



Sixth International Conference on Geosynthetics

Conference Proceedings

25–29 March 1998
Atlanta, Georgia USA

Soil Reinforcement Applications
Geotechnical & Hydraulic Applications

Cooperating Organizations

Geoinstitute of ASCE (American Society of Civil Engineers)
Canadian Geotechnical Society
International Association of Geosynthetics Installers
EDANA (European Association for the Nonwovens Industry)
Geosynthetic Institute



**Organized under the auspices of the International
Geosynthetics Society Sponsored by the
Industrial Fabrics Association International
and the North American Geosynthetics Society**

Table of Contents: Volume 2

SOIL REINFORCEMENT APPLICATIONS

Reinforced Soil Design Issues

Design Procedures for Reinforced Walls - A Historical Perspective R.R. Berg, T.M. Allen & J.R. Bell.....	491
---	-----

Aspects of Partial Factor Design of Reinforced Soil Walls T.S. Ingold	497
--	-----

A Comparison of Design Approaches for Reinforced Soil Structures in Europe J. Penman & R.A. Austin	501
---	-----

Recent Developments of the "Displacement Method" P. Lemonnier, P. Gotteland & A.H. Soubra	507
--	-----

Locally Loaded Geosynthetic Reinforced Soil Structure: Calculation Method E. Haza, P. Gotteland & J.P. Gourc	511
---	-----

Measuring Geotextile Strains with Strain Gauges S.R. Boyle & R.D. Holtz	517
--	-----

Soil Confinement Effect on Stress-Strain Properties of Geosynthetics Z. Yuan, R.H. Swan Jr., R.C. Bachus, V. Elias.....	523
--	-----

The Testing of Geosynthetic Reinforcements P.E. Stevenson, T.R. Skochdopole & A.D. Kelkar	529
--	-----

Geosynthetic Reinforcement: Are Geotextiles and Geogrids Interchangeable? C.J. Sprague	539
---	-----

Effect of End-Restraint in Geogrid-Soil Structures H. Ochiai, N. Yasufuku, T. Kawamura, T. Yamaji & T. Hirai	545
---	-----

Application of Dilatancy Models to Soils Reinforced by Geosynthetics H. Ohta, M. Hirata, A. Iizuka, T. Yamakami & K. Ohmori	551
--	-----

Reinforced Soil Walls

Failure of Two Fabric Reinforced Segmental Block Walls in South Africa F.W. Gassner & G.M. James	559
---	-----

Preloaded-Prestressed Geogrid-Reinforced Soil Bridge Pier T. Uchimura, F. Tatsuoka, M. Tateyama & T. Koga	565
--	-----

Table of Contents: Volume 2

Use of Fabric Reinforced Soil Walls for Integral Bridge End Treatment R.A. Reid, S.P. Soupir & V.R. Schaefer	573
Field Performance Test of a Geosynthetic-Reinforced Soil Wall with Rigid Facing Y.Tsukada, Y. Ochiai, H. Miyatake & N. Tajiri	577
Multi-Anchored Soil Retaining Walls with Geosynthetic Loop Anchors H. Brandl	581
Mechanically Stabilized Earth Wall Design: External Stability M.S. Meyers, R.A. Wetzels & R.R. Berg	587
Brick Faced Retaining Walls Reinforced with Geosynthetics - A Numerical Analysis M. I. M. Pinto, R.V.C. Pereira, M.L. Lopes & A. Mendonca	593
Large Deformations FEM Analysis of a Reinforced Earth Structure R. Arab, P.Villard & J.P.Gourc	597
Evaluation of Foundation Support for Geosynthetic Reinforced Soil Wall on Sloping Ground J. Otani, T. Hirai, H. Ochiai & S. Shinowaki	601
Parametric Study for Geosynthetic Reinforced Walls Under Sustained Earthquakes A. Carotti & P. Rimoldi	605
Influence of Reinforcement Stiffness, Length and Base Condition on Seismic Response of Geosynthetic Reinforced Retaining Walls R.J. Bathurst, K. Hatami	613
Reinforced Slopes	
The Verrand High Reinforced-Soil Structure G. Sembenelli & P. Sembenelli	619
Geogrid Reinforcement of Slopes for Earthquake Resistance at New U.S. Embassy in Caracas, Venezuela J.R. Lambrechts	625
The Construction of Steep Reinforced Slopes in Hilly Terrain C.R. Lawson & T.W. Yee	629
Case Study: Bluewater Retail & Leisure Destination-Major Reinforced Soil Slopes to Form Steep Sided New Lakes J.H. Dixon	637

Table of Contents: Volume 2

Soil Bioengineering/Biotechnical Stabilization of a Slope Failure R.B. Sotir, J.T. Difini & A.F. McKown	643
Finite Element Analysis of Instrumented Geogrid Reinforced Slope A. Ghinelli & M. Sacchetti	649
Durability and Long Term Behavior	
The Assurance of Durability J.H. Greenwood	657
Long-Term Experience with Reinforced Embankments on Soft Subsoil: Mechanical Behavior and Durability K.H. Blume & D. Alexiew	663
Durability of Polyester and Polypropylene Geotextiles Buried in a Tropical Environment for 14 Years J.W. Cowland, K.C. Yeo & J.H. Greenwood	669
Study on Creep-Rupture of Polyester Tendons: Full Scale Tests P. Orsat, M. Khay & M. McCreath	675
Coated PET-Geogrids, Wovens and Yarns - Comparison of Longtime Performance Under Tension J. Müller-Rochholz, D. Alexiew, C. Recker & S.E. Lothspeich	679
The Effect of Oxygen Pressure, Temperature and Manufacturing Processes on Laboratory Degradation of Polypropylene Geosynthetics A. Salman, V. Elias & A. DiMillio	683
Conventional and Stepped Isothermal Methods for Characterizing Long Term Creep Strength of Polyester Geogrids J.S. Thornton, J.N. Paulson & D. Sandri	691
The Stepped Isothermal Method for Time-Temperature Superposition and its Application to Creep Data on Polyester Yarn J.S. Thornton, S.R. Allen, R.W. Thomas & D. Sandri	699
Modeling and Extrapolation of Creep Behavior of Geosynthetics T.Y. Soong & R.M. Koerner	707
Slow Strain Rate Modulus Assessment via Stress Relaxation Experiments T.Y. Soong & A.E. Lord, Jr.	711
Long Term Behavior Characterization of Soft Composites Under Biaxial Loading P. Mailler & M. Sotton	715

Table of Contents: Volume 2

GEOTECHNICAL & HYDRAULIC APPLICATIONS

Construction with/on Marginal Soils

Design Guidance for Reinforced Soil Structures with Marginal Soil Backfills B.R. Christopher, J.G. Zornberg & J.K. Mitchell	797
Reinforcement of a Saudi Sabkha Soil Using Geotextiles S.A. Aiban, O.S.B. Al-Amoudi, I. Ahmed, H. Al-Abdul Wahhab	805
Long-Term Deformation of Reinforced Cohesive Soil Fills and Walls M. Fukuoka	811
Development of Woven Geotextiles for Reinforcing Cohesive Soil Filled Slopes - A New Approach S. Ariadurai, I.L. Whyte & P. Potluri	815
Large Scale Pullout Tests of Geotextile in Poorly Draining Soils S.H. Chew, S.A. Tan, K.H. Loke, P. Delmas & C.T. Ho	821
Soft Clay Embankment Reinforced by Geosynthetic Horizontal Drains M. Kamon, T. Akai, M. Fukuda & Y. Nanbu	825
Centrifuge Modeling of an Innovative MSES for Marginally Stable Slopes M.B. Mahmud & T.F. Zimmie	829
Hydraulic Effects of Using Dual-Function Geosynthetics in the Design of Multi-Layer Structures P. Gotteland	833
Land Reclamation and Ground Improvement	
The Mobilized Strength of Prefabricated Vertical Drains W. Voskamp, G. Troost & G.R. Koerner	839
Investigation of Some Factors Affecting Discharge Capacity of Prefabricated Vertical Drain N. Miura, J. Chai & K. Toyota	845
Design of a New Geocomposite Vertical Wick Drains for Ground Improvement J.N. Mandal & V.S. Kanagi	851
Critical Evaluation of Laboratory Drain Tests Simulating Field Conditions G.P. Karunaratne, S.A. Tan, S.H. Chew & S.L. Loh	855
Geotextiles for the El Dorado International Airport in Colombia A. Malagón	859

Table of Contents: Volume 2

Testing and Analysis of Soft Foundation Treatment for Donggang Diking Project Q.Y. Luo	865
Electrokinetic Geosynthetics and Their Applications I.M. Nettleton, C.J.F.P. Jones, B.G. Clarke & R. Hamir	871
A Study of the Behavior of Geogrid Reinforced Stone Column J.S. Sharma	877
Bearing Capacity	
Geosynthetic Reinforced Unpaved Roads on Very Soft Soils: Construction and Maintenance Effects E.M. Palmeira	885
Numerical Analysis of a Pavement Base Reinforced with Geogrid M. Abramento	891
Improvement of Bearing Capacity of Soft Clay using Geogrids Y. Tanabashi, K. Yasuhara, K. Hirao, N. Kiyokawa & H. Itoh	895
The Bearing Capacity of a Reinforced Sand Layer Overlying a Soft Clay Subgrade M.J. Kenny	901
Supporting Capability of Geogrid Reinforced Soil Foundations N. Yasufuku, H. Ochiai & K. Kawamata	905
Theoretical Solutions for Stress and Strain Fields of a Geosynthetic-Reinforced Foundation Vertically Loaded by a Concentrated Force J. Han	911
Bearing Capacity of Strip Footing on Geogrid-Reinforced Slope C.S. Yoo & D.Y. Lee	915
A Study on the Coir Reinforcement for Strengthening Soft Soil Subgrades K. Rajagopal & S. Ramakrishna	919
Treatment of Container Stockyard Using Stress Distribution Ability of Geonet Z. Hong & H.R. Dao	923
Roads and Pavements	
A Geotextile-Wrapped Aggregate Highway Drain Evaluation G.P. Raymond, R.J. Bathurst & J. Hajek	929

Design Procedures for Reinforced Soil Walls — A Historical Perspective

R.R. Berg

P.E., Consultant, Ryan R. Berg & Associates, Inc., St. Paul, Minnesota, USA

T.M. Allen

P.E., State Geotechnical Engineer, Washington Department of Transportation, Olympia, Washington, USA

J.R. Bell

Ph.D., P.E., Professor Emeritus, Oregon State University, Corvallis, Oregon, USA

ABSTRACT: The progression of analysis procedures, used in the United States, for internal design of geosynthetic reinforced soil retaining walls are summarized in this paper. Procedures are presented in chronological order over the past twenty-four years, to track changes in practice, from first use through current codes. Both the resistance and the load computations, and the combined effect of the two, are examined. It is concluded that large changes in design conservatism have not occurred since first use of geosynthetic reinforced soil walls; and that performance of existing structures is applicable to new design codes and guidelines. This documentation is directed towards researchers, practitioners, and regulators, and gives guidance for future research and development of codes for reinforced soil walls.

KEYWORDS: History, Reinforcement, Retaining walls, Safety factors, Reinforcement specifications & guidelines.

1 INTRODUCTION

Geosynthetic reinforced soil (GRS) retaining walls were first used in North America in 1974 for construction of geotextile reinforced walls supporting logging roads in northwestern United States. Use of GRS walls have grown steadily since this initial project. Significant increases in the use of GRS walls were realized with the introduction of geogrid soil reinforcement elements in 1982 and with the introduction of segmental retaining wall units in 1985. Today, GRS walls are routinely used on private land development projects and are becoming more commonplace in transportation works. It is anticipated that recent guidelines (Elias and Christopher 1997; FHWA 1997) and codes (AASHTO 1997) for highway works will spur use of GRS walls and that they will be routinely used throughout North American highways.

Growth in usage of GRS walls is partially attributable to the success of constructed works. Confidence in engineering of these walls today is based upon performance of GRS structures to date. To better understand this behavior, it is useful to the engineer to understand how design procedures have evolved over time. Were the successfully performing structures constructed to date designed with procedures more or less conservative than current guidelines and codes? This question is addressed within, specifically for the internal stability of GRS walls, by examining changes in the geosynthetic reinforcement design tensile strength and soil load determination procedures.

2 GEOSYNTHETIC TENSILE RESISTANCE

Internal stability analysis of a reinforced soil wall is performed to quantify required strength and vertical spacing of

the geosynthetic reinforcements. A safe, long-term allowable design strength (LTADS) of the geosynthetic reinforcement needs to be quantified for this analysis. Procedures for quantifying LTADS of geosynthetics have evolved over time, as summarized below. Note that connection strength limitations are not addressed, thereby, assuming that connection does not limit LTADS for purposes of comparisons within this paper. Common terminology is used within this paper to present the various procedures. In general, the basic form of the equation used to calculate the LTADS is:

$$LTADS = \frac{T_{ULT}}{RF \times FS} \quad (1)$$

where

T_{ULT} = average value of ultimate wide width strength;
RF = product of reduction factors, or partial factors of safety, to account for creep, installation damage, chemical degradation and biological degradation; and

FS = overall factor of safety for other (e.g., material, geometric, loadings) uncertainties.

2.1 Forest Service Procedures

A 1977 U.S. Forest Service (USFS) manual (Steward et al. 1977) documents a design procedure for geotextile walls. The procedures in this manual were used for the design of a forest service wall constructed in 1974 (Bell et al. 1975), the first GRS wall built in North America. The LTADS is computed with Equation 2. The ultimate strength of the geotextile reinforcement (time frame is prior to introduction of geogrids) is measured with the Oregon State University (OSU) ring test. The OSU ring test ultimate tensile strength,

$T_{ult-OSU}$, is approximately 80% of the wide width tensile strength (ASTM D4595 1986) for nonwoven needle-punched geotextiles. A FS of 1.5 to 1.75 is recommended, with the higher factor generally for use with heavy live loads (e.g., log haul trucks). Reduction factors, RFs, are not used for these temporary walls.

$$LTADS = \frac{T_{ult-OSU}}{FS} \quad (2)$$

2.2 Geogrid Procedure

An allowable strength procedure for geogrids was presented in a 1983 (Netlon) manual published in the United Kingdom. This procedure is presented in Equation 3. The creep limited strength, T_c , is the highest (tested) load level that precludes exceeding 10% strain or rupture, over the design life. An installation damage factor, RF_{ID} , is used to further reduce the creep-limited strength. This factor is quantified as the ratio of the ultimate strength of undamaged to damaged specimens. An overall factor of safety value of 1.35 is recommended.

$$LTADS = \frac{T_c}{RF_{ID} \times FS} \quad (3)$$

The approach in Equation 3 was modified for North American practice (Tensar 1986), for a particular product. The RF_{ID} was incorporated into the overall FS, as shown in Equation 4. An overall factor of safety value of 1.5 was recommended for use with Equation 4.

$$LTADS = \frac{T_c}{FS} \quad (4)$$

For the product addressed in the 1983 (Netlon) and 1986 (Tensar) manuals, the LTADS value calculated with Equation 3 is approximately equal to the value computed with Equation 4 for gravelly sand soils.

2.3 1987 Task Force 27 Procedure

The Task Force 27 (AASHTO 1990) procedure (implemented as early as 1987) for computing a LTADS uses a partial reduction factor approach (Bonaparte and Berg 1987). The LTADS is the lesser of the following two, limit state and serviceability state, equations.

$$LTADS \leq \frac{T_l}{RF_D \times RF_{ID} \times FS} \quad (5a)$$

$$LTADS \leq \frac{T_w}{RF_D \times RF_{ID}} \quad (5b)$$

Where

T_l = highest tension level at which the creep strain-rate continues to decrease with log-time within the required design lifetime and which precludes brittle or ductile failure;

T_w = tension level at which total strain is not expected to exceed 5% within the design lifetime; and

RF_D = durability reduction factor, 1.10 minimum.

A minimum $RF_{ID} = 1.25$ with Equation 5a is required if fill source is unknown at time of design. A 1.5 minimum FS is also required with Equation 5a. No minimum RF_{ID} is stated for Equation 5b.

2.4 1989 FHWA Report

The FHWA research report (Christopher et al. 1989) presented two procedures for quantifying LTADS of geosynthetics. The first procedure, stated as being complex and requiring extensive long-term strength testing, is the partial reduction factor approach presented by Bonaparte and Berg (1987). The second procedure, which can be used in absence of sufficient test data, is to calculate the LTADS with the following simplified equation:

$$LTADS = \frac{T_{ULT} \times CRF}{RF_{ID} \times RF_D \times FS} \leq T_s \quad (6)$$

where

T_s = long-term tension capacity of the geosynthetic at a selected design strain (usually 5% or less); and

CRF = creep reduction factor (ratio of creep limit strength obtained from creep tests to ultimate strength).

RF_D and RF_{ID} should be based upon product specific data, but not less than 1.1, each. A minimum FS value of 1.5 is recommended for permanent walls.

2.5 1991 AASHTO

The 1991 American Association of State Highway and Transportation Officials (AASHTO) Standard Specifications for Highway Bridges followed procedures for LTADS computation as presented in the Task Force 27 (AASHTO 1990) report (i.e., Equations 5a and 5b). However, a minimum RF_{ID} of 1.25 was stated.

2.6 1993 NCMA Procedure

Two optional methods for calculating LTADS are presented within the National Concrete Masonry Association (NCMA) design manual. Method A is a partial reduction factor

approach with a minimum RF_{ID} of 1.05, adapted from an FHWA publication (Berg 1993), as follows:

$$LTADS = \frac{T_{ULT-MARV}}{RF_{CR} \times RF_{ID} \times RF_{CD} \times RF_{BD} \times FS_{MU} \times FS_{to}} \quad (7a)$$

where

$T_{ULT-MARV}$ = minimum average roll value of ultimate tensile strength, which is typically 5 to 15% lower than T_{ULT} ;

RF_{CR} = partial factor of creep deformation (ratio of T_{ULT} to creep limit strength), based upon not exceeding a 10% total strain;

RF_{CD} = partial factor for chemical degradation;

RF_{BD} = partial factor for biological degradation, with a minimum combined RF_{CD} and RF_{BD} of 1.1;

RF_{MU} = partial factor for material uncertainty, 1.5 minimum; and

FS_{to} = factor of safety against tensile overstress, 1.2 minimum.

Method B is similar to European practice and borrows heavily from the work of Jewell and Greenwood (1988). This method decouples the FS against overall uncertainties from the calculation of LTADS, and uses creep rupture to define CRF. The LTADS is calculated as:

$$LTADS = \frac{T_{ULT-MARV} \times CRF}{RF_{BD} \times RF_{CD} \times RF_{ID} \times RF_{CE} \times FS_{to}} \quad (7b)$$

where

RF_{CE} = material factor for extrapolation of creep data, 1.3 to 1.5 typical for permanent walls.

2.7 1994 and 1996 AASHTO

The 1994 and 1996 AASHTO Standard Specifications for Highway Bridges followed equations (i.e., 5a and b) for LTADS computation as presented in the 1991 AASHTO manual. However, the overall factor of safety, FS, minimum was increased to 1.78. A minimum RF_{ID} and RF_D of 1.1 and 1.05, respectively, were stated in the commentary.

2.8 Current FHWA/AASHTO Guidelines

The current FHWA (Elias and Christopher 1997) and AASHTO (1997) guidelines present the following equations for quantifying LTADS.

$$LTADS = \frac{T_{ULT-MARV}}{RF \times FS} \quad (8)$$

Where

RF = product of applicable reduction factors (i.e., $RF = RF_{CR} \times RF_D \times RF_{ID}$), with a minimum value of 1.1 for both RF_D and RF_{ID} , and with RF_{CR} based upon creep rupture; and FS minimum of 1.5 is recommended.

An alternative procedure for LTADS is to use a default overall reduction value, RF, of 7, as shown in Equation 9. Application of this alternative is limited to conditions stated within the guidelines.

$$LTADS = \frac{T_{ULT-MARV}}{7 \times FS} \quad (9)$$

2.9 Current NCMA Guidelines

The current NCMA (1997) design manual uses the same equation (similar nomenclature) as the current FHWA/AASHTO (i.e., Eq. 8).

3 LOAD DETERMINATION

The lateral driving load to be resisted by the geosynthetic reinforcements is a function of the soil mass and surcharge loads, and, in some analyses, the overturning moment on the reinforced fill due to the retained backfill. The soil mass and surcharge loads are factored by a lateral earth pressure coefficient to compute reinforcement loadings. Design and analysis procedures over time have varied by the assumed lateral pressure coefficient and inclusion or not of the overturning moment effect. In general terminology, the tension in the i th layer of reinforcement, not including surcharge loads, is calculated as:

$$T_i = K \sigma_{vi} s_{vi} \quad (10)$$

where

K = lateral pressure coefficient;

σ_{vi} = vertical pressure at the depth of the i th layer; and

s_{vi} = effective vertical spacing (i.e., $\frac{1}{2}$ distance to reinforcement above plus $\frac{1}{2}$ distance to reinforcement below) of the i th layer of reinforcement. The procedures for determining the lateral load are summarized in Table 1 in terms of lateral pressure coefficient used and whether or not overturning (OT) effects are included in the computation of σ_{vi} .

The USFS manual (Steward et al. 1977) focused on the design of geotextile wrap-around walls for log-haul roads. These walls have a relatively short design life and are subject to large live loadings. The load is determined using the approach described by Bell et al. (1975). An at-rest lateral earth pressure coefficient (i.e., $1 - \sin \phi'$) is used. The normal pressure (σ_{vi}) is the sum of the weight of the rein-

Table 1. Load computation procedures.

Procedure	K	σ_{vi}
1977 USFS	at-rest	w/o OT
Geogrid - 1983	active Rankine	w/ OT
- 1987	active Rankine	w/o OT
1987 Task Force 27	active Rankine	w/ OT
1989 FHWA	1.0 to 1.5 active Rankine	w/o OT
1991, 1994 & 1996 AASHTO	active Rankine	w/ OT
1993 & 1997 NCMA	active Coulomb	w/o OT
1997 FHWA /AASHTO	active Rankine	w/o OT

OT — Overturning force from retained backfill.

forced fill (i.e., product of unit weight of soil, γ , and height of fill above i th layer of reinforcement, h_i), uniformly distributed surcharge loads (w_s), and other surcharge loads.

The 1983 (Netlon) geogrid wall design manual recommended use of active lateral earth pressure coefficient, K_a , with either the tie-back wedge or the coherent gravity analysis procedure. The tie-back wedge method with overturning effect was used extensively for design of geogrid walls in North America starting in 1983 (e.g., Berg et al. 1984; Tensar 1986; Berg et al. 1987). A Rankine active lateral earth pressure coefficient (i.e., $\tan^2(45 - \phi/2)$) is used with this procedure. The vertical pressure, assuming a Meyerhof-type of pressure distribution of the overturning force generated by the retained backfill, is shown in Equation 11, for level backfill conditions. The subscripts w and b refer to the reinforced wall fill and the retained backfill, respectively, and l is the length of reinforcement.

$$\sigma_{vi} = \gamma_w h_i + w_s K_{ab} \left(\gamma_b h - i + 3 w_s \right) \left(\frac{h_i}{l} \right)^2 \quad (11)$$

The overturning of component of σ_{vi} was deleted from the load computation (Simac 1990; Tensar 1990), at least in private practice, subsequent to and based upon discussions at the 1987 NATO Workshop on geosynthetic reinforced soil walls (Jarrett and McGown 1988). The method for calculating LTADS did not change, therefore, Equation 4 is applicable with this revised load determination procedure.

In the 1987 Task Force 27 (AASHTO 1990) procedure, the tie-back wedge method of analysis is recommended for analysis of geosynthetic reinforced retaining walls. The tension in the reinforcement is calculated as a function of the vertical stress induced by gravity, uniform normal surcharges

and active thrust from the retained fill (i.e., Eq. 11), multiplied by the Rankine active earth pressure coefficient.

FHWA research in the late 1980's (Christopher et al. 1989) led to a recommended stiffness approach for quantifying the lateral pressure coefficient. With this approach, a Rankine lateral earth pressure coefficient equal to K_a was recommended for geotextile reinforcements. A varying coefficient of $1.5 K_a$ at the top of wall to $1.0 K_a$ at a distance of 6 m below top of wall, and lower, was proposed for geogrid reinforcements.

The 1991, 1994, and 1996 AASHTO Standard Specifications for Highway Bridges followed procedures for load computation as presented in the Task Force 27 (AASHTO 1990) report.

Rankine theory was used for quantifying the K_a coefficient until the NCMA design procedure for segmental retaining walls (Simac et al. 1993) was published. A Coulomb theory is recommended in this manual, which allows for direct incorporation of the beneficial effects of wall face batter and interface friction between the fill soil and wall face. The NCMA procedure (Simac et al. 1993; NCMA 1997) for calculating the internal stability lateral load (without surcharge loads) is:

$$P_a = \frac{1}{2} \gamma_w K_{aC} H_e^2 \cos(\delta_i - \psi) \quad (12)$$

where

P_a = active earth force acting over the effective height of the wall, per unit width of wall;

γ_w = moist unit weight of wall infill soil;

K_{aC} = Coulomb active earth pressure coefficient;

H_e = effective height for battered walls;

δ_i = wall to soil friction angle; and

ψ = total wall inclination from vertical.

The second edition of the NCMA design manual (1997) does not change the procedure for determining the soil load for internal stability analysis. The NCMA design procedure is one of the two procedures currently in widespread use in North America. The other procedure in widespread use was developed for the design of highway walls, with select granular fill, and is referred to as the simplified coherent gravity method.

The new FHWA manual (Elias and Christopher 1997) and the recent update to AASHTO bridge manual (1997) incorporated features of the stiffness, tie-back wedge, and coherent gravity approaches for analysis of walls — resulting in the simplified coherent gravity method. With this procedure an active Rankine lateral earth pressure, over the entire wall height, is recommended for computation of geosynthetic (both geotextiles and geogrids) reinforcement loads. Overturning effects are not included in the vertical pressure.

The changes in procedures to quantify the LTADS of geosynthetic reinforcement and the internal lateral load on GRS walls are quantified in Table 2. The values in Table 2 are based upon typical ranges of values for the partial factors used in practice, from the authors' experience. The resistance, R, is the LTADS in terms of percentage of ultimate wide width strength (%T_{ULT}). The load, L, is the total load on the wall, without surcharges, using the assumptions listed in Table 2, expressed as P/H², where P is the total force on the wall per unit length of wall. The R/L in Table 2 is a normalized ratio for comparing the various procedures, and not a design parameter. The lower the %T_{ULT} used the more conservative the procedure. Also, with other factors remaining equal, the higher the assumed load the more conservative the method. Therefore, the lower the R/L, the more conservative the combination of resistance and load computations. The trend of R/L ratios over time and range of individual procedures are illustrated in Figure 1.

Table 2. Quantifying R/L ratios.

Procedure	Resistance (%T _{ULT})	Load (P/H ²)	R/L Ratio
1977 USFS	~ 53	4.3	~ 12.3
Geogrid			
- '83	25 to 40	3.54	7.1 to 11.3
- post-87	25 to 40	2.77	9.0 to 14.4
1987 Task Force 27	20 to 28	3.54	5.7 to 8.0
'89 FHWA			
- Geogrid	20 to 27.5	3.2	6.3 to 8.6
- Geotextile	10 to 27.5	2.77	3.6 to 9.9
1991 AASHTO	20 to 27.5	3.54	5.8 to 7.8
1993 NCMA	16 to 28	2.3	7.0 to 11.7
1994 & 1996 AASHTO	18 to 24.3	3.54	5.1 to 6.9
'97 FHWA & AASHTO	14.6 to 26	2.77	5.3 to 9.4
- w/ Default	8.6	2.8	3.1
1997 NCMA	19 to 35	2.3	8.3 to 15.2

Assumptions:
 wall fill $\phi = 34^\circ$ $\gamma = 19.6 \text{ kN/m}^3$
 retained backfill $\phi = 30^\circ$ $\gamma = 18.8 \text{ kN/m}^3$
 H = 6 m (1989 FHWA geogrid case) $l/H = 0.7$
 batter = 0° , $\delta = \frac{3}{4} \phi$, and FE = 1.3 (NCMA cases)

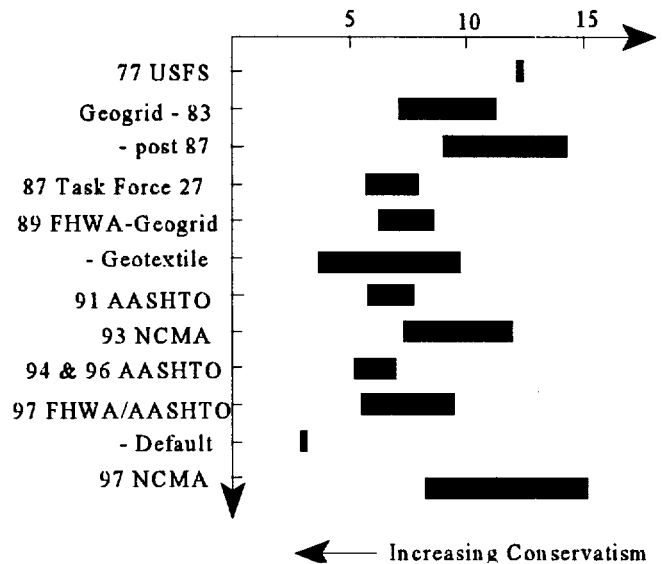


Figure 1. R/L ratio trends and ranges.

5 CONCLUSIONS

The trend of change in the resistance to load relationship (R/L ratio) is illustrated in Figure 1. Observed trends are generalized and based upon assumptions previously stated. More precise results could be revealed by examining specific case histories over time. The following can be concluded from this plot.

1. Transportation specific procedures (i.e., FHWA, AASHTO) are more conservative than non-transportation specific procedures (i.e., geogrid, NCMA).
2. Transportation procedures have, generally, increased in conservatism throughout their development, primarily due to increases in resistance reduction factors. Calculated loads have decreased somewhat during this period.
3. The 1997 FHWA/AASHTO default value of 7 is more conservative than all of the procedures examined.
4. Large changes in conservatism with transportation procedures have not occurred since 1987.
5. Large changes in conservatism with non-transportation procedures have not occurred since first use in 1975.
6. Performance of existing structures is applicable to new design codes and guidelines.

6 REFERENCES

AASHTO (1997) *Interims to Standard Specifications for Highway Bridges*, Sixteenth Edition, 1996, American Association of State Highway and Transportation Officials, Washington, DC, USA.

- AASHTO (1996) *Standard Specifications for Highway Bridges, Sixteenth Edition*, American Association of State Highway and Transportation Officials, Washington, DC, USA.
- AASHTO (1994) *Standard Specifications for Highway Bridges, Fifteenth Edition*, 1992 with 1993 and 1994 Interims and Commentary, American Association of State Highway and Transportation Officials, Washington, DC, USA.
- AASHTO (1991) *Standard Specifications for Highway Bridges, Fourteenth Edition*, 1989 with 1990 and 1991 Interims and Commentary, American Association of State Highway and Transportation Officials, Washington, DC, USA.
- AASHTO-AGC-ARTBA (1990) *Task Force 27 Report: In Situ Soil Improvement Techniques*, American Association of State Highway and Transportation Officials, Washington, DC, USA, 324 p.
- ASTM (1997) D 4595 - 86 (Reapproved 1994) Standard Test Method for Tensile Properties of Geotextiles by the Wide-Width Strip Method, *Soil and Rock (II): D 4943 - latest, Geosynthetics*, Vol. 04.09, West Conshohocken, PA, pp. 961 - 971.
- Bonaparte, R., and Berg R.R. (1987) Long-Term Allowable Design Loads for Geosynthetic Soil Reinforcement, *Proceedings of the Geosynthetics '87*, IFAI, Vol. 1, New Orleans, LA, USA, pp. 181-192.
- Bell, J.R., Stille, A.N. and Vandre, B. (1975) Fabric Retaining Walls, *Proceedings of the 13th Annual Engineering Geology and Soils Engineering Symposium*, Moscow, ID, USA.
- Berg, R.R. (1993) *Guidelines for Design, Specification, & Contracting of Geosynthetic Mechanically Stabilized Earth Slopes on Firm Foundations*, U.S. Department of Transportation, Federal Highway Administration, Washington, DC, USA, FHWA-SA-93-025, 87 p.
- Berg R.R., La Rochelle, P., Bonaparte, R., and Tanguay, L. (1987) Gaspe' Peninsula Reinforced Soil Seawall - Case History, *Proceedings of Soil Improvement - A Ten Year Update*, J.P. Welsh, Ed., Geotechnical Special Publication No. 12, ASCE, pp. 309-328.
- Berg, R.R., Bonaparte, R., Chouery, V.C., and Anderson, R.P. (1986) "Design, Construction, and Performance of Two Geogrid Reinforced Soil Retaining Walls," *Proceedings of the IIIrd International Conference on Geotextiles*, Vienna, Austria, pp. 401-406.
- Christopher, B.R., Gill, S.A., Giroud, J.P., Juran, I., Schlosser, F., Mitchell, J.K. and Dunicliff, J. (1989) *Reinforced Soil Structures: Volume I. Design and Construction Guidelines*, U.S. Department of Transportation, Federal Highway Administration, Washington, DC, USA, FHWA-RD-89-043, 287 p.
- Elias, V. and Christopher, B.R. (1997), *Mechanically Stabilized Earth Walls and Reinforced Soil Slopes, Design & Construction Guidelines*, FHWA-SA-96-071, U.S. Department of Transportation, Federal Highway Administration, Washington, DC, USA, 371p.
- FHWA (1997), *Degradation Reduction Factors for Geosynthetics, Federal Highway Administration Geotechnology Technical Note*, U.S. Department of Transportation, Federal Highway Administration, Washington, DC, USA, 5 p.
- Jarrett, P.M. and McGown, A., eds. (1988) *The Application of Polymeric Reinforcement in Soil Retaining Structures, Proceedings of the NATO Advanced Research Workshop on Application of Polymeric Reinforcement in Soil Retaining Structures*, Kingston, ON, Canada, June 1987, Kluwer Academic Publishers, Dordrecht, The Netherlands, 637 p.
- Jewell, R.A. and Greenwood, J.H. (1988), Long-Term Strength and Safety in Steep Slopes Reinforced by Polymer Materials, *Geotextiles and Geomembranes*, Vol. 7, pp. 81-118.
- NCMA (1997) *Design Manual for Segmental Retaining Walls*, 2nd Edition, J. Collin Ed., National Concrete Masonry Association, Herdon, VA, USA, 289 p.
- Netlon Limited (1983), *Guidelines for the Design & Construction of Reinforced Soil Retaining Walls Using Tensar Geogrids*, Blackburn, England, 39 p.
- Simac, M.R., Bathurst, R.J., Berg, R.R., and Lothspiech, S.E. (1993) *Design Manual for Segmental Retaining Walls*, 1st Edition, National Concrete Masonry Association, Herdon, VA, USA, 336 p.
- Simac, M.R. (1990) *Design Methodology for MIRAGRID™ Reinforced Soil Retaining Walls*, Mirafi Inc., Charlotte, NC, 110 p.
- Steward, J.E., Williamson, R. and Mohny, J. (1977), *Guidelines for Use of Fabrics in Construction and Maintenance of Low-Volume Roads*, USDA, Forest Service, Portland, OR, USA.
- Tensar (1986), *Guidelines for the Design of Tensar Geogrid Reinforced Soil Retaining Walls, TTN:RW1*, The Tensar Corporation, Morrow, GA, USA.
- Tensar (1990), *Guidelines for the Design of Tensar Geogrid Reinforced Soil Retaining Walls, TTN:RW1.1*, The Tensar Corporation, Morrow, GA, USA.

Aspects of Partial Factor Design of Reinforced Soil Walls

T. S. Ingold

Consulting Engineer and Honorary Professor of Geotechnical Engineering, The University of Birmingham, UK

ABSTRACT: In assessing margins of safety, geotechnical engineers have traditionally worked in terms of lumped factors of safety, often defined as the ratio of restoring force to disturbing force, that are calculated using soil parameters which are judged to be representative. This approach is lucid in so far as it deals with raw, unfactored, values of soil properties. In contrast, partial factor design deals with design disturbing forces, which are raw values artificially enhanced by partial factors, and design restoring forces which are raw values artificially depressed by partial factors. How these partial factors are applied has a major affect on the end result with this also being heavily influenced by the use of characteristic values of soil parameters. Certain approaches to partial factor design are more lucid than others and this is illustrated by making comparisons between some of the approaches prescribed in BS 8006 : 1995, "Strengthened/reinforced soils and other fills", and the pre-standard Eurocode ENV-1997-1 : 1994, "Geotechnical design - Part 1 : General rules".

KEYWORDS: Reinforced soil, Retaining walls, Design, Safety factors, Specifications

1 INTRODUCTION

Traditionally, geotechnical engineers factor design values of soil properties by judgment with this judgment, perhaps aided by regression analyses, accounting for a multitude of variables such as test method, validity of test results and variability of results. The resulting value is a raw, unfactored, value which is used for design.

In assessing soil induced forces involved in, say, base sliding of a retaining wall, of given geometry, then, for a cohesionless soil of given unit weight γ , these forces will be a function of ϕ' , the effective stress internal angle of shearing resistance of the soil. The function maybe K_a , if considering a raw lateral disturbing force, D , or $\tan\phi'$ if considering a raw horizontal restoring force, R . The lumped factor of safety against sliding may then be defined, traditionally, as $F=R/D$. Provided F equals, or exceeds, some prescribed value, typically 1.5 to 2.0, then there is deemed to be an adequate, definitive, margin of safety against forward sliding. Although definitive, F is a combined margin of undefined error and/or ignorance. Nonetheless, prescribed values have stood the test of time.

In contrast, non-geotechnical engineers often have the luxury of designing with well controlled materials, and loads, whose parameters are well documented. In this case it is possible to generate a general distribution of, say, material strengths and applied loads. Statistical analyses may be applied to these distributions to determine theoretical values of partial load and partial material factors which are then applied to statistically determined values of load and strength. The end result is that, when the partial factors are applied it, is possible to define the probability of the design load exceeding the design strength. So, for example, such an approach may define a probability of failure of 1 in 10,000. Clearly, this approach is totally different to the lumped factor of safety approach.

There has long been a move in Europe towards partial factor design and so the code of practice, BS 8006 : 1995,

"Strengthened/reinforced soils and other fills" was written in a partial factor format. The essence of this is that a partial load factor, f_t , is used to enhance a raw disturbing force, D , whilst a partial material factor, f_m , is used to depress a raw restoring force, R . An adequate margin of safety, against attaining an ultimate limit state, is deemed to operate when the identity $f_t D \leq (R/f_m)$ is satisfied. A similar approach is proposed in the European pre-standard Eurocode 7, or just EC-7, which is formally entitled Eurocode ENV-1997-1 : 1994, "Geotechnical design - Part 1 : General rules".

2 BS 8006 AND EUROCODE 7

BS 8006 prescribes a variety of different partial material factors, $f_m > 1$, with different numerical values, to be applied to material strengths, such as those for soil or soil reinforcement, to define a design strength. It is important to note that soil unit weight, γ , and $\tan\phi'$ are allotted a partial material factor of unity. So, in other words, these two parameters are not factored. Load factors, $f_t > 1$, with different numerical values, are applied to loads to determine design loads and these factors differ in magnitude from one prescribed loading condition to another. In addition, there is a further group of partial material factors, such as $f_s > 1$, which applies to specific failure modes such as bearing capacity, forward sliding or reinforcement pull-out. Table 1 presents some selected examples of partial load factors.

Table 1. Selected partial load factors from BS 8006

Load factor, f_t , applied to	Loading case		
	A	B	C
Mass of the reinforced soil body	1.5	1.0	1.0
Earth pressure behind structure	1.5	1.5	1.0

Table 2. Selected partial factors from BS 8006

Soil material factor, f_m , applied to $\tan\phi'$	1.00
Factor, f_s , on sliding across reinforcement	1.30
Factor, f_{ms} , on ultimate bearing capacity	1.35

BS 8006 considers two limit states; the ultimate limit state of collapse and a predefined serviceability limit state appropriate to the structure under consideration. In assessing the latter, all partial factors are set to unity per Case C in Table 1. In assessing the ultimate limit state of collapse, the code is formulated in such a way that partial factors with a value greater than unity are only applied to raw pressures or forces. So, taking the example of base sliding, stability is deemed satisfied if $f_r D \leq (R/f_m)$.

Since BS 8006 partial factors operate on what are effectively raw forces, the identity $f_r D \leq (R/f_m)$ may also be expressed as $R/D \geq f_r f_m$. This formulation is identical to the traditional lumped factor of safety format in which R/D must equal or exceed a prescribed minimum value of F . For forward base sliding the prescribed value of F traditionally falls between 1.5 and 2.0. Loading case A of Table 1, a worse case for base sliding, implies a value of f_r of 1.5 and, for a perfectly rough basal reinforcement, Table 2 implies a material factor, $f_s = f_m$, with a value of 1.3. The product of these two factors is 1.95 which is essentially the value of the conventional lumped factor of safety F .

Indeed, the values of partial factors in BS 8006 were formulated such that $f_r f_m = F$. This formulation, with due regard for any interaction between various factors, was extensively calibrated against well established and proven design methods, as well as observed performance of existing structures, to render numerical values of partial factors which, with regard for commercialism, are consistent with adequate margins of safety. Perhaps more importantly, partial factors are applied in a lucid manner which has a linear effect on design loads and strengths.

Table 3. Selected partial factors from EC-7

Case	Favourable load	Unfavourable load	$\tan\phi'$
A	0.95	1.00	1.10
B	1.00	1.35	1.00
C	1.00	1.00	1.25

Eurocode 7 has a similar format to BS 8006 but has three loading cases pertaining to the ultimate limit state, per Table 3, as opposed to two cases, cases A and B of Table 1, in BS 8006. Like BS 8006, EC-7 sets all partial factors to unity when considering a serviceability limit state. EC-7 does not prescribe material factors which can be applied to assess internal stability nor partial factors which apply to specific failure modes such as base sliding.

For loading cases A and C, EC-7 prescribes the use of a materials factor, $f_m > 1$, on $\tan\phi'$. This gives a design value of friction angle $\phi_d = \tan^{-1}([\tan\phi'] / f_m)$. If, for example, lateral soil thrusts were being calculated to BS 8006 then ϕ' is not factored and the resulting coefficient of earth pressure used in design is K_a , the conventional coefficient of active earth pressure. If ϕ_d is used as the design value then the resulting earth pressure coefficient might be denoted as K_d . It is reasonable to assume that the f_m value defined in EC-7 is a component used with the objective of achieving a uniform, target, overall margin of safety, but, if the effects of f_m are assessed it transpires that resulting margins of safety are not uniform.

Figure 1 shows a plot of K_d/K_a against f_m for a range of unfactored values of ϕ' . For soil with $f_m = 1$, per BS 8006, and $\phi' = 20^\circ$ then $\phi' = \phi_d = 20^\circ$ and the value of K_d/K_a is unity since $K_d = K_a$, but if $f_m = 1.25$, per EC-7, the value of K_d/K_a increases by 15 % so implying a concealed load factor component of 1.15. For $\phi' = 50^\circ$ then, as before $K_d = K_a$ per BS 8006, but according to EC-7, K_d/K_a increases by 38 % so implying a concealed load factor component of 1.38. So, the EC-7 approach introduces a non-linearity in margins of safety which penalise better quality soils and fills. This non-linearity varies according to which aspect of stability is being considered. If calculating tensile forces applied to reinforcement then K_a and a sine function is involved. If considering base sliding then both a sine and tangent function are involved.

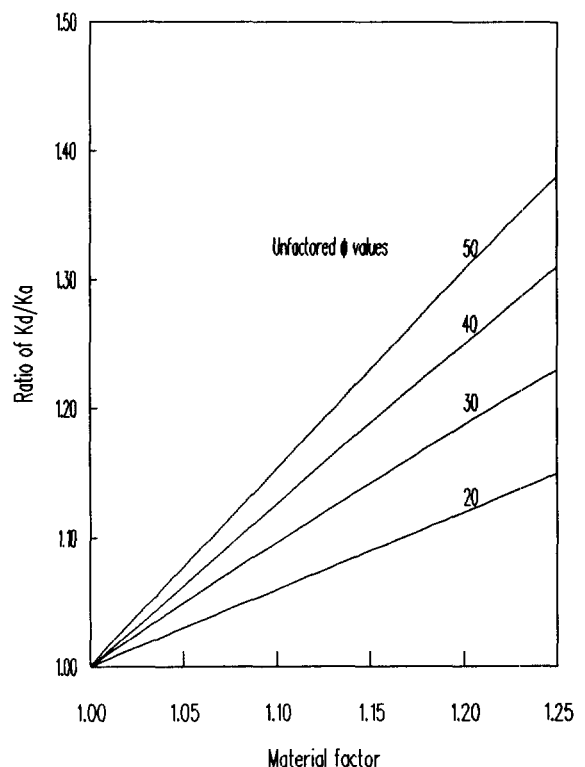


Figure 1. Nonlinear effect of partial material factor on design value of lateral earth pressure coefficient

3 BASE SLIDING

Eurocode 7 does not give partial factors for internal stability so the following sections illustrate various aspects of the BS 8006 and EC-7 approaches by considering base sliding and bearing capacity in terms of ϕ' and the ratio, λ , of wall base width, L , to wall height, H .

Conventional, lumped factor of safety, design defines the factor of safety against base sliding as :

$$(\gamma LH \tan \phi') / (\frac{1}{2} K_a \gamma H^2) = F \quad (1)$$

If F is some limiting target value to be achieved and L/H is written as λ , then Equation 2 can be rearranged as :

$$(2 \lambda \tan \phi') / (FK_a) = 1 \quad (2)$$

The corresponding EC-7 formulation is :

$$(2 f_w \lambda \tan \phi_d) / (f_t K_d) = 1 \quad (3)$$

where $\phi_d = \tan^{-1}([\tan \phi'] / f_m)$ and f_w is a load factor on favourable dead load which may be less than unity. The corresponding BS 8006 Case B formulation is :

$$(2 \lambda \tan \phi') / (f_s f_t K_a) = 1 \quad (4)$$

For given raw values of ϕ' values of λ can be determined for a given partial factor set.

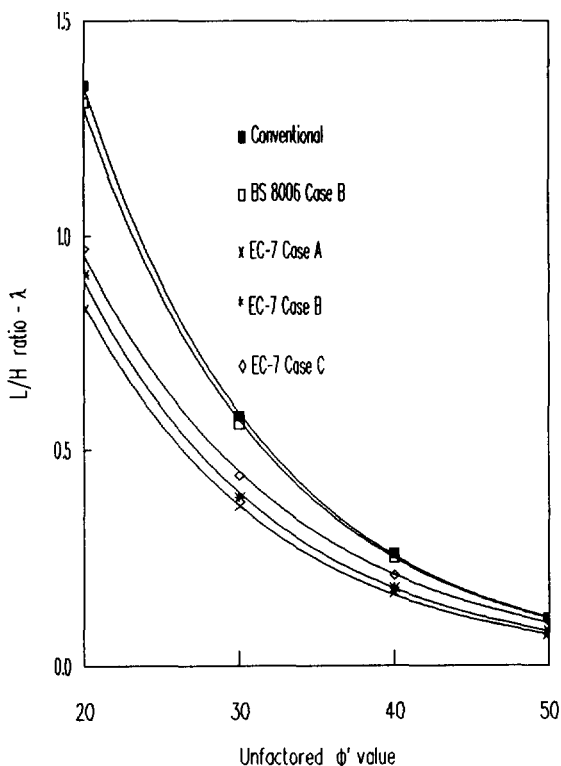


Figure 2. Base width to height ratio - λ against ϕ' values

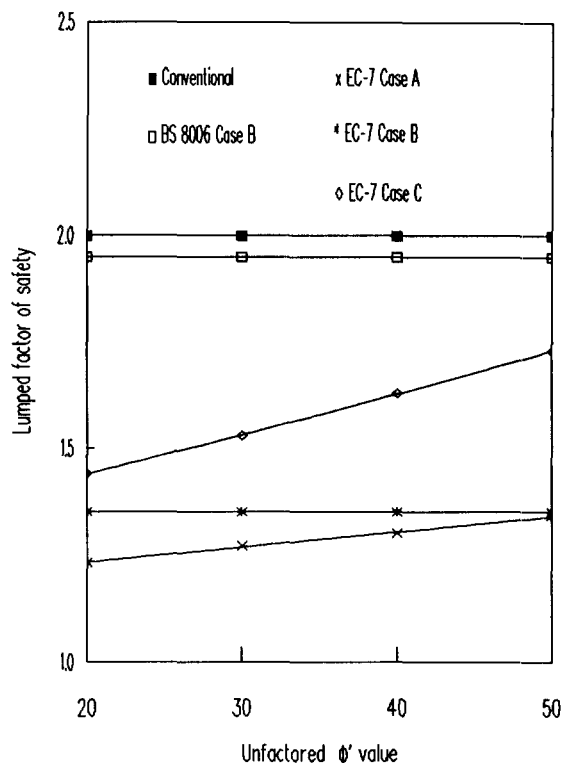


Figure 3. Conventional lumped factor of safety against ϕ'

For each partial factor set and a given value of ϕ' , Figure 2 presents the value of λ required by a given partial factor set to achieve an adequate margin of safety as defined by that partial factor set. As expected, values of λ for the conventional lumped factor of safety approach and BS 8006 Case B almost coincide. The EC-7 partial factor sets are closely grouped and, for a given value of ϕ' , these generally indicate a requirement for a lower value of λ than BS 8006. To investigate the reasons for this, the λ values derived from each partial factor set were reanalysed to determine what conventional lumped factor of safety they would produce.

The results of these reanalyses are presented graphically in Figure 3 which is a plot of equivalent lumped factor of safety against unfactored ϕ' . As expected conventional analysis produces a constant factor of safety, of 2.00, which is independent of ϕ' . The same applies to BS 8006 Case B, with a constant value of 1.95, and to EC-7 Case B where the constant value is 1.35. Case A produces a variable factor of safety as does Case C which is the worst case for base sliding. The non-linearity effect of applying a material factor, greater than unity, to $\tan \phi'$ is well illustrated by Case C where the equivalent factor of safety increases from 1.44 for $\phi' = 20^\circ$ to 1.73 for $\phi' = 50^\circ$. It can be seen that in general EC-7 results in lower margins of safety against base sliding than BS 8006 and, in particular, it penalises better quality fills and soils which have higher ϕ' values.

4 BEARING CAPACITY

To investigate the effects of different partial factor sets on margins of safety against bearing capacity failure, analyses have been carried out on a simple wall, with a constant value of λ of 0.7, founded at ground surface. The common theme of all partial factor sets is that the design ratio, ρ , of available design bearing capacity to applied design pressure should be equal to or greater than unity. The results of these analyses are presented in Figure 4 as plots of ρ against ϕ' . For all partial factor sets a ρ value of unity or greater is obtained for ϕ' greater than 30 to 33°. In particular the worst threshold case from BS 8006, Case B, is obtained at $\phi' = 32^\circ$ whilst from EC-7 the worst case is Case C which is obtained at $\phi' = 33^\circ$. This indicates that, for the wall geometry analysed, BS 8006 and EC-7 render almost identical margins of safety against bearing capacity failure.

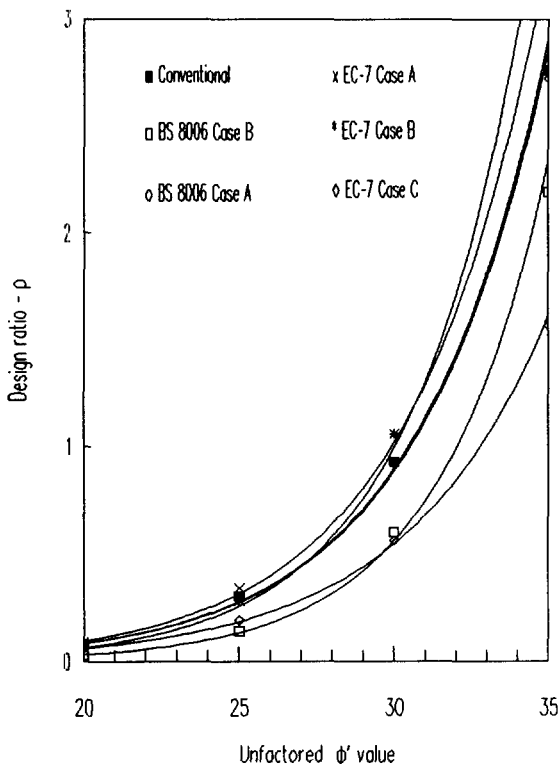


Figure 4. Variation of design ratio, ρ , with unfactored ϕ'

5 CHARACTERISTIC VALUES

The above analyses assume deterministic values of soil properties such as ϕ' but BS 8006 and EC-7 imply the use of characteristic values. If statistical methods are used, the characteristic value should be derived such that the calculated probability of a worse value governing the occurrence of a limit state is not greater than 5%. Upper or lower values are used according to the problem.

Designing with characteristic values of ϕ' for fills is not problematical since the designer can require a specified characteristic value. However, the effects of using characteristic values for insitu soils may be problematical.

Consider a wall imposing a pressure of 120 kN/m². A designer might have 9 test results for the ϕ' value of the foundation soil which are 32, 33, 34, 35, 36, 35, 37, 40 and 33°. The mean is 35° which leads to an ultimate bearing capacity of 670 kN/m² and lumped factor of safety of 5.6. The characteristic value is 31° which leads to a ultimate bearing capacity of 350 kN/m² and a lumped factor of safety of 2.9. If the designer had say only 3 results of 32, 35 and 38° the mean would still be 35° and the designer would calculate the same result as before. The characteristic value of this set is 30° for which the bearing capacity is 300 kN/m² with a notional factor of safety of 2.5. Hence, quality, quantity and distribution of test data may have as large an influence on margins of safety as the various partial factors which may be applied.

6 CONCLUSIONS

Traditionally geotechnical design employs lumped factors of safety and a key element in deriving these is the veracity of the soil parameters used. This is largely a matter of engineering judgment. In theory, if factors of safety are greater than unity, then there should be no failure. In fact failures do occur occasionally and these often call into question the judgment of the designer.

In Europe the move is away from lumped factor of safety design towards partial factor design. Since partial factors are applied to enhance raw loads, and to reduce raw strengths, the designer deals with design loads, and strengths, which are distorted from raw values. The aim of this distortion is to wean geotechnical design away from a deterministic approach to a probabilistic approach.

Some of the mathematical manipulations prescribed in partial factor design, such as factoring characteristic ϕ' values, tend to produce distorted, nonlinear, design values. This tends to cloud the application of engineering judgment and it remains to be seen whether partial factor design introduces a real probability of failure which is lower or higher than that currently associated with traditional lumped factor of safety design.

REFERENCES

- BSI (1995) *Code of practice for Strengthened/reinforced soils and other fills*, BS 8006 : 1994, British Standards Institution, London, UK.
- CEN (1994) *Geotechnical design - Part 1 : General rules*, Eurocode ENV-1997-1 : 1994 Comité Européen de Normalisation, Brussels, Belgium.

A Comparison of Design Approaches for Geosynthetic Reinforced Soil Structures In Europe

J.Penman and R.A.Austin

Tensar Division, Netlon Limited, New Wellington Street, Blackburn, UK

ABSTRACT: The use of geosynthetic materials to reinforce soil structures has become widespread in recent years. Traditional methods for the design of these structures using polymeric reinforcement are based on a limit equilibrium approach which can lead to a conflict in the design of different parts of the same structure. In a bridge for example, the deck itself is likely to be designed using a limit state approach while the supporting reinforced soil abutment could be designed using a limit equilibrium method.

For reinforced soil walls, the most popular design methods currently used in Europe are based on the tie-back wedge approach. For reinforced soil embankments the most common methods use modified forms of Bishop or Janbu equations for circular and non-circular slip surfaces respectively, the method outlined in the UK Department of Transport technical note HA 68/94 or chart based design methods. All these wall and embankment design methods are based on limit equilibrium principles.

The publication of the UK code of Practice for strengthened/reinforced soils and other fills, BS 8006 introduced alternative methods for the design of reinforced soil structures using limit state principles. The paper describes the advantages and limitations of both limit equilibrium and limit state approaches and outlines the economic implications of using the various methods in different conditions.

KEYWORDS: Design, Limit equilibrium, Limit state, BS 8006, Walls, Embankments

1 INTRODUCTION

When reinforced soil techniques were originally developed, only three or four methods were routinely used for the design of structures. With the wider acceptance of this developing technology, many countries now have at least one approved method for the design of walls and embankments and each is slightly different to the ones used elsewhere.

Since the introduction of modern soil reinforcement techniques by Vidal in the 1960's and the pioneering work for the design of reinforced soil embankments undertaken by Jewell in the 1970's, we have moved on to other more refined and flexible methods of analysis. However, the original coherent gravity method, Vidal (1966) and revised embankment design charts, Jewell (1990) are still very much in use today.

Whilst it is appreciated that many other design methods and Standards exist, this paper focuses on the methods most commonly used at present for the design of geosynthetic reinforced soil structures in Europe.

2 LIMIT EQUILIBRIUM METHODS

2.1 General

The limit equilibrium approach for the design of reinforced soil structures is based on the application of global factors of safety. Thus for external stability calculations, minimum target values are set which must not be exceeded in the design, while for internal stability calculations, a factor of

safety is applied to the reinforcement creep limited strength to determine the safe design strength.

Full details of the limit equilibrium design methods discussed in this paper can be found in Netlon Limited (1997).

2.2 Reinforced Soil Walls

2.2.1 Tie-back Wedge Method

This method was one of the earliest developed for reinforced soil walls and is still very much in use today. Most of the more recent limit equilibrium design methods for geosynthetic reinforced soil walls could be regarded as variations of this traditional approach.

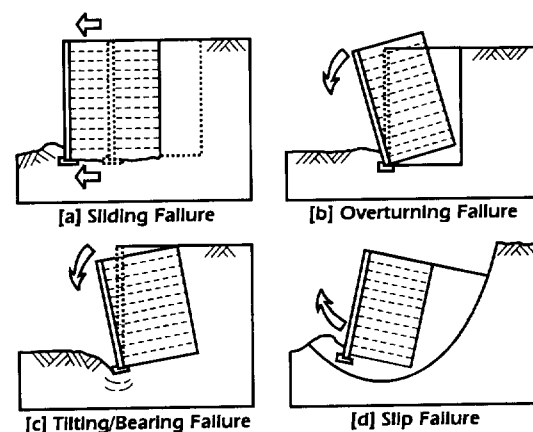


Figure 1. Main failure mechanisms for reinforced soil walls

The external stability of the structure is assessed based on the assumption that it behaves as a rigid body and the possible failure mechanisms are shown in Figure 1. Due to the large strains which develop in the soil, critical state soil parameters (ϕ'_{cv} , c'_{cv}) are generally adopted in design.

Although overturning failure is usually included in external stability calculations, in the absence of any large horizontal loads (e.g. in bridge abutments), it is unlikely to be a problem. A target factor of safety of 2.0 is usually adopted for sliding while for bearing, the vertical pressure exerted by the reinforced soil block is normally calculated and compared with the allowable bearing pressure of the foundation soil. In the past, a trapezoidal pressure distribution was generally adopted for bearing capacity calculations, the vertical pressure being greater at the toe than at the back of the structure. This approach has now largely been replaced by a uniform Meyerhof pressure distribution which takes account of the eccentricity of the applied load at the back of the block in the calculation of the applied pressure.

In general, the base width of the reinforced soil block is chosen to satisfy external stability requirements with regard to sliding, overturning and bearing. A slope stability computer program is then used to check for potential slip failures at the back of the structure.

The internal stability of a reinforced soil wall is essentially concerned with the tension and pull-out failure mechanisms shown in Figure 2. For the purposes of the analysis, a uniform frictional fill is assumed and horizontal soil pressures are taken to be in the active condition throughout the structure; the at rest pressure which may develop during the construction phase will reduce to the active pressure when temporary supports are removed.

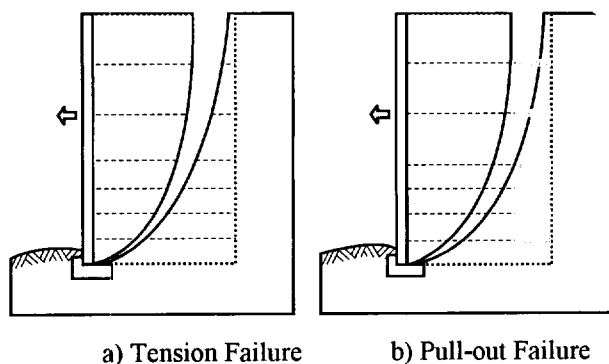


Figure 2. Tie-back wedge internal failure modes

In order to assess potential rupture, it is assumed that the reinforcement will carry tension as a result of the self-weight of the fill and the external loading. These tension components can be evaluated separately and combined to give the total tension to be carried by an individual layer of reinforcement. External vertical and horizontal line loads may also be included thus enabling forces from bridge abutments and parapets to be taken into account.

In order to investigate potential pull-out failure of the reinforcement, it is necessary to consider separately the possibility of inclined failure planes passing through the wall forming unstable wedges of soil bounded by the front face of the wall, the ground surface and the potential failure plane, Figure 3. For the purposes of the analysis, it is assumed that each wedge behaves as a rigid body and friction between the facing and the fill is ignored. A series of potential failure planes emanating at various heights behind the face of the wall are investigated and for each, a check is made to ensure that the total restoring force provided by all layers of reinforcement cut by the wedge exceeds the out of balance force, usually by a factor of two.

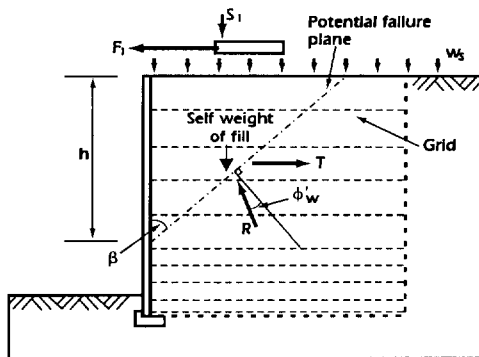


Figure 3. Tie-back wedge pull-out failure mechanism

2.2.2 The Deutsches Institut für Bautechnik Design Method

This design method, based on German DIN standards, has gained widespread acceptance in mainland Europe and is becoming increasingly popular in other parts of the world.

Although the method is based on the tie-back wedge approach, there are a number of important variations. For external stability calculations, these include a reduced target factor of safety of 1.5 for sliding and a specific method for the consideration of bearing failure which by modifying the Terzaghi bearing capacity equation, takes account of the inclination of the resultant force due to the active pressures at the back of the reinforced soil block. An additional check is included to ensure that the resultant force acts in the middle third of the base, this effectively replacing the overturning calculation in the traditional tie-back wedge method.

Internal stability calculations concentrate mainly on a consideration of reinforcement pull-out with the traditional single-part wedge being replaced by a two-part mechanism, the base of the upper wedge passing along the back of the reinforced soil block. An additional check is however required for structures with flexible faces; for each layer of reinforcement, it is necessary to ensure that the design strength (or the anchorage strength if a full-strength connection is not used) is not exceeded by the active pressure on the face.

It is stated in BS 8006 that provided a reinforced soil structure is unlikely to undergo excessive differential settlement, peak effective shear strength parameters can be used for design i.e. ϕ'_p , c'_p . It should be appreciated however that with the exception of some industrial fills (e.g. Pulverised Fuel Ash), an effective cohesion value of zero is normally adopted.

BS 8006 clearly distinguishes two parts to the design process, the ultimate and serviceability limit states. As such it is the only document discussed in this paper which refers directly to the key issue of boundary deformation. Unfortunately, BS 8006 is vague in terms of how serviceability should be addressed and much is therefore left to the individual designer.

4 COMPARISON OF DESIGN METHODS

4.1 General

A number of designs have been undertaken for each of the various methods described above; the analyses were carried out using Netlon Limited's Winslope and Winwall computer programs for the design of reinforced soil structures, Figures 6 and 7. Each design was based on the use of the Tensar® range of HDPE geogrids and where possible, soil parameters were chosen such that the geogrid quantities were not governed by the normal maximum practical spacing criteria.

As the limit equilibrium and limit state methods use constant volume and peak shear strength properties respectively, clearly any comparison between methods adopting these two approaches is sensitive to the relationship assumed between the constant volume and peak values for a particular soil. For the purpose of this exercise, a $\tan\phi'_p / \tan\phi'_{cv}$ ratio of 1.3 has been used throughout. For each design case, the most cost effective method was given a cost rating of 1.00, the relative cost

of using the other methods being based on typical current prices of the products used in the design.

4.2 Wall Design Methods

The results of the cost comparison exercise for walls are shown in Table 1. The most striking feature that comes out of the comparison exercise is the inefficiency of the traditional tie-back wedge approach for all but the smallest of structures. The main reason for this is the longer grid lengths required to satisfy the target factor of safety of 2.0 for sliding, although the method of dealing with the internal stability requirements is also slightly less efficient for the tie-back wedge than the Bautechnik and BS 8006 methods.

The Bautechnik method, in general uses shorter grid lengths than the BS 8006 method but the grid quantities required to satisfy internal stability criteria are significantly less in the BS 8006 method. Overall, for the examples considered in this paper, it would appear that for structures up to 3m high, the traditional tie-back wedge approach may be the most cost effective while for medium sized structures (3m to 8m high), the approach outlined in BS 8006 provides the most cost effective layouts. It should be appreciated however that for different soil and loading conditions, the 'switch in efficiency' between design methods will be at different heights of structure. Similarly, the relationship between the constant volume and peak strength properties for a particular soil will have a considerable effect on the relative performance of the limit equilibrium and limit state methods.

In addition to comparisons being made based on height of structure, the way the design methods deal with inclined faces and water pressure was also investigated. For inclined faces (Cases 7 and 8) the benefits gained by reducing the active earth pressures were equally well reflected in all three methods but when water pressure is present (Cases 9 and 10), it would seem that the BS 8006 method deals with these in a slightly more cost effective manner.

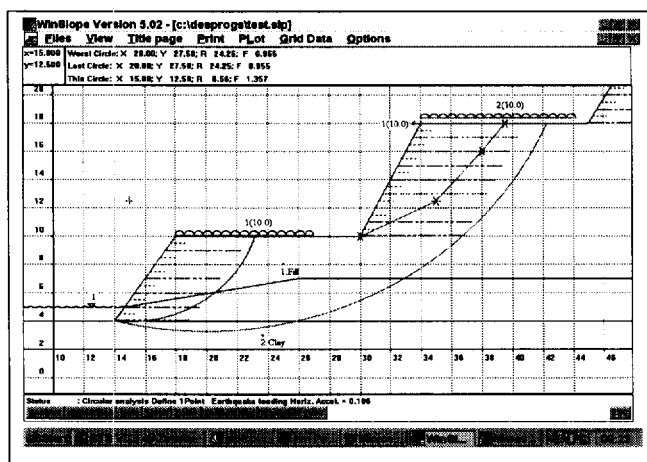


Figure 6. Winslope computer program

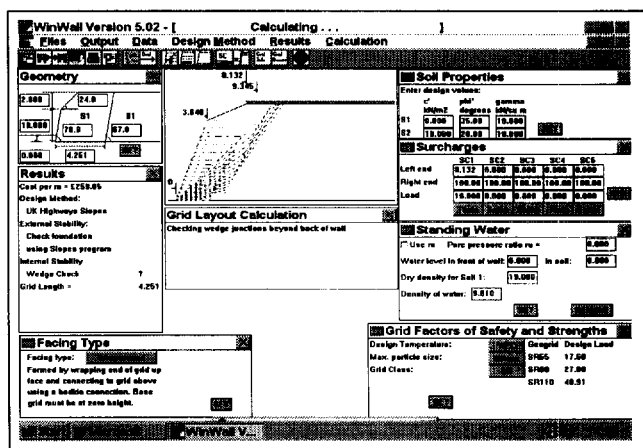


Figure 7. Winwall computer program

4.3 Embankment Design Methods

The results of the cost comparison exercise for embankments are shown in Table 2. It should be appreciated when examining the results that the actual reinforcement layout used to determine the cost ratio for a particular design method is based on both the minimum reinforcement requirement derived from the analysis and the maximum vertical spacing between reinforcement layers; for the latter this was 1.0m throughout. Although this undoubtedly has an effect on the overall costs used in the analysis, it is unlikely to affect the overall cost ranking of the design methods.

Possibly the most noticeable feature of the results for embankments is the significant economy attained by using a limit state approach rather than the traditional limit

equilibrium method for slip circle analyses. It would appear that the difference becomes greater for higher embankments and for shallower embankments constructed with comparatively weak fill (e.g. high plasticity clay).

The two types of HA 68/94 analysis carried out demonstrate the economy which can be attained by using a computerised approach to this method, with the inclusion of inter-wedge friction as opposed to the simplified method using the tables within HA 68/94. It should be appreciated however that in order to use a high value for inter-wedge friction (such as the value of 0.5 used in this exercise), it is necessary to check the stability of two-part wedges behind T_{max} (Love and Bond, 1996).

Table 1. Results of comparison exercise for walls

Case	Description	Bautechnik		Tie-back Wedge		BS 8006	
		Cost Ratio	Grid Length	Cost Ratio	Grid Length	Cost Ratio	Grid Length
1	3m high, 90° wall, $\phi'_{cv}=28^\circ$	1.08	2.00m	1.00	2.60m	1.10	3.00m
2	4m high, 90° wall, $\phi'_{cv}=28^\circ$	1.08	2.60m	1.13	3.40m	1.00	3.00m
3	5m high, 90° wall, $\phi'_{cv}=28^\circ$	1.06	3.00m	1.05	4.30m	1.00	3.00m
4	8m high, 90° wall, $\phi'_{cv}=28^\circ$	1.03	4.80m	1.22	6.80m	1.00	5.60m
5	12m high, 90° wall, $\phi'_{cv}=28^\circ$	1.00	7.20m	1.49	10.30m	1.14	8.40m
6	16m high, 90° wall, $\phi'_{cv}=28^\circ$	1.00	9.60m	1.64	16.60m	1.17	11.60m
7	4m high, 80° face, $\phi'_{cv}=28^\circ$	1.18	2.40m	1.34	3.80m	1.00	3.00m
8	8m high, 80° face, $\phi'_{cv}=28^\circ$	1.09	4.80m	1.41	7.60m	1.00	5.60m
9	As case 2 with water pressures	1.05	3.50m	1.45	5.60m	1.00	4.00m
10	As case 4 with water pressures	1.02	6.30m	1.67	10.30m	1.00	5.90m

Table 2. Results of comparison exercise for embankments

Case	Description	Bishop (Limit Eq.)		Bishop (Limit State)		HA 68/94 ($\phi'_{12} = 0$)		HA 68/94 ($\phi'_{12} = 0.5$)	
		Cost Ratio	Base Grid Length	Cost Ratio	Base Grid Length	Cost Ratio	Base Grid Length	Cost Ratio	Base Grid Length
1	4m high, 60° face, $\phi'_{cv} = 30^\circ$	1.23	2.80m	1.00	2.00m	1.33	2.00m	1.24	2.30m
2	8m high, 60° face, $\phi'_{cv} = 30^\circ$	1.37	5.30m	1.15	4.80m	1.08	5.25m	1.00	4.75m
3	12m high, 60° face, $\phi'_{cv} = 30^\circ$	1.66	8.00m	1.38	7.00m	1.12	8.00m	1.00	8.00m
4	4m high, 45° face, $\phi'_{cv} = 30^\circ$	1.34	3.40m	1.00	2.40m	1.43	3.40m	1.23	2.80m
5	8m high, 45° face, $\phi'_{cv} = 30^\circ$	1.50	6.00m	1.00	4.60m	1.47	6.75m	1.28	5.75m
6	12m high, 45° face, $\phi'_{cv} = 30^\circ$	1.66	8.00m	1.00	7.00m	1.29	10.0m	1.11	8.50m
7	4m high, 1 in 2 face, $\phi'_{cv} = 30^\circ$	1.72	4.80m	1.00	3.80m	1.87	7.30m	1.68	6.50m
8	8m high, 1 in 2 face, $\phi'_{cv} = 30^\circ$	1.56	10.50m	1.00	7.00m	2.03	14.5m	1.83	13.00m

n.b. ϕ'_{12} =inter-wedge friction

Perhaps the most surprising feature of the results is the relative performances of the HA 68/94 and limit state slip circle methods. It would appear that despite the absence of a global factor of safety on soil strength for the HA method, with the exception of reasonably large embankments with steep faces (greater than or equal to 60°), there are considerable savings to be attained using the limit state slip circle approach.

5. CONCLUSIONS

The paper has reviewed the design methods most commonly used in Europe for the design of reinforced soil structures. It is clear that while there are many similarities between the methods used for the design of reinforced soil walls, several important differences exist which in some cases result in significant variation in the amount of reinforcement required to satisfy the various design criteria. Similar differences are observed in embankment design methods.

Overall it is not possible to indicate one particular design method for walls or embankments which consistently yields more cost effective reinforcement layouts. It would appear however that the limit state methods proposed in BS 8006 are economic in most cases.

There is the possibility that individual designers will select their own favourite methods for walls and embankments without being aware of the appropriateness of other approaches. However, when a particular method is chosen simply based on cost, it is important that the designer understands fully the design philosophy and reasons for the economy. In the case of HA 68/94 for example, the adoption of a high inter-wedge friction angle requires additional checks to be made to ensure a safe embankment design is achieved.

ACKNOWLEDGEMENT

The writers would like to acknowledge the efforts of Mr. Paul McCombie in developing the design software used for the analyses referred to in this paper.

REFERENCES

British Standards Institution. BS 8006: *Code of practice for strengthened reinforced soils and other fills*: 1995, BSI, London.

Certificate No. Z-20.1-102, Deutsches Institut für Bautechnik, Berlin, 1990.

Department of Transport, *HA 68/94 Design methods for the reinforcement of highway slopes by reinforced soil and soil nailing techniques*, HMSO, UK, 1994

Jewell, R, *Revised design charts for steep reinforced slopes*, Proc. Symp. Reinforced embankments - theory and practice, Cambridge, Thomas Telford, pp18-30, 1990.

Love, J and Bond A, *discussion on 'The computerised design of reinforced soil structures' by Penman, J and McCombie, P (1996)*, Ground Engineering, Emap Construct, London, January/February 1997, p36.

Netlon Limited, *The design of reinforced soil structures using Tensar geogrids*, 1997

Penman, J and McCombie P, *The computerised design of reinforced soil structures*, Ground Engineering, Emap Construct, London, November 1996, pp 36-37 and December 1996, p33.

Vidal, H, *La terre armée*, Annls L'Inst Tech de Batement et des Travaux Publics, Serie Matériaux 30, Puppement No. 223-4, July-August 1966.

displacement field along the failure surface defined by a vertical top displacement y_1 (see Figure 1), (ii) the anchored membrane concept (see Figure 2), and (iii) the geosynthetic extensibility. The local equilibrium of each sheet is considered, coupled with the tension constitutive model of the reinforcement and of that in friction of the soil-geosynthetic interface (elasto-perfectly plastic behavior). Faced with the problem of the determination of the soil stiffness modulus, a simplified mechanism of the membrane behavior has been considered by the authors: (a) The reinforcement tension is constant all along the membrane zone B_1B_2 (see Figure 2) and is equal to the ones at B_1 and B_2 ; (b) This tension is either assumed to act in the horizontal direction or in the direction of the tangent to the failure surface (maximum inclination); And (c) the modeling of the geosynthetic behavior is considered either with a small or large displacements assumption. Note that the corresponding software "Cartage" is widely used in France for practical design work.

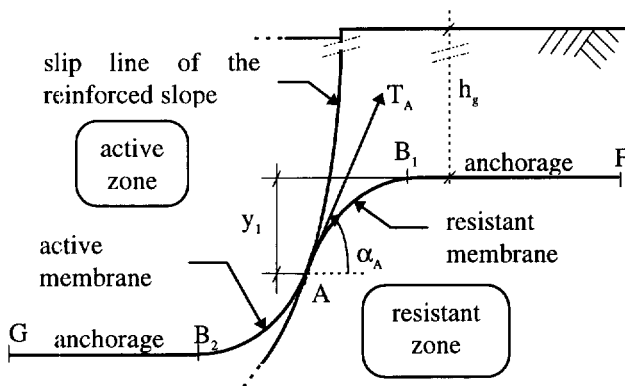


Figure 2: Anchored membrane concept.

2.2 Modified "Displacement Method"

This method considers a more rigorous mechanism (circular shape) of the membrane behavior. The determination of the reinforcement tension T_A (see Figure 2), which is also assumed to be constant all along the circular membrane zone, is based on the local equilibrium of this zone. Thus, the reinforcement tension and its inclination α_A depend on the vertical top displacement y_1 and the soil stiffness modulus. Note that the corresponding software "Membrane" is used essentially for research (Gotteland, 1991).

2.3 "Variational Displacement Method"

The problem has been split into two different parts:

- Global equilibrium of the sliding mass
Applying the variational limit equilibrium method, elaborated by Baker and Garber (1977) in the case of unreinforced slopes, to the one of reinforced slopes, it

has been shown that (i) the trace of the critical failure surface is a log spiral (see Figure 1), and (ii) the only moment equilibrium equation of all forces acting on the sliding mass is enough for the determination of the safety factor FS , defined with respect to the shear strength parameters of the soil.

- Local equilibrium of the reinforcement sheets

In order to assess the reinforcement contribution to the stability, the variational calculus has been applied to the equilibrium of the membrane zone in the neighborhood of the failure surface, considering the principle of the "displacement method" (i.e.: the anchored membrane concept, see Figure 2). The variational approach allows the determination of the optimal shape (log spiral) as well as the optimal position of the sheet for which one obtains the extremal tension at the intersection with the failure surface. Thus, the tension is no longer assumed to be constant along the membrane zone. Furthermore, this method provides the tension distribution and the relative soil-geosynthetic displacements all along the sheets.

2.4 Comparison Of The Different Models

Table 1 shows the comparisons of some principles of the three above mentioned models, regarding (a) the global equilibrium of the sliding mass (columns 1 to 3) and (b) the local equilibrium of the reinforcements (columns 4 to 6). Note that the listed principles are those which differ from each other. It appears that the "Displacement Method" has gained in rigour in its two latter developments (i.e. less a priori assumptions). The improvement provided by the "Modified" model consists of a more rigorous determination of the reinforcement tensions. With the present model, it provides an improvement on the determination of both the safety factor (no a priori assumptions concerning the failure surface shape, nor the normal stress distribution along this surface), and the reinforcement tension (no a priori assumptions concerning the shape of the membrane zone, nor its critical position).

3 COMPARATIVE CASE STUDY

In order to show the developments of the "displacement method", the three above mentioned models have been applied to a 6m high wall reinforced with 11 geosynthetic layers. All other data required for the analysis are presented in Figure 3. For all three models, the safety factor FS of the soil in shear is set to 1.5. Note that all "Cartage" results correspond to the assumption of large displacements with a horizontal reinforcement tension (see §2.1).

Table 1. Comparison of some principles of the three models

Name	1. Limit equilibrium method	2. Failure surface shape	3. Search for critical failure surface	4. Critical position of the membrane zone (as rest)	5. Tension in B ₁ B ₂ (see Fig.2)	6. Inclination of tensions (null) or (maximum)
“Cartage”	“Perturbation”	any (circular more used)	manual	(as rest)	(constant)	(null) or (maximum)
“Membrane”	“Perturbation” Fellenius Bishop Jambu	(circular) (bilinear) (mixed)	manual	(fixed)	(constant)	(fixed)
Present model	Variational	Log-spiral*	automatic	result of minimisation process*	non constant*	result of minimisation process*

Notes: Terms in parentheses () refer to a priori assumptions, and the one followed by * refers to analytical result.

3.1 Failure Surfaces

Concerning the two first models (i.e. “standard” and “modified”), and for each potential slip line (circular shape) considered, a critical vertical top displacement y_{ic} corresponding to $FS=1.5$ is determined. The critical slip circle (represented in a dotted line in Figure 3), which is the same in both models, corresponds to the larger y_{ic} value considering six different potential slip circles (Gourc et al, 1989).

For the present model, the slip line shape is a log spiral and the critical position (represented in Figure 3) corresponds to the critical y_i value (called y_{ic}) which provides a safety factor $FS=1.5$ as its minimum value, considering 860 different log-spirals passing through the toe of the wall.

Note that these two lines are rather close to each other in the lower half part of the wall, then the log-spiral is placed further away from the facing than the circle. Nevertheless, regarding the difference in the determination of the critical position of the failure surface in each model, the scatter between these positions is small.

3.2 Critical Vertical Top Displacements

Concerning the critical vertical top displacements y_{ic} , the standard model gives 26mm, the modified one gives 50mm, and the present one gives 88mm (see Figure 3). Thus, it seems that there is a tendency in the development of the method for an increase of this key parameter.

3.3 Critical Tension Distributions

Figure 4 shows the distribution of the critical tensions and of their inclinations along the failure surfaces. It is interesting to note that the tension distribution of the present model is close to the one of “Cartage” in the

upper half part of the wall, and close to the one of “Membrane” in the lower half part. Plus, the present model gives the lowest maximal tension T_{max} (presented in Figure 4), which is reached in the lowest sheet in each model. Nevertheless, the scatter between these tension distributions is rather small.

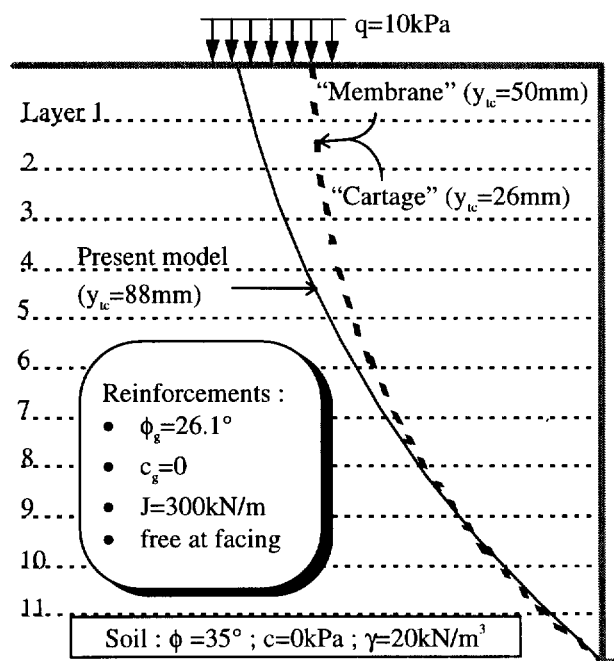


Figure 3. Case study - Critical positions of the theoretical failure surfaces

3.4 Critical Tension Inclination Distributions

Concerning the tension inclinations, the distributions as given by “Membrane” and the present model (null for “Cartage”) are very different from each other. “Membrane” distribution decreases continuously with the depth, while the one of the present model passes through a minimum value at the second layer (see

Figure 4), then from the 8th layer and deeper it reaches the maximal inclination distribution, which corresponds to tensions tangent to the failure surface (the log-spiral of Figure 3).

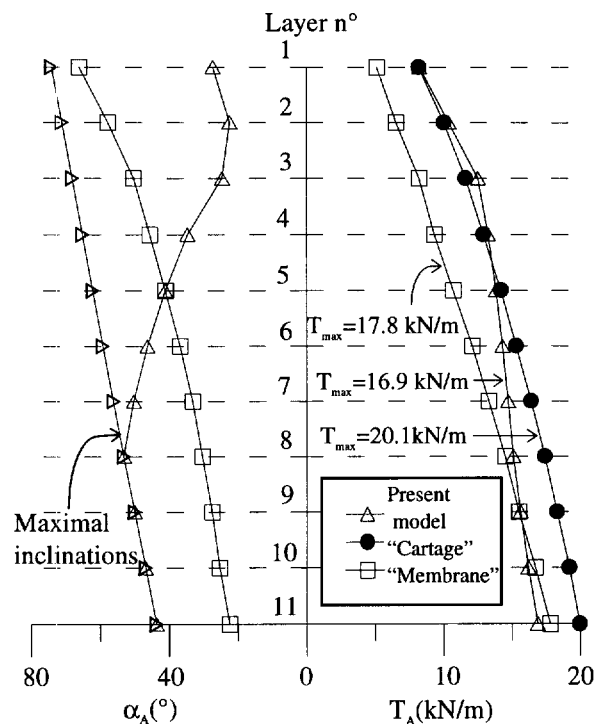


Figure 4. Comparative study (case study of Figure 3)

3.5 Discussion

The present comparison study shows that (i) the critical failure surfaces obtained with the three models are close to each other (see Figure 3), (ii) the reinforcement tension distributions along the failure surface are similar (see Figure 4), but (iii) the obtained critical vertical top displacements y_w has been increased significantly from one model to its following development (92% between the two first, and 76% between the two last). However, the latter parameter is difficult to correlate to actual measurements, and further research should be performed on the validation of these models on real structures build and tested to failure.

4 CONCLUSION

This paper presents the recent developments of the "displacement method". This method, which is the standard in France for the design of geosynthetically reinforced earth structures, has since been improved at least twice. The first improvement concerns the determination of the reinforcement tensions, the second one also concerns the determination of the safety factor of the structure. Indeed, the originality of the latter is

the application of the variational calculus on both the equilibrium of the sliding mass and the one of the membrane zone in the vicinity of the failure surface. This analysis allows a significant decrease in the number of a priori assumptions considered in the previous models. A comparative study on a 6m high wall has shown that the rigour tends to increase the obtained critical top displacement.

REFERENCES

- Baker, R. and Garber, M. (1977) "Variational Approach to Slope Stability", *9th Int. Conf. on Soil Mechanics and Foundation Engineering*, Tokyo, Japan, Vol. 2, pp. 9-12.
- Fidler, P., Gotteland, Ph., Gourc, J. P. and Haidar, S. (1994) "Evolution of the 'Displacement Method' applied to soil reinforced structures", *Int. Conf. on Geotextiles, Geomembranes and related products*, Singapore, pp.225-228.
- Gotteland, Ph. (1991) *Renforcement des sols par géosynthétiques ; dimensionnement et validation* Ph.D thesis, Grenoble University, France, 384 p.
- Gourc, J. P., Ratel, A. and Delmas Ph. (1986) "Design of fabric retaining walls : the Displacements Method", *Third Int. Conf. on Geotextiles and geomembranes*, Vienna, Austria, session 3A/1, pp. 289-294.
- Gourc, J. P., Ratel, A. and Gotteland, Ph. (1988), "Design of reinforced soil retaining walls : Analysis and comparison of existing methods and proposal for a new approach". *The Application of Polymeric Reinforcement in Soil Retaining Structures*, Nato Asi Series, Applied Sciences, Vol. 147, pp.24-67.
- Gourc, J. P., Gotteland, Ph. and Delmas, Ph. (1989), "Parametric study of geosynthetic reinforced retaining walls using the displacement method". *Geosynthetics '89*, San Diego, USA, pp. 112-123.
- Lemonnier, P. (1995) *Application de la méthode variationnelle au problème de la stabilité des talus renforcés par des nappes géosynthétiques*, PhD thesis, I.N.S.A Lyon, France, 483 p.
- Lemonnier, P. and Soubra, A. H. (1997) *Recent development of the "displacement method" for the design of geosynthetically reinforced slopes - Comparative case study*, Rencontres'97, CFG, Reims, France, Vol. 2, pp. 28AF-31AF (10p.).
- Yoshioka, A., Delmas, Ph., Gourc, J. P. and Gotteland, Ph. (1990) "Validation of the 'displacement method' on an experimental reinforced wall at failure" *Int. Conf. on Geotextiles, Geomembranes and related products*, The Hague, Netherlands, Vol. 1, pp.61-66.

Locally Loaded Geosynthetic Reinforced Soil Structure: Calculation Method

E. Haza

Ph.D., Lirigm, Grenoble University, France

P. Gotteland

Assistant Lecture, Lirigm, Grenoble University, France

J.P. Gourc

Professor, Lirigm, Grenoble University, France

ABSTRACT: This article presents a proposed method for the preliminary design of geosynthetically reinforced soil structures, adapted to the case of localised surface loads. The first section describes two modifications made to the basic calculation method: firstly, to consider the deformable nature of geosynthetics and, secondly, to consider a local equilibrium calculation of each reinforcement. In the second section, an attempt is made to validate the proposed initial modifications on the basis of results obtained using an experimental structure locally loaded up to its failure point. The local approach seems satisfactory.

KEYWORDS: Retaining wall, Reinforcement calculation method, concentrated top load, Prediction, Experimentation.

1. INTRODUCTION

Geosynthetically reinforced soil embankments with flexible facings are commonly used in France for retaining purposes; their ability to bear is also currently being studied at the Grenoble Lirigm laboratory. This article will concentrate on this function for case where the head of the structure is locally loaded.

Little is known about structures with flexible reinforcement sheets which are locally loaded at the head. Observation of the way in which instrumented embankments fail (Matichard and al., 1992, Lensiewska and al., 1992) shows that the reinforcing sheets in the upper part of the embankment are placed under high stress by the slab which perforates the embankment, and that the tensile force and slope of the reinforcing sheets in the shear zone are greatly reduced towards the base of the embankment. This behaviour is the reverse of that of a structure with no localised overload or which is evenly overloaded, where the sheets at the base are under greatest tensile forces.

On a reference experimental structure (Gourc and al., 1995) (Photo 1), an attempt will be made to validate a preliminary design method for these structures which is quick and easy to use: the modified double-block method (shortened to DB), based on the limit equilibrium calculation principle. This method is sufficiently widely used to study the stability of structures which are either not overloaded or evenly overloaded.



Photo 1. The GARDEN experimentation

2. THE DOUBLE-BLOCK METHOD (DB)

With the DB method, the active part of the embankment is divided into two rigid blocks placed side by side and assumed to be slipping. The slip line is bilinear, with kinematic convexity condition.

The points where the slip line intersects the facing (point A) and the upper surface of the embankment (point C), as well as the positions of the slope break point and the inter-block line (point B) are selected by the user (Figure 1).

The limit equilibrium of the double block is calculated by applying a resultant horizontal thrust P , redistributed throughout the reinforcing sheets j (tensile forces T_j) (Figure 1). The slip line is assimilated to the line along

which the maximum tensile forces are accommodated in the reinforcing sheets. The equality $\Sigma T^j = P$ is checked.

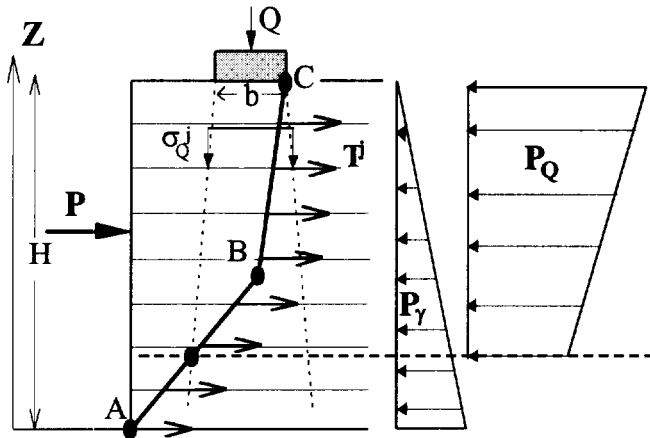


Figure 1. Double-Block method principle.

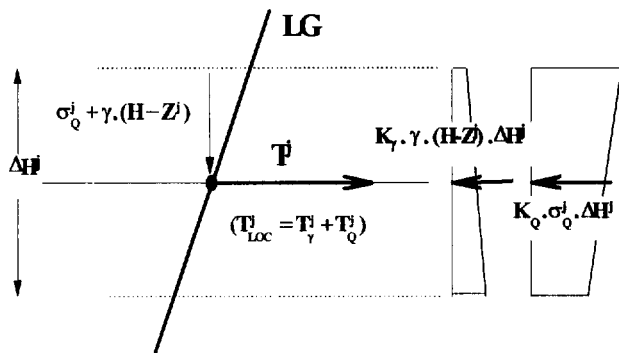


Figure 2. Local equilibrium of a reinforcing sheet j.

The distribution used for the resultant vertical stress of the localised overload Q is almost vertical inside the embankment (angle of distribution $\phi_{soil}/4$). The vertical stress at the reinforcing sheet j which is applicable in the distribution zone will be called σ_Q^j .

The safety coefficient F is applied to the mechanical properties of the earthfill. The theoretical failure of an embankment is thus obtained when $F=1$.

Two approaches are proposed for the preliminary design, one known as *overall* and the other *local*.

2.1 Overall Approach (OA)

Overall equilibrium of the unstable area is considered to be ($\Sigma T^j = P$).

In a first option (OA1), the tensile forces T_{OA1}^j , mobilized in the reinforcement sheets, are fixed; the value of F is deduced.

A second option (OA2) consists in fixing F and then deducing a uniform tensile force distribution throughout

the reinforcement ($T_{OA2}^j = T_{OA2}$, except on case of anchorage problem). The critical slip line is obtained for the maximum value of T_{OA2} .

2.2 Local Approach (LOC)

Another approach consists in studying the local equilibrium of the complex [soil+reinforcing sheet] at the level of each reinforcing sheet for a predefined slip line (Figures 1 and 2).

The action of the localised head load Q is separated from the action of the deadweight of the soil. This means that a different distribution can be considered for each of these actions along the slip line.

The double-block equilibrium thrust P_Q is calculated for the double-block only subjected to Q, for a density of the soil body in the double-block assumed to be zero. In accordance with the observations already made, the distribution made is one whereby the upper reinforcing sheets which are under greater tensile forces. The distribution of P_Q is trapezoidal. The proposed hypothesis consists in assuming that the reinforcing sheets are under tensile forces only if their intersection with the slip line is included in the top load area of influence (Figures 1 and 2).

A thrust coefficient K_Q is calculated on the basis of P_Q to determine local tensile forces T_Q^j :

$$K_Q = \frac{P_Q}{\sum_j \sigma_Q^j \cdot \Delta H} \quad (1) \quad \text{and} \quad \begin{cases} T_Q^j = K_Q \cdot \sigma_Q^j \cdot \Delta H^j \\ \Sigma T_Q^j = P_Q \end{cases} \quad (2)$$

For the action of weight of the soil, the conventional triangular distribution hypothesis is considered. The thrust P_γ is calculated, equilibrium resultant of the double-block under its own weight, on the basis of which the thrust coefficient K_γ and the local tensile forces T_γ^j are deduced.

$$\begin{cases} T_\gamma^j = K_\gamma \cdot \gamma \cdot (H - Z^j) \cdot \Delta H^j \\ \Sigma T_\gamma^j = P_\gamma \end{cases} \quad (3)$$

The tensile force in the reinforcing sheet j is then obtained by (Figure 2): $T_{Loc}^j = T_Q^j + T_\gamma^j$.

Given the cases examined, where the overload Q is high compared with the soil weight, the tensile forces T_Q^j will be generally high compared to the tensile forces T_γ^j , and thus predominant in the design of the structure.

3. COMPARISON WITH EXPERIMENTAL RESULTS

3.1 Experimental structures

The GARDEN programme ("Geotextile": Application in Reinforcement: Experimentation and Normalisation) consisted in loading to failure point two embankments with cellular facings (Löffel type), at an 80° slope (Photo 1).

These embankments have a total height $H = 4.35$ m, and are reinforced by geosynthetics having a tensile strength (T_p) and different stiffness moduli, with local head loading (Gourc and al., 1995). The loading system is presented on the Figure 3.

An exhaustive assessment of the behaviour of these two structures has been made (Haza, 1997). They were hardly instrumented (Figure 4).

One of these embankments is shortly presented here : the embankment reinforced by a non-woven polyester geosynthetic (NW embankment, Figure 5). The other embankment is reinforced by a woven polyester geosynthetic (W embankment, figure 6).

The mechanical properties of the earthfill are $\phi = 36^\circ$, $C = 4$ kPa and $\gamma = 19$ kN/m³.

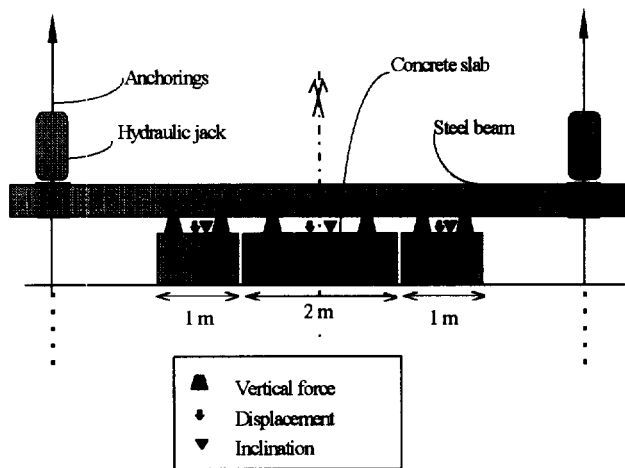


Figure 3. Loading system of both experimental embankments.

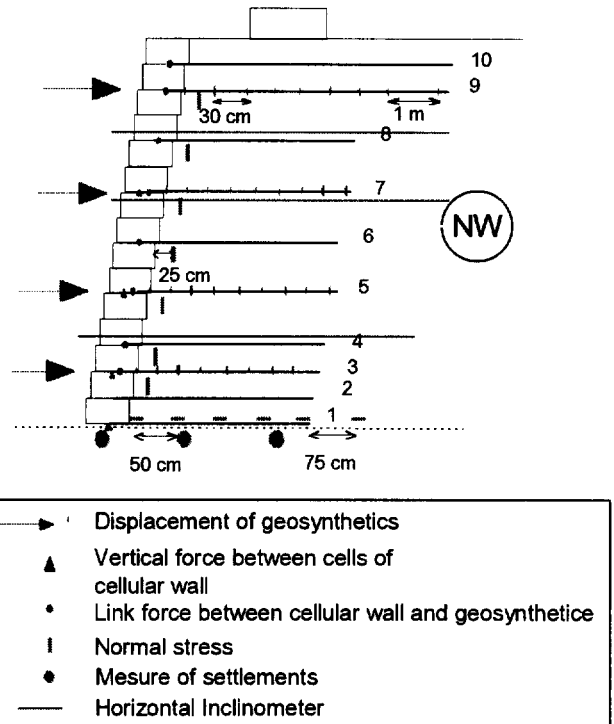


Figure 4. Instrumentation of the NW embankment.

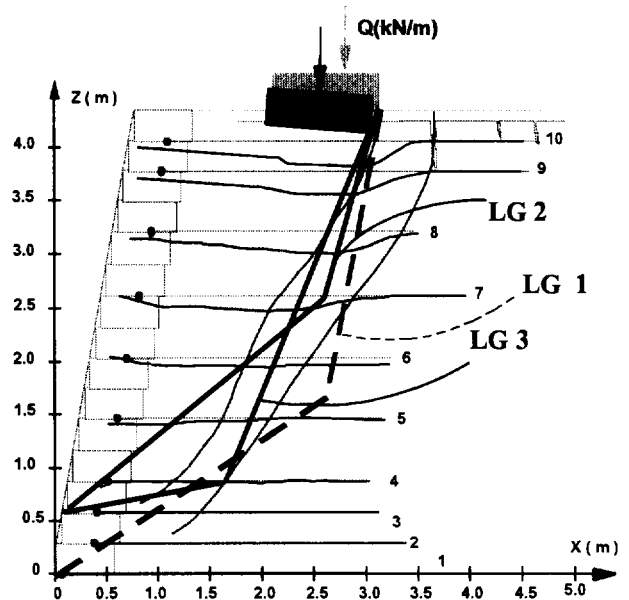


Figure 5. NW embankment profile - slip lines retained for the reverse calculations.

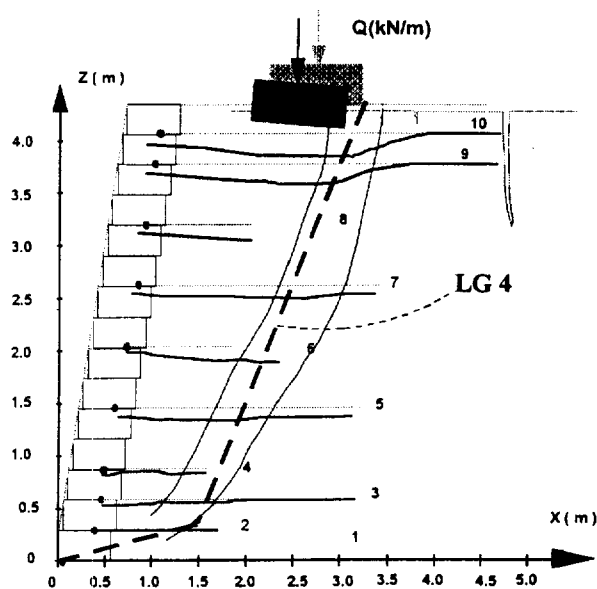


Figure 6. W embankment profil - slip line retained for the reverse calculations.

3.2 Preliminary design stage

3.2.1 Definition of profiles: overall approach (OA)

The preliminary design of these experimental structures was carried out using the overall approach (OA2): the safety coefficient was fixed ($F = 1$, theoretical failure reached), as was the maximum load considered at the conceptual design stage $Q = 330$ kN/m.

The critical slip line was obtained (LG 1 in the NW embankment, Figure 7). The selected tensile strength of the geosynthetic used was equal to T_{OA2} ($T_f = T_{OA2} = 25$ kN/m in the NW embankment).

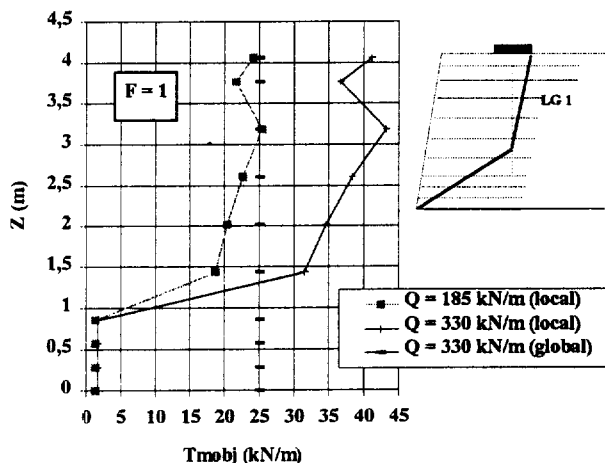


Figure 7. Preliminary design stage - tensile force distribution (NW embankment).

However, since the anchoring strength of the two upper sheets is low ($< T_f$), these sheets were made longer. Thus, the NW embankment is reinforced by eight 3 m long sheets and two 4 m long upper sheets and the W embankment is reinforced by three 3 m long sheets and two 4 m long upper sheets (Figures 5 and 6).

3.2.2 Forecast failure load: local approach (LOC)

For $Q = 330$ kN/m, $F = 1$ and slip line LG 1 defined above, the tensile force distribution T_{LOC}^j gives values much higher than $T_f (= 25$ kN/m) in the upper two thirds of the NW embankment (Figure 7).

A new loading condition Q was then calculated compatible with a maximum tensile force value T_{LOC}^j closer to T_f . A value of $Q_{LOC}^F = 185$ kN/m was obtained for a maximum value of $T_{LOC}^j = 25$ kN/m (Figure 7). The same value of Q_{LOC}^F was obtained for the W embankment, for a maximum value of $T_{LOC}^j = 44$ kN/m ($= T_f$).

3.3 Feedback from experimentation

At the end of the test, the maximum load applied on the two embankments was $Q_{EXP} = 230$ kN/m.

By measuring the displacement of reinforcing sheet points at failure, the range of maximum reinforcement sheet strain zones can be obtained (Figures 3 and 4). The distribution of experimental tensile forces T_{EXP} can then be estimated (Figure 8, in the NW embankment). Observations of the two embankments confirmed that the upper sheets work much harder than the others, and tend to bend considerably (Gotteland and al., 1997).

The critical slip line selected for the preliminary design in the NW embankment (LG 1) was not exactly within the range of maximum tensile force values. In the following discussion, two other slip lines included within this range, LG 2 and LG 3, were considered in the NW embankment for carrying out the reverse calculation using the DB method. The slip line LG 4, included within the range of maximum tensile force values, was considered in the W embankment for the reverse calculation (Figures 5 and 6).

3.3.1 Reverse calculation: overall approach (OA)

The forecast failure load in the overall approach (§ 3.2.1) was 330 kN/m, a value much higher than the load observed under experimental conditions ($Q_{EXP} = 230$ kN/m).

The overall approach (OA1), with $Q_{EXP} = 230$ kN/m and $T_{OA1}^j = T_{EXP}^j$ applied along the line LG 2 and the deeper line LG 3, gives safety coefficient values of $F = 0.66$ and $F = 0.995$ respectively (Figure 8). Therefore,

with the overall approach, the safety coefficient F depends closely on the slip line chosen, although the two lines considered are relatively close. A satisfactory result is obtained for line LG 3 ($F \approx 1$).

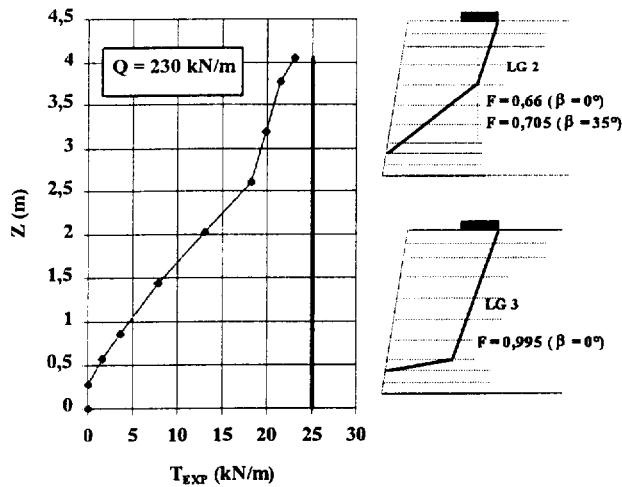


Figure 8. Experimental tensile force distribution in the NW embankment.

3.3.2 Overall approach: proposed development

In the shear zone, flexible reinforcing sheets become deformed. Therefore, the stress that builds up here does not remain horizontal.

A vertical component of the tensile forces along the shear line, taken into account in the active double-block equilibrium, was introduced into the calculation (Haza, 1997).

In the light of the observations, it is proposed to divide up the active zone of the embankment into two simplified zones :

- a "top" zone (above point B, Figure 1), where the tensile forces that build up in the reinforcements are all inclined at the same angle β ,
- a "bottom" zone (below point B, Figure 1), where the tensile forces remain horizontal.

As before, the option (OA1) is applied in the NW embankment with $Q = Q_{EXP} = 230$ kN/m, by imposing $T_{OA1}^j = T_{EXP}^j$ but inclining the "top" forces at $\beta = 35^\circ$ (inclination of sheet n°10 measured when the structure was dismantled). To ensure that only the upper reinforcing sheets were inclined, line LG 2 is considered because point B is high up in the embankment. $F = 0.705$ in place of 0.66 was obtained. By inclining these forces, a slight increase in the safety coefficient F was observed; it nevertheless remains less than 1.

3.3.3 Local Approach (LOC)

During the preliminary design, the foreseeable failure load obtained ($F = 1$) is less than the failure load measured experimentally ($Q_{LOC}^F (=185$ kN/m) < $Q_{EXP} (=230$ kN/m)).

To compare the results of the local approach with the overall approach, the slip lines LG 2 and LG 3 are also used in the NW embankment (Figure 9), and the slip line LG 4 in the W embankment (Figure 10).

By applying $F = 1$ and $Q = Q_{EXP} = 230$ kN/m, the tensile forces distribution calculated along the slip line LG 2 is much higher than the distribution obtained experimentally, whereas along LG 3 it is closer. Thanks to the low position of point B on line LG 3, the deeper-lying reinforcement sheets in the embankment can also take part in the overload double-block equilibrium because they are directly involved in load distribution within the embankment (Figure 9). The thrust P_Q is thus distributed among a greater number of reinforcement sheets, thereby reducing the tensile forces T_{LOC}^j . Meanwhile, the tensile forces distribution calculated along the slip line LG 4 in the W embankment is not so close to the distribution obtained experimentally (Figure 10). The very large vertical space between the sheets at the middle level of the W embankment can be an explanation of this result.

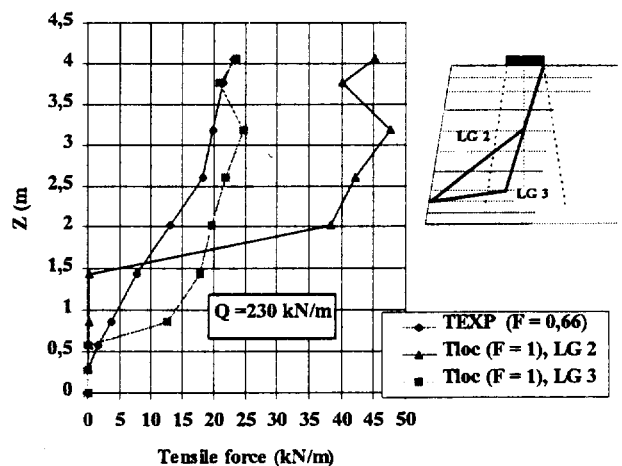


Figure 9. Reverse calculation by the local approach (NW embankment)

As the point B (Figure 1) is near the bottom of the embankment, its exact position has little bearing on the values of T_{LOC}^j ; the same is true for the position of point A, as the level of participation of the lower sheets remains very low.

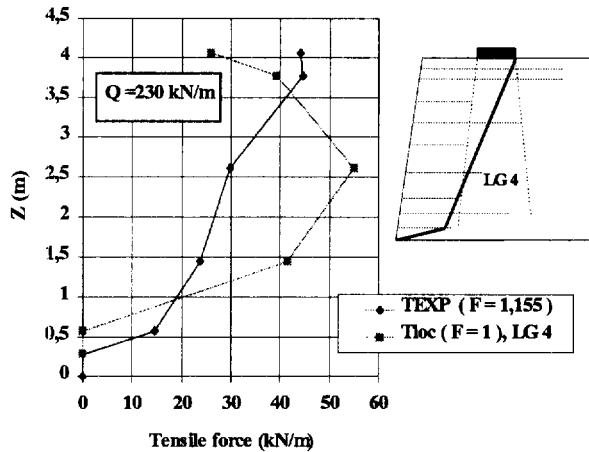


Figure 10. Reverse calculation by the local approach (W embankment).

This type of slip line, emerging at C, just upstream of the loading slab, with a high angular opening, would seem to match the local approach modelling system used here.

The same type of slip line could be used for the design of reinforced embankment whose geosynthetic is more or less stiff. Indeed, we observed, during the GARDEN experimentation, that the position of the experimental slip line is similar in both embankments (Figures 5 and 6). However, the stiffness moduli of the geosynthetics were different ($J_{NW} = 95 \text{ kN/m}$, $J_w = 340 \text{ kN/m}$).

4. CONCLUSIONS

The operating and failure mechanisms of geosynthetically reinforced earth structures, with local head loading condition, are still relatively unknown. This paper proposes the outlines of a simple and fast calculation method for the preliminary design of such structures. Two modifications to the double-block method, the first to take into account the deformable nature of the reinforcing material (Overall Approach), and the other to take into

account a distribution of the tensile forces produced by Local Approach, are used to approximate the observed behaviour on experimental structures subjected to massive deformation.

The Local Approach proposed gives promising results and should become even more satisfactory with possible allowance being made for the angle of inclination of the tensile forces, i.e., consideration for the deformable nature of the reinforcing sheets.

We have suggested (Haza, 1997) a design method which needs now to be validated on several experimental results.

REFERENCES

- Gotteland P., Gourc J.P., Villard P. (1997) Geosynthetics reinforced structures as bridge abutments; Full scale experimentation and comparison with modelisations, *Proceedings of the Int.Symposium on Mechanically Stabilized Backfill*, Denver, U.S.A., 10 p., to be edited.
- Gourc J.P., Gotteland P., Haza E., Perrier H., Baraize E. (1995) Geotextile Reinforced Structures as Bridge Abutments : full scale experimentation, *Proceedings of the VIth International Conference on Geosynthetics*, Nashville, USA, pp 79-92.
- Haza E. (1997) Massif en terre renforcé par géosynthétiques, chargé localement en tête : expérimentation et méthode de calcul , Ph. D, *University of Grenoble*.
- Matichard Y., Thamm B., Sere A. (1992) Behaviour of a geotextile reinforced earthwork under surface loading, *Proceedings of seiken symposium NO.11*, Tokyo, Japan, pp 117 - 130.
- Yoshioka A., Delmas P., Gourc J.P., Gotteland P. (1990) Validation of the « displacement method » on an experimental reinforced wall at failure, *Proceedings of the IVth Int. Conf. on Geotextiles, Geomembranes and Related Products*, The Hague, Neatherland, pp 61 - 66.

Measuring geotextile strains with strain gages

Stanley R. Boyle
 Engineer, Shannon & Wilson, Inc., Seattle, Washington, USA

Robert D. Holtz
 Professor, Department of Civil Engineering, University of Washington, Seattle, Washington USA

ABSTRACT: Laboratory research was undertaken to evaluate the effectiveness of electrical resistance strain gages to measure geotextile strains. At low strains, typical of those observed in geosynthetic reinforced soil slopes and walls, the strain gages were found to underrecord total strain and incremental strain in both in-isolation and in-soil load-elongation tests on both polypropylene and polyester woven geotextiles. The degree of underrecording decreased with increasing geotextile strain. Strain gages were effective for measuring the strain distribution in geotextiles and for monitoring geotextile creep.

KEYWORDS: Geotextiles, reinforcement, strain gages, strain measurements, testing

1 INTRODUCTION

To evaluate the effectiveness of electrical resistance strain gages for measuring strains in reinforcement geotextiles, a series of load-elongation tests were performed on woven polypropylene and polyester geotextiles to which strain gages had been attached. Specimens 100 mm long by 200 mm wide were tested in isolation and confined in soil. Three polypropylene woven slit film geotextiles (PP1, PP2, and PP3) and two polyester woven multi-filament geotextiles (PET1 and PET2) were included in the test program, Table 1.

Table 1: Geotextiles tested.

Material	Material and Description	Strength ¹
PP1	Polypropylene, woven, slit-film	26 (15) ²
PP2	Polypropylene, woven, slit-film, 2 layer stitch-bonded	49 (15) ²
PP3	Polypropylene, woven, slit-film, 3 layer stitch-bonded	77 (15) ²
PET1	Polyester, woven, multi-filament	215 (10) ³
PET2	Polyester, woven, multi-filament	175 (10) ²

¹ Wide width strength, kN/m, and associated (elongation, %), ASTM D 4595.

² Manufacture supplied data from Industrial Fabrics Association International (1990, 1992).

³ Average value from Allen et al. (1992).

In-isolation wide width tests were performed using an MTS testing machine which had been fitted with hydraulically operated clamps, in accordance with ASTM D 4595. The geotextiles were loaded to failure at rates of 10%/min and 1%/min. In an attempt to eliminate end effects, overall elongation of the geotextiles was measured using a "scissors" type displacement measurement device,

Figure 1. The scissors were attached to the geotextiles by pushing needles, mounted at the end of each arm, through the geotextile. The distance between the needles at the beginning of each test, approximately 60 - 75 mm for 100 mm gage length specimens, was used as the initial gage length for calculating overall strains in the woven geotextiles. No measurable reduction in strength resulted from insertion of the needles.

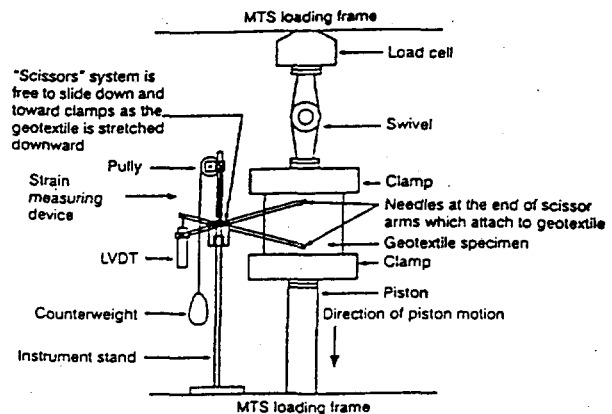


Figure 1: In-isolation test device.

In-soil tests were conducted using a plane strain unit cell device (UCD), Figure 2. During UCD tests, horizontal deformation of the soil is resisted by an applied lateral confining pressure and by tensile loads induced in the reinforcement. Elongation and tension in the geosynthetic specimen are measured, respectively, by LVDT's and load cells connected to the clamps which grip the reinforcement at both ends. Stiff end plates, to which the clamps are mechanically linked, ensure the reinforcement and soil

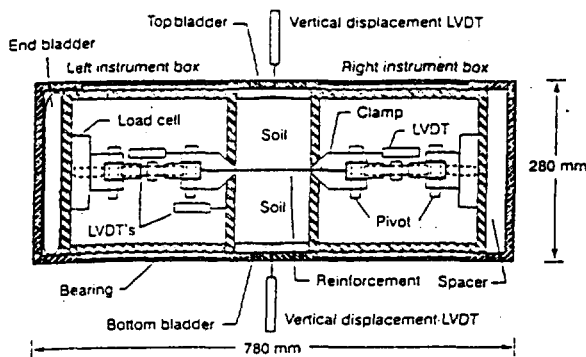


Figure 2: Unit Cell Device (UCD).

displace equally in the lateral direction during loading and that the faces of the specimen remain orthogonal. Because the UCD is a load control device, with load applied vertically to the soil specimen, neither the vertical nor horizontal (reinforcement) strain rates could be controlled, but they could be measured.

Dimensions and yield strain of the high-elongation strain gages used in the testing program are presented in Table 2. A single gage was attached at the center of each in-isolation specimen. Two or three gages were used in the in-soil tests; they were positioned along the length of the geotextile specimen to permit measurement of the strain distribution. After preparing the surface with a primer, the Tokyo Sokki Kenkyujo, Co., Ltd. Model YL-series gages were attached to the polypropylene woven geotextiles using a cyanoacrylate type CN adhesive. The BLH, Inc. SR-4 type, model PA-series gages were attached to the polyester geotextiles using an SR-4 adhesive, without priming the surface. To protect the strain gages during soil compaction and load application in the in-soil tests, the strain gages and their lead wires were coated with type MB-4 rubber cement and then covered with a small piece of 0.3 mm thick latex rubber.

Table 2: Strain gages tested.

Gage Type	Gage Length and Width (mm)	Backing Length and Width (mm)	Yield Strain (%)
YFLA-2	2 x 1.8	7.5 x 4	10 - 15
YL-10	10 x 3	20 x 7	10 - 20
YL-20	20 x 3	30 x 7	10 - 20
PA-3	19 x 11	51 x 13	10
PA-7	6.4 x 7.5	29 x 9.5	8

Additional details on the in-isolation test procedure and results; UCD design, operation, test procedure and results; geotextile sample preparation; and strain gage tests are presented in Boyle (1995a, b), Gallagher (1995), and Boyle et al. (1996).

2 RESULTS

2.1 In-isolation Test Results

The YL-20 strain gages, attached to the woven polypropylene slit-film geotextiles, PP1, PP2, and PP3, appeared to work adequately until they reached the gage yield strain or the backing started to debond from the geotextile, conditions that typically occurred between 6% and 12% strain. In all cases the YL-20 strain gages reported less strain than was recorded for the overall specimen.

To facilitate evaluation of strain gage performance we looked at the ratio of strain gage strain to total strain (SR), defined as:

$$SR = \epsilon_{sg}(t) / \epsilon_{total}(t) \quad (1)$$

where:

$\epsilon_{sg}(t)$ = strain gage strain at time t

$\epsilon_{total}(t)$ = total overall strain at time t

The SR for a given strain gage-reinforcement combination changed throughout each test and differed from one test to another, Figure 3. After the first 1% strain the SR typically increased to a maximum that occurred between 3% and 8% overall strain.

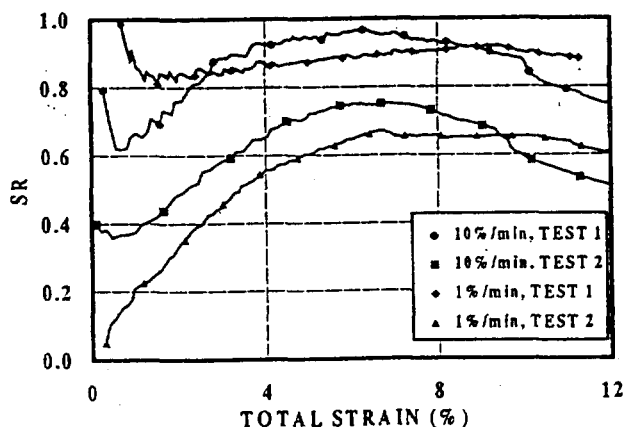


Figure 3: SR versus overall specimen strain for in-isolation test on PP2 with YL gages.

To reduce the influence of initial strain readings on the analysis, an incremental strain ratio, ISR, was defined:

$$ISR = \frac{\epsilon_{sg}(t_2) - \epsilon_{sg}(t_1)}{\epsilon_{total}(t_2) - \epsilon_{total}(t_1)} \quad (2)$$

For the YL gages, as shown in Figure 4, the ISR results fell in a slightly narrower band than was exhibited by the SR. The pattern of ISR versus total strain for the three polypropylene geotextiles were similar. The ISR generally increased to a maximum between 3% and 8% total strain, and then decreased at larger strains (Gallagher, 1995; Boyle, 1995a). The decrease in ISR, and SR, after about 8% strain likely results from debonding of the strain gage from the geotextile or may be due to yielding of the strain gage. At small strains, i.e., 0.5%, ISR values were typically in the range 0.1 to 0.5. The ISR values for the YL-20 gages tested in isolation increased to a maximum at strains greater than 3%. These maximums were typically between 0.8 and 1.2, although values as high as 1.3 were found. Thus, at higher strains, the incremental strain measured by the strain gages was relatively accurately measured. However, strains of this magnitude have not been commonly reported for instrumented wall case histories (Allen et al., 1992; McGown et al., 1993).

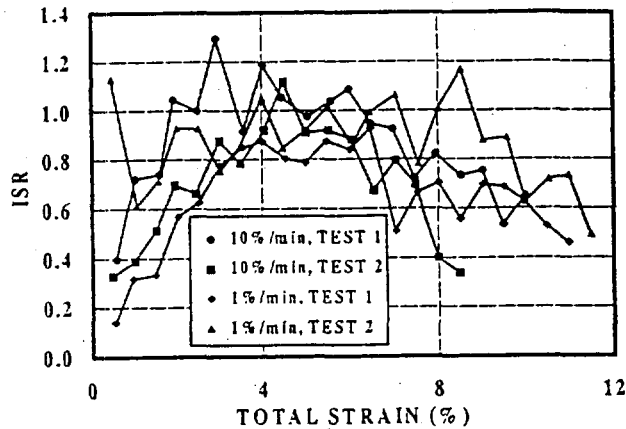


Figure 4: ISR versus overall specimen strain for in-isolation test on PP2 with YL gages

Tests with PA-3 gages attached to polyester reinforcement PET2 met with only limited success. Only two of the in-isolation tests conducted with these strain gages produced reasonable results (Gallagher, 1995). For these two tests, the initial ISR values of 0.78 and 0.91 were higher than the initial values for the YL-20 gages attached to the polypropylene geotextiles. The maximum ISR values were approximately 1.1. ISR values on this order indicate the strain gages were not underrecording incremental strain substantially. However, the non-incremental strain ratio, SR, did underrecord strains, and was sensitive to the initial "zero" strain gage reading selected. Because the PA-3 gages tended to debond from the polyester geotextile at strains between 1% and 3%, evaluation of strain gage performance at higher strains was not possible on the woven polyester geotextiles.

2.2 In-Soil Test Results

The pattern of strain recorded by the YL strain gages when attached to the polypropylene geotextiles, including creep strain, was similar to the pattern for overall lateral (geotextile) strain in the majority of the UCD strain gage tests conducted, Figure 5. This similarity, plus the smooth, continuous nature of the data, was interpreted as evidence that the strain gages were behaving properly. As in the in-isolation tests, the gages underrecorded total strain, Figures 5, 6, and 7. For YL gages attached to polypropylene reinforcements PP1, PP2, and PP3, the SR ranged from 0.3 to 1.0. As occurred in the in-isolation tests, during the initial stages of each test SR increased with increasing strain, Figure 6. Since total strain was limited (by the UCD device) to less than 6% in the in-soil tests, debonding or yield of the strain gages did not occur.

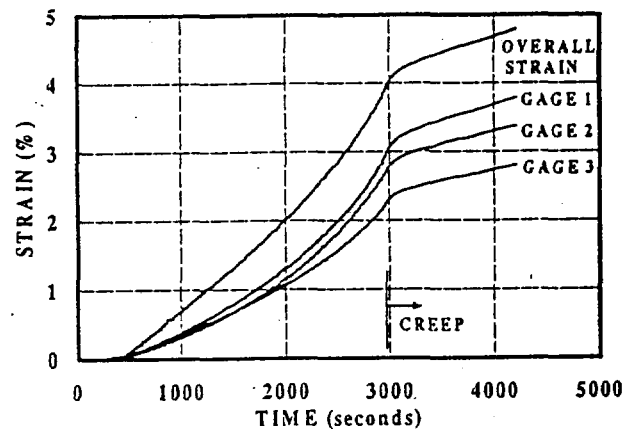


Figure 5: Overall specimen strain and strain gage measured strain for in-soil test, PP2 with YL-10 gages.

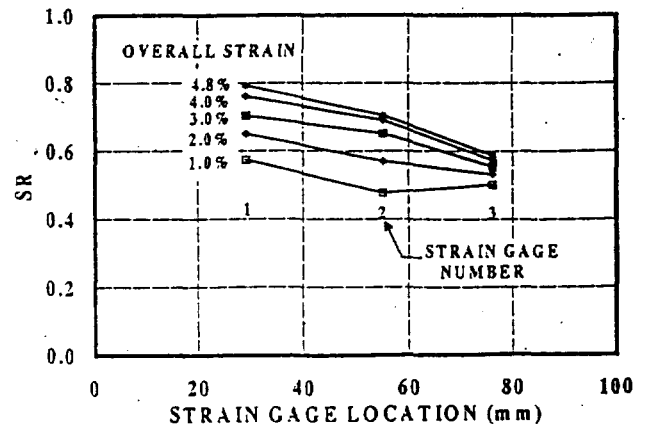


Figure 6: SR for gages at different locations along in-soil test specimen, PP2 with YL-10 gages.

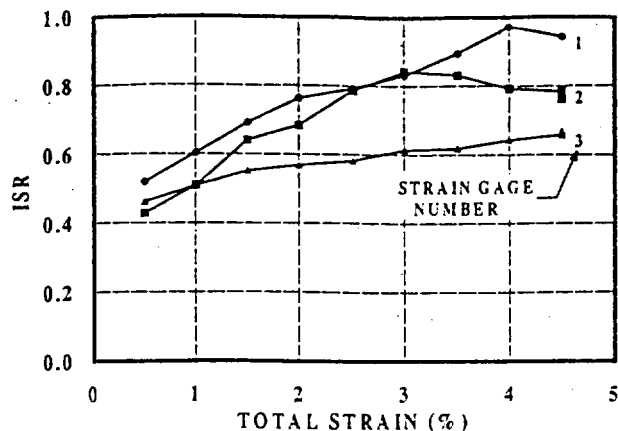


Figure 7: ISR for gages at different locations along in-soil test specimen, PP2 with YL-10 gages.

There was less fluctuation in the ISR values for the YL strain gages in in-soil tests than was recorded in the in-isolation tests, Figure 7. The smoothing of the response may be due to the reduction of specimen flexibility by confinement in soil. As with the in-isolation tests, the ISR for in-soil tests tended to increase with increasing overall specimen strain. Initial ISR values (e.g., at 0.5% strain) for the three different length YL gages were between 0.20 and 0.80. At higher strains ISR generally fell in the range 0.3 to 1.10, although maximums as high as 1.32 were observed, see Table 3. While SR or ISR values near 1.0 would indicate relatively accurate measurement of geotextile strains, the SR and ISR did not approach or exceed 1.0 until strains greater than 3% were attained. This is three times the strain reported in geosynthetic reinforced walls (Allen et al., 1992; McGown et al., 1993).

Table 3: Range of SR and ISR values.

Strain	YL-series gages		PA-series gages	
	In-Isolation	In-Soil	In-Isolation	In-Soil
SR				
0.5%	----	0.3 - 0.8	----	0.3 - 0.7
4% - 6%*	0.5 - 1.0	0.4 - 1.0	----	0.3 - 0.7
ISR				
0.5%	0.2 - 0.7	0.2 - 0.8	0.8 - 1.0	0.4 - 0.7
4% - 6%*	0.8 - 1.3	0.3 - 1.3	0.7 - 1.1	0.1 - 0.9

* Range at 1% to 2% used for PA gages.

Only two in-soil tests were conducted with PA-7 gages, both mounted on Reinforcement PET1. In these tests the ISR at 0.5% strain fell between 0.4 and 0.7, but ranged as wide as 0.1 to 0.9 at higher strains. These values are lower than was observed in the in-isolation tests for PA-3 gages attached to PET2. As with the in-isolation tests, the PA

gage responses were somewhat erratic and strains to only a few percent were recorded.

2.3 Discussion

The SR and ISR values for the YL gages in the in-soil tests were more uniform and less erratic than for the in-isolation tests. While the in-soil and in-isolation ISR values were similar, there was slightly less variation in the in-soil ISR values at each strain level, Table 3. From these tests, neither in-soil or in-isolation resulted in more accurate measurement of geotextile strains. At strains less than 2% the initial ISR for in-isolation tests were somewhat, though not significantly, lower than for in-soil tests. At strains from 4% to 6% in-isolation ISR values were slightly higher than in-soil values. Initial ISR values were also slightly lower for in-soil tests with YL-2 gages (7.6 mm length) than for the longer YL-10 (20.5 mm) and YL-20 (30.5 mm) gages. The PA gages did not behave better in-soil than in-isolation, and we experienced difficulties with their adhesion to the geotextiles under both test conditions. The in-isolation ISR values were closer to 1.0 than were the in-soil ISR values. This difference may be related to the different strain gage lengths; the longer PA-3 gage may be better at recording overall strain than the shorter PA-7 gage.

An insufficient number of tests were performed to conclude that the strain gages attached to geotextiles behaved better in in-soil tests than in in-isolation tests, or vice-versa, or that longer gages perform better than shorter ones. There is, however, sufficient data to conclude that strain gages of the type tested can be expected to underrecord both total and incremental strain when attached to woven polypropylene slit-film or woven polyester multi-filament geotextiles, especially at low strains. A number of factors may contribute to this phenomenon:

- Overall strain includes global rearrangement of the fibers and tightening of the weave. Tightening of the weave with increasing strain may partially explain the increase in SR and ISR values, and their leveling off after the first few percent strain.
- Strain gages are intended for application to smooth, flat surfaces; these conditions are not met when the gages are attached to woven geotextiles where the gages pass over multiple weaves in both the machine and cross-machine directions. The height and length of these "bumps" may be expected to change throughout the test as the reinforcement is strained. This change in degree of flatness of the gage may modify the gage resistance, thus affecting the output.
- The strain gages were not attached to a single geosynthetic fiber oriented in the direction of straining. They were attached to three parallel slit film strips or three parallel filament bundles, and the gages crossed strips and filament bundles oriented perpendicular to the

direction of strain. The independent action of the parallel slit-films or filament bundles to which the gages were attached can be expected to influence gage performance.

- d) In the in-soil tests, it is possible, even likely, that the geotextile sheets were arched very slightly when tested. The presence of such an arch, while unconfirmed, would result from the soil not being perfectly flat when the UCD specimen was constructed or from deformation of the soil during loading. During straining this arch may be increased, removed, or reversed, depending upon specimen behavior. Any change in the reinforcement orientation would influence the gage reading. This effect may be compensated for by attaching complementary gages directly opposite each other on each side of the geotextile specimen.

With the exception of item (d), these complicating factors are inherent to the nature of woven geotextiles and must be recognized as contributors to uncertainty when interpreting strain gage data.

Because the gages attached to the geotextiles did not accurately record overall strains, to estimate the true strain in a geotextile from strain gage measurements, it is necessary to apply a correction factor, CF. Such a factor can be computed by taking the reciprocal of SR and ISR (i.e., $CF_{SR} = 1/SR$ and $CF_{ISR} = 1/ISR$). Emphasizing typical test results, instead of the full range of variation presented in Table 3, we believe representative correction factors for the geotextile reinforcements and strain gages used in our program are as follows:

Table 4: Correction factors.

Strain (%)	YL - series gages		PA -series gages
	0.5	4 - 6	0.5
CF_{SR}	2.5-1.0	1.7-1.0	2.5-1.4
CF_{ISR}	5 - 1.7	2.0-0.9	2.5-0.9

The selection of representative correction factors is somewhat subjective, and is based upon our assessment of the quality of all of the tests conducted in the program, and involves some engineering judgment. Because of the spread in CF values, and the somewhat subjective nature in their selection, it is impractical to select a single correction factor to apply to a given strain gage reading. Instead, if correction factors are to be applied, we recommend a probable range be computed for the corrected strain gage measurement, and that this range be used in estimating overall geotextile strain from strain gage measurements. When using strain gage data to estimate true geotextile strains, our test program illustrates that the potential for error is greatest at low strains (less than 1%). This is unfortunate because for geosynthetic reinforced walls, for example, reported typical strain values are often of this magnitude (Allen et al., 1992; McGown et al., 1993).

In our program, the difference between the measured overall geotextile strain and that measured with strain gages is similar to that reported by Allen et al., (1992) for a 12.6 m high instrumented geotextile reinforced wall. The reinforcements and strain gages used in our program were the same or similar products and by the same manufacturers as those used by Allen et al. For measuring overall geotextile strain in the field, Allen et al., used mechanical extensometers. The extensometers tended to record greater strain than the electrical resistance strain gages in almost all cases.

Despite the apparent limitations and inaccuracies associated with using strain gages to measure overall and incremental strain of geotextiles, the test results provide evidence that strain gages can be effectively used to measure strain distribution and creep of geotextiles confined in soil, Figures 5, 6, and 7. The effectiveness of using strain gages to measure strain distribution and to record creep in geotextiles, as was found in our laboratory program (Boyle, 1995a), was also observed by Allen et al., (1992) in a full scale instrumented wall. Therefore, despite the inability to use strain gages to determine the true strain in geotextiles with confidence, strain gages appear to be useful instruments for determining the distribution of strain along woven geotextiles and for recording creep.

3 CONCLUSIONS

In this study, in the first few percent strain, i.e., at strains typically observed in geosynthetic reinforced walls, strain gages underrecorded by 20% to 80% both total and incremental strain. The degree of underrecording decreased at strains between 4% and 8% strain, and the incremental strain ratio was on the order of 1.0 in some cases. Because of the inaccuracies involved, we suggest that a range of probable geotextile strain values, not a single value, be reported when adjusting field strain gage data. This is an especially important consideration at small strains, e.g., less than 1%.

Despite our inability accurately measure the true geotextile strain using strain gages attached to woven geotextiles, we did find that strain gages could be effectively used to identify the distribution of strain along the geotextiles. Strain gages were also found to be effective for monitoring creep in geotextiles.

ACKNOWLEDGMENTS

This research was funded by the Washington State Department of Transportation, and their financial support is greatly appreciated. We thank T.M. Allen for his many helpful discussions and M. Gallagher for his assistance in conducting the laboratory tests.

REFERENCES

- Allen, T.M., Christopher, B.R., and Holtz, R.D. (1992), "Performance of a 12.6 m high geotextile wall in Seattle, Washington," *Geosynthetic-Reinforced Soil Retaining Walls*, Proceedings of the International Symposium on Geosynthetic-Reinforced Soil Retaining Walls, Denver, J.T.H. Wu ed., A.A. Balkema Publ., Rotterdam, pp. 81-100.
- Boyle, S.R. (1995a), *Deformation of Geosynthetic Reinforced Soil Retaining Walls*, Ph.D. Dissertation, University of Washington, 391 p.
- Boyle, S.R. (1995b), "Unit cell tests on reinforced cohesionless soils", *Proceedings of Geosynthetics '95*, Nashville, Vol. 3, pp. 1221-1234.
- Boyle, S.R., Gallagher, M. and Holtz, R.D. (1996), "Influence of strain rate, specimen length, and confinement on measured geotextile properties", *Geosynthetics International*, Vol. 3, No. 2, pp 205-225.
- Gallagher, M. (1995), *In-isolation wide width tests on geotextiles*, Master of Science Thesis, University of Washington.
- Industrial Fabrics Association International, 1989, "1990 Specifiers Guide", *Geotechnical Fabrics Report*, Vol. 7, No. 7, 120 p.
- Industrial Fabrics Association International, 1992, "1993 Specifiers Guide", *Geotechnical Fabrics Report*, Vol. 10, No. 7, 196 p.
- McGown, A., Yogarajah, I. and Yeo, K.C. (1993), "Choice of soil properties for limit state analysis of reinforced soil retaining structures", *Retaining Structures*, Proceedings of Conference on Retaining Structures, Cambridge, C.R.I. Clayton, ed., Thomas Telford Publishers, London, pp. 529-540.

Soil Confinement Effect on Stress-Strain Properties of Geosynthetics

Z. Yuan, R. H. Swan, Jr., and R. C. Bachus
GeoSyntec Consultants, Atlanta, Georgia, USA

V. Elias
Earth Engineering & Sciences, Inc., Baltimore, Maryland, USA

ABSTRACT: A confined extension test device was designed and fabricated for measuring the response of geosynthetic materials confined in soil. A series of confined extension tests was performed on each of five selected geosynthetic materials using the confined extension test device. Each test series consisted of one unconfined extension test and two confined extension tests, each conducted at a different level of normal stress. The test data were presented in the form of stress versus strain curves. Using the test data, secant moduli at select strain levels were calculated. A comparison was made between unconfined and confined moduli for each geosynthetic material to quantify the soil confinement effect on stress-strain properties. A comparison was also made between the relative increase of moduli at the same strain level among the five geosynthetic materials to demonstrate the different responses of these geosynthetic materials under soil confinement.

KEYWORDS: confined extension test, soil confinement, geosynthetics, geogrids, geotextiles, stress, strain, modulus.

1 INTRODUCTION

In the design of geosynthetic-reinforced soil structures, the tensile strength and modulus of the reinforcing material are important design parameters. These two parameters are commonly obtained from the wide-width tensile test, described in the American Society for Testing and Materials (ASTM) Standard Test Method D 4595. This test is conducted under unconfined (i.e., in-air) conditions which do not fully simulate field conditions. Under field conditions, the geosynthetics are almost always confined within soil. Questions have been raised regarding the potential beneficial effects on the stress-strain properties of the geosynthetics due to soil confinement.

To address these questions, several researchers have studied the effect of soil confinement on stress-strain properties of various geosynthetic materials using different test devices. These devices include: (i) the in-soil test device developed by McGown et al. [1982] and modified by Wilson-Fahmy et al. [1993]; (ii) the zero-span test device by Christopher et al. [1986]; (iii) the pullout test device by Holtz [1977] and Juran et al. [1991]; (iv) the modified triaxial test device by Ling et al. [1991] and Wu [1991]; (v) the plane strain unit cell device (UCD) by Boyle [1995]; (vi) the automated plane strain reinforcement (APSR) cell by Whittle et al. [1993]; and (vii) the modified direct shear test machine by Leshchinsky et al. [1987]. Characteristics of these test devices were described in detail in the final report to the Federal Highway Administration (FHWA) by Yuan et al. [1997].

After an extensive literature review and several series of test trials using different in-soil confined extension test devices, it was found that an in-soil test apparatus based on the initial design by McGown et al. [1982] including the revisions by Wilson-Fahmy et al. [1993] could be modified to provide a nearly constant strain rate and a nearly constant tensile load over the confined test specimen length. Using this device, the confined response of a geosynthetic material measured using the in-soil test apparatus can be directly compared with the unconfined response (ASTM D 4595) of a geosynthetic material to assess the overall effect of soil

confinement. This led to the decision to design and fabricate a new device which is conceptually similar to the in-soil test apparatus for use in a comparative testing program. Using the modified device, herein referred to as the confined extension test device, the confined stress-strain response of geosynthetics at different confining stresses were compared with the unconfined response of the same geosynthetic to evaluate the effect of soil confinement.

2 TEST PROGRAM

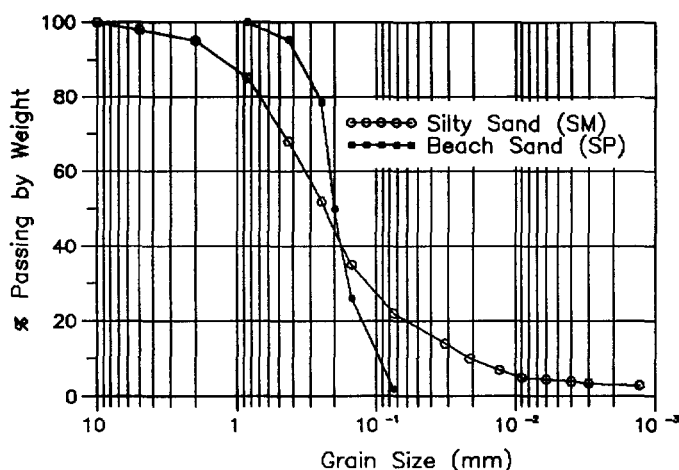
2.1 Testing Materials

The materials used in the testing program included five geosynthetic and two soil materials. A brief description of each geosynthetic material and its ultimate wide-width tensile strength as tested in accordance with ASTM D4595 are summarized in Table 1. Beach sand and silty sand were

Table 1. Summary of geosynthetic properties.

Geosynthetic Materials	Description	Tensile Strength (kN/m)
Geosynthetic PP-10	Staple-filament needle-punched polypropylene nonwoven geotextile	19.7
Geosynthetic PP-11	Slit-film and multi-filament polypropylene woven geotextile	70.1
Geosynthetic PP-12	Mono-filament polypropylene woven geotextile	40.3
Geosynthetic PE-13	Extruded polyethylene geogrid	86.0
Geosynthetic PET-14	Polyester geogrid	85.5

used as the two soils in the testing program. For each of the two soil materials, a particle-size analysis was performed; results are shown in Figure 1. Based on the



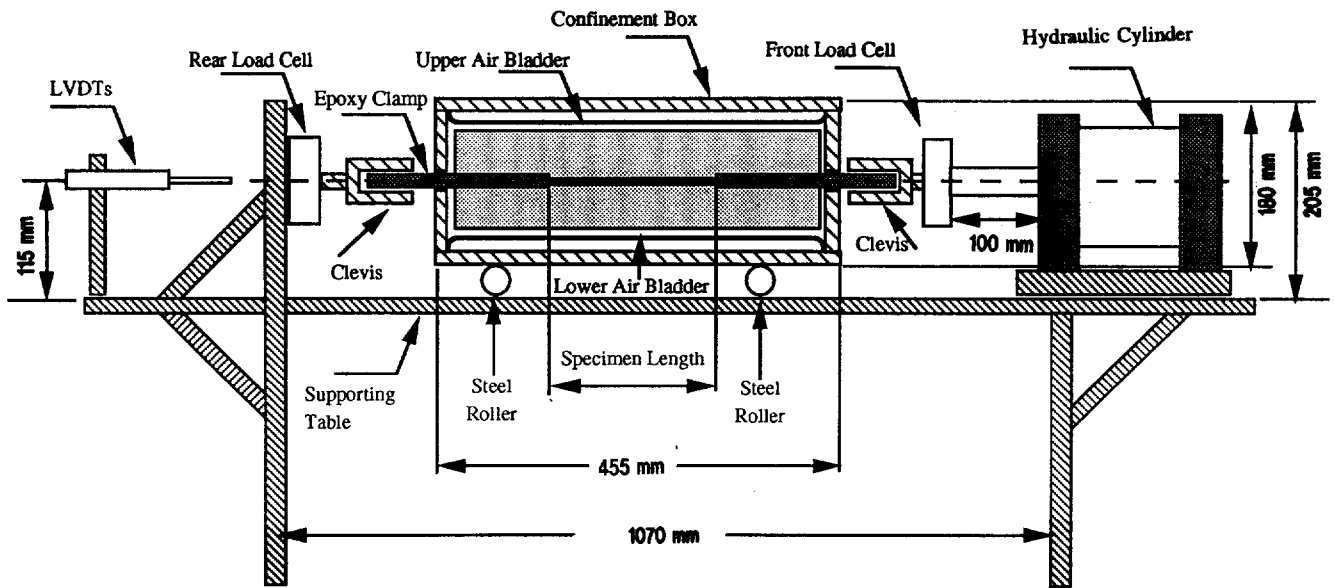


Figure 2. Details of confined extension test device.

constant rate of displacement as measured on the front specimen clamp.

Tensile loads were measured at the front and rear end of the geosynthetic specimen using two electronic load cells. Displacements at the front and rear ends of the geosynthetic specimens were measured using two linear variable differential transformers (LVDTs), each connected to a "tell-tail" wire which was attached to the geosynthetic specimen within the confinement box. Load and displacement data were recorded using a computer data acquisition system.

There were five major test variables involved in the testing procedure established for conducting confined extension tests. These variables were: (i) pretension force; (ii) strain rate; (iii) aspect ratio; (iv) thickness of the confining soil; and (v) boundary friction on the upper and lower surfaces of confining soil. The first three test variables were selected in accordance with ASTM D 4595 as follows:

1. **Pretension Force:** A total pretension force equal to 1.25 percent of the expected breaking force was applied to each geosynthetic specimen. However, the total pretension force was not less than 45 N or greater than 222 N in any case. The pretension force was applied to the geosynthetic specimen prior to placement of the upper confining soil layer.
2. **Strain Rate:** A constant rate of strain of 10 percent per minute was applied to the geosynthetic specimen in the confined extension test.
3. **Aspect Ratio:** An aspect ratio of 2:1 was used for geotextile specimens with a specimen width of 200 mm. For the geogrid, the test specimen was trimmed in such a way that it had a length containing at least two complete apertures in the direction of testing and a width containing at least five ribs in the cross-test direction.

The soil thickness and boundary conditions were selected

based on the results of two preliminary confined extension tests, as will be described below.

The effect of soil thickness on the confined response of geosynthetics was investigated through a series of confined extension tests on Geosynthetic PP-10 confined between two layers of beach sand with thicknesses ranging from 10 to 76 mm. The test results, as shown in Figure 3, indicate that there was little difference among the confined responses of Geosynthetic PP-10 when it was confined between 25-to 76-mm thick soil layers. However, the effect of soil confinement was reduced when the thickness of the soil layer was reduced to 10 mm due to the fact that cracks developed throughout the thickness of the soil layers, resulting in partial confinement of the geosynthetic specimen. To provide full confinement of the geosynthetic specimen, a soil thickness of 76 mm was then selected for all of the confined extension tests in this study.

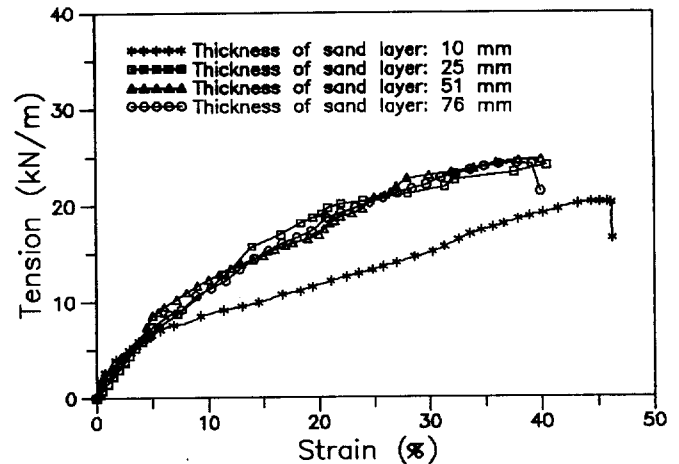


Figure 3. Responses of Geosynthetic PP-10 confined within various thicknesses of beach sand layers.

The effect of the boundary friction on the confined response of geosynthetics was investigated through a series of confined extension tests on Geosynthetic PP-10, each test conducted under one of the following two boundary conditions:

1. Condition 1: no lubrication between the air bladder and confining soil while the confinement box was allowed to move; and
2. Condition 2: lubrication between the air bladder and confining soil while the confinement box was fixed to the supporting table during testing.

The lubrication was achieved by placing two layers of lubricated latex membranes on the contact surface between the bladder and confining soil. In each test the geosynthetic specimen was confined between 10-mm thick beach sand layers in order to directly compare the effect of the boundary condition. The test results, as shown in Figure 4,

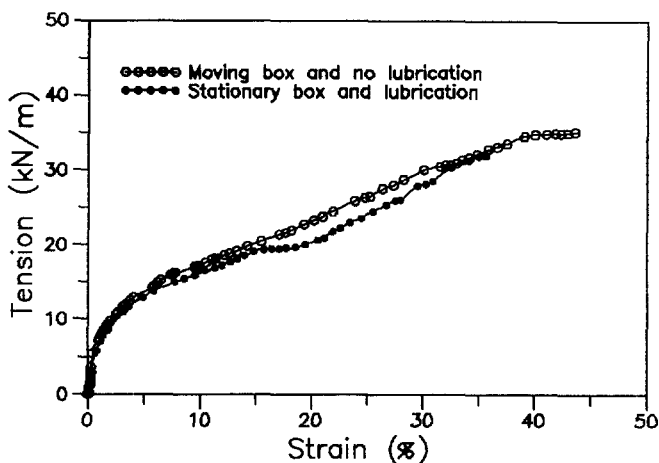


Figure 4. Confined responses of Geosynthetic PP-10 under lubricated and unlubricated boundary conditions.

indicate that the confined stress-strain curves of Geosynthetic PP-10 are very similar when tested in accordance with conditions 1 and 2. Because of the small difference between these results, condition 1 was selected for the boundary condition during the testing program.

3 TEST RESULTS

Ten test series were conducted in the testing program. Each test series consisted of one unconfined and two confined extension tests on one of the five selected geosynthetic materials. Each geosynthetic material was confined within beach sand (Test Series 1 through 5) or silty sand (Test Series 6 through 10) under two different normal stresses (69 and 138 kPa). For each test, tensile loads and displacements were measured at the front and rear end of the geosynthetic specimen by load cells and LVDTs, respectively, and recorded using the computer data acquisition system. The load and displacement data were subsequently used to develop the tensile force (i.e., load

divided by initial specimen width) versus strain (i.e., total displacement divided by initial specimen length) curves.

To quantify the improvement due to the soil confinement, secant moduli at 1, 5, and 10 percent strain levels and peak strength were calculated for each test and summarized in Table 3. For this paper, the secant modulus at 5 percent strain was selected to quantify the effect of soil confinement. The improvement of secant moduli at 5 percent strain was plotted versus confining pressure for each geosynthetic material confined in the beach sand and in the silty sand as shown in Figures 5 and 6, respectively.

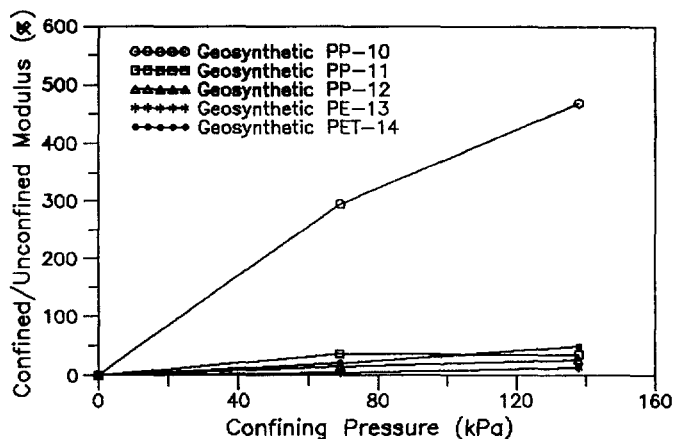


Figure 5. Confinement effect of beach sand on secant modulus at 5 percent strain.

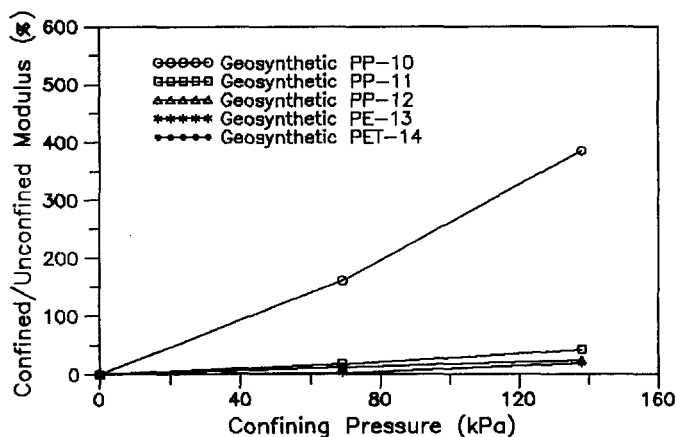


Figure 6. Confinement effect of silty sand on secant modulus at 5 percent strain.

In these plots "improvement" is defined as the ratio of the confined secant modulus to the unconfined secant modulus at a strain level of 5 percent. These figures clearly demonstrate that the Geosynthetic PP-10 is significantly affected by soil confinement and the other four geosynthetic materials are less affected by soil confinement. The comparison between Figures 5 and 6 indicates that the confinement effect of the beach sand is greater than that of the silty sand.

Table 3. Summary of confined extension test results.

Test Series Number	Geosynthetic Material ⁽¹⁾	Confining Material ⁽²⁾	Confining Pressure (kPa)	Modulus at 1% Strain (kN/m)	Modulus at 5% Strain (kN/m)	Modulus at 10% Strain (kN/m)	Peak Strength (kN/m)
1	PP-10 in machine direction	in-air beach sand beach sand	0	81.9	59.0	62.7	19.8
			69	137.1	232.5	162.4	26.5
			138	341.9	335.8	246.8	37.1
2	PP-11 in cross machine direction	in-air beach sand beach sand	0	674.7	618.1	560.4	88.0
			69	828.5	840.7	706.8	95.7
			138	790.0	836.8	715.2	108.6
3	PP-12 in machine direction	in-air beach sand beach sand	0	559.6	417.1	326.5	49.7
			69	783.4	480.8	381.2	56.2
			138	957.9	527.0	424.7	61.8
4	PE-13 in machine direction	in-air beach sand beach sand	0	1135.9	832.7	680.5	85.6
			69	1221.7	868.6	693.4	85.9
			138	1290.4	948.5	675.4	86.7
5	PET-14 in machine direction	in-air beach sand beach sand	0	989.7	930.3	837.0	92.3
			69	907.5	1097.4	914.0	94.5
			138	962.1	1361.1	983.4	103.7
6	PP-10 in machine direction	in-air silty sand silty sand	0	81.9	59.0	62.7	19.8
			69	116.9	153.3	108.1	24.3
			138	277.8	286.0	233.8	31.5
7	PP-11 in cross machine direction	in-air silty sand silty sand	0	674.7	618.1	560.4	88.0
			69	934.3	731.4	620.6	98.6
			138	1089.6	879.9	769.4	104.4
8	PP-12 in machine direction	in-air silty sand silty sand	0	559.6	417.1	326.5	49.7
			69	644.3	467.4	364.5	52.8
			138	754.1	520.5	393.0	60.0
9	PE-13 in machine direction	in-air silty sand silty sand	0	1135.9	832.7	680.5	85.6
			69	1296.3	854.0	726.0	84.5
			138	1322.9	991.6	768.4	87.4
10	PET-14 in machine direction	in-air silty sand silty Sand	0	989.7	930.3	837.0	92.3
			69	1174.8	1046.3	875.7	97.7
			138	1397.9	1250.4	984.9	105.1

Notes: (1) For Geosynthetics PP-10, PP-11 and PP-12, each test specimen was 200 mm in width and 100 mm in gage length. For Geosynthetics PE-13 and PET-14, each test specimen had two full apertures in the machine direction and five ribs in the cross-machine direction.

(2) For each confined extension test, the geosynthetic specimen was confined between two 76-mm thick layers of beach sand or silty sand.

4 CONCLUSIONS

A confined extension test apparatus was designed, fabricated, calibrated, and used in a comparative testing program. The advantages of the test apparatus fabricated for this study include: (i) ease of the test set-up; (ii) well-defined boundary conditions; and (iii) ease of test interpretation. Based on the results of the calibration tests, a nearly uniform distribution of tensile strain along the specimen length was achieved. Because of this relatively uniform distribution, the confined stress-strain response of the geosynthetic was readily obtained from the measured data and used for a direct comparison with the unconfined response of the geosynthetic to evaluate the effect of soil confinement. Further evaluations can be performed using this device to study the effects of full and partial confinement and creep behavior of geosynthetic materials.

Based on the results of the ten confined extension tests series, the following conclusions can be drawn:

1. Soil confinement significantly improves the moduli and strength of Geosynthetic PP-10. As the confining pressures increases, the moduli and strength of this material similarly increases. The 5 percent moduli of Geosynthetic PP-10 increased by approximately 200 to 400 percent when confined in the beach sand and 50 to 300 percent in the silty sand under confining pressures of 69 and 138 kPa.
2. Under the same confining pressure, the confined response (i.e., modulus and strength) of Geosynthetic PP-10 in beach sand is greater than that of Geosynthetic PP-10 in silty sand.
3. There is a noticeable effect of confinement with respect to the confined response for the two woven geotextiles and two geogrids (Geosynthetics PP-11, PP-12, PE-13, and PET-14) when confined in the beach sand and in the silty sand; the increase of the 5 percent moduli ranged from approximately 5 to 30 percent among Geosynthetics PP-11, PP-12, PE-13, and PET-14 at a normal stress of 138 kPa. These increases can be considered significant with respect to unconfined moduli of the same materials although considered less significant when compared with the increase of the 5 percent moduli for the nonwoven geotextile (Geosynthetic PP-10).
4. Improvement of the confined stress-strain properties for a given geosynthetic material may be primarily related to: (i) internal friction between fibers or yarns; (ii) alignment of curved fibers or yarns (i.e., tortuosity); and (iii) interlocking of soil within openings or apertures of geosynthetics.

ACKNOWLEDGEMENTS

The research presented in this paper was supported by the FHWA. The support of the FHWA is greatly appreciated. The authors would like to thank Drs. B. Christopher, R.M. Koerner, and R.D. Holtz for their comments on the original

report of this research program submitted to the FHWA on which this paper is based.

REFERENCES

- Boyle, S.R. (1995), "Unit Cell Test on Reinforced Cohesionless Soils", *Proceedings of Geosynthetics '95*, Nashville, Vol. 3, Feb, pp. 1221-1234.
- Christopher, B.R., Holtz, R.D., and Bell, W.D. (1986), "New Tests for Determining the In-Soil Stress-Strain Properties of Geotextiles", *Proceedings of 3rd International Conference on Geotextiles*, Vol. 3, Vienna, pp. 683-688
- Holtz, R.D. (1977), "Laboratory Studies of Reinforced Earth Using a Woven Polyester Fabric", *International Conference on the Use of Fabrics in Geotechnics*, Paris, Vol 2, pp. 149-154.
- Juran, I., Farrag, K.H., and Richmond, L. (1991), "Short and Long Term Performance of Polymeric Geogrids", *Proceedings of Geosynthetics '91*, Vol. 2, Atlanta, Feb, pp. 587-599.
- Leshchinsky, D. and Field, D.A. (1987), "In-Soil Load Elongation, Tensile Strength and Interface Friction of Nonwoven Geotextile", *Proceedings of Geosynthetics '87*, New Orleans, pp. 238-249.
- Ling, H.I., Wu, J.T.H., and Tatsuoka, F. (1991), "Effectiveness of In-Membrane Test in Simulating Strength and Deformation Characteristics of a Nonwoven Geotextile Under Operational Conditions", *Proceedings of Geosynthetics '91 Conference*, Atlanta, Feb, Vol. 2, pp.601-614.
- McGown, A., Andrawes, K.Z., and Kabir, M.H. (1982), "Load-Extension Testing of Geotextiles Confined In-Soils", *Proceedings of 2nd International Conference on Geotextiles*, Las Vegas, pp. 793-798.
- Whittle, A.J., Larson, D.G., Germaine, J.T., and Abramento, M. (1993), "A New Device for Evaluating Load-Transfer in Geosynthetic Reinforced Soils", *ASTM STP 1190*, pp. 1-15.
- Wilson-Fahmy, R.F., Koerner, R.M., and Fleck, J.A. (1993), "Unconfined and Confined Wide-Width Tension Testing of Geosynthetics", *ASTM STP 1190*, pp. 49-63.
- Wu, J.T.H. (1991), "Measuring Inherent Load-Extension Properties of Geotextiles for Design of Reinforced Structures", *Geotechnical Testing Journal*, Vol. 14, No. 2, Jan, pp. 157-165.
- Yuan, Z., Swan, R.H., Bachus, R.C., and Elias, V. (1997), "Development of Protocol Confined Extension/Creep Testing of Geosynthetics for Highway Applications", Submitted to the Federal Highway Administration, U.S. Department of Transportation.

The Testing of Geosynthetic Reinforcements

Peter E. Stevenson

Project Manager, The Tensar Corporation, Atlanta, Georgia

Todd R. Skochdopole

Manager of Research and Development, The Tensar Corporation, Atlanta, Georgia

Ajit D. Kelkar, Professor, North Carolina A&T State University, Greensboro, NC

ABSTRACT: Concurrent with a product development program, a review of the testing of reinforcements was conducted. Review of more than 100 published articles revealed that: (1) Researchers have identified 14 issues of concern to the design engineer as well as the manufacturer of geosynthetic reinforcements. (2) The geosynthetic and geotechnical community have not fully exploited the technical resources (data base and knowledge) of the textile industry. (3) Data for reinforcement products is inconsistently reported, resulting in potential misinterpretation. (4) Little research has been conducted on the testing of high performance geosynthetic reinforcements. This paper will review the above and present a test methodology that: (1) addresses the issues of concern, (2) is based on detailed research and experimentation, (3) is easily verified, is repeatable and reproducible.

KEYWORDS: Mechanical properties, tensile strength, modulus, testing, woven fabrics, knit fabrics, specifications.

1 INTRODUCTION

Much research has been conducted on the type of wide width testing represented by ASTM D4595 and ISO 10319 in hopes of establishing a relationship between laboratory testing and the plane strain conditions a geosynthetic experiences in use. The references cited in this paper represent the key portion of the work that deals with some aspect of wide width testing of geosynthetics. 53 references in the literature explore wide width testing. Less than 10 address reinforcements and 5 of the 10 report serious concerns about current methodology and the results of its application to high strength materials (Haliburton 1978; Myles et al. 1986; Rowe et al. 1986; Leschinsky et al. 1990; Brand et al. 1991). In the period from 1977 (Finnigan 1977) through the present, 14 issues of concern have been identified with the testing of reinforcements with many of these concerns yet unresolved. The research reported here focuses specifically on the testing of textile products employing high tenacity industrial quality multifilament textile yarns from such polymers as polyester (PET), polyamide (nylon), and polyvinyl alcohol (PVA).

The specific concerns about testing of reinforcing products expressed in the literature are: (1) the effect of sample gauge (length) on reported values including tensile strength, extension and modulus, (2) the effect of test speed, i.e. strain rate on reported values: one specific issue is the difference between ASTM at 10% and ISO at 20% per minute, (3) the effect of fabric structure (weave) on reported values, (4) the effect of jaw or grip types on reported values, (5) the control of sample slippage in grips, (6) the amount of tolerable slippage in clamping devices, (7) the accuracy of various extension measurement systems,

(8) the effect of the extension measurement system on the reported values, (9) the effect of sample width on reported values, (10) the effect of preload on reported values, (11) the definition, measurement and reporting of modulus, (12) which modulus is important?, (13) what portion of the sample does a reported modulus represent?, (14) is there a demonstrated relationship between single end yarn test values and fabric test values?

The research reported in this paper is directed toward developing a repeatable and reproducible test method for textile reinforcements. This presentation focuses on 8 of the concerns. The issues addressed are sample length, sample gauge (area of extension measurement), method of extension measurement, fabric structure, test preloads and modulus. Reference is made but specific research is not reported for jaw types, slippage, sample width and yarn to fabric relationship. The investigation includes both conventional roller grip systems and pressure clamping systems. The pressure clamping system incorporates a technique used in other disciplines for very strong materials. This technique is the application of sacrificial tabs to the clamping area of the specimen, thus permitting very high jaw pressures without specimen damage. A second modification to test protocol involved the use of long samples, 0.508 m between grips. Long samples have two benefits, first the sample geometry is similar between roller and tab systems and longer samples reduce the effect of variation in test speed on results. It is important to note that, the techniques employed in this work are applicable to conventional textiles produced from multifilament yarns based on polymers whose glass transition point is at or above the testing temperature. It is the authors opinion that the techniques in the test method that produce meaningful

information for very strong textiles will not be necessary for other textile based geosynthetics such as nonwovens or separation membranes. A specific caution applies to robust fabrics produced from polypropylene yarns. While the variations in test results caused by variation in testing speed can be substantially neutralized for fibers, yarns and fabrics produced from nylon and polyester, the same cannot be said for polypropylene textiles unless tests are conducted at temperatures below -10°C . Given an accurate description of applicability, technique, preparation, equipment, and clear and accurate reporting requirements, this methodology can be incorporated in the standard test methodologies already extant in the geosynthetics industry.

2 RESULTS OF THE INVESTIGATION

2.1 The Importance of Fabric Structure on the Testing of High Strength Reinforcements.

Several researchers have noted that the structure of a product has a profound impact on the performance of that product in a testing protocol. Research can be interpreted to describe the structure of the reinforcement (fabric) as the dominant condition of the testing protocol (Rowe and Ho 1986). This concept is confirmed by a text sponsored by the NGO (Balkema 1986), which conducts a detailed discussion of the effects of fabric and yarn crimp, sample width, and cross contraction under load in confined and unconfined tests with the conclusion that the structure of

the fabric and the size of the sample will dominate the protocol and dictate the hierarchy of the results. Figures 1 and 2 present comparative test results for two groups of fabrics. For both groups all conditions are uniform except sample structure. Figure 1 presents 6 fabrics produced to the same performance specification, (5 of these fabrics employ a common warp in different structures, the sixth was produced separately). Figure 2 presents an additional 5 fabrics, all from a common warp of a different polymer. The wide variation in the curves and the shape of the curves demonstrates the dramatic effect of fabric structure on the results from a tensile test. Fabric structure is manipulated by the designer/producer to achieve a performance level. Test conditions cannot "correct" the impact of structure on results because structure clearly has

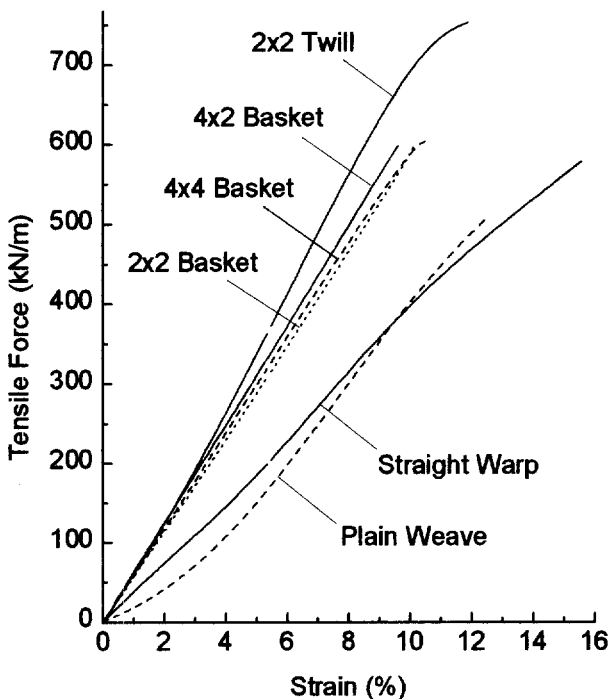


Figure 1. Performance Variation of Polyester Fabric Structure

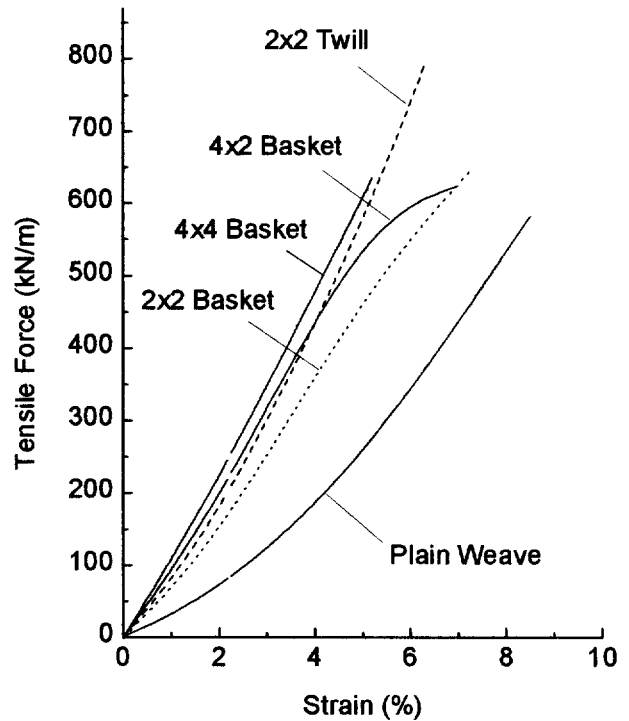


Figure 2. Performance Variation of PVA Fabric Structure an impact on performance.

2.2 The Effect of Preloads on Test Results

Three widely referenced test methods for the reporting of geosynthetic properties are ASTM D4595, ISO 10319:1993 and BS 6906. Subtle differences in test conditions and important differences in reporting exist between the methods. Both ISO and the British Standard cite a maximum preload of 1% of breaking strength while ASTM allows 1.25% not to exceed 0.73 kN/m. The ASTM method appears more conservative for very high strength materials: however, ISO and BSI recommend stress strain curves that

include any initial elongation established in the application of preload. ASTM allows the presentation of data without reporting the initial elongation and acknowledges in a note that ASTM does not have agreement on the point of origin (zero position). Myles (1986) clearly defined the logic and the method in which to record the test initiation, a “daylight” point and total offset to be used for calculation

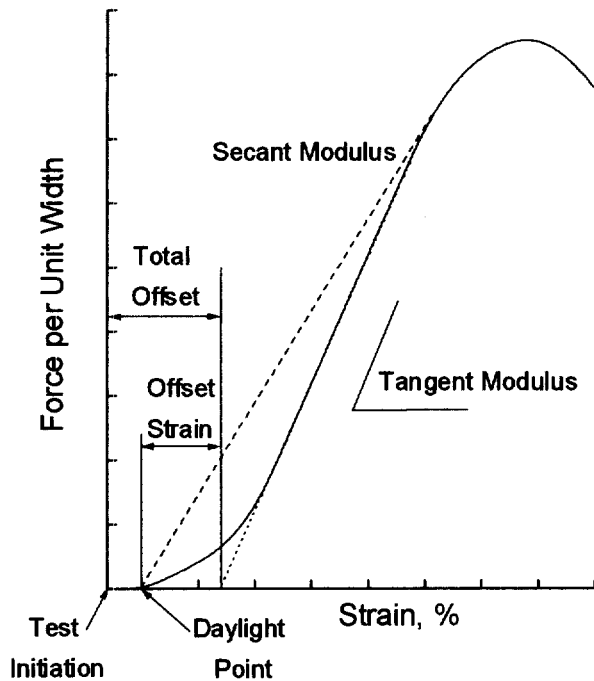


Figure 3. Stress-Strain Curve with Complete Test Results

of secant and tangent moduli as shown in Figure 3.

The test methods cited above are employed equally for a wide range of geosynthetics. The significance of tensile strength and modulus are not the same for all classes of geosynthetics. Unreported stress, strain and modulus data on a filter is not a concern to the designer. Any such unreported data on products used in critical structures is, or should be, a significant concern. One illustration of the importance of accurate reporting is the effect of preloads. Figure 4 presents the effect of preload variation on a set of identical samples tested on roller grips. The significance of geosynthetic performance at low strain is increasingly recognized as significant to the working range of successful construction projects (Craig 1997, Fakher et al. 1996). Current specifications are frequently governed by strength requirements at strains of 5%. Because testing preload has such profound effect on reported data at low strain values, it is essential that the design engineer have both a good understanding of test protocol and accurate data in order to employ reinforcements in such designs. Figure 4 demonstrates that application of a 222 N preload results in a 15 to 20% increase in reported load at 5% strain and that

successively higher preloads more than double T5 values. Ultimate strength is nearly independent of preload; however, there can be a modest decrease in ultimate strain as preload increases. Figure 5 demonstrates that preloads

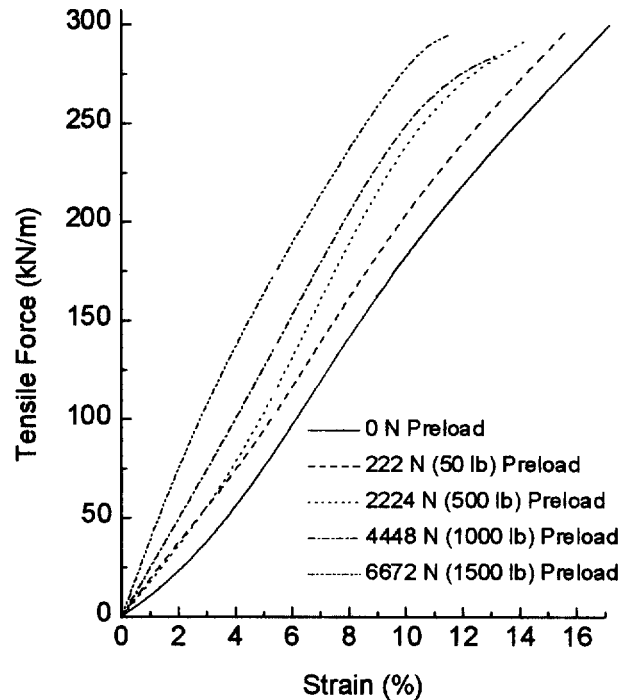


Figure 4. Effect of Preload on Identical Samples Using Roller Grips

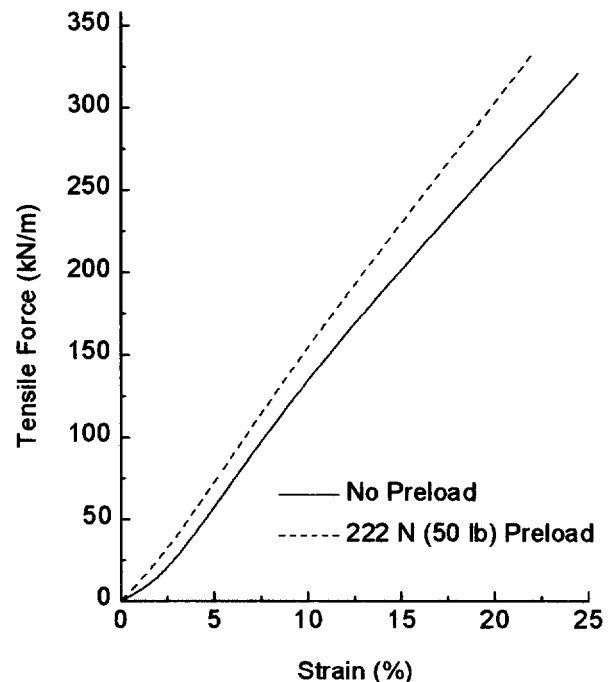


Figure 5. Effect of Preload on Identical Samples Using Tab Grips

produce the same data inflation in the tab system that was seen in figure 4 for roller testing. Figure 6 presents 2 widely different fabric structures produced to the same specification tested under no preload and under a high preload using roller grips. Clearly preloads inflate data regardless of fabric structure or gripping system. When employing roller grips, the use of preload in testing of very strong geosynthetic reinforcements is obviously necessary in order to remove slack and to seat samples in the testing device. The recording of preloads applied in testing of very strong geosynthetic reinforcements is important, and the full reporting of extension when applying preloads is essential to insure data is presented in complete form. The reporting of tests performed on high strength textiles should

are related to segments of the stress strain curve. The ISO and BSI definitions are compatible with ASTM in language; however, the ISO and BSI curves, with the reporting of extension from test initiation, clearly include data that ASTM excludes. The point is that the reporting of a value at 2% or 5% strain on a secant calculated from a body of data that omits part of the specimen extension data should be of little value to the designer of a critical structure.

During the execution of a test, data for the entire curve can be recorded. With the salient data available for analysis, information concerning any, and every, segment of the load elongation curve can be observed. Initial modulus should be defined as the linear portion of the test curve from the initiation point to the point where the curve

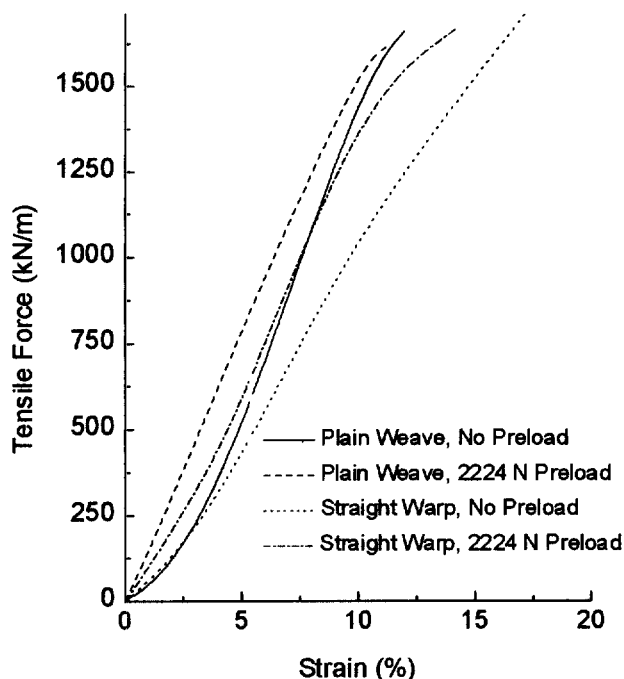


Figure 6. Effect of Preload Regardless of Structure, Using Roller Grips

include test initiation, daylight point and the total offset as mentioned by Myles (1986).

2.3 The Definition of and Reporting of Modulus

Due to poor agreement between sources, the definitions of modulus can be problematic for the authors of specifications and test reports on reinforcing geosynthetics. The problem is the selection of the portions of the curve to be included in the calculations. ASTM D4595 defines initial tensile modulus as “the ratio of change in tensile force per unit width to a change in strain (slope) of the initial portion of the force per unit width strain curve.” ASTM also defines offset modulus and secant modulus in similar terms with the clear intent that all of these concepts

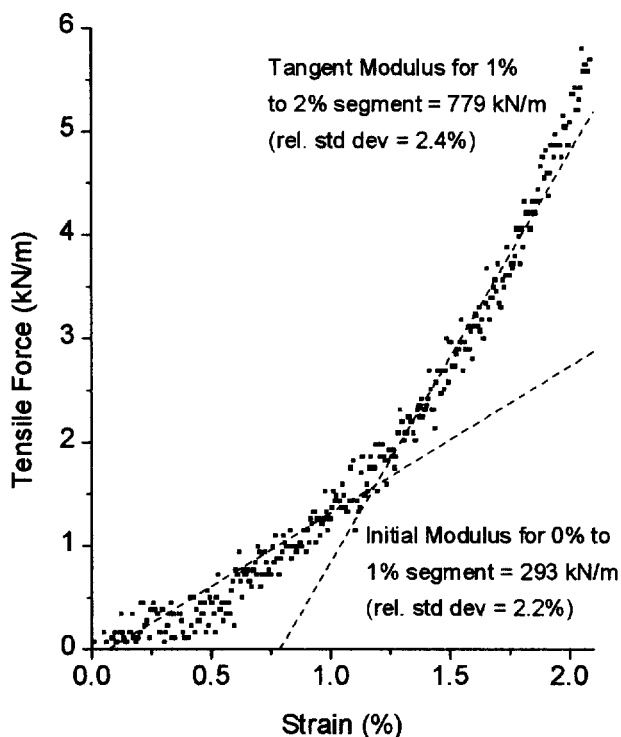


Figure 7. Measurement of Initial Modulus Data Using Tab System with No Applied Preload

shifts to non linearity. Figure 7 presents 2 best fit lines for 2 segments of a stress strain curve. Segment (a) represents 0 to 1%. Segment (b) represents 1 to 2%.

2.4 The Effect of Sample Gauge on Test Results

One of the principle concerns of the research community in its review of wide width testing on reinforcements was the effect of sample gauge. The authors conclude that the 100 mm sample gauge has proven to be inadequate for reinforcements. Finnigan (1977), Sisson (1977) and Van

Leeuwen (1977) all cited standard testing protocols for strong fabrics as the textile strip method in which sample length was typically 2 to 4 times the width. Recognition that the strip concept of sample configuration is most appropriate for strong tensile members is recognized repeatedly throughout the literature, ASTM D5035, a strip test, is representative of the standard method for testing strong textiles and employs long thin specimens. The NGO (Balkema 1986) provide discussion of the mechanisms of testing and effects of gauge, width and structure. The concept of long sample lengths is common to the textile industry reflecting the producers understanding that short sample lengths inflate strength and extension while deflating modulus. Pan et al. (1997) showed that a small variation in length of textile reinforcements had a large effect on results. Experiments were conducted using long samples, up to 0.508 m, in the sacrificial tab method in search of a neutral gauge for multifilament textile products using polyester, polyamide or other industrial fibers. Data indicates that a small variation in length of textile reinforcements has a large effect on results. The experiments indicate that for multifilament textile products using polyester, polyamide or other industrial fibers both the effects of sample length and of variations in test speed are greatly reduced by long specimens. Figure 8 presents the effect of strain rate on initial modulus as a function of specimen length. Initial modulus is defined as "the linear portion of the test curve from the test initiation point to the point where the curve shifts to nonlinearity". Figure 9 presents the effect of strain rate on segment (3%-ULT)

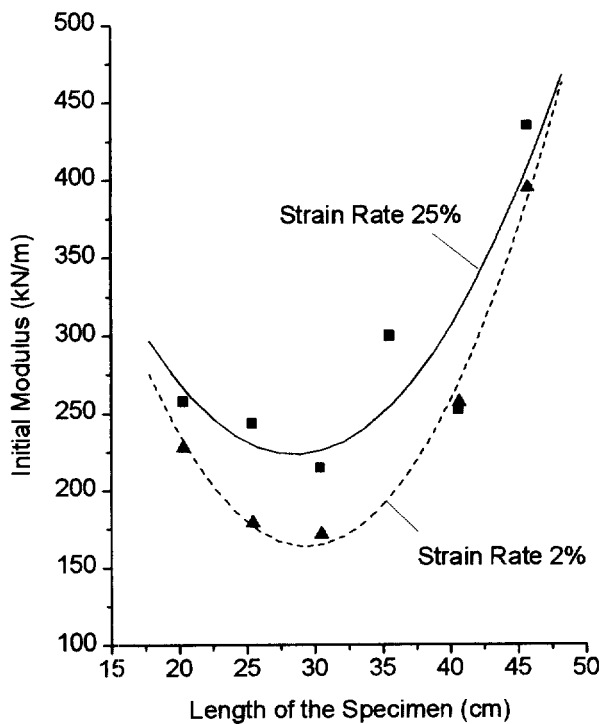


Figure 8. Effect of Strain Rate on Initial Modulus

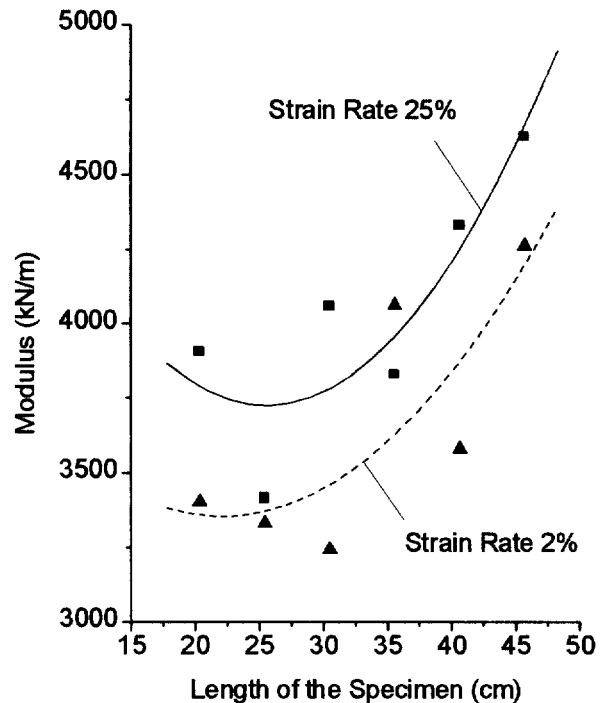


Figure 9. Effect of Strain Rate on Segment (3%-ULT) Modulus

modulus as a function of specimen length and Table 1 presents a comparison of standard deviation for initial and segment modulus.

Table 1. Comparison of Standard Deviation for Initial and Segment Modulus

Length of Specimen, cm	% Strain Rate per min	% Standard Deviation of Initial Modulus	% Standard Deviation of Segment Modulus
20.3	25	2.2	0.8
20.3	2	0.9	0.5
25.4	25	2.1	0.8
25.4	2	1.3	0.4
30.5	25	2.6	1.1
30.5	2	1.1	0.4
35.6	25	2.7	0.9
35.6	2	1.4	0.8
40.6	25	2.2	1.6
40.6	2	1.0	0.4
45.7	25	2.6	1.3
45.7	2	1.0	1.3

2.5. Strain Measurement

The measurement of strain in testing of geosynthetics is widely acknowledged to be difficult and it is particularly so for the high strength materials used in reinforcements. The ISO method dictates that the extensometer be capable of measuring the distance between two reference points on the specimen without any damage to the specimen or slippage in relation to the specimen and resulting in a measurement representing the true movement of the reference points. The four strain measurement techniques cited in the literature and the ISO test method are mechanical, optical, infrared or electrical devices. Mechanical devices include both crosshead movement (displacement of the clamps) and lvdt's (linear displacement measurement devices) or mechanical devices attached to the specimen. Optical devices include video and laser systems. All of which observe a small section of the specimen. The principle issues are specimen damage, rate of strain and confirmation of accuracy. The experiences reported by Brand and Pang (1991) and Leschinsky and Fowler (1990) define the difficulties experienced in accurate measurement of strain on very strong geosynthetic materials regardless of device type, and reflect the broad concern that accuracy needs to be verified by comparison of two or more measurement techniques. Figure 10 presents a comparison of curves from specimens in which extension was recorded simultaneously for both displacement and an optical device. The excellent agreement at low strain is most significant to the designer

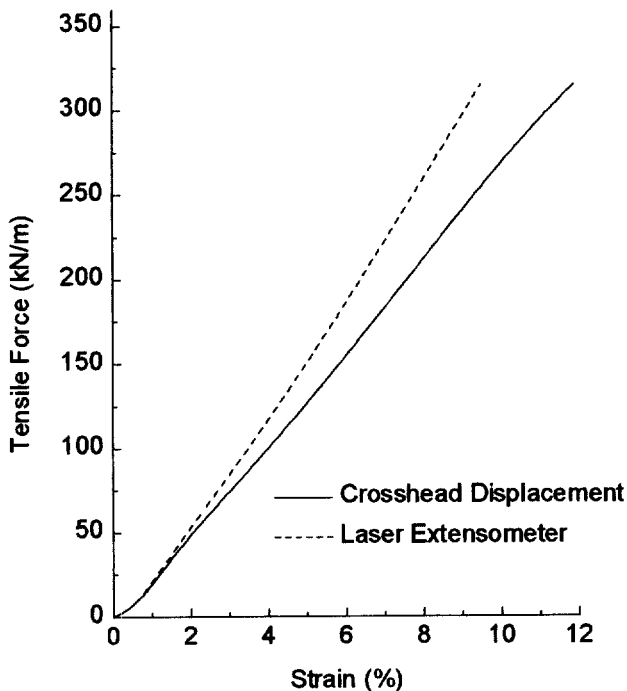


Figure 10. Effect of Extension Measurement Device Using Tab System

of reinforced structures.

Specimen damage or distortion that influence test results can be evidenced in two principal forms. Sample slippage in clamps resulting in partial or major deformation can influence test results necessitating that the specimen be discarded. More frequent is the seating slippage typical of roller devices and the slight distortion of samples in the clamp area in normal strip tests. In both instances, accurate measurement and recording of strain is essential to determine whether the slippage materially affects the results. Figure 11 compares the results of identical specimens with data recorded by lvdt and by crosshead.

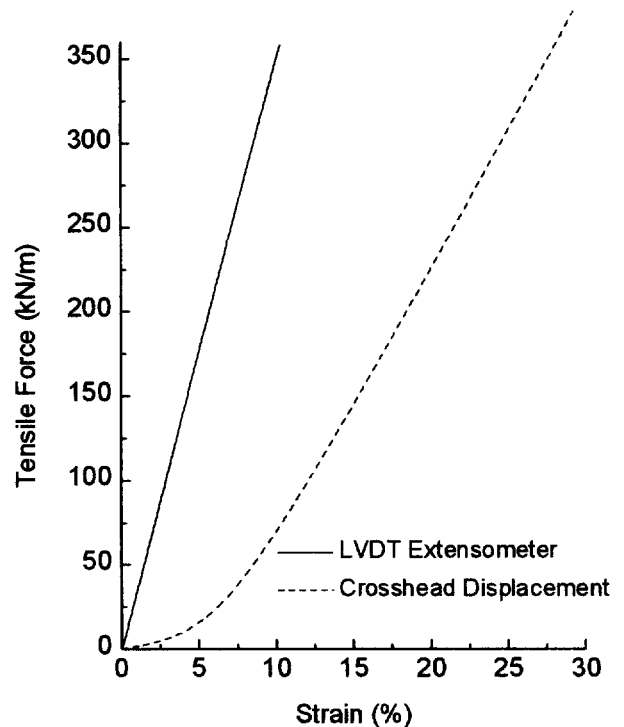


Figure 11. Effect of Extension Measurement Device Using Roller Grips

The crosshead data presentation shows initiation and the process of sample slippage during the test. The lvdt data is presented from preloaded initiation only and masks the slippage and elongation at initiation. It is interesting to note that the device has the effect of truncating the stress strain curve at ultimate while recording consistent data at low loads.

Figure 7 illustrates that for non slipping grips, crosshead displacement data from a correctly calibrated instrument will provide strain information for an entire sample geometry rather than a small nonrepresentative sector. Some practitioners have expressed concern about the accuracy of displacement measurement. The conventional testing machine does experience deformation in the

conduct of a tensile test. Error introduced by this deformation is corrected by subtracting machine displacement from the data. To demonstrate accuracy we tested a calibrated aluminum bar. The specified modulus of the specimen was 68.95 GPa. Strain gages recorded a modulus of 68.1 GPa. Crosshead displacement recorded modulus of 54.0 GPa. Displacement values corrected for machine deformation were 68.4 GPa, essentially zero error. Tests conducted on fabrics with loads at 31.1 kN and extension of 12 to 16% experienced machine deformation of less than 0.1%. Failure to correct for this deformation results in test error of less than 0.5% leading to the conclusion that displacement is an accurate measurement.

Finally, rate of strain is shown to be problematic in measurement as it is calculated as a percentage of sample gauge (a length measurement). For those geosynthetics that can be tested in a 100 mm length by 200 mm width geometry, the speed of the test is easily recorded by conventional means. High strength materials are typically tested in the much different longer than wide geometry, dictated by equipment load capacity and clamping devices. Brand and Pang (1990) report that strain rate for an entire sample tested by roller grips was typically 6% not the expected 10% prescribed by the method ASTM D4595. The NGO, Balkema (1986) explains that the phenomena occurs because of differences in strain characteristics in different portions of the specimen. Strain in the vicinity of the clamps is plane in nature while strain in the center of the sample tends to be linear. Goswami et al. (1996) present variation in strain for different sites on the specimen as the norm for textile type materials. The necessity to observe either the total area or a large portion of the specimen to accurately record strain rate necessitates the simultaneous employment of a combination of techniques such as displacement and optical devices and a mandatory comparison of the data. The definition of sample length, the strain measurement gauge used, the strain measurement system used and the observed test speed must be clearly reported.

2.6 Jaws, grips and other devices

Strong geosynthetics such as reinforcements experience great difficulty in sample gripping. Experienced researchers (Haliburton 1978; Myles 1986, 1987; Rowe et al. 1986; Richardson et al. 1987; Leschinsky and Fowler 1990; Brand and Pang 1991) cite grip failure as a key concern. The principal test methods, ASTM, ISO and BSI, recognize the issue of the difficulty of sample gripping and permit the utilization of roller or capstan grips. Roller grips typically require sample lengths of 1.829 m, width up to 0.203 m and typical spacing between rollers of 0.508 m. Because the sample geometry used in rollers is larger than most extension measurement tools, it seems obvious that displacement could be a critical measure of sample strains.

Unfortunately, the large amount of slippage that occurs in roller grips throughout the test negates the application of these techniques for low strain values in roller testing, although displacement can be quite accurate in recording ultimate strain. Equally problematic is the application of other devices. Typical optical devices observe a pencil line wide strip 0.203 m high, and mechanical/electronic devices also observe a very narrow, 0.101 m long section of a specimen with the result that when applied to roller tested specimens, these extension measurement systems represent the area observed and not the specimens performance.

Roller grips have several other awkward characteristics beside large sample geometry including the need to permit a sample to seat itself. The process of seating, also described as the application of preload, involves a certain extension of the sample. Accurate reporting requires that this extension be recorded as per Figure 3. Another issue of difficulty caused by large sample geometry of 1.829 m length, 0.508 m grip separation and sample widths up to 0.203 m is incompatibility with the general definition of wide width sample geometry: 100 mm gauge length by 200 mm width. In terms of strain measurement, this definition results in the apparent observation of, and reporting on, of a 0.101 m section of a 0.508 m or longer sample. Leschinsky and Fowler (1990) and Brand and Pang (1991) reported that different areas of a fabric were seen to extend at different rates and that any 100 mm by 200 mm section of a large sample would not be representative of the sample, or the product. The phenomenon that extension is not uniform over a large sample is documented elsewhere in textile literature (Goswami et al. 1996).

Sample widths vary according to the test device load capability, but in every case an equal number of yarn ends should be tested in each specimen of a sample or a testing program. In our work the separation from center of barrel to center of barrel was fixed at 0.508 m. Extension was measured by displacement or lvdt with the lvdt found to be acceptable for measurement of low strain values but strongly influenced by sample geometry at ultimate. Figure 9 compares identical specimens with extension recorded by displacement compared to lvdt. The lvdt could be observed to distort the specimen, break fiber and prematurely fail the specimen at very high strain.

The jaw used in the sacrificial tab system employed in our work is a hydraulic clamp with a wide pressure range. For very strong fabrics with tensile exceeding 700 kN/m, grip pressures exceeded 20.7 MPa insuring control of slippage in the grips. The typical specimen length exceeds 0.610 m permitting mounting of 0.0508 m sacrificial tabs on each end of the specimen and leaving a 0.508 m separation between clamps. As in roller testing, sample width is dictated by load cell capability but in every case an equal number of yarn ends is maintained between specimens.

2.7 Sample preparation

Care is taken in mounting samples in grips to avoid skew. Sacrificial tabs of light metal are adhesive bonded on both sides of specimens destined for pressure clamps, with tab separation of a minimum of 0.508 m. Adhesives are selected to have minimal influence on samples. For many light load fabrics, under 130 kN/m, protective tabs are unnecessary.

The sample preparation technique attempts to achieve yarn (and filament) alignment. The sacrificial tab permits very high pressures across the clamped face of the specimen which prevents the specimen from slipping out of the clamp. Simultaneously, the soft adhesive that binds the tab to the sample permits some relative slippage within the specimen permitting the maximum degree of uniform alignment and engagement of a high proportion of the filaments in the specimen. Slippage is observed in the two procedures at different times. Slippage is first observed on rollers in the early stages of the test, continues through much of the procedure and reduces to nil when approaching ultimate. Slippage is observed in pressure clamps at the end of the test. This small distortion develops late in the test and allows the continued loading of a majority of the filaments in the specimen.

3 CONCLUSIONS

The following conclusions are presented in the same order as the listing of the 14 concerns. 1. For textiles with uniaxial orientation of strength members (yarns), sample length influences test results. Shorter lengths inflate tensile values while deflating modulus. A practical solution to insure comparable results is to employ sample lengths in pressure grips that are comparable to roller grip separation distances. This permits the observation of similar geometry of the specimens. 2. Increased test speed inflates results; however, longer samples reduce the effect. Polyolefin materials are far more greatly affected by variation in speed. 3. Fabric structure dominates testing. Manipulation of other testing aspects: polymer, fiber form, test speed, sample geometry, grips, or protocols cannot reduce the impact of structure on fabric performance. 4. Test grips are part of a system and each system, roller or pressure can be employed to achieve accurate and repeatable results. 5. Slippage is also part of the system when testing strong materials and is in fact desirable in order to achieve consistent and meaningful results. 6. Tolerable slippage is observed and recorded by developing correlation between extension measurement systems. 7. Extension measurement is a critical element and a contentious issue in testing of high strength fabrics. Certain devices, lvdts, can be satisfactory for part of the test and may invalidate another portion of the test. There is a potential lack of confidence

in, or familiarity with, displacement and its influence of sample geometry and speed. Accurate displacement measurement can be performed simultaneously with other measurements and compatibility of two measurements insures good understanding of the test process and the recognition of flawed results. The test operator must take care to report the strain measurement gauge and the sample length, particularly when these measurements are different. 8. Extension measurement is defined by sample geometry, test speed, the physical area the device measures and the location of the device on the sample. Extension measurement techniques must be reported in detail to avoid undue masking of results. 9. Strong reinforcements are essentially uniaxial in orientation with each strength member (yarn) parallel to the next. In strip testing, whether 1.016, 0.203 or 0.0508 m in strip width, the entire sample is gripped and width does not play a significant role in the test except where the grip system is incapable of achieving uniform pressure. For reinforcements, sample width identifies the limits of the apparatus, not the reinforcement. In all cases testing must insure that an equal number of yarn ends are tested from sample to sample within a nominal specimen width. 10. Preload is a necessary element in testing of strong materials if roller systems are used. If not properly reported, preloads can mask test result information. 11-13. Modulus is the second contentious issue in testing of reinforcements. Clearly the meaningful moduli are related to certain segments of the data curve. In terms of reinforcements for critical structures it is not agreed whether the meaningful value is a secant of a very large segment or the actual value of a specific segment, for example: the modulus of the segment between 2% and 5% strain. 14. The relationship between single end yarn data and fabric performance is clearly evident; however, the relationship is not represented by a simple ratio. Some of the influences on the translation efficiency of a yarn strength to a fabric are: processing conditions, fabric structure, and testing systems. For a given product from a specific system, the relationship of yarn to fabric is a constant.

REFERENCES

- A.A. Balkema Publishers*, Old Post Road, Brookfield, VT 05036-9704, USA Fax 1 802 276 3837 ISBN 90 6191 624 0
- Bais-Singh, Smita and Goswami, Bhuvanesh, C., 1996, "Deformation Behavior of Spun-Bonded Nonwovens: Measurement" Proceedings of INDA-TEC 96, *International Nonwovens Conference*, Hyatt Regency Crystal City, Crystal city, VA., pp. 29.1-29.19
- Brand, E.W. and Pang, P.L. R., 1991, "Durability of Geotextiles to Outdoor Exposure in Hong Kong",

- Journal of Geotechnical Engineering*, Vol. 117, No. 7, pp. 979-1000.
- Craig, B. "Report on the joint BGS/IGS meeting "Use of Geosynthetic Materials with Improved Reinforcement Capabilities", 4 December, 1996, University of Manchester, Ground Engineering, April, 1997.
- Fakher, A., Jones, C.F.J.P., & Zakaria, N-A.B., "The Influence of Dimensional Analysis on the Interpretation of Model Loading Tests on Reinforced Ground", *Earth Reinforcement: Proceedings of the International Symposium on Earth Reinforcement, Fukuoka, Kyushu, Japan 12-14 November 1996*, Edited by Hidetoshi Ochaii, Noriyuki Yasufuku, Kiyoshi Omine A.A. Balkema Publishers, Old Post Road, Brookfield, VT 05036-9704, USA Fax 1 802 276 3837 ISBN 90 5410 833 9
- Finnigan, J.A., 1977, "The Creep Behavior of High Tenacity Yarns and Fabrics Used in Civil Engineering Applications", *Proceedings of the International Conference on the Use of Fabrics in Geotechnics, L'Ecole Nationale Des Ponts et Chaussees*, Vol. 2, Paris, France, April, 1977, pp. 305-309.
- Geotextiles and Geomembranes, edited by R. Veldhuijzen Van Zanten, pp. 61-78
- Haliburton T.A., Anglin C.C. and Lawmaster, J.D. 1978, "Testing of Geotechnical Fabric for Use as Reinforcement", *Geotechnical Testing Journal*, Vol. 1, No. 4, pp. 203-212
- Jones, C.F.J.P., Fakher, A, Hamir, R. & Nettleton, I.M. "Geosynthetic Materials with Improved Reinforcement Capabilities", *Earth Reinforcement: Proceedings of the International Symposium on Earth Reinforcement, Fukuoka, Kyushu, Japan 12-14 November 1996*, Edited by Hidetoshi Ochaii, Noriyuki Yasufuku, Kiyoshi Omine A.A. Balkema Publishers, Old Post Road, Brookfield, VT 05036-9704, USA Fax 1 802 276 3837 ISBN 90 5410 833 9
- Leschinsky, D. and Fowler, J., 1990, "Laboratory Measurement of Load Elongation Relationship of High-Strength Geotextiles", *Geotextiles and Geomembranes*, Vol. 9, No. 2, pp. 145-164.
- Myles, B. and Carswell, I.G., 1986, "Tensile Testing of Geotextiles", *Proceedings of the Third International Conference on Geotextiles*, Vol. 3, Vienna, Austria, April 1986, pp. 713-718
- Pan, N, Chen, H.C., Thompson, J., Inglesby, M.K., Khatua, S., Zhang, X.S., and Zeroinian, S.H., 1996, "Fiber Initial Modulus as a Function of Fiber Length", *The Fiber Society, General Technical Conference*, Hotel Viking, Newport, Rhode Island, October 14-17,
- Rowe, R.K. and Ho, S.K., 1986, "Determination of geotextile Stress-Strain Characteristics Using a Wide Strip Test" *Proceedings of the Third International Conference on Geotextiles*, Vol. 3, Vienna, Austria, April 1986, pp. 885-890.
- Sissons, C.R., 1977, "Strength Testing of Fabrics for Use in Civil Engineering", *Proceedings of the International Conference on the Use of Fabrics in Geotechnics, L'Ecole Nationale Des Ponts et Chaussees*, Vol. 2, Paris, France, April, 1977, pp. 287-292
- Van Leeuwen, J.H., 1977, "New Methods of Determining the Stress-Strain Behaviour of Woven and Non Woven Fabrics in the Laboratory and in Practice", *Proceedings of the International Conference on the Use of Fabrics in Geotechnics, L'Ecole Nationale Des Ponts et Chaussees*, Vol. 2, Paris, France, April, 1977, pp. 299-304.

GEOSYNTHETIC REINFORCEMENT: ARE GEOTEXTILES AND GEOGRIDS INTERCHANGEABLE?

C. Joel Sprague, P.E.

Sprague & Sprague Consulting Engineers, Greenville, SC, USA

ABSTRACT: Geosynthetically reinforced soil structures have become acceptable, cost-effective alternatives to conventional geotechnical structures. Yet, it is interesting to note that many geosynthetically reinforced soil structures are specified in such a fashion that only geogrid but not geotextile reinforcement may be used, or vice versa. Why is this? This paper explores this question using tables and charts of relevant, performance-oriented properties and a survey of more than 50 State DOT and FHWA engineers questioned about their preferences related to the use of geotextiles and geogrids for reinforcement applications. In general, there appear to be no overriding technical or economical reasons to rely on proprietary, product-specific designs/specifications when using geosynthetic reinforced soil structures. Conversely, there are several arguments for the widespread use of generic design, specification, and procurement procedures.

KEY WORDS: geotextiles, geogrids, reinforcement, specifications

1 INTRODUCTION

Though the use of tensile inclusions in soil structures dates back several thousand years to the construction of religious structures in ancient Babylonia, it was only three decades ago that Henri Vidal, a French architect, pioneered modern earth reinforcement techniques. These techniques involved the incorporation of resisting elements into a soil mass to complement the soil's compressive strength and together to act in a composite fashion to improve the mechanical properties of the soil mass. Vidal patented his system, which used steel strips to provide the reinforcement, and named the system "Terre Armee" in France and "Reinforced Earth" in the United States. The first Reinforced Earth wall was constructed along California State Highway 39 in 1972.

Mitchell and Villet (1987) detailed and expanded on this historical perspective, noting that beginning in the early 1970's, experimentation using geotextiles as soil reinforcement was conducted in Europe and the United States. The U.S. Forest Service constructed full-scale wrapped-face walls in the Siskiyou and Olympic National Forests using geotextiles in 1974 and 1975 and developed construction and design guidelines based on this experience. Under FHWA sponsorship, highway departments in New York, Colorado, and Oregon constructed geotextile reinforced walls in the early 1980's. These geotextile reinforced walls were compared to walls constructed with steel inclusions and all were found to perform well.

This success attracted other candidate forms of plastic inclusions such as geogrids. Beginning in about 1984, Tensar geogrids were introduced specifically for soil reinforcement. These geogrids were manufactured of

polyethylene - a different polymer than used in the geotextiles. Polypropylene and polyester were the polymer of choice for geotextiles.

Since 1986, the use of reinforced soil systems, which are also called mechanically stabilized earth (MSE), in the United States has significantly increased. The primary types of MSE systems which have emerged include: mechanically stabilized earth walls (MSEW); reinforced soil slopes (RSS); reinforced embankments over soft foundations (RESF); and reinforced liners and caps. MSEW and RSS have become especially important in highway construction as their use reduces the required width of new right-of-way and facilitates construction within existing limited right-of-way. RESF are recognized as a cost-effective alternative to traditional techniques for constructing earthen embankments over low strength foundations. Additionally, critical environmental applications of geosynthetic reinforcement have emerged, including the reinforcement of landfill and lagoon liner and cap systems on steep slopes and over weak subgrades or underlying voids.

Free draining granular material is the preferred backfill material in reinforced soil structures. Therefore, the use of reinforced soil structures - primarily MSEW and RSS - has been somewhat limited in cases where high quality backfill material is not readily available. Mitchell and Zornberg (1994 & 1995) observed that the inherent low strength, moisture instability, possible volume changes, and creep potential, along with the corrosive potential of saturated soils, are common concerns associated with the use of fine-grained, cohesive backfills. They further noted that as successful experiences are documented and consistent design methodologies are developed for these poorly

draining backfills, even greater growth in the use of reinforced soil structures will be possible.

Clearly, there has been substantial acceptance of geosynthetic reinforced soil structures and much of the growth has been the result of aggressive marketing by companies providing candidate geosynthetic soil reinforcement materials. Therefore, much of the experience gained to-date is with those reinforcement materials which are marketed most aggressively and "packaged" with proprietary designs. Yet, this growth has been fraught with argument as competing proprietary systems claim superior performance or dependability. In response, independent researchers and Federal and State engineers have advanced the development of generic design techniques and material specifications such as AASHTO (1997) MSEW specifications and the FHWA's RSS guidelines by Berg (1993) and the DEMO 82 educational effort discussed by DiMaggio (1996). This new generation of generic design techniques and specifications recognizes the suitability of both geotextiles and geogrids for soil reinforcement.

This paper details the key issues associated with the use of geosynthetics as soil reinforcement and provides comparative data for common reinforcing geosynthetics. Additionally, required product documentation, relative costs, and a summary of geosynthetic reinforcement use by state Departments of Transportation (DOT) are presented.

2 REINFORCEMENT DESIGN INPUTS

2.1 Overview

Geosynthetic reinforcement systems incorporate geotextiles and/or geogrids as horizontal layers within a soil backfill to resist outward movement of the reinforced soil mass. The geosynthetic interacts with the soil by adding a tensile force and this tensile force is transferred to the soil mass through unique geosynthetic/soil interaction mechanisms. Both tensile force and soil interaction must be determined for each candidate geosynthetic.

2.2 Allowable Tensile Strength

The allowable tensile strength of a geosynthetic is input into reinforced soil analyses in order to determine the reinforced factor of safety. Allowable geosynthetic design strengths must be determined by testing and analysis methods that account for the long-term dimensional stability and durability of the full geosynthetic structure. Dimensional stability is characterized by the ability of the geosynthetic to sustain long-term load in-service without excessive creep strains. Durability factors include site damage, chemical degradation and biological degradation. These factors may theoretically cause deterioration of either the geosynthetic's tensile elements or the geosynthetic/soil stress transfer mechanism of the geosynthetic structure according to Berg

(1993). To account for dimensional stability and durability, allowable tensile strength, T_a , for the geosynthetic is determined using a partial factor of safety approach such as Equation 1 from Berg (1993).

$$T_a = T_{ult} / (FS_{CR} \times FS_{ID} \times FS_{CD} \times FS_{BD} \times FS_{JNT}) \quad (1)$$

T_a = allowable geosynthetic tensile strength;

T_{ult} = ultimate geosynthetic tensile strength;

FS_{CR} = partial factor of creep deformation;

FS_{ID} = partial factor of safety for installation damage;

FS_{CD} = partial factor of safety for chemical degradation;

FS_{BD} = partial factor of safety for biological degradation;

FS_{JNT} = partial factor of safety for joints.

The allowable tensile strength, T_a , is often referred to as the long-term design strength, or LTDS. (Long-term allowable design load, or LTADL, is also used by some.) Many geosynthetic manufacturers can provide typical LTDS values for each of their candidate reinforcement materials. It is important to recognize that these "typical" LTDS values reflect factors of safety derived from laboratory and/or field testing which may or may not simulate the project conditions under consideration. Therefore, the designer must consider whether the partial factors of safety inherent in any "typical" LTDS value are applicable.

2.3 Partial Factors of Safety.

The partial factors of safety used to calculate the allowable tensile strength of the geosynthetic are intended to address the issues which provoke the greatest arguments between competing reinforcing systems. These factors of safety are either based on laboratory/field testing of the candidate material or are assigned based on "default" values derived from worst-case experience. An example of default values as recommended by Berg (1993) and typical testing-derived values is shown in Table 1.

Table 1. Typical Geosynthetic Reinforcement Default and Testing-Derived Values for Partial Factors-of-Safety

FS	Partial Factors of Safety					Composite
	ID	CR	CD	BD	J/S	
Default	3.0	5.0	2.0	1.3	2.0	78
Tested	1.2	2.0	1.1	1.0	1.01	2.64

KEY: FS=factor of safety; ID=installation damage; CR=creep; CD=chemical degradation; BD=biological degradation; J/S=joint/seam

The magnitude of default values virtually assures that a material supplier will do product-specific testing to derive the factors of safety to be used to calculate allowable tensile strength. If one were to use only default values, the

candidate geosynthetic would be able to claim an allowable tensile strength equal to only 1/78th of the ultimate tensile strength of the material. Certainly, this would likely make the candidate material uneconomical. Conversely, product-specific testing can be done to clearly define the unique limitations of a material without excessive conservatism. Guidance is commonly given in well written specifications such as Berg (1993) on how to determine factors of safety through laboratory/field testing. For example, one state DOT (WSDOT,1996) requires that ASTM D 5818 be the basis for FS_{ID} and that ASTM D 5262 along with a detailed data extrapolation technique be the basis for FS_{CR} . Additionally, this DOT gives a general approach to determining FS_{CD} and FS_{BD} based on the geosynthetic polymer. FS_{JNT} is not addressed, so presumably joints/seams are not permitted. It is important to note that the use of partial factors of safety does not identify any combined effects of the various forms of degradation. In the future, FS values derived from testing that examines the combined, and perhaps synergistic effects of two or more forms of degradation will be used. These types of testing are currently under development.

As shown in Table 1, using factors of safety derived from testing, the allowable tensile strength would typically be on the order of 38% of the ultimate (i.e. composite $FS=2.64$), rather than the 1.2% of ultimate resulting from the use of default values. Composite factors of safety for calculating LTDS are commonly range from 2.0 to 4.0, depending primarily on the polymer.

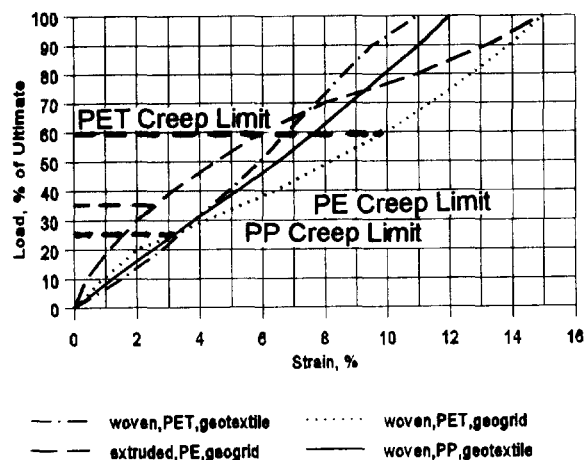


Figure 1. Geosynthetic Strength Characteristics

2.5 Creep.

As shown in Table I, creep potential is usually the greatest "factor" in LTDS calculations. Characteristic strength properties and associated creep limits of various geosynthetic types are presented in Figure 1. Creep potential limits the allowable tensile strength to no more than the creep limited load and strain. Therefore, as shown

in Figure 1, PET geosynthetics can safely mobilize higher strengths and strains than can PE or PP. This explains the generally lower composite factor of safety used to calculate LTDS for PET geosynthetics ($FS = 1.8 - 2.0$) versus that used for PE or PP ($FS = 3 - 4$, or more).

3 GEOSYNTHETIC/SOIL INTERACTION

3.1 Overview

As noted earlier, along with tensile strength, a geosynthetic's interaction with the soil must be characterized as a part of the design process. Geogrids mobilize a different kind of interaction with the soil than the frictional behavior relied on by geotextiles. Instead of a continuous frictional surface, geogrids have large openings, or apertures, which allow the soil to be continuous through the inclusion. Geogrids transfer stress to the soil through passive soil resistance on transverse members of the grid and limited friction between the soil and horizontal surfaces of the geogrid. Geotextiles transfer stress to the soil through the friction created across its entire surface area.

Two types of soil/geosynthetic interaction must be quantified: pullout and direct shear. In both cases, the quantification of stress transfer must be accomplished through laboratory testing. As with Factors of Safety, specific guidance, especially on the range of normal loads to be used, is commonly given in well written specifications on how to determine pullout and direct shear coefficients through laboratory/field testing.

3.2 Pullout Resistance.

Pullout coefficients are used in stability analyses to compute mobilized tensile force at the front and tail of each reinforcement layer in MSEW and RSS systems. According to Berg (1993) design of MSEW and RSS for permanent applications requires evaluation of long-term pullout performance with respect to three basic criteria:

1. pullout capacity should be adequate to resist the design tensile force with an appropriate factor of safety; and
2. allowable displacement should be greater than the relative geosynthetic to soil displacement required to mobilize the design tensile force; and
3. the pullout load should be smaller than the critical creep load.

The long-term pullout interaction coefficient is quantified by laboratory testing such as is outlined by Berg (1993). For geotextiles, this simply requires a quick effective stress pullout test since only surface friction is involved. For geogrids, sufficient long-term junction strength must be considered in addition to or as a part of pullout testing, since soil bearing on transverse ribs may be an important component of grid pullout resistance. This may require

creep testing of the junctions or the entire soil/grid system or cutting transverse ribs to remove the junctions from the testing. Therefore, much more testing may be required in order to qualify a candidate geogrid for pullout resistance as compared to a geotextile. The C_i value from pullout testing is used to calculate the bond length behind a critical failure surface using Equation 2.

$$L = PO_{ult} \text{ or } PO_{0.75 \text{ in}} / (2 \times C_i \times \sigma \times \tan\phi) \quad (2)$$

Where:

L = bond length beyond a failure plane; σ = normal load; $\tan\phi$ = the tangent of the soil's friction angle; C_i = interaction coefficient (See Tables 2a and 2b); PO_{ult} = the highest load resisted by the embedded reinforcement; and $PO_{0.75 \text{ in}}$ = the pullout capacity associated with a movement of less than 0.75 inches (19mm) of the leading edge of the reinforcement sample.

Table 2a: Typical Short-term Geosynthetic/Soil Interaction Coefficients for Pullout, C_i

Interface with Soil	Normal Stress					
	500 psf		1000 psf		2000 psf	
	Clay	Sand	Clay	Sand	Clay	Sand
W,PP,GTX	0.60	0.90	0.65	0.90	0.70	0.90
W,PET,GTX	0.70	1.00	0.80	1.00	0.90	0.95
W,PET,GG	0.70	1.00	0.90	1.00	0.90	1.00
EX,PE,GG	>0.7	>0.9	>0.7	>0.9	>0.7	>0.9

KEY: W=woven; EX=extruded; PP=polypropylene; PET=polyester; GTX=geotextile; GG=geogrid. Based on Cowell & Sprague (1993); Collin & Berg (1993); unpublished reports

Table 2b: Typical Long-term Geosynthetic/Soil Interaction Coefficients for Pullout, C_i

Interface with Soil	Normal Stress					
	500 psf		1000 psf		2000 psf	
	Clay	Sand	Clay	Sand	Clay	Sand
W,PP,GTX	0.60	0.90	0.65	0.90	0.70	0.90
W,PET,GTX	0.70	1.00	0.80	1.00	0.90	0.95
W,PET,GG	n/a	0.90	n/a	1.00	n/a	1.00
EX,PE,GG	>0.7	>0.9	>0.7	>0.9	>0.7	>0.9

KEY: W=woven; EX=extruded; PP=polypropylene; PET=polyester; GTX=geotextile; GG=geogrid; n/a=not available. Based on Cowell & Sprague (1993); Collin & Berg (1993); unpublished reports

Cowell and Sprague (1993) provided the following general conclusions based on extensive pullout testing:

1. Geogrids and geotextiles having similar strength properties also have similar ultimate pullout capacities and coefficients of interaction.
2. The pullout capacity at 0.75 inches of displacement for the geotextiles tested was significantly lower (50 to 67%) than that obtained for geogrids of similar strengths.

3. Junction strength of geogrids and the contribution to pullout resistance contributed from transverse ribs does not have a significant affect on pullout performance. (See long-term values in Table 2b)

One additional conclusion can be drawn concerning the sensitivity of a design to variation in C_i . If equation 2 is solved for length, given a required pullout, it can be shown that for C_i in the range of 0.7 to 0.9, a minimum length of 1 m controls for reinforcement layers below approximately 1 m of soil depth.

3.2.1 Pullout in the Design of RSS Structures.

The ultimate load is taken to be less than or equal to the LTDS and from this the bond length required is calculated. A factor of safety, typically on the order of 1.5, is applied to this length. In RSS applications, strains are typically controlled by using a 10% creep limit strain in the selection of the LTDS. RSS structures can tolerate more movement than MSEW, therefore $PO_{0.75 \text{ in}}$ is not typically used for RSS.

3.2.2 Pullout in the Design of MSEW Structures.

For the design of MSEW structures, especially those with concrete facing panels, not only is the required bond length calculated as with RSS structures, but the limiting strain of the wall face can be critical. It is important to check if the LTDS can be mobilized within a limiting strain in order to assure that wall face movements remain within tolerable limits. Therefore, both the C_i and the $PO_{0.75 \text{ in}}$ must be checked to see how they may affect the design.

3.3 Direct Shear.

Direct shear coefficients are used in checking the factor of safety against sliding of an overlying soil mass. This sliding is a consideration in all reinforced soil systems. Soil/geosynthetic direct shear resistance is determined by laboratory testing. As can be seen in Table 3, geotextiles and geogrids are both highly efficient in transferring interface shear stresses, especially with sand.

Table 3: Typical Geosynthetic/Soil Interaction Coefficients for Direct Shear, C_s

Interface with Soil	Normal Stress					
	500 psf		750 psf		1000 psf	
	Clay	Sand	Clay	Sand	Clay	Sand
W,PP,GTX	0.60	0.85	0.60	0.90	0.60	0.90
W,PET,GTX	0.75	0.90	0.80	0.95	0.90	0.95
W,PET,GG	0.80	0.90	0.85	0.95	0.90	0.95
EX,PE,GG	>0.9	>0.9	>0.9	>0.9	>0.9	>0.9

KEY: W=woven; EX=extruded; PP=polypropylene; PET=polyester; GTX=geotextile; GG=geogrid. Based on Koutsourais, et al (1991); The Tensar Corp. (1986); unpublished reports

3.4 Other Interaction Considerations.

MSEW designs may also require quantification of the geosynthetic/facing connection strength using large-scale pullout testing for each unique geosynthetic/facing combination. Still, experts continue to debate the magnitude of the forces, if any, which are exerted at the face.

4 DOCUMENTING GEOSYNTHETICS

Consideration and approval of candidate geosynthetics by owner/agency personnel requires that the geosynthetic supplier provide sufficient evidence of the proposed material's suitability and additional evidence of the manufacturer's/supplier's capabilities. The Federal Highway Administration (FHWA) requirements for documentation in all submittals are detailed by Berg (1993) as follows:

- * History of material development.
- * Current capability to supply material.
- * Polymer and additive composition of geosynthetic.
- * Practical applications of material.
- * Representative list of users.
- * Typical LTDS and interaction values.
- * Typical unit costs.
- * Laboratory test data, comprehensive literature review, and the interpretation and extrapolation used to determine the partial factor of safety should be presented for:
 - Creep performance: Range of loads for 10000 hours.
 - 75 year creep extrapolation.
 - Installation damage.
 - Ultimate strength.
 - Chemical resistance.
 - Biological degradation.
 - Joint (seam/connection) strength.
 - Long-term pullout coefficient.
 - Direct sliding coefficient.

5 COST CONSIDERATIONS

An important factor in the increasing acceptance of a technology is increasing cost-effectiveness. Although there are many factors associated with the as-built cost of any geosynthetic reinforced soil structure, including project size, backfill type, and contractor familiarity to name a few, it is useful to examine the relative material costs associated with various candidate geosynthetic reinforcements. Commonly, geogrids are somewhat more costly per unit LTDS than are woven geotextiles but, geogrids may be more cost-effective for providing lower initial strain levels and higher soil interaction, if needed. Typical pricing of geogrids ranges from 0.0015 to 0.001 \$/m² per unit LTDS for low to high strengths, respectively. Woven geotextiles commonly range from .001 to .006 \$/m² per unit LTDS.

6 STATE OF PRACTICE

As note earlier, the FHWA has taken the lead in providing guidance in the implementation of generic design techniques and material specifications associated with geosynthetic reinforced soil systems. Still, individual owners/agencies are free to exercise their own judgements as to the appropriateness of following the FHWA lead. Tables 4a and 4b summarize a telephone survey of state Departments of Transportation (DOTs) conducted by the author in the fall of 1996. The survey solicited responses on the use of geosynthetic reinforced soil structures, reinforcement preferences, and reasons why preferential specifications may be used on any given project.

Table 4a. Survey of State DOTs - Use of Geosynthetic Reinforced Soil Systems

U.S. Region	Number of States Using Reinforced Soil System								
	MSEW			RSS			RESF		
	C	T	n/u	C	T	n/u	C	T	n/u
Northeast	1	4	2	3	3	1	1	0	6
Mid-Atl.	3	1	2	3	0	3	2	0	4
Southeast	2	4	2	4	2	2	4	2	2
Midwest	2	2	2	3	2	1	1	1	4
Southwest	2	2	1	2	2	0	1	2	2
Plains	4	0	0	1	2	0	0	0	0
West	5	1	0	3	2	1	1	1	4
Far West	5	1	1	3	1	3	4	1	2
Total States	24	15	10	22	14	13	14	7	28

KEY: MSEW=mechanically stabilized earth walls; RSS=reinforced soil slopes; RESF=reinforced embankments over soft foundations; C=commonly used; T=Trials use only; n/u=not used.
NOTE: RI,NV,PR did not respond.

Table 4b. Survey of State DOTs - Geosynthetic Reinforcement Preferences

U.S. Region	Number of States						
	Preferred Reinforce't			Reason for Preference			
	Gen- Future	Gen- eric	Gen- Future	Prop- erties	Exper- ience	Cns/ Vendor	
Northeast	0	5	2	3	0	2	6
Mid-Atl.	0	2	2	2	0	1	4
Southeast	3	6	2	3	0	3	4
Midwest	1	4	0	5	0	1	5
Southwest	1	5	0	1	2	2	4
Plains	0	4	0	2	2	3	4
West	0	4	1	3	1	3	4
Far West	2	3	3	2	3	2	2
States Re- sponding	44	44	44	44	43	43	43

KEY: Gtx=geotextile; GG=geogrid; Gen.Future=plan generic use in future
NOTE: RI,NV,PR did not respond. 5 states did not indicate a preference. 6 states did not state a reason for a preference.

Tables 4a and 4b reveal the following trends:

1. Most Departments of Transportation (DOTs) are commonly using at least one form of geosynthetic reinforced soil structure.
2. Geogrids have been the most often used geosynthetic reinforcement to-date, largely because of vendor/consultant influences and greater experience with these materials.
3. Many DOTs intend to use non-preferential, more generic design/specification approaches in the future.

A further indication of the acceptance of and support for geosynthetic reinforced soil structures is the recently initiated effort to develop manuals and software and teach associated courses on mechanically stabilized earth technology. Geosynthetic reinforcement and associated design/construction technologies will be presented. This effort is called Demonstration Project No. 82, or Demo 82 for short, and has as its explicit purpose according to DiMaggio (1996): "to optimize the acceptance and implementation of mechanically stabilized earth technology in routine design and construction practice."

7 CONCLUSIONS

Generally, geotextiles and geogrids are interchangeable in reinforcement applications. It appears that there are no overriding technical or economical reasons to rely on proprietary, product-specific designs/specifications when using geosynthetic reinforced soil structures. Conversely, the following observations support the use of generic design, specification, and procurement procedures:

1. Geotextiles and geogrids have been successfully used for over 2 decades in all types of reinforced soil structures.
2. Generally accepted design techniques have been developed which are equally compatible with geotextiles and geogrids.
3. Geotextiles and geogrids have been tested and found to provide suitable and comparable tensile and soil/geosynthetic interaction properties.
4. Geotextiles and geogrids can be quickly tested to confirm compliance with generic project-specific requirements.
5. A wide range of suitable, proven products is available representing the full range of strength/strain/interaction properties typically required in reinforced soil structures.
6. Many owners/agencies now commonly using geosynthetic reinforced soil structures are inclined to encourage more generic design, specification, and procurement of geosynthetic reinforcement in the future to assure fairness and cost-effectiveness.

The generic design, specification, and procurement of geosynthetic reinforced soil structures appears to evolve naturally as the designer/owner gains sufficient understanding of and experience with the associated technology.

ACKNOWLEDGMENTS

The author would like to thank David Andrews of Synthetic Industries for his valuable review of the original report upon which this paper is largely based.

REFERENCES

- AASHTO (1997), "Interim Specifications - Standard Specification for Highway Bridges Division I, Section 5 - Retaining Walls & Division III, Section 7 - Earth Retaining Systems", American Association of State Highway and Transportation Officials (AASHTO), Washington, DC.
- Berg, R.R. (1993), "Guidelines for Design, Specification, and Contracting of Geosynthetic Mechanically Stabilized Earth Slopes on Firm Foundations, FHWA-SA-93-025, FHWA, Washington, D.C.
- Collin, J.G., and Berg, R.R. (1993), "Comparison of Short-term and Long-term Pullout Testing of Geogrid Reinforcement", Geosynthetic Reinforcement Testing Procedures, ASTM, Philadelphia, PA, pp. 184-194
- Cowell, M.J. and Sprague, C.J. (1993), "Comparison of Pullout Performance of Geogrids and Geotextiles", Proc. of Geosynthetics '93, Vancouver, IFAI, pp. 579-592.
- DiMaggio, J.A. (1996), "Update on Demonstration Project No. 82", Geotechnical Fabrics Report, Oct./Nov., p. 43.
- Koutsourais, M.M., Sprague, C.J., and Pucetas, R.C. (1991), "Interfacial Friction Study of Cap and Liner Components for Landfill Design", Geotextiles and Geomembranes, Vol. 10, Nos. 5-6.
- Mitchell, J.K. and Villet, W.C.B. (1987), "Reinforcement of Earth Slopes and Embankments", NCHRP Report No. 290, Transportation Research Board, Washington, D.C., pp. 5-8, 126-129.
- Mitchell, J.K., and Zornberg, J.G. (1994), "Reinforced Soil Structures with Poorly Draining Backfills, Part I: Reinforcement Interactions and Functions", Geosynthetics International, Vol. 1, No. 2, pp. 103-147.
- Mitchell, J.K., and Zornberg, J.G. (1995), "Reinforced Soil Structures with Poorly Draining Backfills, Part II: Case Histories and Applications", Geosynthetics International, Vol. 2, No. 1, pp. 265-307.
- The Tensar Corporation (1986), "Guidelines for the Design of Tensar Geogrid Reinforced Soil Retaining Walls", TTN:RW1.
- WSDOT (1996), "Geosynthetic Reinforcement Product Submission and Approval Requirements", Washington State Department of Transportation, FOSSC Materials Laboratory, Tumwater, WA.

Effect of End-Restraint in Geogrid-Soil Structures

H. Ochiai, N. Yasufuku, and T. Kawamura
Department of Civil Engineering, Kyushu University, Fukuoka, Japan

T. Yamaji
Ministry of Transport, Tokyo, Japan

T. Hirai
Mitsui Petrochemical Industrial Products, Ltd., Tokyo, Japan

ABSTRACT: Reinforcing effects of geogrid-soil structures depend on the end-restraint condition of the geogrid. Two types of end-restraint, fixed-end and sliding-end, were experimentally investigated by using a prototype shear apparatus that has been developed for this purpose. Main conclusions are: 1) In order to obtain a significant effect of reinforcement, one end of each geogrid in the soil structure should be fixed on the facing of the soil structure in such a way that the geogrid and the soil in the moving soil mass do not move relative to each other, and 2) For the fixed-end type, there exists an additional confining effect which increases the normal stress on the potential sliding plane in addition to the effect due to the tensile force of geogrid.

KEYWORDS: Reinforcement, Geogrids, End-restraint

1 INTRODUCTION

Earth reinforcement techniques have become useful and economical solutions to many problems in geotechnical practice but there are some points concerning the reinforcing mechanism of soil-reinforcement system that

need to be clarified.

In geogrid reinforced soil structures, such as the one shown in Figure 1, the end-restraint condition of the geogrid may have considerable influence on the reinforcing effect. In this research, two types of end-restraint, fixed-end and sliding-end, have been investigated experimentally by using a small prototype shear apparatus which has been developed for this purpose. An expression has been proposed to evaluate the reinforcement effect quantitatively.

2 MODEL OF END-RESTRAINT

The two types of end-restraint investigated are shown in Figures 1a and 1b.

Fixed-end: Figure 1a shows the fixed-end type of restraint. One end of the geogrid is fixed on the facing and the geogrid and the soil in the moving soil mass do not move relative to each other.

Sliding-end: Figure 1b shows the sliding-end type of restraint. The geogrid is not fixed on the facing and the geogrid and the soil may move relative to one another.

3 TEST APPARATUS AND TEST PROCEDURE

3.1 Test apparatus

The apparatus has two bellofram-cylinders on the right and left sides to model the types of end-restraint. In the fixed-end type, the left side of the geogrid is fixed to the upper box and the tensile force of geogrid is provided by the right bellofram-cylinder. In the sliding-end type, the tensile force of geogrid is provided by both sides of the bellofram-cylinder.

A sketch of the test apparatus and the shear box are shown in Figure 2, details can be found in Ochiai et al (1996). The shear box is rectangular in shape and is of size 200 × 200 × 380mm. The shear box has two halves, the

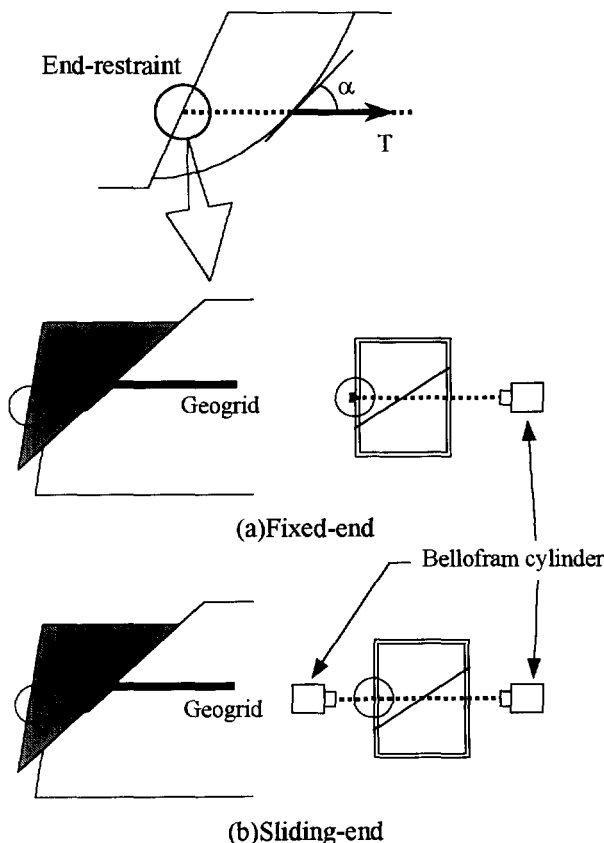


Figure 1. Model of end-restraint in in-situ and laboratory test conditions

upper box and the lower box, with a common sliding plane. The two halves of the shear box are connected and guided by frictionless linear motion bearings on the sliding plane. Three types of shear boxes with different sliding angles are prepared for this study. The shear force, S , along the sliding plane is provided by the vertical surcharge load. The normal component of the tensile force on the geogrid on the sliding plane is canceled out by the reaction on the linear motion bearings. Therefore, the normal component of reinforcement effect due to tensile force of geogrid, $T \cdot \sin \alpha \cdot \tan \phi$, cannot be mobilized in the tests.

3.2 Specimen

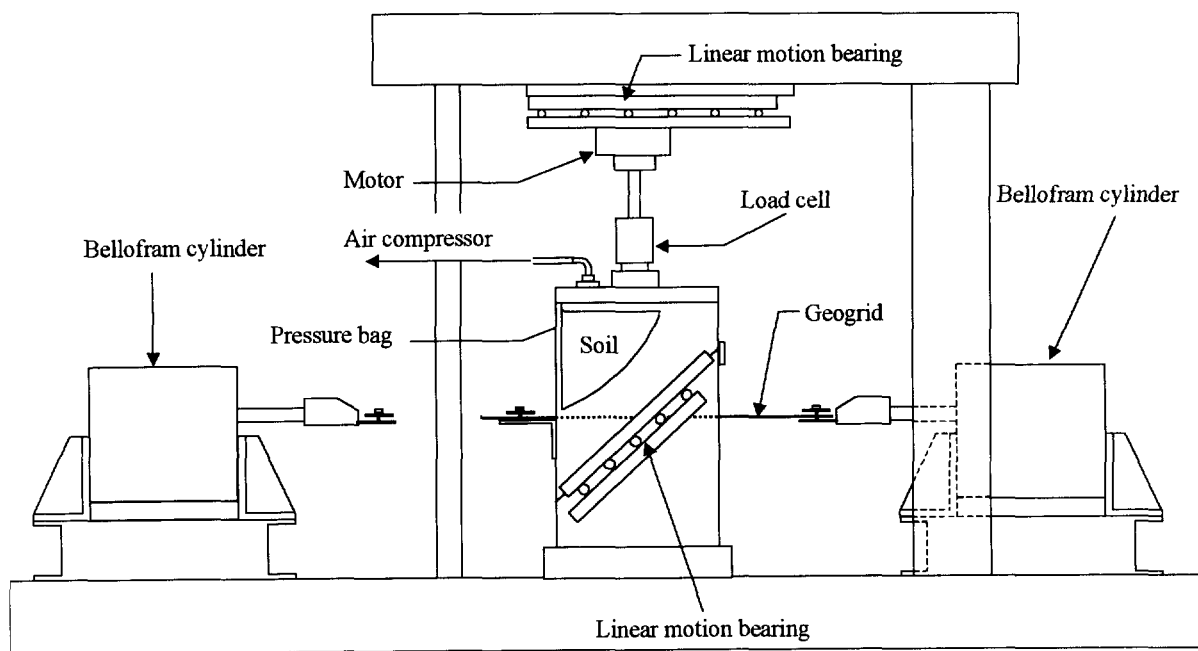
Dry Toyoura sand, which is a standard sand used for testing

in Japan, was used and four kinds of geogrids with varied shape properties were used as reinforcement materials. The physical and strength properties of sand are shown in Table 1 and Figure 3 respectively. The strength values of sand were obtained using the test apparatus shown in Figure 2 for the conditions of the relative density, $D_r=90\%$, and the sliding angle, $\alpha=30^\circ, 40^\circ, 50^\circ$.

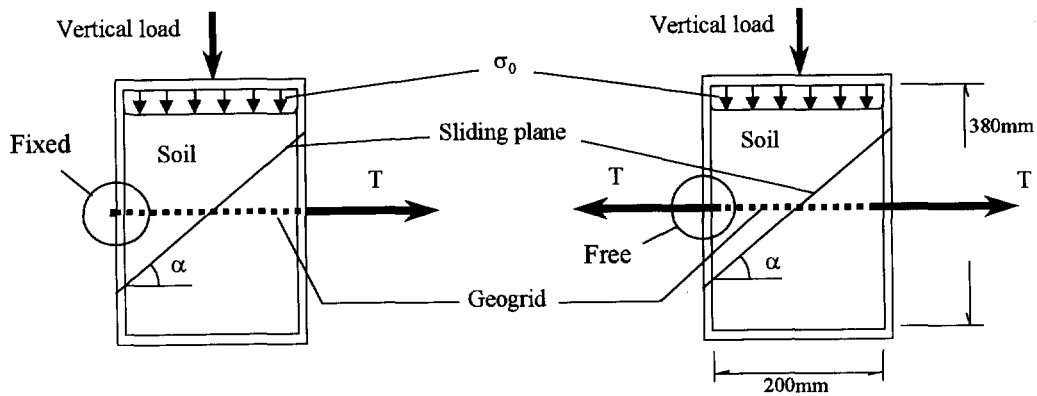
The geogrid measurements are defined in Figure 4 and the properties of geogrids are summarized in Table 2.

3.3 Test procedure

Sand is poured through multiple sieves in order to construct a homogeneous specimen. The relative density of the sand, D_r , is about 90%. After applying a constant tensile force to



(a) Test apparatus



(b) Shear box in fixed-end test

(c) Shear box in sliding-end test

Figure 2. Sketch of test apparatus and the shear box

the geogrid, T , and an overburden pressure, σ_0 , the tests are carried out by vertically loading at a constant speed of 0.35mm/min which is the same as the speed used in the

Table 1. Physical properties of sand

Specific gravity of soil particle, G_s	2.64
Maximum void ratio, e_{max}	0.971
Minimum void ratio, e_{min}	0.601
Uniformity coefficient, U_c	1.7
Mean particle size, D_{50} (mm)	0.18

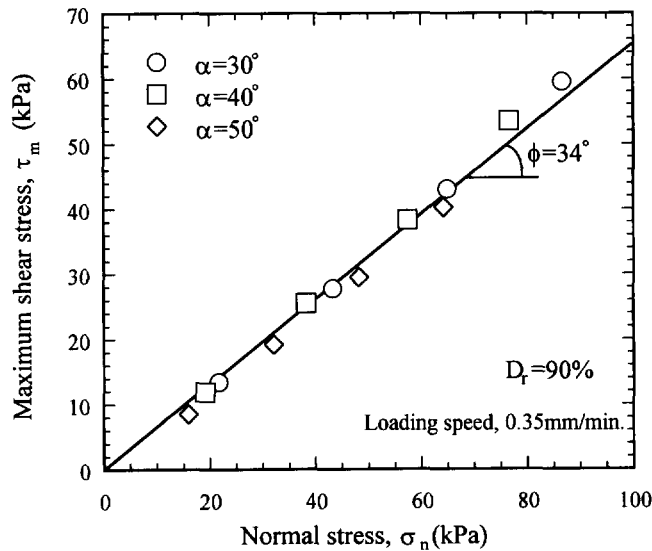


Figure 3. Strength properties of sand

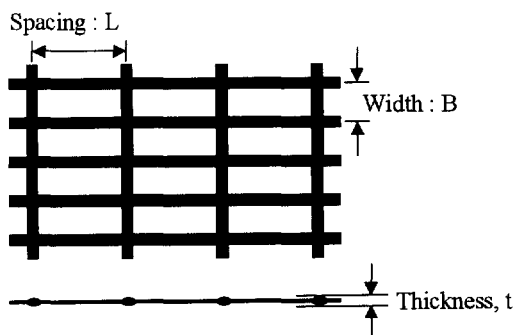


Figure 4. Geogrid measurements

Table 2. Properties of geogrids

	Tensile strength (kN/m)	Spacing L(cm)	Width B(cm)	Thickness t(cm)
Geogrid A	76.6	0.89	0.94	0.13
Geogrid B	37.2	5.42	2.79	0.10
Geogrid C	28.4	2.97	0.83	0.06
Geogrid D	76.6	1.78	0.94	0.13

tests on sand samples. The test conditions are summarized in Table 3.

Table 3. Test conditions

Type of end-restraint	Fixed-end, Sliding-end
Tensile force applied to geogrid, T (kN)	0.373, 0.981, 1.961
Overburden pressure, σ_0 (kPa)	25, 50, 75, 100
Sliding angle, α ($^\circ$)	30, 40, 50

4 TEST RESULTS AND DISCUSSION

4.1 Effect of end-restraint

Figure 5 shows the typical relationships between shear force on the sliding plane, S , and shear displacement, D , obtained from a series of tests. The same tendency is observed in the fixed-end and sliding-end types. The curves in Figure 5 are approximated by hyperbolas given by the equation

$$S = \frac{D}{a \cdot D + b} \quad (1)$$

a and b are constants in which $1/a$ is the asymptotic line of the curves and is approximated as the maximum value of shear force, S_m , on the sliding plane. The relationships between the ratio, $S_{m(F)}/S_{m(S)}$, and the normal stress on the sliding plane, σ_n , are shown in Figure 6 in which $S_{m(F)}$ and $S_{m(S)}$ are the maximum values of shear forces for the fixed-end and the sliding end tests respectively. The maximum value of shear force for the fixed-end test is larger than that of the sliding-end test. Higher reinforcing effects in fixed-

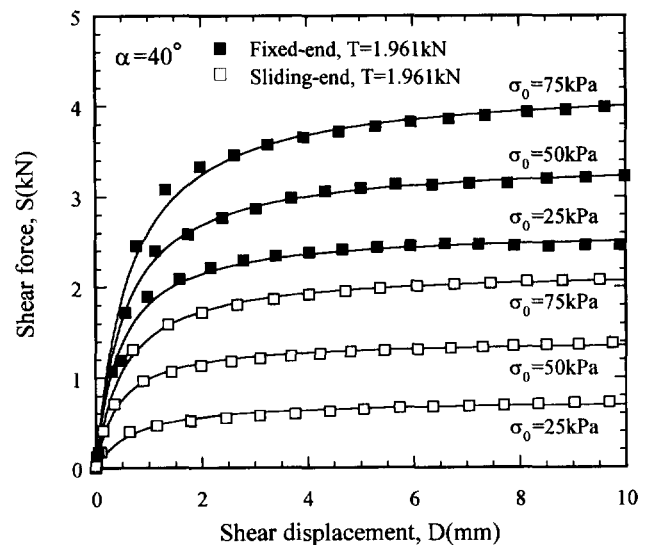


Figure 5. Relationships between shear force, S , and shear displacement, D

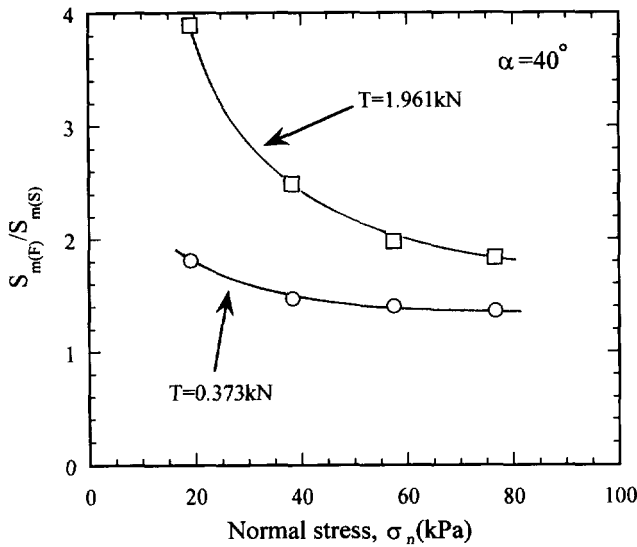


Figure 6. Relationships between $S_{m(F)}/S_{m(S)}$ and normal stress, σ_n

end tests were observed in both small normal stress values and large tensile force of geogrid. The reinforcing effects in sliding-end test is not mobilized, especially in small normal stresses, σ_n , because there is little friction between geogrid and soil.

The maximum values of shear stress measured in the tests are used to investigate the reinforcing effect in the two types of end-restraint conditions. The maximum value of shear stress on the sliding plane is calculated as

$$\tau_m = \frac{S_m}{A'} \quad (2)$$

where A' is the area of the sliding plane. Typical test results are shown in Figure 7. For sand samples, the relation between $\tau_{m(N)}$ and σ_n is a straight line through the origin with an inclination of $\tan\phi$ as shown in Figure 3;

$$\tau_{m(N)} = \sigma_n \cdot \tan\phi \quad (3)$$

in which ϕ is the internal friction angle of sand.

For geogrid-reinforced sand, the relationship will, in general, be expressed as follows;

$$\tau_{m(R)} = \tau_1 + \{(1 + \beta) \tan\phi\} \sigma_n \quad (4)$$

where τ_1 is the intercept on the τ_m axis and $\beta \cdot \tan\phi$ is the increment in slope of the reinforced lines from the sand line. The values of τ_1 and β depend on the end-restraint conditions. The value of τ_1 in the sliding-end type is approximately equal to zero, whereas the value in the fixed-end type changes with the tensile force of geogrid, T , as shown in Figure 7. The values of β in the two end-restraint

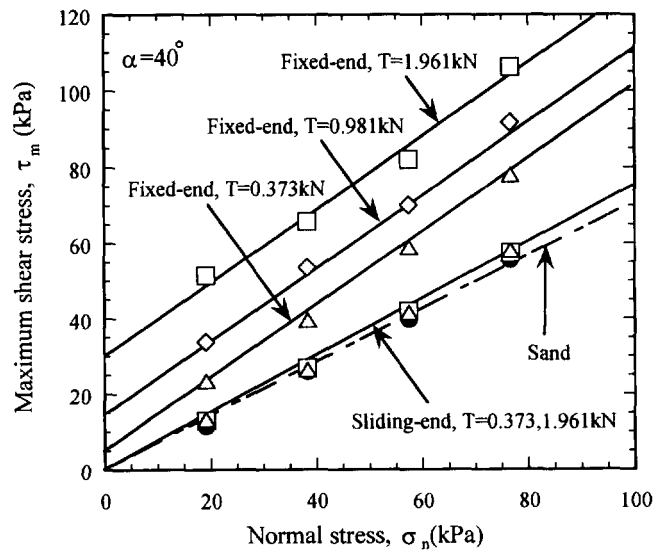


Figure 7. Relationships between maximum shear stress, τ_{max} , and normal stress, σ_n

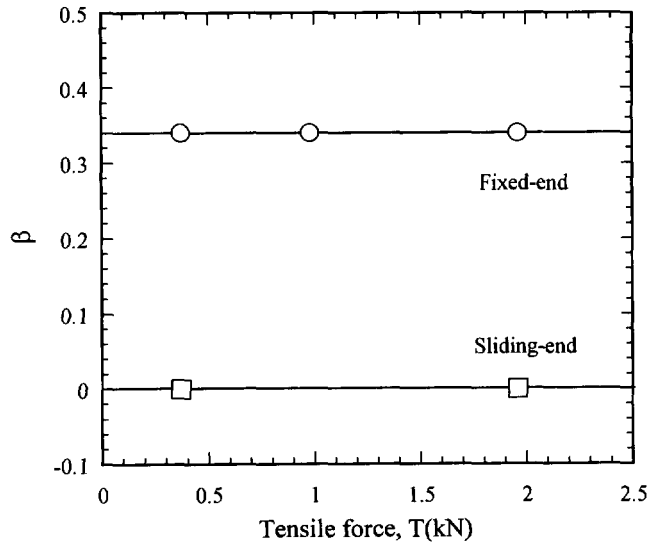


Figure 8. Relationships between β and tensile force, T

conditions are summarized in Figure 8 where β is approximately equal to zero in the sliding-end type and has a constant value in the fixed-end type irrespective of the tensile force of geogrid, T , i.e.

$$\text{Fixed-end: } \tau_1 \neq 0, \beta \neq 0 \quad (5)$$

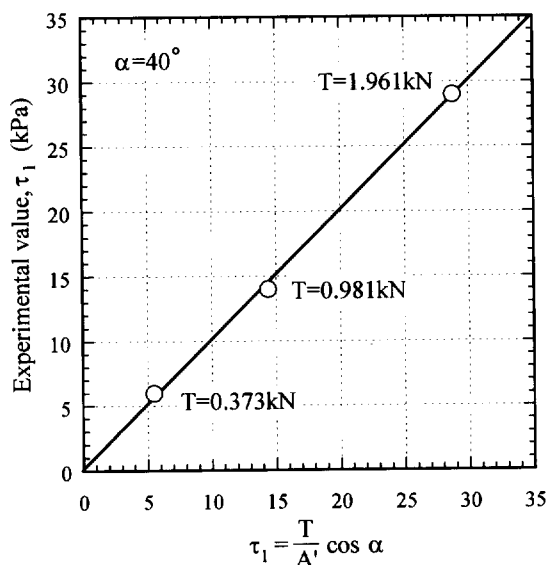
$$\text{Sliding-end: } \tau_1 \approx 0, \beta \approx 0 \quad (6)$$

In conclusion, a significant effect of reinforcement cannot be obtained in the sliding-end type. In order to obtain a significant effect of reinforcement, the geogrid should be fixed on the facing of the soil structure in such a way that the geogrid and the soil in the moving soil mass do not move relative to each other.

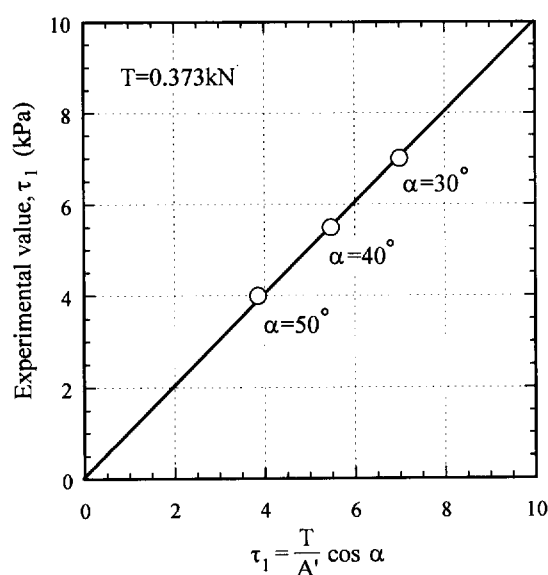
4.2 Evaluation of reinforcement effect in fixed-end type

4.2.1 Evaluation of τ_1

The design of the apparatus is such that the normal component of tensile force on the sliding plane is not transmitted to the soil and therefore a component of reinforcement effect, $T \cdot \sin \alpha \cdot \tan \phi$, due to tensile force of geogrid, T , cannot be mobilized in the tests. Therefore, the observed reinforcement effect due to the tensile force, T , is a component along the sliding plane, τ_1 .



(a) Different tensile forces of geogrid, T



(b) Different sliding angles, α

Figure 9. Comparison between experimental results and calculated values of τ_1

$$\tau_1 = \frac{T}{A'} \cos \alpha \quad (7)$$

The calculated values from Equation (7) and the experimental results in Figure 7 are almost the same as shown in Figures 9a and b. Therefore, Equation (7) well expresses the experimental results under different tensile forces, T , and sliding angles, α .

4.2.2 Evaluation of the coefficient β

The β in Equation (4) can be considered to be a coefficient for the increment in normal stress on the sliding plane due to the placement of geogrid in soil. The coefficient β will therefore depend on the density of the soil and the shape of geogrid. A shape index, R , for evaluating the shape characteristics of the geogrid has been proposed by the authors (Ochiai et al, 1996) as follows;

$$R = \frac{2t(B+L) \frac{A}{B \cdot L}}{A} = 2t \left(\frac{1}{B} + \frac{1}{L} \right) \quad (8)$$

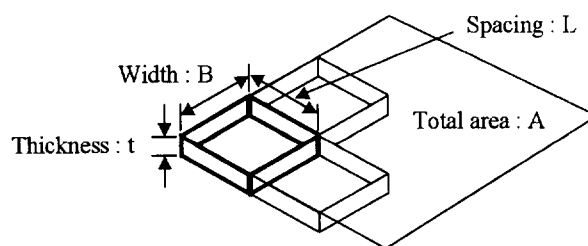


Figure 10. Description of measurements in the shape index

where notations in Equation (8) are shown in Figure 10. It is noted that the value of R represents the effects in which the soil is confined into the aperture of geogrid, and is pressed by the surface of geogrid. Four kinds of geogrids with different values of R were used in this study. A unique β - R relationship can be observed by comparing the shape index R and the coefficient β as shown in Figure 11.

In fixed-end tests, where the geogrid and the soil in the moving soil mass do not move relative to each other, the geogrid restricts the deformation of soil and therefore an additional normal stress, $\beta \cdot \sigma_n$, is induced on the sliding plane as illustrated in Figure 12. This effect of soil reinforcement may be called the confining effect (Ochiai et al 1996).

Thus, the maximum value of shear stress, $\tau_{m(F)}$, measured in the fixed-end tests may be expressed as

$$\tau_{m(F)} = \frac{T}{A'} \cos \alpha + (1 + \beta) \sigma_n \tan \phi \quad (9)$$

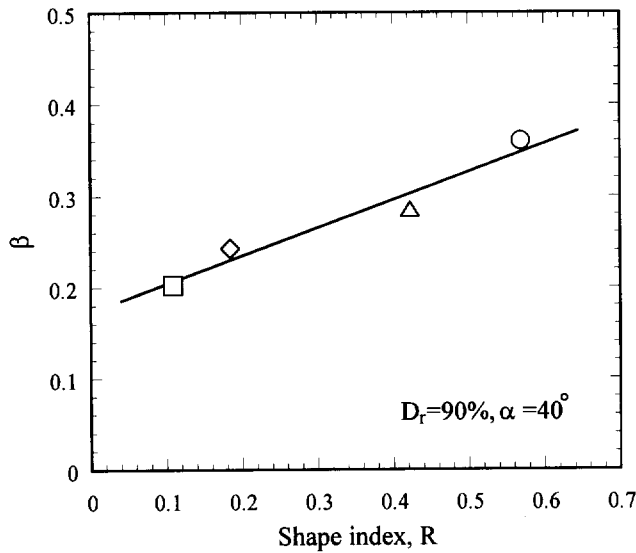


Figure 11. Relationship between β and shape index, R

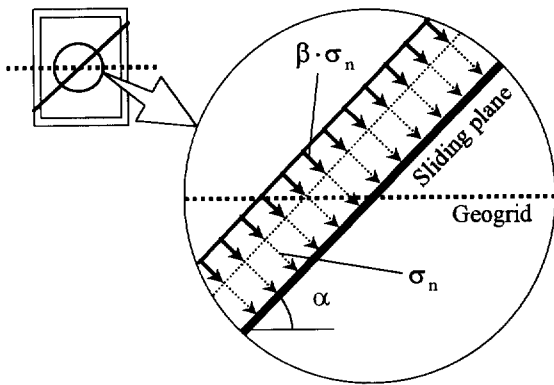


Figure 12. Condition of normal stress around the geogrid

5 REINFORCEMENT EFFECT IN GEOGRID-SOIL STRUCTURES

The test apparatus used in this study was designed such that the normal component on the sliding plane of tensile force of geogrid, $T \cdot \sin \alpha$, is directly transmitted to the lower box and not to the soil. Therefore, the normal component of reinforcement effect due to the tensile force of geogrid, $T \cdot \sin \alpha \cdot \tan \phi$, is not mobilized in the test. However, this component of reinforcement effect is considered to exist in in-situ conditions and is therefore added to the value obtained from the laboratory test. Thus the maximum values of shear stress in geogrid-soil structures may be expressed as follows;

$$\tau_{m(F)} = \frac{T}{A'} (\cos \alpha + \sin \alpha \cdot \tan \phi) + \{(1 + \beta) \sigma_n\} \tan \phi \quad (10)$$

where $\beta \cdot \sigma_n$ is an additional normal stress on the sliding

plane induced by the restriction of soil deformation due to the placement of geogrid in soil.

6 CONCLUSIONS

A series of tests has been performed to clarify the effect of end-restraint in geogrid-soil structures. It has been concluded that:

1. In order to obtain a significant effect of reinforcement, one end of the geogrid should be fixed on the facing of the soil structure in such a way that the geogrid and the soil in the moving soil mass do not move relative to each other.
2. For the fixed-end type, there exists an additional confining effect which increases the normal stress on the potential sliding plane in addition to the effect due to the tensile force of geogrid. The maximum value of shear stress, $\tau_{m(F)}$, in the geogrid-soil structure may therefore be expressed as

$$\tau_{m(F)} = \frac{T}{A'} (\cos \alpha + \sin \alpha \cdot \tan \phi) + \{(1 + \beta) \sigma_n\} \tan \phi$$

REFERENCE

- Ochiai, H., Yasufuku, N., Yamaji, T., Guang-Li Xu and Hirai, T. (1996) "Experimental evaluation of reinforcement in geogrid-soil structure", *Proc. of International Symposium on Earth reinforcement (IS Kyushu 96)*, Balkema publishers, Vol. 1. pp. 249-254

Application of Dilatancy Models to Soils Reinforced by Geosynthetics

H. Ohta

Professor, Department of Civil Engineering, Kanazawa University, Kanazawa, Ishikawa, Japan

M. Hirata

Graduate Student, Department of Civil Engineering, Graduate School of Kanazawa University, Kanazawa, Ishikawa, Japan

A. Iizuka

Associate Professor, Department of Architecture and Civil Engineering, Kobe University, Kobe, Hyogo, Japan

T. Yamakami

Technical Officer, Department of Civil Engineering, Kanazawa University, Kanazawa, Ishikawa, Japan

Y. Yokota

Engineer, Maeda Kohsen Co. Ltd, Fukui, Japan

K. Ohmori

Instructor, Department of Civil Engineering, Kanazawa University, Kanazawa, Ishikawa, Japan

ABSTRACT: This paper aims at rationally explaining the mechanical behavior of the soil structure reinforced by geosynthetics. The attention is paid to confining effect by the geosynthetics under shearing in this paper. The confining effect is interpreted as the mechanical interaction such that the reinforcement material works so as to prevent dilative deformation of soils. Then, elasto-plastic constitutive models which can describe the dilative deformation of soils under shearing are introduced and applied to the finite element simulation of the mechanical behavior of soil structure reinforced by geosynthetics. A full-scale in-situ model test, which was carried out in Kanazawa, Japan, is chosen to analyze. After verification of applicability of employed methodology to the analysis of the model test, the computed results are compared with the monitored behaviors of the soil structure reinforced by geosynthetics in the model test.

KEYWORDS: Geosynthetic reinforcement, Dilatancy of compacted soils, Elasto-plastic model, Finite element simulation

1 INTRODUCTION

The behavior of the soil structure reinforced by geosynthetics is governed by the mechanical interaction of soils and geosynthetic materials. In the numerical simulation of the behavior of such soil structure, appropriate modeling of its mechanical interaction is required. The authors tried to explain the reinforcement mechanism by geosynthetics throughout a series of finite element numerical simulations for a full scale in-situ model test (Ohta et al, 1996), where soils were simply modeled as non-linear elastic materials by employing the hyperbolic constitutive relation. However, observed behaviors in the in-situ model test could not be well explained. Particularly, the development of strain localization, which was prominently observed in the test, could not be well expressed. This has led the authors to feel the importance of introducing the contraction/dilatation characteristics of soils under shearing into the numerical simulation. Then, this paper focuses on the dilatancy characteristics of soils and the reinforcement mechanism is tried to be interpreted as that the geosynthetics work so as to confine the dilation of soils under shearing. The elasto-plastic models for soils are introduced to describe the dilatancy characteristics of compacted soils of which the reinforced soil structure is composed. An idea to specify input parameters needed in the analysis for the compacted soils is proposed and a series of finite element simulations of full scale in-situ model test are carried out. Finally the results obtained are

compared with monitored behaviors in the test.

2 MODEL TO DESCRIBE DILATANCY OF COMPACTED SOILS

2.1 Sekiguchi and Ohta's Model

A model employed in this paper is the elasto-plastic constitutive model proposed by Sekiguchi and Ohta (1977). This model had been primarily developed for naturally consolidated-saturated clays and can be regarded as an extension of the original Cam Clay model. The shear behavior of heavily over-consolidated clays is represented by strain-softening material with dilation in this model. The positive volumetric strain (dilation) which the model yields varies with the over-consolidated ratio, OCR . Higher OCR produces greater dilation under shearing. When this model is applied to the compacted unsaturated soils that tend to dilate under shearing, some idea on how the compacted soils can be modeled as the heavily over-consolidated saturated clays is required. The section 4.2 is devoted to evaluate the material properties of compacted soils as the heavily over-consolidated clay.

When this model is incorporated into a finite element code, a problem arises, that is, the conventional judgement criterion by Hill (1958) cannot distinguish the subsequent loading (elasto-plastic response) in the strain softening region from the unloading (elastic response). Asaoka et al. (1994) introduce a new criterion which can judge the

subsequent loading in the strain-softening region. The new judgement criterion is employed here and is briefly summarized as follows.

When the plastic strain increment is given by the following associated flow rule as,

$$\dot{\epsilon}_{ij}^p = \Lambda \frac{\partial f}{\partial \sigma_{ij}}, \quad (1)$$

proportional constant Λ can be expressed in terms of plastic strain increment as,

$$\Lambda = \frac{L}{X}, \text{ and } L = \frac{\partial f}{\partial \sigma_{ij}} C_{ijkl}^e \dot{\epsilon}_{kl}^p, \\ X = \frac{\partial f}{\partial \sigma_{ij}} C_{ijkl}^e \frac{\partial f}{\partial \sigma_{kl}} + h, \text{ } h = \frac{\partial f}{\partial \sigma_{ij}} \delta_{ij}, \quad (2)$$

where $\dot{\epsilon}_{ij}^p$ is the incremental plastic strain tensor, σ_{ij} is the stress tensor, C_{ijkl}^e is the elastic stiffness tensor, f is the yielding function. In the case of Sekiguchi and Ohta's model, the yielding function f is given as,

$$f = MD \ln \frac{p}{p_0} + D \eta^* - \epsilon_{ij}^p \delta_{ij} = 0, \quad (3)$$

where M is the critical state parameter, D is the dilatancy coefficient proposed by Shibata (1963), p and p_0 are mean stresses at the current state and at the reference state, respectively, η^* is generalized deviatoric stress ratio defined by

$\eta^* = \sqrt{\frac{3}{2} \left(\frac{s_{ij}}{p} - \frac{s_{i_0 j_0}}{p_0} \right) \left(\frac{s_{ij}}{p} - \frac{s_{i_0 j_0}}{p_0} \right)}$, s_{ij} is the deviatoric stress tensor ($= \sigma_{ij} - p \delta_{ij}$). Now, since the plastic coefficient X of Eq.(2) always stays positive, the loading or unloading can be judged by the sign of scalar function L of Eq.(2) as,

loading (elasto-plastic)	if $L > 0$	
neutral	if $L = 0$	(4)
unloading (elastic)	if $L < 0$	

This judgement criterion is incorporated into the finite element program, DACSAR (Iizuka and Ohta, 1987). 4-node quadrilateral constant strain element is employed in the finite element discretization. Fig.1 indicates the verification of F.E. program. Computed effective stress paths of triaxial undrained shear are compared with theoretical curves where q is the deviatoric stress by

$$q = \sqrt{\frac{3}{2} s_{ij} s_{ij}}.$$

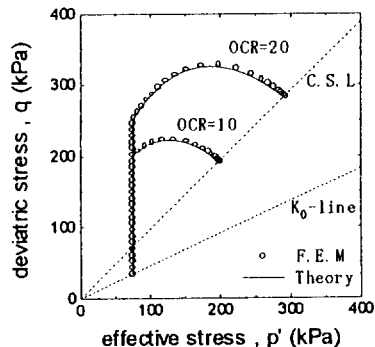


Figure 1 Stress paths of Sekiguchi and Ohta's model

2.2 Drucker and Prager's Model

Another model employed is the elasto-plastic constitutive model of which the yielding function is Drucker and Prager's type. This model always yields the dilation without strain-softening. The amount of dilation is determined by the input parameters, c and ϕ regardless of how much the soils are over-consolidated. Drucker and Prager's yielding function is given as,

$$f = \alpha I_1 + \sqrt{J_2} - k = 0, \quad (5)$$

where I_1 is the first invariant of stress tensor ($I_1 = p$), $\sqrt{J_2}$ is the second invariant of deviatoric stress tensor ($\sqrt{3} \sqrt{J_2} = q$) and α and k are constants relating with the cohesion c and the internal friction angle ϕ as,

$$\alpha = \frac{\tan \phi}{\sqrt{9 + 12 \tan^2 \phi}} \text{ and } k = \frac{3c}{\sqrt{9 + 12 \tan^2 \phi}}. \quad (6)$$

The associated flow rule is employed and the model is incorporated into the finite element program, DACSAR. Fig.2 compares computed effective stress paths of triaxial undrained shear with theoretical ones. Good agreements are obtained.

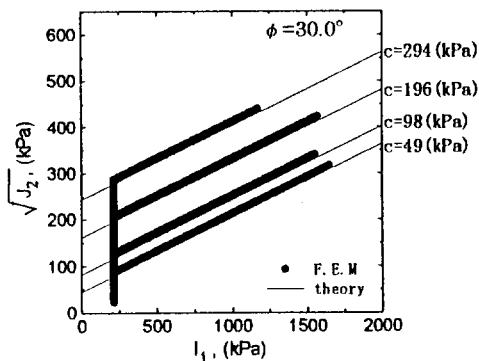


Figure 2 Stress paths of Drucker and Prager's model

3 SIMULATION OF FULL SCALE IN-SITU MODEL TEST

3.1 Full Scale In-situ Model Test

A full scale in-situ model test was conducted during the period from July, 20, to August, 8, '92 in Kanazawa, Japan, in order to investigate the reinforcement mechanism by geosynthetics (Nishimoto et al., 1992, Ohta et al., 1996). A beam shaped soil structure reinforced by geosynthetics was designed and the resistance capability of the structure against the bending moment was investigated. Fig.3 shows the side view of the test embankment that was 2.75 m high, 42.5 m long and 4.5 m wide, including supporting berm. In the construction of the test embankment, the soil was spread over up to 10 cm thickness and compacted sufficiently by the vibration roller. The degree of compaction was controlled by the dry unit weight

measured by RI (radioisotope) method. The geosynthetics (Adem#G-6, Maeda Kohsen Co.) were placed at every 50 cm. The experiment began by removing steel H piles, which were supporting the reinforced portion by geosynthetics, in the order by the number in Fig.4. The deformation of the reinforced soil structure was measured by photographic observation of the position changes of markers installed at every 25 cm interval on the side of the embankment. The measured maximum deformation at each step is summarized in Table 1. In the experiment, when the #10 steel H pile was removed at Step 9, the structure failed.

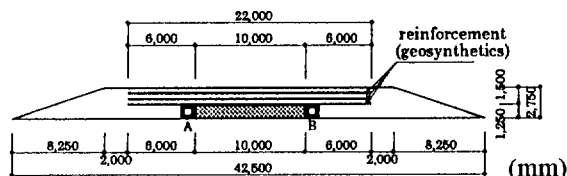


Figure 3 Side view of test embankment

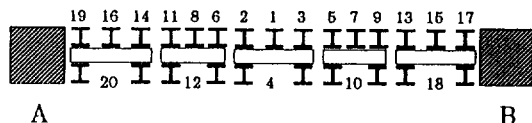


Figure 4 Position of supporting steel H piles
Table 1 Step in experiment and results

step	No. of steel pile to be moved	maximum deformation (m)
1	No.1	0.000
2	No.1~No.2	0.150
3	No.1~No.3	0.319
4	No.1~No.5	0.438
5	No.1~No.6	0.590
6	No.1~No.7	0.770
7	No.1~No.8	0.880
8	No.1~No.9	>1.200
9	No.1~No.10	>1.200

3.1 Applicability of Constitutive Models

The soils were sampled from the test site and served to one-dimensional compression (oedometer) tests and constant volume shear box (CV-SBT) tests in the laboratory. The soil samples were consolidated in the shear box by the vertical pressure of 39.2, 78.4, 156.8 and 313 kPa and then were sheared under the constant volume. Fig.5 shows the effective stress paths obtained from CV-SBT tests for undisturbed compacted soil samples. Experimental effective stress paths in Fig.5 are quite similar to typical behaviors of over-consolidated clays. The authors believe that constitutive models which can explain dilation of a soil element are applicable to the compacted soils, when the effective stress paths in Fig.5 are compared with those in Figs.1 and 2.

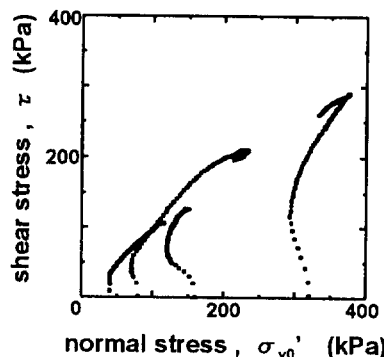


Figure 5 Effective stress paths of compacted soils

3.2 Evaluation of Material Parameters Needed in Analysis

The soils used in the full-scale test were sampled from the site and were prepared at the water content of 20, 23, 25, 27 and 30 %. These loose disturbed soils were served to CV-SBT tests. The soils were consolidated in the shear box by the vertical pressure of 39.2, 78.4, 156.8 and 313 kPa and then were sheared under the constant volume. The results obtained are shown in Fig.6, where the upper figure of Fig.6 presents the relationship between the dry unit weight ρ_d and the consolidation pressure σ'_v and the lower one shows the equivalent 'undrained' strength, s_u , obtained from CV-SBT for very loose disturbed samples. The increase rate of 'undrained' strength results in $s_u/\sigma'_v = 0.234$.

Next, the undisturbed compacted soil samples of which natural water contents varied from 20.6 to 23.4 % in-situ were served to the consolidation and shear tests in the same manner. The plots of test results for undisturbed samples are added to Fig.6 and then Fig.7 is obtained. The plots for undisturbed samples seem to form straight lines with in-situ water contents as shown in Fig.7. When these lines are extended to compression lines obtained from consolidation tests in the shear box for very loose disturbed samples, the equivalent pre-consolidation pressures σ'_{v0} can be estimated. Thus, the equivalent pre-consolidation pressures σ'_{v0} and the equivalent over-consolidation ratios can be specified for in-situ compacted soils as in Table 2.

The 'undrained' strengths (\blacktriangle) obtained from shear tests for undisturbed compacted samples can be converted to its equivalent N.C. 'undrained' strengths by using the following equation,

$$\left(\frac{s_u}{\sigma'_{v0}}\right)_{NC} = OCR^{-\bar{\lambda}} \left(\frac{s_u}{\sigma'_v}\right)_{OC} \quad \text{and} \quad \bar{\lambda} = 1 - \bar{c}_s / c_c \quad (7)$$

where c_c and \bar{c}_s are gradients of compression lines in Fig.6 and the equivalent swelling line in $e - \log \sigma'_v$ space of Fig.7. Thus converted strengths are plotted in the lower figure of Fig.7 as \blacksquare and agree with the broken line indicating $s_u/\sigma'_v = 0.234$.

Then, input parameters needed in Sekiguchi and Ohta's model can be specified as follows. The N.C. undrained

strength obtained from the constant volume shear box test has been theoretically derived from Sekiguchi and Ohta's model as (Ohta et al., 1985),

$$\left(\frac{s_u}{\sigma'_{v0}}\right)_{NC} = \frac{1+2K_0}{3\sqrt{3}} M \exp(-\Lambda), \quad (8)$$

where K_0 is the coefficient of earth pressure at rest, M is the critical state parameter ($= \frac{6\sin\phi'}{3-\sin\phi'}$, ϕ' : effective internal friction angle) and Λ is the irreversible ratio (see, Iizuka and Ohta, 1987). Therefore, by employing the empirical relations: $M = 1.75\Lambda$ (Karube, 1975), $K_0 = 1 - \sin\phi'$ (Jaky, 1944), Eq.(8) can be expressed as the function of only ϕ' shown in Fig.8. Now, since the increase rate of strength $(s_u/\sigma'_{v0})_{NC}$ is given as 0.234 in Fig.6, the effective internal friction angle is specified as 27.5 degree for in-situ compacted soils. Other parameters needed in Sekiguchi and Ohta's model are also specified in the manner shown in Fig.9. Thus obtained input parameters are summarized in Table 3. In the numerical simulation, since the equivalent pre-consolidation pressures of in-situ compacted soils vary in wide range from 931 to 2058 kPa as in Table 2, two cases ($\sigma'_{v0} = 980$ kPa: Case 1, 1960 kPa: Case 2) are considered.

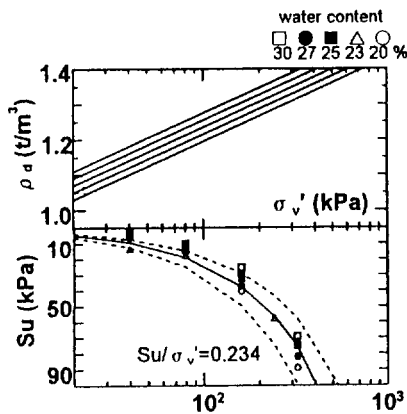


Figure 6 Experimental relation of ρ_d , σ'_v , and s_u

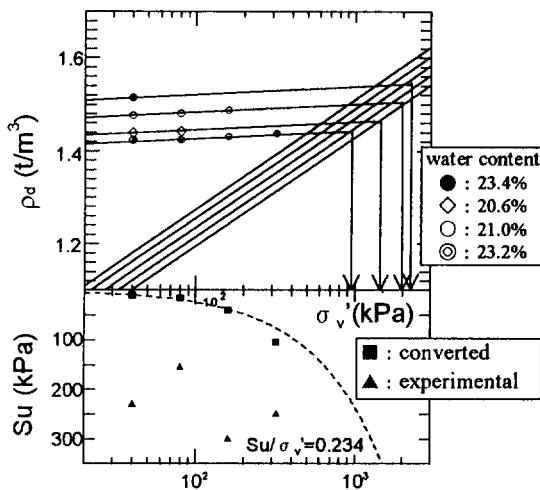


Figure 7 Evaluation of preconsolidation pressure

Table 2 Specified over-consolidation ratio

effective overburden pressure σ'_{v0} (kPa)	water content w (%)	equivalent preconsolidation pressure σ'_{v0} (kPa)	over consolidation ratio OCR
39.2	23.4	2058.0	52.50
78.4	20.6	1470.0	18.75
156.8	21.0	1960.0	12.50
313.6	23.2	931.0	2.97

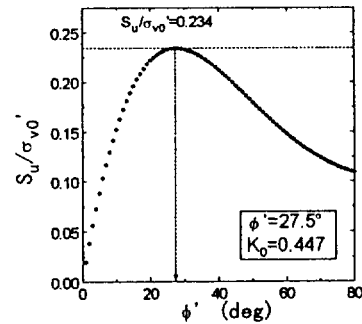


Figure 8 Evaluation of effective internal friction angle

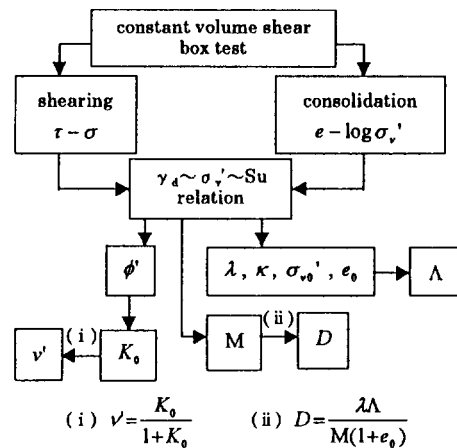


Figure 9 Specification procedure of parameters

Table 3 Parameters for Sekiguchi and Ohta's model

Λ	K_0	M	λ
0.85	0.54	1.09	1.92
D	e_0	v	
0.85	0.77	0.35	

Triaxial CU tests were also carried out for undisturbed soil samples. The results obtained are summarized in Table 4 and the input parameters (c' and ϕ' in terms of effective stress) needed in Drucker and Prager's model can be specified. However, two test results shown in Table 4 happened to quite differ each other. Therefore, two cases in the numerical simulation are considered as shown in Table 4.

Table 4 Parameters for Drucker and Prager's model

	case3	case4
effective cohesion : c'	0.18	0.11
effective internal angle : ϕ'	34.1	26.3
Lame's constant : λ (kN/m ²)	333.2	245.0
Lame's constant : μ (kN/m ²)	166.6	122.5
unit weight of the soil : ρ_t (t/m ³)	1.707	

Fig.10 indicates the experimental result of uniaxial extension test for geosynthetics materials used in the field model test. The linearly elastic model is applied to represent the stress and strain relationship of the geosynthetics in Fig.10 and the bar element in the F.E. simulation is employed. The input parameters are summarized in Table 5.

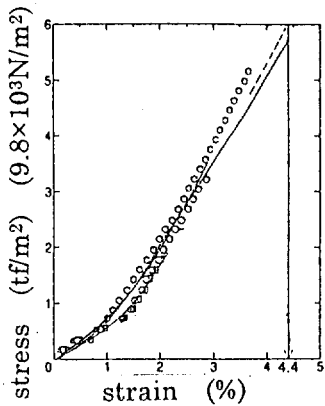


Figure 10 Stress and strain relation of geosynthetics

Table 5 Parameters for geosynthetics

geosynthetics	
max. extension force : N_f (kN/m)	58.8
sectional area : $A \times$	1337.7
Young's module : E (kN)	

3.3 Comparison of Finite Element Simulations

The finite element mesh employed in the simulation of the full-scale in-situ model test is shown in Fig. 11. The 4-node constant strain finite element and the forward incremental calculation scheme are used. The supporting portion indicated by shaded part in Fig.7 is removed following the order in the experiment as shown in Table 1. Table 6 indicates the step number when the axial force of a

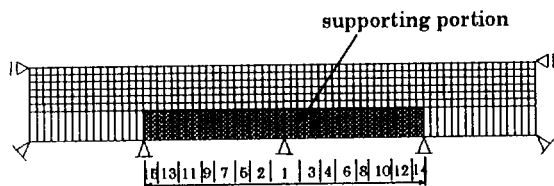
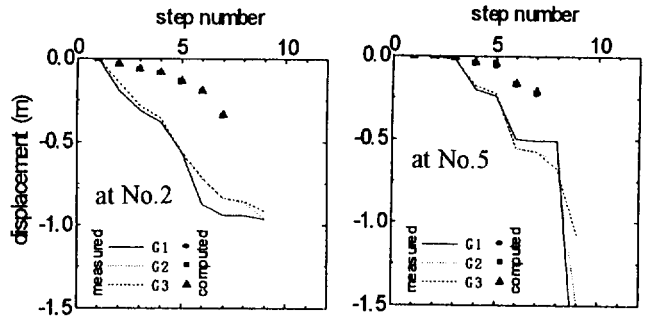


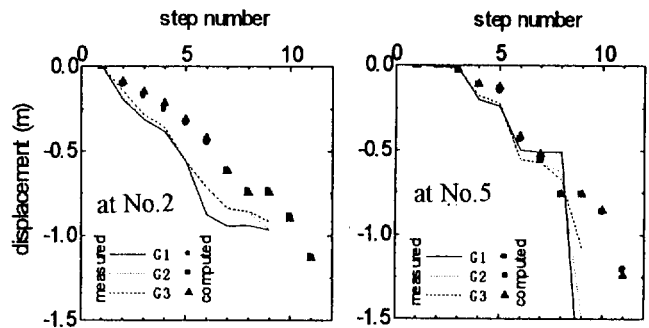
Figure 11 Finite element mesh in simulation

Table 6 Step number when the structure failed

Sekiguchi-Ohta's model	case1	step=7
	case2	step=8
Drucker-Prager's model	case3	step=12
	case4	step=11



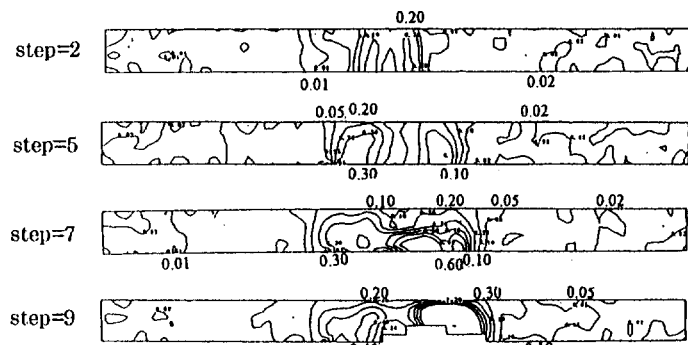
(a) In case of Sekiguchi and Ohta's model



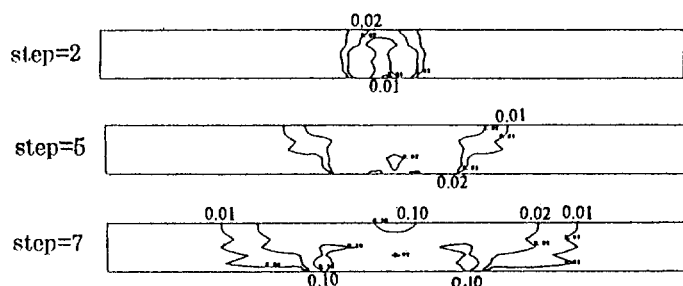
(b) In case of Drucker and Prager's model

Figure 12 Computed and monitored deformations

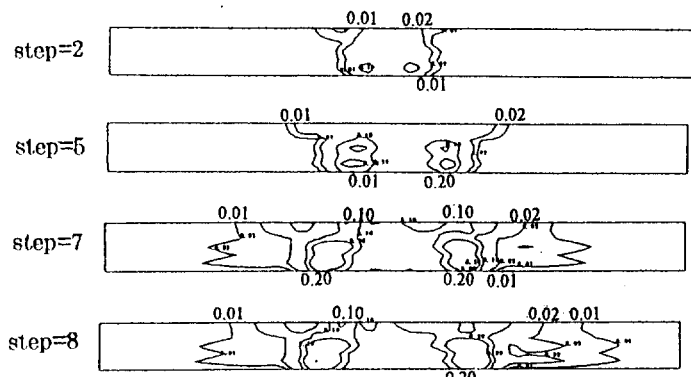
bar element exceeded its strength and the structure failed. In Figs.12, the computed predictions and the monitored behaviors are compared above positions of steel H piles of No.2 and No.5 (refer to Fig.4), in which the horizontal axis in the figure represents the step number shown in Table 1. The labels G1, G2 and G3 indicate the geosynthetics placed, that is, G1 is at the upper layer, G2 is at the middle layer and G3 is at the lower layer. As seen from figures, the monitored deformations are larger than our predictions. It would be because the geosynthetics hung down in experiment when the support was removed and then soils between geosynthetics were loosened. Figs.13 illustrates the contours of shear strain distribution. The results of Case 1 (Sekiguchi and Ohta's model) and Case 4 (Drucker and Prager's model) are chosen to be compared with the monitored result in Fig.13, because there was not much differences between results of Case 1 and Case 2 nor between results of Case 3 and Case 4. Fig.13(d) is added to be compared with the numerical result of the hyperbolic model which does not consider the dilation under shearing (Ohta et al., 1996). At earlier step such as at Step 2, the hyperbolic model does not explain the sharp distribution of strain localization which is observed as in Fig.13(a). The dilatancy models seem to qualitatively explain the monitored development of strain localization from earlier



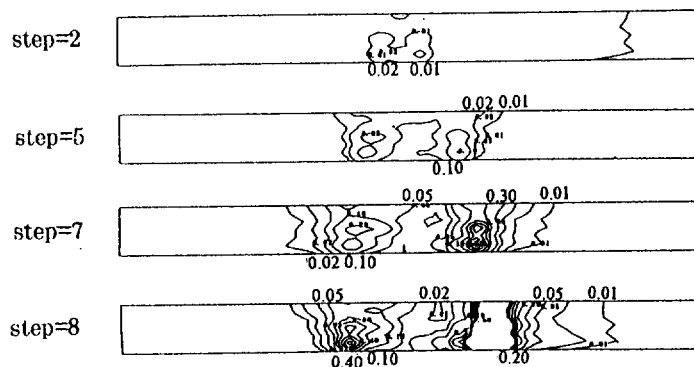
(a) Observed shear strain distribution



(b) In case of Sekiguchi and Ohta's model



(c) In case of Drucker and Prager's model



(d) In case of hyperbolic model

Figure 13 Comparison of shear strain distribution, γ

step. In the case of Sekiguchi and Ohta's model, the shear strain localization concentrates in narrower zone, which is closer to monitored tendency, but distributes in wider region in the case of Drucker and Prager's model. However, the quantitative agreement with monitored distribution of shear strain has not been achieved. The authors guess that it is because the soils were considerably loosened resulting in being less stiff when the steel H piles were removed.

4 CONCLUDING REMARKS

A beam shaped soil structure reinforced by geosynthetics was designed to investigate the resistance capability of the structure against the bending moment and was constructed as a full-scale model test. The monitored behavior of the full-scale model test and its numerical predictions are compared. In numerical simulation, dilatancy models are introduced in order to capture the development of strain localization in the beam shaped soil structure reinforced by geosynthetics. Specification procedure of input parameters needed in the models is presented. The compacted soils used in the full-scale model test are represented by the over-consolidated clays equivalent to them. It is found that dilatancy models qualitatively explain the monitored behaviors in the field model test. However, the above results were obtained for a rather unique test setup and more precise examination on general applicability of dilatancy models is required.

REFERENCES

- Asaoka, A., Nakano, M. and Noda, T. (1994) "Soil-water Coupled Behaviour of Saturated Clay near/at Critical State", *Soils and Foundations*, Vol.34, No.1, pp.91-105.
- Hill, R. (1958) "A general theory of uniqueness and stability in elastic-plastic solids", *J.Mech. Phys. Solids*, Vol.6, pp.236-249.
- Iizuka, A. and Ohta, H. (1987) "A Determination Procedure of Input Parameters in Elasto-viscoplastic Finite Element Analysis", *Soils and Foundations*, Vol.27, No.3, pp.71-87.
- Karube, D. (1975) "Unstandardized Triaxial Testing Procedures and Related Subjects for Inquiry", *Proc. 20th Symposium on Geotechnical Eng.*, pp.45-60 (in Japanese).
- Nishimoto, T., Tsutsui, H. and Morikage, A. (1992) "Joint Project of Full Scale Model Test for Reinforcement by Geosynthetics", *Research Institute Report, Magara Co.* (in Japanese).
- Ohta, H. and Hata, S. (1977) "Strength of Dynamically Compacted Soils", *Proc 9th ICSMFE, Tokyo*, Vol.1, pp.239-242.
- Ohta, H., Hiura, Y., and Kuniyasu, I. (1978) "Strength Mobilized in Compacted Earth Structures at Failure", *Proc. Symposium on Soil Reinforcing and Stabilizing Techniques in Eng. Practice*, Sydney, pp.385-401.
- Ohta, H., Nishihara, A. and Morita, Y. (1985) "Undrained Stability of K_0 -consolidated Clays", *Proc. 11th ICSMFE*, Vol.2, pp.613-616.
- Ohta, H., Goren, S., Iizuka, A., Yamakami, T., Yamagishi, K. and Moroto, N. (1996) "Numerical Simulation of Beam-shaped Soil Structure Reinforced by Geosynthetics", *Proc. Int. Symp. on Earth Reinforcement, Fukuoka*, Vol.1, pp.255-260.
- Sekiguchi, H. and Ohta, H. (1977) "Induced Anisotropy and Time Dependency in Clays", *Proc. 9th ICSMFE, Specialty Session 9*, pp.229-237.
- Shibata, T. (1963) "On the Volume Changes of Normally Consolidated Clays", *Annals, Disaster Prevention Research Institute, Kyoto University*, No.6, pp.128-134, (in Japanese).

Failure Of Two Fabric Reinforced Segmental Block Walls In South Africa

F.W.GASSNER

Director, Wates Meiring & Barnard, Consulting Engineers, Halfway House, Johannesburg, South Africa

G.M. JAMES

Geosynthetics Marketing Director, Kaytech Geotechnical & Industrial Fabrics, Pinetown, South Africa

ABSTRACT: The paper describes the collapse and deformation of two geotextile reinforced segmental concrete block walls in the Gauteng province. The investigation into the factors leading to the distress of the walls is recorded, as well as the back analysis of the structures. Conclusions are drawn regarding the factors that resulted in the distress. A short description of the remedial works implemented, is also provided.

KEYWORDS: Construction, Failures, Reinforcement, Retaining Walls, Woven Fabrics.

1. INTRODUCTION

The paper describes the failure and remediation of two geotextile reinforced concrete block retaining walls. The failures occurred due to a number of differences between the as-constructed and specified details of the walls, resulting in full-scale collapses of sections of the walls. The failures occurred after an exceptionally heavy rainy season in February 1996. The collapsed sections, as well as sections that had deflected excessively were rebuilt. The sections of the walls that remained standing were strengthened, to bring them upto acceptable stability levels.

One wall is adjacent to an athletics track, while the other wall supports a seating embankment for a hockey field, and carpark.

2. SPECIFIED WALL

The design of the walls was carried out in mid-1993.

The detail of the wall next to the athletics track is shown in Figure 1. The wall is 3.6 m high at a slope of 70°, using 300mm deep dry stack concrete blocks up the face. The reinforcement depth of the woven multi-filament polyester geotextile was specified as 1,6m deep (0.44 H) at a varying vertical spacing. The vertical spacing selected was a multiple of the concrete block height, and to balance or exceed the lateral earth

pressure. The specified geotextile has a tensile strength of 25kN/m.

The wall was designed based on using a silty sand backfill to the geotextile-reinforced fill, with the concrete blocks providing the local stability at the face of the wall. The design shear strength of the backfill was based on:

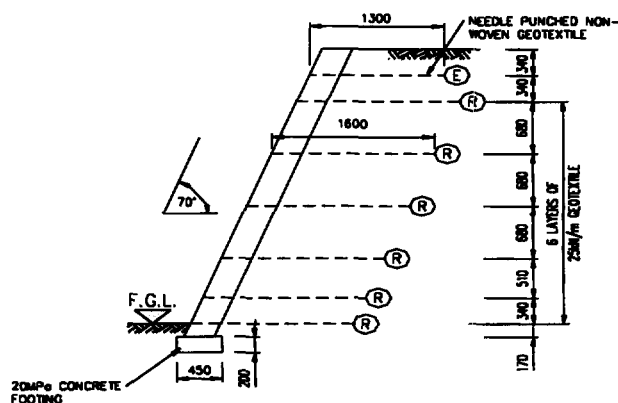


Figure 1: Specified detail of athletics track wall

$$\alpha' = 33^\circ$$

$$c' = 0\text{kPa}$$

The design was based on the fill under the athletics track having the same shear strength parameters as given above. The athletics track, and the encompassed sportsfield, was provided with both surface and subsoil drainage. The site is also located in an area where the

annual evaporation exceeds the annual precipitation. Hence, the design allowed for no phreatic surface in the backfill.

The shear resistance of the concrete blocks was included in determining the depth of reinforcement required and excluded in determining the reinforcement force required.

The design of the hockey-field wall was based on the same principles, as outlined above. The detail of this wall is shown in Figure 2.

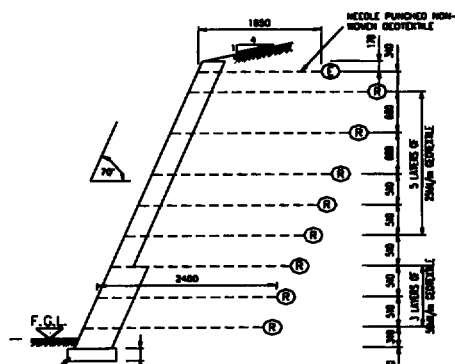


Figure 2: Specified detail of hockey field wall

FIGURE 2

The depth of the reinforcement geotextiles was specified as 2.4m (0.49 H), for the highest section of 4.9m high. The bottom part of the wall was reinforced using woven multi-filament polyester geotextiles with a maximum tensile strength of 50 kN/m. The upper part was reinforced with woven polyester geotextiles of a maximum tensile strength of 25 kN/m. The height of wall reduced along the length of the wall, and at a height of 2.6m, the wall reverted to a gravity structure. Hence this backfill was not reinforced, but 500mm deep blocks were used over the lower section of the wall.

The design was based on a 1:4 slope of the fill at the top of the wall.

3. FAILURE DESCRIPTION

3.1 Athletics track wall

The facing blocks of the wall collapsed, as a result of the lower blocks being sheared by the horizontal deformation of the wall and reinforced backfill. At the top of the fill extensive large cracks formed, upto 75mm

wide. Heavy rainfall resulted in sheet flow runoff from the field flowing into some of the cracks.

Immediately after the collapse of the athletics track wall, seepage was noted over the lower 700mm of the backfill, in areas where stormwater had not flowed into the tension cracks of the soil.

The deformed soil mass kept moving vertically over the next few weeks, until a vertical displacement of around 0.7m existed at 2.4m to 2.8m from the back of the wall. This position coincided with the trench for the irrigation pipes of the sportsfield, and the edge of the athletics track subsoil drainage. Sections of the pipes had been repaired in the past, and the pipe junctions were pulled apart by the movement of the failed wall. The foundation of the concrete blocks had rotated by around 14°, and moved laterally. The deflected reinforced soil mass remained intact for numerous months, before being removed by excavation for remediation of the wall.

3.2 Hockey field wall

The facing of the wall next to the field light mast collapsed over a 20m section, with a portion of the surcharge slope at the top of wall lying on top of the collapsed blocks. A 7m long section adjacent to this moved horizontally by over 150 mm, and opened up a 75mm wide tension crack near the top of the surcharge slope. The concrete blocks near the bottom of this wall section were also extensively cracked.

To the south of the light mast the wall supported a car park with a wall height of 3.74m and a wall slope of 70°. The area 2.5m behind the top of the wall settled by around 100mm, and a crack of 20mm wide existed at the back of the settled area. The wall had an outward bulge of between 130mm and 170mm near the mid-height. These measurements can not be exactly quantified, as no completion survey had been carried out on the wall, upon completion of construction.

4. AS-CONSTRUCTED DETAILS

4.1 Athletics track wall

The detail of the as-constructed wall is shown in Figure 3. This detail applies over most of the wall length. The end sections of the wall of lower height had no geotextile in the backfill, but a larger and heavier concrete block was used.

The bottom layers of reinforcement geotextile were missing in the fill, as well as the top layer of reinforcement geotextile. The short layer of non-woven geotextile at the top of the wall was installed to minimise the risk of erosion gullies forming behind the blocks.

This wall had a short section where no geotextiles were installed in the backfill, but the rest of the wall backfill was reinforced with either three or four layers of a woven multi-filament polyester geotextile with a tensile strength of 25kN/m.

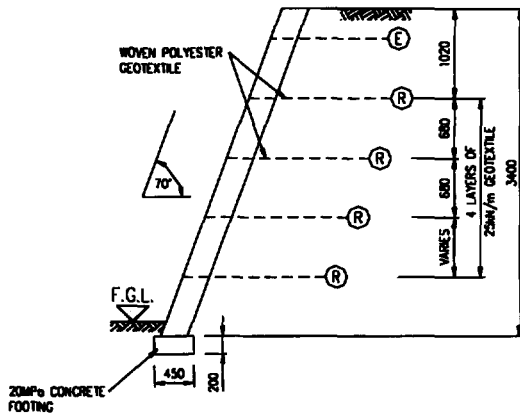


Figure 3: As-constructed athletics track wall

The backfill to the reinforced section as well as under the athletics track, consisted of a silty clay to clayey sand, with a Plasticity Index varying between 24 and 32, and a liquid limit above 43. The soil also classified as medium expansive on the van der Merwe chart for active soils. The tested shear strength of the soil is:

$$\phi' = 26,3^\circ$$

$$c' = 6 \text{ kPa}$$

4.2 Hockey field wall

The detail of the as-constructed wall is shown in Figure 4 and Figure 5.

The wall in Figure 4 was specified to be constructed as per the athletics track wall detail, to a maximum height of 3.74m. The car park at the top of the wall started 2m from the back of the wall, at the highest section of the wall. The depth of the reinforcement geotextiles was specified as 1,8m deep, and they were installed to that depth. The spacing and type geotextiles were however not installed to specification, with sections of the wall having the erosion control geotextile replacing sections of the upper two layers of

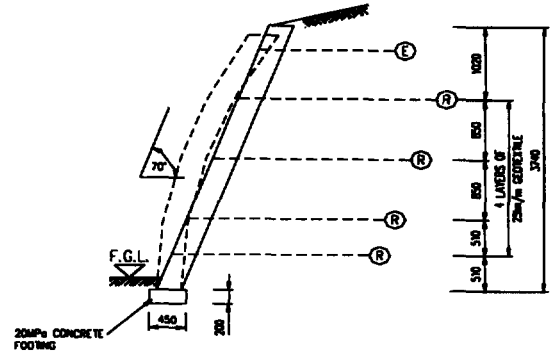


Figure 4: As-constructed hockey field wall, below carpark

reinforcement geotextiles. The tensile stiffness of the non-woven geotextile is between 20% to 30% of that of the woven reinforcement geotextile specified.

The wall in Figure 5 was built to a maximum height of 3.7m, compared to a design height of 4.9m. The toe of the wall and the breakpoint of the top of the slope above the wall were fixed, resulting in a steeper surcharge slope at the top of the wall. This slope varied between 17° and 25° to the horizontal, compared to the 14° design slope. The backfill to the wall, as well as the slope above the wall, consisted of a clayey sand to gravely silt.

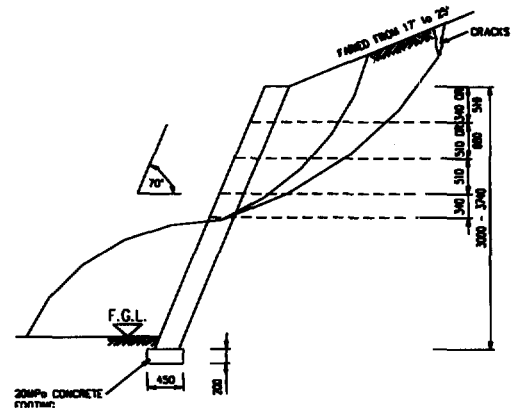


Figure 5: As-constructed hockey field wall, below sloped section

Laboratory analyses of soil samples from both walls confirmed that they were active soils, with a low shear strength, similar to the backfill of the athletics track wall. The reinforcement to the backfill varied considerably over the highest portion of the wall. A 20m section of the highest wall collapsed, while other sections deflected excessively. During reconstruction of the wall, a layer of alluvial soil was also exposed near the base of the reinforced fill where the wall had collapsed. The sections

where the wall had been designed and built as gravity walls, performed satisfactorily. The slope at the top of the wall was less than 14°.

5. BACK ANALYSIS:

The failures of the walls was back analysed, based on the following design deviation conditions:

- Reduced shear strength of poor backfill.
- Incorrect reinforcement geotextiles position.
- Geometry deviation.
- Seepage through backfill.

Each condition was analysed separately, and then in combinations, to determine the impact on the wall stability, resulting from the non-compliance's with the original design. The analysis was carried out using a dual wedge analysis program.

5.1 Reduced Shear Strength and Position of Geotextiles

Due to the variation of moisture content in South African soils between summer and winter, the 'cohesion' measured in laboratory tests on active soils (high PI), is seldom realised in the field over the long term. Hence the case of no cohesion was included in the analysis, as the walls had stood for nearly three years. For the back analysis, the full concrete block shear strength (including mechanical interlock) was included.

Wall I = Athletics track

Wall II = Hockey field

P/R = Ratio of provided to required

Case – Poor Backfill:	P/R
Wall I	
As-Constructed (3 layers)	0,86
As-Constructed (4 layers)	1,00
Geotextile spacing as specified	1,36

Wall II – Collapse

As specified slope at top, bottom geotextile missing	0,64
As specified slope at top, geotextiles as specified	2,5

Wall II – Deflected

As-Constructed (overall stability)	1,19
As specified geotextiles	1,87
As-constructed (force in geotextiles)	1,11

The analysis shows that the reduced shear strength of the soil plus the incorrect spacing of the geotextiles brings the wall close to ultimate limit state for wall I, and "beyond" ultimate limit state for the collapsed wall II. The deflected wall II results in service loads in the geotextiles with a margin of only 10% above what would be normally considered a maximum for the ultimate limit state for the geotextiles used. Geotextiles loaded to this level are expected to give rise to large deflections and excessive creep. This was clearly the case on site.

The reduced shear strength of the soil on its own is unlikely to result in a state of collapse. For a collapse to occur, one would expect the ratio of provided to required to be well below 1,0.

The "temporary situation," where a cohesion of 6kPa is effective, results in a reduction in the stresses of the geotextiles by a factor of 2.5. Also, the factor of safety for overall stability of Wall I is 1.9 and Wall II is 2.3. Hence, no stability or deflection problems would be expected. This was the case for a period of three years from construction.

5.2 Geometry Deviation

Wall II has a further complication, where the slope above the wall was constructed at a slope, which is very close to incipient failure, for a shallow sloughing failure. It can be shown that should such a failure be mobilised, that the upper 1.0m height of the wall, as built, would be at a point of incipient failure. Such a slide results in the top of the wall being pushed over, releasing the clamping effect of the blocks at the front of the geotextiles. Hence, the local stability at the top of the wall is at the limit of equilibrium, where the slope at the top of the wall approached the shear strength of the fill. ($c' = 0\text{kPa}$).

The overall stability was also analysed, based on variation of the angle of the upper slope. The result of this analysis is shown below:

Case – Poor Backfill:	P/R
25° slope at top, as specified geotextiles	0,79
17° slope at top, as specified geotextiles	0,95
14° slope at top, as specified geotextiles	1,15

5.3 Seepage

The effect of a phreatic surface in the reinforced backfill to the wall was analysed. For this a simple r_u

$$= \left(\frac{\sigma}{\gamma_w h_w} \right) \text{ factor was used on the lower failure surface}$$

of the dual wedge analysis. Using a value of $r_u=0,1$, the following results were obtained.

Case: Poor Backfill with Phreatic

Surface:	P/R
As-Built (3layers)	0,82
As-Built (4 layers)	0,91
Geotextiles – as specified	1,15
Geotextiles as specified, granular backfill	2,3

Again, it can be seen that a phreatic surface alone would probably not have been sufficient to collapse the wall.

From the above analyses, it can be concluded that in order for the wall to fail, at least two non-compliance's to the original design were required. On this basis the following scenarios were identified as having resulted in the collapses:

Wall I (Athletic track): Missing geotextiles at the base of the wall in conjunction with low shear strength soil.

Wall II (Hockey wall): Steep surcharge slope, in conjunction with low shear strength soils.

Incorrect spacing of geotextiles with the low shear strength soils lead to serviceability failure of the carpark wall.

6. REMEDIATION OF THE WALLS

6.1 Athletic Track Wall

The athletics track wall was rebuilt, using an imported granular fill. The fill was reinforced with five layers of a woven polyester geotextile with a tensile strength of 50kN/m, at a uniform depth of 2.5m into the fill. Due to space constraints, the excavation next to the athletics track had to be temporarily supported, using driven soil anchors. In the area where the soil remained very wet, subsoil drains were installed at the interface between the clayey soil and the imported granular fill. The owner of the sportsfield was also requested to carry out leakage

tests on the irrigation system to minimise the risk of saturation and erosion due to leaking water pipes.

6.2 Hockey Field Wall

The section of the hockey field wall that had been built too low, and had not deflected excessively, was reinforced with either one, two or three rows of 6m long soilnails, spaced at 1,6m horizontally. These soilnails consisted of 20mm diameter galvanised high tensile steel bars encased in grout.

The number of nails depended on the extra height of wall to be placed ontop of the existing wall, and the final height of the wall. The maximum wall raise was 1,8m ontop of an existing 3,1m high wall. The nails were designed to ensure overall stability of the wall, and the added wall height was reinforced with woven polyester geotextiles. These geotextiles were specified to have a tensile strength of 50kN/m, spaced at 680mm vertical centres and 2,5m deep. A silty sand was specified for the backfill.

The collapsed wall sections, and sections where the backfill and wall had deflected excessively (visibly), were rebuilt. The poor shear strength of the soil dictated that the depth of the geotextiles needed to be 77% of the final wall height. The granular fill used for the reinforced fill allowed the use of a cheaper woven polypropylene tape multi-filament geotextiles with a tensile strength of 35kN/m over the upper 3,5m of the wall, and a woven polyester geotextiles of 50kN/m for the lower section.

All the above work was completed by end of 1996, and has been performing satisfactorily to date.

7. CONCLUSIONS

From the above, the following conclusions can be drawn:

- Geotextile reinforced backfill walls are structures that are robust to variations from the design specifications.
- Collapse of such a structure is usually as a result of two or more substantial deviations from the design specifications.
- Geotextile reinforced retaining walls have a ductile and a brittle component. The brittle component is the facing, while the backfill acts as a ductile component of the structure.

ACKNOWLEDGEMENTS

The authors wish to thank the owners of the retaining walls, as well as the wall contractors, for their permission to publish this case history.

REFERENCES

1. HA68/94, 1994, Design Methods for the Reinforcement of Highway Slopes by Reinforced Soil and Soil Nailing Techniques. Design Manual for Roads and Bridges, Vol. 4, Section 1, Part 4, HMSO.
2. The Practice of Soil Reinforcement in Europe, 1995. Dr. T.S. Ingold (Editor), Symposium by IGS, 18 May 1995, Thomas Telford, London.
3. Nelson N.S.C., Wu J.T.H, 1993, Investigating Performance of Geosynthetic – Reinforced Soil Walls, Report No. CDOT-UCD-R-93-21, University of Colorado, Denver.
4. Greenwood J.H., 1990, The Creep of Geotextiles, 4th International Conference on Geotextiles, Geomembranes and Related Products, Den Hoedt (ed.), The 28 May to 1 June, 1990, The Haque, Netherlands.
5. Report No. 1555/1008/1/G, Wates, Meiring & Barnard (Pty) Ltd, March 1995, “Geofabric Pullout Tests”.
6. Day, R.W., Axten G.W. (1989), “Surficial stability of compacted clay slopes”, Journal of Geotechnical Engineering, ASCE, 115(4), p577-580.
7. Pradel D, Raad G (1993), Affect of Permeability on Surficial Stability of Homogenous Slopes, Journal of Geotechnical Engineering, ASCE, Vol. 119(2), p315-332.

Preloaded-Prestressed Geogrid-reinforced Soil Bridge Pier

T.Uchimura

Research Associate, Department of Civil Engineering, University of Tokyo, Japan

F.Tatsuoka

Professor, Department of Civil Engineering, University of Tokyo, Japan

M.Tateyama

Senior Research Engineer, Japan Railway Technical Research Institute

T. Koga

Kyushu Railway Company (JR Kyushu)

ABSTRACT: The first prototype preloaded and prestressed geogrid reinforced soil bridge pier was constructed to support temporary railway girders. An abutment of geogrid-reinforced soil retaining wall, which was not preloaded nor prestressed, was also constructed. The behavior of the pier and the abutment during and after construction and in service was carefully observed. By preloading and prestressing, the gravel backfill of the pier became very stiff against static and dynamic load compared to the abutment. Cyclic triaxial loading tests on the backfill gravel were performed to understand the contribution of the preloading and prestressing to the high performance of the pier.

KEYWORDS: Preloading, Prestressing, Geogrid-reinforced soil, Bridge pier, Full-scale loading test, Cyclic triaxial test

1 INTRODUCTION

A new construction method, the preloaded and prestressed (PLPS) reinforced soil method, has been proposed; a reinforced backfill is made very stiff against vertical load by vertical preloading and prestressing (Tatsuoka et al. 1996a.)(Figure 1). A similar method taking advantage of preloading has been proposed by Adams (1997), but it does not take advantage of effects of prestressing. The mechanisms of the PLPS method, which will be mentioned later, were demonstrated by tests on a full-scale model embankment and creep-relaxation tests on large triaxial specimens of the backfill gravel (Uchimura et al. 1996).

In this paper, the construction and the behavior of the first prototype PLPS geogrid-reinforced soil bridge pier is

reported. This pier was constructed in the summer of 1996 to support temporary railway girders and has been opened to service since the summer of 1997. The comparison of the behavior between the PLPS pier and an ordinary geogrid-reinforced soil abutment, which was not preloaded nor prestressed, proved that preloading and prestressing can restrain three kinds of vertical compression of the backfill: creep compression under long-term static compressive load; the amplitude of compression by dynamic loading (i.e. transient cyclic loading); and residual compression by many times of cyclic loading.

Cyclic triaxial loading tests on the backfill gravel was performed to understand the effects of preloading and prestressing on the behavior of the pier under cyclic load in service. The results showed that when a very well compacted backfill is sufficiently preloaded and prestressed at an appropriate stress level, the settlement at the pier crest and the reduction in the tie rod tension caused by many times of cyclic loading can be very small.

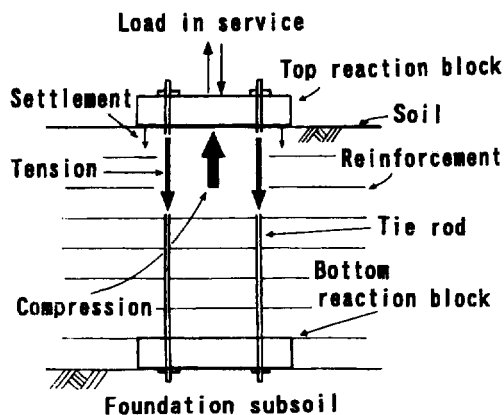


Figure 1. A schematic diagram of preloaded and prestressed reinforced soil (Tatsuoka et al. 1996a.).

2 OUTLINE OF PLPS METHOD

2.1 Construction Procedures

The typical construction procedures are as follows (Tatsuoka et al. 1996a):

1. The sub-soil is improved if necessary, usually by in-situ cement-mixing; a pile foundation is not used because of its high cost.
2. A rigid bottom reaction block, which is usually a reinforced concrete (RC) block, is constructed at the

bottom level of the backfill.

3. Four steel tie rods are installed vertically with their bottom ends anchored to the bottom reaction block.
4. The backfill is constructed, being reinforced with geogrid and involving the tie rods within it. Usually, well-graded gravel is used. Good compaction of the backfill is essential.
5. A top reaction block is constructed on the top of the completed backfill.
6. Hydraulic jacks are set at the top ends of the tie rods, supported by the top reaction block.
7. The backfill is preloaded by using the jacks. To develop as large as possible compression of the backfill during this stage, high preload kept constant for a long period or many times of cyclic loading may be applied.
8. The load is decreased from the preload level to a prescribed non-zero prestress level.
9. The top ends of the tie rods are fixed to the top reaction block (usually by using nuts), and the jacks are removed. After this, a vertical stress remaining in the backfill in equilibrium with the tie rod tension works as prestress.

2.2 Mechanisms

The mechanisms of this method could be summarized as follows (Tatsuoka et al. 1996a) :

1. The backfill needs to be reinforced to support much higher preload than an unreinforced backfill.
2. The preloading and subsequent unloading makes the backfill stiffer and nearly elastic against external loads applied on the top reaction block. The amount of unloading from the preload level should be larger than the maximum design load; otherwise, the compressive stress activated in the backfill during service may exceed the maximum stress during preloading, resulting in occurrence of larger plastic deformation of the backfill. On the other hand, the load should not be decreased to a very low level or zero to avoid swelling and associated softening of the backfill (Tatsuoka et al. 1996b).
3. The compressive prestress activated in the backfill under prestress condition leads to high stiffness, thus a high integrity, of the backfill.
4. The load working on the top of the backfill is always in equilibrium with the sum of the external load applied on the top reaction block and the tie rod tension. Therefore, when external compressive load is applied, the reduction in the tie rod tension associated with vertical compression of the backfill results in a reduction of load increment on the backfill. This mechanism decreases the backfill settlement.
5. Large part of the tensile strains in the reinforcements induced by preloading remains after the load is decreased to the prestress level. Therefore, the reinforcement can confine the backfill more efficiently.
6. If a well compacted backfill is preloaded by sufficiently large load for a long period, relatively large creep

deformation develops in the backfill, resulting in very small long-term rate of the relaxation of the tie rod tension under the prestressed condition..

7. The backfill may deform in the simple shear mode during a seismic event. When the backfill is very well compacted, large dilatation of the backfill may occur associated with seismic shear deformation. But such dilatation is restrained by the tie rods, resulting in a considerable increase in the tie rod tension and compressive stresses in the backfill. Therefore, a high seismic stability can be expected.

3 PROTOTYPE PLPS GEOGRID-REINFORCED SOIL BRIDGE PIER

3.1 Design and Construction

The first prototype PLPS geogrid-reinforced soil bridge pier was constructed to support two 16.5 m long steel bridge girders for a single railway track in Fukuoka City, Japan (pier P1 in Figure 2a). The bridge is planned to be used for about three years from August 1997. The cross-section of the pier is 6.4 m x 4.4 m, and the height of the backfill is 2.7 m. The design dead load by the girder weight and live load by train loads including impact load are 196 kN and 1,280 kN, respectively.

On the other hand, one of the abutments for the girder was constructed as an ordinary geogrid-reinforced soil retaining wall (GRS-RW) without preloading and prestressing (abutment A2 in Figure 2a).

First, a subsoil of an about 9 m-thick very soft clay deposit was improved by in-situ cement-mixing forming nine 9 m-long 0.8 m in diameter cement-mixed soil columns (Figure 2b). In addition, the whole cross-section of the pier was improved by cement-mixing for the 1 m-thick surface soil layer to form the bottom reaction block. The lower ends of four steel tie rods, which were originally produced for prestressed concrete, were anchored into the cement-mixed soil columns for a length of 4 m. The nominal yield tensile force of each tie rod is 1,034 kN.

The backfill was constructed with a help of gravel-filled bags stacked along the four sides of each gravel layer, while wrapping around the bags with the reinforcement. A well graded gravel of crushed sandstone ($D_{max} = 30$ mm, $D_{50} = 0.9$ mm, $U_c = 16.5$, $\phi = 60^\circ$) was used. A hand-operated 30 kg-vibration compactor and a hand-operated 60 kg-tamper were used to compact the backfill; larger machines could not be used because of small available working space. A geogrid reinforcement of polyvinyl alcohol coated with polyvinyl chloride (PVC) was used, whose nominal rupture strength is 73.5 kN/m and the nominal stiffness is 1,050 kN/m at strains less than 1 percent. The arrangement of the reinforcement was determined for a GRS-RW with one facing at the end under

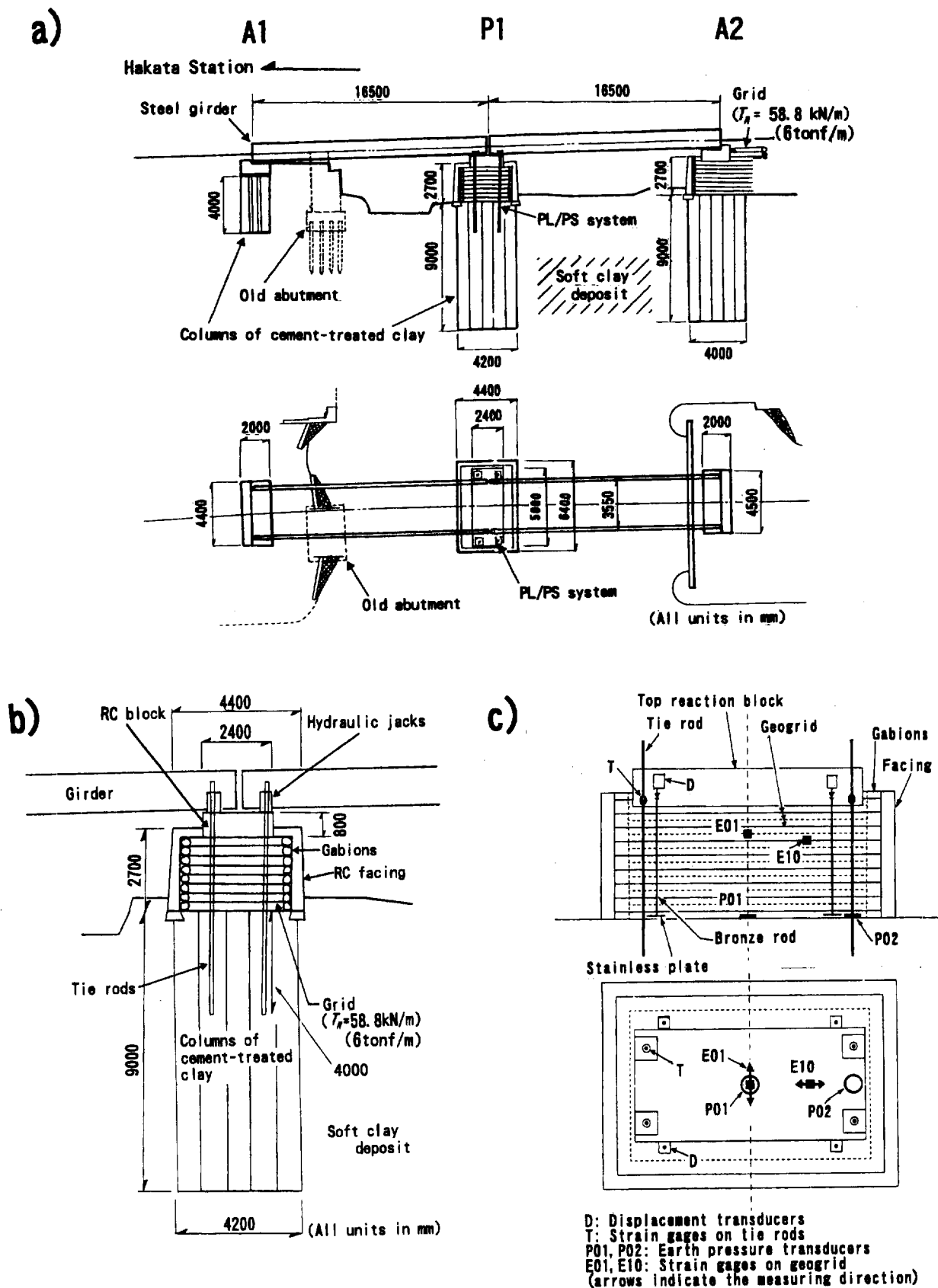


Figure 2. a) A bridge construction project involving the first prototype PLPS reinforced soil pier; b) detail of the pier; c) arrangement of the instrumentation described in this paper (Tatsuoka et al. 1996b).

plane strain condition with the same height as the actual pier, instead of the actual pier having a rectangular prismatic shape. As the result, the vertical spacing of the reinforcement was designed to be 30 cm. However, the pier has two pairs of wall faces in two orthogonal directions; therefore, each cross-section having one pair of wall faces were designed independently. By overlapping the two cross-sections, the actual average vertical spacing of the reinforcement became 15 cm.

The construction of the backfill took five days by a team of five workers. Preloading started ten days after casting the top reaction RC block (5 m-long, 2.4 m-wide and 0.8 m-thick). Then, full-height rigid facings were cast-in-place on the four wall faces. The total construction period was about 1.5 months. The construction cost for the pier was about a half of that for an equivalent conventional RC pier supported by a pile foundation.

The abutment A2 was constructed by the same method using the same materials as the pier, except that it has only one wall face retained by reinforcement with a vertical spacing of 30cm, and the both sides are exposed slopes (1.5:1.0 in H:V) without a facing.

3.2 Instrumentation

For the measurement of vertical compression, four stainless anchor plates for the pier and two plates for the abutment were embedded at the bottom of the backfill (Figure 2c). Brass rods placed inside PVC pipes were vertically installed through the backfill and connected to the anchor plates at the lower ends. The vertical displacement of the top of the rods relative to the top of the backfill have been measured with displacement transducers. The average compression of the pier and the abutment was calculated based on these measurements.

The tie rod tension has been measured with electric resistance strain gages attached to the tie rods. The earth pressure has been measured at the center (P01) and near the tie rods (P02) at the bottom level of the backfill with strain-gage-type pressure transducers of 20 cm in diameter. The tensile strains of the reinforcement have been measured by strain gages attached to the grid at 32 points. Strains in horizontal two directions, orthogonal each other, have been measured separately.

3.3 Preloading

For a period of ten week days, preload was applied by using four hydraulic jacks (Figure 3). The total net preloading period was 72 hours, however, because the preloading was allowed only during daytime due to a restraint at the site. During nighttime, the tie rods were fixed to the top reaction block with the backfill under prestressed condition.

In the first day, the vertical load was increased step by

step up to 1,960 kN (from the origin to Point 1 in Figure 4); each step consisted of a load increment of 196 kN applied within 2 minutes or less and a pause keeping the load constant for 30 or 60 minutes. In the fifth day, the load was decreased to 905 kN (Point 10), followed by reloading. In the sixth day, the load was increased to 2,350 kN (after Point 11). In the seventh day, the load was decreased to zero (Point 13), followed by reloading. In the tenth day, the load was decreased to about 1,100 kN (Point 16) and then the backfill was left under prestressed conditions for three days. Finally, the load was increased to 2,350 kN (Point 17), maintained for three hours, decreased again to 980 kN (Point 18), and since then, the backfill has been left under prestressed condition.

Figure 4 shows the relationship between the total tie rod tension, T , and the backfill compression. During the preloading stage, the tie rod tension was the same as the amount of the preload working on the crest of the backfill. A total settlement of 8 mm occurred through the whole preloading period. During unloading and reloading by 1,400 kN in the last day, the rebound and re-compression were nearly the same and equal to only 0.4 mm, indicating a very high stiffness and nearly elastic deformation of the backfill. According to Tatsuoka et al. (1996a), the Young's modulus E for vertical elastic strains of such gravels measured by triaxial tests can be expressed as $E = E_0 \cdot (\sigma_v / p_0)^m$, where $m=0.57$ and E_0 is the E value when the vertical stress σ_v is equal to $p_0 = 98$ kPa. Based on this relationship, by fitting the theoretical elastic rebound and reload curves to those measured with the pier, $E_0=400$ MPa is obtained. The theoretical curve for elastic settlement is also plotted to start from the origin in Figure 4; this curve indicates the elastic component of the compression. The plastic component of the compression is obtained as the difference between the elastic component and the integrated value of the instantaneous compression increments caused at each loading step. The difference between the total compression and the instantaneous (elastic plus plastic) component is the time-dependent (viscous) component. The viscous component is found to be more than a half of the total compression and its ratio to the total compression increases with the load level. Therefore it is important to remove potential creep deformation of the backfill by sufficient preloading.

It may also be seen from Figure 4 that the average stiffness of the backfill when reloaded from Point 10 is noticeably smaller than the value when reloaded from a higher load level (e.g., from Point 7). Moreover, the average stiffness when reloaded from the zero load (from Point 13) is smaller than the above. This behavior is likely due to the effects of swelling and softening of the backfill when the load is decreased largely or to zero. This result shows the importance of maintaining sufficiently high prestress in the backfill (Tatsuoka et al. 1996b).

Figure 5 shows the relationship between the total tie rod

tension and the earth pressure measured at the center (P01) and near the tie rods (P02) at the bottom of the backfill. The average pressure, equal to the applied load divided by the total cross-sectional area (5.8 m x 3.8 m) of the pier, is nearly the same as the measured earth pressure increments. Furthermore, the earth pressures at P1 and P2 are almost the same as each other, while showing a highly linear relationship with the tie rod tension. These results show

that the stress distribution was nearly uniform at the bottom of the backfill and that the bottom reaction block made by in-situ cement-mixing functioned as a nearly rigid mass.

3.5 Long-term Behavior under Static Load Condition

After the preloading stage, the full-height rigid concrete facings were cast-in-place, and then two steel girders, each

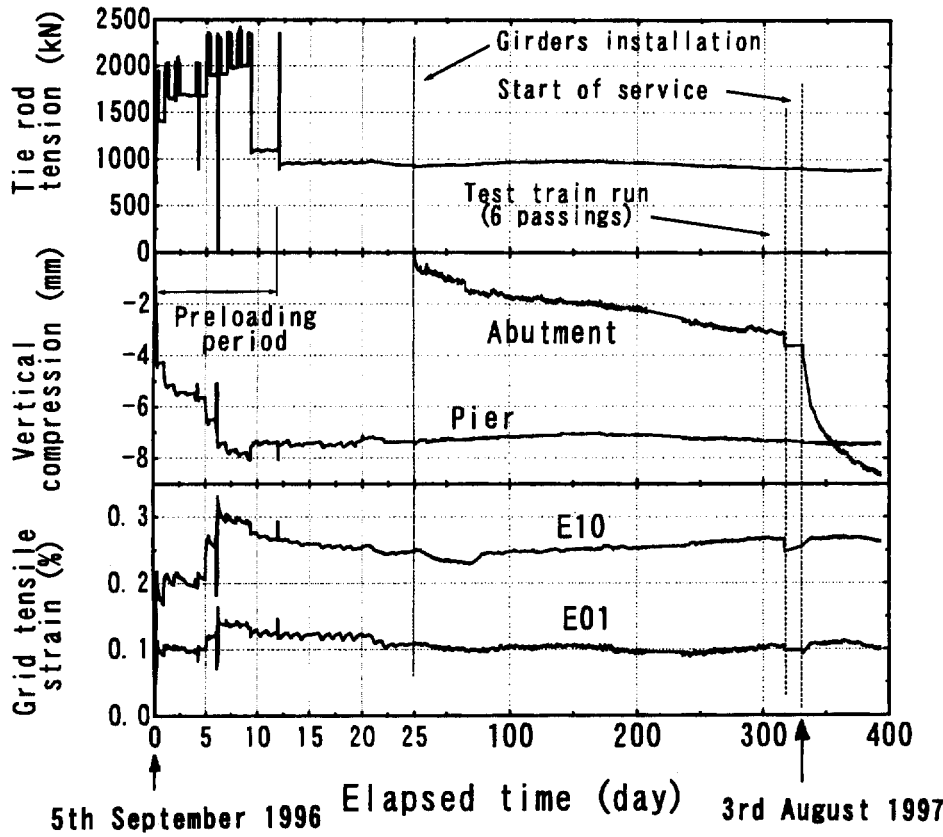


Figure 3. Long-term behavior during and after preloading and in service; tie rod tension; vertical compression of the pier and the abutment; tensile strain of the grid.

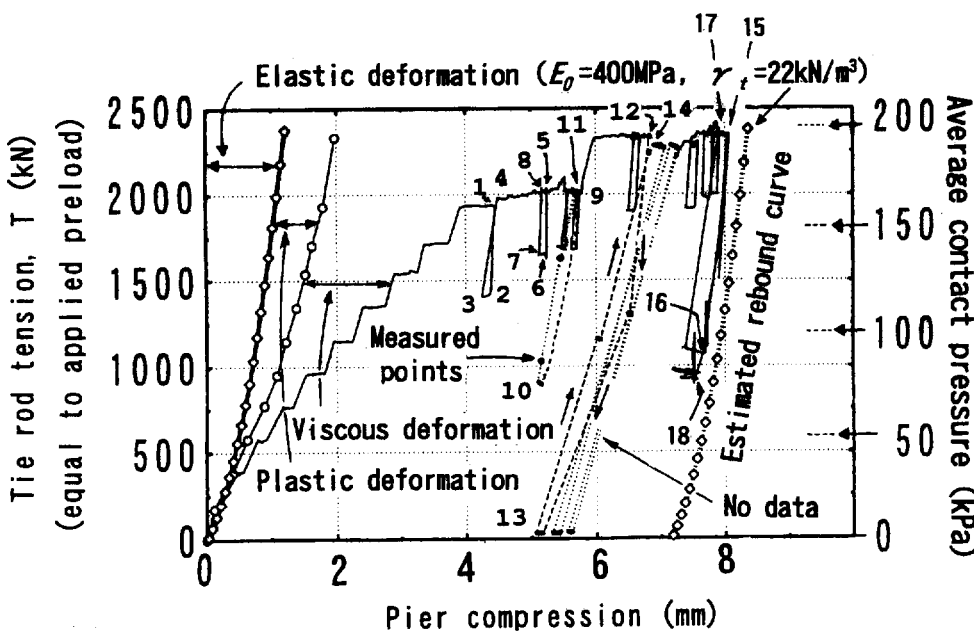


Figure 4. Relationship between the tie rod tension and the settlement of the pier (Tatsuoka et al. 1996b).

weighing 211 kN, were installed on the pier and the abutments. The instantaneous compression of the pier by a girder weight of 211 kN was only 0.04 mm, while that of the abutment by a girder weight of 105 kN was ten times larger, equal to 0.4 mm. Then, the behavior of the pier and the abutment was observed for ten months (Figure 3).

The tie rod tension and the compression of the pier P1 appear to have changed slightly for this long period, but this is likely to be annual change due to temperature effects. The tensile strain in the reinforcement kept almost constant without showing any creep extension.

On the other hand, the abutment A2 showed noticeable creep compression by the self weight and the girder weight. Although the measurement of the abutment compression started just before the girder installing, the total compression has reached 3.1 mm by the summer of 1997.

The difference shows the first advantage of preloading and prestressing that makes long-term creep deformation of the backfill under static load condition very small.

3.6 Short-term Behavior at Train Passing

On 19 July 1997, a diesel locomotive of 637 kN in weight passed 6 times over the bridge for inspection. The residual compression of the pier P1 was 0.02 mm, while that of the abutment A2 was 0.52 mm.

Since 3 August 1997, the bridge has been opened to

service. Figure 6 shows the behavior of the pier P1 and the abutment A2 at the first train passing in service; the train consisted of 2 coaches, each weighing 353 kN without passengers.

The amplitude of compression of the pier was 0.02 mm, which was equivalent to a vertical strain of 0.001 percent; this very small strain also suggests nearly elastic behavior of the pier. The tie rod tension responded to the pier compression. The change in tensile strain in the

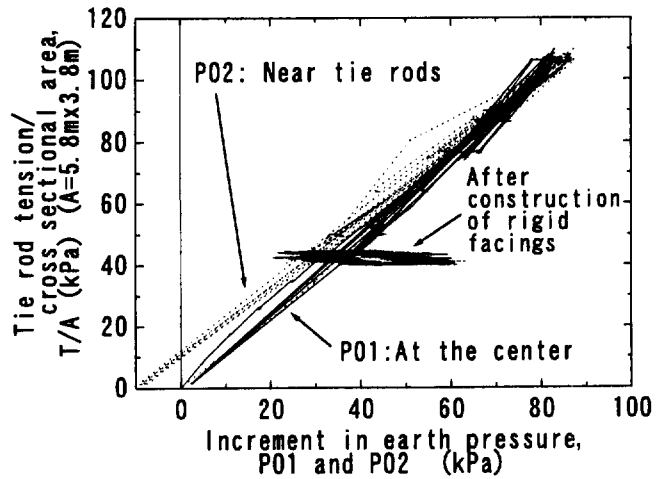


Figure 5. Relationships between the earth pressure P1 and P2 and the tie rod tension.

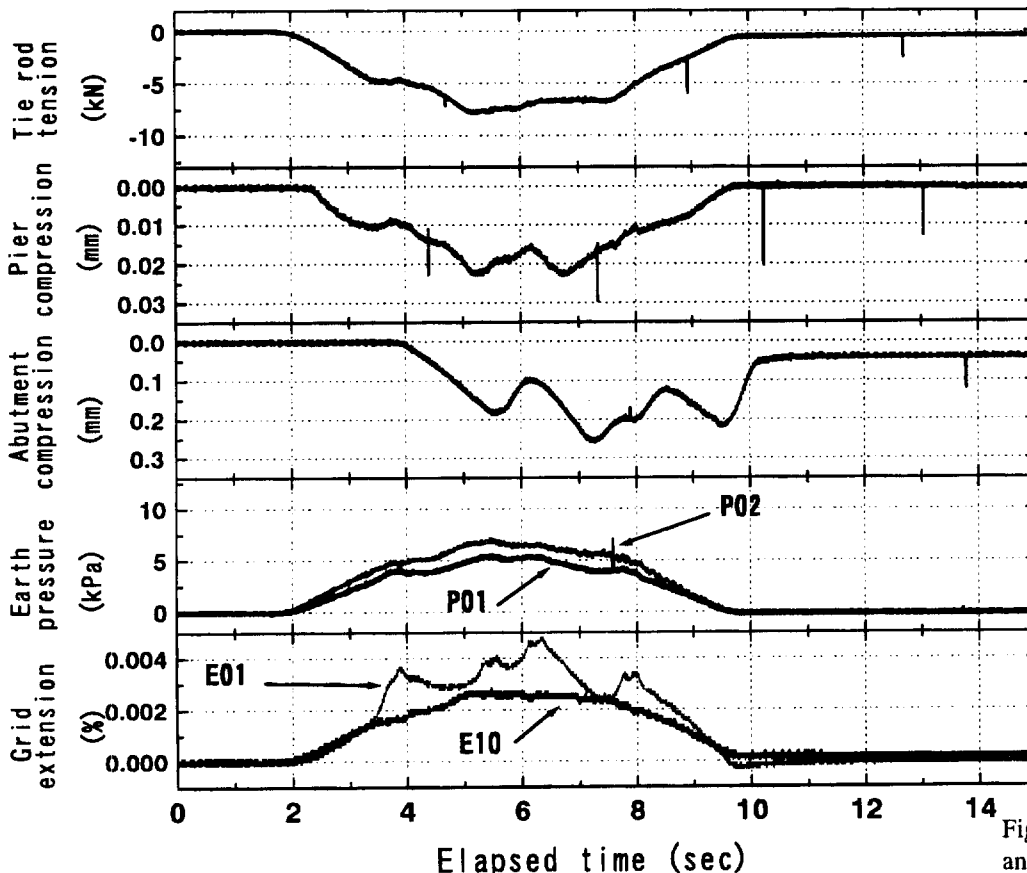


Figure 6. Behavior of the pier and abutment at train passing.

reinforcement was very small and elastic, which was due to very small compression of the pier. Apparently, the train road was not supported by the corresponding very small increase in the tensile force in the reinforcement alone, but the backfill having highly elastic properties with high stiffness actually supported the train load; these backfill properties could be achieved by sufficiently large preloading and prestressing, which was possible only with a help of reinforcement.

On the other hand, the amplitude of the compression of the abutment was 0.2 mm; this is not a harmful quantity, but 10 times larger than that of the pier.

The difference shows the second advantage of preloading and prestressing that makes the amplitude of compression by dynamic loading very small.

3.7 Long Term Behavior in Service

The behavior of pier and abutment in service has been observed for 2 months (Figure 3). On average, 125 trains, each consisting of two to four coaches, each weighing 30 to 40 tons without passengers, pass over the bridge every day.

The residual compression of the pier was 0.08 mm. Corresponding to that, the tie rod tension decreased by 17.3kN. The tensile strains in the reinforcement did not change largely; as a whole, they have been constant. On the other hand, the abutment showed a residual compression of 5.1 mm. It is still compressing rapidly, even though the compression rate is decreasing. Some maintenance will be necessary. This difference shows the third advantage of preloading and prestressing that makes the residual compression by many times of cyclic loading very small.

4 BEHAVIOR AGAINST CYCLIC LOAD

The comparison of the behavior between the pier and the abutment subjected to many times of train passing showed several advantages of preloading and prestressing, by which temporary and residual compression of the backfill against cyclic loading was very effectively restrained. In order to understand these effects of the PLPS method, cyclic triaxial compression tests were performed at a constant confining pressure ($\sigma_h = 49$ kPa) on a large square prismatic unreinforced specimen (23 cm x 23 cm x 60 cm high) of the backfill gravel ($\rho_d = 1.95$ g/cm³ and $w = 3.3$ percent) (Figure 7). Axial and lateral strains were measured by a set of LDTs, a device to measure small local strains on the surface of the specimen. An LDT consists of a phosphor bronze strip with strain gages attached at the center, supported at the both ends with two hinges glued to the specimen surface. Figure 8a shows the time history of the deviator stress $q = \sigma_v - \sigma_h$. The primary loading (PL) was conducted at a stress rate of $dq/dt = 49$ kPa/min. C1 and C2 mean creep loading stages for 6 hours at a constant

$q = 98$ and 196 kPa, respectively. CYC1 to CYC5 mean cyclic loading stages of 500 cycles, in which q changed between 98 and 196 kPa for CYC4 and between 0 and 98 kPa for the others. PL simulated a short-time preloading without creep compression, while C2 simulated a long-time preloading with creep compression at the peak load.

Figures 8b and 9 show the test results. Even after some creep (C1), the vertical compressive strain ϵ_v increased noticeably (by 0.013 percent) during the first cyclic loading stage CYC1. During CYC2 after PL, the increase in ϵ_v by cyclic loading was nearly zero. On the other hand, during CYC3 after C2 and CYC5 after CYC4, ϵ_v decreased during cyclic loading (by 0.006 percent and 0.007 percent respectively). During CYC4, ϵ_v increased noticeably (by 0.023 percent) by cyclic loading, but the double amplitude stiffness $\Delta q / \Delta \epsilon_v$ is about 2.5 times larger than those during CYC1 to CYC5 at the lower q level.

The test results suggest the following:

1. If the backfill is not preloaded, it may be compressed largely by cyclic loading (CYC1). This trend of behavior was actually observed with the abutment A2.
2. For the same amplitude of cyclic stress and number of loading cycles, the settlement of the backfill becomes very small after preloading; this trend becomes more obvious after the occurrence of the creep deformation or cyclic loading during the preloading stage. This trend of behavior was actually observed with the pier P1.
3. The higher prestress on the backfill causes higher stiffness of the backfill during cyclic loading. But if the stress level is near the maximum stress during preloading, residual compression becomes larger.
4. To make both of the amplitude and residual value of compression by cyclic loading very small, the backfill should be preloaded at sufficiently high stress level, and the prestress should be some non-zero level; otherwise it leads

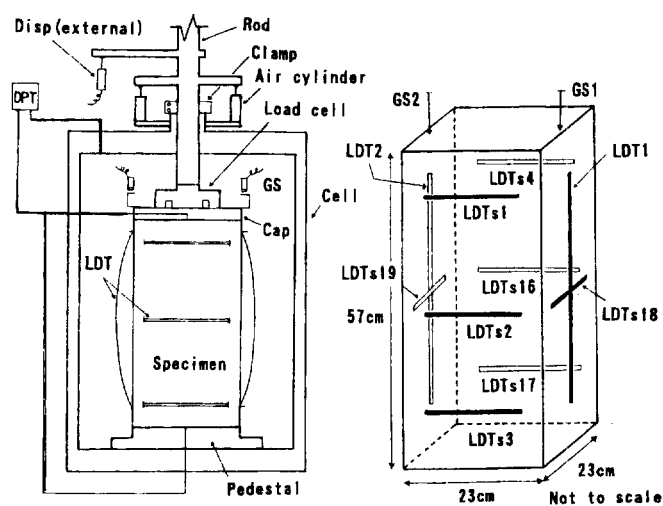


Figure 7. Schematic diagram of the large scale triaxial test (Uchimura et al. 1996).

to a large amplitude of compression during cyclic loading. On the other hand, the prestress should not be very high so that the maximum stress during cyclic loading does not approach the maximum stress during preloading. Some intermediate prestress level is appropriate.

5 CONCLUSIONS

The behavior of the first prototype PLPS geogrid-reinforced soil bridge pier was observed during and after construction and in service. Compared to a bridge abutment of geogrid-reinforced soil constructed without preloading and prestressing in the adjacent place at the same time, the pier showed very small transient and long-term deformation. The different performances demonstrated significant effects of the preloading and prestressing procedures in restraining creep compression under long-term static compressive load; the amplitude of compression by dynamic loading; and residual compression by many times of cyclic loading. The results of triaxial cyclic loading tests on a specimen of the backfill gravel also showed a high efficiency of preloading and prestressing, particularly preloading with creep compression or cyclic loading, to restrain temporary and residual compression of the backfill. Both field and laboratory observations showed that it is not preferable to unload the prestress to zero because it leads to a large amplitude of compression during cyclic loading. On the other hand, to make the residual compression very small, prestress should not be very high so that the maximum stress during cyclic loadings does not approach the maximum stress during preloading.

ACKNOWLEDGMENTS

The authors deeply appreciate the help in this research of Messrs. Tsuru, H. and Maeda, T. of Kyushu Railway Company Dr. Koseki, J. and Mr. Sato, T. of Institute of Industrial Science, University of Tokyo, Mr. Maruyama, D. of University of Tokyo and Mr. Nakamura, H. of Nihon University, and Messrs. Sugimura, Y. and Ishihara, M., graduate school of the university of Tokyo.

REFERENCES

- Adams, M. (1997) "Performance of a prestained geosynthetic reinforced soil bridge pier", Int. Sym. On Mechanically Stabilized Backfill, Balkema, Feb.1997 (Wu eds.), Denver, CO, USA (to appear).
- Tatsuoka, F., Uchimura, T. and Tateyama, M. (1996a) "Preloaded and prestressed reinforced soil", Soils and Foundations, JGS, Vol. 37, No. 3, pp.79-94
- Tatsuoka, F., Tateyama, M, Uchimura, T. and Koseki, J. (1996b) "Geosynthetic-Reinforced Soil Retaining Walls as Important Permanent Structures, The 1996-1997 Mercer

Lecture", Geosynthetic International, IGS, Vol. 4, No. 2, pp.81-136

Uchimura, T., Tatsuoka, F., Sato, T., Tateyama, M. and Tamura, Y. (1996) "Performance of preloaded and prestressed geosynthetic-reinforced soil", Balkema, Int. Symp. on Earth Reinforcement, Fukuoka, Japan, (Ochiai et al., eds), Vol. 1, pp.537-542.

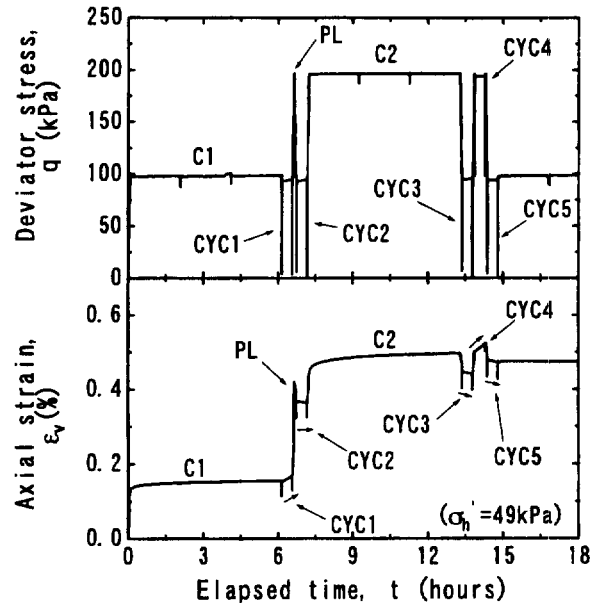


Figure 8. Time histories of a) deviator stress, q and b) axial strain, ϵ_v . Only the first and the last loading cycles are shown for each cyclic loading.

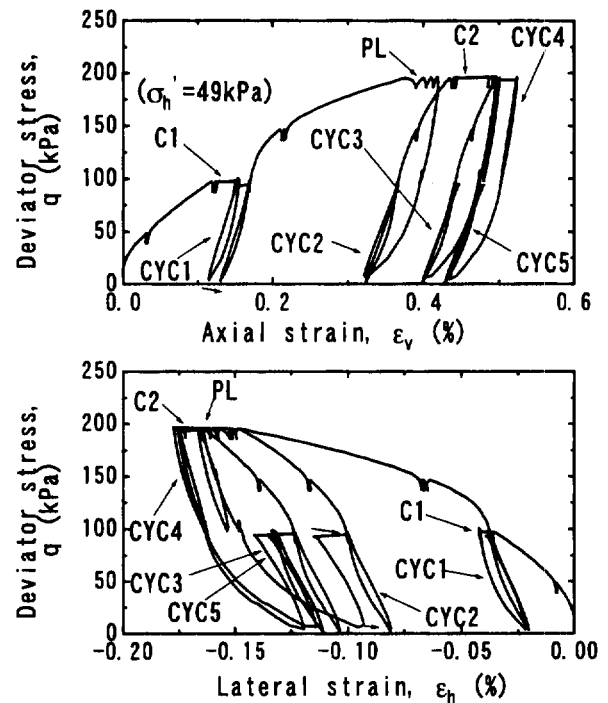


Figure 9. Results of a triaxial cyclic loading test. Relationships between a) deviator stress, q and axial strain ϵ_v , b) q and lateral strain, ϵ_h .

Use of Fabric Reinforced Soil Walls for Integral Bridge End Treatment

R.A. Reid

Assistant Professor, Civil & Environmental Eng. Dept., South Dakota State Univ., Brookings, South Dakota, USA

S.P. Soupir

Graduate Research Assistant, Civil & Environmental Eng. Dept., South Dakota State Univ., Brookings, South Dakota, USA

V.R. Schaefer

Professor, Civil & Environmental Eng. Dept., South Dakota State University, Brookings, South Dakota, USA

ABSTRACT: The problem of void development under bridge approach slabs has been correlated to the use of integral abutment bridges (Schaefer and Koch, 1992). The observation of the occurrence of voids under approach slabs, even in cases where no traffic had yet occurred led to a hypothesis of thermally-induced movements of bridge beams/abutment walls as the mechanism causing the void development. As a result of identification of the mechanism of void development, changes to the approach system needed to be made to accommodate this mechanism. A method used by the Wyoming Department of Transportation, and subsequently by the South Dakota Department of Transportation, uses a fabric reinforced soil wall behind the abutment to build a vertical, self contained wall capable of holding a vertical shape and forming a void behind the abutment. This paper will detail the design concept used by the South Dakota Department of Transportation, present data obtained from instrumented bridges currently being monitored, and show how this system alleviated the integral bridge abutment approach problems.

KEYWORDS: Geotextile, Temperature Effects, Retaining Walls, Integral Abutment, Pavements

1 INTRODUCTION

The problem of void development under bridge approach slabs has been correlated to the use of integral abutment bridges (Schaefer and Koch, 1992). The observation of the occurrence of voids under approach slabs, even in cases where no traffic had yet occurred, led to a hypothesis of thermally-induced movements of bridge beams/abutment walls as the mechanism causing the void development. As a result of identification of the mechanism of void development, changes to the approach system needed to be made to accommodate this mechanism. For this project the approach system design consisted of a geotextile reinforced soil wall behind the abutment resulting in a vertical, self-contained wall capable of holding a vertical shape and forming an air gap between the abutment and retained backfill. This design was based on a system used by the Wyoming Department of Transportation (WYDOT). It was hypothesized that the gap behind the abutment would allow for the thermally-induced movement of the abutment without affecting the backfill. Three bridges were constructed in South Dakota using this design. The field portion of this study consisted of monitoring the variations in gap width between the abutment and geotextile wall and development of voids under the approach slab. This paper will review the design of the bridge systems and geotextile soil wall, data collection and measurement, preliminary analysis and conclusions.

2 PREVIOUS RESEARCH

Although numerous factors contribute to the differential movements between bridge abutments and the approach areas to the bridge, previous research has shown that void development under approach slabs to integral abutment bridges occurs due to the elongation and contraction of the bridge beams due to temperature variations. As the bridge beams expand and contract they alternately push into and pull away from the backfill behind the abutment wall, leading to the development of a void near the abutment wall under the approach slab. The observation of such voids in the field has been reported by Jorgenson (1983), Kramer and Sajer (1991), and Schaefer and Koch (1992). The size of the void varies markedly, with Schaefer and Koch (1992), who surveyed 140 bridges in South Dakota, reporting measured voids from 13 to 360 mm (1/2 to 14 in.) in depth and extending as much as 3 m (10 ft.) away from the abutment wall. The study concluded that the development of the voids under the approach slab to integral abutment structures was an inherent problem in the use of integral abutment systems. The void development was not considered to be isolated to one mechanism resulting from abutment movement, but rather to be the result of the cumulative effects of embankment bulging as the backfill deforms, approach slab uplift, backfill densification as particle breakage occurs, and backfill deformation as passive failure occurs in the backfill. The relative contribution of each of these mechanisms

has not been discerned to date. It was suggested that the largest increases in void size occurred when passive failure likely occurred and this mechanism was probably the most important one.

Edgar, et al. (1989) investigated the use of a reinforced soil wall as a means to prevent void development under the approach slab in highway embankments. This research determined that retaining the backfill with a geotextile wall, thereby creating a gap between the retained fill and bridge abutment, reduced the applied stresses to the soil to near zero. The reduction of the passive stress to near zero eliminates the passive failure mechanism in void development. Consequently, this system was adopted for use in the construction of three bridges in South Dakota based on the hypothesis that the presence of a gap between the abutment and retained fill would prevent or greatly reduce void development under the approach slabs.

3 BRIDGE BACKFILL DESIGN

The backfill design used by the WYDOT was adapted by the South Dakota Department of Transportation (SDDOT) for replacement of a single concrete bridge, 134 m (440 ft) in length, on Highway 73 across the White River near Kadoka, SD in the spring of 1996. This design was also used on two concrete bridges, 122 m (400 ft) in length, on Interstate 29 across the Big Sioux River south of Brookings, SD. The southbound bridge was constructed in the fall of 1996 and the northbound bridge in the summer of 1997. These three bridges are being monitored to measure seasonal variations in the gap spacing and for the development of voids under the approach slab. This design has been adopted for all new bridge construction in South Dakota.

Design of the backfill system followed current SDDOT bridge design and construction practices except for the presence of the woven geotextile wall. Prior to the implementation of this design methodology, backfill material consisted entirely of select granular material. This expensive backfill was used since it had been shown to reduce void development because of its greater passive resistance. This backfill contained material with less than five percent passing the #200 sieves and extended the depth of the abutment and back at typically a 1:2 slope. A design developed by the WYDOT incorporated the use of a gap between a reinforced soil wall and the abutment wall. During construction of the three bridges monitored in this project, a 15.4 cm (6 in) cardboard spacer was placed against the concrete abutment. The wrapped face geotextile wall was then constructed against the cardboard, which acted to maintain the gap and control the alignment of the wall face. The first three layers of the reinforced soil wall were 30.5 cm (1 ft) thick and the top layer thickness

varied with respect to grade specifications. A fabric overlap of 1.2 m (4 ft) was used on all layers of the wall. Upon completion of the wall, the cardboard spacer was saturated with water and removed. The backfill material was the same select backfill used in previous SDDOT designs. Based on the results of this project, the state may specify less expensive backfill materials in the future. The drainage pipe was installed in the bottom most layer of the geotextile wall. A general illustration of this backfill design is shown in figure 1.

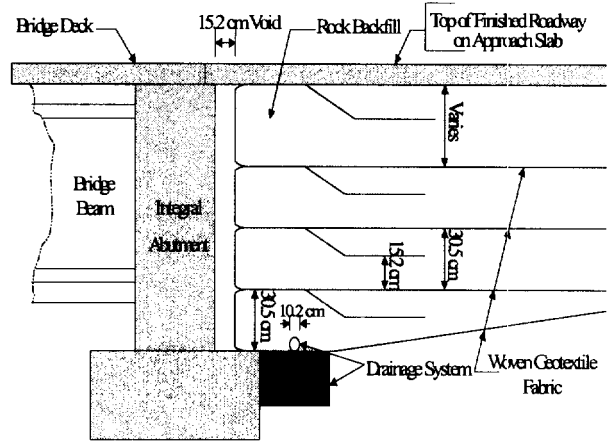


Figure 1. Typical geotextile reinforced soil wall behind the bridge abutment.

4 DATA COLLECTION

Over the course of this three-year project (1996-1999) physical measurements of the gap width, bridge length, and void development were obtained. More detailed instrumentation of these bridges was not feasible due to limited funding.

The gap width between the reinforced soil wall and the bridge abutment was monitored to determine if the abutment came in contact with the reinforced soil wall, thereby creating a passive pressure condition on the backfill. Also, if the abutment and wall do not come in contact, this data would be used to determine if a smaller gap width would be appropriate. To monitor gap width on the White River abutments, four vertical rows of four holes each were drilled through each abutment between the bridge beams. In each row, the approximately 5 cm (2 in) diameter hole locations were evenly spaced on the vertical profile of the wall. Initial measurements of the gap width at each hole location were recorded after the supporting cardboard had been removed. For the I-29 bridges, four vertical rows of three holes each were installed in each abutment

between the bridge beams.

A second series of holes were formed into the approach slab to monitor the formation of voids beneath the slab. These holes were installed with removable caps to cover the hole but allow access for measurement. Void measurement locations measuring 5 cm (2 in) in diameter are located at 0.46 m (1.5 ft), 0.76 m (2.5 ft), 1.68 m (5.5 ft), and 4.72 m (15.5 ft) back from the face of the abutment. These measurements can be made along the centerline, along the centers of the driving lanes, and at the edges of the approach slab.

Physical measurements were also taken to monitor the thermal expansion and contraction of the bridge deck. Nails driven into the bridge deck served as bench marks for measurements of bridge deck movement. Three benchmarks were installed at 0.6 m (2 ft) from the guardrails at the midpoint of the span of the bridge and on the north and south ends of the bridge. Additional benchmarks were placed on the centerline of the bridge at the midpoint and on both ends.

In addition, air temperatures were recorded each time field measurements were made.

5 DATA

The gap width of the White River Bridge has been monitored for a full one-year temperature cycle. Gap width measurements are being taken on two Interstate 29 bridges. The southbound lane has been monitored since completion in November of 1996 and at the time of writing is going through its first high temperature cycles. The northbound lane is near completion and initial gap width readings have been recorded. Figure 2 shows the approximate gap measurement hole locations in between the bridge beams. Due to the space limitations of this paper, only the results from the south abutment of the White River Bridge are shown, see figure 3.

Due to the distance from Brookings this bridge is located, readings on the gap width for the White River bridge were made about every three months, with readings scheduled to ensure readings were taken in the high temperature and low temperature periods in a one-year cycle.

Monitoring of the void development under the approach slab on the White River Bridge will start after the summer of 1997. The thermal expansion and contraction of the bridge system relative to the backfill system is currently being evaluated. No significant findings can be presented on these subjects until two full years of data have been recorded.

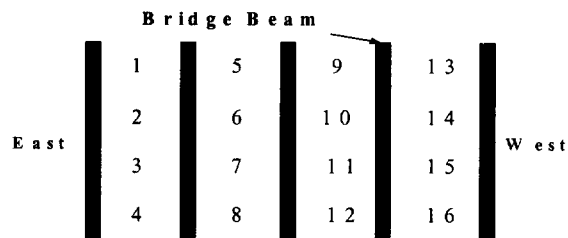


Figure 2. White River Bridge south abutment hole configuration.

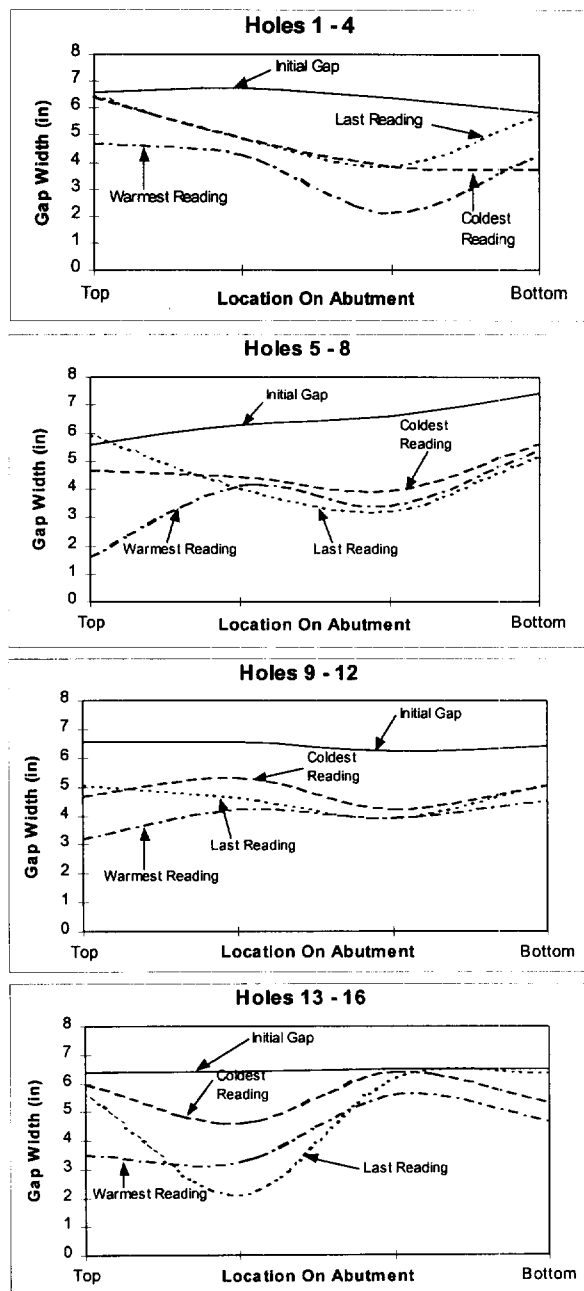


Figure 3. White River Bridge south abutment gap width for a one-year temperature cycle.

Gap width measurements taken from the White River Bridge and the one completed I-29 Bridge show changes in the gap width due to seasonal variations in temperature. The south abutment of the White River Bridge was constructed first. Based upon the limited number of readings taken thus far, the gap widths on this bridge are somewhat more scattered than the others. This has been attributed to the construction of the wall, which was visually observed and noted to be less than ideal. The south abutment was the first reinforced soil wall built by that particular construction company and was the first wall to be constructed by the State of South Dakota in a bridge end backfill application. Construction techniques were refined considerably following construction of the south abutment, which lead to a higher quality of construction for the north abutment. Due to improved construction practices, the north abutment displayed a larger initial gap measurement. Thus, it is essential to ensure all the layers of the wrapped faced reinforced soil wall are pulled very tight to reduce deformations after the cardboard is removed. The results show that experience in construction improved the performance of the north abutment backfill system.

The top of the abutment, which is integral to the bridge deck, undergoes the most movement. In most cases, the gap width for the upper two-thirds of the abutment changes more than the lower third. This suggests that a point of rotation exists in the foundation piling system below the bridge abutment. It can be observed in figure 3 that the minimum measured gap corresponds to the warmest temperatures, 100°F (38°C). Even measurements corresponding to the coldest temperature, 0°F (-18°C), are smaller than the initial gap, indicating a closure of the gap as the abutment cyclically moves. However, the data also shows that the initial gap has not fully closed in even the warmest temperatures, indicating the geotextile wall is functioning as intended. In all cases, the gap has remained open and prevented the abutment from pushing against the backfill and void development has not occurred.

7 CONCLUSIONS

At this early stage of the project conclusions as to the effectiveness of this design methodology in preventing void development will not be made. The data must be recorded over a longer time period to establish the repeatability of the data. Additional monitoring is necessary to distinguish how much of the gap closure is due to the initial movement of the wrapped face geotextile wall or is due to temperature induced abutment movement. The quality of construction of the backfill wall may also affect closure of the gap.

Therefore, quality control measures must be taken during construction. However, from one year's data it appears that the 15.2 cm (6 in) gap will provide sufficient space to allow for both movement of the abutment, movement of the soil wall related to inadequate construction, and movement due to creep of the geotextile soil wall.

8 ADDITIONAL WORK

Additional research, not discussed in this paper, is also being performed as part of this project. Alternative backfill materials and designs are being studied and tested in a SDDOT model bridge facility and will be the subject of future papers.

9 ACKNOWLEDGMENTS

This research was funded by the South Dakota Department of Transportation, project SD96-02. The support of the SDDOT is sincerely appreciated.

The contents of this report reflect the views of the authors who are responsible for the facts and accuracy of the data presented herein. The contents do not necessarily reflect the official views or policies of the South Dakota Department of Transportation, the State Transportation Commission, or the Federal Highway Administration. This report does not constitute a standard, specification, or regulation.

10 REFERENCES

- Edgar, T.V., Puckett, J.A., and D'Spain, R.B. (1989), "Effects of Geotextiles on Lateral Pressure and Deformation in Highway Embankments," Final Report to the Wyoming Highway Department, Department of Civil Engineering, University of Wyoming, Laramie, WY.
- Jorgenson, J.L. (1983), "Behavior of Abutment Piles in an Integral Abutment in Response to Bridge Movements," Transportation Research Record 903, Transportation Research Board, Washington, D.C., pp. 72-79.
- Kramer, S. L. and Sajer, B. (1991). "Bridge approach slab effectiveness." Final Report, Research Project GC 8286, Task 35, Washington State Transportation Center, University of Washington, Seattle, Washington, December.
- Schaefer, V.R. and Koch, J.C. (1992), "Void Development Under Bridge Approaches," Final Report No. SD90-03 to the South Dakota Department of Transportation, Department of Civil and Environmental Engineering, South Dakota State University, Brookings, SD.

Field Performance Test of a Geosynthetic-Reinforced Soil Wall with Rigid Facing

Y. Tsukada, Y. Ochiai and H. Miyatake

Public Works Research Institute, Ministry of Construction, Tsukuba, Japan

N. Tajiri

Fukken Co., Ltd., Consulting Engineers, Hiroshima, Japan

ABSTRACT: Geosynthetic-reinforced soil walls have gained wide acceptance in the world as retaining walls of roads and so on. The functions of their facings and reinforcing materials laid in them vary, and different design methods have been proposed to date. The present paper describes the experimental results of an outdoor, full-scale, reinforced soil wall and the evaluation of the results, the experiment being a part of a series of experimental studies to elucidate the reinforcing mechanism of geosynthetic-reinforced soil walls with concrete facings and establish a design method which takes account of the effect of such wall facings.

The test wall of 8 m-high was constructed on a soft ground, and its facing was of concrete blocks. Its behavior has been observed during the construction and for two years thereafter. During the time period, it was exposed to heavy rains and not so large earthquakes. The focus of this paper is the evaluation of the stability of reinforced soil walls based on the experimental results.

KEYWORDS: Geosynthetic-reinforced wall, Field test, Design, Long-term observation, Stability analysis

1 INTRODUCTION

Various approaches have been taken to the design and construction of geosynthetic-reinforced soil walls. In particular, researchers have proposed a number of design methods, maintaining that wall facings contribute to the reinforcing effect of the walls (Tatsuoka 1992, Leshchinsky 1993, NCMA 1993, and Gotteland et al. 1992). Regarding roads of which less severe constraint of deformation is required, the Public Works Research Institute (PWRI) of the Ministry of Construction has been pursuing experimental studies on the reinforcing effect of various types of wall facings (Tajiri et al. 1996, Nakajima et al. 1996, and Ochiai & Fukuda 1996). As shown in Figure 1, a full-scale vertical reinforced soil wall of 8 m-high with concrete-block facings (under an overloaded embankment of 9.8 kN/m²) was constructed, and its behavior has been observed during the construction and for two years thereafter. The present paper compares and contrasts the observed behavior with the

behavior assumed and predicted by the current design method, and discusses subjects which require due consideration in the design of reinforced soil walls in future.

2 SPECIFICATIONS OF TEST WALL

To design the test wall shown in Figure 1, its design conditions were set based on the previous test results and so on. The banking material was sandy soil, and its internal friction angle ϕ_s' , cohesion c' , and unit weight γ_s were 29°, 0 kN/m², and 18.6 kN/m³, respectively. The dimensions of the concrete blocks to be used were 50 cm in height, 100 cm in width, and 35 cm in depth, and their hollows were to be filled with crushed stone. Their unit weight was 21.1 kN/m³. A zone of crushed stone about 30 cm thick was to be provided at the back of the concrete-block facing as a drainage, and its internal friction angle ϕ_g' and unit weight γ_g were 45° and 19.6 kN/m³.

The internal friction angles between materials were set as follows: $\delta_1=(2/3)\phi=19^\circ$ between banking soil and blocks, $\delta_2=0$ between reinforced soil mass and banked soil behind, $\delta_3=(2/3)\phi_g=30^\circ$ and $\delta_3=(1/2)\phi_g=22^\circ$ (two cases) between blocks, $\delta_{bf}=\delta_3$ between blocks and concrete foundation, and $\delta_{sg}=\phi_s'=29^\circ$ between banking soil and reinforcements. Reinforcing geosynthetic to be used was geogrid (Tensar SR-55), of which the design tensile strength T_d was 29.4 kN/m.

To determine the arrangement of the reinforcements, comparative design was performed by using the following design methods: PWRI method (Onodera et al. 1992), Geogrid Research Board (GRB) method (Yamanouchi & Fukuda 1993), Leshchinsky method (1993), and monolithic wall method which assumes that short reinforcements and a facing unite with each other to exert the soil retaining effect. Figure 2 shows the stability analysis mode by the PWRI method. For the stability analysis under the seismic condition, the horizontal seismic coefficient k_h of 0.10 was assumed.

Figure 3 summarizes the specifications of reinforcements found by the comparative calculation. The focus of this study was put on the verification of the reinforcing mechanism by

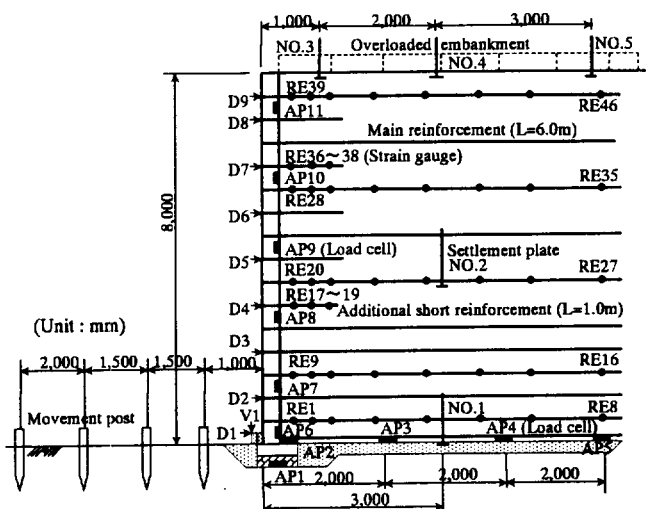


Figure 1. Cross-section and reinforcement pattern of test wall.

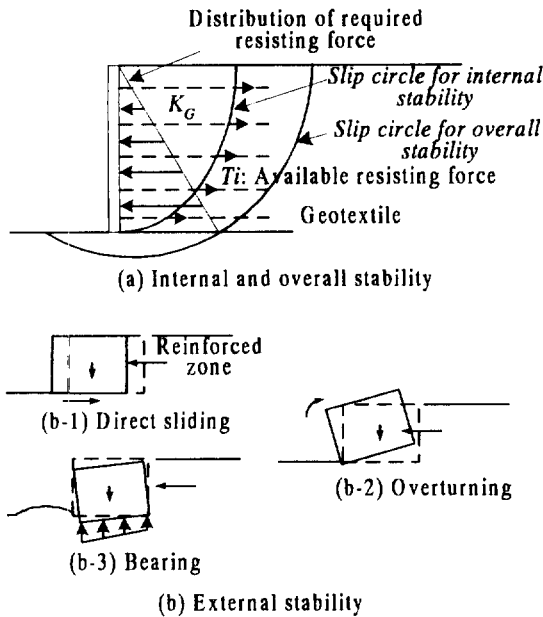


Figure 2. Failure mode of PWRI's design method.

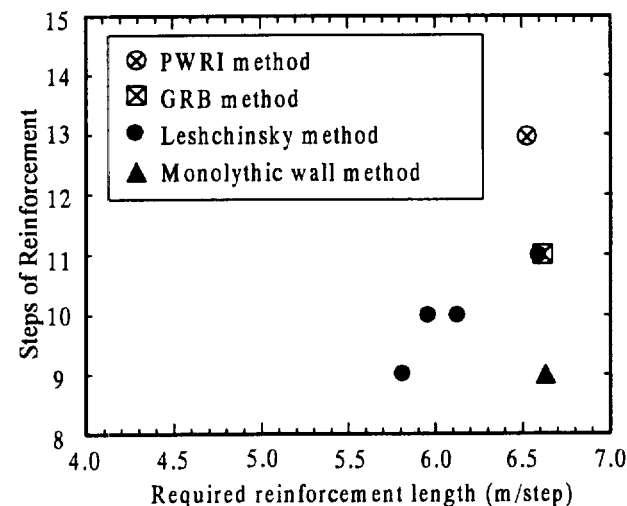


Figure 3. Required reinforcement length and steps.

constructing the test wall into a critical state, the calculation results taken into account. Namely, the test wall was based on the ordinary condition, the number of reinforcement layers was set at 11 on reference to the results by the Leshchinsky method, and the length of reinforcements L was set at 6.0 m (see Figure 1). To prevent the blocks not connected to main reinforcements from coming out of the wall surface, short reinforcements of 1.0 m-long were connected to them. The wall given these conditions and specifications, its stability was calculated by the PWRI's method as shown in Table 1. The overall stability F_s by the slip circular method was found to be 1.055, a state near the critical condition. Under the seismic condition of $k_h=0.10$, it (F_s) was found to be 0.917, an unstable state.

Table 1. Stabilities of test wall calculated by PWRI method.

Analysis mode	Ordinary condition	Seismic condition ($k_h=0.10$)
Overall stability (Circular slip)	$F_s=1.055 < 1.2^*$ NO	$F_s=0.917 < 1.0^*$ NO
Direct sliding	$F_{sd}=2.142 > 1.5^*$ OK	$F_{sd}=1.844 > 1.2^*$ OK
Overturning (Eccentricity)	$ e =0.690 < L/6^*$ OK	$ e =0.566 < L/3^*$ OK
Bearing capacity	$q_{max}=252 < q_a^*$ NO	$q_{max}=264 < q_a^*$ NO

L : length of main reinforcement, (=6.0m).
 q_a : allowable bearing capacity, (=49kN/m²) estimated from N -value (6) after Nakajima et al. 1996.
 *: design criteria.



Photo 1. Overview of test wall (June 1997).

3 FIELD MEASUREMENT OF TEST WALL

The long-term observation of the test wall has been conducted with the measuring instruments shown in Figure 1 for about 800 days including the construction period. The wall experienced the heavy rainfall of 81.5 mm/d ($t=189$ d) and the of 191.5 mm/d ($t=559$ d). The wall was also exposed to three small to medium earthquakes, but maintained its stability as Photo. 1.

3.1 Horizontal Displacements of Test Wall

Figure 4 shows the displacements of the wall surface measured during the observation period. The maximum horizontal displacement was approximately 100 mm, and the wall surface took a bulgy shape, the center portion in height most prominent. The displacements immediately after the construction were small enough.

Since the overhanging of wall surfaces mars their scenes and offends our sense of security, it would be preferable to give the wall surfaces small backward leans in their construction. The deformation of the wall slowed down considerably and settled after some 800 days passed in the observation.

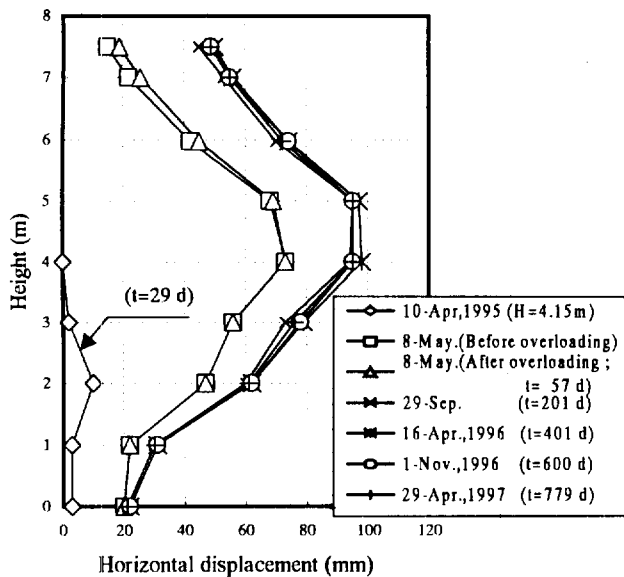


Figure 4. Horizontal displacement of test wall.

3.2 Earth Pressure on Wall Facing and Subgrade Reaction

Figure 5 shows the distribution of earth pressure on the back of the facing during and after the construction of the wall. The measured values were larger in the upper zone and smaller in the lower zone than the values calculated on the basis of Coulomb's earth-pressure theory.

As shown in Figure 6, the subgrade reactions were equal to or smaller than the overburden pressure in the area distant from the facing, and exceeded largely the pressure by the dead weight of the concrete blocks at the bottom of the facing. This does not

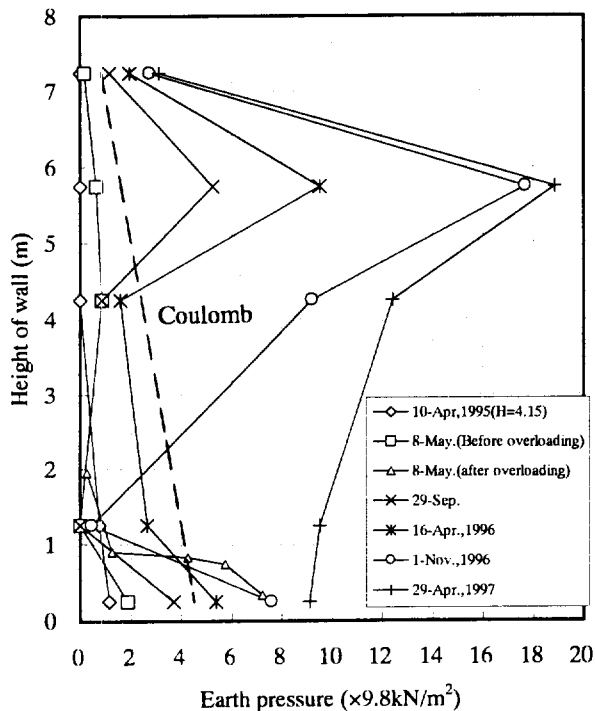


Figure 5. Earth pressure distribution on back of facing.

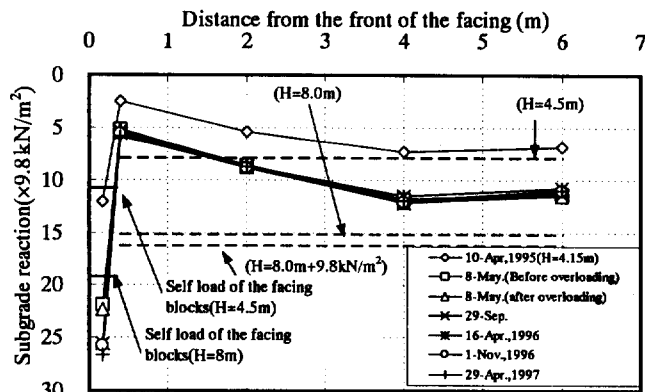


Figure 6. Distribution of subgrade reaction at bottom.

agree with the assumption, made in the design manual of the PWRI regarding the external stability analysis for the bearing capacity of foundation grounds, that the reinforced zone of an embankment behaves as a rigid body and the distribution of the subgrade reaction takes a trapezoidal shape, the reaction decreasing linearly from the facing toward the rear.

3.3 Strain of Reinforcements

Figure 7 shows the distribution of the strain of the reinforcements measured by foil strain gauges bonded on them. The maximum strain of each reinforcement was observed in the immediate vicinity of the facing. This distribution pattern is typical of walls with high-rigidity facings. At the completion of the test wall, the maximum strains were approximately 1%, 8.8 kN/m in terms of tensile force, which were smaller than the design strength of 29.4 kN/m. The maximum strains of the additional short reinforcements were at the same level as those of the main reinforcements.

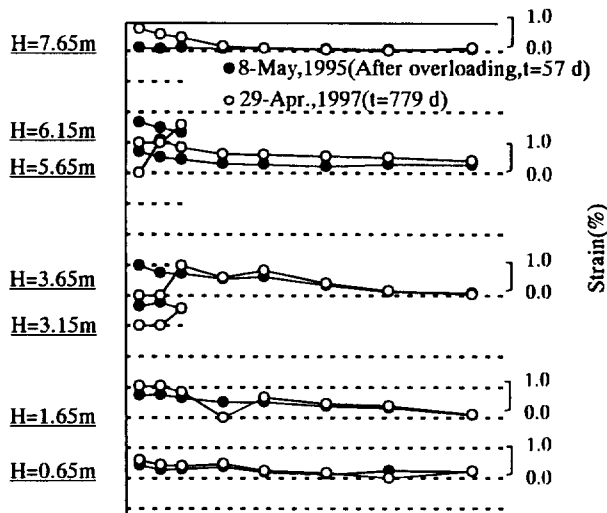


Figure 7. Distribution of strain of reinforcements.

4 DISCUSSION ON STABILITY OF TEST WALL

4.1 External Stability Analysis

In the PWRI design method, its external stability for the bearing capacity of the foundation ground is examined by checking whether the subgrade reaction is contained within the bearing capacity or not. The top layer of the foundation ground of the test wall was a filled Kanto-loam layer 2.15 m thick. As its N -value was about 6, its bearing capacity was estimated at 49 kN/m² or so. On the other hand, the maximum subgrade reaction was estimated at 252 kN/m² under the ordinary condition and 264 kN/m² under the seismic condition ($k_s=0.10$), suggesting the instability of the test wall. Besides, the subgrade reactions observed were about 261 kN/m² under the facing and about 117 kN/m² under the embankment. Thus, it can not be explained why the test wall has maintained its stability.

On the other hand, since almost the whole test wall consisted of soil and it could basically be regarded as an embankment, another stability analysis was performed by using a circular slip surface which runs into the foundation ground. The soil-filling history of the ground taken into account, its strength parameters in the original state and in the state immediately before the construction of the test wall were estimated. With the safety factor F_s of 1.027 thus found, the stability of the test wall could be explained (Nakajima et al., 1996).

Thus, it was suggested that the external stability analysis for the bearing capacity of foundation grounds can basically and advantageously be replaced by the circular slip stability analysis using slip surfaces which run into the foundation grounds.

4.2 Stability Analysis under Seismic Conditions

The test wall underwent three small to medium earthquakes so far in 1996: the first was of $M=4.7$ and estimated acceleration at Tsukuba 14 gals on August 16; the second, $M=6.2$ and 26gals on September 11; and the third, $M=5.4$ and 45 gals on December 21. The stability analyses of the wall under the third earthquakes (45 gals, $k_s=0.05$) turned out as follows: the safety factors against slip circle $F_s=0.989<1.0$; the safety factors against direct sliding $F_{sd}=2.326>1.2$; and the stabilities against overturning $e=0.373<L/3$, indicating the instability against slip circle in particular. Nevertheless, the wall maintained its stability during the earthquakes. Accordingly, it would also be necessary to review the seismic-stability analysis method of the PWRI design method.

5 CONCLUSIONS

Based on the long-term observation results of the full-scale reinforced test wall 8-meter high, the behavior of the test wall was compared and contrasted with that assumed and predicted by the PWRI's design method, to identify future subjects toward the establishment of a more rational design method. Main findings are as follows:

1. The arrangement of the reinforcements of the test wall was determined to construct the wall into a critical state under the ordinary condition, critical when evaluated by the PWRI design method. During the some 800 days observation, the test wall was exposed to heavy rains and small to medium earthquakes. Although the test wall, given such specifications, was supposed to lose its stability, it maintained its stability. Accordingly, it is necessary to establish a more

rational design method in future.

2. The PWRI design method is built on the concept of limit equilibrium. However, the following inconsistencies were observed: (i) the measured earth pressures on the back of the test wall's facing in the lower zone were smaller than the active earth pressures estimated by the Coulomb's earth-pressure theory, (ii) the measured values of the tensile force on the reinforcements were smaller than the values estimated in designing the test wall, and (iii) the distribution of the subgrade reaction did not take the trapezoidal shape which is assumed of concrete retaining walls, and the design and measured values of the subgrade reaction exceeded the bearing capacity of the foundation ground.
3. The bearing capacity, one factor in analyzing the external stability of walls, need not be examined, if their external stability is examined by the circular slip stability analysis using slip surfaces which run into their foundation grounds.

REFERENCES

- Gotteland, Ph., J. P. Gourc, H. Wilson Jones and J. Baraize (1992) Cellular walls associated with geosynthetics: A laboratory model study, *Proc. Int. Symp. on Earth Reinforcement Practice (IS Kyushu '92)*, Fukuoka, Japan, pp.337-343.
- Leshchinsky, D. (1993) Geosynthetic reinforced steep slopes and walls: Effects of facing blocks, *1st Tokushima Int. Seminar on Slope Stability Engineering*, Tokushima, Japan, pp.95-133.
- Nakajima, T., N. Toriumi, H. Shintani, H. Miyatake and K. Dobashi (1996) Field performance of a geotextile reinforced soil wall with concrete facing blocks, *Proc. Int. Symp. on Earth Reinforcement Practice (IS Kyushu '96)*, Fukuoka, Japan, pp.427-432.
- NCMA (1993) "Design manual for segmental retaining walls (Modular Concrete block retaining wall systems) 1st edition", National Concrete Masonry Association, Virginia, USA, 336p.
- Ochiai Y. and N. Fukuda (1996) Experimental study on geotextile-reinforced soil walls with different facings, *Proc. 1st European Geosynthetics Conf. (EUROGEO 1)*, Maastricht, Netherland, pp.113-120.
- Onodera, S., S. Naemura, A. Nakane and S. Maruo (1992) A design method for steep reinforced embankments with geotextiles, *Proc. Int. Symp. on Earth Reinforcement Practice (IS Kyushu '92)*, Fukuoka, Japan, pp.391-396.
- Tajiri, N., H. Sakaki, J. Nishimura, Y. Ochiai and K. Dobashi (1996) Full-scale failure experiments of geotextile-reinforced soil walls with different facings, *Proc. Int. Symp. on Earth Reinforcement Practice (IS Kyushu '96)*, Fukuoka, Japan, pp.525-530.
- Tatsuoka, F. (1992) Keynote lecture: Roles of facing rigidity in soil reinforcing, *Proc. Int. Symp. on Earth Reinforcement Practice (IS Kyushu '92)*, Fukuoka, Japan, Vol. 2, pp.831-870.
- Yamanouchi, T. and N. Fukuda (1993) Design and observation of steep reinforced embankment, *Proc. 3rd Int. Conf. on Case Histories in Geotechnical Engineering*, St. Louis, USA, Vol. 2, pp.1361-1378.

Multi-Anchored Soil Retaining Walls with Geosynthetic Loop Anchors.

H. Brandl

Professor, Institute for Geotechnical Engineering, Technical University, Vienna Austria

ABSTRACT: The paper deals with reinforced modular block walls using loop anchors. The bearing behavior of such structures is the deadman principle, but there exists simultaneously a composite effect between modular units, straps, and soil. Accordingly, several hypotheses of calculation are presented, based on model tests and comprehensive in-situ measurements on construction sites since the year 1977. Recommendations for on-site installation, filling, and backfilling of the structure are also given.

KEYWORDS: Retaining walls, Slope stabilization, Geo „Others“, Design by Function

1 SCHEME OF LOOP ANCHORED WALL SYSTEMS

Figure 1. illustrates the scheme of a loop anchored wall system. Generally, the front side of the wall consists of L-shaped elements (modular prefabricated reinforced concrete units) arranged in displaced position to each other and connected by tension straps (loop anchors) to anchor elements (e.g. half tubes) on the back of the wall. Similarly, for embankments both facings can be constructed of L-shaped elements (e.g. Figure 3).

The core of the wall consists of soil being placed in layers and compacted. The prefabricated elements and the loop anchors prevent the soil from giving way. Thus the fill material increases the bearing capacity, and the whole structure acts as a composite body - similar to crib walls but more flexible. Accordingly, the effect of the loops is primarily not a soil reinforcement, and friction is merely of secondary importance.

In order to avoid long term corrosion problems and to provide a flexible behavior of the retaining wall, geosynthetics have been preferred since about 15 years as tie-elements: High modulus polyester has proved especially suitable. Aramid is relatively expensive but exhibits less strain and creep. Consequently, a combination of polyester and aramid yarns is especially useful in critical cases. Special loops consist of geocomposites comprising a polyester tie element with a strip drain, and this core being wrapped by a non-woven geotextile. These composite loops have proved suitable for low-permeable fill material of a high water content.

The retaining structure with anchor loops is not only used for retaining walls but also for

- Noise protection walls.
- Bridge abutments.
- Protective structures against avalanches, mud flows.
- Quay walls and bank protection.
- Increase of the height of embankment dams.

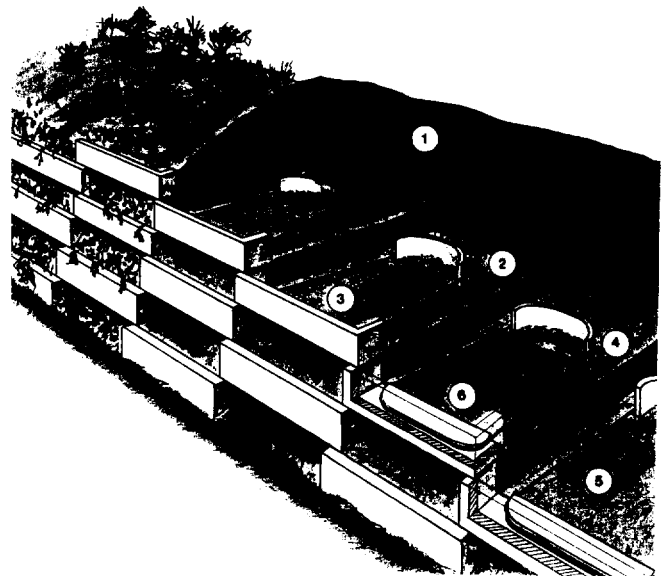


Figure 1. Loop anchored wall system - Schematic.

- | | |
|-------------------------------|----------------------------------|
| 1 Natural soil or backfill | 2 Fill material |
| 3 Modular wall facing element | 4 Anchor element |
| 5 Loop anchors | 6 Section through facing element |

2 MODEL TESTS AND FIELD MEASUREMENTS

Small scale tests (1:20) in the laboratory were combined with 1:1 - field measurements on several construction sites. The maximum wall height was 21 m.

From Figure 2 it can be seen that overturning is the dominating mode of the global wall displacement. But in detail the structure does not tilt like an ideal monolith: There are differential movements among the layers, thus indicating internal shear deformations. The layers are pushed outside in steps, remaining rather horizontal. With

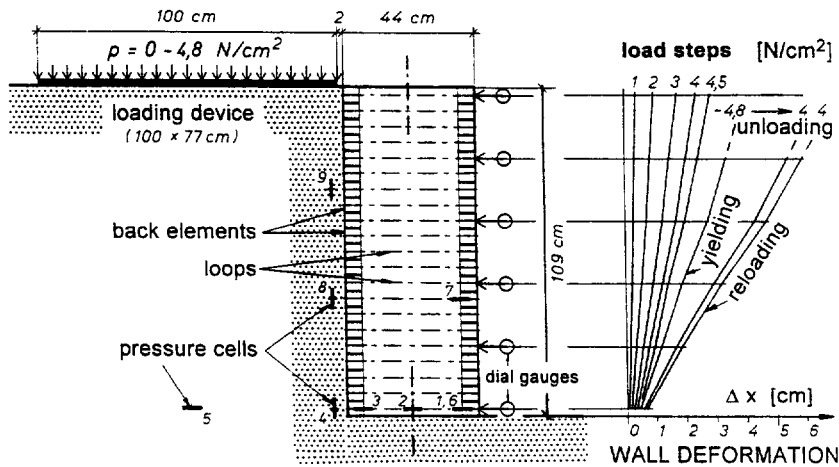


Figure 2. Laboratory test No.2. Scale 1:20, hence wall height $H = 21,8\text{m}$ in nature. $1\text{ N/cm}^2 = 10\text{ kPa}$

increasing surcharge load, structural failure begins on top of the wall where the composite behavior of the wall is not yet as strong as in greater depth. The bond effect among backfill, loops and modular elements increases with the overburden pressure. This could be proven especially clearly by cutting some of the loops. In this case a rearrangement of internal forces took place, thus avoiding failure to a high extent. Collapse of the wall is announced by large movements and does not occur suddenly.

This bearing deformation behavior is characteristic of multi-anchored soil retaining walls with geosynthetic loop anchors. It could be found not only in model tests but also

on numerous construction sites. Figure 3 shows a loop anchored retaining wall as a catch-system for avalanches and mud flows which threatened a highway and railroad on toe of a steeply inclined slope. Figure 4 illustrates the base pressure during the construction period and its long-term behavior. The stress distribution exhibits a maximum near the inner pressure cell which is caused by the embankment-like cross section of the retaining system. This differs widely from the behavior of gravity walls.

The tensile forces in the loops are plotted in Figure 5 showing a typical long-term decrease within the first years after wall completion. Four strain gauges were mounted on

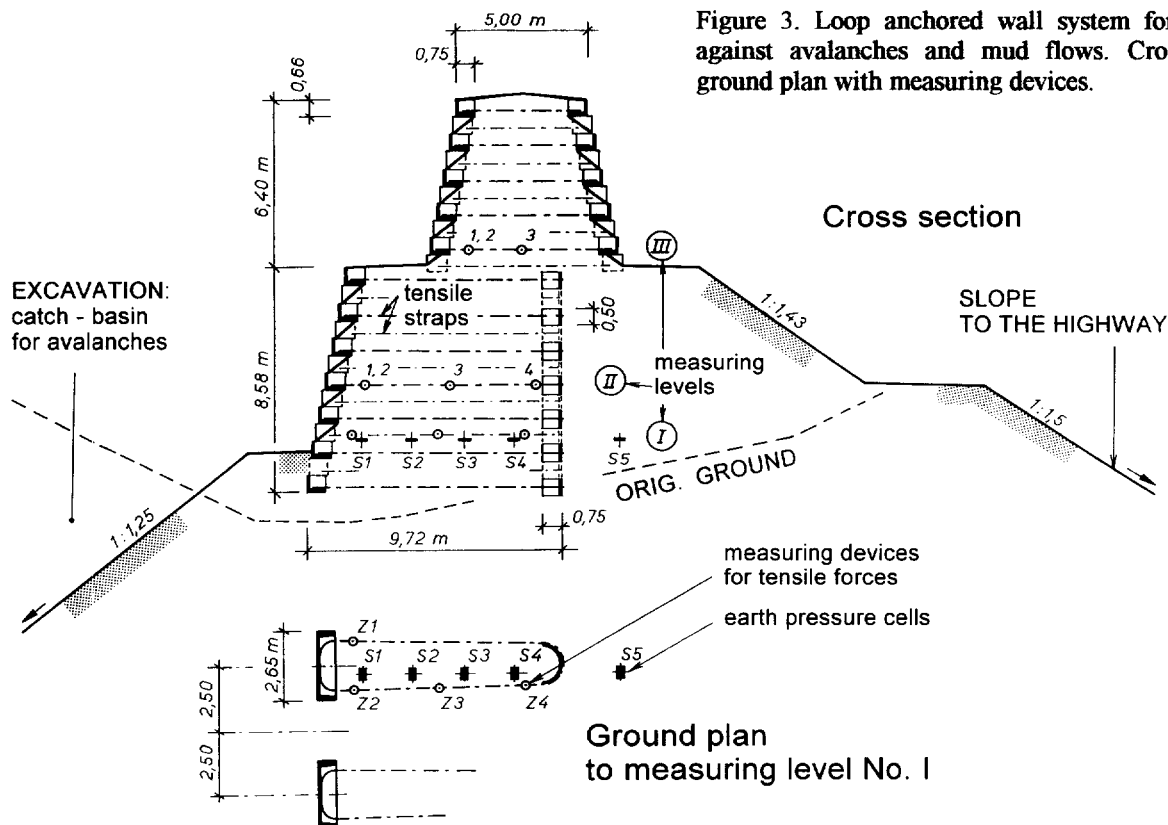


Figure 3. Loop anchored wall system for a catch-basin against avalanches and mud flows. Cross section and ground plan with measuring devices.

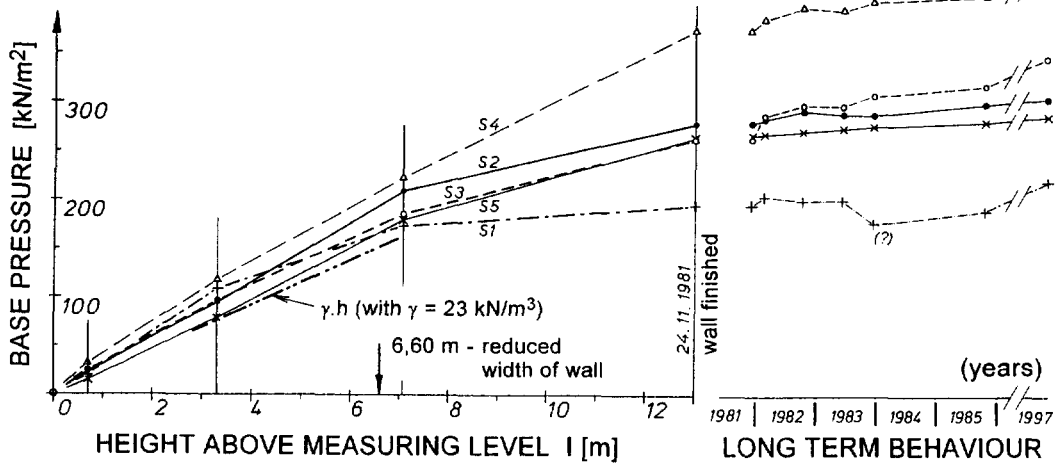
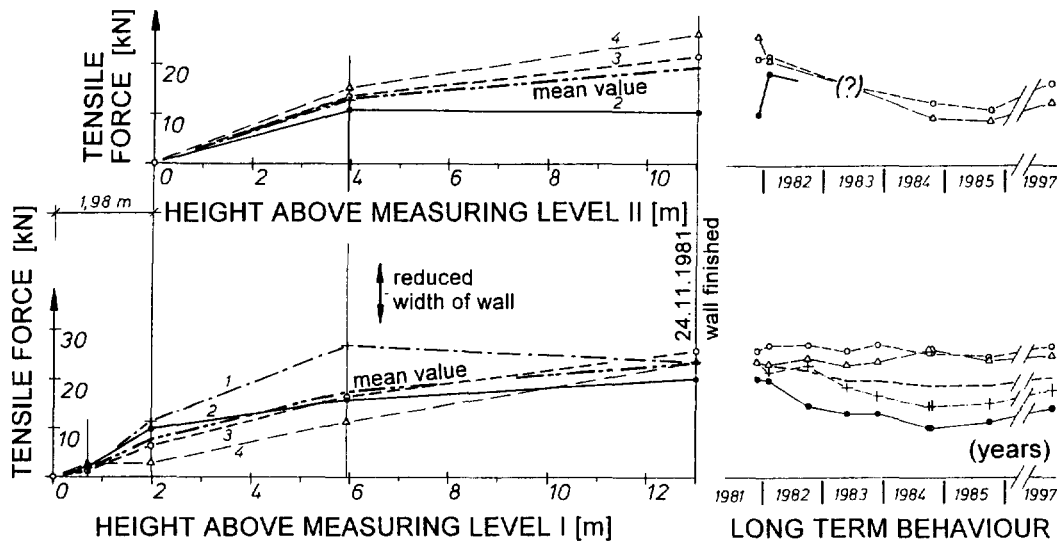


Figure 4. Measured base pressures versus wall height and long-term behavior (to Figure 3).

Figure 5. Measured tensile forces versus wall height and long-term behavior (to Figure 3).



each loop. The measured tensile forces are smaller than calculated, especially in the lower part of the retaining system. After reaching a certain overburden, additional wall heights cause less increase in tensile force than could be expected by the dead weight of $\gamma \cdot z$ and $\sigma_h = K \cdot \gamma \cdot z$. This is caused by a variable coefficient of lateral earth pressure. Similar to reinforced soil, K varies with depth from K_0 at the top, to K_a below several meters depth. Furthermore, low tensile forces can be explained by arching or silo pressure conditions in the fill and by an increasing modulus of the fill. A gradual increase of the bond effect between soil, loops, and anchor elements plays an additional role. Loops generally experience stress reduction, as the soil progressively takes over a higher portion of load. Creeping of the loops could be widely excluded, because some sections of the retaining system had loops of coated steel - and the results were fairly

similar. The difference between theoretical and actual tensile forces represents an additional safety factor compared to conventional calculation.

3 DESIGN AND CALCULATION

In order to develop a practicable design method, several hypotheses and theoretical assumptions were compared. Their accuracy and limits of application had to be verified on the basis of small scale tests, field experiments, in-situ measurements and site experience.

For design, external, internal, and local stability analyses have to be performed. The external stability comprises base sliding, overturning, and ground failure. It is calculated similarly to conventional retaining walls, the structure being considered a „quasi-monolith“, but with a statically

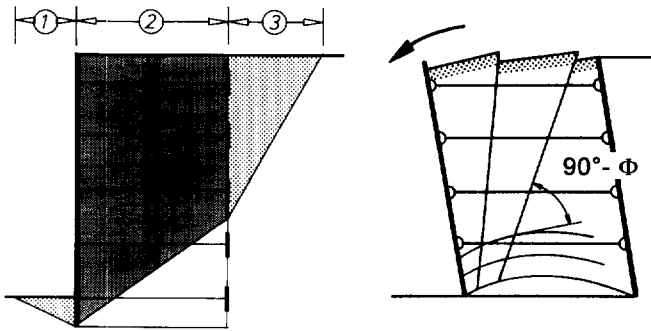


Figure 6. Internal failure mechanisms of loop anchored walls. Left: Block theory (assuming three slices). Right: Cofferdam scheme.

reduced, fictive width of the wall. According to the deformability of the wall, the active earth pressure can be assumed at the back of the wall and an angle of wall friction, $\delta = \phi$. The resultant of all acting forces should run generally within the core of the cross section. Commonly, block-like overturning is not a relevant failure mechanism.

The internal stability comprises three failure mechanisms: pull-out, tensile overstress, internal sliding (including possible slope failure). Furthermore, the local stability of the segmental wall units has to be proven: facing connection and bulging (shear transfer failure). The calculation can, above all, be performed similarly to that of cellular cofferdams, assuming a lateral earth pressure between the active limit value and the earth pressure at rest, depending on the stretchability of the loops.

For assessing the tensile forces, T , in the loops two boundary analyses have proved suitable:

$$T = K_{ah} \cdot \sigma_1 \cdot \Delta A \quad \text{.....for } \delta = \phi$$

$$T = K_a \cdot \gamma_f \cdot z \cdot \Delta A \quad \text{.....for } \delta = 0$$

whereby

K_a = active earth pressure coefficient

z = depth of the loop beneath top of wall

γ_f = unit weight of the fill material

σ_1 = front edge pressure (fictious value of „quasi-monolith“)

ΔA = portion of the wall area referring to one loop

δ = angle of wall friction

ϕ = friction angle of fill material.

The maximum calculated T should be considered the design value.

The influence of surcharge loads on the back or directly on the crown of the wall can be assessed by conventional calculation methods. Traffic loads are idealized by static replacement loads. Contrary to reinforced soil, a friction loss along the tie elements caused by dynamic loads is not relevant.

Site observations have disclosed that the internal stability of loop anchored walls is actually higher than assessed by conventional calculation. This refers especially to internal

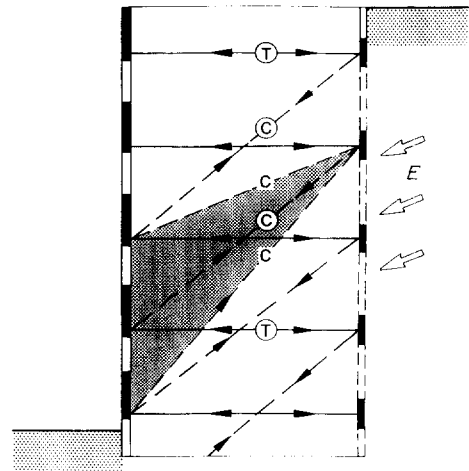


Figure 7. Idealization of soil (fill material) and structural members of a loop anchor wall system as a truss like retaining structure.

E = earth pressure

C = soil in compression

T = anchor loops acting in tension

sliding of slender structures. For a slenderness of $B/H \geq 0.6$, Janbu's block method has proved suitable. The methods of Kranz and others provide by far too small safety factors. Sliding analyses based on block theories (e.g. Figure 6/left) underestimate the actual safety factor of very slender structures. Numerous site observations have shown that in such cases values of only $FS_{calc.} = 0.4$ to 0.8 are calculated, whereas the walls have been exhibiting a fully stable behavior since 10 years and more (checked by long term monitoring). Consequently, such slender structures should be designed similar to cofferdams with multiple anchorage (Figure 6/right).

Another calculation method idealizes the loop anchor wall system as a truss-like structure. According to Figure 7, the loops are the truss members acting in tension, and the soil between the loops and modular units represents the truss members in compression. This truss-like behavior increases with compaction degree of the fill material. A high compressive strength and dilatant properties of the soil enable it to interact with the loops and the anchor elements on the front and back side of the retaining structure. Vertical, possibly prestressed anchors through the prefabricated anchor elements at the back of the wall would provide further improvement.

Experience has shown that loop anchored walls hardly fail on a plane passing through the toe. Commonly, the critical failure plane runs through the face of the structure at a point $1/4 H$ to $1/3 H$ above the toe (H = wall height). In case of high surcharge loads, failure may occur at even higher points.

If inextensible (metallic) loops are used, the failure of the wall can occur rather rapidly according to potential overstress of adjacent loops - like a zip effect. Contrary to

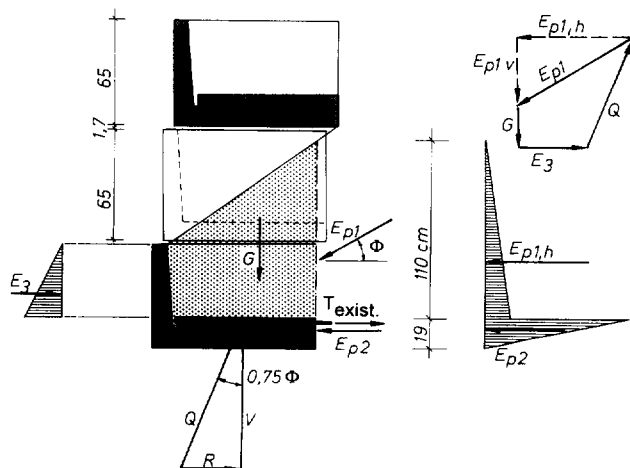


Figure 8. Forces on the facing element of a loop anchor wall system and force polygon for the soil fill on the concrete element.

T_{exist} = existing tension force
 G, G_B = dead weights of soil and concrete element

that, overstressing of extensible loops (polymeric anchors) first of all leads to creep and only limited load shedding. The deformation increases, thus indicating in time the necessity of strengthening the structure.

The connection between the tie elements and the facing of a permanent soil reinforcement wall is a critical part of the design. Contrary to that, anchor loops allow a full strength solution without requiring special starter elements embedded in the modular facing. Figure 8 illustrates the load transfer in a typical modular structure. Vertical wall friction can be assumed $\delta_v = \emptyset$, and horizontal friction $\delta_h = 0.75 \emptyset$.

Loop anchored walls require smaller widths than conventional reinforced soil structures. This reduces the slope cut, which is especially important if the retaining structure has to be placed into unstable terrain. No special footing is necessary except on soft soil.

The structure allows adaptation to various site conditions, geometries, and varying loads, and it behaves fairly insensitive to differential settlement, to dynamic loads, and to earthquakes. Furthermore, full-face draining and intensive greenery planting are possible.

4 LONG TERM BEHAVIOR

Regarding the long term behavior of loop anchored wall systems, two factors have to be considered before all: Creeping and effect of hydrolysis on polyester.

Monitoring of loop anchored wall systems has disclosed that creeping can be widely neglected. Figure 9 shows the tensile strength-extension characteristics of various loops. At a working stress level of about $\leq 30\%$ for the initial ultimate tensile strength of geosynthetic straps, long term creep elongation could be expected less than 1% occurring

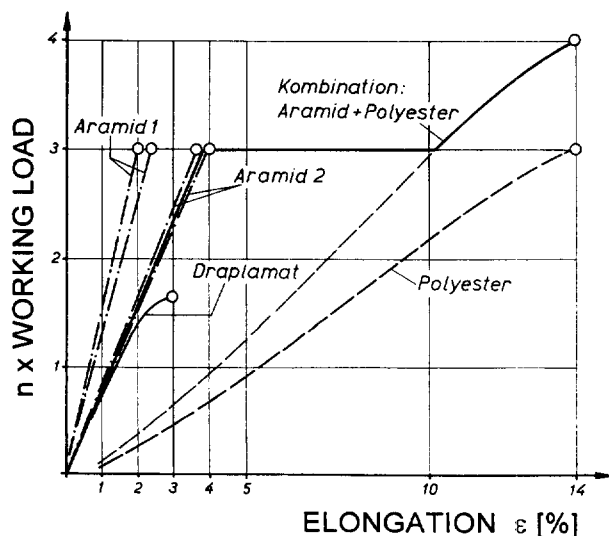


Figure 9. Tensile strength - elongation characteristics of various loops. Draplamat is a coated steel strap.

after construction. The (allowable design) extension is likely to be $< 5\%$ in total for polyester and $< 1\%$ for aramid and draplamat.

There is a significant difference between the load-deflection characteristics of a loop and a reinforcing strip. Contrary to laboratory tests on free tie elements, creeping gradually decreases on the site where the loops are embedded in soil. This effect increases with composite effect, hence with compaction degree and friction/adhesion. Changes in ambient operating temperature between 10 to 40 ° C practically do not alter the creep characteristics.

Draplamat consists of coated steel tendons and is cheaper than aramid. Polyaramid loops can exhibit even greater shear strength and lower extension than steel straps (Figure 9). Such tie elements are sometimes preferred for very high retaining structures and high loads. Mostly, the ultimate tensile strength of draplamat is similar to that of aramid, i.e. $\sigma_T = 2600 \text{ N/mm}^2$. The strain at failure is $\epsilon_f = 3\%$ and 2 to 4% respectively. Commonly used polyester straps exhibit $\sigma_T = 1050$ to 1250 N/mm^2 and $\epsilon_f = 10$ to 14%.

Composite loops consisting of aramid and polyester have proved suitable for structures in unstable slopes and seismic areas. Overstressing is indicated by a period of great deformation which is succeeded by strain hardening. This ductile behavior enables a timely strengthening of the structure before failure might occur. Consequently, such retaining systems are especially suitable for designing by the observational method.

When polyester fibres are directly exposed over longer periods of time at $\text{pH} > 11$, the presence of water (exactly OH ions) can have a detrimental and destructive effect, resulting in chain scission, reduced molecular weight and strength loss. Consequently, a coating of polyester loops is

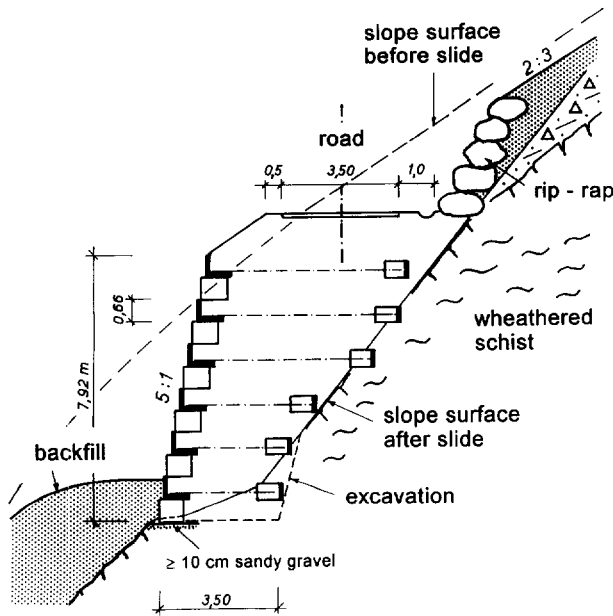


Figure 10. Loop anchored wall to reconstruct a road in a steep slope after landslide had occurred.

sometimes required. Generally, hydrolysis is not relevant if well engineered materials are used for loop anchored wall systems.

5 CONSTRUCTION PRINCIPLES

Commonly, indigenous and waste fill materials can be used for loop anchored wall systems. This provides significant savings in construction costs. The maximum grain size of the fill should not exceed 2/3 of the thickness of a layer. Cohesive or cohesive-frictional material provides more stable structures than purely frictional fill. On the other hand, sufficient drainage is essential if the retaining structure supports a slope. In such cases the grains finer than 0,06 mm should be limited to 15%. Furthermore, this value avoids frost damages within the composite structure. Sandwich filling, with alternating cohesive and non-cohesive layers has also proved suitable.

Usually, the fill material and the backfill of the structure should be compacted to $D_{pr} = 97$ to 100% of standard Proctor density. The higher value is for widely grained fill material and a distance of more than 1 m behind the back of the wall. Near the front face, a lower compaction is preferred (about $D_{pr} = 92\%$) to avoid local damage and to facilitate the planting of greenery. Compaction should begin about 1 m behind the face elements and proceed toward the backside of the wall. Thus, a slight prestressing of the loops is obtained, and the front blocks remain in their position. The back members of the deadman anchorage have to be well embedded in densely compacted soil. The front zone shall be compacted as last part.

During wall construction, the anchor loops must be protected from local overstress (e.g. passing of heavy vehicles or site equipment). This can be performed by a cover of sand, by a stable coating, or by excavating small trenches where the loops are placed. Polyester loops should be isolated from direct contact with concrete facing elements. Accordingly, a coating is recommended if polyester loops are installed. Commonly, robust loop coatings of polyethylene or PVC are used. Coating of the modular concrete elements has also proved suitable.

The concrete elements do not require a special interlock, e.g. by slotting dowels into preformed locating holes. Experience has shown that an accurate positioning of successive layers of blocks can be fully obtained simply by a precise installation of the elements. But bituminous soft-fibrous boards should be placed between the concrete elements to avoid local overstressing and edge cracking. Furthermore, such interlayers improve the flexible behavior of the structure, and they may compensate possible installation deficiencies. Flexible interlayers, covering the whole contact zone, have proved more suitable than small boards.

Commonly, loop anchored wall systems are stepped back at 5 to 15 cm per layer to provide an attractive face inclination and to improve planting conditions. Furthermore, facing elements can be colored to give specific aesthetic effects. Small unit sizes allow an adaption to various geometry, including stepped foundations and wall heights and varying length of anchor loops (e.g. Figure 10).

The main advantages of the loop anchor wall system are:

- Modular standards of the pre-fabricated elements.
- The assembling of the wall requires only a light crane; no special technical knowledge is required.
- Short construction period.
- The excavated soil can be used as fill material in most cases.
- No footings (except on soft subsoil).
- Well adaptable to locally differing conditions (geometry, soil, loads, etc.).
- Rather insensitive to differential settlements, to dynamic and cyclic loads, and to earthquakes.
- No sudden rupture in case of overloading, but gradually increasing failure indications, due to the great plastic reserves.
- Excellent drainage of the fill and backfill.
- Sufficient place for plant growth (hence also „green walls“).

REFERENCES

- Brandl, H., Dalmatiner, J. (1986) „New earth retaining structure and other retaining structures of reinforced or multi-anchored earth“, Volume 280 of *Straßenforschung*, Federal Ministry of Economic Affairs, Vienna, Austria.

Mechanically Stabilized Earth Wall Design: External Stability

M.S. Meyers, PhD, PE

Senior Geotechnical Engineering Specialist, U.S. Army Corps of Engineers, St. Paul District, St. Paul, Minnesota, USA

R.A. Wetzel, PhD, PE

E.S. McCullough, PhD, PE

Professors, Department of Civil and Environmental Engineering, University of Wisconsin-Platteville, Platteville, Wisconsin, USA

R.R. Berg, PE

Consultant, Ryan R. Berg & Associates, Inc., St. Paul, Minnesota, USA

ABSTRACT: Design of mechanically stabilized earth (MSE) walls includes internal and external stability analyses. External stability, which includes sliding, overturning, bearing capacity, global stability, and compound stability analyses, generally governs the required length of reinforcement and the wall embedment depth. This paper discusses the components of external stability design of MSE walls, the focus being on bearing capacity and the impact of non-generalized site conditions on reinforcement lengths and embedment depths required to satisfy bearing capacity and sliding design criteria. Results indicate that the minimum L/H ratios of 0.6 or 0.7 taken for granted by many designers are not satisfactory for non-generalized site conditions. This paper is directed towards members of the geosynthetics community who design and construct MSE walls.

KEYWORDS: Bearing capacity, Segmental retaining walls, Geosynthetic reinforcement, Foundations, Embedment depth.

1 INTRODUCTION

Design and construction of mechanically stabilized earth (MSE) walls has dramatically increased with the advent of segmental retaining wall (SRW), or modular block, units. Design of MSE walls is routinely completed by many engineers (e.g., civil, structural, geotechnical) with varying technical expertise. The need to fully understand the concepts of MSE wall design appears to have diminished with the widespread availability of computer software and design charts provided by manufacturers, suppliers of geosynthetic reinforcement and SRW units, and others.

Design of MSE walls includes internal and external stability analyses. Most designers find that completing the internal stability design, which tends to focus on the economic placement of the geosynthetic reinforcement, is straightforward. For very generalized site conditions, such as a wall with horizontal backslopes and front slopes, general design rules-of-thumb may be satisfactory for determining the reinforcement length. For non-generalized site conditions, however, such as a wall with a front slope and/or backslope, external stability is likely to govern the design of the wall, especially with respect to required reinforcement lengths and wall embedment depth.

External stability includes: sliding, overturning, bearing capacity, global stability, and compound stability. Many designers do not have all of the tools required to complete all of the components of the external stability analysis for non-generalized site conditions. Most current MSE wall design software products do not address all of the components of external stability design for non-generalized site conditions.

This paper discusses the components of external stability design of MSE walls. The focus of the paper is on bearing capacity and the impact of non-generalized site conditions on required reinforcement lengths and wall embedment depths.

The purpose of the paper is threefold: (i) to rekindle a classical geotechnical engineering oriented approach to the design of MSE walls with respect to external stability; (ii) to highlight the significance of non-generalized site conditions on bearing capacities for MSE wall system foundations; and (iii) to disseminate findings regarding the ultimate bearing capacity of MSE wall system foundations, for both generalized and non-generalized site conditions.

2 CURRENT DESIGN PRACTICE

2.1 Design Methodology

Several design guides for MSE wall systems are available. This discussion will focus on two of the generic design guides which are available: the National Concrete Masonry Association (NCMA) design manual (1996); and the Federal Highway Administration (FHWA) design guidelines (Elias and Christopher 1997). The general design approach for both methods consists of two interrelated but separate procedures: design for internal stability; and design for external stability. A generic MSE wall cross-section is presented in Figure 1.

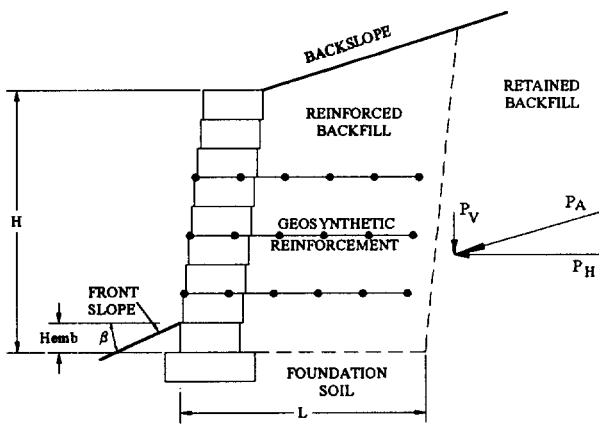


Figure 1. Typical geosynthetic-reinforced MSE wall cross-section (after NCMA, 1997).

2.1.1 Internal Stability

Internal stability refers to the interactions between the soil, facing units, and geosynthetic reinforcement in the reinforced soil zone. The spacing and tensile strength of the reinforcing layers are determined in this analysis, along with a check of the connection strength between the facing units and the reinforcement.

2.1.2 External Stability

The reinforced soil zone is considered to act as a composite gravity mass for the purposes of external stability analyses other than composite stability analyses. Forces acting on this mass include: the weights of the soil and facing units; the lateral earth pressure of the retained backfill; and any surcharge loads. Sliding, bearing capacity, overturning, settlement, compound stability, and global stability are possible failure modes that must be considered.

2.1.3 Empirical Design Criteria

The base width, L , of the reinforced soil zone is usually established from external stability analyses. In addition, certain minimum values for L have been established from experience. The NCMA guidelines recommend that L shall not be less than $0.6H$ regardless of the results of stability calculations. FHWA guidelines recommend a minimum L of $0.7H$.

To insure a safe allowable bearing capacity is achieved, minimum wall embedment depths, H_{emb} , have been established for the bottom of the wall below finished grade. These values vary from $H/20$ for walls with a horizontal slope in front of the wall to $H/5$ for slopes of 3 horizontal to 2 vertical (3H:2V). A minimum wall embedment depth of 0.5 m, except for structures founded on rock, where no

embedment of the wall is required, is stated in the FHWA guidelines. NCMA guidelines require a minimum wall embedment of 0.15 m.

2.2 Lateral Earth Pressures

Lateral earth pressures are calculated differently in the two design procedures. With the NCMA guidelines, lateral earth pressures for both internal and external analyses are based on Coulomb earth pressure theory, which can account for the inclination of the wall facing units, the back slope angle, wall friction, and MSE mass-retained backfill friction. The vertical component of earth pressure is neglected in NCMA internal and external stability calculations.

Using the FHWA guidelines, lateral earth pressures are based on Coulomb theory for external stability and Rankine theory for internal stability. Face batters are ignored for batters less than or equal to 10 degrees from the vertical. The earth pressure direction is considered to be parallel to the back slope angle for external stability. A horizontal earth pressure direction is used for internal stability, with and without sloping backfills.

2.3 Bearing Capacity

As this paper is primarily concerned with bearing capacity determinations, the analysis methods for sliding, overturning, settlement, compound stability, and global stability are not discussed herein; a complete discussion of these analyses is contained in the literature (Elias and Christopher 1997; Holtz et al. 1997; Simac et al. 1993; and Berg et al. 1989).

Conventional bearing capacity analyses are carried out assuming that the reinforced soil mass acts as a continuous strip footing of width, L . The vertical stress on the base of the footing should be less than the allowable bearing capacity of the foundation soil. The vertical stress is assumed to act uniformly over a footing of effective width, B' , which is determined from

$$B' = L - 2e \quad (1)$$

where e is the eccentricity of the resultant vertical force on the base. The ultimate bearing capacity, q_{ult} , may be determined from the Terzaghi bearing capacity equation using the Vesic bearing capacity factors:

$$q_{ult} = c N_c + q N_q + 0.5 \gamma B' N_\gamma \quad (2)$$

Allowable bearing capacity, q_{all} , is determined by dividing the ultimate bearing capacity by an appropriate factor of safety, which is typically 2.0 for MSE wall systems (NCMA, 1997; U.S. Army Corps of Engineers, 1989 and 1990) to 2.5 (Elias and Christopher, 1997):

$$q_{all} = q_{ult} / FS \quad (3)$$

Design procedures in the FHWA guidelines require that the eccentricity, e , not exceed $L/6$, and if it does, the reinforcement length must be increased. A limitation on eccentricity is not required in the NCMA procedures.

Both the NCMA and FHWA design procedures consider only the vertical components of foundation loads in ultimate bearing capacity calculations. Thus, effects of the inclination of the resultant foundation load, which typically reduce the ultimate bearing capacity of a foundation, are neglected.

The NCMA and FHWA design procedures do not address the presence of a ground slope in front of the wall, except with respect to general guidance and recommendations of minimum embedment depths for typical ground slopes in front of the wall. The ultimate bearing capacity of a wall with a front slope is reduced by an amount proportional to the angle β of the front slope, assuming no bench in front of the wall. A ground slope bearing capacity factor is included in the bearing capacity equation (Bowles, 1996). Equation (2), with β measured counterclockwise in degrees from the horizontal, is modified to:

$$q_{ult} = c N_c g_c + q N_q g_q + 0.5 \gamma B' N_\gamma g_\gamma \quad (4)$$

where:

$$g_c = 1.0 - \beta/147 \quad (5)$$

and

$$g_q = g_\gamma = (1 - 0.5 \tan \beta)^5 \quad (6)$$

Assuming a cohesionless soil and all other conditions equal, a 3H:1V front slope reduces the ultimate bearing capacity by approximately 60 percent; a 2.5H:1V front slope reduces the ultimate bearing capacity by approximately 68 percent; and a 2H:1V front slope reduces the ultimate bearing capacity by approximately 76 percent. These are staggering reductions in ultimate bearing capacity values, which are typically not directly accounted for in most MSE wall design software.

Bowles (1996) also presents a procedure for determining the ultimate bearing capacity of foundations on slopes, with and without a bench in front of the foundation, independent of the application of a ground slope bearing capacity factor to the general bearing capacity equation.

A goal of this paper is to verify the NCMA and FHWA minimum embedment depth and reinforcement length guidelines and to enlighten the reader as to a more thorough understanding of the impacts of various front slope and backslope combinations on the ultimate bearing capacity of MSE wall systems.

3 GEOTECHNICAL SITE CONDITIONS

3.1 Generalized Site Conditions

MSE wall systems are often designed for generalized sites conditions, such as: a horizontal front slope; a nominal surcharge loading; adequate foundation soil shear strengths; and a depth to groundwater which does impact the bearing capacity of the foundation soils. For these generalized site conditions, the guidance and recommendations regarding embedment depths and L/H ratios may well be applicable. In many instances however, especially of late, many MSE wall systems are being carried to extreme heights in locations where the generalized site conditions discussed above do not exist. Such conditions are referred to in this paper as non-generalized site conditions.

3.2 Non-Generalized Site Conditions

Many MSE walls are being designed and constructed with backslopes and ground slopes in front of the wall which can vary from 3H:1V to 1.5H:1V. In addition, foundation soil shear strengths may be lower than is typically assumed for generalized site conditions (Meyers et al. 1997). These non-generalized site conditions obviously result in lower ultimate bearing capacities than would be determined for the generalized site conditions. In addition, compound stability may govern the design in some instances. As such, the general guidance and recommendations regarding embedment depths and L/H ratios may not provide sufficient safety factors against failure.

4 METHODOLOGY

4.1 General

A spreadsheet was developed to analyze the sliding stability and ultimate bearing capacity of MSE wall foundations for the generalized and non-generalized site condition combinations presented in Table 1. A cohesionless soil with an angle of internal friction equal to 30 degrees and having a unit weight of 19.6 kN/m³ for the wall fill, retained backfill, and foundation soil were assumed for these analyses. Only the NCMA methodology was used for the analyses. The NCMA bearing capacity equations were modified to include a ground slope factor, assuming no bench in front of the wall. Analyses include determination of bearing capacity factors of safety and L/H ratios.

4.2 L/H Ratio Determinations

The minimum length of geosynthetic reinforcement required to just meet a factor of safety equal to 1.5 against sliding failure was determined for various wall height, surcharge,

Table 1. Combinations Analyzed For Ultimate Bearing Capacity of MSE Walls.

Case	Front Slope	Back Slope	Surcharge (kN/m ²)	Embedment Ratio Denominator ^a
1	0	0	0	20, 10, 7, 5
2	0	3H:1V	0	20, 10, 7, 5
3	0	2H:1V	0	20, 10, 7, 5
4	0	0	12	20, 10, 7, 5
5	3H:1V	0	0	20, 10, 7, 5
6	3H:1V	3H:1V	0	20, 10, 7, 5
7	3H:1V	2H:1V	0	20, 10, 7, 5
8	3H:1V	0	12	20, 10, 7, 5
9	2H:1V	0	0	20, 10, 7, 5
10	2H:1V	3H:1V	0	20, 10, 7, 5
11	2H:1V	2H:1V	0	20, 10, 7, 5
12	2H:1V	0	12	20, 10, 7, 5

^aWall embedment depth equal to H/Embedment Ratio Denominator (e.g. $H_{emb} = H/5$).

and backslope combinations. The critical sliding plane was taken as the reinforced fill-foundation soil interface (i.e., at depth equal to H). This required reinforcement length, or a minimum reinforcement length of 0.6H, whichever was greater, was then used in the bearing capacity computations to determine the factor of safety against bearing capacity failure for various wall heights, backslope, front slope, surcharge, and wall embedment depths. A minimum embedment depth of 0.15 m was used. A bench in front of the wall was not included in the analyses.

Minimum length of geosynthetic reinforcement required to just meet a factor of safety equal to 2.0 against bearing capacity failure were determined for various wall heights, backslope, front slope, surcharge, and wall embedment depths. The minimum L/H ratio for the various backslope, front slope, embedment depth, and surcharge combinations was, thus, defined as the longer of the lengths required to: (i) meet a factor of safety of 2.0 against bearing capacity failure; (ii) meet a factor of safety of 1.5 against sliding failure; and (iii) meet a minimum L/H ratio of 0.6.

5 RESULTS

5.1 Bearing Capacity Factors of Safety Determinations

Typical bearing capacity factor of safety results are presented in Figure 2, which plots the bearing capacity factor of safety against the foundation embedment depth (as a ratio of the wall height) for several different front slopes of a typical MSE wall condition assuming a horizontal backslope and a surcharge of 12 kN/m². As is to be expected, for a horizontal front slope, the factors of safety are well above 2.0 and indicate that a minimum embedment ratio of H/20 or 0.15 m, which ever is greater, should be satisfactory with respect to the sliding and bearing capacity components of external stability, for walls varying in height from 1.5 to 12 m.

The bearing capacity factors of safety are reduced dramatically when the only variable modified is the front slope, which was increased from horizontal to 3H:1V. A minimum embedment ratio of H/20 or 0.15 m is still satisfactory for the wall height and embedment ratio combinations analyzed. However, with the factor of safety approaching 2.0 for the shorter embedment depths, the designer should have a higher degree of confidence in the definition of the design parameters used in the sliding and bearing capacity analyses.

For a 2H:1V front slope, a factor of safety of 2.0 is not attained for most wall height and embedment depth ratio combinations. Either a greater geosynthetic reinforcement length is required or an increased embedment depth ratio is required. Since an embedment depth ratio of H/7.5, which results in a bearing capacity factor of safety of just 2.0 for a wall height of 12 m, corresponds to an embedment depth of 1.8 m, it may be more economical to increase the effective width of the footing by increasing the length of geosynthetic reinforcement.

5.2 Minimum L/H Ratios

Typical minimum L/H ratio results are presented in Figure 3, which is a bar graph plot of the range of L/H ratios required to satisfy both sliding and bearing capacity design requirements against the various combinations of front slopes, backslopes, and surcharges for wall heights which vary from 1.5 m to 12 m, assuming an embedment depth ratio of H/20 and no bench in front of the wall. A thick horizontal line is drawn across the bar graphs at an L/H ratio equal to 0.6, the minimum L/H ratio recommended by the NCMA Manual.

An L/H ratio greater than 0.6 is required to satisfy the sliding and bearing capacity requirements for many of the design cases. The following conditions require a L/H ratio greater than 0.6:

1. A backslope of 2H:1V, regardless of the front slope.
2. A front slope of 2H:1V, regardless of the backslope.
3. A front slope of 3H:1V, if a backslope other than horizontal is used.

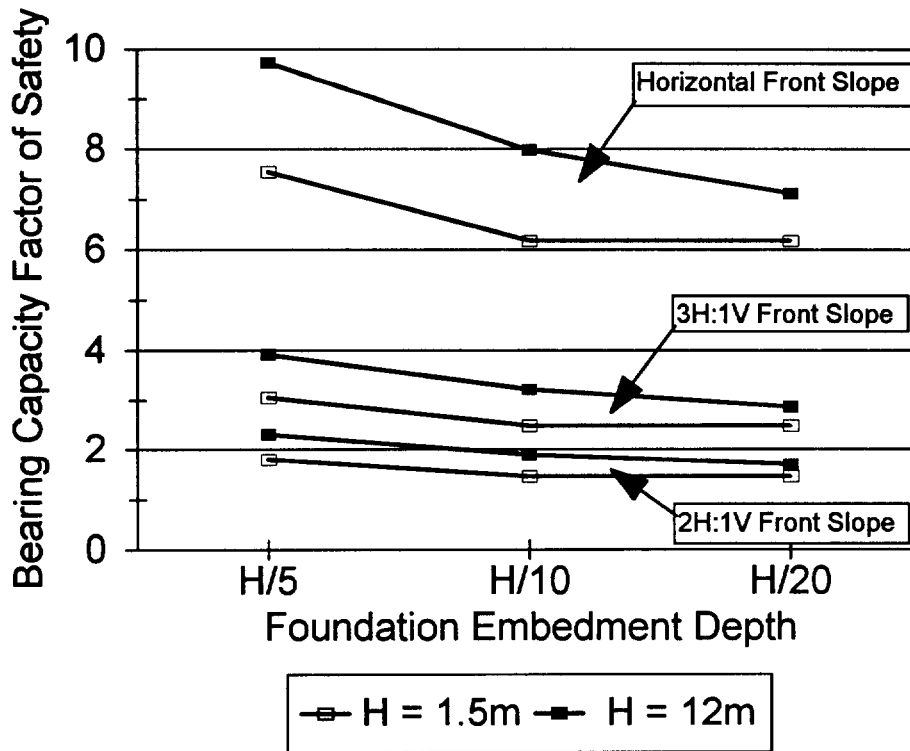


Figure 2. Typical bearing capacity factors of safety for various wall embedment ratios.

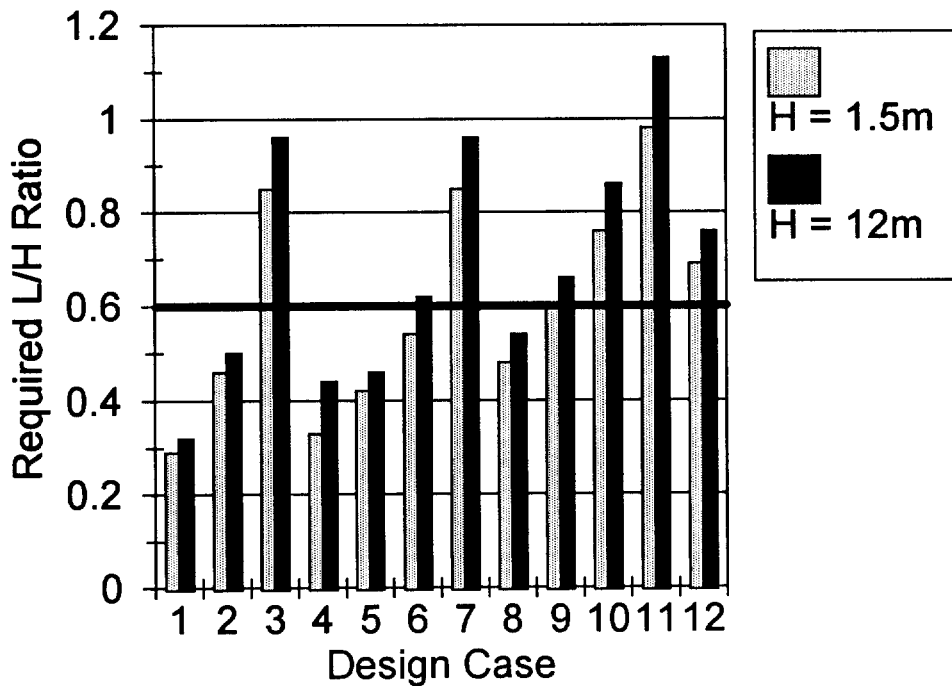


Figure 3. Minimum L/H Ratios for the combinations listed in Table 1.

Since the embedment ratio of H/20 represents the shortest embedment depth investigated, the required L/H ratios for increased wall embedment depths are not quite as large. However, the same design cases (No. 1, 2, and 3 noted above) require L/H ratios greater than 0.6 for wall embedment depth ratios of H/10, H/7, and H/5.

6 CONCLUSIONS

This paper has presented a basic review of the determination of the ultimate bearing capacity of MSE wall systems. The impact of various combinations of front slopes, back slopes, surcharges, embedment depths, and wall heights on ultimate bearing capacity is presented and discussed.

Conclusions, based on the assumptions previously listed, are:

1. The ground slope in front of a MSE wall system can significantly impact the ultimate bearing capacity beneath an MSE wall.
2. The magnitude of the angle of the ground slope in front of an MSE wall is proportional to the reduction in ultimate bearing capacity for the wall.
3. A backslope of 2H:1V requires an L/H ratio greater than 0.6, regardless of the front slope and wall embedment depth used.
4. A front slope of 2H:1V requires an L/H ratio greater than 0.6, regardless of the backslope and wall embedment depth used.
5. A front slope of 3H:1V requires an L/H ratio greater than 0.6, if a backslope other than horizontal is used, regardless of the wall embedment depth used.
6. A L/H ratio of 0.6, with a wall embedment depth ratio of H/20, is most likely satisfactory for generalized site conditions limited to horizontal front slopes and backslopes and a surcharge of 12 kN/m² or less.

7 RECOMMENDATIONS

The intent of this paper was to investigate the impact of non-generalized site conditions on the bearing capacity of MSE wall systems. The authors note that performance of comprehensive sliding, bearing capacity, and compound stability analyses are particularly important for all projects with non-generalized site conditions, especially where a front slope or backslope of any magnitude is to be used. The site conditions will dictate the minimum reinforcement length, L, and wall embedment depth ratio for the MSE wall structure.

8 DISCLAIMER

The opinions and recommendations included in this paper are solely those of the authors and do not represent the views of the US Army Corps of Engineers or the University of Wisconsin-Platteville.

9 REFERENCES

- Berg, R.R., Chouery-Curtis, V.E., and Watson, C.H. (1989) "Critical Failure Planes in Analysis of Reinforced Slopes", *Geosynthetics '89*, IFAI, San Diego, CA, USA, pp. 269- 278.
- Berg, R.R. and Meyers, M.S. (1997) "Analysis of the Collapse of a 6.7 m High Geosynthetic-Reinforced Wall Structure", *Geosynthetics '97*, IFAI, Long Beach, CA, USA, Vol. 1, pp. 85-104.
- Bowles, J.E. (1996) *Foundation Analysis and Design, Fifth Edition*, McGraw-Hill Book Company, New York, USA.
- Elias, V. and Christopher, B.R. (1997) *Mechanically Stabilized Earth Walls and Reinforced Soil Slopes Design and Construction Guidelines, Participants Manual, FHWA Demonstration Project 82, Ground Improvement*, Federal Highway Administration, Washington, D.C., USA, 371 p.
- Holtz, R.D., Christopher, B.R., and Berg, R.R. (1997) *Geosynthetics Engineering*, Bitech Publishers, Vancouver, B.C, Canada, 452 p.
- Meyers, M.S. and Schwanz, N.T. (1993) "MSE Segmental Block Wall System in a Riverine Environment", *Geotechnical Fabrics Report*, IFAI, Volume 11, Number 4, pp. 22-27.
- Meyers, M.S., Schwanz, N.T., and Berg, R.R. (1997) "Specifying and Bidding Segmental Concrete Faced MSE Walls on U.S. Army Corps of Engineers, St. Paul District Projects", *Geosynthetics '97*, IFAI, Long Beach, CA, USA, Vol. 2, pp. 789-801.
- National Concrete Masonry Association, (1997) *Design Manual For Segmental Retaining Walls (Modular Block Retaining Wall Systems), Second Edition*, Herndon, Virginia, USA.
- U.S. Army Corps of Engineers (1989) *EM 1110-2-2502, Retaining and Flood Walls*, U.S. Army Corps of Engineers, Washington, D.C., USA.
- U.S. Army Corps of Engineers (1990) *ETL 1110-2-322, Retaining and Flood Walls*, U.S. Army Corps of Engineers, Washington, D.C., USA.

Brick-Faced Retaining Walls Reinforced with Geosynthetics - A Numerical Analysis

M. Isabel M. Pinto

Assistant Professor, Department of Civil Engineering, University of Coimbra, Coimbra, Portugal

R. V. C. Pereira,

Research Assistant, Department of Civil Engineering, University of Coimbra, Coimbra, Portugal

M. L. Lopes

Assistant Professor, Department of Civil Engineering, University of Porto, Porto, Portugal

A. Mendonça

Research Assistant, Department of Civil Engineering, University of Porto, Porto, Portugal

ABSTRACT: The paper presents a study on the behaviour of brick-faced retaining walls reinforced with geosynthetics. This new method of construction for low height retaining walls combines the reinforced earth techniques with a conventional brick wall. While the walls are being built reinforcement sheets are anchored to the wall by the bed joints of the brickwork. After cure, backfilling is done in layers and a surcharge load is applied.

The influence of the reinforcement configuration's length and spacing is studied by using a numerical model based on the finite elements method. The reliability of the model is checked by comparing the numerical results with those obtained from laboratory studies on small scale models. A brief description of the bidimensional model used is presented and followed by the definition of the geometry of the analysed structure. The backfill, reinforcement and face materials of the retaining wall are characterized.

KEY WORDS: Geosynthetic reinforcement, Retaining walls, Finite element analysis, Nonwoven Fabrics.

1 INTRODUCTION

Nowadays retaining walls reinforced with geosynthetics are being constructed frequently throughout the world. Therefore the establishment of reliable criteria of behaviour for each type of these structures is of the utmost importance.

This paper presents a study carried out on brick faced retaining walls reinforced with geosynthetics, built on rigid foundations. The effect of varying the reinforcement configuration both its length and spacing was investigated by using a two dimensional numerical model based on the finite elements method. The validity of the model is checked by comparing the results with those obtained from laboratory studies on small model walls.

This study follows an experimental test program (Pinto 1992, Pinto and Cousens 1996) on this type of wall and the development of a numerical model for reinforced retaining walls (Lopes 1992, Lopes et al 1994).

2 EXPERIMENTAL STUDY

The method of construction is similar to that proposed by Dalton (1977) for low height retaining walls and combines the reinforced earth technique with a conventional brick wall.

The walls were built "in situ" in a test tank near its free end. The internal dimensions of the tank are 240 mm wide x 490 mm high x 630 mm long. It is made mainly of steel in order to ensure minimum deformations so that plane strain conditions could be considered. The walls were 300 mm high x 240 mm wide and half a brick thick (20.5 mm).

The reinforcement material was a non-woven fabric used as interfacing in dressmaking, with a deformability modulus of 6.9 kN/m and a thickness of about 0.3 mm.

The walls were built with scale model bricks sawn from full size bricks "class B engineering bricks" as recommended by BS 5628 (1978). While the walls were being built, reinforcement sheets were anchored to the wall by the bed joints of the brickwork. After cure backfilling was done in 30 mm layers (each layer being compacted by a small vibrating plate in order to achieve the required density) while the reinforcement were extended horizontally into the backfill. Finally a surcharge load was applied.

Different reinforcement lengths and spacings were tested. The walls were instrumented in order to measure the wall movement and the horizontal earth pressure acting on the rear face of the wall.

3 NUMERICAL MODEL

The numerical model was developed for reinforced retaining walls and simulates the construction process. It is based upon the finite elements method and assume the validity of the plane strain conditions. The soil and the face are simulated by bidimensional elements with 5 nodes (Doherty et al 1969), the soil-face and the soil-reinforcement interfaces by joint elements with 4 nodes (Goodman et al 1968) and the reinforcement by elements with 2 nodes.

The construction process was simulated according to Kulhawy (1977). When a finite element is activated its self weight is divided by the element nodes and applied to the system. The deformability modulus of these elements is very small in order to simulate a material with weight and

without stiffness, however, before the placement of the next layer of backfill (next stage) the deformability modulus returns to its real value. The vertical and the horizontal stresses correspond to the overburden pressure, and to the at rest state respectively. The movement of the nodes of the activated elements is considered to be the same as the top nodes of the previous elements.

4 NUMERICAL ANALYSIS

4.1 Problem Conditions

In order to carry out the study a total of 5 finite element meshes were created, one for an unreinforced wall, and four for reinforced walls. These include two lengths (8 and 12 cm) and two spacings (3 and 4 brick courses, i. e., 45 and 60 mm respectively) for the reinforcement.

Figure 1 shows a finite element mesh for the wall reinforced every 3 brick courses with 12 cm long reinforcement sheets.

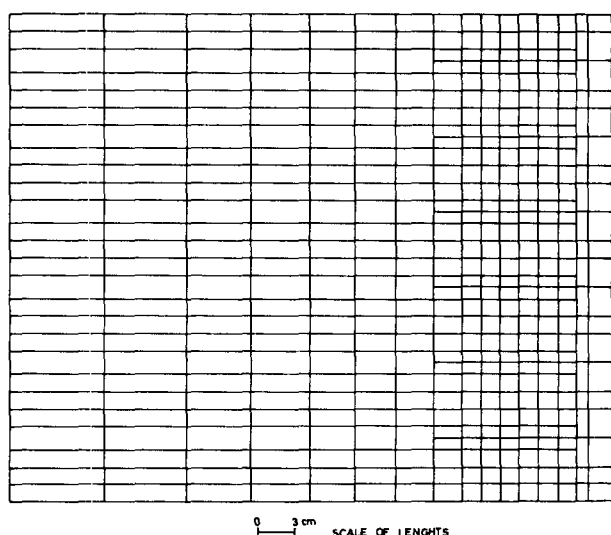


Figure 1. Finite element mesh.

Each mesh starts with only 20 elements, corresponding to the face of the wall. New elements are progressively activated in order to simulate the backfilling process: 300 for the backfilling, 126 for the interfaces and 48 for the reinforcement. Each reinforcement element is activated immediately after the placement of some soil on top of it. At the end of the backfilling stage the full mesh (which is activated in 10 steps) has a total of 494 elements and 495 nodes. The surcharge is then simulated by an equivalent load applied to the upper nodes of the top elements.

The boundary conditions were defined taking into account the geometry of the test tank (left lateral boundary) and the foundation condition (bottom boundary). In the former, the horizontal movement is prevented while in the latter, neither horizontal nor vertical movements are allowed in order to simulate a rigid foundation.

The soil of the backfill is a medium grain size containing about 15% of fine sand, with limiting densities of 14.4

kN/m^3 and 16.8 kN/m^3 . Other characteristics of the soil are given in Table 1.

Table 1. Soil characteristics.

γ (kN/m^3)	K_0	ϕ ($^\circ$)	c (kPa)	ν	E (kPa)
16.3	0.36	40	0	0.35	7000

γ denotes density, K_0 at rest coefficient, ϕ angle of friction, c cohesion, ν Poisson's ratio and E deformability modulus.

Table 2 shows the characteristics of the interfaces. The deformability modulus of the wall was assumed to be 25000 kPa after comparative studies on unreinforced walls.

Table 2. Interface characteristics.

	Soil - Reinforcement	Soil - Face
c_a (kPa)	0	0
$\text{tg } \delta$	0.73	0.75
K_t (kPa/m)	2000	750

c_a denotes adhesion, δ angle of friction and K_t stiffness modulus.

4.2 Results

4.2.1 Reliability of the numerical model

The reliability of the numerical model was checked by comparing the numerical results with those obtained from the laboratory tests. The comparisons were made both during the backfilling stage and under a surcharge load equivalent to a 270 mm high embankment on top of the backfill. In general a good degree of agreement was found when comparing the movement of the wall and the horizontal pressures acting on the rear face of the brickwall.

The influence of the increase of the backfill on the movement of the wall is shown in Figure 2 for a wall reinforced every 3 brick courses with 8 cm reinforcement length.

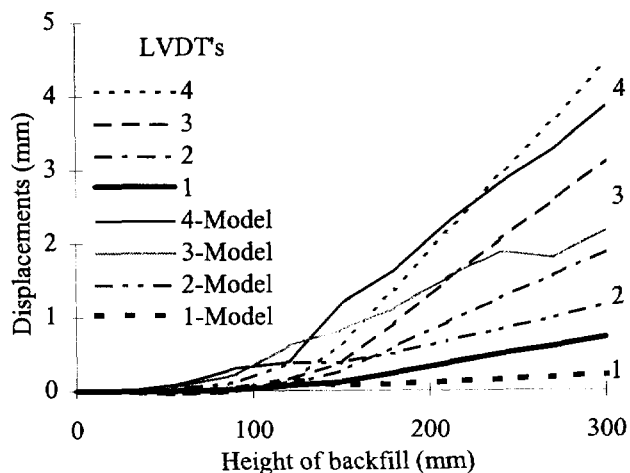


Figure 2. Displacements during backfill.

Figure 2 shows the variation of the displacement of the wall at different heights: 40, 115, 200 and 280 mm from the base of the wall, which corresponds to the position of the LVDT's 1, 2, 3 and 4 respectively. This figure shows in general, good agreement between the results obtained from the numerical model and those obtained from the laboratory tests. Small differences are however noticed as the values from the numerical model are lower than those from the laboratory. This is more evident near the end of backfilling stage and was also noticed during surcharging.

Figure 3 shows the displacements along the height of a wall reinforced every 4 brick courses with 8 cm reinforcement length during surcharging. The results from the numerical model and the laboratory test show a similar profile with values close to each other, but again, with the numerical model giving lower values when compared with the laboratory tests.

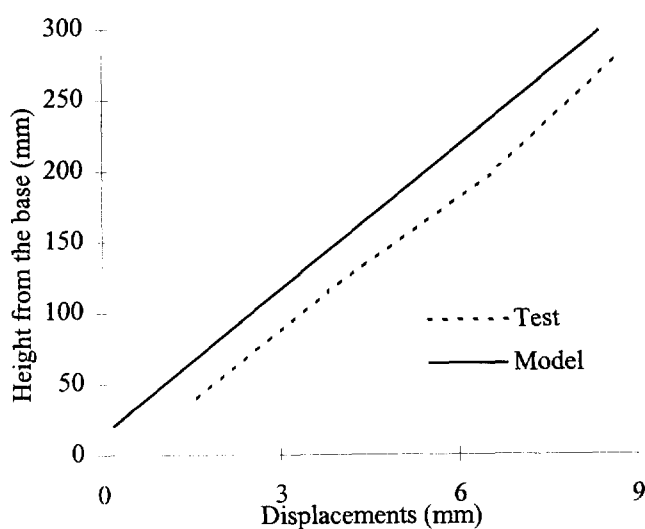


Figure 3. Displacements during surcharging.

The difference observed might be explained by a combination of two effects: the compaction which is not simulated by the numerical model and was found to be important during the laboratory test program (Cousens and Pinto 1996); and the restriction of displacement on the base of the wall imposed by the boundary conditions of the numerical model necessary to simulate the rigid foundation.

4.2.2 Influence of the reinforcement configuration

A study of the influence of the reinforcement length and spacing configuration was carried out. The movement of the face of the wall (Figure 4) and the stresses developed on the reinforcement (Figure 5) were considered.

When comparing the curves plotted in Figure 4, corresponding to the same reinforcement length (i.e. 3b.c.-8 cm with 4b.c.-8 cm and 3b.c.-12 cm with 4b.c.-12 cm), it can be seen that displacements decrease with a decrease of spacing for both reinforcement lengths.

Comparisons between curves corresponding to the same spacing (i.e. 3b.c.-8 cm with 3b.c.-12 cm and 4b.c.-8 cm with 4b.c.-12 cm) reveal a decrease of displacements with

an increase of length for both reinforcement spacings.

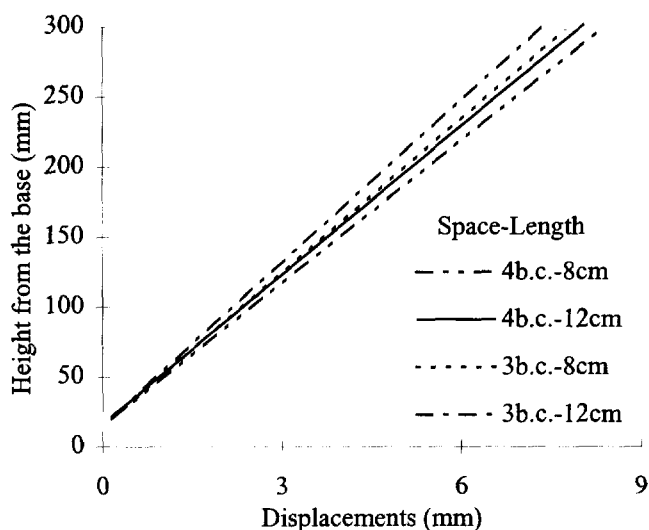


Figure 4. Displacements during surcharge for different reinforcement conditions.

The influence of the reinforcement configuration can also be studied comparing curves 3b.c.-8 cm and 4b.c.-12 cm of Figure 4. These curves correspond to walls with the same total amount of reinforcement (1152 m^2 for each wall) although differently distributed along the height of the wall. Figure 4 shows smaller displacements for the situation with lower spacing (3b.c.-8 cm) as opposed to that with long reinforcement (4b.c.-12 cm), suggested that the spacing is more important than the length of the reinforcement.

Figure 5 shows the variation of the stresses along the reinforcement length for walls with different reinforcement conditions. The curves plotted correspond to the most solicited layers of each wall which are those positioned at about mid-height. However, similar results were obtained for other layers. All curves show a non-linear behaviour, characteristic of highly deformable materials. The stresses are highest at the connection with the wall, and decrease towards the free end, which is characteristic of rigid walls (Shen et al 1979). Unlike walls with flexible faces, walls with rigid faces do not follow the vertical movement of the soil mass, consequently some bending takes place on the reinforcement, which generates tensile stresses.

The influence of the spacing can be studied comparing curves 3b.c.-8 cm with 4b.c.-8 cm and 3b.c.-12 cm with 4b.c.-12 cm in Figure 5. A decrease of the stresses can be related to a decrease in spacing, for both lengths. The influence seems to be more important on walls with the longest reinforcement.

When comparing curves corresponding to the same spacing (i.e. 3b.c.-8 cm with 3b.c.-12 cm and 4b.c.-8 cm with 4b.c.-12 cm) it can be seen that higher stresses are associated with shorter reinforcement, for both spacings, and specially for lower spacing.

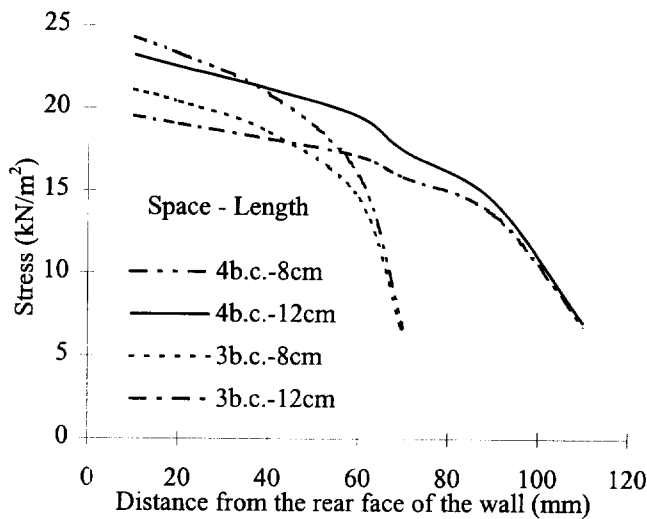


Figure 5. Stresses along the reinforcement length during surcharge for different reinforcement conditions.

Comparing stresses on walls with the same amount of reinforcement (i.e. 3b.c.-8 cm and 4b.c.-12 cm) it can be seen that lower stresses are associated with lower spacing. This is in agreement with the findings relating to the movement of the wall where the most important factor was found to be the spacing as opposed to the length. The difference of stresses between the two reinforcement situations increases towards the top of the wall.

5 CONCLUSIONS

A satisfactory degree of agreement was found when comparing the numerical results with those obtained from the laboratory tests.

From the study carried out it can be concluded that both the reinforcement length and spacing are important as far as the behaviour of the structure is concerned.

In fact, small movement and low stresses on the reinforcement are associated with longer reinforcement and lower spacing between reinforcing layers. This might be explained by the relative movement between the soil and the face of the wall which decreases both with the increase of the reinforcement length and with the decrease of the reinforcement spacing. Due to this movement some bending takes place on the reinforcement generating tensile stresses. The lower the movement the lower the generation of these stresses.

The spacing seems more important than the length of the reinforcement for both the movement of the wall and the development of tensile stresses on the reinforcement.

ACKNOWLEDGMENTS

The authors would like to express their thanks to the financial support of JNICT through the Project

PBIC/C/CEG/2387/95, to PRAXIS XXI of the "Ministério da Ciência e Tecnologia" and FEDER through the Project 3/3.1/CEG/2598/95 and to the Scholarship PRAXIS XXI/BM/8009/96.

REFERENCES

- BS 5628: Part1. (1978) "Structural Use of Masonry", British Standards Institution.
- Cousens, T.W. and Pinto, M. Isabel M. (1996) "The Effect of Compaction on Model Fabric Reinforced Brick-Faced Earth Retaining Walls", International Symposium on Earth Reinforcement, Fukuoka, Balkema, Rotterdam, ISBN 9054108339, Vol. 1, pp. 339 - 344.
- Dalton, D.C. (1977) "Fabric Reinforced Brick Retaining Wall", West Yorkshire Metropolitan County Council, Internal Report.
- Doherty, W.P., Wilson, E.L. and Taylor, R.L. (1969) "Stress Analysis of Axisymmetric Solids Utilizing Higher Order Quadrilateral Finite Elements", Report No. S.E.S.M. 69-3, Structures and Materials Research, Department of Civil Engineering, University of California, Berkeley.
- Goodman, R.E., Taylor, R.L. and Brekke, T.L. (1968) "A Model for the Mechanics of Jointed Rock", Journal of the Soil Mechanics and Foundation Division, Vol. 94, SM3, pp. 637-659.
- Kulhawy, F.H. (1977) "Embankments and Excavations", Chap. 16, "Numerical Methods in Geotechnical Engineering", C. Desai and J. Christian Eds. McGraw-Hill Book Company, New York.
- Lopes, M.L. (1992) "Muros Reforçados com Geossintéticos", PhD Thesis, University of Oporto, Porto, Portugal (in Portuguese).
- Lopes, M.L., Cardoso A.S. and Yeo, K.C. (1994) "Modelling Performance of a Sloped Reinforced Soil Wall using Creep Functions", International Journal of Geotextiles and Geomembranes, Vol. 13, No. 3, pp. 181-197.
- Pinto, M. Isabel M. (1992) "Model Studies of Fabric-Reinforced Brick-Faced Earth-Retaining Walls", PhD Thesis, University of Leeds, U.K.
- Pinto, M. Isabel M. and Cousens, T.W. (1996) "Geotextile Reinforced Brick Faced Retaining Walls", International Journal of Geotextiles and Geomembranes, Vol. 14, No. 9, pp. 449-464.
- Shen, C.K., Mitchell, J.F., DeNatale, J.S. and Romstad, K.M. (1979) "Laboratory Testing and Model Studies on Friction in Reinforced Earth", Proceedings of the International Conference on Soil Reinforcement, Paris, pp. 169-174.

Large Deformations FEM Analysis of a Reinforced Earth Structure

R. Arab

Lirigm, Joseph Fourier University, Grenoble, France

P. Villard

Lirigm, Joseph Fourier University, Grenoble, France

J.P. Gourc

Lirigm, Joseph Fourier University, Grenoble, France

ABSTRACT: This paper describes the use of finite element (FE) method in large deformations to predict the behaviour of reinforced soil walls loaded on the top by a concrete slab load. The measured results are compared to the numerical ones for both the simulations done. A parametric study was also carried out to investigate the effect of some important parameters for design, such as the geotextile length, the facing stiffness and the position of top load application considering a geotextile-reinforced retaining wall with a continuous and vertical facing.

KEYWORDS: Finite element analysis, Retaining wall, Geotextile reinforcement, Top load.

1 INTRODUCTION

This paper outlines the use of the finite element (FE) method for the analysis of two full scale experimentations on segmental walls (4.35 m height by 5 m wide) loaded on the top and constructed with extensible reinforcement : one with non woven geotextile and another with woven geotextile. The reinforcement distribution in the two reinforced walls are not exactly the same as illustrated in Figures 1 and 2, this is justified by the difference in mechanical properties between the two geotextiles. The experimentation was performed and reported by Gourc et al., (1995). The analysis of the reinforced soil walls was performed using a finite element program GOLIATH developed at Lirigm which is appropriate to simulate the great deformations of this kind of structures and the membrane behaviour of the geotextiles in the slinding process.

The comparison between the predicted and the experimental results shows the difficulties to simulate correctly field prototype structures behaviour.

In this study, the effect of some parameters such as reinforcement length, facing stiffness and the position of load application is examined, considering a reinforced-retaining wall with a continuous and a vertical facing.

2 NUMERICAL MODELLING

2.1 Materials

A plane strain finite element analysis in large deformations was performed using the finite element (FE) program GOLIATH. The finite element mesh adopted for the analysis is shown in Figure 3. The fill is modelled by three

node isoparametric elements. The soil was assumed to be an elastic-perfectly plastic material with a Mohr-Coulomb failure criterion (E_s, ν_s, c_s, Φ_s) with a non associated flow rule with a dilatancy angle ψ_s . The unit weight of the soil is $\gamma_s = 19 \text{ kN/m}^3$. The foundation of the structure is supposed to have an elastic behaviour ($E = 60 \text{ MPa}, \nu = 0.33$).

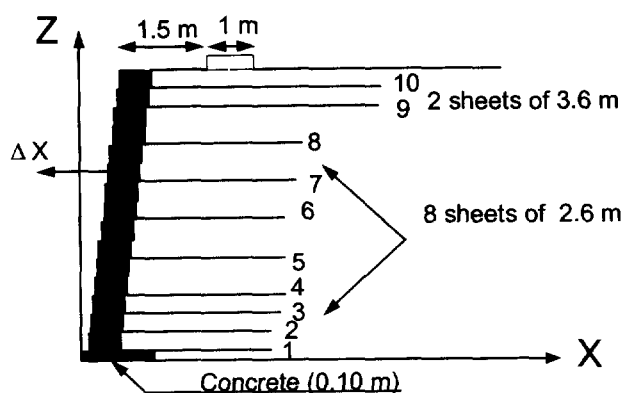


Figure 1. Non Woven wall (NW) profile and notations

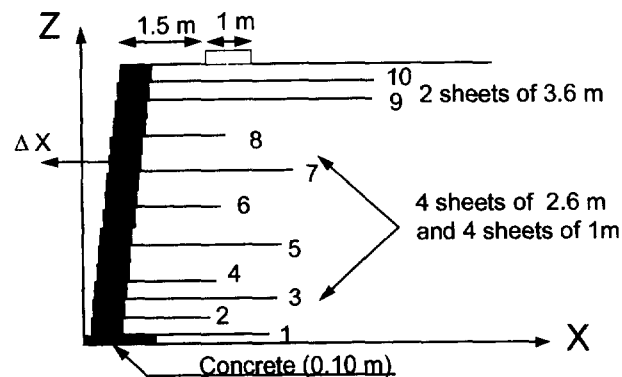


Figure 2. Woven wall (W) profile and notations.

The facing is modelled using four node isoparametric elements and was supposed to be elastic (E_f, ν_f) with a unit weight $\gamma=22 \text{ kN/m}^3$. Backfill, foundation, and facing element are modelled in large strain.

The facing is assumed to be continuous and the sheets are assumed to be fully bonded to the soil (no relative displacement).

The geotextile sheets were modelled using linear elastic bar elements in large displacement with negligible compressive strength and no bending stiffness (which allows the simulation of the membrane behaviour).

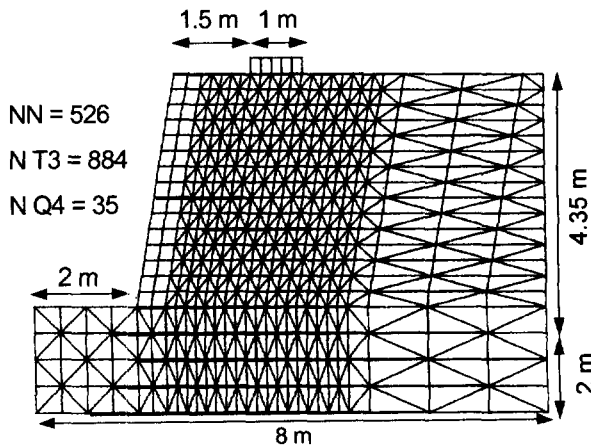


Figure 3. Finite element mesh adopted.

The geotextile stiffness are respectively $J_{NW}=95 \text{ kN/m}$ and $J_W=340 \text{ kN/m}$ for a non woven and woven fabrics.

2.2 Construction and loading

The compaction process is not simulated in this analysis. The full height of the wall is initially constructed applying body forces on the structure with ten load increments of 0.1g. Then the concentrated load is applied step by step through a linear elastic slab ($E = 1500 \text{ MPa}, \nu = 0.2$) with 10 kPa increments until 100 kPa, followed by 2.5 kPa increments until failure.

The two reinforced walls have been analysed by Arab et al., 1996 using the set 1 of parameters as summarised in Table 1 which was modified after additional laboratory test (set 2) as indicated in table 1.

Table 1. soil and facing parameters for the modelisation

	E_s (MPa)	ν_s	ϕ_s (°)	ψ_s (°)	E_f (MPa)	ν_f
Set 1	20	0.3	36	6	25	0.2
Set 2	35	0.3	36	16	20	0.2

3 RESULTS OF ANALYSIS

The predicted slab settlements versus surcharge Q obtained

with the two sets of parameters, are compared to the experimental one, respectively on Figures 4 and 5 for the two reinforced walls. The large settlement values considered shall be noticed.

For low value of the top load, the predicted settlement of the slab is very close to the measured one. It is worth noting that below the critical surcharge (breakpoint) the deformations and the displacement for the two structures are very small. Above this surcharge value the deformations increase significantly with the top load.

The measured slab settlement curves versus top load shown a breakpoint which corresponds to about 130 kN/m called the "critical surcharge". This is not predicted by the simulations. The breakpoint is very significant for designer because below it, only small deformations and displacements occur.

In the case of the Non Woven wall (NW) the predicted settlement obtained great with the two sets of parameters is lower than the measured one, particularly the solution calculated with the first set. However for the Woven structure (W) the measured settlement curve is enclosed by the numerical ones.

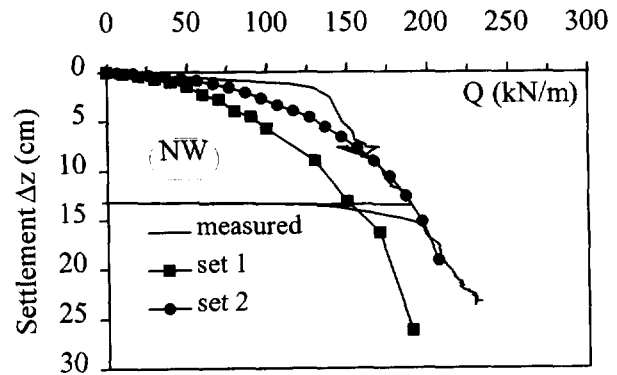


Figure 4. Slab load settlement versus top load (NW wall).

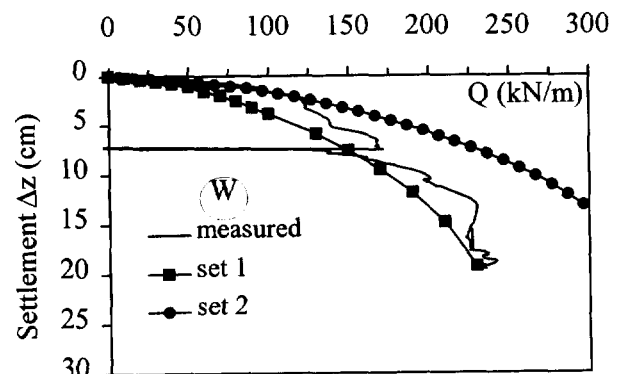


Figure 5. Slab load settlement versus top load (W wall).

The low settlement measured below the "critical surcharge" in the case of the Non Woven wall (NW) is probably due to the compaction effect. Under compaction, the extensibility and the texture of the geotextile combined

to the fine sand used to construct the Non Woven (NW) reinforced wall induce a better improvement of the mechanical characteristics than in the case of the Woven structure (W).

4 PARAMETRIC STUDY

A parametric study was carried out to investigate the effect of mechanical and geometric parameters for gaining an insight into the effects of several of the important design factors, such as the geotextile length, the facing stiffness and the position of top load application considering a geotextile-reinforced retaining wall with a continuous and vertical facing. The structure geometry, the finite element mesh and the material properties of backfill, foundation, facing used are those corresponding to set 2 as summarised in Table 1 unless otherwise stated. The geotextile stiffness adopted corresponds to the non woven fabrics ($J_{NW}=95$ kN/m).

4.1 Effect of geotextile length (L)

The effect of reinforcement length L is examined by considering different lengths of reinforcement while the height H of the wall reinforced by eight sheets with a constant spacing $\Delta H=0.58$ m is kept the same. The range of L/H considered varies from 0.36 to 0.8. As shown in Figure 6 the influence of increasing length of the geotextile is no more significant when L reaches $0.5H$. The short reinforcement sheets ($L/H=0.36$) contribute to the increasing of the bearing capacity as demonstrated by comparison with the unreinforced retaining wall (No reinf). This demonstrates that not only the reinforcement tensile beyond the failure surface will be considered in the design methods.

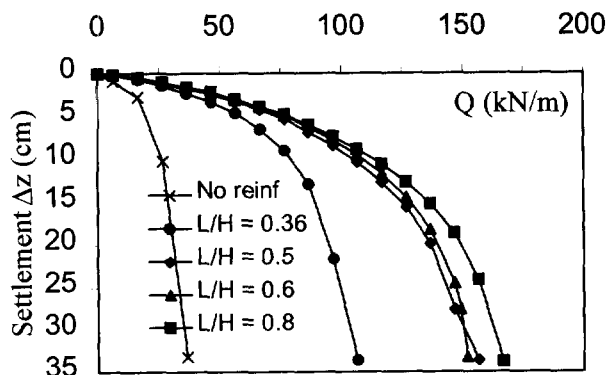


Figure 6. Effect of reinforcement length on the slab settlement under surcharge.

4.2 Effect of wall facing stiffness

The rigidity of the wall facing depends of the construction mode. The effect of facing stiffness on the performance of

geosynthetic-reinforced soil retaining wall is not fully understood and is usually ignored in the design. An analysis is performed considering a retaining wall reinforced by $N_p=8$ sheets of geotextile. The sheets are equally spaced, $\Delta H=0.58$ m and are 2.6 m long ($L / H = 0.5$). Different facing stiffness were examined ($E = 5, 10$ and 20 MPa). A wrapped facing was also analysed ($E = 0$ MPa). The slab settlement versus surcharge and the lateral deflections of the facing induced by a top load of $Q=60$ kN/m for all the cases considered are illustrated respectively on Figures 7 and 8.

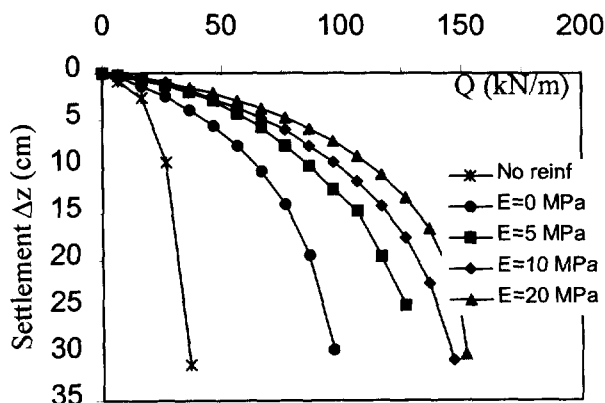


Figure 7. Effect of facing stiffness (E) on the slab load settlement.

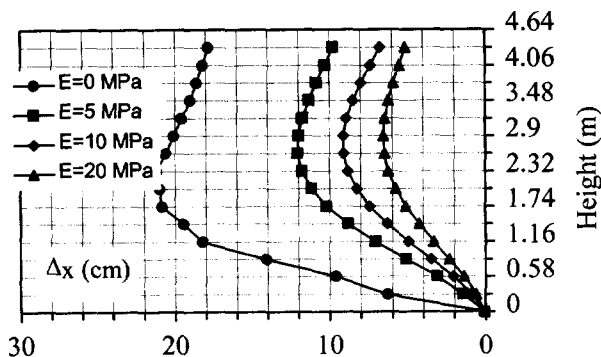


Figure 8. Effect of facing stiffness (E) on the wall facing horizontal deflection Δx .

In the absence of a facing or with a facing of low stiffness, the wall deformed greatly, particularly at high top load.

4.3 Effect of the position of top load

To examine the effects of the position of the top load, different distance of slab position from wall face were considered ($d = 1, 1.5$ and 2.5 m). The height of the wall, the number of reinforcement layers and their length were the same as previously i.e. ($H = 4.35$ m, $N_p = 8$, $L/H = 0.5$). The slab settlement curves versus top load are illustrated in Figure 9 for the three cases. When the rear of the geotextile is not horizontally beyond the upstream

corner of the slab, the failure occurs roughly as in the case corresponding to $d = 2.5$ m. The mean shear strain field ($\epsilon_1 - \epsilon_3$) for the cases $d = 1.5$ m and $d = 2.5$ m are shown in Figures 10 and 11. We notice from these patterns that when the reinforcement length does not include horizontally the slab width a shear band develops from downstream side of the slab to the bottom of the facing.

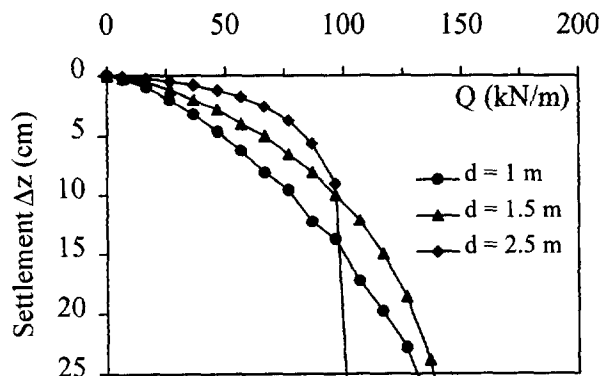


Figure 9. Effect of the point application of the top load on the slab settlement.

5 CONCLUSION

A finite element method has been used to model two experimental walls reinforced by extensible reinforcement. Despite the assumption done, the predicted results are quite satisfactory until large deformations. However some physical phenomenon observed are not predicted like the experimental "breakpoint" of the diagram surcharge-settlement. To simulate this phenomenon, it would be necessary to take into account the compaction effect and the construction stages. However lack of experimental data on the compaction mode and effect makes such approach very difficult.

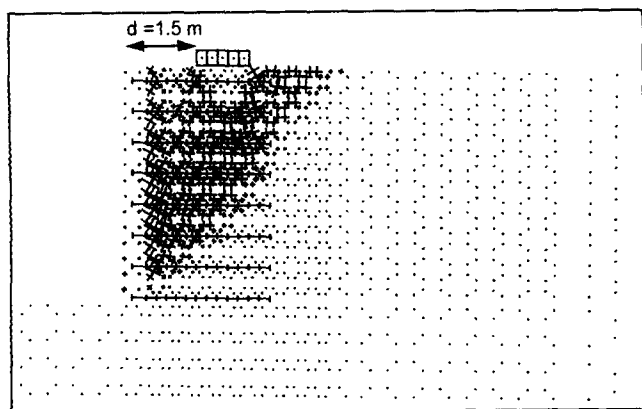


Figure 10. shear strain field ($\epsilon_1 - \epsilon_3$) induced by a top load $Q=90$ kN/m (scale : 1.5).

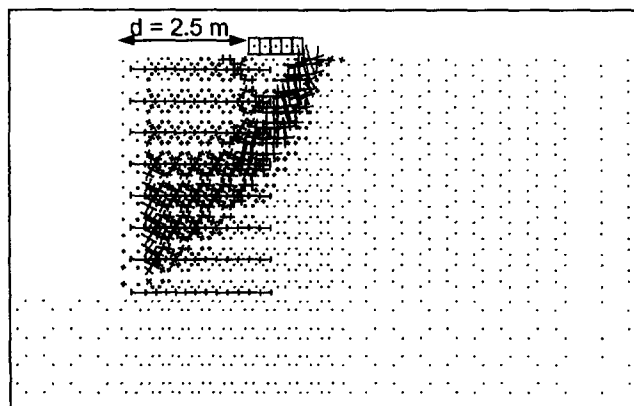


Figure 11. shear strain field ($\epsilon_1 - \epsilon_3$) induced by a top load $Q=90$ kN/m (scale : 1.5)

In addition, numerical simulations have been performed to investigate the effects of some parameters on the behaviour of reinforced soil wall loaded on the top. The parameters considered included the reinforcement length, the facing stiffness and the point of application of the top load. All of these parameters influence the behaviour of the structure. But the most important geometric parameter is the ratio of the reinforcement length to wall height. For a ratio equal or greater than 0.5 there is no significant increasing on the bearing capacity. It is also found that the reinforcement length has to be extended beyond the potential failure surface developing from the upstream side of the slab to cover the width of the slab load.

REFERENCES

- Arab R., Villard P, Gourc J.P (1996). Mechanism of Reinforcement from two field trials. *International Symposium on Earth Reinforcement Practice, Kyushu, Japan*, pp. 303 - 308.
- Arab R. (1997). Modélisation des massifs renforcés sollicités localement en tête. Doctorat thesis, University Joseph Fourier of Grenoble.
- Gourc J.P., Gotteland P.H., Haza E., Perrier H., Baraize E. (1995) Geotextile reinforced structures as bridge abutments : full scale experimentation, *Geosynthetics 95, Nashville, USA*, pp. 79-93.
- Ling H.I., Tatsuoka F. (1995). Simulating Performance of GRS-RW by Finite Element Procedure. *Journal of Geotechnical Engineering*. vol.121, n°4, pp. 330-340.
- Helwany M.B., Tatsuoka F., Tateyama M., Kojima K. (1996). Effects of facing rigidity on the performance of geosynthetic-reinforced soil retaining walls. *Soils and Foundation. Japanese geotechnical Society*. vol. 36, n°1, pp. 27- 38.

Evaluation of Foundation Support for Geosynthetic Reinforced Soil Wall on Sloping Ground

J. Otani

Associate Professor, Department of Civil & Environmental Engineering, Kumamoto University, Kumamoto, Japan

T. Hirai

Manager, Mitsui Petrochemical Industrial Products, Tokyo, Japan

H. Ochiai

Professor, Department of Civil Engineering, Kyushu University, Fukuoka, Japan

S. Shinowaki

Graduate Student, Department of Civil & Environmental Engineering, Kumamoto University, Kumamoto, Japan

ABSTRACT: The purpose of the paper is to evaluate the effects of deformation of geosynthetic reinforced soil wall backfill on the bearing resistance of the foundation ground using the results of finite element analysis. Here, the reinforced soil wall constructed on relatively soft sloping ground, which is a real construction site in Japan, is taken into consideration and a series of parametric study is conducted, in which the effects of the condition of foundation ground and a backcut angle behind the reinforced backfill are discussed, and also the effectiveness of soil improvement at the toe of the wall is also evaluated. The conclusions drawn from this study are: (1) the effect of the backcut angle behind the reinforced backfill on the bearing resistance of foundation ground is less, so that this effect does not have to be considered on the design calculation of bearing capacity; and (2) when the foundation ground is relatively soft, the deformation property of the reinforced backfill deeply affects to the reaction at the base of the reinforced backfill. The soil improvement technique at the base of the reinforced backfill is one of the effective methods.

KEYWORDS: Bearing Capacity, Finite Element Analysis, Reinforcement, Retaining Walls, Steep Slope

1 INTRODUCTION

Applications of geosynthetics to the embankment or retaining wall have been most popular techniques among all the earth reinforcement practices around the world. This is because the behavior and failure mechanism of these reinforcing structures have been successfully evaluated under the contributions by many researchers. The results of these researches have been presented in recent international conferences and symposia (e.g. Proceedings edited by Yamanouchi et al., 1988, Ochiai et al., 1992, and Ochiai et al., 1996). But recently, such as in Japan, these applications have been applied to more severe conditions such as relatively soft sloping ground or various backcut angles behind the backfill. And those conditions have to be considered on the stability calculation in order to design these structures safely.

In the current design method, the stress distribution at the base of the retaining soil wall has been assumed by the moment equilibrium with assumption of Coulomb earth pressure theory. However, this distribution is affected by the deformation and strength properties of the reinforced backfill and it also depends on the property of foundation ground. These properties have not been considered in the current design method so far and besides, in-situ conditions at the construction site, e.g. the backcut angle, is variously changed.

The purpose of the paper is to evaluate the effects of deformation of geosynthetic reinforced soil wall backfill on the bearing resistance of the foundation ground using the results of finite element analysis. Here, the reinforced soil

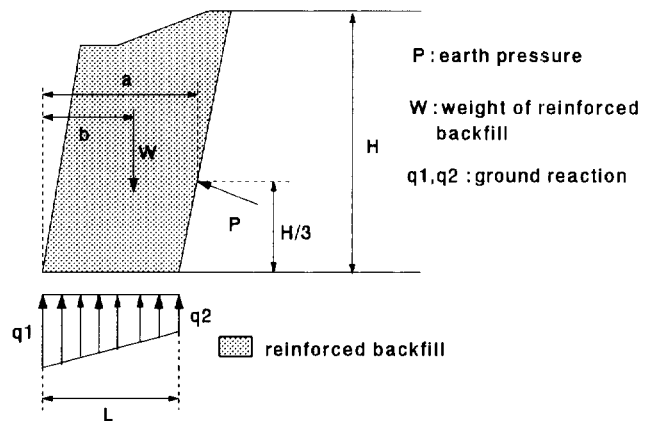


Figure 1. Forces on the reinforced backfill in the design.

wall constructed on relatively soft sloping ground, which is a real construction site in Japan, is taken into consideration and a series of parametric study is conducted, in which the effects of the condition of foundation ground and a backcut angle behind the reinforced backfill are discussed. And also the effectiveness of soil improvement at the toe of the wall is also evaluated.

2 CALCULATION OF BEARING RESISTANCE ON CURRENT DESIGN METHOD

Current design calculation of the stability concerning bearing capacity of foundation ground at the base of the reinforced backfill is summarized based on the design

manual by Public Works Research Center(PWRC) in Japan. This design calculation is based on the equilibrium of all the loads subjected to the reinforced backfill as shown in Fig.1. As shown in this figure, the ground reaction at the base of the reinforced backfill is always set to be trapezoidal shape and this is based on the assumption that the ground under the backfill is always rigid and the effect of ground settlement is not evaluated in the design method. As described above, the application of these structures is extended to the relatively soft foundation ground nowadays. When the foundation ground is relatively soft or the backcut angle behind the reinforced backfill is changed, this trapezoidal assumption may not be true and has to be examined. This is a key issue here in this paper and is discussed based on the results of finite element analysis.

3 FINITE ELEMENT ANALYSIS

3.1 Problem to be solved

The finite element analysis is conducted for the real construction site in Japan and this is shown in Fig.2(a). The geosynthetic reinforced soil wall was constructed on the sloping foundation with its slope angle of 25° . The ground conditions are also shown in the figure and these are summarized as follows:

- For natural ground:
 - a) Ground I: clay with gravel (SPT N-value = 2 - 5);
 - b) Ground II: weathered dacite (SPT N-value = 12 - 50);
 - c) Ground III: dacite (SPT N-value is more than 50).
- For artificial ground:
 - d) Reinforced ground: compacted Ground I;
 - e) Improved ground: improved by cement.

It is noted that the Ground I is a sloping soft ground and the application of soil improvement technique at the toe of the wall was taken into consideration. The geogrid type of reinforcing material was used at the site. As shown in Fig.2(a), there are 11 layers of geogrid and three different types were used (Tensar SR55, SR80 and SR110), in which SR110 was used for the first four layers from the bottom, SR80 for fifth to seventh layers and SR55 for top four layers.

3.2 Method of analysis

In order to evaluate not only 1) the effect of backcut angle behind the reinforced backfill but also 2) that of soil improvement in the ground, a series of finite element analysis is conducted. The method used here is elasto-plastic finite element method using Drucker-Prager failure criterion with non-associated flow rule(Otani et al.,1992). The geogrid type of geosynthetics is modeled by beam element in the analysis with perfectly elasto-plastic assumption. The material properties were determined from material tests in laboratory. The interaction between soil and geogrid is ignored. The soil testings for both in-situ and laboratory have been conducted for the soils at this

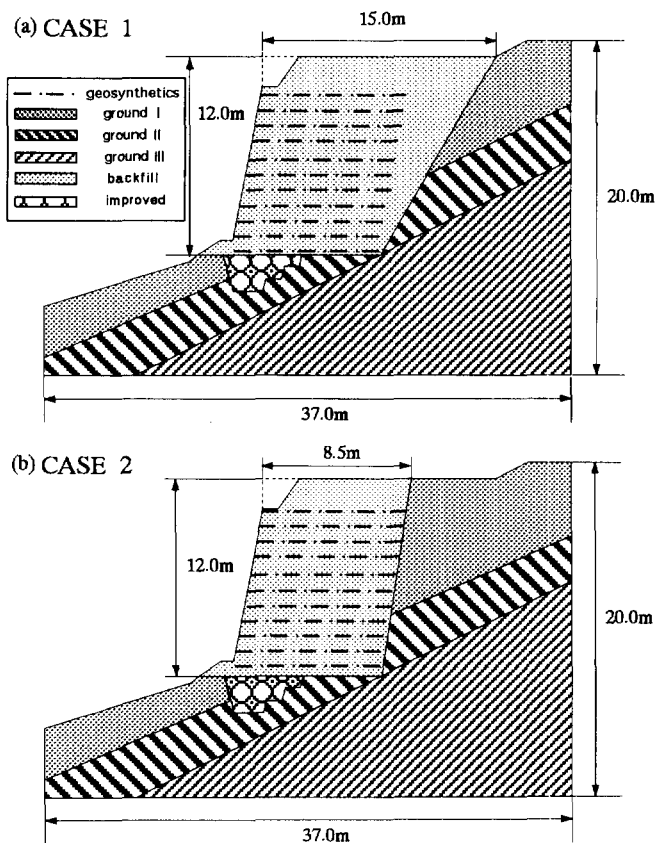


Figure 2. Problems to be analyzed.

construction site, so that the material property of the ground was determined from these testings and is shown in Table 1. In the analysis, the case shown in Fig.2(b) is also analyzed in order to evaluate the effect of backcut angle. The analysis is conducted with loading condition of step-by-step construction of the backfill. It is also noted that the joint element is used between natural slope and the backfill in order to express the discontinuity phenomenon, in which this interaction is modeled as a friction property with setting the shear stiffness of the soil itself in the joint element. The total cases of the analysis are listed as follows:

- CASE 1: ground condition of natural sloping ground as shown in Fig.2(a)
- CASE 1-1: for rigid foundation ground;
 - CASE 1-2: without improvement; and
 - CASE 1-3: with improvement,

- CASE 2: ground condition of natural sloping ground as shown in Fig.2(b)
- CASE 2-1: for rigid foundation ground;
 - CASE 2-2: without improvement; and
 - CASE 2-3: with improvement.

It is noted that the case of rigid foundation is also analyzed for the comparative study and this is conducted by assuming all the natural ground to be Ground III without improvement technique.

Table 1. List of material property of the ground.

	Young's modulus	poisson's ratio	cohesion	friction angle	unit weight
	$E(\text{kN/m}^2)$	ν	$c(\text{kN/m}^2)$	$\phi(^{\circ})$	$\gamma(\text{kN/m}^3)$
ground I	$4.90 \cdot 10^3$	0.30	18.63	29	$1.67 \cdot 10^2$
ground II	$2.94 \cdot 10^4$	0.25	0.00	32	$1.77 \cdot 10^2$
ground III	$2.94 \cdot 10^5$	0.20	0.00	41	$2.62 \cdot 10^2$
backfill	$1.47 \cdot 10^4$	0.40	10.79	23	$1.63 \cdot 10^2$
improved	$5.88 \cdot 10^4$	0.35	95.12	31	$1.73 \cdot 10^2$

4 RESULTS AND DISCUSSION

Figure 3 shows the results of deformation for all the cases, in which CASE 1-1 is shown in Fig.3(a); Fig.3(b) for CASE 1-2; Fig.3(c) for CASE 1-3; Fig.3(d) for CASE 2-1; Fig.3(e) for CASE 2-2; and Fig.3(f) for CASE 2-3. Comparing the results between CASE 1-1 and CASE 1-2 or CASE 2-1 and CASE 2-2, the deformation around the base of the reinforced backfill for the case of rigid foundation is much less than that for the case of without improvement. The lateral deformation is also remarkable for the case of without improvement. But this is improved by the application of soil improvement technique as shown in Fig.3(c) and Fig.3(f). Figure 4 shows the results of both distributions of settlement and vertical pressure beneath the reinforced retaining backfill. Looking at the shape of stress distribution at the base of the

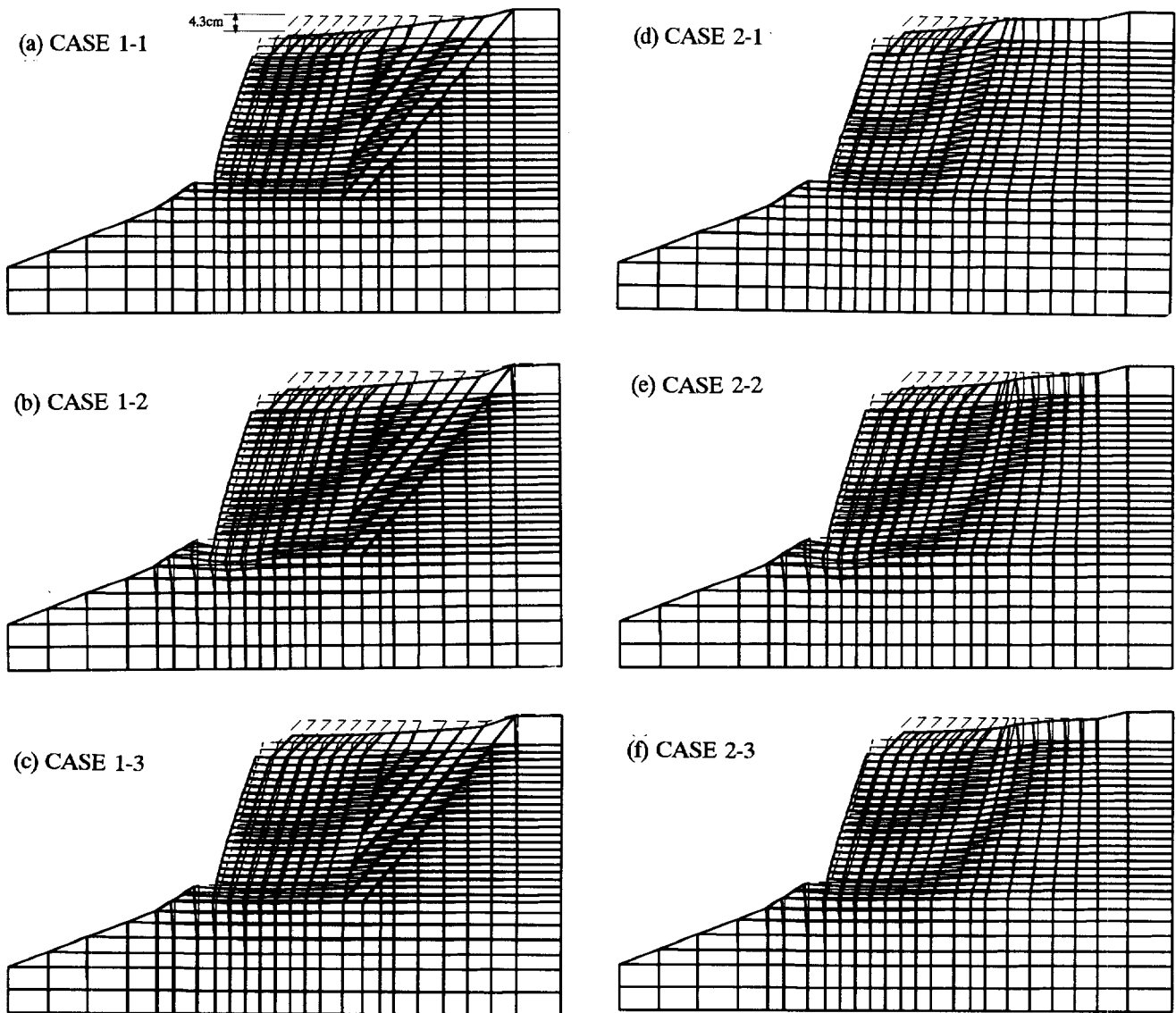
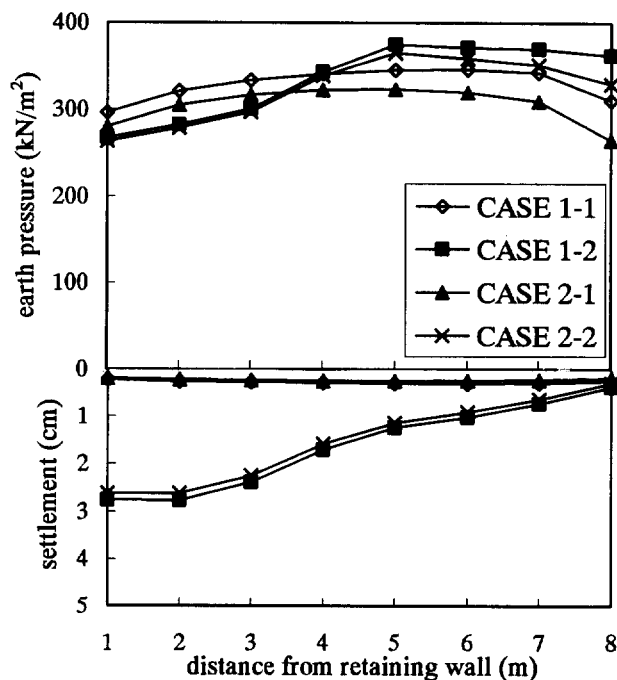


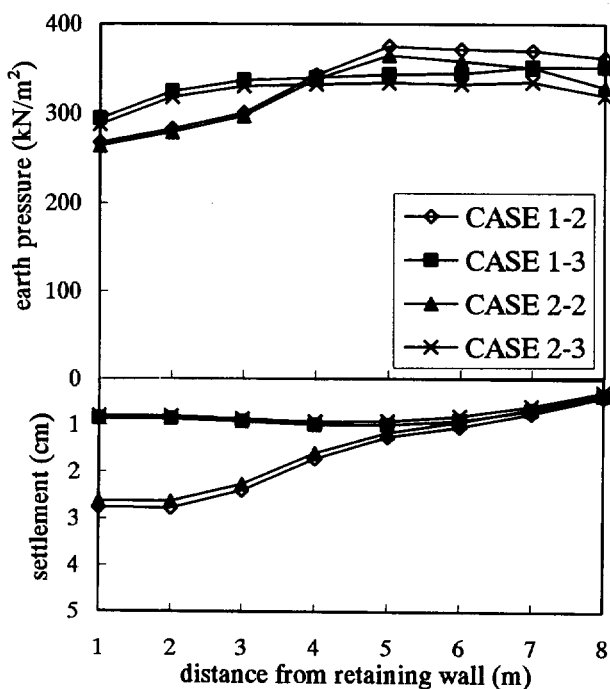
Figure 3. Deformation Property from analysis results.

backfill, it is not always the trapezoidal shape. So that it affects the calculation of overall stability for the reinforced soil wall and this depends on the deformation property of the reinforced backfill. It is also pointed out that not only

the force equilibrium on the reinforced backfill but also the local deformation around the toe of the wall have to be checked for its overall stability. For comparing the effect of slope angle of natural ground behind the reinforced backfill, it is obviously realized that it is not much difference between two cases (CASE 1 and CASE 2).



(a) Effect of rigidity of foundation ground



(b) Effect of soil improvement technique

Figure 4. Distributions of earth pressure and settlement at the base of reinforced backfill.

5 CONCLUSIONS

Recently, the earth reinforcement practice has been applied to the cases with more severe conditions such as on relatively soft sloping ground or various backcut angle behind the backfill. These conditions on the bearing capacity of foundation ground were evaluated.

The conclusions drawn from this study are listed as follows:

- (1) The effect of the angle of natural slope behind the reinforced backfill on the bearing resistance of foundation ground is less, so that this effect does not have to be considered on the design calculation of bearing capacity.
- (2) When the foundation ground is relatively soft, the deformation property of the reinforced backfill deeply affects to the reaction at the base of the reinforced backfill. Therefore, this should be considered in the design calculation.
- (3) For overall stability of the reinforced wall on relatively soft sloping ground, not only the force equilibrium on the reinforced backfill but also the local deformation around the toe of the wall should be checked.
- (4) The improvement technique around the toe of retaining wall makes the settlement less and earth pressure equivalent at the base of the reinforced backfill.

The field measurements such as earth pressure and deformation of the reinforced backfill at this site are still on the way at this moment. When the results of this paper is compared with this in-situ measurement, it is promised that the analysis results are quantitatively evaluated.

REFERENCES

- Ochiai,H.,Hayashi,S. and Otani,J.(1992) "Earth Reinforcement Practice", Balkema, Rotterdam, Netherlands.
- Ochiai,H., Yasufuku,N. and Oomine, T.(1996) "Earth Reinforcement", Balkema, Rotterdam, Netherlands.
- Public Works Research Center (PWRC) (1994) "Design and construction manuals of geotextile-reinforced structures", (in Japanese).
- Otani,J., Ochai,H. and Hayashi,S.(1992) "Restraining effect of geogrid reinforced soil in finite element analysis", IS Kyushu '92, JGS, Fukuoka, Japan, Vol.1, pp.147-150.
- Yamanouchi,T., Miura,N. and Ochiai,H.(1988) "Theory and Practice of Earth Reinforcement", Balkema, Rotterdam, Netherlands.

PARAMETRIC STUDY FOR GEOSYNTHETIC REINFORCED WALLS UNDER SUSTAINED EARTHQUAKES

A. Carotti

Professor, Dept. of Structural Eng., Politecnico di Milano, Milan (Italy)

P. Rimoldi

Director, Tenax SpA, Geosynthetics Division, Viganò (Italy)

Abstract

The Authors propose a newtonian model for the dynamics of geogrid reinforced soil retaining walls, based on a scheme with lumped masses having elastic, viscous and coulombian interactions. The model allows to evaluate the local amplifications by integrating the elasticity and inherent damping with the contribution of the geogrid layers. The aim of the present paper is the drawing, for the different cases analyzed, of design charts which will allow engineers to evaluate the number and characteristics of the geosynthetic reinforcing layers required to satisfy given safety requirements, as a function of the characteristic parameters of the earthquake. A trial-and-error procedure for the seismic analysis of geogrid reinforced walls is outlined.

Keywords: Geogrids, Dynamic Mechanical Analysis, Retaining Walls, Seismic Design, Seismic Loads.

1. INTRODUCTION

A non-linear multidof newtonian model for the seismic dynamics of slopes and walls on horizontally accelerated bedrock (Carotti and Rimoldi, 1997), is taken as the basic mathematical and computational support for a pseudo-static design procedure for geosynthetic reinforced walls.

From the multidof model, a series of 2-D response spectra and design charts have been obtained; from such plots the following kinematic and mechanical information can be deduced:

- maximum values of the seismic response at the top of the wall;
- spectral values of the active coefficient of earth pressure K_{aE} under seismic condition.

Based on these charts, a trials-and-errors procedure for checking the seismic feasibility of statically designed reinforcements is presented for various peak accelerations at bedrock and various frequency contents of the accelerogram.

A first major group of parameters are discussed in the present paper; successive developments, which are under way, will take into consideration other characteristics, including the interlayer stiffness and viscous damping.

2. NON-LINEAR NEWTONIAN MODEL WITH GEOGRIDS

From laboratory tests (Montanelli and Moraci, 1997), we assume the following mechanical actions between the geogrids and the soil layers on top and bottom, as a consequence of the soil-geogrid interlocking:

1. an increase of the interlayer soil stiffness, proportional to the elastic stiffness of the geogrids. From monotonic tensile tests on geogrids (Fig. 1) the load-strain curve has been reduced to a tri-linear curve and the stiffness value in each linear segment have been identified. We have focused the attention on the 1st stage, with strain threshold $\epsilon_1 = 0.03$. If L_g is the geogrid length in the direction of the seismic acceleration, F is the tensile force applied to the geogrid and Δl its elongation, we postulate that, in condition of interlocking between the geogrids and the soil layers, the contributed inter-layer stiffness is:

$$K_{gi} = \frac{F}{\Delta l} = \frac{F}{\epsilon_1 \cdot L_g} \quad (1)$$

2. An increase of the interlayer viscous damping force, equal to the inherent viscous damping of the geogrid. From sinusoidal cyclic tests (Montanelli and Moraci, 1997) with frequency $f = 1.0$ Hz (see Fig. 2) and from the examination of an average elliptical cycle, the average viscous force F_{vinc} (force in counterphase

to the velocity, when the displacement is nil) has been obtained, together with the value of the peak velocity (product of the peak displacement, obtained from the test plot, and of the circular frequency $\omega = 2\pi f$ of the test). From the ratio force/velocity the damping coefficient is immediately obtained. In details :

$$C_{gi} = \frac{F_{visc}}{\Delta l \cdot \omega} = \frac{F_{visc}}{\varepsilon \cdot L_g \cdot \omega} \quad (2)$$

where Δl is the differential interlayer displacement ($x_i - x_{i-1}$), when perfect interlocking between soil and geogrid has been assumed.

- An increase of the interlayer damping due to the friction between the geogrid and the soil layers, under the weight of the soil. The frictional damping due to the i-th geogrid (where N is the number of geogrid layers) is:

$$F_{Ci} = -tg \phi_{sg} \cdot g \cdot \sum_{k=i}^n M_k \cdot sign(\dot{x}_k) \quad (3)$$

where the signum function $sign(\dot{x}_k)$ introduces the non linearity in the model. The direction of the frictional force is determined by the sign of \dot{x}_k . In Eq. (3) ϕ_{sg} is the soil-geogrid interface friction angle; g is the gravity acceleration.

The Newtonian equations of motion for the N-DOF non-linear model with geogrids (N soil layers with N geogrid layers) can be obtained taking into account the elastic stiffness K_{gi} , the viscous damping C_{gi} and the Coulomb-type friction force F_{Ci} induced by the geogrids, defined in Eq.s (1)÷(3).

Indicating with \hat{M} the distributed load on top of the wall, the Newtonian equation of motion for the i-th layer is:

$$M_i \cdot \ddot{x}_i = -K_i(x_{i-1} - x_i) - C_i(\dot{x}_{i-1} - \dot{x}_i) + K_{i+1}(x_i - x_{i+1}) + C_{i+1}(\dot{x}_i - \dot{x}_{i+1}) - K_i(x_{i+1} - x_i) - C_i(\dot{x}_{i+1} - \dot{x}_i) + K_{i+1}(x_i - x_{i+1}) + C_{i+1}(\dot{x}_i - \dot{x}_{i+1}) + tg \phi_{sg} \cdot g \cdot \left(\sum_{k=i}^n M_k + \hat{M} \right) sign \dot{x}_i - tg \phi_{sg} \cdot g \cdot \left(\sum_{k=i+1}^n M_k + \hat{M} \right) \cdot sign \dot{x}_{i+1} = -M_i \cdot \ddot{x}_i \quad (4)$$

where $g \cdot \left(\sum_{k=1}^n M_k + \hat{M} \right)$ represents the total gravity load acting on the i-th geogrid layer.

3. CONTROL OF DYNAMIC EQUILIBRIUM FOR GEOGRID REINFORCED WALLS

The steady dynamic equilibrium for a 1-DOF (one Degree Of Freedom) linear oscillator under sinusoidal resonant excitation is described in Fig. 3, where the inertia force is balanced - at maximum displacement

- by the elastic recalls.

In this non-linear model (see Carotti and Rimoldi, 1997), the contribution of the friction force to the equilibrium (at maximum displacement) of the i-th reinforced layer of the wall must be taken into consideration.

In the present research, a geogrid reinforced earth wall is assumed, with a cohesionless backfill and possible permanent surcharge loads on the top surface; the vertical spacing S_v of the geogrids and the overall length L are taken as constant.

Here the following hypotheses are introduced:

- the static earth pressure P_{st} is balanced even in seismic conditions by the friction F_{C_i} and by the tensile strength Tg_i of the geogrids;
- in seismic conditions, the forces F_{C_i} furtherly provide an increase of damping, the forces Tg_i provide an increase in terms of damping and stiffness;
- the dynamic earth pressure Pa_d can be obtained through the superposition of effects of the static earth pressure Pa_s and the seismic earth pressure Pa_{ge} (suffix "G" for geogrids and "E" for earthquake):

$$Pa_d = Pa_s + Pa_{GE} \quad (5)$$

- The earth pressures can be described with the Rankine type equations:

$$Pa_d = \frac{1}{2} Ka_d \gamma H^2 \quad (6)$$

$$Pa_s = \frac{1}{2} Ka_s \gamma H^2 \quad (7)$$

$$Pa_{GE} = \frac{1}{2} Ka_{GE} \gamma H^2 \quad (8)$$

Therefore :

$$Pa_d = \frac{1}{2} (Ka_s + Ka_{GE}) \gamma H^2 \quad (9)$$

and :

$$Kad = Ka_s + Ka_{GE} \quad (10)$$

- due to the previous hypothesis, the dynamic forces can be studied independently from the static ones; therefore now on only the equilibrium of the dynamic forces will be considered.

The conditions of dynamic equilibrium and the mechanical interaction between the two adjacent layer, (i-1)-th and i-th, are described in Fig. 3, which gives an imagine at maximum displacement (zero velocity) of the wall. Being in conditions of zero velocity, at this point of time the viscous damping force Fv is zero.

As said above, only the dynamic forces are

considered here, without the static earth pressure P_{a_i} .
 Let F_{IN_i} ; $F_{e_{(i-1)}}$; F_{e_i} represent, respectively, the overall inertia force and the elastic recalls above and under the i -th layer; and let $F_{c_{(i-1)}}$; F_{c_i} ; P_{agE_i} represent the upper and lower Coulomb friction force, and the active earth pressure due to the i -th layer.

With the assumption that the 1st modal shape is dominating (Carotti and Rimoldi, 1997), then all the displacements of the single layers are in phase. Hence we can assume that there is a balance between the elastic recall forces of the soil itself: therefore F_{e_i} is almost equal to $F_{e_{(i-1)}}$ and computationally they can be neglected.

Under these hypotheses, in condition of dynamic equilibrium we have (see Fig. 3):

$$P_{axE_i} = F_{IN_i} + T_{g_i} \quad (11)$$

$$F_{IN_i} = -M_i \cdot \ddot{x}_{v_i}$$

where T_{g_i} is the tensile strength in the geogrid under the i -th soil layer (see Fig. 3):

$$T_{g_i} = F_{c_i} \quad (12)$$

When the expression of Eq. 8 is introduced, a pseudo-static expression for the coefficient of active earth pressure K_{agE} under seismic excitation can be obtained:

$$K_{agE} = \frac{2 \cdot P_{agE}}{\gamma \cdot H^2} \quad (13)$$

4. PRELIMINARY PARAMETRIC DISCUSSION

The following design parameters has been taken into consideration for discussing the effects of geosynthetic reinforcement on the seismic response of the wall.

a) Soil:

$$\gamma = 18 \text{ kN/m}^3 ; \phi = 25^\circ - 40^\circ ; c = 0$$

$$\text{shear modulus } G = 10^4 \text{ kN/m}^2 ;$$

$$H = 3 \text{ m} - 6 \text{ m} - 9 \text{ m}.$$

The first three natural frequencies and damping ratios for the 3 m and 6 m high walls, without reinforcements, are given in Table 1.

Tab. 1 - Natural frequency f and damping ratio ξ for some of the walls considered in the parametric study.

	H = 3 m.		H = 6 m.	
	f (Hz)	ξ (%)	f (Hz)	ξ (%)
1st mode	5.63	4.9	2.95	1.3
2nd mode	14.43	14.3	8.8	3.8
3rd mode	25.89	22.6	14.45	6.3

b) Geogrids:

We have considered the geometrical and mechanical characteristics of the TENAX TT401 Samp mono-oriented geogrid, which have the following properties:

$$\text{Unit weight: } w = 0.77 \text{ Kg/m}^2$$

$$\text{Polymer density: } \rho = 0.950$$

$$\text{Tensile strength: } T = 80 \text{ kN/m}$$

$$\text{Elongation at peak: } \varepsilon_{\text{peak}} = 13\%$$

$$\text{Strength at 2\% strain: } T_{2\%} = 26 \text{ kN/m}$$

$$\text{" " 5\% " : } T_{5\%} = 48 \text{ kN/m}$$

Taking into consideration the cross sectional area of the longitudinal stretched rib of the geogrids: $A_r = 1.6 \text{ mm} \times 6.5 \text{ mm} = 10.4 \text{ mm}^2$, and a number of 50 ribs/m, the resistant section is: $Ar = 5.2 \times 10^{-4} \text{ m}^2/\text{m}$:

And therefore,

$$\sigma_{\text{peak}} = T/Ar = 154 \text{ MPa}$$

$$E_{\text{peak}} = \sigma_{\text{peak}}/\varepsilon_{\text{peak}} = 1185 \text{ MPa}$$

$$\sigma_{2\%} = T_{2\%}/Ar = 50 \text{ MPa}$$

$$E_{2\%} = \sigma_{2\%}/0.02 = 2500 \text{ MPa}$$

Other data used in the model are:

- soil-geogrid interface friction angle:

$$\phi_{\text{sg}} = \arctan(\tan \phi / f_{\text{ds}})$$

where the direct shear factor f_{ds} has been assumed equal to 0.80;

- constant vertical spacing: $S_v = 0.6 \text{ m}$;

- geogrid length: $L = 0.5 H - 1.0 H$

where H is the wall height.

c) bedrock excitation:

the following classes of acceleration time histories have been implemented:

c1) a stationary gaussian zero-means white noise, low-pass filtered with fixed bandwidth (0,5 Hz) and variable peak acceleration, varying between 0.1 g to 1.1 g.

c2) as above but with parametrically fixed peak acceleration $a_g = 5 \text{ ms}^{-2}$ and variable bandwidth: all the bandwidths considered have the same left cut-off frequency (zero Hz) and different right cut-

off frequencies, ranging from 1 Hz to 10. By this way the effects of many historic earthquakes can be modelled and simulated: from very low frequency “near-fault” earthquakes, to earthquakes with increasingly wider bandwidths as the San Salvador (1986), Mexico City (1985) and El Centro (1940) records.

Using these types of bedrock excitation it is possible to obtain the following spectra:

1. spectra under excitation c1: spectra of top relative displacement and top absolute acceleration of active earth pressure coefficient K_{agE} and the overall active earth pressure P_{agE} for two different geogrid lengths, are given in Figg. 4, 5, 6. Such spectra are obtained by plotting the maximum value of the response quantity (extracted from the time history) vs the peak acceleration of the bedrock.

The family of parabolic curves are monotonically increasing with the base peak acceleration. Both K_{agE} and P_{agE} decrease with increasing geogrid length L .

2. spectra under excitation c2: spectra as above vs variable bandwidth of the bedrock acceleration, are given as well in Fig. 4, 5, 6, respectively for the 3 m, 6m, 9m high walls. The amplification effect when the seismic bandwidth includes the natural frequencies of the wall (see Tab. 1) is evident: spectra show the possibility of controlling such amplifications by means of geogrid reinforcements of variable lengths.

Note 1: the 1st mode of vibration is dominating in reinforced soil structures. Hence resonance occurs around the frequency of the 1st mode (compare Figg. 4, 5 with Tab.1).

Note 2: For soil without geogrids, in order to stress the influence of geogrids, the model has taken into account only the viscous damping and not the Coulombian one (which has been accounted for in the model with geogrids). As a consequence the model for soil alone is not sensitive to the parameter ϕ (in favour of safety); hence in the charts all the curves without geogrids are the same. This limitation will be eliminated in the future developments of the model.

5. DESIGN CHARTS FOR GEOGRID REINFORCED WALLS IN SEISMIC CONDITIONS

The analysis has been extended to the ranges of practical interest of the main soil and geogrid parameters. Design charts are given in Figures 4, 5 and 6. The following procedure can be used for the seismic analysis of geogrid reinforced walls:

STEP 1: design the reinforced block in static conditions. Adopting, as example, the “tie-back wedge” method, the following three parameters shall be determined :

- minimum length of geogrids L_{min} ,
- vertical spacing S_v ,
- overall number of geogrids: n_{grid} .

STEP 2: the seismic input is established. At first, a standard 0 - 5 Hz bandwidth and variable peak acceleration are assumed (characteristic statistical parameters of the time record, including RMS, crest-factor and variance, can be imposed),

STEP 3: the design charts in Figg. 4 - 6 are then entered and the seismic active pressure coefficient K_{agE} is obtained.

STEP 4: the dynamic earth pressure coefficient K_{ad} is determined with Eq. 10; then the stability analysis of Step 1 is re-calculated with reference to K_{ad} and allowing for a reduction of the safety factor FS according to each National Code (usually a 20% reduction of FS is envisaged in the seismic Codes for earthworks, e.g.: a reduction from 1.3 to 1.06 of the $FS_{\text{inversion}}$; a FS_{pullout} reduction from 1.5 to 1.2 etc.)

STEP 5: if any of the before mentioned checks at Step 4 are not satisfied, then by a trials-and-errors procedure the following corrections may be introduced:

- increase the number of geogrids and/or the geogrids length L ,
- with these new values, the design procedure starting from Step 3 is repeated,
- as long as all the checkouts are satisfied.

STEP 6: the sequence from Step 2 to Step 5 can be repeated for a different choice of the seismic input.

If the effects of variable bandwidths and fixed peak-acceleration must be investigated, spectra at the bottom in Figures 4 -6 will be considered.

REFERENCES

- Carotti A., Rimoldi P., (1997) “Time and Frequency Domain Analysis for the Seismic Design of Geogrid-Reinforced Soil Slopes and Walls”, Proceedings of Geosynthetics '97 Conf., Long Beach, Ca (USA).
- Montanelli F., Moraci N. (1997) “Behaviour of Geogrids under cyclic loads”, Proc. Geosynthetics '97 Conf., Long Beach, California, USA.

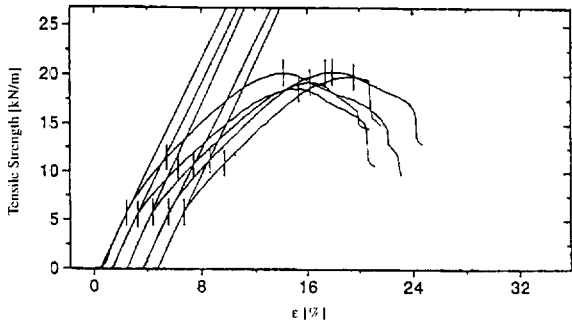


Figure 1: Scheme of the mechanical interaction between soil layers and geogrids in conditions of dynamic equilibrium at maximum displacement (from Carotti and Rimoldi, 1997).

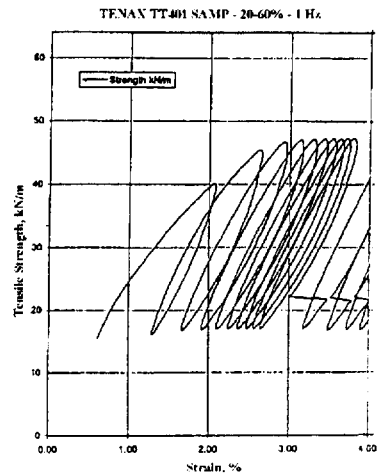
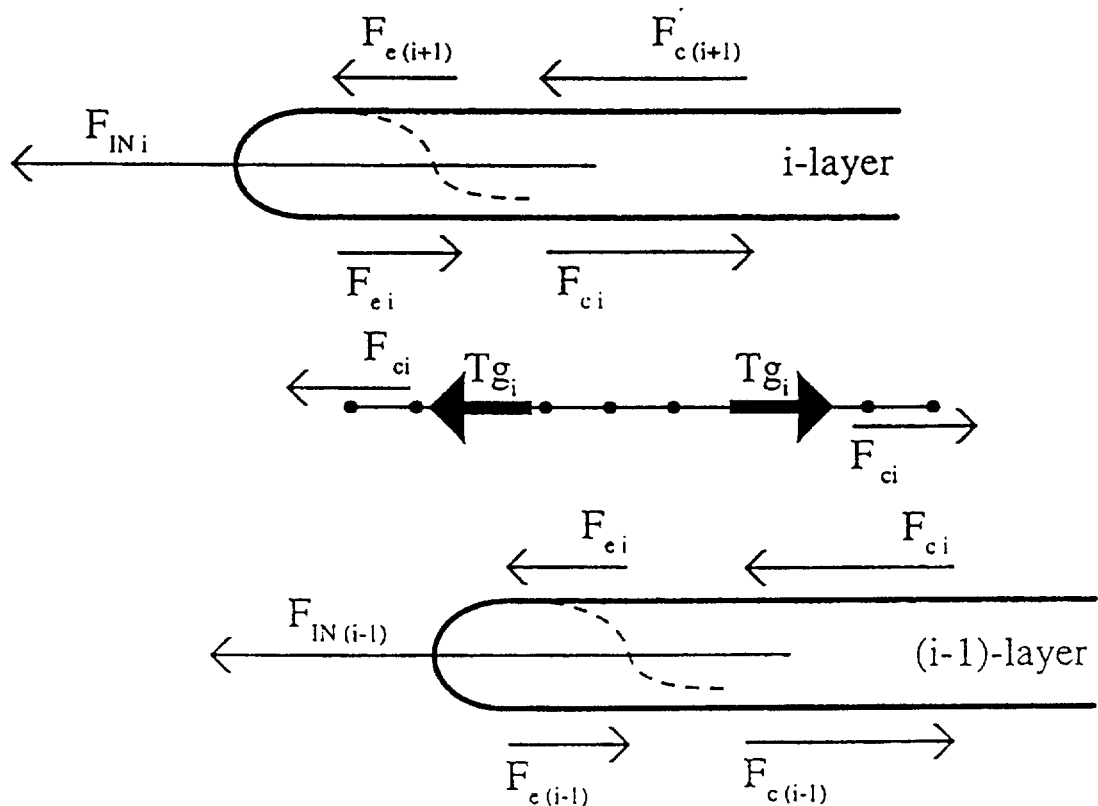


Figure 2: A cyclic tensile test for a typical HDPE geogrid (from Carotti and Rimoldi, 1997).



Force field at maximum displacement:
 F_e = Interlayer elastic recall force field
 F_c = Interlayer coulombian friction force field
 F_{IN} = Inertial force field

Figure 3: Scheme of the mechanical interaction between soil layers and geogrids in conditions of dynamic equilibrium at maximum displacement.

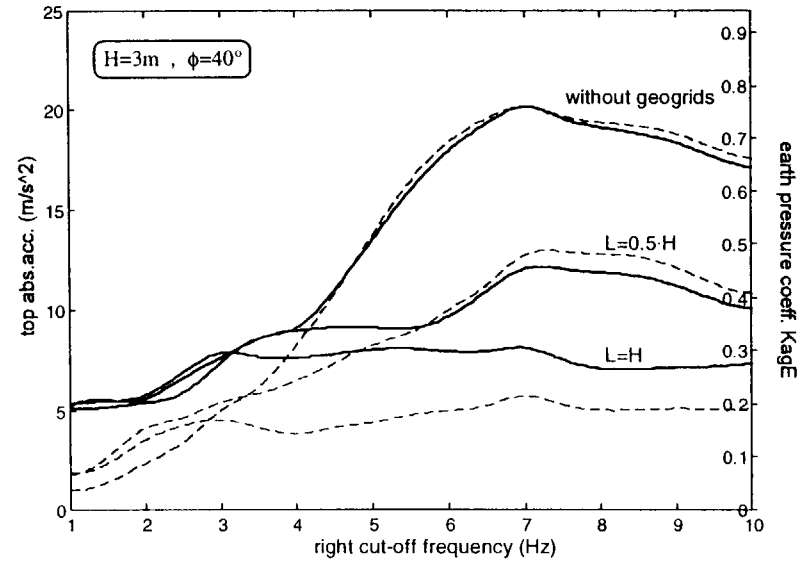
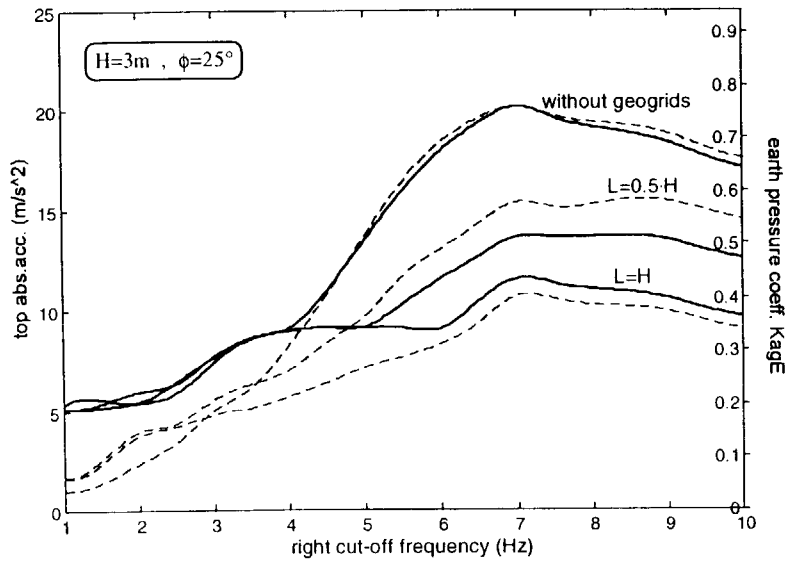
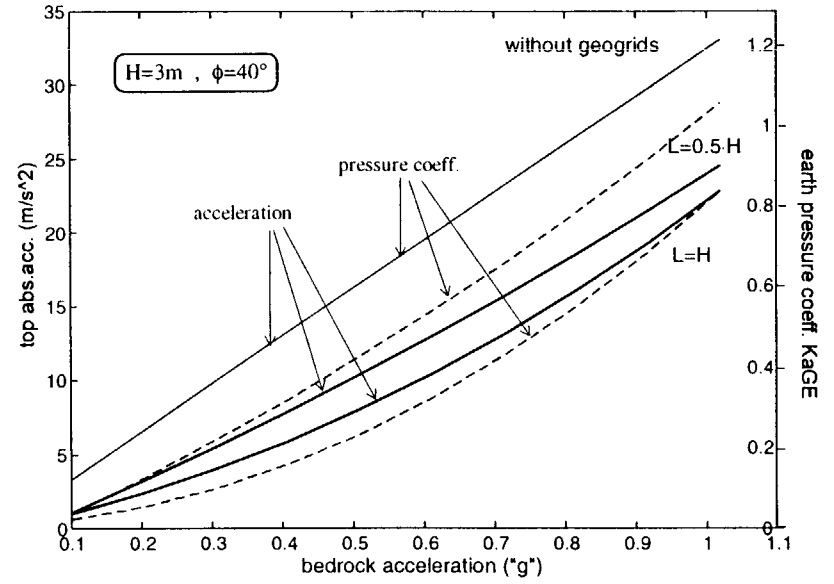
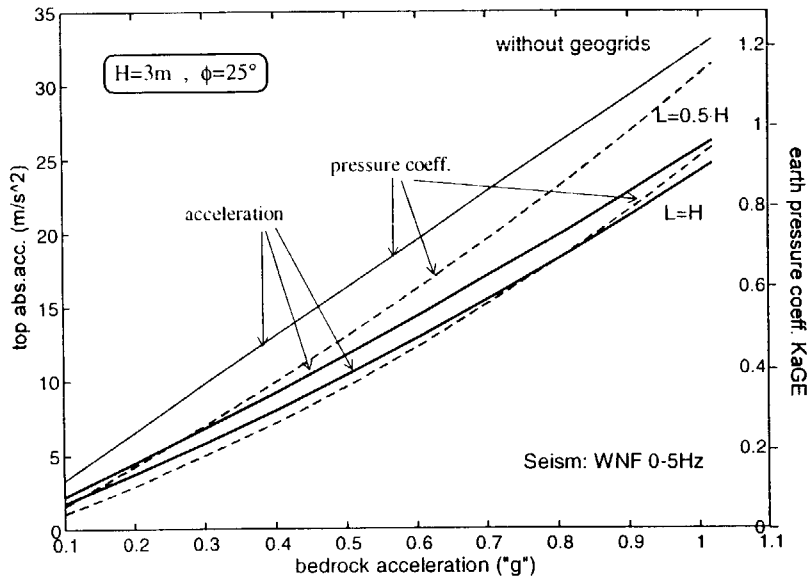


Figure 4 : Design charts for a 9.0 m high wall.

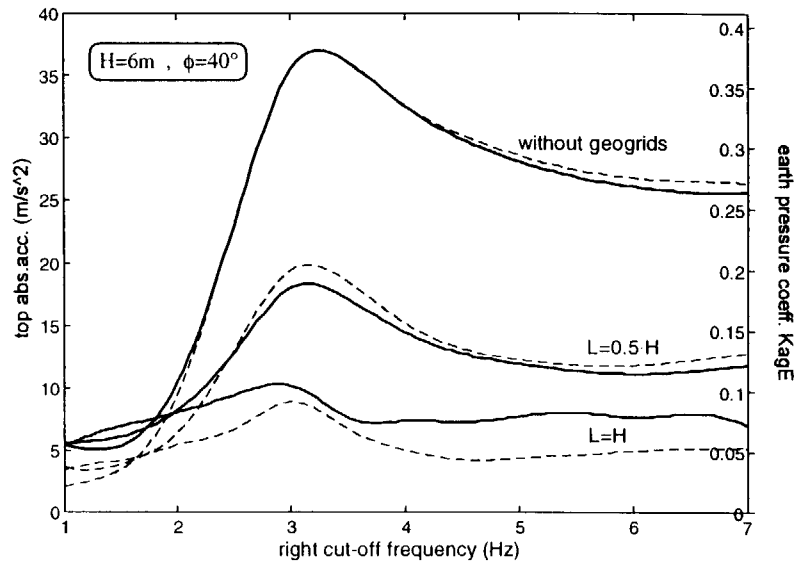
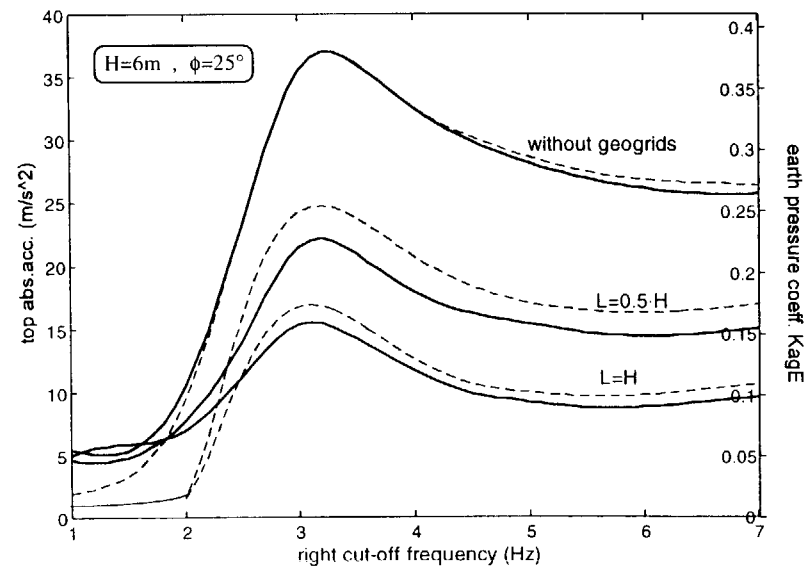
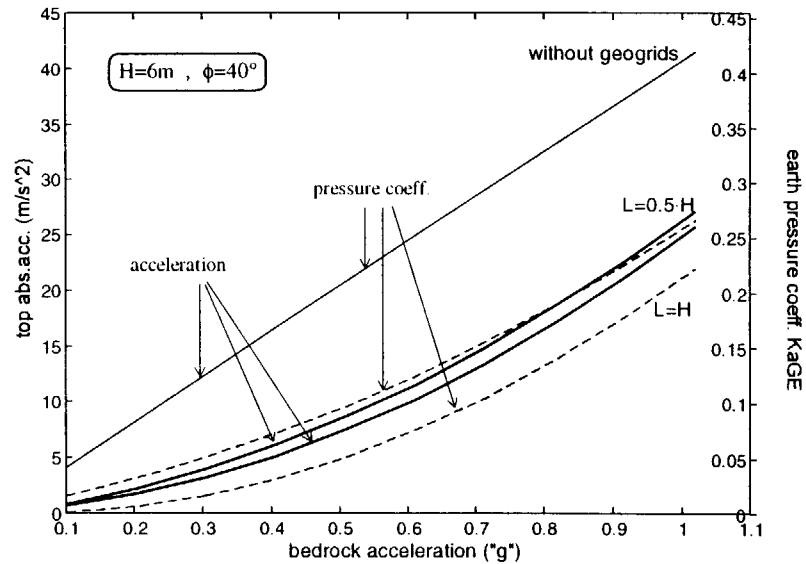
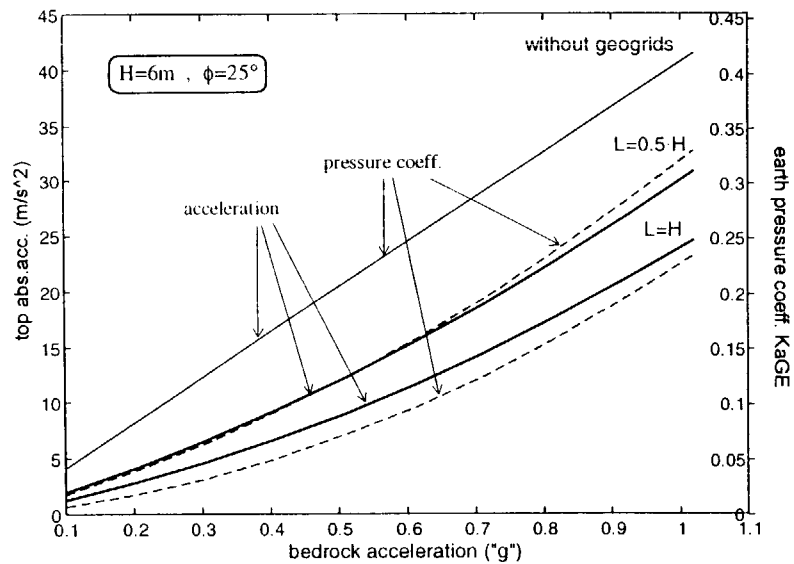


Figure 5 : Design charts for a 6.0 m high wall.

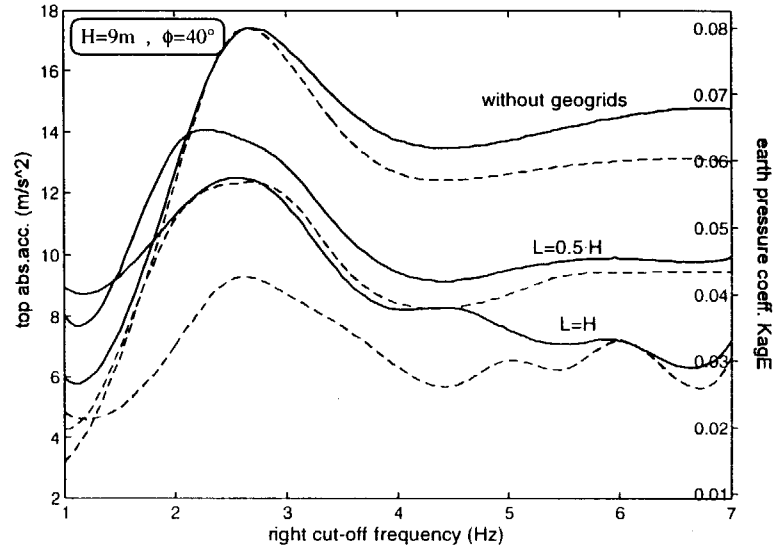
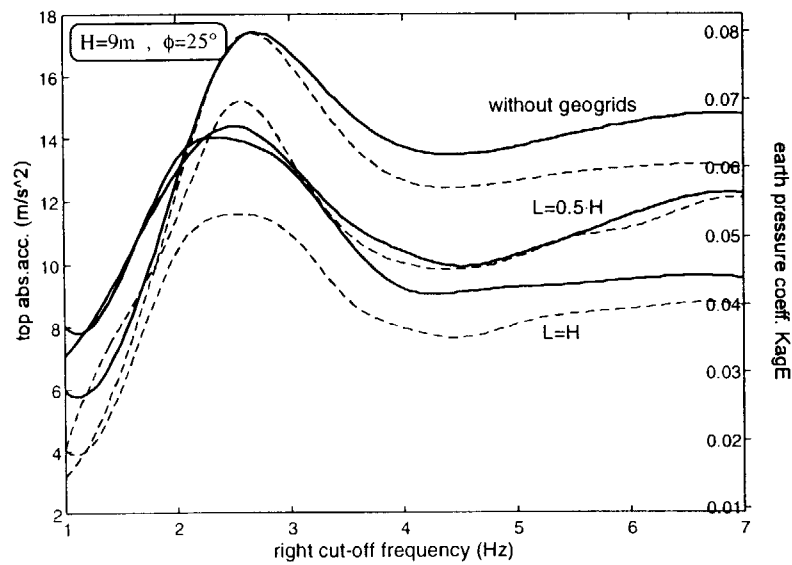
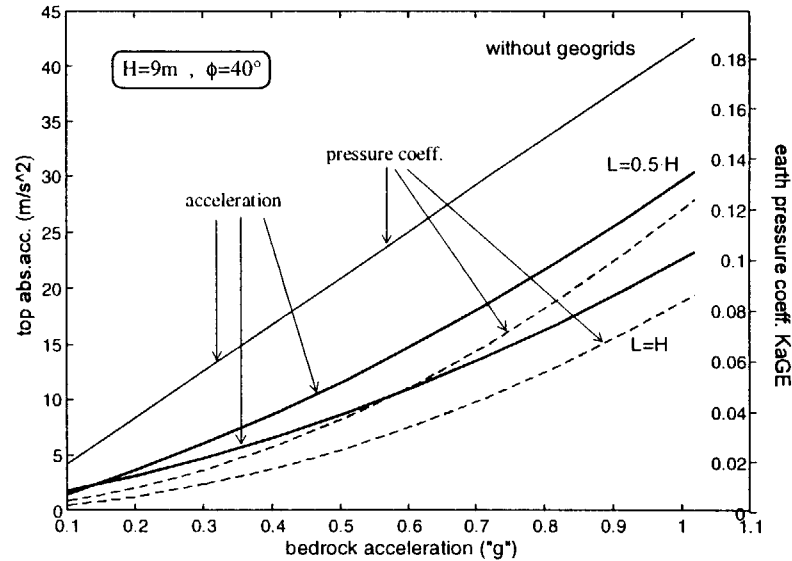
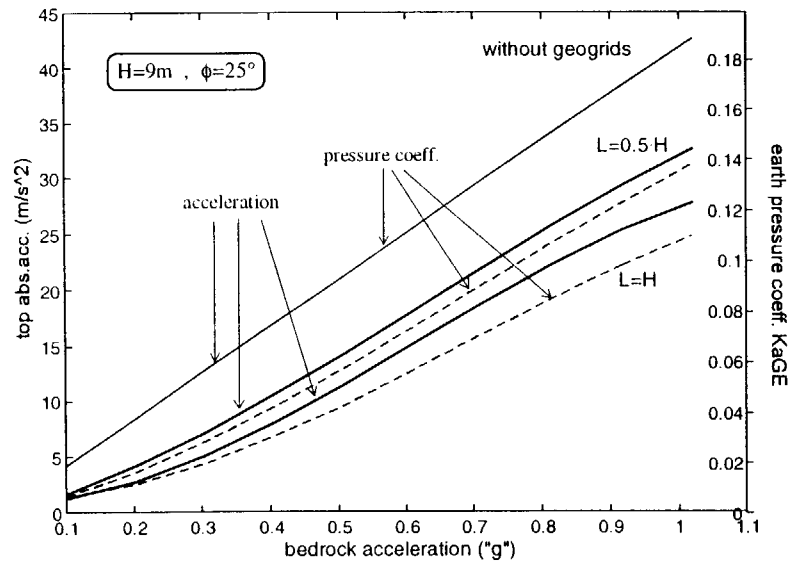


Figure 6 : Design charts for a 9.0 m high wall.

Influence of Reinforcement Stiffness, Length and Base Condition on Seismic Response of Geosynthetic Reinforced Retaining Walls

R.J. Bathurst

Professor, Department of Civil Engineering, Royal Military College of Canada, Kingston, Ontario, Canada

K. Hatami

Research Associate, Department of Civil Engineering, Royal Military College of Canada, Kingston, Ontario, Canada

ABSTRACT: The paper reports selected results from a set of numerical experiments that were carried out to investigate the influence of reinforcement stiffness, length and base boundary condition on the seismic response of a geosynthetic reinforced full-height panel wall. The two-dimensional explicit finite difference program FLAC was used to carry out the numerical experiments. The paper illustrates how program FLAC may be a useful research tool to corroborate current empirical guidelines for the pseudo-static analysis and design of geosynthetic reinforced wall structures or to propose new guidelines. For example, the numerical results illustrate that the dynamic response of the simulated walls is very sensitive to base foundation condition.

KEYWORDS: Retaining walls, Geosynthetic reinforcement, Seismic analysis, Finite difference, Parametric study.

1 INTRODUCTION

In North America, geosynthetic reinforced soil walls are routinely designed using pseudo-static limit-equilibrium methods for sites with peak horizontal ground accelerations $\leq 0.29g$. A limitation of pseudo-static methods is that they cannot consider the effect of duration of seismic loading, acceleration amplification through the backfill soil, and foundation condition on the development of reinforcement loads and structure deformations (Bathurst and Alfaro 1996; Bathurst and Cai 1995). The results presented in this paper are part of an ongoing project directed at understanding the dynamic response of geosynthetic reinforced wall structures due to earthquake. The results presented in this paper show that the two-dimensional explicit finite difference program FLAC may be a useful tool to investigate the seismic performance of reinforced wall structures. Ultimately, numerical simulation results of the type demonstrated here may be used to verify or modify currently accepted pseudo-static design methods.

2 MODEL

The example walls were chosen to have the same height and number of uniformly spaced reinforcement layers as the base case example reported by Rowe and Ho (1992) (Figure 1). A preliminary set of static analyses were carried out using the same geometry, material properties and reinforcement layout as that reported by Rowe and Ho to confirm that FLAC (version 3.30) analyses for the end of construction loading case give similar results to their finite element analyses. However, boundary conditions were then modified for the current study to accommodate the need for a larger mesh and other details related to the two different foundation conditions investigated.

Each wall was modeled as a continuous panel with a height of 6.0 m and a width of 0.14 m. The bulk and shear moduli of the wall were $K_w = 20,000$ MPa and $G_w = 10,000$ MPa, respectively. The wall was hinged at its toe using beam elements. The soil was modeled as a purely frictional elastic-

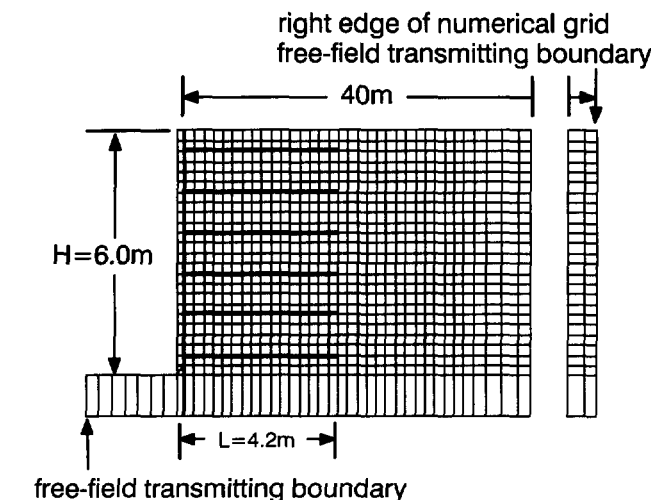


Figure 1. Numerical grid for example problem with fixed base condition.

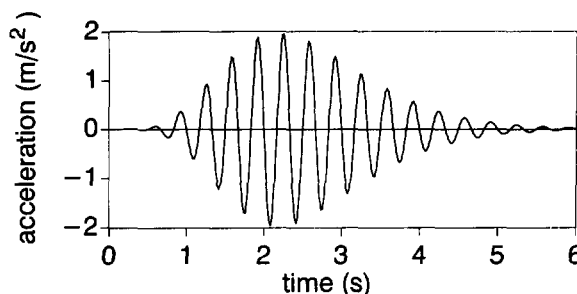


Figure 2. Base acceleration-time history.

plastic material with a Mohr-Coulomb failure criterion and non-associated flow rule. The friction angle of the soil was $\phi = 35^\circ$, dilatancy angle $\psi = 6^\circ$ and unit weight $\gamma = 20$ kN/m³. The bulk and shear moduli of the soil were $K_s = 27.5$ MPa and $G_s = 12.7$ MPa, respectively.

A uniformly spaced reinforcement was considered in the model. The reinforcement was modeled using linear elastic cable elements with negligible compressive strength and an equivalent cross-sectional area of 0.002 m^2 . The stiffness of the reinforcement (J) was a variable in this set of parametric analyses. The tensile yield strength of the reinforcement was $T_{\text{yield}} = 200 \text{ kN/m}$ to ensure that reinforcement rupture was not a failure mechanism.

The interface between the reinforcement (cable elements) and the soil was modeled by a grout material of negligible thickness with interface friction angle $\delta_g = 35^\circ$. The bond stiffness and bond strength of the grout model were taken as $k_{\text{bond}} = 2 \times 10^6 \text{ MN/m/m}$ and $s_{\text{bond}} = 10^3 \text{ kN/m}$, respectively. The interface and grout properties were selected to simulate a perfect bond between the soil and reinforcement layers. The soil-wall and soil-foundation interfaces (for the sliding wall cases) were modeled using a thin soil layer of 0.05 m thick. However, the friction angle of the interface layer between the reinforced soil and the panel wall was set to $\phi_{\text{int}} = 20^\circ$ and the dilatancy angle to $\psi_{\text{int}} = 0^\circ$.

The numerical grid was selected to represent an infinitely wide region. To achieve this condition the soil region was extended to 40 m beyond the back of the wall and a *free field* boundary condition was applied at the truncated boundaries at the left and right edges of the grid to allow for the radiation of elastic waves to the far field.

The soil and reinforcement elements were constructed in layers while the panel wall was braced horizontally. The propped panel supports were then released in sequence from the top of the structure as reported by Rowe and Ho. After static equilibrium was achieved, the full width of the foundation was subjected to the acceleration history illustrated in Figure 2.

Table 1. Numerical simulation configurations.

Test	Base condition	L/H	J (kN/m)
1	fixed	0.7	500
2	fixed	0.7	1000
3	fixed	0.7	2000
4	sliding	0.7	500
5	sliding	0.7	1000
6	sliding	0.7	2000
7	fixed	1.0	500
8	fixed	1.0	1000
9	fixed	1.0	2000
10	sliding	1.0	500
11	sliding	1.0	1000
12	sliding	1.0	2000

3 PARAMETRIC ANALYSES

The test configurations considered in the current investigation are summarized in Table 1. The base foundation condi-

tion was either fixed (i.e. the toe of the wall was slaved to the foundation but was free to rotate) or free to slide horizontally along a thin 0.05 m thick layer of soil and rotate about the toe. The stiffness (J) and length (L) of the reinforcement were also varied as shown in the table. The synthetic horizontal acceleration record shown in Figure 2 was applied to nodes along the entire base of the numerical grid at equal time intervals of $\Delta t = 0.05 \text{ s}$. The accelerogram simulates a ground motion with both increasing and decaying peak acceleration portions. The peak amplitude of the input acceleration was $0.2g$ with a dominant frequency of 3 Hz which is typical of medium to high-frequency content earthquakes. A mass proportional damping of $\zeta = 0.05$ was assumed for the model. The total duration of the input excitation was limited to 6 seconds in order to minimize computational time.

4 RESULTS

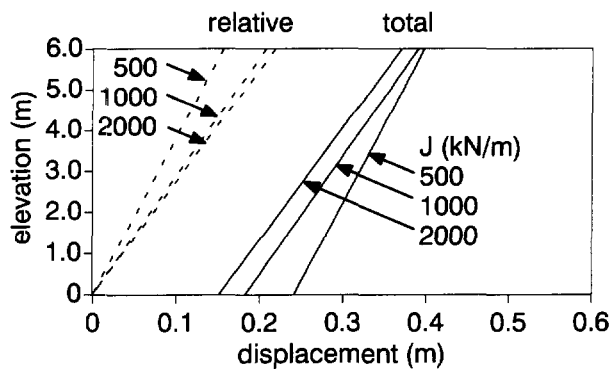
4.1 Wall Displacements

Wall displacements predicted at the end of the excitation period are shown in Figure 3. For the same base condition, the *total* wall deflections diminish with increasing reinforcement stiffness. Similarly, for the same base condition and reinforcement stiffness, there is less total wall displacement for $L/H=1.0$ compared to configurations with $L/H=0.7$. However, the plots show that for the range of reinforcement stiffness values used, the base condition (fixed or sliding) has a greater influence on wall deflection than the magnitude of reinforcement stiffness. In addition, the *relative* wall deflections taken with respect to the wall toe are less for the sliding foundation case than for the fixed toe case.

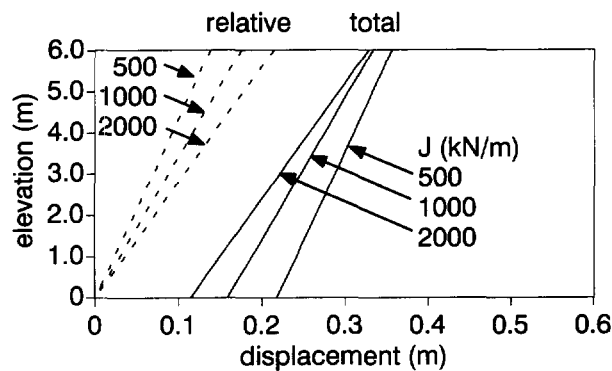
4.2 Reinforcement Forces

In general, reinforcement forces were observed to accumulate with duration of seismic shaking. Figure 4 shows the relative distribution of axial forces in the reinforcement layers at the end of the 6 second acceleration record. The reinforcement forces at the connections were almost always greater than the internal reinforcement forces at all stages of the numerical experiments including end of construction. This trend can be attributed to the relative downward movement of the reinforced soil zone relative to the continuous wall panel.

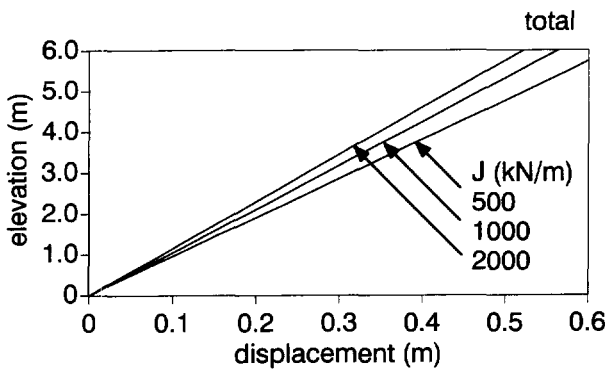
Figures 5a and 5b show the distribution of maximum *total* reinforcement force (typically at the end of the shaking duration when ground accelerations have returned to static conditions) and the distribution of forces at the end of construction for each experiment (initial). The largest reinforcement forces at the end of construction and after dynamic loading were predicted for the sliding foundation case. The distributions of maximum total reinforcement forces are very different for sliding and fixed foundation cases. The influence of toe fixity and the structural panel member on reinforcement forces is clear in the two figures. The maximum reinforcement force occurs at the bottom layer for the sliding cases while the peak reinforcement layer occurs at the second from bottom layer for the fixed toe condition. The maximum total



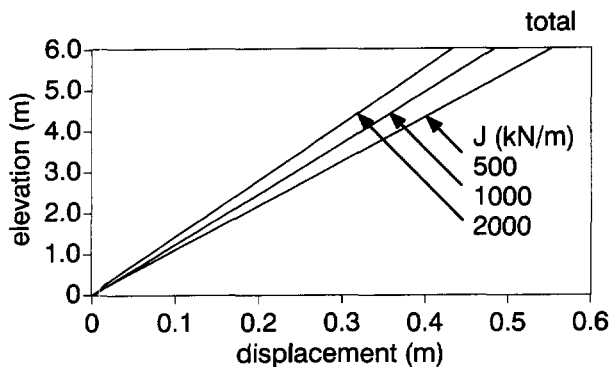
a) sliding base ($L/H=0.7$)



b) sliding base ($L/H=1.0$)



c) fixed base ($L/H=0.7$)



d) fixed base ($L/H=1.0$)

Figure 3. Wall displacements predicted at end of seismic record (time = 6 s).

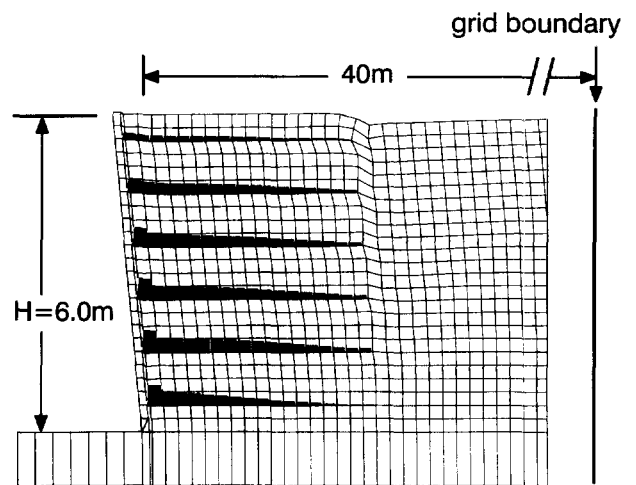


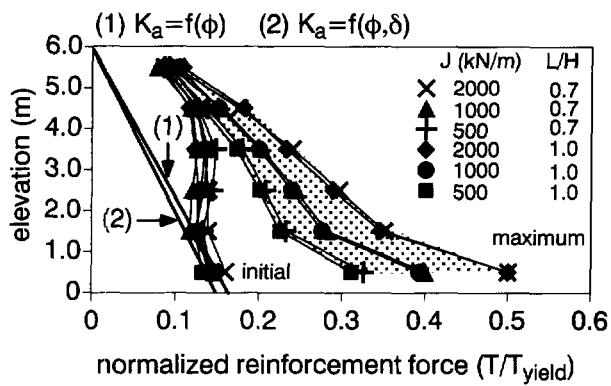
Figure 4. Reinforcement forces at $t = 6$ s for fixed base condition with $L/H=0.7$ and $J=2000$ kN/m.

reinforcement force distributions are relatively insensitive to reinforcement ratio (L/H) for the two values investigated but relatively sensitive to the reinforcement stiffness value under dynamic loading. Reinforcement loads increase with reinforcement stiffness. Superimposed on these two figures are predicted reinforcement forces using Rankine earth pressure theory and Coulomb earth pressure theory. These curves do not capture the trend in reinforcement loads at the end of construction for both foundation conditions and are generally very much lower in magnitude than the peak reinforcement forces generated as a result of shaking.

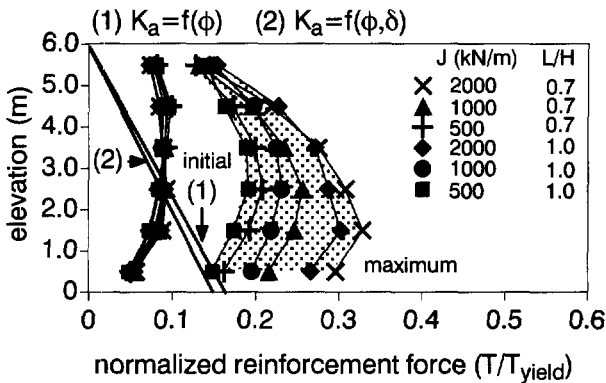
Figures 6a and 6b show the peak dynamic increment force recorded in all simulations. These values are calculated by subtracting the total dynamic load curves in Figure 5 from the corresponding initial static values. Superimposed on the figures are the predicted dynamic increment forces using the current AASHTO (1996) method with a peak ground acceleration of 0.2g. In general, the empirical AASHTO method underestimates the magnitude of additional reinforcement forces. In addition, the trend in additional reinforcement load cannot be captured by the empirical AASHTO curves for the fixed toe condition.

4.3 Other

Figure 7 shows a plot of shear zones in the failed volume of soil within the reinforced zone and in the retained fill. This figure is typical of all numerical simulations reported in this paper. There was no evidence of a well-defined Rankine type failure surface contained within the reinforced soil zone. Rather, the reinforced soil zone acted as a parallel sided monolithic mass. Large shear strains were recorded at the wall-soil interface and at the reinforced soil-retained soil interface. The failure volume can be approximated by a bilinear wedge with the orientation of the linear segment in the retained soil approximately 31° from the horizontal. This failure surface orientation is consistent with Mononobe-Okabe earth pressure theory when ground acceleration amplification is considered (i.e. peak accelerations in the soil were as great as 2 to 3 times the 0.2g peak input value at the base of the structure).

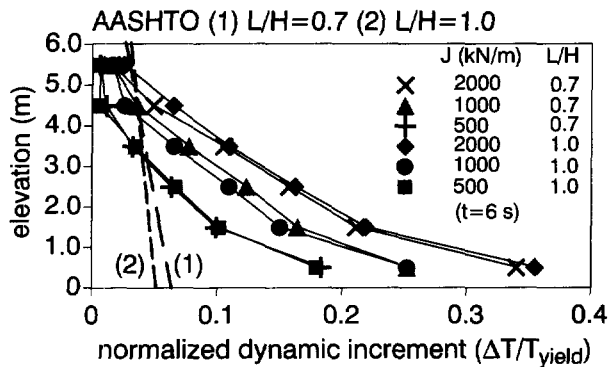


a) sliding base (total forces)

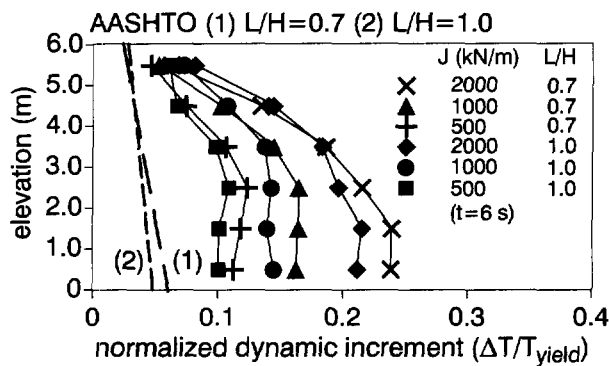


b) fixed base (total forces)

Figure 5. Total reinforcement forces.



a) sliding base (dynamic increment force)



b) fixed base (dynamic increment force)

Figure 6. Dynamic increment reinforcement forces.

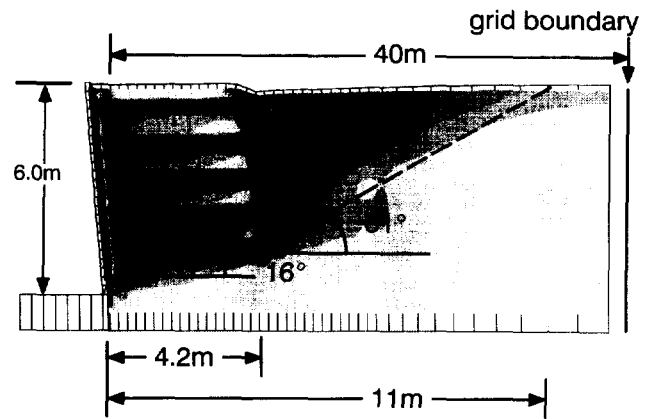


Figure 7. Shear zones at $t = 6$ s for fixed base condition with $L/H=0.7$ and $J=2000$ kN/m.

5 CONCLUSIONS

Program FLAC holds promise as a numerical simulation tool to investigate the seismic response of geosynthetic reinforced soil walls. In particular, the numerical results may be used to corroborate current empirical guidelines for the pseudo-static analysis and design of geosynthetic reinforced wall structures or to propose new guidelines. More work remains to investigate a wider range of wall geometries and facing types before predictions based on program FLAC can be used as an aid to the development of simplified seismic design guidelines. However, it is important to note that the seismic response values reported in this paper have not been verified against laboratory models of any scale. The writers are currently carrying out reduced-scale shaking table tests of geosynthetic reinforced soil walls that will be used to calibrate numerical simulations and to verify simulation results.

ACKNOWLEDGMENTS

The funding for the work reported in the paper was provided by the Department of National Defence (Canada).

REFERENCES

- AASHTO (1996) *Standard Specifications for Highway Bridges*, 16th Edition, American Association of State Highway and Transportation Officials, Washington, D.C., USA, 677 p.
- Bathurst, R.J. and Alfaro, M.C. (1996) "Review of seismic design, analysis and performance of geosynthetic reinforced walls, slopes and embankments", *Proc. of the Int. Symp. on Earth Reinforcement Practice*, IS-Kyushu'96 Fukuoka, Kyushu, Japan, 12-14 November 1996, 30 p.
- Bathurst, R.J. and Cai, Z. (1995) "Pseudo-static seismic analysis of geosynthetic reinforced segmental retaining walls", *Geosynthetics International*, Vol. 2, No.5, pp. 789-832.
- FLAC (1995) (Version 3.30) Itasca Consulting Group, Inc. 708 South Third Street, Minneapolis, MN 55415, USA.
- Rowe, R.K. and Ho, S.K. (1992) "A review of the behavior of reinforced soil walls", *Proc. of the Int. Symp. on Earth Reinforcement Practice*, IS-Kyushu'92, Fukuoka, Japan, 11-13 November 1992, pp. 801-830.

The Verrand High Reinforced-Soil Structure

G. Sembenelli

Geotechnical Consultant, SC Sembenelli Consulting, Milan, Italy

P. Sembenelli

Geotechnical Consultant and Managing Director, SC Sembenelli Consulting, Milan, Italy

ABSTRACT: The Verrand Embankment is a 27.5 m High Reinforced Soil Structure topped by a 10 m high unreinforced embankment, located at the bottom of a steep V-shaped valley, in the Italian Alps. Scope of the structure, which was completed by the end of 1996, was threefold: providing a stabilising weight to the natural slope, providing a disposal for material from tunnel excavation and providing access beyond the embankment. The reinforced portion mainly consists of three 9 m high blocks, with face angle about 60° from the horizontal. The reinforcements are non-woven geotextiles. The Paper describes the project geometry, fill and reinforcing materials as well as the construction sequence. Monitoring data, collected since the early construction phases, are also presented and discussed.

KEYWORDS: Reinforced slope, Geotextiles, Case study, Construction, Deformations

1 INTRODUCTION

A new highway connecting the Monte Bianco Tunnel with the city of Aosta, in the Italian Alps, requires the construction of a bridge, some 600 m long, parallel to a very steep slope, about 35 to 40° from the horizontal. The slope forms the left side of a V-shaped valley, created by the Dora Baltea River.

The geology of the site is quite complex. Originally, the valley was filled by a very large earth and rock slide. During the latest glaciation the slide materials were overconsolidated by the action of a thick layer of ice. Locally, concretions of carbonate-rich waters had also formed. By the end of Würmian glaciation the increased erosive potential of the river deeply cut the overconsolidated deposits. The slope material, which is observed today, can be described as a silty sand matrix containing gravel and large boulders, slightly cemented. The surficial part of the mass is often decompressed. The natural water table daylight in the bottom half of the slope.

Presently the slope is close to limit conditions and repeated slides of limited extent occur, whenever the river cuts into the toe of the slope. A particularly large slide took place, in the early years of the century, near the village of Verrand.

Pier #4 of the bridge is located within the perimeter of this slide. It was thus decided that the slope had to be stabilised with a high buttressing embankment.

The steepness of the valley sides imposed the use of reinforced soil technologies, so that the volume of fill and thus the stabilising weight could be maximised. As a side result of this solution, a large volume of muck from nearby tunnel jobsites could be disposed in an environmentally acceptable way.

2 PROJECT DESCRIPTION

The Verrand Embankment, shown in plan on Fig. 1, is a 27.5 m High Reinforced Soil Structure overlaid by 10 m of unreinforced, 1.5H to 1V embankment. The structure is some 150 m long for a total volume of about 120 000 m³, out of which 50 000 m³ are reinforced fill.

The reinforced portion mainly consists of three 9 m high blocks, with face angle of 60° from the horizontal. The blocks are stepped to create 5 m wide sloping berms, almost parallel to the riverbed grade. A 5 m wide service ramp runs on the lower berm and cuts the second and third blocks. A ramp was necessary for construction and to provide access beyond the buttress.

The area where the lower block is founded was cleaned and excavated to reach a competent foundation. Also the natural slope was cleaned and stepped in order to get a better interlocking with the new fill. This operation was carried out as filling progressed.

The toe of the HRSS had to be protected from river action by a cyclopean wall, about 4 m high. Additional riverbed training and erosion preventive works are presently underway.

A deep drainage was located at the contact between fill and natural slope, in order to keep water away from the reinforced fill. The drainage system consisted of two sloping collectors along the sides and one collector at the toe. All collectors were created backfilling a trench with selected gravel, wrapped in a geotextile separator. The drainage system also included geonet bands placed on the slope at 10 m spacings, across the collectors. Drainage in form of bands instead of a continuous sheet was selected in order to avoid creating a low friction contact between the new fill and existing slope. In addition, a number of nearly horizontal drain holes heading in the main drainage collector were drilled to depress the piezometric level as far as possible inside the slope. The main collector discharges to the river, on both sides of the embankment.

A surface drainage system was also foreseen. Rain water is collected and carried to the river by a system of ditches and collectors, running along the berms and along the slopes. Collectors along the slopes are included in the facing system and consist of trapezoidal channels on galvanised steel.

3 THE REINFORCED SOIL

The first step in designing a reinforced soil structure is selecting the facing technology, on account that it strongly

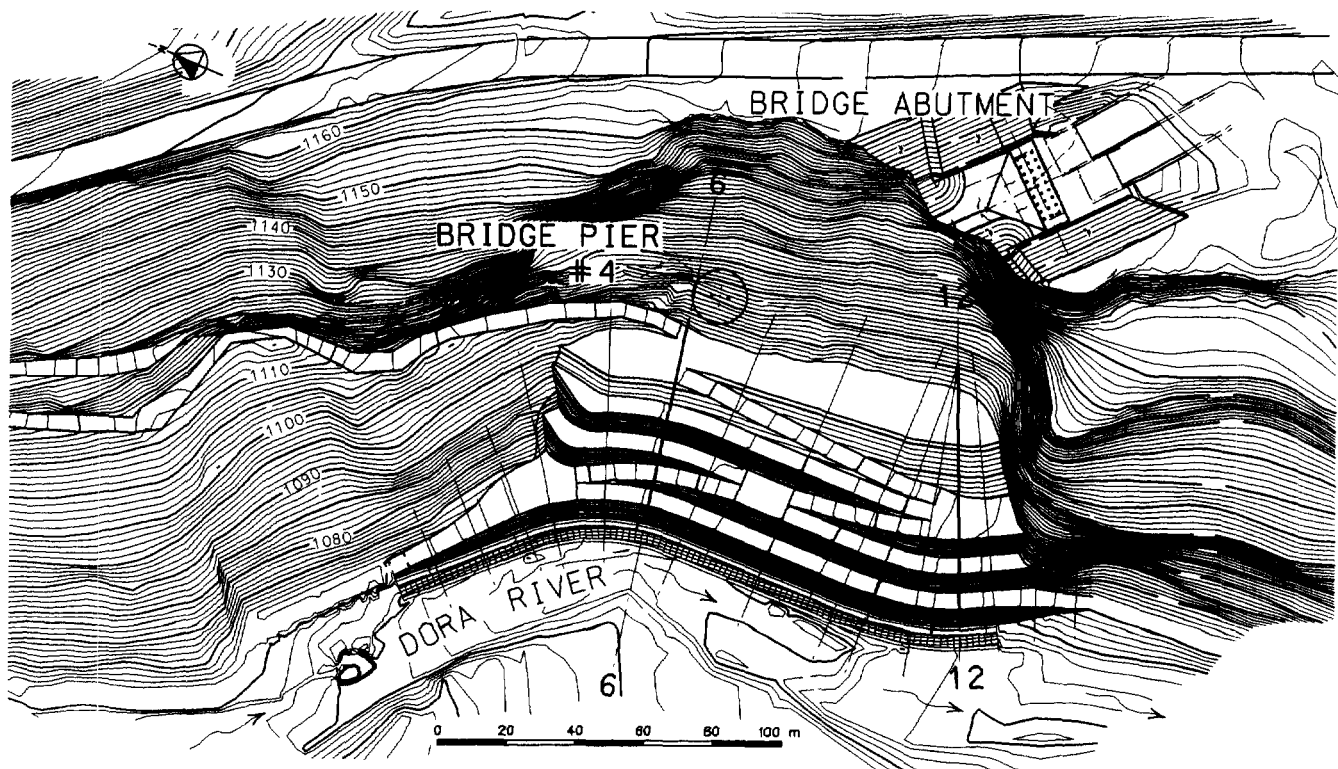


Figure 1. Plan of the Verrand High Reinforced Soil Structure

influences the construction process and the overall structural behaviour. Due to environmental constraints, it was chosen one patented facing systems, resulting in a completely grassed surface, once construction completed.

The basic element of the selected facing technology are 0.5 or 0.6 m high, L-shaped forms made by a welded wire steel mesh, left in place. Each form element is to be bent to an angle which is the one selected for the slope. Short steel tendons holding the two arms of the forms keep the section undeformed during lift compaction. A light woven geotextile is placed inside the form to retain the soil. The fill material is usually spread and compacted in half form high lifts, stopped 0.4 m short from the form. A band of topsoil is placed between the woven geotextile and the lift edge, in order to create a support for vegetation growth. The surface is finally hydroseeded so that it becomes completely and permanently grassed in a short time.

The appearance of the grassed surface at Verrand HRSS before and after hydroseeding is shown in Fig. 2.

An heavy vibrating roller is normally used to provide the necessary compaction effort. The roller actually used at Verrand was a DYNAPAC CA35 Class (7 static tons on drum), instead of the specified CA 25 class (5 static tons on drum). The roller moves parallel to the slope, covering the whole spread of both fill and topsoil placed over the geotextiles, up to the forms.

4 MATERIALS FOR CONSTRUCTION

The fill material placed within the reinforced section was

well graded crushed rock with a relatively large sand and silt fractions, obtained by processing tunnel muck. This material mainly came from tunnelling in schists. The tunnel muck was first crushed in order to reduce its maximum grain size to 150-200 mm and then mixed with material obtained from open air excavations. The latter material was added considering that a relatively high content in sand and silt fines could reduce the potential for damaging the reinforcements.

The specifications for fill materials could not be excessively tight, on account of the fact that random tunnel muck from different excavations fronts were used to supply the needed volume.

The backfill was basically the same material with maximum size in the order of 500 mm. No processing was required for the backfill.

The reinforcements used at Verrand were anisotropic nonwoven geotextiles, continuous filament, needle-punched, Polyester (PET) fibre of three grades, manufactured by Fritz Landolt A.G., Switzerland. The nominal tensile strengths of the geotextiles were 40, 100 and 120 kN/m and their main characteristics are summarised in Table 1.

The reinforcements of grade 1000 and 1200 are quite thick and sometimes the unrolled sheets were undulated. This required special care during placement, in order to avoid wrinkles under the lifts, which might reduce the overall stiffness of the reinforcements. The above deformation were mainly considered to be a consequence of the production process.



Figure 2. View of the Verrand High Reinforced Soil Structure after completion. Vegetation is not yet fully developed in the upper part.

Table 1. Main characteristics of geotextiles FLN-TEXA used as reinforcement at Verrand HRSS

Type	Mass	Machine direction		Transverse direction	
		Strength	Elongation at failure	Strength	Elongation at failure
[-]	[g/m ²]	[kN/m]	[%]	[kN/m]	[%]
350	350	48.5	36.8	21.8	37.6
1000	900	115.5	38.3	47.8	36.2
1200	1050	132.7	40.1	55.4	39.6

Geotextiles survivability was checked by full scale tests, under the worst expected condition, i.e. with the coarsest fill compacted in 0.3 m thick lifts. After placing the geotextiles sheets on a compacted layer of fill, 3 additional fill lifts were spread and compacted with the same roller used in construction. The reinforcements were then carefully dug out. Exhuming operations are very difficult and

some additional damage is inevitably produced.

The most damaged zones of the unearthed sheets were thoroughly mapped. From those zones, specimens were taken, described and tested according to UNI-8639 (Italian) Standard. This testing procedure requires 100 mm wide and 200 mm long tubular (folded) specimens (Cazuffi et al., 1986).

Damages were not uniformly distributed over the geotextiles, but rather concentrated in patches. This is probably related to coarse particles segregation processes in the fill, as shown in Fig. 3. The tendency for damages to concentrate close to the outer slope was observed. Apparently segregation tends to increase along the edge of a given lift. Special attention should be devoted to avoid excessive segregation and hence excessive damages near the face, considering that here tensile stresses are the greatest. The extent of the damaged areas was about 50% of the reinforcements width.

Damage was classified under three main types: tears, through-going punctures and partial punctures. Tears were large damages probably related to the unearthing operations and were not considered in the analyses. Through-

going punctures are the most significant damages on account that they produce an appreciable loss of strength. They are small cuts, either rounded or linear, randomly oriented, 10 to 30 mm long. Partial punctures are small indentations, where the filaments are displaced and not necessarily cut.

Within the most damaged zones, the number of observed through-going punctures ranged from a minimum of 40 per square meter (30 per sq. yard) to a maximum of 100 to 120 per square meter (80 to 100 per sq. yard). The corresponding average strength loss was in the order of 50 to 60%. The above results could be observed on all the reinforcement examined and are in good agreement with previously published works (Sembenelli, 1995).

On account that the most damaged zones spread over about half the width of each reinforcement, it may be concluded that the actual strength retained by the whole reinforcement is 70 to 75% of that of the undamaged material. Correspondingly, the appropriate Factor of Safety to account for installation damage is $F_d = 1.35$ to 1.45.

Our observations suggest that the maximum particle size has more influence on the width of the damaged areas than on the level of damage itself.



Figure 3. Compacted fill material surface under a reinforcement. Segregation of coarse particles in foreground is clearly visible

5 DESIGN OF THE REINFORCEMENT DISTRIBUTION AND LENGTH

The selection of the reinforcement requirements (force and length) was based on the limit equilibrium. In the Writers' opinion, when dealing with complex High Reinforced Soil Structures, this is still the most suitable design tool available.

The total horizontal force necessary for equilibrium was determined on a homogeneous unreinforced cross section. The required tensile force to be taken by the reinforcements was then computed as the force required for obtaining a minimum Factor of Safety $F_s = 1.3$ against sliding. The computations were carried out with the Simplified Janbu Method, working directly on horizontal forces.

The assumed geotechnical characteristics of the fill material were: total unit weight $TUW = 21 \text{ kN/m}^3$, cohesion $c = 0 \text{ kPa}$ and angle of friction $\phi = 35^\circ$. Tri-axial CD strength values, obtained from 100 mm diameter, compacted specimens, were larger than the assumed ones. However, a conservative value of the friction angle was selected to take into account the reduction of friction at high confining pressures and high strain levels. With this, the conditions of the lower block and situations of excess of silty fines were covered.

Several design sections were analysed, in order to cover all typical configurations. On each section a number of potential sliding surfaces were selected, so that part of a single block as well as one or more blocks were cut. The computed maximum horizontal force needed for equilibrium at each potential sliding surface was hence distributed over its height. Finally, the minimum required reinforcement was computed as the envelope of the above values.

The geotextiles tensile strength values were reduced to account for installation damage, long term durability and creep. The Design Strength was finally assumed to be 27% of the Wide-Width (500 mm) strength determined according with CNR-UNI (Italian) standards (Cazzuffi et al., 1986).

The length of the reinforcements was selected so that the computed minimum factor of safety for surfaces passing just beyond the reinforcements would be $F_s = 1.3$.

Detailed drawings of each reinforcement level were provided to the Contractor to ensure a proper distribution of the overall strength and to minimise wastage. This required a large number of construction drawings including plans, front views and cross sections. The curved contours of the reinforced embankment surface required detailed drawings to show the exact location in plan of both the reinforcement sheets and their overlaps.

The heaviest reinforcements were located within the lower blocks, not only to fulfil strength requirements but also to provide greater stiffness. Grade 350 reinforcements were used only locally in the very upper portion of the upper block. Additional reinforcements at the base of the top unreinforced fill were introduced to reduce the earth pressure on the reinforced blocks.

A typical reinforcement distribution is shown in Fig. 4. It is worth noting that the inner side profile of the reinforcements is stepped in order to meet the overall stability requirement.

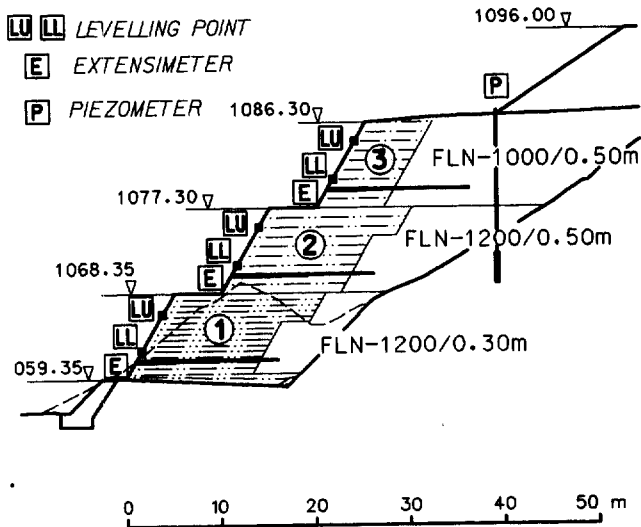


Figure 4. Design cross section 12 with blocks numbering, reinforcements and instrumentation

6 CONSTRUCTION

Construction started in summer 1994. The lower block and about 3 m of the mid block were completed by November 1994. From winter 1994 through April 1996, construction was stopped, due to non-technical reasons. Fill could not be placed between late November and early April anyway, on account of the cold climate.

After resuming construction, the reinforced portion was completed early in September 1996 and the unreinforced fill was hence added to final grade. Actual construction took about 9 months.

The flow of material from neighbourhood excavations was slow so that a standard production, say 300 to 500 m³/day for a crew of 3 men, could not be sustained.

Hydroseeding was carried out early in 1996 for the lower part, already completed at that time, and at the end of 1996, for the upper blocks. Some delay between completion of construction and seeding is usually tolerated, though not beneficial for the facing which remains unprotected.

A large flood, in the order of 600 m³/s, occurred in the summer of 1996. The estimated return period of such flood was 50 years. The water level rose to the top of the toe wall, but no effects were noted on the reinforced embankment, though a scour, up to 2 m deep, produced in the riverbed.

7 BEHAVIOUR

Since early construction, vertical and horizontal displacements were monitored, with topographic surveys of reference points at cross sections 6 and 12. On the same cross

sections, long-base extensometers were placed to measure horizontal average strains. Due to installation problems, however, no one of the bases gave reliable readings.

The selected reference points were special plates and the heads of the extensometers. Horizontal displacements were measured from stations located on the opposite bank of the river, so that the distance between station and measuring points was in the order of 100 m. The location of the reference points on cross section 12 are shown in Fig. 4. Plates and extensometers are similarly located in section 6. It should be noted that the extensometer 2E in section 6 is below the service road.

The main data recorded are summarised in the time histories of Fig. 5 and 6. The shape of all displacement

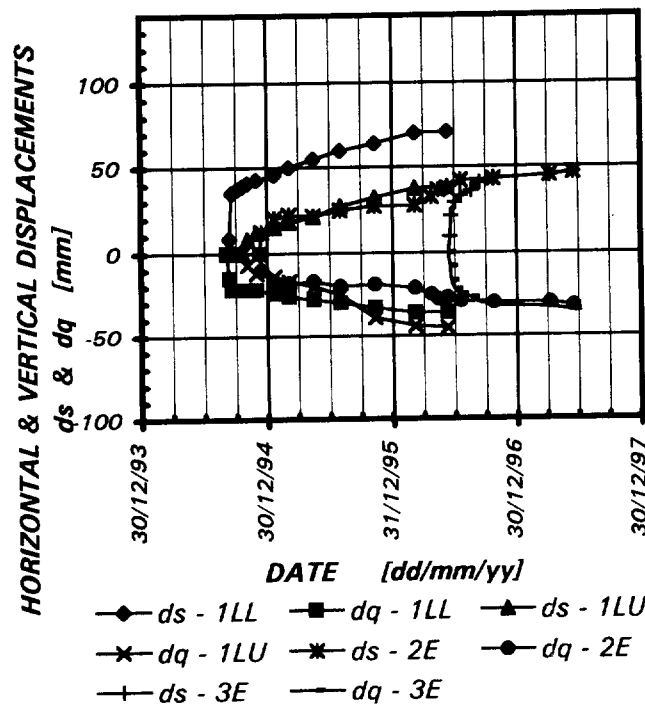


Figure 5. Horizontal and vertical displacements measured on section 6. See Figure 3 for key

curves is hyperbolic and a horizontal asymptote appears to be reached after 9 months, from completion.

At Section 6, the maximum horizontal displacements is in the order of 70 mm, on the lower plate of the lowest block. The upper blocks exhibited lesser horizontal displacements, in the order of 50 mm. Vertical displacements range between 30 and 45 mm.

At Section 12, the measured horizontal displacements of the lower block are somehow larger, with maximum in the order of 100 mm. The horizontal displacements of the upper blocks were approximately 50 mm. Vertical displacements are about 70 mm, in the lower block, and 40 mm, above.

The normalised Horizontal Displacements with respect to the relevant height vary over a wide range, between

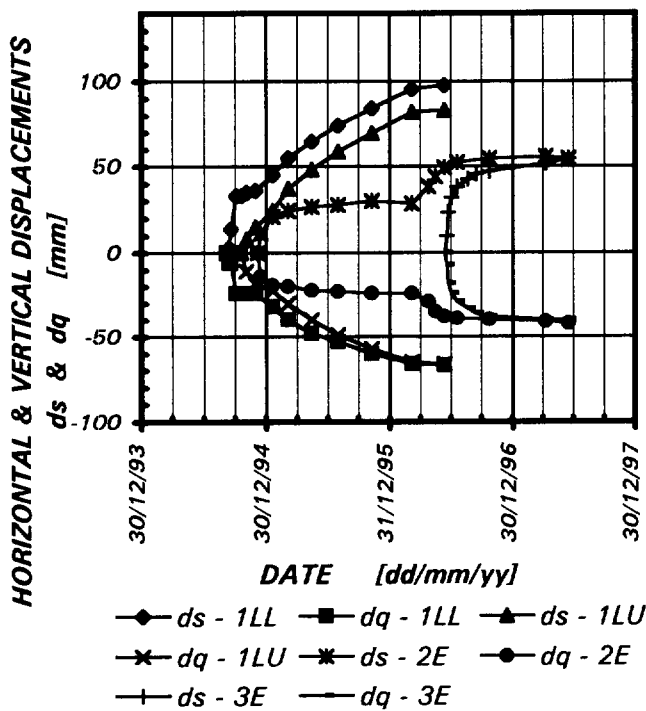


Figure 6. Horizontal and vertical displacements measured on section 12. See Figure 3 for key

$ds/H = 0.25 \%$ to $ds/H = 0.56 \%$. A good correlation between the normalised height and the average slope above the reference point, to which displacements are referred, seems to exist as shown in Fig. 7. Data from Champagne HRSS, a similar structure built according with the same facing technology, are also included for reference (Sembenelli, 1995). The experimental points from Verrand HRSS fit to a logarithmic curve, with a satisfactory correlation. Only one point from Champagne HRSS lays close to the above fitting curve while the other ones lay on an almost parallel curve. This latter points actually refer to a different condition, which included an arched facing and geogrids reinforcements (Sembenelli, 1994).

All points, which fall close to the fitting curve, are related to structures built with well graded (silty) sand and gravels, reinforced with non-woven geotextiles.

Casagrande Standpipe Piezometers will also be installed in order to monitor the water table in the long term.

ACKNOWLEDGMENTS

The Owner of the Monte Bianco-Aosta Highway is RAV - Raccordo Autostradale Valle d'Aosta spa, Roma, Italy. The permission for publishing the above is deeply acknowledged.

VIADOTTI COURMAYEUR a.t.i., a Joint Venture headed by ASTALDI spa, Roma, Italy, is the Contractor in charge of construction. Most of the measurements were carried out by the Contractor's personnel, whose support is also acknowledged.

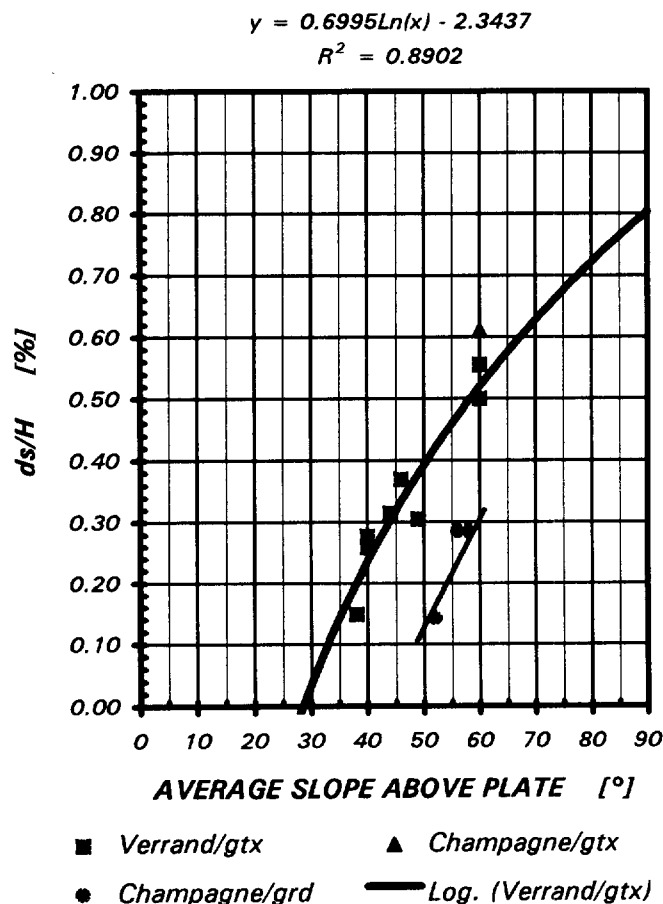


Figure 7. Normalised horizontal displacements vs. average slope

REFERENCES

- Cazzuffi, D., Venesia, E., Rinaldi, M., and Zocca, A. (1986) "The Mechanical Properties of Geotextiles: Italian Standard and Interlaboratory Test Comparison" *Third International Conference on Geotextiles, Geomembranes and Related Products*, Vienna, Austria, Vol. 3, pp. 695-700
- Christopher, B.R., Gill, S.A., Giroud, J.P., Juran, I., Mitchell, J.K. and Dunnicliff, J. (1989) *Design and Construction Guidelines for Reinforced Soil Structures*, Report No. FHWA-RD-89-043, McLean, VA
- Jewell, R.A. (1990) "Strength and Deformations in Reinforced Soil Design" *Fourth International Conference on Geotextiles, Geomembranes and Related Products*, The Hague, Netherlands, Vol. 3, pp. 913-946
- Sembenelli, G. and Sembenelli, P. (1994) "Experiences with High Reinforced Soil Slopes" *Fifth International Conference on Geotextiles, Geomembranes and Related Products*, Singapore, Vol. 1, pp. 479-482
- Sembenelli, G. and Sembenelli, P. (1995) "An Approach to High Reinforced Soil Structures" in *The Practice of Soil Reinforcing in Europe*, Ed. by T.S. Ingold, Thomas Telford, London, UK, pp. 139-152

GEOGRID REINFORCEMENT OF SLOPES FOR EARTHQUAKE RESISTANCE AT THE NEW U.S. EMBASSY IN CARACAS, VENEZUELA

J.R. Lambrechts

Vice President, Haley & Aldrich, Inc., Cambridge, Massachusetts

ABSTRACT: Construction of a new U.S. Embassy building in Caracas, Venezuela posed a number of site stabilization challenges that were overcome with extensive use of geosynthetics. The new site contained several deep, steep sided valleys that had been previously filled in an uncontrolled manner. These 15 to 30 m thick fills were stabilized by installing more than 200,000 sq.m. of geogrid to provide necessary seismic stability in what was the largest application of geogrids in South America, and ranks high in worldwide use at a single building site. Two large walls supported with geo-mechanical stabilization were incorporated into slope stabilization design. This paper reviews the site conditions, design requirements that prompted the use of geogrid stabilization, and the unique application for stabilizing long sloping valley fills placed on bedrock.

KEYWORDS: Geogrids, Slope stabilization, Reinforcement, Seismic design.

The construction of the new U.S. Embassy building in Caracas, Venezuela required extensive site stabilization with geogrid to make the long, steep slopes on the site resistant to the local severe earthquake design conditions. Stability considerations that were incorporated into slope reinforcement designs required special construction to provide resistance to interface sliding of reinforced fill along the surface of underlying sloping bedrock. Other applications of geosynthetics included support of retaining walls and surface slope stabilization using cellular confinement systems in landscape areas of steep final ground surface.

1 SITE CONDITIONS

1.1 Local Geology

The site of the new embassy is in the Alameda area of southeastern Caracas, near the top of a high ridge that rises more than 150 m above a major southern trending valley corridor in this city of 5 + million people. At the edge of the Caribbean tectonic plate, the region is seismically active, and mountains and hilly terrain are present throughout. The bedrock in the area of the embassy is a dark gray micaceous, calcareous schist, which is a member of the Las Mercedes Formation.

The local hilly topography results from erosion of the bedrock. The tropical environs has produced deep weathering of the bedrock. A mantle of residual soils that has developed over the weathered bedrock is typical for such environs, with gradual transition from weathered bedrock upward through decomposed bedrock, which becomes residual soils, and finally topsoil.

1.2 Original Site Preparation for Development

An area of several square miles south and east of the embassy site was developed in the early 1980's, with level

building lots being formed on previously steep sloping hillsides. The initial site development in the early 1980's involved considerable earthwork to make level building lots in the originally hilly terrain. This involved bulldozing off topographic high ridges to fill in the deep intervening, incised valleys.

Several building lots were combined to make a site large enough to accommodate the security needs of a U.S. Embassy. Most of the embassy site had been transformed from hilly terrain, to a series of relatively level plateaus by extensive cutting and filling. Figures 1.a and 1.b present the pre- and post-development site topographic conditions, with the major fill areas labeled. The principal building and land uses of the new embassy are also indicated.

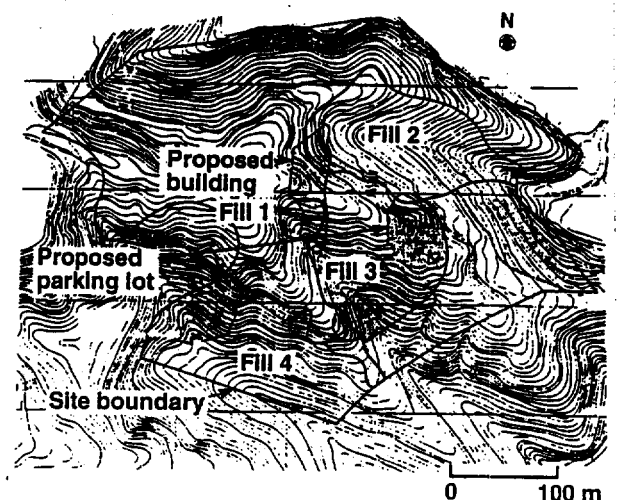


Figure 1.a Pre-Development Site Topography

2 DESIGN CONSIDERATIONS

Site use requirements for the proposed embassy necessitated adding fill on the slopes of Fills 2 and 3, and changes in grading on Fill 4. Also, in certain areas adjacent to the new building, filling was necessary for landscaping, with slopes as steep as 45 deg. However, the calculated stability of the Fill slopes existing before construction was marginal for even static conditions. Conditions for Fill 2 are shown on Figure 2, indicating new fill necessary for required final site grading and critical stability surfaces. Similar Factors of Safety were found for Fill 3. Factors of Safety were calculated using the program GEOSLOPE for the Janbu procedure to study irregular sliding models. The constraining effects of the buried valleys were considered, and applied by increasing the calculated Factors of Safety by 10 %, per findings of Baligh and Azzouz (1975).

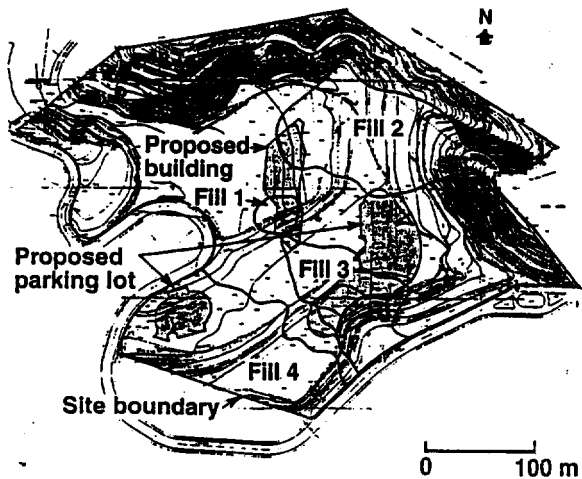


Figure 1.b Conditions After Development Grading

Ground surface across the majority of the developed site area varies El. 945 m to El. 990, but lower levels to El. 915 occur at the bottom (east end) of Fill 2. Bedrock was exposed at ground surface after site development in the flat areas and on slopes between the Fills. Only about half of the Fill 4 area, at the southwest side of the site, is within the site limit, with the remainder continuing across the road and onto the sites on the other side of the street. Similarly, Fill 3 continues downhill beyond the site limit and road, and beneath the lot across the street. The design of stabilization for each Fill area had to account for these conditions.

The Fills were found to be 20 m to 35 m thick, with density being generally loose to compact. The fill was a mixture of the topsoil, the residual soils, and the decomposed and weathered bedrock. Gradation of fill generally varied from silty coarse to fine sand, to medium to fine sandy silt, all with trace clay and rock fragments. Some organic matter was also randomly present. Since there had been little clearing and grubbing prior to valley filling, in many borings topsoil and residual soil were found below fill. Also, as a result of the bulldozing of ridges, vegetation was sometimes found buried in bottoms of fills. Based on results of test boring Standard Penetration Test N-values, the following strengths were assigned to the various strata:

Stratum	Friction Angle (deg)	Unit Weight (kN/m ³)
Uncompacted Fill	30	19.6
Residual Soil (& Topsoil)	25	20.4 (18.8)
Decomposed Rock	35	21.2
Schist Bedrock	40	22.0
Compacted Backfill	33	20.4

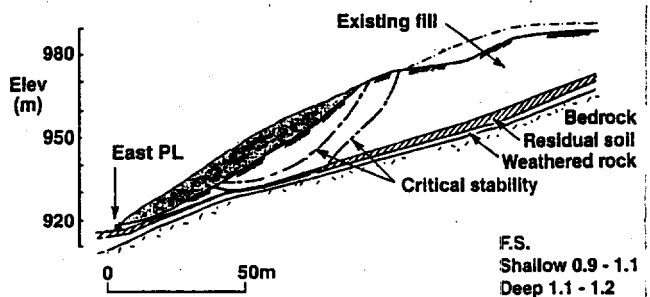


Figure 2. Stability Conditions of Original Fill 2

Primary geotechnical design considerations stem from the severe regional seismicity, which requires design for Richter magnitude 7.0. From earlier site specific seismicity study, the design earthquake was determined to produce bedrock horizontal acceleration of 0.30g. This was used in seismic slope stability analyses, which lowered calculated factors of safety to considerably below 1. Major reconstruction of the large site fills was therefore imperative.

Design for developed site required static Factor of Safety of 1.5, and for seismic conditions a FS of at least 1.0, plus the requirement that toe of slope not move beyond the property line as result of earthquake shaking. To satisfy these requirements, it was found necessary to remove and replace considerable amount of the existing fill in the three major Fills.

3 DESIGN OF SLOPES USING GEOGRID

In designing the stabilized fills for surface slopes as steep as 2 hor. to 1 vert., extensive use of geogrid reinforcement was essential to meet design criteria. Slope stability Factors of Safety were calculated using friction angle of reinforced fill judged to be at least 5 deg. more

than compacted backfill; i.e., 38 deg. Generalized profile through Fill 2 in Figure 3 shows the extent of reinforced fill necessary to meet design requirements for both the resist deep seated and shallow instability. As indicated, the dynamic conditions were the more severe, and thus necessitated more geogrid than would have only static considerations.

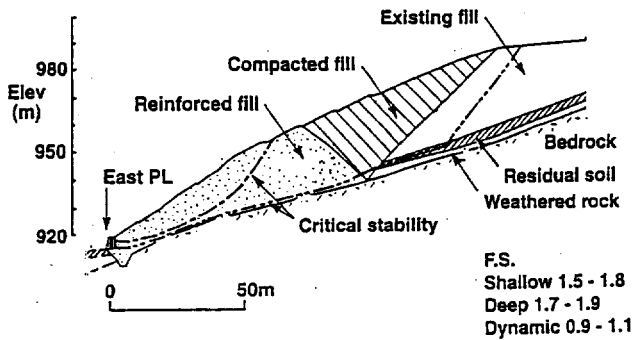


Figure 3 Calculated Stability for Reinforced Fill Buttress in Fill 2

However, design consideration was necessary to prevent a possible sliding surface from occurring on the interface between reinforced fill and bedrock, which would have been at the lower strength of the unreinforced fill. A means was devised to anchor the geogrid reinforced fill into the bedrock using "step cuts" into the weathered rock (below the decomposed rock). The need to "tie" the reinforced fill into the bedrock illustrated in Figure 4; the T_g force would have to be developed to bolster base friction is to prevent sliding along the bedrock surface.

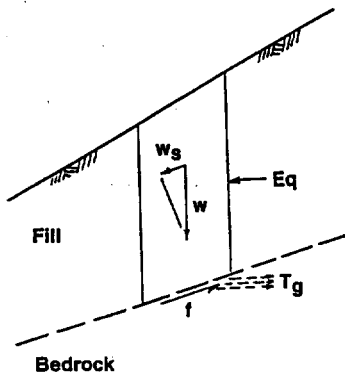


Figure 4 Sliding Block Model for Slope Stabilization

The necessary tension force from the geogrid was determined from the slope stability calculations as increments of load applied to bottoms of slope slices to hold the slice in place, thus supplementing base friction. The geogrid force, T_g , provides the increase in frictional

resistance to make up the 5 deg. difference in friction angle between the compacted unreinforced fill and the reinforced fill. This force was then converted into equivalent length of geogrid using reasonable grid spacings and applying the equation shown in Figure 5. The equation parameters were derived from FHWA (1989).

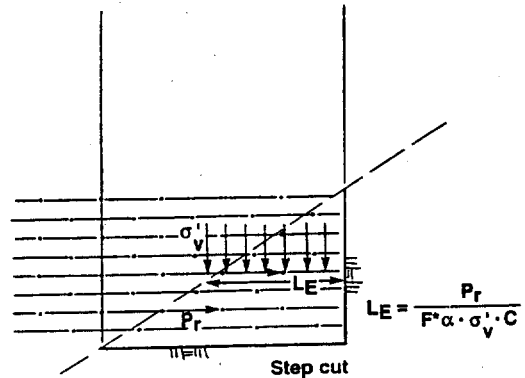


Figure 5 Model for Determining Embedment Length

The key feature to make the geogrid reinforcement effective was the use of "step cuts" into the top of bedrock, as shown in Figure 5. The width of the step cuts had to be long enough to engage the L_e of the geogrid. This was generally accomplished by limiting the height of cut to 2 m. since the slope of bedrock was relatively gentle, see Figure 3. The upper layers of geogrid in each step cut were less than fully effective, but this was taken into account in the overall stabilization design.

Further, the effectiveness of the engagement zone was enhanced by use of coarse to medium sand as a 1 m minimum thickness "slope drain" layer between the reinforced fill and bedrock. The slope drain contained less than 5% fines and is used to keep piezometric pressures from building up in the base of the reinforced fill. Although bedrock was not found to freely yield groundwater, infiltration over the life of the project from surface irrigation, rainfall, or the surface drainage system were considered possible sources which the slope drain would protect against. Leaks in drain pipe lines are considered possible given the seismic potential of the area.

The non-uniformity of the valley fills led to intricate zoning of the reinforced fills in design drawings. Typical sections of the fills are shown on Figures 6.a, 6.b and 6.c. In the Fill 3, the stability of the on-site fill was provided for with the arrangement shown in Figure 6.a. The Fill 3 section proceeded further downslope beyond the property limit, so the deeper overall stability of the valley fill could not be fully improved. However, the reinforcement provided makes the slope within the site secure against earthquake loadings.

At the sides of the Fill 3 valley, the soil fill was joined to the bedrock as shown in Figure 6.b, with a series of step cuts. Also of importance in the design of the geogrid

was the retained fill wall at the top of the slope which was designed as a geogrid supported precast concrete wall. Spacing of geogrid layers is shown on the cross-sections. At both locations above Fill 3, a retaining wall was constructed to achieve area needed for parking lots. The wall was designed to use pre-cast concrete panels supported by geogrids extended back sufficient distance for seismic loading conditions.

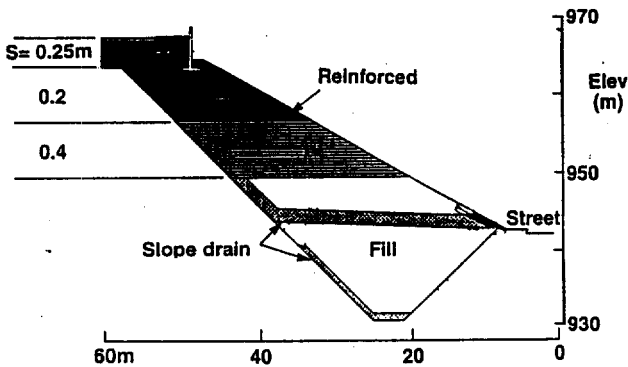


Figure 6.a Fill 3 Deep Buttress

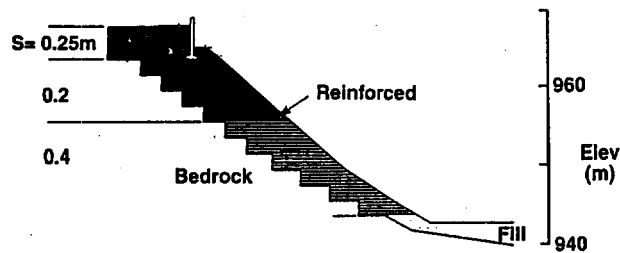


Figure 6.b Fill 3 Provisions for Fill over Rock Slope

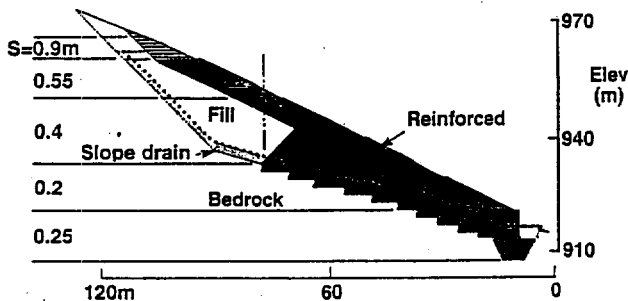


Figure 6.c Fill 2 Cross Section of Reinforcement

Fill 2 profile shown on Figure 6.c provides heavy reinforcement at the toe to create a buttress, with geogrids anchored in the step cuts. Further up the slope, reinforcement was provided only to provide stability of the

"surficial" slope, since the overall stability was sufficient with the large buttress formed in the bottom part of the slope. At the bottom of the Fill 2 slope, another retaining wall was provided for grade separation at the property line. It also will act as buttress in the event adjacent ground support is removed (by earthquake or excavation).

The contract documents set the following requirements for geogrid material:

Weight, per square m.	644 g/sq.m
Minimum Opening Size, in.	15.2 mm
Long-Term Allowable Design Load	14.6 kN/m
determined per GRI GG4 (1991)	

Material chosen by the Contractor was Mirafi 10 T. In limited areas around the building where small slopes were reinforced to provide 45 deg. inclinations, Mirafi 7 T was used, since the LTADL was less. To maintain landscape slopes adjacent to the building that were at 45 deg. inclinations stable against surface runoff, Geoweb cellular confinement system was installed and interconnected with the layers of geogrid.

Stabilization of the three large fills to provide site slopes, roads and parking areas that would be stable under the design earthquake conditions involved removal of deep fill, and reconstruction with geogrid reinforced backfill. At the time of installation in 1992-3, the more than 200,000 sq.m of geogrid used was the largest installation in South America. About 8,500 sq. m of cellular confinement was also installed.

ACKNOWLEDGMENTS

The Foreign Buildings Office of the U.S. Department of State supervised the design and construction of the Caracas embassy project, and their permission to publish this paper is gratefully appreciated. Project Architect was Gunnar Birkerts Associates of Birmingham, MI. Ammann and Whitney of New York City was the site civil engineer. General Contractor for the construction was Perini International, of Framingham, MA. Haley & Aldrich served as the geotechnical consultant for the project, including design of the geogrid system, and provided on-site geotechnical consultation during building foundation and geogrid installation during earthwork construction.

REFERENCES

Baligh, M. and Azzouz, A. (1975), "End Effects on Stability of Cohesive Slopes", Journal of the Geotechnical Engineering Division, ASCE, Vol. 101, No. GT11, Nov., pp. 1105-1117.

FHWA (1989), "Reinforced Soil Structures", Report No. 89-043, Vol. 1, Nov. 1989.

The Construction of Steep Reinforced Slopes in Hilly Terrain

C.R. Lawson
CEO, TC Nicolon Asia, Malaysia

T.W. Yee
Manager, TC Nicolon Asia, Malaysia

ABSTRACT: The flexibility of reinforced soil makes it an ideal solution for the construction of steep reinforced slopes in hilly terrain. However, due to the nature of hilly terrain, four major construction constraints can arise. These are the lack of a firm foundation on which to construct the reinforced slope; excavation instability or the occurrence of bedrock that limits the width of the base of the reinforced zone; the presence of groundwater emanating into the excavation from behind the reinforced zone; and the overall instability of the hilly terrain that limits the geometry of the reinforced slope. A parametric study was performed to evaluate the effect of these constraints on reinforced slope stability. Guidelines for maximising reinforced slope geometry, the role of drainage, and the modular approach to design are given for reinforced slopes constructed in hilly terrain.

KEYWORDS: Reinforced slopes, Hilly terrain, Construction constraints, Slope geometry, Drainage, Instability

1 INTRODUCTION

The use of reinforced soil as a technique to construct steep, stable slopes is a common practice. Today, much is known of the performance of reinforced soil slopes designed and constructed to "standard" geometries. Standard geometries include the presence of a flat, firm foundation beneath the reinforced slope; no limitations on the width of the reinforced zone for stability purposes; and no unusual loading regimes above the reinforced zone.

Reinforced soil is also an ideal technique for the construction of steep slopes in hilly, or mountainous, terrain. The technique results in a retaining structure that is flexible (i.e. it can undergo deformation without exhibiting structural distress) and highly cost-effective. This is important because the topography of hilly terrain dictates the adoption of significant earthworks structures, in some cases founded on suspect and unstable foundation materials. In addition, groundwater is normally present in this type of topography. This is particularly so in tropical climates where heavy rainfall can result in severe groundwater conditions. In this environment the construction of stiff, brittle structures is to be avoided.

In South East Asia, development effort is spreading from the coastal areas into the hinterland of many countries. For the majority of these countries, large areas of the hinterland consist of hilly and mountainous terrain. The overall topographical and geomorphological geometry of this terrain coupled with the need to maximise stable earthworks platforms for infrastructure and other development purposes results in reinforced slopes of significant magnitude. Slope heights over 20 m and slope angles greater than 60 degrees are not uncommon.

An example of such a reinforced slope, whose final height will be over 40 m, is shown in Figure 1 (it is currently at a height of 30 m). It should be emphasised that slopes of this magnitude require good construction quality. Two examples of good construction quality shown in this

example is the use of grass-impregnated soil bags for the slope facing and the use of tiered catchment drains for the collection of surface and subsurface water run-off. The use of grass-impregnated soil bags enables a stable slope face to be developed while at the same time promotes quick vegetation growth. The use of tiered catchment drains enables the quick removal of surface water run-off as well as being the exit drains for the subsurface drainage galleries within the reinforced slope.

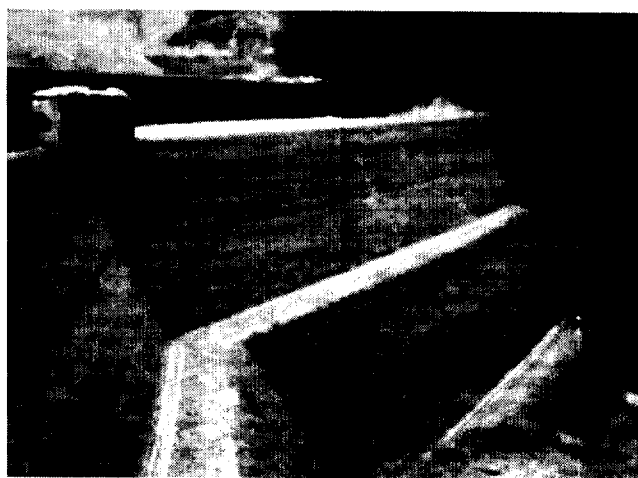


Figure 1. Example of a high, reinforced slope constructed in hilly terrain.

2 REINFORCED SLOPE CONSTRAINTS IN HILLY TERRAIN

The geomorphological and topographical nature of hilly, or mountainous, terrain poses considerable constraints on the design and construction of steep reinforced slopes. The general geomorphology is similar to that shown in Figure 2a where the terrain consists of a soil-filled slope overlying a dipping bedrock stratum. The soil-filled slope either has formed naturally or is the result of the dumping of earthfill

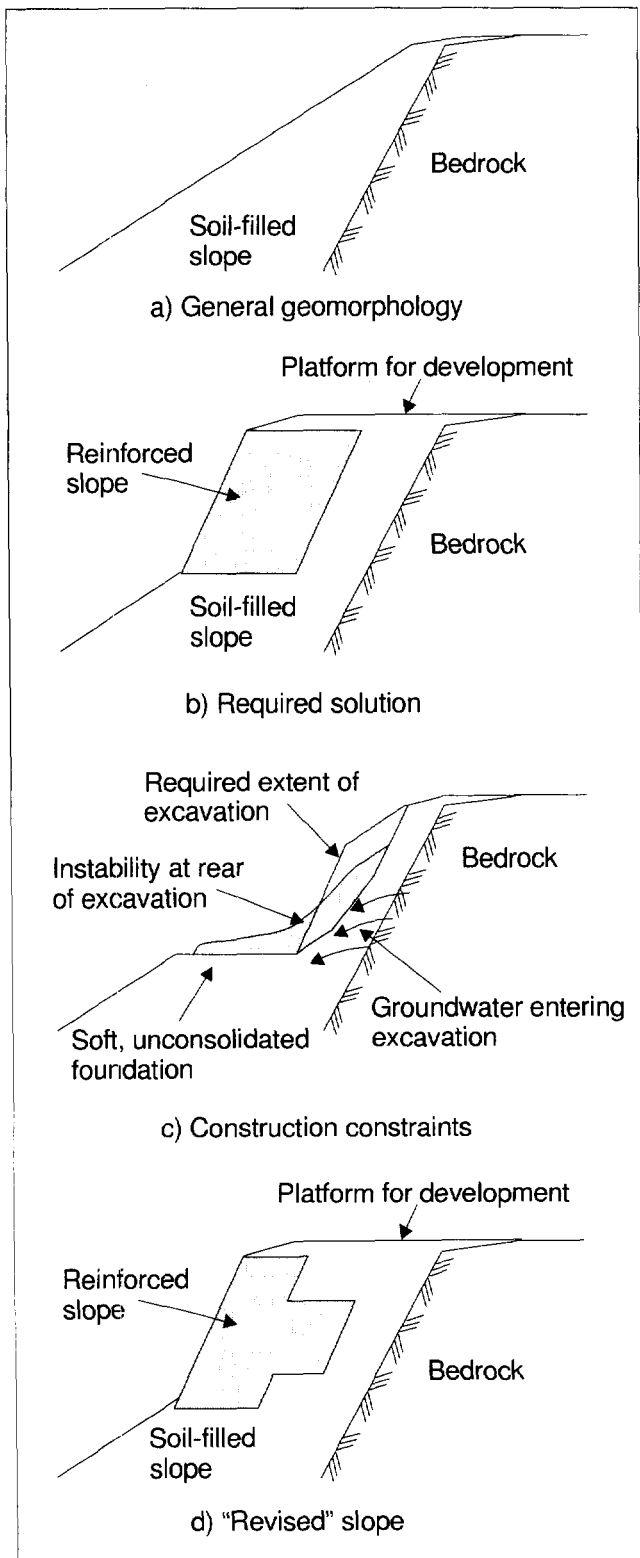


Figure 2. Constraints on construction of reinforced slopes in hilly terrain.

from nearby construction sites. In South East Asia these soils are normally saprolytic, residual or colluvial deposits. In many instances these soils are not compacted and

consequently exhibit relatively high hydraulic conductivities enabling easy penetration by groundwater.

When a reinforced slope of standard geometry is proposed for construction in this type of terrain (Figure 2b) a number of constraints may exist that considerably affects the final design geometry. These are (Figure 2c):

- The ability to excavate the soil-filled slope in order to provide an adequate base width for the reinforced slope. Slope instability at the rear of the excavation may limit the base width possible.
- The foundation at the base of the reinforced slope may be uncompacted and soft. This may constrain the geometry of the reinforced slope.
- The presence of groundwater during excavation of the soil-filled slope can promote slope instability at the rear of the excavation and can prevent the formation of a firm foundation beneath the proposed reinforced slope.

While each of the above constraints has a marked effect on the design geometry of the final reinforced slope it is impossible to foresee these events with any degree of certainty until construction is in progress. Consequently, in many instances it is necessary to carry out a revised reinforced slope design once the construction constraints are known. To accommodate these construction constraints the final design geometry of the reinforced slope may resemble that shown in Figure 2d.

The revised reinforced slope geometry shown in Figure 2d is not what one would consider a "standard" reinforced slope geometry inasmuch as:

- The foundation surface dips down from the toe of the reinforced slope and is not horizontal.
- The foundation may not be firm but may be soft and compressible.
- Instability at the back of the excavation limits the width of the reinforced zone at the base of the reinforced slope.
- The presence of the bedrock stratum may limit the extent of the reinforced zone and may concentrate shear stresses behind the reinforced zone.

Because of the above features, the use of design procedures based on "standard" geometries is only of limited use. When establishing an appropriate, safe geometry for the required reinforced slope all of the above features need to be considered. Because of some of the unusual topographical and geomorphological features involved in hilly terrain it is important to have an understanding of their effect on the resulting geometry of the reinforced slope. This is especially the case where required reinforced slope heights are to be maximised.

Table 1. Geotechnical parameters used in the parametric study.

	Reinforced soil	Foundation soil			Backfill soil	Bedrock
		Firm	Moderate	Soft		
Bulk density (kN/m ³)	18	18	16	15	18	22
Friction angle (°)	35	35	32	30	35	45
Cohesion (kPa)	150	150	20	10	10	5,000
Bulk modulus (MPa)	115	115	65	15	85	20,000
Shear modulus (MPa)	70	70	40	10	50	15,000

3 PARAMETRIC STUDY

To evaluate the effect of various geometric and material parameters on the stability of reinforced slopes in hilly terrain a parametric study was performed. It was considered that the boundaries of external stability were important aspects that required assessment for reinforced slopes constructed in hilly terrain. In addition, stresses and deformations were also considered important parameters for investigation. Because of the specific nature of this type of terrain and the need to evaluate the effect of foundation compressibility as one of the aspects of reinforced slope stability, it was concluded that a sophisticated modelling procedure would be required. Consequently, the parametric study was performed using a continuum method approach (FLAC 1995).

3.1 Slope Geometry Analysed

A slope geometry indicative of that encountered in hilly, or mountainous, terrain was used as a basis for the parametric study. This is shown in Figure 3. The reinforced zone has variables H , L and β .

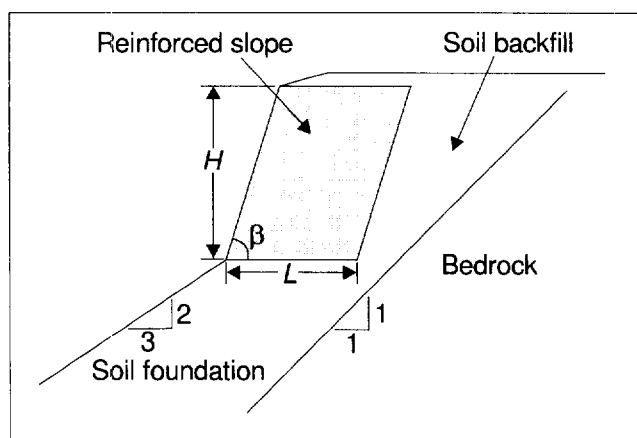


Figure 3. Reinforced slope geometry used in the parametric study.

A bedrock stratum, on a 1:1 dipping plane, is present near the heel of the reinforced zone. The presence of this bedrock stratum concentrates shear stresses within the backfill zone behind the reinforced zone, thus accelerating a potential global failure mode. The location of the bedrock stratum also restricts large vertical deformations at the heel

of the reinforced zone. This condition is considered common in hilly terrain.

The reinforced zone is seated on a soil foundation with a surface slope of 3:2 (34° to the horizontal). This slope angle is close to the natural angle of repose for various soil types and is considered common in hilly terrain.

3.2 Material Parameters Used

The various geotechnical parameters used in the study are listed in Table 1. The soil in the reinforced zone was assumed a compacted cohesive-frictional fill indicative of the saprolytic, residual and colluvial soils found in South East Asia. In the reinforced zone, the reinforcement was modelled by means of an additional apparent cohesion within the compacted soil. To ensure the maintenance of internal stability within the reinforced zone the layers of reinforcement would have to impart an apparent cohesion of 130 to 140 kPa according to the method proposed by Hausmann (1976). Consequently, a total cohesion of 150 kPa was assumed for the reinforced zone.

Three different foundation soil conditions were adopted for the parametric study – firm, moderate and soft (see Table 1). Standard design methods for reinforced slopes always assume a firm foundation beneath the reinforced slope. While never specifically stated, a firm foundation can be assumed to be one where it is impossible for a bearing failure to occur, or where another type of external instability occurs before the onset of bearing failure. For the parametric study, the firm foundation has been given the same properties as the reinforced zone. This was done to ensure that foundation failures beneath the reinforced zone could not occur, given the specific geometry of the problem. With a foundation having these properties the only external failure modes are global, sliding, compound or overturning instability.

The soft foundation soil parameters listed in Table 1 may be considered indicative of loosely placed soil or fill. While not implicit, groundwater may be also present within the loose fill.

The moderate foundation soil parameters are considered indicative of naturally deposited soil without any form of densification carried out. This is considered to be the most prevalent type of foundation condition encountered in hilly terrain in South East Asia.

It has been assumed that the soil backfill consists of compacted local soil taken from the excavation of the

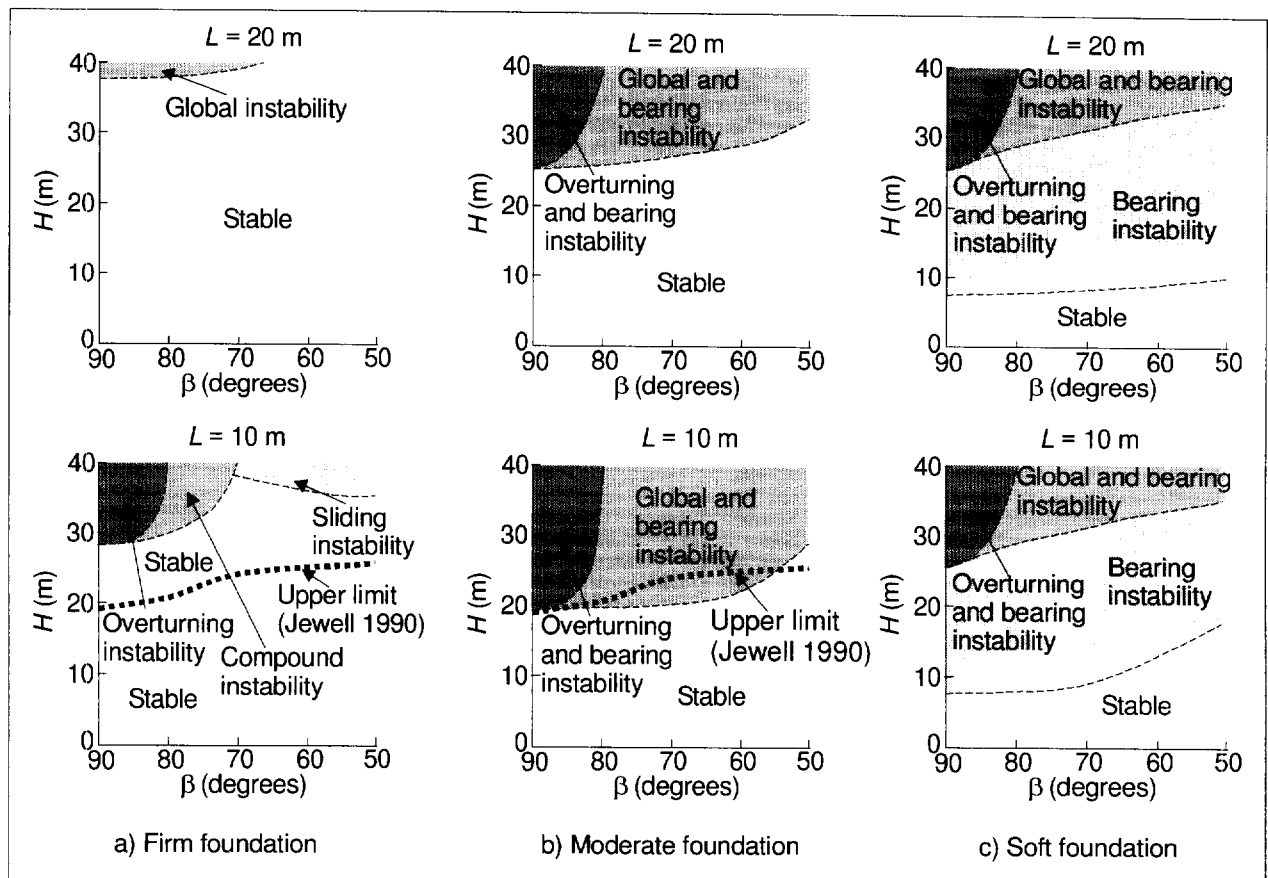


Figure 4. External stability boundaries for reinforced slopes constructed according to the geometry shown in Figure 3.

reinforced slope. The bedrock is an incompressible stratum that cannot fail internally.

For the parametric study, a reinforcement layer was included at the base of the reinforced slope. The inclusion of this layer was not to enhance the internal stability of the reinforced zone but to determine what additional tensile loads are exerted on the base reinforcement layer, given the different foundation conditions and potential failure modes occurring. In addition to the base reinforcement layer a horizontal interface was included between the reinforcement layer and the surface of the soil foundation. This interface layer was given a bond coefficient $a' = 0.7$ which, while being lower than expected for modern geosynthetic reinforcements, would be considered to provide conservative (i.e. safe) stability solutions.

A second interface was included between the compacted backfill and the rear of the reinforced zone. For this interface a bond coefficient of $a' = 1.0$ was used for all cases.

3.3 External Stability Boundaries for Reinforced Slopes

From the parametric study it was possible to determine the boundaries of acceptable external stability for reinforced slopes analysed according to the geometry shown in Figure 3. Figure 4 contains plots of regions depicting stable and unstable behaviour for the cases of reinforcement length L

$= 10$ m and $L = 20$ m and for firm, moderate and soft foundation conditions.

For the firm foundation case, Figure 4a, and for reinforcement length $L = 20$ m global instability begins at around 40 m height for the reinforced slope. Global instability occurs along the boundary of the bedrock stratum (see Figure 3). "Standard" design methods such as the chart method proposed by Jewell (1990) would indicate that significantly higher slopes were possible for $L = 20$ m, however, these methods cannot take into account the geomorphological features shown in Figure 3. For the reinforcement length $L = 10$ m case shown in Figure 4a external instability can be induced by overturning, compound or sliding depending on the reinforced zone geometry. The calculated upper limit according to Jewell (1990) has also been plotted. The results show that an additional slope height of 8 to 10 m can be adopted compared to that calculated using "standard" design methods.

For the moderate foundation case, Figure 4b, and for reinforcement length $L = 20$ m the onset of external instability occurs around 25 to 30 m in height depending on the slope angle. The onset of global and bearing instability occurs before other forms of instability, e.g. sliding, etc. Comparison with the firm foundation case shown in Figure 4a shows the effect of the change in foundation properties on the achievable reinforced slope geometry. For the

reinforcement length $L = 10$ m case shown in Figure 4b external instability is also induced by global and bearing but (as expected) at a lower slope height than for $L = 20$ m. The calculated upper limit according to the design charts of Jewell (1990) has also been plotted. The results show that there is fair agreement, however, this is considered to be by chance as “standard” design methods cannot account for bearing instability, which is the major mode of instability in this case.

For the soft foundation case, Figure 4c, and for reinforcement length $L = 20$ m the onset of external instability occurs around 8 to 10 m in height depending on the slope angle. As to be expected the dominant mode of instability is bearing failure. For the reinforcement length $L = 10$ m case shown in Figure 4c external instability is also induced by bearing failure at comparable slope heights to the $L = 20$ m case.

3.4 Vertical Stress at Base of Reinforced Slope

The vertical stress acting across the base of the reinforced slope was also recorded from the parametric study. This stress was derived in the form of a vertical stress ratio (VSR), being:

$$VSR = \frac{\sigma'_{vb}}{\gamma H} \quad (1)$$

where: σ'_{vb} = vertical stress along the base of the reinforced slope; γ = bulk density of the soil in the reinforced slope; and H = height of the reinforced slope.

While the vertical stress at the base of the reinforced slope varies across the width of the reinforced zone, for simplicity, the vertical stress ratio at the toe of the slope (VSR_{toe}) and at the heel of the slope (VSR_{heel}) were the only two locations recorded.

Figure 5 shows the results obtained for the firm foundation case. At the toe of the reinforced slope (Figure 5a) VSR_{toe} ranges from 1.2 to 0.35 according to slope angle and H/L ratio. For slope angles greater than 75° $VSR_{toe} \geq 1.0$. This is consistent with retaining wall theory. For slope angles less than 75° $VSR_{toe} < 1.0$, the value reducing as the slope angle reduces. At $\beta = 75^\circ$, $VSR_{toe} = 1.0$.

At the heel of the reinforced slope (Figure 5b) the magnitude of VSR_{heel} is greatly dependent on the H/L ratio of the slope. Relatively high values of VSR_{heel} are obtained for $H/L = 0.5$. The reason for this is the effect of the development of full friction between the reinforced zone and the soil backfill. This effect reduces as the slope angle reduces. For $H/L = 1.0$ there is still some effect of backfill friction giving $VSR_{heel} > 1.0$ for slope angles greater than 55° . For $H/L \geq 1.5$ the effect of backfill friction is negligible and consequently, $VSR_{heel} = 1.0$ for slope angles greater than 65° .

Figure 6 shows the results obtained for the moderate foundation case. In general, the results are similar to those

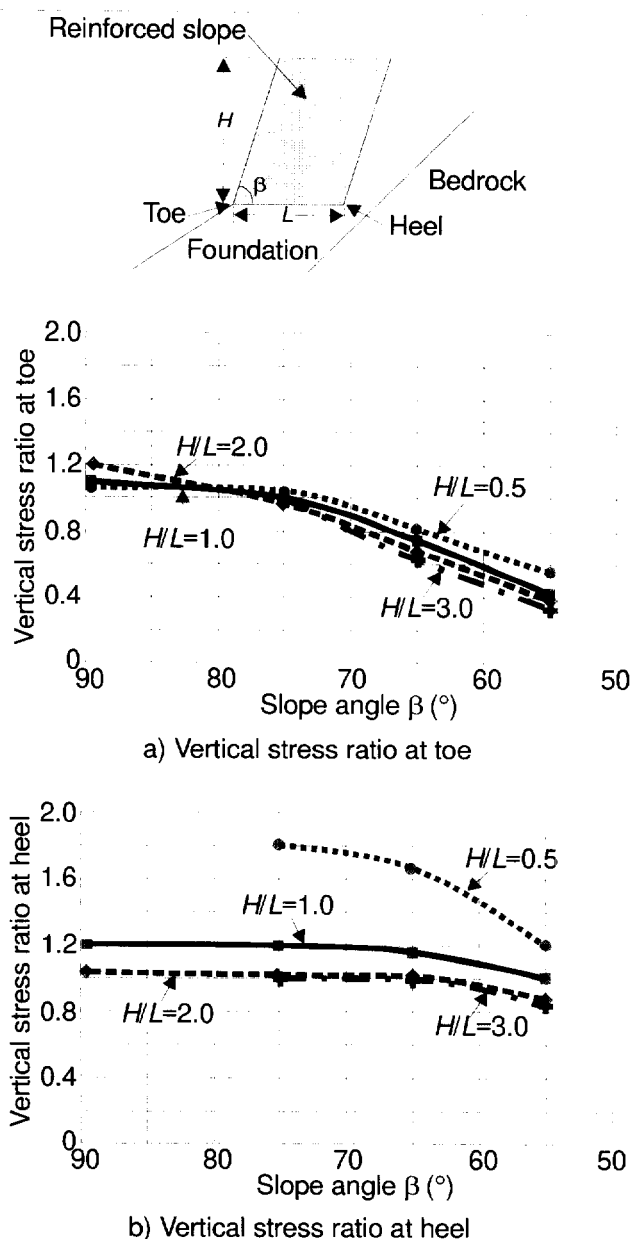


Figure 5. Vertical stress ratio at the base of the reinforced slope for the firm foundation case.

presented in Figure 5 for the firm foundation case. However, the moderate foundation, being more compressible than the firm foundation, enables a more uniform stress distribution to develop across the base of the reinforced zone than is the case with the firm foundation. Consequently, the curves plotted in Figure 6 show more agreement between the VSR_{toe} and VSR_{heel} values than is the case for the firm foundation.

3.5 Additional Load in Reinforcement at Base of Reinforced Slope

Standard design methods that assume the presence of a firm foundation calculate reinforcement loads according to

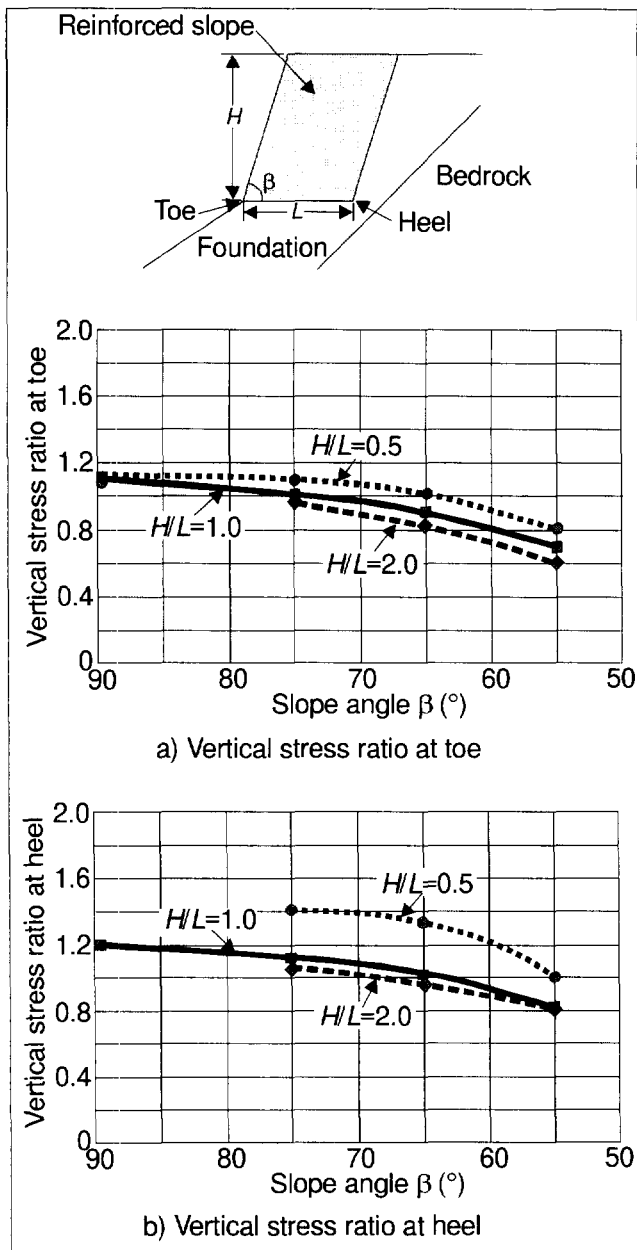


Figure 6. Vertical stress ratio at the base of the reinforced slope for the moderate foundation case.

internal stability requirements only. However, in situations where the foundation is compressible additional tensile loads may be imparted to the reinforcements as the reinforced slope deforms. These additional tensile loads would be a maximum at the base of the reinforced slope. The parametric study was also used to calculate the magnitude of these additional tensile loads imparted to the reinforcement layer at the base of the reinforced slope.

Table 2 contains a summary of the results obtained. It is noted that for stable conditions the additional loads imparted to the base reinforcement layer are relatively small and may be neglected for all cases except the soft foundation case. For the soft foundation case the additional loads are greatest, at around 10 kN/m. For most reinforced

slope applications the design loads carried by the reinforcements are between 30 and 60 kN/m. Thus, only for soft foundation conditions would the additional reinforcement load be significant.

Table 2. Additional reinforcement load at base of reinforced slope due to different foundation conditions.

Foundation	Additional reinforcement load	
	Stable conditions	Onset of instability
Firm	≈ 1 kN/m	≥ 20 kN/m
Moderate	≈ 3 kN/m	≥ 30 kN/m
Soft	≈ 10 kN/m	≥ 40 kN/m

However, at the onset of instability the additional load applied to the base layer reinforcement increases significantly, even for the firm foundation case. This increase in reinforcement load should provide added incentive to ensure that reinforced soil slopes do not approach external instability as the additional loads applied to the base layer reinforcements could lead to their premature rupture with subsequent collapse of the structure.

4 THE ROLE OF DRAINAGE

The influence of good drainage on the performance of reinforced slopes constructed in hilly terrain should not be underestimated. This is especially the case in wet, tropical climates where significant flows of surface and subsurface water can occur. In these environments well- designed and constructed drainage systems are essential and should be considered an integral part of reinforced slope design and construction.

Water may penetrate the constructed slopes in two ways – as groundwater flow from the existing undisturbed deposits behind the slopes, and as surface water run-off due to rainfall. To accommodate these events a recommended drainage layout is shown in Figure 7.

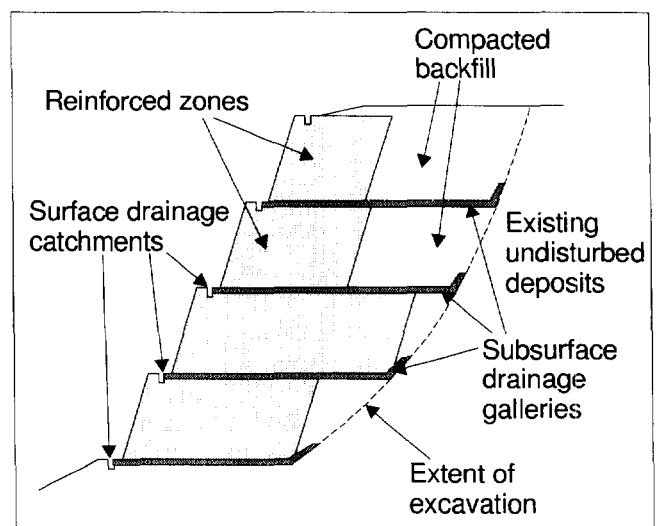


Figure 7. Recommended layout of drainage system within high, reinforced slopes.

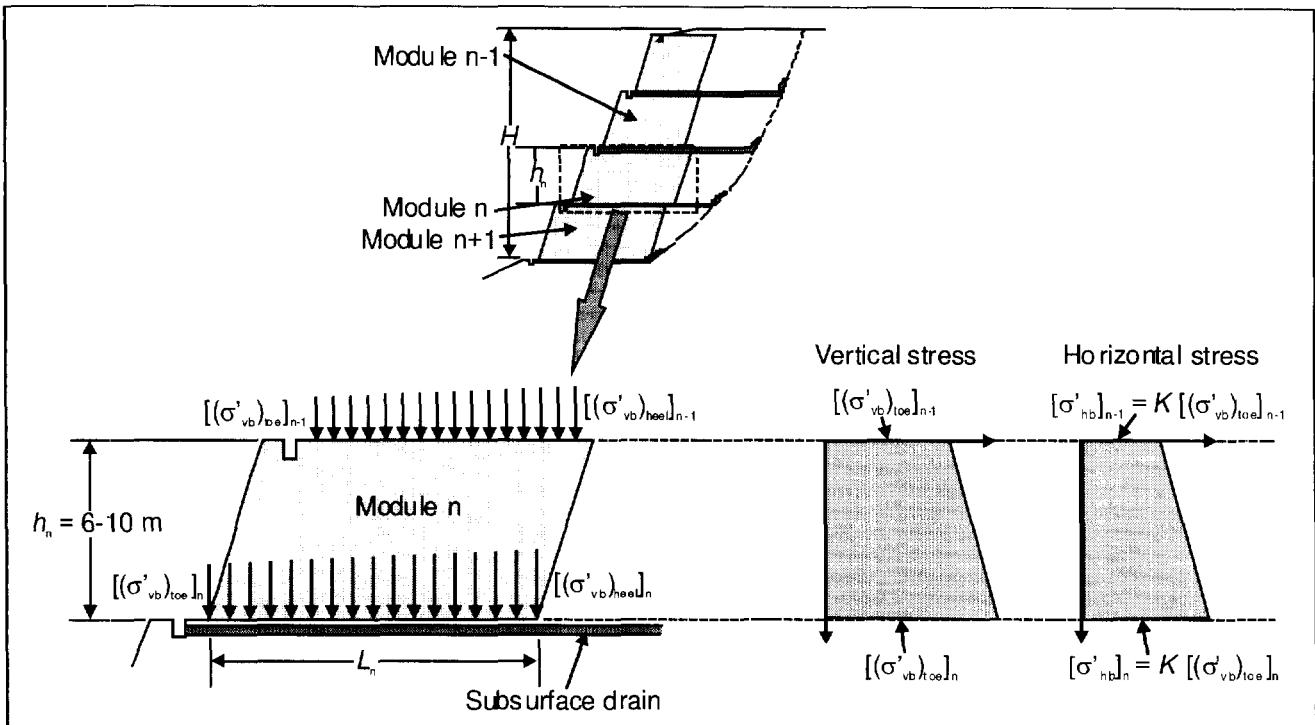


Figure 8. Modular approach to the design of steep reinforced slopes.

To ensure the effective removal of groundwater from behind the constructed slope subsurface drainage galleries should be constructed within the fill zone, preferably at every tier level in the reinforced slope. Since the compacted backfill material is normally the same material as that excavated at site, when replaced and compacted it exhibits significantly less hydraulic conductivity than the adjacent undisturbed deposits. Consequently, to remove the groundwater effectively it is essential that the subsurface drainage galleries be extended beyond the compacted backfill zone to interface with the existing undisturbed deposits. The subsurface drainage galleries can be of the form of drainage blankets or feeder drains. The materials used for the drains are normally small aggregates (for drainage) with geotextile filters. The outlets of the subsurface drainage galleries extend beneath the reinforced soil zones and exit within the surface catchment drains at the toes of the reinforced slope tiers.

If the excavated soil is suitable it is normally used with the geosynthetic reinforcement to construct the reinforced soil zones. This is common practice in South East Asia where the saprolitic, residual and colluvial soils exhibit good shear resistance when combined with geosynthetic reinforcement. The use of the locally available soil also provides the most economical solution. When these soils are compacted to form the reinforced zones it is difficult for surface water to penetrate these fills especially when one considers the nature of the surface geometry of steep slopes. Consequently, surface water damage is normally confined to surface erosion. To protect against surface erosion, open catchment drains should be constructed at the toe of each reinforced zone tier to prevent excess surface

run-off, Figure 7. To prevent surface soil loss it is normal practice either to use an erosion control mat on the surface of the slope or to use grass-filled soil bags. Grass-filled soil bags are normally used for the steeper reinforced soil slopes.

5 MODULAR APPROACH TO DESIGN

The design of steep reinforced slopes in hilly, or mountainous, terrain lends itself to a modular approach inasmuch as the reinforced slope can be divided into similar regions, or modules, within the height of the reinforced slope. Each module can be assessed for internal stability as well as sized appropriately to ensure external stability of the whole reinforced slope. A modular approach to design also enables added flexibility in the sizing of the individual modules, standardisation and simplification of the reinforced soil components within each module, and the ability to readily re-size specific modules if construction conditions are not the same as assumed during the design phase.

Figure 8 shows the general basis for the modular design approach. The reinforced slope is designed as a series of reinforced soil modules. Each module consists of its reinforced soil zone along with its associated integral drainage system. Each reinforced soil module can be 6 to 10 m in height, but is more commonly 6 to 8 m. During construction, it is common practice to step-back the face of each succeeding module between 1 to 1.5 m. This enables enough space for the construction of the surface catchment drain.

The length of each module, L_n in Figure 8, needs to be assessed with regard to the maintenance of internal and external stability. The results shown in Figure 4 may be used as a basis for the assessment of external stability.

The internal stability of each module is assessed by plotting the horizontal stress distribution through the module and ensuring that there is adequate reinforcement capacity to resist the horizontal stresses. The procedure used to determine the horizontal stress distribution through each module is shown in Figure 8. First, the vertical stress distribution at the top and the base of each module is determined, e.g. by using the results in Figures 5 and 6. Second, the vertical stress distribution through each module can then be determined using the vertical stress at the toe of each module as the basis. Third, the horizontal stress distribution can then be determined by adopting an appropriate value of K , the ratio of horizontal to vertical stress. Values of K as proposed by Jewell (1990) may be used. Checks for adequate reinforcement bond capacity can be performed by deriving a vertical stress distribution through each module based on the vertical stress at the toe and the heel of each module.

6 CONCLUSIONS

The paper has concentrated on a specific, but important, aspect of reinforced slopes – that of their construction in hilly, or mountainous, terrain.

While the use of “standard” design methods may be appropriate for assessing the internal stability of reinforced slopes constructed in this type of terrain, their use for assessing the overall dimensions of the reinforced zone for external stability purposes is not appropriate. Specific aspects such as local topography and geomorphology, as well as foundation conditions need to be considered, and these can result in significantly different solutions compared with those solutions provided using standard design methods and charts.

Good drainage should form an integral part of any reinforced slope design in hilly terrain, especially in tropical climates where high rainfall is prevalent. Attention to the controlled removal of both surface and subsurface water is crucial for good performance.

A modular approach to the design of steep reinforced slopes offers a number of advantages over the conventional approach of considering the reinforced zone as one single mass. Its major benefit lies in the flexibility of being able to consider the reinforced slope as separate regions (modules) that can be sized according to their location in the slope, and reinforced according to the magnitude of the vertical stresses acting at the top and the bottom of each module. The modular approach enables a number of the components of reinforced slope design to be standardised, and allows the slope geometry to be easily adjusted according to local construction conditions.

REFERENCES

- FLAC (1995) *Fast Lagrangian Analysis of Continua*, Itasca Consulting Group, Version 3.3.
- Hausmann, M.R. (1976) “Strength of Reinforced Earth”, *Proceedings Eighth Australian Road Research Conference*, Vol.8, Section 13, pp. 1-8.
- Jewell, R.A. (1990) “Revised Design Charts for Steep Reinforced Slopes”, *Reinforced Embankments, Theory and Practice*, Thomas Telford Ltd, UK. pp. 1-30.

Case Study. Bluewater Retail & Leisure Destination - Major reinforced soil slopes to form steep sided new lakes.

J.H. Dixon

Tensar International Ltd, New Wellington Street, Blackburn, UK

ABSTRACT: Bluewater is a new £360M (\$580M) retail and leisure destination located in a former chalk quarry in England. Enabling Works involved bulk filling and the formation of a number of lakes. Two of these lakes were formed with slopes at 70° to the horizontal, about 10m high, and which in places were surcharged with highway embankments. Lakes 1 and 2 were constructed with several hundred linear metres of reinforced soil slopes, incorporating high density polyethylene uni-axially oriented geogrids. Lake 1 was also lined with a geomembrane which, to avoid damage could not be placed on or near the slope face. The geomembrane was therefore located underneath and behind the rear face of the reinforced soil block. This detail posed unusual design considerations involving sliding stability and the analysis of a number of load cases for different combinations of water level. The design and construction of these lakes including three innovative facing details are discussed.

KEYWORDS: Geogrid, Steep slope, Reinforced embankment, Geomembrane lake liner.

1 INTRODUCTION

Bluewater, developed by Lend Lease is located approximately 30km east of London. On completion, in March 1999, it is intended to be the largest and most prestigious retail development in Europe, containing 140,000m² of retail space, 13,000 car parking spaces, nearly 12,000m² of leisure space and with a million trees and shrubs landscaping the area.

The site is located in a former deep chalk quarry. The construction of several lakes was included within an Enabling Works contract which principally involved bulk filling with approximately 3M m³ of a local silty sand. Two of the lakes, Lakes 1 and 2, were formed with steep sides in order to maximise their water volume and depth for environmental reasons.

Lake sides sloping at 70° to the horizontal and approximately 10m high were selected. In places these slopes were to be surcharged by highway embankments and landscaping fill under a later contract. The Client's Consulting Engineer, Waterman Partnership, recognised at an early stage the economic and practical advantages of reinforced soil techniques.

As the ground water level was known to vary significantly it was decided to line Lake 1 with a geomembrane in order to retain a constant lake water level. There were concerns about the long-term durability of the geomembrane and in particular its vulnerability to potential damage from burrowing wildlife or boat impact if it were placed on, or close to, the slope surface. It was therefore decided to locate it underneath and up the rear face of the reinforced soil block.

2 REINFORCED SOIL DESIGN

2.1 Outline Design Brief

The Engineer invited Tensar International Ltd to assist with specialist design support in developing the reinforced soil design beyond the concept stage.

Lake 1, with the geomembrane lining located below the reinforced soil block, presented two unusual reinforced soil design challenges:

- The potential for sliding of the reinforced soil block over the geomembrane.
- The combination of the large number of possible water levels (within both the lake and the external ground) and various imposed loadings conditions, phased with the subsequent highway and landscaping contracts.

Furthermore, the design brief called for a low-cost durable face with a 120 year life and high security against wash out of the fill.

2.1.2 Basic Design Parameters

The fill which was to be sourced from an adjacent quarry was a silty fine sand (Thanet Sand). Its design parameters were:

$$\phi'_{cv} = 31^{\circ}, c' = 0, \gamma_{opt} = 19.3\text{kN/m}^3 \text{ and } \gamma_{sat} = 20.2\text{kN/m}^3$$

A series of 30cm x 30cm laboratory shear box tests was commissioned to measure the frictional shearing resistance between the various specified geosynthetic materials and this fill.

The selected lining system was 1mm thick modified low density polyethylene (LDPE) geomembrane protected by a 700g/m² polypropylene needle punched geotextile. The critical interface shearing angle (ϕ_{is}) for this combination was measured at 20° .

Two strengths of high density polyethylene (HDPE) geogrid reinforcement were selected; Tensar 40RE (Type 1) and Tensar 80RE (Type 2). These are manufactured from extruded sheets and orientated (stretched) in the machine direction. Their Index QC strength in the longitudinal direction is 40kN/m and 80kN/m respectively and rib thicknesses (t_f) 0.7mm and 1.3mm and (t_b) 1.9mm and 3.6mm respectively (Figure 1). Shear tests on these two grid types with the chosen fill material indicated friction angles in excess of 26° (i.e. a coefficient of soil interaction $\mu > 0.8$).

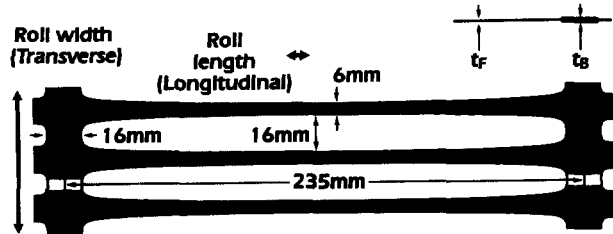


Figure 1 Geometry of the grid reinforcement

2.2 External Stability

The shear box testing confirmed that a critical potential failure mechanism for Lake 1 was sliding over the geomembrane lining system. It was therefore decided to incline the lining at an angle α of approximately 5° below the reinforced soil block (This equated to a fall of 1.5m from toe to heel over the width of the block).

The basal reinforcement layer remained horizontal and was positioned a minimum distance of 100mm above the lining system at the face. This ensured that the critical interface frictional value would not be further reduced.

The factor of safety against sliding over the inclined geomembrane was calculated by resolving forces about the geomembrane (Figure 2).

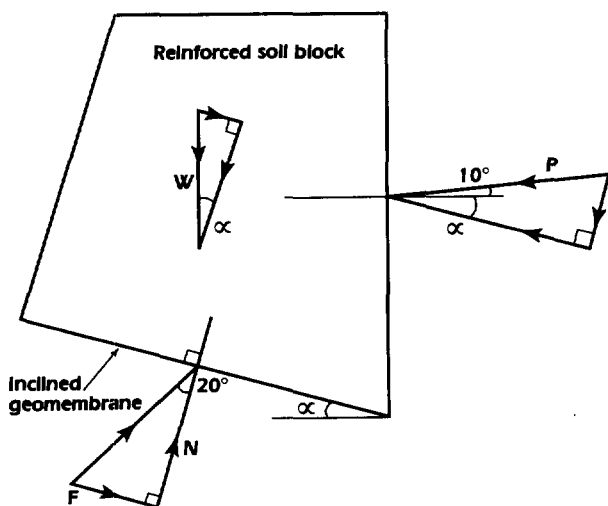


Figure 2 Force resolution on reinforced soil block.

Note: the net mobilising force (P) is assumed to act on an angle to the rear of the reinforced soil wall = $\frac{1}{2} \times \phi'_{ls}$. W = weight of the reinforced soil block and F and N are the frictional and normal forces acting on the inclined geomembrane.

By resolving forces perpendicular to the geomembrane:

$$W \cos \alpha + P \sin (10^\circ + \alpha) = N \quad (1)$$

By resolving forces parallel with the geomembrane:

$$F = N \tan 20^\circ \quad (2)$$

$$FoS = \frac{F + W \sin \alpha}{P \cos (10^\circ + \alpha)} \quad (3)$$

$$FoS = \frac{[W \cos \alpha + P \sin (10^\circ + \alpha)] \tan 20^\circ + W \sin \alpha}{P \cos (10^\circ + \alpha)} \quad (4)$$

Where FoS = Factor of Safety against sliding over the lining system. (i.e. the resisting force divided by the sliding force).

FoS for design was specified as 1.5 for the temporary condition and 2.0 for the completed works. Figure 3 shows the cross section through the north side of Lake 1 and the particular loading condition which was found to be critical for sliding stability i.e. the condition prior to the placement of landscaping fill and with the lake water level lower than its final design level.

The width of the reinforced soil block is dimensioned to provide sufficient weight (W) to satisfy FoS.

Lakes 1 and 2 were also checked for other external stability conditions, including sliding over the reinforcement.

2.3 Internal Stability

The specialist designer's experience of other reinforced soil structures with a similar geometry was that design principles based on the German Institut für Bautechnik (DIBt) would produce a stable and economical solution. Internal stability calculations take the form of a two-part wedge analysis through the reinforced soil block. A series of two-part wedges are examined with the lower part of the wedge originating at the structure face and passing through the block, and the upper part of the wedge passing up the back face of the reinforced soil block. The active pressure, above that point where the lower part of the wedge cuts the back face of the reinforced soil block, is added to the disturbing forces acting on the two-part wedge to give the total disturbing force. In the case of internal stability, the resultant active

force is taken to act on angle equal to the friction angle of the soil block rear face.

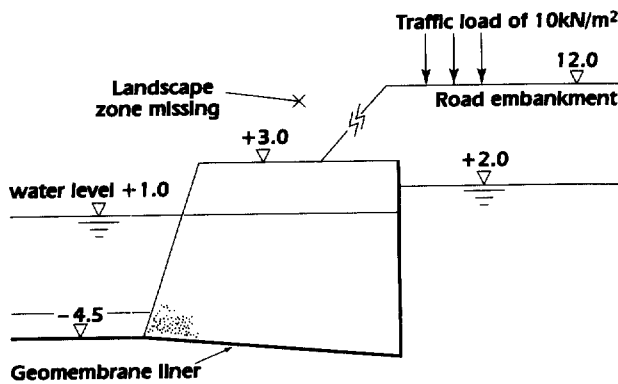


Figure 3

Reinforcement must be provided to resist the disturbing force on each two-part wedge by intercepting the wedge being considered. The two-part wedge stability calculation should be carried out from the toe of the structure, the bottom grid layer, at all levels where the grid spacing alters and at every level where the grid type alters.

The reinforcement design strength is obtained from the creep-limited strength appropriate to the design life and in-soil temperature. Specific partial factors are then applied to take account of such factors as installation damage. Finally, an overall FoS = 1.75 is applied to the strength.

The reinforcement layout was derived by analysis with lower part wedge angles (θ) set at 3° intervals (Figure 4) using the specialist designer's computer program - Winwall. (Tensar International, 1995)

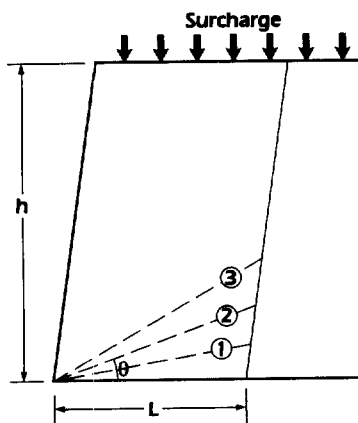


Figure 4 Two-part wedge analysis.

For Lake 1, the critical condition for internal stability was identified as the completed structure fully landscaped under the rapid 'draw-down' condition with the lake empty (perhaps during a future maintenance operation) and the backfill behind the reinforced soil block fully saturated. A typical reinforcement layout for the north side of Lake 1 is shown in Figure 5. The maximum vertical reinforcement spacing was set at 60cm.

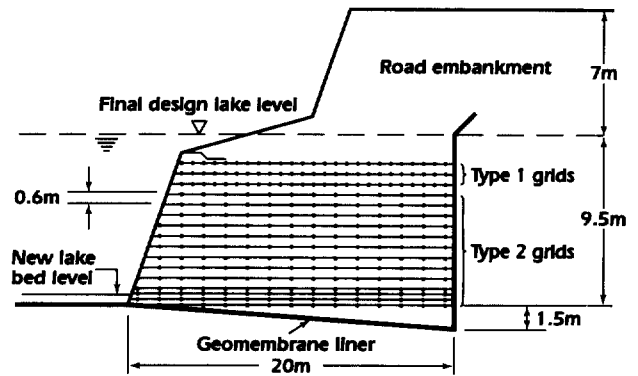


Figure 5 Typical reinforcement layout.

Note: The road embankment (part of a later contract) was constructed using reinforced soil.

2.4 Face Detail

The face of the reinforced slopes had to be relatively inexpensive while possessing high durability and damage resistance. The Engineer ruled out a proprietary segmental concrete block face on the grounds of cost, and instead selected a geogrid wrap-around face. With this detail, the horizontal reinforcement layers are extended up the temporarily supported face of the fill and then returned back horizontally and connected with a full-strength joint to the next layer of reinforcement. There was sufficient information on the durability of the specified grids to satisfy long-term serviceability questions (Wrigley, 1987).

The face also had to remain permeable and retain the silty sand fill. Attention was therefore focused on the selection of a geotextile filter to line the wrap-around face. It was recognised that any damage or malfunction of this geotextile could lead to a steady wash out of fines and ultimately to collapse.

Netlon 1004R geotextile was specified. It has independent certification from the German Federal Waterways Authority (BAW) based on rigorous performance testing with a range of soils including silty sand. These tests assess:

- filter performance by filtering a real soil in turbulent conditions and also examining the resultant permeability after impregnation with soil particles.
- residual tensile strength following exposure to abrasion (16 x 5000 revolutions of a rotating drum containing gravel and water).
- puncture resistance in a test replicating rock armour units being dropped on a soil supported sample.

This non-woven geotextile is manufactured by needle punching two separate geotextiles, one containing staple (short) fibres of polypropylene and the other, a polyester, to create an integrated 800g/m² duplex material. This efficient double layer arrangement provides a coarse fibre pre-filter which, additionally, interacts with the soil to achieve a degree of mechanical stabilisation of soil particles which may otherwise be prone to migration.

Despite this certified evidence of the geotextile's robustness and field experience with similar products under extremely severe test conditions (Dixon et. al, 1990), the Engineer was concerned about its vulnerability to damage e.g. from accidental impact, burrowing animals, nesting birds and long term exposure to ultra violet (UV) radiation.

The Engineer, therefore, specified an outer grid wrap-around face retaining a 15cm wide layer of 5 - 10cm sized hard durable fill as cover protection to a geotextile wrap-around local to the face of the silty sand fill (Figure 6).

With the specified grids it is possible to create a full-strength connection between adjacent lengths using an HDPE bodkin (Figure 7). In a wrap-around detail this bodkin provides a more positive joint than simply relying on a frictional anchorage. Furthermore, when the higher grid length is tensioned during installation this helps pull the lower wrap-around face tight.

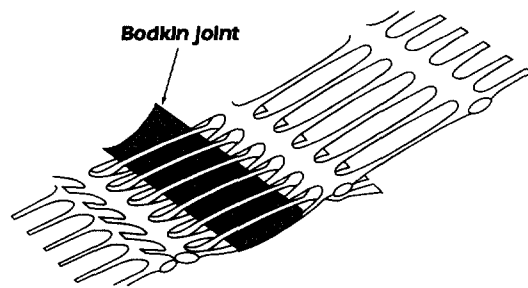
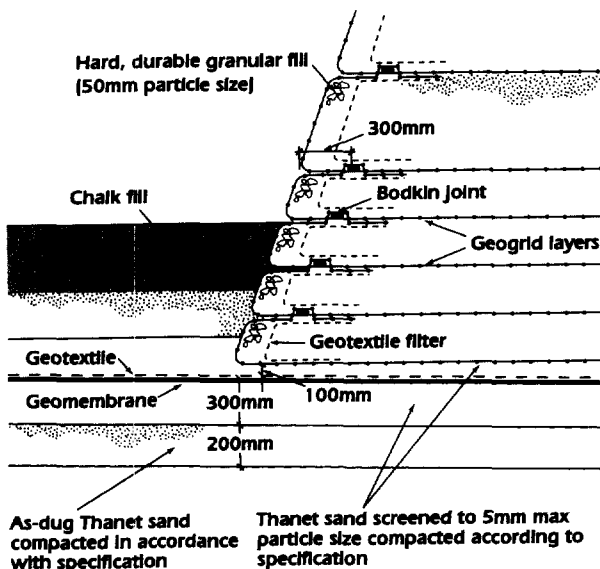


Figure 7

3 CONSTRUCTION

3.1 Contract Award

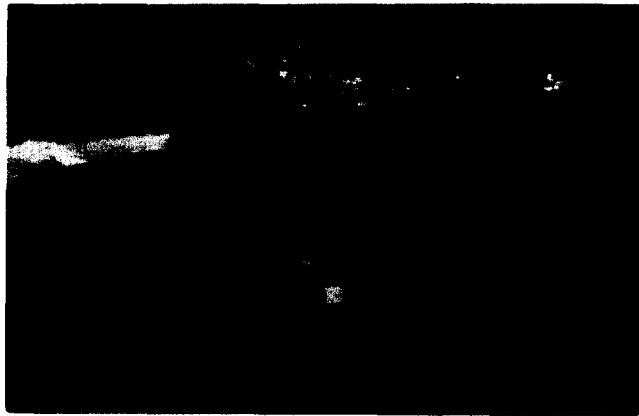
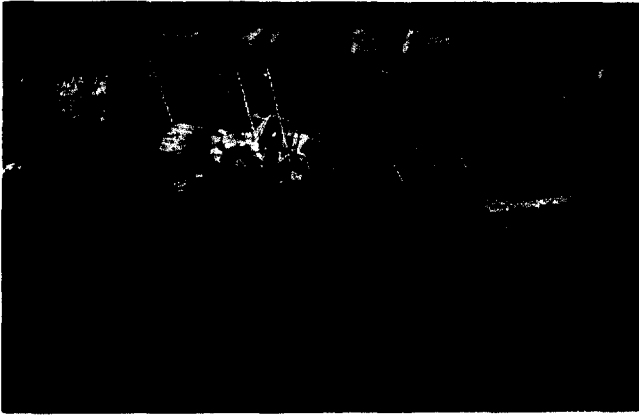
The Enabling Works contract was let by Bluewater Construction Management Team (BCMT) to O'Rourke Civil Engineering Limited in early 1996 following a competitive tendering process. O'Rourke chose to use the specified geosynthetics. They appointed a specialist sub-contractor to supply and install the lining system for Lake 1 and opted to construct the reinforced soil slopes themselves.

3.2 Lake 1

Lake 1 is oval in plan with a perimeter slope length of approximately 500m. Reinforced soil installation began in April 1996. The Contractor selected a 2.4m high timber formwork system, supported by scaffold tube and fittings, for temporary support to the grid wraparound face (Figures 8 & 9). A 60cm high inner plywood former with lifting holes, tapering in cross section from 20cm at the top to 15cm at the bottom, was used to form the inner geotextile wrap-around.

The grids were cut to design length on site. Bodkin joints were used to avoid wastage from end of roll off-cuts. These lengths were abutted against the inside face of the shutter and nominally joined by cable ties to avoid any gaps opening during installation. The internal former was then placed against the grid face and the geotextile was wrapped around the internal face of the former. A geotextile overlap of 50cm was specified. The silty sand fill was placed and compacted in lifts to a depth of 60cm. This fill was found to have sufficient short-term cohesion that the former could be carefully raised and the resulting void filled, by hand, with coarse material without any slumping of the geotextile face.

Figure 6 Cross-section showing face detail.



Figures 8 & 9

The grid wrap-around face was next returned over the coarse fill and connected to the next grid layer using a bodkin. The free end of the upper grid was then hand tensioned using a steel beam.

The face of Lake 1 was slightly reprofiled by local steepening to accommodate 20cm horizontal ledges at the top of each 2.4m lift on which the shutter could be seated. The overall slope remained at 70° . (The geomembrane which extended up the rear of the reinforced soil block also required its own temporary shuttering).

These details resulted in relatively slow outputs of around 40 - 50m² of completed face area per day using two gangs. In order to improve this, the Contractor developed a face detail which replaced the shutter and plywood former with an internal steel mesh former. This was produced by site cutting 5mm diameter steel mesh sheets and bending them into 'U' shaped units 60cm high x 28cm wide. These units were positioned to act as a permanent face former (Figure 10) and then filled with the coarse fill. Since the steel mesh aperture was 20cm x 20cm, the vertical face of the unit was lined with geogrid Type 1 before filling. The top of the unit was cross braced using steel tie wire.



Figure 10

The geotextile was then wrapped up the rear face of the filled unit and the bulk fill placed behind. The main grid length was then wrapped up the front face of the unit and bodkined and tensioned as normal.

This alternative method proved a little quicker, particularly for the higher levels, although the alignment, while acceptable, was less consistent.

The reinforced soil slopes of the Lake are constructed with approximately 60,000m² and 80,000m² of geogrids Types 1 and 2 respectively supplied in 50m x 1.3m rolls. They were constructed in approximately 3 months.

3.3 Lake 2

The water level of Lake 2 was designed to fluctuate with that of the surrounding chalk aquifer and so no geomembrane lining was necessary. About half of the slope length of Lake 2 was formed from the existing chalk quarry face.

Reinforced soil construction took place in the Winter and Spring of 1997. In order to simplify and accelerate installation the Contractor, with assistance from the grid manufacturer, proposed a radically different face comprising site-cast, ordinary-Portland-cement concrete blocks (with 50MPa 28 day compressive strength). These blocks were 2.7m long, 0.6m high and 0.3m wide and contained either one or two layers of 'starter' lengths of cast in Type 2 geogrid (Figure 11). The deeply embedded thick transverse bar of the grid has been shown to provide an anchorage in excess of the design strength of the reinforcement.

HDPE grids have been shown to be unaffected by the highly alkaline environment associated with concrete embedment. (Wrigley, 1987)

This solution was attractive to the Contractor who had already established a batching plant on site and estimated

that he could produce blocks at about a third the cost of typical proprietary segmental units.

For simplicity, the blocks were produced with a stepped vertical face and so the slope profile was amended (Figure 12).

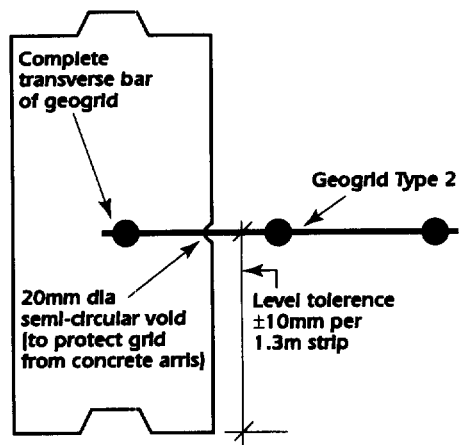


Figure 11 Cross-section of typical block.

These blocks overcame the need for both the shuttering and the coarse fill. The main grid lengths were connected to the starters using bodkins and the geotextile was used to prevent wash out of fines through any small gaps between blocks.

The blocks were cast at a rate of up to 36 per day. Over 1,000 blocks each weighing approximately 1 tonne were required. Installation was much less labour intensive when compared to Lake 1.

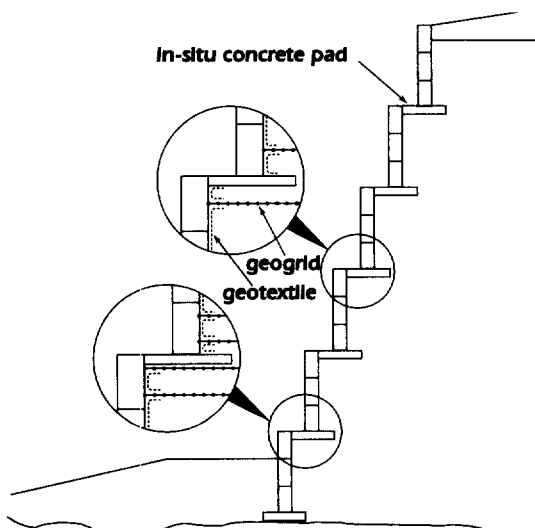


Figure 12

4 CONCLUSIONS

This paper explains the design approach used to address the unusual situation of a reinforced soil lake slope overlying a geomembrane lining system.

The construction details of the three reinforced steep slope facings on this major UK project are also described.

Although the retail park is not scheduled to open until early 1999, Lake 1 (lined) had been substantially completed by the end of 1996 and Lake 2 by the Spring of 1997. There has been no sign of any movement or instability in the reinforced soil structures.

ACKNOWLEDGEMENTS

The writer is indebted to Lend Lease, BCMT, Waterman Partnership and O'Rourke Civil Engineering Limited for permission to produce this paper and to J Cannon who carried out much of the original reinforced soil design.

REFERENCES

- Tensar International (1995) In-house Publication "Winwall, Version 1.14, In-house reinforced wall and slopes design program to Institute für Bautechnik and UK DoT reinforced slope design method (HA68/94)".
- Dixon, J.H. and Osborn, S. (1990) "Field trials to evaluate geotextile puncture resistance", *Proc 4th Int Conf on Geotextiles, Geomembranes and Related Products*, Balkema, Rotterdam. P641 ISBN 90 61 911192.
- Wrigley, N.E. (1987) "Durability long-term performance of Tensar polymer grids for soil reinforcement," *Materials Science and Technology*, Vol 3.

Soil Bioengineering\Biotechnical Stabilization Of A Slope Failure

Robbin B. Sotir

Principal, Robbin B. Sotir & Associates, Marietta, Georgia

John T. Difini

Engineer, Haley & Aldrich, Inc., Cambridge, Massachusetts

Andrew F. McKown

Vice President, Haley & Aldrich, Inc. Cambridge, Massachusetts

ABSTRACT: This paper describes the basic principles of steep slope stabilization using soil bioengineering to reconstruct and stabilize a section of slope along Massachusetts Turnpike at Mile 79.3 E.B. Discussions will focus on the principles of soil bioengineering and reinforced soil slope (RSS) designs, benefits of this interdisciplinary environmentally sound approach, and case study details: vegetation harvesting and storage, design, installation and project status as of October 1997. Design of a fill material, satisfying both agronomic needs of vegetative components and engineering requirements for slope stability, is described. Meeting environmental and aesthetic goals was paramount.

Use of tensile inclusions made from live branches and polymeric geogrids made it possible to construct a highly steepened 4V:1H vegetated earthen buttress slope.

RSS is useful in constructing steepened slopes, improving stability and reducing required fill volumes. Soil bioengineering uses woody vegetation installed perpendicular to the slope face on constructed fill terraces. The installed branches offer immediate reinforcement as supplemental tensile inclusions.

KEYWORDS: Soil Bioengineering, Biotechnical, Slope, Stabilization, Vegetation.

1 INTRODUCTION

Mechanically stabilized earth (MSE), or reinforced soil slope (RSS) embankment systems are commonly used for the widening and reconstruction of existing roads and highways. This paper focuses on the benefits achieved by combining the principles of soil bioengineering and reinforced soil slope design to reconstruct a failed slope on the Massachusetts Turnpike.

2 SYSTEM OVERVIEW

2.1 Soil Bioengineering and Biotechnical Slope Stabilization Techniques

Soil bioengineering techniques have been used around the world for centuries and were used in the United States by the Department of Agriculture's Soil Conservation Service in the 1930s. They have since been incorporated into the USDA's National Resources Conservation Service Engineering Field Handbook as Chapter 18, "Soil Bioengineering for Upland Slope and Erosion Control." Soil bioengineering uses mechanical, hydrological, biological, and ecological principles to develop living structures for the stabilization and revegetation of cut and fill slopes. Living woody plant material forms the main structural component. Soil bioengineering is typically used in conjunction with sound engineering data and design, a fact that is especially evident on this project.

In this case, live cuttings from woody plants were installed in the ground in specific configurations and served immedi-

ately as soil reinforcements, horizontal drains, barriers to earth movement and hydraulic pumps or wicks. Much the same as with geogrids, additional stabilization occurs when the roots develop along the length of the embedded stems. Woody vegetation, when properly designed and installed in these specific configurations, can create stable, composite earth masses. Its functional value has been well established. These cuttings can be used alone or in combination with geosynthetic materials.

When living vegetation is combined with inert components such as geogrids, the approach is referred to as biotechnical stabilization. Essentially the vegetated geogrid is a composite of soil bioengineering and an RSS system in which the slope will always be dependent upon the RSS structural measures for stability. This case study project represents an excellent example of how to combine technologies.

2.2 Engineering a Reinforced Soil Slope

The design approach to engineering an RSS is a generic process that is typical from slope to slope.

2.3 Anticipated Benefits

The combination of RSS and soil bioengineering systems typically provides the following benefits:

- Immediate slope stabilization and erosion control
- Elimination of the need to purchase additional rights-of-way since slopes can be reconstructed at very steep angles
- Reduction of maintenance costs, as there is no need to return to the site to add soil or gravel, or to hydroseed
- Modification of soil moisture regimes using backslope

drainage systems and/or the brushlayer branches which act as wick drains

- Enhancement of opportunities for wildlife habitat and ecological diversity
- Improved aesthetic quality and scenic beauty through revegetation and naturalization of the slope.

3 CASE STUDY

3.1 Project Site

The project site is located immediately adjacent to the eastbound lane of the Massachusetts Turnpike at Mile 79.3 in Charlton, Massachusetts. The slope was approximately 144.87 meters (475 feet) in length, ranged from 3.05 meters (10 feet) to 15.25 meters (50 feet) in height and had a slope angle of approximately 1V:1.5H. Stabilization was needed to remediate ongoing surficial sloughing failures. These failures ultimately formed a large exposed, unvegetated area that was increasingly vulnerable to progressive surface erosion and further failure. Groundwater seepage, saturated surficial soils, and seasonal freeze-thaw cycles exacerbated the instability of this north-facing slope. On both sides of the failed area, the slope was well vegetated and appeared stable; however, it was apparent that the failure was expanding on both sides, as shown in Figure 1.

Subsurface conditions at the site include widely graded, slightly cohesive, dense to very dense glacial till overlain by shallow surficial topsoil and forest mat. Bedrock is typically located within 3.05 meters (10 feet) of the base elevation of the slope. However, during construction an outcrop of poor rock was discovered along a 7.62 meter-long (25 feet) section of slope. The rock sloped unfavorably toward the roadway and required controlled blasting to cut it to a stable surface on which the slope could be reconstructed.

3.2 Project Background

Due to the nature and extent of the failure conditions, the Massachusetts Turnpike Authority (MTA) decided it was imperative to correct this situation by reconstructing the slope. See Figure 1. If not treated, these conditions would inevitably lead to further slope failures, additional maintenance costs and an expanding, unsightly, unvegetated slope along a scenic



Figure 1. Overall view of the project from the west-bound lane (Sept. 1994), prior to slope excavation and slope reconstruction

stretch of the Turnpike. A concrete barrier was installed along the base of the slope to contain the failed soil mass and prevent it from moving onto the roadway.

The aim of the project was to design and construct a 4V:1H earthen buttress immediately in front of the cut slope to provide internal, external, and compound stability. The soil bio-engineering approach was adopted to meet the requirement of an aesthetically pleasing and environmentally sound reconstruction, and to assist in controlling internal drainage. This combined approach uses vegetated geogrids to provide the much-needed surficial stability and to support long-term vegetative growth with almost no maintenance requirements. The geogrid is a hybrid design that incorporates brushlayers in the frontal, wrapped portion of the RSS. Over time the live branches take root and increase the internal stability of the reinforced slope.

3.3 Remedial Design

The remedial design called for excavating the failed slope back approximately 6.1 meters (20 feet) to the same slope angle (4V:1H) as the proposed slope and constructing a steepened, biotechnically stabilized earthen buttress. The slope was stabilized with layers of primary and secondary geogrids, burlap, vegetated geogrids at the face, and live fascines over the top of the finished slope. Figure 2 shows a cross section depicting the existing slope (dashed line) and the remedial design.

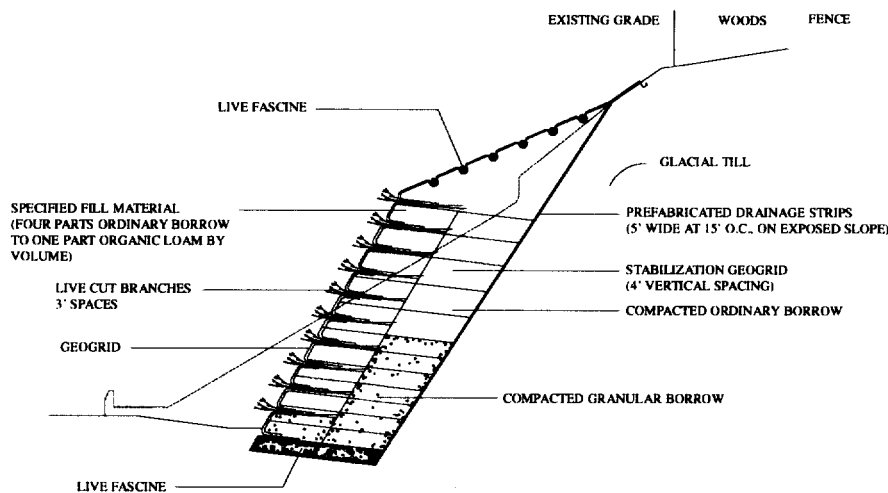


Figure 2. Cross section of remedial slope design

The primary geogrid was designed to provide global, internal, and compound stability to the slope. This grid extends approximately 6.1 meters (20 feet) from the face to the back of the slope. The vertical spacing of the primary geogrid is .61 meter (2 feet) over the lower half of the slope and 1.22 meters (4 feet) over the upper.

As shown in Figure 3, the secondary geogrid, burlap, and brushlayers (which together constitute the vegetated geogrid) were primarily designed to provide facial stability to the slope. As shown in Figure 2, the secondary geogrid and burlap "wrap" the face of each vertical lift between each row of brushlayer branches. The burlap temporarily prevents soil from sloughing out of the face through the grid openings until the plant materials produce leaves and roots. The face wrap extends .91 meters (3 feet) into the slope at the bottom of each vertical lift and five feet at the top. All lifts were constructed using a continuous batter board to control the slope of the face. A front view of the vertical and lateral limits of the vegetated geogrid lifts and brushlayers is provided in Figure 4.

Brushlayers consisting of 2.44 to 3.05 meter (8 to 10 feet) long willow (*salix* sp.) and dogwood (*cornus* sp.) branches were placed on the constructed earthen terraces between each .91 meter (3 feet) vertical lift. These brush-layers, which are installed in layers with the growing ends exposed, extend from the face approximately 3.05 meters (10 feet) back to the mid-point of the slope. During the growing season, these brushlayers will root and produce leaves, stabilizing the face of

the slope. They will also provide some measure of internal stability initially and over the long term. The alternating sequence of constructed earthen terraces and live branch brushlayers is shown in Figure 5.

Drainage panels (1.52 meters (5 feet) wide, spaced 4.57 meters (15 feet) on center) that extend vertically along the back side of the slope were designed to accommodate the migration of groundwater into the reinforced portion of the slope, preventing the buildup of hydrostatic pressures in that area. These panels connect

into a .305 meter (1-foot) thick crushed-stone drainage layer at the base of the slope, which extends the full length and width of the slope.

As shown on Figure 1, four types of backfill were used to reconstruct the slope in addition to the crushed-stone drainage layer at the base. These backfills are granular borrow, ordinary borrow, 50/50 mix, and specified fill. The first three constitute the structurally competent "core" while the specified fill at the face provides a media amenable to plant growth. The specified fill used in the front 3.05 meters (10 feet) of each lift is a blended material consisting of four parts ordinary borrow to one part organic loam by volume. It should be noted that the lifts were constructed to slope away from the face (~20°)



Figure 3. Close-up view of the vegetated geogrid along the front face.

For design of

the slope, stability analyses were conducted to determine: (1) the width of the reinforced zone required to provide a minimum safety factor of 1.5 for deep-seated failure surfaces, and (2) the vertical spacing and design strength of soil reinforcement elements required to provide a minimum factor of safety of 1.3 for both internal

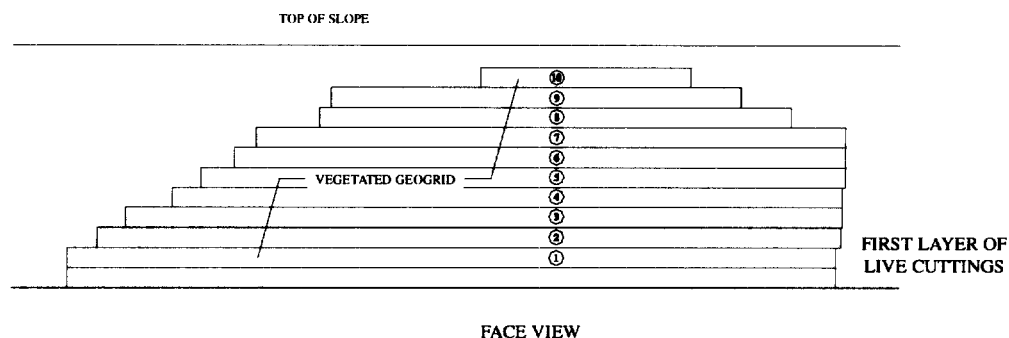


Figure 4. Front view of as-built slope illustrating limits of slope remediation activities.

and that fertilizers were added to each lift to further optimize the growing conditions for the installed brushlayers.

A 1V:3H cut was made above the steep slope and live fascine bundles were installed to prevent surface erosion and to rapidly revegetate the slope with woody plant materials. As illustrated in Figure 6, a live fascine is a collection of live cut branches grouped together in a bundle and secured with twine. The bundle was placed in trenches and anchored with dead stout stakes and live stakes. These structures provide immediate mechanical stabilization and erosion control and will eventually grow and reinforce the surface soil mantle. In this particular application, they also act as a drain, collecting water and transporting it laterally to both ends of the site.

3.4 Stability Analyses

A series of slope stability analyses were conducted to design the RSS and assess the stability of the slope under temporary construction conditions (i.e., the cut slope condition). These analyses were conducted using the University of

and compound failure surfaces. For temporary construction conditions, stability analyses were conducted to configure the cut so that a minimum factor of safety of 1.2 was maintained during the construction process. The computer output for the global stability analysis used to determine the lateral extent of the reinforced zone is provided in Figure 7. The failure surface yielding a minimum factor of safety of 1.5 generally defines the extent of the reinforced zone.

3.5 Agronomic and Geotechnical Considerations

The design and construction of this slope presented several



Figure 5. The alternating sequence of constructed earthen terraces and live branch layer

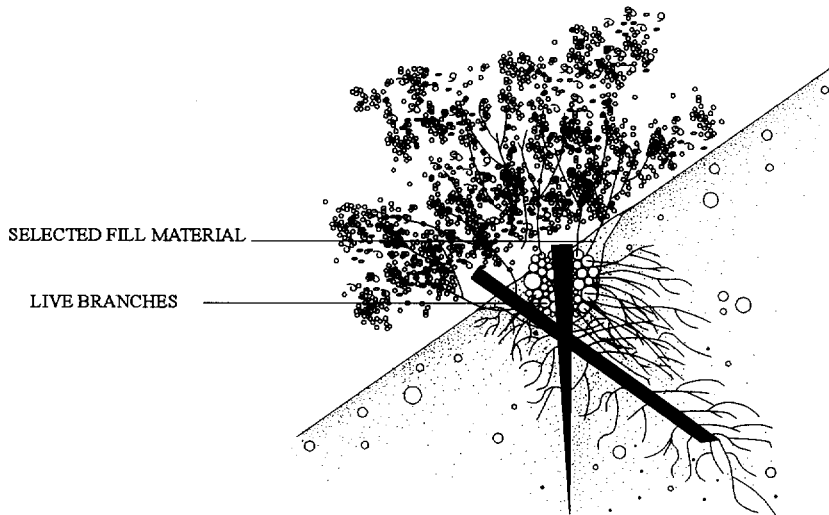


Figure 6. Establishing live fascine.

challenges involving the need to balance agronomic and geotechnical requirements. The factors to be balanced were these: (1) the need for water and nutrients in the slope to sustain and promote vegetative growth versus the desire to remove water so as to eliminate hydrostatic pressures; (2) the need to use organic matter in the slope to provide nourishment for plant growth and development versus the desire to construct the slope with free-draining, inorganic, granular soils; and (3) the need to construct the slope during the fall and winter months while the vegetative plant materials were in a dormant state versus the desire to construct the slope during warmer weather to prevent soil freezing problems and weather delays. A final agronomic consideration was that the plant materials needed to be properly stored following harvesting to protect them from shock. A brief discussion of each of these topics follows.

• **Drainage** - The original design called for a continuous backslope drainage system to intercept groundwater before it enters the reinforced portion of the slope and divert it to the gravel subbase and drainage system beneath the slope. The backslope drainage system was originally designed to consist of free-draining crushed stone, with filter fabric against the naturally deposited gla-

cial soils. However, since it was desirable to allow some water to migrate to the willow and dogwood branches in the slope, the design was modified to utilize 1.52 meter (5 feet) wide prefabricated drainage strips spaced 4.57 meters (15 feet) on center in place of the continuous crushed-stone backslope layer. That allows some groundwater to migrate into the reinforced zone without permitting hydrostatic pressures to develop on the back side of this zone. The brushlayers also function as horizontal drains, reducing the possibility of hydrostatic pressures.

• **Organic material** - To provide favorable conditions for plant growth, it was desirable from an agronomic standpoint to incorporate organic material in the backfill. To accommodate this, the outer 3.05 meters (10 feet) of slope, starting approximately 1.52 meters (5 feet) up from the base of the slope, was backfilled with a blended material consisting of four parts of ordinary borrow to one part loam by volume.

By carefully selecting the mixture and the location within the slope and checking the global stability and location of failure planes, it was possible to satisfy both the agronomic and geotechnical design requirements.

• **Construction time frame** - The freezing of subgrade soils that contain high organic material and water was a daily concern, since the construction was done mostly during the winter

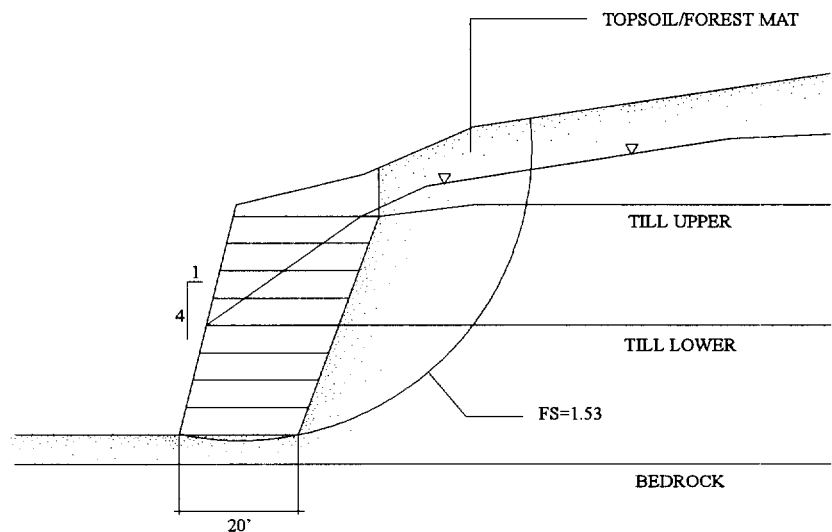


Figure 7. Factor of safety for deep-seated global failure surface.



Figure 8. The condition of the project site, July 1996.

months. To minimize the impact of freezing, the lifts were adequately compacted at the end of each workday, and were inspected the following day for the occurrence of heave or formation of ice lenses; in addition, unsuitable frozen subgrade soils were removed when needed. Furthermore, frequent snow-storms limited the number of workdays on the project's already tight schedule. Accumulating snow, which had to be plowed from the previously constructed lifts before work could continue, shrunk staging and storage areas significantly. It should be noted that a near record snowfall in excess of 254 centimeters (100 inches) occurred during the winter this slope was constructed, following an unseasonably warm fall.

• Harvesting, handling and storage of cuttings - The harvesting of suitable, biotechnically capable plant material and installation of the soil bioengineering systems needed were carefully planned, coordinated and maintained. Numerous potential harvest sites were located before the project started. Sites were then selected based on the quality of material, site accessibility, and proximity to the project site. These harvesting sites contained large stands of willow (*Salix* sp.), a species well-suited for soil bioengineering construction. Refrigerated trucks were used to transport and store the live cut branches, which allowed the cuttings to be stored for long periods of time, such as a month or more. Proper temperature and humidity controls were maintained to keep the branches in dormancy and prevent the cuttings from dying out. The use of refrigerated trailers allowed the contractor to transport larger quantities of material to the site, providing installation crews with immediate access to live cuttings when needed and improving overall operations and efficiency.

4 CONCLUSIONS

The face of the major slope reconstruction, the vegetated geogrid, looks very good. As shown in Figure 8, the slope is stable and the vegetation is well developed. The cut slope above is also well vegetated and appears stable.

This biotechnical installation should continue to root and grow, thus providing for increased surface protection, soil reinforcement, and an aesthetically pleasing revegetated slope. Over time, natural invasion from the surrounding plant community is expected to occur, causing the system to blend into the naturally wooded scenic setting of the area. Thus the long-term mechanical and ecological goals of the project will be satisfied.

REFERENCES

- Gray, D.H. and Sotir, R. (1995). *Biotechnical and Soil Bioengineering Slope Stabilization. A Practical Guide for Erosion Control*, John Wiley & Sons, New York, NY, USA.
- Kraebel, C.J. (1936). *Erosion control on mountain roads*. USDA Circular No. 380, 43 pp.
- Coppin, N., Barker, D., and Richards, I. (1990). *Use of Vegetation in Civil Engineering*. Butterworth's: Sevenoaks, Kent, England.
- Gray, D.H. and Leiser, A.T. (1982). *Biotechnical Slope Protection and Erosion Control*, Van Nostrand Reinhold, New York, N.Y. USA.

Finite Element Analysis of instrumented geogrid reinforced slope

A. Ghinelli

Professor, Department of Civil Engineering, Florence University, Italy

M. Sacchetti

Researcher, Department of Civil Engineering, Florence University, Italy

ABSTRACT : A 15 m high green faced reinforced slope was built in 1996 to consolidate a landslide situated on the Montone hill in the province of Perugia (Italy). The reinforced slope was built using as fill material locally available soils and as reinforcement HDPE mono-oriented extruded geogrids. A section of the slope has been fully instrumented in order to verify its long term behavior. To evaluate the field stress and deformation behavior of the Montone reinforced slope a finite element analysis has been carried out. The paper describe the model technique developed to evaluate the filed stress and deformation of steep reinforced slope using special interface elements. The results of finite element analysis are in good agreement with the field measured results.

KEYWORDS: Steep slope, Geogrids, Field test, Finite Element analysis

1 INTRODUCTION

The Montone hill located in the province of Perugia (Italy), was interested in the past by several instability and erosive phenomena along its slopes, which caused great damage at historical buildings and at road network.

During the last decades important landslides concerned the North-East slope of Montone hill, particularly along the Montone-Pietralunga main road. These phenomena that involved an area of about 15.0 m high and 200.0 m long, produced in proximity of the Fosso Fornaci a road interruption.

In one of the sub-project for the consolidation of the Montone hill, near the Fosso Fornaci, was foreseen to restore the interrupted main road and to stabilize the natural slope by rebuilding it with the local soils reinforced with HDPE geogrids. The reinforced slope presents a maximum height of 15.5 m and a length of about 53.0 m (see Figure 1). Due to the importance of the project, a section of the slope has been instrumented in order to verify its long-term behavior.

The paper deals with the stress and deformation analysis of the Montone reinforced slope by finite element analysis. A procedure to model the fill soil, the reinforcements and the soil-reinforcement interaction using discrete finite elements are described. The properties of the soil fill and of the reinforcement geogrids are also presented.

Field measurement taken over two months period after construction are reported and compared with numerical analysis results.

The paper shows a good agreement between compared results. This fact highlights the possibility to use element finite methods to predict filed behavior of reinforced slopes without rigid face and with a complex geometry.

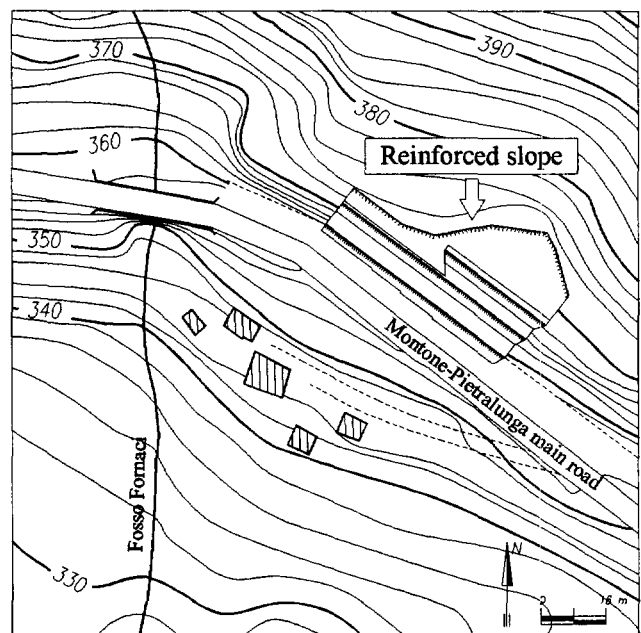


Figure 1. Reinforced slope location

2 REINFORCED SLOPE DESCRIPTION

In the last decades the North-East slope of Montone hill was interested by important landslides and erosive phenomena that produced in proximity of the Fosso Fornaci an interruption of the Montone-Pietralunga main road.

For better understanding the reasons of slope instability an intensive geophysical and geotechnical test campaign and a back-analysis study on the old landslide bodies were carried out (Coluzzi et al., 1997).

To restore the interrupted main road and to stabilize the natural slope a green faced reinforced slope was built. The

construction commenced in the summer of 1996 after the landslide body has completely been removed from the main road and after the existing ground surface has been remodeled.

The reinforced slope shows a running length of 53.0 m and a maximum height of 15.5 m, split up in three bodies respectively of 5.3, 5.6 and 4.6 m of height, with 1:1.73 side slope, separated by two horizontal berms of 4.1 m and 3.1 m length (see Figure 2).

As above mentioned the reinforced slope was built using as fill material locally available soils and as reinforcement HDPE mono-oriented extruded geogrids. In particular the entire slope was supplied of 23 reinforcement layers, 0.65 m vertically spaced, with length variable between 4.5 m and 3.15 m.

The green faced reinforced slope was built using the TENAX RIVEL system (Rimoldi et al., 1996), which consist in the use of sacrificial steel mesh form-works that help in the face construction and permit to obtain a very uniform geometry of the slope. A thick drainage system was placed beneath the reinforced bodies.

The Jewell method (Jewell, 1990) was used to design the reinforced slope, whereas global stability analysis was carried out using the STABGM, a code based on the Bishop's modified method (Coluzzi et al., 1997).

The main geotechnical properties of the fill soil and mechanical properties of the reinforcement geogrids

adopted to design are reported in Table 1.

Table 1. Geotechnical properties of the fill soil and mechanical properties of the reinforcement geogrids adopted to limit equilibrium design

	Unit	Design value
FILL SOIL		
Unit weight	[kN/m ³]	19.7
Friction angle	[°]	26
Effective cohesion		-
Interstitial pressure ratio	[-]	0
REINFORCEMENT		
Peak tensile strength	[kN/m]	60
Strength at 2% strain	[kN/m]	17
Long term design strength	[kN/m]	25

2 INSTRUMENTATION

Due to the importance of the project, a section of the was provided with extensive instrumentation.

The main purpose of the instruments installed is to

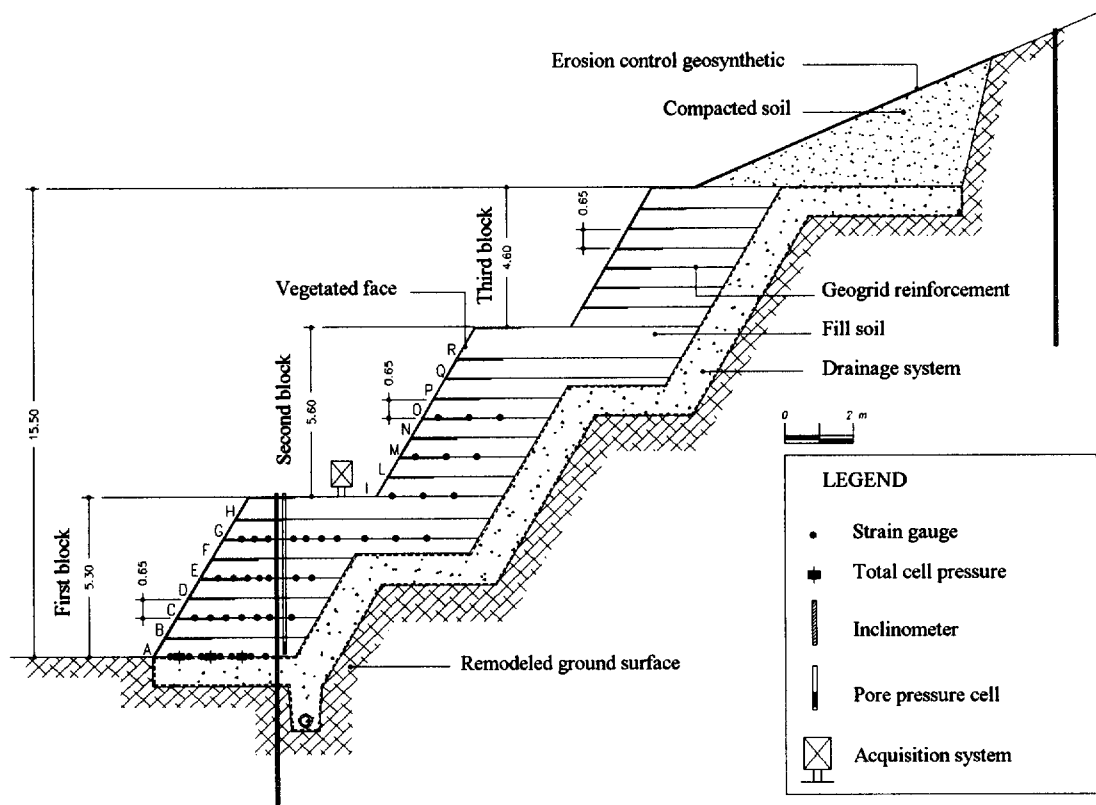


Figure 2. Cross section of the instrumented geogrid reinforced slope

check the overall deformation of the slope and to indicate the long-term behavior of the reinforcements under field stress conditions. Moreover, field measurements are very valuable input data for subsequent numerical analysis with finite element method.

The instrumented section was equipped with 40 strain gauges (electrical wire resistance type) positioned on geogrid ribs of the first and second reinforced block; 3 total vertical pressure cells positioned at the bottom of the first reinforced block; 2 vertical inclinometers installed on the first block and on the top of the third block; 1 pore pressure cell and 1 acquisition system installed on the first block (see Figure 2). Descriptions of instrumentation types and installation procedure are detailed in Coluzzi et al. (1997).

The strain gauges and total pressure cells has been activated after construction, whereas inclinometers and pore pressure cell are not yet active. After about one month measurements 9 strain gauges are "dead".

3 FINITE ELEMENT ANALYSIS

For reinforced slopes, deformation and stability are the two main concerns. Nevertheless an accurate assessment of deformations in field condition can only be achieved through a stress-deformation analysis, such as a finite element analysis.

To evaluate the field stress and deformation behavior of the Montone reinforced slope a finite element model of the entire structure has been developed. The numerical simulation has been performed using the CRISP90 computer code (Britto et al., 1990), developed at Cambridge University in the eighties, which uses many soil constitutive models, and capable to simulate drained and undrained geotechnical problems with static load conditions. In particular to simulate the field behavior of steep reinforced slope, without rigid facing, a modeling technique has specifically been developed. This technique foresee to use the following elements:

- "BAR" elements, with linear-elastic or linear elasto-plastic behavior, for reinforcements.
- "LSQ" (Linear Strain Quadrilateral) and "LST" (Linear Strain Triangle) elements, with linear elastic-plastic behavior, for fill soil.
- "SLIP" elements, with behavior based on the Goodman & Taylor (1968), for soil-reinforcement interface.
- "LSQ" and "LST" elements, with linear-elastic behavior, for foundation soil.

To obtain a true and correct forecast of the stress and deformation behavior of reinforced slope by numerical finite element analysis it is necessary to define and subsequently to simulate the very complex interaction mechanisms establishing between the fill soil and the

reinforcement geogrids. In this pattern the use of "SLIP" elements with frictional and adhesive behavior, which permits relative displacements, seems to be able to simulate the above mentioned interaction mechanics.

The finite element model created consist of 2107 nodes and 872 elements (161 reinforcement elements, 322 interface elements and 389 soil elements) (see Figure 3). Computational problems connected with the dimension of the overall stiffness matrix imposed heavy limitations on the elements number of soil foundations. Therefore we decided upon to model a little portion of natural slope with very simple linear-elastic elements having adequate resistance and stiffness to support the reinforced body.

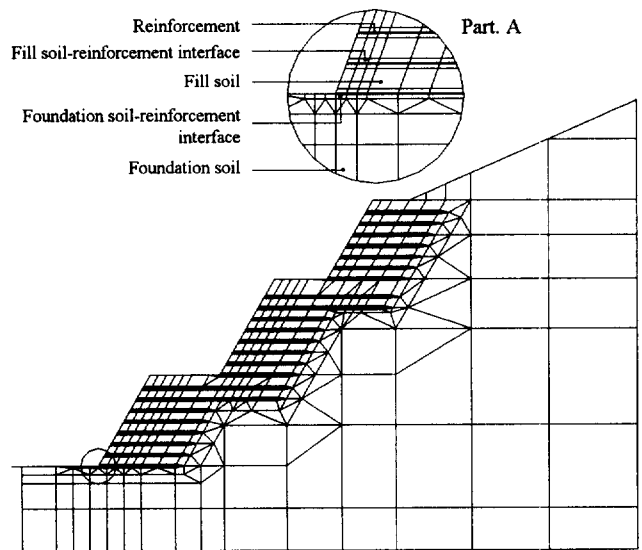


Figure 3. Finite element model

4 MATERIAL PROPERTIES

With the final purpose to obtain a more realistic numerical simulation a series of field tests on the reinforced slope and laboratory tests on materials taken from reinforced bodies were carried out. From these tests were assessed the most important mechanical parameters to introduce into numerical model. The tests undertaken are:

- Field density tests, carried out on all three reinforced bodies, that supplied the unit weight of the fill soil.
- Field pull-out tests, performed on geogrid layers, about 0.50 m wide with different anchorage length, purposely embedded into the bottom reinforced body, that given the pull-out factor of reinforcement.
- Rigid plate load tests, carried out on the first reinforced body using circular plates with 300 mm and 600 mm diameter, that supplied the principal deformation parameters of the fill soil.
- Classification tests, performed on several samples of

fill soil taken from reinforced slope, that supplied the limit indexes and the particle size distributions.

- Direct shear tests with standard box of 60x60 mm, performed on samples of fill taken from reinforced slope, that given the shear resistance of fill with particle size finer than ASTM10 sieve.
- Tensile creep tests, carried out on geogrids samples, using different tensile loads and temperatures (Cazzuffi et al., 1997), taken from the reinforced slope after end construction, that given the long-term tensile stiffness of reinforcement.

The most important test results achieved are summarized in Table 2.

Table 2. Geotechnical properties of fill soil and mechanical properties of reinforcement geogrids adopted to finite element analysis

	Unit	Design value
FILL SOIL		
Unit weight	[kN/m ³]	18.4
Friction angle	[°]	33
Effective cohesion	-	-
Initial elastic modulus	[MPa]	35.2
Poisson ratio	[-]	0.2
REINFORCEMENT		
Tensile stiffness	[kN/m]	500
FOUNDATION SOIL		
Unit weight	[kN/m ³]	20.0
Friction angle	[°]	23
Effective cohesion	[kPa]	100
Elastic modulus	[MPa]	10
Poisson ratio	[-]	0.4
INTERFACE		
Pull-out coefficient	[-]	1

5 FINITE ELEMENT ANALISYS RESULTS

The state of deformation at end construction of the Monotone reinforced slope, achieved with numerical analysis, is showed in Figure 4.

Figure 5 shows the comparison between the distribution of reinforcement strains achieved with numerical analysis (light dots and dashes) and achieved from field measurement (dark dots) after two months of the end construction, relating to the first reinforced body (layers A to H). Figure 6 shows the same comparison relating to the second reinforced body (layers I to R).

With reference to numerical analysis results, all layers presents the same shape strain distributions, excepting the

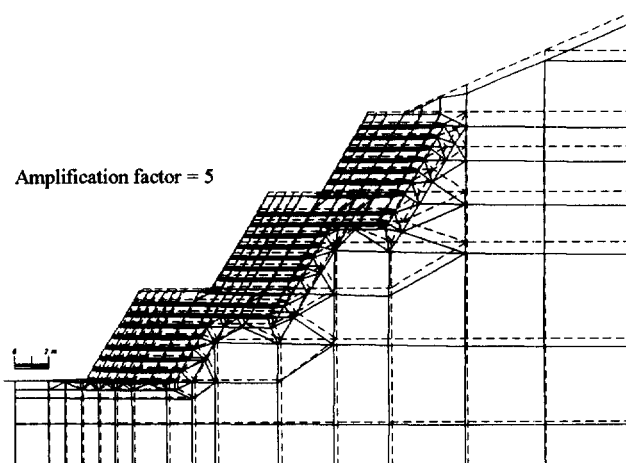


Figure 4. Deformation state of entire reinforced slope

layers G and H on the first body and Q and R on the second body. In particular the second layer of each body (respectively B and L) has the largest strain whereas the top layer (respectively F and P) has the smallest. The peak reinforcement strains occurred in the bottom layers closer to the slope surface than the top layers. The very particular strain profiles of layers G and H on the bottom body and Q and R on the second body are mainly related to their specific border conditions.

From Figures 5 and 6 it is also possible to highlight a close affinity between measured values and calculated values, excepting the at layers A and G. The reasons of this disagreement may be attributable to specific border conditions. In fact for layer A the distribution of strains along its length depends also from foundation soil-geogrid interface characteristics, while for layer G the distribution of strains is influenced by different confinement pressure conditions and different support soils along its length. The presence of a second peak in the strains profile in proximity of different contour condition confirm the above mentioned consideration.

At the last Figure 7 shows a very good agreement between numerical and measured distribution of total vertical pressure at the bottom of the first reinforced body. In the same figure the total vertical pressure has been compared also with "static" pressure due at the weight of reinforced slope. The different envelope is obviously due to thrust of backfill.

6 CONCLUSION

To evaluate the field stress and deformation behavior of the Montone green faced reinforced slope a finite element model of the entire structure has been carried out. A modeling technique has specifically been developed to simulate the field behavior of reinforced slope without

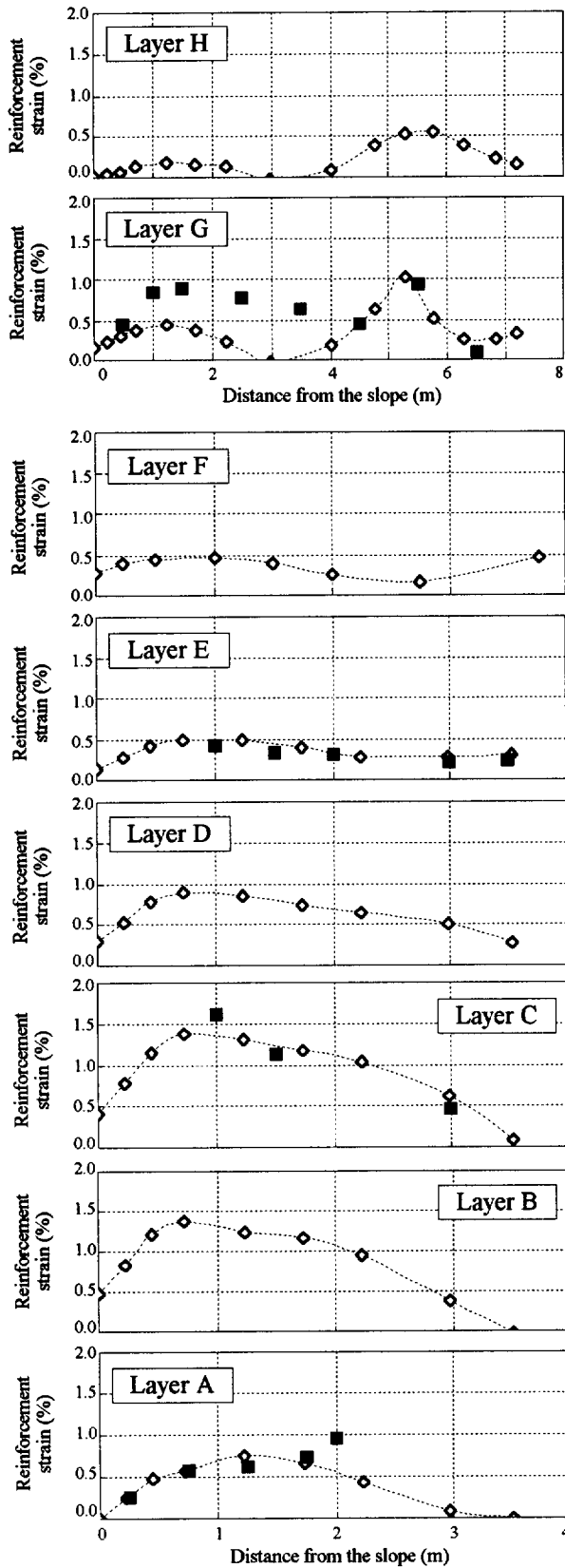


Figure 5. Strain distributions on the reinforcement geogrids of the first reinforced block

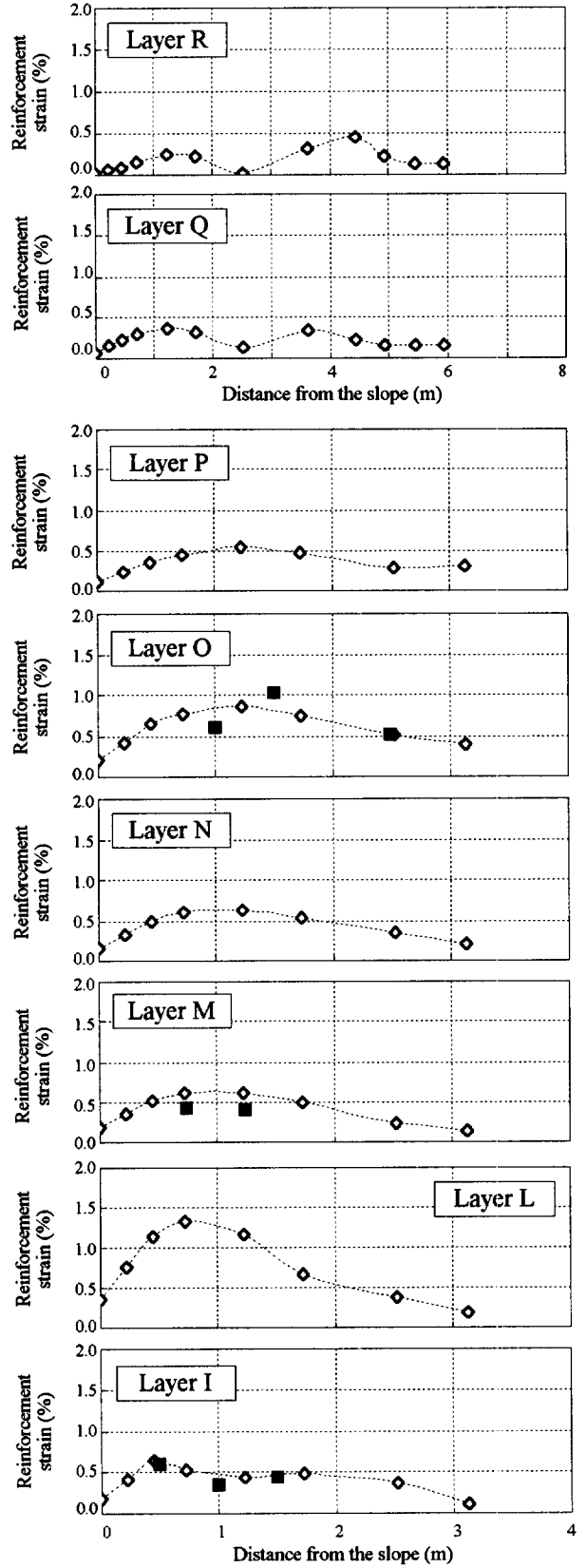


Figure 6. Strain distributions on reinforcement geogrids of the second reinforced block

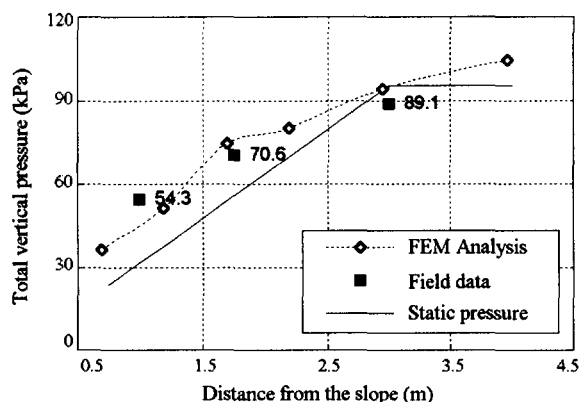


Figure 7. Total vertical pressure at the bottom of the first reinforced block

rigid facing which foresee the use of “SLIP” elements with frictional and adhesive behavior, which permits relative displacements, to simulate the complex interaction mechanisms establishing between the soil fill and the reinforcement geogrids.

A series of field and laboratory tests was carried out to assess the most important mechanical parameters to introduce into numerical model.

The performance of the Montone reinforced slope was monitored by a specific instrumentation installed in a section of the slope during its construction. Field measurement showed the mobilization of tensile resistance on the geogrids and the distribution of total vertical pressure at the base.

The strain distribution results of finite element analysis are in good agreement with field measurement results taken after two months of the end construction. Nevertheless the border conditions have a remarkable influence on the base reinforcement layer and on the layers disposed between each reinforced body. This influence is negligible in the others reinforcement layers.

The good agreement achieved confirm the validity of modeling technique developed and highlights the concrete possibility to use of element finite methods to obtain detailed information about stress and deformations under field condition.

ACKNOWLEDGMENT

The field measurement is a co-operative project in association with the Department of Civil Engineering of Florence University, TENAX SpA, Viganò, Italy, and R.P.A., Perugia, Italy. The contribution of these organization is acknowledged.

A particular acknowledgment to the SEAS SpA, Perugia, Italy, for precious assistance given during the execution of all the field tests.

REFERENCES

- Britto, A. and Gunn, M. (1990) *Critical State Soil Mechanics via Finite Elements*, Ellis Horwood Limited, Chichester, England.
- Cazzuffi, D., Ghinelli, A., Sacchetti, M. and Villa, C., (1997) “European Experimental Approach to the Tensile Creep Behaviour of High-Strength Geosynthetics”, *Geosynthetics'97*, Long Beach, CA, pp.253-266.
- Coluzzi, E., Montanelli, F., Rimoldi, P. and Zinesi, M. (1997) “Preliminary Results From an Instrumented Geogrid Reinforced Slope for The Stabilisation of The Montone Hill in Central Italy”, *International Symposium on Mechanically Stabilized Backfill (MSB)*, Colorado USA.
- Goodman, R.E., Taylor, R.L. and Brekke, T.L. (1968) “A Model for The Mechanics of Joined Rock”, *Journal Soil Mechanics Foundations Division*, ASCE, Vol. 99, pp.637-659.
- Jewell, R.A. (1990) “Strength and Deformation in Reinforced Soil Design”, *Proc. IV Int. Conf. on Geotextiles, Geomembranes and related Products*, The Hague, Netherlands, pp.913-946.
- Rimoldi, P. and Jaecklin, F. (1996) “Green Faced Reinforced Soil Walls and Steep Slopes: The State-of-The-Art”, *Geosynthetics: Applications, Design and Construction*, De Groot, Den Hoedt & Termaat Editors, Balkema, Rotterdam, pp.361-380.

The Assurance Of Durability

John H Greenwood

ERA Technology Ltd, Cleeve Road, Leatherhead KT22 7SA, UK

ABSTRACT: The design engineer requires assurance that the geosynthetics he uses will function over a particular service lifetime. This paper introduces the CEN Guide to Durability which provides guidance to the user of geotextiles for non-reinforcing and, to a limited extent, reinforcing applications on the resistance to weathering, chemical and biological effects. "Normal service conditions" are defined for which testing is restricted to a minimum and there is exemption for materials where there is sufficient field experience. The designer of reinforced soil will require in addition information on potential reductions in strength, expressed as partial safety factors, and methods are described for deriving these factors expressed as in BS 8006.

KEYWORDS: Degradation, Polymeric ageing, Predictions, Reinforcement, Safety factors

1 INTRODUCTION

The design engineer requires assurance that the geosynthetics he uses will function over a particular service lifetime. In the absence of long-term experience, it is necessary to make predictions, which of necessity are based on changes in properties measured over shorter periods, or under more severe or accelerated conditions. For most applications an assurance of a minimum level durability is sufficient, and standards committees on both sides of the Atlantic have defined practical tests intended to assure a minimum durability.

Reinforced soil design requires additional calculation of the reduction in strength due to environmental or other factors and the calculation of a corresponding partial factor for use in design.

2 NON-REINFORCING APPLICATIONS

2.1 "Normal Service Conditions" and When to Test

The CEN Guide to Durability of Geotextiles and Geotextile-Related Products (CEN 1998) has been written by members of Working Group 5 (Durability) of CEN Technical Committee TC189, Geotextiles, to guide the user and to provide the background to the recommendations it makes. Starting with definitions of durability, "required" and "available" properties, design life and end of life, it then describes the polymer structure, polymer types and manufacturing processes relating to the principal types of geotextile. The environments above and below ground are noted, with particular reference to the temperature, humidity, organic and chemical content of soils and of their potential effects on the polymer. In addition mechanical

load will cause creep or rupture, particularly of soil reinforcements, while transverse load in coarse soils can lead to mechanical damage and to compressive creep of drainage composites. Under some circumstances mechanical load can accelerate chemical attack (or vice versa), although this is not seen as a major problem in the highly oriented polymers used in fibres and geogrids.

The final chapter of the Guide provides guidance on what testing is necessary and when, introducing the concept of a window of "normal service conditions" for which only very limited testing is necessary. Recognising that the geotextiles have been used for upwards of 25 years after which, with few exceptions, the only significant degradation found has been that caused by mechanical damage, the normal service conditions are defined as:

- functional design lifetime less than 25 years
- pH value between 4 and 9
- soil temperature not greater than 25°C
- natural soil, excluding landfills and contaminated land.

It is recognised that the soil may be dry, partially or fully saturated, aerobic or anaerobic, and may contain common transition metals in ionic form such as Fe²⁺ and Fe³⁺.

For non-reinforcing applications in natural soil where the geotextile has a functional design life of less than five years, even when the soil structure itself has a longer lifetime, the only tests required are for mechanical damage and weathering. For all other applications with design lives of up to 25 years, screening tests for the hydrolysis of polyester and for the oxidation resistance of polypropylene and polyethylene will be required in addition. A soil burial

test for biological resistance is not required for these polymers, but should be performed on new materials, vegetable based products, geocomposites, coated materials and any others of doubtful quality (such as materials recycled after consumer use). Other polymers require separate assessment, including polyamides which can be subject to both hydrolysis and oxidation.

An important feature of the Guide is the inclusion of a clause allowing manufacturers to use a demonstration of satisfactory long-term service as an alternative to screening tests. The user will decide whether the site conditions experienced were sufficiently similar to the new design conditions for the field evidence of good durability to be accepted, and whether the new product is sufficiently similar to the old. So far, most studies on exhumed samples have shown little evidence of degradation other than mechanical damage due to compaction in coarse fills on installation. The assessment of field experience is mentioned further in Section 3.8.

2.2 Mechanical Damage

A simulated site test for mechanical damage has been described by Watts and Brady (1990) and a database of measurements has been compiled by Allen and Bathurst (1994). The results are generally expressed as a reduction in tensile strength (see below, Section 3.4), but for visual observation holes and tears may be more significant for applications in filtration and separation.

2.3 Weathering Tests

The screening test for weathering test, ENV 12224, will be a fluorescent tube test based on current practice in artificial weathering and is described further in Greenwood et al. (1996). Drawing on the results of intercomparison tests on a range of stabilised and specially prepared unstabilised geotextiles, the Guide recommends that, unless they are to be covered on the day of installation, all materials should be subjected to accelerated weathering for a UV radiant exposure (total ultraviolet light below 400 nm wavelength received per unit area) of 50 MJ/m². This corresponds to approximately 250 hours in a weatherometer and to one summer month's exposure on site in southern Europe. As with mechanical damage, loss of strength is taken as the indicator of degradation for all applications, since it can be measured quantitatively and more accurately than, for example, hydraulic permeability.

For applications in soil reinforcement or otherwise dependent on long-term strength, geotextiles which retain over 80% of their strength in the weathering test should be covered within one to four months, while those which retain 60% to 80 % of their strength should be covered within 2 weeks. For non-reinforcing applications the acceptable bands of retained strength are over 60% and 20% to 60% respectively. The time to cover depends on the season and location in Europe, it being unreasonable to apply the same

rule on a hot summer's day by the Mediterranean as on a short winter's day in Scandinavia. If the material fails the test it has to be covered on the day of installation.

Correlation between the reduction in strength and the time to cover on site is believed to be a useful and practical concept. Extended artificial weathering tests using similar methods are required for materials which are to be exposed for longer durations.

2.4 Hydrolysis and oxidation

Apart from the soil burial test for biological resistance (ENV 12225), which was described by Greenwood et al (1996), the only tests required for non-reinforcing applications with service lives from 5 to 25 years are the screening of polyester geotextiles for resistance to internal hydrolysis and of polypropylene, polyethylene and polyamide for resistance to oxidation. It is well established that normal textile grade polyester degrades slowly under moist conditions, and high tenacity polyesters even more slowly. Based on current quality control practice in polyester manufacture, ENV 12447 proposes immersing the geosynthetic in water at 95°C for 8 weeks and determining the percentage reduction in strength. This is a simple and directly relevant screening test that avoids the problems of determining carboxyl end-group count and molecular weight. The screening test for oxidation of polyethylene and polypropylene is an oven ageing test at 110°C for polypropylene and at 100°C for polyethylene. The passmark is 50% of tensile strength and the durations are longer for reinforcing than for non-reinforcing applications.

2.5 Beyond Normal Service Conditions

Outside the "window" of normal service conditions the Guide recommends the designer to consider further tests. For example, for pH values below 4 and above 9, screening tests in concentrated alkali and in acid under aerobic conditions have been developed. For landfill sites, contaminated land, or for very long durations under hydrolysing or oxidising conditions, Arrhenius type accelerated testing should be considered.

3 REINFORCING APPLICATIONS

3.1 General

The design of reinforced soil is not covered in detail by the CEN Guide to Durability but is governed by codes such as BS 8006 which specify a safety factor f_m for the durability of the material which is applied to the design strength. Design lives are long, typically 50 to 120 years. Definition of f_m requires a numerical estimate of the reduction in strength that will occur by the end of the design life. f_m is the product of several partial safety factors (>1) as listed in Table 1 but for only some of them does the code specify the

means of calculation. Methods for deriving these factors from the properties of the reinforcement are not included in the Guide, but some have been drafted elsewhere (for example WSDOT 1997). The following Sections are intended to point out some of the items which should be addressed.

Table 1. Partial safety factors as defined by BS 8006: 1995.

f_{m11}	applied where the base tensile strength is not the characteristic strength	statistical*
f_{m112}	= 1.0 for polymers	
f_{m121}	statistical scatter of long-term data	statistical
f_{m122}	uncertainty of extrapolation	uncertainty
f_{m211}	mechanical damage	reduction
f_{m212}	long-term effect of mechanical damage	uncertainty
f_{m22}	chemical effect of the soil environment	reduction/ uncertainty

*For the use of these definitions see Section 3.9

3.2 Specifications

The general service environment including the soil types, temperatures and gradations, the expected loads and the design life must first be defined. The information required includes:

- tensile properties including characteristic strength
- creep and rupture tests
- damage tests
- chemical description of the material
- chemical durability tests
- field experience (if any)
- quality assurance statement.

The range of loads, temperatures, times and soil gradations used, in particular those for the creep and rupture tests, must correspond to the service environment. Without a complete set of data it is necessary to resort to default and uncertainty factors which too often turn out to be controversial. The ultimate goal must be to define a procedure which is independent of the operator and excludes all uncertainty factors.

3.3 Separation of Long-Term Strength from Long-Term Strain

Until there is an integrated theory of creep and stress-rupture the calculation of partial safety factors for strength and strain should be kept separate. While strength is sensitive to mechanical damage and to environmental influences such as weathering and possible long-term

chemical degradation, creep strain at lower loads is affected by little except load and temperature.

3.4 Mechanical Damage

As mentioned in Section 2.2, the effect of mechanical damage is generally expressed as the ratio in strengths of a damaged material compared with the undamaged material and expressed as a percentage. The partial safety factor f_{m211} will then be the inverse of the ratio. Methods are being developed for performing damage tests in the laboratory using standard fills. The reduction in strength for the fills on the site being considered can be interpolated by plotting the reductions in strength against a soil parameter such as d_{50} (WSDOT 1997).

Very little information exists on the effect of mechanical damage on long-term strength, if any, and in this situation the method of Allen and Bathurst (1996) could be used to define f_{m212} .

3.5 Environmental effects

The principal potential degradation mechanisms for commonly available geotextiles are those which are the subject of screening tests (Section 2.1). Internal hydrolysis, the slow degradation of polyester fibres in water irrespective of pH, has been studied by a number of authors and the reduction in strength of high tenacity fibres has been predicted. From measurements of both retained strength and molecular weight after immersion in water (pH7) at elevated temperatures the rate of bond breakage can be derived as a function of temperature. The strength of the polyester at long times and lower temperatures can then be derived by extrapolation using Arrhenius' formula. The predictions in Table 2 use the calculations of Burgoyne and Merii (1993) for the two fibres they used, PET1 and PET2, while the results of Schmidt et al (1994) for tests at 50 to 70°C have been extrapolated assuming that the rate of loss of strength is linearly proportional to the rate constant. All refer to high tenacity fibres with number-average molecular weight $M_n > 25000$. A similar calculation has been made by Salman et al (1997) for a polyester with $M_n = 18200$.

Table 2. Percentage retained strength following internal hydrolysis.

	50 years		120 years	
	20°C	30°C	20°C	30°C
Burgoyne (PET1)	98	92	96	87
Burgoyne (PET2)	96	85	92	74
Schmidt et al.	95	89	85	64
Salman et al.	84	54	62	0

These predicted reductions in strength can be used to derive the reduction factor f_{m22} . It should be noted that the data

refer to saturated conditions and that internal hydrolysis will take place more slowly in unsaturated soils. Alkaline hydrolysis, which reduces the strength due to surface attack, should be considered in addition for soils with a pH of 9-10 or above.

There is no generally accepted method for predicting the reduction in strength of polyolefins due to oxidation, but that of Salman et al (1997) provides an example.

Extrapolations based on logarithmic scales as in Arrhenius' method can have wide confidence limits and an estimate should be made of the sensitivity of any prediction to changes in the input data. It may therefore be necessary to set an additional factor to account for the uncertainty of the extrapolation, but this factor should be handled separately as described in Section 3.9.

Weathering is discussed in Section 2.3. If a reduction in strength is anticipated due to weathering during installation, then this must be included in the calculation of f_{m22} .

3.6 Stress-Rupture

As with all extrapolations, stress-rupture results must be examined for any evidence of a change of behaviour, whether in the shape of the curve, the elongation at break or the appearance of the broken specimen. Any change in the mechanism of failure will invalidate the extrapolation.

Long-term design strength is currently predicted by fitting a curve to the stress-rupture data, conventionally plotted as in Fig. 1, and extrapolating it from shorter times at high loads to longer times at lower loads. The most commonly used fit is:

$$T = T_0 - b \log t \quad (1)$$

where T is applied tension (load) expressed as a percentage of the tensile strength of the same batch of material, t is time and T_0 and b are constants. With $x = \log t$, $y = \sigma$, and the subscript av indicating a mean,

$$S_{xx} = \sum (x_i - x_{av})^2 \quad (2)$$

$$S_{yy} = \sum (y_i - y_{av})^2 \quad (3)$$

$$S_{xy} = \sum (x_i - x_{av})(y_i - y_{av}) \quad (4)$$

$$b = S_{xy} / S_{yy} \quad (5)$$

and the straight line fit is:

$$T_0 = y_{av} - x_{av} / b \quad (6)$$

The regression line is then extrapolated to the design lifetime to give the unfactored design strength T_{CR} , again as a percentage of the batch tensile strength. The regression line is expected to cross the line $T = 100\%$ at a time comparable with the duration of a tensile test.

Table 3: Example of stress-rupture results (fictitious).

load as % tensile strength		time to rupture (h)	
85		1.2	
85		7	
85		21	
80		19	
80		61	
80		225	
75		345	
75		716	
75		2,014	
70		3,970	
70		9,836	
70		>18340	
x_{av}	2.351	b	-0.214
y_{av}	77.5	n	12
S_{xx}	19.06	K	0.0442
S_{yy}	375	t	1.812
S_{xy}	-80.27	s	0.4340
predicted stress rupture load for 1000000 h			60.5%
lower confidence limit for 1000000 h			54.7%
f_{m121} based on statistical procedure			1.11

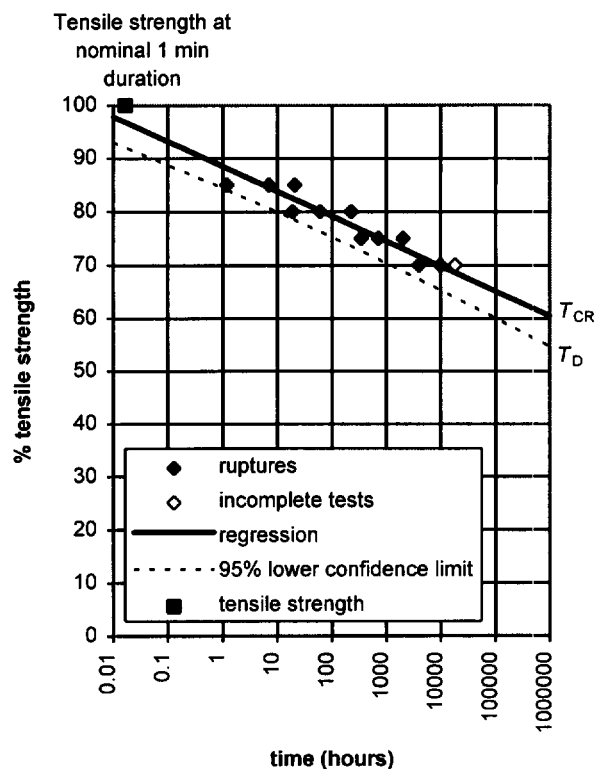


Fig. 1 Stress-rupture diagram

Statistically, the lower confidence limit is given by a formula which combines the variance of the data with the variance of the gradient of the line:

$$y = y_{av} + b(x - x_{av})/K - (ts/K)[K(1 + 1/n) + (x - x_{av})^2/S_{yy}]^{1/2} \quad (7)$$

where n is the number of measurements, t is the value of Student's t corresponding to $(n - 2)$ and the appropriate (one-sided) probability level, and

$$s = [(S_{xx} - S_{xy}^2/S_{yy})/(n - 2)]^{1/2}; \quad K = b^2 - t^2s^2/S_{yy} \quad (8)$$

This curve forms the lower branch of a hyperbola that draws away from the stress-rupture line on extrapolation and meets the design life at T_D such that $T_{CR} / T_D = f_{m121}$ (see example with numerical data in Table 3 and stress-rupture diagram in Fig. 1). WSDOT (1997) defines the reduction factor as equalling $100/T_{CR}$ and applying it to the MARV strength, which in the BS 8006 system is equivalent of applying f_{m111} and then setting $f_{m121} = 1$. In either case it is important not to double-count the variability due to scatter. The question of whether design should more correctly be based on residual strength has been raised elsewhere (Greenwood 1997).

Methods for defining f_{m122} , the uncertainty factor which reflects the considerable step of predicting 50 to 120 year performance from rupture data over much shorter periods, are based on the duration of the longest test result. The methods allow extrapolation up to ten times without further penalty and then increase f_{m122} progressively to reach values of 2 for extrapolation by a factor of 100 based on T_d (BS 8006), or 1.2 or 1.4, depending on the likelihood of a knee, based on the confidence limit as defined by WSDOT (1997). Following current practice in the calculation of stress-rupture characteristics, it is proposed that the duration of an incomplete rupture test should be acceptable for this procedure provided that it lies to the right of the curve as in Fig. 1.

Any such procedure should include measurements made at different temperatures, firstly to allow design strengths to be defined for different design temperatures and secondly to accommodate predictions made by time-temperature shifting. If this is done, the longest duration used to define f_{m122} may be redefined as the longest test after time-temperature shifting (WSDOT 1997). A maximum temperature shift of 20°C below the lowest test temperature is proposed.

Measurement of stress-rupture data is laborious, expensive and can give similar results on similar products. Small and Greenwood (1991) combined results from a range of polyethylene geogrids to produce a general stress-rupture curve for the range. Such measurements on products from the same range of products are generally acceptable but the rules for acceptance require definition (WSDOT 1997).

3.7 Combination of Partial Safety Factors

Following Greenwood and Yeo (1996) partial safety factors should correctly be classified and combined as follows:

reduction factors	multiply
statistical factors	combine statistically to give the correct final probability level
uncertainty factors	choose an appropriate overall factor not less than the largest partial factor

The resultant factors defined by the three classes should then be multiplied.

3.8 Creep Strain

In the absence of a satisfactory method for predicting the creep of the soil-reinforcement composite, current practice is to measure the unrestrained creep of geosynthetics for soil reinforcement in air. This yields maximum and thus conservative values for strain.

The comments made at the start of Section 3.6 concerning the extrapolation of stress-rupture apply equally well to creep. Again, there is no fundamental materials based equation for curve fitting. The equation

$$\varepsilon = \varepsilon_0 + \varepsilon_1 \log t \quad (9)$$

is normally sufficient for polyester and a power law

$$\varepsilon = \varepsilon_0 + \varepsilon_1 t^n \quad (10)$$

is a useful model for the primary creep of polyethylene with $\varepsilon =$ strain. $\varepsilon_0, \varepsilon_1$ and ε_2 (below) are all functions of applied load, the shape of which is reflected in the isochronous curves. For polyethylene it is necessary to predict the onset of secondary (constant strain rate) creep. This can be done by adding a constant strain rate term $\varepsilon_2 t$ and curve fitting to tests at higher values of load which exhibit secondary creep. If a relation is established between ε_2, T and applied load, for example by using Sherby-Dorn diagrams, then the onset of secondary creep can be predicted at lower values of T .

As for stress-rupture, creep strain curves can be time-temperature shifted, offering the possibility of abbreviated testing (see for example Thornton et al 1997). It should be noted, however, that since the elongation at break is itself a function of time and temperature the shift factor for creep strain may differ from that for stress-rupture of the same material.

The accuracy of the prediction of creep strain has been examined by Müller-Rochholz and Koslowski (1996) and found to lie within 0.7% strain for polyesters and polyethylene at 7% strain, predicted from 24 h to 24000 h. These levels of accuracy are comparable with the variability in short term creep modulus, suggesting that a partial safety factor for uncertainty of strain extrapolation is superfluous. As 10 year creep strain measurements on polyester based products are become available, the only partial safety factor

required for creep strain extrapolated to 100 years, given that temperature has already been taken into account, should be to reflect the variability in the initial strain or modulus of the material. This argument will not apply to creep rupture data until corresponding 10 year data are available.

3.9 Field Experience

The above predictions will increasingly be complemented, and eventually replaced, by experience from site. Statements that no degradation took place should always be accompanied by an estimate of what degradation might have been predicted given the site conditions. A conclusion that "no degradation occurred, and none was expected" serves only as a demonstration that no unexpected phenomena are present.

4 CONCLUSIONS

A document on the durability of geotextiles is in place for the guidance of civil engineers. Further details are necessary to cover the definition of partial safety factors used in the design of reinforced soil.

ACKNOWLEDGEMENTS

I acknowledge the many contributions made by members of CEN TC189/WG5 toward the first part of this publication. The second part is based partly on work supported by the Geotechnical Engineering Office, Hong Kong, and is published with the permission of the Director of Civil Engineering of the Hong Kong Government. The views expressed are those of the author. The Directors of ERA Technology Ltd are thanked for permission to publish.

REFERENCES

- BS 8006: (1995) *Code of Practice for Strengthened/Reinforced Soils and Other Fills*, British Standards Institution, London
- CEN (1998). *Geotextiles and Geotextile-related products: Guide to Durability*. CEN Report, Brussels, in press.
- ENV 12447 (1997). *Geotextiles and Geotextile-Related Products. Method for determining the resistance to hydrolysis*. CEN, Brussels
- ENV 12224 (1996). *Geotextiles and Geotextile-Related Products. Determination of the Resistance to Weathering*. CEN, Brussels.
- ENV 12225 (1996). *Geotextiles and Geotextile-Related Products. Method for determining the microbiological resistance by a soil burial test*. CEN, Brussels.
- Allen, T.M. and Bathurst, R.J. (1994) "Characterisation of Geosynthetic Load-Strain Behaviour after Installation Damage", *Geosynthetics International*, Vol. 1, No. 2, pp. 181-199.
- Allen, T.M. and Bathurst R.J. (1996) "Combined Allowable strength Reduction Factor for Geosynthetic Creep and Installation Damage", *Geosynthetics International*, Vol. 3, No. 3, pp. 407-439.
- Burgoyne, C.J. and Merri, A.L. (1993) "Hydrolysis tests on polyester yarns", Cambridge University Department of Engineering Technical Report CUEDID-Struct/TR138, Cambridge, U.K.
- Greenwood, J.H., Trubiroha, P., Schröder, H.F., Franke, P. and Hufenus R. (1996) "Durability Standards for Geosynthetics: the Tests for Weathering and Biological Resistance", *Geosynthetics: Applications, Design and Construction*, eds. de Groot, M., den Hoedt, G. and Termaat, R.J., Balkema, Rotterdam, Netherlands, pp. 637-642.
- Greenwood, J.H. and Yeo, K.C. (1996) "Assessment of Geogrids for Soil Reinforcement in Hong Kong", *Earth Reinforcement*, eds. Ochiai, H., Yasufuku, N. and Omine K., Balkema, Rotterdam, Netherlands, pp. 363-367.
- Greenwood, J.H. (1997) "Designing to Residual Strength of Geosynthetics Instead of Stress-Rupture", *Geosynthetics International*, Vol. 4, No. 1, pp. 1-10.
- Müller-Rochholz, J. and Koslowski, C. (1996) "Creep prediction", *Geosynthetics: Applications, Design and Construction*, eds. de Groot, M., den Hoedt, G. and Termaat, R.J., Balkema, Rotterdam, Netherlands, pp. 1027--1030.
- Salman, A., Elias, V., Juran, I., Lu, S. and Pierce, E. (1997) "Durability of Geosynthetics Based on Accelerated Laboratory Testing", *Geosynthetics '97*, Long Beach. IFAI, St. Paul MN, USA, pp. 217-234.
- Schmidt, H.M., te Pas, F.W.T., Risseeuw, P. and Voskamp, W. (1994) "The hydrolytic stability of PET Yarns under medium alkaline conditions", *Fifth International Conference on Geotextiles, Geomembranes and Related Products*, Singapore, Vol. 3, pp. 1153-1158.
- Small, G.D. and Greenwood, J.H. (1993) "A Review of the Phenomenon of Stress-Rupture in HDPE Geogrids", GEO Report No 19, Geotechnical Engineering Office, Hong Kong, 77p.
- Thornton, S.J., Allen, S.R. and Thomas, R.W. (1997) "Approaches for the Prediction of Long-Term Viscoelastic Properties of Geosynthetics from Short-Term Tests", *Geosynthetics '97*, Long Beach. IFAI, St. Paul MN, USA, pp. 277-291.
- Watts, G.R.A. and Brady, K.C. (1990) "Site damage trials on geotextiles", *Fourth International Conference on Geotextiles, Geomembranes and Related Products*, The Hague, Netherlands, pp 603-607
- WSDOT (1997) "Geosynthetic Reinforcement Product Submission and Approval Requirements". *Test Method 925*. Washington State Department of Transportation, USA.

Long-Term Experience with Reinforced Embankments on Soft Subsoil: Mechanical Behavior and Durability

K.-H. Blume

Dipl.-Ing., Federal Highway Research Institute, Bergisch-Gladbach, Germany

D. Alexiew

Dr.-Ing., HUESKER Synthetic GmbH & Co., Gescher, Germany

ABSTRACT: Two projects of embankments on soft ground with high-strength basement reinforcement are shortly described. Started in 1981 and 1986, respectively they belong to the first one's using preloading plus reinforcement for autobahns and highways in Germany. Site conditions, construction stages, measurement data and evaluation are presented, including long-term reinforcement strain measurements. The geotextiles are still under tension. In 1995 high-tenacity polyester woven was exhumed from underneath the first embankment and analyzed for evaluation of durability. Important preliminary results are reported, showing negligible loss of strength in 14 years. In conclusion, findings and recommendations for focal points of design, long-term reinforcement behavior and durability are summarized.

KEYWORDS: Embankments, Reinforcement, Long-term-measurements, Soft soils, Durability

1 INTRODUCTION

In Germany, in the construction of highways on soft saturated subsoils, increased use is being made of the preloading method. The advantages compared to soil replacement are not only the high cost savings but also countryside, environmental and ground water protection. The development of the preloading method is closely connected with the development of geosynthetics. The reinforcement function is of particular importance as it can be required not only to ensure the short-term stability during construction, but also the final long-term stability.

Since around 1970, the Federal Highway Research Institute (Bundesanstalt für Straßenwesen -BAST) has been involved in such projects on federal highways and autobahns. Investigation and measuring programs have been performed on large-scale test embankments. The aim was to ascertain the behavior of the soft subsoil and the long-term behavior of high-strength geosynthetic reinforcement. Some of the experimental embankments were just loaded up to ground failure to verify the assumptions and results of the stability calculations.

For the Federal autobahn project BAB A 26, connecting the cities of Hamburg and Stade, a test embankment was built near the town of Rübke (designated as 'Rübke-embankment' here) by the BAST in 1981, simulating a real autobahn-section on saturated peat with high-strength basement reinforcement. The project, materials used and deformation behavior until now are reported below.

Based on this experience the entire highway B 211 at the town of Grossemeer was built in 1986 under similar conditions using a reinforcement of even higher strength (designated as 'Grossemeer-embankment' here). The measurements in this case were extended by direct strain measurements on the high-strength woven used, which are continued up to now. The project, materials and most important measurement results including the long-term strains are shortly described.

In autumn 1995, after a 14-years-service period, parts of the high-tenacity polyester woven from underneath the 'Rübke-embankment' were exhumed. Tests and analyses were carried out for evaluation of durability. The most important findings are also presented.

2 TEST EMBANKMENT AT RÜBKE

2.1 Description Of The Full-Scale Test

The dimensions of the embankment were in compliance with the standard cross section RQ 26 planned for the autobahn. Geometry and essential characteristic values of the peat subsoil are shown in Figure 1. The consolidation calculations resulted in a required preloading height of 3.6 m. A part of preloading had to be removed after consolidation. The stability calculations were performed according to DIN 4084 (Bishop's method) modified by reinforcement retaining force. Only low short- and long-term strains were allowed. The calculations resulted in a reinforcement mobilizing at least 90 kN/m at maximum 5% short-term strain, with an ultimate tensile strength (UTS) of at least 200 kN/m and ultimate strain $\leq 10\%$. Only 1% creep strain in two years was allowed under 90 kN/m tension force. A high-strength polyester woven geotextile (Stabilenka® 200) was selected. The test comprises preloading with a subsequent consolidation period of just under two years, removal of preload, a reloading and the long-term measurements of the deformation behavior.

The test embankment was constructed directly on the terrain without any soil replacement. First of all the woven was laid on the grass in July 1981.

Loads, heights and settlements to date are shown in Figure 2.

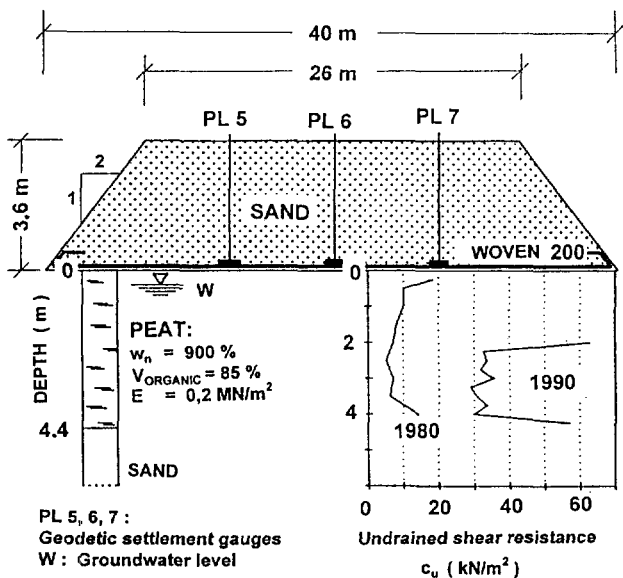


Figure 1. Full-scale test embankment at Rübke (not to scale).

2.2 Course Of The Test And Measurement Results

Measurements of settlement, pore water pressure, base pressure, inclination and groundwater level were performed.

In this test, it was not possible to perform strain measurements directly on the fabric. Because, at this time, a measuring system with robust, precise and water-proof strain gauges was not available. Four years later, long-term resistant strain gauges were developed and applied for the 'Grossenmeer-embankment' (see section 3).

The development of the settlement shows a significant drop in the settlement rate, which was below 1 cm/year in the first year after the reloading. Nowadays the settlement rate is less than 0.5 cm/year with a decreasing tendency. The BASt is continuing the measurements.

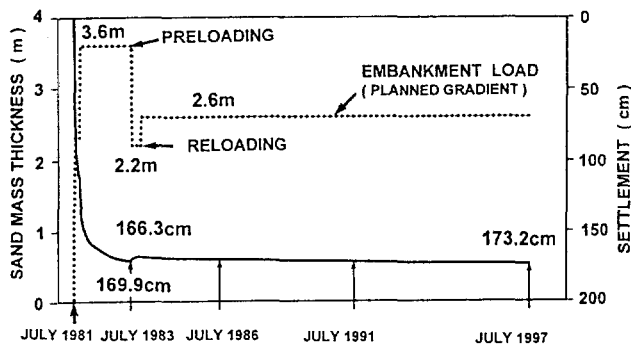


Figure 2. Load and settlement at Rübke from July 1981 until July 1997.

The high permeability of the peat in the unconsolidated state has made a rapid consolidation settlement easier.

For an embankment thickness of 2.3 m, the degree of consolidation was already 80% after two-months. Very high primary settlements of around 1.1 m were measured. The

transition primary / secondary settlements at a degree of consolidation of 90% occurred after 5.5 months. The total settlement of the peat mounted to around 1.6 m. The peat was compressed by around 40%.

The average strain of reinforcement derived from the settlement profiles (not shown) amounted up to 3%. Maxima and minima could not be registered due to absence of strain gauges (compare with section 3, 'Grossenmeer').

During filling and consolidation relatively low horizontal displacements occurred at the toe of embankment: maximum 18 cm in the peat and 12 cm on the ground surface. In a distance of 10 m from the toe of the embankment horizontal displacements of 1 cm to 3 cm were registered. The increase of undrained shear strength is shown in Figure 1.

2.3 Assessment Of The Measurement Results

The measurement results confirmed the feasibility of controlled construction of reinforced embankments on very weak subsoil (peat) by preloading, removing of preload and partial reloading to justify the final gradient. Due to the controlled preloading and the reinforcement, no failure-type deformations occurred, neither in the embankment nor in the foundation soil. The high-modulus geotextile (see section 2.1) allowed only small lateral spreading/squeezing deformations. Based on the average strain only the reinforcement looked understressed compared to design assumptions and calculations. But note, that strain (and tensile force) could had been higher e.g. in the usually critical zone (from the point of view of stability) under the slope and near the toe (see section 3.3). Summarizing: the simplified design calculations according to DIN 4084 agreed well enough for engineering purposes with the measured behavior. Nevertheless, continuous measurements are an important tool to control the construction progress.

The measurement results and the collected experience from July 1981 until March 1985 were adequate to recommend the preloading method with high-strength reinforcement for the entire new autobahn route BAB A 26.

3 HIGHWAY EMBANKMENT AT GROSSENMEER: TEST AND REFERENCE SECTIONS

3.1 Description Of The Project

Due to the positive results from the 'Rübke-embankment', the BASt recommended the preloading method with geotextile reinforcement for the construction of the new federal interstate highway B 211 at the town of Grossenmeer.

The BASt performed measurements on two sections. The first one with steeper slopes, called here 'test embankment', had to be integrated later after reshaping in the standard highway embankment. The second one, called here 'reference section', was already from the beginning a standard highway embankment. The test program was extended here by direct short- and long-term strain measurements of

the high-strength basement reinforcement.

The highway embankment at Grossenmeer has a length of around 2 km. The weak subsoil consists of layers of peat and organic silts in all 3 m to 5 m thick, underlayered by dense sand. According to pre-design calculations, typically an embankment thickness of 4.5 m height was selected for the stage of consolidation (preloading). The consolidation period was expected to be about two years. After that layers of different adequate thickness had to be removed to fit the planned final gradient.

The following design soil parameters were assumed for the stability calculations according to DIN 4084:

- Soft subsoil: Undrained shear strength $c_u = 8 \text{ kN/m}^2$
Unit weight $\gamma_n = 11 \text{ to } 13 \text{ kN/m}^3$
- Sand: Angle of internal friction $\phi' = 32.5^\circ$
Unit weight $\gamma_n = 18 \text{ kN/m}^3$

The calculation resulted in an allowable embankment height of only 2.6 m without reinforcement. To achieve the aimed preloading height of 4.5 m and the required FOS = 1.2 (global stability, temporary stage) according to DIN 4084, a reinforcement tensile force of about 200 kN/m was required (Blume 1995, Blume 1996). For reasons of deformation compatibility the corresponding short-term strain was limited to 5%, and the total strain (short-term plus creep) was not allowed to exceed 6% for several years. Based on the stress-strain and creep curves a high-tenacity polyester woven with an UTS = 400 kN/m and 10% ultimate strain was selected (Stabilenka® 400).

The earthwork for the entire 2 km-stretch was carried out from June 1986 until June 1987, followed by a consolidation period of 15 months. After then in some sections the embankment thickness had to be increased additionally from 4.5 m up to 6.5 m (including the 'reference section', see below) to compensate the unexpected high settlements. After a new consolidation period of 17 months, parts of the preloading thickness were removed in March 1990 for fitting the final gradient. The highway was opened to traffic in October 1990.

Since October 1990, after the end of the measurements directly accompanying construction, measurements have been and are being performed on the long-term deformation behavior of the subsoil, of the completed highway and on the strain behavior of the basal reinforcement.

3.2 Description Of The Tests

The main aim of both the 'test embankment' and the 'reference section' was to provoke the highest possible stress in the woven, selecting sections of the highway having particularly unfavorable subsoil conditions. Knowledge was to be gained of the long-term behavior of the reinforcement.

Under the 'test embankment', which was planned as a 'crash test', extremely high reinforcement stress had to be generated by rapid construction (4.5 m in four days), and by a steep slope of 1 V : 2 H. Nevertheless, ground failure had to be avoided because of the later integration in the stan-

dard highway embankment, after reshaping. Around 40 m away, in the 'reference section' with a standard (flatter) slope of 1 V : 3 H, the loading process lasted around a year.

For the direct geotextile strain measurements, the BAST developed a suitable strain measuring system which does not influence the strain of the fabric. Robustness, precision and water-resistance were proved in advance in contact with soil and under water also.

Settlements, pore water pressure, inclination and groundwater level of the subsoil were measured. The strain measurements were performed on, in total three cross sections, two of them in the 'test embankment' and one in the 'reference section'. In each case 9 strain gauges were installed at 2 m space. Additionally, settlement gauges were placed near the strain gauges (Figure 3 a, d).

3.3 Measurement Results And Assessment

The most important results are depicted in Figure 3 a, b, c for the 'test embankment' and in Figure 3 d, e, f for the 'reference section'. Note, that embankment material, single layer thickness, height (4.5 m) and reinforcement are the same.

The construction periods and slope inclinations are quite different, as mentioned above.

In Figure 3 b, c the graphs show the development only within the first 4 days (height from zero to 4.5 m). After that the increase in strain became less and, after 2 months, came almost to a halt (not shown). In the subsequent 25 months the strains asymptotically came up to a maximum final strain of about 7% below the slope and 6% below the center of the embankment (not shown).

In Figure 3 e, f the graphs show the processes within around one year (height from zero to 4.5 m stepwise). The line with the number 1 corresponds to the 4th day (1.5 m sand), and with the numbers 2 to 5 to the 30th day after placing of the respective sand layer, at nearly constant time intervals.

Although the distance between the 'test embankment' and the 'reference section' is only around 40 m, the subsoil conditions seem to be considerably different, resulting in unexpected high settlements of the latter. In both cases a weak zone below the slopes was identified. Nevertheless, slope failure was not observed in the embankment body itself, neither for the 'test embankment', nor for the 'reference section'. On the contrary, the horizontal displacement of the subsoil near the toes became large, for the 'test embankment' up to 40 cm, destroying the inclinometer tubes. The ground tended to a 'squeezing-out', but a real failure did not occur. Note, that the typical subsoil-squeezing-mode cannot be checked by Bishop's method (DIN 4084) used for design calculations. Nowadays this mode should be checked e.g. according to Michalowski and Lei Shi (1993).

The reasons for the surprisingly high reinforcement-strains (and corresponding stresses) below the slopes in both cases are apparently both the weak zones and the squeezing-out tendency.

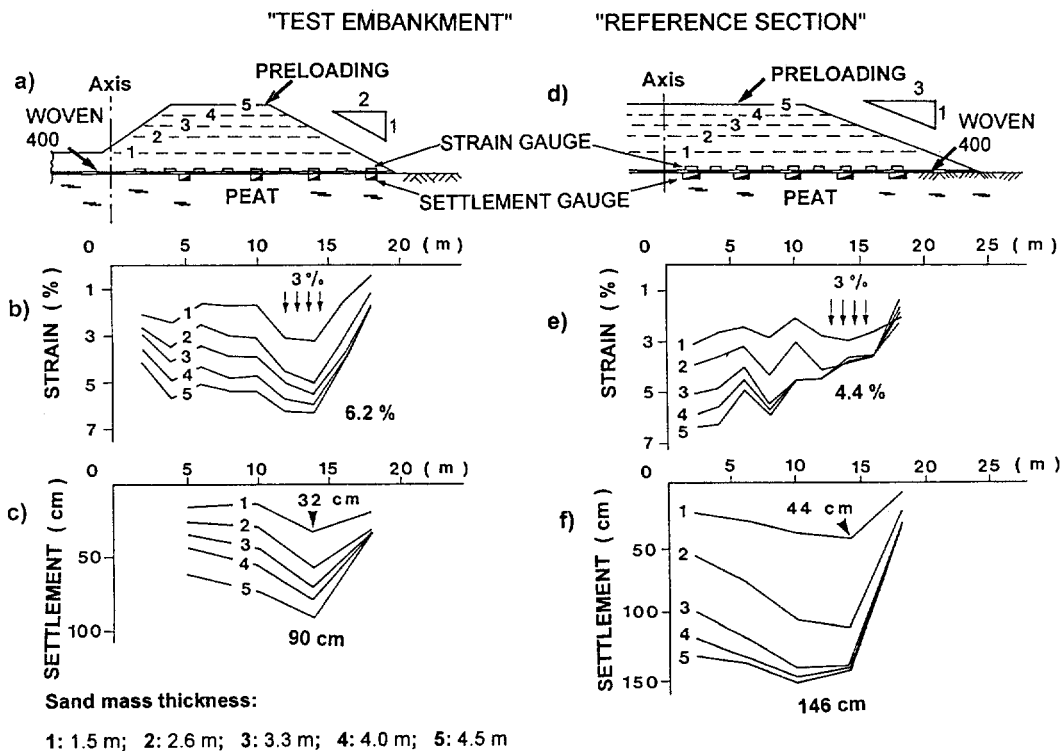


Figure 3. Grossemeer: construction stages, settlements and strains

The strain increase and the horizontal deformations came to a halt shortly after completion of the construction. Based on the observation, it can be concluded that the reinforcement prevented both slope failure of the embankment and ground failure due to squeezing of the soft layers.

The reinforcement strains exceeded at some locations the values of 5% (short-term) and 6% (long-term) assumed in design. The real mobilized tensile forces were higher than expected according to the stability calculations (DIN 4084, Bishop's method). The stress ratio (tensile force/UTS) exceeded 50% clearly.

In 1993, the strain measurements in the 'test embankment' were terminated due to adjacent building activities. Only the results of the continued long-term measurements from the 'reference section' are reported below.

Note, that in Figure 3 d, e, f only the period from June 1987 to June 1988 is depicted. After that in Autumn 1988 the height of the 'reference section' was increased to 6.5 m to compensate the high settlements, and was reduced again just in Spring 1990 (Figure 4).

So far, at the center of the embankment, maximum strains between 6.8% and 7.6% and maximum settlements of the soft subsoil of between 190 cm and 205 cm have been measured. The strains presented in Figure 4 from commencement of construction in July 1986 until July 1997 remained practically unchanged after removal of the preloading height and opening of the highway to traffic in October 1990.

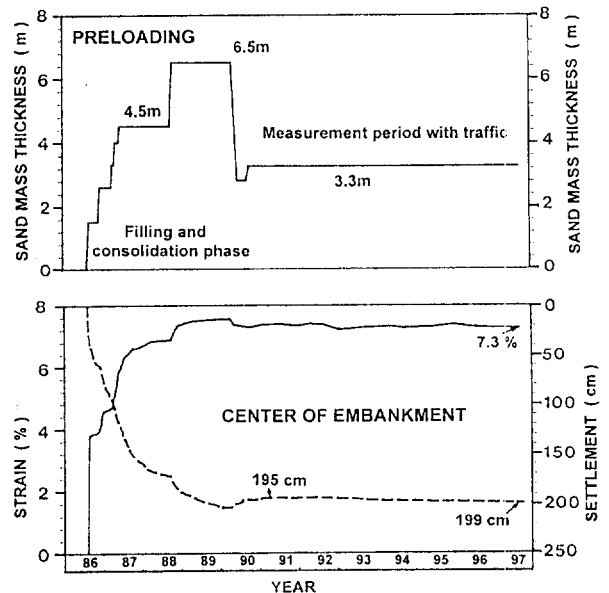


Figure 4. Variation of load, strain and settlement in the Grossemeer 'reference section' (1986 to 1997).

The constant strain level indicates that the reinforcement is still under tension after 10 years. It is difficult to evaluate the effective tensile forces from the registered strains with high precision now. In comparison with the short-term behavior a reduction in the effective tensile stress could be expected theoretically due to some factors. Relaxation could

play a (negligible) role; for the high-tenacity polyester used relaxation due to creep is very low. Furthermore, installation/compaction damage and environmental effects could have reduced the really available mobilized tensile force.

For the evaluation of relaxation the isochrones could be used, and the percentage of installation damage in sands is known in good confidence, being in the range of 5% to 10% for the reinforcement used. For evaluation of environmental effects the best way is to exhume and analyze an analogous reinforcement material, which has been embedded under similar conditions for a long time. For this purpose the Rübke-embankment offered a good possibility (see section 2).

4. INVESTIGATION OF A HIGH-STRENGTH POLYESTER WOVEN AFTER 14 YEARS EMBEDDED IN SOIL

4.1 Description Of Exhumation And Tests

In 1995, the BAST initiated the investigation of exhumed fabric samples. Since it is not possible to take samples from Grossemeer, the BAST proposed, samples to be taken at Rübke (see section 2).

In September 1995, around 120 m² of the high-strength woven were exhumed from the embankment base after 14 years in use. The entire geotextile was lying below the terrain in the peat and groundwater due to settlements. By an excavator, embankment parts were removed down to the woven, from the slope to the center of embankment. At the beginning, it was possible to remove the remaining sand by hand. Due to the rapid rising of water, it was unavoidable to pull out and up most of the woven directly by the excavator. Thus, abrasion and damage of the fabric could not be fully avoided.

It was observed during uncovering, that the woven was still under tension before cutting. A considerable effort was necessary to lift up the edge of the woven by a shovel (Figure 5). This observation corresponds to the strains under the Grossemeer 'reference section', which indicate considerable tensile forces until today also (Figure 4). Discoloration of the fabric due to contact with the rotted grass and the peat were clearly visible. In some places, grains of sand had penetrated its structure.

Samples for the testing institutes, participating in the investigations, were taken from four different geotextile areas after exhumation, corresponding to defined different positions in the base.

For each of the four areas the following tests were performed:

- (1) Yarn tensile tests according to DIN 53834, T 1 with 15 individual tests per each area
- (2) Analyses for determination of the carboxyl end groups (CEG) and of the molecular weights of the high-tenacity polyester
- (3) Scanning electron microscopy (SEM) of filaments
- (4) Chemical analysis of the groundwater (pH-values).

4.2 Evaluation Of The Results Available To Date

The evaluation of the investigations regarding durability are almost completed. The most important results to date are presented here. The final evaluation and details will be reported separately.

The results of yarn tensile tests form a better criterion for evaluation of strength loss due to environmental effects than the wide-width strip tests. Damage caused by installation, compaction and (in this case) removal and exhumation, and sand-grain inclusions in the woven structure has a less pronounced influence on the cleaned single yarn (although it can not be eliminated). The graphs in Figure 6 show the stress-strain behavior of the exhumed yarns. Each curve represents the average of 15 tests per area.



Figure 5. Rübke: the woven being still under tension after 14 years.

The specific yarn strength of the 'virgin' (brand new) high-tenacity polyester used (Diolen[®]: CEG < 27 meq/kg; number average molecular weight M_n > 25000; further exact data are known also) is shown in Figure 6, too. To perform a durability evaluation on the safer side, an increased possible average value of 'virgin' strength of 86 cN/tex (instead of 84.6 cN/tex) could be assumed. Thus, the residual strength is around 83% of the 'virgin' strength. The ultimate strain is practically unchanged. Note, that the yarn-strength-loss of around 17% includes (in chronological order) the effects of weaving of the yarns producing the fabric, of installation and compaction damage, of biological and chemical degradation (chemical attack plus hydrolysis) and of exhumation process.

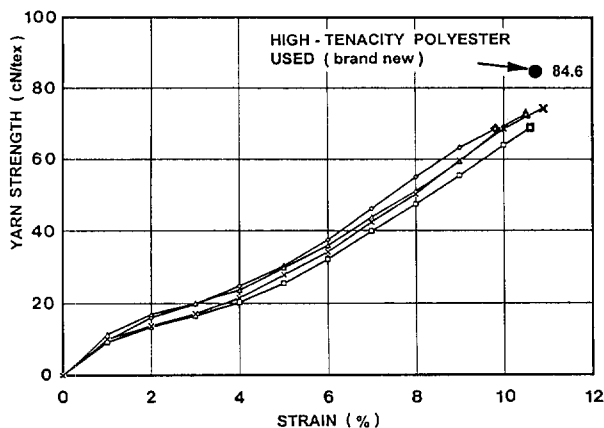


Figure 6. Specific yarn strength after 14 years in soil under groundwater level for the four different sampled areas according to DIN 53834, T 1.

The loss of yarn-strength due to the manufacturing process is 7% to 12%, on the average 9% (HUESKER Synthetic 1996). Further, for the woven mentioned loss of strength during compaction in sands of 5% to 10% has been observed. The loss of strength due to exhumation process is hardly to be identified exactly, but it can be set to 1% to 5% in this case. (Note, that a gentle exhumation was not possible, as mentioned above.)

The comparison of the percentage terms described above (weaving, compaction and exhumation) with the registered total loss of yarn-strength of about 17% results in 0% to 3% loss of strength due to environmental effects in this case.

Further, the SEM-photomicrographs performed indicate no chemical damage of the filament surface; it is completely smooth.

The comparison of molecular weights and number of CEG of 'virgin' and exhumed material leads so far to the conclusion, that 1% to 2% of strength-loss could be caused by changes in the polymer itself.

These latter evaluations of the microscopic and chemical investigations correspond well to the evaluation of loss in strength based on mechanical yarn-tests as mentioned earlier.

The pH-value of the groundwater is 6.6 on the average. This fact together with the SEM leads to the conclusion, that no chemical attack ('external' hydrolysis) has taken place.

The loss of strength of about 1.5% per 10 years, evaluated by different methods in this case, may be explained by 'internal' hydrolysis ('aging') in the groundwater and (unlikely) by biological effects (rotted grass, peat).

5 SUMMARY AND CONCLUSIONS

Two projects of embankments on soft subsoil with high-strength basement reinforcement have been started in Germany in 1981 ('Rübke') and 1986 ('Grossenmeer')

respectively.

The 'Rübke-embankment' is a pure test-embankment for the autobahn BAB A 26. The 'Grossenmeer-embankment' is an integral part of the federal highway B 211. In both cases high-modulus polyester woven is used with 200 kN/m and 400 kN/m UTS, respectively, and 10% ultimate strain. For stability calculations DIN 4084 (Bishop's method) has been used, modified by reinforcement force. Measurement programs are performed up to now, including direct strain measurements at 'Grossenmeer'.

Woven from 'Rübke' was exhumed after 14 years under tension below groundwater to evaluate durability.

1. Stability calculations according to DIN 4084 are correct enough to prevent failure of embankment and/or subsoil, at least when high tensile force at low strain is mobilized to restrain deformations.
2. High-moduli for a long period (low creep) are important, because the reinforcement works after consolidation also. In the projects described it is still under tension after 15 and 11 years, respectively.
3. The high-strength reinforcement used proved to resist overstressing successfully for a long period.
4. Local weaker subsoil zones can easily result in reinforcement overstressing and/or failure tendency; it should be kept in mind when selecting safety factors.
5. Subsoil squeezing-out is recommended to be checked additionally to DIN 4084-calculations by other methods.
6. The analyses of durability and operation conditions indicate in this case, that (internal) hydrolysis under stress in groundwater is the main reason for the registered negligible loss of strength.
7. The loss of strength due to 'aging' (environmental effects) is 1.5% to 2% in 14 years for the high-tenacity polyester woven used.

REFERENCES

- Blume, K.-H. (1995) "Großversuch zum Tragverhalten textiler Bewehrung unter einer Dammaufstandsfläche", 4. Informations- und Vortragsveranstaltung über "Kunststoffe in der Geotechnik", Special Issue 1995, DGGT, Germany, pp. 78 - 88.
- Blume, K.-H. (1996) "Long-term measurement on a road embankment reinforced with a high-strength geotextile", EuroGeo 1 1996, Maastricht, The Netherlands, Conference proceedings, Balkema, Rotterdam, 1996, pp. 237 - 244.
- HUESKER Synthetic GmbH & Co. (1996), "Internal test reports summary", Gescher, Germany (unpublished).
- Michalowski, R.L., Lei Shi (1993), "Bearing capacity of nonhomogeneous clay layers under embankments", Journal of Geotechnical Engineering, Vol. 119, 1993, No. 10, ASCE, pp. 1657 - 1669.

Durability of Polyester and Polypropylene Geotextiles Buried in a Tropical Environment for 14 Years

J.W. Cowland
Geotechnical Engineering Office, Hong Kong

K.C. Yeo
Geotechnical Engineering Office, Hong Kong

J.H. Greenwood
ERA Technology, United Kingdom

ABSTRACT: The demolition of a 14 year old embankment on soft clay provided the opportunity to exhume samples of the geotextiles that had been used to reinforce the base. Specimens of these woven polyester and woven polypropylene geotextiles were then tested to assess their durability. From tensile and hydrolysis tests it was found that the polypropylene geotextile largely retained its strength, and the polyester geotextile lost about 15% of its strength. A portion of the polyester strength loss was attributed to hydrolysis.

KEYWORDS: Durability, Polyester, Polypropylene, Geotextiles, Tropical Environment.

1. INTRODUCTION

In 1982, a 3.5 km long coastal road embankment was constructed on soft clays in a tidal area of Hong Kong. The base of this embankment was reinforced with woven polyester and woven polypropylene geotextiles. Figure 1 shows a typical cross-section of the embankment.

In 1996, part of this embankment was demolished to make way for a river improvement scheme, which provided the opportunity to exhume some of these materials. Large pieces of both the polyester and the polypropylene geotextiles were carefully removed from the embankment by hand, and tests were carried out to determine their durability.

Tensile tests were carried out to determine the strengths of the recovered geotextiles, and they were also examined under a scanning electron microscope to determine the extent of site damage. Carboxyl end group counts, and molecular weight determinations, were performed on the polyester geotextile to evaluate the extent of hydrolysis. This paper presents the results of these durability tests.

2. GEOTEXTILES

A single layer of reinforcing geotextile was used beneath the embankment. Rolls 5 m wide were placed on the intertidal mud flats and stitched together. The project commenced with a polyester geotextile, which was substituted in places by a polypropylene geotextile. The exhumation encountered areas of both materials.

2.1 Polyester

The woven polyester geotextile was a multifilament material, with a weight of 450 g/m². Quality control tests at the time of construction demonstrated a characteristic tensile strength of 200 kN/m in the warp. The maximum tensile strength was often 220 kN/m, at a strain of 8%, with a 10% strain at break. In the weft the characteristic tensile strength was 45 kN/m, with a 20% strain at break.

Ten strain gauges were attached to one roll of the polyester geotextile during laying, and a 9% extension was recorded after the placing of the fill material.

2.2 Polypropylene

The woven polypropylene geotextile was a fibrillated tape material, with a weight of 570 g/m². Quality control tests demonstrated a characteristic tensile strength of 200 kN/m in the warp, with a strain of 12% at the maximum tensile strength, and 40 kN/m in the weft.

3. ENVIRONMENT

The coastal road embankment was constructed in the intertidal zone of a mangrove swamp. The geotextiles were placed by hand directly onto the very soft dark grey organic silty clay, which contained a large number of shells. The fill material, essentially a brown gravelly silty sand of granitic origin, was mechanically placed on top in 0.5 m layers.

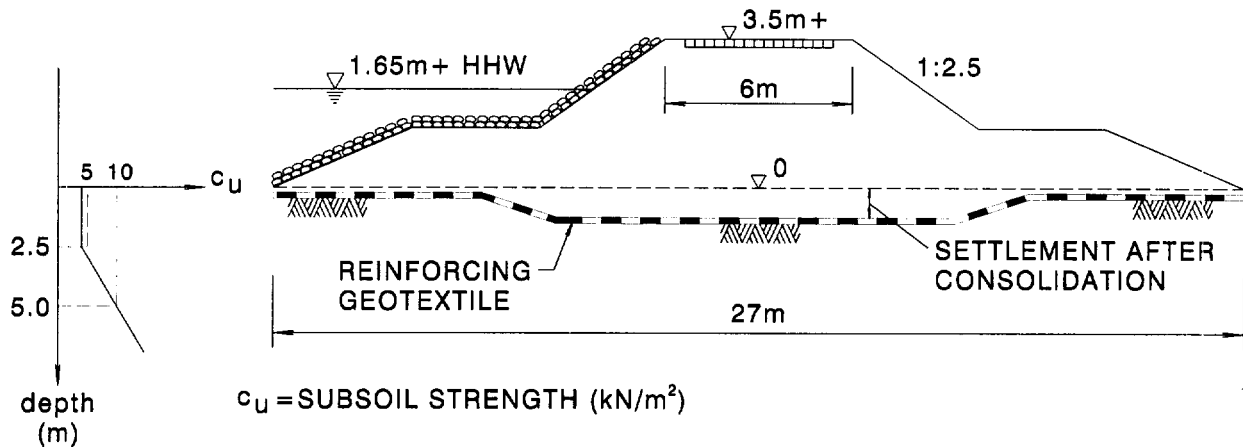


Figure 1. Cross-Section of the Embankment

During exhumation, pieces of pH indicator paper were placed in the water surrounding each geotextile, and they all indicated a pH of 7. It should be noted, though, that the portion of the exhumed embankment where the polyester geotextile was located was adjacent to the estuary of the Shan Pui River, which flows through the Yuen Long Industrial Estate, and is polluted.

The Hong Kong Observatory has been measuring soil temperature, for agricultural purposes, for over 25 years. At a depth of 3 m below ground level, the average soil temperature has consistently been found to be 26°C.

4. EXHUMATION AND SAMPLE SELECTION

The polypropylene geotextile was encountered during the initial stage of demolition of the embankment. With the full cooperation of the site staff, careful hand excavations were then made to recover large pieces of both the polyester and the polypropylene geotextiles. These large pieces were then washed with a hose of water to remove some of the adhering soil, their appearance carefully observed and recorded, before being transported to the laboratory.

The appearance of the black polypropylene geotextile was relatively uniform, and appropriate samples were taken for tensile testing, and examination for site damage.

The white polyester geotextile had more marked differences in appearance, especially in colour. One area was greyish white, and showed some signs of installation damage, whilst another area was stained brown and grey. Samples for testing were selected from areas that were visually undamaged (to the human eye), although stained.

5. DURABILITY TESTING

5.1 Tensile Tests

Ten specimens of the polyester geotextile, and ten specimens of the polypropylene geotextile, were subjected to wide width tensile tests, in accordance with BS 6906: Part 1 (1987), except that individual specimens were tested at different rates of strain. Two specimens of each geotextile were tested in the warp direction at 100, 10, 1, 0.1 and 0.01 per cent/minute strain. The specimens were gripped with roller clamps, and their extensions measured using a non-contacting video extensometer.

The results are shown in Table 1. Examples of the load strain curves for both the polyester and the polypropylene geotextiles, at a constant strain rate of 10%/min, are shown in Figure 2. None of the polyester specimens showed any visible signs of damage before testing, although some staining was evident on all specimens. Specimen F of the polypropylene material showed visible fraying of some of the warp fibres, and this probably accounts for the low value of tensile strength.

The results are summarised in Figure 3.

5.2 Scanning Electron Microscope Examination

Three specimens of the polypropylene geotextile were examined in a scanning electron microscope, one on both sides. Their appearance, as shown in Plate 1, was typical of a fibrillated tape geotextile. Most of the damage was confined to the surface. Both warp and weft were damaged equally. Soil residue had penetrated the textile.

Table 1. Tensile Test Results

Rate of strain (%/minute)	Polypropylene Geotextile			Polyester Geotextile		
	Sample	Maximum strength (kN/m)	Strain at maximum strength (%)	Sample	Maximum strength (kN/m)	Strain at maximum strength (%)
100	A	246.4	10.7	A	168.2	5.5
100	B	259.5	11.2	B	153.8	4.9
10	C	216.9	12.6	C	177.7	5.5
10	D	215.4	11.5	D	164.2	5.4
1	E	213.1	14.5	E	173.9	5.5
1	F	†144.8	11.1	F	142.2	5.1
0.1	G	210.9	15.3	G	159.1	5.3
0.1	H	167.2	13.7	H	163.8	5.2
0.01	I	160.6	15.6	I	108.8	3.7
0.01	J	188.6	20.8	J	140.5	5.2

† Damaged specimen

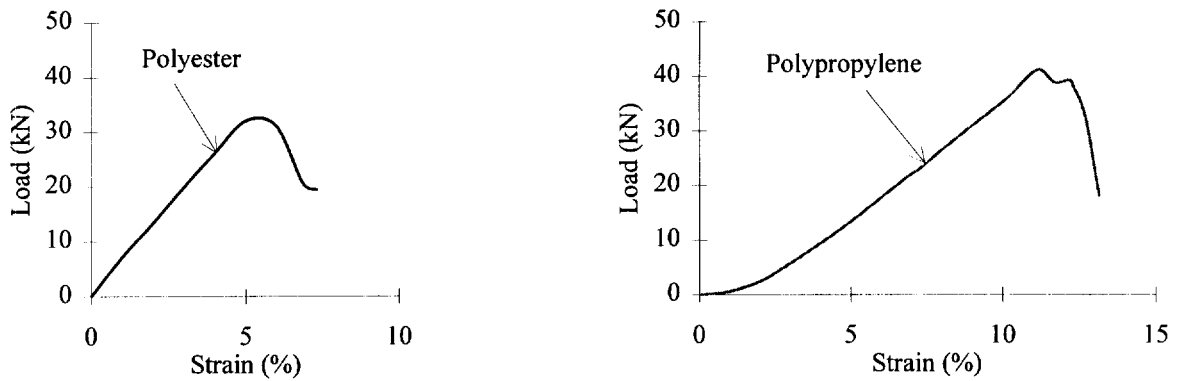


Figure 2. Examples of Load Strain Curves

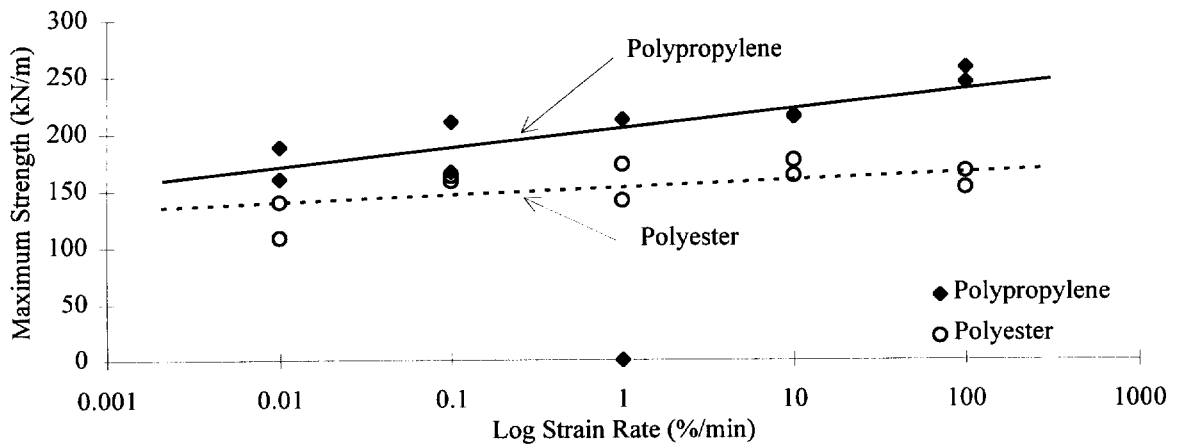


Figure 3. Change of Maximum Tensile Strength with Strain Rate

Plate 1. Scanning Electron Micrograph of Polypropylene Geotextile

Plate 2. Scanning Electron Micrograph of Polyester Geotextile

Plate 3. Scanning Electron Micrograph of Polyester Geotextile

Plate 4. Scanning Electron Micrograph of Polyester Geotextile

Table 2. Hydrolysis Test Results

Specimen	Staining	Intrinsic viscosity	Viscosity molecular weight	Carboxyl end group (CEG) (meq./ μg)			Mean CEG (meq./ μg)
1	Greyish white	1.08	38,200	28.9	25.9	29.8	28.2
2	Grey / brown	0.61	19,200	30.4	30.1	29.8	30.1
3	Grey / brown	0.64	20,300	29.6	30.2	29.4	29.7

Two specimens of the polyester geotextile, one from the area stained brown and grey, and the other from the area stained greyish white, were examined in the scanning electron microscope. There was no damage visible to the unaided eye in either specimen. Examples of the micrographs are shown in Plates 2, 3 & 4; in which the warp direction is horizontal.

Locally there was damage to the fibres in the form of splits, indentations or openings in the fibre surface parallel to the axis. In places the surface of the fibres appeared flaky. This was sometimes, but not always accompanied by local distortion, as shown in Plate 3. Individual soil particles and smeared areas were present, primarily attached to the warp fibres.

X-ray analysis of an area stained brown and grey showed that the smeared areas contained aluminium, silicon and some iron, and were therefore likely to be from an iron containing clay. Analysis of the discrete particles showed that some were clay, but others consisted mostly of sulphur. Analysis of an area stained greyish white found similar distributions of sulphur containing particles. The clay was found to contain silicon and aluminium as before, but no iron.

5.3 Hydrolysis Tests

Nine carboxyl end group tests were carried out on the polyester geotextile, using the non-aqueous titration method of Pohl (1954), but with bromocresol green as the indicator. Three tests were performed on a specimen of the material stained greyish white and six were performed on two specimens of the material stained brown and grey. The results are shown in Table 2.

Three intrinsic viscosity measurements were made, in accordance with ISO 1628-1 (1984), using o-chlorophenol as the solution medium; from which the viscosity molecular weight, which approximates to the weight average molecular weight, was then calculated. These results are also shown in Table 2.

6. DISCUSSION OF RESULTS

6.1 Polypropylene

The loss of strength of the polypropylene geotextile after burial for 14 years was relatively insignificant. Also, as shown by comparison of a test at 10%/minute strain (Figure 2) and the original properties, there was little change to the strain characteristics.

In addition, examination in the scanning electron microscope found only surficial surface damage to the material. Thus, it is concluded that this woven polypropylene geotextile has survived installation, and burial in the ground for 14 years at 26°C., with little change.

6.2 Polyester

The polyester geotextile lost about 15% of its strength after installation and burial for 14 years in a saturated ground at 26°C.

From Table 1 it can be seen the strain at maximum strength was less than that measured before installation. Figure 2 shows that the strain at break was also less. The relatively flat gradient of the polyester change of strength with strain rate plot, shown in Figure 3, indicates that it is not particularly strain rate sensitive.

The carboxyl end group test results ranged from 26 to 30 equivalent ends/microgram, which when compared with the range of 25 to 50 normally required for the production of high tenacity polyester fibres, indicates little hydrolytic degradation. The results for the material stained brown and grey were slightly higher than for the greyish white material.

The weight and number average molecular weights of the original geotextile are believed to have been at least 33,000 and 12,400 respectively. The intrinsic viscosity measurements and molecular weight determinations showed that material from the areas stained brown and grey was only two thirds of the original molecular weight.

Taking all these measurements into account, especially the loss of molecular weight, it is concluded that a portion of the 15% loss of strength of this woven polyester geotextile was due to hydrolysis. The rest may be due to installation damage (Brady et al, 1994).

The analysis of Burgoyne and Merii (1993) and the Arrhenius diagram of Schmidt et al (1994) both predict a loss of less than 5% due to hydrolysis after 14 years in saturated soil at 26°C. Salman et al (1997) predict a larger loss, and Schmidt et al indicate that a 30% loss of molecular weight would be associated with a 14% loss of strength.

The relationship between a change of carboxyl end group count and the change in the molecular weight depends on the distribution of molecular weights. Local hydrolysis may be associated with the presence of metal ions in the degraded areas.

This loss of strength does not preclude the use of similar polyester geotextiles for the basal reinforcement of embankments on soft clay, as the strength of the reinforcement is only required for a few months, until the clay has consolidated. It is suggested, though, that similar durability studies be carried out on polyester geotextiles and geogrids exhumed from permanent reinforced fill.

ACKNOWLEDGEMENTS

This paper is published with the permission of the Director of Civil Engineering of the Hong Kong Special Administrative Region Government. J.H. Greenwood thanks the Directors of ERA Technology for permission to publish.

The authors wish to thank G.W. Lovegrove and F. Teague for their records and recollections of the construction of the embankment, and Mrs. P.J. Howard for performing the scanning electron microscopy.

REFERENCES

- Brady K.C., Watts G.R.A., Nagarkatti A.S. & Greenwood J.H. (1994). "Installation Damage Trials on Geotextiles", Research Report 382, Transport Research Laboratory, Crowthorne, U.K.
- British Standards Institution (1987). BS 6906: Part 1. "Methods of Test for Geotextiles: Determination of the Tensile Properties using a Wide Width Strip", BSI, London.
- Burgoyne C.J. & Merii A.L. (1993). "Hydrolysis Tests on Polyester Yarns", Cambridge University Department of Engineering Technical report CUEDID-Struct/TR138, Cambridge, U.K.
- International Organisation for Standardisation (1984). ISO 1628-1: "Guidelines for the Standardisation of Methods for the Determination of Viscosity Number and Limiting Viscosity Number of Polymers in Dilute Solution", ISO, Switzerland.
- Pohl H.A. (1954). "Determination of Carboxyl End Groups in a Polyester, Polyethylene Terephthalate", Analytical Chemistry, Volume 26, pp. 1614-1616.
- Salman A., Elias V., Juran I., Lu S. & Pierce E. (1997). "Durability of Geosynthetics Based on Accelerated Laboratory Testing", Geosynthetics 97, Long Beach, U.S.A., pp. 217-234.
- Schmidt H.M., te Pas F.W.T., Riseeuw P. & Voskamp W. (1994). "The Hydrolytic Stability of PET Yarns Under Medium Alkaline Conditions", Proceedings of the 5th International Conference on Geotextiles, Geomembranes and Related Products, Singapore, Volume 3, pp. 1153-1158.

Study on Creep-Rupture of Polyester Tendons : Full Scale Tests

P. Orsat
Freyssisol, Freyssinet International and Cie, Velizy, France

M. Khay
Centre d'Experimentation Routiere, Le Grand Quevilly, France

M. Mc Creath, Linear Composites Ltd, Keighley, United Kingdom

ABSTRACT: The behaviour under creep of polymeric materials used to reinforce soil structures is an essential criterion in the study of the durability of structures. The report presents the results of full-scale tests carried out to study the behaviour under creep of polyester tendons. Loading tests to rupture were performed on tendons for assumed life periods of 2, 10, 30, 100, 300 and 1000 days. Samples taken before rupture at different ages allow determination of the residual strength characteristics of the tendons. The results obtained confirm the law of the linear behaviour of creep rupture versus the logarithm of time. It also shows that the residual strength of tendons subjected to creep tests remains greater than that calculated from the stress rupture curve and very close to the initial test strength of polymeric materials.

KEYWORDS: Polyester, creep rupture, residual strength, creep.

1 INTRODUCTION

The results of creep rupture tests on polyester fibres are generally expressed in the form of creep rupture curves of the type: load in relation to log (time) as shown in Figure 1. The admissible tension load at time "t" is determined by extrapolation of the tensile strength data obtained from creep tests at time t_0 . Safety coefficients are applied to the tensile strength to allow for uncertainty due to extrapolation. Knowing the true strength of the material under the effect of creep related to time is of major interest when defining these safety coefficients.

It is important, therefore, to establish the residual strength of tendons used i.e. what is their actual breaking load Tf_1 at time " t_1 ", under a given load applied Tf_2 , when off loading takes place some time before creep rupture, as per the creep rupture line at time " t_2 " (Figure 2).

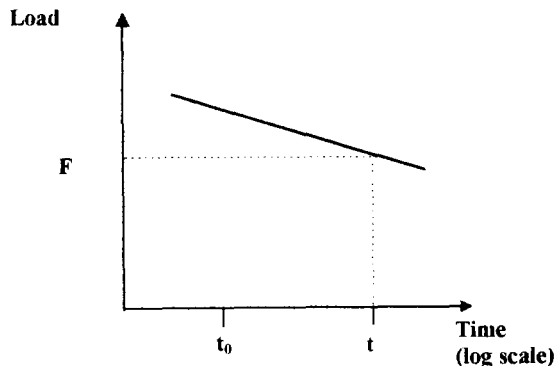


Figure 1. Creep rupture curve.

The report presents the results of a study carried out in order to establish the characteristics of creep rupture of polyester cables used as tendons in reinforced fill and to evaluate their residual strength before rupture (Linear Composites Ltd 1995).

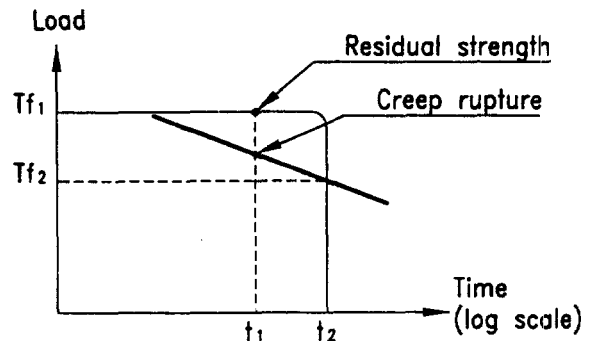


Figure 2. Residual strength.

2 TESTS

The loading test was performed to full scale in a covered test pit under ambient atmospheric conditions. A device allowed maintenance and monitoring of the temperature in the pit at about 18°C. Tendon test pieces were loaded to a constant value calculated for different rupture times. For each series, the tests were continued on the one hand up to creep rupture of the test pieces, and on the other hand by

taking samples at different times before rupture for determination of their residual strength in a laboratory tensile test.

2.1 Tested Material

For this study and for experimental purposes, the tests were performed on Parafil polyester tendons of the same nature as polyester reinforced strips used in the reinforced fill. These were composed of polyester fibres covered with a polyethylene sheath. The test pieces, prepared specially for these tests, were 550 mm long and comprised two termination devices at their extremities.

2.2 Loading Weights

These tendons are characterised by:

- their Nominal Breaking Load "N.B.L." defined as 10 kN,
- their actual breaking load i.e. the mean of 20 samples tested as initial reference. However, this value can vary between various series of samples tested due to termination dimension as pre-tensioning conditions during samples preparation.

The weights consist of concrete blocks which are adjusted by adding additional weights before loading the samples.

2.3 Table 1

This table gives the plan of the experiments carried out. The set of samples was prepared successively for the tests. In general, 16 samples were loaded for each creep rupture point and 6 samples for each strength retention point.

Table 1. Plan of experiments performed.

Phase	Reference	Loading for		Test performed		Type	
	Sample	Test pieces	Rupture at (days)	Test pieces	Time (day)	Test pieces	
0		2	5	2	5	Creep	
1	1	20	2	12	2	12	Creep
			10	16	10	16	Creep
			30	14	30	14	Creep
2	2	20	100	40	2.10	4x6=2	Resi. strength
					30.60	4	
					100	16	Creep
					30	6	Resid. strength
					300	34	100
3	3	5	1000	24	200	6	
					300	16	Creep
					30	6	
					100	6	Resid. strength
					200	6	Resid. strength
			300	6			

2.4 Determination of Creep Rupture Loads

The calculation of the creep rupture loads for each phase of the tests was determined from the experimental results obtained during a previous study and readjusted by a series of rupture tests under creep. This relationship subsequently recalculated after each test phase, was used for calculating the weights for the following phase. The weights were calculated with reference to the tensile strength of the test samples.

2.5 Determination of the Reference Tensile Strength

Characterisation of the 550 mm long tendons due to be tested was established using tensile tests at a strain rate of 100 mm/min. Table 2 gives the results for the tendons for the three series of samples tested.

Table 2. Reference tensile strength.

Series	1	2	3			
Samples	20	20	5			
	Loads kN	Extension at rupture (%)	Loads kN	Extension at rupture (%)	Loads kN	Extension at rupture (%)
Mean	15.85	10.09	14.72	9.7	15.57	10.3
S.D. ¹	20	0.31	56	0.5	71	0.7
V.C. ² %	1.3	2.9	3.8	4.8	4.5	7.0

¹Standard Deviation - ²Variation Coefficient

All tendons tested came from the same batch of cable. However, slight changes were introduced in the termination conditions (dimension and pre-stressing rate during preparation stage). This can explain the slight changes observed for reference tensile strength measurement between phases.

3 TEST RESULTS

Table 3 gives the creep test results. The graph in Figure 2 shows an adjustment by linear regression of the relation load - f(log(time)) with very good correlation.

The creep rupture equation line obtained is:

$$Tf(\%) = 88.8 - 2.38 \log(t_{\min}) \quad (1)$$

where: Tf(%) = actual breaking load (in % of original breaking load) at time t ; and t = time in minutes.

This equation has been established using creep rupture results at 2, 10, 30 and 100 days. It will be confirmed by 300 days tests which are still on going.

Table 3. Rupture time under creep.

Phase	Weight values (kN)	Rupture time under calculated creep (day)	Rupture under observed creep (day)		
			Mean	S.D. ¹	V.C. ² %
0	13.40	2	0.05	0.05	100
	12.62	2	1.21	0.91	74.9
1	12.41	10	10.34	7.47	72.2
	12.20	30	15.51	10.81	69.7
2	11.95	100	81.87	62.61	76.5
3	11.75	300	*	*	*

* Test under way

¹ Standard Deviation - ² Variation Coefficient

Table 4 gives the results of the determination of residual strength for tendons subjected to creep tests. These show that, for different loads and before termination of their foreseeable life span, the residual strength is not affected by the load (Cf. Figure 3).

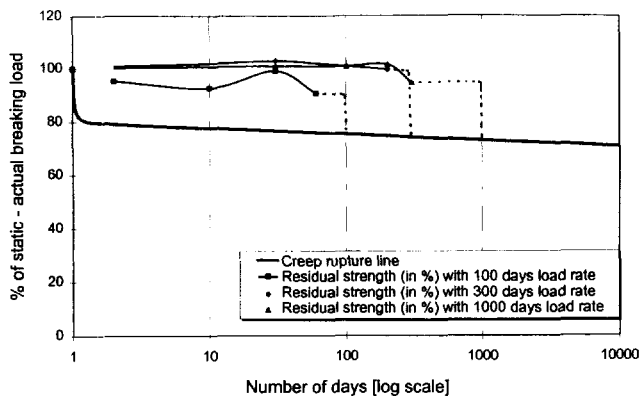


Figure 3. Creep rupture curve and residual strength.

Table 4. Residual strength of tendons subjected to creep test.

Phase	Refe. ³ (kN)	Time of rupture calculated creep ⁴ (day)	Age of the test (day)	Measure residual strength % of the reference tension		
				Mean	S.D. ¹	V.C. ² %
2	14.72	100 (81,2%)	2	95.2	4.6	4.9
			10	92.5	3.5	3.7
			30	99.0	4.8	4.8
			60	90.4	1.7	1.9
			300	102.8	3.1	3.0
3	15.57 (74,2%)	100 (74,2%)	100	100.8	5.3	5.2
			200	99.5	1.9	1.9
			30	100.9	8.8	8.7
			1000	100.7	6.2	6.2
			200	101.4	2.3	2.3
		300	94.5	7.1	7.5	

¹ Standard Deviation - ² Variation Coefficients - ³ Reference

⁴ Rate of loading in relation to reference

For phase 2, the variations observed, as well as the fall in measured residual strength, may result from problems related to the termination devices on the tendons, which were improved for phase 3.

4 DISCUSSION

The objective of this project was to firmly establish the long-term tensile behaviour of Paraweb soil reinforcing products. However, the creep and creep rupture behaviour of webbing is difficult to study because slip-free methods of holding the web are complex and expensive and preclude the multi-sample approach. Polyester cable was used in this work to simulate webbing because it performs in an identical manner to the equivalent web and is easier to hold in standard terminations. The breaking load of the cable was limited to about 15 kN so that the concrete weights could be restricted to a maximum of 14 kN.

The test results for creep rupture and strength retention are shown in Tables 3 and 4 and graphically in Figure 3. The anticipated creep rupture performance was confirmed and the regression equation established.

Evidence of retention of strength under load approaching 100% is clearly demonstrated for three different loads (it is clear that the phase 2 results were slightly lower than anticipated. This was due to minor termination difficulties which were resolved for phase 3).

Evidence is also presented confirming the retention of initial strength until close to the creep rupture point.

This strength retention phenomenon brings into question the current techniques (based on creep rupture) used to establish safety factors for design loads. The following example demonstrates the anomaly:

- taking the Characteristic Breaking Load (CBL mean - 1.64 SD) of series 2 as 13.8 kN,
- assume a typical factor of safety (which includes the effects of creep rupture) of 3 on CBL,
- the design load for the tendons becomes:

$$DL = \frac{CBL}{3} = \frac{13.8}{3} = 4.6 \text{ kN}$$

- using the creep rupture equation, if we calculated the time to rupture for a load of 4.6 kN from:

$$\log(t_{\min}) = \frac{88.8 - 31.25}{2.38}$$

this results in $t = 2.3 \times 10^{18}$ years.

The evidence presented in this paper suggests that if this tendon was off-loaded after "only" 120 years its breaking load would still be close to 100%.

It is believed, therefore, that the phenomenon of strength retention should be a major consideration when calculating design loads. Clearly, providing the final design load is below the predicted creep rupture load for 120 years, safety factors should be applied to the retained load i.e. the initial strength of the geotextile. In addition any factors for transient load increases during the life of the structure should be based on the retained, i.e. initial strength.

5. CONCLUSION

1. This work has confirmed the linear nature of the creep rupture performance of polyester tendons on a load versus log time basis.
2. The residual strength of the tendons when subjected to the creep tests remains far above the creep rupture curve and is unaffected by time under load until close to the creep rupture life.
3. A new approach to design load safety factors should be considered which take into account residual strength (as opposed to the current BNSR 1991).

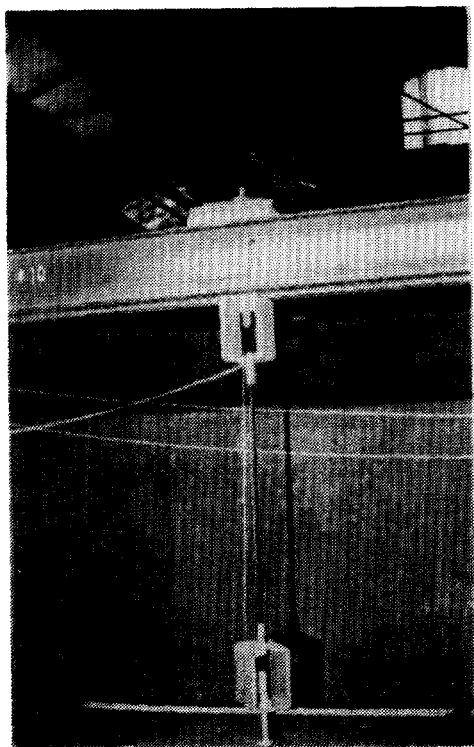


Figure 3. Close view of sample under testing

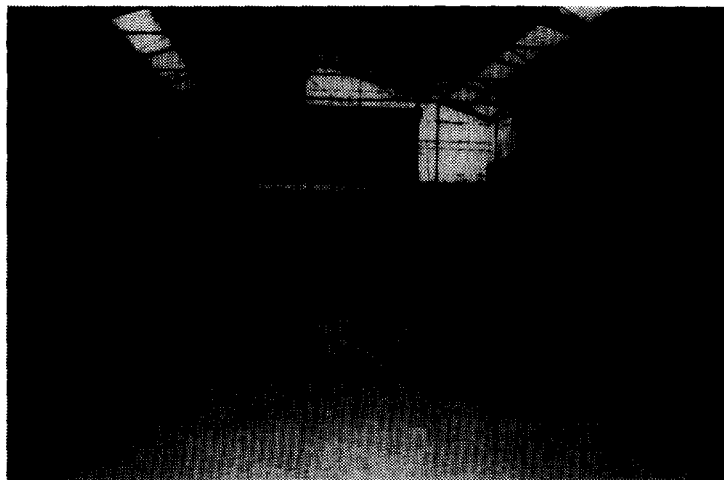


Figure 5. A pit view with all the samples under testing.

ACKNOWLEDGMENTS

The authors wish to thank Messrs H. Perrier, G. Vincelas and D. Lozach for their participation in the tests. The study was financed by the Freyssiol Department of Freyssinet International and Cie and by Linear Composites Ltd.

REFERENCES

- BNSR (1991) Commission Géotextile et Produits Apparentés "Safety coefficients for geotextiles and products" - Project GTX 71.
- Linear Composites (1995) "Note on creep and the application of creep / stress rupture curves to the choice of design values".

Coated PET-geogrids, wovens and yarns - comparison of longtime performance under tension

J. Müller-Rochholz

Professor, Department of Civil Engineering, Fachhochschule Münster, Labor für Baustoffe, Münster, and Institute for textile Building and Environmental Techniques (tBU), Germany

D. Alexiew

Chief Engineer, HUESKER Synthetic, Gescher, Germany

C. Recker

Civil Engineer, Fachhochschule Münster and tBU, Germany

S.E. Lothspeich, P.E. (civil engineer), HUESKER Inc., Charlotte, NC, USA

ABSTRACT: The load/deformation behavior of geogrids is the dominant characteristic for the bearing behaviour of the composite soil-geogrid. As deformations of soil shall be small during implementation of geogrid and very small after construction high modulus at low deformations and low creep are the aims. As polyester normally has a orientation phase at low deformations the attempt was made to use other polyester yarns for geogrids. Short-time and creep tests show significantly better behavior in initial load bearing capacity and creep behavior.

KEYWORDS: Creep, Design deformation, Polyester, Geogrid

1 INTRODUCTION

The coaction of reinforcing geosynthetic and soil is the basis of design methods. Examples are given by OECD Expert Group I8 (1991). The following figures are taken from the OECD report.

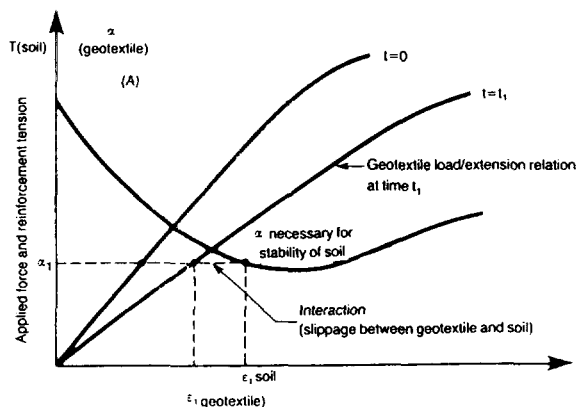
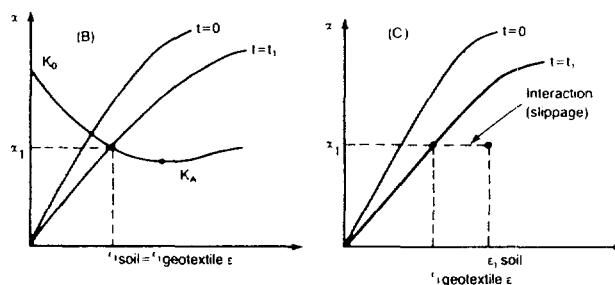


Figure 1 a. Calculation of slope stability and compatibility of soil and geotextile reinforcement



(A) General principles of calculation of the internal stability
(B) Two part wedge method
(C) Displacement method

Figure 1 b. Calculation of slope stability and compatibility of soil and geotextile reinforcement

The curves show load/extension curves for the geosynthetic („isochronous stress-strain curves) and the soil curve. Independent from the design approach, it is to be seen that a steeper curve for $t = t_1$ (for example $t_1 = 10^6$ h = 114 years) leads to structures with low movement. A big difference between $t = 0$ and $t = t_1$ leads to movement in a post construction phase i.e. service period. For the post construction deformation values are given between .5 % for rigid structures and 1 % for not sensitive structures by the OECD Expert Group I8 (1991).

So a reinforcing material should have a curve with low deformation in the design-relevant area

(deformations of $\leq 3\%$) and the smallest difference possible between $t = 0$ and $t = t_1$.

As some polymers have orientation phases of the macro molecules at relativ low deformation, this orientation should be eliminated by stretching during production or other thermo-mechanical pretreatment.

This investigation deals with two types of polyester (PES-) yarns and grids woven from these yarns.

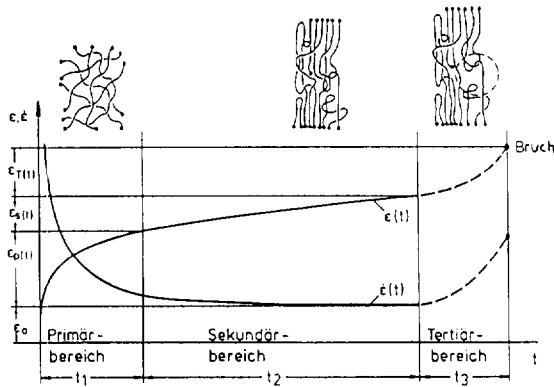
2 GENERAL DEFORMATION BEHAVIOR

Geosynthetics deformation behavior is influenced by

- deformation in the textile structure
- polymer type
- thermo-mechanical treatment of tapes, yarns, fibres etc.

The deformation in the textile structure of woven materials may be influenced by kind of weaving and warp tension. Knitwear may have straight load bearing elements, thus having no construction deformation. The same is valid for extruded and stretched grids.

Polyester materials are characterized by a orientation phase between 20 and 30 % of short-time strength. The phenomenon is visualized in Figure 2 (C. Koslowski, 1996) versus time, as this orientation occurs under sustained load at lower stresses.



- ϵ_T = tertiary creep deformation
- ϵ_s = secondary creep deformation
- ϵ_p = primary creep deformation
- ϵ_0 = initial deformation

Figure 2. Creep deformation and creep rate

3 TARGET OF THE INVESTIGATION

The tests reported here should show, whether a different yarn [called New Technology (NT) in this report] gives better performance at low deformation values than a

standard PES-yarn. Short-time tensile, tensile creep and creep rupture tests were conducted, this report deals with short-time tensile and creep tests.

3.1 Short-time Tests

The short-time tests were carried out with two grids of identical nominal maximum force. All tests were performed on identical equipment by same staff according to ISO 10319 i. e. 1 % preload, 20 %/min strain rate, videoextensometer. Figure 3 shows the stress-strain curves, which (best to be seen for the product with 150 kN/m) miss the typical orientation phase, characterized by a degressive gradient from about 1 % strain up to 4 %. Also the ultimate deformation is about 9 % for the NT-materials compared with about 12 % for the standard material.

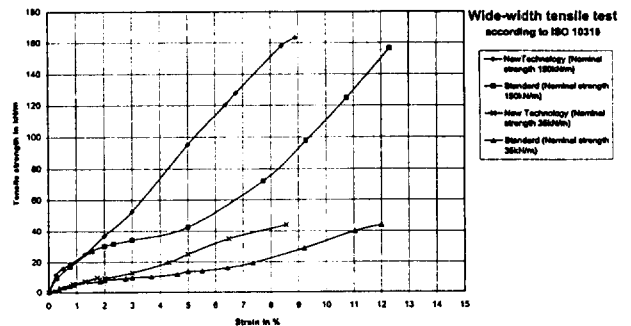


Figure 3. Stress-strain curves - woven polyester-geogrid

3.2 Creep Tests

For the creep comparison we took old values for the standard materials [published by J. Müller-Rochholz and R. Kirschner at the 4th International Conference on Geotextiles, Geomembranes and Related Products, The Hague, Netherlands (1990)], therefore sometimes stress/strength values and temperatures are close but not identical.

Creep curves for yarn and geogrids of different strength woven of this yarn are shown in Figures 4 a and b. The problem in testing is to be seen by the remark „clamp failure“. If stress level is very close to the bearable load, any lateral stress may cause rupture.

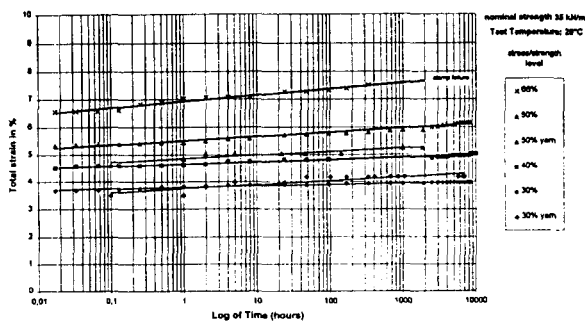


Figure 4 a. Creep curves - woven polyester-geogrid „new technology“ (35 kN/m)

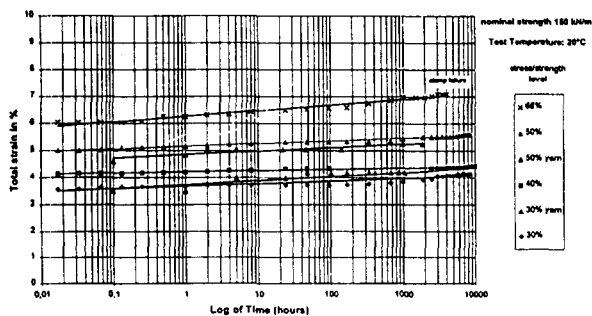


Figure 4 b. Creep curves - woven polyester-geogrid „new technology“ (150 kN/m)

Figure 5 shows 1 year NT-values at 30 % stress level and 3 years lines of standard PES of lower (= 25 %) stress level, showing ca. 1 % higher strains for the lower stress level of standard yarns.

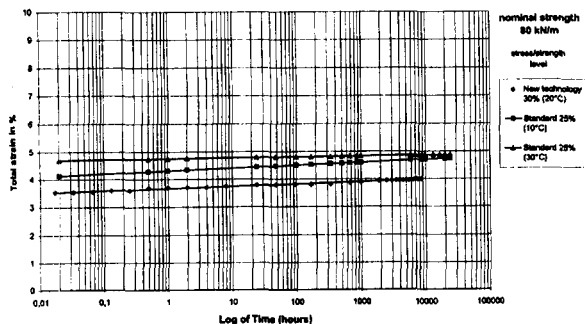


Figure 5. Creep curves - woven polyester-geogrid

In Figure 6 identical stress levels (50 %) of products are compared at differing temperatures showing the low influence of temperature for PES and ca. 2 % less strain for the NT-materials. In this figure results of yarn creep tests supplied by the producer are plotted additionally. There is a different stress level for the standard yarn. The coincidence of yarn and product strains shows low construction influence.

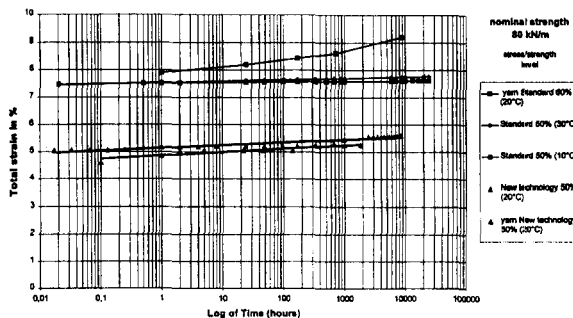


Figure 6. Creep curves – woven polyester-geogrid (80 kN/m)

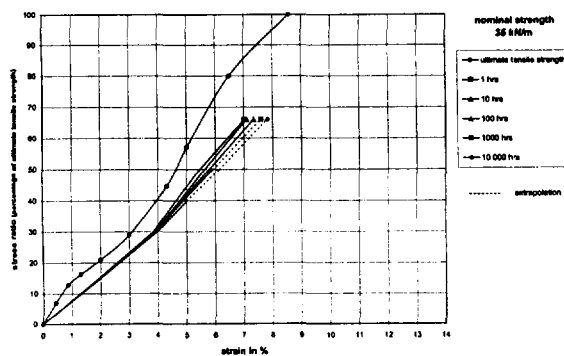


Figure 7. Isochronous curves – woven polyester-geogrid „new technology“

From these creep curves isochronous stress-strain curves were derived, showing in Figure 7 the close lines for 1 h up to 10000 hrs. Two lines of Figure 7 are transferred to Figure 8 to see the difference between the products with different yarns; which leads to strain differences f. e. at 20 % stress-level of > 3,5 % strain at 10000 hrs for standard to < 1,5 % for NT-products or at strain level of 2 % to stress levels from 5 % (standard) to 15 % (NT).

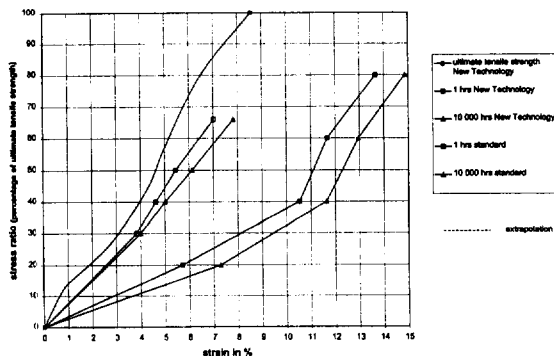


Figure 8. Isochronous curves – woven polyester-geogrid

4 CONCLUSION

It can be shown that the thermo-mechanical treatment of yarns (here: Polyester) may lead to significant changes in the load deformation behavior especially in the application relevant area of admissible deformations/stresses. So the load bearing capacity at 2 % strain is tripled.

REFERENCES

- OECD Expert Group I8 (1991) *Ground Engineering Applications of Geotextiles in Road Construction and Maintenance*, Transport and Road Research Laboratory Crowthorne, UK.
- Koslowski, C. (1996) *Geokunststoffe, Extrapolation von Kurzzeitkriechversuchen (≤ 1000 h) auf Langzeitwerte*, Final thesis work at Fachhochschule Münster
- Müller-Rochholz, J., Kirschner, R. (1990) "Creep of geotextiles at different temperatures", *4th International Conference on Geotextiles, Geomembranes and Related Products*, The Hague, Netherlands, Editor G. den Hoedt A.A. Balkema/Rotterdam/Brookfield

The Effect of Oxygen Pressure, Temperature and Manufacturing Processes on Laboratory Degradation of Polypropylene Geosynthetics.

A. Salman
Consultant, Westbury, NY

V. Elias
Principal, V. Elias and Associates P.A., Bethesda, MD.

A. DiMillio.
Geotechnical Research Project Manager, Federal Highway Administration, McLean, VA.

ABSTRACT: To qualify geosynthetics for in ground reinforcement use, it becomes mandatory to assess their durability within a short time with respect to environmental parameters to which they will likely be subjected for 75 to 100 years. This requires the development of accelerated tests permitting prediction of potential degradation under actual use conditions. It is known that polyolefin may oxidize resulting in polymeric molecular chain breaks directly resulting in strength loss of the material. The available studies of polyolefins oxidation indicate that rates of oxidation are very low at ambient temperatures, however in the context of the lifetime of civil engineering applications, may not be negligible. Comprehensive studies of polyolefin oxidation indicated that the rate of reaction among other factors, depends on the oxygen partial pressure in the system as well as on temperature. Complex antioxidant mixtures are commonly used to reduce the rate of oxidation for commercial polyolefin products during processing and in end use.

KEY WORDS: Geosynthetics, durability testing, oxidation, life prediction, antioxidant consumption

1. RESEARCH OBJECTIVES

This study was focused on considering the prime factors affecting the rate of degradation which are temperature, oxygen partial pressure, manufacturing process and effectiveness of antioxidants.

The scope of this reported research was limited to the laboratory investigation of thermooxidative degradation of a few typical commercial products selected to represent geosynthetic materials potentially used in highway applications. It is only a part of a larger FHWA study to develop durability testing protocols for geosynthetics.

The scope of the study is limited in that:

- a small number of commercial geosynthetic products are considered;
- only "severe" conditions of treatment, as compared to the in-service conditions, are used to accelerate degradation to achieve measurable chemical and mechanical changes during 2 to 3 years of laboratory incubation time.

2. LABORATORY ASSESSMENT PROCEDURES

The basic principles of thermooxidative degradation of polyolefin polymers indicate that environmental conditions such as oxygen partial pressure may have a significant impact on the rate of mechanical deterioration caused by oxidation. In order to assess the influence of oxygen partial pressure on the rate of mechanical degradation for

polyolefin geosynthetics, the following initial conditions have been selected for accelerated laboratory testing:

1. Oven aging in circulating air (21% O₂) to represent surface and near surface conditions
2. Oven aging in stagnant atmosphere containing 8% O₂ balanced by N₂ to represent reduced oxygen found in reinforced fills (Yanful, 1993).

The overall effect of antioxidant additives is assessed by testing a specially manufactured polypropylene textile P-3a. This material is identical to the commercial products P-3 in terms of polymeric composition and manufacturing, except that it was manufactured with a minimum amount of additives required for production purposes.

3. GEOSYNTHETIC MATERIALS TESTED

Results from 2 commercial and 1 research grade geotextiles are reported in this study. The materials are differentiated by manufacturing process, composition and antioxidant additives. The main characteristics are shown in Table 1.

3.1 Testing procedures

The testing procedure consists of: (i) sample preparation; (ii) oven aging of prepared samples at different levels of oxygen concentration (iii) mechanical testing to determine tensile strength using a Wide Width Strip Test (ASTM D-4595); (iv) chemical testing to determine Oxygen Induction Time (OIT) by Differential Scanning Calorimetry

Table 1. Major characteristics of selected commercial polyolefin geosynthetic products.

Product code	Type	Unit weight (g/m ²)	Tensile strength (kN/m)	Antioxidant type
P-3	PP Needlepunched-continuous filament non-woven geotextile	440	1.20±0.06	Hindered Amine (HALS), with trace carbon additive for color
P-3a	PP Needlepunched-continuous filament nonwoven textile	200	0.35±0.03	Research grade manufactured with a minimum amount of additives
P-4	PP Needlepunched staple nonwoven geotextile	370	1.50±0.05	Phenolic and phosphite

(DSC) at 175°C; and (v) analysis of surface morphology by SEM and/or optical microscopy. The major features of the testing procedure are outlined below.

To perform accelerated thermodegradation of polyolefin geosynthetics in air (21% O₂), forced-draft ovens with a temperature uniformity of ±1% and substantial fresh air intake are used in a compliance with ASTM D-3045, "Heat aging of plastics without load". To conduct aging in a stagnant atmosphere containing 8% O₂, a special chamber was designed and manufactured. This apparatus provides a temperature uniformity of ±1°C, and allows control of oxygen concentration in the chamber. The specimens are suspended in the oven or in the chamber without pretension and without touching each other.

The temperature of exposure varied from 50° to 90°C. At least 5 consecutive retrievals were made over the period of aging at each specific condition with each retrieval represented by a minimum of 5 specimens.

The study further indicated that Oxidative Induction Time (OIT) measurements for these geotextiles appeared to be ineffective in monitoring strength degradation for the products tested.

Measurements of remaining OIT for the geotextiles reported did not correlate with remaining strength or antioxidant consumption as measured by induction time.

4. LABORATORY ACCELERATED DEGRADATION RESULTS

Each of the selected geosynthetic products tested exhibits a unique pattern of degradation under the tested environmental conditions. Surface morphology studies are discussed in the context of measurable deterioration of mechanical properties observed for the aged geosynthetics.

4.1 Nonwoven continuous filament geotextiles, P-3 and P-3a

The monitoring of weight changes during exposure to elevated temperatures in different atmospheres, indicated

no statistically significant variation of weight for the P-3 and P-3a geotextiles.

SEM study of the fiber surface morphology indicated that there are no apparent changes on the fiber surface on a microlevel, for either geotextile, aged in different atmospheric environments and at temperatures varying from 50° to 90°C.

The progressive strength loss versus time for the P-3 and P-3a geotextiles, are shown on Figure 1, indicates a non linear strength loss and the presence of an induction period. The induction period is defined as the initial period of oven aging, when no statistically significant changes of a tensile strength is observed. The P-3a geotextile exhibits no induction period for the same range of test temperatures.

One of the properties which affects the rate of thermooxidation processes is the composition and concentration of antioxidant additives in commercial products. The effect of antioxidant additives on the rate of mechanical degradation of polyolefin geosynthetic products is clearly illustrated by the relative performance of two products, P-3 and P-3a. The P-3 product contains a HALS type of antioxidant additive, and P-3a is a specially manufactured textile with only a minimum amount of antioxidants required for production purposes. The beneficial effect of antioxidants is clearly demonstrated by the summarized comparisons between degradation rates for these two products which is shown in Figure 1. There is an indication that at the lowest temperature tested of 50°C, the effect of the antioxidants is more pronounced than at the highest temperature of exposure of 80°C which is closer to the upper limit of effectiveness of about 135°C, for HALS type antioxidants (Fay, King, 1994).

Samples of the P-3 commercial geotextile were exposed to elevated temperatures of 70°, 80° and 90°C in a stagnant atmosphere of 8% oxygen balanced by nitrogen. The summary of results is shown on Figure 2.

Results indicate that the rate of mechanical degradation in stagnant diluted air is much slower than the rate of degradation in circulating air ovens. It can be observed that in stagnant diluted air (8% O₂) P-3 exhibits an initial

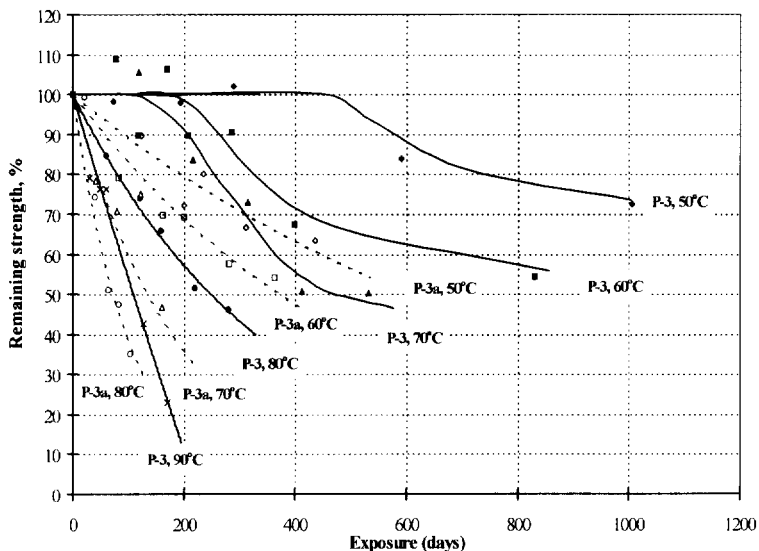


Figure 1. Effect of antioxidant additives on the rate of thermooxidation for the P-3 commercial product and P-3a research grade textile.

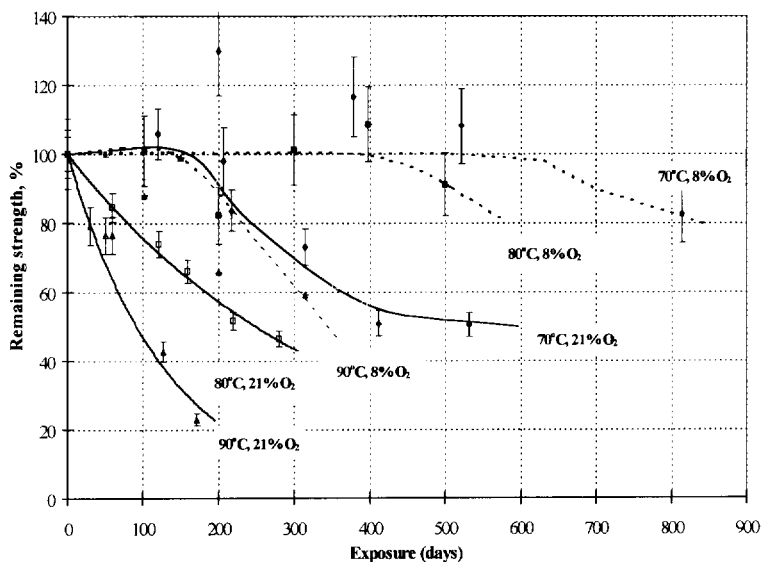


Figure 2. Tensile strength for continuous filament geotextile P-3 during oven aging in stagnant diluted air at 8% O₂ and in circulating air at 21% O₂.

tensile strength increase when tested at 70°C. However, tensile strength decreases with exposure time.

4.2 P-4, nonwoven staple geotextile

Commercial geosynthetic P-4 does not exhibit shrinkage or swelling over the period of aging in circulating air and stagnant diluted air ovens.

Analysis for microscopic changes on fiber surface morphology has been conducted by SEM of fibers "as received" and fibers taken from the specimens aged in circulating air oven at 50°C. The virgin fibers appear to

be smooth and clean, however, there are traces of initial cracks on the surface of virgin fibers transverse to the fiber length. The SEM study further indicates a progressive development of circumferential cracks on the fiber surface during exposure to elevated temperatures in circulating air.

The SEM study of fiber surface morphology for this geotextile aged in stagnant diluted air (8% O₂) at 70 °C, indicated no development of circumferential cracks on the surface of fibers after the 473-day thermal treatment. No changes of the fiber diameters have been observed.

Weight changes for P-4 measured over the period of exposure to elevated temperatures in different atmospheric conditions are minimal. The weight changes measured vary within the range of 0 to 2 percent.

The observed development of fiber cracking explains the rapid loss of tensile strength during thermooxidation in intense circulating air. It appears that this material loses 50% or more of its initial strength during the first 50 days of exposure in temperatures varying from 50° to 80°C as shown on Figure 3.

The results of mechanical testing for P-4 aged in a stagnant atmosphere of diluted air (8% O₂, 92% N₂) are at first quite unexpected. The specimens aged at 70° and 80°C in stagnant diluted air exhibit a strength increase by factor of 1.8 after first 80 days of exposure followed by statistically insignificant changes of tensile strength. However, no tensile strength increase is observed at 90°C. The summarized experimental results for mechanical degradation in these conditions are also shown on Figure 3.

4.3 Summary of laboratory data on the rate of mechanical deterioration caused by thermooxidation

Results of tensile strength monitoring for these two polypropylene geosynthetics, indicate that each of the products studied, exhibits a unique pattern of tensile strength changes during exposure to elevated temperatures under differing environment conditions (oxygen partial pressure). However, the common features are as follows:

1. Oven aging in stagnant diluted air at 8 percent oxygen results in the decrease of the rate of tensile

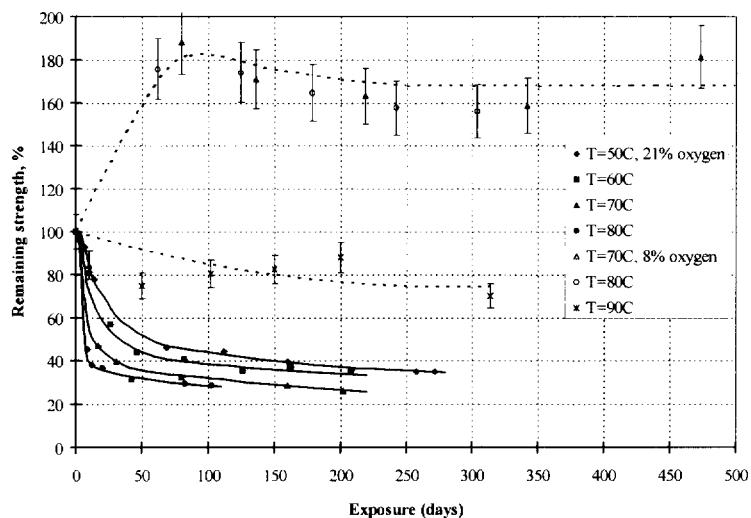


Figure 3. Tensile strength loss for geotextile P-4, aged in circulating air at 21% O₂ (solid line) and at 8% O₂ (dashed line).

- strength loss as compared to the rate observed in circulating air (21% O₂) at the same temperature.
2. The two commercial products tested, exhibit a different morphology in their virgin state. SEM microphotographs at a magnification of 3000x reveal the presence of initial crazes/cracks on the surface of virgin fibers for nonwoven staple geotextile P-4. There is no indication of surface imperfections under the same magnification, for the virgin fibers of the nonwoven continuous filament product, P-3. This difference in fiber morphology is one of the causes for the differences in degradation patterns for P-3 and P-4 product.
3. Staple product P-4 exhibits very low resistance to oxidation in circulating air (21% O₂) at elevated temperatures which results from intensive surface cracks growth over the period of aging. By contrast, the continuous filament product P-3 exhibits no fiber surface crack development during oxidation under the same conditions, and a much lower rate of mechanical deterioration.
4. Aging in stagnant diluted air (8% O₂) results in the healing of the initial crazes on the fiber surface of the P-4 product. This may explain the tensile strength increases by a factor of about 1.5-1.6, observed in stagnant diluted air. Product P-3 exhibits the increase of tensile strength by a factor of 1.2-1.3, under the same conditions of aging.
5. It appears that the effectiveness of antioxidant package can be measured by the developed induction time for products with no cracks or crazes in their as manufactured state.

Intensive surface crack growth in circulating air as well as crack healing in stagnant diluted air, indicate that there may be other or additional mechanisms to ther-

mooxidation, which contribute to mechanical degradation for staple product P-4 under accelerated temperature testing. The crack disappearance phenomena may occur due to an increase of molecular diffusion rate in the polymer leading to crack healing, analogous to the cold welding of metals. When the rate of diffusion and crack healing prevails over the rate of oxidation, a strength gain effect is observed. This adds to the complexity of the degradation process at high temperatures and brings to question the validity of oven aging as the appropriate accelerator for thermooxidative degradation studies especially for products which exhibit initial cracks/crazes in their as manufactured state.

The nonwoven continuous filament product, P-3, exhibits a more classic behavior and the temperature accelerated data lends itself to analysis within a framework of polymer chemistry.

5. A NUMERICAL MODEL FOR DEGRADATION RATE AND LIFE EXPECTANCY

The main objective of durability studies for commercial geosynthetic products is to estimate a degradation rate and corresponding life expectancy for in-service conditions.

The results of tensile strength losses for P-3 during oven aging in circulating air (21% O₂) at elevated temperatures up to 70°C exhibit a substantial period of time with no changes of mechanical strength followed by a nonlinear decay of strength. Experimental data obtained in stagnant diluted air (8% O₂), show a significant decrease in the rate of mechanical degradation as compared to the rate in circulating air (Figure 1). These patterns of degradation indicate that conventional "Arrhenius modeling" as suggested in the literature (Wisse and Berkenfield, 1982; Koerner, Lord and Hsuan, 1992) may be too simplistic to describe the degradation behavior of geosynthetic products. Therefore, the basic principles of kinetics of chemical reactions in general, and kinetics of thermooxidation in particular, such as the Basic Autoxidation Scheme (BAS) (Bolland, 1948; Kelen, 1982) must be considered in formulating an appropriate numerical model for materials which in their virgin state are completely intact and exhibit no cracks/crazes.

An interpretation procedure using BAS has been recently developed by the authors (Salman, Elias et al., 1997) and is used to interpret the laboratory results for P-3, which exhibits a more classic behavior.

5.1 Interpretation Procedure

In chemical kinetics (Adamson, 1973) the rate R of a reaction $A+B+C+\dots \rightarrow \text{Products}$ at constant temperature is expressed as a function of composition of the system, according to mass action law as:

$$-\frac{d[P]}{dt} = R = k[A]^x[B]^y[C]^z \quad (1)$$

where $[A]$, $[B]$, and $[C]$ are the concentrations of reactants, and k is the rate constant being independent of the concentration of the reactants but dependent on temperature.

The order of the rate law is the sum of the exponents $(x+y+\dots)$. The important cases are zero, first and second-order reactions. The rate should be determined experimentally (Atkins, 1986).

The rates k of most reactions increase with temperature according to the Arrhenius law as:

$$k = Ae^{-E_a/RT} \quad (2)$$

with A - the pre-exponential factor, usually considered as a constant which is independent of temperature; E_a - the activation energy; R - the ideal gas constant; and T - the temperature in $^{\circ}\text{K}$.

The kinetics of autoxidation for the general case of antioxidant presence, consist of two phases. The first phase (induction period) describes the consumption of antioxidants, with the reaction constant for consumption defined by an Arrhenius-type dependency. During the second phase, the oxidation and corresponding mechanical degradation is described by the kinetics of the BAS.

The data usually obtained in the laboratory, does not provide sufficient information on the kinetics of antioxidant depletion during aging. Therefore, the order of reaction for antioxidant consumption cannot be determined directly from experimental data. Analysis of integrated rate laws for kinetics of chemical reactions (Adamson, 1973) yield a general expression for induction time versus temperature at any given level of antioxidant depletion $[A]/[A_0]=c$. Assuming that the reaction constant for antioxidant consumption obeys the Arrhenius law, the following relationship is indicated:

$$\ln \frac{1}{t_{ind}} = C_1 + C_2 \frac{E_a}{RT} \quad (3)$$

where C_1 and C_2 are the constants for a particular antioxidant and given level of depletion c .

This relationship (3) suggests a procedure for estimating induction time at a given temperature T_0 $^{\circ}\text{K}$ as follows:

1. The induction period t_{ind} is determined at each temperature of exposure, defined as the period of no statistically

significant changes in mechanical strength. It is determined by extending a tangent line to the slope of the post induction degradation curve until it intersects the no strength loss line. With limited data it requires some judgment.

2. A linear regression analysis is conducted for the function $\ln(1/t_{ind})$ versus the reciprocal temperature $(1/T^{\circ}\text{K})$. The obtained linear equation $\ln(1/t_{ind}) = a(1/T)+b$ is used to find the value of the induction period at any given temperature, T_0 $^{\circ}\text{K}$ as follows:

$$t_{ind} = 1/\{ \exp[a(1/T_0)+b] \} \quad (4)$$

The determination of induction period at elevated temperatures is shown in Figure 4 for P-3 commercial geosynthetic, aged in circulating air at 21 percent oxygen and reduced oxygen at 8 percent.

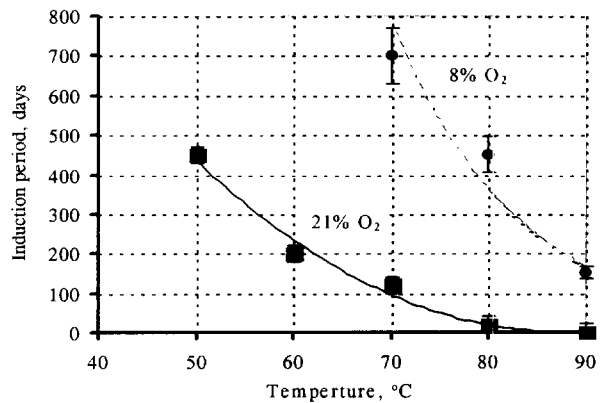


Figure 4. Induction period for P-3 aged in circulating air at 21% (solid line) and 8% (dashed line) O_2 .

3. The solution of the equation for linear regression of $\ln(1/t_{ind})$ versus reciprocal temperature at 20°C (Figure 5), yields a value for P-3 of anticipated induction period $t_{ind} = 51$ years at 21% O_2 and 240 years at 8% O_2 . For P-3a which does not exhibit an induction period at the temperature tested, no prediction at ambient temperature can be made from the data.

Interpretation of data for mechanical degradation observed in the post induction period, requires the determination of the order of reaction for the product tested, with a subsequent estimate of anticipated rate of degradation (strength loss per 100 years) or time to 50 percent strength loss at any given temperature. In this study zero-, first- and second-order reactions are considered. The procedure of determining the order of reaction and degradation rate estimates are as follows:

1. Functions representing the kinetics of zero-, first- and second-order are used to fit the experimental data for the measured mechanical degradation, after the induction period for each temperature of aging.

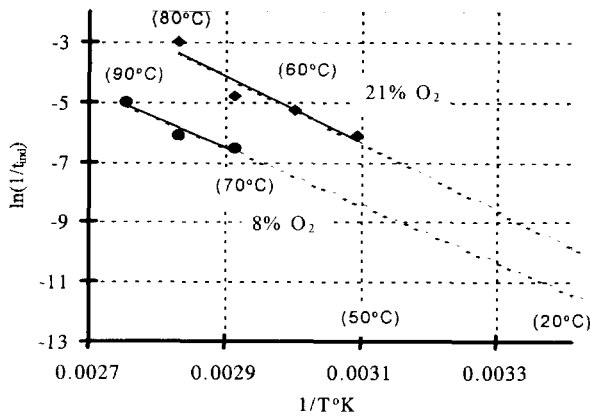


Figure 5. Linear regression analysis of $\ln(1/t_{ind})$ versus $1/T^\circ K$ for P-3.

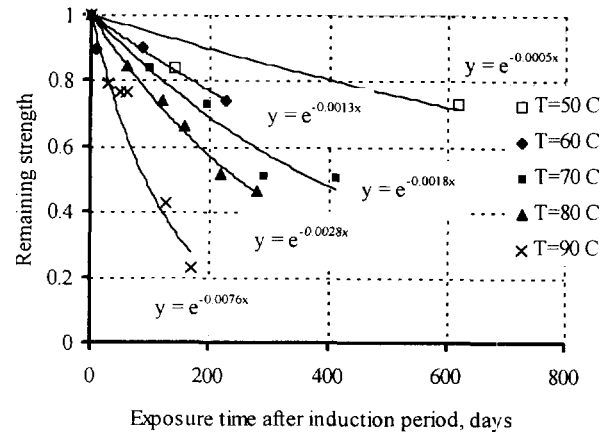


Figure 6. Exponential curve fitting corresponding to a first-order reaction, after an induction period, for P-3 at 21% O_2 .

2. The obtained values of the logarithm of reaction constant $\ln(k)$ for the chosen type of kinetics, are plotted versus reciprocal temperature of aging (Arrhenius plot).
3. A linear regression analysis is used to find the equation for $\ln(k)$ as a function of reciprocal temperature $1/T$, $\ln(k) = a(1/T) + b$. This equation yields the value of k for the temperature of interest, T_0 ; $k(T_0) = \exp[a(1/T_0) + b]$.
4. The obtained $k(T_0)$ value of the rate constant is used to calculate a normalized retained strength at a given time $x(t) = F(t)/F_0$ or to calculate time t_i to reach certain level of retained strength $c = F_i/F_0$ at a given temperature T_0 K for a specific reaction:

$$x(t) = 1 - k(T_0)t; t_i = \frac{1 - c}{k(T_0)} \text{ - for zero-order reactions; } \quad (5)$$

$$x(t) = \exp(-k(T_0)t); t_i = \ln(1/c)/k(T_0) \quad (6)$$

- for first-order reactions; and

$$x(t) = \frac{1}{1 + k_1(T_0)t}; t_i = \frac{1 - c}{k_1(T_0)c} \quad (7)$$

- for second order reactions law.

The results of exponential curve fitting corresponding to a first-order reaction which has the greatest likelihood (R^2) for approximating the experimental data, are shown in Figure 6.

A first-order reaction is predicted by the BAS model for kinetics of mechanical degradation of polyolefins without antioxidants at a constant oxygen pressure. Therefore, the priority in the selection of the reaction order, is given to the exponential law (first-order).

Figure 6 summarizes the result of a linear regression analysis for the reaction constant k corresponding to a first-order reaction for mechanical degradation for P-3 in circulating air at 21 percent oxygen.

The solution of a linear regression line equation and sequential substitution of the obtained value of the reaction constant k into a first-order reaction, yields an estimate of 50 percent strength loss at 20°C of 38 years after the induction period of 51 years at 21% O_2 and 240 years at 8% O_2 . The obtained estimates of anticipated strength is valid only for the conditions of testing, e.g. circulating air at 21% O_2 and in stagnant diluted air at 8% O_2 .

It appears, that the estimate for the induction period of 51 to 240 years with no strength loss, suggests that antioxidant consumption rate and ambient regime primarily determine the practical durability of this commercial product.

For the research grade textile P-3a, the interpretation of data in circulating air at 21% O_2 , yields an estimate of anticipated time to 50 percent strength loss at 20°C as of 29 years. This result is in a good agreement with the estimate of degradation rate after the depletion of antioxidants, for the P-3 geotextile. The interpretation of data in stagnant diluted air at 8% O_2 yields an estimate of anticipated time to 50% strength loss at 20°C as of 47 years for the P-3a textile which is a decrease by a factor of 1.6 when compared to the degradation rate in air at 21% O_2 (FHWA, 1997). This result is in general agreement with an estimate of the reduction of the degradation rate in diluted air at 8% O_2 based on the integrated law of chemical kinetics (Equation 1).

Arrhenius equation for reaction rate constant could be rewritten as: $\ln(k) = C - U/RT$, where U is apparent activation energy, and $R = 8.31$ J/mol. Solving this equation with respect to U , one obtains value of $U = 61$ kJ/mol, which is in a reasonable agreement with the value of 65 kJ/mol, reported by Wisse and Birkenfeld (1982) for PP geosynthetic with extracted antioxidants tested at 21% O_2 .

Tests for P-4 in stagnant diluted air indicate that some process other than oxidation, controls the behavior of this

material at elevated temperatures. Therefore, both elevated temperature aging results and the numerical model developed within the framework of BAS, cannot be directly applied to laboratory data obtained for the P-4 product or other products with initial cracks or circumferential cracks developed during aging at elevated temperatures. For these geosynthetics, alternate testing methods at ambient temperature and elevated oxygen pressure (50 to 100 atm) as indicated by the BAS, result in mechanical degradation rates in for shorter time and may be more applicable.

6. ALTERNATE TESTING PROTOCOL AT ELEVATED OXYGEN PRESSURE

In a simplified process of polyolefin oxidation, it is assumed that the rate of reaction at constant temperature depends on the concentration of original polymer [A] and the concentration of oxygen [B], in equation (1). Data reported in the literature (Kelen, 1982) indicate that the rate of oxidation may be proportional to the concentration of oxygen in the system, which corresponds to a first order reaction. Therefore, an increase in oxygen pressure should result in the proportional increase of the rate of mechanical degradation for polyolefins. For example, the exposure of polyolefin based geosynthetics to an atmosphere of pure oxygen may result in the acceleration of the degradation rate by a factor of 5 as compared to the rate anticipated in air (21% oxygen) at ambient temperature. The further increase of oxygen pressure to 50 atm should result in an acceleration of the reaction by a factor of 250, as compared to the rate of oxidation under ambient conditions.

6.1 Testing conditions and experimental results

An atmosphere of pure oxygen at a pressure of 50 and 100 atm has been selected for an initial feasibility assessment of high oxygen pressure accelerated degradation for polyolefin geosynthetics. It is anticipated that this condition may accelerate the degradation rate by a factor of 250 in 50 atm and by a factor of 500 in 100 atm as compared to the rate under ambient (1 atm, 21% O₂, 20°C) conditions. Strip size specimens of three geosynthetics previously tested (P-3, P-3a and P-4), were placed in high pressure chamber filled with pure oxygen at 50 and 100 atm at 20°-22°C. The chamber was ventilated and refilled with oxygen once a day.

Tensile strength tests were conducted on strip-size specimens for materials as received and after the incubation. Relative changes of tensile strength are presented in Table 2.

6.2 Interpretation of test results

The simplified and preliminary kinetics for oxidation under oxygen pressure yields an acceleration factor of 250 for oxygen pressure of 50 atm and factor of 500 for oxygen pressure of 100 atm. Strength losses from oven aging in circulating air at 21% oxygen and under high pressure oxygen incubation at ambient temperature were calculated within the framework of the Basic Autoxidation Scheme and are shown on Table 3. The comparison is based on strength losses in equivalent periods of time.

Table 2. Tensile strength loss for geosynthetics aged in pure oxygen at 50 and 100 atm and 20°C.

Condition	Equivalent time at ambient condition*, years	Strength loss, %	Material		
			P-3	P-3a	P-4
Oxygen pressure, atm	Incubation time, days				
50	60	40	0	42	10
100	30	40	0	N/A	N/A
100	90	120	16	N/A	N/A

* 21% O₂, 20°-22°C

Table 3. Comparison between oven aging and high oxygen pressure strength loss estimates.

Equivalent time at ambient conditions, years	High pressure oxygen strength loss, % (oven aging strength loss estimate, %)	Material ⇒		
		P-3	P-3a	P-4
40		0/(0)	42/(63)	10/(100)
80		N/A/(50)	N/A	N/A
120		16/(100)	N/A	N/A

N/A - not available

Results of this limited study indicate that oxygen pressure can be used as an accelerator and that a preliminary acceleration factor can be predicted by the simplified kinetics of oxidation for polyolefins. The estimates of strength loss over 40 years based on data developed under high oxygen pressure conditions are within the range of estimates obtained in oven aging in circulating air for some products or yield more reasonable results as indicated by actual performance. As expected, the P-3 product with an estimated 50 years induction period, exhibits no tensile strength loss over a period equivalent to 40 years. The research grade textile P-3a yields a strength loss of 42% tested under high oxygen pressure condition which is in reasonable agreement with the 63% strength loss over 40 years, obtained for oven aging in circulating air. The difference may be attributed to the

intrinsic variability of mechanical properties for the P-3a product, nonuniformity of the degradation process at different temperatures and in high oxygen pressure etc.

Furthermore and of significant importance is the preliminary finding that the estimated strength loss in 40 years measured for the P-4 nonwoven staple fiber geotextile is more consistent with the anticipated and reported performance for this geosynthetic. Interpretation of P-4 losses from oven aging protocols suggests a 50% strength loss in 6.5 years, which is unreasonable in light of the actual performance of this material over 10 years as measured from retrieved sites. Examination of P-4 samples incubated under high oxygen pressure indicates no changes in surface morphology.

7. SUMMARY

Interpretation of experimental data suggests the following:

1. Kinetic models developed within the framework of the Basic Autoxidation Scheme (BAS) appear to provide a satisfactory analysis of the experimental data and permit conservative estimates of time against strength loss at ambient temperature to be made for products which exhibit no cracking/crazes in their as produced state.
2. The rate of antioxidant depletion and the rate of mechanical degradation in stagnant diluted air appears to be lower than in circulating air and may provide better model of in-ground conditions.
3. Products with effective antioxidants may exhibit induction times well in excess of their useful life in civil engineering applications. Oven aging temperatures must be low enough to permit measurements of induction time, which is a method to quantify the effectiveness of the antioxidant package.
4. High oxygen pressure appears to be a viable accelerator for oxidative strength loss measurements and appears to be a viable testing protocol for products where high temperature changes the surface morphology. However more development is necessary to establish more exact relationships.
5. Estimates of strength loss versus time under ambient conditions based on high oxygen pressure degradation are in a satisfactory agreement with estimates obtained from oven aging in circulating air for the monofilament product tested.

ACKNOWLEDGMENTS

This study was funded by Federal Highway Administration under DTFH 61-91-R-00054, "Durability of Geosynthetics for Highway Applications". Their permission to publish the developed data is appreciated. We wish to acknowledge the contributions of T.M. Allen for his con-

tinuous interest and suggestions and Dr. V.V. Krongauz for his helpful discussions.

REFERENCES

- Adamson A.W., 1973, "A textbook of physical chemistry", Academic Press, New York, 1079 p.
- Atkins P.W., 1986, "Physical chemistry" Third edition, Oxford University Press, 857 p.
- ASTM D-3045, Heat aging of plastics without load", American Society for Testing and Materials, Philadelphia, PA, USA.
- ASTM D-4595, "Standard Test Method for Tensile Properties of Geotextiles by the Wide-Width Strip Method", American Society for Testing and Materials, Philadelphia, PA, USA.
- Bolland J.L., 1948, "Kinetic studies in the chemistry of rubber and related materials. VI. The benzoyl peroxide catalyzed oxidation of ethyl linoleate", *Trans. Faraday Soc.*, Vol. 44, pp. 669.
- Fay J.J., King R.E., 1994 "Antioxidants for geosynthetic resins and applications", *Proc. 8th Conference GRI, Dec. 94*, Philadelphia, pp. 74-91.
- FHWA, 1997, "Durability of geosynthetics for highway applications", Draft Final Report, DTFH 61091-R-00054.
- Kelen T., 1982, "Polymer degradation" Van Nostrand Reinhold Company, New York, p. 211.
- Koerner R.M., Lord A., Hsuan Y.H., 1992, "Arrhenius modeling to predict geosynthetic degradation" *Geotextiles and Geomembranes*, No 11, pp. 151-183.
- Salman A., Elias V., Juran I., Lu S., Pearce E., 1997, "Durability of geosynthetics based on accelerated laboratory testing", *Geosynthetics '97*, San Diego, CA, pp 217-234.
- Wisse J.D.M., 1988, "The role of thermo-oxidative aging in the long-term behavior of geotextiles". *Durability of geotextiles, RILEM*, Chapman and Hall, London, pp. 207-216.
- Wisse J.D.M., Birkenfeld S., 1982, "The long term thermo-oxidative stability of polypropylene geotextiles in the Oosterschelde Project", *Second International Conference on Geotextiles*, Las Vegas, USA, Vol 1, pp. 283-288.
- Yanful E.K., 1993, "Oxygen diffusion through soil covers on sulfuric mine tailings", *Journal of Geotechnical Engineering*, Vol. 119, No. 8, pp. 1207-1228.

Conventional and Stepped Isothermal Methods for Characterizing Long Term Creep Strength of Polyester Geogrids

J. S. Thornton

President and Principal Scientist, Texas Research International, Inc., Austin, Texas, U.S.A.

J. N. Paulson

Vice President, Strata Systems, Inc., Atlanta, Georgia, U.S.A.

D. Sandri

Western Regional Engineer, T.C. Mirafi, Inc., Lake Forest, California, U.S.A.

ABSTRACT: Conventional methods of time-temperature superposition (TTS) are compared to a new procedure for time-temperature superposition called the stepped isothermal method (SIM). Creep and creep rupture properties of two polyester geogrid products are investigated. The conventional TTS approaches studied consumed a total of 18,000 hours of test time. In addition with both polyester products it was found difficult to separate temperature dependence of creep strain response from specimen to specimen variation in elastic strain response to loading events. Using the new SIM method, over 15 load specific master creep modulus curves were generated, some of which extended to over 100 year design lifetimes, each from a single specimen in a test that was completed in less than 18 hours. The results of the conventional and SIM procedures were found to be equivalent for the polyester products examined.

KEYWORDS: Time-temperature superposition, shift factors, unconfined creep tests, creep strain, creep modulus, creep rupture, polyester fibers, geogrid, accelerated testing.

1 INTRODUCTION

The Stepped Isothermal Method (SIM) for time-temperature superposition (TTS) has been formally introduced at this symposium in a companion paper [Thornton, et. al. (1998)] emphasizing the theoretical aspects of the procedure development and giving examples selected from tests on a polyester (PET) yarn. Thornton, et.al (1997) described SIM for a single temperature step on a wide width PET geogrid sample.

The present paper introduces the application of SIM to two PET fiber based geogrid products designated Product A and Product B from two different geosynthetic material manufacturers in the USA.

Utilization of TTS principles have been applied often to polypropylene and polyethylene products. However, extensive use of TTS for polyester products has been inhibited by three factors. First the creep rates for PET, which are generally linear (or nearly so) in semilog plots, are relatively low, in the range of 0.1 to 0.2% strain per time decade. Secondly, the specimen to specimen variation in the load vs. strain relationship is relatively high, given the small resultant creep strains. A 1% uncertainty in strain level for a given load is not atypical. The third factor is that the temperature dependence of creep curves under the same applied load is comparatively small. Differences in exposure temperatures of 20°C cause less than 1% difference in creep strain at the same exposure time. The above factors conspire to make the TTS process for PET so uncertain that many replicate samples are needed to establish the shift factors and the proper strain level locations for shifted creep curves.

SIM overcomes these difficulties because a master curve is

generated on a single sample which is maintained under load as it is exposed to a series of isothermal dwells separated by increasing temperature steps. Because recovery is prevented by this procedure, the master curve is made up of juxtaposed segments in contrast to the overlapped segments that comprise a conventional master curve. When specimens are taken to rupture, the shifted times to rupture obtained from the SIM procedure can be used to construct creep rupture curves. The experimental efficiencies that result from SIM lead to large cost and time savings.

2 OBJECTIVE

The objective of this paper is to introduce the application of the SIM to the characterization of long term creep and creep-rupture of two PET based geogrid products. The results of conventional time-temperature superposition are provided for comparison purposes.

3 MATERIALS AND METHODS

Products A and B are from two different manufacturers in the U.S.A. The methods of construction differ significantly, Product A is manufactured by the weft insertion weaving process and Product B is manufactured by a knitting process. Both products are coated to protect the fibers from abrasion. Comparative load vs. strain and secant modulus vs. strain curves for the two materials are given in Figure 1. Both products are made from high tenacity, high molecular weight (>25,000), alkali tolerant (max. 30 carboxyl end group) fibers. The double hump in both load vs. strain curves is

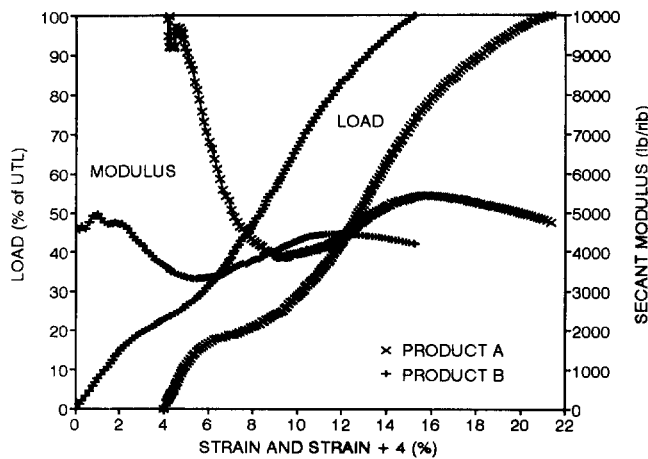


Figure 1. Load and secant modulus vs. strain curves for Products A and B.

characteristic of drawn PET fibers. The initial modulus of Product A is higher than that of Product B due to construction differences. Both products exhibit gradual peaks in secant modulus at strains corresponding to about 75% of the ultimate tensile strength (UTS).

The stepped isothermal creep and creep rupture tests were performed by TRI/Environmental, Inc. of the U.S.A. These tests were all performed in a Model 3111 Instron environmental chamber modified with a Watlow Series 982 temperature controller at a series of temperatures 14°C apart beginning at 26 ± 0.5°C. The 26°C starting temperature was sufficiently above laboratory ambient temperature that adequate temperature control could be achieved by heating only. The tests were performed in an Instron 4505 Load Frame under computer control. Strain was monitored using an extensometer (typically Instron 2620-T24) with a nominal gage length of 2 in. The load cell used was Instron with a rated load capacity of 2248 pounds.

The conventional creep tests on Product A and creep-rupture tests on Product B were performed by ERA Technology, Ltd. of the U.K. Test conditions were 20 ± 2°C/65 ± 2% RH, 40 ± 2°C and 60 ± 2°C for both test programs. Two ribs were utilized in the creep tests and a single rib in the creep rupture tests. The gage lengths were 60mm and 75mm. Roller grips and dead weight loading frames were used in both tests and the strain transducers used were LVDTs.

The Product A and B materials used in SIM tests by TRI and conventional tests by ERA were from different manufacturing lots.

4 RESULTS AND DISCUSSION

4.1 Creep of Product A

4.1.1 Conventional Time-Temperature Superposition

Figure 2 shows the results of eleven long term creep tests of Product A. The tests were conducted at 21, 31 and 56% of

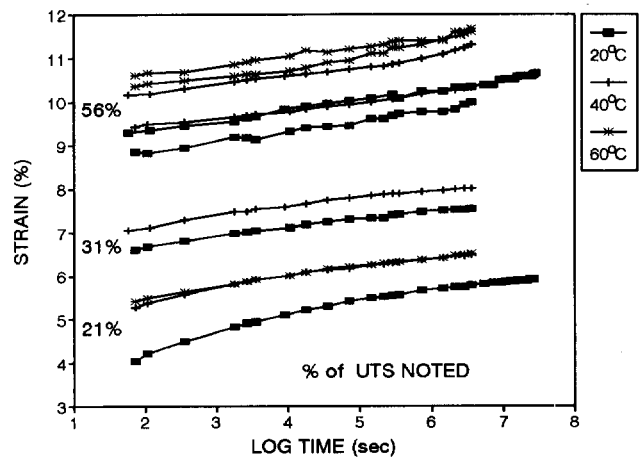


Figure 2. Creep strain vs. log time for Product A at 21%, 31% and 56% of UTS and 20°C, 30°C and 40°C.

the ultimate tensile load of the material and at 20, 40 and 60 degrees Celsius. Two of the tests at 20°C were of 8000 hour duration (one at 21% UTS and one at 56% UTS) and the balance of the tests were 1000 hour duration. Replicate tests were performed at 56% UTS at 20, 40 and 60°C.

These data illustrate one of the major problems with conventional time-temperature superposition of PET products: specimen-to-specimen variation tends to mask the effect of temperature on test results. In Figure 2 at 21% of UTS, the creep strain curve for 60°C lies on top of the creep strain curve for 40°C. At 56% of UTS, one creep strain curve at 20°C lies over another at 40°C. Also at 56% of UTS, the separation between the two 40°C curves is nearly as great as between the higher 20°C curve and the lower 60°C curve. Clearly, it can be concluded from Figure 2 that the specimen-to-specimen variation exhibited is of the same magnitude as a 20°C change in test temperature.

Figure 3 presents the averages of the two creep strain results at each temperature for 56% of UTS. The average curves display reasonable separation despite variability of the individual curves.

Figure 4 shows the creep data of Figure 3 in terms of creep modulus, which is the quotient of the creep stress by the creep strain. As discussed in the companion paper [Thornton, et.al (1998)] creep modulus, as a more fundamental quantity, is preferred over creep strain when comparing the properties of different materials or even different lots of the same material.

Conventional time-temperature superposition was applied to the creep modulus data of Figure 4 to obtain the master curve of Figure 5. The 40°C and 60°C curves were shifted horizontally to the right (representing an acceleration) until they overlapped the 20°C curve in a reasonable fashion. The horizontal shift of creep strain vs. log time data on a semi log plot is equivalent to multiplying the time for each data point of the curve by the same shift factor. The logarithm of the shift factor is the horizontal distance along the log time scale that the curve is moved. The logarithm of the shift factor used on the 40°C data was about 2.5 and that for the 60°C data was about 5. This means that the 40°C curve was shifted

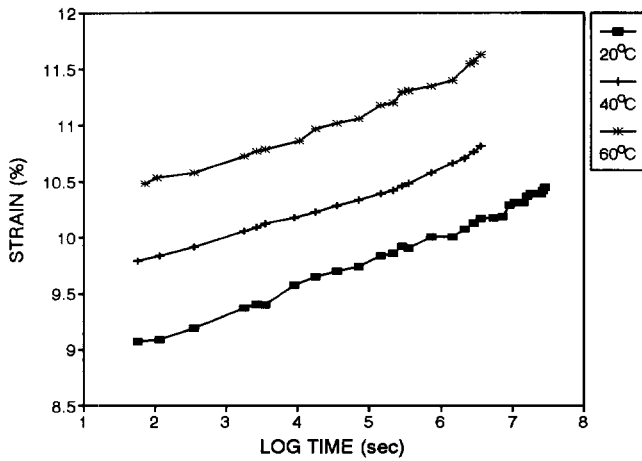


Figure 3. Creep strain vs. log time for Product A at 56% of UTS and 20°C, 30°C and 40°C. Results to 1000 hr. are the average of 2 specimens; results beyond 1000 hr. (20C) are from one specimen shifted vertically to continue the trend established up to 1000 hr.

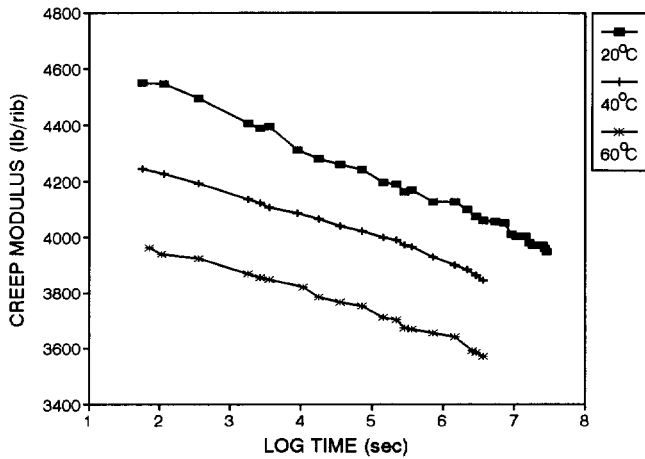


Figure 4. Creep modulus vs. log time for Product A at 56% of UTS and 20°C, 30°C and 40°C.

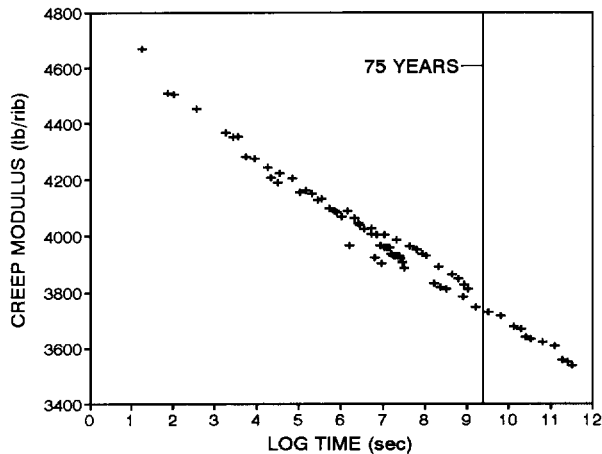


Figure 5. Master creep modulus vs. log time for Product A at 56% UTS for a reference temperature of 20°C.

To the right by two and one-half decades and the 60°C curve was shifted to the right by five decades to achieve the master curve. Since the 20°C curve was fixed in this procedure, 20°C became the reference temperature.

4.1.2 Stepped Isothermal Method (Product A)

Four tests which represent replicate specimens tested at 40% and 56% of UTS were completed on Product A. Since the SIM procedure is described in some detail in the companion paper, only a brief description of the procedure as applied to one of the 40% UTS tests (1801) is given here. The stepped temperature profile for test 1801 is shown in Figure 6, where thermocouple readings representative of the temperatures of the specimen and the grips are displayed. Note that there is a brief exposure to 99°C, which is well above the glass transition temperature (often quoted as 82°C) of PET.

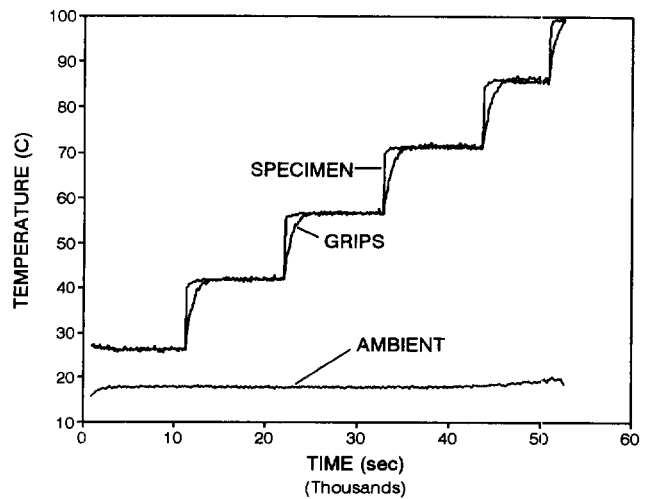


Figure 6. Stepped temperature profile for SIM test 1801 (40% UTS).

The first four isothermal steps are each about 10,800 sec. long, the fifth step about 7000 sec. long and the final step is about 1700 sec. in length. The creep response under the influence of the constant applied load and the temperature profile is presented in Figure 7. The first strain response at 26°C is a normal and complete creep curve, while the subsequent responses at 42°C, 57°C and so on, appear normal, only lacking the initial ramp up portions. Thus, each new temperature exposure sets off a fresh creep response under the constant applied load. Additional interesting features of this graph are the thermal contractions that accompany the increases in temperature. A negative coefficient of expansion is a characteristic of PET fibers. The one shown here is about 35 parts per million per degree Celsius. The load and strain data of this figure were converted to creep modulus and plotted in Figure 8.

Figure 9 contains the creep modulus information of Figure 8 plotted against log time. In addition, the creep modulus responses for the second through the sixth temperature steps

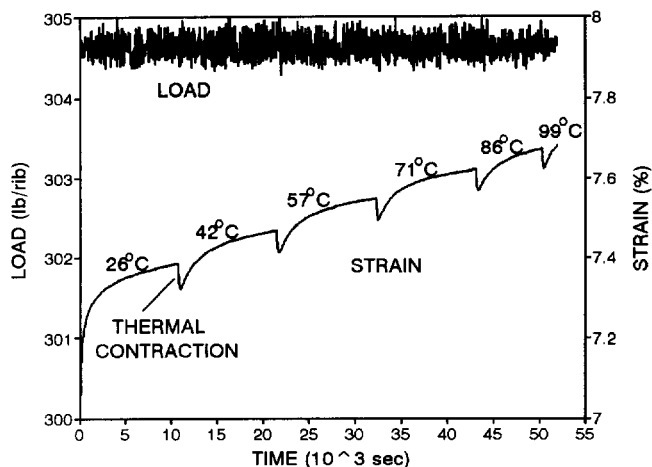


Figure 7. Creep strain response and applied load vs. time for SIM test 1801 (40% UTS).

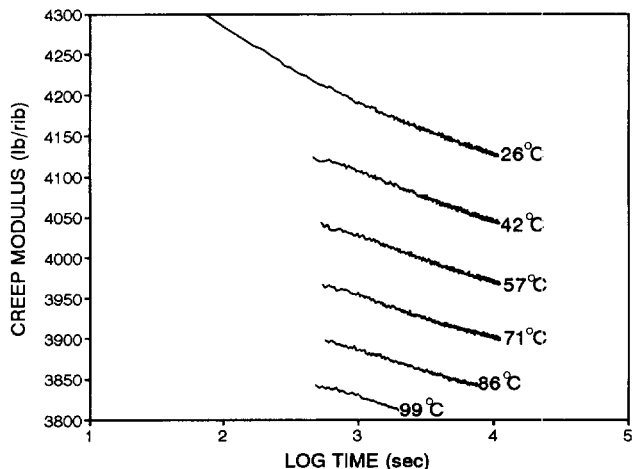


Figure 10. Creep modulus vs. log time for SIM test 1801 (40% of UTS) showing effect of vertical shifts to eliminate thermal contractions between steps.

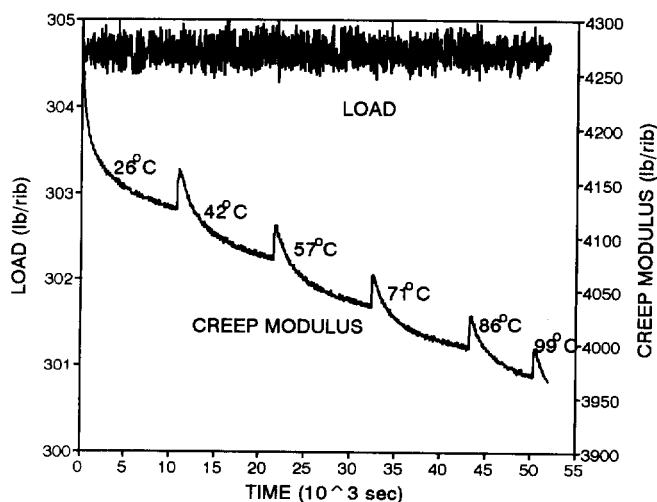


Figure 8. Creep modulus and applied load vs. time for SIM test 1801 (40% UTS).

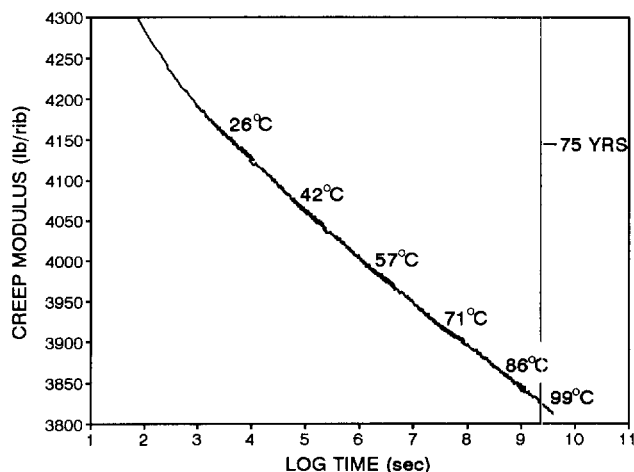


Figure 11. Master creep modulus vs. log time for SIM test 1801 (40% of UTS).

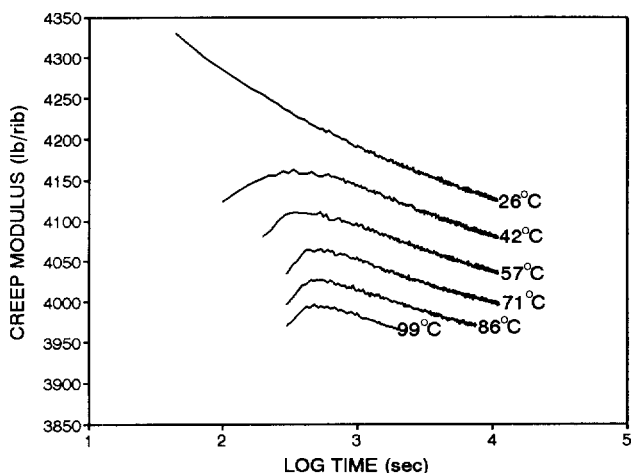


Figure 9. Creep modulus vs. log time for SIM test 1801 (40% UTS) with effect of rescaled start times.

are rescaled to new starting times between 100 and 300 seconds, increasing 2 to 2.5 on the log scale. The next figure, Figure 10 shows the intermediate result of vertical shifts to remove the thermal contractions from the creep data.

Finally, the master creep modulus curve is obtained by horizontal shifts of the segments stacked up in Figure 10 to achieve the result shown in Figure 11 for the reference temperature given by the first step, 26°C. The duration depicted by this master curve is 9.596665 log seconds which converts to over 100 years. Without the 99°C segment of 1700 sec. The shifted time would have been about 32 years.

Master creep modulus curves for the other three tests were created using the method just described.

4.1.3 Comparison of Conventional and SIM Results

Master creep modulus curves for the tests described in the previous two sections are shown in Figure 12. The agreement

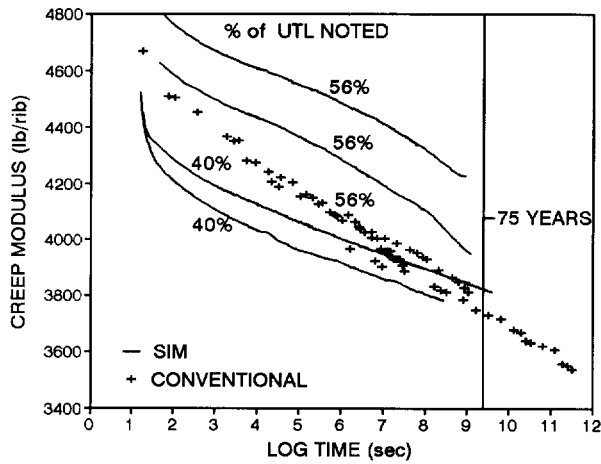


Figure 12. Master creep modulus vs. log time curves by conventional and SIM for Product A at 56% and 40% of UTL.

is quite good especially considering the data were generated several years apart on two different lots of material at separate laboratories.

The separation between the two 56% and the two 40% SIM curves are indicative of specimen to specimen variation. Since data from six specimens were combined to give the conventional (56%) curve, the individual effect of specimen-to-specimen variation is somewhat suppressed, but the overall scatter in the data for the conventional curve reflects uncertainty in both specimen-to-specimen variations and selections of the factors used for the time-temperature shifts. A set of creep strain curves, were computed from the master creep modulus curves and are presented in Figure 13.

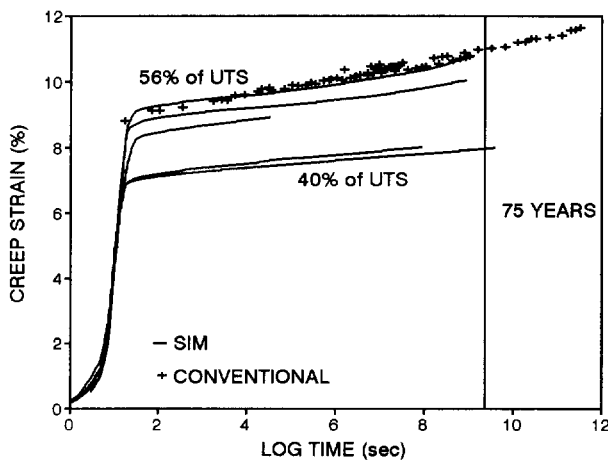


Figure 13. Strain response to long term loading at 40% and 56% of UTS for Product A.

Figure 14 consists of curves relating the cumulative shift factors used in the time-temperature superposition procedures to create the master curves. The single curve of the factors used to generate the conventional master curve is the one on the left of this figure. A family of four curves to the right define the shift factors for the four SIM master curves. The

SIM shift factor curves are essentially the same, appearing not to depend on load level. The slopes of the conventional and SIM curves differ somewhat as do the origins of the curves. The difference in the origins is arbitrary, depending only on the selection of reference temperature. The difference in slopes is not so arbitrary, but given the sample to sample variation problems inherent in the conventional master curves may not be significant. Note that the shift factor curve that extends to 99°C maintains linearity and constant slope beyond the reach of the other curves.

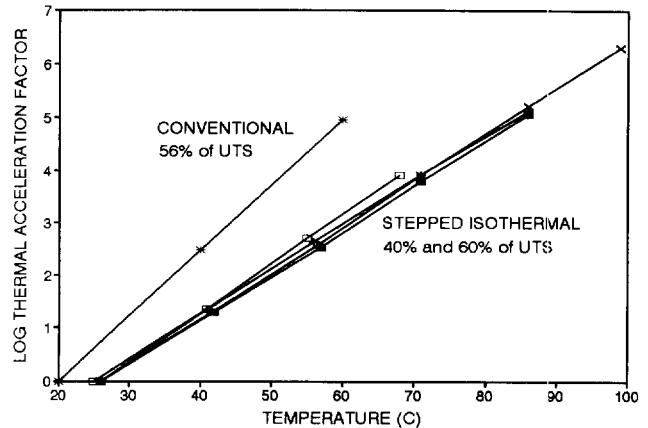


Figure 14. Shift factors used to construct the Product A master creep modulus curves.

4.2 Creep-Rupture of Product B

4.2.1 Conventional Time-Temperature Superposition

There are several ways to do conventional TTS for creep rupture data. The first starts with separate linear regression plots of the rupture strengths vs. log times to rupture for each test temperature. The regression lines for each plot are then shifted horizontally along the log time axis to achieve the optimum fit of a combined regression line through all the data. If, in addition to the rupture strength and time-to-rupture data there are creep strain measurements available, as in the present case, then it is possible to obtain additional estimates of the shift factors using the creep modulus curves at the different test temperatures, in a manner similar to that illustrated in Section 4.1.1. The two ways just described should give similar creep rupture regression lines. However, if at the same rupture stress the creep strains at rupture vary with temperature then the factors for shifting rupture regression lines will differ from those for shifting creep modulus curves.

Figure 15 presents the separate linear regression plots of rupture load as % of UTS vs. log time to rupture for tests performed at 20°C, 40°C and 60°C. The regression lines are not parallel, which makes the TTS uncertain. Horizontal shifts to make the regression lines colinear resulted in several visually acceptable curves, using shift factors between 1.91 and 2.3 for the 40°C to 20°C shift and 3.8 and 4.6 for the 60°C to 20°C shift.

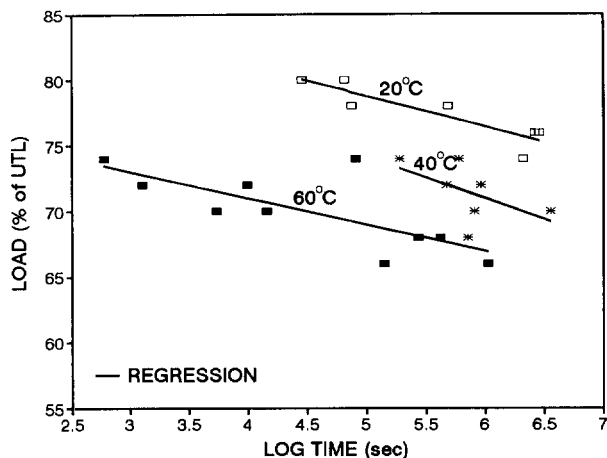


Figure 15. Conventional Load vs. time to rupture data with regression Lines for Product B at exposure temperature of 20°C, 40°C and 60°C.

Creep strain data taken during the creep rupture tests are presented in Figure 16, and the creep modulus curves derived therefrom are shown in Figure 17. Notice that the creep modulus data tend to be separated by test temperature, more so than the creep strain data. The natural groupings of the creep modulus data suggest they can be shifted en masse, despite the slightly different load levels applied at the three test temperatures. This is a consequence of the fact that as a quotient, modulus does not change as much as load with strain in the 65 to 80% load range (see Figure 1). More exact estimates of the log shift factors might be obtained by examining smaller groups of individual curves arranged by applied load. However, this would work only to the extent that sample to sample variation effects were controlled by testing numerous replicates. Figure 18 presents the modulus data of Figure 17 shifted by factors of 1.95 (40°C to 20°C) and 3.90 (60°C to 20°C). Using these factors, the data of Figure 15 are shifted to give the master curve of Figure 19.

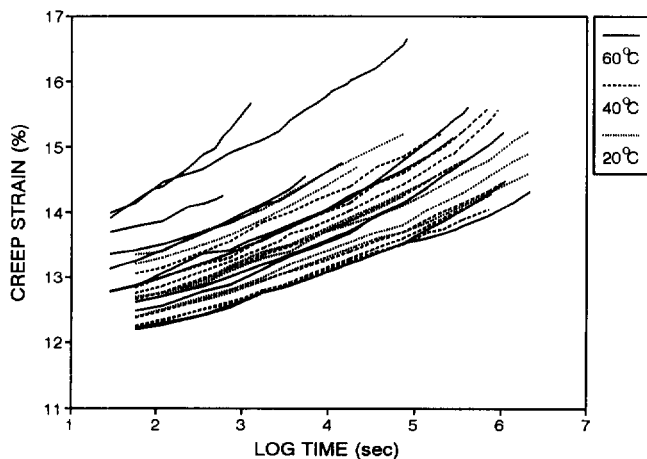


Figure 16. Creep strain vs. log time curves for the conventional Product B rupture tests.

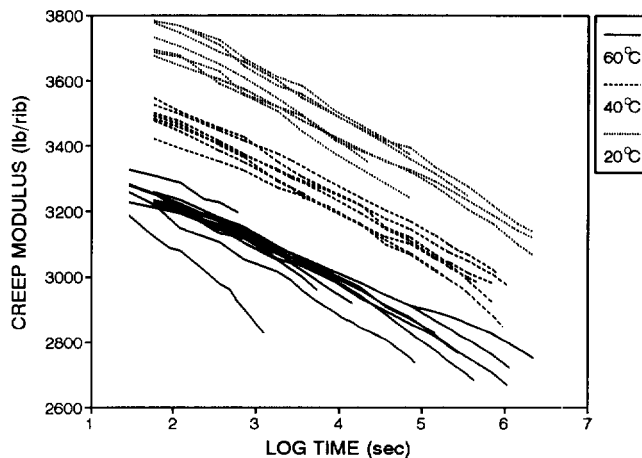


Figure 17. Creep modulus vs. log time curves for the conventional Product B rupture tests.

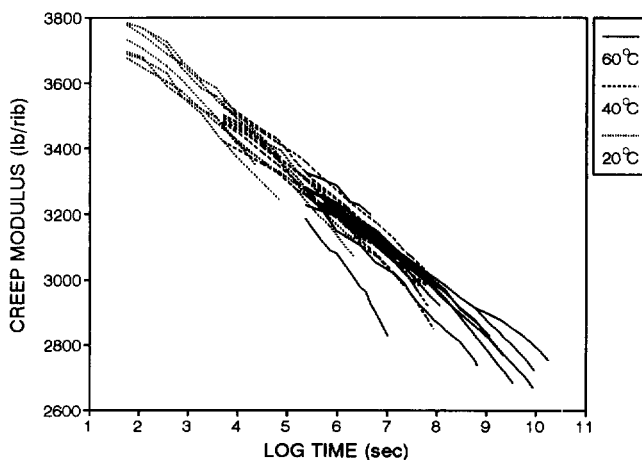


Figure 18. Shifted creep modulus curves for the conventional Product B rupture tests.

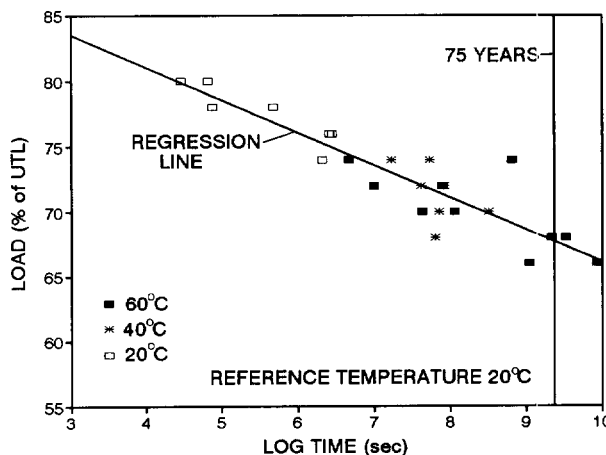


Figure 19. Conventional master load vs. log time to rupture data and regression line at a 20°C reference temperature.

4.2.2 Stepped Isothermal Method (Product B)

Creep modulus master curves for each specimen were generated using the same procedure described in Section 4.1.2. These are displayed in Figure 20. Note that 5 of the curves terminated in rupture, and the balance did not. We use the term runout to describe the result of a test where rupture did not occur before the test was terminated. Runouts that are close to the loads resulting in rupture can be used in the statistical analysis to help locate the regression line.

Figure 21 presents the creep strain curves derived from the creep modulus master curves.

An expanded set of creep-rupture loads vs. log times to rupture for the SIM tests are shown in Figure 22. The runout loads and log times, included for information, were not included in the regression calculation. The 75 year rupture load at a reference temperature of 26°C is 65.6% of UTS. Less than one decade of extrapolation beyond the temperature shifted results was needed to return this result.

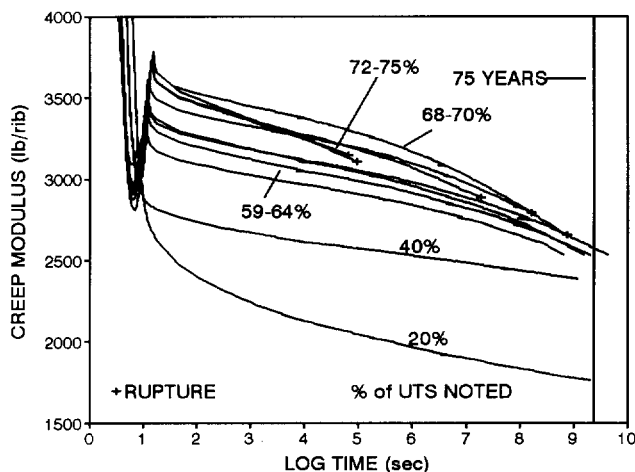


Figure 20. Master creep modulus vs. log time curves for SIM tests on Product B. Load levels and rupture events are noted.

Table 1 provides a guide to the shifted rupture times of Figures 20 - 22. The log shift factors used to construct this table are based on 0.093 decades per °C. Thus a 14°C temperature step creates a time shift of about 1.3 decades.

Table 1. Logarithm of the shifted times at the reference temperature (26°C) corresponding to the unshifted times at the exposure temperatures.

Range Shifted time Log $A_T(t-t')$	Maximum value	
	Exposure Temperature, °C	Unshifted cumulative time, sec
0.0-4.0	26	1×10^4
4.0-5.3	40	1×10^4
5.3-6.7	54	1×10^4
6.7-8.0	68	1×10^4
8.0-9.3	82	1×10^4

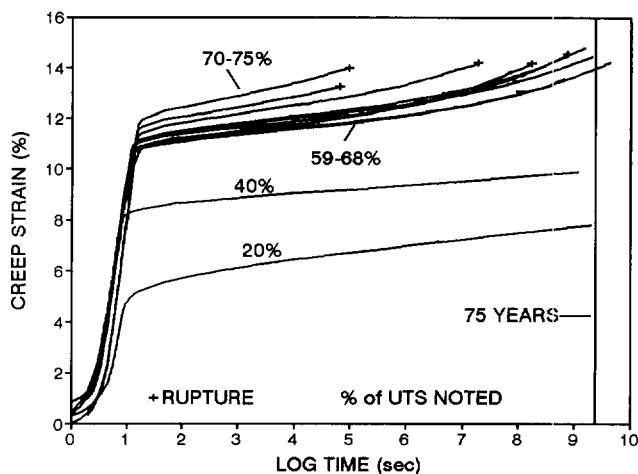


Figure 21. Creep strain curves computed from the data of Figure 20.

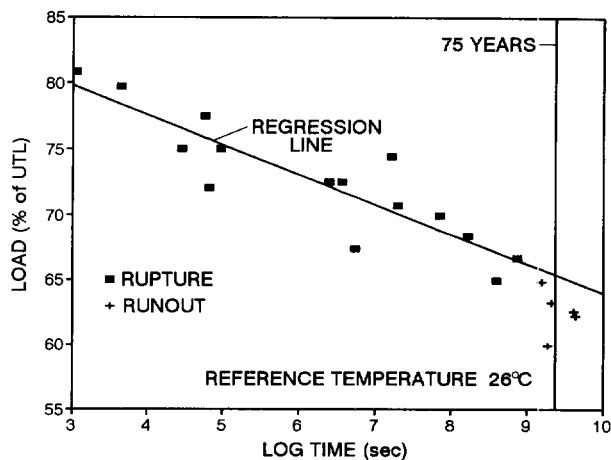


Figure 22. SIM master load vs. log time-to-rupture data and regression line for Product B.

4.2.3 Comparisons

Regression lines for the conventional and SIM creep rupture results are compared in Figure 23, and shift factors used to accomplish TTS, in Figure 24. Rupture loads at 75 years for a reference temperature of 20°C are 67.7% for conventional and 66.5% for SIM TTS. Despite an apparent small difference in shift factors for the conventional and SIM approaches, results for the regression lines and the projected rupture loads at 75 years are very close. Figure 25 compares all shift factors for Products A and B.

5 CONCLUSIONS

- The use of SIM as a special application of TTS for polyester geogrids appears to be validated by the results presented herein. Differences, if any, in the shift factors obtained in SIM and conventional approaches are not large.

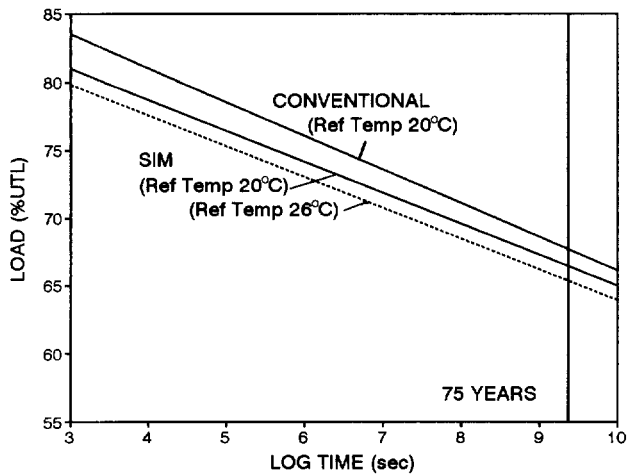


Figure 23. Comparison of conventional and SIM regression lines for Product B.

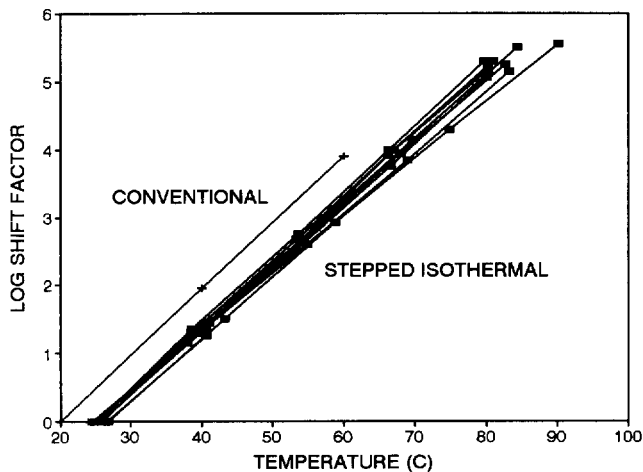


Figure 24. Comparison of log shift factors for Conventional and SIM rupture master curves.

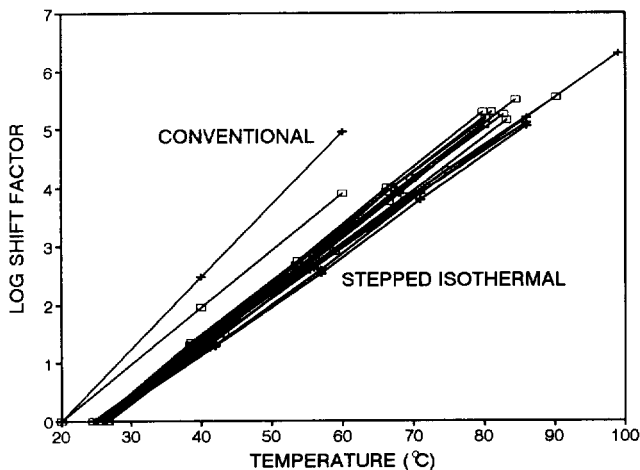


Figure 25. Comparison of all shift factors for creep and creep rupture for Products A and B.

- An advantage of SIM in this regard is that it reduces the uncertainty of shift factors used to construct master curves.
- Since a SIM master curve is generated from a single specimen, the precise location of the completed curve is uncertain, due to specimen-to-specimen variation. This is not a great disadvantage if several SIM tests are to be done, as in developing a creep rupture curve. Alternatively, if only a single SIM test is done and its location is important, the location can be determined from the results of a few very short term conventional creep experiments.
- The apparent insensitivity of SIM master curves to abrupt transition behavior for tests at 40% of ultimate and higher at and above the glass transition temperature is consistent with a creep mechanism associated with they crystalline regions of the polymer.
- The slopes of SIM generated creep strain curves increase significantly with increase in applied load, but the shift factors are not greatly sensitive to applied load for the range of loads studied here. Thus the increases in slopes are not caused by decreases in shift factors.
- The shift factors for Products A and B (Figure 25) are similar despite differences in construction and load vs. strain behavior confirming the notion that the shift functions are manifestations of basic material properties.
- Obtaining creep strain data in conjunction with performing creep rupture tests is recommended where TTS is to be done. If rupture times at elevated temperatures are shifted based on the basis of achieving superposition of creep strain or modulus curves then the shift factors for creep and those fro rupture will be the same. Rupture times from SIM tests can be obtained no other way.

ACKNOWLEDGMENTS

The authors are indebted to Dr. John H. Greenwood for helpful suggestions and experimental efforts at ERA Technology, Ltd., for both products A and B over several years, Shawn L. Arnett of TRI/Environmental, Inc. and J.M. Palmer of ERA are acknowledged for conducting the experimental program. Funding from Texas Research International, Inc., Strata Systems, Inc., and T.C. Mirafi, Inc. is greatly appreciated. T.C. Mirafi, Inc. is also acknowledged for providing seed funding for SIM development.

REFERENCES

- Ferry, J.D. (1980) *Viscoelastic Properties of Polymers*, 3rd Edition, John Wiley and Sons, New York, NY, USA.
- Thornton, J.S., Allen, S.R., Thomas, R.W. and Sandri, D. (1998), "The Stepped Isothermal Method for TTS and Its Application to Creep Data on Polyester Yarn," *Sixth Int'l Conference on Geosynthetics, Atlanta, USA*.
- Thornton, J.S., Allen, S.R., and Thomas R.W., (1997), "Approaches for the Prediction of Long Term Viscoelastic Properties of Geo Synthetics from Short Term Tests," *Geo '97, IFAI, Vol. 1, Long Beach, CA, USA, pp 277-291*.

The Stepped Isothermal Method for Time-Temperature Superposition and Its Application to Creep Data on Polyester Yarn

J. S. Thornton

President and Principal Scientist, Texas Research International, Inc., Austin, Texas, U.S.A.

S. R. Allen

Vice President and Program Manager, TRI/Environmental, Inc., Austin, Texas, U.S.A.

R. W. Thomas

Vice President and Technical Director, TRI/Environmental, Inc., Austin, Texas, U.S.A.

D. Sandri

Western Regional Engineer, T. C. Mirafi, Inc., Lake Forest, California, U.S.A.

ABSTRACT: The stepped isothermal method (SIM) is a new procedure for assessing the long term viscoelastic behavior of polymeric materials. SIM is a special case of time-temperature superposition (TTS) that is convenient for characterizing viscoelastic materials. It utilizes a single specimen which is loaded continuously through a sequence of timed isothermal exposures at increasing temperature in stair step fashion. Generating master curves involves rescaling the times for the elevated temperature and utilizing horizontal shifts in such a way that smooth curves are achieved. Relationships between the rescaling times and the resulting horizontal shift factors as well as the relative magnitudes of the temperature and time steps are investigated to demonstrate that the SIM can tolerate reasonable variations in these parameters and provide master curves and shift factors comparable to those obtained by conventional time temperature superposition. Conventional and SIM results are obtained on a 3 ply, 1000 denier poly(ethylene terephthalate) yarn. PET is an ideal object for study because its creep properties are well behaved. Also, as the basic ingredient for a number of commercially viable geosynthetic fabrics and grids, the properties of PET yarn are of special interest on their own.

KEYWORDS: Stepped isothermal method, time-temperature superposition, shift factors, unconfined creep tests, creep strain, creep modulus, creep rupture, polyester yarn, accelerated testing.

1 INTRODUCTION

Polymer scientists have been using time-temperature superposition techniques for at least 4 decades to describe long term viscous or viscoelastic properties of polymers [see, for example, Ferry (1980)]. The fundamental notion is that elevating temperature accelerates the response to mechanical load. Deformations, such as creep strain, occur relatively rapidly when load is first applied, but the rate of increase decreases with time. Consequently, graphs produced with log time as the abscissa are indispensable for describing viscoelastic behavior.

The precise way that increasing temperature accelerates these physical processes, governs how creep response can be "shifted" along a log time scale. Ferry (1980) refers to TTS as the method of reduced variables for corresponding states. A temperature dependent time factor, a_T , relates the ratio of the time, t_T , for a viscoelastic process to proceed a given amount at an arbitrary temperature to the time, t_R , for the same process at a reference temperature.

$$a_T = \frac{(t_T)}{(t_R)}$$

At temperatures greater than the reference temperature a_T is less than 1. For this reason, some in the accelerated testing business refer to a_T , as an attenuation factor and A_T , defined as its reciprocal, as an acceleration factor. Both, collectively, are referred to as shift factors.

Early master creep (or relaxation) curves using TTS were specialized to small strain linear viscoelastic situations. Single specimens were used (to reduce specimen to specimen variation) and these were permitted to recover between creep exposures by removing the load (without removing the specimen from the apparatus to avoid problems of repeatable clamping stress transfers) for a time period that was long compared to the loading time between creep tests (10 times the loading time would generally effect 99+% recovery of the creep strain of the prior creep test).

Most engineering applications that engage time-dependent behavior of polymeric materials deal with non-linear viscoelastic behavior. For such situations, creep master curves are generated using several specimens to reduce the uncertainties of non-identical specimens, and each is only tested one time because recovery is generally too complex to consider doing. Hence, the corresponding states must come from averaging a range of states from the several specimens tested at each exposure temperature. Despite the preoccu-

pation of this paper with large strain nonlinear viscoelastic effects we believe it will be helpful preparation to review the Boltzman Superposition Principle, which is the first mathematical statement of linear viscoelasticity.

From this brief review we will see that tracking the creep response to a series of loading steps includes starting a new clock with each new step. Boltzman (1876) proposed that, a) the creep response of a material is a function of the entire loading history, and b) each loading step is treated as an independent event, and c) the total creep response is the sum of the individual responses to those independent events. In mathematical notation the time dependent strain $e(t)$ is

$$e(t) = \int_{-\infty}^t D(t-t') \frac{d\sigma(t')}{dt'} dt'$$

The integral is over all time to the present hence the limits are from $-\infty$ to t . The first factor $D(t-t')$ is the compliance function where t' symbolizes the times at which increments of stress $d\sigma$ are applied; so that $t-t'$ starts a new clock that activates the compliance function at the application of each stress increment. The second factor $d\sigma(t')/dt'$ represents the loading program which is summed by the integration process. The response of a linear viscoelastic material to a two-step loading program is illustrated in Figure 1. As illustrated in this figure, each loading event begins a new clock and evokes an independent creep response. The new creep response is on top of (added to) the background of continuing responses to the history of loading events. The idea of a series of loading events activating new responses and starting new clocks at $t-t'$ will be utilized for explaining the SIM as we shall see shortly.

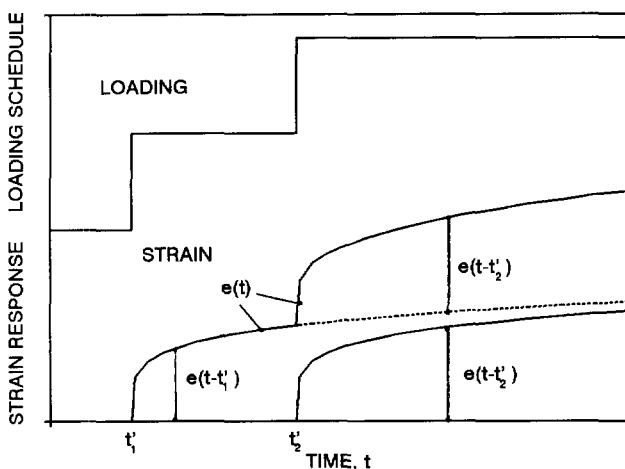


Figure 1. Boltzman Superposition Principle applied to the case of two loading steps

2 THE SIM PROCEDURE

The stepped isothermal method (SIM) procedure for creep consists of a series of timed isothermal creep tests performed

at a sequence of increasing temperatures. These are somewhat analogous to the loading steps of the previous section. As in an ordinary creep test, the load is held constant and the creep strain is measured for the duration of the test. The number, heights and the durations of the temperature steps are designed to produce a master curve of creep compliance (or preferably its reciprocal, the creep modulus) over a long term period defined by the test objective. For the geosynthetics community, long term generally means 75 years or sometimes 1,000,000 hours, which is 114 years. For our work on PET, we've found that 14°C temperature steps and 10,000 second isothermal step durations are convenient and workable for most tests on PET base products. Five 10,000 second isothermal exposures between 26°C and 82°C will usually achieve the desired long term objective. The time step of 10,000 seconds has been used frequently in the literature [see, for example, Murayama et.al (1968)]. Also, in previous work, Thornton, et.al (1997) showed that as the basis for long term extrapolations creep and relaxation modulus curves at 3 hours were as well developed as curves at 24 hours for that purpose. The typical starting temperature of 26°C comes from desiring a temperature above our maximum summer laboratory ambient temperature of 23°C that could be controlled by heating only. The typical ceiling temperature of 82°C came from the temperature usually assigned as the glass transition temperature for PET. Above 82°C one would ordinarily expect to encounter glass transition behavior with PET. However, as we'll see later, at high loads the creep mechanism engages crystalline regions of the polymer which do not participate in the glass transition. Our study of shorter and longer times and higher and lower temperature steps has confirmed that our standard SIM temperature steps of 14°C and time steps of 10,000 sec, while aggressive, are usually acceptable.

Preparation for the SIM test involves mounting the specimen in the grips, achieving temperature equilibrium, and applying a small (< 1%) preload on the specimen. Ramping the load to the predetermined stress level begins the test. This is done rapidly (typically 60%/minute strain rate) to minimize the creep deformation that occurs during the ramp-up process. We've gotten into the habit of "starting the clock" for the first leg of the creep test at the start rather than the end of the ramp. This preserves the ramp-up process for the record. With generally less than 20 seconds involved in the ramp-up and 75 or 114 years the long term objective, a starting time correction from the start to the peak of the ramp has no measurable impact on the final master curves.

The first creep exposure of the SIM procedure is a normal creep test in the sense that the specimen does not have a history of creep loading. The second and subsequent creep exposures are complicated slightly by having the thermal histories of the previous steps. This slight complication however, represents the essence of the SIM method. Since recovery is not permitted during the time that the temperature step takes place, and since the temperature step is accomplished rapidly, within 1 to 2 minutes, the mechanical

state of the sample is nearly the same after the temperature step as it was before the temperature step took place. Inherent in the SIM is the necessity that the corresponding states at both the lower and the higher temperature are stable ones that would be readily achievable under, say a conventional TTS approach. That condition would not be achieved if, for example, the temperature step was so large that the sample had to undergo a rapid change to achieve a steady state creep rate.

Just as each loading step is treated as an independent event for Boltzman's Principle, we assign a starting time, t' on the old clock to each temperature step. The time on the new clock starts at 0 which is obtained by setting $t-t' = 0$. The response history for the thermal steps is easier to account for than with the loading steps because the load has not changed. The assumption is that with the temperature step only the rate of creep has been changed, not the mechanism. Based on the notion that for a pair of corresponding states obtainable at two temperatures, the one at the higher temperature must have occurred at an earlier time than the one at the lower temperature, we begin the rescaling procedure by finding that earlier time, t' , that represents the virtual starting time of the higher temperature step. Exactly how we choose t' is illustrated in Figure 2.

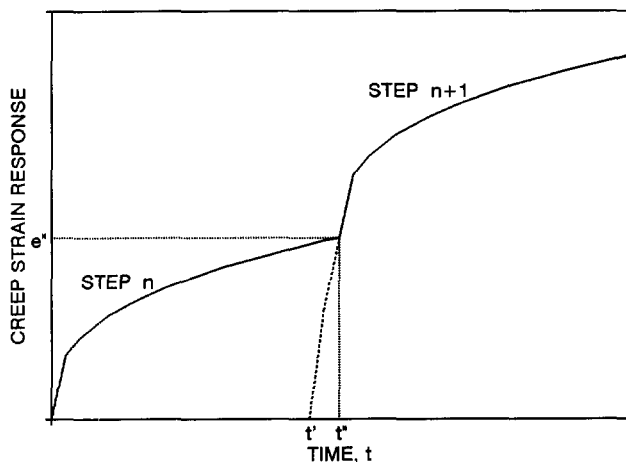


Figure 2. Strain response for two temperature steps

Here, we see the strain response for two temperature steps. In Figure 2 the precise time of the application of temperature step $n + 1$ is t'' . In the SIM at t'' , the effect of history has been to bring the strain response to e'' . In a hypothetical independent creep test at the temperature of step $n + 1$ the creep strain e'' would have been achieved at a time t_1 after the start time. Overlaid on Figure 2, the starting point of that hypothetical creep curve would be at t' . Thus, $t_1 = t' - t''$. We refer to the value of $(t-t')$ at the beginning of the step (i.e. at $t = t''$) as the initial value of $t-t'$. We know that we have the best value for t' if the slopes of the creep curves in semi logarithmic representations are the same before and after the temperature change.

In the SIM procedure it is necessary to remove the effects of thermal expansion to insure that the strain response is due to loading effects only. This is accomplished by a simple vertical shift for each temperature change.

The final SIM procedural step is the horizontal shifts to achieve juxtaposition of the creep modulus segments. If the rescaling step has achieved the slope matching boundary condition, then there will be little if any effort needed to determine the horizontal shifts needed. In practice, we generally do the rescaling and the horizontal shifting steps together in an iterative fashion to achieve a smooth creep modulus master curve.

The SIM procedure just described for processing creep modulus data is summarized in bullet form in Table 1.

Table 1. SIM procedure for processing creep modulus data

- Plot the creep strain and creep modulus data as function of linear time to identify the times for the temperature step changes.
- Using creep modulus as the parameter of interest, plot this parameter vs. log time.
- Rescale the times for the individual creep modulus segments by plotting them vs. the logarithm of the initial value of $(t-t')$ where t' is adjusted to account for history. This will be achieved when the slope of the beginning of a new segment is exactly the same as the ending slope of the previous segment.*
- Remove thermal expansion effects by vertical shifts.
- Shift horizontally to achieve exact juxtaposition of the rescaled and vertically shifted individual creep modulus segments.*

*the rescaling and shifting steps may require some iteration.

3 OBJECTIVE

The objective of this paper is to introduce the SIM and a standard protocol for its use. This will be accomplished by first comparing SIM results using the standard protocol to conventional TTS results and next by examining the effects of variations from the standard protocol. Finally, demonstrating the effectiveness of SIM by using it to characterize the long term creep and creep rupture properties of a polyester yarn, completes this introduction.

4 MATERIALS AND METHODS

Figure 3 represents stress vs. strain and secant modulus vs. strain curves for a 3 ply polyester yarn chosen for the current investigation on the basis of its well behaved creep properties and commercial importance. The rapid loading secant modulus is included in this illustration because the creep modulus is a secant modulus. When the loading path up a stress-strain curve is interrupted at a particular stress for a creep test, the beginning creep modulus for the creep test will

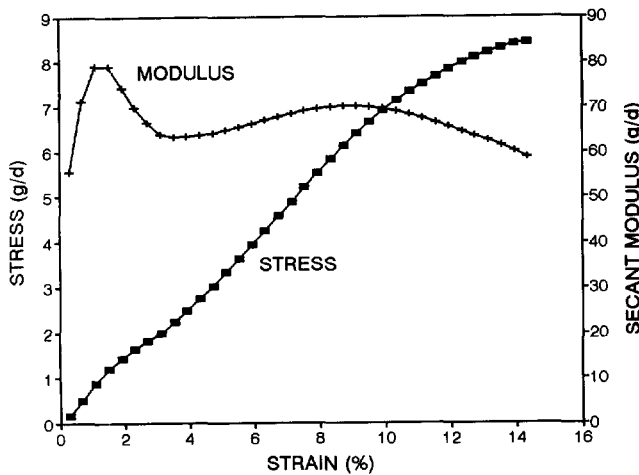


Figure 3. Stress and secant modulus vs. strain for the 3 ply, 1000d polyester yarn under rapid loading conditions.

be the same as the rapid loading secant modulus at that stress. Most of the tests reported in this paper were conducted in the vicinity of the second modulus peak at stresses between 5 and 7 g/d. Note that the secant modulus varies only within a range of about 3% around 70 g/d, in that stress range. The creep mechanism probably involves some straightening and breaking of tie molecules between crystalline regions in vicinity of the second modulus peak. Even for creep tests at stresses as low as 3 g/d the mechanism is probably similar to that of the higher stresses. At stresses below about 1.5 g/d the creep mechanism is associated more with the initial modulus peak and involves conformational changes involving the breakdown of the entanglement network as well as molecular uncoiling [Van den Heuvel et.al. (1993)]. This figure shows that initial creep modulus for tests at less than 1.5 g/d applied stress will be substantially higher than tests at above 3 g/d applied stress.

The creep tests were all performed in a Model 3111 Instron environmental chamber modified with a Watlow Series 982 temperature controller at a series of temperatures 14°C apart \pm 0.5°C. The 26°C starting temperature was sufficiently above laboratory ambient temperature that adequate temperature control could be achieved by heating only. The tests were performed in an Instron 4505 Load Frame under computer control. Strain was computed from cross head travel and a 10 inch gage length. Instron Model 2111 "horn" grips were used along with an Instron load cell with a rated load capacity of 224 pounds. The specimen and the grips were completely enclosed in the environmental chamber.

5 RESULTS AND DISCUSSION

5.1 Conventional TTS

As a special case of TTS, SIM should provide master curves as good as and potentially better than the conventional procedure. Thus, the ability of SIM results to match exactly those of conventional TTS is not the goal; to show they give

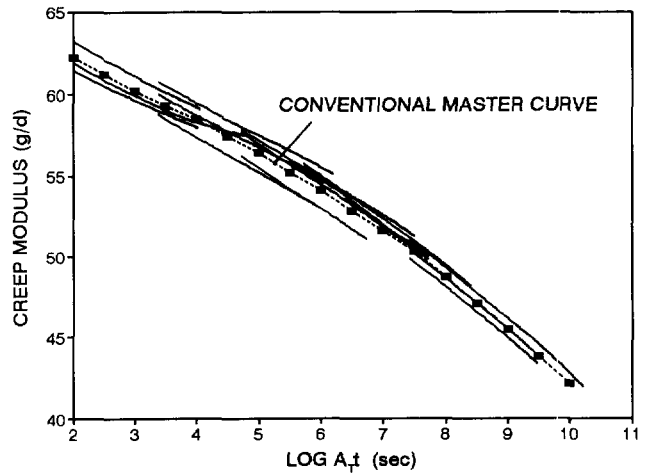


Figure 4. Conventional master creep modulus curve.

comparable results, builds confidence in both procedures.

A total of 15 polyester yarn specimens, consisting of 3 each at the temperatures of 26, 40, 54, 68, and 82°C were tested for creep at an average stress of 62% of UTL over time periods of 10,000 to 60,000 sec. The resulting creep modulus curves were shifted to obtain a good visual representation by a conventional master creep modulus curve. These results are shown in Figure 4. Note the range of the individual modulus values is 3 to 5% of the master curve values. The conventional master curve appears in some of the subsequent figures to provide a comparison with SIM master curves.

5.2 Standard SIM Steps

Figures 5 through 9 illustrate the SIM applied to a yarn specimen subjected to a constant stress of 5.21 g/d, which is about 62% of the ultimate tensile strength (UTS) of this material. Figure 5 shows the measured creep strain and the computed creep modulus as a function of linear time. Each time step is approximately 10,000 sec and each temperature

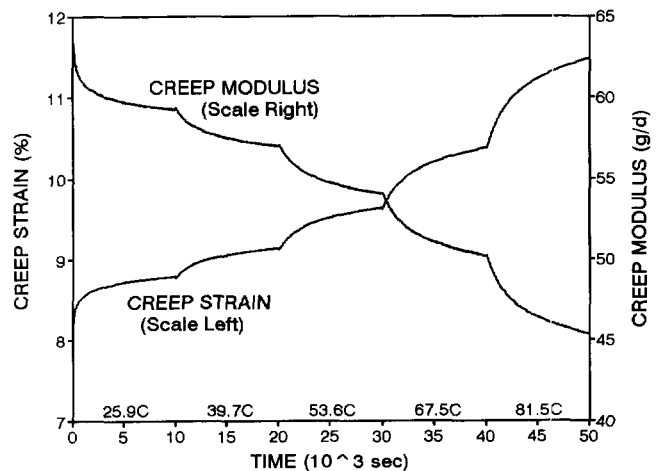


Figure 5. Creep strain and creep modulus vs. linear time for a specimen tested at 62% of UTS.

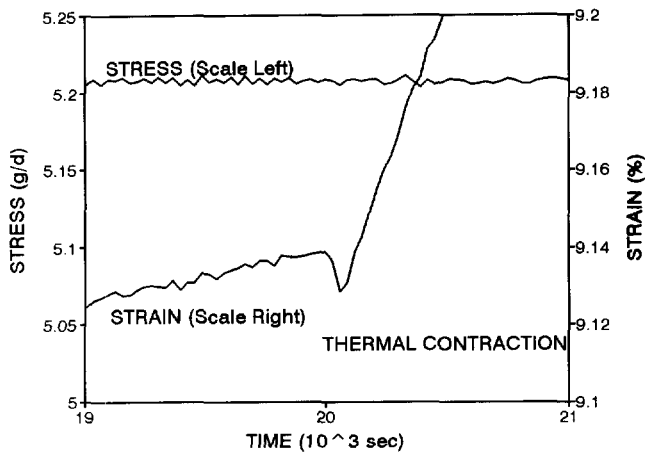


Figure 6. Enlargement of a portion of Figure 5 showing a thermal contraction after a 13.9°C temperature step.

step approximately 14°C beginning at 25.9°C and ending with 81.5°C as shown along the bottom of the figure. There are tiny cusps at the temperature step change points which are manifestations of a negative thermal expansion coefficient (α_T). One of them is shown in enlarged scale in Figure 6. The magnitude of α_T for this example is about 7ppm/°C. Such negative thermal expansions are easy to identify because they produce length changes opposite to the creep strains. Positive thermal expansions may require separate experiments to quantify. Next, Figure 7 presents the creep modulus data as a function of log time. The effect of the time rescaling step is illustrated in Figure 8. Rescaling has a dramatic effect on the shapes of the curve segments. Part of this is due to the nature of logarithmic scales, but as indicated earlier, the initial slopes of the rescaled curves are influenced by the new starting times. Figure 9 gives the master creep modulus curve resulting from the horizontal shifts. The abscissa is now labeled LOG $A_T [t-t']$ to indicate the data has been both rescaled and shifted.

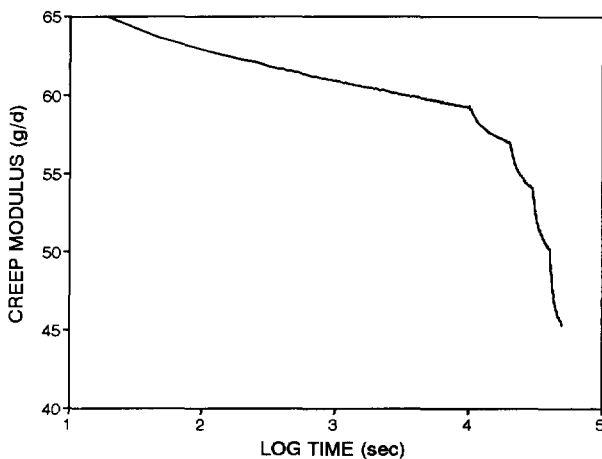


Figure 7. Creep modulus data from Figure 5 plotted vs. log time.

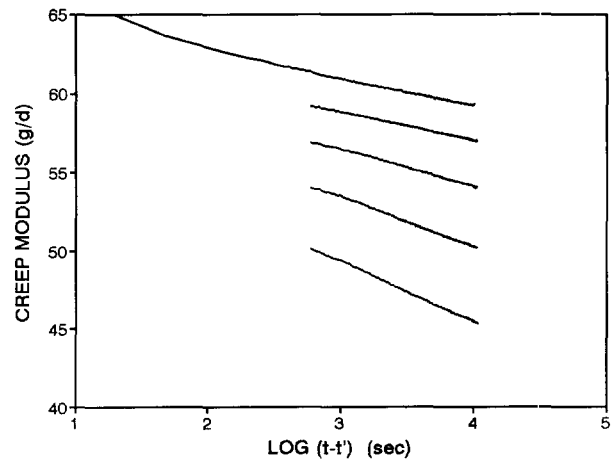


Figure 8. Creep modulus data from Figure 7 rescaled for new starting times vs. log $[t-t']$

5.3 Effect of the Choice of $t-t'$ on A_T

The purpose of this section is to explore the effect on A_T of non optimum selections of rescaling times $t-t'$, when generating master curves.

Figure 10 displays the influence of three choices for rescaled times $t-t'$ on the shapes of the resulting creep modulus master curves. The middle curve, labeled 600s, for the initial value of $t-t'$, is near optimum, and this is the same curve displayed in Figure 9. The other two do not show slope continuity at the points of juxtaposition. One of these shows concave features for $t-t'$ considerably larger than optimum, in this case 1500s, the other convex features for $t-t'$ considerably smaller than optimum, here 300s. The reach of the master curves is governed by the horizontal shift factors, and by inspection we observe that a smaller value for $t-t'$ requires a larger log A_T to achieve juxtaposition, and visa versa. A quantitative relationship between the initial value of $t-t'$ and the average log shift factor per degree of temperature

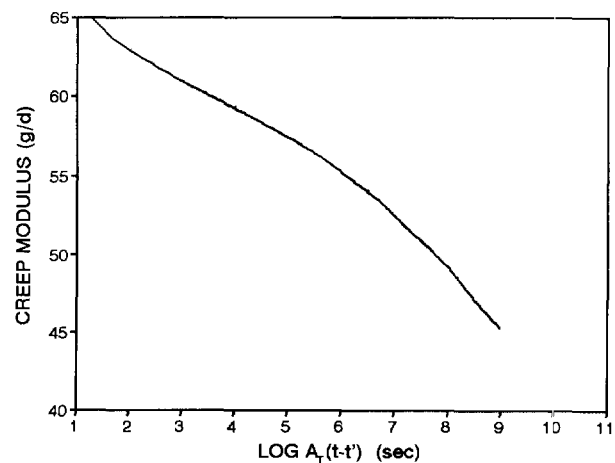


Figure 9. Creep modulus data from Figure 8 horizontally shifted to achieve the master curve shown.

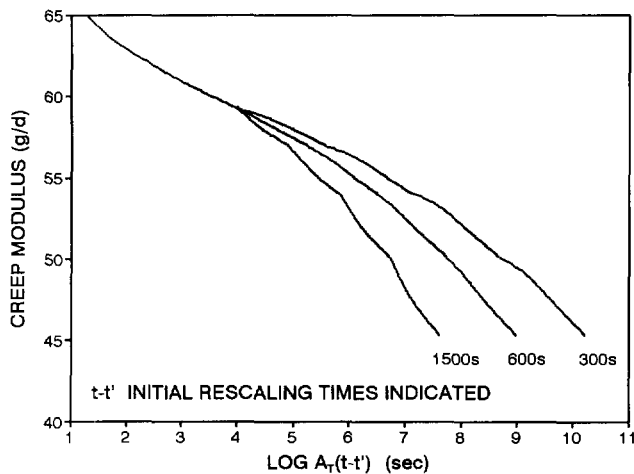


Figure 10. Effect of choice of rescaling times on the shape of the creep modulus master curve.

step, is given in Figure 11.

Figures 10 and 11 show that while it is possible to generate master curves that achieve juxtaposition with a wide combination of $t-t'$ and A_T selections, there will be a much limited selection of combinations (perhaps only one optimum combination) where the slopes of the adjacent curve segments will match at the points where they meet. For clarity, we have exaggerated the effects on A_T and the resulting master curves by illustrating the effects of large deviations from optimum selections of $t-t'$. Near optimum selections of $t-t'$ are easy to achieve, however, and uncertainties in the reach of resulting master curves are not expected to be above 0.1 log cycle.

5.4 Effect of Time and Temperature Step Magnitudes

When designing a SIM test it is important to pick the times at each temperature increment and the size of the temperature changes imposed to achieve the desired results. One of the important requirements is that the temperature step bridges

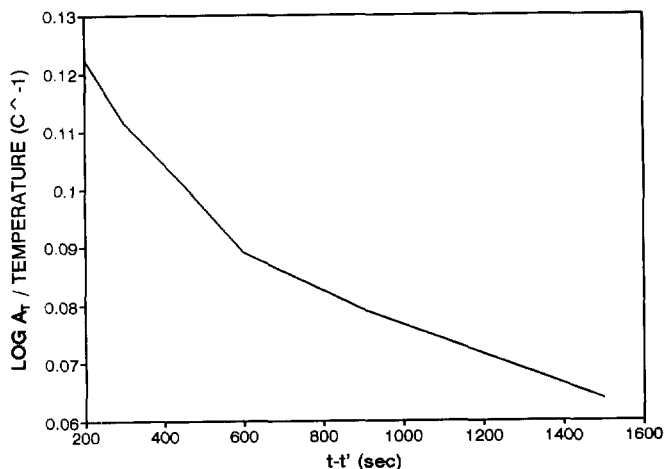


Figure 11. Effect of rescaling times on the horizontal shift factors used to construct master curves.

two corresponding states. The only way we know to effect this is to insure that both states be very nearly steady states, by which we mean that the creep rates are not changing (at least not rapidly) with time. Thus, the creep rate, $de/d\log t$, before a temperature step would be ideally, exactly the same as after the step. This situation we desire will be more achievable for small temperature steps and large time steps, but that is the direction of higher cost.

The matrix of SIM tests we conducted to explore the effect of time and temperature step magnitudes is given in Table 2. The conditions studied were A through G. The two not studied were cases Y and Z, the conditions for which were considered too extreme to be instructive. The A through G tests were conducted on yarn specimens loaded to 62% of UTS. The number of steps and the maximum temperature

Table 2. Matrix of SIM tests on variable time and temperature steps

Step times, sec	7°C steps	14°C Steps	28°C Steps
1000	A(9)[82]	B(5)[82]	Y
10,000	C(7)[68]	D(5)[82]	E(3)[82]
100,000	Z	F(4)[68]	G(3)[82]

achieved in the SIM tests are given in parentheses and brackets respectively. All tests were started at 26°C. The results of the SIM tests are presented in Figure 12. The SIM results have been normalized to a creep modulus of 62.4 g/d at log time 2 and are presented with a creep modulus curve developed by conventional TTS which was also normalized to 62.4 at log time 2. We note that three of the SIM results compare favorably with the conventional results, these are conditions C, D and F. Conditions A and B result in smooth

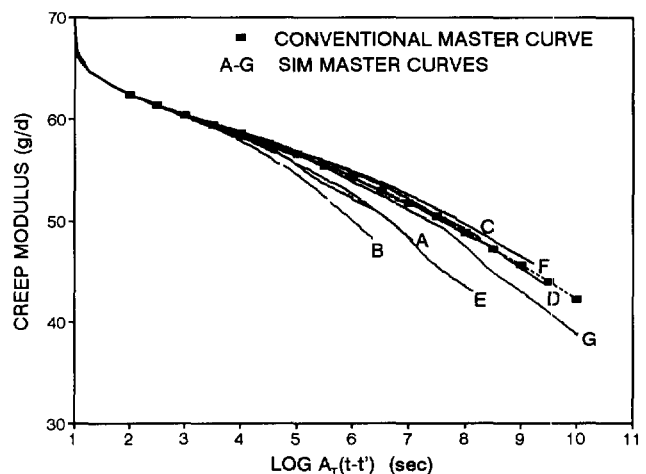


Figure 12. Resulting creep modulus master curves from the variable time and temperature steps of the Table 1 Matrix, compared to the conventional master curve of Figure 4. All curves have been normalized to a modulus of 62.4 g/d at log time 2 (sec).

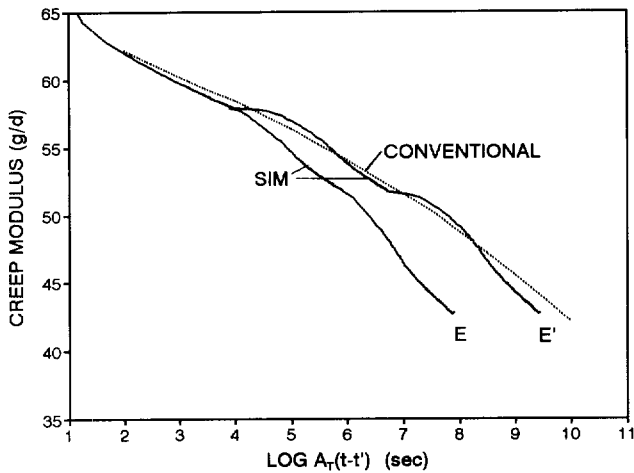


Figure 13. Characteristic curve shapes for an excessive temperature step (condition E of Table 2).

master curves, but the short reach of these curves indicate clearly that the time steps are inadequate for stable creep conditions to have been achieved. Conditions E and G do not result in smooth master curves despite achieving both the slope matching and juxtaposition boundary conditions. Condition E is examined in more detail in Figure 13.

Slopes are matched at the points of juxtaposition in curve E of Figure 13, yet a convex curvature followed by a concave curvature indicates that the creep rate accelerated immediately after the temperature step change. A larger shift factor would bring the steady state regions of the curves into a better alignment with the conventional TTS data as shown in curve E' but at the expense of slope matching at the points of juxtaposition.

SIM tests conducted with inadequate temperature or time steps will result in master curves of shorter reach than those with adequate steps. The exaggerated examples investigated here would be easy to identify and rectify by substituting tests utilizing smaller temperature and/or longer time steps. More

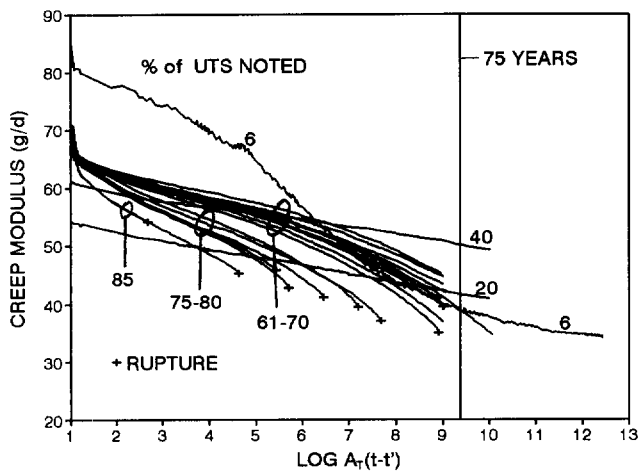


Figure 14. Creep modulus master curves as a function of stress level.

subtle inadequacies might go undetected, but would result in master curves that would err on the conservative side.

Conditions C, D, and F yield satisfactory SIM master curves. Condition D, as the most economical is recommended as a standard protocol for PET.

5.5 Effect of Stress Levels

To assess the effect of stress levels on the master creep modulus curves and the associated shift functions, over twenty-five creep tests were performed at stress levels between 6% and 85% of the 26°C UTS. Nine of the specimens were taken to rupture. These nine were among the ones tested at above 67% of UTS. Following the SIM procedure, the raw creep data was converted to master creep modulus curves, and the resulting family of curves is presented in Figure 14. Note that at the very lowest stress (6%) the beginning creep modulus values are higher than those at the higher stresses. Also, note that the modulus curve of 20% falls below the one at 40%. These are natural consequences of the trend in the secant modulus curve in Figure 3. The shift factors for those master curves are graphed against the step temperatures in Figure 15. The results presented in Figure 15 indicate that the shift factors for the low stress master curves are higher than those generated at higher stress levels. This may be understood in terms of the differences in the creep mechanisms operative at the different stress levels. Refined creep strain curves, computed from the master creep modulus curves of Figure 14 are presented in 16.

The several creep ruptures indicated in Figure 16 are associated with creep strain curves that display higher creep rates but otherwise appear as reasonable creep curves. The shift factors used to generate the curves leading to rupture are not distinguishable from those at lower stresses down to 61% of UTS, most of which do not lead to rupture (see Figure 15, Stress > 61%).

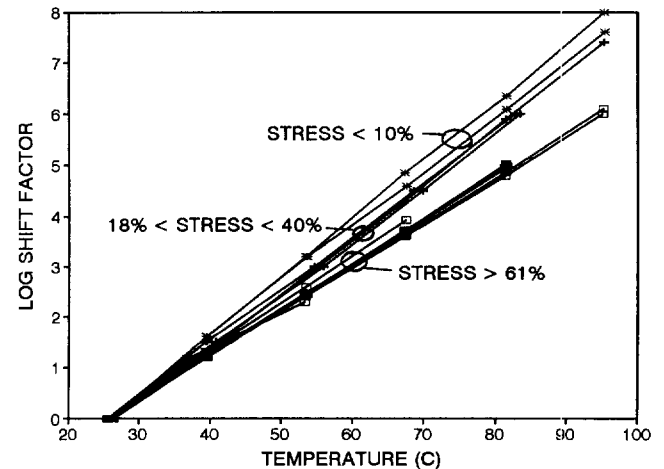


Figure 15. Shift factors vs. temperature for the master curves of Figure 14.

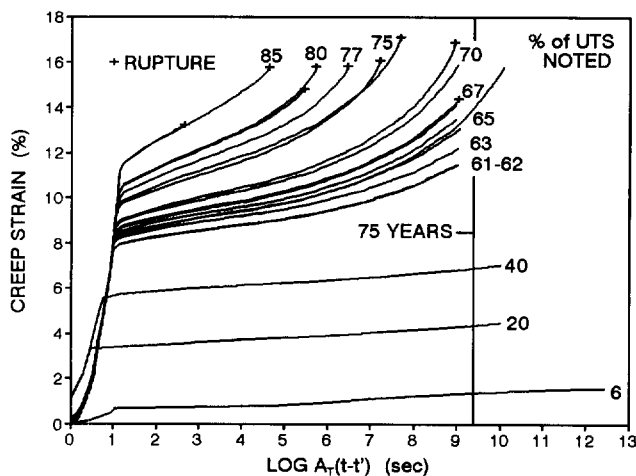


Figure 16. Creep strain vs log time curves computed from the master curves of Figure 14

The plot of creep rupture stress vs. log time to rupture is presented in Figure 17. Nine rupture points are indicated along with three run out points. Significantly, one data point goes well beyond the 75 year time line, so that the 75 year intercept is a conservative interpolation rather than an extrapolation. The 75 year intercept of the regression line is at 68% of the 26°C UTS. Table 3 provides a guide to the shifted rupture times of Figure 17.

Table 3. Logarithm of the shifted times at the reference temperature (26°C) vs the unshifted times at the exposure temperatures.

Shifted time Range Log $A_T(t-t')$	Maximum values (approximate)	
	Exposure Temperature, °C	Unshifted cumulative time, sec
0.0-4.0	26	1×10^4
4.0-5.3	40	2×10^4
5.3-6.7	54	3×10^4
6.7-8.0	68	4×10^4
8.0-9.3	82	5×10^4

6 CONCLUSIONS

- Utilization of SIM for TTS reduces the uncertainty of the shift factors used to construct master curves.
- Both the conventional and the stepped isothermal methods of time-temperature superposition can produce master curves that extend well beyond 100 years.
- Utilization of SIM reduces greatly the test time needed for characterizing long term creep properties over conventional TTS or extrapolation methods.
- The time and temperature steps of 10,000 sec and 14°C appear to be acceptable for SIM creep testing of PET yarn under most conditions.
- Inadequate temperature and or time steps result in master

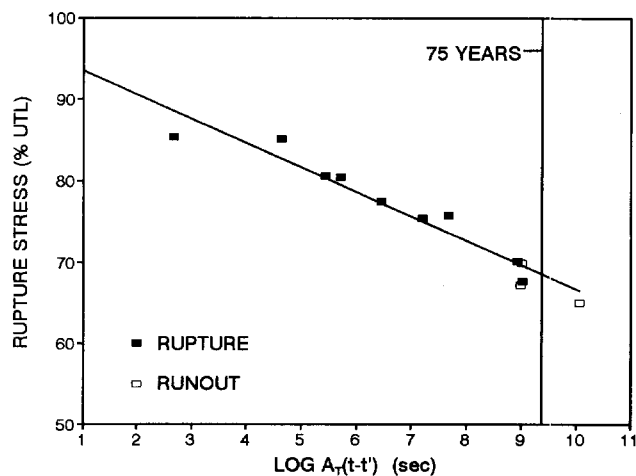


Figure 17. Creep rupture data and regression line for the polyester yarn.

curves with shorter reach than curves generated from tests with adequate steps, but such inadequacies will be conservative.

- The shift factors for creep display a linear direct dependence on temperature and an inverse dependence on stress, the latter may be caused by a difference in creep mechanism between low and high applied stress levels.
- Since creep rupture is merely an event that takes place at the end of a creep strain curve, the shift factors used to generate the creep strain vs. shifted time curves are the factors that determine the shifted time of the rupture event.

ACKNOWLEDGMENTS

The authors are indebted to Shawn L. Arnett of TRI/Environmental for conducting the experimental program. Funding from T.C. Mirafi, Inc. and Texas Research International, Inc. for research leading to the discovery of the SIM as well as the characterization of the 3 ply PET yarn reported herein is gratefully acknowledged.

REFERENCES

- Ferry, J.D. (1980) *Viscoelastic Properties of Polymers*, 3rd Edition, John Wiley and Sons, New York, NY, USA.
- Heuvel, C.J.M. v.d., Heuvel, H.M., Faassen, W.A., Veurink, J., and Lucas, L.J., (1993), "Molecular Changes of PET Yarns during Stretching Measured with Rheo-Optical Infrared Spectroscopy and Other Techniques," *J. Appl. Polymer Sci.*, Vol. 49, pp. 925-934.
- Murayama, T., Dumbleton, J.H., and Williams, M.L., (1968), "Viscoelasticity of Oriented Polyethylene Terephthalate," *J. Appl. Polymer Sci.*, Vol. 6, pp. 787-793.
- Thornton, J.S., Allen, S.R., and Thomas R.W., (1997), "Approaches for the Prediction of Long Term Viscoelastic Properties of Geo Synthetics from Short Term Tests," *Geosynthetics '97*, IFAI, Vol. 1, Long Beach, CA, USA, pp 277-291.

Modeling and Extrapolation of Creep Behavior of Geosynthetics

Te-Yang Soong

Research Engineer, Geosynthetic Research Institute, Drexel University, Philadelphia, Pennsylvania, USA

Robert M. Koerner

Professor and Director, Geosynthetic Research Institute, Drexel University, Philadelphia, Pennsylvania, USA

ABSTRACT: The creep behavior of geosynthetic materials can be described by a rheologic model consisting of a finite number of Kelvin units connected in series, i.e., the so-called Kelvin-chain model. With properly selected spring moduli and dashpot viscosities, the combined effect of all Kelvin units in the model can be used to describe the results of experimental creep data. Once such a model is established, it can then be used to extrapolate the creep behavior of the tested material beyond the laboratory measured time frame. This paper presents a systematic procedure for obtaining the optimum model based on relatively short-term creep data. The long-term predicting capability of the model is then justified by supplemental experimental data.

KEYWORDS: Creep, Modeling, Geotextile, Geogrid, Geomembrane, Geosynthetic Clay liner, Geocomposite Edge Drain

1 INTRODUCTION

Whenever stresses are imposed on a viscoelastic material like geosynthetics (via tension, compression, shear, torsion, bending, etc.), they must somehow be internally sustained by the material's molecular structure. If the stresses remain constant over a sufficiently long period of time, the molecular structure will attempt to accommodate them via some type of deformation, e.g., the creep phenomenon. Examples of applications where creep is of concern are the following:

- Tensile creep of geotextiles in mechanically stabilized earth structures,
- Tensile creep of geogrids in mechanically stabilized earth structures,
- Compressive creep of geonets and drainage geocomposites in the liner systems of landfills,
- Out-of-plane deformation of geomembranes in landfill and waste pile covers due to differential settlement and up-lifting gases,
- Internal creep shear of geosynthetic clay liners on steep side slopes
- Compressive deformation (creep) of geopipes in various situations.

In actual designs, creep is generally included via reducing the allowable stress by a proper creep reduction factor, Koerner (1998). In an ideal situation, the creep reduction factors are determined experimentally, e.g., conducting 10,000-hour (or longer) creep test at several stress levels.

Unfortunately, creep tests are by their nature time-consuming and thus expensive. Furthermore, accurate creep tests are difficult to perform owing to the difficulty in maintaining the desired environment over a long period of time. In this study, a rheologic model which provides long-term prediction capability is presented. It is hoped that via careful interpretation and extrapolation of short-term creep data, accurate long-term creep behavior can be predicted.

2 THE KELVIN-CHAIN MODEL

It has been shown that the creep behavior of a wide range of materials can be described by a Kelvin-chain model which consists of a finite number of Kelvin units in series, Roscoe (1950). In addition, a spring can be added to the original Kelvin-chain model. This provides to the model the capability of simulating the initial instantaneous (elastic) strain which is typically seen in creep measurements. Figure 1 shows the modified Kelvin-chain model used in this study.

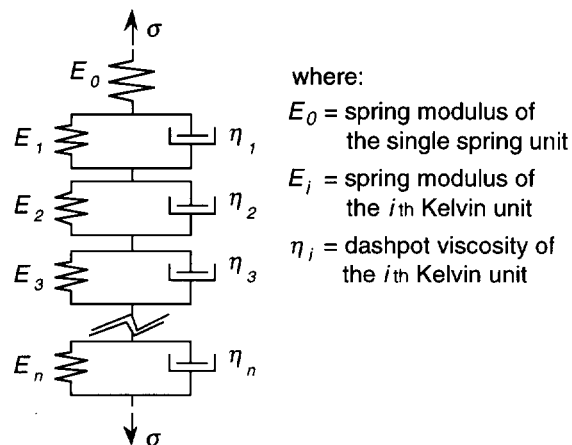


Figure 1. The Kelvin-chain model

A Kelvin unit consists of a spring and a dashpot in parallel. In the Kelvin-chain model, each Kelvin unit is identified by the letter "i" and characterized by a retardation time, τ_i , where $\tau_i = \eta_i / E_i$. Experiences show that in an ideal Kelvin-chain model, the spring modulus in each Kelvin unit is generally inversely proportional to its corresponding dashpot viscosity. In other words, Kelvin units consisting of high-modulus springs possess dashpots with low viscosities. The relative degrees vary. When such

a model is subjected to an external stress, σ , as seen in Figure 1, an instantaneous deformation is created in the single spring. Note that this deformation stays constant regardless of the time scale as long as the applied stress remains. Subsequently, the Kelvin units with higher spring moduli and lower dashpot viscosities will be deformed. Note that such deformations will also be retarded more rapidly. Succeedingly, the units with lower spring moduli will respond to the external stress owing to the higher resistance from the dashpots. However, continuous deformations will be observed in these units over a longer period of time, until their corresponding retardation times are reached.

Figure 2 illustrates the above concept by plotting a set of creep data along with the calculated curve corresponding to a Kelvin-chain model consists of four Kelvin units and a single spring. It is seen that the calculated curve (a superposition of five individual curves) accurately modeled the experimental data. The individual behavior of each component in the model is also shown in the figure where the concept of "retardation time" is clearly demonstrated.

3 THE MODELING PROCEDURE

To utilize a Kelvin-chain model, the creep behavior is viewed as a so-called strain function:

$$\epsilon(t) = \epsilon_0 + \sum_{i=1}^n \frac{1}{E_i} (1 - e^{-t/\tau_i}) \quad (1)$$

where: $\epsilon_0 = 1/E_0 =$ the elastic strain (i.e., strain induced immediately after the stress is applied) caused by a unit stress (i.e., $\sigma = 1$). Note that the end of the elastic deformation portion of the experimental data, i.e., ϵ_0 , is defined herein as the point of which the second derivative first changes its sign, generally from negative to positive. In Equation 1, the retardation times, τ_i 's, are values which can be arbitrarily chosen providing some restrictions are satisfied, Bazant (1988), Bazant and Prasanna (1989). However, any two adjacent Kelvin units having a relationship of $\Delta(\log\tau_i) = 1$ generally gives sufficiently smooth creep curves; Bazant and Xi (1995). That is to say, if the smallest retardation time is chosen as 10^{-3} hour, the subsequent retardation times will generally be selected as 10^{-2} hr., 10^{-1} hr., 10^0 hr., 10^1 hr., etc.

Furthermore, an "N"-unit Kelvin-chain model can generally simulate creep data of "N" orders of magnitude on the time scale. Note, however, if extrapolation of the experimental data is desirable, more Kelvin units are necessary. For example, if a extrapolation out to 10^4 hours is desirable using a 1000-hour creep data (i.e., one-order extrapolation), one additional Kelvin unit with retardation time of 10^4 is necessary.

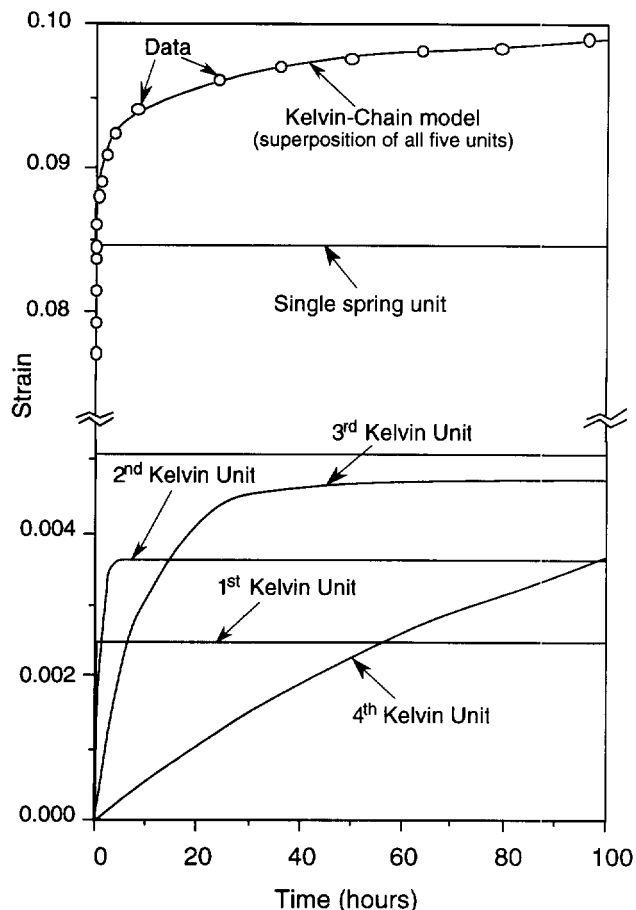


Figure 2. Creep data simulated by a Kelvin-chain model consisting of four Kelvin units and one single spring.

As to the selection of E_i 's, it is determined by optimum fitting of the creep data under the constraints of the pre-selected retardation times.

It is clear that a regression analysis (optimum fitting) for determining six or more unknowns (numbers of E_i 's, in this case) can be extremely time consuming. A procedure which reduces the numbers of the independent variables to only two, regardless the actual number of E_i 's, is recommended herein.

The following expression is proposed to serve the aforementioned purposes [see Bazant and Xi (1995) for detailed mathematical derivations]:

$$\frac{1}{E_i} = 1.151(a)(3\tau_i)^3 \left[\frac{-2n^2(3\tau_i)^{2n-3}(n-1-(3\tau_i)^n)}{(1+(3\tau_i)^n)^3} + \frac{n(n-2)(3\tau_i)^{n-3}(n-1-(3\tau_i)^n) - n^2(3\tau_i)^{2n-3}}{(1+(3\tau_i)^n)^2} \right] \quad (2)$$

In Equation 2, “a” and “n” are the new targeted unknowns (instead of E_i 's) associated with the modeled creep data. Note that the new fitting involves only two variables and is obviously much simpler.

By varying the two independent variables “a” and “n” in Equation 2, different combinations of E_i 's with respect to the pre-selected retardation times, τ_i 's, can be obtained. This allows a comparison of each calculated result of Equation 1 to the actual experimental data. The calculated result is then optimized using the least-squares approximation (weighting by “time” is recommended) and iteration of this process will eventually converge on the actual experimental data. The resulting optimum model can then be used to predict experimental creep behavior beyond the actual measured data.

4 EXAMPLES

Six sets of very different geosynthetic materials creep data were used to verify both the simulating and the long-term predicting capabilities of the proposed Kelvin-chain model. They are the following geosynthetic materials:

- (a) 1500-hr tensile creep of a nonwoven needle-punched PP geotextile at 50% of its wide-width tensile strength at a temperature of 22°C [Allen et al (1982)],
- (b) 10,000-hr tensile creep of a PET geogrid at 70% of its short-term tensile strength at a temperature of 23°C (data courtesy of Strata Systems, Inc.),
- (c) 1000-hr confined tensile creep of a stiff, unitized HDPE geogrid at 60% of its ultimate tensile strength under a normal stress of 28 kPa at approximately 23°C [Wilson-Fahmy et al (1995)],
- (d) 20,000-hr biaxial tensile creep of a HDPE geomembrane under a constant stress ($\approx 60\%$ of its ultimate strength) at approximately 23°C [Duvall (1993)],
- (e) 1,000-hr internal shear creep of a geosynthetic clay liner (GCL) at 40% of its short-term shear strength at approximately 23°C,
- (f) 1,000-hr compressive creep of a edge-drain geocomposite at 45% of its short-term compressive strength at approximately 23°C (data courtesy of Monsanto Company).

The results are shown in Figures 3 to 8 corresponding to each of the above tests, respectively. Note that the results shown in Figure 4 are plotted on a logarithmic scale to give a different perspective. Seen in each of the figures are (1) initial portion of the data (one order of magnitude shorter in time than the entire data), as solid circles, for establishing the Kelvin-chain model; (2) the optimum Kelvin-chain model calculated creep behavior, as solid curves; (3) one order of magnitude extrapolation using the established model, as dashed curves and (4) the rest of the creep data, as

open circles, for verifying the predicting capability of the model.

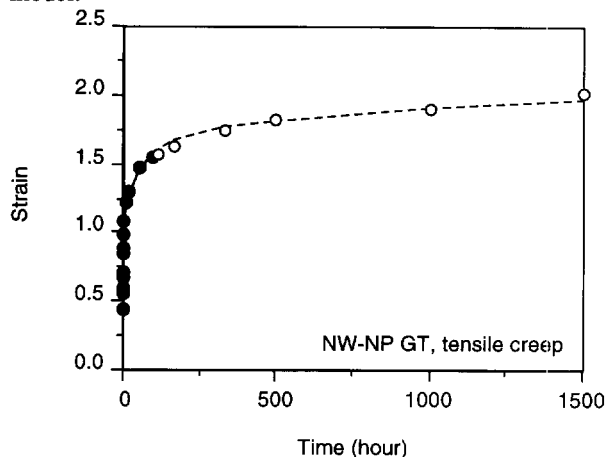


Figure 3. Experimental and modeled data of material (a)

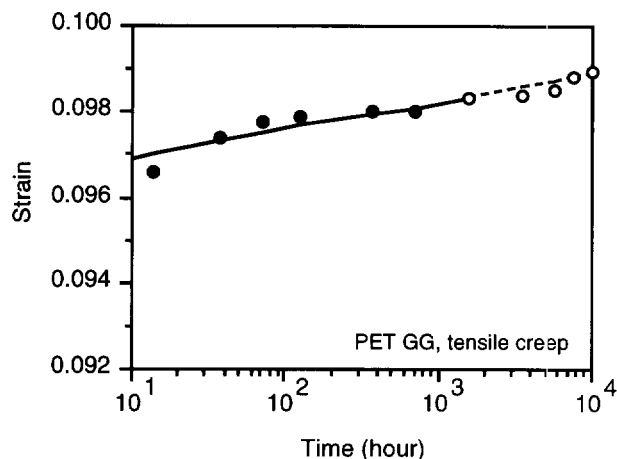


Figure 4. Experimental and modeled data of material (b)

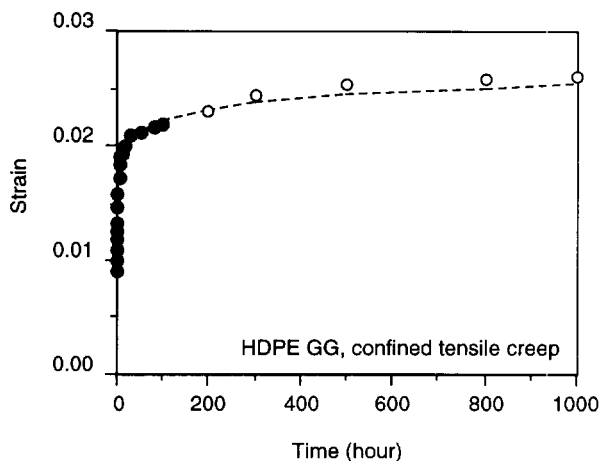


Figure 5. Experimental and modeled data of material (c)

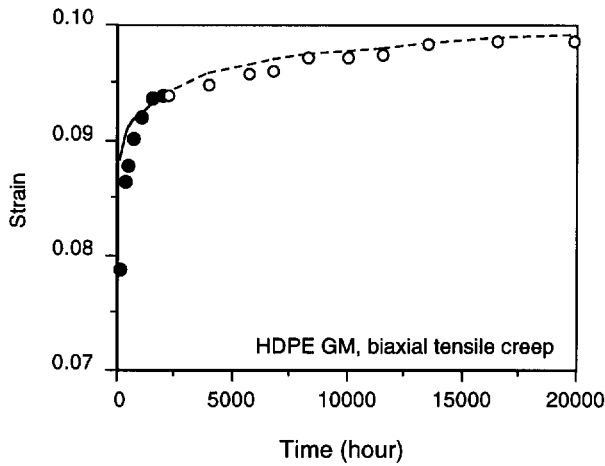


Figure 6. Experimental and modeled data of material (d)

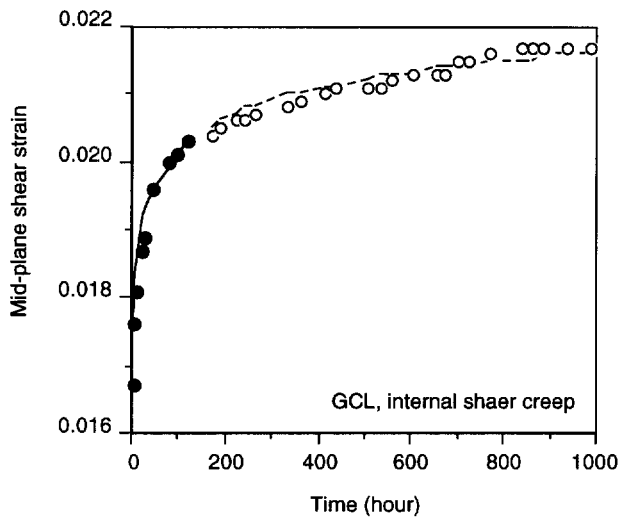


Figure 7. Experimental and modeled data of material (e)

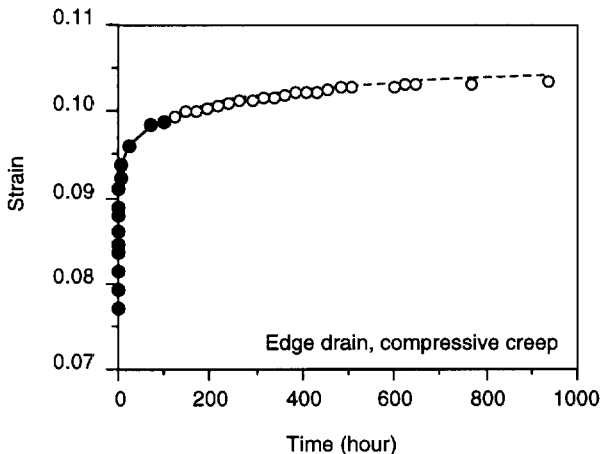


Figure 8. Experimental and modeled data of material (f)

5 SUMMARY AND CONCLUSIONS

Geosynthetics, being viscoelastic materials, must be evaluated for their creep sensitivity under a variety of constant stress situations. Laboratory tests can be performed for relatively long time periods, yet extrapolation to site specific lifetimes is usually necessary and the technique used is obviously critical. The Kelvin-chain model presented in this paper, and its application to a wide variety of geosynthetic materials, is shown to result in an accurate prediction of the data and is recommended for general use. This model is shown to be viable for at least one order of magnitude based on the results presented herein. Analytically it is possible to extrapolate beyond one order of magnitude, but substantiate data is sparse and further corroboration is required in this regard.

6 ACKNOWLEDGMENT

The funding for the preparation of this paper was provided by the Geosynthetic Institute's consortium of member organizations and the U.S. EPA. Financial support via David A. Carson under contract CR-821448 is sincerely appreciated.

7 REFERENCES

- Allen, T., Vinson, T.S. and Bell, J.R. (1982) "Tensile Strength and Creep Behavior of Geotextiles in Cold Regions Applications", *2nd Int. Conf. on Geotextiles*, Las Vegas, NV, USA, Vol. 3, pp. 775-780.
- Bazant, Z.P. ed. (1988) *Mathematical Modeling of Creep and Shrinkage of Concrete*, John Wiley & Sons, Inc., New York, NY, USA
- Bazant, Z.P. and Prasannan, S. (1989) "Solidification Theory of Concrete Creep II: Verification and Application", *J. Engrg. Mech.*, ASCE, Vol. 115, No. 5, pp. 1691-1703.
- Bazant, Z.P. and Xi, Y. (1995) "Continuous Retardation Spectrum for Solidification Theory of Concrete Creep", *J. Engrg. Mech.*, ASCE, Vol. 121, No. 2, pp. 281-288.
- Duvall, D.E. (1993) "Creep and Stress Rupture Testing of a Polyethylene Geomembrane Under Equal Biaxial Tensile Stress", *Geosynthetics '93*, IFAI, Vancouver, BC, Canada, Vol. 2, pp. 817-830.
- Koerner, R. M. (1998) *Designing with Geosynthetics*, 4th Ed., Prentice Hill Book Co., Englewood Cliffs, NJ, 792 pgs.
- Roscoe, R. (1950) "Mechanical Models for the Representation of Viscoelastic Properties", *British J. of Appl. Physics*, Vol. 1, pp. 171-173.
- Wilson-Fahmy, R.F., Koerner, R.M. and Harpur, W.A. (1995) "Long-Term Pullout Behavior of Polymeric Geogrids", *J. Geotech. Engrg.*, ASCE, Vol. 121, No. 10, pp. 723-728.

Slow Strain Rate Modulus Assessment Via Stress Relaxation Experiments

Te-Yang Soong

Research Engineer, Geosynthetic Research Institute, Drexel University, Philadelphia, Pennsylvania, USA

Arthur E. Lord, Jr.

Professor, Department of Physics & Atmospheric Science, Drexel University, Philadelphia, Pennsylvania, USA

ABSTRACT: Geosynthetics are usually deformed very slowly in actual applications. Conversely, most mechanical properties (e.g., modulus) are determined in the laboratory under relatively fast strain rates. The use of such experimental values in engineering design is felt to give an inaccurate assessment of actual behavior. This paper presents a procedure to simulate laboratory generated stress relaxation test results by the Maxwell-Weichert rheologic model. Once such a model is established and calibrated, it can be used to determine the more realistic, “design-oriented”, modulus of the tested material. In this paper, the 0.3% secant modulus of a 1.5 mm HDPE geomembrane tested at various strain rates was successfully predicted using the Maxwell-Weichert model. It is felt that the same approach can be applied to other geosynthetic materials for determining realistic moduli values for use in engineering design.

KEYWORDS: Modeling, Geomembranes, Modulus, Stress relaxation

1 INTRODUCTION

Geosynthetics are usually deformed very slowly (i.e., on the order of weeks, months or years) in actual applications. Conversely, most mechanical properties (e.g., modulus) are experimentally determined in the laboratory under relatively fast strain rates (i.e., on the order of seconds, minutes or hours). Since it is well known that the mechanical properties of viscoelastic materials like geosynthetics are strongly strain-rate dependent, the use of such experimental values in actual engineering design is a concern in that changing in the polymer structure, e.g., stress relaxation, cannot occur as it likely does in the field.

In this paper, a Maxwell-Weichert rheologic model established using laboratory generated stress relaxation test results at fast strain rates, is presented. Once such a model is established and calibrated, it can be used to calculate values of modulus at slow strain rates. It is hoped that via the above procedure, more suitable initial moduli values for the use of engineering design can be determined.

2 BACKGROUND

The strong dependence of mechanical properties on how fast the material is deformed (time scale) is a result of the viscoelastic nature of geosynthetics. Two well-known examples of such dependence are the stress relaxation behavior and the strain-rate dependent modulus. Both phenomena are illustrated graphically in Figure 1. Conceptually, two replicate specimens are deformed to a specific strain level, ϵ_0 , under two different strain rates, i.e., $\dot{\epsilon}_1$ and $\dot{\epsilon}_2$. This strain level is then held constant for both cases and the stresses are monitored over time. Eventually, after considerable time, the curves come to the same equilibrium residual stress level. It is seen, in the left-hand

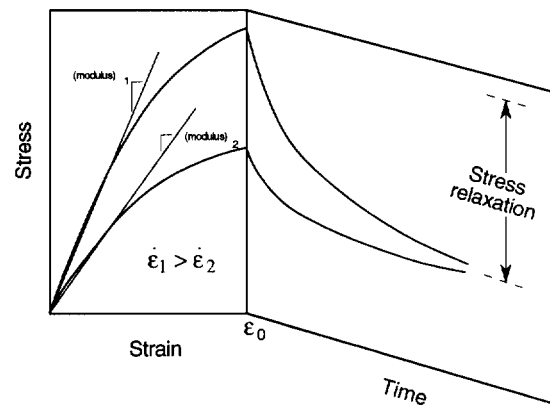


Figure 1. Viscoelastic nature of geosynthetics illustrated by the strain-rate dependent secant modulus and the stress relaxation behavior.

portion of the curves, that the modulus (in this case, a secant modulus) of the tested material is proportional to the strain rate. Regarding the right-hand portion of the curves, the trend of decreasing stresses with time demonstrates the concept of stress relaxation.

It is reasonable to assume that the above two phenomena are inter-related since both of them are results of the unique viscoelastic nature of the tested material. It is also reasonable to assume that using the result of one experiment (e.g., a stress relaxation test) one should be able to predict the result of a related test (e.g., the strain-rate dependent modulus). The objective of this study is to develop the above concepts.

3 THE MAXWELL-WEICHERT MODEL

Figure 2 shows the Maxwell-Weichert rheologic model used in this study, Aklonis et al (1972). A typical model consists of “N” Maxwell units, which are springs and dashpots in series, placed in a parallel combination with a single spring at the end. The springs represent the elastic properties (E is the elastic modulus) and the dashpots represent the viscous properties (η is the dashpot viscosity) of the modeled material. In this study, the units become less strong and more viscous as one moves to the right in the parallel combination. Each Maxwell unit is characterized by a spring modulus, E_i , and a corresponding retardation time, τ_i , where $\tau_i = \eta_i/E_i$. The final spring, with an elastic modulus of E_R , represents the totally relaxed or residual modulus value.

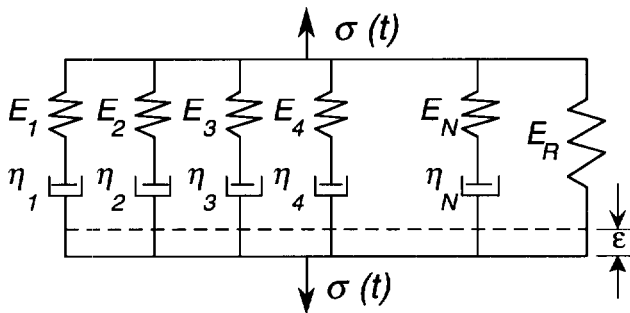


Figure 2. A Maxwell-Weichert model subjected to a constant strain.

In a typical stress relaxation test, it takes an initial stress to deform a Maxwell-Weichert model to reach the desired strain because of the resistance of all Maxwell units has to be overcome. In stress relaxation tests, this is the maximum stress. Once the desired strain is reached, the dashpots start to flow and therefore release the stresses in the springs. As a result, the stress required to maintain a constant strain decreases with time. Since the units in a Maxwell-Weichert model consist of dashpots with viscosities over a wide range, i.e., some dashpots can be easily stretched and others are more difficult, they can be used to simulate stress relaxation of geosynthetics at different stages. Ultimately, when the stresses in all Maxwell units are fully dissipated, the residual stress is modeled by the final spring.

When a Maxwell-Weichert model is subjected to a constant strain, as in a stress relaxation test, the following expression can be used to describe the stress/strain relationship in each of the Maxwell units:

$$\frac{d\varepsilon_i}{dt} = \frac{d\varepsilon}{dt} = \frac{1}{E_i} \frac{d\sigma_i}{dt} + \frac{\sigma_i}{\eta_i} = 0 \quad (1)$$

where ε_i = strain in unit “i”, ε = the constant strain applied and σ_i = stress in unit “i”.

The solution of Equation 1, which represents the stress in unit “i” at any time “t”, is as follows:

$$\sigma_i(t) = \sigma_{i0} e^{-t/\tau_i} \quad (2)$$

where σ_{i0} = the initial stress in unit “i”.

The total stress at any time “t” in the entire Maxwell-Weichert model, is the sum of the stresses in all of the elements, i.e.,

$$\sigma(t) = \sigma_{10} e^{-t/\tau_1} + \sigma_{20} e^{-t/\tau_2} + \dots + \sigma_{N0} e^{-t/\tau_N} + \sigma_R \quad (3)$$

where σ_R = the stress in the final single spring.

Alternatively, the stress relaxation process can be described by a time-dependent relaxation modulus, $E(t)$, where

$$E(t) = \frac{\sigma(t)}{\varepsilon} = \sum_{i=1}^N \left(\frac{\sigma_{i0}}{\varepsilon} e^{-t/\tau_i} \right) + \frac{\sigma_R}{\varepsilon} \quad (4)$$

or

$$E(t) = \sum_{i=1}^N (E_i e^{-t/\tau_i}) + E_R \quad (5)$$

Equation 5 can then be used to simulate the stress relaxation test results. Figure 3 illustrates the modeling concept by plotting a set of stress relaxation data along with the calculated curve corresponding to a Maxwell-Weichert model. This example consists of four Maxwell units and a single spring. It is seen that the calculated curve (a superposition of five underlying individual curves) accurately modeled the laboratory data. The individual behavior of each unit in the model is also shown in the figure.

In Equation 5, the retardation times, τ_i 's, are values which can be arbitrarily chosen. If we choose adjacent Maxwell units to have a relationship of $\Delta(\log\tau_i) = 1$, it generally gives satisfactory simulation. That is to say, if the smallest retardation time is chosen as 10^{-3} hour, the subsequent retardation times will generally be selected as 10^{-2} hr., 10^{-1} hr., 1 hr., 10^1 hr., etc. As to the selection of E_i 's, they are determined by optimum fitting of the stress relaxation data under the constraints of the pre-selected retardation times.

4 MAXWELL-WEICHERT MODELING OF HDPE GEOMEMBRANES USED IN THIS STUDY

Large-scale stress relaxation test results on a commercially available 1.5 mm thick HDPE geomembrane were used to illustrate the use of Maxwell-Weichert model. See Soong, et al (1994) for a detailed description of the laboratory test setup and conditions. The tests were conducted at five

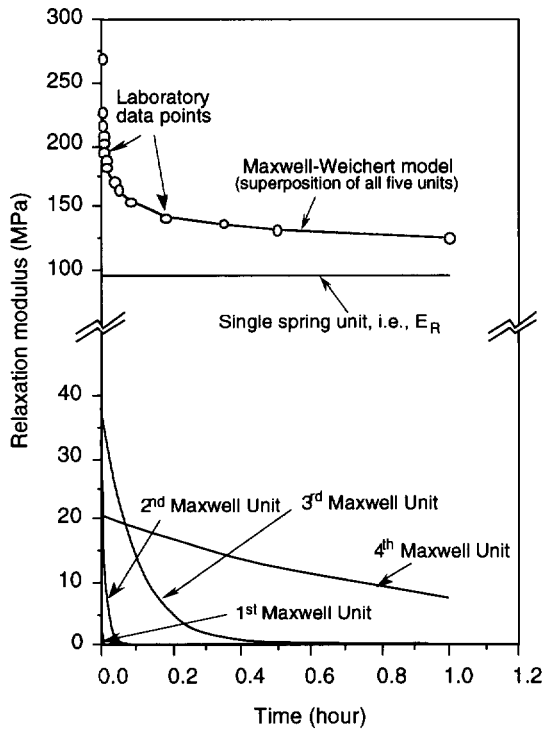


Figure 3. Stress relaxation data simulated by a Maxwell-Weichert model consisting of four Maxwell units and one single spring.

different temperatures under a constant tensile strain of 3%. Seven Maxwell units with retardation times varying from 10^{-4} to 10^2 hours and one additional spring were used in each of the five models for five different temperatures. The values of E_i 's in all of the models were determined by applying a least-squares regression procedure, under the restraints of the pre-selected retardation times, until the calculated behavior converged to the laboratory results. The laboratory data along with the calculated relaxation behavior are shown in Figure 4 by plotting the relaxation modulus against time on a log-log scale. There is excellent agreement between the laboratory and the calculated results.

Once a Maxwell-Weichert model is established, it can be used to calculate the modulus of the modeled material at different values of strain rate. The following section presents the detailed procedure.

5 CALCULATING THE STRESS UNDER VARIOUS STRAIN RATES

When the modeled material, e.g., a geomembrane, is deformed under a constant strain rate "C", the following expression can be used to describe the stress/strain relationship in each of the Maxwell unit:

$$\frac{d\epsilon_i}{dt} = \frac{d\epsilon}{dt} = \frac{1}{E_i} \frac{d\sigma_i}{dt} + \frac{\sigma_i}{\eta_i} = C \quad (6)$$

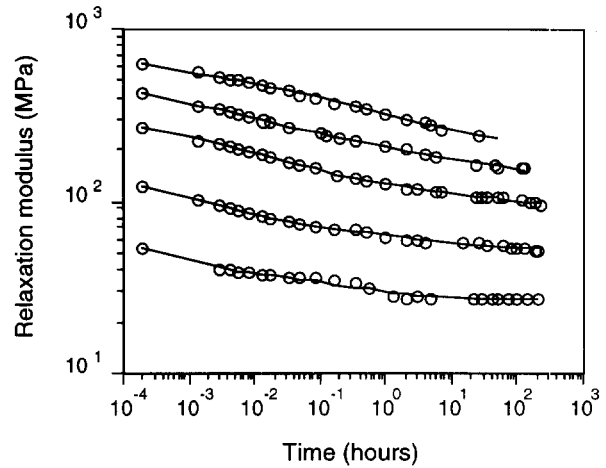


Figure 4. Laboratory generated (open circles) and calculated stress relaxation behavior (solid lines) of a 1.5 mm thick HDPE geomembrane at various temperatures.

Equation 6 can be solved as:

$$\sigma_i(t) = C\tau_i E_i (1 - e^{-t/\tau_i}) \quad (7)$$

Consequently, the expression for the entire model can be written as:

$$\sigma(t) = C \left[\sum_{i=1}^N \tau_i E_i \left(1 - e^{-\frac{t}{\tau_i}} \right) \right] + C(E_R)t \quad (8)$$

Since the experimental data was developed at 3% strain, we must modify Equation 8 if it is to work for general values of strain (e.g., 0.3% strain).

Popelar, et al (1990) presented an empirical relationship to incorporate the strain dependence in the establishing of viscoelastic models for HDPE pipes. The relationship was interpolated and extended for this study and the following expression, a modification of Equation 8, results:

$$\sigma(t) = C \left[\sum_{i=1}^N \tau_i \left(\frac{E_i}{a + b(Ct)} \right) \left(1 - e^{-\frac{t}{\tau_i}} \right) \right] + \left(\frac{E_R}{a + b(Ct)} \right) Ct \quad (9)$$

where $Ct = \epsilon =$ strain at time "t".

Table 1 lists values of the constants "a" and "b" corresponding to various strain levels used for conducting the stress relaxation tests. Note that when the desired strain level is equal to that used in the stress relaxation test, no modification is necessary.

Table 1. Constants in Eq. 9 as a function of strain level

Strain level used in the stress relaxation test, ϵ_p	Constants ¹ in Equation 10	
	a	b
1.0%	0.70	30.5
2.0%	0.53	23.3
3.0%	0.43 ²	18.9 ²
5.0%	0.31	13.7
7.5%	0.23	10.2
10.0%	0.19	8.1

1. Values are for modulus in units of MPa.

2. Appropriate constants for this study.

6 JUSTIFICATION OF CALCULATED INITIAL MODULUS VALUES

The 0.3% secant modulus of the tested HDPE geomembrane can be determined as follows:

1. A strain rate, i.e., a value of "C", is assumed.
2. The relation " $0.3\% = Ct$ " gives the value of "t".
3. The time "t" is inserted into Equation 9 to obtain the corresponding stress, $\sigma(t)$, at 0.3% strain.
4. The relation " $\sigma(t)/0.003$ " gives the 0.3% secant modulus of the modeled material.

The above procedure was applied to five separate Maxwell-Weichert models corresponding to five different temperatures over a range of strain rates from 0.0001% to 100% per minute. The results are shown in Figure 5 by plotting the 0.3% secant modulus against strain rate on a log-log scale. The experimental values of some supplementary tensile tests conducted at 30°C under various strain rates are also shown, in open circles, to exam the validity of the aforementioned prediction procedure. As seen in the figure, the agreement between the experimental data and the calculated values is quite satisfactory.

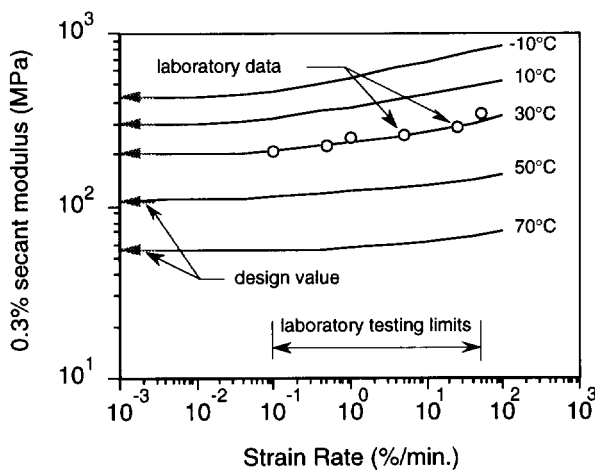


Figure 5. Strain-rate dependent 0.3% secant moduli of the 1.5 mm HDPE geomembrane used in this study.

Also seen in Figure 5 is that at a given temperature, the values of 0.3% secant modulus of the tested HDPE geomembrane remain practically unchanged when strain rates are slower than 0.01% per minute. Such values are considered more suitable in engineering design than those obtained routinely in the laboratory. Such recommended design moduli of the tested HDPE geomembrane are collected and re-plotted against temperature in Figure 6. It is felt that this type of data, shown here for modulus, is the type of data that should be used in design to simulate field conditions.

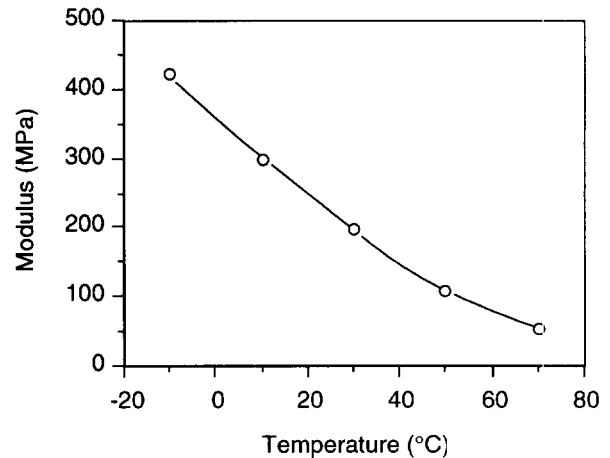


Figure 6. Design modulus of the HDPE geomembrane used in this study (corresponding to a very slow strain rate, i.e., $\leq 10^{-2}\%$ /min simulating a situation of stress relaxation).

8 CONCLUSIONS

This paper presents a recommended procedure to simulate stress relaxation test results by the Maxwell-Weichert rheologic model. Once such models are established and calibrated, they can be used to determine realistic, "design-oriented", moduli of the modeled material and thereby assess the stress relaxation phenomenon. To verify the procedure, the 0.3% secant moduli of a 1.5 mm HDPE geomembrane at various strain rates were successfully predicted.

9 ACKNOWLEDGMENT

The funding for the preparation of this paper was provided by the Geosynthetic Institute's consortium of member organizations and the U.S. EPA. Financial support via David A. Carson under contract CR-821448 is sincerely appreciated.

10 REFERENCES

- Aklonis, J.J., Macknight, W.J. and Shen, M. (1972) *Introduction of Polymer Viscoelasticity*, Wiley-Interscience, New York, NY, USA.
- Popelar, C.F., Popelar, C.H. and Kenner, V.H. (1990), "Viscoelastic Material Characterization and Modeling for Polyethylene", *Polymer Engineering and Science*, Vol. 30, No. 10, pp. 577-586.
- Soong, T.-Y., Lord, A.E., Jr. and Koerner, R.M. (1994) "Stress Relaxation Behavior of HDPE Geomembranes", *5th Intl. Conference on Geotextiles, Geomembranes and Related Products*, Singapore, Vol. 3, pp. 1121-1124.

Long term behavior characterization of soft composite under biaxial loading

P. MAILLER

Geosynthetic tests manager, Institut Textile de France D.R. LYON, av, Guy de Collongue, BP 60, 69132 Ecully cedex

M. SOTTON

General manager, Institut Textile de France D.R. LYON, av, Guy de Collongue, BP 60, 69132 Ecully cedex

ABSTRACTS: Amongst the many composite materials, soft composites containing a thermo-plastic matrix with textile reinforcement are used in civil engineering and building construction in the form of tensile membranes.

To justify permanent use of these structures, it is necessary to know their stiffness and failure behavior, and to predict their long term behavior under combined loading. So we must develop experimental characterization techniques and rheological models taking into account the specific properties of these materials and their long term behavior.

The material studied is a polyvinylchloride reinforced with high tenacity polyester plain weave fabric and is used for tensile or inflatable structures.

KEYWORDS: Durability, Soft composite, Biaxial loading, Creep, Rheological behavior

1 INTRODUCTION

The aging of reinforced PVC fabrics is caused mainly by superficial cracks of the matrix. The exposed fibers are then attacked by U.V.. The main characteristics affected are the tensile strength and the tear strength. These characteristics can fall by up to 60%. So it is necessary to characterize, to predict and to model this aging to take it into account in the time of building conception.

This paper presents a theorico experimental method for the characterization of long term behavior of soft composites. The study is made on a coated fabric but the method can easily be apply to every kind of soft composites

As it is shown on figure 1 this characterization can be done by accelerated tests at the scale of the constituents (fiber, matrix) or at the scale of the textile architecture. The prediction must be validated by real time tests.

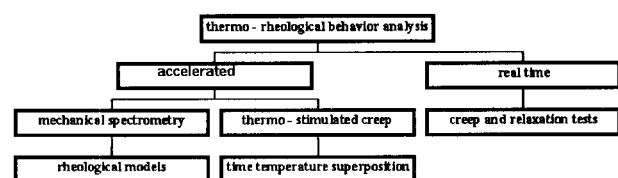


Figure 1 : Study organigram

2 MATERIAL STUDIED

The material studied is a high tenacity plain weave polyester (ref. ENKA 174 S) coated with PVC. The weight of the coated fabric is 800 g/m² for a thickness of 0.6 mm and a fiber content of 24%. The PVC has no mechanical properties, is only used to protect the polyester from U.V. attack. The material is orthotropic on the scale of the textile architecture and behaves as a membrane.

3 VISCOELASTIC MEASUREMENT

3.1 Elaboration of rheological model

Simple viscoelastic tests were performed at different frequencies with a DMTA (Dynamic Mechanical Thermal Analysis).. To choose a well suited model, we draw with the experimental results Cole-Cole diagrams (Cole et al. 1941) and we compare those diagrams with model ones. The results are shown on figure 2. The complex modulus E^* can be written

$$E^* = E' + iE'' \quad (1)$$

Cole-Cole diagrams are made by plotting E'' modulus as a function of E' modulus.

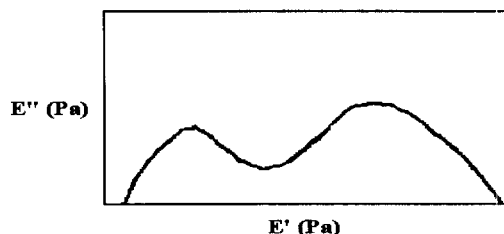


Figure 2 : Evolution of E' and tangent δ with temperature

Our experimental results can be approached by a Zener biparabolic model (Huet et al. 1984). This model can be done either with an assembly in series or/and parallel of springs and dashpots or with an assembly in series or/and parallel of fractional elements. The basic fractional is a model of one mechanism (spring pot) which constitutive law satisfies : (Koller 1984)

$$K.D_t^\alpha . X(t) = F(t) \quad (2)$$

where α is the order of the fractional derivation ($0 \leq \alpha \leq 1$). After several mathematical operations we obtain the equation of the model. (equation 3 and figure 3)

$$E^*(i\omega) = E_0 + \frac{E_\infty - E_0}{1 + (i\omega\tau)^{-k} + \delta(i\omega\tau)^{-h}} \quad (3)$$

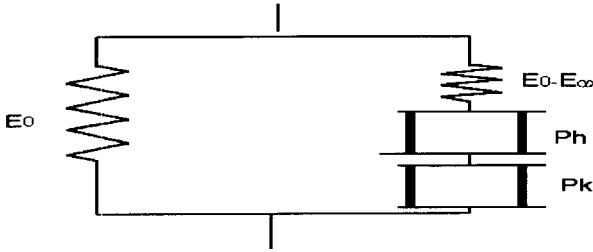


Figure 3 : Limited biparabolic Zener

The values of the parameters h, k, E_0 are determined by enlarging the external parts of Cole-Cole diagrams. In order to determinate the value of E_∞ , we divide every part of Cole-Cole diagram in two zones. The first one corresponding to high frequencies is approximated to an arc of a circle whose center is under the real axis, the second corresponding to low frequencies is approximated to an arc of a circle whose center is under the real axis and cuts it in E_∞ .

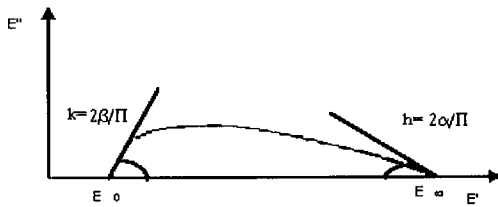


Figure 4 : Determination of the different parameters

To determinate the value of δ , we give arbitrary values of the term $\omega\tau$ and we adjust the value of δ until the experimental and calculated values are matched. (figure 5)

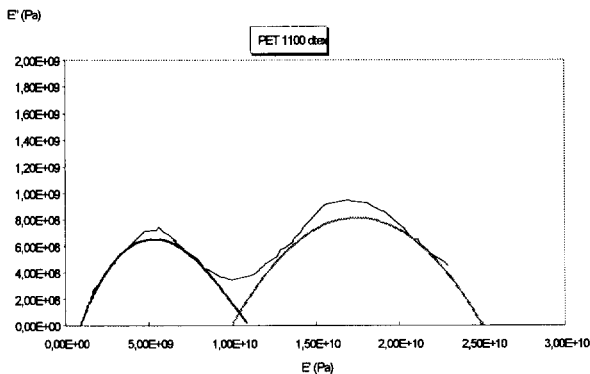


Figure 5 : Experimental/theoretical Cole-Cole

Table 1 gives the values of the parameters of the model for the polyester fibers.

zone 1					zone 2				
E0 GPa	E∞ GPa	h	k	δ	E0 GPa	E∞ GPa	h	k	δ
2.9	11	0.22	0.13	2.5	9.9	25	0.14	0.14	1

From equation (3) of Zener model it is possible to find temporal expressions (relaxation modulus $E(t)$ and creep modulus $J(t)$). Operational relaxation and creep modulus can be expressed with the help of Carlson Laplace transforms'. (Boufera et al. 1990), (Cost 1964) Equations 4 and 5 give us the temporal expression of the relaxation ($E(t)$) and creep ($J(t)$) functions.

$$E(t) = E_0 + \frac{E_\infty - E_0}{1 + \left(\frac{t}{\tau}\right)^k + \delta\left(\frac{t}{\tau}\right)^h} \quad (4)$$

$$J(t) = \frac{1 + \left(\frac{t}{\tau}\right)^k + \delta\left(\frac{t}{\tau}\right)^h}{E_0\left(1 + \left(\frac{t}{\tau}\right)^k + \delta\left(\frac{t}{\tau}\right)^h\right) + E_\infty - E_0} \quad (5)$$

3.2 Time temperature superposition

In the second part of this investigation, we determine the time variation of $E(t)$ by application time temperature superposition. The tests are made on the DMTA between -150 °C and 200 °C at five frequencies (0.3 to 30 Hz). Superposition of the data curves permits us to obtain a master curve for a reference temperature of 25 °C.

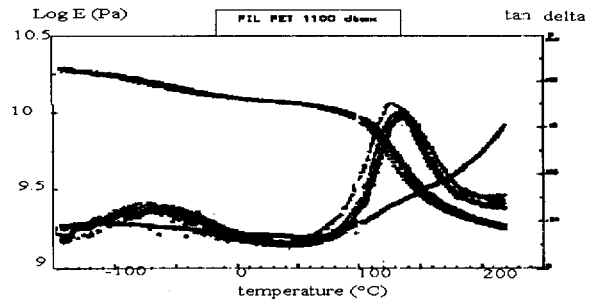


Figure 6 : Test at several frequencies on polyester fiber

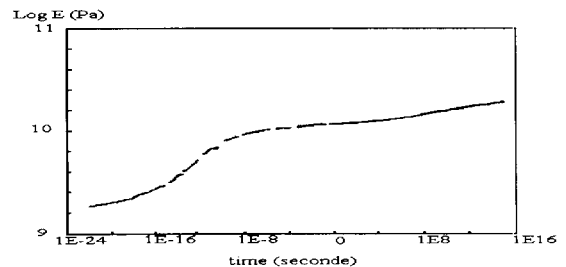


Figure 7 : Master curve at 25 °C for polyester fiber

This master curve can be fitted with an exponential function (Kabir 1984).

$$E = E_0 \cdot t^a \quad (6)$$

where $\log E_0 = 10.09$ Pa and $a = -0.013$ Pa/s.

In this part we have determined the creep curves of polyester fibers either by applying the time temperature superposition principle or by mechanical spectrometry and definition of a rheological model.

4 THERMOSTIMULATED CREEP ON LARGE DIMENSION SPECIMENS

The Institut Textile de France in collaboration with the Laboratoire Mécanique et Matériaux Université Lyon 1 (with the support of the Région Rhône Alpes) have developed a biaxial testing apparatus to carry out tests on large dimension specimens on soft or stiff composites. (Mailler 1996)

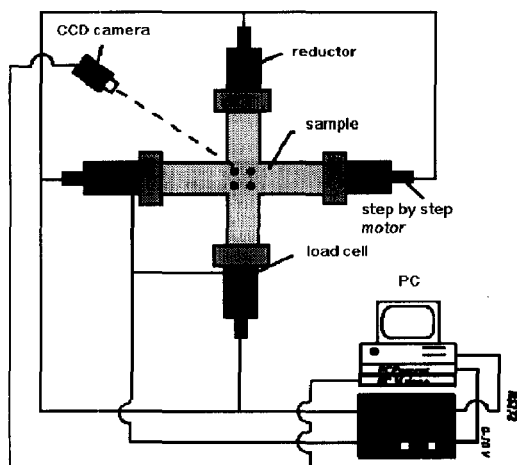


Figure 8 : Biaxial testing apparatus

The mains characteristics of this apparatus are given below.

- maximum load of 15 000 daN,
- sample of $1 \times 1 \text{ m}^2$ with a maximal deformation of 50%,
- four step by step motors permit to drive the apparatus either in displacement or load with several load or displacement ratio between the two axes,
- a thermal enclosure permits us to realize test between $-40 \text{ }^\circ\text{C}$ to $200 \text{ }^\circ\text{C}$.

We made a series of creep test in the following conditions:

- 1/1 320 daN/30 cm in warp and 320 daN/30 cm in weft,
- 2/1 320 daN/30 cm in warp and 160 daN/30 cm in weft,
- 1/2 160 daN/30 cm in warp and 320 daN/30 cm in weft.

The displacements are measured in the central part of the specimen with an optical method. Using a CCD camera, we follow the displacement of the barycentre of marks drawn on the surface of specimen.

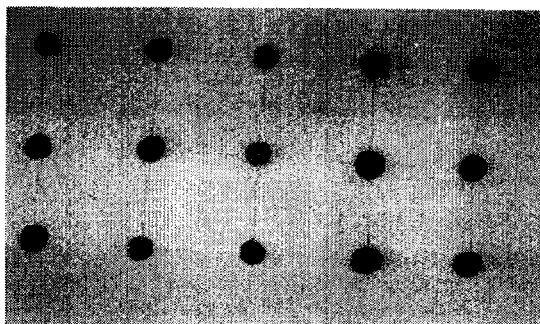


Figure 9 : Biaxial specimen (marks on surface)

The strains are then calculated using a pseudo finite element made with four points. These strains are calculated in the center of these elements and take into account the large deformations of this kind of material.

Figure 10 illustrates biaxial creep curves at $25 \text{ }^\circ\text{C}$ for a load ratio of 1:1.

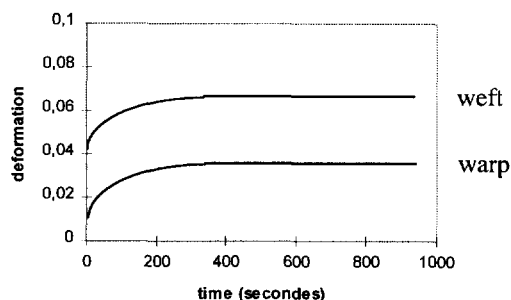


Figure 10 : Biaxial creep curve at $25 \text{ }^\circ\text{C}$ (1/1)

With similar curves at several temperature we construct a master curve taking into account the stresses applied in the central part of the specimen and using an inverse method to calculate the E modulus. The basis of this method is given below.

At a given time we have,

$$\begin{bmatrix} \sigma_1 \\ \sigma_2 \end{bmatrix} = \begin{bmatrix} \varepsilon_1 & \varepsilon_2 & 0 \\ 0 & \varepsilon_1 & \varepsilon_2 \end{bmatrix} \times \begin{bmatrix} C_{11} \\ C_{12} \\ C_{22} \end{bmatrix} \quad (7)$$

where σ_i are the stress, C_{ij} are the coefficients of the rigidity matrix and ε_i the strain.

If we consider two different times on two different tests (for example two load ratios) we have,

$$\begin{bmatrix} \sigma_1^1 \\ \sigma_2^1 \\ \sigma_1^2 \\ \sigma_2^2 \end{bmatrix} = \begin{bmatrix} \varepsilon_1^1 & \varepsilon_2^1 & 0 \\ 0 & \varepsilon_1^1 & \varepsilon_2^1 \\ \varepsilon_1^2 & \varepsilon_2^2 & 0 \\ 0 & \varepsilon_1^2 & \varepsilon_2^2 \end{bmatrix} \times \begin{bmatrix} C_{11} \\ C_{12} \\ C_{22} \end{bmatrix} \quad (8)$$

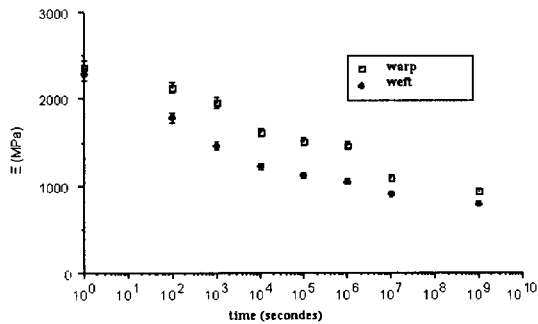


Figure 11 : Biaxial master curve at 25° C

These curves can be fitted by a logarithmic function:

$$E(t) = E_0 + a \log t \quad (9)$$

where a warp = -170 MPa/s , a weft = -165 MPa/s , E_0 warp = 2400 MPa, E_0 weft = 2060 MPa

In an attempt to validate this predicted creep curves, we carried out real time tests on specimens exposed during 380 days in situ at Lyon. We measured the displacement under a constant load and we defined the creep curves (Figure 12). The knee indicates an augmentation of deformation du to higher temperatures in summer time.

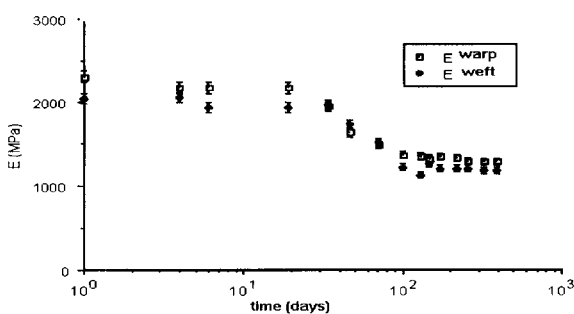


Figure 12 : Creep curves obtained by real time tests

5 CONCLUSION

All those results can be compared with real time tests (Figure 12). The three different approaches (at the scale of the constituents, at the scale of the textile architecture and the real time tests) give us similar results.

In a general point of view this results are similar to the literature (Toyada et al 1990,1992,1994) and give a residual tension stress of 50% in 3 years with a little evolution in 7 years. This is in accordance with our results which show us an asymptotic stabilization of creep.

This work permits the designers to take the durability into account during the design process.

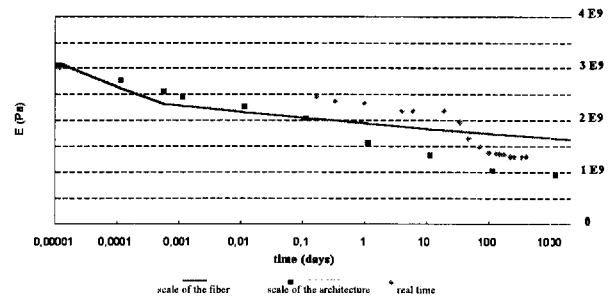


Figure 13 : Comparison of real time test and accelerated tests

REFERENCES

- Cole K.S., Cole R.H. (1941) "Dispersion and absorption in dielectrics; Alternative current characteristics". T Chem Phys. vol 9 p341
- Huet C., Bourgoïn D., Richemond S. (1984) "Rhéologie des matériaux anisotropes" Compte rendu du 19^{ème} colloque national annuel, Paris Cepadues ed p 591
- Koller R. C. (1984) "Application of fractional calculus to the theory of viscoelasticity" Journal of Applied Mechanics vol. 51 pp 299-307
- Boufera A., Doan C., Hamelin P. (1990) "Comportement viscoélastique des matrices polymères" Comportement des composites à renforts tissus - Comportement dynamique des composites. Ed Pluralis 1990 pp 47-68
- Cost T. (1964) "Approximate Laplace transform inversion in viscoelastic stress analysis" AIAA journal vol. 2 pp 2157-2166
- Kabir (1984) "In isolation and soil behavior of geotextile" Theses University of Glasgow
- Mailler Ph. (1996) "Rhéologie des membranes composites souples orthotropes sous chargement multi axial" Thèse de doctorat UCB LYON I 1996
- Toyada, Nireky, Juntunen, Ohnuma (1990) "Durability of PVC coated fabrics for membrane structures" I.A.S.S.S. Dresden and Cottbus
- Toyada, Wu, Tori (1992) "Deterioration with time of PVC coated fabric for tent warehouses, some experimental results" Textile Composite in Building Construction Part 1, Ed Pluralis
- Toyada, Sakabe, Tori, Itoh, Konishi (1994) "Weatherability of membrane structure materials as determined by their exposure conditions" ESN I Gakkaishi, vol. 50 N° 10

A Model for the Ultimate Pull-out Resistance of Geogrids

R.H. CHEN

Professor, Institute of Civil Engineering, National Taiwan University, R.O.C.

Y.S. LEE

Ph.D. Candidate, Institute of Civil Engineering, National Taiwan University, R.O.C.

ABSTRACT: A three-parameter model is proposed to predict the ultimate pull-out resistance of geogrids. Twenty-seven pull-out tests were performed using three types of geogrids embedded in Ottawa Sand and kaolinite clay. The proposed model can take into account the nonlinear relation of the ultimate resistance with the normal stress. Using this model and analyzing the test results, the above mentioned phenomenon can be described and the ultimate resistance can be predicted very well.

KEYWORDS: Pull-out test, Ultimate pull-out resistance, Geogrid.

1 INTRODUCTION

In the design of reinforcements, laboratory pull-out tests are performed to understand the pull-out resistance of reinforcements in soils. The parameters needed in the limit equilibrium methods, such as apparent cohesion c and frictional angle ϕ are obtained. It is a common practice to employ the Mohr-Coulomb criterion for the design. However, this criterion does not usually predict the ultimate pull-out resistance very well. Hence, a three-parameter model for predicting the ultimate pull-out resistance is presented in this study to take into account the deformation modulus of geogrids and applied normal stress. This model was verified by twenty-seven pull-out tests. According to the results verified, this model can describe the relation between the ultimate pull-out resistance and the applied stress, and predicts the ultimate pull-out resistance of other geogrids.

2 THE PROPOSED MODEL

In design practice, the assumptions on the pull-out resistance of geogrids in soils are: (a) the shear stress at the interface between geogrid and soil is constant, (b) the shear stress at the interface follows the Mohr-Coulomb criterion. Hence the pull-out resistance is presented as:

$$\tau = c + \sigma \tan \phi \quad (1)$$

$$P = 2 A \tau \quad (2)$$

where:

τ : the shear stress at the interface

c : apparent cohesion intercept

σ : applied normal stress

ϕ : frictional angle

P : ultimate pull-out resistance

A : embedded area of geogrids

On the other hand, the proposed three-parameter model is

as follows:

$$\tau = \sigma \left[a_1 + a_2 \exp\left(-a_3 \frac{\sigma}{E}\right) \right] \quad \text{for sandy soils} \quad (3)$$

$$\tau = a_1 + \sigma a_2 \exp\left(-a_3 \frac{\sigma}{E}\right) \quad \text{for cohesive soil} \quad (4)$$

$$E = \frac{T}{\epsilon} \quad (5)$$

where:

a_1, a_2, a_3 : parameters to be determined.

E : deformation modulus of geogrid, which can be determined by Eq.(5).

T : the tensile force of geogrid in the tensile strength test.

ϵ : the strain of geogrid in the tensile strength test.

In this model, the a_1 , a_2 and a_3 parameters are obtained by pull-out tests. Eq.(3) is suitable to sandy soils, and Eq.(4) is suitable to cohesive soils. This proposed model compared with the Mohr-Coulomb criterion has the following characteristics:

1. The model uses the applied normal stress σ and the geogrid deformation modulus E to describe the ultimate pull-out resistance.
2. If the modulus of geogrid is infinite, the pattern of the simplified proposed model is similar to the ordinary shear strength model such as Mohr-Coulomb criterion.
3. The expansion of the exponential function in Eq.(3) or Eq.(4) has infinite terms. For this reason, the proposed model is convenient to describe test results smoothly, compared to the Mohr-Coulomb criterion that has only two parameters.

Table 1. Fundamental properties of geogrids.

Item (kN/m)	Grid A	Grid B	Grid C
Ultimate tensile strength	110	80	55
Deformation modulus at 5% strain	1320	960	660
Deformation modulus at 10% strain	880	640	440

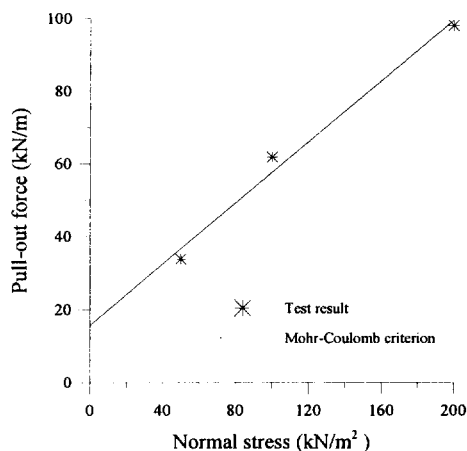


Figure 1. Normal stress versus ultimate pull-out resistance for grid A embedded in Ottawa Sand ($D_r=85\%$).

3 TEST EQUIPMENT AND TEST MATERIAL

The dimension of the pull-out box is 60cm × 35cm × 20cm (length × width × height). The range of pulling rate is from 0.0006 to 107 mm/min. The capacity of pulling force is 12.5 tons applied by electric motor. The vertical load system consists of a rubber air bag and a jack. Load cells and LVDT are used to measure the pulling force and the displacement. A data acquisition device, an AD card, and a personal computer are used for test controlling and recording. Test materials include geogrid, sand, and clay. The material properties of three types of Tensar geogrid used in the tests are summarized in Table 1. The sand is Ottawa sand (No. C109) that has specific gravity 2.65, maximum void ratio 0.732, and minimum void ratio 0.387. The strength parameters are $c = 0.7 \text{ kN/m}^2$, $\phi = 36^\circ$, for relative density $D_r = 85\%$; and $c = 5 \text{ kN/m}^2$, $\phi = 32^\circ$, for $D_r = 50\%$. The clay is kaolinite that has specific gravity 2.62, maximum dry density 12.8 kN/m^3 , the optimum water content 31.5%. The strength parameters from the consolidated undrained test are $c = 18 \text{ kN/m}^2$, $\phi = 15.6^\circ$, for dry unit weight $\gamma_d = 12.4 \text{ kN/m}^3$ and water content $\omega = 29\%$.

The dimension of geogrid specimen is 45 cm × 10 cm (length × width), there are three apertures in the longitudinal direction and five apertures in the transverse direction. The distance between the first transverse rib and the front wall of

Table 2. The ultimate pull-out resistance.

(a) Ottawa Sand ($D_r=85\%$)

Normal stress (kN/m^2)	Grid A (kN/m)	Grid B (kN/m)	Grid C (kN/m)
50	33.8	30.9	28.2
100	61.8	57.2	47.9
150			56.2
200	98.1	74.7	

(b) Ottawa Sand ($D_r=50\%$)

Normal stress (kN/m^2)	Grid A (kN/m)	Grid B (kN/m)	Grid C (kN/m)
50	25.3	22.0	18.5
100	48.2	42.1	33.5
150		53.0	51.2
200	86.1		

(c) Clay

Normal stress (kN/m^2)	Grid A (kN/m)	Grid B (kN/m)	Grid C (kN/m)
50		18.2	15.1
100	26.5	24.5	17.5
200	35.9	30.7	23.5
300	43.0		

the pull-out box is 12 cm. The pulling rate is 1 mm/min.

4 TEST RESULTS AND ANALYSIS

The ultimate pull-out resistance of test results is summarized in Table 2. According to the test results, the ultimate resistance increases with the normal stress but the relation is not proportional. The example using the Mohr-Coulomb criterion together with the pull-out test result is shown in Figure 1. From the figure, the Mohr-Coulomb criterion does not appear to be very accurate in regression result, but also the cohesion intercept is greater than zero in sands. Considering the aforementioned phenomenon, a three-parameter model is therefore proposed. The procedure used to analyze the test result is described in the following:

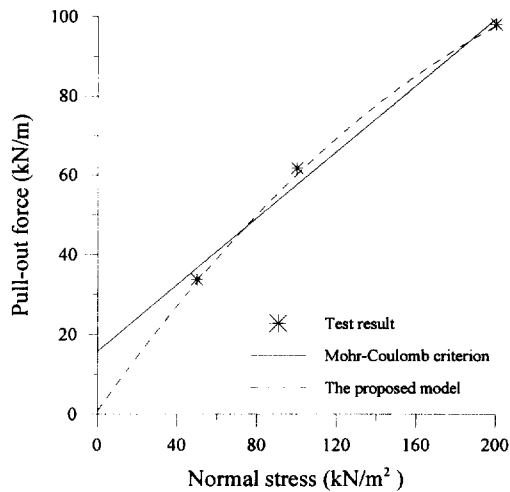
1. Determine the deformation modulus.

Geogrid is a flexible material, and its modulus varies with strain. Hence a predictive model must take this behavior into consideration. For simplicity, the proposed model adopts the deformation modulus as the secant modulus at 5% strain when the strain is less than 5%, and the secant modulus at 10% strain for strain more than 5%.

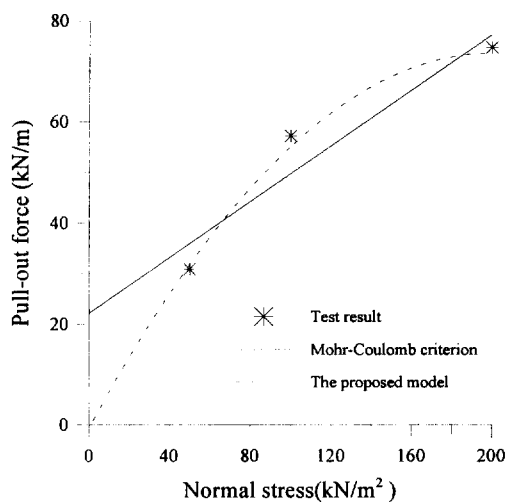
2. Determine a_1, a_2 and a_3 parameters.

The three parameters are to be determined by using Eq.(3) for sands, and using Eq.(4) for clays.

3. Compute the ultimate pull-out resistance.



(a) Grid A



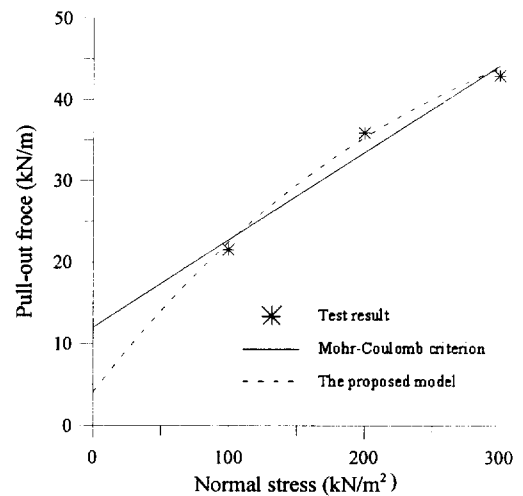
(b) Grid B

Figure 2. The comparison of the proposed model and Mohr-Coulomb criterion for pull-out tests in Ottawa Sand ($D_r=85\%$).

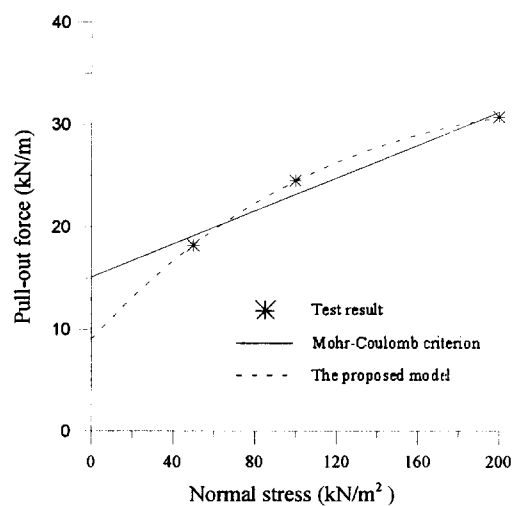
The ultimate pull-out resistance is computed considering various modulus and normal stress using Eq.(3) for sands and Eq.(4) for clays.

The parameters for computation are summarized in Table 3. The comparison of the proposed model and the Mohr-Coulomb criterion for the ultimate pull-out resistance of geogrids in sands are shown in Figure 2.

It is obvious that the proposed model is better than the Mohr-Coulomb criterion. For instance, the proposed model describes the relation of the ultimate pull-out resistance and the normal stress very well and the apparent cohesion intercept is zero. The model also describes non-proportional relation of the ultimate pull-out resistance with the normal stress. In the other case for kaolinite clay, the comparison is



(a) Grid A



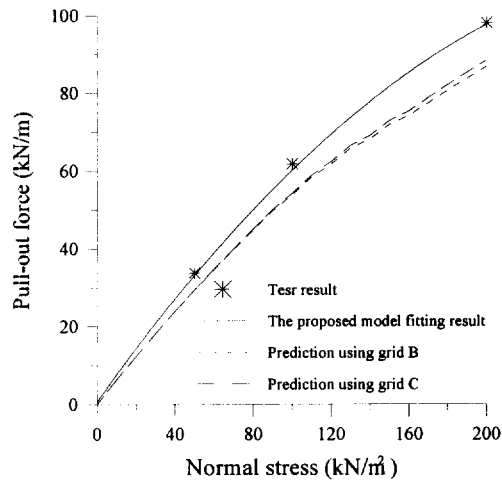
(b) Grid B

Figure 3. The comparison of the proposed model and Mohr-Coulomb criterion for pull-out tests in clay.

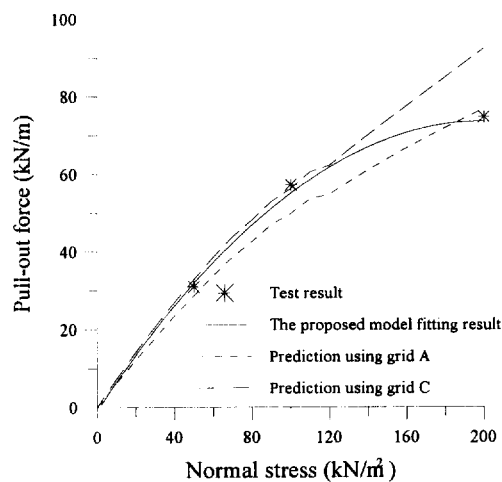
shown in Figure 3. Analyzing and comparing the result, the result from this model is similar to that of the Mohr-Coulomb criterion. Besides, this model predicts the ultimate pull-out resistance well.

From the above mentioned results, the proposed model is a good application to predict the ultimate resistance for alternating normal stress.

Furthermore, the proposed model seems also be able to predict the ultimate pull-out resistance of other geogrids. For instance, it predicts the ultimate resistance of geogrid B by using the parameters of geogrid A or C. The results of this prediction are shown in Figure 4. It is found that the predictions are within 10%~20% error. In engineering practice, it seems acceptable.



(a) Grid A/Ottawa Sand (Dr=85%)



(b) Grid B/Ottawa Sand (Dr=85%)

Figure 4. The result of the proposed model predicting the ultimate pull-out resistance.

5 CONCLUSIONS

Summarizing from the mentioned explanation and discussion, the advantages of the proposed model are as follows:

1. The dimensionless term σ/E is used to describe the ultimate pull-out resistance, and its application on studying test result shows good.
2. Although there are three parameters in this model, more than two parameters in the Mohr-Coulomb criterion, the convenience and power of this model is justified.
3. As the modulus E approaches infinity, the model can be simplified to become a special case of the Mohr-Coulomb criterion.
4. The model predicts the ultimate pull-out resistance of

Table 3. Parameters of the proposed model.

(a) Ottawa Sand ($Dr=85\%$)

Item	a_1	a_2	a_3
Grid A	0.46	0.37	6.2
Grid B	0.23	0.47	3.0
Grid C	0.25	0.45	3.0

(b) Ottawa Sand ($Dr=50\%$)

Item	a_1	a_2	a_3
Grid A	0.42	0.17	5.5
Grid B	0.14	0.55	5.0
Grid C	0.37	0.065	6.0

(c) Clay

Item	a_1	a_2	a_3
Grid A	4.0	0.22	2.2
Grid B	9.0	0.22	3.4
Grid C	11.7	0.07	0.7

geogrids more well than the Mohr-Coulomb criterion. It also can be used to predict the ultimate pull-out resistance of other geogrids within acceptable error.

5. Using this model, the non-proportional relation of the ultimate resistance with the normal stress can be described.

REFERENCES

- F.H.W.A. (1991) *Reinforced Soil Structures, Design and Construction Guidelines*, Vol. 2, U.S. Department of Transportation, D.C., USA.
- Ingold, T.S. (1984) "A Laboratory Investigation of Soil-Geotextile Friction", *Journal of Ground Engineering*, Vol. 17, pp.21-28.
- Koerner, R.M. (1990) *Designing with Geosynthetics*, 2nd ed., Prentice-Hall, New Jersey, USA.
- Lee, Y.S., Chen, R.H., and Chen, T.C. (1996) "A Three-Parameter Model for the Ultimate Pull-out Force of Geogrids", *Proceedings of the International Symposium on Earth Reinforcement*, Fukuoka, Japan, pp.69-72.

An Approach to Analyze the Pull-out Resistance of Woven Geotextiles

Ashoke K. Karmokar

Assistant Professor, Department of Material Systems Engineering, Tokyo University of Agriculture and Technology, Faculty of Technology, 2-24-16 Naka-cho, Koganei-shi, Tokyo 184-0012, Japan

Hisayoshi Kabeya

Professor, Department of Material Systems Engineering, Tokyo University of Agriculture and Technology, Faculty of Technology, 2-24-16 Naka-cho, Koganei-shi, Tokyo 184-0012, Japan

ABSTRACT: The pull-out resistance of geotextiles is generally the result of complex phenomena occurring at the soil-geotextile interface. In this study, an attempt is made to analyze the pull-out resistance by considering that soil shearing and soil-geotextile friction at the interface are liable to develop the resistance. The usefulness of this approach is pointed out in terms of the prediction of pull-out resistances of soil-geotextile system. For illustration, the pull-out resistances of two woven geotextiles with Toyoura sand are predicted, and compared with those of experimental values. The surface asperity of geotextile is identified as an important factor influencing shearing and friction components at the interface.

KEYWORDS: Friction, Geotextiles, Pull-out Resistance, Shear Strength, Woven Fabrics

1 INTRODUCTION

The operational circumstances of many soil structures reinforced with geotextiles reveal that the geotextile is at least partly subjected to a pull-out force. This is leading to the pull-out method which is used for the evaluation of soil-geotextile interfacial interaction. The results of a pull-out test are, however, difficult to interpret because of complex interactions at the interface. Nevertheless, a few attempts at a numerical approach have been made to analyze the behavior involved in the pull-out operation of a geogrid (Wilson-Fahmy and Koerner 1993; Yogarajah and Yeo 1994), but hardly any attempts have ever been made for a geotextile. This is probably because of the structural complexities that a geotextile presents compared with a geogrid. In this study, a semi-empirical approach is adopted to analyze the pull-out resistance developed by the woven geotextiles with sand. The structural parameters of the geotextiles and their interactions with the sand are well accounted for in this approach.

2 ANALYTICAL PROPOSITION

The pull-out resistance is assumed to be developed due to interactions comprising soil shearing and soil-geotextile friction. Therefore, pull-out resistance (P) could be written as

$$P = S + F \quad (1)$$

where, S = shearing force, F = frictional force. Let the total area at the interface be A, out of which the areas responsible for soil shearing and soil-geotextile friction are A1 and A2, respectively. Thus, Equation (1) becomes

$$P = \tau.A1 + f.A2 \quad (2)$$

where, τ = soil shear stress, f = soil-geotextile frictional force per unit area. The relationship for the determination of frictional force is

$$f = \mu_f N \quad (3)$$

where, μ_f = coefficient of friction between soil and raw material of geotextile (hereafter the raw material frictional behavior is termed as 'skin-friction'), N = normal stress.

To predict pull-out resistance, therefore, we need the values of τ , μ_f and shearing/friction area at the interface.

3 MODEL ILLUSTRATION

For illustration, two plain woven geotextile samples were considered, and their interactions with Toyoura sand were taken into account. A few details of the geotextile samples and sand are given in Table 1 and Figure 1, respectively.

A prototype apparatus (Kabeya et al. 1993) was used for conducting the pull-out experiments. Four levels of normal pressure, e.g., 2.5, 5.0, 7.5, and 10.0 kPa, were maintained on the soil-geotextile-soil system during experiments (low pressures were to avoid fabric deformation inside soil).

Table 1 Specifications of woven geotextile samples.*

Descriptions	Sample (S1)	Sample (S2)
Polymer type	Polypropylene	Polyester
Yarn type	Flat tape	Multi-filament
Yarn count (Tex)	130 × 120	530 × 530
Yarn crimp (%)	4.3 × 1.6	5.5 × 3.7
No. of yarns (/cm)	6.3 × 6.3	5.6 × 5.6
Thickness (mm)	0.60	1.00
Area density (g/m ²)	170	600

*Samples were obtained from Taisei Corporation, Japan

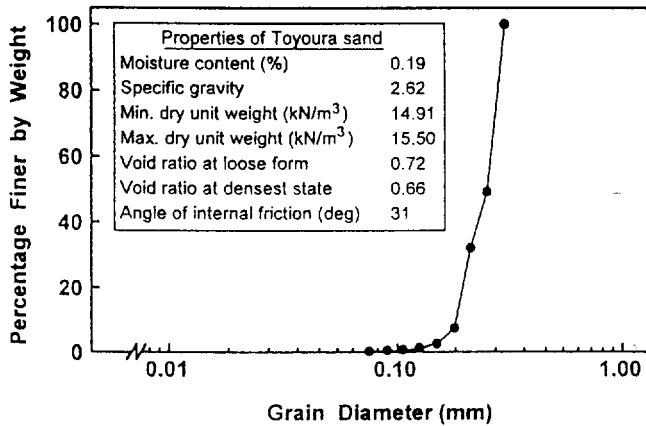


Figure 1 Grain size distribution of Toyoura sand.

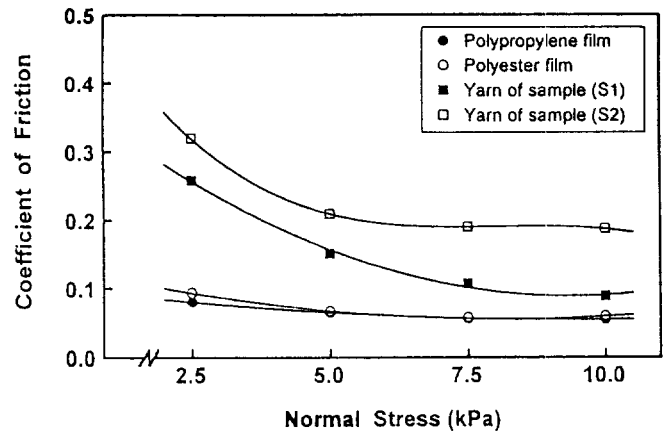


Figure 2 Skin-frictional coefficient with Toyoura sand.

3.1 Frictional Experiments

The polymer types of the two selected geotextiles were polypropylene (sample S1) and polyester (sample S2). Consequently, the pull-out tests on polypropylene (PP) and polyester (PET) films with sand were carried out for determining the sand-geotextile skin-friction coefficients. By this method, however, the frictional representation may not be truly possible, as finishes in the geotextile and the film are necessarily different. Thus, to find out the actual frictional coefficients, the following approach was used.

The individual yarn was unraveled from the geotextile sample and heat-set under decrimped-taut condition. The decrimped yarn was then used in the pull-out experiments with Toyoura sand. In pull-out experiments, therefore, the occurrence of soil shearing at the interface which may be initiated by the crimps was very unlikely, as the yarn was decrimped and merely tape or filament (with marginal twists) in kind. Consequently, the yarn-sand pull-out resistance development was thought to be solely due to friction. The sand-film (geotextile) skin-friction coefficient is obtained by using the following empirical relationship

$$\mu_f = F' / (A' \cdot N) \quad (4)$$

where, μ_f = coefficient of skin-friction, F' = frictional force, A' = interfacing area, N = normal stress.

The results are shown in Figure 2 where it may be seen that the set of values obtained by the above approach are higher than those obtained with the respective films. These differences in values could be attributed to their different surface textures. However, the coefficients of skin-friction obtained here could reasonably be taken as actual values.

3.2 Shearing Experiments

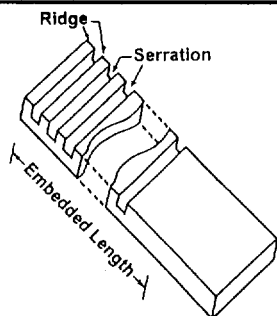
For characterizing the shear behavior of sand, generally, we conduct direct shear box tests in laboratory. However, possibly a different state occurs due to different shearing

situations at the soil-geotextile interface in the pull-out method, and at the interface of the two boxes in the direct shear box method. At the soil-geotextile interface, the soil shear behavior is believed to be influenced by the presence of the surface concavities of the geotextile. The concavity wall may put up passive bearing resistance to the soil shear stress. As concavities are numerous, so the contribution of passive bearing resistance to soil shear stress is also significant. In the direct shear box test, such resistance comes only from the back wall of the shear box for total interface area, and consequently, the shear stress occurring with this method is lower in value. Thus, it is important to conduct shear tests under simulated pull-out interfacing conditions, so that the passive bearing resistance of soil brought by cross elements could be taken into account.

For this, channel-like parallel serrations were engraved on acrylic plates (Table 2). Each plate was then used as the reinforcing element in the pull-out experiments. The conditions maintained in the experiments were similar to those during soil-geotextile pull-out testing. The engraved area on the plate (channel) is believed to be responsible for soil shearing, and the flat area to be responsible for friction in the pull-out operation. With defined areas for shearing and friction on the plate, it was possible to distinguish the soil shearing and soil-acrylic plate friction components, provided the sand-acrylic plate frictional coefficient was known. For the sand-acrylic plate frictional coefficient, the pull-out tests on smooth acrylic plates with Toyoura sand were conducted.

Figure 3 was drawn to show the trend of soil shear stress against serration width in the acrylic plate for different levels of normal pressure. The shear stress corresponding to the pitch of respective geotextile samples could now be obtained from this figure by extrapolating the respective trends. It is noteworthy to mention at this stage that as the shear area in the acrylic plate decreases, the variability in pull-out resistance (i.e., soil shear stress) increases. This is one of the reasons why we did not use acrylic plates with serration widths of less than 5 mm in this study.

Table 2 Specifications of serrated acrylic plates.



Designation of plates	P20	P15	P10	P5
Number of serration	2	3	4	5
Serration length (mm)	48	48	48	48
Serration width (mm)	20	15	10	5
Serration depth (mm)	5	5	5	5
Shearing area (cm ²)	23.2	26.1	23.2	14.5
Ridge width (mm)	10	10	10	10
Friction area in 10 cm embedded length (cm ²)	92.8	89.9	92.8	101.5

3.3 Interfacial Shearing and/or Friction Area

Evaluating the shearing/friction area at the soil-geotextile interface is a two stage process, namely, the measurement of the surface roughness of geotextile samples, and the correlation between surface roughness and soil properties involved in the interface interaction process. The brief description for each of the stages is given below.

3.3.1 Evaluation of surface roughness

An empirical approach was followed for measuring the surface roughness of geotextile samples because the two other commonly used methods e.g., mechanical scanning and laser scanning methods, were tried, but they failed to give definite outcomes. due to procedural limitations. In this method, replicas of the two geotextile samples were reinforced with a contrasting color matrix to form a solid block. The block was then milled gradually (in cross-plane direction) at regular intervals. For milling, a precision end-milling machine was used in our laboratory. The milling was done for a cut-out thickness of 0.1 mm in each step. Therefore, it may be said that the technique used here characterizes the surface as a combination of undulating lines, as may be obtained in other scanning methods. The photograph of each milled surface (i.e., at steps of 0.1 mm milled thickness) was taken with a camera fixed to the milling machine. As a next process, each photographic negatives was enlarged by a projector and imaged over the sensitive screen of a digitizer. The digitizer was interfaced with a computer, by which undulating lines were digitized into corresponding numerical values of X_i , as the distance along the fabric plane, and Y_i , as the distance of surface contours from the top fabric plane (see inset of Figure 4).

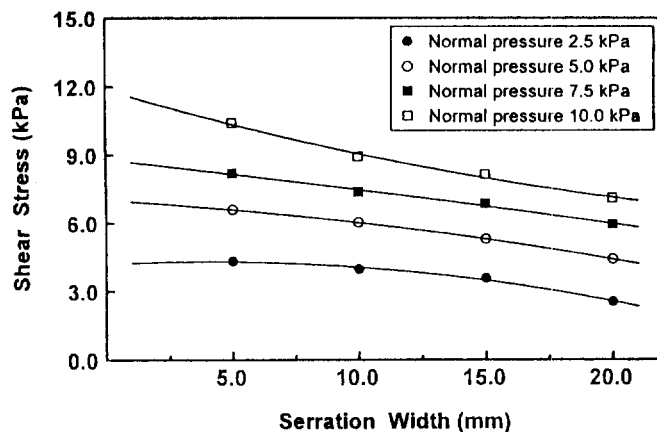


Figure 3 Effect of serration width on shear stress.

Consequently, two dimensional arrays (X_i , Y_i) for each undulating line were obtained. The reassembling of these undulating lines by a computer program gives a view of the surface of the geotextile sample, as shown in Figure 4.

3.3.2 Correlation of surface roughness with soil properties

The two parameters, namely, the depth, and the slope of surface concavities were used for expressing the surface roughnesses of geotextile samples. These two parameters were then weighed, as stated below, against the two soil parameters, viz., the average soil particle diameter (D_{50}), and the soil shear angle (ϕ) of Toyoura sand, respectively, for determining interfacial shearing/friction area.

The measurements of concavity depths at different points at distances 0.1 mm apart yield a frequency distribution for each of the geotextile samples. It is assumed that when the absolute concavity depth at any point (element) is more than the size of soil particle employed, then that element will be responsible for soil shearing at the interface. On the other hand, if the concavity depth is less than the size of the soil particle, the element will be responsible for friction at the interface. Thus, corresponding to the value of concavity depth equals to average soil particle diameter (D_{50}) of Toyoura sand, the percentage of elements causing shearing and friction at the interface may be found out. By knowing the total embedded area maintained during experiments (both faces of the geotextile), we were able to calculate the interfacial shearing and friction area.

Similarly, the concavity slopes calculated between any two consecutive measuring points (0.1 mm apart) give a frequency distribution for each geotextile sample. It is our assumption that when the calculated slope is less than the angle of soil shearing (ϕ), that slope will be responsible for soil-geotextile friction, and when the slope is more than the angle of soil shearing, that slope will be responsible for soil shearing at the interface. Using the same line of action stated above, therefore, we were able to draw a partition in the population of concavity slope distribution.

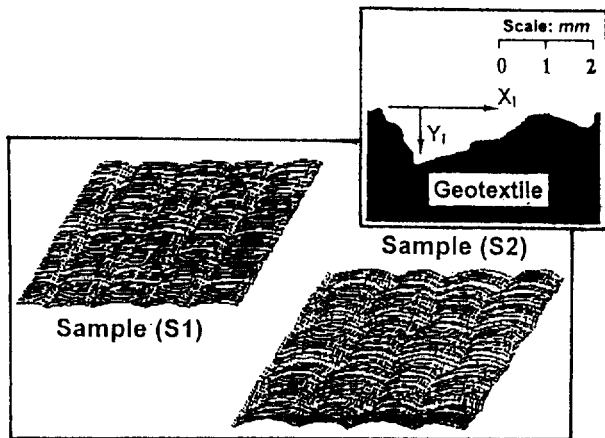


Figure 4 Surface view of geotextile samples.

However, it is a common perception that the interfacial interactions between soil and geotextile are quite complex phenomena, and the ways we tried to correlate concavity depth and concavity slope with soil properties individually may not be totally justified. This is because, even if there is sufficient concavity depth (greater than particle diameter), interfacial soil shearing may not occur when the slope at that point is less than the shear angle of the soil. Similarly, it may be argued that, even if the concavity slope is higher than the soil shear angle, the interfacial shearing may not occur when the concavity depth is less than the particle diameter. For this reason, therefore, an attempt was also made to introduce the interaction between concavity depth and concavity slope, for finding the correct shearing and/or friction area at the interface.

3.4 Calculated Pull-out Resistance

Using the three sets of shearing/friction areas, obtained from the concavity depth distribution, the concavity slope distribution, and the interaction of the two, the pull-out resistances were calculated. It were observed that the pull-out resistances calculated using the areas corresponding to depth distribution and slope distribution were in poor agreement with those obtained experimentally, although the general trends were found the same. In contrast, the pull-out resistances calculated using the interaction induced shearing/friction areas were in good agreement with the experimental pull-out resistances (Figure 5). As stated before, the reason for this may be the interactive effects due to both the depth and the slope of surface concavities of geotextiles, rather than individual actions.

4 SUMMARY

With the multiplicity of structural parameters of geotextiles and complexities in the design procedure for geotechnical applications, we very often encounter the

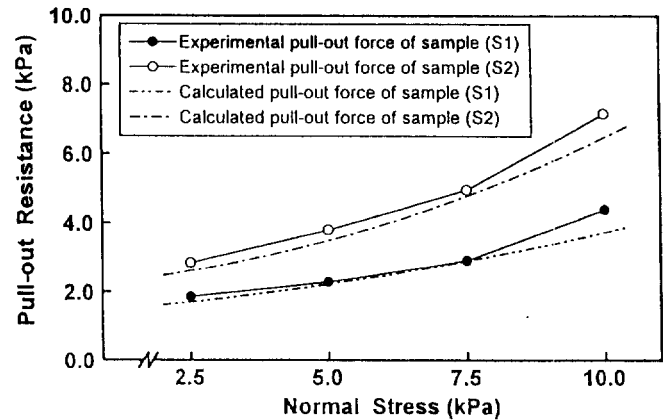


Figure 5 Experimental/calculated pull-out resistance.

need to know the pull-out force that a geotextile will exert with the soil type. Using the proposition described before, we may have the option of dealing with the problem of determining pull-out resistance. By knowing the soil-geotextile skin-friction behaviors, the soil shearing properties, and the interfacial shearing or friction areas for the soil-geotextile system, we could proceed to calculate the constituents shearing and friction at first, and then the pull-out resistance.

The illustration reported in this study indicates that depending on the surface asperities of the geotextile, and their interactions with the soil, the contributions of shearing and friction in the pull-out resistance will vary. It is identified that the effect of the surface asperity of the geotextile is merely to influence the shearing and friction area at the interface. Comparisons of experimental and calculated values of the pull-out resistance show that the correlation between surface asperities and soil properties for evaluating the interfacial shearing and/or friction area is an interactive process of factors such as depth and slope of surface concavity of geotextiles.

REFERENCES

- Wilson-Fahmy, R.F. and Koerner, R.M. (1993) "Finite Element Modeling of Soil-Geogrid Interaction with Application to the Behavior of Geogrids in a Pull-out Loading Condition", *Geotextiles and Geomembranes*, Vol. 12, pp. 479-501.
- Yogarajah, I. and Yeo, K.C. (1994) "Finite Element Modeling of Pull-out Tests with Load and Strain Measurements", *Geotextiles and Geomembranes*, Vol. 13, pp. 43-54.
- Kabeya, H., Karmokar, A.K., Kamata, Y. and Tsunoda, S. (1993) "Influence of Surface Roughness of Woven Geotextiles on Interfacial Frictional Behavior — Evaluation Through Model Experiments", *Textile Research Journal*, Vol. 63, No. 10, pp. 604-610.

A NEW APPROACH IN MODELING OF SOIL-GEOTEXTILE INTERFACE BEHAVIOR IN PULLOUT TESTS

S. B. Mallick,
Civil Engineering Department, Auburn University

D. J. Elton
Civil Engineering Department, Auburn University

and

S. Adanur
Textile Engineering Department, Auburn University

ABSTRACT: A nonlinear elastic finite element model was developed using GAP elements to investigate the failure criteria and the separation behavior at the soil-geotextile interface during pullout tests. Pullout resistance calculated from this model was compared to that obtained from laboratory pullout tests reported earlier in the literature. The data showed the pullout resistance obtained from the finite element model was approximately equal to that obtained from the laboratory pullout tests. Results from the model also indicated the existence of material nonlinearity close to pullout load application point.

KEY WORDS: Finite element, Numerical modeling, Interface-element, Geotextile, Pullout

1. INTRODUCTION

When a geotextile is used as reinforcement material in a slope, one of the predominant causes of failure is the slippage or pullout of geotextile from the soil mass. Such a behavior can be modeled by the pullout tests in a laboratory. A simple experimental set-up was designed and pullout tests were carried out in the laboratory (Mallick et. al, 1997). In conjunction with experimental study a theoretical model is required to visualize the pullout mechanism. Such a model can be validated against the results obtained from the laboratory pullout tests.

Finite element analysis conducted by Katagiri et. al (1990) has shown a linear relationship between normal pressure and shear stiffness of the soil-geotextile interface. A joint element technique was used to connect the upper and lower surface of the geogrid with the soil particles. The results showed that the analyzed strain sufficiently agreed with the measured strain. Floss and Gold (1990) conducted a finite element analysis on the efficiency of a single geotextile reinforced two-layer system. Soil continuum was modeled by an eight node isoparametric element with quadratic shape functions. The geotextile was modeled with isoparametric bar elements. To model the soil-geotextile interaction, thin-layer elements were used at the interface. An elastoplastic nature of analysis with

Mohr-Coulomb yield criterion was adopted to limit the transfer of load from the soil to the geotextile.

Wu (1987) also developed a finite element model to predict the stress-deformation behavior of a soil-fabric system. The interface region was modeled by connecting the nodes with unilateral normal and tangential springs. The fabric was represented by a special element which could only withstand tension. No resistance to bending and compression was allowed in this element. To simulate the viscoelastic behavior of the polymeric geogrid, varying elastic moduli was used for different sections of the geogrid in a finite element analysis. The residual shear modulus at the interface was selected on the basis of the assumption that the partial slippage would occur once the shear strength was reached.

A review of literature shows that the behavior of the soil-geotextile interface depends on the successful modeling of load transfer mechanism from geotextile to soil. This mechanism is again dependent on the choice of a proper element to model the soil-geotextile interface. This study was carried out to investigate the applicability of a new type of interface element in modeling a pullout test with geotextiles.

2. MODELING OF INTERFACE WITH GAP ELEMENTS

In the numerical model developed in this study a new type of element was used to model the soil-geotextile interface.

Ten isotropic GAP elements were used to model the load transfer mechanism at the soil-geotextile interface. Slip-separation behavior of the interface is governed by the status of the GAP elements. The GAP or friction element (available in the element library of MSC/NASTRAN) has several advantages over the thin-layer or spring elements previously used to model the soil-geotextile interface. This is because GAP elements can simulate several situations which are observed in a pullout test. These situations are:

Open GAP: Simulates no contact at the interface

Closed GAP: Simulates the contact between soil and geotextile at the interface under vertical loading

GAP sticking with static friction: Simulates the building of pullout resistance at the interface.

Resistance increases until the pullout load overcomes the static friction at the interface. After the static friction is overcome, GAP elements start slipping with kinetic friction and pullout resistance drops as the reinforcement is pulled out of the soil layers. A horizontal shear stiffness for the gap element was used to simulate the frictional force at the interface. As the load was applied, the stick-slip behavior of the interface was examined with the behavior of GAP elements under the specified loading condition.

3. NUMERICAL MODELING OF PULLOUT MECHANISM

A two dimensional plane strain nonlinear model was developed to simulate the stress-strain behavior of a geotextile subjected to a pullout load (Figure 1). A large scale general purpose computer program, MSC/NASTRAN, was used to analyze the model. The above model was tested for initial pullout displacement of 40 mm. For this displacement, stress-strain relationship for soil and geotextile materials were considered to be linearly elastic. For the correct simulation of stick-slip behavior of the interface, geometric nonlinearity was incorporated in the model.

4. ELEMENTS AND PARAMETERS USED FOR THE MODEL

Soil: Cover material was modeled using a elastic, four node, isotropic, quadrilateral element. The following material properties were used for the quadrilateral elements:

Modulus: 100 Mpa
Poisson's ratio: 0.3
 ϕ : 32 degrees
c: 0 (dry sand)

Interface Element: The following parameters were selected as the properties of the GAP elements.

axial stiffness: 80.E+7 N/m²
transverse stiffness: 9.E+7 N/m²
coefficient of static friction: 3.0
coefficient of kinetic friction: 0.1

Reinforcement: Reinforcement was modeled with four one dimensional linear rod elements with no bending stiffness. The following parameters were selected as the properties of the rod elements.

thickness: 0.001m
modulus: 5250 kN/m

Loading: The above model was tested for a 7 kPa normal pressure and 40 mm pullout displacement at the tension end of the geotextile. Ten iterations were used in the model to reach 40 mm forced displacement.

5. EXPERIMENTAL

Details of the experimental study can be found from Mallick et. al (1997). A simple pullout box was designed and pullout tests were conducted with different types of geotextiles and sands. Figure 2 shows the details of the experimental set-up. A pullout load was applied at the rate of 1 mm/min at the tension end of the geotextile. Pullout load and the corresponding front end displacement were measured during a pullout test.

6. RESULTS

Figure 3 shows the calculated (from finite element model) and measured load-displacement behavior at the front end of the geotextile. From the output it was observed that the calculated load response of the geotextile at different displacement levels are very close to the load measured during the experiment. Calculated loads are slightly higher than the measured loads at all displacement levels.

Figure 4 shows the calculated pullout resistance along the length of the geotextile. From the results it can be noted that the pullout resistance obtained from element number two is smaller than that obtained for element number one. This discrepancy in the output shows the need for a varying modulus input for the different sections of the geotextile. As the pullout resistance sharply increases from element 3 to element 4, nature of the load response graph shows a need for nonlinear modeling for the geotextile material close to the load application point.

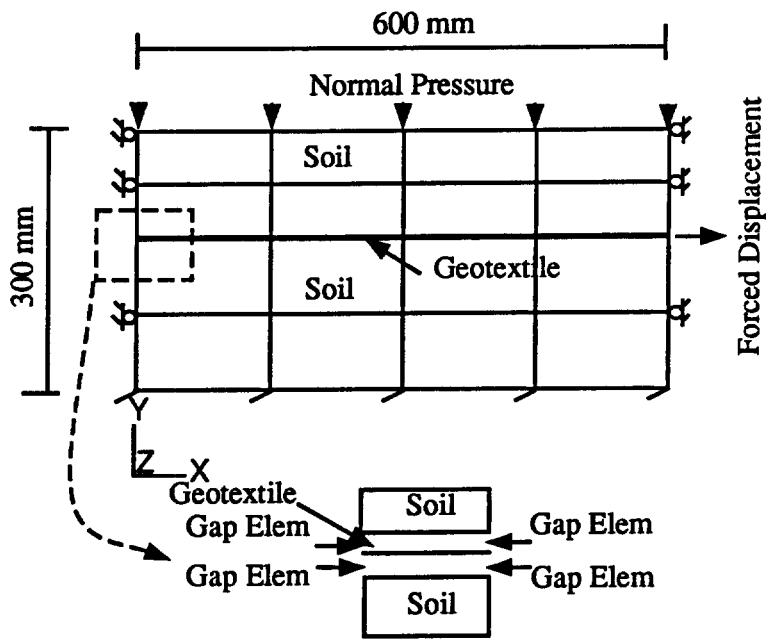


Figure 1. Finite Element Model

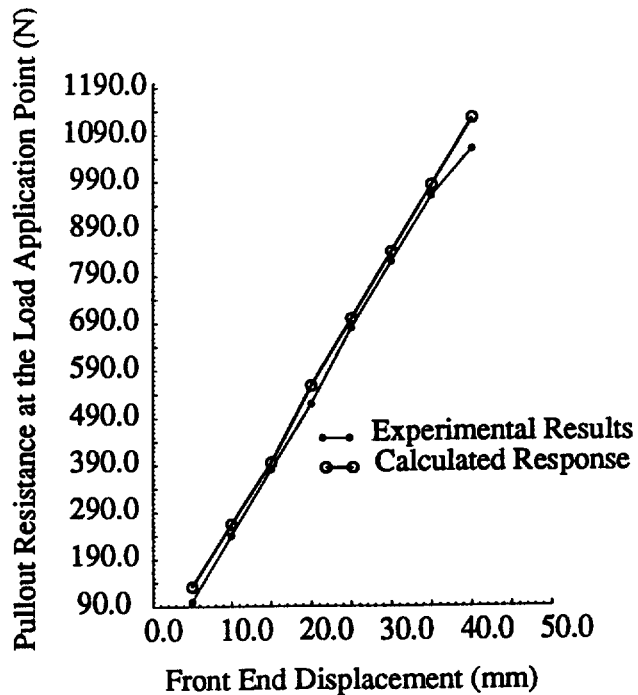
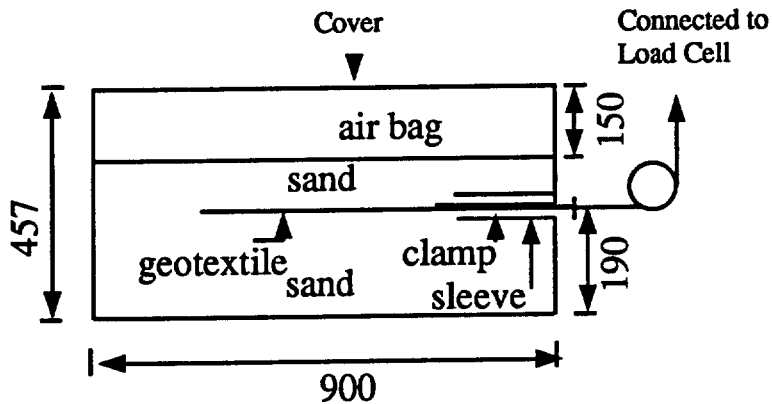


Figure 3. Calculated and Measured Load-Displacement Behavior at the Front End of Geotextile (Element No. 4)



Note: all dimensions are in mm

Figure 2. Experimental Setup

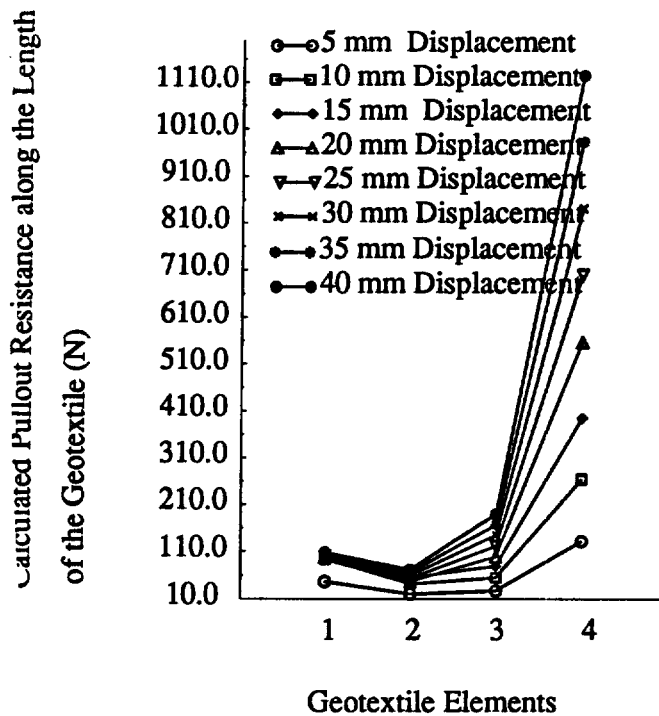


Figure 4. Calculated Pullout Resistance along the Length of Geotextile

From the force-displacement output of GAP elements it was observed that up to 15 mm displacement, all ten GAP elements were sticking to the rod elements and no slip was calculated at the interface. At 15 mm displacement, GAP elements 5 and 10 (both at the load application point) started slipping with kinetic friction. No sliding was observed from the analysis.

Analysis of Fabric Reinforced Sand", Ph.d. Dissertation, 1987, The University of Michigan, Ann Arbor.

Yogarajah, I., and Yeo, K. C., "Finite Element Modeling of Pullout Tests with Load and Strain Measurements", *Geotextiles and Geomembranes*, 13 (1994) pp 43-54

7. SUMMARY AND CONCLUSION

A finite element model was developed to simulate the behavior of a geotextile under pullout load. GAP or friction elements were used to simulate the contact problem at the soil-geotextile interface. Data showed that the model can accurately predict the pullout resistance developed at the front end of the geotextile. Analysis results show that the pullout resistance in the reinforcement increased sharply from element three to element four (at the load application point). This sharp increase in the load response indicate that a nonuniform stress distribution due to a nonlinear stress-strain behavior exists close to tension end of the geotextile. This particular stress-strain behavior can be modeled with localized nonlinear-elastic stress-strain relationship.

From the results of the analysis it can be concluded that, even for the small displacement of 40 mm at the front end of the geotextile, local material non-linearity should be incorporated into the model. GAP element properties should be selected with extreme caution because the performance of the model depends on the correct stick-slip behavior of the gap elements.

8. REFERENCES

Floss, R. and Gold, G., "Use of the FEM for the Single Reinforced Two-Layer System", *Geotextiles, Geomembranes and Related Products*, Den Hoedt (ed.), 1990, Balkema, Rotterdam, ISBN 90 61911192.

Katagiri, T., Haneda, H., Mamoru, M., *Steep Reinforced Embankment Using Geogrid: Laboratory Pullout Test of Geogrid and Its Finite Element Analysis*", *Geotextiles, Geomembranes and Related Products*, Den Hoedt (ed.), 1990 Balkema, Rotterdam, ISBN 90 6191 1192

Mallick, S. B., D. J. Elton., and S. Adanur. An Experimental Characterization of Soil-Woven Geotextile Interface in Large Box Pullout Tests. *Proceedings of Geosynthetics '97*, IFAI, Volume 2, page 927 -940. Wu, Cho-Sen, "Finite Element

Influence of Grid Configuration on Interface Shear Strength Soil/Geogrid Systems

T. Zettler

Research Assistant, Department of Civil and Environmental Engineering, Syracuse University, Syracuse, New York

G. Kasturi

Research Assistant, Department of Civil and Environmental Engineering, Syracuse University, Syracuse, New York

S. K. Bhatia

Chair, Department of Civil and Environmental Engineering, Syracuse University, Syracuse, New York

A.H. Abdel-Rehman

Assistant Professor, National Research Center, English Research Institute, Pilot Laboratory, Dokki, Cairo, Egypt

R. Bakeer

Professor, Department of Civil and Environmental Engineering, Tulane University, New Orleans, Louisiana

ABSTRACT: Despite the increased use of geogrids in modern engineering practice, there is a lack of information on their in-situ performance. The performance of geogrids vary based on manufacturing and design conditions. Each type of geogrid has a different grid configuration or aperture sizes. To assure a sufficient design one should learn about the basic mechanism of soil/geogrid interaction and influence of their configuration on their performance. This paper presents the results of a study of the influence of grid configuration on the direct shear strength of geogrid-soil interfaces. The results demonstrate that there is an optimum configuration which offers the optimum interaction between soil/geogrid. The results of this study have been the basis of development of a new soil/geogrid interface finite element.

KEYWORDS: Friction, Finite Element Analysis, Geogrids, Reinforcement, Shear Strength

1 INTRODUCTION

Over the last two decades, inclusion of geosynthetics in soil reinforcement has greatly increased. Their material properties allow for an increased stability of foundation soils, retaining walls, and many other earth structures. Practical experience coupled with field performance has demonstrated the positive impact of geosynthetic inclusions in regard to economics and stability of the reinforced continuum.

Structures are increasingly built on difficult soils and larger and higher walls are being built; the need for reinforcement mechanisms such as geosynthetics becomes more apparent.

Inclusion of this media in design introduces a tensile strength factor to a soil mass which previously was largely only able to support compressive stresses.

Due to their ability to carry large tensile stresses, geogrids are being used more frequently especially in the design of retaining walls. However, their behavior in shear and pullout conditions is complex and still not clearly understood.

In addition to the adhesion and friction components acting on the interface surfaces of the geogrids with soil, other shear stress components can also affect the

interaction behavior of geogrids. Passive stresses due to the interlocking of soil particles along the cross ribs would definitely influence the measured resistance.

In general, the geogrids offer a three-fold advantage as a reinforcement:

1. offers tensile strength to soil;
2. offers shear resistance due to the friction between the transverse and longitudinal ribs of the grid;
3. offers additional pull-out resistance due to the bearing resistance of the soil interlocked within the grid holes.

When employing a geogrid into a design, there are two potential failure mechanisms:

1. "Bond Resistance Mechanism". The geogrid must be properly anchored into the soil. If there are no provisions made for this, the geogrid would have the potential to "slide out". Then, failure will occur above and below the soil reinforcement interface.
2. "Direct sliding". If the reinforcement interface does not have a large enough interface frictional strength, the soil either above or below the

reinforcement would have the potential to slide along the reinforcement. This occurs when the soil/reinforcement strength is less than that of the actual soil by itself.

Design of geogrids changes according to their function and manufacturing process. Each geogrid may differ in aperture size, configuration, and tensile strength. Geogrids available today have uniaxial or biaxial configurations.

Configuration of the geogrid openings plays an important role in their performance. The ratio of the open space area to the total surface area, dimensions of the openings, and orientation of the openings are some factors that would affect a geogrid performance.

In order to have optimum benefit of geogrids, the designer must have a general knowledge of the characteristics of both the "pullout" and "direct shear" capabilities of the specific geogrid. At the present time, there is little information to be found concerning these capabilities for a general type of geogrid. In addition, there is not enough information on in-situ behavior of geogrids.

To provide a step towards understanding basic understanding of soil-geogrid interaction, this research concentrated on the effects of varying the grid configuration and hole size in a series of direct shear tests while keeping the aperture ratio fairly constant. Thus, any variance seen in the shear strength capability would be a direct result of the configuration alone and is, therefore, indicative of the passive resistance during shearing. Due to time limitation, pullout resistance was not investigated.

As mentioned earlier, it would be impossible to test every possible configuration of geogrids. Currently, work is in progress to create a finite element model which would simulate the various types of soil/geosynthetic interface reactions (Abdel-Rehman 1997). The experimental data presented in this paper has been used to verify the finite element.

The results reported in this paper will be used to verify a numerical interface model and element with more applicable postulates to accurately describe the geogrid performance in a finite element analysis. Once the model has been proven, it can be used to simulate many configurations and situations.

2 LITERATURE REVIEW

Rowe and Fisher (1985) conducted tests concerning both the pullout and shear strength characteristics of geotextiles and geogrids. For testing purposes, a geogrid with openings representing approximately 55

percent of the gross area of the material was used. Thus, the ribs represented 45 percent of the gross area.

In shearing of geogrid/soil, Rowe and Fisher (1985) observed that "the soil adjacent to the geogrid moves relative to both the ribs of the geogrid and the soil in the openings of the ribs". In their research, "recognizing that the rib-soil interface represents approximately 45 percent of the gross area, the apparent friction angle can be determined from:

$$\tan^{-1} (0.45 \tan \phi_{\text{rib-soil}} + 0.55 \tan \phi_{\text{soil}}) \quad (1)$$

where: ϕ = interface friction angle. They observed that in direct shear tests the interface friction angles were similar whether the grid was sheared in the longitudinal direction or the transverse direction ($\phi_{\text{rib-soil}} = 31.5^\circ$). Also, the angle was similar to that of the soil itself ($\phi_{\text{soil}} = 31-32^\circ$).

Reasoning presented for such behavior was that "in direct shear, the entire rib-soil interface and soil-soil interface between ribs is mobilized and hence the apparent friction angle is close to that of the soil". The work by Rowe and Fisher was one of the first to focus on geogrid/soil interaction. However, they did not focus on different configurations of the geogrid. Bergado et al. (1993) also conducted research on geogrid/soil interaction. With geogrids, "the direct shear interaction mode is controlled not only by the friction between the soil and the grid surface but also by the friction of the soil itself" (Bergado et al. 1993). The resistance due to direct shear has two components including the shear resistance between the soil and the reinforcement-plane surface area, and the soil-to-soil shear resistance at the grid opening (Jewell et al. 1984). Jewell et al (1984) and Bergado et al. (1993) also provided understanding on the interaction of soil/geogrids mechanics during shearing. The direct shear resistance can be quantified as:

$$P_s = \sigma_n A [\alpha_{ds} \tan (\delta + (1 - \alpha_{ds}) \tan \phi_{ds})] \quad (2)$$

where: ϕ_{ds} = friction angle of soil in direct shear; δ = skin-friction angle between soil and reinforcement shear surface; α_{ds} = ratio between reinforcement shear area and total shear area; σ_n = normal stress at the shear plane; and A = total shear area.

From this research, Bergado et al. concluded that depending on the apertures of the grid, the shear resistance between the grid and soil can be equal to or larger than the shear resistance of the soil itself (1993).

This added resistance would come from the passive resistance created along the rib interface.

3 SCOPE OF RESEARCH

3.1 Test Apparatus

The device used for direct shear testing was built specifically to test the interface properties of geosynthetics, including geogrids. The equipment consists of a computer, a control panel, and a split shear box. The machine is fully automated and computer controlled and built according to ASTM D5321 standards for direct shear testing.

The control panel is used to operate the split shear box. It displays the normal load being applied by a set of pneumatic pistons located below the shear box. It also displays the horizontal and vertical displacements occurring during the testing. LVDTs are placed in contact with the upper shear box for horizontal displacement measurement and in contact with the loading yoke for vertical displacement measurement. The control panel also controls the rate of shear displacement via a worm gear connected to the lower box.

The split shear box consists of top and bottom parts. The top part, which remains stationary at all times, has the dimensions of 30.5 by 30.5 by 5.1 cm. The bottom part, which is displaced, has dimensions of 40.6 by 30.5 by 5.1 cm. The bottom part is longer than the top part to allow for a larger displacement area. The top and bottom parts are slightly separated to eliminate added friction.

3.2 Soil Properties

Soil used for the testing is a mostly fine grained sand. Properties are as follows: $C_u = 0.45$; $C_c = 1.23$, $d_{10} = 0.52$ mm; $d_{40} = 0.29$ mm; $d_{60} = 0.15$ mm; $\phi_{\text{soil}} = 32.3^\circ$.

3.3 Geogrid Configurations

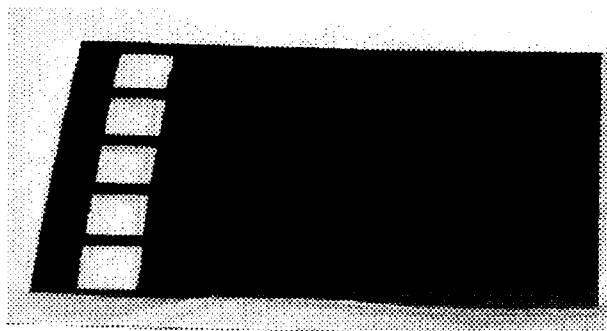
Simulated geogrid sheets were using in the tests. The geogrids are made from samples of high density polyethylene (HDPE) solid sheets (geomembrane). The HDPE is a 60 mil. HDPE sheets were cut to the dimensions of 33 by 47 cm. The different geogrid patterns are then designed and cut into the sheet

Nine patterns were tested. The patterns were determined such that constant opening areas are maintained as much as possible. In doing so, any differences in the results among the different configurations would be a result of additional passive stresses of the new configuration.

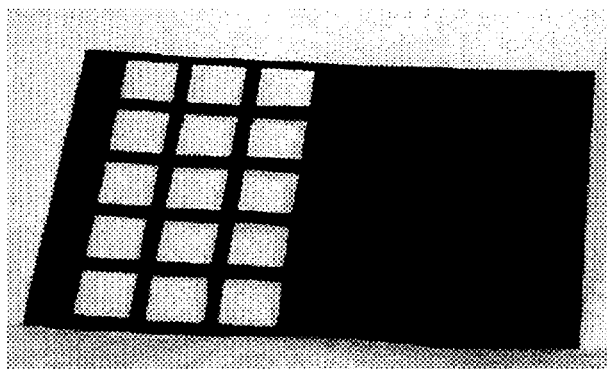
Each hole, independent of the pattern, was cut to be 25 cm². Three different holes sizes are used: Series A (5 by 5 cm), Series B (2.5 by 10 cm), and Series C (4

by 6.4 cm). Each sample of a particular hole size has an increasing number of rows of holes.

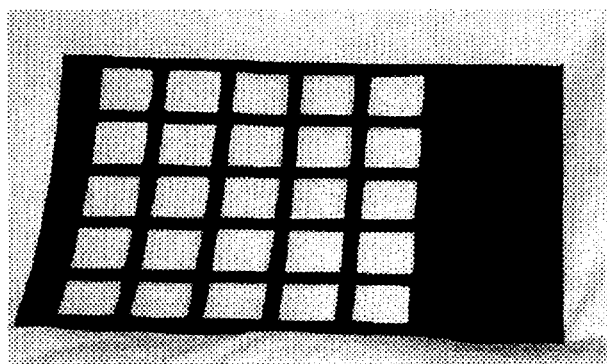
The nine samples were as follows: 5 by 5 cm holes with 1, 3, and 5 rows (Figure 1); 2.5 by 10 cm holes with 1, 2, and 3 rows oriented longitudinally; and 4 by 6.4 cm holes with 2, 4, and 6 rows oriented transversely.



Pattern 1



Pattern 2



Pattern 3

Figure 1. Typical configuration of geogrids (Series A).

4 TESTING PROGRAM

Several tests were performed to ensure the repeatability of the tests. For the geogrids/soil tests the bottom part of the direct shear machine was filled

with sand and tamped by hand for compaction. The geogrid was secured to the bottom part of the machine. Only the end of the geogrid being pulled (closest to the control panel) was securely clamped. This is done to limit stretching of the sample. The opposite end is left free. The top part is then placed on top and filled with sand. Again the sand is tamped by hand. The top part is slightly raised after the addition of the sand to eliminate added friction between the two metal surfaces of the top and bottom parts of the direct shear machine. The loading apparatus is then added to apply the normal load.

Tests were conducted in the dry state. Each test was run at a normal load of 69.64 kPa, representing an average normal stress.

During shearing, the bottom part of the machine is pulled at a displacement rate of one mm/min. Total testing time was approximately one hour with the data acquisition recording performance every minute.

Several experiments were conducted on a pure sheet of HDPE geomembrane (60 mil) to provide a reference for tests on the geogrids. The interface friction angle of the HDPE geomembrane with the same sand used in the rest of the testing was measured to be $\delta_{\text{mb soil}} = 23.5^\circ$.

Each geogrid is tested at least three times while attempting to keep all conditions the same. Figure 2 shows the full set of results of three tests under the same conditions. The subsequent figures represent average values of three identical tests.

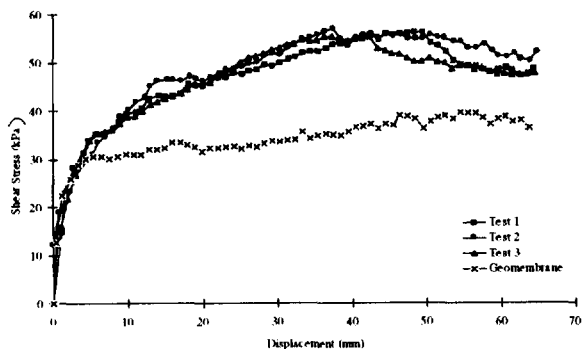


Figure 2. Shear stress vs. displacement (5 by 5 cm holes and 5 rows) (See Figure 1).

As can be seen in Figure 2, results of the three tests are fairly consistent. The slight variations can be attributed to minor differences in normal loading application or set up of the test. For example, the degree of compaction may vary since it is performed manually.

5 TEST RESULTS

The results are presented in Figures 3, 4, and 5, and in these figures each curve represents an average of three tests. Results for the geomembrane are also the average of three tests.

5.1 Geogrid Sample A: 5 by 5 cm Holes

As can be seen below, the holes in the geogrid provided an added component of resistance over the geomembrane (Figure 3). However, it is not until five rows of squares in the geogrid are used that a substantial increase is evident. There is a slight increase in resistance on the membrane for geogrids with one and three holes. The first two patterns did not show a peak in shear strength. This could be due to the thin width of the grid between holes which may have resulted in some stretching during the testing.

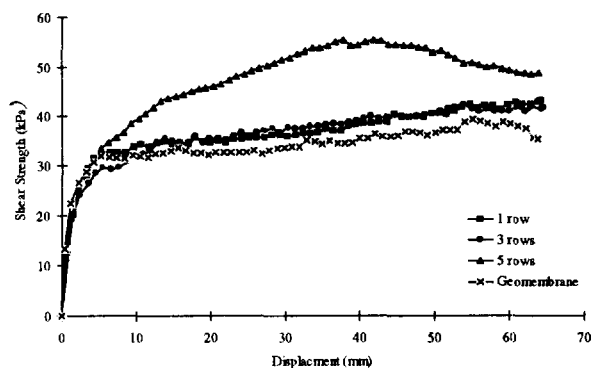


Figure 3. Results of sample A: shear stress vs. displacement (See Figure 1).

5.2 Geogrid Sample B: 2.5 by 10 cm Holes

For this sample, there was a steady increase in the added component of resistance over the geomembrane (Figure 4). However, in all geogrids with one row, there was no real added resistance. It should be noted that as the shearing continued the patterns showed a distinct peak and increase in resilience, however, the residual shear strength for both were very similar. The third pattern with five rows of holes reached and maintained a much larger shear resistance over the membrane.

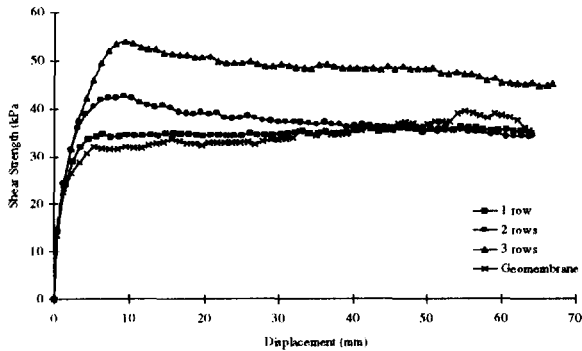


Figure 4. Results of sample B: shear stress vs. displacement.

5.3 Geogrid Sample C: 4 by 6.4 cm Holes

This test showed similar results as for Sample B. However, shear resistance was slightly larger than for Sample B.

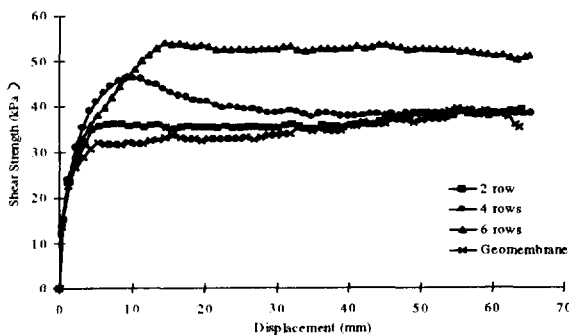


Figure 5. Results of sample C: shear stress vs. displacement.

6 DISCUSSION

All samples (A, B, and C) were prepared such that the aperture ratio stayed approximately similar for the different patterns (Table 1). The aperture ratio is the ratio of the area of the holes to the total area of the sample before cutting.

For the first test of each series (aperture ratio in the range of 8 to 13 percent), there is no noticeable amount of added resistance.

For Series B and C, there is some added resistance as the ratio increased to approximately 25 percent. However, in Series A there was not much of an advantage to increasing the aperture ratio to 25 percent.

Once the ratio increased to 40 percent, there is a significant resistance added by the grid.

The results given in Table 1 demonstrate that the configuration of the grid does have an effect on the shear resistance of the continuum.

Table 1. Calculated Data for the various grid configurations.

Series	Pattern	Aperture Ratio	$\delta_{\text{measured}}^*$	$\delta_{\text{measured}}^{**}$
"A"	1 row	8%	24.3	31.7
	3 rows	24%	25.7	31.4
	5 rows	40%	27.2	38.6
"B"	1 row	13%	24.7	27.3
	2 rows	26%	25.9	31.5
	3 rows	39%	27.1	37.5
"C"	2 rows	13%	24.7	29.2
	4 rows	23%	25.7	33.6
	6 rows	34%	26.7	37.8

Notes: *See equation (1). **See equation (3).

Values for the "apparent" friction angle (δ) were determined using the equation provided by Rowe and Fisher (1985) and given in Table 1. To determine the "measured" friction angle from the test results, the maximum shear stress was obtained for each configuration, assuming cohesion equal to zero:

$$\delta_{\text{measured}} = \tan^{-1} (\tau_{\text{max}} / \sigma) \quad (3)$$

where: σ = normal stress.

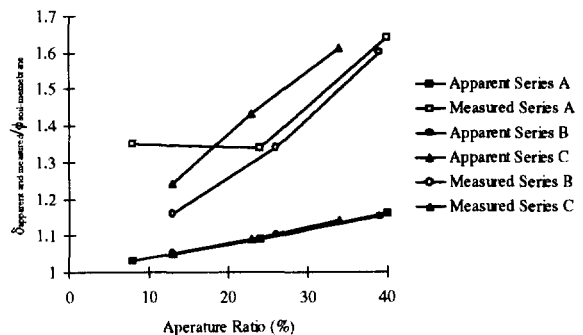


Figure 6. Apparent versus measured friction angles.

Figure 6 shows that the apparent friction angle was always less than the measured friction angle (calculated using equations 1 and 3 respectively). At times, these values may even exceed the interface friction angle of the soil alone. This can be attributed to many factors.

After conducting a test, it was often observed that the sand particles have moved up and long the surfaces of the ribs. This may cause the friction angle

to increase as it would if the membrane were textured in that area.

Also, it was noted that the sand had to move up and then along the ribs before the shearing could occur. This created an almost wave-like pattern on the membrane which offered an extra resistance surface. As the number of holes in a pattern increases, the resistance magnifies creating the large measured friction angle.

It was also observed that holes near the edge of the pattern did not contribute as much resistance as did the holes in the center. Thus, when patterns were tested with holes only in the center there is a large increase in measured resistance. To verify this, a pattern was cut in which one row of square holes (50 by 50 cm) was placed only in the center of the grid (see results in Figure 7).

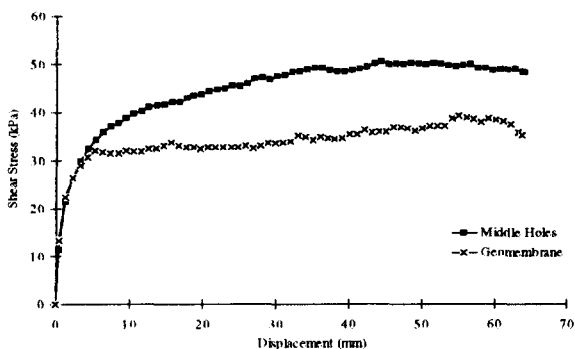


Figure 7. Testing with one row of squares in center of grid: shear stress versus displacement.

As can be seen when comparing results of Figures 3 and 7, the maximum resistance obtained was greater when the holes were in the center. This indicates that more resistance is generated by the center holes.

In the case of Series A (Figure 1), the ribs between the holes were relatively thin. Some stretching or twisting may have occurred during shearing. This may explain the lack of a defined peak shear strength in the first two patterns in the series (Figure 3). Because of the lack of a definite peak value, it is difficult to evaluate the measured friction angle accurately.

This being the case, it appears that Series C offered the most benefit, since the apparent friction angles versus measured are the most similar.

This research provides a basic study on the mechanisms of geogrids/soil. The results are being used by Tulane University to test and verify a finite element model being developed (Abdel-Rehman, 1997). In order to develop such a model, basic test results such as this one are necessary for verification. Ongoing research is being conducted in this field by

the two universities involved in this research. It is promising that the model will allow for even more definite results of a most suitable configuration of geogrid based on actual design criteria.

7 CONCLUSION

The results presented show that grid patterns, location, and aperture ratio significantly influence interface frictional resistance. The following general conclusions can be determined:

1. Grid configuration plays a vital role on the shear strength capability of a geogrid. Certain configurations provide larger amounts of passive resistance over other patterns.
2. The results of this study has been used as a basis of a finite element program being developed for modeling soil-structures reinforced with geosynthetics.

ACKNOWLEDGMENTS

The writers would like to thank those individuals who helped with this research. Especially, we would like to thank Ms. Kristen Refkofsky for the many hours spent on testing geogrids.

REFERENCES

- Abdel-Rehman, A. (1997) "Modeling of Soil/Geosynthetic Interaction in Reinforced Earth Works", *Ph.D. Dissertation*, Civil Engineering, Tulane University.
- Alfaro, M.C., Hayashi, S., Miura, N. and Watanabe, K. (1995) "Pullout Interaction Mechanism of Geogrid Strip Reinforcement", *Geosynthetics International*, Vol. 2, No. 4, pp. 679-698.
- Bergado, D.T., Chai, J.C., Abiera, H.O., Alfaro, M.C. and Balasubramaniam, A.S. (1993) "Interaction between Cohesive-Frictional Soil and Various Grid Reinforcements", *Geotextiles and Geomembranes*, Vol. 12, pp. 327-349.
- Jewell, R.A., Milligan, G.W.E., Sarsby, R.W. and Dubois, D. (1984) "Interaction between Soil and Geogrids", *Proceedings of Symposium on Polymer Grid Reinforcement*, Thomas Telford Ltd., London, pp. 18-19.
- Rowe, R.K., and Fisher, D.G. (1985) "Determination of Soil-Geotextile Interface Strength Properties", *2nd Canadian Symposium on Geotextiles and Geomembranes*.

Soil Interaction Characteristics of Geotextiles and Geogrids

M. Koutsourais
Regional Manager, TC Mirafi, USA

D. Sandri
Senior Engineer, TC Mirafi, USA

R. Swan
GeoSyntec Consultants, USA

ABSTRACT: Geosynthetic design in soil reinforcement applications require that the soil interaction characteristics of the reinforcement product be evaluated. The soil interaction characteristics are determined by performing direct shear and pullout tests under a specific soil condition and range of normal pressures. Polymeric reinforcement products used in soil reinforcement applications consist of geotextiles and geogrids which vary in texture, flexibility and open area. This paper presents soil interaction data of geotextiles and geogrids in both cohesionless and cohesive soil types. The data is used to compare soil interaction properties for various geosynthetic reinforcement products in both cohesionless and cohesive soils. Results indicate that geogrids and geotextiles offer similar soil interaction values. Interaction coefficients range from 0.9 to 1.0 in sands and from 0.6 to 0.9 in clays depending on geosynthetic surface texture, stiffness and applied normal stress.

KEYWORDS: Friction, Geogrids, Geotextiles, Pull-out resistance, Pull-out test, Reinforcement, Shear strength, Woven fabrics

1 INTRODUCTION

Geogrids and geotextiles are often used to construct reinforced retaining walls, steepened slopes, embankments on soft foundations, vertical landfill expansions, and soil veneer covers of landfills. However, a generally accepted but incorrect belief exists among Civil engineering professionals that geogrids interact or interlock with the soil being reinforced better than do geotextiles such as woven polyester fabrics. As a result, geogrids are often chosen over equally well-suited geotextiles. In order to curtail such mis-selection of materials and encourage accurate selection of design parameters, the interaction between the soil and the geosynthetic reinforcement must be evaluated.

Today, soil reinforced structures are designed with a variety of geosynthetics and soil types. The soil interaction characteristics between various geosynthetics and fine grained (clay) soils becomes increasingly important as more and more reinforced soil structures are designed with marginal (cohesive) fill materials and various types of geotextiles and geogrids. As a result, quantifying the soil interaction characteristics between these materials and developing design values for various soil and geosynthetic combinations is essential.

In keeping with current state-of-practice design references (AASHTO (1992), Christopher et. al. (1990), Simac (1993)), minimum anchorage lengths (L_a) may vary from 0.3 to 1 meter (1 to 3 ft). The actual required embedment length is a function of the amount of effective overburden (i.e. depth of reinforcement), soil type above and below the

geosynthetic, and the interaction properties between the soil and geosynthetic.

Many researchers (Batt (1991), Cowell (1993) Geoservices (1990), Ingold (1983), Jewell (1980), Juran (1988), Koerner (1986), O'Dowda (1987), Palmeira (1990), Rowe (1985), Swan (1987)) have investigated the soil interaction characteristics between geosynthetics and sand. Cowell and Sprague (1993) presents a comparative study of pullout data and soil interaction values between woven polyester geogrids and high-strength, high-modulus polyester geotextiles in a uniform fine sand. The results presented by Cowell and Sprague (1993) and of previously published research show that geogrids and geotextiles provide similar soil interaction coefficients in sand between 0.90 and 1.0.

To supplement the research documented by Cowell and Sprague (1993) and others, direct shear testing of various high-strength polyester and polypropylene geotextiles in sand was conducted as well as both direct shear and pullout testing of polyester geogrids and high-strength polyester and polypropylene geotextiles in a lean clay. The data can be used to compare the results obtained by direct shear and pullout testing for determination of the coefficient of interaction. The data can also be used to compare the soil interaction properties of various geosynthetic reinforcement products and to develop recommended design soil interaction properties in different soil conditions.

2 TESTING CONCEPTS, AND TYPICAL RESULTS

2.1 Purpose

The direct shear and pullout tests measure the total resistance to sliding and pullout of a geosynthetic with a soil substratum and superstratum. Total sliding and pullout resistance may be a combination of sliding, rolling, interlocking of soil particles and geosynthetic surfaces, and shear strain within the geosynthetic specimen. The data developed can be used in the design of geosynthetic-reinforced retaining walls, steepened slopes, and embankments constructed on weak foundation soils. The data is also useful for applications in which the geosynthetic is subject to sliding such as applications which require the geosynthetic to be placed on a slope and for determination of geosynthetic overlap requirements.

The interaction developed between the soil and the geosynthetic is determined by performing direct shear and pullout tests under various soil types and a range of normal pressures. The data obtained is used to determine the coefficient of shear-stress-interaction, C_i , which measures a reinforcement product's efficiency in transferring stresses from adjacent soil particles to the geosynthetic reinforcement. The coefficients are simply the percentage of the internal shear strength of the soil that can be mobilized at the soil/geosynthetic interface as shown by equation (1).

$$C_i = \tau_i / \tau_s = (c_a + \sigma_n \tan \delta) / (c + \sigma_n \tan \phi) \quad (1)$$

where:

- τ_i = shear stress at interface
- τ_s = shear stress of soil
- δ = interface friction angle
- ϕ = internal friction angle of soil
- c_a = interface adhesion
- c = soil cohesion
- σ_n = normal soil pressure

The coefficient of interaction is used in reinforced soil structure design to determine required reinforcement embedment lengths beyond the anticipated failure plane to prevent pullout of the reinforcement. A commonly accepted method of calculating this embedment length beyond the failure plane, l_a , is indicated by equation (2).

$$l_a = (P \times FS_{po}) / (2 C_i (c + \sigma_n \tan \phi)) \quad (2)$$

where:

- P = Pullout force per unit length of reinforcement
- FS_{po} = Design factor-of-safety with respect to pullout

The coefficient of soil and geosynthetic interaction can be expressed only in terms of the soil used in testing and is a function of the applied normal stress, soil gradation,

plasticity, in-place density, and moisture content, as well as the unique physical and mechanical characteristics of the geosynthetic. However, it is useful for design guidance to be able to characterize C_i values by geosynthetic and soil "type".

2.2 Direct Shear

The direct shear test used to determine the shear resistance of a soil/geosynthetic combination is ASTM D5321-92, "Standard Test Method for Determining the Coefficient of Soil and Geosynthetic or Geosynthetic and Geosynthetic Friction by the Direct Shear Method". The coefficient of friction between a geosynthetic and soil is determined by placing the geosynthetic and one or more contact surfaces, such as soil, within a direct shear box. A constant normal stress is applied and a tangential (shear) load is imposed on the apparatus such that one section of the box moves in relation to the other. Shear loading is applied via a 10 cm/min (0.04 in/min) constant rate device capable of measuring load.

The shear force is recorded as a function of the horizontal displacement of the moving section of the shear box. The test is performed for a minimum of three different normal stresses. The peak and/or residual shear stress is plotted against the applied normal stresses with the test data represented by a "best fit" straight line whose slope is the coefficient of friction between the two materials where the shearing occurred. The y-intercept of the straight line provides the 'adhesion' as measured by the test.

2.3 Pullout

The general test method used to determine the pullout resistance of a geosynthetic in soil is GRI GG-5/GT-6 - "Geogrid/Geotextile Pullout". The pullout test is performed by compacting soil in the lower half of the pullout box with subsequent placement of the geosynthetic specimen on top of the compacted soil and attached to a loading harness. The soil is then compacted in the upper half of the pullout box. The specific normal stress is applied to the upper layer of compacted soil through the use of a rigid loading platen and dead weight for the normal stress or through the use of an air bladder loading system. After application of the normal stress, the pullout specimen is immediately subjected to a 10 cm/min (0.04 inch/minute) constant rate of extension "pullout" force. Pullout displacement continues until a constant or decreasing load is recorded or the geosynthetic sample fails in rupture. Tests which fail in rupture would require re-doing at lower normal stresses in order to induce slippage and hence measurement of resistance to sliding.

The pullout force is recorded as a function of the horizontal displacement of the pullout specimen. The test is performed for a minimum of two different normal stresses. The peak pullout force is plotted against the applied normal stresses used for testing. The coefficient of interaction, C_i ,

is back-calculated using equation 3.

$$C_i = (P)/(2 I_a (c + \sigma_n \tan \phi)) \quad (3)$$

3 TEST PROGRAM

3.1 Geosynthetic Types

The reinforcement products chosen for this research consist of a woven polypropylene geotextile (W, PP, GT), woven polyester geotextiles (W, PET, GT) and polyester geogrids (W, PET, GG). Table 1 summarizes the geosynthetic types investigated.

Table 1. Summary of Geosynthetic Materials Investigated

P r o d	Type ¹	Weight, g/m ² (osy)	Ultimate strength, kN/m (lbs/ft)	Weave
A	W, PP, GT	420 (12)	70 (4800)	twill
B	W, PET, GT	440 (13)	105 (7200)	plain
C	W, PET, GT	680 (20)	200 (13800)	twill
D	W, PET, GT	950 (28)	300 (20580)	basket
E	W, PET, GG	186 (5.5)	39 (2700)	knitted
F	W, PET, GG	390 (12)	109 (7460)	knitted

¹W = woven, PET = polyester, PP = polypropylene, GT = geotextile, GG = geogrid

The products were chosen based on their different structure, weave pattern and polymer type. This range of products also compliments the matrix of products tested and presented by Cowell and Sprague (1993). They ranged in ultimate tensile strength from 73 kN/m (5000 lbs/ft) to 364 kN/m (25000 lbs/ft).

The woven polypropylene geotextile evaluated in the program is characterized as being relatively stiff, having a rough surface texture and exhibiting a low percent open area (<30%). The woven polyester geotextiles evaluated are characterized as being flexible, having a smooth surface texture and exhibiting a low percent open area. The coated polyester geogrids evaluated are characterized as being flexible with a high percent open area (>30%). The samples tested cover a range of weights, tensile strengths and weave patterns as noted in Table 1 for detailed evaluation and comparison.

3.2 Soil Types

The two soil types tested in conjunction with the geosynthetic products referenced above include a uniform fine sand (SP) and a lean clay with sand (CL). Figure 5 illustrates the gradations of the two soil types.

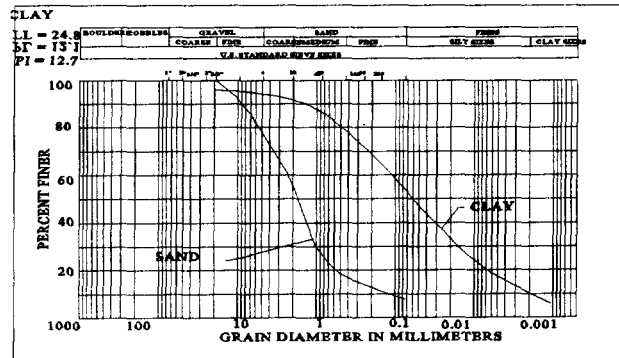


Figure 5. Soil Gradation Curves

3.3 As-tested soil properties

A modified proctor was performed on the sand in accordance with ASTM D1557. The maximum dry density was determined to be approximately 18.4 N/m³ (117 pcf) at an optimum moisture content of 8.8%. Post test evaluations indicated an average 94% of maximum dry density at an average moisture content of 17.4% had been achieved.

The clay soil used for direct shear and pullout testing had a liquid limit (LL) = 24.8; plastic limit (PL) = 12.1; plasticity index (PI) = 12.7; maximum dry unit weight of 18.6 N/m³ (118.5 pcf); and optimum moisture content of 12.5%. The clay was moisture conditioned for compaction to 95% of the maximum dry unit weight and 1% dry of the optimum moisture content based on ASTM D698.

3.4 Matrix of Test Conditions

Tables 2 and 3 summarize the program matrix and conditions for direct shear and pullout testing, respectively. All direct shear samples were 30.5 cm wide by 30.5 cm long.

Samples used in pullout testing are noted below. Pullout samples had dimensions of 45.7 (wide) by 91.5 (long) cm. An exception to the above was in test number 1 where the sample was 46.5 cm by 92.7 cm.

Table 2. Summary of Direct Shear Test Conditions

Test no.	Soil type	P r	Initial soil conditions ¹		Normal stress (Pa)
			γ_d , kN/m ³	ω , (%)	
1	Sand	A	17.2	17.4	34, 69, 103
2	Sand	B	17.2	17.4	34, 69, 103
3	Sand	C	17.2	17.4	34, 69, 103
4	Clay	A	17.5	11.5	14, 28, 55
5	Clay	B	17.5	11.5	14, 28, 55
6	Clay	D	17.5	11.5	14, 28, 55
7	Clay	E	17.5	11.5	14, 28, 55
8	Clay	F	17.5	11.5	14, 28, 55

¹ γ_d = Dry unit weight, ω = water content

Table 3. Summary of Pullout Test Conditions

Test no.	Soil type	P r	Initial soil conditions ¹		Normal stress (Pa)
			γ_d , kN/m ³	ω (%)	
1	Clay	A	117.5	11.5	14, 28
2	Clay	B	117.5	11.5	14, 28, 55
3	Clay	C	117.5	11.5	28, 55
4	Clay	D	117.5	11.7	7, 14
5	Clay	E	117.5	11.4	28, 55

¹ γ_d = Dry unit weight, ω = water content

4 RESULTS

A summary of the direct shear results in sand (TRI, 1995) is shown in Table 4. Soil interaction coefficients via direct shear testing range between 0.92 and 1.0.

A summary of the direct shear and pullout test results in clay (GeoSyntec, 1996) are shown in Tables 5 and 6, respectively.

The soil interaction coefficients for the flexible polyester geotextiles and geogrids range from 0.71 to 0.93 in direct shear and from 0.82 to 0.91 in pullout under the full range of normal stresses tested. The soil interaction coefficients for the woven polypropylene geotextile range from 0.58 to 0.64 in direct shear and 0.66 to 0.71 in pullout.

Table 4. Summary of direct shear results in sand - peak sliding resistance (N/m²) vs normal stress

Test No.	Soil	P r	Normal Stress, Pa			Friction angle, δ	C _i
			34	69	103		
	C/S ¹	-	26	44	65	32 °	-----
1	Sand	A	25	44	61	30 °	0.9
2	Sand	B	38	65	92	32 °	1.0
3	Sand	C	35	55	78	32 °	1.0

¹ C/S = Control Sand

4.1 Interpretation of results

The results demonstrate that direct shear and pullout testing in sand will yield similar soil interaction coefficients for all geosynthetic types tested. These values are typically in excess of 0.90 and provide good agreement with results of pullout testing presented by Cowell and Sprague (1993) on similar products.

Similar results which demonstrate high sand-geosynthetic action values are abundant in the literature. No significant correlation appears to exist between percent open area, reinforcement geosynthetic texture, its stiffness or other such properties. All reinforcement geosynthetics seem to do well in sand.

Results of direct shear testing in clay provide interaction values ranging from 0.71 to 0.93 for polyester products and somewhat lower values of 0.58 to 0.64 for polypropylene product A. The results demonstrate a lack of correlation between interaction behavior and percent open area or geosynthetic structure. However, the data suggests superior polyester performance when compared to polypropylene. In fact, the high-strength polyester geotextiles provide interface shear strengths as great as the internal shear strength of the soil itself. Further, the peak interface shear strengths were all mobilized at approximately the same displacement (5 cm) as was the peak strength of the soil itself. Good compatibility exists between each geosynthetic type and sand.

In general, the results of pullout testing in clay are in agreement with those noted above for direct shear testing in clay.

Compared to direct shear results, pullout testing provides approximately 13% to 17% higher soil interaction values at low normal stresses of less than 20 Pa (< 4 psi) and essentially the same soil interaction values at higher normal stresses (>28 Pa (4 psi)).

The flexible polyester geosynthetics provide approximately 25% higher soil interaction values when compared to the stiff woven polypropylene geotextile. The

woven polyester geotextiles provide similar soil interaction values when compared to the geogrids.

Observations from the test results indicate that the percent open area of the geosynthetic has negligible, if any, influence on the soil interaction coefficients in clay. However, the surface texture and stiffness or rigidity of the geosynthetic has a significant effect on the soil interaction within clay. The geotextile weave pattern has negligible, if any, effect on the soil interaction characteristics of the geotextile.

5 DESIGN RECOMMENDATIONS

Table 7 provides soil interaction coefficients for use in conservative design of reinforced soil structures. Values are subject to verification testing during construction.

The results provided herein and found in the literature suggest that relatively high interaction values can be confidently employed with all reinforcement geosynthetics irrespective of texture, percent open area or polymer type. An interaction coefficient in sand of 0.9 is recommended.

Greater variability is observed in interaction testing in clay. Test results incorporating polyester reinforcement geosynthetics range from 0.7 to 0.9+. Therefore, a

conservative guidance value of 0.7 appears to be reasonable.

A slightly lower design interaction value of 0.6 is recommended for polypropylene products used in clay.

Design values recommended above range from 0.6 to 0.9 with values used for critical structures being verified by actual soil-geosynthetic testing during construction. However, it is also recommended that validation testing during construction be required on a selective basis with great consideration for its true impact on design. A parametric study of most reinforcement applications will demonstrate that the greatest factor affecting required embedment length is normal stress (i.e. reinforcement depth), not C_i . In practice, its affect on structure design and performance is only significant in the upper portions of reinforced soil structures. In fact, once below a depth of about 1 m (3 ft), the embedment length of most commonly marketed reinforcement geosynthetics is governed by minimum embedment length criteria rather than C_i or pullout.

Recognizing the true impact of soil-geosynthetic interaction for each design scenario will guide the designer in evaluating whether to use the above recommended values or require testing during construction.

Table 5. Summary of Direct Shear Results in Clay - Peak Sliding Resistance (N/m^2) vs. Normal Stress (psi)

Test No.	Soil	Product	Normal Stress, Pa			Adhesion, c_a (N/m^2)	Friction Angle, δ	C_i
			14	28	55			
	Control Clay	---	16.5	28.2	49.6	6211	38	-----
4	Clay	A	9.6	17.2	31.7	1911	28	0.58 - 0.64
5	Clay	B	11.7	22.0	44.1	477	38	0.71 - 0.89
6	Clay	D	13.1	24.1	46.2	1911	39	0.79 - 0.93
7	Clay	E	13.1	22.7	43.4	2388	37	0.79 - 0.88
8	Clay	F	13.8	23.4	44.6	3822	36	0.83 - 0.89

Table 6. Summary of Pullout Test Results - Ultimate Pullout Capacity (N/m) vs. Normal Stress

Test No.	Soil Type	Product	Normal Stress, Pa				C_i
			7	14	28	55	
1	Clay	A		20,030	36,400		0.66 - 0.71
2	Clay	B		25,500	45,500		0.82 - 0.91
3	Clay	D			45,500	80,200	0.88 - 0.90
4	Clay	E	17,800	27,400			0.83 - 0.89
5	Clay	F			44,600	78,700	0.87

Table 7. Recommended Design Soil Interaction Coefficients

Product	Sand	Clay	
		PET	PP
Rough textured, stiff PP GT	0.9	--	0.6-0.7
Smooth textured, flexible PET GT and GG	0.9-1.0	0.7-0.9	--
Recommended value	0.9	0.7	0.6

REFERENCES

AASHTO Interim Specifications (1992), "Standard Specification for Highway Bridges", Fourteenth Edition, 1989 as amended by the Interim Specification.

ASTM (1996), "Standard Test Method for Determining the Coefficient of Soil and Geosynthetic or Geosynthetic and Geosynthetic Friction by the Direct Shear Method", Volume 04.09.

ASTM, Draft Standard Test Method D 35.01.87.02, "Measuring geosynthetic Pullout Resistance in Soil".

Batt, D. and Bowers, M. (1990), "Preliminary Report of Pullout Testing of Miragrid 5T in Sand in the University of Cincinnati Pullout Box", May.

Christopher, B.R., Safdar, A.G., Giroud, J.P., Juran, I., Mitchell, J.K., Schlosser, F., and Dunncliff, J., (1990), Reinforced Soil Structures, Volume I. Design and Construction Guidelines, FHWA-RD-89-043, November.

Cowell, M.J. and Sprague, C.J. (1993), "Comparison of Pull-Out Performance of Geogrids and Geotextiles", Geosynthetics, '93 Conference, Vancouver, BC, Canada, pp. 579-592.

GeoServices, Consulting Engineers, Inc. (1990), "Pullout and Interface Direct Shear Testing of Miragrid 7T Geogrid and Perini Project Number 126", May, Norcross, GA.

GeoServices Consulting Engineers, Inc. (1990), "Pullout Testing of Selected Mirafi Geogrids", GeoServices Project No. P1268, April, Norcross, GA.

GeoSyntec Consultants, Inc. (1996), "Nicolon/Mirafi Geogrid and Geotextile Direct Shear and Pullout Testing within Compacted Clay Soil", Draft Report No. GLI3839.

Geosynthetic Research Institute (1991), "Test Method for Geogrid Pullout", GG5.

Geosynthetic Research Institute (1992), "Test Method for Geotextile Pullout", GT6.

Ingold, T.S. (1983), "Laboratory of pull-out testing of geogrid reinforcements in sand", Geotechnical Testing J., ASTM, 6(3), pp. 101-111.

Jewell, R.A. (1980), "Some effects of reinforcement on the mechanical behavior of soil", Thesis presented to Cambridge University, Cambridge, UK, in partial fulfillment of the requirements for the Degree of Doctor of Philosophy.

Juran, I., and Chen, C.L., (1988) "Soil-Geotextile Pull-out Interaction Properties: Testing and Interpretation", Proceedings of the TRB 67th Annual Meeting, January 11-4, 1988, Paper No. 870159, pp. 38

Juran, I., Knochenmus, G., Acar, Y.B. & Arman, A. (1988), "Pull-out response of geotextiles and geogrids", Proc. Symp. on Geosynthetics for Soil Improvement, ASCE, Nashville, USA, Geotechnical special publication No. 18, pp. 92-111.

Koerner, B. (1986), "Direct shear/pull-out tests on geogrids", Report No. 1, Department of Civil Engineering, Drexel University, USA.

O'Dowda, C.S. and Barratt, D.A. (1987), "Field Pull-Out Tests on Geogrids", Ground Engineering Division Structures Dept., Transport and Road Research Laboratory, Crowthorne, Berkshire.

Palmeira, E.M., and Milligan, G.W.E., (1990) "Large Scale Pull-out Test on Geotextiles and Geogrids", 4th International Conference on Geotextiles Geomembranes and Related Products, Vol. 2, pp. 743-746.

Rowe, R.K., Ho, S.K. & Fisher, D.G. (1985), "Determination of soil-Geotextile Interface Strength Properties" Second Canadian Symp. on Geotextiles, pp. 25-34.

Simac, M.R., Bathurst, R.J., Berg, R.R., Lothspeich, S.E. (1993), Design Manual for Segmental Retaining Walls, National Concrete Masonry Association, First Edition, Herndon, VA.

Swan, R.H., (1987) "The Influence of Fabric Geometry on Soil/Geotextile Shear Strength", Geotextiles and Geomembranes, 6, pp. 81-87.

TRI Environmental, Inc. (1995), "Test Results for Interface Friction Tests", TRI Log No. E3001-70-09, Test Dates 6/24-29/1995, June.

Performance of Geotextile-Reinforced Embankment on Soft Bangkok Clay

D.T. Bergado and P.V. Long

Professor and Research Associate, School of Civil Engineering, Asian Institute of Technology, Bangkok, Thailand.

P. Delmas and K.H. Loke

Polyfelt/Bidim Geosynthetics, Bezons, Cedex, France and Polyfelt Sdn. Bhd., Kuala Lumpur, Malaysia.

N. Miura

Professor and Director, Institute of Lowland Technology, Saga University, Saga 840, Japan.

ABSTRACT: Three full scale test embankments were constructed to failure on soft Bangkok clay. One of the embankments was unreinforced and served as control embankment. The second embankment was reinforced with multi-layer reinforcements consisting of four layers of low strength nonwoven geotextiles. The third embankment was reinforced with one layer of high strength (200 kN/m ultimate strength) nonwoven/woven geotextile at the base. The test embankments were constructed using silty sand and were fully instrumented. The geotextile reinforcements were also instrumented to measure their deformations. Back-analyses were made using the limit equilibrium method. The primary failure occurred at the same deformation as the unreinforced embankment during the bearing capacity failure in the foundation. Just prior to this stage, the limiting strain in the geotextile can be taken equal to the critical strain at 3% and the direction of the reinforcing force can be taken as horizontal. The secondary failure occurred at the embankment collapse coinciding with the rupture of the reinforcement and the limiting strain can be taken as the sum of the critical strain during primary failure and localized strain during secondary failure and the direction of the reinforcing force can be taken as bisectonal. The results confirmed the existence of soil/geotextile composite behavior that modified the soil shear strength at the intersection of the failure plane and geotextile reinforcement. Consequently, the respective collapse heights of the multi-layer and high-strength geotextile-reinforced embankments were 1.1 and 1.6 times the unreinforced embankment.

KEYWORDS: Geotextiles, Nonwoven fabrics, Reinforcements, Embankments, Soft soils

1 INTRODUCTION

In this paper, the performances of 3 full scale test embankments, constructed on soft Bangkok clay, have been described and analyzed. All three test embankments have been built to failure. The unreinforced embankment served as control embankment and was designated as CE embankment. The second embankment, designated as MGE embankment, was reinforced with 4 layers of low strength, nonwoven, needle-punched geotextile consisting of one layer of TS700 (280 g/m² and ultimate strength of 19 kN/m) and 3 layers of TS420 (130 g/m² and ultimate strength of 9 kN/m). The third embankment, the HGE embankment, was reinforced with one layer of high-strength, woven/ nonwoven (composite) geotextile (PEC 200) with nominal mass of 700 g/m² and ultimate strength of 200 kN/m. The geotextile instrumentations and preliminary theoretical analyses have been published previously (Bergado et al, 1994; Loke et al, 1994). The objectives of this paper are to present, evaluate, and analyze the performances of all 3 test embankments based on the measured and monitored data and subsequent theoretical back-analyses using the limit equilibrium method (LEM). Most of the data and results presented in this paper were derived from the work of Long (1997) under the supervision of the first author.

2 SITE CONDITION AND SOIL PROFILE

The layout of the test embankments is given in Figure 1. The embankment designations CE, MGE, and HGE have been defined previously. Two boreholes down to 12 m depth and 6 field vane tests down to 10.5 m depth were done. The locations of boreholes and vane tests are also shown in Figure 1. Continuous Shelby tube (inside diameter = 0.075 m) samples were obtained from the boreholes while undrained shear strength at 0.50 m intervals were obtained from the vane tests. The generalized soil profile and soil properties are presented in Figure 2. The uppermost 11 m in the soil profile can be divided into 3 sublayers. The weathered crust forms the topmost 2 m thick sublayer consisting of heavily overconsolidated reddish-brown clay. This sublayer is underlain by a soft, grayish clay sublayer down to about 8 m depth with natural water content varying from 60 to 80%. The medium stiff clay sublayer with silt seams and fine sand lenses can be found from 8 to 11 m depth. The liquid limit of the soft clay ranges from 70 to 102% and the plasticity index is about 60%. The groundwater level at the test site varied seasonally from 0.50 m depth in the rainy season to 1.50 m depth in the dry season. The undrained shear strength from field vane test are also given in Figure 2.

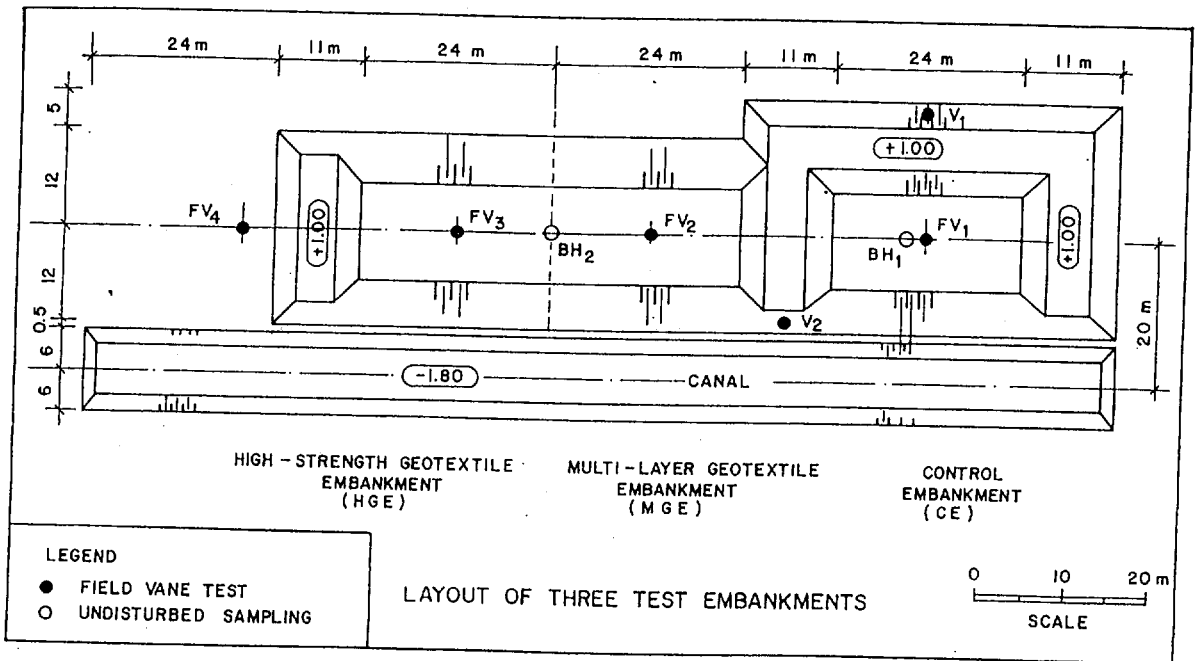


Figure 1. Layout of test embankments with locations of field investigations.

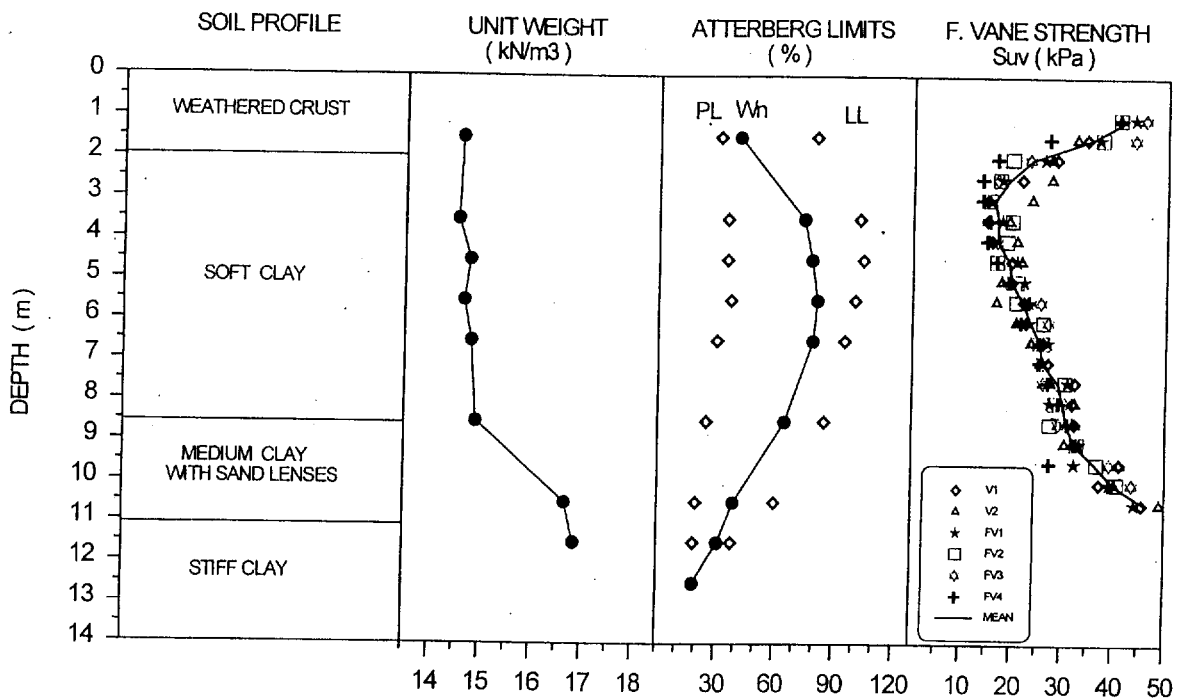


Figure 2. General soil profile and soil properties at the site.

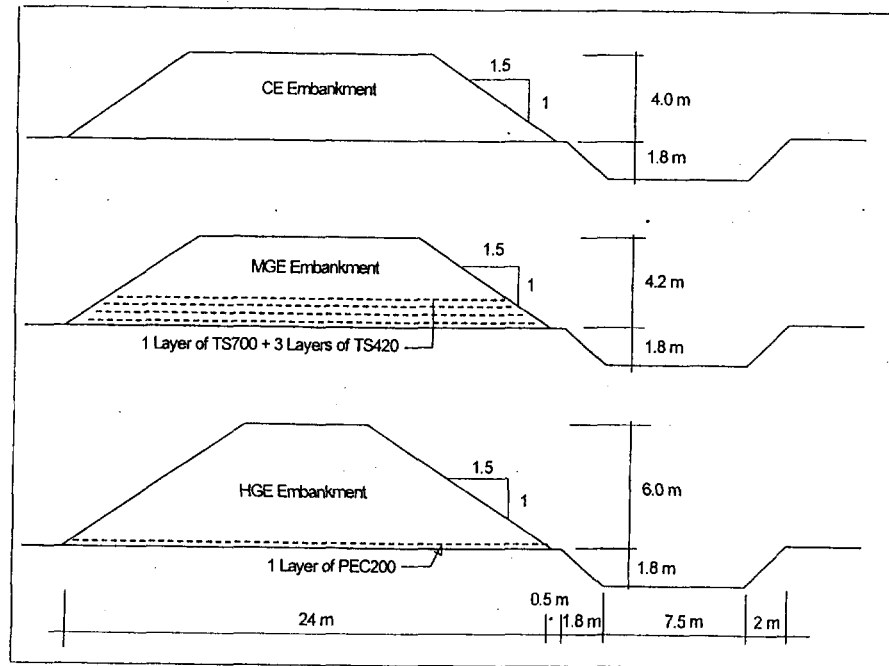


Figure 3. Cross-sections of three test embankments.

3 EMBANKMENT DESIGN AND INSTRUMENTATIONS

The cross-sections of the three test embankments are given in Figure 3. All embankments were designed with side slopes of 1V to 1.5 H. A canal was excavated to 2 m deep and 7.5 m wide along the toe of the test embankments to reduce the volume of fill required to reach failure and to ensure that the failure will occur in the canal side.

The silty sand, widely used locally for highway construction, was utilized as embankment material. Using standard Proctor compaction, the maximum dry density and optimum moisture content were obtained as 18 kN/m³ and 10%, respectively. The failure envelopes from large (shearing area = 0.54 m²) and conventional (shearing area = 0.0032 m²) shear box tests for the embankment material compacted to 95% of standard Proctor compaction with water contents of 9.5% and 13.0% are plotted in Figure 4. The conventional and large shear box test results correspond to peak and critical state strength parameters, respectively.

The foundation instrumentation of MGE and HGE embankments is presented in Figure 5. The same instrumentation system was used for CE embankment except for surface settlement, S2, and standpipe piezometers SP4, SP5 and SP6. The instruments consisted of piezometers, surface and subsurface settlement plates, and inclinometers for measuring pore pressures, vertical settlements and lateral displacements, respectively. The displacements in the geotextiles reinforcements were measured by wire extensometers, Glotzl extensometers, and 100 mm long special strain gages (Figure 6).

4 EMBANKMENT CONSTRUCTION TO FAILURE

Before the embankment construction, the ground surface was cleared by excavating to 0.20 m depth and levelled. Then, the canal was excavated. Immediately, thereafter, the control embankment (CE) was constructed in layers with compaction lift thickness of 0.30 m. The sequences of embankment construction are shown in Figure 7. Very small deformations were observed at embankment height lower than 2.50 m. The magnitudes and rates of vertical settlements as well as the lateral movements increased significantly when the embankment height exceeded 3.5 m corresponding to 65 kPa embankment loading. The CE

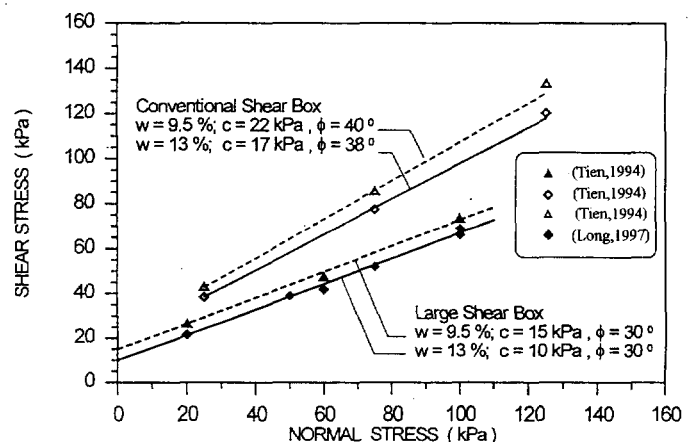


Figure 4. Failure envelopes of embankment fill from conventional and large scale direct shear tests.

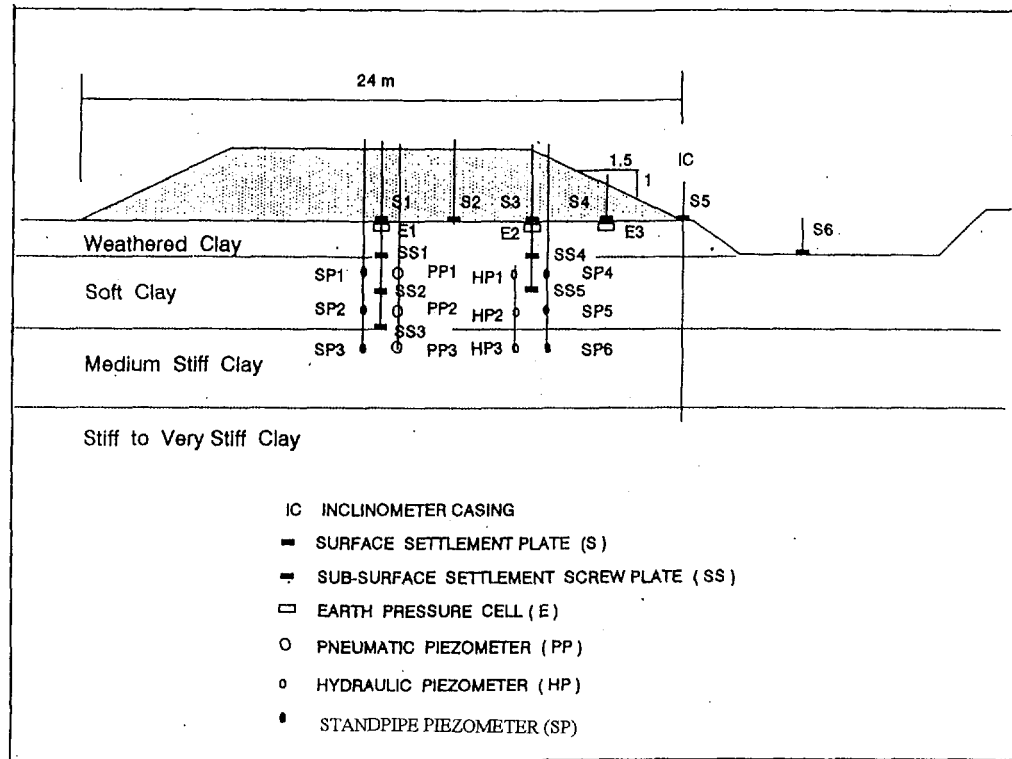


Figure 5. Foundation instrumentations of the embankments.

embankment reached a net height of 4 m (or 80 kPa embankment loading) at failure. The measured excess pore pressures from pneumatic piezometers are plotted in Figure 8 together with the rate of embankment loading. The cross-section measured after failure is plotted in Figure 10 including the failure locations indicated by bamboo stakes and by inclinometer.

Both MGE and HGE embankments were built at the same time with the same rate of filling, construction procedure and quality control as the CE embankment (see Figure 7). Up to the embankment height of 3.75 m or 75 kPa embankment load, the measured strains in the geotextiles were smaller than 1.0%. The rates of vertical and lateral displacements as well as geotextile strains increased significantly when the embankment height exceeded 3.75 m. At this stage, the maximum strains in the geotextile reinforcements were 3% and 2.3% in the MGE and HGE embankments, respectively. The failure of MGE embankment occurred at 4.2 m height (88 kPa embankment loading) that completely ruptured the low strength geotextile reinforcement. The MGE embankment failure induced deformations in the HGE embankment. The cross-section of MGE embankment at failure as compared with CE embankment is also shown in Figure 10. During the failure stage of MGE embankment, the measured maximum strain in the high strength reinforcement was 8.5% which indicated that the induced failure caused 6% additional strain in the high strength reinforcement. The HGE em-

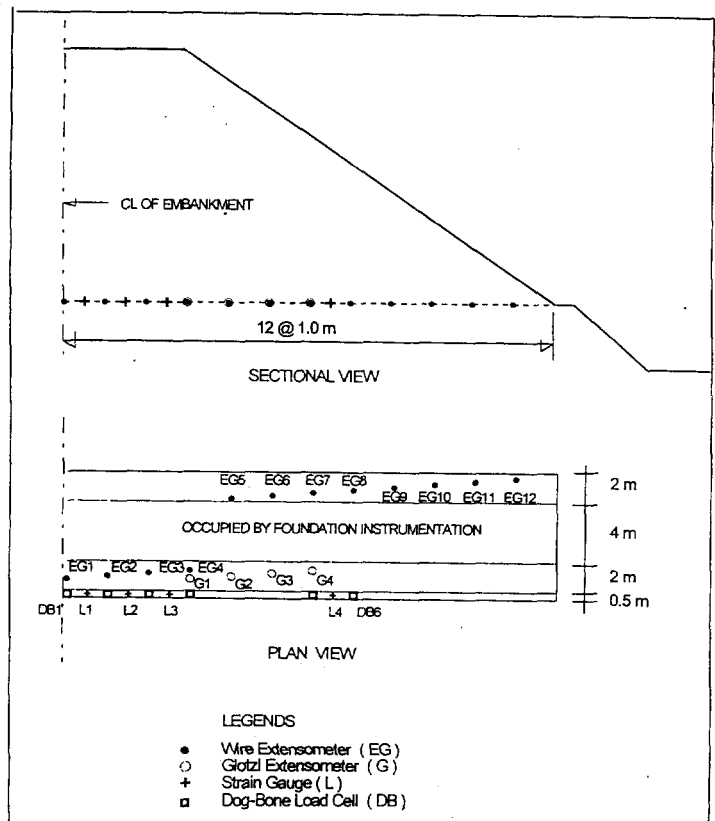


Figure 6. Geotextile instrumentations in HGE embankment.

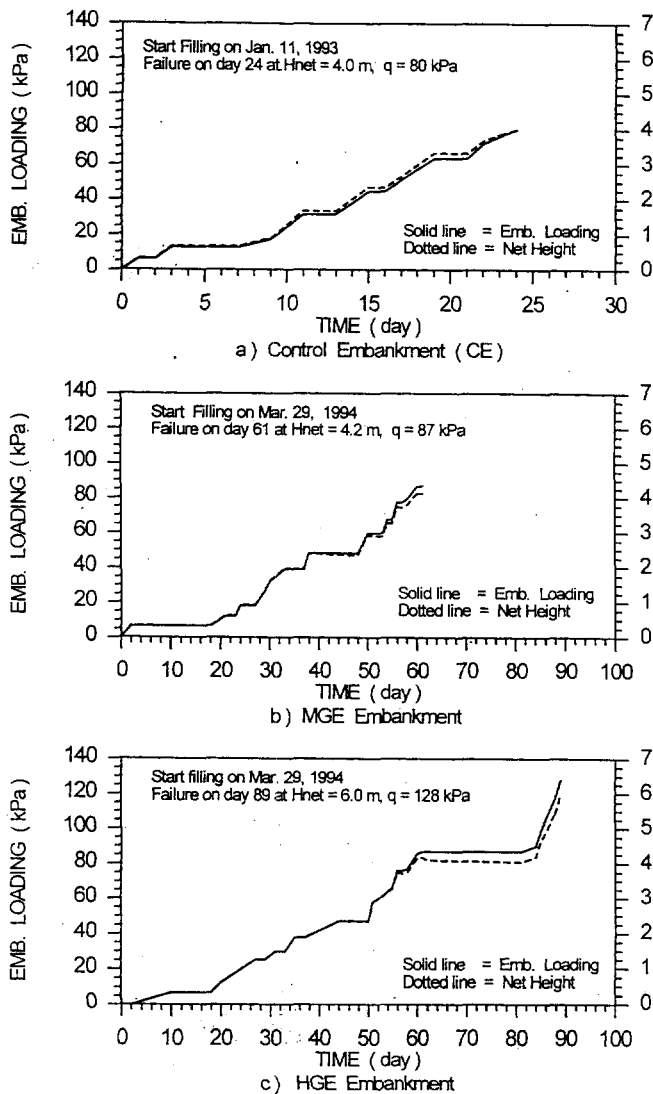


Figure 7. Construction sequences of three test embankments.

bankment height was further increased until a net height of 6 m (or 128 kPa embankment loading) was reached wherein the maximum recorded displacement was 670 mm corresponding to 12% strain and rupture of the high strength reinforcement. The excess pore pressures from pneumatic piezometers underneath the HGE embankment are given in Figure 9 together with the rate of embankment loading. The measured displacements in the high strength reinforcements at selected locations from wire extensometers are plotted in Figure 11 together with the base of embankment construction.

The collapse height corresponds to the maximum net embankment height that can be constructed. The net embankment height is defined as the difference between the current embankment crest elevation and the original elevation of the embankment base. The critical height, on the other hand, is the height at which the deformations in the foundations are equal to that of the unreinforced embankment prior to failure. Thus, the critical height and the collapse height can be considered as the embankment heights corresponding to the bearing capacity failure of the founda-

tion (primary failure) and the collapse of the reinforced embankment together with its foundation (secondary failure), respectively.

There were 35 rainy days during the construction of MGE and HGE embankments as compared to none for CE embankment. Thus, the actual collapse loads of MGE and HGE embankments were 88 kPa (4.6 m fill thickness) and 128 kPa (6.7 m fill thickness) which are, respectively, 1.1 and 1.6 times higher than the CE embankment.

5 CRITICAL STRAIN IN GEOTEXTILE REINFORCEMENT

The critical strain in geotextile reinforcement, ϵ_c , is defined as the maximum strain mobilized in the reinforcement when the reinforced embankment reaches the critical height (prior to primary failure). The measured strains prior to primary failure of HGE and MGE embankments are 2.3% and 3.0%, respectively. The Almere test embankment (Rowe, 1992) reinforced by one layer of geotextile yielded the strain of 2.5% at critical height of 2.05 m. The Sackville embankment (Rowe et al, 1995) using one layer of polyester woven geotextile yielded 3% strain at 5.7 m fill thickness when primary failure occurred. The critical strain of 3% was also obtained at Guiche test embankment (Delmas et al, 1992) with one layer of woven/nonwoven geotextile. Thus, the critical strain lie in a small band of values ranging from 2.3 to 3.0% for a very large range of geotextile stiffness ranging from 350 kN/m to 5,000 kN/m in various soil profiles.

6 BACK-ANALYSES OF STABILITY USING LIMIT EQUILIBRIUM METHOD

The limit equilibrium method (LEM), assuming circular slip surface, was used for back-analyses of stability in both

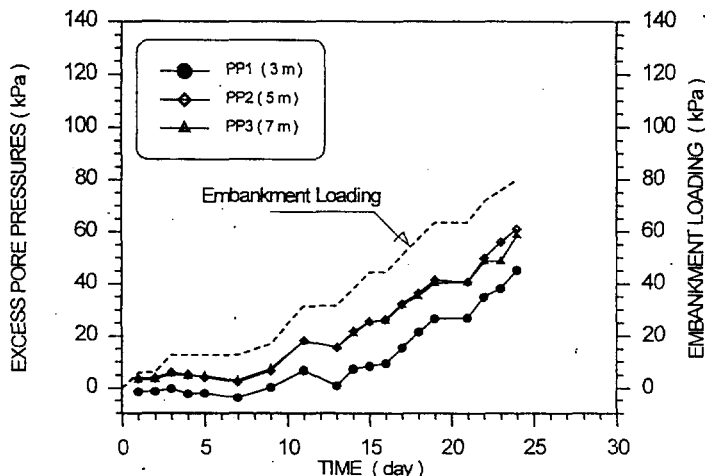


Figure 8. Excess pore pressures from pneumatic piezometers in CE embankment.

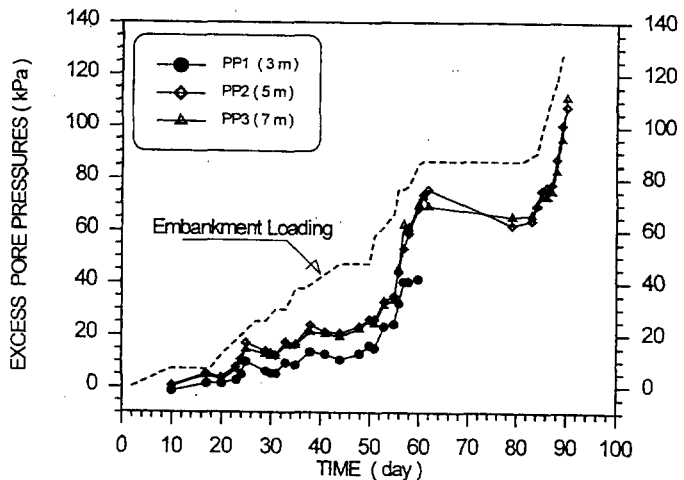


Figure 9. Excess pore pressures from pneumatic piezometers in HGE embankment.

unreinforced and reinforced embankments. The computer software PCSTABL6 (Purdue University) based on Bishop's simplified method (Bishop, 1955) with modification to include the effect of the reinforcement, was utilized.

For the CE embankment, the field compaction have total unit weight (γ) of 18.5 kN/m³ and moisture content (ω) of 9.5%. Corresponding to this condition, the peak strength consists of 40 degrees friction angle and 22 kPa apparent cohesion and the corresponding critical state values were 30 degrees friction angle and 15 kPa apparent cohesion (see Figure 4). The mean values of the field vane shear strength with correction factor of 0.80 were used as undrained strengths of the soft clay foundation. The calculated factor of safety for the actual slip surface of CE embankment at 4.0 m net height were 1.02 and 0.98 for the strength parameters of embankment fill at peak and post-peak, respectively.

For the stability of MGE and HGE embankments, the reinforcing force can be either assumed as a free-body force or a force modifying the soil strength. Following the approach of Bonaparte and Christopher (1987), the former assumption was applied in the HGE embankment and the latter assumption was used in the MGE embankment. For the case of the reinforcement modifying the soil shear strength, the resultant force in the direction tangent to the slip surface, T_R , can be calculated as follows:

$$T_R = T(\cos \alpha + \sin \alpha \cdot \tan \phi) \quad (1)$$

in which α is the angle between the direction of the reinforcement and the tangential direction of the slip circle, and ϕ is the friction angle of the embankment fill.

The direction of reinforcement force at the onset of failure can be represented by the inclination factor, I_f , defined as follows:

$$I_f = 1 - \alpha/\alpha_0 \quad (2)$$

where α_0 is the angle between the initial (horizontal) direction of the reinforcement and the tangential direction of the slip surface. The values of I_f of 0, 0.5, and 1.0 correspond to horizontal, bisectonal, and tangential directions, respectively. The reorientation of the reinforcement is caused mainly by the bending of reinforcement due to local deformation. Thus, the value of inclination factor, I_f , should be selected according to the magnitude of the localized strain in the geotextile, ϵ_{lc} , at the vicinity of the slip surface. From the results of large direct shear tests and finite element modeling (FEM), Bergado et al (1996) suggested that the maximum value of I_f is 0.50 corresponding to the bisectonal direction. The bisectonal direction has also been successfully assumed by Rowe and Soderman (1984), Low and Duncan (1985) and Rowe (1992).

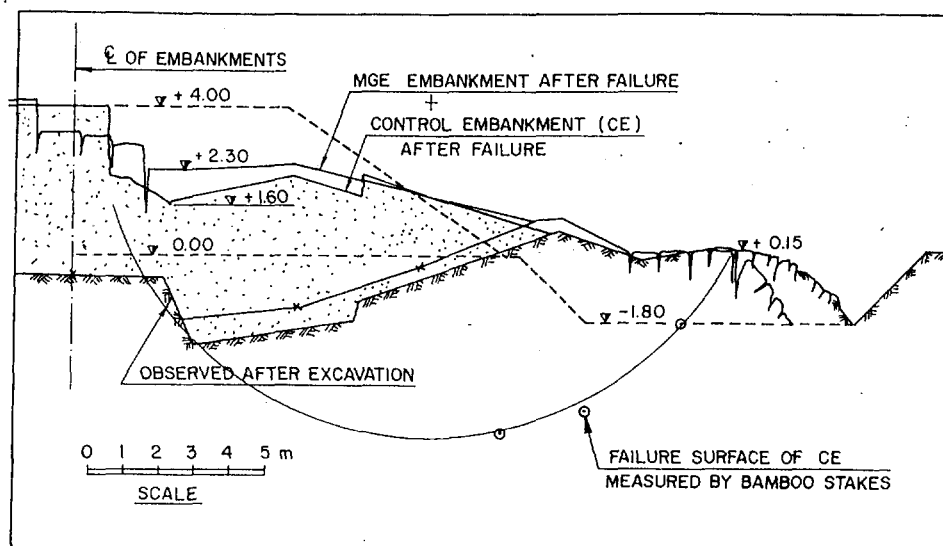


Figure 10. Cross-section of CE and MGE embankment after failure.

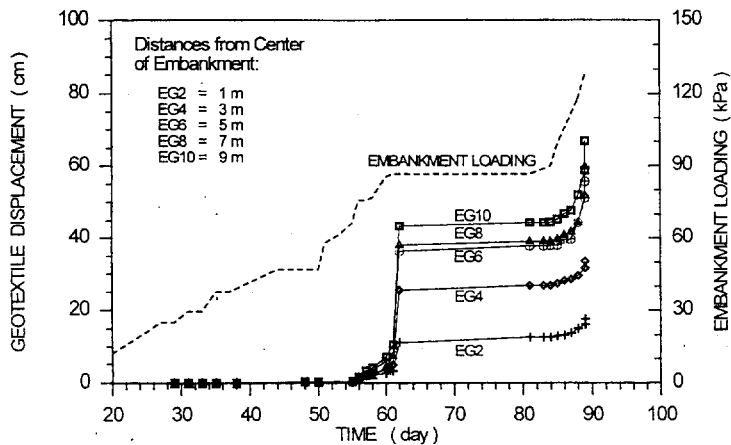


Figure 11. Displacements in geotextile measured by wire extensometer.

The ultimate reinforcement force, T_{ult} , was computed corresponding to the value of the limiting strain, ϵ_{lm} , which includes the localized strain, ϵ_{lc} , whenever I_r is greater than 0. The strength parameters of backfill soil correspond to the field compaction condition ($\gamma_t = 19.2 \text{ kN/m}^3$ and $w = 13\%$) influenced by rainy days. The corresponding friction angle (ϕ) and apparent cohesion (c) were $\phi = 38$ degrees and $c = 17 \text{ kPa}$ at peak strength, respectively, and $\phi = 30$ degrees and $c = 10 \text{ kPa}$ at critical state, respectively. The undrained strengths in the soft clay foundation were similar as the CE embankment.

The failure of MGE embankment at 4.2 m net height was back-analyzed. At the critical height, assuming peak strength parameters of embankment fill, no localized geotextile deformation ($\epsilon_{lc} = 0$) and horizontal direction of reinforcing force ($I_r = 0$) with measured strain of reinforcement of 3%, the factor of safety (FS) was 0.98. At the onset of failure (FS = 1.0) with $I_r = 0.5$ (bisectonal direction of reinforcing force and using critical state strength parameters of embankment fill, the back-analyzed geotextile strain was found to be 13%.

The stability of HGE embankment at net embankment heights of 4.2 m (critical height) and at 6.0 m (collapse height) were back-analyzed. Using the measured strain in the geotextile of 2.3% and assuming $I_r = 0$ and peak strength parameters for embankment fill, the calculated FS was 1.0. This indicates that the HGE embankment reached critical height at 4.2 m and the bearing capacity failure (primary failure) was unavoidable, even without the interference of MGE embankment. After induced failure of adjacent MGE embankment, the measured strain in the high strength geotextile was 8.5% corresponding to tensile strength of 145 kN/m. At this stage, assuming $I_r = 0.5$ and using critical strength parameters of embankment fill, the safety factor of 1.25 was obtained. Therefore, the embankment construction can be continued which was done. The HGE embankment collapse at net embankment height of 6 m with measured strain in the geotextile of 12 to 14% corresponding to rupture strength of 200 kN/m for high

strength geotextile. At 6 m net height, the FS value for HGE embankment was found to be 1.0 using either the actual failure surface or the most critical and deeper failure surface. Therefore, regardless of the influence of MGE embankment failure at net height of 4.2 m, the HGE embankment should fail at net embankment height of 6.0 m.

7 MAGNITUDE AND ORIENTATION OF REINFORCING FORCE

Two important variables are involved in the circular slip stability analyses, namely: the inclination factor, I_r , and the limiting strain, ϵ_{lm} , at the onset of failure. Based on the measured strain, the results of back-analyses by LEM indicated that reinforcing force can be horizontal direction ($I_r = 0$) at critical height just prior to bearing capacity failure (primary failure) as well as the reinforcing force can be bisectonal ($I_r = 0.50$) at collapse height. Rather than assumed arbitrarily, an improved method is introduced to estimate the limiting strain, ϵ_{lm} , as follows:

$$\epsilon_{lm} = \epsilon_c + \epsilon_{lc} \quad (3)$$

in which ϵ_c is the critical strain corresponding to the critical height (just prior to bearing capacity failure or primary failure) and ϵ_{lc} is the localized strain associated with the slip failure. The value of ϵ_c was found to be 2.3% to 3% as mentioned previously. Based on large direct shear tests and subsequent FEM modeling, Bergado et al (1996) proposed a new method to calculate the localized strain, ϵ_{lc} , as follows:

$$\epsilon_{lc} = 225 (I_r) (S^{-0.4}) \quad (4)$$

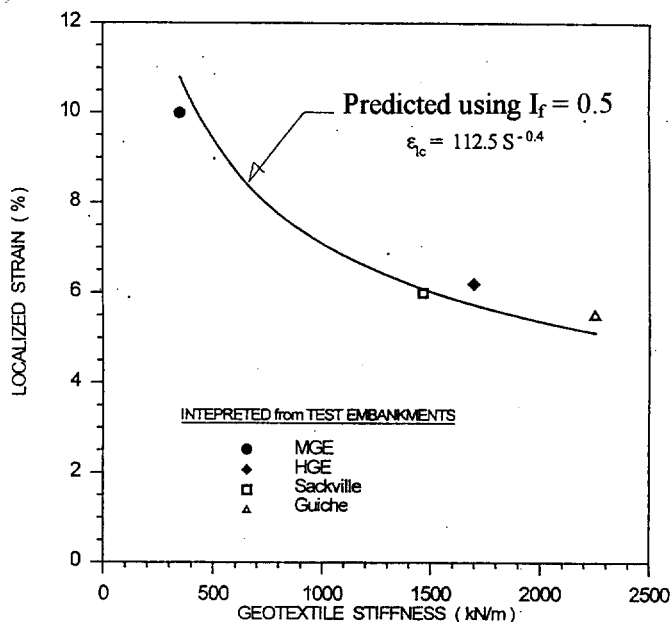


Figure 12. Localized strains in geotextile from field data and as predicted by Equation 4.

The value of S is the total stiffness of all reinforcement layers in the embankment and should be determined as secant stiffness at 5% strain. The value of I_r can be assumed as $I_r = 0$ or $I_r = 0.50$ corresponding to critical embankment height and collapse height, respectively. Equation 4 is plotted in Figure 12 for various values of stiffness, S . The data derived from Sackville (Rowe et al, 1995) and Guiche (Delmas et al, 1992) embankments are also included in Figure 12.

8 CONCLUSIONS

The full scale test embankment program including the site conditions, instrumentations, and embankment construction have been described. The test embankment program yielded valuable data which can be used to improve the design method of geotextile reinforced embankment on soft ground. Based on the results, the following conclusions can be made:

1. The geotextile reinforcements improved the collapse heights of MGE and HGE embankments by 1.1 and 1.6 times, respectively, higher than CE embankment.
2. The critical strain, ϵ_c , in the geotextile reinforcement just prior to bearing capacity failure or primary failure of foundation soil can be taken as 2.3 to 3% irrespective of geotextile stiffness and condition of the foundation soil.
3. The limiting strain, ϵ_{lm} , at slip failure can be taken as the sum of critical strain, ϵ_c , and the localized strain, ϵ_{lc} , associated with the slip failure.
4. The geotextile reinforced embankment on soft ground with limitation on foundation deformation not exceeding the unreinforced embankment just prior to the bearing capacity failure or primary failure (embankment height, $H < \text{critical height, } H_c$), the mobilized tensile force in the reinforcement can be obtained assuming the limiting strain equal to critical strain which can be taken as 3% ($\epsilon_{lm} = \epsilon_c = 3\%$). The direction of reinforcing force can be taken as horizontal ($I_r=0$) and the peak strength parameters of embankment fill are suitable.
5. For embankments designed with allowable large deformations where the embankment height, H , can exceed the critical embankment height, H_c , the mobilized reinforcing force should correspond to the limiting strain, ϵ_{lm} , which is the sum of critical strain, ϵ_c , and localized strain at failure, ϵ_{lc} . The value of ϵ_{lc} can be obtained from the in-soil stiffness of the reinforcement using $I_r = 0.50$ and using the shear strength parameters of embankment fill at critical state.
6. For single layer reinforcement placed directly on the ground at the base of embankment, the reinforcing force can be taken as free-body force. For multi-layer reinforcements with frictional embankment fill, the effects of reinforcing force in modifying the soil strength at the vicinity of failure surface should be considered.

ACKNOWLEDGEMENTS

The authors are deeply indebted to the generous financial support of Polyfelt Geosynthetics, Austria and to their past and present staff such as G. Werner, K.H. Loke, J. Smith, P. Delmas, and B.R. Christopher for their technical advises and suggestions.

REFERENCES

- Bergado, D.T., Long, P.V., Loke, K.H., Christopher, B.R. and Delmas, P. (1994), "Geotextile Reinforcement in Full Scale Test Embankment on Soft Ground", *Proc. Fifth Intl. Conf. on Geotextiles and Geomembranes and Related Products*, Singapore, pp. 21-24.
- Bergado, D.T., Long, P.V. and Werner, G. (1996) "Deformation Behavior of Geotextile Reinforcement at Vicinity of the Shear Surface", *First European Geosynthetics Conference (EuroGeo 1)*, Maastricht, The Netherlands, pp. 177-182.
- Bishop, A.W. (1955) "The Use of Slip Circle in the Stability Analysis of Slopes", *Geotechnique*, Vol. 5, No. 1, pp. 7-17.
- Bonaparte, R. and Christopher, B.R. (1987) "Design and Construction of Reinforced Embankments over Weak Foundation", *Transp. Res. Record* 1153, pp. 26-39.
- Delmas, P., Queroy, D., Quaresma, M. and De Saint, A. (1992) "Failure of an Experimental Embankment: Guiche", *Geotextiles and Geomembranes and Related Products*, Den Hoedt (ed.), Balkema Printers Rotterdam, the Netherlands.
- Loke, K.H., Ganeshan, V., Werner, G. and Bergado, D.T. (1994) "Composite Behavior of Geotextile Reinforced Embankment Soft Clay", *Proc. Fifth Intl. Conf. on Geotextiles and Geomembranes and Related Products*, Singapore, pp. 25-28.
- Long, P.V. (1997) "Behavior of Geotextile-Reinforced Embankment on Soft Ground", *Doctoral Engineering Dissertation*, School of Civil Engineering, Asian Institute of Technology, Bangkok, Thailand.
- Low, B.K. and Duncan, J.M. (1985) "Analysis of the Behavior of Reinforced Embankment on Weak Foundation", *Report VPI/CE-CT-85-H*, Virginia Polytechnic Institute, Blacksburg, V.A., U.S.A.
- Rowe, R.K., Granendran, C.T., Landva, A.O. and Valsangkar, A.J. (1995) "Construction and Performance of a Full Scale Geotextile Reinforced Test Embankment, Sackville, New Brunswick", *Canadian Geotechnical Journal*, Vol. 23, pp. 512-534.
- Rowe, R.K. (1992) "Reinforced Embankments on Cohesive Deposits", *International Symposium on Application of Geosynthetics Technology*, Jakarta, Indonesia, pp. 1-19.
- Rowe, R.K. and Soderman, K.L. (1987) "Reinforcement of Embankment on Soils Whose Strength Increases with Depth", *Geosynthetics '87*, New Orleans, pp. 266-277.
- Tien, M.H. (1994) "An Investigation of Interaction of Geotextile and Low Quality Backfill Soil by Direct Shear Tests", *Master of Engineering Thesis*, Asian Institute of Technology, Bangkok, Thailand.

Reinforced Piled Embankments in Sweden - Design Aspects

Y. Rogbeck
M Sc, Swedish Geotechnical Institute, Linköping, Sweden

S. Gustavsson
M Sc, Scandiaconsult, Malmö, Sweden

I. Södergren
M Sc, Swedish National Road Administration, Borlänge, Sweden

D. Lindquist
B Sc, Swedish Geotechnical Institute/University of Washington, Seattle, USA

Abstract: This paper describes a case study of a reinforced piled embankment and presents a proposed calculation model. The height of the embankment was 1.7 m, which is lower than that normally accepted for embankment piling according to Swedish regulations. The project includes a field study of displacement and strain in the reinforcement for the alternatives soil fill and cavities below the reinforcement. The cavities were simulated by using foam mattresses below the reinforcement. Displacements at the reinforcement level in the area with soil fill were about 20 mm, while displacements over the mattresses were about 200 mm, i.e. 10 times larger. Calculations were carried out using two analytical models, BS 8006 and Carlsson, and a finite difference method, FLAC. Comparisons are made between measured values and calculated values. In this case the FLAC calculations are judged to give a good picture of the actual behaviour in the construction. The analytical models are too conservative because they do not take the foundation support from the soil beneath the reinforcement into account. The various calculation models were compared to each other and a suggestion for design using an analytical model is made. The model is two-dimensional but an attempt was made to take the three-dimensional behaviour into account. This was done in this case by taking the three-dimensional load and distributing it over the two-dimensioned surface. Aspects of design are provided.

Keywords: Geogrids, Piles, Embankments, Reinforcement, Design, Case study.

1. MÖNSTERÅS CASE STUDY

Embankment piling has been used in Sweden for many years. During recent years some projects have been carried out with reinforcement over embankment piling or deep stabilisation. Monitoring has been carried out in an embankment at Mönsterås.

The case study was of a reinforced piled embankment constructed in 1996 on a section of Route 632 in Mönsterås, Sweden. The Swedish National Road Administration (SNRA) ordered the construction, Scandiaconsult managed it and the Nordic Construction Company was the contractor. The field studies were carried out by Scandiaconsult and the Swedish Geotechnical Institute (SGI). A number of different alternatives were studied in the process of selecting soil improvement on the stretch of road in question, explained below.

- Excavation/refill. Discarded because of the effects this would have on the surroundings. Both on the nearby quay construction and the environment. Furthermore, it would require considerable heavy truck traffic in central Mönsterås.
- Light fill. For sufficient load relief, the light fill would cause uplift at the maximum groundwater level.
- Concrete mat foundation on piles. Feasible but expensive, about twice as expensive as embankment piling.

1.1 Soil conditions

The soil consisted of an upper layer of 1 to 3 m of fill beneath which was 2 to 4 m of loose sediments of gytija and clay which rest on sand and till. The depth to the bedrock was not carefully examined but is probably limited. The thickness of the soil layer in a cross-section of the embankment area varies.

The fill was deposited over a long period of time. The oldest part of the fill was placed with a grillage beneath it. The fill consisted mainly of non-cohesive soil but there was also some

wood and construction waste. The fill varied in stiffness. For design calculations, a dimensioning friction angle of 32° was used.

The gytija, the thickness of which varies between 0.5 and 2.0 m, contained layers of silt and fine sand. The gytija was loose with an uncorrected shear strength, according to field vane shear tests, between 10 and 50 kPa. The water content varied between 40 % and 200 % with one measurement of 430 %. For design calculations, a dimensioning, undrained shear strength of 8 kPa was used.

The clay, the thickness of which varied between 0.5 and 2.0 m, contained layers of fine silt. The uncorrected shear strength of the clay varied, according to vane shear tests, between 10 and 70 kPa. The water content varied between 20 % and 60 %. For design calculations, a dimensioning, undrained shear strength of 10 kPa was used.

Both the gytija and the clay were assessed as being normally consolidated for the existing conditions.

The composition and thickness of the till were not closely examined, but generally it had a high relative stiffness. However, in some areas there were looser layers of sand in the upper surface of the till. For design calculations, a dimensioning friction angle of 35° was used.

Parts of the embankment area have been flooded at the maximum groundwater levels.

1.2 Design and construction

The construction consisted of precast concrete piles which were driven down to a firm bottom. The length of the piles was 3 to 6 m. Pile caps were placed above the piles covering 25 % of the embankments surface area. The reinforcement consisted of a biaxial polyester geogrid, with 84 kN/m tensile strength at break and a tensile strength of 16 kN/m at 3 % strain according to EN ISO 10319 (TexGrid TG 75-75). The geogrid was laid in one layer. The embankment fill consisted of crushed rock, 0 to 200 mm. A cross-section of the construction is shown in

Figure 1. The height of the embankment is 1.7 m which is lower than that normally accepted in Swedish regulations. In order to obtain permission to build the construction, the designer was forced to verify that the design would function as intended. Verification took place through calculations supplemented with field monitoring.

The embankment fill was compacted with a 2-ton roller. The first layer over the reinforcement was 0.5 m when compacted. Thereafter compaction took place in 0.3 m lifts. In the area with measurement equipment, a 600 kg vibratory plate compactor was used in order not to destroy the monitoring equipment. The fill was placed in two stages. In the first stage fill was placed to 0.7 m over the reinforcement and in the second stage to the total of 1.6 m above the reinforcement.

1.3 Design

For design of the soil reinforcement, calculations were carried out according to British Standard (BS 8006, Draft) 1995, Equation 1 and according to (Carlsson 1987), Equation 2. The most significant differences between the models are the forces in the reinforcement due to the vertical load. These differences arise from the way that the models analyse the arching effect. These forces are compared in Table 1. The results differed, in this case with the lowest forces in the reinforcement according to BS 8006. The procedure used in BS 8006 produces relatively large jumps in the calculation results at certain embankment heights. The jumps depended on whether or not an arching effect arose and how the load was distributed between piles and reinforcement. Care should be taken, especially with new standards and results should be checked which are near such limits. The geometry of the Mönsterås project was close to such a limit. The SNRA therefore decided to carry out such a check within the framework of the SGIs planned work on the regulations for the SNRA in Sweden.

The calculations according to BS 8006 are as follows:

For $H > 0.7$ (c-a) the distribution over pile load/soil load is;

$$p'_c / \sigma'_v = (C_c \cdot a / H)^2$$

For $H > 1.4$ (c-a) the distributed load on and the force in the soil reinforcement are;

$$W_T = \frac{1.4c f_{fs} \gamma (c-a)}{c^2 - a^2} [c^2 - a^2 (p'_c / \sigma'_v)]$$

$$T_{rp} = \frac{W_T (c-a)}{2a} \sqrt{1 + \frac{1}{6\epsilon}} \quad (1)$$

The calculations according to Carlsson are as follows:

$$d = (c-a) \sqrt{\frac{3\epsilon}{8}}$$

$$P_b = \frac{(c-a)^3}{16 \tan 15^\circ} \gamma \frac{1}{2d} \sqrt{1 + \frac{16d^2}{(c-a)^2}} \quad (2)$$

- Where H = embankment height (1.7 m)
- c = centre distance between pile caps (2.4 m)
- a = pile cap width (1.2 m)
- d = displacement (d)
- C_c = pile type factor, end-bearing piles ($1.95 H/a - 0.18$)
- γ = unit weight of embankment fill (20 kN/m^3)
- f_{fs} = partial coefficient for soil load (1.0)
- ϵ = strain
- W_T = the distributed vertical load acting on the reinforcement (kN/m)
- $T_{rp} = P_b$ = force in the reinforcement (kN/m)

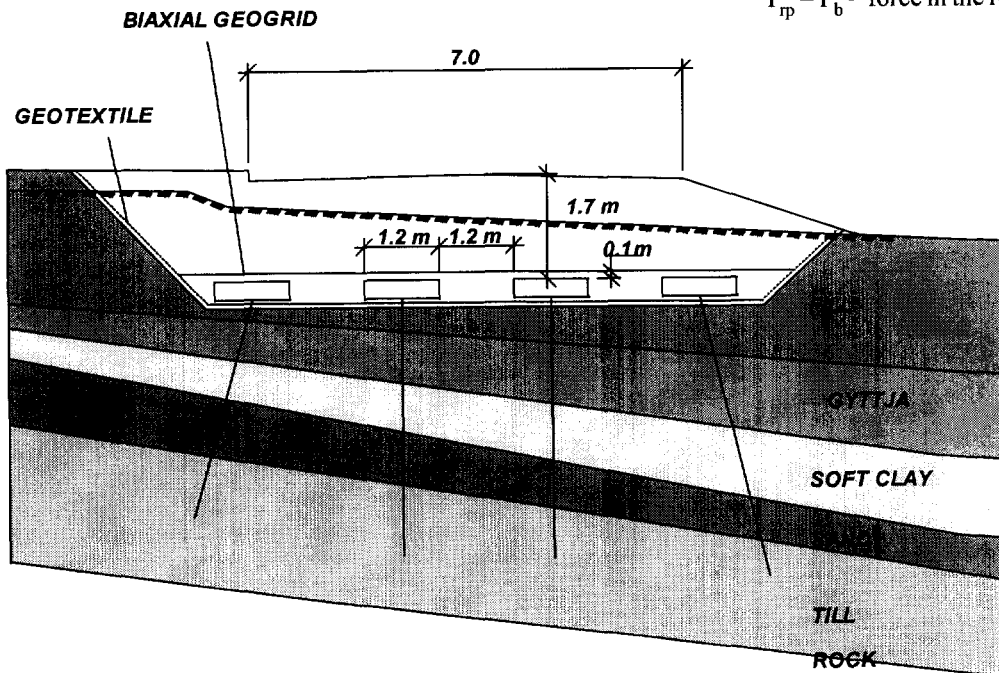


Figure 1. Cross-section of Route 632 in Mönsterås.

Calculations using the BS 8006-model (fictive three-dimensional) gave a force on the basis of the vertical load between the pile caps of 18 kN/m at a strain of 6 %. Calculation according to Carlsson (two-dimensional) gave a force of 26 kN/m and a displacement of 0.18 m at a corresponding strain. In order to verify these results, other calculations were carried out using the two-dimensional finite difference program, Fast Lagrangian Analysis of Continua (FLAC), Version 3.30 (Itasca 1995). The calculations showed that there was arch formation, even for the low embankment height studied here, and that the displacement at the road surface was negligible. Calculations were carried out for cases with both cavities and soil fill under the reinforcement. The elastic modulus times area, EA = 400 kN/m, was used for the FLAC calculations. In implementation, however, a somewhat more rigid reinforcement was used. Table 1 shows the results from the calculations.

Table 1. Design results of the analytical and finite difference models.

Method	Strain ϵ (%)	Displacement d (m)	Force F_v (kN/m)
Carlsson	2	0.10	42
	6	0.18	26
BS 8006	2	0.10	28
	6	0.18	18
FLAC Foundation support cavity	0.08	0.01	1
	3.5	0.13	14

1.4 Field monitoring of strain and displacement in the reinforcement

The quality control was supplemented with measurements in an attempt to clarify the effect of the reinforcement and compare measured values with the calculation models. The monitoring was carried out in two areas of the embankment, as shown in Figure 2. One area consisted of the normal construction with soil fill between the pile caps. The other area consisted of foam mattresses between two rows of pile caps in order to simulate a cavity under the reinforcement. The mattresses were 0.55 m high and had an area of 1.2 m by 6.0 m. The monitoring consisted of vertical displacement and strain measurements in the reinforcement and displacement measurements on the road surface.

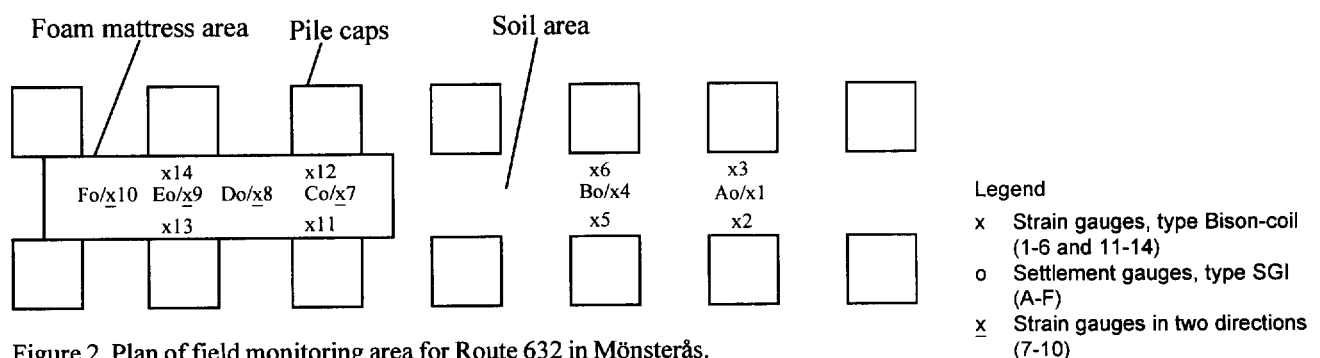


Figure 2. Plan of field monitoring area for Route 632 in Mönsterås.

The vertical displacements of the reinforcement were measured using settlement gauges, type SGI. The measurement results are shown in Figure 3. The displacement in the area with the soil fill was about 20 mm. Displacement measured over the mattresses between the pile caps was 173 and 206 mm while displacement on the diagonal was 212 and 213 mm. The larger displacement on the diagonal is probably due to three-dimensional effects. However, the full effect is not obtained since the mattresses are only lying between the pile caps in one direction and soil fill is between the pile caps in the cross direction.

The strains in the geogrids were measured with Bison coil strain gauges screwed into the geogrids. They are designed for synthetic geogrids and have a measurement accuracy of 2.5 micrometers. Theoretically, the largest strains are obtained at the cap edge. Where there is a cavity under the reinforcement, the strain is nearly uniform between the pile caps. To examine the differences between the cap edge and the middle of the cavity, measurements were carried out both between the pile caps and at the cap edge. The strain measurements between the caps also gave the opportunity to compare these with measured displacements. Field measurements of horizontal movements were made, which were then calculated into strains and forces.

The strains are shown in Figures 4 and 5. The strain gauge locations are shown in Figure 2. In spite of a high measurement accuracy in the strain gauges, the distribution of results at the pile cap edge is large. This may be due to edge

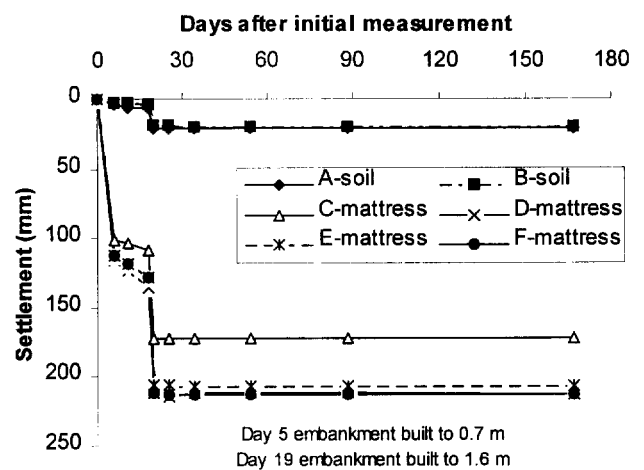


Figure 3. Measured vertical displacement in the area with soil fill and foam mattresses respectively.

effects. In the mattress area the strains close to the edge of the pile caps were 0.5, 1.6, 2.1 and 4.5 %. At the midpoint between and along the pile caps the strains were 0.4, 0.6, 0.7 and 1 %. At the midpoint between and across the pile caps they were 1.8, 2.9, 3.0 and 3.2 %. Corresponding tensile forces were 5 to 23, 4 to 9 and 12 to 17 kN/m.

1.5 Monitoring of displacements on the road surface

The displacements on the road surface were measured with settlement plates placed 0.7 m under the surface and surrounded by protective tubing. The embankment fill material was assessed as being non-susceptible to frost heave. Measurements of the displacements in the surface did not begin until all the embankment fill had been placed in November 1996. Displacements also occurred during the laying and compaction processes. Unfortunately these displacements could not be documented.

The measured displacements varied between 5 and 10 mm. Most of these were formed within one month after the embankment fill had been completed. No significant differences on the road surface were observed between the area with and without mattresses.

1.6 FLAC calculations to evaluate the field behaviour

To find the reasons for the differences between predicted and measured displacements and geogrid strains supplementary FLAC calculations were carried out. The primary aim was to study the case where a cavity arises under the reinforcement between the pile caps.

The embankment was symmetrical about its centre line so only one side of the embankment was modelled. If the mattress had also been used in side sections, rather than just the centre of the embankment, the modelled section could have been reduced to 1.2 m in width. Instead, the modelled section

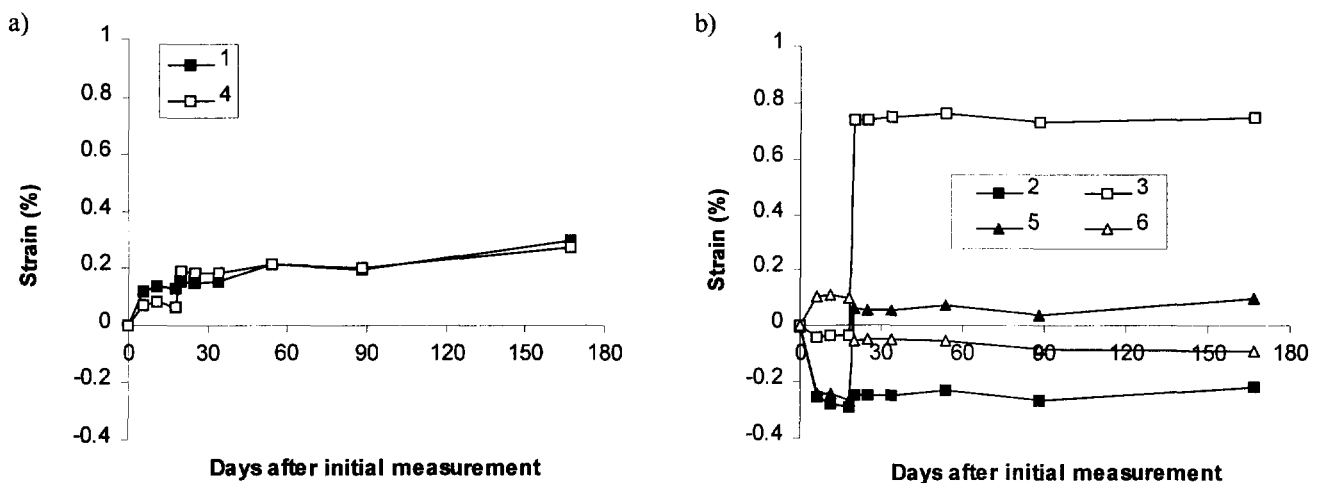


Figure 4. Measured strains in the reinforcement for case with soil. a) along and in the middle between the pile caps. b) across and at the pile caps.

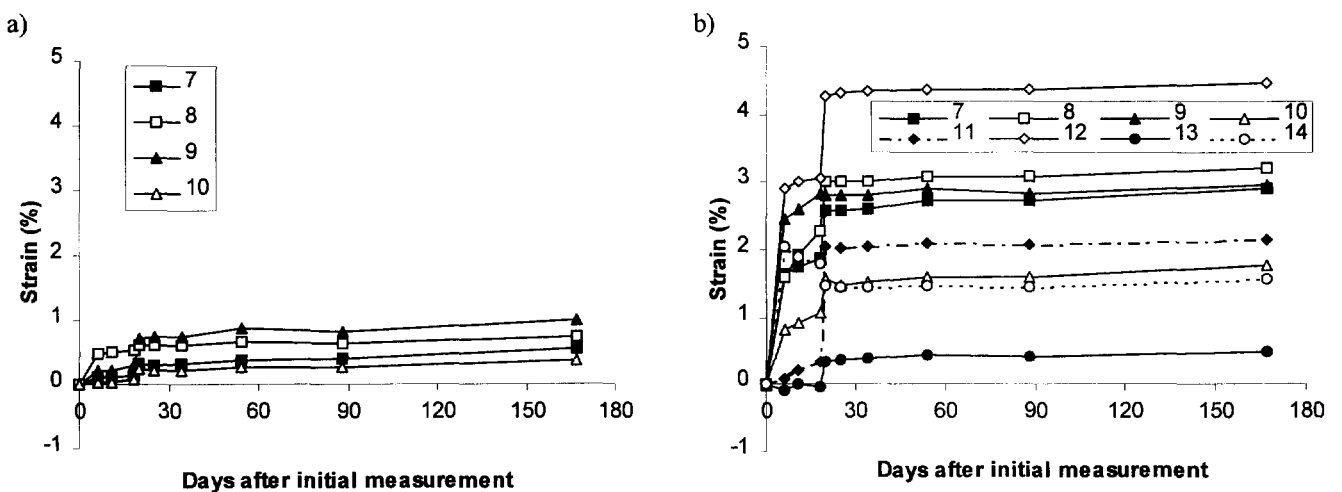


Figure 5. Measured strains in the reinforcement for case with soil fill and foam mattresses. a) along and at the midpoint between the pile caps. b) across the pile caps both at the midpoint between and at the pile caps.

was 3.6 m wide and 2.15 m high. It spanned horizontally from the centre of the mattress area across a footing and soil area to the centre of the second footing. Vertically it spanned from the bottom of the mattress to the top of the fill. The material locations were shown in Figure 1. A variety of grid meshes were tested. A 36 x 28 grid was selected to optimise the calculation time and precision of the results.

The geogrid was modelled using the cable element in FLAC. Values used in this analysis for the cable element are shown in Table 2. The cable element was chosen, rather than the beam element, because the cable element can model the soil/geogrid interaction. The Mohr-Coulomb plasticity model was used for the soil. The mattress was modelled elastically with its moduli based on laboratory unconfined compression tests. Finally, the footings were modelled as null elements with fixed boundary points.

Table 2. Cable element input values used to model a geogrid.

FLAC parameter	Magnitude and units
elastic modulus · area	600 kN/m
perimeter	2 m/m
yield	75 kN/m
kbond	17,000 kPa (maximum)
sbond	0 kPa
sfriiction (assumed = soil)	42°

Ideally the kbond and sbond should be obtained from laboratory and field pullout tests using the fill material. Because these tests were not available, Equation 3, based on the definitions in (Itasca 1995), was used to obtain values for the kbond.

$$kbond = (sbond + perimeter \cdot \sigma' \cdot \tan(sfriiction)) / \delta_{max} \quad (3)$$

The perimeter was chosen to be the maximum of 2 m for the geogrid, as opposed to its surface area, because there is frictional resistance on both the top and bottom of its surface and significant passive resistance where the holes in the grid meet the spanning grid elements. σ' is the overburden pressure at the level of the geogrid. It should be noted that the kbond increases with the overburden pressure as the embankment is constructed. Finally, δ_{max} is the geogrid displacement when the maximum pullout resistance is reached. For the geogrid used in this project 3 mm was used.

The maximum displacement occurred at the mattress/geogrid interface at the midpoint between pile caps. The displacement and tensile force distribution in the geogrid are shown in Figure 6.

Compaction of the fill was modelled as a static pressure applied during the construction of the embankment. The compactive effort was modelled by adding an equivalent static load of 20 or 50 kPa and stepping to equilibrium. When equilibrium was reached the load was removed and FLAC stepped again to a new equilibrium. The equivalent static load used in FLAC for compaction was only an estimate. Therefore, two values were chosen in-between the compaction equipment's static load and its centrifugal vibratory force of 12 and 100 kPa, respectively. The incremental displacements and the effect of the static compaction loads for the base case are shown in Figure 7. The compaction was modelled at 0.5, 0.7, 1.0, 1.3 and 1.6 m embankment heights. The effect on displacement at the geogrid was only significant for the first two compactions.

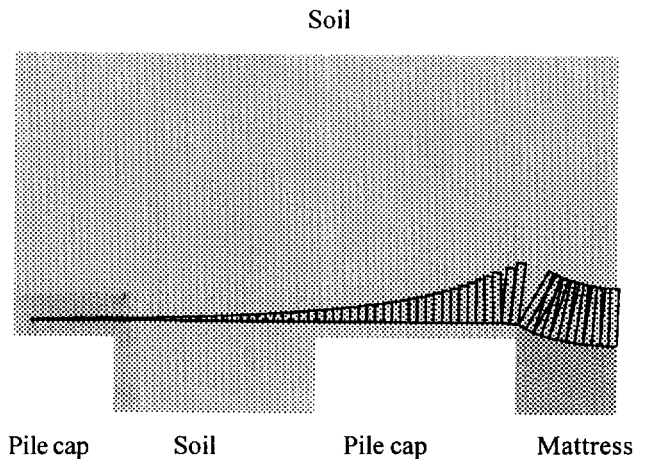


Figure 6. Base case displacement and tensile force distribution in the geogrid.

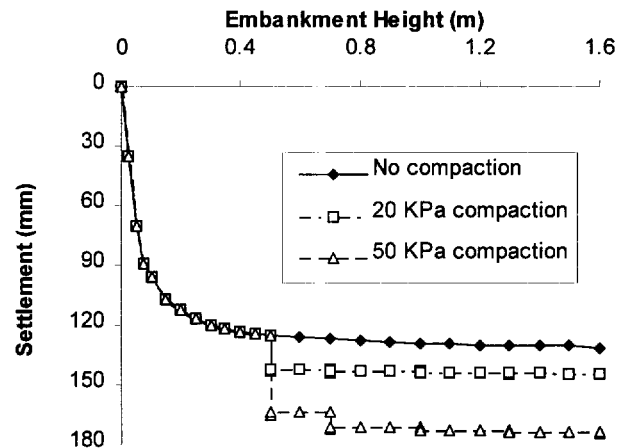


Figure 7. Base case maximum geogrid settlement versus embankment height.

The arching effect between pile caps reduced the incremental portion of load carried by the geogrid as the fill height increased. Thus the displacement did not increase at the same rate as the embankment was constructed. The arching effect between pile caps is shown in Figure 8. Figures 6 and 8 show that the surface displacement is relatively small.

Five models were analyzed in FLAC. The base case model had the geogrid, mattress, pile caps, and fill all modelled as they are in the field. A fictive 3D model attempted to account for the three dimensional effects of the lateral spacing between pile caps by increasing the weight of the fill by the equivalent increased area of 50 %. Next, air was modelled between all the pile caps to compare the design assumptions with the FLAC results. Because the air was modelled in all the areas around the pile caps the geogrid had relatively high tensile stresses from settlements on both sides of the pile cap. Also the geogrid was not able to move toward either side as it could in the mattress case. Compared to the mattress model, the air model had smaller displacements and higher geogrid tensile forces and strains. The final two models had soil modelled below the geogrid as it was in most of the embankment. Unlike the mattress and air, the soil was stiffer than the gytija below the footing. Therefore much of the displacement

Soil

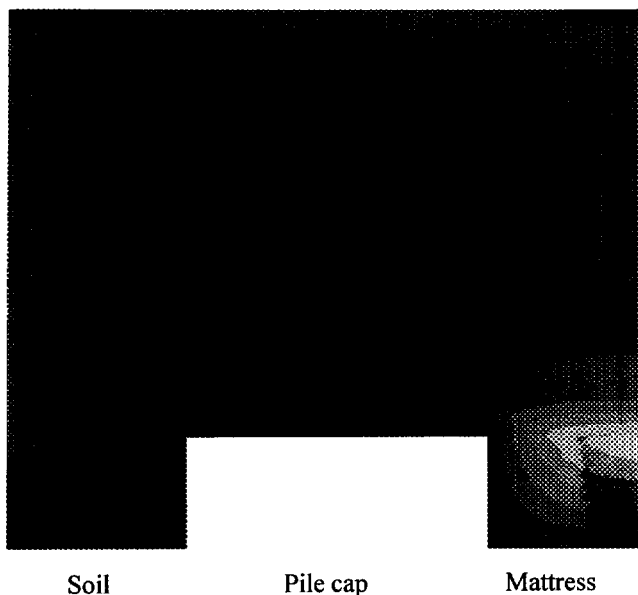


Figure 8. Arching effect as shown by y-displacement contours.

occurred in the gytja. Thus the soil models required that the lower fill and gytja be included in the calculations. The material properties of the gytja were not known with much certainty, so the soil model calculations are provided to show only approximate magnitudes.

The results from the FLAC calculations are summarized in Table 3.

In these models the most important input parameters affecting the magnitude of the settlement in the embankment were the following: moduli of the soil or mattress between pile caps, elastic modulus times area of the cable, amount of compaction, depth of fill when compacted, the soil/geogrid bond properties and the fill properties.

1.7 Comparison between calculations and field measurements

A comparison was made between the values obtained in design and the values measured for vertical displacements and forces in the reinforcement.

For the case with the mattress the calculated tensile force was 10 kN/m and the displacement about 0.14 m in FLAC. Modelling compaction of the fill increased the displacement between 10 and 50 mm and the tensile force between 3 and 9 kN/m. The forces measured in the area with mattresses were generally somewhat higher than calculated, as was the displacement. One of the causes may be three-dimensional behaviour. FLAC calculations in two dimensions were estimated to give a good understanding of the behaviour of the construction, but it was somewhat uncertain. One way of taking the three-dimensional behaviour into account was to increase the density by 50 %, which corresponds to a load distribution according to Figure 11. Such a calculation gave a displacement of 0.18 to 0.2 m when the compaction effect was taken into account. This was closer to the results in the field which were 0.17 to 0.21 m. The strain in the geogrid in the field between the caps was 3 %, which the FLAC calculation also showed for the compaction case. For the case with soil below the geogrid the displacement according to the FLAC calculation was 12 mm and the tensile force was 0.4 kN/m without compaction. If the fictive three-dimensional effects were taken into account as mentioned above then the calculated displacement was 23 mm. Modelling compaction of the fill increased the displacement between 10 and 45 mm and the tensile force between 1 and 9 kN.

In the soil case the displacements without compaction corresponded better to the field measurements. On the other hand the displacements are small and there are large uncertainties in the properties for the soil below the pile caps. Therefore the model of the case with mattresses is more reliable.

Because the resistance of the foundation soil is considerable the analytical calculation models in this case gave a misguided picture of the actual behaviour of the construction. The FLAC calculations on the other hand gave a good picture of the behaviour on the condition that the pertinent input data was used. If a cavity should arise under the reinforcement then the analytical models are thought to be appropriate, but the three-dimensional effects should be taken into account.

Table 3. Results from FLAC.

Model Description	Maximum Settlement* (mm)	Maximum Cable Tensile Force (kN)	Maximum Cable Strain (%)
Base case no compaction	141	10	1.7
Base case 20 kPa compaction	155	13	2.2
Base case 50 kPa compaction	188	19	3.1
Fictive 3-D no compaction	171	14	2.3
Fictive 3-D 20 kPa compaction	181	17	2.8
Fictive 3-D 50 kPa compaction	205	23	3.9
Design grid air no compaction	152	15	2.4
Design grid air 20 kPa compaction	167	18	3.0
Design grid air 50 kPa compaction	195	25	4.2
Soil case no compaction	12	0.4	0.07
Soil case 20 kPa compaction	22	1.5	0.25
Soil case 50 kPa compaction	56	7	1.2
Soil fictive 3-D no compaction	23	1.6	0.3
Soil fictive 3-D 20 kPa compaction	35	3.5	0.6
Soil fictive 3-D 50 kPa compaction	70	11	1.8

* The results are shown to the nearest mm for comparison purposes only. Model predictions are not this precise.

2. PROPOSED ANALYTICAL CALCULATION MODEL

With an active reinforcement, the size of the caps can be reduced. It is also possible to choose a lower embankment height than the 2.5 metres which is today the lowest permitted in Swedish regulations.

In order to be able to propose a model which is suitable for design of reinforcement over embankment piling, the SGI carried out a pre-study by the assignment of the SNRA where a number of calculation models were compared. In that comparison, BS 8006 appeared to be a promising model. In the second stage of the project, BS 8006 was compared with FLAC calculations to get a closer idea of the actual behaviour. That comparison showed that at the degree of cap coverage which is normally used in Sweden between 20 to 30 % (to be compared with those on which the method is based, which are usually around 8 to 16 %) the calculations did not agree. Better agreement was reached when Carlsson's method was compared to the FLAC calculations. This method had been modified to take into account the three-dimensional effects and reduced embankment heights.

2.1 Prerequisites

The calculation assumes arch formation and that the reinforcement is deformed during loading. The reinforcement is assumed to be placed in one layer. The function of the reinforcement is greatest if it is placed closest to the pile caps, but it should for practical reasons be about 0.1 m above the pile caps.

In order to ensure that the displacements in the road surface are not too large, the embankment height should be at least as large as the distance between the pile caps, a minimum of 1.0 m high, and the degree of cap coverage should be at least 10 %.

It is recommended that calculations should be carried out for an initial strain of a maximum of 6 % and with a remaining creep strain after the construction period and during the lifetime of the construction of an additional 2 % at most. Figure 9 shows the symbols used in the proposed calculation model.

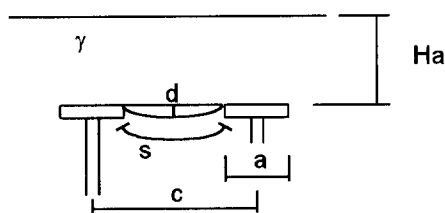


Figure 9. Symbols used in the proposed calculation model.

where c = distance between the pile centres (m)
 a = side length of the pile caps
 Ha = embankment's height above the reinforcement (m)
 γ = unit weight of embankment fill (kN/m^3)
 d = maximum displacement of the geosynthetic (m)
 s = arc length of the displaced geosynthetic (m)

2.2 Vertical load transfer

The method is based on the formation of an arch which spreads the soil load onto the pile caps. The cross-sectional area of the soil under the arch, which is the load carried by the rein-

forcement geogrid, is approximated using the soil wedge described in Figure 10. This applies even if the embankment height is lower than $(c-a)/2 \cdot \tan 15^\circ$, which is the height of the soil wedge.

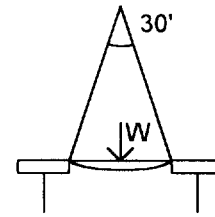


Figure 10. The soil wedge which is carried by the geosynthetic.

The weight of the soil wedge, W , according to Figure 10 is:

$$W = \frac{(c-a)^2}{4 \cdot \tan 15^\circ} \cdot \gamma \quad \text{kN per metre in depth.}$$

The arc length of the geogrid when it is displaced by the load of the soil wedge, can be calculated as follows:

$$s = (1 + \varepsilon)(c-a) = c-a + \frac{8}{3} \cdot \frac{d^2}{c-a}$$

where the displacement, d , is dependent on the strain in the geosynthetic, ε , according to:

$$d \approx (c-a) \sqrt{\frac{3}{8} \cdot \varepsilon}$$

The force in the reinforcement, F , in two-dimensions is calculated using the catenary equation:

$$F_{2D} = W \cdot \frac{(c-a)}{8d} \sqrt{1 + \frac{16d^2}{(c-a)^2}}$$

The three-dimensional effects are estimated through load distribution according to Figure 11, where the load is distributed over the surface according to the figure and is taken up by the reinforcement along the edge of the pile cap. The force is calculated as follows:

$$F_{3D} = \frac{1 + c/a}{2} F_{2D}$$

where,

F_{3D} = the dimensioned force in the reinforcement due to the vertical load in three dimensions

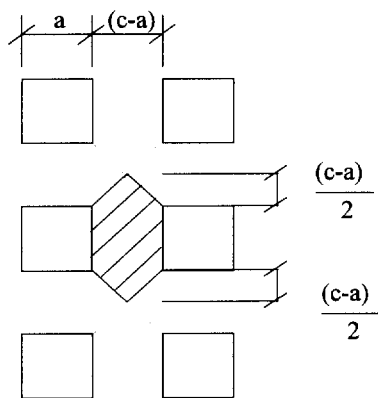


Figure 11. Load distribution to estimate the forces in the three-dimensional case.

2.3 Transverse sliding across the bank and pull-out of the reinforcement

For the necessary reinforcement length on account of transverse sliding across the bank, the bond length and the pull-out length of the reinforcement can be determined according to BS 8006.

3. CONCLUSIONS

In design with analytical models, the foundation support of the soil between the pile caps is not normally taken into account, but field measurements showed that the effect can be considerable. For the relatively low embankment height used here, it appeared that the displacement which arises in the reinforcement does not affect displacements in the road surface. In this case, the FLAC calculations are judged to give a good picture of the actual behaviour of the construction. Three-dimensional effects should however be simulated. Here they were fictively simulated by increasing the density of the fill.

Analytical calculation models are judged reasonable if there is a risk that a cavity will arise under the reinforcement. They are though often more conservative than if FLAC calculations are made for cavities. The proposed calculation model has proved to give better agreement with the FLAC calculations than other methods at the degrees of cap coverage which are normally used in Sweden, i.e. 20 to 30 %. Soil with poor properties can give support initially but settlement can arise even after the construction period. Thus in low embankments there is a risk that settlement which arises after the completion of the road could cause displacements in the road surface, and this must be taken into account in design. The force in the reinforcement is also greater if the soil settles than if there is resistance. Future changes to the load situation, e.g. a ground water lowering, can affect the foundation support of the soil and in such cases it should be assumed that a cavity has arisen.

Compaction of the fill above the reinforcement significantly affects the tensile force and moderately affects the displacement of the reinforcement. This is very important if the compaction is carried out at low fill heights above the reinforcement. The effect of compaction is not normally taken into account in calculations but should be considered if foundation support from the soil is assumed.

The results of the field study showed a large difference in the strain measurements close to the pile cap edge, possibly due to edge effects. This makes the cap edge strains difficult to compare with the calculation model. The strains measured in the center of the pile caps show a smaller difference and compare well with the FLAC model. Some effects of three-dimensional behaviour could be seen in the field measurements. A larger area with mattresses would have better simulated what actually happens if a cavity appears under the reinforcement. In this case the measurements were conducted on a road construction and the risk of having to rebuild large areas of the embankment, if the displacement of the road surface proved too great, was not acceptable.

For many cases the analytical calculation models that assume cavities below the geogrid are too conservative in estimating the forces in the geogrid. The finite difference model showed much better agreement with field measurements because it included the soil foundation support beneath the reinforcement. A study by (Jones et al, 1990) concluded that current simplified analytical procedures are conservative due to quantifying the arching mechanism and that they can not accurately take into account partial foundation support. There is a need for finite element or difference methods to model the complex interaction behaviour. Additional full-scale field testing and modelling is necessary to better understand the processes involved here.

The three-dimensional effects should be studied with field studies using larger areas with simulated cavities. Modelling should also be done with three-dimensional programmes to verify the differences between two- and three-dimensions. Until three-dimensional programmes become more common there is a need to model in two-dimensions, with relevant additions to take the three-dimensional behaviour into account.

ACKNOWLEDGEMENTS

The authors would like to thank Mr. F. Burman, SGI, who carried out the measurements, Mr. M. Åberg, SNRA, assistant project leader, Mr. P-E Bengtsson, SGI, for his views on the choice of parameters and Mr. T. Eng, Engtex, for help with the properties of the reinforcement.

The project described in the article was funded by SNRA and SGI.

Douglas Lindquist's participation in the project was possible thanks to a grant from the Valle Scandinavian Exchange.

REFERENCES

- British Standard, BS 8006 (1995) *Code of practice for strengthened/reinforced soils and other fills*. BSi.
- Carlsson B. (1987) *Reinforced soil, principles for calculation*, Terratema AB, Linköping. (In Swedish).
- Itasca Consulting Group, Inc. (1995). *Fast Lagrangian Analysis of Continua (FLAC) Version 3.3 User's Manual*.
- Jones, C.J.F.P., Lawson, C.R., Ayres, D.J. (1990) Geotextile reinforced piled embankments, *4th Int. Conf. on Geotextiles, Geomembranes and Related Products*, The Hague, 28 May-1 June 1990, page 155-159.

Embankment Support Over Piles Using Geogrids

C G Jenner and R A Austin

Tensar Division, Netlon Limited, New Wellington Street, Blackburn, UK

D Buckland

Clwyd County Council Highways Department, Clwyd, UK

ABSTRACT:

The construction of embankments over soft ground is a common engineering problem. In situations where the underlying soil is highly compressible or for approach embankments to bridges, minimising the total and differential settlement of a new road construction can govern the method of construction.

The paper describes the use of stiff biaxial polypropylene geogrids within granular fill to support embankment loads above piles and vibro concrete columns, VCCs. This technique has been used successfully on many road embankment projects in Europe due its cost effectiveness and ability to deliver an effective embankment support system within a short time frame.

The design and construction of geogrid reinforced load transfer platforms is discussed, including the platform used on the A525 Rhuddlan Bypass in North Wales, where due to underlying soil conditions, a piled solution employing VCCs was used, to carry the embankment loads through the soft layers into the firmer strata below.

To ensure that the load transfer platform (LTP) performed as expected, instrumentation was included in the platform construction to monitor platform settlement, geogrid strains and deflections. The installation and results of the instrumentation monitoring are described.

KEYWORDS: Embankments, Geogrids, Piles, Design, Monitoring

1 INTRODUCTION

The growing use of geosynthetic solutions for construction over soft and variable ground confirms their importance in overcoming complex geotechnical problems.

Increasingly utilised under embankments constructed on piles or vibro concrete columns (VCCs), is a geogrid reinforced granular load transfer platform. Used in several major UK projects, the technique is growing in popularity in Europe because it offers a rapid, cost effective solution within a predictable construction programme.

The platform functions by transferring loads imposed by the embankment to pile caps via a grid-reinforced basal layer. Biaxial geogrids, with high stiffness at low strain, are placed in several layers to interlock with, and reinforce the granular fill to create a flexurally stiff platform which distributes loads evenly and reliably to the piles. The supporting piles or VCCs pass through the soft soil layer and transmit load to the stable ground beneath, thus reducing settlement and removing the need to pre-consolidate the ground to remove permanent settlement and improve ground bearing properties.

2 LOAD TRANSFER PLATFORM CONCEPTS

The design of a load transfer platform can be carried out in different ways:

1. Tension membrane approach, using high strength tension membrane theory.
2. Improved arching approach, using low strength reinforcement.

The most common approach for embankment support over piles is to adopt the tension membrane approach. This requires the reinforcement to carry the full amount of any vertical load above the geosynthetic, less allowance for load shedding in the overlying fill.

The improved arching approach differs from the tension membrane theory only in respect to the calculation of the vertical load shedding and relies on the ability of the reinforcement used to interlock with the granular embankment fill and enhance the natural arching angle of the fill, thus reducing the vertical load to be supported by the reinforcement. Both design methods can be carried out in accordance with the limit state design principles defined in BS 8006.

When constructing load transfer platforms using the improved arching approach, the mechanism of load transfer is one of arching taking place in the granular platform. The purpose of the geogrids spanning across the pile/VCC heads is to enhance the transfer of vertical loading onto the piles/VCCs and subsequently through the piles/VCCs to the foundation soils.

In order to control differential settlement at the proposed ground surface, the geogrids need to adequately retain the soil between the arching angles of adjacent VCCs. A minimum height of fill above the load transfer platform of at least the platform thickness is normally employed to ensure that the arch is always loaded and that the VCC positions are not reflected up to the ground surface causing surface undulations.

Stiff integral biaxial geogrids, due to their unique element geometry and junction strength, interact with the fill and create a composite beam where the fill's shear strength properties are utilised effectively. The improved arching design approach is specific to a type of integral geogrid which has been proven to enhance the natural arching angle of granular fill when a multi-layer solution is employed, Guido 1987.

Research into the load transfer characteristics of the geogrid/fill composite has shown that the load spread through fill can be conservatively taken as 45° providing that the peak internal angle of friction of the fill is at least this value.

Whichever design approach is used, the design must ensure that the geosynthetic is sufficiently well anchored in the fill material, to permit the transfer of the design load into the reinforcement. This requirement can lead to long anchorage lengths where high strength reinforcement solutions are employed.

Geogrid load transfer platforms designed adopting the enhanced arching approach have been successfully used on a number of major projects in Europe, including the Gdansk Urban Highway, Topolnicki 1996 and the Second Severn Crossing Toll Plaza, Maddison et al. 1996.

3.0 CASE STUDY

3.1 A525 Rhuddlan Bypass

Rhuddlan is a small town standing between the coastal town of Rhyl and the main A55 trunk road, in Denbighshire (formerly Clwyd), North Wales. During the summer months large traffic volumes leave the A55 and travel through the centre of Rhuddlan on their way to the coast causing severe congestion.

In May 1995 a two year £11 million contract was started for the construction of 2km of 7.3m wide two lane dual carriageway bypass to the town, which included upgrading an existing section of highway and the construction of a

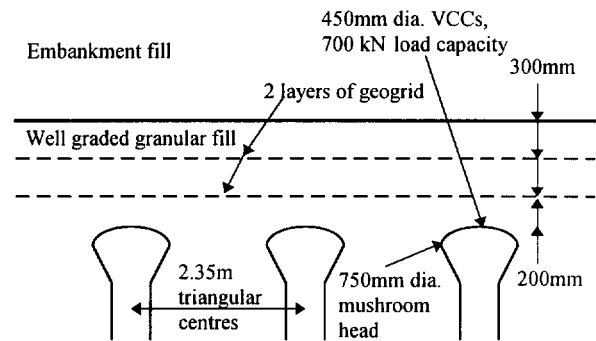


Figure 1 Typical cross-section through Rhuddlan bypass load transfer platform.

430m long 11-span twin deck viaduct, with a 46m centre span over the River Clwyd.

The approach embankment to one side of the viaduct crossed an area of 7-8m of peat and soft silty alluvial strata overlying sands and gravels. To support the embankment over this area the construction contract specified cast in situ driven piles under a 800mm thick un-reinforced rolled concrete supporting raft. Contractor Edmund Nuttall proposed a VCC and load transfer platform solution as an economic and rapidly constructed alternative to the specified design.

The accepted solution for the embankment support was to install VCCs at the appropriate centres to support the loads from the embankment which varied in height from 4m to 7m. The layout of the VCCs was a triangular pattern with centre to centre dimensions of 2.65m, 2.35m, 2.05m, and 1.75m, the closer centres supporting the higher sections of the embankment.

3.2 Load transfer platform design

The geogrid reinforced load transfer platform varied in height, 650mm, 800mm and 950mm, depending on the particular VCC layout with the number of geogrid layers being 3No. in the 950mm thick sections and 2No. in the 800mm and 650mm sections. As the distance between the VCCs reduced the load transfer platform thickness required for the arching mechanism to develop also reduced.

The LTP was designed assuming a grid strain of 5% in 120 years. This level of strain was assumed to represent the ultimate limit state condition for the platform, which can only occur in conditions where the underlying soil would degrade or collapse, i.e. waste fills. Such conditions did not occur on this site. For the in-service condition some support to the fill beneath the developed arch will always be provided by the underlying soil, leading to a reduced level of strain in the geogrid. A typical cross section through the construction used is shown in Figure 1

Table 1 Properties of Geogrids used in the Rhuddlan Bypass Load Transfer Platform

Grid Property		Tensar SS1	Tensar SS2
		Grid Type 1	Grid Type 2
Quality Control Strength*	LD	12.5 kN/m	17.5 kN/m
	TD	20.5kN/m	31.5 kN/m
Approximate Peak Strain	LD	12.0%	12.0%
	TD	10.0%	10.0%
Load at 2% Strain*	LD	4.5 kN/m	7.0 kN/m
	TD	6.0 kN/m	12.0 kN/m
Load at 5% Strain*	LD	9.5 kN/m	14 kN/m
	TD	15.0 kN/m	23.0 kN/m
Typical Rib Thickness	LD	0.7mm	1.20mm
	TD	0.5mm	0.90mm

* Determined as a lower 95% confidence limit in accordance with ISO 2602 1980 (BS 2846 Part 2 1981).

and properties of the reinforcement used are given in Table 1. Approximately 18 000m² of biaxial geogrid was installed to construct the 6000m² of load transfer platform over VCCs installed by Keller Foundations Ltd.

Due to the critical nature of the project the Client, Clwyd County Council requested the Contractors alternative design was subjected to Category II checks and certification. An independent verification of the design was therefore carried out by Clwyd County Council's Design and Construction Division Bridges Group - the designer of the structures.

3.3 Monitoring of geogrid strain

To ascertain the performance of the load transfer platform, the bridge designer specified that strain gauges and inclinometers were installed in the reinforced fill. At two locations, inclinometer and strain gauges were installed to monitor development of the arch and geogrid strain.

Prior to installation of the strain gauges, a calibration exercise was undertaken in a tensile testing machine to correlate the strain recorded by the gauges with the actual strain in the grid, Figure 2.

On site, vibrating wire strain gauges were clamped in pairs to both layers of grid, at the centre of the geogrid design span geogrid to measure strain over a 260mm gauge length, Figure 3. At locations A and B, an inclinometer and two pairs of strain gauges were installed on each layer of grid. Station A was under the viaduct bank seat with a vertical pressure of 121 kN/m² applied to the top of the reinforced fill. At Station B the platform was supporting a 4m high embankment.

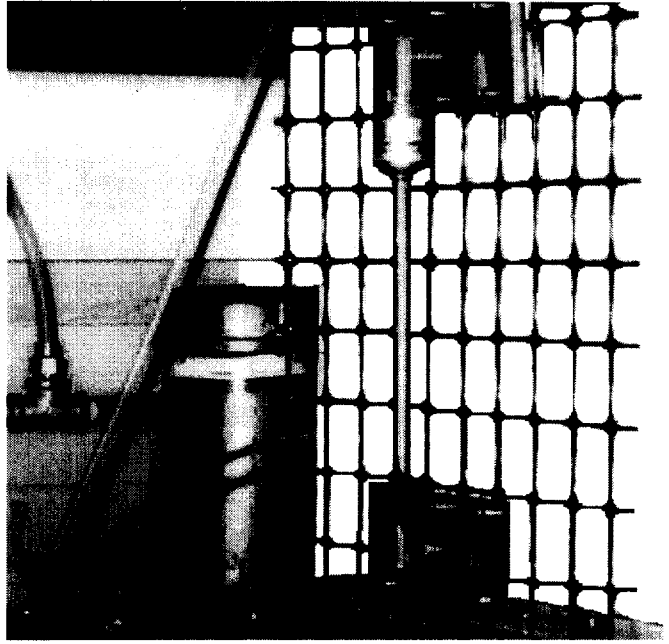


Figure 2 Laboratory calibration of strain gauges.

3.4 Results of strain monitoring

Readings taken over a period of one year show that strain developed in the grid during construction, after which the strain remained virtually unchanged, Figure 4 & 5. Once the initial strain had developed during construction the LTP rapidly achieved a state of equilibrium and the grid strains stabilised, with no evidence of creep being apparent. As used in the LTP design, partial support of the fill under the arch was shown to have occurred by a reduced level of strain in the geogrid from that assumed being recorded.

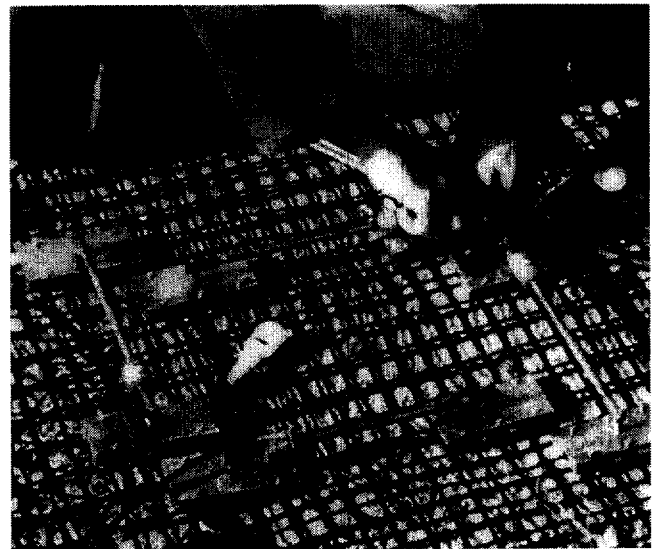


Figure 3 Installation of strain gauges on geogrid

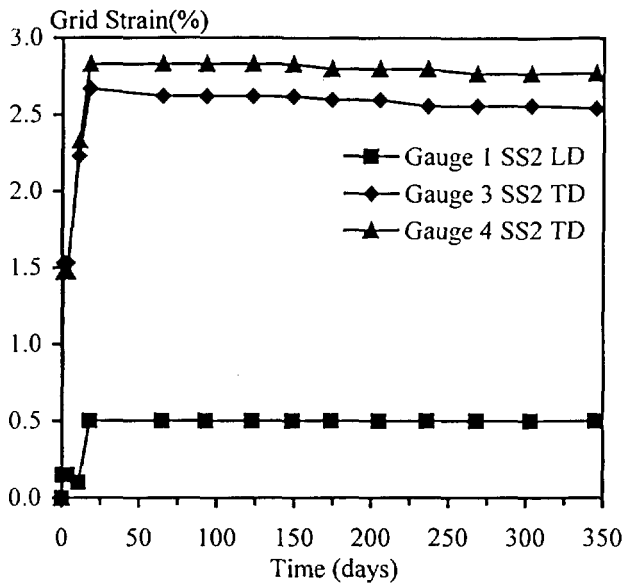


Figure 4 Geogrid strain readings at Station B Lower Grid - Grid Type 2

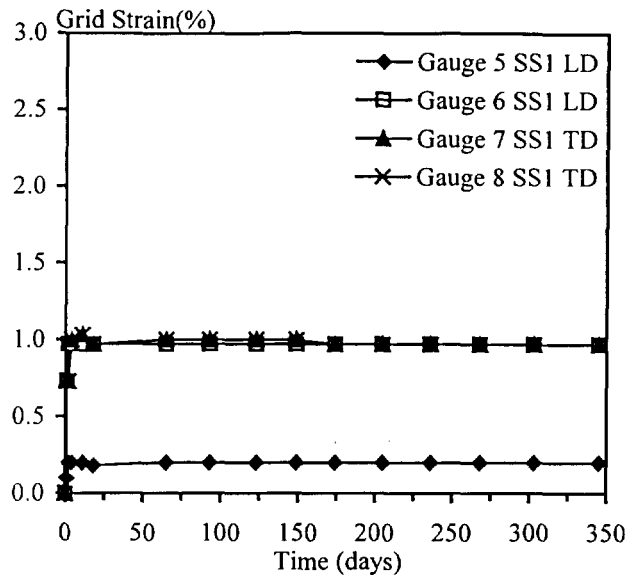


Figure 5 Geogrid strain readings at Station B Upper Grid - Grid Type 1

One of the simplified assumptions made during the design check was that half the weight of the fill under the arch would be supported by the foundation soil and half by the geogrid layers. It was further assumed that the strain in the upper grid would be less than that in the lower grid. The initial strain calculated by this approach was found to be of similar magnitude to that recorded by the strain gauges over the monitoring period.

4.0 CONCLUSIONS

1. The geogrid reinforced load transfer platform used on the Rhuddlan Bypass project provided a cost effective solution to the problem of embankment construction over soft ground.
2. The monitoring undertaken revealed that the geogrid reinforcement was providing restraint to the fill to enable enhanced arching within the fill to occur.
3. Recorded geogrid strains were as allowed for in the design.
4. Due to the interlock of the geogrid with the fill and the development of a composite material, no evidence of creep of the geogrid was recorded.
5. Higher grid stains were recorded in the lower grid than the upper grid as anticipated in the design.
6. The use of low strength, stiff biaxial geogrids and the enhanced arching design approach is a viable alternative to the use of high strength reinforcement and tension membrane theory, for the construction of embankments over piles.

ACKNOWLEDGEMENTS

The Authors wish express their thanks to the Highways and Transportation Department of the former Clwyd County Council and subsequently the Technical Services Department of Denbighshire County Council for the provision of monitoring data for inclusion in this paper.

REFERENCES

- British Standards Institution. BS 8006:1995, "Code of practice for strengthened reinforced soils and other fills", BSI, London.
- Guido, V.A., Knueppel, J.D., Sweeny, M.A., 'Plate Loading Tests on Geogrid-Reinforced Earth Slabs', Proceedings: Geosynthetics '87, IFAI, New Orleans, USA. pp. 216-225.
- Maddison, J.D., Jones, D.B., Bell, A.L. and Jenner, C.G., (1996), "Design and performance of an embankment supported using low strength geogrids and vibro concrete columns", Geosynthetics: Applications, Design and Construction, Proceedings EuroGeo1, Balkema, Maastricht, Holland, pp. 325-332.
- Topolnicki, M, (1996), "Case History of a geogrid-reinforced embankment supported on vibro concrete columns", Geosynthetics: Applications, Design and Construction, Proceedings EuroGeo1, Balkema, Maastricht, Holland, pp. 333-340.

Two- and Three-Dimensional Numerical Analysis of the Performance of Piled Embankments

G. Kempton
Consultant, Terram Ltd, Pontypool, UK

D. Russell
Geotechnical Engineer, Foundations & Geotechnics Division, Mott MacDonald, UK

N. D. Pierpoint
Geotechnical Engineer, Foundations & Geotechnics Division, Mott MacDonald, UK

C. J. F. P. Jones
Professor of Geotechnical Engineering, University of Newcastle-Upon-Tyne, UK

ABSTRACT: Empirical methods have been in use for some time to design geosynthetic materials to carry embankment loads over piles. Some methods have used simple two-dimensional models based on little more than load spreading procedures which generally ignore three-dimensional effects. Other methods have attempted to address the three-dimensional nature of the problem by basing the design method on behaviour observed in experimental work. The paper describes work which has been carried out using two- and three-dimensional finite difference techniques that better represents the problem's full complexity. A study has been carried out which compares the two- and three-dimensional analyses for various piled embankment geometries. A comparison is also made between the two and three-dimensional finite difference analyses and the current British design standard, BS 8006. The paper also gives recommendations for design.

KEYWORDS: Design, Embankments, Finite Element Analysis, Geosynthetic Reinforcement, Soft Soils.

1. INTRODUCTION

Construction of roads, railways and buildings is increasingly carried out on foundations that would previously have been considered unsuitable. In order to construct these structures with confidence and within the available time it is often necessary to adopt a piled solution. Piles are installed through the soft subsoil material. The piles are much stiffer than the subsoil and therefore differential settlements occur. These differential movements generate shear stresses within the embankment which increase the load on the piles and decrease the load on the subsoil. This mechanism is called arching.

In order to place the relatively expensive piles as far apart as possible, a relatively inexpensive geosynthetic material is included at the base of the fill. The geosynthetic picks up the vertical load not carried directly by the piles and goes into tension. The difficulty in design is to assess the amount of vertical load which is carried by the geosynthetic and the tension which this load generates in the geosynthetic.

A typical piled embankment layout is shown in Figure 1. For analysis and design a two-dimensional (2D) model, Figure 2, has often been used. However, in reality, the problem is three-dimensional (3D), Figure 3.

A research project has been undertaken to better understand the behaviour of the piled embankment system. The finite difference programs FLAC and FLAC^{3D} (ITASCA, 1993) have been used to carry out a series of 2D and 3D numerical analyses. These are compared to assess the appropriateness of each approach.

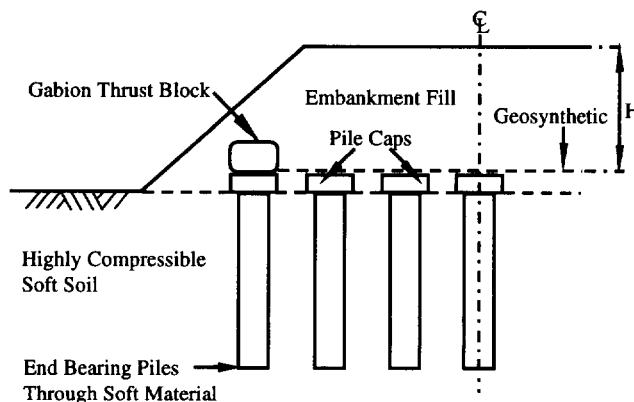


Figure 1. A cross-section through a typical piled embankment.

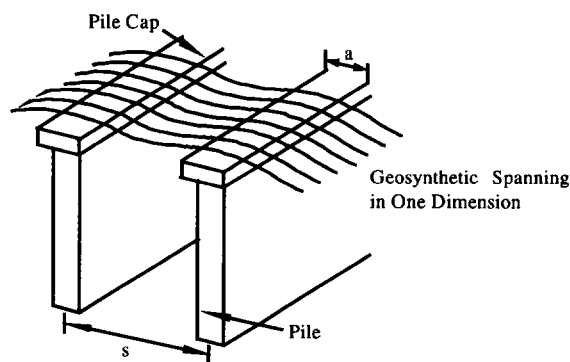


Figure 2. Two-dimensional representation of the piled embankment problem.

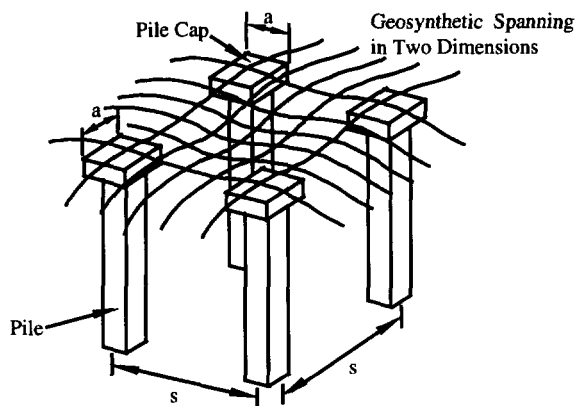


Figure 3. Three-dimensional representation of the piled embankment problem.

Due to the uncertainty of the subsoil behaviour it is generally assumed that the entire vertical load of the embankment is carried by the piles, either by soil arching or transferred by the geosynthetic.

In order to compare design methods a parameter, the Stress Reduction Ratio S has been defined (after Low, Tang and Choa, 1994). The Stress Reduction Ratio is defined as the ratio of the average vertical stress carried by the geosynthetic p_r to the average vertical stress γH due to the embankment fill of height H :

$$S = \frac{p_r}{\gamma H} \quad (1)$$

The stress reduction ratio S is written S_{2D} or S_{3D} for two- and three-dimensional conditions respectively.

2. NUMERICAL ANALYSIS

An initial series of 2D numerical analyses was performed using the finite difference program FLAC. A cross section of the embankment was considered in plane strain for which the pile is represented as a strip foundation. A typical mesh geometry is shown in Figure 4(a).

However, the piled embankment problem is truly 3D (Figure 3); neither plane strain nor axisymmetric analyses accurately reproduce the behaviour. (In axisymmetric analysis, an umbrella shaped arch resting on a single central pile cap is produced). A second series of analyses was performed using the 3D finite difference program FLAC^{3D}. A typical mesh geometry for these analyses is shown in Figure 4(b). In 3D the arching can be thought of as producing a dome resting on four pile caps. In both the 2D and 3D analyses, the fill material was modelled as linear elastic with a Mohr-Coulomb yield criterion ($E' = 20 \text{ MPa}$, $\nu' = 0.2$, $\phi' = 30^\circ$, $c' = 5 \text{ kPa}$ and $\gamma = 20 \text{ kN/m}^3$). The geosynthetic, installed at the base of the fill, consisted of one-dimensional linear elastic elements capable of sustaining axial tension but no bending (a single line of elements in 2D and a grid of elements in 3D with a stiffness $J = 9500 \text{ kN/m}$). In the analyses presented the subsoil was not included (which reproduced

the assumption made in all current design methods), although analyses have subsequently been carried out where the subsoil was included. The pile was assumed rigid with the base of the mesh fixed vertically to represent the pile cap.

For both the 2D and 3D analyses, the embankment fill material was modelled as being installed in a number of lifts. After each lift deformation occurs and the geosynthetic tension increases. The analysis therefore models an embankment constructed very slowly under drained conditions with full consolidation of the subsoil between lifts.

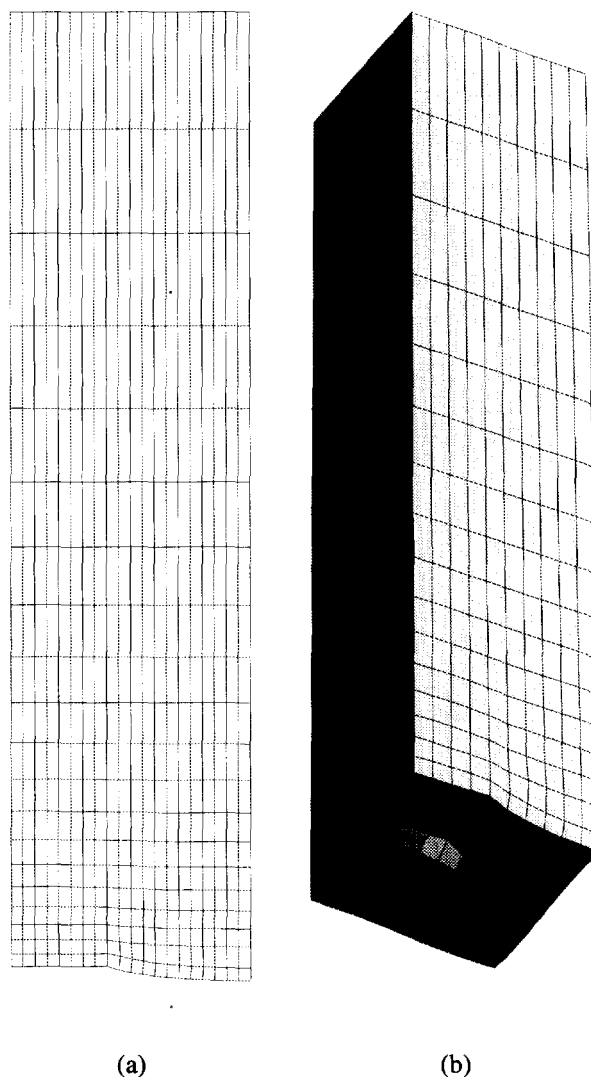


Figure 4. Mesh geometry for (a) 2D analyses, and (b) 3D analyses.

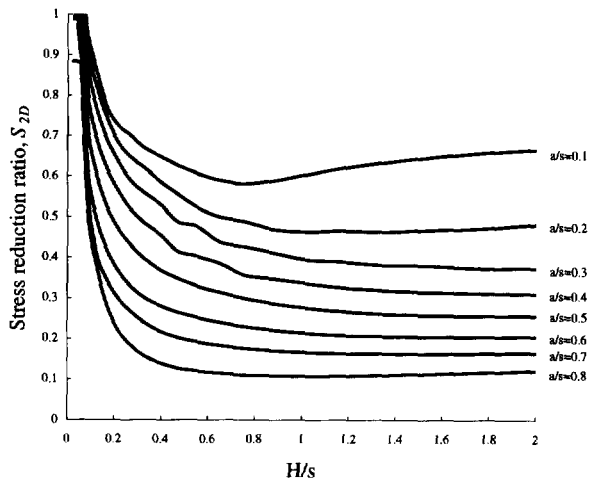


Figure 5. Stress reduction ratio in two-dimensional analyses.

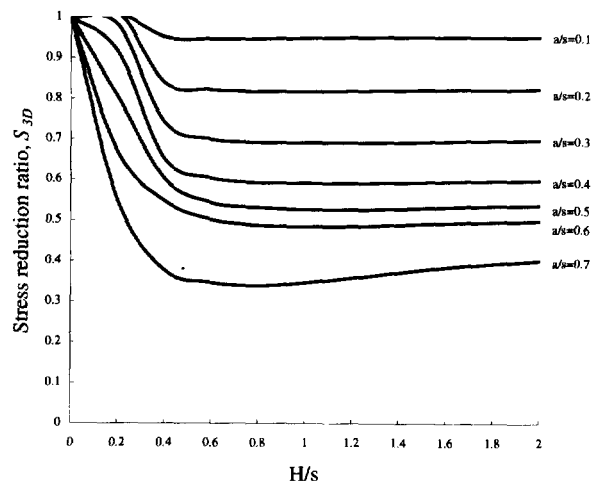


Figure 6. Stress reduction ratio in three-dimensional analyses.

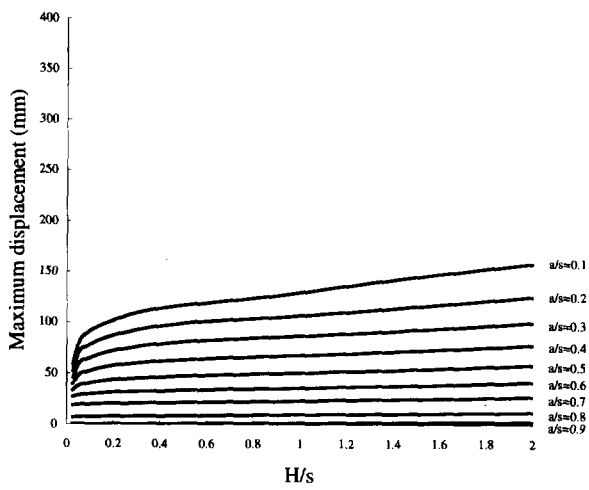


Figure 7. Maximum displacement in two-dimensional analyses.

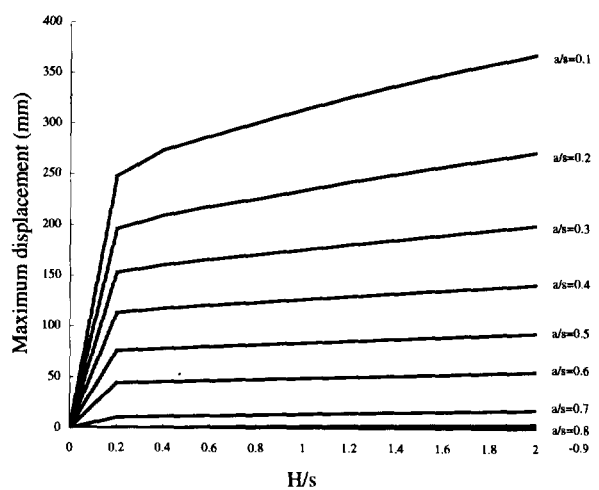


Figure 8. Maximum displacement in three-dimensional analyses.

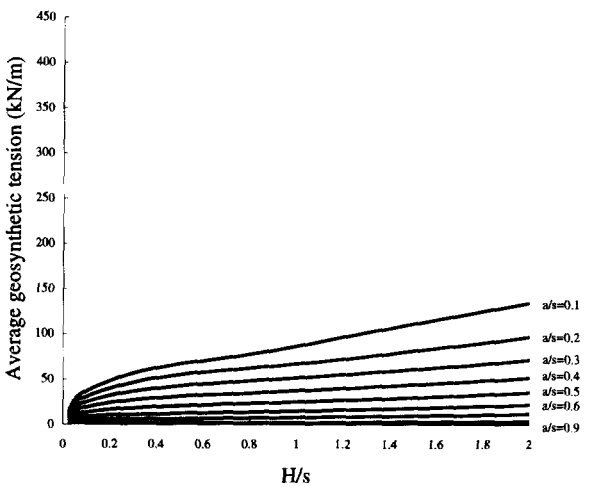


Figure 9. Average geosynthetic tension in two-dimensional analyses.

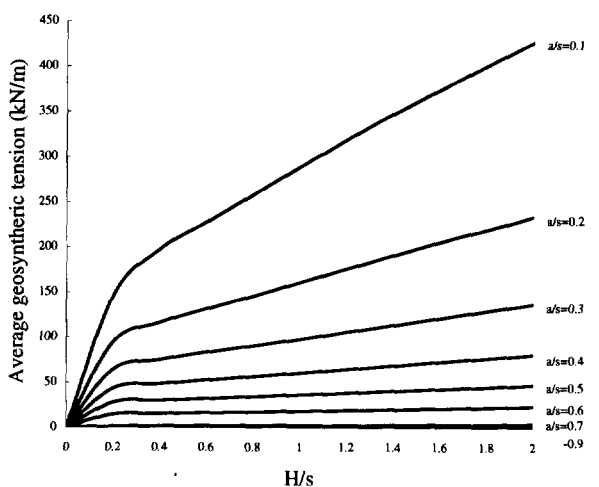


Figure 10. Average geosynthetic tension in three-dimensional analyses.

Analyses were performed in which the pile width a to pile spacing s ratio was varied with the fill and geosynthetic properties held constant. The behaviour of the system was assessed in terms of the stress reduction ratio (Figure 5, Figure 6), the average tension generated in the geosynthetic (Figure 7, Figure 8), and the maximum displacement at the base of the embankment (Figure 9, Figure 10), for 2D and 3D analyses respectively.

3. DISCUSSION OF ANALYSIS RESULTS

In both the 2D and 3D analyses, the stress reduction ratio decreases as a/s ratio increases. This is a result of the piles being closer together allowing arching to develop. Also, the stress reduction ratio decreases as the height increases until a critical height is reached after which the stress reduction ratio is virtually constant. This behaviour is explained by the ability of the arching mechanism to develop as the height increases. There is a point at which 'full arching' develops. When this occurs the load carried by the geosynthetic increases proportionally to the embankment height.

The stress reduction ratio determines the maximum displacement and the geosynthetic tension. The higher the stress reduction ratio the larger the maximum displacement and the larger the geosynthetic tension.

The numerical analyses presented demonstrate the need to analyse the piled embankment in 3D rather than 2D. Comparing Figures 6 and 7, it can be seen that the stress reduction ratio is significantly higher in the 3D analyses than in the 2D analyses for any given a/s ratio. Consequently, the maximum displacement at the base of the embankment and the tension generated in the geosynthetic are underestimated if the 3D nature of the problem is ignored. This behaviour is intuitively correct as the proportion of pile is less in the 3D case (a^2/s^2) than in the two-dimensional case (a/s).

4. BS 8006 DESIGN METHOD

The method used in the current BS 8006, Code of practice for strengthened/reinforced soils and other fills (1995) to design geosynthetics over piles was initially developed by Jones et al. (1990). An assessment of the degree of arching taking place in the embankment fill is made using Marston's formula for positive projecting subsurface conduits (Spangler and Handy, 1973; Young and O'Reilly, 1983). BS 8006 introduces a critical height concept, Figure 11, with the critical height assumed to be equal to $1.4(s-a)$, where s is the pile spacing and a is the width of the pile cap.

If the embankment height is below the critical height Figure 11(a), the load carried by the geosynthetic is the embankment load reduced due to the arching in the embankment fill plus any surcharge loading on the top of the embankment. For embankment heights greater than

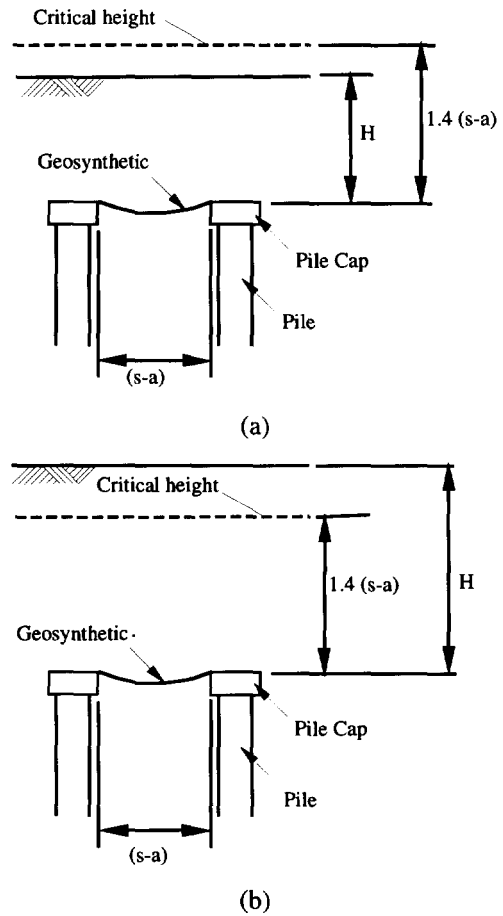


Figure 11. BS 8006 critical height concept.

the critical height, Figure 11(b), it is assumed all loads above the critical height are transferred directly to the piles as a result of arching in the embankment fill.

The load on the geosynthetic is assumed to be a distributed load between adjacent pile caps and the resultant deflected shape of the geosynthetic a parabola. The tension in the geosynthetic, ignoring partial factors of safety, is calculated using the following equation:

$$T = \frac{w_T(s-a)}{2a} \sqrt{1 + \frac{l}{6\varepsilon}} \quad (2)$$

where w_T is the distributed load on the geosynthetic and ε is the strain in the geosynthetic. w_T can be calculated using one of the following expressions, depending on the embankment height:

For $H > 1.4(s-a)$

$$w_T = \frac{1.4s\gamma(s-a)}{s^2 - a^2} \left[s^2 - a^2 \frac{p'_c}{\sigma'_v} \right] \quad (3)$$

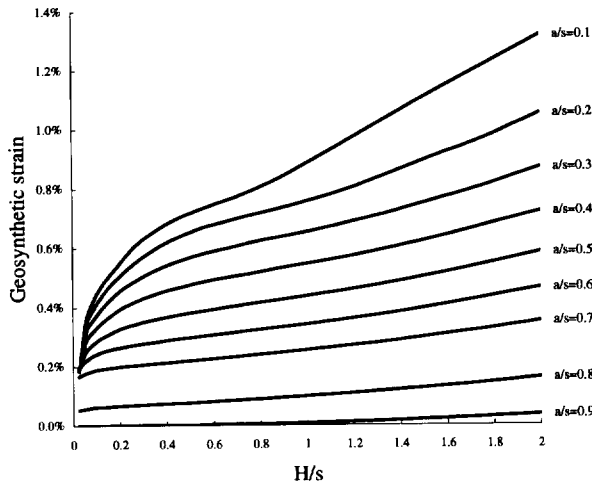


Figure 12. Geosynthetic strain from 2D FLAC analyses.

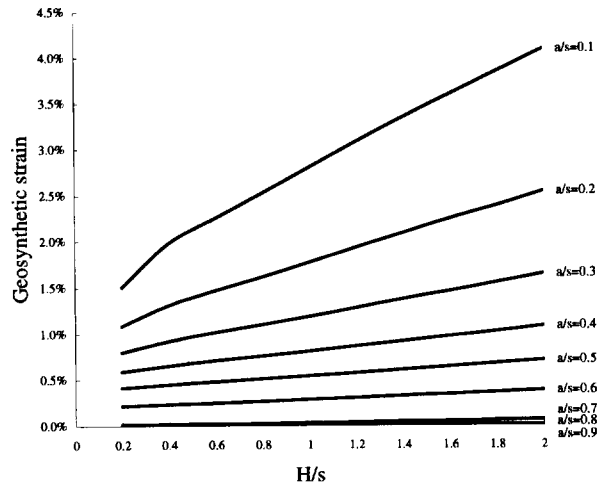


Figure 13. Geosynthetic strain from 3D FLAC analyses.

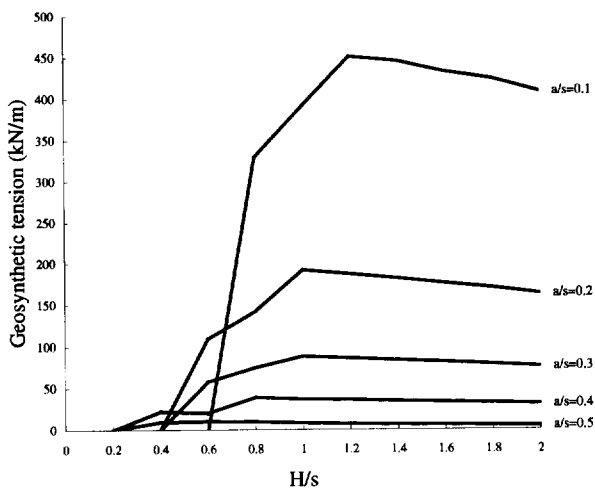


Figure 14. Geosynthetic tension in 2D based on BS 8006.

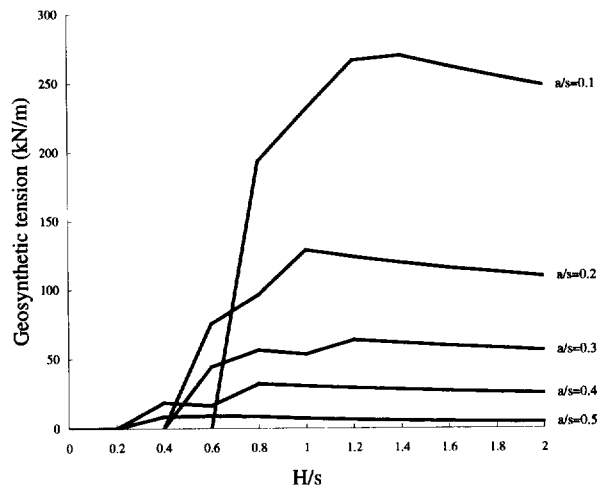


Figure 15. Geosynthetic tension in 3D based on BS 8006.

For $0.7(s-a) \leq H \leq 1.4(s-a)$

$$w_T = \frac{s(\gamma H + w_s)}{s^2 - a^2} \left[s^2 - a^2 \frac{p'_c}{\sigma'_v} \right] \quad (4)$$

Where γ is the soil unit weight, w_s is a uniformly distributed surcharge loading, p'_c is the vertical stress on the pile cap and σ'_v is the average vertical stress at the base of the embankment. p'_c/σ'_v can be calculated using the following expression:

$$\frac{p'_c}{\sigma'_v} = \left[\frac{C_c a}{H} \right]^2 \quad (5)$$

Where for the end bearing pile used in this study C_c is defined as:

$$C_c = 1.95 \frac{H}{a} - 0.18 \quad (6)$$

Partial factors of safety have been omitted from the above equations. No account is taken of the subsoil in assessing the load to be carried by the geosynthetic. BS 8006 recommends that the initial design strain should be limited, for practical purposes, to less than 6%.

For comparison purposes the tension in the geosynthetic was calculated for H/s ratios from 0.2 to 2.0 and a/s ratios from 0.2 to 0.8. The design strain values used in Equation 2 were taken from both the 2D and 3D FLAC analyses in Figure 12 and Figure 13, respectively. The tensions determined from the BS 8006 design method are presented in Figure 14 for 2D and Figure 15 for 3D.

A marked difference was found between the geosynthetic tensions calculated using BS 8006 and those resulting from the FLAC analyses.

It was found that BS 8006 overestimated the geosynthetic tension for all geometries in 2D and underestimated the tension in 3D. For a/s between 0.2 and 0.6 and with H/s between 0.6 and 1.4 the BS 8006 geosynthetic tensions were approximately 30% lower than the 3D FLAC analysis. For the other

geometries the difference was larger. For values of a/s less than 0.6 BS 8006 gave a negative tension value. If the BS 8006 partial load factor for soil unit weight is applied, all calculated geosynthetic tensions are 30% higher.

5. RECOMMENDATIONS FOR DESIGN

The analyses presented have been compared with various design methods (Russell and Pierpoint, 1997). The comparison showed that there is a reasonable agreement with the Terzaghi (1943) and the Hewlett & Randolph (1988) design methods. The other design methods used in the UK, BS 8006 (1995) and Guido (1987), appear to give results that differ significantly from the numerical analyses for some geometries. The most appropriate design method is dependent on the geometry of the particular piled embankment.

The major uncertainty is the vertical load that the soft subsoil can carry in the long term without producing excessive settlement. This is a very difficult prediction to make as the stiffness of the fill, geosynthetic, piles and subsoil all contribute to the distribution of stresses and therefore, displacement. If the subsoil contribution is overestimated then large settlements of the surface of the embankment can result (Azam et al, 1990). Currently the authors recommend a conservative approach to design with the contribution from the subsoil calculated based on the allowable settlement at the surface of the embankment. This contribution may be negligible for high embankments but can be significant for low embankments or lightly loaded building floor slabs.

Research is underway to look at the role of the subsoil in more detail and to provide recommendations for design. In the mean time the use of numerical analysis methods is strongly recommended.

5. CONCLUSIONS

A series of 2D and 3D numerical analyses have been carried out to investigate the behaviour of piled embankments. The analyses show large differences between the 2D and 3D cases. A 3D model is required to accurately model the wide range of piled embankment geometries used in practice.

The 3D parametric study has shown that the minimum stress reduction ratio develops at an H/s ratio of approximately 0.5. A significantly lower stress reduction ratio is calculated in 2D analyses.

A comparison was made between the BS 8006 design method and the 2D and 3D FLAC analyses. BS 8006 overestimated the geosynthetic tension when compared with FLAC 2D and under estimated the tension when compared with FLAC 3D.

Recommendations for design have been made. The major uncertainty is the amount of vertical load that can be resisted by the subsoil. Due to the current lack of

information, the authors recommend a cautious approach. For high embankments, the resistance from the subsoil is likely to be a small proportion of the total load. For lower embankments, or building slabs, the subsoil resistance may be significant but must be assessed with care to ensure that the long term surface settlements meet construction specifications.

REFERENCES

- Azam, T., Ramsn, K. and Ali, F. H. (1990), Geotechnical assessment of distressed piled embankments on soft ground, *Seminar on Geotechnical Aspects of the North South Expressway*, Kuala Lumpur, Malaysia.
- BS 8006 (1995), *Code of Practice for strengthened/reinforced soils and other fills*, British Standards Institute.
- Guido, V.A., Kneuppel and Sweeney, M.A. (1987), Plate loading tests on geogrid-reinforced earth slabs, *Geosynthetics '87*, New Orleans, pp. 216-225.
- Hewlett, W.J. and Randolph, M.F. (1988), Analysis of piled embankments, *Ground Engineering*, Vol. 21 No. 3.
- ITASCA Consulting Group Inc (1993), *FLAC/FLAC^{3D} - Fast Lagrangian analysis of Continua*. ITASCA Consulting Group, Minneapolis, Minn, USA.
- Jones, C.J.F.P., Lawson, C.R., Ayres, D.J. (1990), *Geotextile reinforced piled embankments, Geotextiles, geomembranes and related products*, Den Hoedt (Ed), 1990, Balkema, Rotterdam, pp. 157-159.
- Low, B.K., Tang, S.K. and Choa, V. (1994), Arching in Piled Embankments, *Journal of Geotechnical Engineering*, ASCE, Vol. 120. No. 11, pp. 1917-1937.
- Russell, D. and Pierpoint, N. D. (1997). A numerical investigation of the behaviour of piled embankments. *Ground Engineering*, November, Thomas Telford.
- Spangler, M.G. and Hardy, R.L. (1973), *Soil Engineering*, Intext Education Publishers, New York.
- Terzaghi, K. (1943), *Theoretical Soil Mechanics*, John Wiley & Sons, New York.
- Young, O.C. and O'Reilly, M.P. (1983), *A guide to design loadings for buried rigid pipes*, Transport and Road Research Laboratory, UK.

Geogrid and Geocell Reinforced Secondary Road Over Deep Peat Deposit

Juha Forsman

Research Engineer, Viatek Group Ltd, Espoo, Finland

Eero Slunga

Professor, Soil Mechanics and Foundation Engineering, Helsinki university of Technology, Espoo, Finland

Pentti Lahtinen

Development Manager, Viatek Group Ltd / SGT, Luopioinen, Finland

ABSTRACT: A reinforced secondary road on the top of a 10 meter thick peat deposit has been constructed at the peat bog of "Leteensuo" in the southern part of Finland. The secondary road contains three different reinforced test sections: two geogrid reinforced and one geocell reinforced sections. This paper presents the description of the construction, field instrumentation and observations of the test sections. The bearing capacity and the settlement of the reinforced roads have been analysed by manual calculation methods. After construction the calculations have been verified on the basis of field observations.

KEYWORDS: Unpaved Roads, Geogrids, Geocell, Instrumentation, Case study

1. INTRODUCTION

A secondary road (Y607) has been constructed on the top of a peat surface using synthetic georeinforcements. The road forms a part of the Finnish Georeinforcement Research and Development Project, which has been introduced by Friberg et al. (1994).

The secondary road on the top of peat contains three different reinforced test sections: two geogrid reinforced and one geocell reinforced sections. The situation of the test sections is beside the Highway between Helsinki and Tampere at Leteensuo peat bog about 15 km to north-west of the city of Hämeenlinna. The private secondary road is constructed beside the highway at summer 1996.

2. TEST SITE

2.1 Geology

In the middle of the peat deposit of Leteensuo the thickness of peat layer is 9...10 m and the degree of humification of it is medium (H4-6) or high (H7-10), Figure 1. On the edges of the deposit the degree of humification is high (H=von Post classification). Under the peat layers there is 5...6 m of clay on the top of glacial till. The level of ground water is near the ground level.

2.2 Index Properties of the Peat

The index properties of the peat samples [water content (w), density (γ), ash content (A_s), acidity (pH), void ratio (e) and the degree of humification (H)] are presented in Figure 2 at station number 244 (Figure 1).

The water content of the peat is about 500...1000 % at the

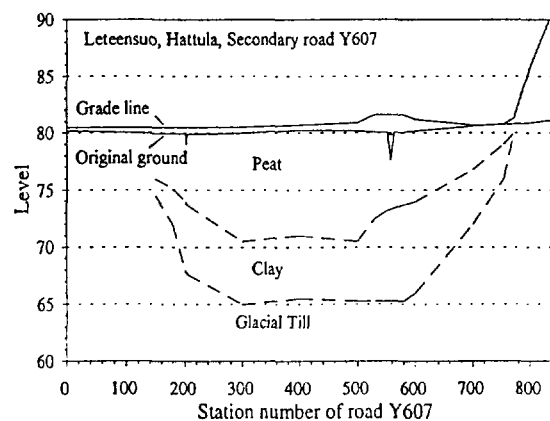


Figure 1. Profile of the secondary road at Leteensuo.

depth of 1...10 m and 300...500 % at the depth of 0...1 m.

2.3 Strength and Deformation Parameters of the Peat

The undrained shear strength of the peat has been determined by vane test (c_u) and fall-cone test (c_{uk}), Figure 2. Drained and undrained triaxial tests with undisturbed peat have been performed using standard triaxial apparatus. The triaxial tests have been performed at a strain rate of 0,6 %/h and with $\sigma_3 = 10...20$ kPa. The strength and deformation parameters have been determined at strains $\epsilon_1 = 1,6..15$ %. The drained Young's modulus varies between 380..150 kPa at strains 1,6..15 % at the depth of 0,8..1,0 m, between 360..100 kPa at the depth of 1,3..2,4 m and between 355..80 kPa at the depth of 3,1..5,3 m.

The undrained Young's modulus varies between 580..140 kPa at strains 1,6..15 %. Cohesion varies between 0.4 kPa and the angle of friction between 3..19°. The peat seems to behave like a yield hardening material, without any rupture.

The strength properties of the peat have been determined also by direct shear tests. One dimensional compression of the peat has been studied by means of incremental loading and constant rate of strain oedometer tests. The results of those laboratory tests have been presented more comprehensively by Lojander et al. (1996).

3. TEST STRUCTURES

The secondary road of Leteensuu contains two geogrid and one geocell reinforced test sections.

The reinforcements have been used to increase the bearing capacity and to reduce the settlement differences of the road. The road embankment has been constructed by the Finnish National Road Administration of Häme Region.

The geogrid or geocell reinforced structures are: 1xgeogrid+crushed gravel (Ch 90..200 and 680..750, Fig. 3a), Geocell+LECA (Ch 200..300, Fig. 3b) and 2xgeogrid+LECA (Ch 590..680, Fig. 3c).

The test structures are illustrated as designed. The fulfilled thicknesses of the aggregate layers were mainly higher than designed. The fulfilled layer thicknesses at the instrumented stations, 170, 240 and 650, are presented in the brackets in Figure 3. The fulfilled layer thickness varies quite much at the 1xgrid and 2xgrid -structures. The layer thickness of the geocell structure does not vary significantly. The layer

thickness has been measured by ground penetrating radar (GPR) survey after construction.

The LECA, Light Expanded Clay Aggregate, has been used as a light-weight fill because of the expected large settlements of the road.

4. MATERIALS OF THE TEST STRUCTURES

4.1 Aggregates

In the 1xgeogrid+crushed gravel -structure there was used crushed gravel with a grain size of 0-65 mm as a bearing layer. In the geocell structure the 500 mm high geocell was filled with blown LECA with a grain size of 4-20 mm. In the 2xgeogrid+LECA -structure there was used about 500 mm layer of LECA with a grain size of 0-65mm. Over the LECA there was a layer of crushed gravel as a bearing layer. Uppermost there was surface layer of gravel (0-16mm). The strength and deformation parameters of the aggregates are presented in Table 1.

4.2 Geosynthetics

Geogrid Tensor SS30 (grid A) has been used at the bottom of the test structures 1xgrid+crushed gravel and geocell+LECA. Geogrid Tensor SR55 (grid B) has been used as a vertical grid of the geocell structure. Geogrid Fortrac 35/20 (grid C) has been used in the test structure 2xgrid+LECA. The properties of the grids are presented in Table 2.

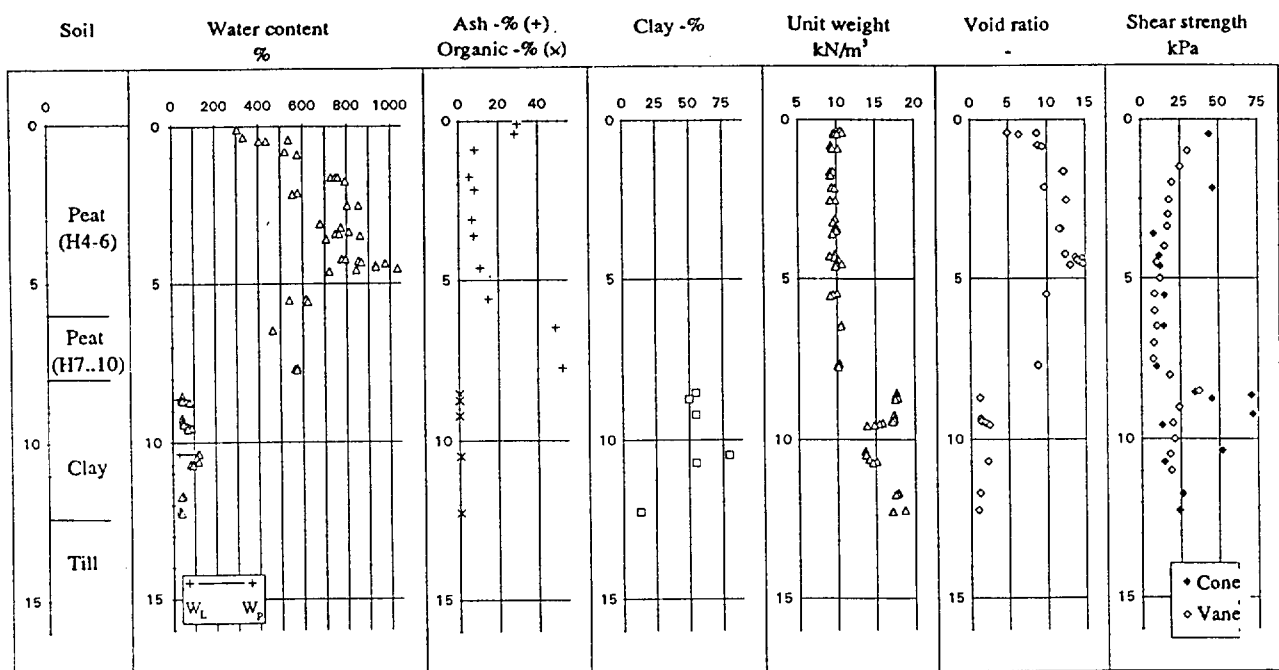


Figure 2. Index properties and undrained shear strength of peat and clay of Leteensuu at station 244.

Table 1. Index, strength and deformation properties of the aggregates.

	Crushed gravel 0-65 mm	LECA 4-20 mm	LECA 0-65 mm
γ_0 [kN/m ³]	19,45	2,99...3,07	4,49...4,81
triaxial test			
ϕ_p c_p [° kPa]	43,8 0	44,5 2	44,5 2
ϕ_c c_c [° kPa]	42,6 0	40,0 2	40,0 2
E_{d50} [kPa]	9...26	11...13	14...16
E_{dr} [kPa]	47...143	-	56

Polypropylene grid A is extruded biaxially drawn. Polyethylene (HDPE) grid B is extruded uniaxially drawn. Polyester grid C is woven and coated with PVC. The weight of grid A is 300 g/m², grid B 500 g/m² and grid C 210 g/m².

5. CONSTRUCTION

5.1 Installation of the Geogrids

All test structures have been built during May-July 1996 in three sections. Over the levelled subsoil there was first put a needlepunched nonwoven geotextile. Over the textile there

Table 2. Properties of the reinforcements.

Label	Index strength kN/m	F_{max}^d = UTS kN/m	ϵ_{max}^d %	J_{sec}^d $\epsilon = 2$ 6 % kN/m
A ^a	30 / 30 ^a	32,6	9,4	780 535
B ^b	55 / - ^b	50,5	10,1	905 650
C ^c	35 / 20 ^c	36,6	11,4	305 230

a. Biaxially drawn b. Uniaxially drawn c. Woven
a. and b. Netlon Limited (1984, 1995)
c. DIN 5387, preload 5mN/tex or ASTM 1682/B52576
d. ISO/DIS 10319.2, Tested at Helsinki Univ. of Tech.

was put the base grid A or C. In the 1xgeogrid structure and in the geocell structure the base grid was installed in the longitudinal direction of the road except the 4 pieces of grid in the 1xgeogrid structure. One of those pieces was instrumented with strain gauges. In the 2xgrid+LECA -structure all grids were installed in transverse direction of the road.

Grid B in the geocell structure was cut to a width of 0,5 m. The grid was installed vertically by wooden piles and nylon cord in the transverse direction of the road. Between the transverse grids there were installed other vertical grids. The grids are connected to each other with iron bars. Vertical grids are connected to base grid with cable ties, Fig. 3b.

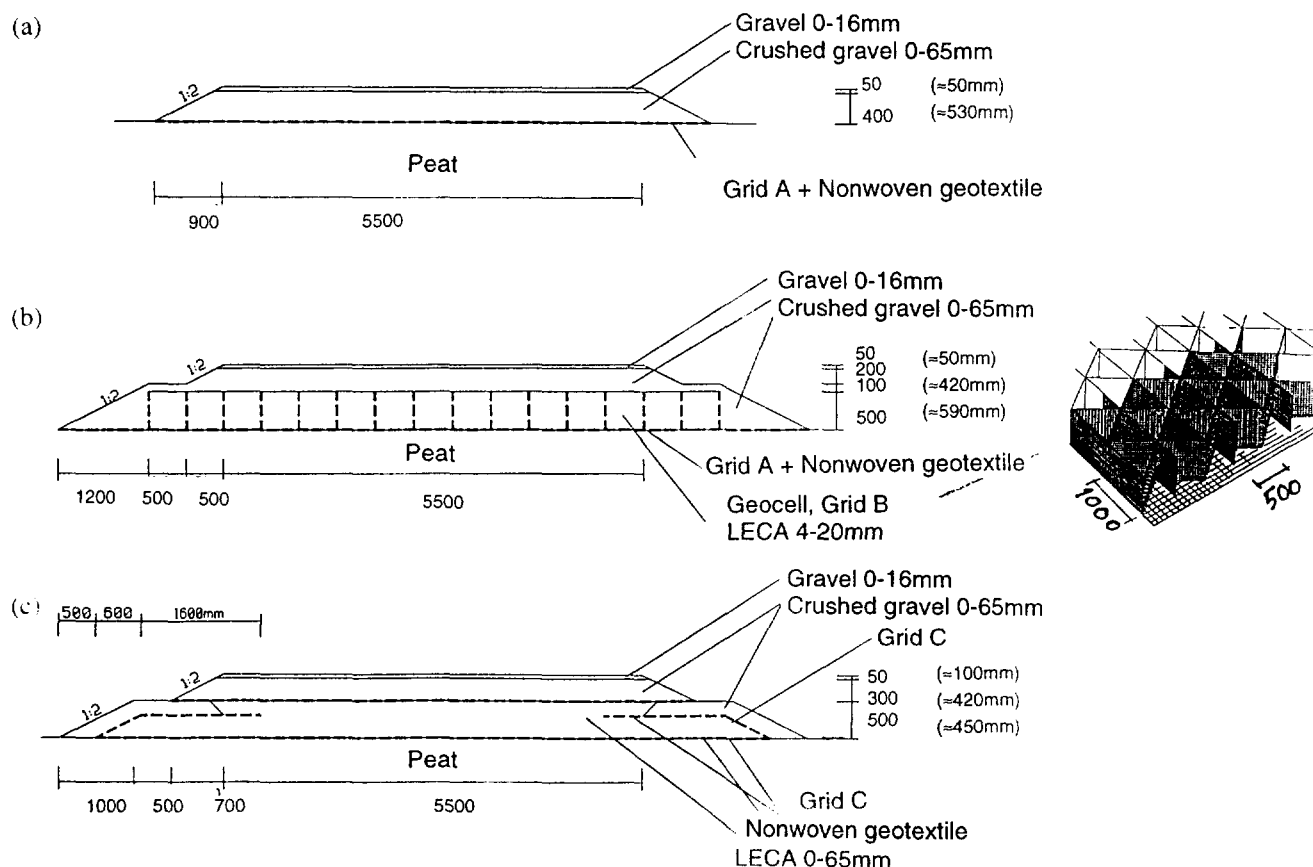


Figure 3. Geogrid and geocell reinforced test structures: (a) 1 x geogrid + crushed gravel, (b) geocell + LECA, (c) 2 x geogrid + LECA. The fulfilled layer thickness are presented in the brackets.

5.2 Installation of the Aggregates

The installation of crushed gravel and LECA of the test structures of 1xgrid and 2xgrid+LECA was performed by lorry and excavation machine. The installation of LECA to geocells was performed by blowing.

The precompaction of the aggregate layers was done by the excavation machine with caterpillar tread. All test structures have been compacted by a vibratory roller.

6. INSTRUMENTATION

6.1 Instruments

The test structures are extensively instrumented. The principles of the instrumentation are presented in Figure 4.

The instrumentation and control methods include: vertical magnetic probe extensometers, horizontal hydrostatic profile gauges, settlement plates, horizontal extensometers, strain gauges, plate load tests and falling weight deflectometer tests (FWD).

6.2 Installation of the Instruments

The vertical magnetic probe extensometers were installed at stations 241,5 and 651,5 to measure the settlements of the ground at different depths. An extensometer consists of ring magnets sliding on a central access pipe and fixed in the ground at preselected measuring levels. A special probe travels within the access tube and observes the positions of the magnets outside the tube.

To measure the settlements and the shape of the base of the road embankment there were installed flexible PEH-pipes for the horizontal hydrostatic profile gauges at the peat surface at six stations.

The horizontal extensometers were installed to stations 171 and 651 to measure the horizontal movements of the base of the road embankment about 0,1...0,15 m above the surface of the peat. The measuring units, precision potentiometers, were installed at the centre line of the road and the anchor plates were installed about 1,3 and 2,7 meters to the side from the centre line of the road. When the anchor plate moves the voltage of the potentiometer changes. The changes are converted to millimetres by a calibration factor determined in laboratory.

The strain gauges were glued to grids to measure the strains of the grids at stations 170, 240 and 650. The strain gauges were glued to the elements of the grids. The measured strains are converted to tensions of the reinforcements by a calibration factor determined in laboratory.

At the surface of peat there were installed 4 steel plates ($\phi=0,45$ m) and at the surface of the LECA 2 steel plates ($\phi=0,30$ m) for plate bearing tests.

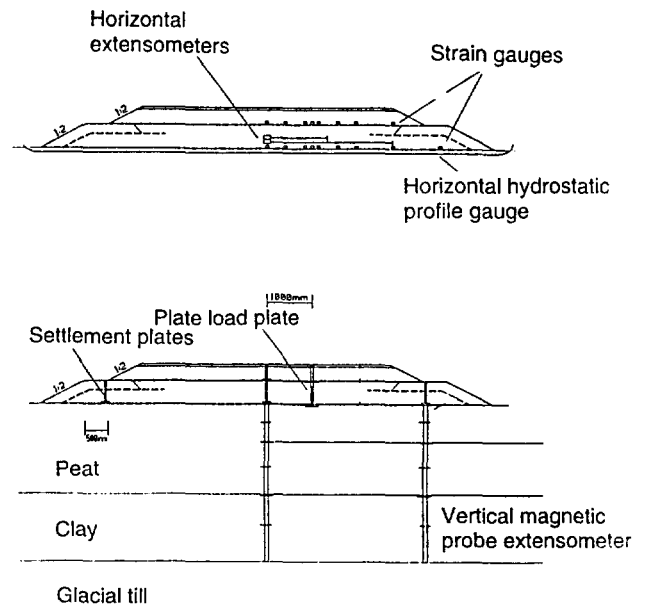


Figure 4. The principles of the instrumentation of the test structures.

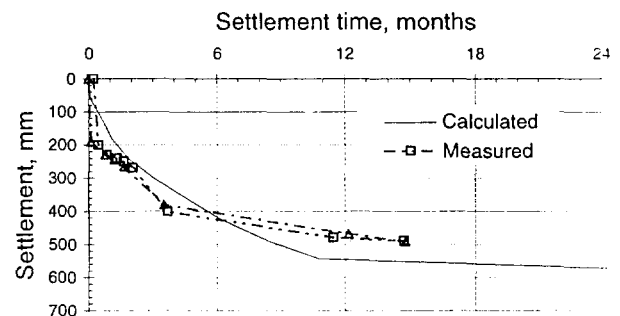


Figure 5. Calculated and measured settlement of the geocell structure at station 240.

7. RESULTS

7.1 Settlements

The settlements at the centre line of the test structures from summer -96 to 8/97 are: 0,41 m at station 174, 0,51 m at station 239..250 and 0,54 m at station 649. The settlements are directly dependent on the thickness of the peat layer (Figure 1). The measured settlements are quite near to the manually calculated settlements during one year, Figure 5. In this case it is really wise to use LECA as a light-weight fill to keep the road surface over the peat surface. The surface of the 1xgeogrid+crushed gravel -structure is now, 1.5 years after construction, about at the same level as the peat surface and in this situation the drainage of the road structure is very bad.

The settlements at different depths in the ground are not illustrated in this article, but they equal quite well to the precalculated deformation distribution.

7.2 E_2 -modulus

The E_2 -modulus at the surface of the peat and LECA has been measured at stations 170, 240, 650 and 700 in 7-8/96, 9/96 and 8/97. The E_2 -modulus was 2..5 MPa and 27..36 MPa. The E_2 -modulus of the road has been measured at the surface by plate load and by FWD-tests, Table 4. The FWD-tests have been made at intervals of 10 or 5 m about 1 m to both sides from the centre line. By plate load and FWD-test measured E_2 -modulus are very near each other. Plate load and FWD-tests in 7-8/96 were made before the installation of the surface gravel (0-16mm).

When looking at the results of the plate load and FWD-tests one has to keep in mind that the E_2 -modulus changes very much at different stations along the road because of the varying thickness of the embankment and the strength of the peat layer. It can be seen from the Table 4 that the E_2 -modulus of the structure 2xgeogrid+LECA is increasing by the time.

7.3 Strains and Tensions of the Georeinforcements

The measuring results of the strain gauges have been converted to tensions by a calibration factor ignoring the potential effects of the creep of the synthetic geogrids and the effects of the confining stress to the modulus of the grid.

The mobilised tension of the base grid of the 2xgeogrid+LECA -structure is illustrated in Figure 6. The tandem-axle with twin tyres is above the strain gauges. The axle-group load of the lorry is approximately over 16 ton. In Figure (a) there is a lorry laden with gravel on the middle of the embankment (Fig. c) and there is illustrated the total mobilised tension of the grid (=tension before the loading + tension caused by the lorry). In Figure (b) there are the changes of the tension of the grid caused by the lorry on the embankment. In Figures (a) and (b) the continuous line illustrates the case when both axles of the tandem-axle are loaded (Fig. d). The dashed line illustrates the case when the whole load is on one axle of the tandem-axle (Fig. e).

The loading with lorry was repeated with all test structures. The mobilised tension of the base grids was 4..5 kN/m in 1xgrid+crushed gravel, geocell+LECA and 2x geogrid+LECA -structures. The mobilised tension of the upper grid of the 2xgeogrid+LECA -structure was about 1..1,5 kN/m. The changes of the mobilised tension of the lower edge of the vertical grid of the geocell were about 3 kN/m.

The lorry loading of the test embankments has been made almost immediately after the construction of the embank-

ment. About 2..4 months later when repeated the loading the mobilised tension has been lower because of the installation of the surface of the road and the strengthening of the peat due to the consolidation.

7.4 Deterioration of the Surface of the Test Structures

The rutting and the deterioration in the form of potholes on the surface of the test structures have been observed ocularly. The shape of the surface has also been measured by the means of levelling. On the basis of the observations after 1 year of the construction there are mostly potholes on the surface of the 1xgrid+crushed gravel -structure. On the surface of the 2xgrid+LECA there are very few potholes but on the surface of the geocell -structure there are more potholes. The most rutted test structures are the 1xgrid and geocell -structures while the surface of the 2xgrid+LECA has behaved better.

8. ANALYSIS BY MANUAL CALCULATION

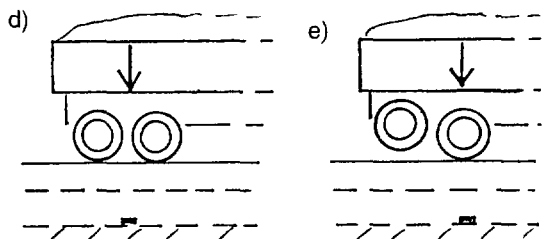
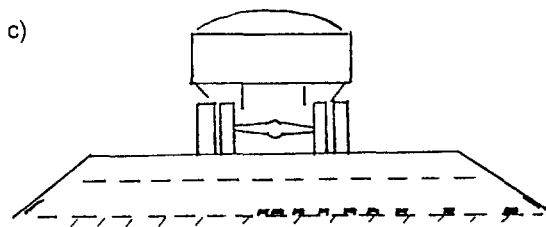
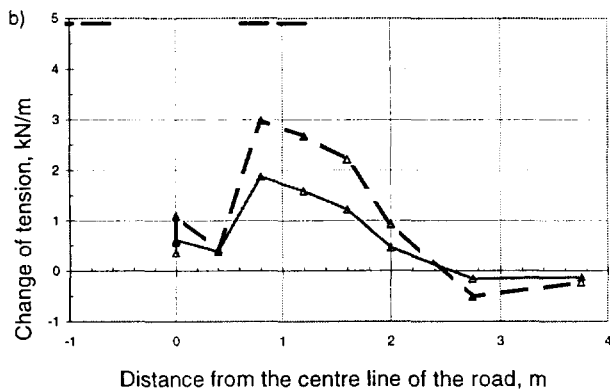
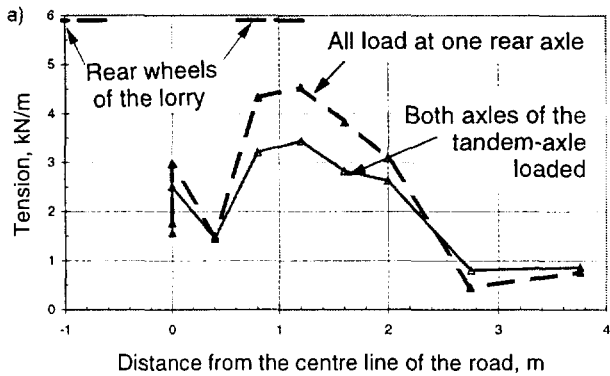
The tension of the grid of the 1xgrid structure has been calculated using the methods presented by Giroud & Noiray (1981) and Houlsby & Jewell (1990). Both methods are for a clay base but in the absence of a better method those are used also for a peat base. In the calculations the next assumptions have been adopted: axle load 100 kN, number of passes 10 000, rut depth 150 mm and the shear strength of the base 25 kPa.

When using the method of Giroud & Noiray the calculated thickness of the embankment is 0,73 m and tension of the base grid is 8 kN/m. When using the method of Houlsby & Jewell the calculated thickness of the embankment is 0,77 m and tension of the grid is 10 kN/m. The calculated thickness of the road structure is a little bit bigger than the fulfilled thickness ($\approx 0,6$ m). The calculated tensions of the grid are about twice as big as the measured ones (4..5 kN/m) in the 1xgrid and 2xgrid -structures.

The method of Houlsby & Jewell is based on the combination of the bearing capacity of the clay subgrade and the effect of the horizontal stresses in the fill/clay interface. The method of Giroud & Noiray is concentrated to the tensioned membrane effect and the bearing capacity of the clay subgrade. According to the theory of Houlsby & Jewell the tension of the grid is concentrated near the loading point while in the theory of the tensioned membrane the tension is supposed to be distributed evenly to a very large area. When

Table 4. E_2 -modulus measured by plate load and FWD-tests at 7-8/96, 9/96 and 5/97.

Station	FWD-tests, MPa				Plate load test, MPa, $E_{2\text{ average}}$		
	E_2 , 9/96	$E_{2\text{ average}}$, 9/96	E_2 , 5/97	$E_{2\text{ average}}$, 5/97	7-8/96	9/96	8/97
90...200	17...69	45	34...95	58	36	53	49
200...300	14...83	43	28...95	55	49	67	65
590...680	38...75	55	40...93	69	50	68	89



- - - - - Geogrid C
 ■ Strain gauge
 / / / / / Peat

Figure 6. Mobilised tension of the base grid of the 2 x grid + LECA-structure caused by a lorry on the embankment. (a) Tension before loading + tension caused by the lorry. (b) The change of the tension of the grid caused by the lorry on the embankment.

studying Figure 6 one can see that the tension is not very largely distributed but the tension is concentrated quite near the loading point.

9. CONCLUSIONS

When constructing a road on a peat area there are two main problems: the low bearing capacity of the peat and the large settlements. The low bearing capacity can be increased and the differences in settlements can be reduced by geogrids. In the case of Leteensuu an adequate bearing capacity of the road has been achieved by a moderate low embankment with geogrids. One and a half years after the construction of the test structures there are no significant differential settlements at the road surface.

The measured tensions of the base grids are about half of the precalculated ones with the methods presented by Giroud & Noiray (1981) and Houlsby & Jewell (1990). The distribution of the tension agrees quite well with the distribution assumed by the theory of Houlsby & Jewell. On the basis of the test construction of Leteensuu it seems to be possible to use both of the dimensioning methods of Giroud & Noiray and Houlsby & Jewell on the peat base.

ACKNOWLEDGEMENTS

The authors like to thank the "Georeinforcement" -project for the financing and promoting of the laboratory tests and the instrumentation of the test structures. Thanks are due also to the organisation of the Finnish National Road Administration of Häme Region for the construction of the test structures.

REFERENCES

- Friberg, P., Lahtinen, P., Slunga, E. & Suni, H. (1994). Finnish Georeinforcement Research and Development Project. *Fifth international conference on geotextiles, geomembranes and related products*, Singapore. 5-9.9.1994. Vol. 3, pp. 1169-1172.
- Giroud, J.-P. & Noiray, L. (1981). Geotextile-Reinforced Unpaved Road Design. *Journal of the Geotechnical Engineering Division, (ASCE)*, Vol. 107, No. GT9, pp. 1233-1254.
- Houlsby, G. T. & Jewell, R. A. (1990). Design of reinforced unpaved roads for small rut depths. *4th international conference on geotextiles, geomembranes and related products*, The Hague. 28.3.-1.4.1990. Vol. 1, pp. 171-176.
- Lojander, M., Forsman, J. & Takala, J. (1996). Mechanical properties of Leteensuu peat. *XII Nordiska Geoteknikermötet*, Reykjavík. 26-28.6.1996. Vol. 1, pp. 123-128.

CONSTRUCTION OF HIGHWAY EMBANKMENT ON SOFT MARINE SOIL USING JUTE GEOTEXTILES

P.Jagannatha Rao

Senior Consultant, Lea Associates South Asia Pvt Ltd., New Delhi

Bindumadhava

Project Manager, Consulting Engineering Services (P) Ltd., New Delhi

N. Venisri

Engineer, Consulting Engineering Services (P) Ltd., Hyderabad

ABSTRACT : The paper presents case study of design and construction of 1.5m high embankment resting on 4m deep soft marine clay subsoil layer. In order to ensure adequate initial factor of safety, it was found necessary to provide a reinforcing fabric at the base of the fill and jute geotextile was successfully used for this purpose. Jute being biodegradable the natural fibre fabric suffers loss of strength with time. In the present case, it was found that the post construction gain in the undrained shear strength of the soft clay subsoil is adequate to compensate the loss in the strength of reinforcing fabric after it is placed in the soil. Thus, the factor of safety always remains at the design level. Construction of the embankment was completed in April 1996 and post construction monitoring showed the embankment performance to be satisfactory.

KEYWORDS : Jute geotextile, Reinforcement, Embankments.

1.0 INTRODUCTION

A major deepwater port was developed at Kakinada in Andhra Pradesh, India and within the port area, a highway network was under construction for transporting cargo from ships to godowns. At the proposed location, subsoil is soft clay upto 4m depth and water table is at about 0.5m below the ground level. The area gets submerged during high tide. Highways constructed earlier faced many problems during and after construction such as subsidence of the fill during construction, excessive post construction settlements, lateral spreading of fill material, etc. It was observed that sometime as much as 30% of the fill sinks into the soft subsoil during spreading of the fill, thus necessitating use of larger quantities of costly granular fill material, pushing up the cost of construction.

In order to mitigate the above problems, various alternatives were examined among which jute geotextile has shown itself to be a promising one from performance as well as cost considerations. The use of geotextiles to improve the performance of embankments over soft subsoil is an effective and well tried form of reinforced soil construction. Geotextiles may be used to improve

- i) embankment stability against bearing capacity failure
- ii) stability against slope failure through the foundation

- iii) allow controlled construction over very soft or difficult foundation soils and make possible more uniform settlement of the embankment.
- iv) act as separator between the embankment material and soft subsoil
- v) function as drainage blanket for draining of pore water during consolidation.

Reinforcement on soft soil is most effective when placed at or close to the foundation surface.

Factor of safety of embankment is usually at its lowest during and immediately after construction and increases thereafter. The increase is a function of the gain in strength of the soft clay. Thus, reinforcement has to be effective only for a short term, the duration depending on the consolidation characteristics of the soft clay layer. In such cases, long term durability of the geotextile reinforcement is of secondary concern.

The reinforcement is needed essentially to improve the stability during construction phase and in the period of consolidation during which the soil attains the required strength. The concept, shown in fig (1) is given by Jewell (1996) and forms the basis of design in the present instance.

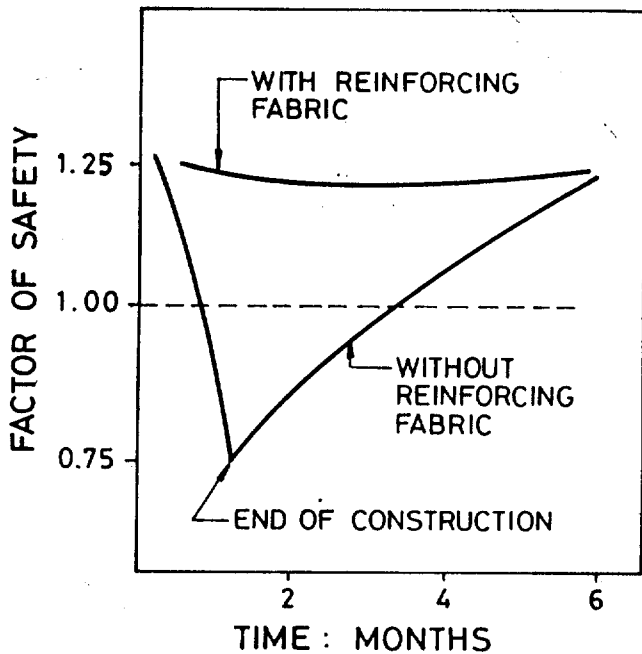


Figure 1 : Variation in factor of safety of fill on soft ground, with and without reinforcing fabric. Based on Jewel (1996)

The primary loading from an embankment is due to the self weight of the embankment fill, which causes horizontal stresses in the fill, which in turn produce lateral forces (i.e.) outward shear stresses. The resulting outward shear stresses which act on the foundation surface reduce the bearing capacity of the foundation subsoil. Hence, the primary role of the reinforcement is to resist the outward shear stresses and relieve the foundation of the effect of lateral forces, thereby increasing the allowable height of the embankment. A layer of reinforcement placed in the embankment would resist lateral displacement by exerting an inward shear stress on the foundation surface thus reduce the lateral spreading of the foundation soil. Since the geotextile is placed between the embankment fill and the subsoil, it also performs the function of separator thereby eliminating the possibility of the soft subsoil squeezing upward into the costly granular fill. This geotextile along with a sand cushion also acts as a drainage layer facilitating the escape of pore water during the consolidation phase.

1.1 Properties of Subsoil

The subsoil upto a depth of 4m from the ground level is mainly clay with occasional mixture of silty sand. The average liquid limit and plasticity index were 60 and 28 percent respectively. The soil in general was found to have a natural moisture content ranging from 70% to 80% with bulk density varying from 1.3 Mg/m³ to 1.45 Mg/m³. Average undrained shear strength of the soil was found to

be 6.0 kN/m² from in-situ vane shear tests, compression index (C_c) 0.225 and coefficient of consolidation (c_v) 2.0×10^{-7} m²/ sec.

1.2 Design Aspects

Design of geotextile used for reinforcement is based on the methodology given by Jewel (1996) and is as follows:

Height of fill (H) = 1.5m

Unit weight (γ) = 16.6 kN/m³,

Angle of internal friction $\phi = 30^\circ$

Depth of foundation soil $D = 4.0$ m

Undrained cohesion $C_u = 6$ kN/m²

Thus vertical stress due to fill (σ_v) = $16.6 \times 1.5 = 24.9$ kN/m².

Factor of safety (FS) against bearing failure for the unreinforced embankment.

$$= \frac{cN_c}{\gamma H} = \frac{6 \times 3.14}{24.9} = 0.75$$

$N_c = 3.14$ in the unreinforced state.

Thus, the bearing capacity is not adequate without reinforcement at the base level. By providing a geotextile reinforcement, the bearing capacity factor, N_c increases to $\pi + 2 = 5.14$

and the factor of safety works out to

$$\frac{6 \times 5.14}{24.9} = 1.23$$

which is a satisfactory value.

The horizontal force to be resisted by tension in the fabric is estimated as

$$P_a = K_a \gamma H^2 / 2$$

$$= \frac{0.33 \times 16.6 \times 1.5 \times 1.5}{2} = 6.16 \text{ kN/m}$$

Hence, required design tension in the fabric = 6.16 kN/m

For a fabric having a tensile strength of 20 kN/m, the factor of safety available is 3.2 and is thus adequate. Once the embankment is in place, the soft clay consolidates and improves in shear strength.

With an average $c_v = 2 \times 10^{-7}$ m²/sec, the time required for 90% consolidation works out to 205 days or about seven months.

Settlement was estimated to be the order of 175 to 200mm, by using standard calculations.

Strength gain at the end of consolidation is of the order of $\Delta S_u = 0.18 \times \Delta \sigma'_v = 0.18 \times 24.9 = 4.48 \text{ kPa}$

Average undrained cohesion at the end of consolidation would thus be of the order of (6.0 + 4.48) say 10 kPa. Factor of safety of the embankment at the end of consolidation without any reinforcing fabric would thus be

$$FS = \frac{10 \times 3.14}{16.6 \times 1.5} = 1.26 \text{ which is satisfactory.}$$

Thus the use of an even a relatively low strength geotextile helps to maintain the factor of safety at an acceptable level of 1.26.

At the end of 7 months, when the strength gain due to consolidation has occurred, the increased shear strength of the subsoil ensures the minimum required factor of safety. The strength of fabric is no longer needed to provide reinforcing effect.

3.0 CHOICE OF FABRIC

In the preceding section, it was demonstrated that a fill can be built on the soft clay by placing a geotextile fabric and a low strength one is adequate. A variety of such geotextiles are manufactured from petroproducts. However, in certain areas of the world, natural fibres such as jute, coir, sisal, kenaf are being increasingly studied and evaluated for use in various geotechnical engineering applications. The objective of such efforts is to make use of desirable properties of above fibres, make a wider variety of fabric products available for geotechnical engineers where suitable use can be found and in some instances with cost advantage, provided performance criteria are met. The 5th International conference on geosynthetics held in September 1994 in Singapore devoted a special session to Natural Fibre Fabrics. This session has clearly impressed the engineers with the potential of natural fibre fabrics for use in geotechnical engineering applications. These fabrics compliment the range of applications of petrobased fabrics.

Since jute is available in India in abundance, a United Nations Development Programme (UNDP) sponsored project on the "Development and Promotion of Jute Geotextile" is in progress in India covering the period 1992-1997. The Indian Jute Mills Association (IJMA) is the coordinating agency for the project. Development of jute and jute based geotextiles, their evaluation and characterization and the use of such fabrics in full scale experimental constructions form objectives of the project. Efforts were concentrated on carrying out full scale field experiments to demonstrate and evaluate the capabilities of selected varieties of jute fabrics for use in surface erosion control of slopes, drainage, separation and to a limited extent, reinforcing function. The fact that jute fabric is

biodegradable, with a limited life and deteriorates in a short period of about two years was always kept in mind in the planning and operation of the project and choice of experimental installations. Full scale field experiments covering these applications have been implemented at different locations in India. Ramaswamy (1994) presents in detail the application of jute geotextiles in erosion control, drainage as well as reinforcement.

As explained in section 1 and shown in design in section 2, in the present instance, it is adequate if the reinforcing function of the fabric is available for period of seven months. The use of fabric has essentially helped in overcoming problems in the placement of the fill and initial low factor of safety. Thus, fabric with a limited life can be tried in this project and its performance evaluated by the field trial. Accordingly, jute geotextile fabric having the basic properties given in Table 1 was chosen for use in the project.

Table 1 : Properties of Jute Geotextile

S.No	Property	Test Value
1	Thickness	3 mm
2	Weight	750 gsm
3	Tensile Strength	20 kN/m
4	Elongation	30%
5	Puncture Resistance	350 N
6	Overlap length	30 cm

The woven jute geotextile fabric was treated with cuproammonium sulphate to increase resistance of the fabric to biodegradability. Talukdar et al (1994) have studied the influence of various chemicals such as copper naphthenate etc. with acrylic binder on the resistance to microbial attack when buried in soil. The results were very encouraging and showed that jute fabrics treated with selected chemicals have better resistance to microbial attack under conditions of burial in soil. Venkatappa Rao et al (1994) have shown on the basis of a careful study that the decrease in the narrow strip tensile strength of soil embedded in soil and remaining in submerged condition is only of the order of 35% after four months. Mohiuddin (1994) provides data to indicate that in jute fabrics treated with copper naphthenate and such other chemicals, the loss of strength is retarded. Thus, it was reasonable to consider that jute fabric used would serve the reinforcing function in adequate measure, in the design life of 7 months.

4.0 INSTALLATION OF GEOTEXTILE

At present, jute geotextile being an experimental product is available in roll width of 0.75m only. Hence, fabrics were stitched at site, using a portable stitching machine to obtain the requisite width. The stitching operation was easy, reliable and fast. Before spreading the geotextile, the site was cleared of any extraneous materials and tree/plant roots. A layer of sand 150 mm thick was spread to serve as a levelling course. The geotextile was laid with its warp direction (strong direction) parallel to the width of the embankment. Top width of the embankment was 7.0m and side slope 1 v1 to 2h1. A trench of size 0.5 x 0.5m was dug in the soil at either toe line of the embankment and along its length. To provide anchorage, the geotextile was placed in the trench. The trench was back filled with sand placed in layers and compacted. The fabric was stretched manually after spreading on the ground so as to render it free of wrinkles and establish good contact with soil and fill. An overlap of 0.30m was provided between two rolls of geotextiles. After spreading the geotextile and anchoring it along the edges, a sand cushion of 30 cm thick was placed to protect the geotextile from damage due to moving vehicles. Placing of fill upto the requisite height was done by rear dumping and spreading. The fill was then compacted by a 6 ton roller. Nearly 300 m of embankment was built under the programme. Construction of the embankment was completed in April 1996. Settlements were observed subsequent to the construction. Simple standpipe type settlement gauge was installed for this purpose. It was found that the settlements conformed to the estimated value. The physical condition of the fill and its surface were monitored periodically and were found to be satisfactory.

The cost of jute geotextile used in the project is of the order of Rs. 18/- or US\$ 0.50 and thus proved to be highly economical compared to products based on petrochemicals, which are costlier in India.

5.0 CONCLUSION

An embankment was built on soft clay subsoil, using geotextile as a reinforcing layer at the base. the geotextile was required to serve as reinforcing fabric for a period of 7 months only. Subsequently the strength gain in the soft clay was adequate to keep the embankment stable. The performance of the fill was found satisfactory. The project demonstrates that where site conditions enable the designer to rely on reinforcing properties of geotextiles for a limited time period, it is possible to use natural fibre geotextile in such applications. This has the effect of finding suitable range of conditions where natural fibre based geotextile can be used in geotechnical applications.

ACKNOWLEDGEMENT

The project was carried out as a part of the UNDP sponsored project "Development and Promotion of Jute Geotextiles". The overall coordinating agency was the Indian Jute Mills Association, Calcutta. The work reported herein was carried out by the authors, while they were at the Central Road Research Institute, New Delhi and the senior author was coordinating the project. The authors thank all concerned in the above organisations for their cooperation in successfully completing the project. The authors also wish to thank officials of Kakinada port and JNTU college of Engineering, Kakinada for help at site in various phases of the project.

REFERENCES

- Jewell, R.A (1996) Soil Reinforcement with Geotextiles, 1st Ed., Construction Industries Research and Information Association, London.
- Mohiuddin. G. (1994). Jute geotextiles. 2nd International Workshop on Geotextiles, Central Board of Irrigation and Power, 1994. pp.70-76. New Delhi
- Ramaswamy. S.D (1994). Potential of Jute Assembled Soil Stabilisers. 2nd International Workshop on Geotextiles, Central Board of Irrigation and Power, New Delhi, 1994. pp. 77-85.
- Talukdar, M.K. Mukherjee, D. and Ghosh S.K. (1994), Performance of Certain Antimicrobial Treated Nonwoven Jute Fabrics. Fifth International Conference on Geotextiles, Geomembranes and Related Products, Singapore 1994, Vol.2 pp. 849-852
- Venkatappa Rao, G. and Abid Alikhan, M. and Narayana Sarma, G.V. (1994). Durability of Geotextiles. Fifth International Conference on Geotextiles, Geomembranes and Related Products. Singapore 1994. Vol. 2. pp.857-860.

PERFORMANCE OF GEOTEXTILE REINFORCED EMBANKMENTS ON VERTICALLY DRAINED SOFT MUDS

K.C. Yeo & J.W. Cowland
Geotechnical Engineering Office, Hong Kong

ABSTRACT: Twenty kilometres of flood protection embankments have been constructed on soft muds in the north-west of Hong Kong, using woven polyester geotextiles as basal reinforcement. Prefabricated vertical drains were installed to accelerate consolidation of the muds. An extensive instrumentation programme was carried out to monitor the performance of the embankments. This paper outlines the design and construction of the embankments. Typical instrumentation results are given, and performance of the embankments are discussed.

KEYWORDS: Case Study, Embankments, Soft Soils, Geotextiles, Pre-fabricated Vertical Drains

1 INTRODUCTION

The northwestern part of Hong Kong contains a broad alluvial floodplain. Development of this low-lying area generally requires the construction of raised platforms. Provision of major flood drainage is essential for land use planning as flood discharges develop rapidly due to heavy rainfall in the wet season.

A series of drainage channel projects are being carried out in these areas to alleviate the flood problem and to

improve the drainage systems. The case study presented in this paper consisted of the construction of three drainage channels of width 125m to 480m, and of lengths 3.2km(Contract A), 4.4km(Contract B) & 2.3km(Contract C) respectively. Small embankments 4m high were constructed on each side of these drainage channels over an area which had been used extensively for fish farming, with small bunds forming the boundaries of the ponds. Figure 1 shows the location of the site.

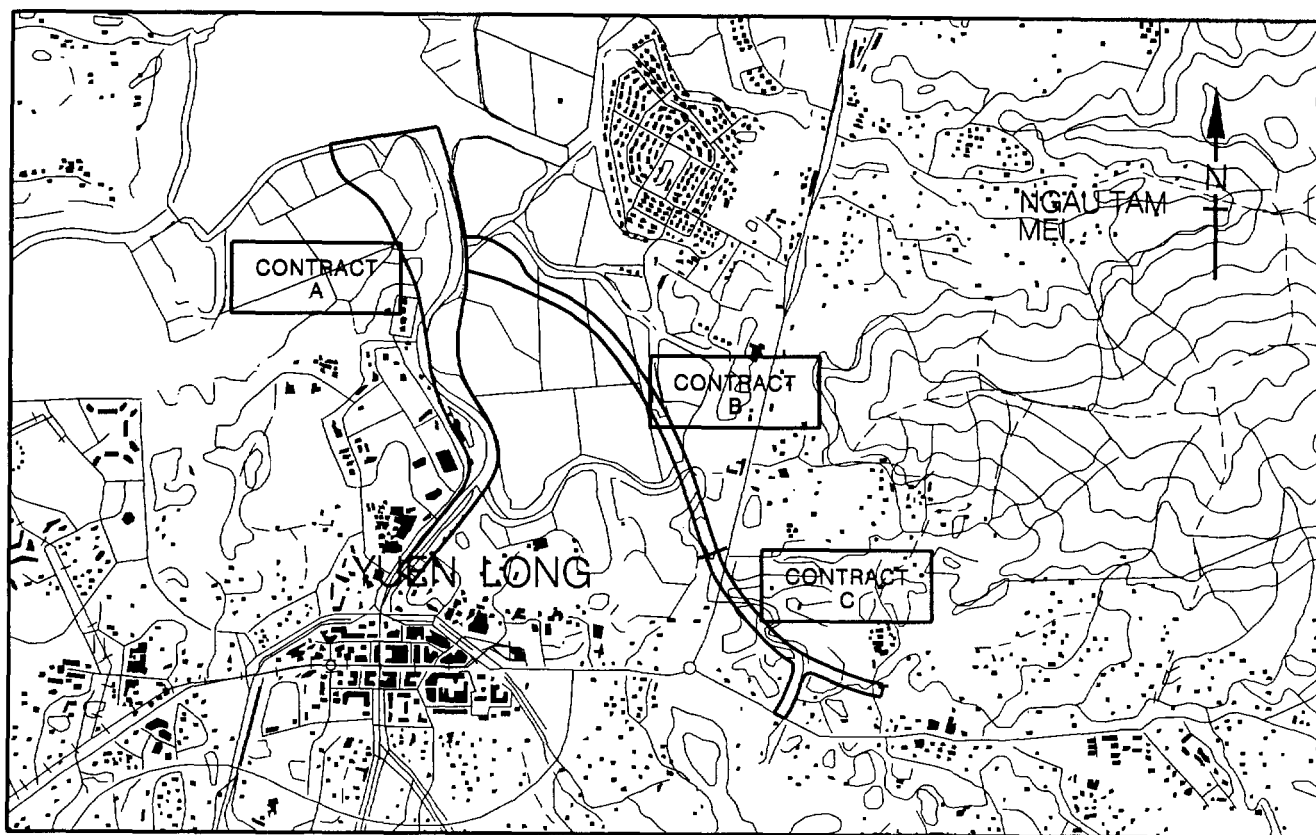


Figure 1. Location of the Site

2 GEOLOGY

The geology of the area comprises muds overlying older alluvial sediments which rest on residual weathered rocks of volcanic or meta-sedimentary origin. The stratigraphy of the site can be categorised as follows:

Fill: generally granular in nature and exists in the bunds of the fish pond area, with thickness varying from 1 to 3 metres.

Pond deposits: generally a very soft to soft dark brown to dark grey silty clay exists at the bottom of the fish ponds for a depth of 1 to 1.5 metres.

Estuarine/Marine deposits: generally a very soft dark grey to black silty to sandy clay with shell fragments, with thickness from 2 to 8 metres.

Alluvial clay/silt: generally a firm to stiff light grey to pinkish brown with reddish brown mottled sandy silty clay with varied depth.

Alluvial sand/gravel: generally a medium dense to dense grey to brownish yellow/light grey silty/ gravelly sand with varied depth.

The thickness of the alluvium was between 10 to 30 metres. It does not possess a uniform succession of strata, but varies from location to location. The insitu materials below the alluvial deposits are coarse tuff/granodiorite. Figure 2 shows the geology of the site.

3 DESIGN AND CONSTRUCTION

The embankments were formed by filling on the existing ground. For embankments constructed over soft muds, the stability of the embankments has been improved by a combination of measures, i.e. installation of prefabricated vertical drains (PVD), application of geotextile reinforcement, staged construction with wide berms and partial removal of pond deposits. As the preconsolidation

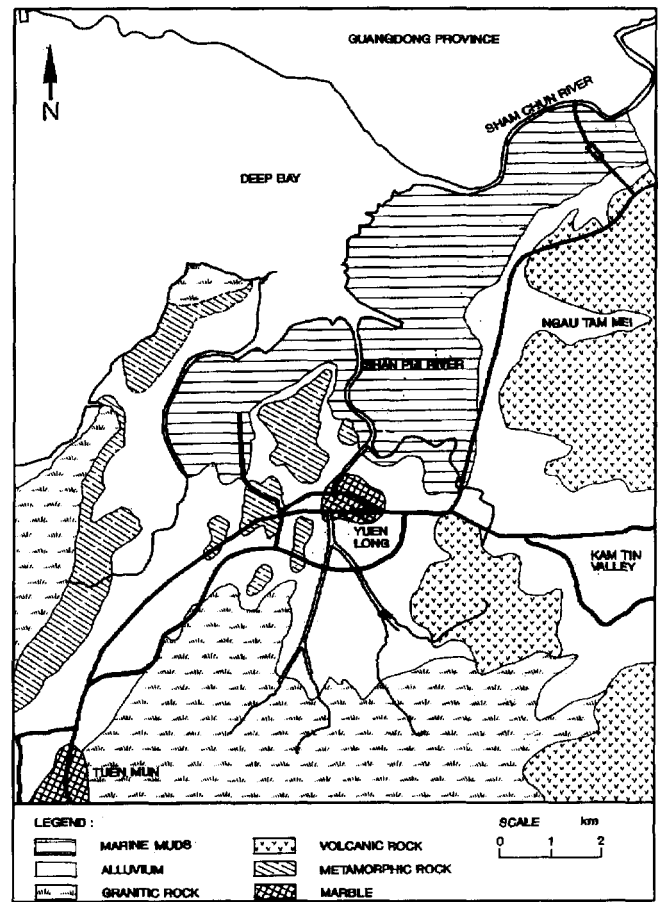


Figure 2. Geology of the Site

pressure of the alluvium was generally higher than the embankment load, most of the settlement occurred only in the marine sediment. The soil parameters adopted for the embankment design are summarised in Table 1. In general, they are on the conservative side.

Table 1. Geotechnical Design Parameters

Design Parameters				Type of Deposit				
				Marine Deposit	Alluvial Clay	Alluvial Silt	Alluvial Sand	Alluvial Gravel
Unit Weight (kN/m^3)				16	19	20	19	19
Shear Strength Parameters	Short Term	Undrained Shear Strength	S_u (kPa)	10	40	40	-	-
	Long Term	Effective Cohesion	c' (kPa)	3	4	0	0	0
		Effective Angle of Friction	ϕ' (Deg)	25	33	33	35	35
Parameters for Settlement	Preconsolidation Pressure		P_o' (kPa)	NC	150 - 300	150 - 300	-	-
	Compression Ratio		$C_c / (1+e_o)$	0.15 - 0.3	0.11 - 0.16	0.12 - 0.18	-	-
Analysis	Recompression Ratio		$C_r / (1+e_o)$	0.015 - 0.03	0.015 - 0.025	0.018 - 0.03	-	-

A typical cross section of the embankment, showing the layout of the geotextiles, prefabricated vertical drains and instrumentation, is shown in Figure 3. The construction adopted both "partial removal of pond deposits" and "no excavation" approaches. The primary basal reinforcements used were a layer of woven polyester geotextile (two different brands) of characteristic strength of 800kN/m or 600kN/m. A second layer of woven polyester geotextiles were used as a separator with characteristic strength of 400 kN/m or 200kN/m. Two different types of PVD (grooved and spun core) were installed to a depth of approximately 15 metres through the marine deposits, to accelerate the consolidation of the foundation soil.

They are simple to read and can be read from a station which is remote from the work area with little interference to the construction activity. However, they are not robust and some of the piezometers were damaged during construction. A number of the pneumatic piezometers were found to malfunction after installation, and yielded erratic results. Therefore it is important to consider the use of more than one type of piezometer for cross checking. For future projects it would be advisable to install some standpipe piezometers to supplement pneumatic piezometers at selective locations for reference.

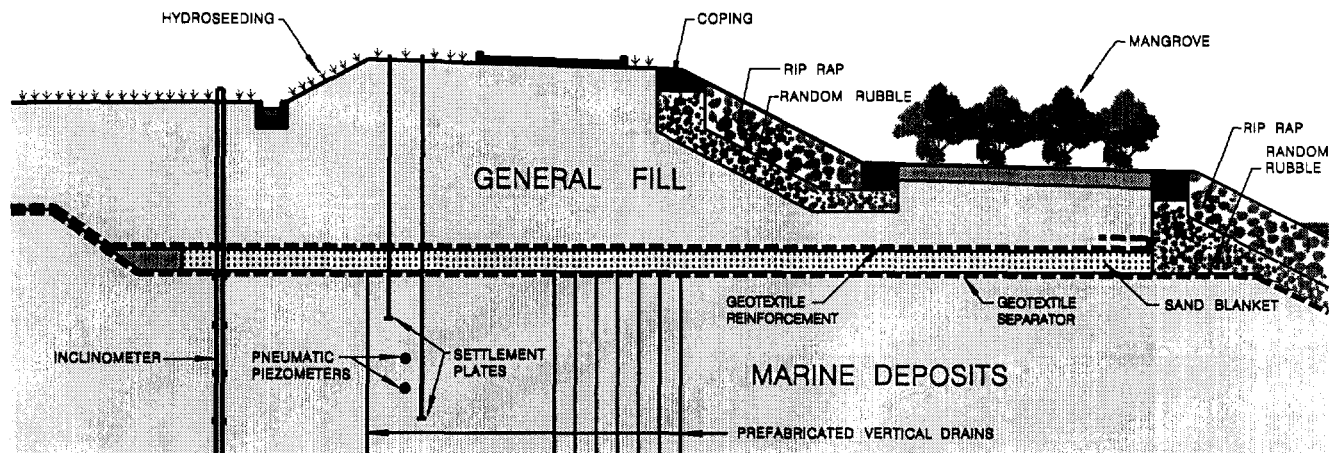


Figure 3. Typical Section of the Embankment

4 INSTRUMENTATION

An extensive network of geotechnical instrumentation was installed, to monitor ground deformation and groundwater pressures during construction of the embankments. More than fifty cross-sections (at 100 metres interval) along the embankments were monitored using pneumatic piezometers, inclinometers (with and without extensometers) and settlement plates, during and after construction.

For embankments constructed over pond and estuarine/marine deposits, monitoring of the excess pore water pressure dissipation within the mud was critical for controlling the filling rate of the embankment. In addition, there were fish ponds along both sides of the channels, and lateral movement of the soft deposits may have damaged the bunds of the fish ponds. Thus it was important to monitor this movement. It was also important to measure the settlement of the mud over time, so that the timing of laying the black top of the service road on the crown of the embankment could be determined.

4.1 Piezometers

Pneumatic piezometers were widely used in this project.

4.2 Inclinometers and Extensometers

Inclinometers were installed to monitor the magnitude and the rate of lateral movement of the foundation soils below the embankment. Casing inclination data were provided in two mutually perpendicular near-vertical planes. Horizontal deformation of the transverse sections was of particular interest as the behaviour of the embankment would be assumed to be in plane strain.

Extensometers were used in conjunction with inclinometers to monitor the changing distance between two to four positions beneath the vertical axis of a particular section, i.e. vertical compression of the foundation soils. Two different types of extensometers were used, i.e. spring anchor extensometers attached outside the inclinometer casing, and flexible corrugated polyethylene pipe with induction coil rings where inclinometer casing was inserted inside the pipe. As the accuracy of extensometers is only 10 - 20 mm. Settlement plates are a useful alternative.

4.3 Settlement Plates

Settlement plates were used to quantify the magnitude of settlement of the embankments with time. Two types of

settlement plates were used, i.e. shallow settlement plates and deep settlement plates. The shallow settlement plate was a 1m x 1m steel plate welded to a hollow tube which was extended with fill height, installed at the base of the embankment before filling. The deep settlement plate was a 110 mm diameter circular plate welded to an steel bar, which was also extended, and installed at the base of the soft deposits by drillhole. The settlement of the plates were monitored using surveying techniques throughout construction. The difference between the settlement measured by the shallow and the deep settlement plates represented the actual settlement of the layer of the soft deposits at any time.

The accuracy of the plate settlement measurement using conventional surveying equipment was found to be close to millimetres.

5 TYPICAL INSTRUMENTATION RESULTS

A typical set of instrumentation results is shown in Figures 4 to 9. Figure 4 summarises the locations of all the instrumentation. The fill level was increased to approximately 4m at the crown in October 1995, as indicated in Figure 5, and a typical set of piezometer measurements shows that the excess pore pressure has built up slowly, and then dissipated over the next three months, as shown in Figure 6. This indicates that the prefabricated vertical drains were working satisfactorily. The ground water re-established at a new level after that, and then fluctuated with seasonal changes. Figure 7 shows the increase in settlement, from the monitoring data of the settlement plates, in response to the increase in pore water pressure during the same period. The increase in settlement reduced when the pore water pressure stabilised, and the

rate of settlement became insignificant. Figures 7 & 8 show the settlement monitoring results at the crown (by extensometers) and at the berm (by settlement plates). The total settlement which occurred at the crown of the embankment was about 150mm, while the settlement which occurred at the berm was about 70mm.

Two plots were employed for the interpretation of inclinometer data. The 'cumulative' plot gave a more graphic representation of the actual deformation pattern and was most commonly used. The 'change' plot, which plots the gradient of the 'cumulative' plot, accentuates the location of the deformation zone, which is useful to identify the shear zone (squeezing) and its magnitude. In general, the shear deformation is expressed in degrees. Figure 9 shows typical cumulative and shear deformation plots in the transverse direction for the inclinometer at a typical section. The plane on which the maximum shear strain occurred was at about 2m below the existing ground level. From the drillhole records, this level coincided with the location of the interface between fill and marine deposits. The magnitude of the maximum shear strain was less than 1 degree.

6 PERFORMANCE OF EMBANKMENTS

The performance of the embankments has been assessed from the monitored behaviour of the instrumentation. The fill level has reached a full height of approximately 4 metres. The excess pore water pressures within the marine deposits have dissipated satisfactorily, with an undissipated pore water pressure of only about 5-10 kPa. In general, the settlement plates have provided reasonably good information on the compression of the marine deposits. The shallow and deep settlement plates indicated that the

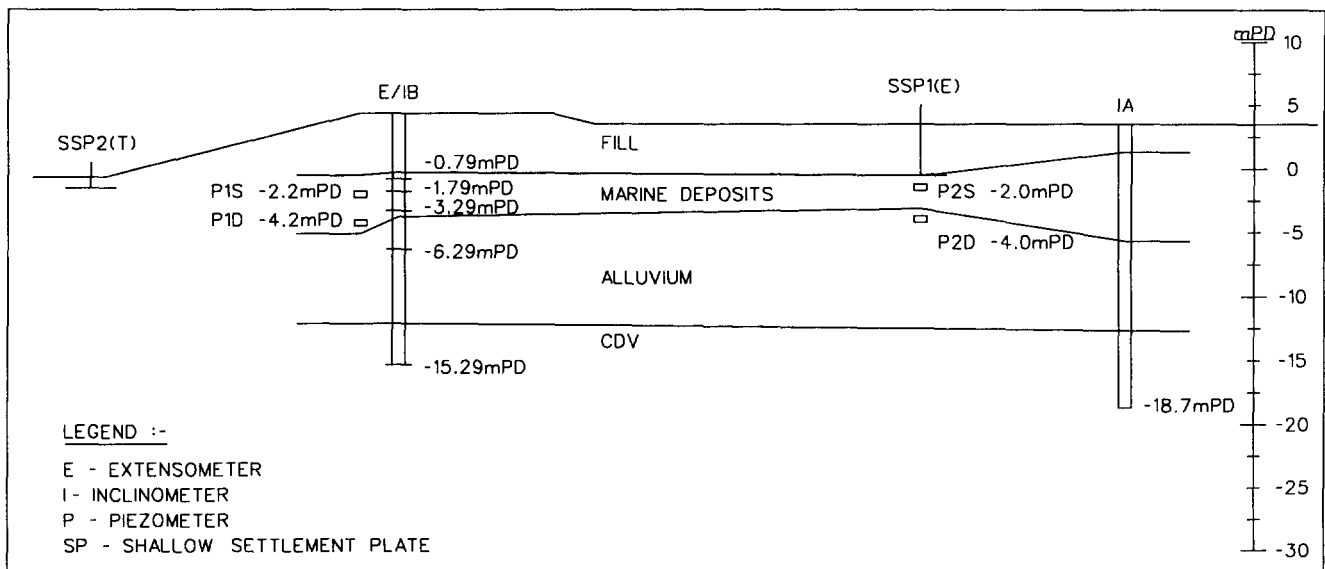


Figure 4. A Typical Instrumentation Section

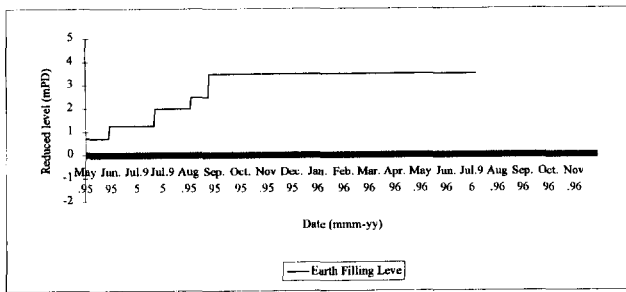


Figure 5. Fill Level Plot

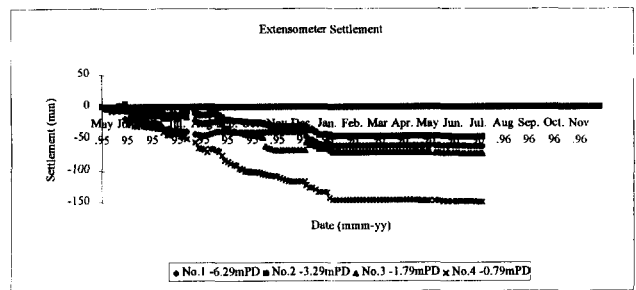


Figure 7. Settlement Plot

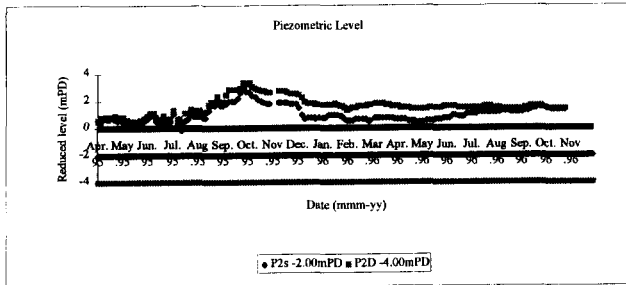


Figure 6. Piezometer Plot

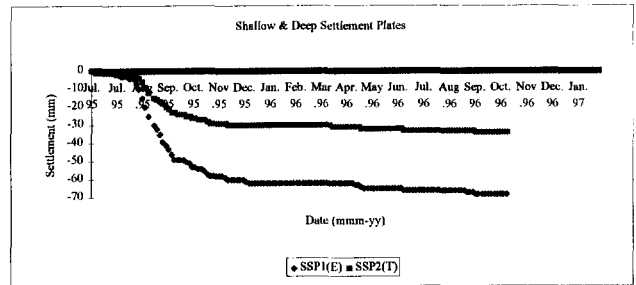


Figure 8. Settlement Plot

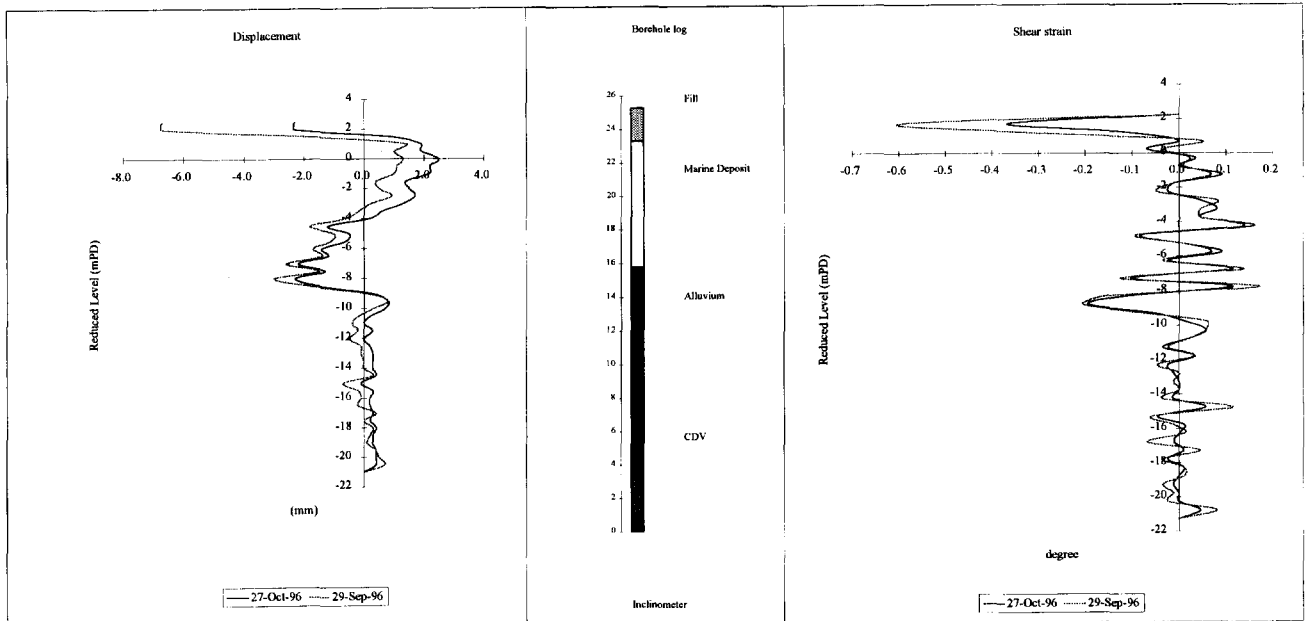


Figure 9. Inclinerometer Plots

settlement for the marine deposits at the embankment crown was between 250mm to 350mm, depending on the thickness of marine deposits, which ranged between 4m to 6m. At the berm of the embankment, the settlement measured by using extensometers was between 60mm to 150mm with thickness of the marine deposits ranged from 6m to 8m. In general, the rate of settlement was insignificant 4-6 months after the end of construction. The inclinometer with extensometer was used to monitor the horizontal and vertical deformation of the ground at

selected locations. At this site it was used to monitor the lateral movement of the earth bunds adjacent to fish ponds. It was found that squeezing of the marine deposits underneath the embankment occurred at the interface between the stiffer alluvium and the marine deposits. In general, the cumulative deformation ranged from 30mm to 100mm along the drainage channel. The maximum shear deformation, in general, occurred at the interface of the marine deposits and the alluvium, with a magnitude of between 0.5° to 2°.

7 COMPARISON OF PERFORMANCE

To assess the effectiveness of the performance of the embankments, four cases of trial embankments on soft soil foundations, which employed similar reinforcement materials or had similar site conditions as Hong Kong, were

It is suggested that a way forward to improve the economy, efficiency and effectiveness of the design of embankments on soft soil foundations in Hong Kong is to construct a trial embankment, to define the critical conditions, and to conduct back analyses, so that the design parameters can be more accurately determined.

Table 2. Comparison of Embankment Performance

Case	Reinforcement Material	Su(kN/m ²)	Soft Clay Depth (m)	Berm	Fill Height (m)	Rft. Strain (%)	Rft. Load (%)	PVD
1986 France Test Embankment	Polyester Woven 225/60	30 Const.	24	Yes (4.5m)	7 8.75 (failed)	2.5	50	No
1989 Canadian Test Embankment	Polyester Woven 216	30 Const.	10	Yes (3.5m)	4 8.2 (failed)	2		No
1982 Hong Kong Deep Bay	Polyester Polypropylene Woven 200/200	5-10 Linearly Increase Ratio 0.25	12	Yes (0.8m)	3.5	9		No
1988 Malaysia Trial Embankment	HDPE Geogrid 80	5-10 Linearly Increase Ratio 0.3	14	No	6	5	40	Yes (Not Functioned)
	HDPE Geogrid 110 × 2			Yes (3m)	8.50	2	25 × 2	Yes (Not Functioned)
1995 Hong Kong DSD Contract A	Polyester Woven 800/100		10	Yes (2m)	4			Yes

reviewed (Delmas, Ph. et al (1992), Rowe, R.K. et al (1994), Cowland, J.W. et al (1997) & Malaysian Highway Authority (1989)).

A comparison of the performance of these trial embankments and the Hong Kong embankment are summarised in Table 2. Although the reinforcement load and strain in the Hong Kong embankments have not been measured, the comparison does indicate that the design of the geotextile reinforcement for these flood protection embankment was conservative.

8 CONCLUSIONS

The use of vertical drains in combination with basal reinforcement proved to be a cost-effective means to construct embankments over soft ground without removal of the muds.

Both types of polyester woven reinforcement geotextiles and the prefabricated vertical drains that were used performed satisfactorily. They enhanced the short-term stability of the embankments and accelerated the time of consolidation of the muds.

Instrumentation plays a important role during construction to ensure safety of the construction work, allow control of the construction pace, and to provide data for measurement of quantities.

The performance of the embankments was very much better than the calculated performance assumed in design, reflecting the conservatism in the choice of soil parameters.

ACKNOWLEDGEMENTS

This Paper is published with the permission of the Director of Civil Engineering of the Government of the Hong Kong Special Administrative Region.

REFERENCES

- Cowland, J W, Yeo K C & Greenwood, J H (1998) "Durability of polyester and polypropylene geotextiles buried in a tropical environment for 14 years", *Paper submitted to the Sixth International Conference on Geosynthetics*.
- Delmas, Ph., Queyroi, D., Quaresma, M., De Saint, Amand & Puech, A. (1992) "Failure of an experimental embankment on soft soil reinforced with geotextile: Guiche", *Geotextiles, Geomembranes and Related Products*, Den Hoedt (ed.) @ 1992 Balkma, Rotterdam.
- Dunnicliff, J (1988) "Geotechnical Instrumentation for Monitoring Field Performance", John Wiley & Sons, 577p.
- Malaysian Highway Authority (1989) "Factual report on performance of the 13 trial embankments", *Proceedings of Int. Sym. on Trial Embankments on Malaysian Marine Clays*, Kuala Lumpur, vol.I.
- Rowe, R.K. & Gnanendran, C.T. (1994) "Geotextile strain in a full scale reinforced test embankment". *Geotextiles and Geomembranes 13*, pp 781-806.

Influence of Geometry and Construction Sequence on Reinforced Embankments on Soft Soils

J.L. Borges

Auxiliary Professor, Department of Civil Engineering, Faculty of Engineering, University of Porto, Portugal

A.S. Cardoso

Associate Professor, Department of Civil Engineering, Faculty of Engineering, University of Porto, Portugal

ABSTRACT: In order to study the influence of some parameters, namely the embankment geometry and construction sequence, on the geotechnical behaviour of reinforced embankments on soft soils, a numerical model based on the finite element method is used. The settlements, horizontal displacements, stresses in the reinforcement (geosynthetic) and global stability are analysed. Several conclusions are indicated.

KEYWORDS: Embankments, Finite Element Analysis, Reinforcement, Settlement Analysis, Soft Soils.

1 INTRODUCTION

In this paper, the influence of two parameters - embankment width and construction sequence (Fowler and Haliburton, 1980; Christopher and Holtz, 1985; Haliburton et al., 1982; Koerner and Welsh, 1980; Ingold and Miller, 1988; Holtz, 1990) - is studied.

A numerical model based on the finite element method (Borges, 1995) is used and, basically, its theoretical hypotheses are: a) validity of the plane strain conditions; b) coupled formulation of the flow and equilibrium equations considering the constitutive relations (elasto-plastic models) formulated in effective stresses (extension of Biot's consolidation theory); this formulation is applied at any phase of the problem, either during the embankment construction or in the post-construction period; c) utilisation of the critical states model [p,q,θ] (Lewis and Schrefler, 1987; Borges, 1995) to simulate the constitutive behaviour of the foundation and embankment soils; d) utilisation of a hardening elasto-plastic model to simulate the «instantaneous» constitutive behaviour of the reinforcements; e) simulation of the viscous behaviour of the geosynthetics (time-dependent constitutive relations) using a rheological model based on the serial association of Kelvin's units; f) simulation of the constitutive behaviour of the soil-geosynthetic interfaces using a hardening elasto-plastic model.

These studies involve the numerical results of a reference embankment, reinforced and unreinforced (analyses 1A and 1B, respectively). Firstly, the results of these cases are compared to the results of other two cases (analyses 2A and 2B) which are similar to the first ones except to their width, that is smaller. Secondly, having the purpose to verify the influence of the way each embankment layer is constructed (in this case, starting, or not, from its extremities to its middle), the results of other analysis (3A) are introduced.

2 DESCRIPTION OF REFERENCE PROBLEM

The analyses 1A and 1B are similar except in the fact that the first one has a reinforcement in the embankment base and the second one does not. They model a 28 days continuous construction of an embankment of 2 m height, symmetric, with a final platform of 10.6 m width and slopes inclined V/H=2/3. The foundation is a 5 m depth saturated clay that lays on a rigid and permeable soil (lower boundary of the problem). Figure 1 shows the finite elements mesh. Only the 2D elements are represented; the geosynthetic and the soil-geosynthetic interfaces are modulated by one-dimensional elements put between the foundation and the embankment elements.

The embankment construction was simulated activating successively the elements that form the different embankment layers. Four layers of 0.5 m were considered. Total time of construction was 28 days (7 days by layer).

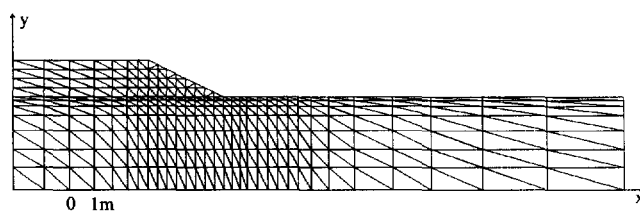


Figure 1. Finite element mesh

The constitutive relations of the embankment and of the foundation were simulated using the critical states model [p,q,θ] with the parameters indicated in Table 1. Tables 2 and 3 show other geotechnical properties and the depth variation of the coefficient of earth pressure at rest, k_0 , and of the over-consolidation ratio, OCR, in the foundation.

Figure 2 shows the mechanical behaviour of the geosynthetic and soil-geosynthetic interfaces (elastoplastic

models). The geosynthetic thickness is 2 mm and its elastic modulus is 1.5×10^6 kPa. Normal and tangential stiffnesses of the soil-reinforcement interfaces are 2.0×10^7 kPa and 1.6×10^4 kPa, respectively.

Table 1. Parameters of the critical states model [p,q,θ] for the foundation and the embankment

	λ	k	Γ	N
Foundation	0.22	0.02	3.26	3.40
Embankment	0.03	0.005	1.80	1.817

Table 2. Geotechnical properties of the foundation and the embankment

	γ (kN/m ³)	v'	ϕ' (°)
Foundation	17	0.25	30
Embankment	20	0.30	35

Table 3. Coefficient of earth pressure at rest, k_0 , and over-consolidation ratio, OCR, in the foundation

Depth (m)	K_0	OCR
0 - 1	0.7	2.43
1 - 1.8	0.7 - 0.5	2.43 - 1
1.8 - 5	0.5	1

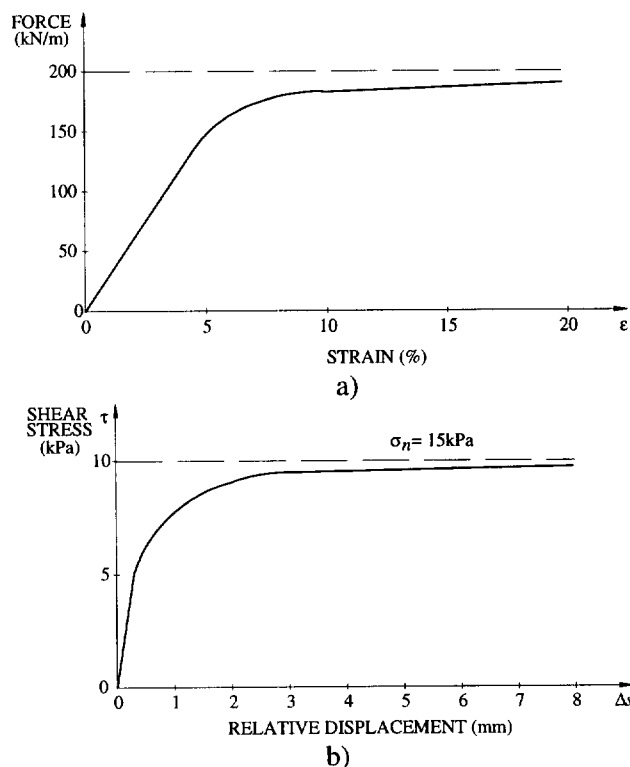


Figure 2. Constitutive curve of the: a) geosynthetic; b) soil-geosynthetic interface

3 INFLUENCE OF EMBANKMENT WIDTH

Because the 2D character of the problem, it is natural that the alteration of the embankment geometry - namely the embankment width - influences the behaviour, either in terms of displacements or in terms of global stability.

To study this question two analyses were done (2A and 2B), which are, as said, similar to the reference analyses (1A and 1B), except to their width, that is smaller (see Figure 3).

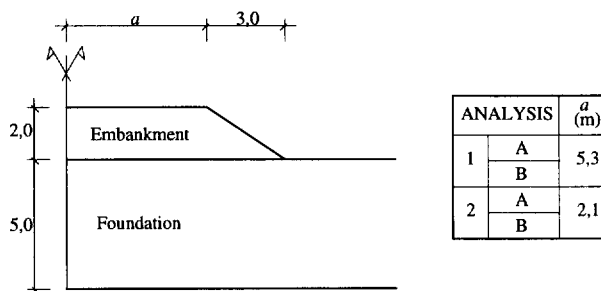


Figure 3. Embankment geometry

Relatively to the geosynthetic traction forces, Figure 4 shows that their maximum values are similar (either at the end of construction or at the end of consolidation) in the 1A and 2A analyses, which shows that the maximum value of the traction, as explained by Borges (1995), does not significantly depend on the embankment width. Increasing this parameter, only increases the area of the geosynthetic in which the traction force has approximately a uniform value (similar to the maximum one), in the middle zone of the embankment base.

Relatively to the embankment settlements (Figure 5), one can see that, in terms of decrease of maximum value of the settlements due to the geosynthetic, this decrease can be more effective in larger embankments. However, the influence on the differential settlements under the embankment platform can be observed in both cases. It is interesting verify that the maximum settlement value increases with the embankment width (different geometry of the problem determines different stresses in the foundation and, consequently, different maximum settlement value at the end of the consolidation).

In terms of global stability, it should be noted that the embankment geometry, namely the b/h relation (see Figure 6), influences the type of failure surface that can occur, i.e., the probability of occurring a failure surface as the one presented in Figure 6a (without cutting the embankment and the reinforcement) is greater when the b/h parameter has a small value. In this case the geosynthetic does not directly contribute with its strength to the global stability, so the embankment width can determine the role of the reinforcement on failure mechanism.

Using the numerical results and limit equilibrium assumptions, it can be obtained the failure surfaces

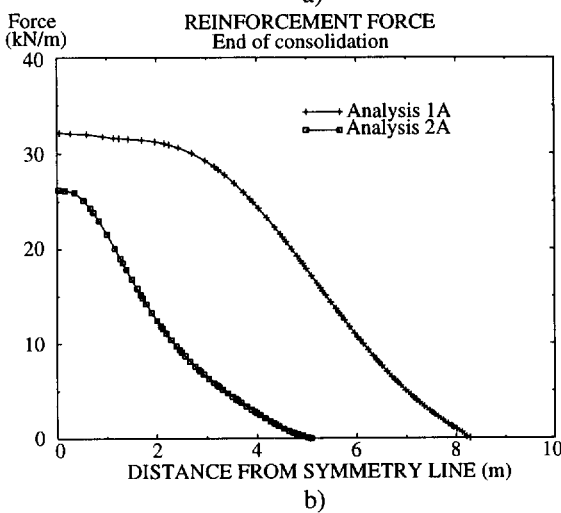
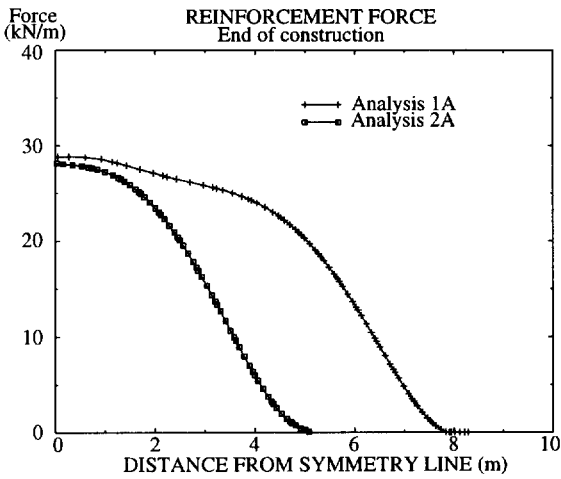


Figure 4. Influence of the embankment width on the reinforcement forces: a) at the end of construction; b) at the end of consolidation

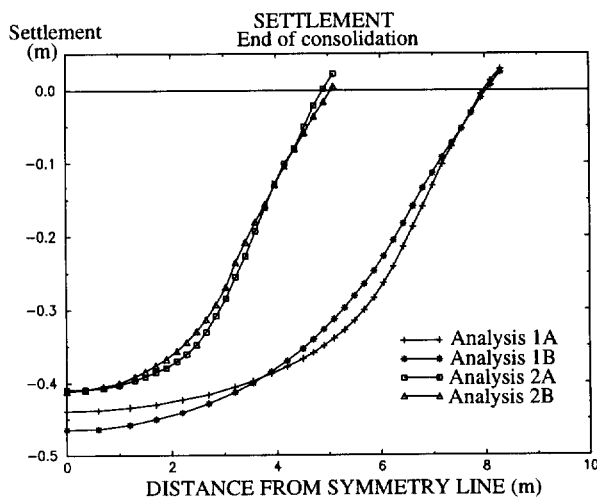


Figure 5. Influence of the embankment width on the embankment settlements at the end of consolidation

concerning the four analysed cases. Figure 7 shows those (cylindrical) surfaces and the respective global stability coefficients, at the end of construction. These calculations were done by a computer program that, in each analysed cylindrical surface, compares acting and failure tangential forces (obtained from the results of the numerical model and the strength characteristics of the materials).

The results show that the increase of the global stability due to the reinforcement (comparing 1A to 1B and 2A to 2B) is less effective for small values of b/h because failure surfaces could be similar to the one represented in Figure 6a. It was the case of 2A analysis.

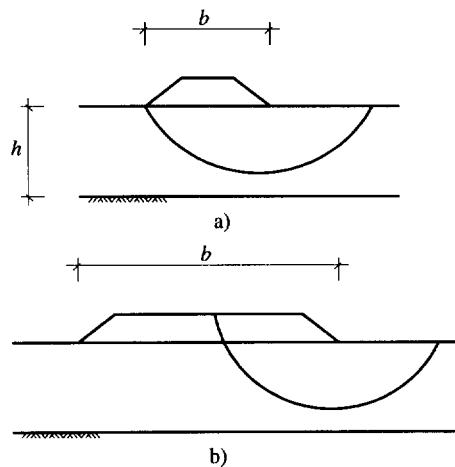


Figure 6. Influence of embankment width on the type of global failure

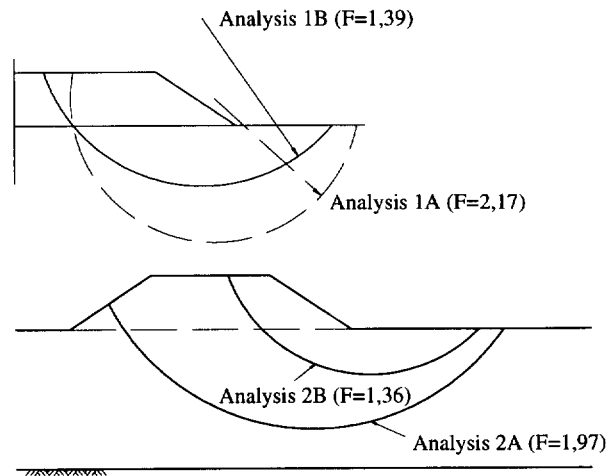


Figure 7. Failure surfaces and respective global stability coefficients (F) at the end of construction.

4 INFLUENCE OF CONSTRUCTION SEQUENCE

To verify the influence of the way each embankment layer is constructed (temporal and spatial evolution), the results

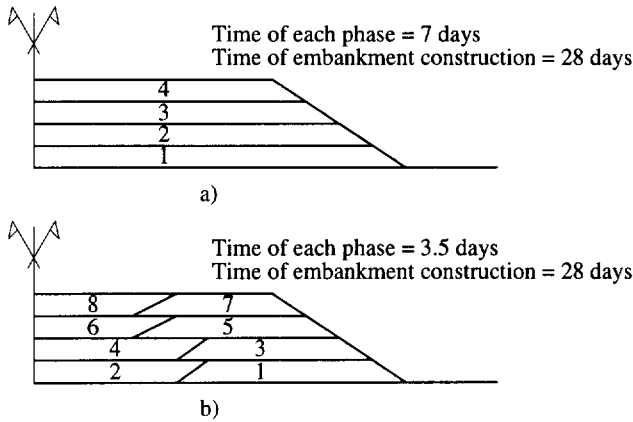


Figure 8. Embankment construction phases: a) analyses 1; b) analyses 3

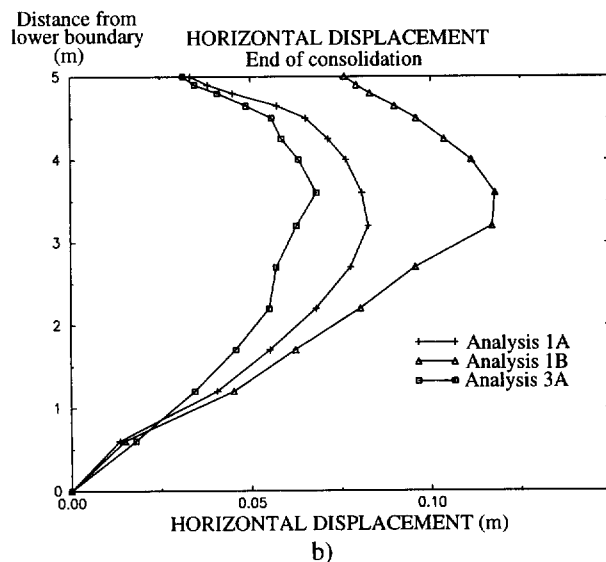
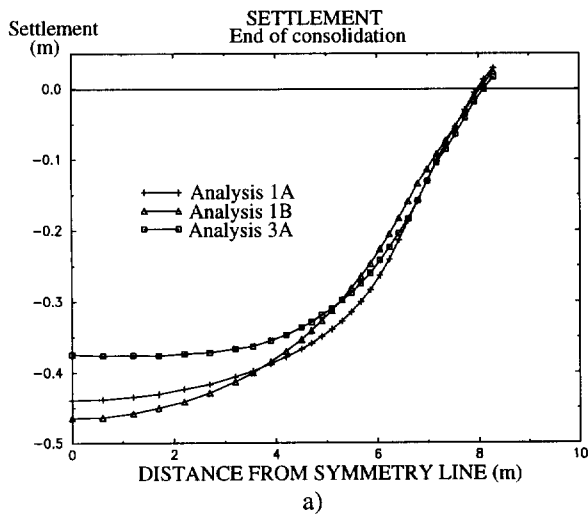


Figure 9. Influence of construction procedures on the: a) settlements; b) horizontal displacements at the vertical line 3.2 m distant from symmetrical line.

of other analysis (3A) are introduced. This analysis is similar to the reference one, 1A, except in what concerns the construction sequence of each layer (see Figure 8).

From the analysis of the numerical results, it can be concluded that the most important alterations concern the long time settlements (Figure 9a). These settlements are significantly reduce in terms of maximum and differential values.

The reason of that behaviour (Borges, 1995) is related to the fact that, at the end of construction, the distribution of excess pore pressures in the middle of the foundation loaded zone is more uniform. This fact implies a decrease of the shear strains in the foundation, which, consequently, leads to the reduction of settlements (as seen in Figure 9a) and of horizontal displacements, as it can be seen, for example, at the vertical line 3.2 meters distant from symmetry line (Figure 9b).

ACKNOWLEDGEMENTS

The writers acknowledge the funding for the work reported in this paper that was provided by the PRAXIX/2/2.1/CEG/42/94 project.

REFERENCES

- Borges, J. L. (1995) "Aterros sobre solos moles reforçados com geossintéticos - Análise e dimensionamento", *PhD Thesis in Civil Engineering*, Faculty of Engineering, University of Porto, Portugal.
- Christopher, B. R. and Holtz, R. D. (1985) *Geotextile Engineering Manual*, Federal Highway Administration, Washington, D.C., FHWA-TS-86/203, 1044 pp.
- Fowler, J. and Haliburton, T. A. (1980) "Design and Construction of Fabric Reinforced Embankments", *The Use of Geotextiles for Soil Improvement*, Preprint 80-177, ASCE Convention, pp. 89-118.
- Haliburton, T. A.; Lawmaster, J. D. and McGuffey, V. E. (1982) *Use of Engineering Fabrics in Transportation Related Applications*, Final Report Under Contract N° DTFH61-80-C-0094.
- Holtz, R. D. (1990) "Design and Construction of Geosynthetically Reinforced Embankments on Very Soft Soils", *International Reinforced Soil Conference*, Glasgow, pp. 391-402.
- Ingold, T. S. and Miller, K. S. (1988) *Geotextiles Handbook*, Thomas Telford, London.
- Koerner, R. M. and Welsh, J. P. (1980) *Construction and geotechnical engineering using synthetic fabrics*, John Wiley and Sons, Inc., New York.
- Lewis, R. W. and Schrefler, B. A. (1987) *The Finite Element Method in the Deformation and Consolidation of Porous Media*, John Wiley and Sons, Inc., New York.

Design Guidance for Reinforced Soil Structures with Marginal Soil Backfills

Barry R. Christopher, Ph.D., P.E.
Christopher Consultants, Roswell, Georgia, USA

Jorge G. Zornberg, Ph.D., P.E.
GeoSyntec Consultants, Huntington Beach, California, U.S.A.

James K. Mitchell, Ph.D., P.E.
Virginia Polytechnic Institute and State University, Blacksburg, Virginia, U.S.A.

ABSTRACT: Use of marginal, poorly draining backfill to construct reinforced soil structures offers significant advantages for numerous applications. This paper reviews the issues associated with using such soils with an emphasis on the use of permeable inclusions as a design alternative to provide internal drainage of the reinforced zone. Case histories demonstrating the successful use of permeable inclusions for addressing both internal and external seepage problems are presented. Adverse conditions of excessive moisture and pore water pressures within the poorly draining backfill are identified. Finally, preliminary guidance for reinforced soil structures using poorly draining backfills is provided to account for these adverse conditions in their design.

KEYWORDS: Reinforcement, Design, Seepage Control, Shear Strength, Drainage.

1 INTRODUCTION

Granular soils have been the preferred backfill material for reinforced soil construction due to their high strength and ability to prevent development of pore water pressures. Stringent specifications regarding selection of granular backfill are provided, for example, by the United States FHWA guidelines (Elias and Christopher, 1996). However, if granular fills were not readily available, or if substantial cost benefits resulted from relaxing fill specifications, poorly draining soils (e.g. silty or clayey soils) have been used in practice. In these cases, proper understanding of the conditions leading to wetting of the fill and to the development of pore water pressures is imperative for an adequate design.

Although marginal soils have been successfully reinforced using impermeable reinforcements (e.g. geogrids, woven geotextiles, metallic reinforcements), failures have also been reported. These failures generally occurred if the generation of pore pressures or seepage related conditions were not correctly addressed during design (Mitchell and Zornberg, 1995).

A promising approach for design of reinforced marginal soils is to promote lateral drainage in combination with soil reinforcement. This may be achieved by using geocomposites with in-plane drainage capabilities or thin layers of granular soil in combination with the geosynthetic reinforcements. This design approach may even lead to the elimination of external drainage requirements. The potential use of permeable inclusions to reinforce poorly draining soils is well documented (e.g. Tatsuoka et al.,

1990; Zornberg and Mitchell, 1994; Mitchell and Zornberg, 1995). The focus of this paper is on the implementation of this technology by providing design guidance based on experience gained in recent case histories. Emphasis is placed on the identification of the adverse conditions that may result in wetting and pore water pressure development within the reinforced marginal fill.

This paper initially identifies the problems related to the use of marginal soils and the potential use of permeable inclusions as a design alternative. Next, experiences from the technical literature and by the authors on recent case histories are presented. Finally, preliminary guidance is provided, considering the identified adverse conditions, regarding the design of reinforced soil structure using poorly draining backfills.

2 BACKGROUND

2.1 Reinforcing Poorly Draining Backfills: Identification of Adverse Conditions

Significant problems are associated with the use of marginal soils in reinforced soil construction. The use of comparatively wet soils leads, for example, to construction problems associated with compaction difficulties during placement. However, the most serious concerns are related to stability problems associated with the potential development of pore water pressures or loss of strength due to wetting within the reinforced fill mass. The following three adverse conditions of pore water pressure generation and/or loss of

strength due to wetting are of concern when reinforcing poorly draining backfills (Fig. 1):

Condition (a): Generation of pore water pressures within the reinforced fill. When fine grained, poorly draining soils are used in reinforced soil construction (particularly if placed wet of optimum moisture), excess pore water pressure can develop during compaction, subsequent loading, and surcharging. The designer must then account for these pore water pressures for the evaluations of stability and consolidation-induced settlements.

Condition (b): Wetting front advancing into the reinforced fill. This is the case for fills placed comparatively dry (i.e. no pore water pressure generation is expected during construction). However, loss of soil shear strength may occur due to wetting of the backfill soils as a consequence of post-construction infiltration. This loss of strength due to wetting could be expected, even if no positive pore water pressures are generated and no seepage flow configuration is established within the fill.

Condition (c): Seepage configuration established within the reinforced fill. Seepage flow may occur within the reinforced soil mass, for example, in the case of sliver fills constructed on existing embankment side slopes and cut slopes in which infiltration occurs from the adjacent ground. Significant seepage forces may occur either during rainy or spring thaw seasons. Water level fluctuations and rapid draw down conditions can also induce seepage forces in structures subjected to flooding or constructed adjacent to or within bodies of water. Seepage forces may also occur during ground wetting, inducing an additional destabilizing effect to the loss in shear strength described by Condition (b).

2.2 Reinforcing Poorly Draining Backfills: Permeable Inclusions as Potential Design Alternative

The potential benefits of using marginal soils to construct steepened slopes are significant and include:

- reduced cost of structures that would otherwise be constructed with expensive select backfill;
- improved performance of compacted clay structures that would otherwise be constructed without reinforcements; and
- use of materials, such as nearly saturated cohesive soils and mine wastes, that would otherwise require disposal.

However, the significant benefits of using poorly draining soils as backfill material can be realized only if a proper design accounts for the three adverse conditions listed in Section 2.1. The use of permeable reinforcements is a potential design alternative to properly handle these conditions, as follows:

Condition (a): Pore water pressures generated during construction within the reinforced poorly draining fill could be dissipated if the geosynthetic inclusions are used not only as reinforcements, but also as lateral drains. New applications in the use of geosynthetics for stabilization in land reclamation projects could be developed. For example, acceleration of drainage of hydraulically dredged materials could be achieved.

Condition (b): A problem frequently reported for embankments of (unreinforced) compacted cohesive soils is the development of surface tension cracks and the subsequent loss of soil strength due to soaking. The wetting front and development of surface tension cracks have been observed by the authors and other investigators (Tatsuoka et al., 1990) to extend only down to the region above the first geosynthetic layer. If the reinforcement is permeable, water that might normally accumulate in the crack can drain when the crack reaches the first layer of reinforcement.

Condition (c): Permeable reinforcements can prevent the development of flow configurations with destabilizing seepage forces within the embankment fill. Internal drainage is of particular concern in road widening projects, because of the potential water seepage from cut slopes into the reinforced fill. Although the adverse effect of seepage forces in engineered slopes could be prevented by designing special drainage systems, a more economical design alternative is to combine drainage and reinforcement capabilities by using permeable reinforcement elements.

In addition to addressing stability problems, the use of permeable inclusions may also be of benefit during construction. Wet soils typically must be dried to provide desired compaction levels and associated design strengths. However, it has been verified that permeable inclusions (e.g. nonwoven geotextiles) help in the compaction of the

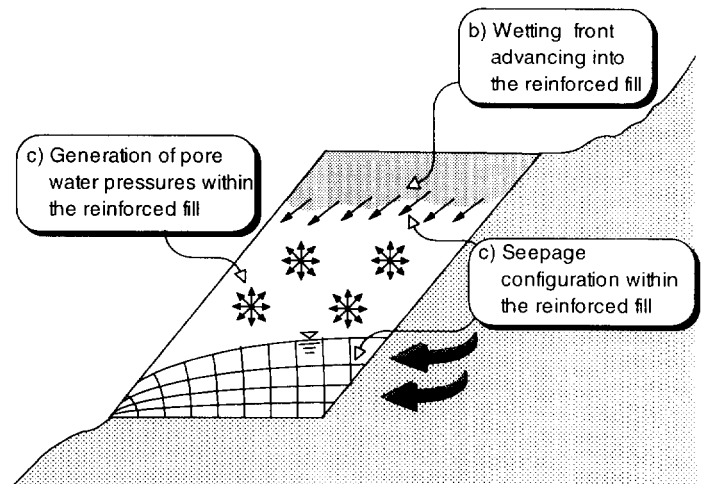


Fig. 1. Different conditions of concern in reinforced soil slopes using poorly draining backfills.

fill both by allowing better distribution of the compaction effort and by draining excess pore water pressure induced during compaction (Indraratna et al., 1991; Zornberg et al., 1995). On several projects, water has even been observed seeping out of the geotextile during compaction of such soils placed wet of optimum. The most significant improvement in compaction has been reported for low plasticity clayey and silty soils. Although some compaction improvement has been observed in plastic soils, the influence would not be nearly as significant. In either case, drying may still be required to facilitate placement and compaction, especially in very wet soils. Test pads are recommended to determine the actual placement requirements and compaction improvements. The increased rate of settlement would also expedite the construction of structures with a low tolerance for settlement (e.g. roads, bridges and buildings) that may be supported by the reinforced structure.

3. EXPERIENCE IN THE USE OF REINFORCED POORLY DRAINING FILLS

Although there are no generally accepted design guidelines for reinforced soil structures using marginal soils, good performance has been observed in cases where the generation of pore water pressures within the fill was mitigated. The observed performance of a 5.6 m high experimental structure built using silt backfill in Rouen, France is a good example (Perrier et al., 1986). Pore water pressures were monitored within the silt backfill. The structure consisted of sections reinforced with woven geotextiles and a section reinforced with a composite nonwoven/geogrid. Fig. 2 shows positive and negative pore water pressures as a function of time recorded at different locations within the fill. The pressure sensor behind the reinforcement region recorded placement excess pore water pressures of as much as 60 kPa at the end of construction. Along the woven geotextile, 3.5 m from the wall face, positive pore water pressures on the order of 20 kPa were registered at the end of construction and dissipated in 350 days. Along the composite geotextile, on the other hand, negative pore water pressures were registered over the entire length of the reinforcement, even at the end of construction. The negative pore water pressure recorded for the geocomposite most likely developed due to the ability of the geosynthetic to maintain partial saturation in the soil or to the unsaturated condition of the geosynthetic itself. Pore water pressures along the composite geotextile were systematically lower than those recorded along the woven textile.

Permeable reinforcements were also used to control pore water pressure during construction and to accelerate post-construction consolidation as part of the reconstruction of an embankment in Pennsylvania (Wayne et al., 1996). A sink hole developed in a section of state

route SR54 due to the collapse of an abandoned railroad tunnel. The traditional repair would have involved the removal and replacement of the 15 m high embankment. However, the native soil (a sandy clay of high moisture content) was deemed unsuitable backfill due to potential stability and settlement problems. Consequently, due to the high cost of granular fill as replacement material (estimated as \$19.60/m³), the Pennsylvania DOT decided to use geosynthetics to provide both drainage and reinforcement to the native soil used as fill. The estimated cost savings are \$200,000 (based on an as built cost of \$4/m³ for the native

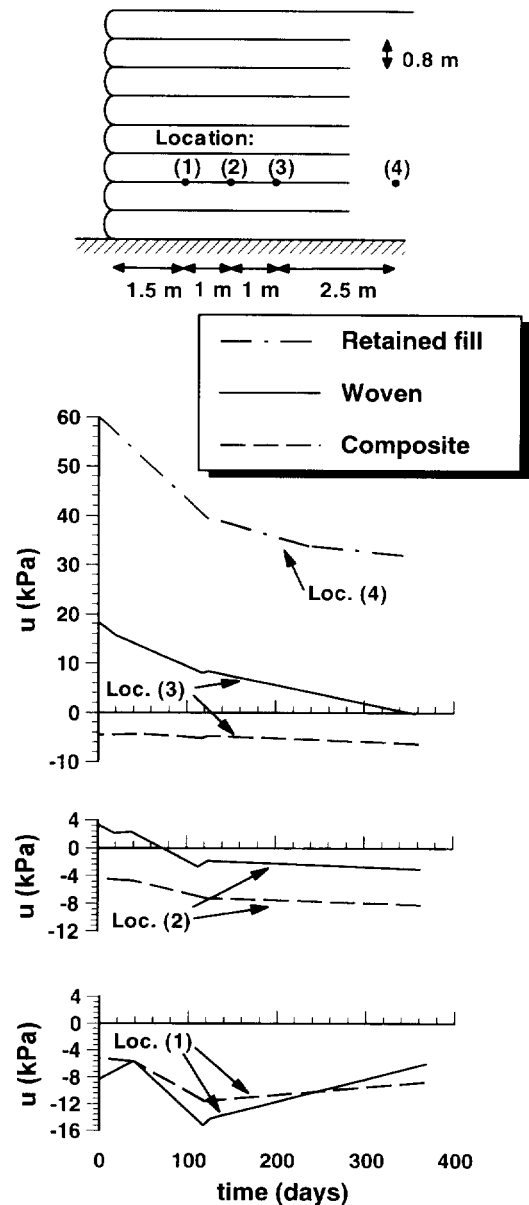


Fig. 2. Pore water pressures (u) in the Rouen reinforced wall, along a woven and a nonwoven/geogrid composite, within a silty backfill (redrawn after Perrier et al., 1986).

soil plus the geotextile). Based on the results of field tests used to evaluate pore pressure response, a nonwoven geotextile was selected to allow pore pressure dissipation in the native soil. The geotextile, with an ultimate strength of 16 kN/m, also provided reinforcement to the 1.5H:1V side slopes. Placement of geotextiles at each compacted lift (0.3 m spacing, i.e. 0.15 m drainage path), led to full dissipation of pore water pressure within approximately 4 days. Only approximately 25% of the pore water pressures were dissipated during the same time period in zones that did not contain geosynthetics. Piezometers installed at the base and middle of the slope confirmed the test pad results. Fig. 3 shows the development and subsequent dissipation of pore pressure during and following construction of the embankment. Geotextile deformations in the side slope were monitored and found to be less than the precision of the gages ($\pm 1\%$ strain).

There is also good evidence that permeable geosynthetic reinforcements can reduce the influence of external seepage behind the reinforced soil mass (e.g. in cut slope applications). Recent centrifuge model studies evaluated the performance of unreinforced and reinforced steep slopes constructed with clay (Mahmud, 1997). Seepage was induced into the reinforced clay by maintaining a constant water level at the back of the structure. Measurement of pore pressure across the base of the structure, indicated a lower phreatic surface if the slope was constructed using permeable geosynthetic reinforcements than if the slope was unreinforced (Fig. 4).

The use of permeable reinforcements to reduce external seepage problems was also demonstrated in a recent project which included one of the highest geotextile-reinforced slopes in the U. S. (Zornberg et al., 1995). As part of a highway widening project, the Federal Highway Administration constructed a permanent, 15.3 m high geotextile-reinforced slope. Several characteristics were unique to the design: the structure was higher than usual geotextile-reinforced slopes, it involved the use of both a high modulus composite and a nonwoven geotextile, and it was constructed using indigenous soils (decomposed granite) as backfill material. Internal drainage was a design concern because of the potential seepage from the fractured rock mass into the reinforced fill, and because of the potential crushing of decomposed granite particles that was anticipated to reduce the hydraulic conductivity of the fill. Widening of the original road was achieved by converting the existing 2H:1V unreinforced slope into a 1H:1V reinforced slope. The final design adopted a high strength composite geotextile in the lower half of the slope and a nonwoven geotextile in the upper half. Piezometer measurements indicated that a seepage flow configuration did not develop within the reinforced soil mass even during the spring thaw, when seepage water infiltrated from the backslope fractured rock into the reinforced fill.

Additional evidences that good structure performance is dependent on maintaining a low water pressure in poorly

draining backfills was provided by Tatsuoka et al. (1990) and Mitchell and Zornberg (1995). However, practice has led theory, and a consistent design methodology for design of reinforced soil structures using poorly draining backfills has not been developed yet.

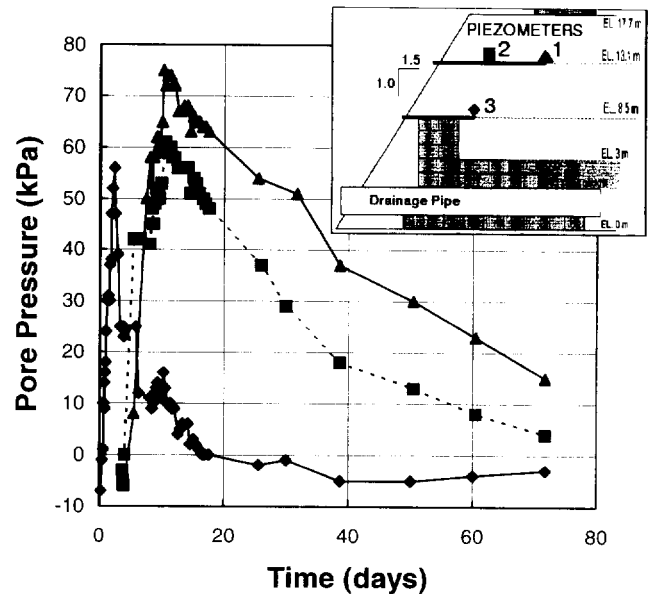


Fig. 3. Pore water pressure measurements in the SR54 reinforced slope (redrawn after Wayne et al., 1996).

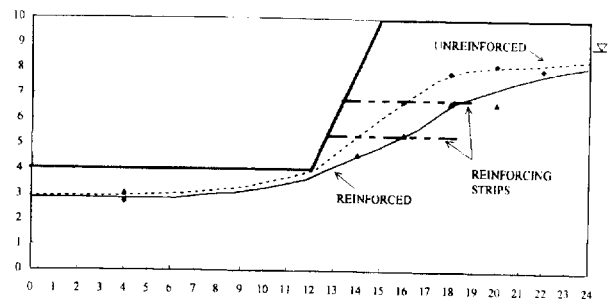


Fig. 4. Centrifuge model results showing the elevation of the phreatic surfaces for unreinforced and reinforced slopes (Mahmud, 1997).

4. DESIGN GUIDANCE

4.1 General Considerations

Good performance in reinforcing marginal soils depends on accounting for excess pore water pressure development within the fill material. Design criteria involved in the use of reinforcement-drainage geocomposites differ from those developed for conventional soil reinforcement applications. A total stress analysis, considering soil parameters representative of placement conditions, usually has been

adopted in the analysis of impermeable conventional reinforcements. The design generally leads to the use of reinforcements with a comparatively high tensile strength to account for a low soil shear strength and the presence of seepage forces. Reinforcement embedment length is comparatively large to account for reduced pullout resistance. External drainage of the reinforced soil structure has often been considered as part of the design to intercept ground water at the back of the structure.

The general design philosophy for permeable inclusions that is proposed in this paper is that transmissivity of the geosynthetic inclusion should be selected so that the geosynthetic inclusions can carry the full in-plane flow without developing positive pore water pressures along the soil-reinforcement interface. While it is also possible to design for positive pore water pressures at the interface, such a design requires evaluations that are beyond the scope of this paper. Consequently, the design procedure described below is only for reinforced soil structures in which the reinforcement transmissivity is conservatively selected so that flow is not impeded within the geosynthetic. The proposed design methodology assumes no build up of excess pore pressure within the permeable reinforcements.

The analysis should account for the three adverse conditions listed in Section 2.1 in order to determine the tensile strength and pullout requirements. The general design philosophy proposed herein is to consider a two-phase evaluation:

Analysis (i) in each adverse condition is performed ignoring the drainage contribution provided by the reinforcements.

This is a total stress analysis which considers that stability is mostly provided by the reinforcements with minimum contribution of the soil shear strength. Due to the conservative nature of this assumption, a relatively low design factor of safety is suggested.

Analysis (ii) in each adverse condition is performed accounting fully for the drainage contribution provided by the reinforcements (i.e. zero pore water pressure is considered within the reinforced fill for analysis purposes). Considering that no pore water pressures are assumed to develop, this is an effective stress analysis. Design factors of safety used in conventional engineering practice are considered in this case.

4.2 Designing for Condition (a): Pore water Pressures Generated within the Reinforced Fill

There is good evidence that geosynthetics with adequate transmissivity and vertical spacing on the order of every compaction lift or every other compaction lift (e.g. 200 to 300 mm) can dissipate excess pore pressure along the interface of the permeable inclusions during construction (Bourdillon et al., 1977). However, excess pore water pressures may develop within the soil mass between

geosynthetic layers during construction, especially if highly plastic soils are used as backfill material. Considering the difficulty in accurately evaluating the distribution of pore water pressures generated during construction a two-phase analysis is proposed. These analyses, summarized in Table 1, are as follows:

- i) Total stress analysis ignoring reinforcement lateral drainage. This analysis neglects the dissipation of pore water pressures through the permeable inclusions to provide a conservative estimate of the stability of the structure at the end of construction. Considering the short-term condition and the conservative assumptions in this analysis, a factor of safety of 1.1 is recommended. This analysis determines minimum reinforcement requirements that will preclude collapse during construction of the structure. That is, it provides reinforcement requirements for a short-term situation in which stability is provided mostly by the tensile forces in the reinforcements with only a minor contribution by the undrained shear strength of the backfill. The undrained soil shear strength of the backfill for this analysis should be based on unconsolidated undrained (UU) triaxial tests. The specimens should be prepared at representative field densities and moisture placement conditions, and tested at these placement conditions under project-specific confining pressures. Although the authors consider testing under unsaturated conditions is an adequate approach, testing under fully saturated conditions represents an additional degree of conservatism that the designer may consider on a project-specific basis.
- ii) Effective stress analysis accounting for full lateral drainage by the reinforcement. Full drainage of the reinforced fill is assumed for the long-term conditions. This analysis provides a realistic evaluation of the long-term stability of the structure, because dissipation of pore water pressures generated during construction should have occurred through the permeable inclusions. This analysis determines the minimum reinforcement requirements that will provide adequate stability under long-term conditions following dissipation of pore water pressures generated during construction of the structure. It is emphasized that the transmissivity of the reinforcements should be selected so that generation of pore water pressures is prevented at the soil-reinforcement interface. Typically, the soil shear strength should be based on isotropically consolidated undrained (CIU) triaxial tests performed on saturated samples with pore pressure measurements or on consolidated drained (CD) triaxial tests. The long term design factor of safety typically required for reinforcement of granular fills (e.g. 1.3 to 1.5) should be used in this analysis.

Table 1. Summary of Analyses for Reinforced Soil Structures with Poorly Draining Backfills

<i>Condition</i>	<i>Characteristics</i>	<i>Analysis i: Ignoring lateral drainage</i>	<i>Analysis ii: Accounting for full drainage</i>
<i>a) Generation of pore water pressures within reinforced fill</i>	Type of analysis:	Total Stress	Effective Stress
	Case:	Generation of pore pressures due to short-term loads	Long-term drained condition due to lateral drainage
	Design Criteria:	FS = 1.1	FS = 1.3 to 1.5 (*)
	Reinforcement Transmissivity:	Ignored in analysis	Conveys fully the flow from consolidation process
	Soil shear strength:	ϕ and c from UU tests. Specimen condition: as placed	ϕ' and c' from CIU or CD tests. Specimen condition: saturated
<i>b) Wetting front advancing into reinforced fill</i>	Type of analysis:	Total Stress	Total Stress
	Case:	Loss of shear strength due to soaking	Unsaturated condition maintained due to permeable reinforcements
	Design Criteria:	FS = 1.1	FS = 1.3 to 1.5 (*)
	Reinforcement Transmissivity:	Ignored in analysis	Prevents advancement of wetting as defined by testing
	Soil shear strength:	ϕ and c from CIU tests. Specimen condition: saturated	ϕ and c from CIU or CD tests. Specimen condition: highest anticipated moisture
<i>c) Seepage flow configuration established within reinforced fill</i>	Type of analysis:	Total Stress	Effective Stress
	Case:	Development of seepage forces within fill	Saturation of fill, without development of seepage forces due to permeable reinforcements
	Design Criteria:	FS = 1.1	FS = 1.3 to 1.5 (*)
	Reinforcement Transmissivity:	Ignored in analysis	Conveys fully the seepage flowing into the backfill
	Soil shear strength:	ϕ and c from CIU tests. Specimen condition: saturated	ϕ' and c' from CIU or CD tests. Specimen condition: saturated

(*) Design criteria for Analysis (ii) should be selected based on design guidelines for reinforced soil structures with granular backfill.

The reinforcement tensile strength eventually selected is the higher value obtained from analyses (i) and (ii). Moreover, the minimum reinforcement length selected for design should be the larger value defined from the two analyses. Note that the analyses described above address internal stability. However, the required length of the reinforcement must also consider external stability of the structure. External stability should consider the undrained soil shear strength for the fill retained behind the reinforced zone if it is to be constructed with similar marginal fill. For cut slopes appropriate pore water pressure assumptions should be made for field conditions.

It should be noted that an effective stress analysis could have been proposed to evaluate the short-term stability of the structure, instead of the total stress Analysis (i). An effective stress analysis would more accurately account for the in-plane drainage capacity of the geosynthetic and the corresponding increase in soil strength. Also, an effective stress analysis would facilitate evaluation of the backfill placement rate that would lead to

an acceptable stability factor of safety during construction. The difficulty in this approach is the accurate determination of the pore water pressures within the fill. They could be estimated from direct measurements in field trials (e.g. test pads) or sealed laboratory specimens (one lift thick with a geosynthetic on the bottom and top connected to drain lines) subjected to stress levels anticipated during construction. Alternatively, pore pressures could be theoretically estimated based on one-dimensional consolidation theory and the assumption of full saturation of the backfill material during construction. An evaluation of this approach is beyond the scope of this paper.

4.3 Designing for Condition (b): Wetting Front Advancing into the Reinforced Fill

As loss of strength may occur because of a wetting front advancing into the reinforced fill. Geosynthetic transmissivity requirements should be established to avoid

advancement of wetting front for expected conditions. A two-phase analysis is also proposed in this case. These analyses, summarized in Table 1, are as follows:

- i) Total stress analysis ignoring the effect of lateral drainage in preventing advancement of a wetting front. This analysis is performed using shear strength properties of the reinforced soil mass defined using saturated specimens. The results of this analysis provide an estimate of the stability of the structure under an advancing wetting front. This analysis is conservative because the backfill is assumed fully saturated, which should not occur in actual practice because the wetting front is intercepted by the permeable reinforcements. Consequently, a factor of safety of 1.1 is recommended in this case. Water pressure that may develop as water fills surface cracks (induced by desiccation, freeze/thaw, or slope movements) should be accounted using boundary water pressures in the analysis.
- ii) Total stress analysis accounting for the effect of lateral drainage in preventing advancement of a wetting front. The total shear strength is defined from unsaturated specimens prepared at the highest moisture anticipated in the fill. Note that the total shear strength defined from unsaturated specimens should be higher than the effective shear strength of the fill. A total stress analysis is considered in this case, instead of an effective stress analysis, in order to account for the beneficial effect of the negative pore water pressures in the unsaturated reinforced fill. The shear strength of the reinforced fill above the top reinforced layer (which may become saturated) should be obtained from saturated specimens. This analysis provides a realistic evaluation of the stability of the structure because it accounts for the lateral drainage of the geosynthetic reinforcements.

4.4 Designing for Condition (c): Seepage Configuration Established within the Reinforced Fill

Post-construction pore water pressures could be generated by a seepage configuration developing within the backfill material. Such a flow configuration may develop seasonally during rainy periods or during spring thaw. A seepage configuration may also develop due to water level fluctuations in structures subjected to flooding or constructed adjacent to or within bodies of water. Finally, seepage forces could be induced by surface water infiltration. The seepage configuration can be determined for an unreinforced embankment using flow nets for seepage analysis. Transmissivity requirements in the geosynthetic inclusions are such that each reinforcement should convey fully the flow quantity it intercepts (as estimated from a flow net defined in an unreinforced

slope). A two-phase analysis is also proposed in this case. These analyses, summarized in Table 1, are as follows:

- i) Total stress analysis ignoring reinforcement lateral drainage. This analysis considers seepage forces defined from a flow configuration that would develop in an unreinforced slope. The results of this analysis provide a conservative estimate of the stability of the structure during a seasonal rapid configuration of seepage flow within the fill. The conservatism of this analysis is because (1) the backfill is assumed as fully saturated, which may not occur in actual practice, and (2) the seepage configuration does not account for the lateral drainage provided by the reinforcements. Therefore, a relatively low factor of safety of 1.1 is recommended in this case (note that seepage forces are considered in the analysis).
- ii) Effective stress analysis accounting for full reinforcement lateral drainage. Full drainage of the reinforced fill is assumed for the typical condition of the structure. This analysis provides a realistic evaluation of the long-term stability of the structure because it accounts for the lateral drainage of the geosynthetic reinforcements. No seepage forces are considered to develop within the reinforced fill if the reinforcements provide adequate internal drainage.

As indicated, the transmissivity and number and location of layers should be selected so that the geosynthetics have in-plane drainage capacity to accommodate the full seepage flowing into the reinforced fill. Otherwise, external groundwater and surface water control systems (e.g. base and back drains and surface collectors) must be incorporated into the design. The soil shear strength in the two analyses (total and effective stresses) should be determined using saturated samples in order to account for the potential loss of shear strength under soaked conditions.

4.5 Reinforcement Requirements

Mechanical and hydraulic properties that must be characterized for alternative reinforcement-drainage geocomposite systems include: tensile strength, pullout resistance, drainage, and filtration. These four characteristics should be carefully evaluated and quantified in order to assess the overall performance of the structures under consideration. The evaluations include at least the following considerations:

- Tensile strength requirements of the geosynthetic, determined as indicated in Table 1, will be typically higher for reinforcement of marginal fills than conventional free draining material. Consideration should be given to soil creep in the determination of long-term design strength.

- Pullout resistance, which require special consideration due to the potential development of pore water pressures at the soil/reinforcement interface and to the creep potential of cohesive soils. For the total stress analyses in Table 1, total stress shear strength properties should be used. For the effective stress analyses, effective shear strength properties should be considered.
- Transmissivity requirements should account for the different conditions indicated in Table 1 (i.e. the total flow induced by consolidation or seepage must be accommodated without inducing positive pore water pressures within the reinforcements). There is good evidence that transmissivity values equivalent to those of needlepunched nonwoven geotextiles are adequate to freely drain cohesive type soil and dissipate excess pore pressure along the interface, provided spacing is on the order of every lift or every other lift of compacted soil (e.g. Bourdillon et al., 1977). They should also be high enough to prevent advancement of a wetting front. Test pads could be used to evaluate the suitability of selected geosynthetics. Increased transmissivity may be required based on flow net analysis of externally induced seepage (Condition c).
- Filtration requirements needed to minimize clogging of the geocomposite should also be evaluated. Design guidance is provided in Holtz et al. (1997) and Koerner (1994).

5 CONCLUSIONS

Marginal poorly draining backfill can be used to safely construct reinforced steepened slopes provided internal and external seepage forces have been accounted for in the analysis. Adverse conditions include: (a) the generation of pore water pressures within the reinforced fill (either during construction or subsequent loading); (b) a wetting front advancing into the reinforced fill, which may cause loss of soil shear strength in a fill initially placed in a comparatively dry condition; and (c) a seepage flow configuration established within the reinforced fill due to seepage from the retained soil or fluctuations in the water level for structures constructed adjacent to or within bodies of water.

Reinforcements with in-plane drainage capabilities offer a design alternative for mitigating these adverse conditions. A two-phase analysis is proposed when using permeable reinforcements to account for both short and long-term conditions. Although the design approach is supported by theoretical soil mechanics, it relies heavily on field experience. Therefore, an element of conservatism is inherently included in the proposed methods. Further refinement of this guidance is being developed by the authors in order to provide quantitative transmissivity requirements for the case of pore water pressures developed during construction. Recommendations are

provided herein regarding the selection of soil shear strength properties and design criteria for the analyses.

REFERENCES

- Bourdillon, M., Didier, G., and Gielly, J., 1977, "Utilisation des Produits Non-tissés pour le Drainage," *Proc. Intl. Conf. on the Use of Fabrics in Geotechnics*, Paris, Vol. 2, pp. 279-284.
- Elias, V., and Christopher, B.R., 1996, "Mechanically Stabilized Earth Walls and Reinforced Soil Slopes, Design and Construction Guidelines" Department of Transportation, FHWA, Washington D.C., 367 p.
- Holtz, R.D., Christopher, B.R. and Berg, R.B., *Geosynthetic Engineering*, 1997, BiTech Publishers Ltd., Richmond, British Columbia, Canada, 452 p.
- Indraratna, B., Satkunaseelan, K.S., and Rasul, M.G., 1991, "Laboratory Properties of a Soft Marine Clay Reinforced with Woven and Nonwoven Geotextiles", *Geotechnical Testing J.*, Vol. 14, No. 3, pp. 288-295.
- Koerner, R.M., 1994, *Designing With Geosynthetics*, 3rd Edition, Prentice-Hall Inc., Englewood Cliffs, 783 p.
- Mahmud, M.B., 1997, "Centrifuge Modeling of an Innovative Rapidly Installed and Economical MSES for Marginally Stable Slopes" Ph.D. Dissertation, Rensselaer Polyt. Inst., Troy, NY, 240 p.
- Mitchell, J.K., and Zornberg, J.G., 1995, "Reinforced Soil Structures with Poorly Draining Backfills. Part II: Case Histories and Applications," *Geosynthetics International*, Vol. 2, no. 1, pp. 265-307.
- Perrier, H., Blivet, J.C., and Khay, M., 1986, "Stabilization de Talus par Renforcement tout Textile: Ouvrages Experimentel et Reel," *Proc. Third Intl. Conf. on Geotextiles*, Vol. 2, Vienna, pp. 313-318.
- Tatsuoka, F., Murata, O., Tateyama, M., Nakamura, K., Tamura, Y., Ling, H.I., Iwasaki, K., and Yamauchi, H., 1990, "Reinforcing Steep Clay Slopes with a Nonwoven Geotextile," *Performance of Reinforced Soil Structures*, Thomas Telford Ltd., pp. 141-146.
- Wayne, M.H., K.W. Petrasic, Wilcosky, E., and Rafter, T.J., 1996, "An Innovative Use of a Nonwoven Geotextile in the Restoration of Pennsylvania SR54," *Proc. Geofilters '96*, Montreal, pp. 513-521.
- Zornberg, J.G., and Mitchell, J.K., 1994, "Reinforced Soil Structures with Poorly Draining Backfills. Part I: Reinforcement Interactions and Functions," *Geosynthetics International*, Vol. 1, no. 2, pp. 103-148.
- Zornberg, J.G., Barrows, R.J., Christopher, B.R., and Wayne, M.H., 1995, "Construction and Instrumentation of a Highway Slope Reinforced with High Strength Geotextiles". *Proc. Geosynthetics '95*, Nashville, TN, Vol. 1, pp. 13-27.

Reinforcement of a Saudi Sabkha Soil Using Geotextiles

S.A. Aiban, O.S.B. Al-Amoudi, I. Ahmed, H.I. Al-Abdul Wahhab

Assistant Professor, Assistant Professor, Research Assistant and Associate Professor, respectively, Department of Civil Engineering, King Fahd University of Petroleum and Minerals, Dhahran, Saudi Arabia

ABSTRACT: Sabkha soils are well distributed over many parts of the world. Paved roads constructed on sabkha terrains often suffer different classes of damage due to the low load-carrying capacity of sabkha deposits, especially when becoming wet. This calls for the improvement of sabkhas prior to any construction. An experimental program was conducted to assess the performance of a problematic sabkha soil from eastern Saudi Arabia and to improve its strength using different techniques. In this paper, the effects of chemical additive type, dry density, moisture content and exposure conditions on the strength and deformation characteristics of the sabkha are presented. The results indicated that the sabkha had an acute water sensitivity depicted by a complete loss of strength when the samples were compacted at moisture contents other than the optimum value or when the sabkha was inundated with water. The results also showed that cement and lime had a marginal effect on the strength of this sabkha while geotextile significantly enhanced its load-bearing capacity.

KEYWORDS: Sabkha, Geotextile, Subgrade, Chemical stabilization, Water sensitivity.

1 INTRODUCTION

Sabkha is originally an Arabic expression to describe indefinitely saline flats that are underlain by sand, silt and clay, and often encrusted with salt. It is an equilibrium surface whose level is largely controlled by the prevailing climatic and hydrological conditions (Johnson et al. 1978). These soils are defined as the subaerial evaporite flats that border partially landlocked seas (called coastal sabkhas), or cover a number of continental depressions (called inland or continental sabkhas), both types usually form under hot and arid climates; and are associated with shallow groundwater tables (Al-Amoudi 1995).

Sabkha is widely distributed in the Arabian Peninsula, especially in the well-populated cities along the Arabian Gulf and Red Sea coasts (Al-Amoudi et al. 1992). Along the western and southwestern shores of the Arabian Gulf, these soils are generally viewed as unconsolidated, heterogeneous, layered or unlayered sediments, that are bathed in highly concentrated brines. Their outer surfaces are generally composed of hygroscopic salts which, when dampened, can render the normally stable surface crusts impassable. These characteristics make the sabkha susceptible to collapse upon flooding.

Sabkha soils are not confined to the Arabian Peninsula, but are well distributed over the globe with various nomenclatures, and often highly bewildering (Ellis 1973). Sabkha extends over many parts of the Middle East, including Egypt, Sudan, Libya, Tunisia,

Algeria and Ethiopia. Sabkha also exists in India, Australia, Southern Africa, Mexico as well as in California, Utah and Texas in the USA (Al-Amoudi et al. 1997).

1.1 Characteristics of Sabkha Soils

During the last two decades, with the upsurge in oil prices, the Arabian Gulf countries have gone through a spectacular phase of both industrialization and urbanization. Inevitably, some of this construction was located on sabkha flats and, therefore, several problems developed in road construction, such as cracking, ravelling, formation of huge potholes and rutting (Farwana and Majidzadeh 1988), despite the fact that the necessary precaution had been taken. A major contributory factor is the very low bearing capacity of the sabkha soil, which often leads to the formation of depressions and excessive differential settlement (Al-Amoudi et al. 1995). The surficial layers of sabkha deposits are well known for their generally low strength, with SPT N-values of 0 to 8, rarely exceeding 10. In addition, there are three other concerns when dealing with sabkha soils (Al-Amoudi et al. 1995). Firstly, the concentrated nature of sabkha brines, which is often four to six times that of a seawater from the same vicinity, can be drawn into the permeable layers of a construction (such as a road) by capillary action and can recrystallize therein, causing expansion and blistering at the surface. Secondly, the severe climatic conditions, under which

sabkha deposits usually develop, can contribute to the instability of the sabkha soil by phase alteration. Lastly, the mineral grains in the sabkha matrix are bonded together by cements that are somewhat water-soluble, such as halite, gypsum, anhydrite and/or aragonite, thus making the sabkha susceptible to collapse upon wetting.

These characteristics mean that sabkha soils do not comply with routine design requirements, as neither their bearing capacity nor compressibility meet normal constructional practices (Al-Amoudi 1994). Such a situation calls for the improvement of sabkha soil prior to any construction to avoid future problems. A recent search of the literature (Al-Amoudi 1995) indicates that many deep soil densification techniques (i.e. vibroflotation, vibroreplacement, dynamic compaction, etc.) have been implemented for large-scale constructions, with varying degrees of success. Chemical stabilization, using cement, lime and emulsion, did not bring a guaranteed improvement for all types of sabkha (Aiban et al. 1996). Geotextiles have also been used to stabilize sabkha soils in both preliminary laboratory studies and the field. Despite the reported success achieved through the use of geotextiles as a means of reinforcing the sabkha soil and/or drainage control, practicality and durability remain the critical factors (Al-Amoudi 1994). Presently, there is relatively meager information on the usage of geotextile for aggregate bases/subbases constructed over weak soils, such as sabkha. Such applications are of great potential to the construction industry in the Arabian Gulf and elsewhere.

This research program was initiated when lime and cement failed to stabilize a problematic "clayey" sabkha soil. Therefore, geotextiles were proposed to improve the load-bearing capacity of this sabkha. Accordingly, an experimental program was initiated to assess the performance of sabkha soil with and without geotextile. Although there are currently many parameters under investigation, the paper reports the effect of density, moisture content and exposure conditions (i.e. as-molded vs. soaked) on the strength and deformation characteristics of sabkha soils.

2 EXPERIMENTAL PROGRAM AND RESULTS

The sabkha sample was retrieved from the gigantic Ar-Riyas sabkha in eastern Saudi Arabia. The characteristics of this sabkha have been described in detail by Al-Amoudi et al. (1997) and Johnson et al. (1978). The soil was collected to embody all the layers up to the water table excluding the salt crust. After being transported to the laboratory, the soil was spread on plastic sheets for air drying and the lumped pieces were broken down using plastic hammers until all the

material passed ASTM # 4 sieve. The soil was thereafter thoroughly mixed, allowed to air dry and stored in plastic drums until testing.

2.1 Geomorphology of the Sabkha

The sabkha surface was observed to be covered by non-crystallized, pure halite layer 3 to 4 cm thick. A layer of brownish clay with anhydrite impurities was the second layer in succession and had a thickness of 2 to 3 cm. A band of anhydrite of about 6 to 7 cm thick was encountered followed thereafter by dark brown clay that had an apparent plasticity and contained some cubical crystals of clear halite (sodium chloride). Thereafter, a layer of halite cubes was encountered at a depth of 20 to 22 cm. The water table is shallow and was encountered at the top of the halite layer which is only 20 cm below the ground surface. Some air bubbles were observed after excavation, indicating the presence of artesian flow. The sabkha layering is shown in Figure 1.



Figure 1. Layering characteristics of the sabkha.

2.2 Sabkha Classification and Compaction

The USCS and AASHTO systems were used to classify the sabkha soil. In addition to water, the characterization tests were conducted using sabkha brine from the same vicinity. The grain-size distribution curves are shown in Figure 2. The plastic limit values

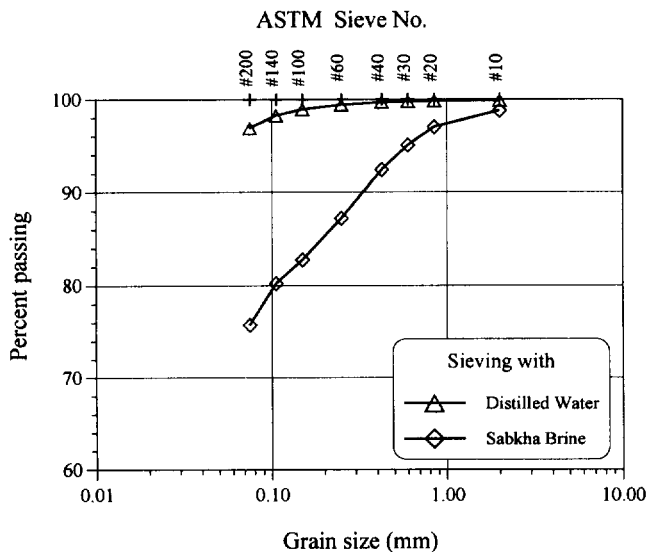


Figure 2. Grain-size distribution of the sabkha.

were 21% and 28% when distilled water and sabkha brine were used, respectively. The corresponding plasticity indices are 17.1% and 13.4%. Based on the sabkha brine results, the soil is classified as CL and A-6 according to the USCS and AASHTO systems, respectively.

The modified Proctor (i.e. compaction) test (ASTM D 1557) was used to determine the maximum dry density ($\gamma_{d \max}$) and optimum moisture content (w_{opt}). The California-bearing ratio (CBR) test (ASTM D 1833) was conducted for samples prepared at different moisture contents to assess the moisture sensitivity of the sabkha. The variation of the dry density and CBR values with the molding moisture content is shown in Figure 3. The CBR results clearly indicate the acute water sensitivity of the sabkha; the as-molded CBR value could reach 64 on the dry side of optimum while on the wet side of optimum, the CBR was as low as 3 only. In addition, the CBR at the w_{opt} was much lower than those at lower moisture contents. Furthermore, the soaked CBR did not exceed 2 regardless of the molding moisture content.

2.3 Chemical Stabilization

The CBR results in Figure 3 indicate a complete loss of strength when the samples were compacted on the wet side of optimum at a moisture content corresponding to 95% of the $\gamma_{d \max}$. The complete strength loss calls for stabilization of the sabkha prior to its usage. Different percentages of portland cement and lime were used to increase the strength of the sabkha and improve its water sensitivity, however, the improvements cannot be considered significant. The results in Figure 4 reveal

that only the addition of 10% cement can, at best, double the maximum unsoaked CBR value after 7 days of curing. These additions reduced the water sensitivity of the sabkha, but could not bring out significant improvements as compared with other sabkhas where an increase in the strength in excess of ten times has been reported (Aiban et al. 1996; Al-Amoudi et al. 1995). It was, therefore, decided to use geotextile to improve the bearing capacity of this sabkha.

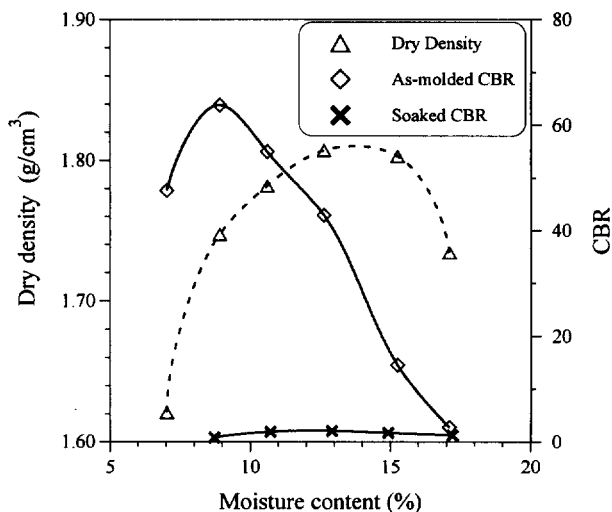


Figure 3. Variations of dry density and CBR values with molding moisture content for untreated sabkha.

2.4 Mold Fabrication

At present, relatively meager information has been developed concerning the use of geotextiles as reinforcement in aggregate bases or under foundations. This is particularly true when using weak and heterogeneous soils, such as sabkhas, as part of a pavement layer system. The only documented laboratory work on the use of geotextiles with sabkha soils is that of Abduljauwad et al. (1994). However, the mold used in their investigation was relatively small and had a diameter of only 320 mm. In this experimental program, a large-scale setup was fabricated at the University central workshop to conduct "representative" tests on sabkha soil reinforced with locally-produced geotextiles. The setup consists of a stainless steel mold having a diameter of 750 mm and a height of 350 mm with a wall thickness of 6.4 mm. The mold rests on a square stainless steel plate having the dimension of 1100 × 1100 mm and 16.5 mm in thickness. Stainless steel material was used in the setup because of the chemical aggressivity of the sabkha. To soak the samples, four

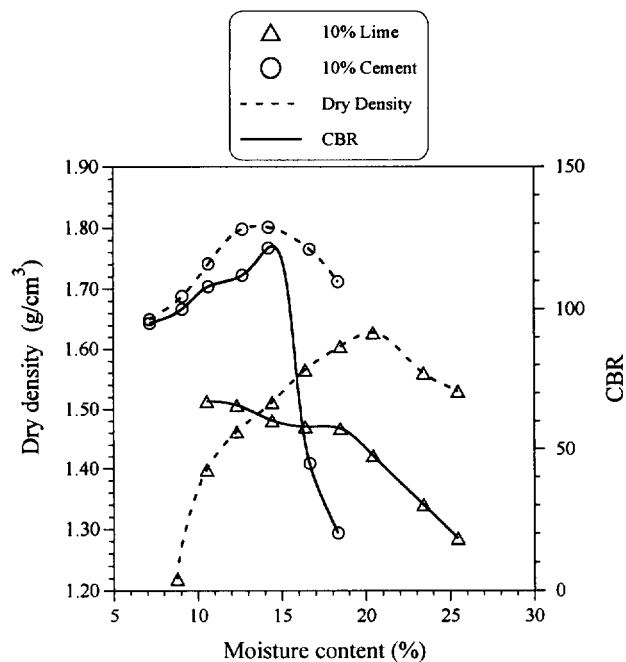


Figure 4. Variation of dry density and unsoaked CBR values with moisture content for sabkha samples treated with 10% cement or lime.

holes were made in the lower portion of the mold which were connected to the top reservoir containing the soaking fluid. The bottom reservoir was provided to maintain a constant water level when testing soaked samples. The setup is schematically shown in Figure 5.

2.5 Sample Preparation and Testing

The sabkha samples were prepared in the large-scale mold as follows (Figure 5): First, a 20 mm layer of coarse sand filter was laid in the mold, thereafter, a layer of geotextile was spread over the sand, which acted as a separator between the sand filter and sabkha matrix while allowing water to flow in an upward direction when the sabkha samples were soaked. The sabkha soil was mixed with the specific amount of water in a large mixer, then a known weight of soil was placed in the mold and compacted to the required dry density using the static compaction method by means of a large jack which acted against a strong reaction beam. The soil was compacted in three lifts of 70, 60 and 70 mm thicknesses. The reinforcing layer of geotextile was thereafter placed on top of the compacted sabkha soil followed by a 62.5 mm thick layer of fine (0.15 to 4.76 mm in size) steel slag aggregate, which was pluviated to its maximum density. The technical specifications of the geotextile are summarized in Table 1. The geotextile is a locally produced non-woven needle punched fabric manufactured from polyester fibers.

So far, all testings of the geotextile-reinforced sabkha were performed under static loading. A displacement control loading was applied using an electrical motor and the deformation rate was set at 1 mm/min. The load was applied on a stiff circular plate having a diameter of 125 mm and a thickness of 10 mm. The load was measured using a load cell while the deformation was measured using four LVDT's mounted on top of the loading plate.

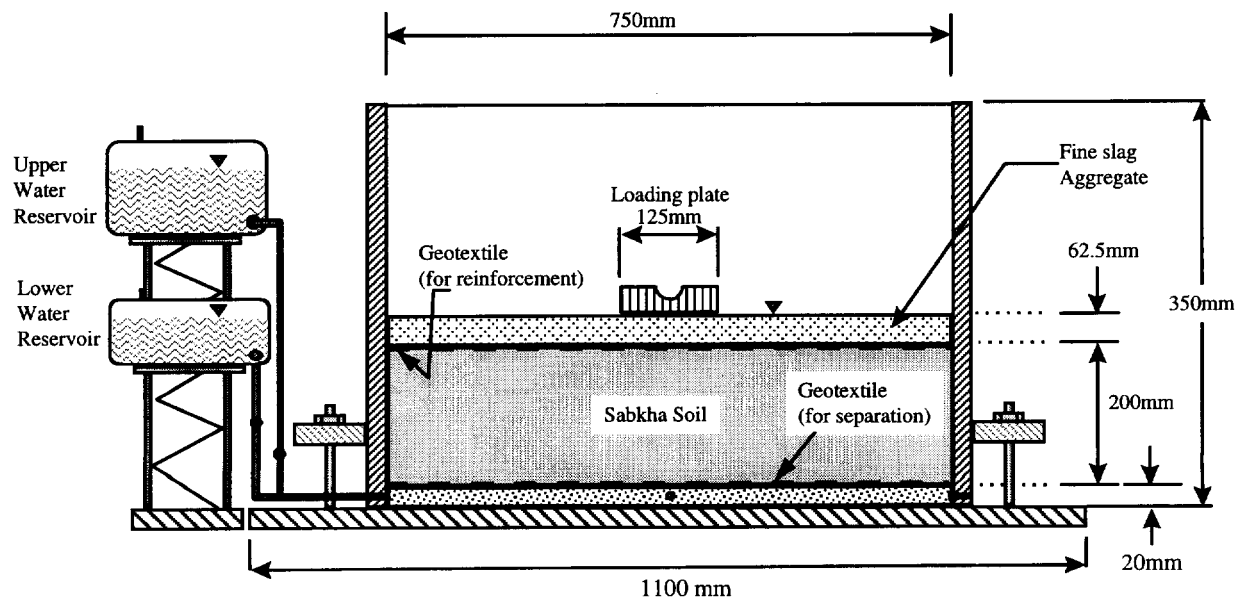


Figure 5. The experimental setup for the sabkha-geotextile system.

Table 1. Technical specifications of the geotextile used as reported by the manufacturer.

Property	Standard	Unit	ALYAF-400
Weight	ASTM D5261	gm/cm ²	400
Thickness under 2 kN/m ²	ASTM D5199	mm	4.5
Strip tensile strength (Longitudinal/transverse)	DIN 53857	N	925/1650
Grab tensile strength (Longitudinal/transverse)	ASTM D4632	N	1025/1525
Grab elongation (Longitudinal/transverse)	ASTM D4632	%	>80/>80
Cone penetration	BS 6906-6	mm	8.5
Permeability, k	BTTG, UK	cm/s	0.14

The loading plate was selected to be circular for many reasons including: (1) to simulate tire imprints which can be assumed circular for the majority of problems (Yoder and Witczak 1975), (2) to allow direct comparison with the California Bearing Ratio (CBR) results due to the relative similarities in the two systems since the CBR applies the load through a circular piston, and finally (3) to enable future theoretical simulations using both numerical procedures and analytical calculations due to the existence of similar solutions for axisymmetric problems.

The loading plate was chosen to have a diameter of 125 mm so that a clearance of 312 mm (five times the radius of the plate) from the sides of the mold can be maintained. This was intended to avoid any boundary interference from the sides of the mold. In addition, there will be enough distance from the end of the geotextile to provide anchorage of the geotextile and thus prevent failure due to pull out of the geotextile.

Figure 6 depicts the results for the specimens prepared at 90% and 95% of the maximum dry density ($\gamma_{d \max}$) on the dry side of optimum and tested under "soaked" conditions, with and without the geotextile reinforcing layer. The data therein indicates that the strength of the system increased significantly when a geotextile layer was introduced. The ultimate strength of the sample without geotextile layer was 68 and 76 kgf at a deformation of 30 mm for the samples prepared at 90 and 95% of $\gamma_{d \max}$, respectively. When a geotextile layer was incorporated in the system, the ultimate strength increased to 248 and 265 kgf for the same deformation. This corresponds to an improvement in the ultimate strength of 365% and 350% compared to that of the corresponding samples without any geotextile layer. With an average improvement of about 357%, the soil-geotextile systems successfully improved the strength of

the present sabkha soil more than the improvement attained using cement or lime at a dosage of 10% by weight of the dry soil.

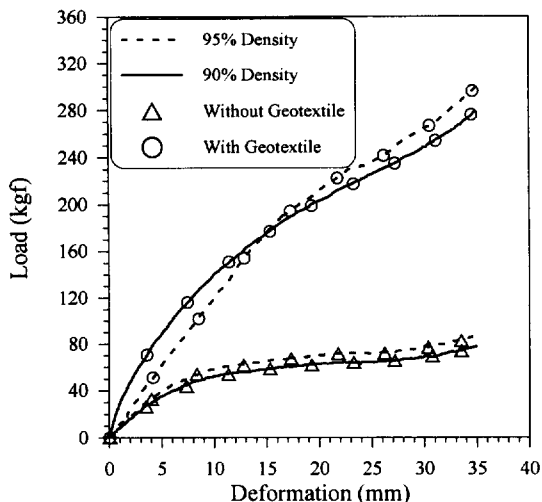


Figure 6. Load deformation curves for soaked sabkha soil with and without geotextile reinforcement.

It is worth mentioning that the two sets of load-deformation curves for the 90 and 95% relative compaction are almost identical regardless of the sabkha's initial density or moisture content. This is mainly ascribable to the fact that the strength of the sabkha is completely lost upon soaking and, thus, the soaked sabkha samples have the same strength. However, the reinforcing geotextile layer improves the load-carrying capacity of the sabkha significantly irrespective of its initial state. It is believed that the fine slag aggregate and some other factors have an effect on these results. It is the intention of the research team to vary the thickness of the fine slag aggregate and the geotextile (type and properties) and investigate their effects, in order to optimize the design of geotextile-sabkha systems.

3 CONCLUSIONS

This experimental program was conducted to compare the influence of chemical additives and geotextile on the load-carrying capacity of a clayey sabkha soil. The results clearly indicated the acute water sensitivity of the sabkha, as evidenced by the complete loss of strength when the samples were prepared at moisture contents other than the optimum value or when the sabkha was soaked. The results also demonstrated the fact that

chemical additives did not improve the strength significantly even when 10% cement or lime was added. However, the use of geotextile improved the load-carrying capacity of the sabkha up to four times that without geotextile. This was the case even for lower degrees of compaction such as 90% of $\gamma_{d \max}$. The utilization of problematic sabkha sites seems to be possible with the use of geotextile; a possibility where other stabilization techniques failed.

In addition, the future program will include testing of cement-treated sabkha samples using the 750 mm mold. This will allow a direct comparison between the effectiveness of the chemical stabilization and geotextile. The boundary conditions of the two sets will be identical except for the treatment procedures. It should be clear that the data presented in this paper does not directly compare the chemical stabilization and the improvement using geotextile, nevertheless, the results vividly demonstrated the poor response of sabkha to chemical stabilization. On the other hand, the data clearly indicates the significant improvement of the load-carrying capacity of the sabkha-geotextile system. Both the CBR and loading in the large 750 mm mold simulate a punching problem albeit with some variation in the boundary conditions.

ACKNOWLEDGMENTS

The authors acknowledge the support provided by King Fahd University of Petroleum and Minerals (KFUPM), and King Abdulaziz City for Science & Technology (KACST). Thanks are extended to Mr. Hassan Zakariya Saleh for his assistance.

REFERENCES

- Abduljawwad, S.N., Bayomy, F.M., Al-Shaikh, A.M. and Al-Amoudi, O.S.B. (1994) "Influence of Geotextiles on the Performance of 'Saline' Sebkhah Soils", *Journal of Geotechnical Engineering*, ASCE, Vol. 120, No. 11, pp. 1939-1960.
- Aiban, S.A., Al-Abdul Wahhab, H.I. and Al-Amoudi, O.S.B. (1996) *Identification, Evaluation and Improvement of Eastern Saudi Soils for Constructional Purposes*, Progress Report No. 4, KACST AR-14-61, Riyadh, Saudi Arabia.
- Al-Amoudi, O.S.B. (1994) "Chemical Stabilization of Sabkha Soils at High Moisture Contents", *Engineering Geology*, Vol. 36, Nos. 3/4, pp. 279-291.
- Al-Amoudi, O.S.B. (1995) "A Review of the Geotechnical and Construction Problems in Sabkha Environments and Methods of Treatment", *Arabian Journal for Science & Engineering*, Vol. 20, No. 3, pp. 405-432.
- Al-Amoudi, O.S.B., Abduljawwad, S.N., El-Naggar, Z.R. and Rasheeduzzafar (1992) "Response of Sabkha to Laboratory Tests: A Case Study", *Engineering Geology*, Vol. 33, No. 2, pp. 111-125.
- Al-Amoudi, O.S.B., Aiban, S.A. and Al-Abdul Wahhab, H.I. (1997) "Variability and Characteristics of Eastern Saudi Sabkha Soils", *XIV International Conference on Soil Mechanics and Foundation Engineering*, Balkema, Rotterdam, Netherlands, Vol. 1, pp. 17-20.
- Al-Amoudi, O.S.B., Asi, I.M. and El-Naggar, Z.R. (1995) "Stabilization of an Arid, Saline Soil Using Additives", *Quarterly Journal of Engineering Geology*, Vol. 28, No. 4, pp. 369-379.
- Ellis, G.I. (1973) "Arabian Salt-bearing Soil (Sabkha) as an Engineering Material", *TRRL Report LR 523*, Crowthorne, Berkshire, England.
- Farwana, T.A. and Majidzadeh, K. (1988) "An Investigation into the Use of Emulsified Asphalt in the Stabilization of Sandy Sabkha", *Proceedings, 3rd IRF Middle East Regional Meeting*, Riyadh, Saudi Arabia, Vol. 3, pp. 3.203-3.213.
- Johnson, H., Kamal, M.R., Pierson, G.O. and Ramsay, J.B. (1978) "Sabkhahs of Eastern Saudi Arabia", In S.S. Al-Sayari and J.G. Zlot (eds.), *Quaternary Period in Saudi Arabia*, Springer-Verlag, Berlin, pp. 84-93.
- Yoder, E.J. and Witczak, M.W. (1975) *Principles of Pavement Design*, 2nd ed., John Wiley & Sons Inc., New York.

Long-term Deformation of Reinforced Cohesive Soil Fills and Walls

M. Fukuoka

Dr., Public Works Research Center, Tokyo, Japan

ABSTRACT: This paper describes a method of estimating long-term deformation of geosynthetic reinforcing walls or embankments mainly due to percolation of rainwater. The triaxial compression test commonly used for obtaining coefficient of linear deformation and Poisson's ratio cannot be used for gravel-mixed soil or unsaturated soil which change soil constants by percolation of rainwater, under low level stresses and long-term loading tests. Moreover, uniform results are very difficult to obtain, because apparatuses differ from place to place and individual errors in tests are large. It is rather common to construct reinforced walls and embankments in front of original slope, a large unreinforced part is left. Deformation of the total structure is influenced by the deformation of the unreinforced part. Method of calculating deformation by use of coefficient of linear deformation is presented by utilizing an actual example. Finally, the behavior of the surface on the reinforced part, which gets high earth pressure by absorbing much rainwater, is analysed. Shear deformation in the reinforced part is presented.

KEYWORDS: Deformation, Testing, Walls, Soil deformation, Design.

1 INTRODUCTION

The author presented a paper titled "Well Documented Case Study of a Reinforced Soil Wall", at the 5th International Conference of the IGS in Singapore in 1994 with M. Itoh et al. (Itoh et al. 1992)

The backfill soil was a cohesive soil prevailing in the central region of Japan's mainland, and the reinforcement was a polyethylene geogrid widely used in Japan.

The purpose of this wall was to test applicability of cohesive soils for reinforcing soil structures. The wall was 7.5m high and has a front slope of 1 to 0.3. Geocomposite strips for drainage were inserted in the fill. After completion of the fill, the wet season followed for about 5 months. Total amount of rainfall was about 400mm, which is about 30 percent of the annual rainfall.

Vertical and horizontal deformations at the shoulder were 880mm and 374mm, respectively. Maximum pore water pressure in the fill was 20 kPa. It is clear that the cause of major deformation is due to the percolation of rainwater into the fill. Strain gages, extensometers, pore water pressure meters, earth pressure cells, settlement plates, horizontal displacement rods and deformation plates at the front wall were installed in the test wall. Material tests for both soil and geogrid were conducted in the laboratory. As no such well documented records like these were found, the author asked M. Itoh to translate the full report into English.

It was distributed to the members of the IGS, who came to the meeting room of the IS-Kyushu. The author hoped that this report be used for cooperative research work aiming for forecasting long-term behavior of reinforcing walls and embankments. The author has been studying this report from various angles of investigation. This paper describes in part the results of this studies as such.

2 BEHAVIOR OF FILL PART WITH NO REINFORCEMENT

Figure 1 is the reinforced part of the test wall with instrumentation layout. Table 1 is properties of geogrid. Figure 2 illustrates strain versus tension of the geogrid. Table 2 gives soil properties.

Figure 3 illustrates the section of the test wall including both reinforcing and non-reinforcing parts. The area ratio between reinforced and non-reinforced parts is $46\text{m}^2 : 85\text{m}^2 = 1:1.5$ from Fig.3.

The area of non-reinforced part is very much larger compared with that of reinforced part. Table 3 gives horizontal displacement of the wall face and the boundary plane between reinforced and non-reinforced parts. Horizontal elongation of the non-reinforced part is much larger than that of the reinforced part at the upper portion of the test wall. As stated above, the non-reinforced part of the fill is very important upon discussing displacement of reinforcing walls. But there were no monitoring systems here, because we were not aware of the importance. The author could not help but use case records which he gathered himself for the purpose of analyzing the behavior of this part. The non-reinforced part can be assumed as a backfill supported by a kind of retaining wall. Regarding the reinforced part of the wall as a common retaining wall, the unreinforced part is backfill. As the reinforced part is massive and heavy, it has enough power of retaining backfill. The face between the reinforced and unreinforced parts can be regarded as a front face of the backfill. The inclination of the face is 1:0.3. The author has about 50 well documented case records of earth pressure measurement, some of which are described in the references at the end of this paper. As the results of earth pressure measurements, wall height and inclination of the back side of the retaining wall are more important than other conditions like soil properties and method of compaction. Therefore, the author determines the earth pressure coefficient based on the case records. Some of the selected case records are described here. Finally, the earth pressure coefficient is decided as 0.3. The earth pressure measurement in the soil mass is terribly difficult. The author has several case records now, and is hoping that a chance will come in the near future. Figure 4 is a gravity concrete retaining wall. Three panel type earth pressure gages, 2m in width, were installed to the back of the wall. Figure 5 shows the earth pressure for 3 large concrete block retaining walls. Coefficients of earth pressure K are described for comparison. Distribution of earth pressure is not triangular. The panel type earth pressure gages are installed not only on the back face of the retaining wall but also on the slope behind the backfill as shown in Fig.6. Precision of the measurement can be checked by using those gages surrounding the backfill. Coefficient of earth pressure is as low as 0.15, which is due to the thickness of the backfill and low energy of compaction. A small-scale laboratory model test was conducted in order to study the effect of backfill width. Sketch of the backfill and test results are given in Fig. 7. The horizontal axis is the coefficient of

earth pressure and vertical axis is the ratio between thickness and height of the backfill (B/H). Inclination of the back face of the retaining wall is 1:0.5. The coefficient of earth pressure decreases remarkably in accordance with the decrease of the B/H, and becomes nearly equal to the final value of the coefficient of earth pressure with the increase of the B/H larger than 0.5. Figure 8 illustrates the external forces acting on the boundaries of the non-reinforced part. The weight of the non-reinforced part is 1.463 MN/m. The earth pressure on the boundary between reinforced and non-reinforced parts is 179 kN/m, assuming the coefficient of earth pressure is 0.3. Reaction from the original ground surface is calculated by the force polygon in the figure. Normal and tangential components of the reaction and mobilized angle of friction are obtained as shown in the figure. Using

cohesion $c=48$ kPa and friction angle $\phi=25^\circ$ from the triaxial compression test, safety factor against sliding is computed. The factor of safety is 6.2. As a matter of fact, such soil constants are too large. Even when considering these conditions, such high factor of safety sufficiently verifies that no sliding, deformation shall be caused. Factor of safety against sliding increases with coefficients of earth pressure higher than 0.3. The factor of safety against sliding decreases with lower coefficient of earth pressure, but this part is absolutely safe. Because the inclination of the original ground surface is gentle. If the inclination is 45° , the situation changes entirely. The non-reinforced part moves out horizontally toward the surface of the wall as the fill settles. There is a case example showing such a phenomenon. Distribution of normal and shear stresses along the original ground

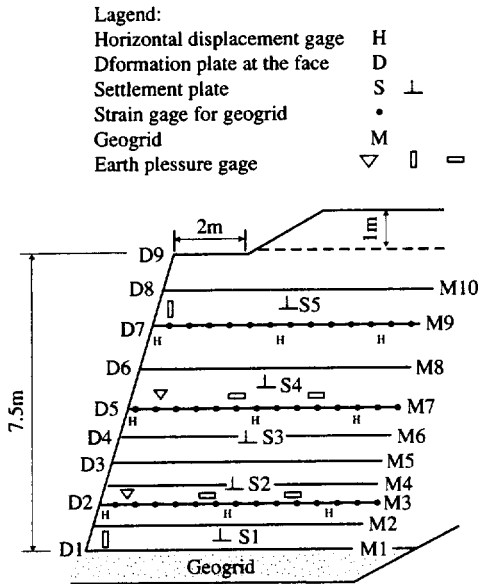


Figure 1 Instrumentation layout.

Table 1 Geogrid properties

Opening dimensions:	110x22mm
Tension at failure:	78kN/m
Elongation at maximum strength:	17%
Material:	Polyethylene

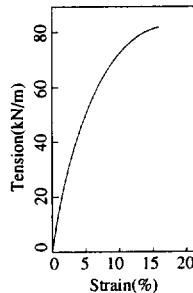


Figure 2 Strain versus tension for geogrid

Table 2 Soil properties

Grain size:	sand 23.3%, silt 53.3%, clay 23.4%
Natural water content:	$w_n = 25.0\%$
Liquid limit:	$w_l = 54.6\%$
Plastic limit:	$w_p = 26.8\%$
Maximum dry density:	$\rho_{dmax} = 1.48 \text{ Mg/m}^3$
Optimum water content:	$w_{opt} = 26.4\%$
Angle of internal friction:	$\phi = 20.6^\circ$
Cohesion:	$c = 42.2 \text{ kPa}$

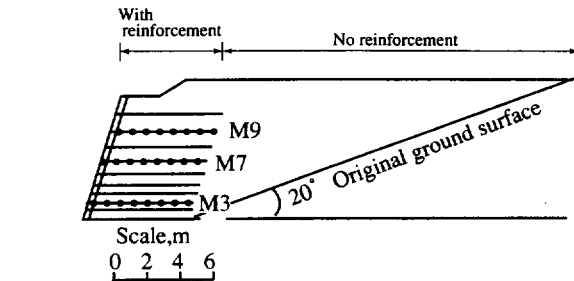


Figure 3 Cross section of the test wall.

Table 3. Horizontal displacement of the wall face, boundary between reinforced and unreinforced parts, and elongation of reinforced part.

Position	May 8			October 7		
	M9	M7	M3	M9	M7	M2
Wall face	23	33	20	242	160	62
Boundary, reinforced & non-reinforced	15	16	4	154	73	17
Elongation of reinforced part parts	8	17	16	88	87	45

Notes: May 8 is date of end of construction.

October 7 is date of end of measurement.

M9, M7, M2 are reinforcing mats in Fig. 3.

Unit:mm

How to read: The wall face at M3 level moved 23mm during construction. It was moving through the rainy season, and finally the amount of movement reached 242mm. Movement of the boundary of reinforced and non-reinforced parts are 15mm (May 8) and 154mm (October 7). Accordingly, elongation of the reinforced part is 23-15=8mm (May 8) and 62-17=45mm (October 7).

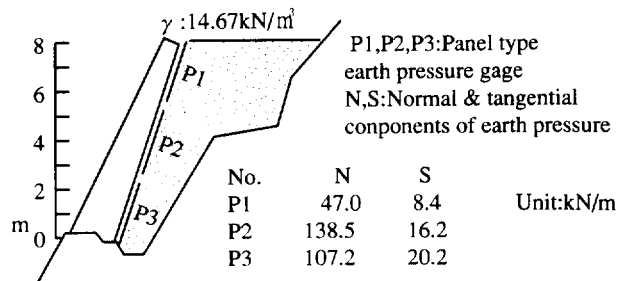


Figure 4 Concrete gravity wall.

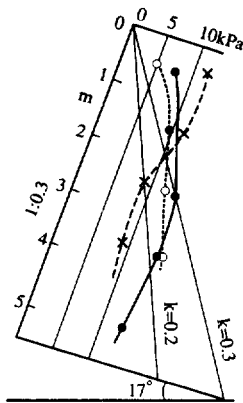


Figure 5 Normal component of earth pressure against large concrete block walls.

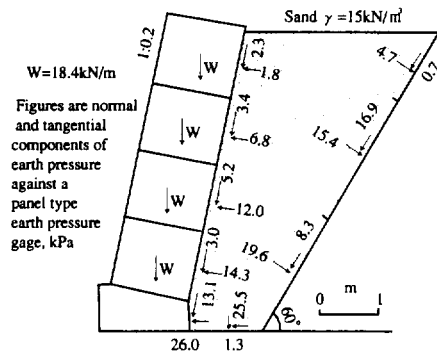


Figure 6 Large concrete block retaining wall.

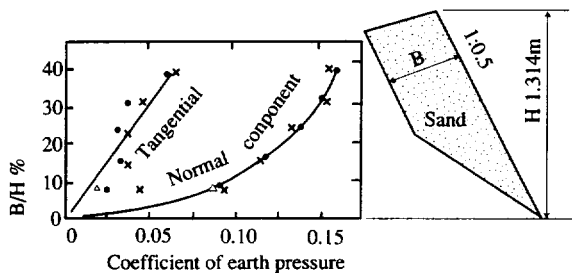


Figure 7 Relationship between thickness of backfill and earth pressure.

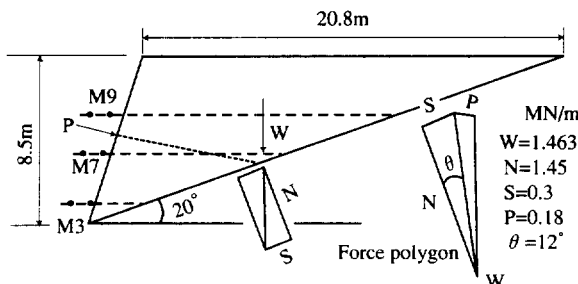


Figure 8 Unreinforced part of the test wall. Method of analyzing earth pressure on the front wall and the back slope of the backfill.

surface is not uniform or triangular as shown in Fig. 6. Maximum shear stress is about 2 times larger than the average value for this case. Therefore, it is necessary to maintain a higher factor of safety to prevent sliding movement. Figure 8 illustrates positions of mats M3, M7 and M9. Records of horizontal displacement gages are indicated in Table 3. Displacement of the surface between the reinforcing and non-reinforcing can be inferred by this table. The lengths of the dotted lines in the figure are widths of the non-reinforced part. They are 2.4, 8.2, 12.9 m respectively. Assuming the strains are uniform along those lines, those strains are calculated as shown in Table 4. Comparing these values with strains at the tail ends of the mats measured by strain gages, quite a neat coincidence was recognized. Vertical settlements were measured by the settlement plates. The variation of those thicknesses between two settlement plates are obtained. These variations are calculated in the form of strain and described in Table 4.

Table 4. Variation of vertical and horizontal deformation in the form of strain.

Position	Horizontal strain			Vertical strain		
	~5/8	~10/7	5/8~10/7	~5/8	~10/8	5/8~10/7
M9	0.108	1.19	1.09	S4~S5	0.75	8.80
M7	0.182	0.89	0.71	S3~S4	0.87	5.92
M3	0.167	0.71	0.54	S2~S3	0.46	16.36
				S1~S2	0.42	12.48
(Position)				(Layer)		

As the forces on the boundary and weight of the backfill are obtained, stress distribution is obtained by trial and error method. This rough method of calculation may be sufficient at this stage.

According to the author's case records, earth pressure does not change so much, if the retaining wall moves forward after the completion of it.

Therefore, only horizontal strain in taking into account and the changes of m and E are back-calculated using equations (1) and (2).

$$\epsilon_h = \frac{\sigma_h}{E} - \frac{1}{mE} \left\{ (\sigma_h + \sigma_v) \frac{1}{m} + \sigma_v \right\} \dots \dots \dots (1)$$

$$\epsilon_v = \frac{\sigma_v}{E} - \frac{1}{mE} \left\{ (\sigma_h + \sigma_v) \frac{1}{m} + \sigma_h \right\} \dots \dots \dots (2)$$

The results are described in Table 5. m-values are ranging between 3.08~3.98, E-values between 0.45~7.30 MPa. E-values before May 8 which had ranged between 2.46~7.30 MPa, decreased to 0.49~1.30 MPa at the end of the test on October 7. The reduction caused a drop by 1/10 of original values.

We can realize how the increase of moisture content has a large effect on soil constants. The wide variety of m and E values are mainly due to the non-uniformity of soil kinds and distribution of moisture content.

Table 5. Coefficient of linear deformation E and Poisson's ratio 1/m in the non-reinforcing part.

Period	~5/8			~10/7			5/8~10/7		
	M9	M7	M3	M9	M7	M3	M9	M7	M3
E:MPa	5.25	7.30	2.46	0.45	1.10	0.83	0.49	1.30	1.25
m	3.35	3.08	3.98	3.39	3.32	3.85	3.39	3.37	3.79

There are a lot of monitoring systems set up in the reinforced part of the wall. Twelve conventional earth pressure gages were installed. No. 1 and 12 measure horizontal earth pressure or stress. No. 2, 3, 4 and No. 7, 8, 9 measure two-dimensional earth pressure, namely, horizontal, vertical and shear stresses. No. 5, 6, 10 and 11 measure only vertical stress. These were located behind the wall face. The other 8 gages were located 1.5m behind the wall face. Table 6 describes earth pressure and horizontal strain 1.5m behind the wall face.

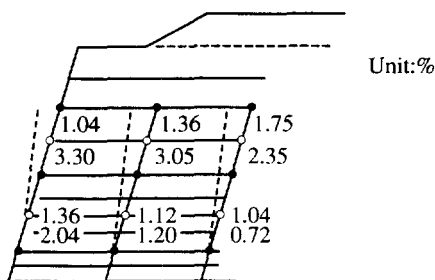
Table 6. Earth pressure near the front face of the wall.

NO.		5/8	5/16	6/20	7/1	10/20
12	σ_h	2.2	1.4	4.4	5.2	5.1
7,8,9	σ_v	45.6	67.0	77.5	37.7	40.5
	σ_h	11.1	9.9	5.5	37.7	34.3
	τ	+5.2	+5.35	-2.30	-22.7	+2.30
	ϵ_h	0.465	0.800	0.891	0.710	1.302
2,3,4	σ_v	79.1	112.7	116.0	37.7	74.4
	σ_h	21.8	30.6	14.6	2.2	1.7
	τ	-5.45	-5.35	-16.1	-7.85	-6.7
	ϵ_h	0.477	1.043	1.017	1.106	1.507

Note: σ_v, σ_h, τ : kPa ; ϵ_h : %
 12→Earth pressure cell which is between D7 and D8,
 7,8,9→earth pressure cells which are between D5 and D6, and
 2,3,4→earth pressure cells which are between D2 and D3 in Fig.1.
 + and - signs of shear stress and counter clockwise and clockwise directions, respectively.
 Rainy season : 5/16~7/1

Looking at the table, earth pressure changes in wide range with the lapse of time. The strain along the reinforcements are elongated in accordance with the horizontal deformation of the soil. As this soil is not elastic, this elongation is never recovered. Vertical stress σ_v and ϵ_h rapidly increase with the start of rainy season. Horizontal stress σ_h of No. 7, 8 and 9 increases gradually with time. Horizontal stress of No. 2, 3 and 4 is large in rainy season. Shear stress is low, and sometimes changes their sign from plus to minus. Shear stress for No. 2, 3 and 4 is high in rainy season.

This paper deals with shear deformation of the fill by use of data from horizontal displacement gages. Figure 9 illustrates distribution of shear strain. Upper figures indicate the shear strains between May 8 and June 20, which is the first part of rainy season, and the lower figures are that between June 20 to October 7, which is the main part of rainy season with much rain. Shear strain in the main part of rainy season is larger than that of the first part.



Legend: ○ : Points measured
 Upper figure : shear strain before rainy season, | between two points
 Lower figure : shear strain during rainy season, | marked with ●

Figure 9 Distribution of shear strain, at points marked with ○

1. A large deformation occurred by percolation of rain water, when a geogrid reinforced test wall with cohesive soil backfill was exposed to the wet season. Deformation of the wall is caused by reduction of soil constants with increase of moisture content. The deformation of soil is irreversible, and the elongated reinforcement caused by the soil deformation is left intact. Therefore, a method of soil test for measuring soil constants is needed. It is important to use a simple laboratory test with no individual errors.

2. There are many cases where the triangular unreinforced part comes behind the reinforced part. Effect of deformation on this part is large to estimate total deformation of the wall. Method of estimating such deformation by use of coefficient of linear deformation and Poisson's ratio is described.

3. Front face of a reinforced soil wall was exposed to percolation of rainwater causing marked change in earth pressure.

This then caused major deformation, whereupon colossal permanent deformation is caused in reinforcing material. Decrease of soil constants may also induce this phenomenon and increase strain in the reinforcement.

4. Shear strain in the reinforced part of the test wall increased with amount of percolated rain.

ACKNOWLEDGMENTS

The author would like to thank M. Itoh of Maeda Corporation for providing us with the report of Toyoshina test wall.

REFERENCES

Fukuoka, M., Akatsu, T., Katagiri, S., Iseda, T., Shimazu, A., Nakagaki, M. (1981) Earth Pressure Measurements on Retaining Walls, Case History Volume, 9th International Conference on Soil Mechanics and Foundation Engineering, Tokyo, pp. 237-296.
 Fukuoka, M. (1984) Earth Pressure on Retaining Walls and Buried Pipes, International Conference on Case Histories in Geotechnical Engineering, St. Louis, Vol. 1, pp. 351-362.
 Fukuoka, M., Tani, S., Ihara, S., Ishizaki, H., Takano, G. (1990) Stability of Retaining Wall Reinforced by Continuous Fiber During Earthquakes, Proc., 4th International Conference on Geotextiles, Geomembranes and Related Products, the Hague, Vol. 1, pp. 27-32.
 Fukuoka, M., Okedoi, K., Ozaki, K., Nakayama, K., Ihara, S. (1992) Stability of Fiber Reinforced Sand Retaining Walls, Proc., 2nd International Conference on Recent Advances in Geotechnical and Soil Dynamics, St. Louis, Vol. 1, pp. 643-648.
 Fukuoka, M. (1994) Friction at Upper and Lower Faces and Tension in Reinforcing Sheets, Proc. on Geotextiles, Geomembranes and Related Products, Singapore, pp. 243-246.
 Itoh, M., Shirasawa, M., Itoh, A., Kumagai, K., Fukuoka, M. (1994) Well Documented Case Study of a Reinforced Soil Wall, Proc. on Geotextiles, Geomembranes and Related Products, Singapore, pp. 255-258.

Development Of Woven Geotextiles For Reinforcing Cohesive Soil Filled Slopes - A New Approach

S. Anbahan Ariadurai

Research Student, Department of Textiles, UMIST, Manchester, United Kingdom

Ian L. Whyte

Senior Lecturer, Department of Civil and Structural Engineering, UMIST, Manchester, United Kingdom

Prasad Potluri

Lecturer, Department of Textiles, UMIST, Manchester, United Kingdom

ABSTRACT: Reinforced ground structures using cohesive soils are difficult to design due to problems relating to consolidation and poor internal drainage. Due to these inherent drawbacks cohesive soils are seldom used as fill materials in reinforced embankments. However, when a geotextile with good filtration and drainage properties is used as a reinforcement, cohesive soils could be successfully used as back-fills in steep embankments. There are few instances of needle-punched nonwoven fabrics, possessing superior hydraulic conductivity, have been used as reinforcements in embankments with back fills of cohesive soil. Non-woven textiles, however, are inferior in tensile properties when compared with the woven textiles. In reinforcement applications, the primary quality required of the fabric is superior tensile properties. Woven geotextiles, which have the required tensile properties, have not been tried as reinforcement for cohesive soils because of their poor transmissivity. Owing to this draw back in woven geotextiles the amount of research done on the transmissivity of woven geotextiles is minimal. By designing novel and innovative woven fabric structures it is possible to increase the transmissivity of the woven geotextiles without sacrificing the tensile properties. This paper presents a new approach that enables woven geotextiles to be designed with superior tensile properties and adequate transmissivity for use as reinforcement in cohesive soil filled earth structures. A theoretical model, derived from the first principles, which predicts the transmissivity values of woven geotextiles is discussed. Laboratory results from tests conducted on some woven geotextiles substantiate the theoretical models and the data is presented.

Keywords - Geotextiles, Woven Fabrics, Reinforcement, Transmissivity, Tensile Strength

1 INTRODUCTION

In recent years, use of geosynthetics has become accepted as a technically sound and cost-effective solution in solving many geotechnical and environmental problems. In the construction of reinforced earth filled embankments, when the in-situ soil is not suitable as a fill - cohesive soils such as clay, it is usual to fill the structure with a suitable imported granular material. With ever increasing cost in material handling, use of readily available materials from the site is one of the best cost-effective options available. However, use of cohesive soils as back-fill in steep embankments has gained little acceptance due to their inherent low permeability and excess pore water pressures. Therefore, if geotextiles of adequate draining capacity and tensile characteristics are developed and used with the in-site cohesive materials considerable savings can be achieved.

A few case histories of test embankments with cohesive soil back fills employing needle-punched nonwoven fabrics are reported (Tatsuoka et al. 1986, Ling et al., 1993). Further, when the motorway M25, between Junctions 15 and 16 on the west side of London in the UK, was widened, the embankment was reinforced with a combination of a geogrid and a nonwoven geotextile (Leiper, 1995). The soil

in this case was recompacted London Clay. Fabian (1990) too has successfully used needle-punched nonwoven geotextiles to reinforce test embankments built with cohesive fills. However, there are no reports of woven geotextiles being attempted as reinforcement for cohesive soils. The main limitation of the currently available woven geotextiles is their poor drainage capabilities. According to the United Kingdom's Department of Transport requirements, the design life for steep slopes is not less than 60 years if the slope is regarded as an earthwork or 120 years if the slope is regarded as a structure (Ingold 1994). Strength and creep are vital properties to provide such a long life; woven fabrics are capable of providing these properties better than nonwovens or any other fabric type. Thus, if the draining capacity of woven geotextiles is considerably improved, they would become the most suitable geotextile material to reinforce a cohesive soil-filled structure.

In order to design woven geotextiles which have the capacity to drain the estimated quantity of water a suitable theoretical model is required. This paper presents a geometrical model which can estimate the transmissivity of woven fabrics. The model, which is validated by laboratory results, is then used to engineer novel woven fabric structures which give improved transmissivity.

2 ESTIMATES OF REQUIRED DRAINAGE

A clay reinforced slope can act as a frictional fill in terms of the effective critical state angle of shearing resistance, provided any excess pore water pressures are rapidly dissipated. The required drainage is a function of the soil consolidation properties, geometry of the reinforcement layers and excess pore water pressures generated by construction. An estimate of the drainage is made using the following assumptions: the clay is fully saturated, with permeability $k = 10^{-8}$ m/s, and compressibility $M_V = 0.25$ m²/MN, subjected to a total normal stress increase $\Delta\sigma = 200$ kN/m² (equivalent to a basal layer in a 10 m high fill) with geotextile reinforcement drains at a relatively wide spacing of 0.5 m and of length 7.5 m. The clay layer between the reinforcement is assumed to be in one dimensional consolidation, with the excess pore water pressure isochrones modelled as a parabolic function. The rate of discharge from the clay is given by the hydraulic gradient (slope of the isochrone) at the clay surface.

At any time 't' the total volume of water expelled from the clay is equal to the settlement volume at that time:

$$V = 2 d L_{GT} b_{GT} R M_V \Delta\sigma \quad (1)$$

at time:

$$t = \frac{T_V d^2}{c_V} \quad (2)$$

where, d = maximum drainage distance, L_{GT} = length of the geotextile, b_{GT} = width of the geotextile, R = average degree of consolidation, M_V = coefficient of volume compressibility, $\Delta\sigma$ = total stress increment, T_V = time factor and c_V = coefficient of consolidation.

For the assumed values, the total volume of water discharged per metre width by consolidation is 0.1875 m³. Hence, 90% consolidation (0.169 m³ water) takes 3.7 hours.

The rate of discharge per square metre from the clay fill (above and below the geotextile layer) is given by

$$Q = \frac{4 k \Delta\sigma}{\gamma_w \sqrt{12 c_V t}} \text{ for } T_V < \frac{1}{12} \quad (3)$$

where, Q = rate of discharge and γ_w = unit weight of water. From equation (3), the rate of discharge of water from the soil when the isochrone reaches the centre of the clay layer can be calculated to be less than 10⁻⁷ m³/s/m², this occurs approximately one hour after the assumed instant load application. Clays typically have permeability of 10⁻⁷ m/s or less, often about 10⁻⁹ m/s, and if permeable layers with permeability of 10⁻⁴ m/s, or greater, are incorporated, then these will act as effective drains.

The computations involved for calculating the required transmissivity for the geotextiles are lengthy and complex (Giroud, 1981). However, one dimensional consolidation theory provides an indication as to the efficiency of these drains. Accordingly, geotextiles placed at small vertical spacing (0.5 m or less), can rapidly consolidate the clay and dissipate excess pore water pressures. The total volume of water is relatively small and the discharge rate diminishes rapidly with time.

3 THEORIES OF FLUID FLOW

Predicting the fluid flow through textile materials has largely been studied with the help of the general theories of fluid flow through porous media. In all of these theories, the fluid flow is given as a function of the total pore space available in the fabric mass and the specific area. However, as the structure of woven fabrics are very different from other porous media, with two distinct drainage paths - within the yarns and between the yarns - a need for a specific theoretical model for woven fabrics was realised.

As a result, a theoretical model which predicts the in-plane fluid flow in woven geotextiles is developed from first principles. This model is found to predict the flow of water in woven fabrics more accurately than the available general models for flow through porous media.

The Poiseuille equation for the average laminar flow velocity through straight parallel capillary tubes of constant circular cross-section is,

$$V = \frac{R_h^2 \Delta p}{8\mu L} \quad (4)$$

and hence

$$Q = \frac{R_h^2 \Delta p}{8\mu L} A \quad (5)$$

where, V is the velocity of the fluid, Δp the pressure difference, μ the viscosity of the fluid, L the length of the drainage medium, A the area of cross-section and R_h the hydraulic radius.

When the Poiseuille's equation is extended to non-circular channels it becomes,

$$Q = \frac{R_h^2 \Delta p}{k \mu L} A' \quad (6)$$

where, A' area of the pore space in the channels and k shape constant which depends on the shape of the channel. However, the cross-sectional area of the pores in the channels is $A\varepsilon$, where, ε is the porosity. Therefore, equation (6) can be written as,

$$Q = \frac{R_h^2 \Delta p}{k \mu L} A \epsilon \quad (7)$$

Thus, if the hydraulic radius R_h of the woven fabric is estimated, from equation (7), the rate of discharge can be calculated.

The hydraulic radius is defined as,

$$R_h = \frac{\text{cross sectional area of the pore}}{\text{wetted perimeter}} \quad (8)$$

When the flow of fluid through a woven fabric is considered, it is clear that there exist pores between the yarns and within the yarns. As the structural parameters of the two porous media are different, it is prudent to treat the two separately. The overall coefficient of in-plane permeability is then obtained by combining the two.

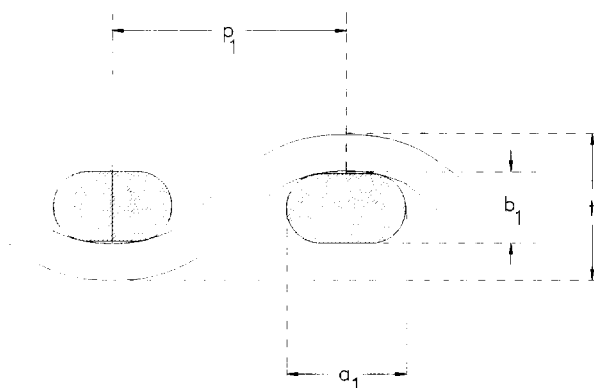


Figure 1. Cross-section of two consecutive yarns in an intersection unit

Figure 1 shows a cross-section of two consecutive yarns of a woven fabric in a plane containing the axis of an intersecting weft yarn. The yarns are considered to have the Kemp's race track sectional geometry (Kemp, 1958). If the major diameter of the warp and weft yarns are ' a_1 ' and ' a_2 ' respectively, and the minor diameter of the warp and weft yarns are ' b_1 ' and ' b_2 ' respectively and the distance between the centre of two adjacent warp yarns is ' p_1 ', we have,

$$\text{total cross-sectional area between two consecutive yarns} = t \times p_1$$

where, t is the thickness of the fabric.

However, the area of solid in the cross-section =
area of the warp yarn + area of the weft yarn.

$$\text{Area of the warp yarn} = \frac{\pi b_1^2}{4} + b_1(a_1 - b_1) \quad (9)$$

$$\text{Area of the weft yarn} = l_2 b_2 \quad (10)$$

where, l_2 is the length of weft yarn between the planes

containing the axes of consecutive warp yarns.

$$\text{However,} \quad l_2 = p_1(1 + c_2) \quad (11)$$

where, c_2 is the crimp in the weft yarn. Therefore,

$$\text{Area of the weft yarn} = b_2 p_1(1 + c_2) \quad (12)$$

Hence, Total area of solid

$$= \left\{ \left[\frac{\pi b_1^2}{4} + b_1(a_1 - b_1) \right] + [b_2 \cdot p_1(1 + c_2)] \right\} \quad (13)$$

Therefore, Area of void between the yarns

$$= t p_1 - \left\{ \left[\frac{\pi b_1^2}{4} + b_1(a_1 - b_1) \right] + [b_2 p_1(1 + c_2)] \right\} \quad (14)$$

$$\text{Wetted perimeter of the pore} = 2p_1 + \pi b_1 + 2 l_2' \quad (15)$$

where, l_2' is the length of yarn in the partial geometry of the Kemp's race track section. Further,

$$l_2' = l_2 - (a_1 - b_1) \quad (16)$$

Therefore, wetted perimeter of the pore

$$= 2p_1 + \pi b_1 + 2[p_1(1 + c_2) - (a_1 - b_1)] \quad (17)$$

Substituting (14) and (17) in (8) we get,

$$R_h = \frac{t p_1 - \left\{ \left[\frac{\pi b_1^2}{4} + b_1(a_1 - b_1) \right] + [b_2 p_1(1 + c_2)] \right\}}{2p_1 + \pi b_1 + 2[p_1(1 + c_2) - (a_1 - b_1)]} \quad (18)$$

A similar treatment is done to find the rate of discharge within the yarns. Considering circular cross-sectional filaments, if the diameter of a single filament in a multi-filament yarn of race track geometrical shape is d_f , the hydraulic radius for the flow within the yarn is derived.

The porosity of the yarn,

$$\epsilon_y = 1 - \frac{\text{Volume of filament yarns}}{\text{Total volume of yarn}}$$

Considering racetrack geometry and unit length,

$$\text{Total volume of warp yarn} = \left[\frac{\pi b_1^2}{4} + b_1(a_1 - b_1) \right]$$

Considering circular filaments,

$$\text{Volume of filaments in warp yarn} = \frac{\pi d_f^2}{4} n_f$$

where n_f is the number of filaments in the yarn.

Therefore, porosity in yarn

$$\epsilon_y = \left[1 - \frac{\left[\frac{\pi b_1^2}{4} + b_1 (a_1 - b_1) \right]}{\left(\frac{\pi d_f^2}{4} n_f \right)} \right] \quad (19)$$

The total cross sectional area of the yarn, considering the race track sectional geometry,

$$= \left[\frac{\pi b_1^2}{4} + b_1 (a_1 - b_1) \right] \quad (20)$$

Then the cross-sectional area of the pore

$$= \left[\frac{\pi b_1^2}{4} + b_1 (a_1 - b_1) \right] \epsilon_y \quad (21)$$

$$\text{total wetted perimeter} = \pi d_f n_f \quad (22)$$

where, n_f is the number of filaments in the yarn.

Therefore,

$$R_h = \frac{\left[\frac{\pi b_1^2}{4} + b_1 (a_1 - b_1) \right] \epsilon_y}{\pi d_f n_f} \quad (23)$$

If the geometrical parameters of the fabric and the yarn are known, the hydraulic radius of the inter-yarn and the intra-yarn porous media can be calculated using equations (18) and (23) respectively. Thus, the rate of discharge between the yarns and within the yarns can be calculated using equation (7) if the appropriate shape constants and the porosity values are known. It is assumed that the shape of the pore within the yarns is of an equilateral triangle and in-between the yarns a rectangular triangle. Therefore, the respective shape constants are 1.67 and 1.63 (Munson et al, 1990). Once the rate of discharge is known the coefficient of in-plane permeability and subsequently the transmissivity of the fabric can be estimated using the equations (24) and (25).

$$\theta = \frac{Q L}{W H} \quad (24)$$

where, θ = hydraulic transmissivity, W = width of the specimen, H = difference in total head across the specimen and L = length of the specimen.

$$k_p = \frac{\theta}{t} \quad (25)$$

where, k_p = coefficient of in-plane permeability and t = thickness of the geotextile.

In Figures 2 and 3, results obtained by the developed theoretical model, indicated by the name UMIST, and other general models are compared with the laboratory results obtained at various normal stress levels. The hydraulic transmissivity testing was performed in accordance with ASTM D 4716 - 87 (ASTM, 1987). The distinctive advantage of this model is its capability to predict the flow in any composite structure which has a number of drainage paths. Fabric C1 is commercially available and M2 is a fabric made in the laboratories of the Department of Textiles of UMIST. Two other fabrics, M1 and M3, made in the laboratory and a second commercial fabric C2 were also tested for their transmissivity. In Table 2 is given the specifications of all the five fabrics tested.

Table 2. Specifications of the fabrics tested.

Fabr	Weave	Fabric sett		Yarn count		Area density (g/m ²)	Thickn-ess ** (mm)
		ends /cm	picks /cm	warp (tex)	weft (tex)		
M1	Plain	4.6	3.33	2200	220	1202	1.70
M2	Matt	4.25	4.27	2200	220	1160	1.66
M3	* Double	4.72	2.36	2200	220	2139	3.60
C1	Twill	4.00	5.14	337	330	297	0.93
C2	Plain	5.91	9.84	228	108	224	0.83

* The count, and the sett correspond to both face and back fabrics individually. ** Thickness at 2 kN/m² stress level.

4 A NOVEL WOVEN FABRIC

A novel woven fabric which incorporates porous tubes in its structure is designed to enhance the drainage property of the woven geotextile without sacrificing its tensile properties. In this fabric two sets of fabrics are woven on top of one another with a tubular structure, into which the porous tubes are inter woven. The whole composite fabric is woven on a shuttle loom. The laboratory transmissivity results obtained are presented in Figure 4 along with the results obtained for fabrics M1, M2 and M3 developed at the laboratory of UMIST.

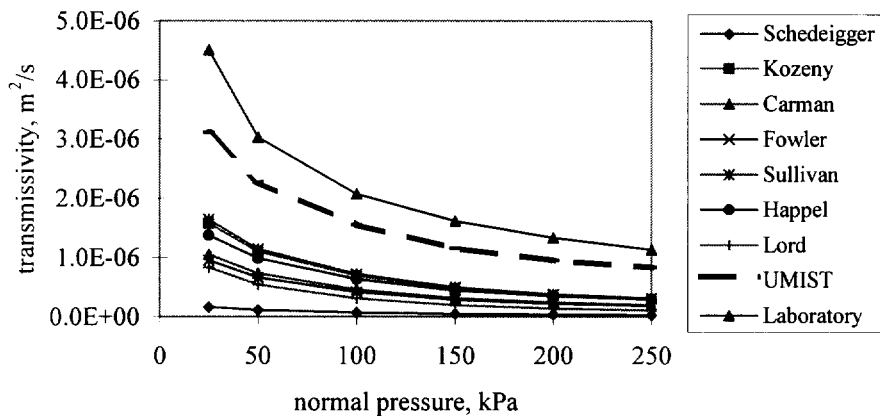


Figure 2. Transmissivity - normal pressure relationship for various theories - Fabric C1

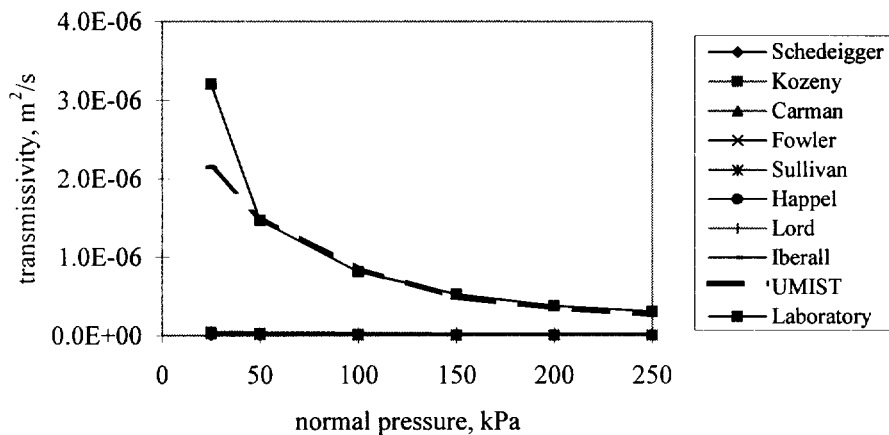


Figure 3. Transmissivity - normal pressure relationship for various theories - Fabric M2

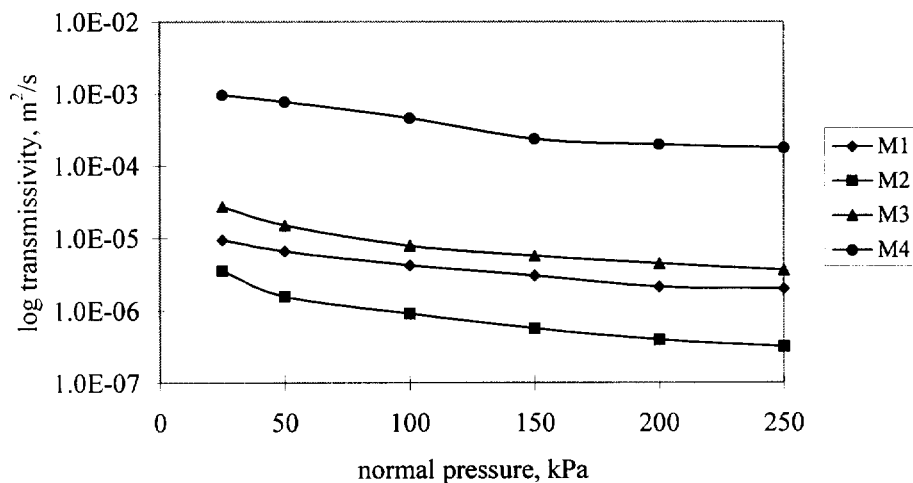


Figure 4. Log transmissivity - normal pressure relationship - Fabrics M1, M2, M3 and M4

5 TENSILE PROPERTIES

Tensile behaviour of the fabrics are of great importance when the geotextile is to be used for reinforcement applications. One of the most critical property is the tensile stiffness, which must be as high as possible to avoid any undesirable deformations and movements in the soil structure. Therefore, during the design and manufacturing of the geotextile fabric careful consideration was given to keep the warp crimp to a feasible minimum level. For typical slopes a maximum allowable reinforcement elongation of 5% will result in outward face deflections of no greater than 100 to 150 mm (Jewel, 1996). From the estimated initial load - strain curve shown in Figure 5, it is clear that the maximum strain levels in all the designed fabrics are within the permissible levels.

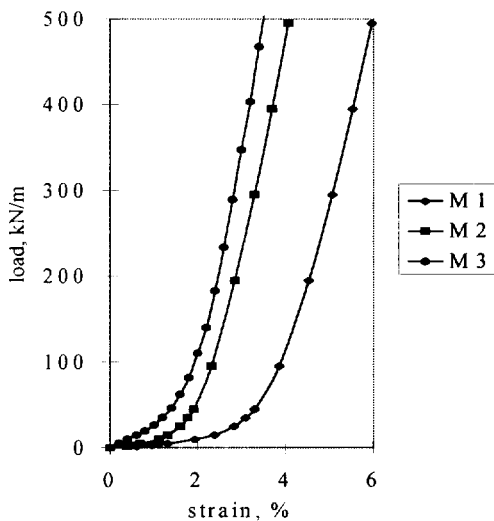


Figure 5. Estimated initial load - strain relationship of fabrics M1, M2 and M3

6 DISCUSSION AND CONCLUSIONS

From Figure 2 and 3 it is apparent that the proposed theoretical model for the flow of water in the plane of the woven fabrics is fairly accurate in predicting the actual flow levels compared to the other general theories of flow in porous media. Although the prediction at lower stress levels is comparatively farther from the actual values, at higher stress levels, which are the stress levels encountered in the field, the predictions are reasonably accurate. Tests done on other three fabrics also follow a similar trend. However, for fabric M3, the predictions at lower levels are comparatively away from the measured values. Nevertheless, at 150 kPa and beyond, the predictions are similar to the other fabrics. Giroud considered a geotextile basal drain to an embankment and calculated that a transmissivity of $3.1 \times 10^{-7} \text{ m}^2/\text{s}$ allowed the geotextile to effectively work as a

drain for compressive stresses of less than about 1 MPa (equivalent to a 50 m high embankment). From Figure 4, where the transmissivity of the geotextiles at various stress levels are indicated, it is clear that the innovative geotextile M4 possesses a transmissivity value that is 100 - 1000 times higher than the transmissivity value predicted by Giroud. Further, from the results given in Figure 4 it can be deduced that with suitable geotechnical designs even geotextiles M1 and M3 can successfully be used as reinforcement geotextiles functioning as drains in clayey soils. Although the cost of these fabrics are higher than the fabrics available in the market, preliminary cost calculations suggest that the savings obtained by the use of in-site soils over imported material will override the fabric cost.

The theoretical model presented in this paper does not take into consideration the fact that soil particles can partially fill the pores in the fabric structure. It is envisaged to study this effect in future research. However, the transmissivity of the novel fabric M4 is sufficiently high to take into account any partial blockage that may occur.

REFERENCES

- ASTM D 4716-87 (1987) Standard test method for constant head hydraulic transmissivity (in-plane flow) of geotextiles and geotextile related products. Annual Book of ASTM Standards, Vol. 04.09. pp 53 - 56
- Fabian, K. (1990) "Time dependent behaviour of geotextiles reinforced clay walls", *Fourth International Conference on Geotextiles, Geomembranes and Related products*, A. A. Balkema, The Hague, Netherlands, Vol. 1, pp. 33 - 38.
- Giroud, J. P., (1981) "Designing with Geotextiles", *Materiaux et Constructions*, Vol. 14, pp 257 - 272.
- Ingold, T.S. (1994) *The Geotextiles and Geomembranes Manual*, Elsevier Advanced Technology, Oxford, UK.
- Jewel, R.A.(1996) *Soil Reinforcement with Geotextile*, CIRIA Special Publication - 123, London, UK.
- Kemp, A. (1958) "An Extension of Pierce's Cloth Geometry to the Treatment of Non-circular Threads", *Journal of the Textile Institute - Transactions*, Vol. 49, pp T44 - T48.
- Leiper, Q. (1995) "A Reinforced Soil Solution for the M25", *Geotechnical Engineering in Highway Design and Construction*, UMIST, Manchester.
- Ling, Hoe I., Tatsuoka Fumio, Wu Jonathan T.H. and Nishimura Jun. (1993) "Hydraulic Conductivity of Geotextiles under Typical Operations Conditions", *Geotextiles and Geomembranes*, Vol. 12, pp 509 - 542.
- Munson, Bruce R., Young, Donald F. and Okiishi, Theodore H. (1990) *Fundamentals of Fluid Mechanics*, John Wiley & Sons, New York.
- Tatsuoka, F., Ando, H., Iwasaki, K. and Nakamura, K. (1986) "Performances of Clay Test Embankments Reinforced with Non-woven Geotextile", *Third International Conference on Geotextiles, Geomembranes and Related Products*, Vienna, Austria, pp 355 - 360.

Large Scale Pullout Tests of Geotextile in Poorly Draining Soils

S. H. Chew, S. A. Tan

Lecturer and Senior Lecturer, Department of Civil Engineering, National University of Singapore, Singapore

K. H. Loke

Regional Technical Manager, Polyfelt Asia Sdn. Bhd., Malaysia

P. H. Delmas

Vice-president, Development Application Europe, Polyfelt

C. T. Ho

Formerly Research Scholar, Department of Civil Engineering, National University of Singapore, Singapore;
Civil Engineer, Civil Engineering Department, Housing and Development Board, Singapore

ABSTRACT: The use of geosynthetics in soil reinforcement applications has been increasingly popular in recent years. Geosynthetic reinforced soil walls are commonly backfilled with clean sand. In regions where clean sand is not cheaply and easily available, a cost-effective design of the wall is to use locally available soil, that may not be free draining. As a result, the designs of reinforced slopes and walls have to take into consideration of the probable build-up of excess pore water pressures, especially during rainy seasons. In recent years, effort is focused on the development of geosynthetic material that can perform not only reinforcement functions but act as a drainage medium as well. Such soil-reinforcement material can rapidly drain off excess pore water to maintain the stability of the system. This paper reports a series of large scale pullout tests in locally available residual soil which is poorly draining.

KEYWORDS: Geotextile, Reinforcement, Pullout tests, Drainage, Deformation.

1 INTRODUCTION

The growth of the petrochemical industries in the recent years has led to the development of numerous synthetic products for various geotechnical engineering purposes. One of the many applications is the use of such materials for reinforcement purposes. This includes using geosynthetic products for slope stabilisation, erosion control, reinforcement of steep slopes as well as construction of vertical earth walls. The use of geosynthetics for soil reinforcement applications, especially, depends on the characteristics of the soil-geosynthetic interface which, in turn, is dependent on the effective stress at the interface. When granular material is used as the backfill material, the effective stress at the interface is more stable due to the unlikelihood of build-up of excess pore water pressure.

Granular backfill, however, may not be easily and cheaply available in many areas, especially in Southeast Asian regions. Under such circumstances, the more cost effective way of constructing reinforced earth walls would be to use the locally available residual soil which is lateritic in nature. Lateritic soils are cohesive-frictional soils but they are not free draining in nature. The soil strength is also dependent on its in-situ water content and soaking may lead to a drastic reduction in the expected strength of such material (Bergado et al. 1993). There is an impending threat of build-up of excess pore water pressure

at the soil-geosynthetic interface during heavy raining seasons, leading to the possibility of instability of the soil mass. Hence, in order to effectively use such material as backfill for reinforced soil system, the geosynthetic used must have the dual function of reinforcing the soil mass and, at the same time, drain away pore water in the soil mass. The essential design criteria for such system were outlined in Chew and Loke (1996).

2 PULLOUT TESTS

2.1 Test Apparatus

The Department of Civil Engineering at National University of Singapore (NUS) has developed a large scale pullout apparatus capable of performing large scale pullout tests on geosynthetic material of various configurations. Recommendations from Farrag et al. (1993) were studied extensively and used as guidelines in the development of the pullout apparatus at NUS. The apparatus measured 1.5 m in length, 1.5 m in width and provides for 30 cm of soil sample to be placed below and on top of the geosynthetic specimen to be tested. Horizontal sleeve plates are provided at the front wall of the pullout apparatus to eliminate boundary effects due to the front wall. The apparatus performs the pullout process at constant strain rate, driven

by a hydraulic machine. Detail description of this large scale pullout apparatus can be found in Chew et al. (1997).

In the first few series of pullout tests performed, the main objectives were to test the ability of the apparatus to function as desired. The series of pullout tests performed by Ng (1995) showed that the pullout apparatus is able to perform pullout at slow constant rates and that boundary effects were minimal. Subsequently, the apparatus were further modified by Ho (1996) to increase its testing capabilities by incorporating drainage systems into the apparatus. The aims of the improvements and modifications were to enable the apparatus to perform pullout tests in various soils, from granular to lateritic.

2.2 Geotextile Material

The geosynthetic material used in the two pullout tests is the PEC-75/25, a high-strength geotextile produced by Polyfelt. Theoretically, this material is a geocomposite as it comprised of a woven geotextile mechanically bonded to a nonwoven geotextile. This geotextile has multi-filament woven polyester yarns in grid-like pattern bonded to thermally bonded nonwoven polypropylene sheet. The maximum tensile strength of the geotextile is 75 kN/m along the longitudinal direction and 25 kN/m along the transverse direction. It derives its strength from the woven polyester yarns while the polypropylene sheet provides a drainage medium.

2.3 Soil Sample

The soil sample used is the locally available residual soil from the western part of Singapore. The soil is lateritic in nature and its optimal compaction is at water content of about 20%. However, it turns soggy and loses strength rapidly when soaked in water for long periods of time. The soil is reddish brown in the colour and consists of well-graded silty sand. Dry sieving tests on the soil revealed that the soil contains about 10-14% of silts, with a D_{50} of 0.24 mm and C_u of 6.2.

2.4 Test Program

A number of series of pullout tests were conducted in the last few years using the NUS Large Scale Pullout apparatus. Various type of geosynthetics has been tested with both sand and with residual soils as backfill material. Tests results were found to be consistent, and with good repeatability. In this paper, the test results of two pullout tests with residual soils will be reported. The first pullout test aimed to study the pullout resistance of the geotextile when embedded in residual soil at its in-situ moisture content. The soil sample in test 1 was prepared and compacted to an average density of 1905 kg/m³ and an average moisture content of 23.5%. In the second test, the objective was to study the reduction in the pullout resistance

of the geotextile in residual soil when the soil is soaked with water to simulate ponding conditions. In this test, the soil was first compacted to an average density of 1887 kg/m³ and an average water content of 23.3%. The soil sample in the test 2 was then subjected to 20 cm of water ponding for 4 days continuously in order to soak the soil sample in the pullout apparatus. In both tests, the rate of pulling at the front of apparatus was 0.80 mm per minute and the tests were carried out until total pullout had occurred. There was also no additional surcharge applied to the surface of the soil backfill, i.e. the pullout tests were conducted under low stress conditions.

2.5 Instrumentation

Aluminium strips with strain gauges were used to measure the pullout resistance mobilized by the geotextile in the course of the pullout process. The aluminium strips were pre-calibrated and a total of 8 were used for measuring the pullout resistance. These were mounted at the front of the geotextile and connected to the clamping plate in front of the pullout apparatus which was pulled forward at a constant and very slow rate by the hydraulic machine.

Displacements at various locations of the geotextile were measured using thin tell-tale wires, with the help of potentiometers with travel range of 100 mm. A total of 7 tell-tales were used in each of the two tests. In addition, potentiometers were used to measure the displacements at the front end of the geotextile. Each of the potentiometers was connected to the data acquisition system together with the strain gauges for the aluminium strips. Readings were recorded at 30 second intervals.

In test 2 where soaking of the soil sample occurred, there was anticipation of possible build-up of excess pore water pressure during the compaction and pullout test. In this test, miniature pore water pressure transducers were used to measure the pore water pressure at various parts of the soil sample. Two of such transducers were placed near the soil-geotextile interface: one just in front of the sleeve plates and the other, about 60 cm from the front wall.

3 PULLOUT RESPONSE OF GEOTEXTILES

3.1 Peak pullout resistance

The pullout responses of the geotextile in residual soil under different soil conditions are shown in figures 1. In test 1, where the soil is compacted at its in-situ moisture content, it can be seen that the pullout resistance of the geotextile increased steadily with front displacement until an apparent peak. The peak pullout resistance registered in the first pullout test was 23.2 kN while in the soaked pullout test, the peak pullout strength was measured at 19.4 kN. This indicates a drop of 16.4% in the peak pullout

resistance when the soil is pond with water. What was worthy to note was the change in the strength of the residual soil before and after the soaking process. Cone penetrometer tests on the soil sample showed an average CBR value of 3% in test 1. For test 2, where the soil was thoroughly soaked for 4 days, the CBR value dropped to an average of only about 1.5%, with the soil at the interface having only 0.75% in CBR value. This showed that the pullout resistance of the geotextile fell by only 16.4% when the strength of the soil at the interface dropped by almost 75%.

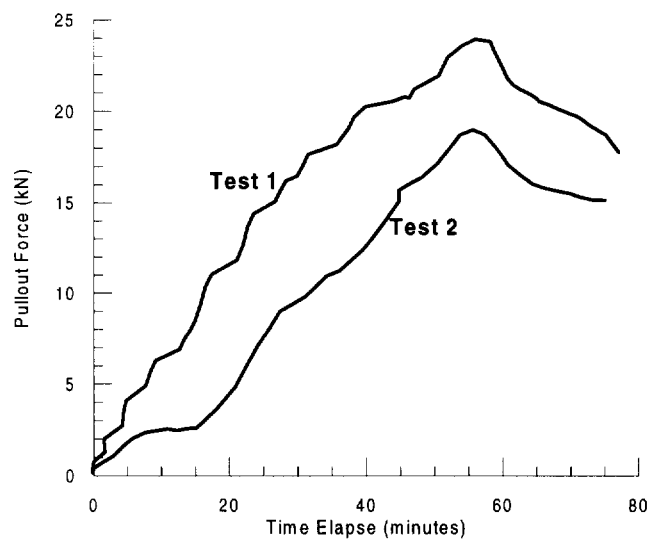


Figure 1 : Pullout response of geotextile in residual soil in tests 1 and 2.

3.2 Displacements during pullout

Figures 2 and 3 show the total displacements measured at various locations of the geotextile for test 1 and test 2 respectively. By total displacements, it meant that the magnitude of displacements recorded consisted of both displacement due to sliding of the geotextile against the soil at the soil-geotextile interface, as well as displacement due to material stretching of the geotextile.

It can be seen that the differential displacement between the front end of the geotextile and a point 30 cm from the front wall was lower for test 2 as compared to test 1. This is expected as the peak pullout resistance that can be mobilised in the second test was lower than the first test, substantiating the fact that the residual soil backfill at the interface was indeed weakened by the soaking process. Note that the first 30 cm of the geotextile was not embedded in soil. Thus this section of the geotextile was undergoing a process similar to the wide-strip tensile test.

Another important observation made in the two pullout tests was that in test 1, the differential displacement between two

consecutive locations along the embedded length of the geotextile was less uniform. Differential displacements were larger at locations nearer to the front wall than locations further from the front wall. This meant that the geotextile developed higher levels of strain nearer to the front wall than at locations further from the front wall. In test 2, however, it was observed that the differential displacement seemed to be quite uniform along the length of the geotextile, showing that the strain development was rather uniform along the length of the geotextile.

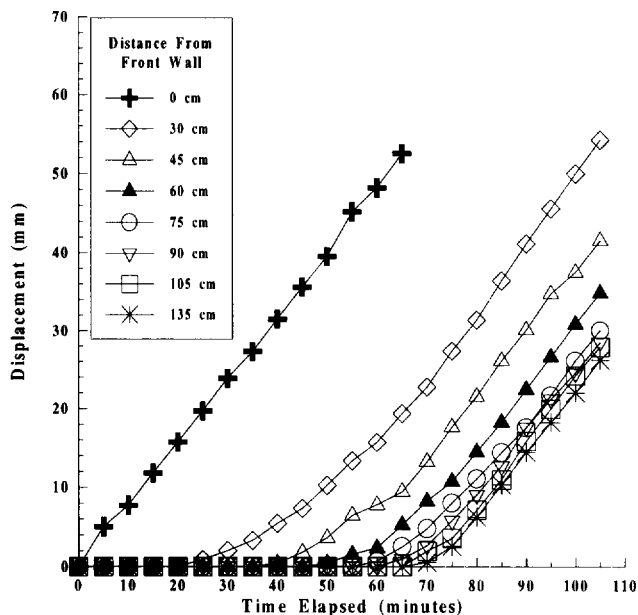


Figure 2 : Displacements at various locations of the geotextile during pullout test 1.

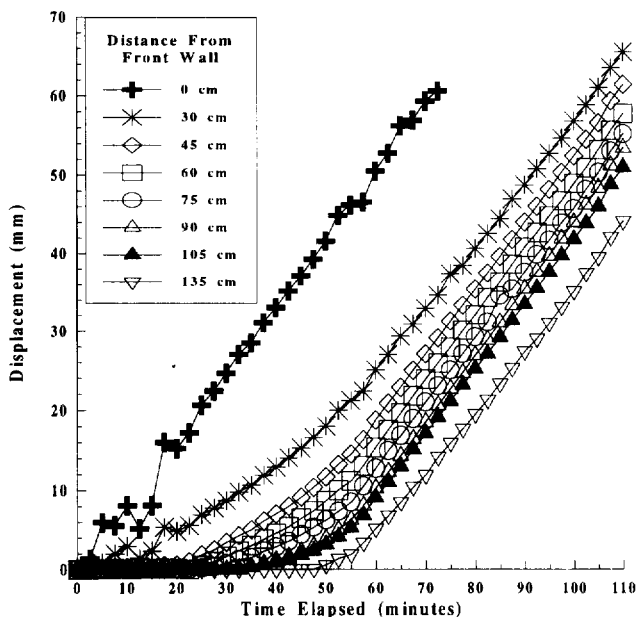


Figure 3 : Displacement at various locations of the geotextile during pullout test 2.

3.3 Pore water pressure measurements

During test 2, pore water pressure transducers were installed in various locations to measure the pore water pressure during the compaction and the pullout stages. While the hydrostatic pore water pressure is about 1.0 kPa at the location 10 cm below the surface of the soil, as indicated as PPT4. The pore water pressure transducer at this point (PPT4) measured a pore pressure of about 3.5 kPa through the test, indicating that there is a built-up of excess pore water pressure of about 2.5 kPa. However, at the location of the soil-geotextile interface, where the hydrostatic pressure is about 2.5 kPa, the pore pressure transducer PPT2 gave pore water pressure reading of practically zero through out the pulling process. This indicates that the geotextile is capability of draining away the water effectively and functioned not only as reinforcement but also as a drainage medium.

Interesting results were obtained from the pore pressure transducer near the sleeve plate (PPT3). At the location of soil-geotextile interface, the transducer just in front of the sleeve plates (PPT3) registered some development of excess pore water pressure during the pullout process, reaching the peak total pore water pressure of about 6.5 kPa at the elapse time of about 60 minutes, which corresponds to the time when peak pullout force occurred. Subsequently, the pore water pressure dissipated rapidly when the geotextile was undergoing pullout.

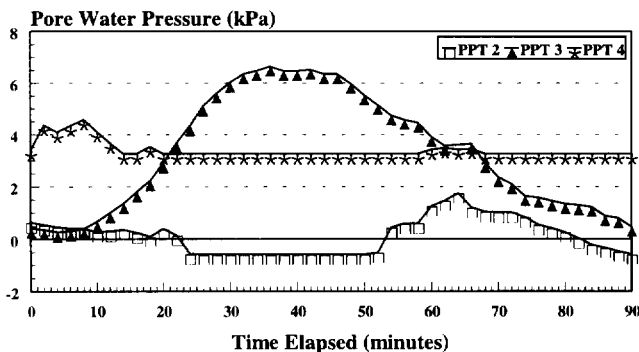
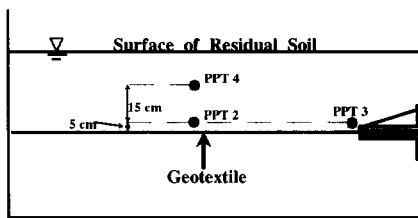


Figure 4 : Pore water pressure measurements during test 2.

4 CONCLUSIONS

The use of residual soil as backfill material for the construction of geosynthetic steep slopes and earth walls

is feasible only if proper drainage mediums are also provided to rapidly drain off the pore water to prevent potential build-up of excess pore water pressure. Hence, the geosynthetic material not only have to functioned as a reinforcement material but also as a drainage medium. One such material is the composite geotextile which consists of high-strength polyester yarns for reinforcement purposes, and a porous nonwoven polypropylene sheet for drainage function. The two large scale pullout tests reported here indicate that high-strength geotextile, coupled with drainage capability, can provide a rational choice as the reinforcement material. The test results indicates that the pore pressure at the soil-geotextile interface is practically zero, except at location near the sleeve plate, while the soil mass above the geotextile were having some excess pore water pressure. This seems to suggest that the geotextile is capable of dissipating excess pore water pressure rapidly during the pullout test. With the provision of this drainage function, peak pullout force dropped by only 16.4% when the residual soil is subjected to ponding. With the use of such material for reinforcement purposes, the reinforced soil concept can be further extended to regions where granular material is not readily available as backfill material.

REFERENCES

- Bergado, D.T., Macatol, K.C., Amin, N.U., Chai, J.C., Alfaro, M.C. and Anderson, L.R. (1993) "Interaction of Lateritic Soil and Steel Grid Reinforcement", *Canadian Geotechnical Journal*, Vol. 30 No. 2, pp. 376-384.
- Chew, S.H. and Loke, K.H. (1996) "Design Criteria for Reinforced Soil Structures using Poorly Draining Backfills", *Proceeding, 12th Southeast Asia Geotechnical Conference*, Kuala Lumpur, Malaysia, pp. 137-145.
- Chew, S.H., Tan, S.A., Ho, C.T. and Loke, K.H. (1997) "Case studies and Large scale Tests on Geosynthetic Soil Reinforcement with Regional Soils", *International Conference on Ground Improvement Techniques*, Macau, pp. 121-129.
- Farrag, K., Acar, Y.B. and Juran, I. (1993) "Pullout Resistance of Geogrid Reinforcements", *Geotextiles and Geomembranes*, Vol. 12, No. 2, pp. 133-159.
- Ho, C.T. (1996) *Pullout Response of Geotextile in Dry and Wet Soils*, B(Eng) Thesis, Department of Civil Engineering, National University of Singapore, Singapore.
- Ng, L.F. (1995) *Pullout Resistance of Geosynthetics Using Large Scale Pullout Apparatus*, B(Eng) Thesis, Department of Civil Engineering, National University of Singapore, Singapore.

Soft Clay Embankment Reinforced by Geosynthetic Horizontal Drains

M. Kamon

Professor, Disaster Prevention Research Institute, Kyoto University, Uji, Kyoto, Japan

T. Akai

Chief Engineer, Technology Research Institute of Osaka Prefecture, Izumi, Osaka, Japan

M. Fukuda

Manager, Osaka Soil Test Laboratory, Osaka, Japan

Y. Nanbu

Chief Engineer, Obayashi Corporation, Osaka, Japan

ABSTRACT: A full-scale test embankment reinforced with geosynthetic horizontal drains (GHDs) was carried out. The GHDs consisted of geocomposite materials and had the functions of reinforcement and drainage. Two kinds of GHDs and slope facing materials were selected, and a soft clay generated from an excavation was used for the filling material. The soft clay embankment, reinforced by GHDs, was designed to be 10 meters high with a steep slope angle. Limit values for the safety of the embankment were selected.

During and after the embankment execution, the settlement and the deformation of the embankment, the induced elongation of the GHDs, the strengths of the filling material, etc. were carefully monitored. The results obtained reveal that the soft clay embankment is stable and that the GHDs provide sufficient reinforcement.

KEYWORDS: Embankment, Geocomposites, Reinforcements, Soft Soils, Steep Slope

1 INTRODUCTION

Recently, embankments reinforced with geosynthetic materials have been used as one of the general construction methods for stabilizing embankments. The good mechanical properties of geogrid, a typical reinforcing material, are widely recognized for their applicability to reinforced embankments filled with sandy soils. Due to the lack of drainage, inferior quality soil such as surplus soil from construction sites can not be used for filling material in reinforced embankments. When soft clay of a low strength is used as a filling material for embankments, the filling is expected to increase in strength owing to consolidation by the effects of dewatering. Therefore, we have developed GHDs which are not only superior strength but also high permeability (Kamon et al. 1994).

This paper describes the results of a case study involving newly developed GHDs applied to a reinforced embankment filled with a soft clay soil.

2 OUTLINE OF THE TEST EMBANKMENT AND BASIC PROPERTIES OF GHDS

Two GHDs were applied to a reinforced embankment 10 meters in height. Plastic cores covered by nonwoven fabric (improved mechanical characteristics) and the reinforced nonwoven fabric (reinforced with high tensile strength yarn) were used. The width of each GHD was 0.3 meters. The basic material properties of the GHDs are summarized in Table 1.

The construction site is in the southern part of Osaka Prefecture, and surplus clay soil from an excavation in

Table 1. Basic properties of geosynthetic horizontal drains

Materials	Zone A	Zone B
	(Plastic core covered by nonwoven fabric)	(Reinforced nonwoven fabric)
Thickness (mm)	3.6	8.7
Unit density (g/m ²)	1636	1581
Pull-out strength (kN)		
at 5% elongation	6.1	8.3
at failure	6.5	12.2
Tensile strength (kN/m)		
at 5% elongation	43.5	43.8
at failure	82.8	72.9
Elongation at failure (%)	32.1	11.4
In-plate permeability (cm/s)		
Normal stress at 98.0kPa	1.6x10 ⁻¹	3.2x10 ⁻¹
Normal stress at 294.0kPa	1.6x10 ⁻¹	1.0x10 ⁻¹

this area was used. The ground conditions in this area include Pleistocene deposits, and the excavated clay soil was in a slightly overconsolidated state.

Table 2. Physical properties of filling material used

Density of solid particle (Mg/m ³)	2.686
Water content (%)	44.2
Clay fraction (<5 μm) (%)	63.3
Liquid limit (%)	57.4
Plasticity (%)	35.3
Cohesion, c _u (kPa)	88.2
Internal friction angle, φ (°)	23.7
Preconsolidation stress, p _c (kPa)	426.3
Coefficient of consolidation, c _v (cm ² /day)	0.589

3 DESIGN OF THE SOFT CLAY EMBANKMENT REINFORCED BY GHDS

The physical properties of the clay soil are indicated in Table 2. The liquidity index was approximately 63% and the clay soil became very soft after remolding.

Based on the in situ failure test results (Kamon et al. 1996), a highly soft clay embankment reinforced by GHDS was constructed. A section of the embankment is illustrated in Figure 1. GHDS were placed over 50% of the embankment with the staggered arrangement shown in this figure. The design factors of the slope stability are summarized in Table 3, which was modified from the Japanese design manual (1992).

The stability of the embankment was calculated according to the following rotational slip method.

$$F_s = \frac{R \cdot \Sigma \{c_i \cdot l_i + (W_i \cdot \cos \theta_i + T_i \cdot \sin \theta_i) \cdot \tan \phi_i + T_i \cdot \cos \theta_i\}}{R \cdot \Sigma (W_i \cdot \sin \theta_i)} \quad (1)$$

where c_i = cohesion of the soil (kPa), w_i = clod weight, ϕ_i = angle of internal friction (degree), and T_i = tensile strength of material (kN/m).

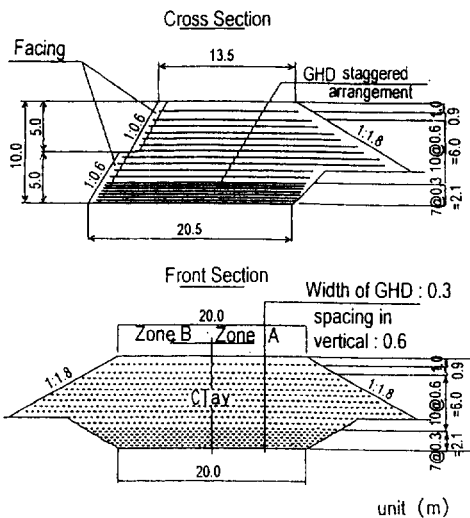


Figure 1. Section of the test embankment

As T_i value, we selected the smaller value between the ultimate tensile strength T_a and the pull out resistance T_{pi} of GHDS. T_{pi} was calculated by Equation (2), namely,

$$T_{pi} = 2 \cdot (0.5c_i + 1.0 \cdot \sigma_v \cdot \tan \phi_i) \cdot L_{ei} \quad (2)$$

where σ_v : vertical earth pressure which works upon the anchorage part of the material at each layer, L_{ei} : anchorage length of the material at each layer, F_s : safety factor, R : radius of the rotational slip surface, l_i : arch length of the slip surface which was divided into sections, and θ_i : sliding angle at the center point of the slip surface which was divided into sections.

The embankment had two different zones reinforced by two different GHDS, each 10 meters high and with a

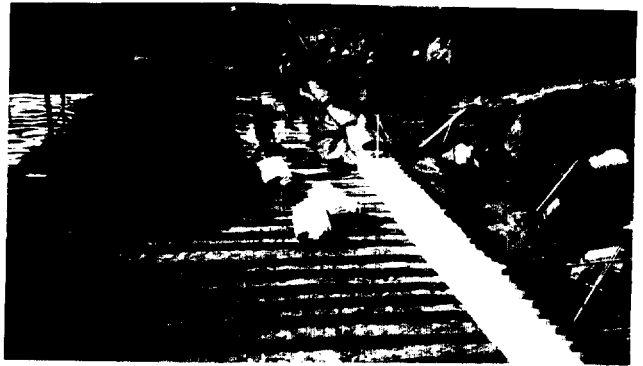


Figure 2. Filling work with GHD and facing material



Figure 3. Completed filling work of 10 m-embankment

Table 3. Design factors and the calculation result of the slope stability

Calculation method of slope stability	Sliding circle method
Seismic design factor	$k_h = 0.2$
Arrangement of GHDS	Staggered; 50%
Design strength of soil (remolded)	$c = 29.4 \text{ kPa}$, $\phi = 0$
Safety factors	Sliding circle (static): 1.3 (dynamics): 1.0 Pull-out safety (static): 2.0 (dynamics): 1.2
Design strength of GHDS	Static (by the creep test result) Dynamics (at 5% elongation by tensile test result)
Calculation result of slope stability	Static: without reinforced = 0.976 with reinforced = 1.405 Dynamics: without reinforced = 0.730 with reinforced = 1.015

1:0.6 slope angle. Figures 2 and 3 show the embankment reinforced by the GHDs during and after the filling work. Two types of facing materials were newly developed and applied to zones A and B, the details of which are omitted in this paper.

4 MONITORING RESULT

4.1 Monitoring System of the Embankment

The filling works were carried out smoothly in both zones. To monitor the slope stability, inclinometers, tensiometers, multi-layer settlement gauges, earth pressure gauges, relative displacement meters, and groundwater monitoring wells were installed in the embankment in order to certify the deformation of the embankment and the status of the GHDs. These monitoring instruments with automatic measuring systems (Figure 4) were mainly installed on the slope and around the predicted sliding circle. The measuring points for each parameter are indicated in Figure 5.

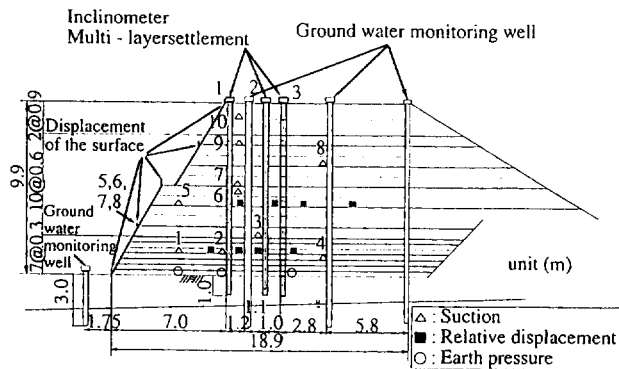


Figure 4 Monitoring system of the embankment

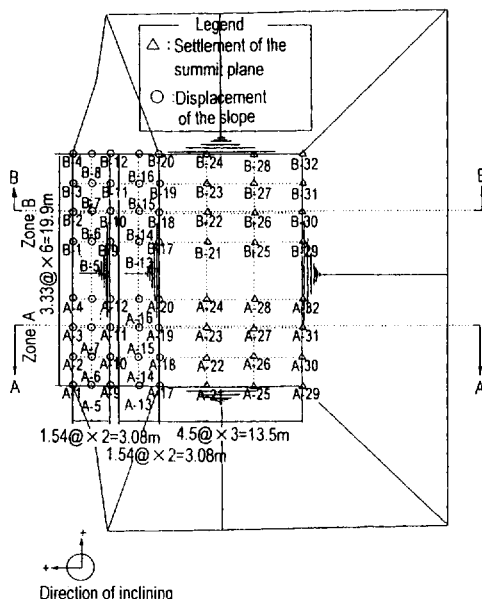


Figure 5. Monitoring points of the embankment

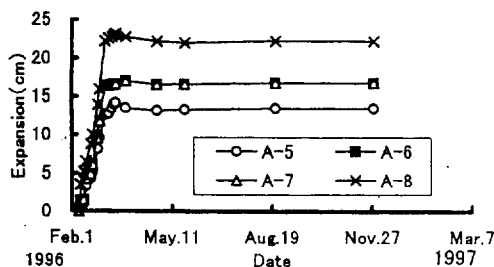


Figure 6. Behavior of the deformation of slope surface

4.2 Deformation of the Embankment

Figure 6 indicates horizontal displacements at the 3-meter high slope of the embankment measured by surveying the total stations. A large horizontal outward deformation at the early stage of the filling work includes a lateral movement by the overburden load as well as the self-weight effect of the filling machine. After the completion of the filling work on March 22, 1996, the horizontal deformation was very small and the embankment became stable by the consolidation of the clay soil.

4.3 Elongation of the GHDs

The results of measuring the strain of the GHDs are illustrated in Figure 7. Strain gauges were set on the fourth and the tenth GHDs where they would be close to the predicted sliding circle. The extensions of the GHDs as well as the compressions were obtained during the filling work. The maximum strains were relatively small values (0.8 to 1.0 %). After the completion of the embankment, no additional strain was observed in the GHDs. This means that the embankment was quite stable.

The difference in the embankment's deformation behavior between zones A and B depends on the elongation and the friction of the GHDs used, but the difference was very small in this case study.

4.4 Physical Properties of the Filled Soft Clay

The shear strength of the filled soil during the filling work was measured by a cone penetration test. Figure 8 shows the results of the distribution of cohesion in the embankment. The results are in zone A and the controlled value was 30 kPa. As the shear strength was less than 30 kPa with a height of 3 - 5 meters, additional filling was carefully performed with the confirmation of the stability analysis. Since the safety of the soft clay embankment is at its lowest in the early stage of the execution, the safety factor of the embankment increased in the drainage function of the GHDs after the completion of the embankment.

The variation in suction for the embankment (zone A) during a rainy season is illustrated in Figure 9. Tensiometers at points A3, 7, and 9 are directly set on the GHDs

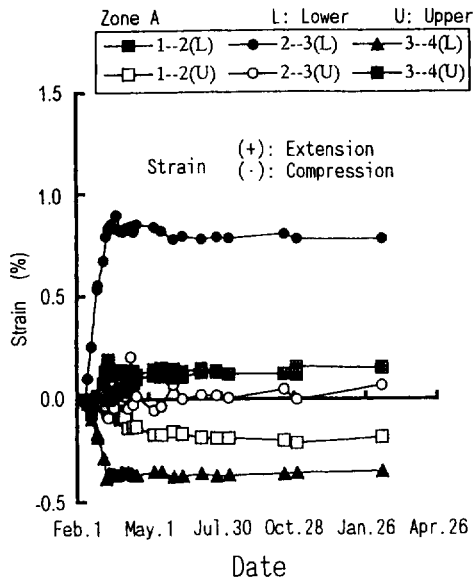


Figure 7(a). Behavior of elongation of GHD (Zone A)

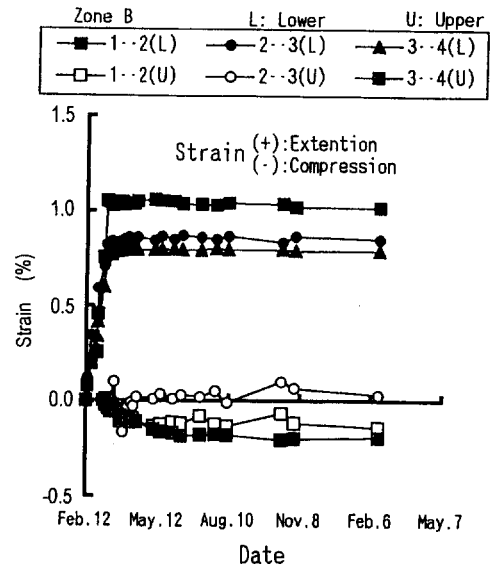


Figure 7(b). Behavior of elongation of GHD (Zone B)

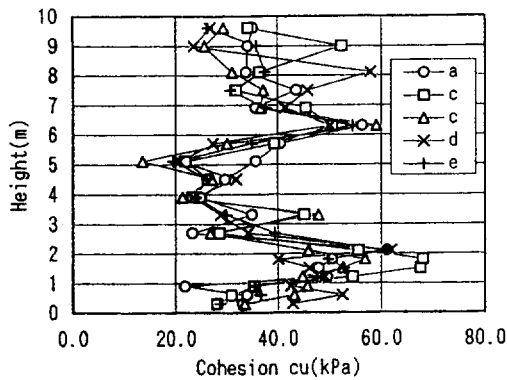


Figure 8. Cohesion distribution of the embankment

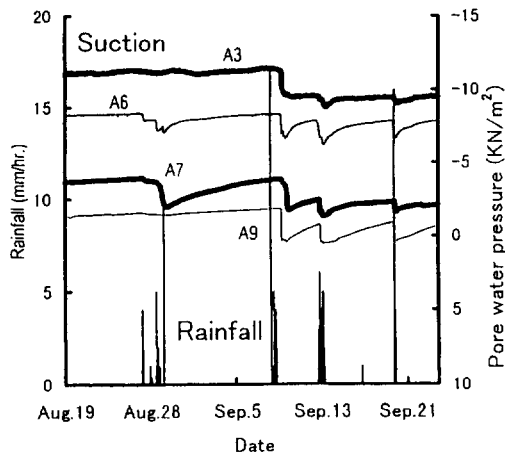


Figure 9. Behavior of tensiometers with rainfall

and A6 was set in the center of the soft clay. The data show negative porewater pressure because of the Pleistocene clay that was filled. This suction (negative porewater pressure) decreases with rainfall, at the surface of the embankment in particular, and increases with dissipation due to the high permeability of the GHDs. It is seen that the GHDs had a high drainage effect and that the safety of the embankment was maintained even with a heavy rainfall.

5 CONCLUSION

The GHDs showed a sufficient tensile reinforcing function and the soft clay embankment with a steep slope was safely constructed using them. The reinforcing and drainage effects of the GHDs can be estimated because of the monitoring results, in particular from the deformation behavior of slope surface and elongation data of the GHDs. Consequently, the GHDs can be used practically in designing reinforced embankments filled with soft clays which are usually disposed of as construction waste.

REFERENCES

Kamon, M., Akai, T., Fukuda, M. and Nanbu, Y. (1996) "In Situ Failure Test of High Water Content Soft Clay Embankment Reinforced by GHDs", *IS-Kyushu '96*, JGS, Fukuoka, Japan, Vol. 1, pp. 215-220.

Kamon, M., Akai, T., Fukuda, M. and Yaida, O. (1994) "Reinforced Embankment Using Geosynthetic Horizontal Drains", *Proc. 5th ICG*, Singapore, Vol. 2, pp. 791-794.

Public Works Research Institute (1992) *Design Manual for Reinforced Earth by Geotextile*, Civil Engineering Research Center, Tokyo, Japan.

Centrifuge Modeling of an Innovative MSES for Marginally Stable Slopes

M. B. Mahmud

Lecturer, Faculty of Civil Engineering, Universiti Teknologi Malaysia, Johor Bahru, Johor, Malaysia

T. F. Zimmie

Professor, Department of Civil Engineering, Rensselaer Polytechnic Institute, Troy, New York, USA

ABSTRACT: Centrifuge model tests were performed to study the feasibility of a new installation method for the construction of mechanically stabilized earth structures (MSES) using geotextile reinforcement. The proposed method allows wide strips of geotextile to be driven horizontally and directly into existing and marginally stable slopes, similar to the installation of vertical wick drains. It does not require excavation of the soil behind the slope face, thus offering a rapid and economical solution for slope stabilization. Model geotextile strips simulated high strength non-woven geotextiles, which serve both as horizontal drain and reinforcement. The contribution of each function to the stability of marginally stable slopes in soft soil is presented in this paper. Typical results from centrifuge model studies show good agreement with other numerical analyses.

KEYWORDS: centrifuge modeling, geotextile reinforced slopes, soil reinforcing, low cost slope stabilization

1 INTRODUCTION

Centrifuge model tests were performed to study the feasibility of a new installation method for the construction of mechanically stabilized earth structures (MSES) using geotextile reinforcement. Conventional geotextile reinforced slopes utilize geosynthetics such as geogrids and geotextiles in the form of continuous sheets. These materials are installed in place after excavation of the slope and successive placement of selected soil as backfill. The proposed method allows wide geotextile strips to be driven horizontally and directly into existing and marginally stable slopes, similar to the installation of vertical wick drains. The geotextile strips perform dual functions, both as horizontal drains and reinforcement. Since excavation of the soil behind the slope face is not required, the method offers a rapid and economical solution to slope stabilization. The advantages of the proposed method over conventional MSES are summarized in Table 1.

Table 1. Conventional MSES versus the proposed method

Conventional MSES	Proposed Method
<ul style="list-style-type: none">• require excavation/removal of "bad" soil• use selected/imported backfill• time consuming (constructed in layers)• require formwork/temporary supports• some need specially designed facing• high cost	<ul style="list-style-type: none">• insitu installation on existing slope (minimal or no excavation)• utilize existing soil• rapid installation• no formwork/temporary support• minimal facing (surface erosion control)• economical

2 SOFT SOIL SLOPES

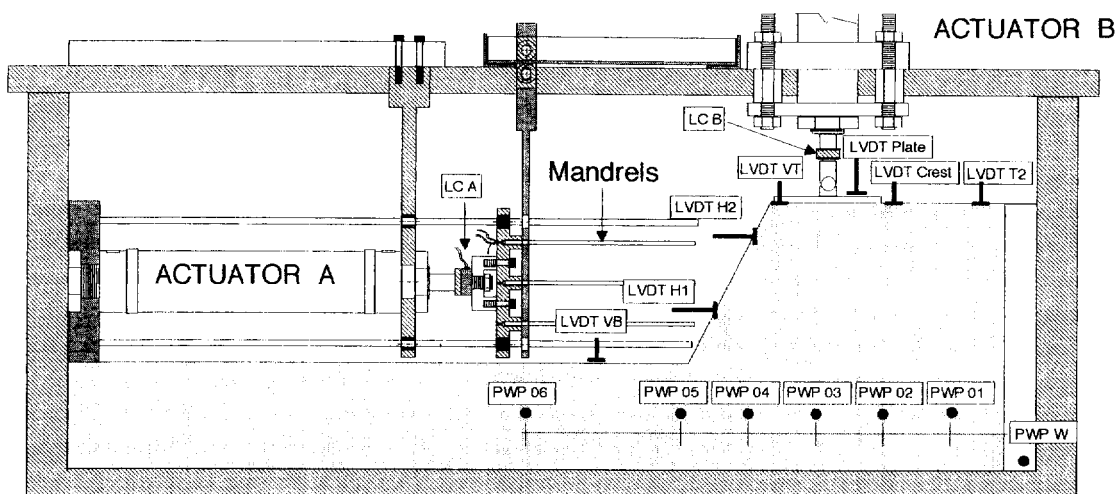
Various full scale studies have been performed dealing with geotextiles performing multiple functions in the stability of reinforced slopes in soft saturated soil. Tatsuoka and Yamauchi (1986) reported on full scale studies performed on two clay test embankments reinforced with planar sheets of non-woven geotextile. The multiple functions of the geotextile, i.e. drainage, tensile reinforcement and compaction control, were the major considerations in the study. Two embankments were constructed using locally available volcanic ash clay, and were fully instrumented to monitor the performance of the embankments over a period of 1.5 and 3 years. The non-woven geotextiles used served well as pore pressure dissipators and the immediate dissipation of pore water pressure was observed after a period of heavy rainfall. The non-woven geotextile was about 3-4 mm thick with an in-plane permeability of 2×10^{-1} to 3×10^{-2} cm/sec and provided the required drainage and hence stabilized the slopes.

Kamon and Akai (1996) constructed full scale reinforced embankments to study the effect of geosynthetic horizontal drains (GHD) on the stability of the embankments. Various types of newly designed GHDs were used in the study. The GHDs were similar to vertical wick drains. The inner cores were wrapped with woven or non-woven geotextiles. These materials were about 12 mm thick, had maximum tensile strengths of about 74.5 kN/m, and exhibited very high in-plane permeabilities. GHD strips, 30 cm wide, were installed during the construction of the clay embankments. The use of GHDs improved the stability of the slopes, increasing the factors of safety (FOS) to about 1.43 and 1.55, compared to a FOS of 1.163 using only conventional geotextiles. Kamon et al. concluded that GHDs can serve the dual functions of reinforcement and drainage for stabilizing soft clay embankments.

It should be noted that the GHDs were installed in a similar manner to conventional MSES systems, i.e. the slopes were excavated in order to install the GHDs or reinforcement.

Loke et al. (1994) also studies the multi-functioning behavior of geotextile-reinforced embankments on soft clay. The full scale embankments, reinforced and unreinforced, were constructed to failure. High strength and multi-layers

non-woven needle punched geotextiles were used in the study. The use of the high strength non-woven geotextiles provided the required drainage and reinforcement for the embankment. Theoretical analyses, using finite difference methods, were performed to determine the critical height of the embankment. The results from the analyses confirmed the behavior of the full scale slope.



(note: LC - Load Cell, LVDT - Linear Variable Displacement Transformer, PWP - Pore Pressure Transducer)

Figure 1 The experimental setup showing various instrumentation used in the study

3 CENTRIFUGE TESTING

3.1 Experimental Setup

The geotechnical centrifuge at Rensselaer was used to perform all model tests presented herein. The capability and performance of the centrifuge, and a summary of various research projects that have been performed using the centrifuge is presented by Van Laak et al. 1997. Model slopes with a slope angle of 63° (1H:2V) were constructed in a large centrifuge strong box (60.96 cm wide x 91.44 cm long). Two actuators, Actuator A and Actuator B shown in Figure 1, were used to drive the mandrel and apply surcharge loading, respectively.

Soft clay material was used in the model slopes which were accelerated to marginal g-levels (factor of safety close to one) to simulate near failure conditions of the slopes. Geotextile strips were then inserted into the slopes, using the remotely controlled mandrel driver, at that particular high g-level (while the centrifuge was rotating). The slopes were then loaded to failure.

Various instrumentation used in the models are shown in Figure 1. Details dealing with the instrumentation and calibrations are presented elsewhere (Zimmie and Mahmud, 1996a).

3.2 Testing scheme

Four model tests are presented in this paper. The models are Unre301, Rein301, Unre403 and Rein401 which represent an unreinforced slope with surcharge loading, reinforced slope with surcharge loading, unreinforced slope with seepage and reinforced slope with seepage, respectively.

Models Unre301 and Rein301 were spun up to 8 g in the centrifuge and maintained at this g-level for a few minutes, then the g-level was increased to 16 g and again maintained at that g-level for a few minutes before finally being increased to 25 g. The surcharge loading was introduced at the 25 g-level, and the load was monitored by the load cell attached to the loading plate. For model Rein301, six geotextile strips were inserted at 25g, prior to the application of crest loading. Both Actuator A and Actuator B (Figure 1), were utilized in the model. Actuator A moves horizontally, inserting geotextile strips housed inside the mandrels into the soil. This operation occurs while the centrifuge is in motion and the model is at the specified high acceleration level in order to simulate prototype soil stresses in the slope. Actuator B is used to apply a surcharge loading on the slope after the strip installation process is complete. Load cells are used to continuously monitor the driving force and surcharge loading.

Models Unre403 and Rein401 were spun up to 25 g in increments of 5 g. The models were maintained at that g level for several minutes before introducing the water. Water was fed into a reservoir behind the slope, from a water tank mounted on the shaft of the centrifuge. An automatic shut-off valve with a remote switch located in the centrifuge control room was used to control the flow of water in flight. Two perforated plates were placed at the headwater and tailwater sides to allow flow within the model. For model Rein401, six reinforcing and drainage strips were inserted at 25 g before introducing the water at the back of the slope.

Centrifuge modeling requirements were carefully observed to achieve similitude. Additional details concerning centrifuge modeling laws pertinent to this study are presented in Zimmie and Mahmud (1996b).

4 RESULTS AND DISCUSSIONS

The crest settlements of models Unre301 and Rein301 plus corresponding loads that caused failure are shown in Figures 2 and 3 respectively. The unreinforced slope model resisted an applied crest load of about 27.2 kg (60 lbs) and the reinforced slope a load of 45.4 kg (100 lbs). Both tests showed approximately the same amount of settlement to failure but the reinforced slope resisted a higher load, as expected. Using limit equilibrium analyses, the factor of safety (FOS) for the unreinforced and reinforced slopes were 1.24 and 1.62 respectively, prior to the application of surcharge loading. The FOS at failure was about 0.45 for both models, computed using the maximum applied loads, indicating that failure probably occurred at load values slightly less than the maximum. Details results and the failure mode of these slopes are presented in Mahmud and Zimmie (1997).

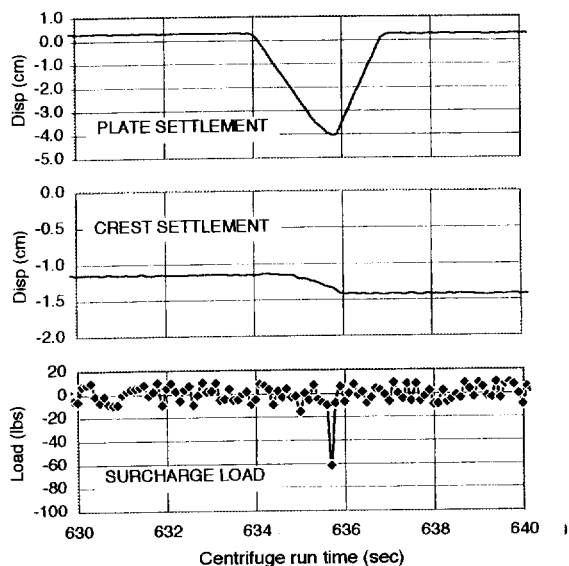


Figure 2 Unreinforced slope with surcharge loading

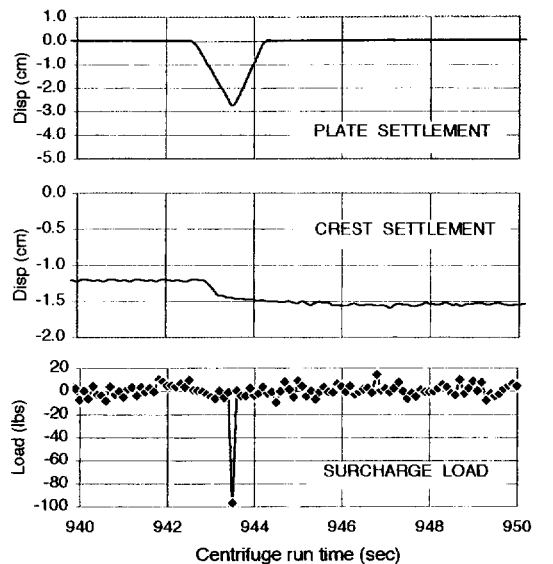


Figure 3. Reinforced slope with surcharge loading

Model Unre403 and Rein401 were performed to emphasize the drainage function of the geotextile strips. The difference in water table between the unreinforced and reinforced slopes plotted from pore pressure transducer data is shown in Figure 4. As shown, the installation of six strips into the slope significantly lowered the phreatic surface and increased the stability of the slope. The FOS of the unreinforced and reinforced slopes computed by limit equilibrium analysis were 0.8 and 1.1 respectively.

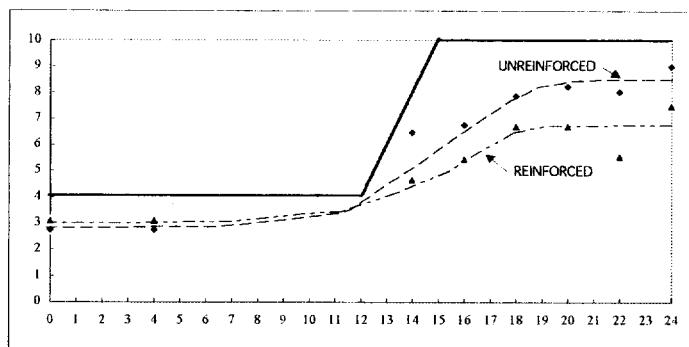


Figure 4. Phreatic surfaces for unreinforced and reinforced slopes (dimension in model units- inches)

5 CONCLUSIONS

The use of geosynthetics as reinforcing elements in reinforced walls can result in savings of about 20-50% as

compared to the use of metallic strips [Christopher and Holtz (1985), and Mitchell and Villet (1987)]. The new installation technique proposed herein will even further reduce the overall construction cost of mechanically stabilized earth structures (MSES). Detailed analysis of the cost of the proposed method is presented by Mahmud (1997). A comparison of unit costs between the proposed method and other reinforced soil structures is shown in Figure 5. Unit costs of the other structures were provided by Holtz et al. (1995). The proposed method is very economical compared to other MSES, largely due to the fact that no excavation of the slopes is required.

This method can rapidly stabilize marginally stable slopes or slopes near failure. The practicality, and time and cost saving aspects of this new method will be beneficial in various slope stabilization schemes including marginally stable embankments, existing slopes and cut slopes.

The centrifuge modeling techniques used in this study are quite economical and less time consuming than the alternative of full scale prototype testing. In fact, it would have been economically impractical to conduct full scale testing during this stage of the study. Proper scaling conditions were carefully observed, and the results of the centrifuge model tests should agree well with the results of full scale tests.

Obviously the feasibility and cost effectiveness of the proposed methodology can only be truly verified after full scale slope installations are completed.

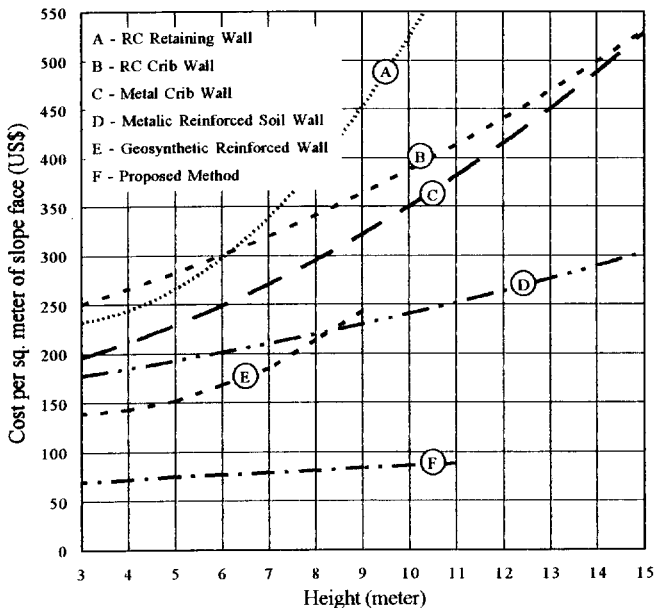


Figure 5. The cost comparison between the proposed method and other methods for reinforcing slopes.

REFERENCES

- Christopher, B. R. and Holtz, R. D. (1985), "Geotextile Engineering Manual", National Highway Institute, FHWA, DTFH 61-80-C-00094.
- Holtz, R. D., Christopher, B. R. and Berg, R. R. (1995), "Geosynthetic Design and Construction Guidelines", FHWA HI-95-038 (May 1995), NHI, Fed. Highway Administration, US-DOT, Washington D. C.
- Kamon, M. & Akai, T., (1996), "In Situ Failure Test of High Water Content Soft Clay Embankments Reinforced by GHDs", In H. Ochiai, N. Yasufuku and K. Omine (eds.), Earth Reinforcement - Proc. of the International Symposium, Vol. 1, Fukuoka, Japan: Balkema, Rotterdam, pp. 215-220.
- Loke, K. H., Ganeshan, V., Werner, G. and Bergado, D. T. (1994), "Composite Behaviour of Geotextile Reinforced Embankment on Soft Clay", Proceedings of the Fifth International Conference on Geotextiles, Geomembranes and Related Products, G. P. Karunaratne, S. H. Chew and K. S. Wong(eds), International Geotextile Society, Singapore, pp. 25-28.
- Mahmud, M. B. (1997), "Centrifuge Modeling of an Innovative, Rapidly Installed and Economical MSES for Marginally Stable Slopes", Ph. D. Thesis (July 1997), Rensselaer Polytechnic Institute, Troy, New York.
- Mahmud, M. B. & T. F. Zimmie (1997), "The Influence of Surcharge Loading on the Stability of Directly Installed MSES", Proc. of the International Symposium on Mechanically Stabilized Backfill (MSB), Denver, Colorado.
- Mitchell, J. K. and Villet, W. C. B. (1987), "Reinforcement of Earth Slopes and Embankments", NCHRP Report no. 290, TRB, National Research Council, Washington D.C.
- Tatsuoka F. and Yamauchi, H., (1986), "A Reinforcing Method for Steep Clay Slopes using a Non-woven Geotextile", Geotextile and Geomembranes, vol. 4, pp. 241-268.
- Van Laak, P., Elgamal, A-W., Zimmie, T. F., and Adalier, K. (1997), "Experimental Facilities: The RPI Geotechnical Centrifuge Facility", NCEER Bulletin, vol 11, no. 2, State University of NY at Buffalo, April 1997, pp. 12-17.
- Zimmie, T. F. and Mahmud, M. B. (1996a), "Instrumentation for Centrifuge Modeling of Geotextile Reinforced Slopes", In H. Ochiai, N. Yasufuku and K. Omine (eds.), Earth Reinforcement - Proc. of the International Symposium, Vol. 1, Fukuoka, Japan: Balkema, Rotterdam, pp. 847-852.
- Zimmie, T. F. and Mahmud M. B. (1996b), "Centrifuge Modeling of a Rapidly Installed MSES", In H. Y. Fang and H. Inyang (eds), Environmental : Proc. of the 3rd International Symposium, Vol. 1 Technomic, Lancaster, PA, pp. 795-804.

Hydraulic Effects of Using Dual-Function Geosynthetics in the Design of Multi-layer Structures

PH. GOTTELAND,
Assistant Lecture, L.I.R.I.G.M.laboratory, Grenoble University, France.

ABSTRACT: This article presents some works to try to model the behavior of multi-layer structures combining a soil having what would be considered as poor mechanical properties for construction purposes, and Dual-Function (draining-reinforcing) Geosynthetics (DFG). We focus on this paper on the hydraulic modeling of a composite soil geosynthetics. We consider for the DFG geosynthetic only the transmissive capacity of the geosynthetic drain for accelerating the dissipation of uplift pressures. Effect of the geosynthetic transmissivity is shown for two types of soil. Modeling of the effect of a local damage of the drain is presented.

KEYWORDS: Drainage, Geocomposites, Modeling, Transmissivity, Installation damage

1 INTRODUCTION

One advantage of using flexible geosynthetics for ground reinforcement would seem to be the possibility of using soils of poor quality, with a high percentage of fines, often with high initial water content and highly sensitive to water. The concept involves associating a drainage function and a reinforcing function for the inclusion (Dual-Function Geosynthetics: DFG). Thanks to the high transmissive capacity of the geosynthetic with high permeability draining function, interstitial uplift pressures induced by placing the soil can be quickly dissipated. At the same time, the tensile strength of the reinforcing geosynthetic improves the mechanical stability of the structure provided by the consolidation of the material (Figure 1).

A modeling system was already presented (Gotteland et al. 1996) with some results of the combined draining-reinforcing effect of a dual-function inclusion for the construction of multi-layer structures alternating a layer of soil with a geosynthetic sheet. We focus on this paper on the hydraulic modeling and on numerical results obtained to assess the effect of some parameters.

2 EMBANKMENTS CONSIDERED

The types of structure concerned are linear structures with vertical or sloping facing with the length being much greater than the other dimensions: height H and width B . Calculations can thus be made in the plane of the structure. The structures could be multi-layer, alternating a layer of soil with a Dual-Function Geosynthetic DFG, of length B , placed horizontally with a spacing of D_h .

The soil supplied is the same and homogeneous over the entire height of the embankment.

The embankment facing is considered as a perfect drain; the upstream boundary between the structure and the in situ soil is considered to be either perfectly draining, or perfectly impermeable depending on the type of construction.

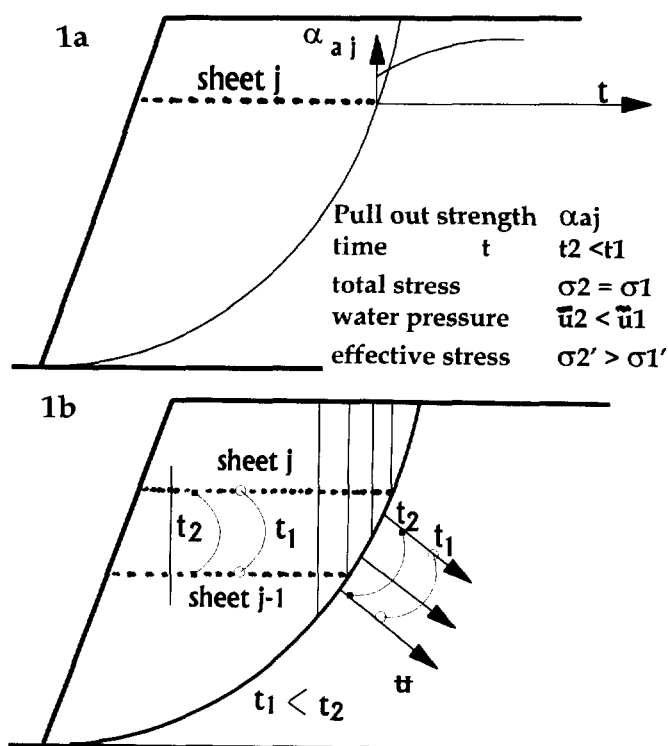


Figure 1: increase of the pull-out strength of the DFG (1a), increase of the shear strength of the soil (1b), by lowering of the pore water pressure in the structure

2.1 The soils

The soils considered in this study are homogeneous fine soils (clays, silts), with high initial water content and permeability, k_s , between 10^{-8} and 10^{-10} m/s. A saturated state may be achieved on completion of placing operations. Compacting may give rise to permeability anisotropy (vertical and horizontal permeability may be different).

2.2 Dual-Function Geosynthetics (DFG)

The DFG inclusions considered are made up of an association of a draining geosynthetic and a reinforcing geosynthetic, for example by the combination of a non-woven and a woven fabric.

As far as only drainage is concerned (hydraulic function), the functional characteristic is the transmissivity θg [m^2/s] with $\theta g = kg \cdot e$ ($kg[m/s]$ permeability, $e[m]$ thickness).

2.3 Draining properties of DFG in the presence of soil

Contact with the soil and applied stresses, over time, lead to a reduction in draining properties of geosynthetics as well as a reduction in soil permeability in the surrounding filtration area. This is known as the clogging phenomenon. The laws governing the variation in these properties are still being studied but simplified approaches can be considered.

The more simple modeling is to consider the transmissivities could be reduced all a long the drain compared to the same values on virgin geosynthetics in order to take these phenomena into account (θg initial = θg reduced $\sim 2 \times 10^{-8} m^2/s$).

We present one other possibility : local reducing of the drain transmissivity for example to modelise a localized clogging or problems of water penetration in the drain.

3 INTERSTITIAL UPLIFT PRESSURES IN A SOIL-GEOSYNTHETIC DRAINING COMPOSITE.

For the hydraulic study, the multi-layer structures studied are broken down into identical elementary element, either by considering two half draining geosynthetic enveloping a soil layer of thickness Dh , or two soil half-layers enveloping a geosynthetic (Figures 2).

For modeling purposes, the construction of a element j is assumed to be instantaneous and completed after time T_j . The time T [days] is the time in days since the start of embankment construction (layer $j=1$), $t=T-T_j$ [days] is the relative time since construction of module j . The construction time between completion of two successive elements is Dt [days].

The stress σ , generated by the weight of the soil layers, is applied uniformly to each element and is imposed instantaneously when constructing the next overlayer.

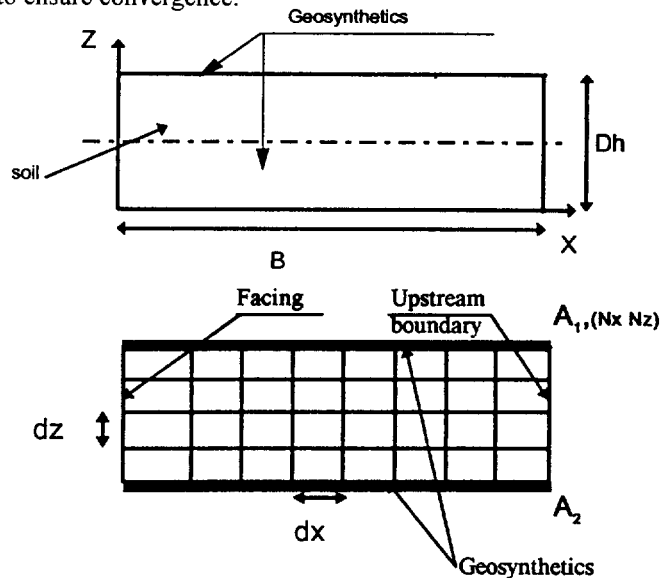
The deadweight of the element j studied is not taken into account.

The soil has an isotropic, linear elastic behavior; after placing, it is assumed to be saturated in water, a fluid considered to be incompressible. The stress s created by an instantaneous increase in interstitial uplift pressure \bar{u} , $\bar{u}(x, z, t=T-T_j=0) = \sigma$.

The transmissivity θg of the geosynthetic is constant with time. Flow in the geosynthetic drain obeys Darcy's law.

The evaluation method for $\bar{u}(t)$ is based on the theory of consolidation. Two approaches are possible: flow in the soil may be considered to be unidirectional (Auriault et al. 77) or two-directional (Bourdillon 76, Gotteland 91).

We consider here the hypothesis of two directional flow in the soil. The consolidation problem is resolved by a finite-difference numerical method. The system is broken down into discrete elements in space (rectangular mesh) and time (explicit scheme). The degree of error in the evaluation of uplift pressures will depend on the size of the mesh dx/dz (a smaller mesh giving a more accurate result) and on the time step, which must be less than the critical time step in order to ensure convergence.



Figures 2: elementary element, discrete mesh

4 MODELING OF CONSTRUCTION

Each element of the multi-layer structure can be studied separately. For each, the effect of the construction stack of successive element on the change in interstitial uplift pressures must be assessed.

A detailed modeling procedure was proposed (Gotteland 91, Gotteland et al 96) in order to assess the effect of the following main parameters on the dissipation times of interstitial uplift pressures in the elements:

- Construction phasing Dt [days]
- Initial uplift pressure $\bar{u}(t=0) = \bar{u} \text{ comp}$ [kPa] (initial remnant pressure after compacting effect)
- Thickness of modules Dh [m]
- Transmissivity of the geosynthetic θg [m^2/s]
- Horizontal and vertical permeability of the soil k_x, k_z [m/s]
- etc.

We retain for this paper, the following simplified modeling procedure : Hypothesis of instantaneous construction of the complete structure ($Dt=0$), with combined influence of compacting and total overload generated by the weight of overlying modules on the consolidation ($\bar{u}(t=0) = \bar{u} \text{ comp} + (n-1) \cdot \bar{u} \text{ stat}$, $\bar{u} \text{ comp}$ is the initial remnant pressure after compacting effect, $\bar{u} \text{ stat}$ increasing by the weight of the soil from an additional element, simplified model 2, Figure 3).

This model provide a greater safety margin because it does not make allowance for consolidation during construction.

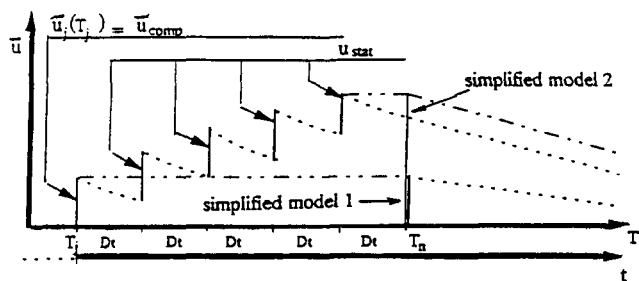


Figure 3: Theoretical modeling of the variation of the uplift pressure during and after construction.

5 STUDY

Some characteristic results of a parametric study are presented in order assess the influence of the variation in transmissivity θ_g of the DFG. Three soils are considered :

	Soil 1 (clay)	Soil 2 (Silty clay)	Soil 3 (Clayey silt)
k_s [m/s]	$1,7 \cdot 10^{-10}$	$1,6 \cdot 10^{-9}$	$2,6 \cdot 10^{-9}$
γ_s [kN/m ³]	17,5	17,5	17,5
Cvs [m ² /s]	$1.47 \cdot 10^{-7}$	$5.4 \cdot 10^{-7}$	$2.8 \cdot 10^{-7}$

k_s [m/s]: permeability, γ_s : soil density [kN/m³],
 $Cvs = k_s \cdot E_{oed} / \gamma_w$ with E_{oed} : oedometric modules of the soil [kPa], γ_w : water density [kN/m³]

Only the uplift pressure distribution in the element at the base is calculated (height of the structure $H = 7$ m, length $B =$ variable , geosynthetic spacing $D_h = 1$ m) with impermeable upstream boundary.

The instantaneous construction hypothesis is considered:
 $\bar{u}(t=0) = 105$ [kPa] (simplified model 2, Figure 3)

5.1 Influence of the transmissivity θ_g of the DFG

Figure 4 shows the variation in dissipation time required to obtain 10% maximum residual uplift pressure in the module in the vicinity of the impermeable upstream boundary (time t such that $\bar{u}(t)_{max} / \bar{u}(t=0) = 10\%$). as a function of DFG transmissivity θ_g .

An interesting phenomenon is seen to occur as a result of the modeling calculation: for low transmissivity values, maximum uplift pressures are dissipated faster in soil 1 (clay) than in soil 3 (silt), and even compared to soil 2 for extremely low values, although soil 1 has lower permeability.

For a more important length B of the drain, the observed phenomena exist for greater value of θ_g . In the same way, if the thickness D_h is smaller ($D_h = 0.5$ m) the same phenomenon is amplified. Notice, that these values of θ_g

are similar of real values of θ_g for non-woven geotextiles used for D.F.G.

For high transmissivity values ($\theta_g = 10^{-5}$ m²/s), the uplift pressure decreases rapidly in the drains for both soils: drainage occurs mainly through the geosynthetic drains. The soil with the high Cvs value dissipates the interstitial uplift pressures more quickly.

For a lower transmissivity value ($\theta_g = 10^{-7}$ m²/s), the uplift pressure in the drains takes much longer to decrease. The explanation seems to be that, for soil 1, the ratio θ_g / k_s is such that most drainage of the soil takes place through the geosynthetic drains. For soil 3, given the low θ_g value, flow is mainly horizontal through the soil; as a result, the drain is subjected to high uplift pressure. Consequently, the draining time being longer, the residual uplift pressure (maximum at the impermeable upstream boundary), is higher for the more permeable soil. Figure 5 shows the uplift pressure distribution for two times $t = 10$ and 20 days for soils 1 and 3 and for $\theta_g = 10^{-7}$ m²/s of the DFG.

The using of a geosynthetic drain seems to be really efficient for low permeability of soil (clay) compared to higher permeability of soil (clayey silt).

The ratio of geosynthetic transmissivity to soil permeability (θ_g / k_s) therefore plays a major role. What can we expect in real life of draining system?

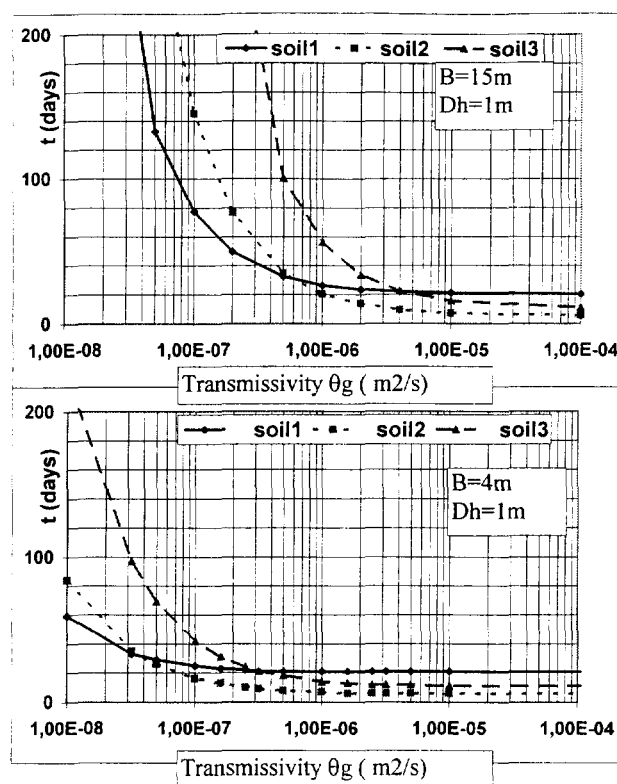


Figure 4: variation in dissipation time ($\bar{u}(t)_{max} / \bar{u}(t=0) = 10\%$) as a function of transmissivity θ_g ($B = 4m, B = 15m$).

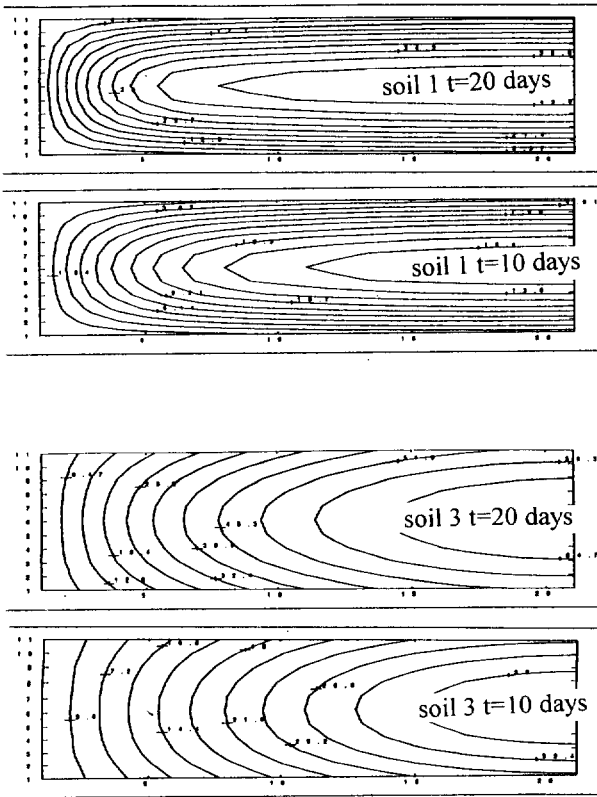


Figure 5: uplift pressure distribution in soil 1 and soil 3 ($\theta_g = 10^{-7} \text{ m}^2/\text{s}$, $B=4\text{m}$, $d_h=1\text{m}$, two times 10 and 20 days)

5.2 Influence of a localized decrease of θ_g

We show the influence that could have a localized reduce of the DFG transmissivity. This decreasing could be produced: by a local damage of the drain, a decreasing of the thickness of the drain induced by a construction blemish, a water moisture penetration difficulty of the drain. This last phenomena was already observed for non-woven geosynthetics.

We had solved this problem with a numerical method; θ_g is locally reduced: (θ_g locally reduced = $\theta_g/100$) in the application treated. In function of the place of the damage, we had an uplift pressure discontinuity in the damage DFG: the uplift pressure is increased at the back and is decreased in front of the damage, in comparison with undamaged DFG (Figure 6). This induce an over distribution of the water flow in the soil-DFG composite: the uplift pressure increase in the undamaged DFG and it is more efficient.

6 CONCLUSIONS

The use of draining-reinforcing dual-function geosynthetics (DFG) means that it is possible to consider employing poor quality soils to build reinforced-earth structures.

From this first original approach, the effect of the main parameters involved can be judged, although it should be

stressed that this is only the preliminary stage of research on this subject. An instrumented structure will have to be built and monitored to refine the hypotheses considered and modeling procedures in order to establish a necessary validation base.

REFERENCES

- Auriault J.L., Cordary D., Giroud J.P., Gourc J.P. (1977) *Etude théorique du rôle des drains textiles dans la consolidation des remblais*. 1st International Conference on Soils and textiles, Paris, pp.273-278.
- Bourdillon M., (1976) *Utilisation des textiles non tissés pour le drainage, application aux remblais de sols fins en cours de consolidation*, Doctoral thesis, Lyon France
- Khay M. (1978) *consolidation de remblai au moyen d'un non tissé; Remblais expérimentaux*, rapport cete, Rouen France
- Gotteland Ph. (1991) *Renforcement des sols par géosynthétiques: dimensionnement et validation*, doctoral thesis Grenoble, France
- Gotteland Ph., Gourc J.P., Aboura A. (1996) *Benefits of using Dual-Function Geosynthetics in the design of multi-layer Structures* Proceedings Geofilters'96, Montreal, pp 553-562

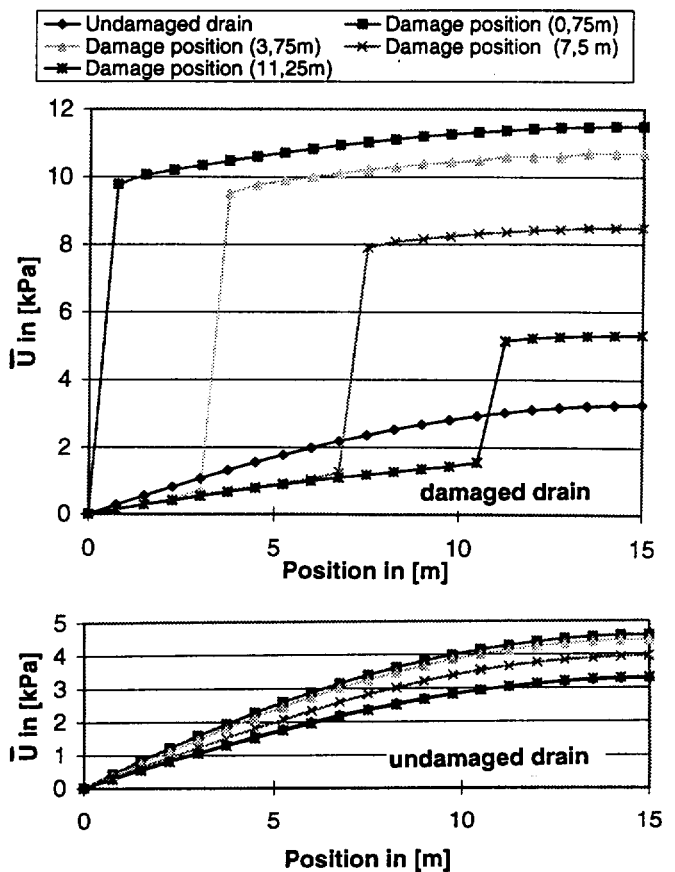


Figure 6: uplift pressure in the damaged and undamaged DFG (θ_g locally reduced = $\theta_g/100$, $\theta_g=10^{-7} \text{ m}^2/\text{s}$, $B=15\text{m}$)

The Mobilized Strength of Prefabricated Vertical Drains

W. Voskamp
Akzo Nobel Geosynthetics bv

G. Troost
Akzo Nobel Geosynthetics bv

G. R. Koerner
Geosynthetic Research Institute, Drexel University, Philadelphia, PA USA

ABSTRACT: This paper focuses on the mobilized strength of prefabricated vertical drains, or PVDs, and is based on the results of theoretical, laboratory and field testing on prototype PVDs. Used herein are PVD simulated units known as load-elongation measuring strips, or LEMS. Results of the paper show that the typical strength of commercially available PVDs are well in excess of the required strength when installed by properly functioning construction equipment.

KEYWORDS: Drainage, Wick Drains, Tensile Strength and Survivability

1 INTRODUCTION

PVDs have replaced conventional sand drains over the past 20 years, by providing an economical solution to rapidly consolidate fine grained saturated soils. When building on such compressible soils, large settlements are anticipated. As the soil cannot compress at a greater rate than release of the excess pore water pressure, such settlement can continue for a long period of time. PVDs are used to expedite this release of pore water hence they decrease the time for settlement and greatly facilitate the stabilization of such sites.

PVDs are approximately 100 mm wide by 2 to 5 mm thick. They are delivered on site in large rolls. Most PVDs consist of a synthetic drainage core surrounded by a nonwoven heat bonded or mechanically bonded geotextile filter. They are installed vertically in the ground by a pile driving type of construction equipment known as a "wick sticker". Spacings are typically at 1 to 5 m throughout the soil to be stabilized. The length of the drains are site specific but usually extend to the bottom of the soft soil involved.

Once the PVDs are installed over a large area, a surcharge load is placed on the ground surface to mobilize excess pore water pressure in the foundation soil. The expulsion of the water is coincident with consolidation of the soil resulting in settlement at the ground surface. Additional surcharge load is placed in incremental lifts in accordance with the design requirements. The duration of the load depends on the soil characteristics, PVD spacing and type of PVD utilized.

There is a wealth of information available on the technique and a tremendous number of PVDs have been successfully installed around the world. The design method for determining the consolidation time versus PVD spacing as well as the required flow rate has been fully described in the literature. For example, Hansbo [1979]

has developed the relationship usually used to determine the PVD spacing as a function of the desired consolidation time. Holtz, et al. [1991] has given guidance on the flow rate capacity of PVDs in the unkinked and kinked conditions.

Conversely, the mechanical strength requirements of PVDs has seen little quantitative analysis and discussion. The only reference, Kremer, et al. [1983], reports the need for a PVD tensile strength of 500 N at a corresponding minimum strain of 2%. They also suggest a maximum strain of 10%. This upper strain limit is imposed in order to avoid unwanted deformations that might compromise the drain's dimensions and thus flow capacity. The technical background for these tensile strength and strain values is not known. Thus, the pursuit of a more rigorous numerical and experimental treatment of the tensile strength requirements during installation of PVDs is the purpose of this paper.

The tensile strength of PVDs is a consideration both during installation and during consolidation. Installation challenges the drain's strength as it threads through rollers of the wick sticker. The strength of the PVD is also challenged during the mandrel withdrawal process. Both of these situations are exacerbated by high installation speeds. In addition, the tensile strength may also be an issue when the drains are collectively used to resist a circular arc failure of the weak, sensitive soil. A large number of PVDs "sewn into the ground" and working as a unit will intercept and resist such a circular arc failure. This, however, is a design issue and is not addressed in this paper.

The paper will describe theoretical, laboratory and field research aimed at determining the mobilized strength of PVDs. The paper will conclude with generic recommendations on the required strength of PVDs based on the results of this investigation.

2 INSTALLATION

Typical equipment used to install PVDs is shown in Figure 1. Lighter trackhoe mounted units are sometimes used when the PVDs are relatively short, e.g., less than 15 m deep. Collectively, we will refer to all PVD installation equipment as "wick stickers". Wick stickers contain a mandrel which encases and carries the PVD while it is being driven. Mandrel designs are product specific. Rhombic mandrels with tapered ends are often used for high speed driving in soft soils. T-shaped mandrels reinforced with a longitudinal steel fin and fitted with harden steel driving tips are used when hard surface layers need to be penetrated. Mandrels are designed to minimize disturbance of the ground and to reduce smear and remolding of the soil adjacent to the PVD.

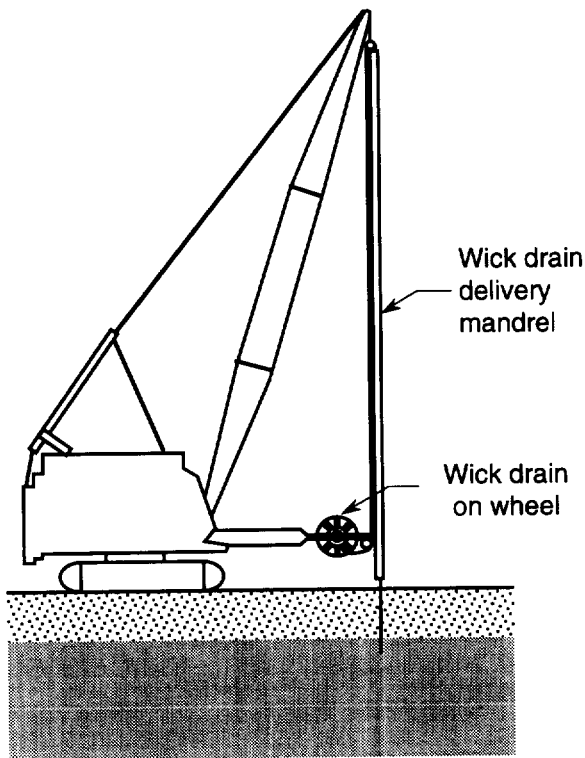


Figure 1. PVD installation rig, a wick sticker.

At the bottom of the mandrel the PVD is fixed to an end assembly that remains in the ground as the mandrel is withdrawn. The purpose of the end assembly is to keep the PVD fixed at the bottom of the soil layer while at the same time keeping soft soil from entering the mandrel as it is driven.

3 THEORETICAL CONSIDERATIONS

PVDs strengths are challenged during installation partly from the drain's self weight and partly from friction between the drain and various parts of the installation equipment. Worst case scenarios are envisioned as maximum forces are developed in the PVD when the mandrel accelerates from a full stop to full speed. Four limiting conditions are identified. These conditions are when the drain is pulled from the roll, as the drain passes through the conveyance system and under the lower roller, as the drain passes over the fixed cylindrical guide roller at the top of the rig, and when the mandrel is retrieved from the penetrated soil leaving the PVD in place.

The first condition investigated is when the drain is initially pulled off the roll. This is a process where the drain is drawn into the mandrel of the installation equipment. This incremental rather than continuous process requires the use of peak rather than average speed for the calculations. By using an angular acceleration of the roll with peak velocity of the wick sticker, a required force of only 14 N is mobilized in the PVD. This occurs at the beginning of each drive when there is a full roll of drain on the reel. The situation is analytically suggested to be as follows:

Velocity of Roll

$$V_{ave} = \frac{L}{D} = \frac{18\text{m}}{18\text{sec}}$$

$$V_{ave} = 1\text{ m / sec}$$

$$2\left(\frac{1}{2}(1)V_{peak}\right) + 16\text{ 1 / peak} = 18$$

$$V_{peak} = 1.06\text{ m / sec}$$

Acceleration of PVD Roll

$$a = \frac{V_{peak}}{t} = \frac{1.06\text{ m / sec}}{1\text{ sec}} = 1.06\text{ m / sec}^2$$

$$\alpha = \frac{a}{r} = \frac{1.06}{0.6} = 1.77\frac{\text{rad}}{\text{sec}^2}$$

Center of Gravity of PVD Roll

$$k^2 = \gamma^2 + r^2$$

$$k = \sqrt{(.1)^2 + .6^2}$$

$$k = 0.61\text{ m}$$

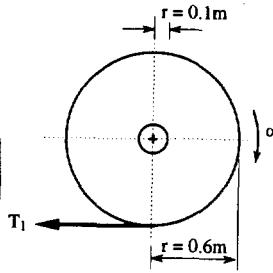
$$\text{mass}_{\text{max}} = m = 25\text{ kg}$$

$$\Sigma M_o = I\alpha$$

$$T_1(0.6) = \frac{1}{2}mk^2\alpha$$

$$T_1 = \frac{1}{0.6} \left[\frac{1}{2}(25)(0.61)^2(1.77) \right]$$

$$T_1 = 13.6 \text{ N}$$



Note, this is the maximum force due to the fact that m and α decrease as the drain is utilized off of the roll.

In the second condition, the drain passes through the conveyance system and under the lower roller. There exists a relationship between the tension in the drain before it enters and after it leaves the roller. This relationship is based on the assumption that the drain is just about to slide into motion. By taking a free body diagram of a small element of the drain the forces acting on the drain are the two forces of tension, the normal component of the reaction of the roller and the friction force. A relationship is obtained knowing that motion is imminent by letting the angular change of the drain approach zero. As seen in the following calculations, only 25 N of strength is required of the PVD in such a condition.

$$\frac{dT}{d\theta} = \mu_s T = 0 \quad \frac{dT}{T} = \mu_s d\theta$$

By integration

$$\ln \frac{T_2}{T} = \mu_s \beta \quad \text{or} \quad \frac{T_2}{T} = e^{\mu_s \beta}$$

Given

$$\beta = \pi \text{ rad, and}$$

$$\mu_s = 0.2$$

Since:

$$F = T_1 = 13.6 \text{ N}$$

Therefore the PVD experiences the following after it exits the lower roller

$$T_2 = e^{\mu_s \beta} T_1$$

$$T_2 = e^{(.2)(3.14)}(13.6)$$

$$T_2 = 25 \text{ N}$$

In the third condition, the PVD is considered to be sliding over the roller at the top of the rig. The tensile force in the PVD is calculated by assuming geometric and frictional characteristics of an upper roller for typical construction equipment. The calculations are similar to that of the lower roller. Liberties were taken in estimating the frictional characteristic of the roller. Conservative values were chosen assuming that the roller would seize-up and become partially fixed. Regardless of these conservative assumptions, a relatively low force of 47 N was mobilized in the PVD for this condition.

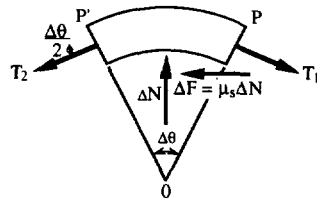
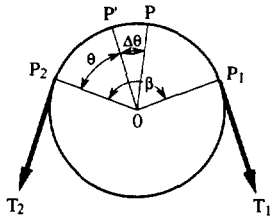
Upper Roller

$$T_3 = e^{\mu_s \beta} T_2$$

$$T_3 = e^{(.2)(3.14)}(25)$$

$$T_3 = 47 \text{ N}$$

The fourth condition is when the mandrel is withdrawn and pulled out of the soil leaving behind the drain and its end assembly. As stated previously, the end assembly anchors the PVD and keeps soft soil out of the mandrel. It is possible, however, that some soil can enter the bottom of the mandrel. This in turn will impede release of the drain and subject it to a tensile force by snagging the PVD at the tip of the mandrel. Assuming such a condition exists, the end assembly constitutes the resisting force, where the



$$\Sigma F_x = 0: (T + \Delta T) \cos \frac{\Delta\theta}{2} - T \cos \frac{\Delta\theta}{2} - \mu_s \Delta N = 0 \quad (1)$$

$$\Sigma F_y = 0: \Delta N - (T + T\Delta) \sin \frac{\Delta\theta}{2} - T \sin \frac{\Delta\theta}{2} = 0 \quad (2)$$

Solving Eq. 2 for ΔN and substituting Eq. 1

$$\Delta T \cos \frac{\Delta\theta}{2} - \mu_s (2T + \Delta T) \sin \frac{\Delta\theta}{2} = 0$$

Divide by $\Delta\theta$

$$\frac{\Delta T}{\Delta\theta} \cos \frac{\Delta\theta}{2} - \mu_s \left(T + \frac{\Delta T}{2} \right) \frac{\sin(\Delta\theta / 2)}{\Delta\theta / 2} = 0$$

Let $\Delta\theta$ approach zero

friction caused by the soil in the end of the mandrel constitutes the driving force. The calculation and assumptions associated with this condition follows. This worst case scenario results in a mobilized strength of approximately 103 N in the PVD.

3.1 Friction in the Mandrel

Using Mohr-Coulomb criteria

$$\tau = \sigma_n \tan \phi + c$$

$$\tau = c \text{ assuming } \phi = 0$$

$$\tau = c = 10,000 \text{ Pa for typical soft clay}$$

$$\Sigma F_y = T_4 - 2\tau e A = 0$$

$$T_4 = 2\tau e A$$

$$T_4 = 2(10,000)(30\%)(.1)$$

$$T_4 = 600 \text{ N}$$

However can such a force be mobilized in the drain?

3.2 Bearing Capacity of End Rod

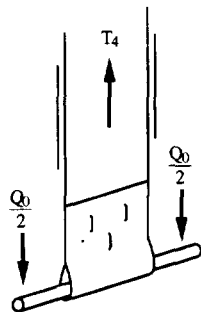
$$Q_o = Q_p + Q_s$$

$$Q_o = A_p p_o + 0$$

$$Q_o = A_p (cN_c + 9N_a)$$

$$Q_o = .002(10,000)(5.14)$$

$$Q_o = 103 \text{ N}$$



Since $Q_o \ll T_4$, T_4 will never be mobilized and therefore Q_o governs

4 LABORATORY INVESTIGATION

The purpose of the laboratory investigation was twofold; to verify, or refute, the theoretical values just calculated (wherein many assumptions were required) and to develop a means of determining the mobilized strength of PVDs in the field. To aid us in these pursuits, we constructed a laboratory wick sticker simulator. A schematic diagram of the laboratory wick sticker simulator is shown in Figure 2. The simulator was constructed in the high bay region of GRI's soils laboratory. The high bay allowed for an upper fixed roller height of 10 m above the floor level.

By positioning a load cell at different locations along the PVD path, one could check the mobilized strength of the drain along the path. Results from this exercise showed that the first, second and third conditions resulted in average load cell responses of 10 N, 18 N and 150 N

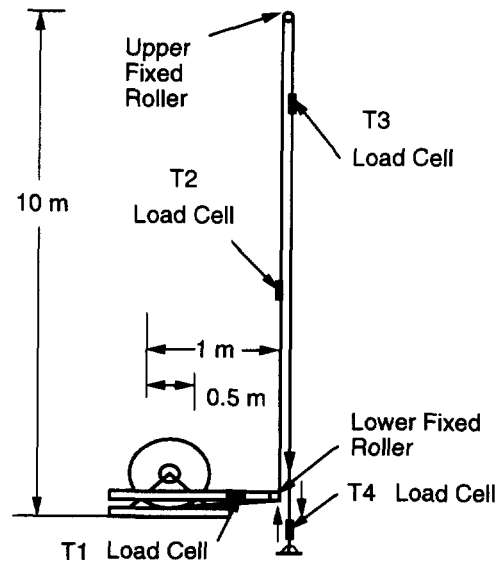


Figure 2 Schematic of laboratory wick sticker simulator.

respectively. To simulate the fourth condition we had to make up a model in the soils lab of an end assembly attached to a PVD being pulled from a freshly remolded column of soft soil. The PVD experienced widely different loads in this simulation depending on the amount of friction imparted in the mock mandrel. Loads in the PVD varied from 25 to 250 N.

These laboratory simulations were interesting, however, it was clear that we could not use the load cell out in the field. It was too cumbersome and fragile to withstand the rigors of field work. Hence we set out on developing a means of determining the mobilized strength of PVDs remotely. Six different techniques were attempted to measure the load elongation response of the PVD. They included:

- Foil strain gages similar to those used by Risseeuw [1986] and Guglielmetti, et al. [1996]
- Load sensitive film which changes color upon being stressed to different levels
- Spray applied coatings which crack to varying degrees after being stressed
- Hole punching to reduce PVD strength
- Side cutting PVD to incrementally reduce its strength
- Development of a simulated PVD unit called "Load-Elongation Measuring Strip" (LEMS)

Of all the techniques attempted, the LEMS showed the most promise. This specially prepared PVD consisting of a polyamide (3 x 3) grid fabric as a core, heat bonded between two 160 g/sq. m. nonwoven PET geotextiles. At 2 m intervals along the LEMS, the geotextile was cut away and specific number of polyamide yarns were cut. This left known numbers of yarns intact which allowed the LEMS to

model progressively weaker PVDs. This procedure was used to develop the curves shown in Figure 3. From this data an average breaking strength of 78 N per yarn was obtained. For comparison purposes, Figure 4 shows the tensile strength behavior of commercially available PVDs. For all tests of Figure 3 and 4 the gage separation was maintained at 100 mm and the strain rate was 10 mm/min.

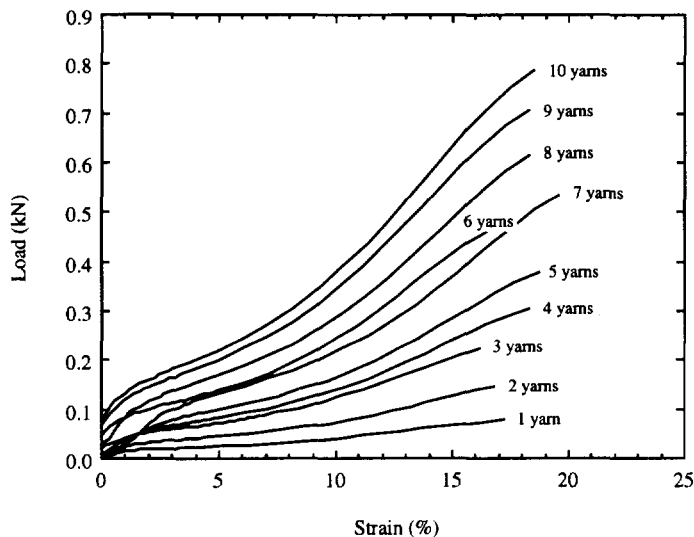


Figure 3 Load elongation behavior of LEMS.

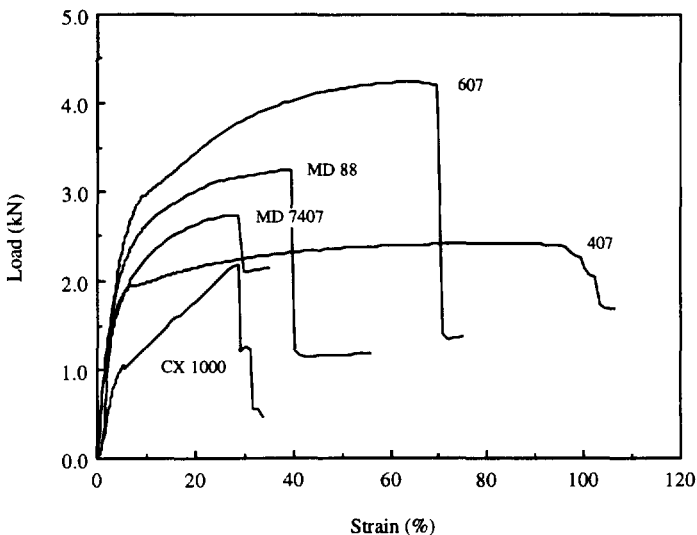


Figure 4 Commercially available PVD load elongation responses.

With the LEMS now calibrated insofar as its strength per yarn is considered, laboratory trials on the wick sticker simulator were undertaken. In conducting these trials friction in the rolls was increased using a brake and weight assembly to sequentially cause failure of the LEMS. The results of approximately 27 trial runs (with different numbers of uncut yarns) provided the results of Figure 5. The trend is linear resulting in a slope of 75 N per yarn. This roughly agrees with the tension testing in the constant rate of extension machine as noted previously. Equipped with this confirmation, we took the LEMS to the field to try and verify our theoretical and laboratory findings.

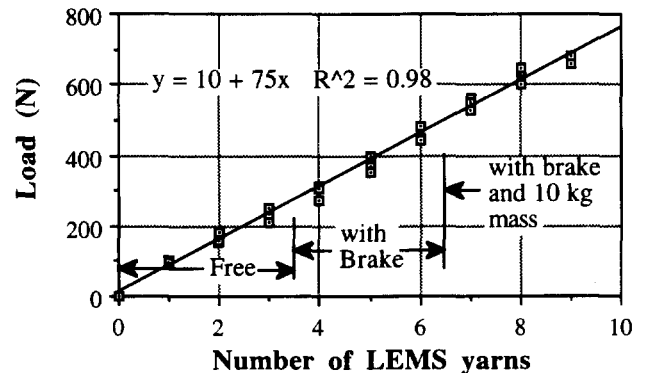


Figure 5 Results of LEMS calibration on simulator.

5 FIELD INVESTIGATION

Field trials with the LEMS material were conducted at a major soft soil stabilization project at the Philadelphia International Airport. Through the cooperation of Day & Zimmerman Infrastructure, Inc. and Geotechnics America, Inc. (the PVD contractor) a field trial of the LEMS was conducted in October of 1997.

As reported by Koerner [1997], the results of the field work are summarized in Table 1.

Table 1 - Field Behavior of LEMS at the Philadelphia International Airport.

No. of Yarns in LEMS	Resulting Strength of LEMS (N)	No. of Repeat Trials	Result of Each Trial
20	1540 N	2	pass/pass
14	1080 N	2	pass/pass
10	770 N	3	pass/pass/pass
5	390 N	3	pass/pass/pass
3	230 N	2	fail/fail

The results of Table 1 indicate that the mobilized PVD strength for this particular construction equipment and site condition is between 390 and 230 N. It must be clearly stated that it is believed that site conditions and

construction equipment will influence results. However, these limited results are insightful none-the-less.

6 SUMMARY AND CONCLUSION

It appears from theoretical calculation, laboratory testing and a limited field investigation that the strength of most commercially available PVDs are greater than required for installation. In addition, it appears that the current trend of increasing the strength requirements of PVDs is unfounded. At present, there does not appear to be any tangible reason for increasing PVD strengths over and above those that are currently being manufactured. For example, Figure 4 indicates that available PVD tensile strengths are from 2000 to 4000 N. Most commercially available PVDs meet or exceed equipment imposed installation stresses as demonstrated in this paper.

In light of the low values of mobilized PVD strengths developed in this study, e.g.,

- theoretically: 14 to 103 N
- experimentally: 10 to 250 N
- field: 230 to 390 N

we are confident in stating that there is an inherent factor of safety for most commercially available PVDs. Of all installation conditions described, it appears that withdrawal of the mandrel is the governing strength condition. Loads during withdrawal of the mandrel are site specific. They depend on the type of anchor plate and will only take place at the tip of the PVD where it connects with the end assembly.

The requirement for discharge of water at this location is limited since it is at the end of the drain. The load in the rest of the drain is probably less than 230 - 390 N. It is interesting to note that this corresponds with an elongation of approximately 2-4% for most PVD.

It is concluded that all commercially available drains have strengths and elongation's at break which are much higher than necessary. Hence, the available factors of safety for mobilized strength is in the range of 4 to 11. We question if the higher factors of safety are warranted in the event that ones construction equipment is functioning properly and geometrically equipped to drive the specific PVD delivered to the specific job site.

ACKNOWLEDGMENTS

The research project was carried out under the general support of the GSI consortium of member organizations. Appreciation is extended in this regard. The authors would like to specifically thank Mr. Timothy Kruppenbacker, construction manager of Day and Zimmermann, Inc. and Mr. John Case, controller of

Geotechnics America, Inc. for their assistance with our field effort.

REFERENCES

- Guglielmetti, J. L., Koerner, G. R. and Battino, F. S. (1996), "Geotextile Reinforcement of Soft Landfill Process Sludge to Facilitate Final Closure: An Instrumented Case Study," Proceedings of GRI-9 Conference on Geosynthetics in Infrastructure, Enhancement and Remediation," R. M. Koerner and G. R. Koerner, Eds., GII Publ., Philadelphia, Pennsylvania, USA.
- Hansbo, S. (1979), "Consolidation of Clay by Band Shaped Prefabricated Drains," *Ground Engineering*, Vol. 12, No. 5, pp. 21-25.
- Holtz, R. D., Jamiolkowski, B., Lancellotta, R. and Pedroni, R. (1991), "Prefabricated Vertical Drains: Design and Performance," Butterworth Heinemann, London.
- Koerner, G. R. (1997), "Field Installation of Prefabricated Vertical Drains," Proceedings of GRI-11 Conference on Installation of Geosynthetics, R. M. Koerner Ed., GII Publication, Philadelphia, Pennsylvania, USA.
- Kremer, R. J., Oostveen, J. P., Van Weele, A. F., DeJager, W. J. and Meyvogel, I. J. (1983), "The Quality of Vertical Drainage," Proceedings of the Eight European Conference on Soil Mechanics and Foundation Engineering, Helsinki, Vol. 2, pp. 721-726.
- Risseuw, P., "Manual for the Attachment of Strain Gauges for Measuring Deformations of Stablenka Reinforcing Fabrics," Enka Industrial Systems, Holland, 1986, p. 23.

Investigation on Some Factors Affecting Discharge Capacity of Prefabricated Vertical Drain

Norihiko MIURA

Professor, Department of Civil Engineering, Saga University, Saga 840, Japan

Jinchun CHAI

Associate Professor, Department of Civil Engineering, Saga University, Saga 840, Japan

Kiyomitsu TOYOTA

Graduate Student, Department of Civil Engineering, Saga University, Saga 840, Japan

ABSTRACT: A series of laboratory tests have been conducted to investigate the effects of (a) trapped air bubbles in drainage path, (b) folding (no kinking) of drain, (c) confining drain by clay, and (d) elapsed time (long term), on discharge capacity of prefabricated vertical drain (PVD). The test results indicate that confining the drain by rubber membrane yielded a much higher discharge capacity than that in clay. It suggests that the discharge capacity test of PVD should be conducted by confining the drain in clay. Also, the discharge capacity reduces significantly with elapsed time, and the long term behavior of PVD should be considered in design. For most commercially available PVDs, a long term discharge capacity of less than 100 m³/year is tentatively suggested for design. The possible air bubbles trapped in the drainage path of PVD has some effect on discharge capacity, and the test data from this study showed about 20% reduction due to this factor. The folding of the drain does not have obvious influence on discharge capacity because it does not change both length and cross sectional area of drainage path much.

KEYWORDS: Prefabricated vertical drain, Laboratory test, Hydraulic conductivity, Drainage.

1 INTRODUCTION

Installing the vertical drain into ground can shorten the drainage length of the deposit significantly, and with some surcharge loading, the engineering properties, in terms of the compressibility and undrained shear strength, of the deposit can be substantially improved. The development of prefabricated vertical drain (PVD) has made this method more attractive due to the portability of the material and lower installation cost. During past few decades, vertical drain improvement has been widely used in soft soil engineering.

For a given soil condition, the behavior of vertical drain improved subsoil is controlled by: (a) drain spacing and equivalent drain diameter, (b) smear effect, and (c) discharge capacity of drain (well resistance). The drain spacing is a known factor and the equivalent drain diameter of PVD can be reliably calculated based on the geometry of the PVD. However, smear effect and discharge capacity have to be determined experimentally. At present, the method for determining the discharge capacity of PVD has not been standardized, and the values reported in the literature are not consistent. Most test methods confine the drain by rubber membrane, such as ASTM D4716-87, and determined values are usually high. However, some low values were reported for confining the drain in clay (e.g. Hansbo 1983). An ideal discharge capacity test should simulate the drain installation, confinement of clay on the filter sleeve of drain, and the deformation of drain during consolidation. It is obvious that a full scale test could be expensive if it is possible. For a small scale laboratory test to be valid, it must consider the important influence factors. In order to improve the laboratory test method and advance the prediction ability on the behavior of vertical drain improved

subsoil, there is a need to investigate the main influencing factors on discharge capacity of PVD.

In this paper, the effect of (a) possible air bubbles trapped in the drainage path, (b) folding (no kinking) of drain which most likely will occur in the field due to consolidation of soil, (c) confining the drain by clay, and (d) elapsed time (long term) on discharge capacity of PVD are systematically investigated. First, the unit cell (a drain surrounded by a soil cylinder) consolidation theory is briefly reviewed to indicate the effect of discharge capacity on the rate of consolidation. Then the laboratory test methods as well as results are presented. The suggestions are made on improving the test method on discharge capacity of PVD.

2 A BRIEF REVIEW ON UNIT CELL THEORY

The basic theory of vertical drain consolidation is unit cell theory which was first proposed by Barron (1948). Further studies on unit cell behavior were made by Yoshikuni and Nakanodo (1974) and Hansbo (1981). Since Hansbo's theory is relatively simple, it has been widely used. The derivation of the theory is based on equal vertical strain assumption. The resulting equation for average degree of radial consolidation (\bar{u}_h) of a unit cell is as follows:

$$\bar{u}_h = 1 - \exp(-8T_h / \mu) \quad (1)$$

$$T_h = \frac{C_h t}{D^2} \quad (2)$$

$$\mu = \ln \frac{n}{s} + \frac{k_h}{k_s} \ln s - \frac{3}{4} + \pi \frac{2l^2 k_h}{3q_w} \quad (3)$$

Where C_h is the horizontal coefficient of consolidation, t is time, D is the diameter of unit cell, k_h is the horizontal permeability of soil, k_s is permeability in smear zone, l is drainage length, q_w is discharge capacity, $n=D/d_w$, and $s=d_s/d_w$ (d_w is the diameter of drain, and d_s is the diameter of smear zone). The last term in Equation 3 represents the well resistance. It can be seen that the larger the discharge capacity, q_w , the smaller the well resistance, and the higher the rate of consolidation. For example, assuming $l=15$ m and $k_h=10^{-8}$ m/sec, if q_w is less than 100 m³/year, it will have a considerable influence on consolidation rate of vertical drain improved subsoil.

3 APPARATUS AND TEST METHODS

3.1 Apparatus and Test Procedure

The apparatus used is a modified triaxial device as shown in Figure 1. The main cell has a diameter of 200 mm and height of 600 mm. The drain sample is set inside the cell similar to that of setting the triaxial test sample. The lower pedestal is fixed at the bottom of the cell and connected to the inlet water flow system. The upper pedestal is movable (for adjusting the length of drain sample) and connected to the outlet water flow system. The drain length can be

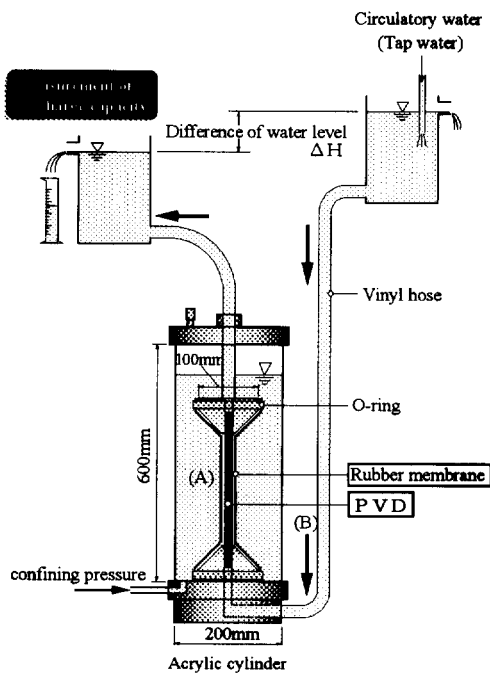


Figure 1. Set-up of discharge capacity test apparatus

tested is 200 mm to 400 mm. The shape of pedestal is made as: one end is cylindrical for fixing the membrane, and rectangular at another end to connect the drain. In this way, when confining the drain by rubber membrane, there will be no gap between membrane and drain. The length of drain inserted into the slot of upper and lower pedestal is about 30 mm each. The diameter of the pedestal is 100 mm. Except the main cell, there are inlet and outlet water containers. The inlet water container is linked with water supply system, and outlet water container is connected to discharge capacity measuring device. After the drain is installed, the cell is filled with water up to about 80% full, and confining pressure is applied by air pressure through an air pressure regulator. For investigating the effect of folding, the drain is folded at one and two point for 10% and 20% vertical strain, respectively. The methods for investigating the possible trapped air bubble effect and confining the drain by clay are described as follows.

3.2 Method for Investigating the Effect of Trapped Air Bubbles

It is considered that installing a drain into ground, the water from soil gradually enters the drain along the whole length of the drain, and there might be some air bubbles trapped into drainage channels. In order to study the possible trapped air bubble effect, a simple air bubble generation device is newly developed. A thin plastic tube is connected to an air tank through an air pressure regulator. Then the tube is placed at the bottom of the drain sample through an inlet hose as shown in Figure 2. The amount of air bubbles generated can be controlled by adjusting the air pressure regulator. The generated air bubbles enter the drain following the water flow. The main test steps are:

- (1) Set-up the drain sample and apply the desired confining pressure as well as hydraulic gradient.

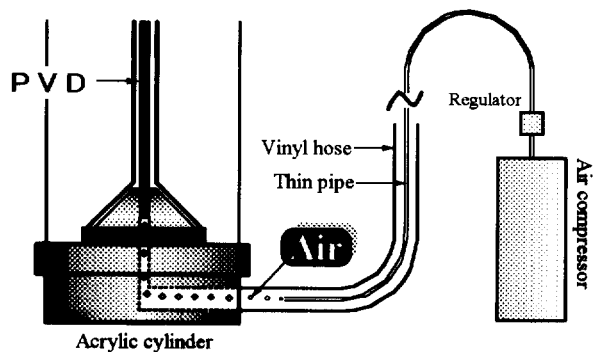


Figure 2. Method for generating air bubbles

- (2) Generate the air bubbles with a diameter of about 1 mm, and a speed of about 100 bubble/min. This process is continued for about 4-6 hours.

- (3) Close the air bubble generation system, and let the water flow continue for more than 2 hours to steady the flow. Then measure the discharge capacity.

3.3 Test Procedure for Confining the Drain by Clay

Hansbo (1983) recognized the importance of confining the drain by clay on determining the discharge capacity. However, due to convenience, most discharge capacity tests conducted by manufacturers are confining the drain by rubber membrane. One of the purposes of this investigation is to compare the discharge capacities determined by clay confinement and membrane confinement. The test method proposed in this study for testing the drain in clay is simple and can test the full size of drain. The following main steps are followed during test:

- (1) Connect the drain sample to lower pedestal, fix the membrane to lower pedestal also, and set the mould for preparing the clay sample in position.
- (2) Make clay sample. The remoulded clay with a water content close to the liquid limit is put into the mould layer by layer keeping the drain in the middle. The diameter of the clay sample is 100 mm. After the required height of clay sample is reached, the upper pedestal is installed and the drain is connected to outlet flow system. Care needs to be paid to prevent the contamination of the top of drain by clay.
- (3) Consolidate the clay sample. For removing the mould, a suction of about 10 kPa is applied to the clay sample. After confining pressure is applied, the suction is gradually released and the sample is left for consolidation under lateral pressure.
- (4) Measure discharge capacity. After the consolidation of clay sample is finished, the discharge capacity is measured under desired hydraulic gradient.

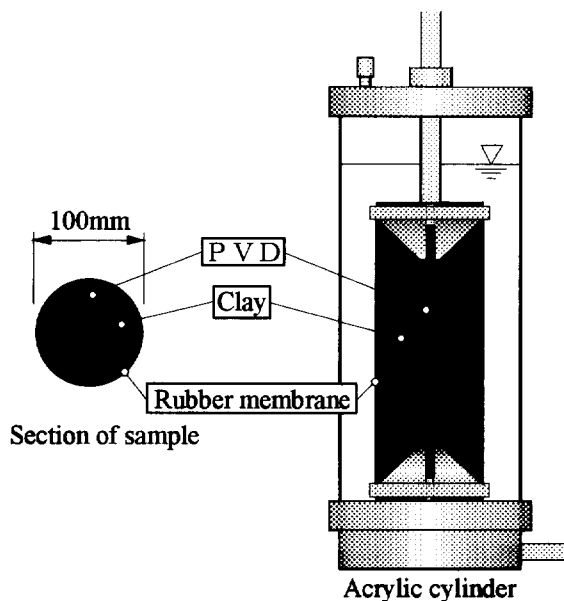


Figure 3. Set-up of confining the drain by clay

The set-up of the drain confined by clay is illustrated in Figure 3. With this method, a test with one consolidation pressure and several hydraulic gradients requires 10 days to complete.

3.4 Considering the Head Lose in Hose System

Another factor which has been noticed during the investigation is head loss in the hose of the test equipment. Since the discharge capacity of drain confined in membrane is normally high, ignoring the head loss in the hose does not introduce much error. For testing the drain in clay, which is close to field condition, the head loss in the testing system needs to be considered. The calibration of the head loss in the hose system can be made by conducting the test without installing a drain sample.

4 TEST RESULTS AND DISCUSSIONS

4.1 Materials Used

The PVD adopted in this study is a commercial products and its properties are summarized in Table 1. The soil used is remoulded Ariake clay. Its index properties are: specific gravity, ρ_s , of 2.60, plastic limit, w_p , of 42.8%, and liquid limit, w_l , of 105.0%. The soil consists of 57.0% clay, 41.7% silt, and 1.3% sand particles. The rubber membrane used has a thickness of 1.0 mm.

Table 1. Physical properties of PVD

Size (mm)	Thickness	2.6
	Width	94
Drainage channel	Depth(mm)	1.5
	Width(mm)	1.8
	No.of channel/drain	40
Unit weight (g/m)		90
Material	Filter	Spun bonded polyester
	Core	Polyolefin
Connection condition between filter and core		Fixed
Structure		

4.2 Short Term Test Results

For ease in quantifying each influencing factor, the test results of confining a straight drain in a rubber membrane are considered as basic ones and other test results are compared with them. The confining pressures for the basic test were 49 and 392 kPa, and hydraulic gradients were

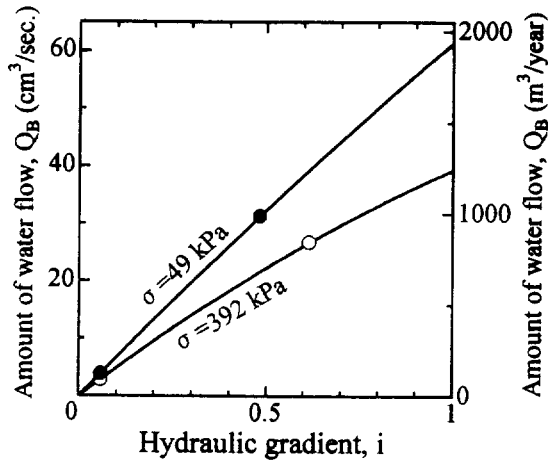


Figure 4. Results of basic test

about 0.08 and 0.8. The results are plotted in Figure 4. It can be seen that as a general tendency the discharge capacity is reduced with increased confining pressure. It is the same as the results reported in the literature (e.g. Hansbo 1987). If extrapolating the results to unit hydraulic gradient ($i=1.0$), a discharge capacity of 1981 $m^3/year$ and 1307 $m^3/year$ can be obtained for confining pressures of 49 kPa and 392 kPa, respectively. The short term test results are summarized in Figure 5. A discharge capacity ratio is used in the figure, which is defined as the amount of water flow, Q , divided by the corresponding value of basic test, Q_b (Q/Q_b). Following discussions can be made for short term test results.

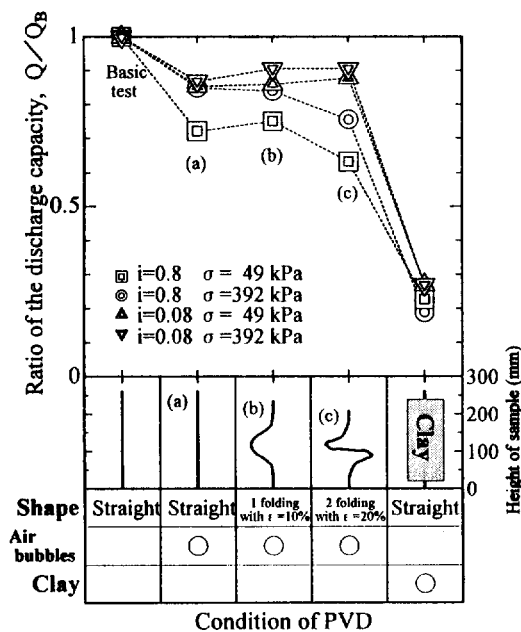


Figure 5. Summary of short term test results

(1) Confining the drain by a rubber membrane can not simulate the actual field condition and the discharge capacity test for determining the design value should confine the drain with clay. When confined by a rubber membrane, it results in a much higher discharge capacity than that in clay. For the case investigated, the clay value is only about 20% of membrane value. Three possible reasons for reduction on discharge capacity of PVD in clay can be considered.

- (a) Reducing the cross sectional area of drainage channel due to deformation of filter under pressure. This has been considered as the main reason. After the test, it was observed that the filter was considerably deformed and the cross sectional area of drainage channel was reduced to 70-50% of original value as shown in Figure 6. The left side of Figure 6 was made by stamping the actually used soil sample on paper. Since the amount of reduction on cross-sectional area is a function of stiffness of filter, as a supplementary information, the tension force versus tension strain relationship of the filter was determined by the laboratory wide strip test, with a strain rate of about 1%/min as shown in Figure 7. For the case of confined in rubber membrane, due to the tension stiffness of membrane, filter can not deform as freely as that in clay.

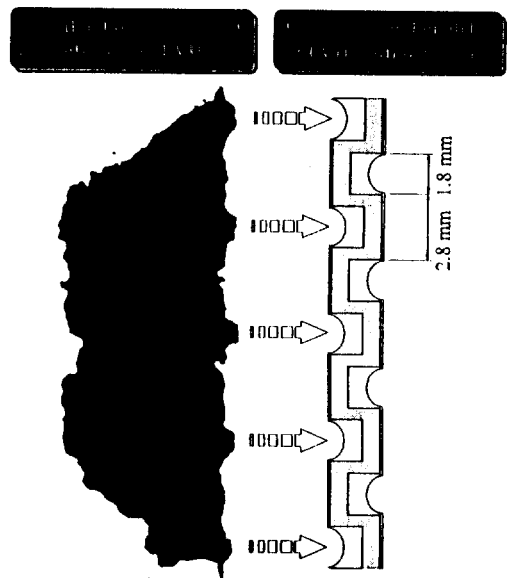


Figure 6. Deformed shape of clay sample adjacent to drain

- (b) Reducing the conductivity of filter in longitudinal direction due to soil particles penetrating into the opening of filter. When confining the drain in rubber membrane, the filter may act as a part of vertical water flow path. In the case of confined by clay, the clay particles will enter the opening of the filter and reduce the conductivity of filter. Since the thickness

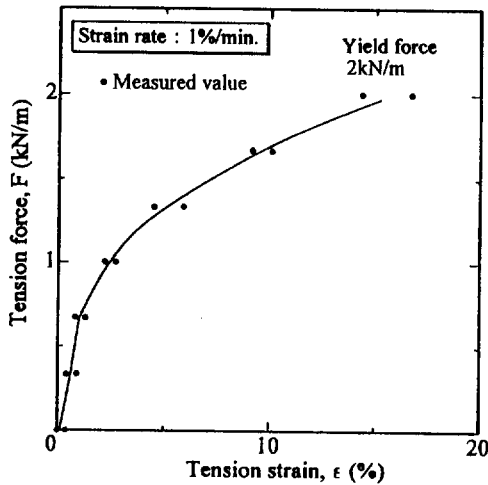


Figure 7. Tensile force versus tensile strain curve for filter

of the filter is only about 0.2 mm, this effect is a minor one.

(c) Clay particles enter the drainage channel. Although the most of filters commercially used satisfy the filtration criteria, the experimental evidence indicates that some amount of very fine particles entered the drainage path and forming loose flocculated sediments on the wall of drainage path. It is considered that the formation of the flocculated sediments is a function of chemical contents of clay.

(2) It seems that not much air bubbles can remain in the drainage path. The data from this study show that the trapped air bubbles reduced the discharge capacity about 20%.

(3) Considering a vertical strain up to 20%, the folding of the drain has minimal effect on discharge capacity, which supports the conclusion drawn by Hansbo (1983). This factor can be explained as the folding of the drain does not change both the length and cross-sectional area of drainage path much. The kinking was not considered in this study because it rarely occurs in the field.

4.3 Long Term Test Results

Only one test of confining the drain in clay was tested for about 5 months. The conditions were: confining pressure of 49 kPa and hydraulic gradient of 0.08. This confining pressure approximately represents the lateral earth pressure in subsoil under a 5 m high embankment or at 10 to 15 m depth of natural subsoil. A lower hydraulic gradient is adopted because, in the field, the average value during consolidation process may not be high. The long term test results are shown in Figure 8, which indicate that the discharge capacity was continuously reduced with elapsed time except the last measurement point. It has been understood that in the interval between the last two measurements, the inlet hose (about 30 mm in diameter and flexible) had been stepped on several times unexpectedly.

Stepping on the water flow hose is just like applying pressure pulses to water flow system. It was observed that some flocculated fine particles were pressured (due to stepping) out of the drainage channel of drain and deposited on the wall of the outlet hose. Based on these results, it is considered that the reasons for the reduction of discharge capacity with elapsed time are (1) creep behavior of filter which reduces the cross-sectional area of drainage path, and (2) clogging caused by flocculated fine particles. As shown in Figure 8, for the case investigated, the creep effect is evaluated as the difference between last measurement point and the reading at about 1 week of elapsed time, which reduced the discharge capacity about 30%. The most reduction can be attributed to the clogging effect which is a function of soil type and filter type. The chemical analysis about the flocculated fine particles as well as the clay mineral is going on and the results will be reported in the future. The discharge capacity reduction with elapsed time was also reported by Koda et al. (1986) for confining the Geodrain in organic soils. For a drain, it is normally expected to work at least half a year. Therefore, in design, long term behavior of drain should be taken into account.

4.4 Discussions

From this investigation, it shows that the most important factors affecting the discharge capacity of PVD are: (a) confining condition, and (b) the duration of test. Therefore, for determining the design value of discharge capacity, the test should be conducted by confining the drain by clay and tested for a longer period (may be few month). If comparing the results from this study with those reported in the literatures, the following comments can be made.

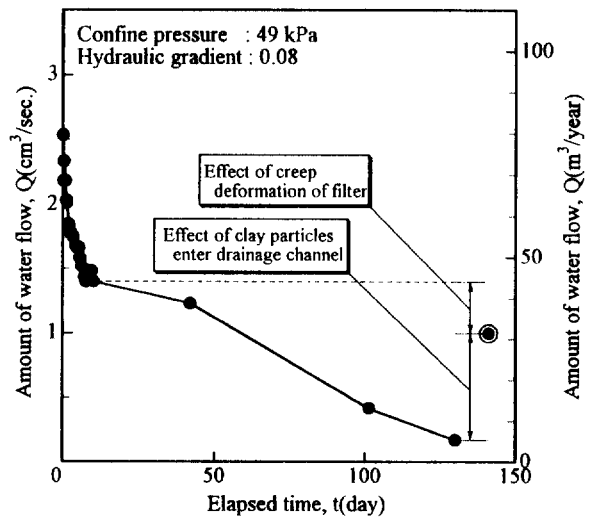


Figure 8. Long term discharge capacity test results

(1) The values of confining the drain by rubber membrane are comparable with the data reported by manufacturers. Due to the apparent high discharge capacity, it may be considered that the well resistance of PVD can be

ignored in design. However, the results of this study suggest that the high value for confining the drain by rubber membrane may not represent the field condition, and well resistance may be an important design factor, especially for long drains. The discharge capacity of confining the drain by rubber membrane may only be used as a quality control test.

(2) In clay short term (about 1 week) value of discharge capacity is in the lower range of the data summarized by Hansbo (1987). Comparing with the specifications about required discharge capacity as summarized by Bergado et al. (1996), it can be seen that with a discharge capacity of few hundreds $m^3/year$, the most specifications can be satisfied. However, the most specifications have no clear requirement about long term behavior.

(3) The long term in clay value (about 5 months) from this study is higher than the data reported by Hansbo (1983) by using the revised CTH (Chalmers University of Technology) method for the similar drain. The revised CTH method also confined the drain in clay with a test duration of less than 1 month. Whether the CTH method considered the head loss in the hose system is not clear, and if not, it might be the reason for the lower value of discharge capacity. The relative lower value of discharge capacity of PVD was also reported by Jamiolkowski et al. (1983). The field discharge capacity may vary with the type of drain, type of clay, and designed consolidation period, but as a rough reference, it is recommended that for most commercial PVD, a design discharge capacity of less than $100 m^3/year$ can be used.

5 CONCLUSIONS

Four influence factors on discharge capacity of PVD are experimentally investigated. These factors are: (a) possible trapped air bubbles in drainage path, (b) folding of drain, (c) confining the drain by clay, and (4) long term behavior. From the test results, following conclusions can be drawn:

1. The discharge capacity of PVD confined in clay is significantly lower than that confined by rubber membrane. It is strongly recommended that for determining the design value, the discharge capacity test should be conducted by confining the drain in clay. The test of confining the drain by rubber membrane not represents the field condition and it might be used for quality control purpose only.
2. The discharge capacity of PVD reduces significantly with elapsed time. For the case investigated, the

long term minimum value is only about 10% of the value at 1 week. This indicates that for design vertical drain improvement, long term behavior of PVD should be considered. For most commercial PVD, a design long term discharge capacity of less than $100 m^3/year$ is tentatively suggested.

3. The possible air bubbles trapped in drainage channel has an effect on discharge capacity. For the case investigated, it shows that the discharge capacity was reduced by about 20% due to the effect of trapped air bubbles.
4. The folding of drain does not influence discharge capacity significantly because it does not change both the length and cross sectional area of drainage path much.

REFERENCES

- Barron, R. A. (1948) "Consolidation of fine-grained soils by drain wells", *Trans. ASCE*, Vol. 113, pp. 718-742.
- Bergado, D.T., Manivannan, R., and Balasubramaniam, A.S. (1996) "Proposed criteria for discharge capacity of prefabricated vertical drain", *Geotextiles and Geomembranes*, Vol. 14, pp. 481-505.
- Hansbo, S. (1981) "Consolidation of fine-grained soils by prefabricated drains", *Proc. 10th Int. Conf. Soil Mech. and Found. Eng.*, Stockholm, Vol. 3, pp. 677-682.
- Hansbo, S. (1983) "How to evaluate the properties of prefabricated drains", *Proc. of 8th ECSMFEE*, Helsinki, Vol. 2 pp. 621-626.
- Hansbo, S. (1987) "Design aspects of vertical drains and lime column installations", *Proc. of the 9th southeast Asian Geotechnical Conference*, Bangkok, Vol. 2, pp. 8-1 to 8-12.
- Jamiolkowski, M., Lancellotta, R., and Wolski, W. (1983) "Pre-compression and speeding up consolidation, General Report", *Special Session 6, Proc. Eighth Europe Conf. Soil Mech. and Found. Engrg.*, Rotterdam, A.A. Balkema, pp. 1201-1226.
- Koda, E., Szymanski, A., and Wolski, W. (1986) "Laboratory tests on Geodrains durability in organic soils", Seminar on Laboratory Testing of Prefabricated Band-Shaped Drains, Milan, Italy.
- Yoshikuni, H. and Nakanodo, H. (1974) "Consolidation of soils by vertical drain wells with finite permeability", *Soils and Foundations*, Vol. 14, No. 2, pp. 35-46.

Design of a New Geocomposite Vertical Wick Drains for Ground Improvement

J. N. Mandal

Department of Civil engineering, Indian Institute of Technology, Powai, Mumbai-400076, India.

V. S. Kanagi

Department of Civil engineering, Indian Institute of Technology, Powai, Mumbai-400076, India.

ABSTRACT: During the past few decades, an increasing need has arisen for various types of civil engineering projects on construction sites underlain by thick deposit of soft cohesive soils. Parallel to the development of the sand drains, different types of prefabricated vertical strip drains were developed and were used exclusively in various projects. In this paper, a new cylindrical prefabricated geocomposite drain (environmental friendly coir and jute) has developed and can be used to accelerate the consolidation of soil thereby making the site available for the use in short time. The relatively low cost of manufacture and installation makes this drain quite attractive. A design methodology has been developed and the results are presented in the form of design charts for the handy use.

KEYWORDS: Prefabricated vertical drains, Soft soils, Drainage, Filtration, Geocomposite.

1 INTRODUCTION

In the recent years many civil engineering projects have been under-taken on the sites which are underlain by thick deposits of soft cohesive soils. In such situations a ground improvement technique is essentially needed to provide adequate soil properties viz., bearing capacity and tolerable post construction total and differential settlements. Preloading and precompression are frequently used in combination with vertical drains, (Hausman, 1990. Holtz, 1987 and Johnston, 1970) especially in areas of very thick deposits of soft soils with high percentage of moisture content. The main purpose of vertical drains is to accelerate the consolidation time by shortening the drainage path. Usually sand drains are used for these purposes (Bergado, et al., 1992). The prefabricated drains were first introduced into the field of geotechnical engineering by Kjellman (1948). Improvement of the Kjellman wick drain included using a grooved plastic core in place of cardboard.

The various types of prefabricated vertical drains, their common installation methods and pertinent characteristics have been documented. (Jamiolkowski et al., 1983 and Koerner, 1994). Most of the prefabricated drains made of natural materials viz., jute and coir has also been studied. (Lee et al., 1989; Ramaswamy, 1994; Dastidar, 1969; Dinesh Mohan, 1977; Sengupta, 1980 and Mandal and Shiv, 1992). As two components of natural geocomposite drains (i.e. jute and coir) are readily available in the Indian subcontinent at low cost, an attempt has been made in the present paper to develop a new design methodology to install geocomposite drains in soft cohesive soils. The design charts are also presented for handy use.

2 GEOCOMPOSITE DRAINS

Generally geocomposite drains are made of synthetic materials, yet some geocomposite drains are made of natural fibre extracted from jute and coir. Different configurations of natural geocomposite drains are shown in Figure-1. The schematic diagram of a natural geocomposite drain for which the nomogram is developed is shown in Figure-2.

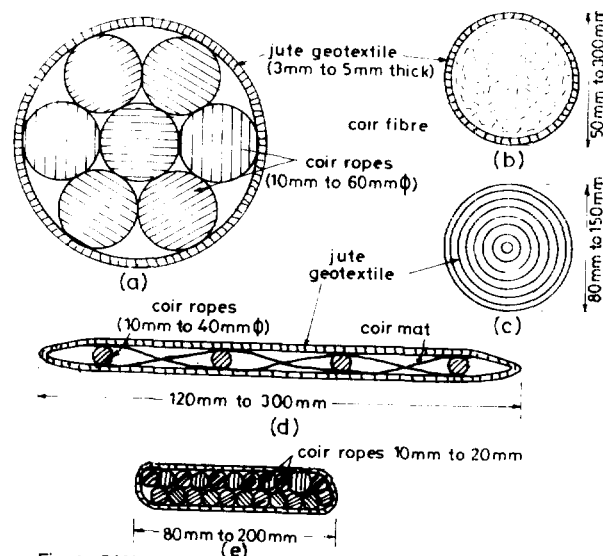


Fig. 1. Different types of geocomposite drains

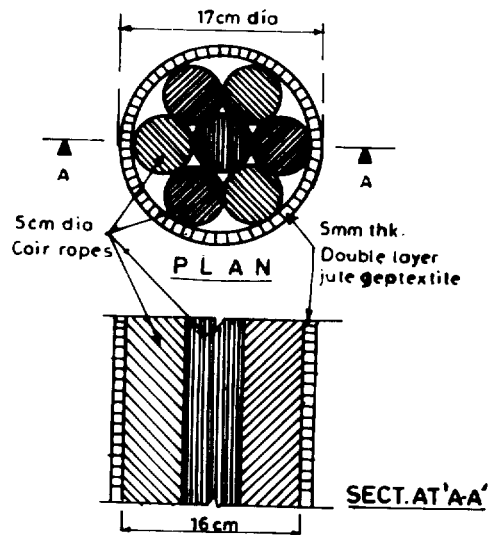


Fig. 2 Geocomposites vertical wick drain

Seven coir ropes of diameter 10mm to 60mm are grouped to form one geocomposite drain. These ropes are tied with jute rope at a spacing of 60cm. This group of coir rope is then wrapped with double layer of jute geotextile. The geocomposite drain diameter varies from 50mm to 200mm. The coir ropes provide longitudinal channels to allow percolation where as the filtering quality of the drain is furnished by the two jute burlap layers.

This geocomposite drain can be designed and manufactured to suit the needs of the specific requirements of different soil improvement projects. It is flexible, rugged, resistant to clogging adequately strong in tension and sufficiently durable. The properties of this geocomposite drain and a typical natural soil are given in Table 1. Jute and coir are by nature strong and not easily decomposable under adverse environmental conditions. The geocomposite drain is relatively resistant to chemical action and loses its strength usually after two years of installation in soft marine clay. (Ramaswamy, 1994)

Table 1 Properties of geocomposite drain and soil

a) Material

1) Jute fibre

Thread diameter : 1.5 to 2.0 mm
weight: 450 g/m²
Tensile strength = 13 KN./m

2) Coir rope

Rope diameter: 10mm to 60mm.
weight: 350 g/m²
Tensile strength = 11 KN./m

b) Geocomposite drain

- i) Components : seven number of coir ropes of diameter 10mm to 60mm wrapped by double layer jute geotextile.
- ii) Diameter: 100mm to 200mm.
- iii) Filter cover permeability $> 10^{-3}$ cm/sec.
- iv) Axial permeability : > 10 cm/sec for confining pressure up to 330 KN /sq.m

c) Marine clay

specific gravity = 2.65
liquid limit = 78%
plastic limit = 38%
plasticity index = 40%

2.1 Function of Natural Geocomposite Drain

The function of geocomposite drains are:

1. The jute fiber has the capacity to accept water through the filter jacket and work as water absorbent material.

2. The coir has the capacity to discharge the water quickly out of the consolidation soil strata.

The natural geocomposite drain has a unique structure that enhances the function as a filter fabric has high permeability and restricts the erosion of soil particles. At the same time it allows very fine particles from the soil to flow in and out of the drain without clogging. Removal of very fine sand particles is beneficial as this allow larger particles to form a highly permeable soil network against the fabric.

3 DESIGN CONSIDERATION

The procedure for the design of vertical drains are based on Terzaghi's one dimensional consolidation theory as suggested by (Barron, 1948, Richart, 1959, Kjellman, 1948 and Hansbo, 1979)

3.1 Design Parameters:

The spacing of the vertical drain is governed by

- soil properties
- boundary and drainage conditions
- desired degree of consolidation
- time available for consolidation
- drain installation pattern and
- height of surcharge or fill load.

The degree of consolidation, surcharge intensity, settlement, pore water pressure and drain parameters are interrelated. The degree of improvement of soil properties depends on percentage settlement, dissipation of pore water pressure, increase in effective stress or

increase of shear strength and the drain spacing can be obtained from (Barron, 1948). A more rigorous approach to drain design has been used in Europe and utilizes a combination of Kjellman's, (1948) original work and Hansbo (1979), the relevant design equation follow:

$$t = \frac{D^2}{8Ch} \left[\frac{\ln\left(\frac{D}{d}\right)}{1 - \left(\frac{d}{D}\right)^2} - \frac{3 - \left(\frac{d}{D}\right)^2}{4} \right] \ln \frac{1}{1-U}$$

which can be simplified, since d/D is small, to

$$t = \frac{D^2}{8Ch} \left[\ln\left(\frac{D}{d}\right) - 0.75 \right] \ln \frac{1}{1-U} \quad (1)$$

where : t = consolidation time

Ch = coefficient of consolidation for horizontal flow

d = equivalent diameter of the wick drain (\approx circumference / π)

D = sphere of influence of the wick drain (for a triangular pattern use 1.05 times the spacing, for a square pattern use 1.13 times the spacing)

U = average degree of consolidation.

From equation 1 a nomogram has been developed which relate degree of consolidation, coefficient of consolidation Ch , and the required drain spacing. The results are plotted in a graphical form as shown in Figure-3.

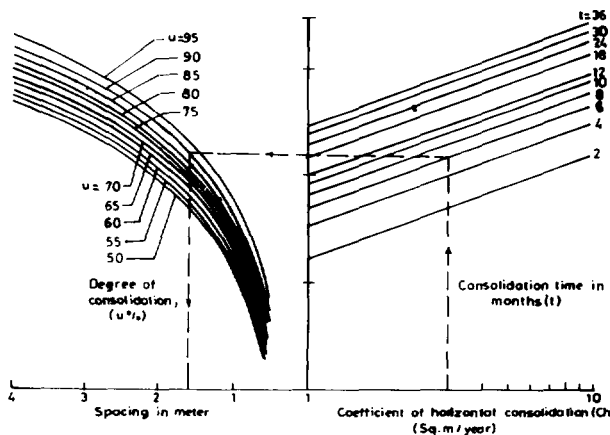


Fig. 3 Nomogram for geocomposite drain (15 cm diameter)

4 CONSTRUCTION PROCEDURE

Geocomposite drains can be lowered into the drill holes made by readily available piling equipment. Koerner (1994) has given varieties of base plates to attach geocomposite drains at bottom of lanes. Similar types of drain plates can be used for lowering the natural geocomposite drain. A coir fabric at the ground surface is proposed for quick drainage of dissipated water beneath the embankment, instead of costly sand blanket. Since geocomposite drain allows faster consolidation the embankment layer thickness may also be increased to complete work at the earliest.

5 CONCLUSIONS

The natural geocomposite vertical drain has been developed to speed up the consolidation process for various types of construction on sites underlain by thick deposits of soft clays. It is flexible, resistant to clogging, resistance to ultraviolet rays, relatively more permeable, strong in tension and sufficiently durable, low cost and environmental superiority over geosynthetics. As with synthetic geocomposite drains the natural geocomposite drain can be designed and manufactured to suit the specific requirements of different soil improvement projects.

ACKNOWLEDGMENTS

The authors are grateful to Prof. S. P. Sukhatme, Director IIT, Powai, Bombay, for his encouragement and the use of facilities.

REFERENCES

- Barron, R. A. (1948), "Consolidation of Fine Grained Soils by Drain Wells", ASCE, Transaction, Paper No. 2346, Vol. 113, PP. 718-754.
- Bergado, D. T., Alfaro, M. C. and Balsubramaniam, A. S. (1992), "Improvement of Soft Bangkok Clay using Vertical Drains" *Geotechnical Engineering Bulletin*, Vol. 1, No. 2, PP. 3-30.
- Dastidar, A. G. , Gupta, S. and Ghosh, T. K. (1969), "Application of Sand Wick in Housing Project, Int. Conf. on Soil Mechanics and Foundation Engineering, Mexico, PP. 59-64.
- Dinesh Mohan (1977), "Consolidation of Ground by Vertical Rope Drains" *Indian Geotech Journal*, Vol 7, No. 2, PP. 106-115.
- Hansbo, S. (1979), "Consolidation of Clay by Band-Shaped Prefabricated Drains", *Ground Engineering*, Vol. 12, No. 5, pp. 16-25.
- Hausman, M. R. (1990), "Engineering Principle of Ground Modification", McGraw Hill International Edition, P.632.
- Holtz, R. D. (1987), "Preloading with Prefabricated Vertical Strip Drains" *Geotextile and Geomembrane*, Vol. 6, PP. 109-131.
- Jamiolkowski, M., Lancellotta, R. and Wolski, W. (1983), "Precompression and speeding up consolidation", General report, specially session 6, Proc.8th ECSMFE, Helsinki, Vol.3, PP. 1201-1226.
- Johnston, S. J.(1970), "Foundation Precompression with Vertical Sand Drains" *Journal of Soil Mech. and Foundation Division*, ASCE, Vol. 96, No. 1, PP. 145-175.
- Kejellman, W. (1948), "Accelerating Consolidation of Fine Grained Soils by Means of Cardboard Wicks", *Proceeding Second Int. Conf. On Soil Mech. and Foundation Engineering*, Rotterdam, Vol. 2, PP. 302-305.
- Koerner, R. M. (1994), "Designing with Geosynthetics", Prentice Hall Englewood Cliffs, New Jersey, Second Edition, USA.
- Lee, S. L., Karunaratne, G. P., Yong, K. Y., and Ramaswamy, S. D. (1989), "Performance of Fiber Drain in Consolidation of Soft Soils", *Proc. 12th Int. Conf. SMFE. Rio De Janeiro, Brazil*, PP. 1667-1670.
- Mandal, J. N. and Shiv, A. (1992), "CAD on Geocomposite Vertical Strip Drains" *Construction and Building Material*, Vol. 6, No. 4, PP. 219-225.
- McGown, A., Marsland, A., Radwan, A. M. and Gabar, A. W. (1980), " Recording and Interpreting Soil Macrofabric Data", *Geotechnique*, Vol. 30, PP. 417-447.
- Ramaswamy, S. D. (1994), "Potential of Jute Assembled Soil Stabilizers", *Proc. 2nd. Int. Workshop on Geotextiles*, 11-12 Jan. New Delhi, PP 77-85.
- Sengupta. D. P. (1980), " Sub-strata Treatment for a Building using Rope Drains", *Indian Geotech. Journal*, Vol. 10, No. 4, PP 322-332.
- Richart, F. E. (1959), "Review of the Theories Sand Drains", *ASCE Trans. Vol. 124*, Paper No. 2999, PP. 709-739.
- Wissa, E. A., Davis, E. H., Christian, J. T. and Heibergs, S., "Consolidation at Constant Strain", *ASCE Journal. of Geotechnical Engg. Vol. 97*, pp. 1393-1413.

Critical Evaluation of Laboratory Drain Tests Simulating Field Conditions

G.P. Karunaratne

Formerly Associate Professor, Department of Civil Engineering, National University of Singapore

S.A. Tan

Senior Lecturer, Department of Civil Engineering, National University of Singapore

S.H. Chew

Lecturer, Department of Civil Engineering, National University of Singapore

S.L. Loh

Research Scholar, Department of Civil Engineering, National University of Singapore

ABSTRACT: The discharge capacity of vertical drains is found to be significantly affected by the testing conditions. This paper presents the drainage performance of prefabricated vertical drains (PVD) under simulated field conditions, using a new drain testing apparatus. This apparatus can simulate realistic field conditions for vertical drains in soft clay deposits. Due to large ground settlement in soft clay, vertical drains may subject to excessive strains and formation of kinks. In general, such drains will have a lower discharge capacity than straight drains. Therefore, in addition to the realistic field properties of soil, critical evaluation of the laboratory determined discharge capacity is needed to understand the field performance of PVD. The testing conditions that can be simulated in this apparatus include varying confinement pressure, kinking of drains and packing in clayey soils. It is seen that different types of prefabricated vertical drains have significantly different discharge capacities under similar testing conditions. A comparative study of the discharge capacity of four drains under various test conditions is also presented in this paper.

KEYWORDS: Prefabricated vertical drains, Confining air pressure, Discharge capacity, Kinking, Testing

1 INTRODUCTION

Prefabricated vertical drains (PVD) are often used to accelerate consolidation of soft clay soils in ground improvement projects. Many types of prefabricated vertical drains are available in the market. To determine the suitability of a drain for a given project an evaluation of discharge capacity is needed. A new drain testing apparatus for PVD was developed at the National University of Singapore (NUS), to closely simulate the field conditions in such tests. The simulated testing conditions include varying confining pressure, kinking of drains and packing of clay around them. Four types of PVDs were tested under these conditions.

Hansbo (1983) recommended that testing of vertical drains should be carried out by placing it in an impervious soil. Lawrence and Koerner (1988) examined the influence of the kinks on the discharge capacity of drains. Based on these two conditions the discharge capacity of kinked drains that have packed clay around them is an important condition to be specified. The results of such tests with the new apparatus are discussed in this paper.

2 NUS DRAIN TESTING APPARATUS

A vertical drain testing apparatus was designed and fabricated to determine the discharge capacity and the transmissivity of prefabricated vertical drains (Loh, 1996). The design of the apparatus adheres closely to the ASTM Standard D4716-87 specifications and the conditions stated in the Hansbo (1983) 'ideal test'. The apparatus consists of three main detachable components: a constant head inlet reservoir, an outlet reservoir and a transparent, cylindrical compressed air chamber as shown in Figure 1.

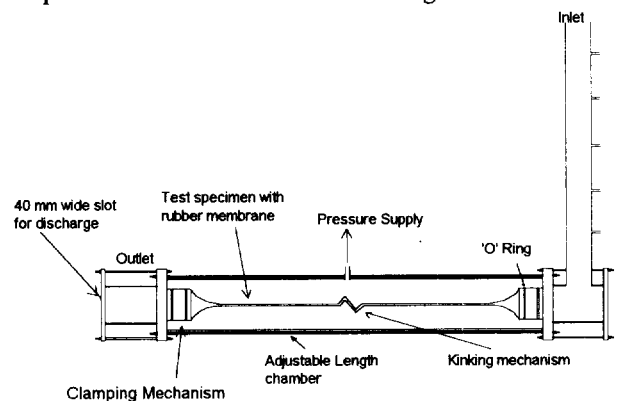


Figure 1: Schematic diagram of the NUS drain testing apparatus (Loh, 1996)

Table 1: Physical properties of the PVD tested

	VD1	VD	VD3	VD4
Mass/unit area (g/mm ²) x10 ⁻⁴	11.81	2.92	4.06	3.4
Core type	Coir	Polypropylene	Polypropylene	Polyester
Core structure		 Continuous channel	 button extrusion	XXXXXXXXXX nylon web
Sleeve filter	Double layer of woven Jute	Polypropylene non-woven	Polypropylene non-woven	Polyester non-woven
Dimensions (W mm x t mm)	100 x 8	100 x 6	100 x 6	100 x 6

The compressed air chamber is designed to be large enough to accommodate a kinking mechanism, which consists of two angle plates. The angle plates can be placed against the drain to form a kink at any desired angle. Hence the discharge capacity of kinked drains can be determined. Remoulded clay can be packed around the drain, which is then encased in a rubber membrane, in order to ensure that the effective lateral pressure of the soil against the drain sleeve is acting as in the field. The liquidity index of the remoulded clay was 0.6 to 0.7. With this layer of clay coming into contact with the drains, there will be a better simulation of the field conditions.

3 TYPES OF DRAINS

Four types of prefabricated vertical drains were investigated in this apparatus. VD1 is made of natural fibres of jute and coir. Two layers of jute burlap (Lee et al 1996) envelop four coir strands of 5-6mm in diameter made of coconut fibre. VD2, VD3 and VD4 are geosynthetic drains with different core types and core structures. VD2 has continuous rectangular channels whereas VD3 has button extrusions formed on the polypropylene core. VD4 has a polyester nylon web type of core (Hausmann, 1990). Salient physical properties of the four prefabricated vertical drains are shown in Table 1.

4 TEST RESULTS

4.1 Confining Pressure

The four PVDs were tested under a range of confining pressures from 20kPa - 300kPa, which is equivalent to a lateral pressure in 30m-40m thick submerged soft clay. High confining pressure is needed to determine the discharge capacity of such PVD installed at great depths. Figure 2 shows the results for the four drains tested. For all drains, it is noted that with an increase in confining pressure, there is a reduction in discharge capacity. This is to be expected as reported by Hansbo (1993), Kamon et al (1992) and Broms et al (1994). The filter sleeve squeezes

into the core with increased confining pressure and hence the effective cross-sectional area of the core is reduced, leading to a reduction in the discharge capacity.

VD1 has the lowest discharge capacity among the drains tested. VD2 and VD3 have polypropylene non-woven filter sleeves, which were partially squeezed into the channels in the core at large confining pressures. This reduction in core space causes a drastic reduction in the discharge capacity. It is observed that the discharge capacity of VD4 is lower than that of VD2 at low confining pressures, but is the highest among the four at 300 kPa pressure. The relatively high discharge capacity is due to the relative stiffness of the nylon web type of core structure and the filter sleeve. The relatively high stiffness is more effective in preventing the filter sleeve from being squeezed into the core at high confining pressures.

4.2 Type of Confinement

It is very important to have a close simulation of the field conditions of the drains in a study of this type. Besides changing the hydraulic gradient and confining pressure, tests were conducted using different confinement methods for each PVD. These included packing of clay around the PVD, with or without a stiff plate, as prescribed in the ASTM in applying pressure on the PVD.

Hansbo (1983) commented that the determination of the discharge capacity of a drain wrapped in a film of polyethylene and placed between two steel plates is inaccurate in this regard. He recommended that, in order to determine the discharge capacity of a drain, clay should be packed around the drains to ensure that the effective lateral pressure of the soil acting on the drain sleeve is similar to that in the field. The ASTM specification and the testing conditions used by many other workers, for instance Chang et al (1994), are similar without any clay directly around the drain. Hence from the above discussion, it was decided to determine the discharge capacity of PVDs with the placement of a rigid plate, as per ASTM, and to compare the results with those conducted with clay packed PVDs, as

proposed by Hansbo (1983). Two rigid perspex plates placed on either side of the PVD served the purpose.

In Figure 3, the drains lined with rigid (perspex) plates have nearly always a larger discharge capacity than those without rigid plates. The drains with the packed clay around fall in between the discharge capacities measured with and without perspex plates. Hence, clay packing is a closer simulation of the field conditions.

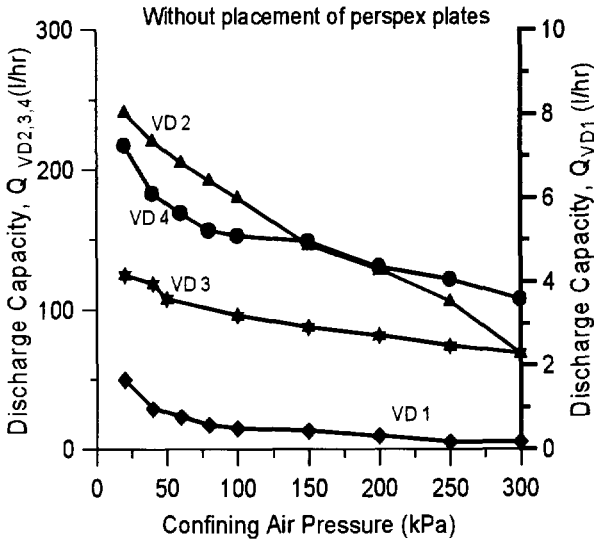


Figure 2: Discharge capacity of different types of PVD

4.3 Kinking of Drains

Another field condition likely to be encountered is the kinking of drains (Lawrence and Koerner, 1988). Two series of kinking tests were conducted. In the first series, an artificial kink with 135° angle was introduced. The second series was a “natural” kink carried out by imposing a 25% axial strain on the drain, similar to the drain deformation in the field. Lawrence and Koerner (1988) observed that with kinks in the PVDs, there is a reduction in discharge capacity.

Figure 4 shows the discharge capacity of straight and kinked drains and Figure 5 shows the percentage reduction of the discharge capacity of kinked drains compared to the straight drains. It is clear that the discharge capacity of straight drains is always higher than that of kinked drains. Although straight VD2 showed much higher discharge capacity than VD3, kinked VD2 showed a greater percentage reduction in discharge capacity than kinked VD3 at 135°. It is apparent that VD3 has a more rigid core structure than VD2. At a confining pressure of 350 kPa, the percentage reduction of discharge capacity for VD4 is the lowest, whereas VD2 has the highest reduction. Tests were also performed with artificial and natural kinks.

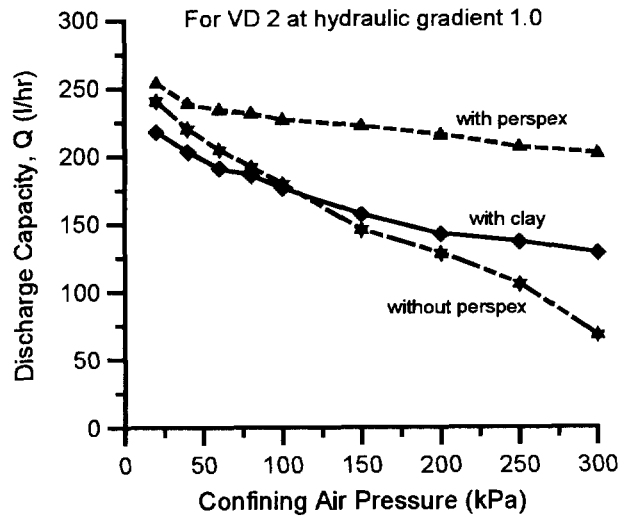


Figure 3: Discharge capacity of VD2 under confinement with/without stiff perspex/clay around

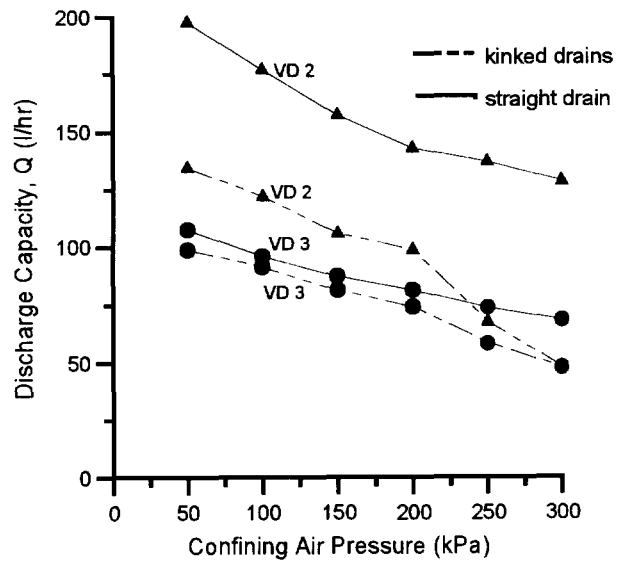


Figure 4: Discharge capacity of kinked and straight drains

Figure 6 gives a comparison of results for the two series of tests with artificial and natural kinks. Drains with natural kinks tend to have a higher discharge capacity than drains with artificial kinks. Discharge capacity of kinked drains obtained from natural kink is more realistic as kinks are formed naturally in the field. Figure 7 shows the discharge capacity of drains with natural kinks and clay packing around the drain. The discharge capacity of VD4 is the highest in the kinked condition. This type of drain has a nylon web type of core which is robust and does not collapse much when kinked. Also its filter sleeve is relatively stiff compared to those of VD2 and VD3 and hence it is not squeezed into the core at high confining pressure. In the case of VD1 the discharge remains very low both in the straight and kinked conditions.

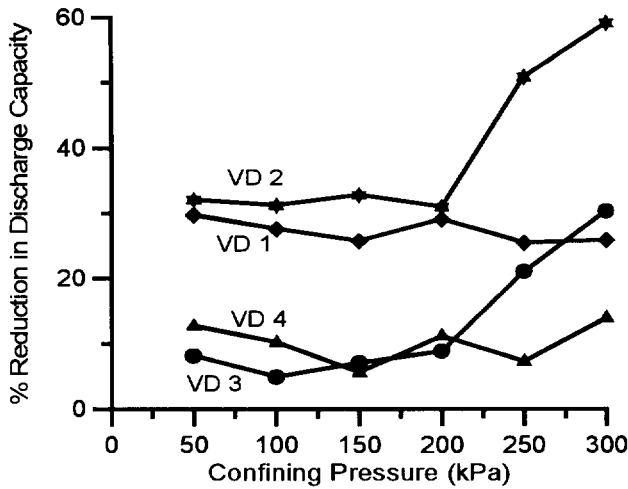


Figure 5: Percentage reduction in discharge capacity of kinked drains

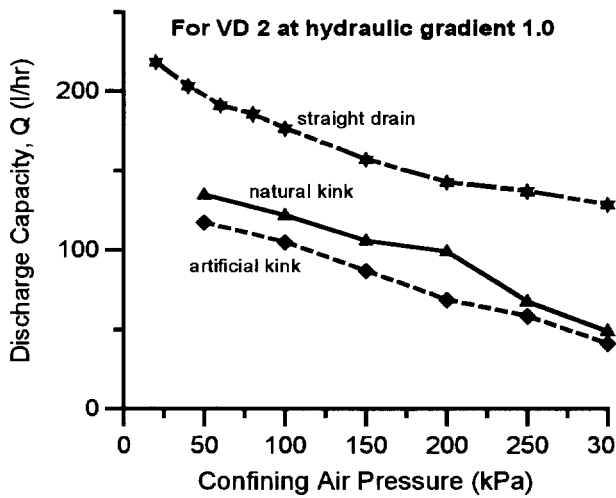


Figure 6: Discharge capacity of VD2 with different types of kinks

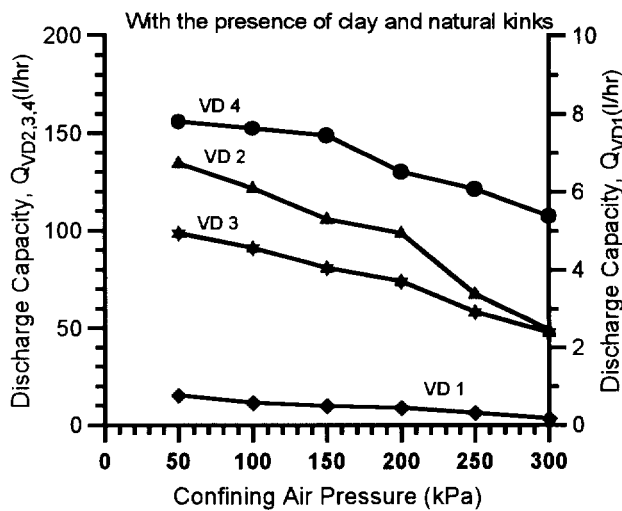


Figure 7: Discharge capacity of PVD with 25% axial compression

5 CONCLUSION

Four types of PVDs were tested in a new apparatus. It is observed that the core structure of the drain plays an important role in the estimation of the discharge capacity. In testing PVDs, the method of confinement of PVDs has a great influence on the discharge capacity. Different confinement modes can yield considerably different results. Other conditions such as kinking of drains are also important when choosing a PVD for a given project. To be more realistic in the measurement of discharge capacity, the confinement pressure on PVD should be applied through a packed layer of clay, where the PVD is to be used, and a natural kink should also be incorporated during the test.

6 REFERENCES

- ASTM D4716-87 (1987), "Standard Test Method for Constant Head Hydraulic Transmissivity (In-plane flow) of Geotextiles and Geotextile related products".
- Broms B.B., Chu J. and Choa V. (1994), "Measuring the Discharge Capacity of Band Drains by a New Drain Tester", *Proceedings of Fifth International Conference on Geotextile, Geomembranes and Related Products*, Singapore, vol. 2, pp 803-806.
- Chang D.T.T., Liao J.C. and Lai S.P. (1994), "Laboratory Study of Vertical drains for a Ground Improvement Project in Taipei", *Proceedings of Fifth International Conference on Geotextile, Geomembranes and Related Products*, Singapore, vol. 2, pp 807-812.
- Hansbo, S. (1983), "How to Evaluate the Properties of Prefabricated Drains", *Proceedings VIIIth ECSMFE*, Helsinki, vol. 2, pp 621-626.
- Hansbo, S. (1993), *Ground Improvement*, Chapman and Hall, CRC Press, Florida, USA
- Kamon M., Pradhan T.B.S and Suwa S. (1992), *Soil Improvement - Current Japanese Materials Research vol. 9*, ELSEVIER Science Publisher Ltd and The Society of Materials Science, Japan
- Hausmann, M. R. (1990), *Engineering Principles of Ground Modification*, McGraw-Hill International Editions.
- Lawrence C.A. and Koerner R.M. (1988), Flow Behaviour of Kinked Strip Drains, *Proceeding Geosynthetic for Soil Improvement - Geotechnical Special Publication No. 18*, pp 22-39.
- Lee S.L. Karunaratne G.P., Aziz M.A. and Yong K.Y. (1996), "Fibredrain and its application in land reclamation and ground improvement", *Proceedings of Joint NUS-Fukken seminar on Land Reclamation and Ground Improvement*, Singapore, pp 1-28.
- Loh S.L. (1996), *Vertical Drains Capacity Test*, B.Eng. Thesis, National University of Singapore.

Geotextiles for the ElDorado International Airport in Colombia

A. Malagón

Civil Engineer, Manager of Ingeniería & Geosintéticos Ltda, Santafé de Bogotá, Colombia, South America

ABSTRACT: This document presents the case history of the utilization, between 1996 and 1997, of 1,220,000 m² of woven geotextiles, reinforcing the foundation of embankments constructed on soft soils, and 25,000 m² of nonwoven geotextiles for filtration, on the second runway of the ElDorado International Airport. In Colombia, geosynthetics have been used since the 1980s; however this is the first job that has been reinforced by high tensile strength geotextiles. The foundation soil at the project site consists of a deep deposit of lacustrine origin, poorly consolidated. The original design was based on improving the characteristics of the soil's resistance through preconsolidation by overload, with the use of wick drains. The building contractor, based on a further investigation of the subsoil, presented and obtained the approval of an alternative, that does not contemplate the preconsolidation nor the wick drains, but rather includes the reinforcement of the foundations of the embankments by woven geotextiles.

KEY WORDS: Airport Construction, Soft Soils, Wick Drains, Geotextiles, and Reinforcement

1. INTRODUCTION

The use of geosynthetics in Colombia was initiated during the 1980s with the utilization of geotextiles for soil separation and filtration, with the specific purpose of avoiding contamination of structures below pavements and porous mediums in drainage systems. Later, geotextiles were used to reinforce foundations and to construct mechanically stabilized soil retaining walls. In the beginning of the nineties decade, the use of geomembranes started mainly to avoid or diminish leaks in such works as (a) water storage, (b) wastewater treatment and (c) disposition of solid contaminants. Other geosynthetics such as geogrids, geonets, and so on, have been used occasionally in limited quantities.

The development of the geosynthetics market in Colombia, without being very great, has been faster than the diffusion and acquisition of the necessary technical know-how for its correct use and specification. In Colombia, there are no technical norms that regulate the specification, the design and the construction with geosynthetics nor is there an impartial entity that can duly assess the engineer. The industry, along with some universities and engineering firms, has made great efforts to spread the technology but the results are limited and in some case arguable.

On the other hand, Colombia suffers from a lack of runways and transportation infrastructure, which has led some investigators to calculate that Colombia is behind its own necessities by about thirty years. To overcome this problem, the Colombian government has decided recently to grant licenses for the most important construction projects and for the rehabilitation of roads, city streets, airports and seaports. Both national and international firms have been invited. This is the case of the ElDorado International Airport, which handles some of the heaviest air traffic in the world with only one runway. The construction of the second runway has been contracted, by granting a license for a term of seventeen years. The

contractor is a consortium of the Spanish firm Dragados and the Colombian firm Conconcreto.

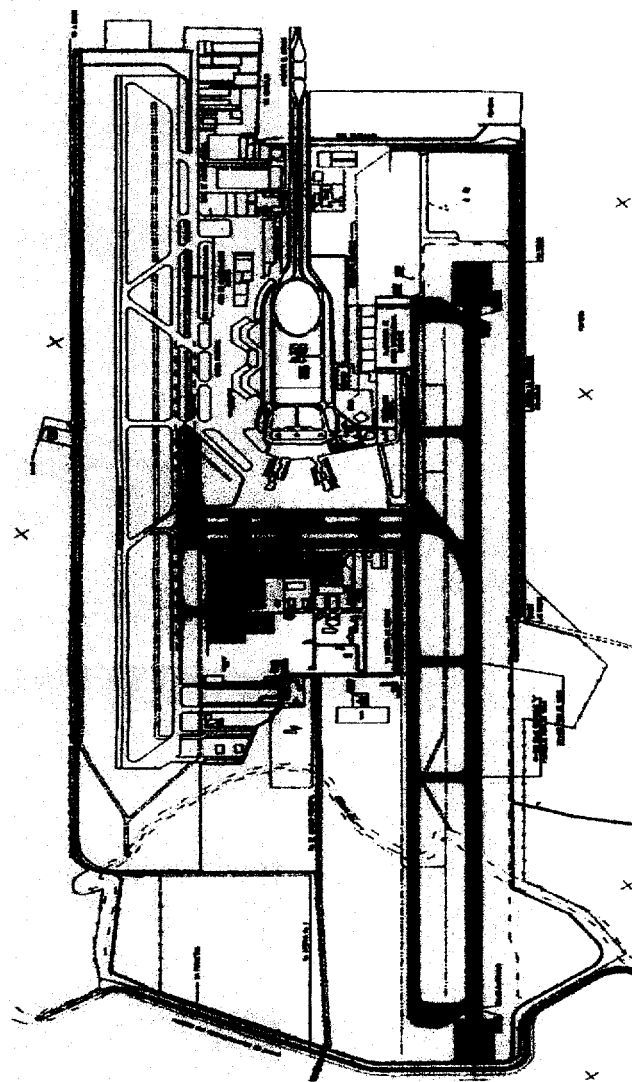


Figure 1. General plan view of the project

The soil on which the runway is being constructed, is a deposit of some 300 meters deep (for this project about 60 meters have been recognized as soft), consisting of lacustrine origin soils mainly clayey with presence of volcanic ash and also some sand lens. The runway goes in an east-west direction which is 3,800 meters long and crosses the Bogotá river bed which was rectified by means of a canal of some 600 meters long, which made the construction possible (see Figure 1). Figure 2 shows the side view of the runway. As can be observed, the initial 2,600 m of the runway - Sector 1 - rest directly on the top layer of native clays, while the final 1,200 m of the runway - Sector 2 - rest on a embankment with maximum height of 4.0 m.

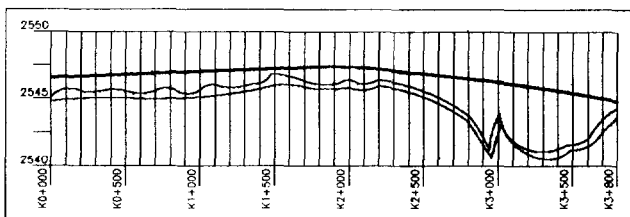


Figure 2. Side view of the runway

The investigation of the subsoil demonstrated its incapacity to support the loads of the embankments and that the runway would suffer great differential settlements, unless adequate measures were taken to avoid this. The designer specified a process of preconsolidation: induced by an overload caused by an embankment 5 meters high, accelerated by the installation of wick drains placed 1.80 meters apart and 10 meters deep (see Figure 3).

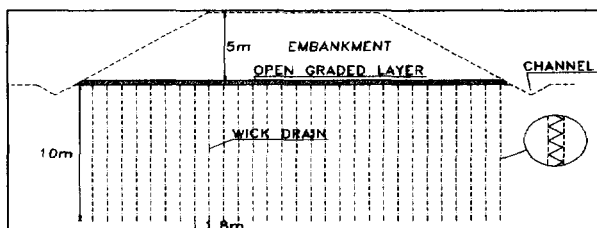


Figure 3. Preconsolidation typical transverse section of the full scale test embankment.

The contractor furthered the investigation of the subsoil through traditional mechanical drilling and through the Cone Penetration Test (CPT), with a continuous measurement of interstitial pressure. In Santafé de Bogotá at that time, there had been no one with the experience required for the project in the use of CPT equipment. When the original design was done, the designer did not have the information that the constructor obtained through his own additional investigation. The results of this investigation made it possible to characterize better the subsoil and led to the conclusion that the treatment of preconsolidation could be avoided. Consequently, the contractor recommended embankment foundation reinforcement in lieu of the acceleration of settlements.

In order to confirm the performance of the original design, a full-scale test embankment has been constructed and monitored.

2. ORIGINAL DESIGN : IMPROVEMENT THROUGH PRECONSOLIDATION

2.1 Foundation Soil

The soils at the work site are predominantly arguieulous of high plasticity (CH), very soft, and belong to the lacustrine deposit named *Sabana* formation, whose depth beneath the runway is 60 m as a minimum. The water table is 1 or 2 m below the terrain surface. According with the bidding documents, there are two geotechnical zones along the runway: Zone 1, on the Bogotá river valley that presents a layer of fine sands located between 4.0 and 11.0 m below the surface, resting on the typical soils of the *Sabana* formation. Zone 2, located out of the Bogotá river valley where the typical geotechnical profile of the *Sabana* formation is present. The designer specified the use of wick drains in order to improve the resistance of the foundation but mainly to make it uniform. This preconsolidation treatment was designed also to reduce the expected differential long-term settlements between zone 1 and 2, due not only to the geotechnical differences but also taking into account the variable height of the embankment (from 0 to 4.0 m).

The wick drains were specified to have a depth of 10 m; 1.80 m spaced and interconnected on the surface through a granular material layer of high permeability. This layer was designed to capture and evacuate the expelled water from the soil, thanks to the application of the overload of an embankment 5.00 meters in height (Figure 3). The estimated time necessary for the completion of the preconsolidation process was 15 months.

2.2 Pavement Structure

In the solicitations, two alternative pavement designs were specified: (a) flexible pavement composed by 13 cm of asphalt carpet, over 38 cm of standard asphalt base and 90 cm of granular material, meeting specifications of subbase course. And (b) rigid pavement composed by 38 cm of concrete slab, over 20 cm of standard asphalt base and 90 cm of granular subbase material.

2.3 Embankment Material

Table 1. Embankment material specifications.

CHARACTERISTIC	SPECIFIED	REAL
Maximum Grain Size	75mm	75 mm
% passing No. 200 sieve	<15%	13.5%
Liquid Limit (I_L)	25%	23%
Plasticity Index (I_p)	6%	6.7%
CBR	-	38

These specifications correspond to a local material, called "Recebo", with a soil friction angle (ϕ) that varies between 25° and 30° when compacted, and is composed by a mix of fine and granular soils.

3. DEFINITIVE DESIGN : REINFORCEMENT OF THE FOUNDATION WITH GEOTEXTILES

Three typical transversal sections were analyzed: (a) transversal section of the runway, (b) transversal section of the platforms and (c) transversal section of the perimeter roadways for vehicle transit.

This document refers mainly to the runway and platforms reinforcement, though it includes the technical characteristics of low strength geotextiles used to reinforce the perimeter roadways.

Based on the new exploration of the subsoil, the contractor was able to establish more precisely the characteristics of the foundation soil and to analyze, for the embankment material used (see Table 1), the two transversal typical sections of the runway (see Figure 4).

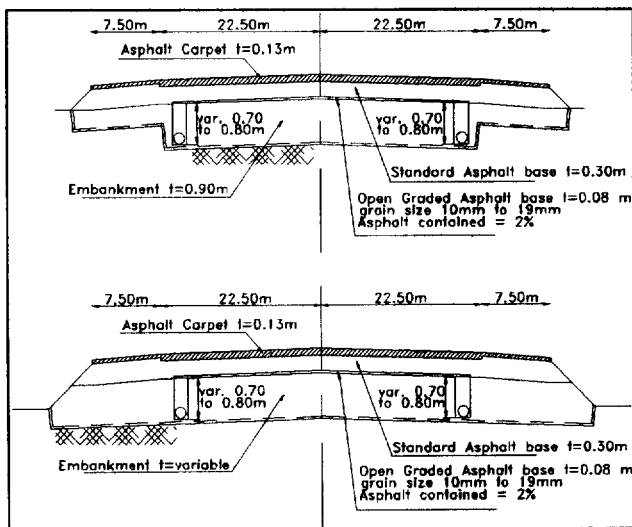


Figure 4. Reinforced Typical Transverse Sections.

Following the design method proposed by Koerner (1990) to determine the required functions of a geotextile in the foundation of embankments on soft soils, the contractor determined the primary and secondary functions of the geotextile. According with the contractor criteria, separation is the primary function for low height embankments, while for high height embankments, depending on the governing mode of failure, reinforcing could be of primary importance (see Figure 5). When Toe or Spreading are the governing failure modes, reinforcement and separation are the geotextile primary functions. When Base failure is governing, separation is the primary geotextile function. For Sector 1, the geotextile was designed for separation. For Sector 2 by means of comparing the embankment height (H), the soft soil depth (D) and the embankment width (B), a toe failure was

determined to be the governing mode and the geotextile was designed for separation and reinforcement.

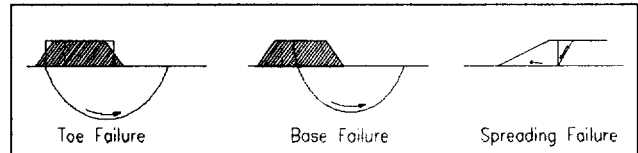


Figure 5 Mode of Failure

3.1 Geotextile Design for Separation Function

The contractor, considering puncture as the most probable separation geotextile-breaking mode, used the following equation to determine the required geotextile puncture resistance:

$$F_{p_{req}} = (\pi d_i d_a) p' S' \quad (1)$$

Where,

$F_{p_{req}}$ = Required geotextile puncture resistance (kN)

d_i = Geotextile opening size (m)

d_a = Average diameter of the puncturing aggregate (m)

p' = Pressure exerted on the geotextile (kPa)

S' = Shape factor of the aggregate particles

$$S' = (1-S)$$

S = sphericity

$$S = 0.4 \text{ for crushed stone}$$

Taking into account that the foundation soils have a passing 200 ASTM sieves $> 50\%$, the contractor decided to specify O95 < 0.3 mm. In consequence for $d_i = 0.3$ mm, $p' = 490$ kPa (imposed by the construction trucks) and $d_a = 70$ mm, we have:

$$F_{p_{req}} = (\pi)(0.3 \times 10^{-3})(70 \times 10^{-3}) 490 (1-0.4)$$

$$F_{p_{req}} = 0.01940 \text{ kN} = 19.40 \text{ N}$$

Using a factor of safety against puncture of 2.0,

$$F_{p_{reqd}} = 38.8 \text{ N}$$

3.2 Geotextile Design for Reinforcement

Using a computer program for geosynthetics design, the contractor determined the required tension at 20% of elongation (T_{20}), based on the following parameters:

Table 2. Geotextile for reinforcement design parameters

Design parameter	Symbol	Unity	Value
Embankment Height	H	M	3.50
Elongation at failure	ϵ_f	%	≤ 20
Fill material Shear stress	τ_f	kPa	19
Foundation soil Shear stress	τ_s	kPa	17.8
Soft soil depth	D	M	14
Angle of slopes to horizontal	β	$^\circ$	26
Fill material Unit weight	γ_f	kN/m ³	17.8

Geotextile resin		PP
Uniform surcharge load	q_s	kPa 10
Damage during construction partial factor	f_{m1}	1.1
Loss of resistance for 20 year partial factor	f_{m2}	1.24
Global Factor of Safety	FS	1.5

The computer program calculates the required T_{20} and minimum anchor length L_a using the Bishop stability method of analysis. For the runway, the results was:

$$T_{20} = 70 \text{ kN/m}$$

$$L_a = 47 \text{ m}$$

4. PRELIMINARY RESULTS OF THE MONITORING ON THE TEST EMBANKMENT AND ON THE FINAL EMBANKMENT

4.1 Test Embankment

The test embankment, 160 m length by 80 m wide and 5 m high, with slopes 2H:1V (see Figure 6), was constructed near the runway where one can expect the largest velocities of settlement, due to the presence of a sand layer in the stratum. As Figure 6 shows, the test embankment was divided in three zones:

Zone A: on top of foundation soil treated with wick drains installed as defined in the original design (1 wick drain / 2.80 m²),

Zone B: on top of foundation soil treated with wick drains installed more closely (1 wick drain / 2.0 m²),

Zone C: embankment on top of foundation soil without wick drains.

To monitoring the test embankment performance, the following set of instruments was installed:

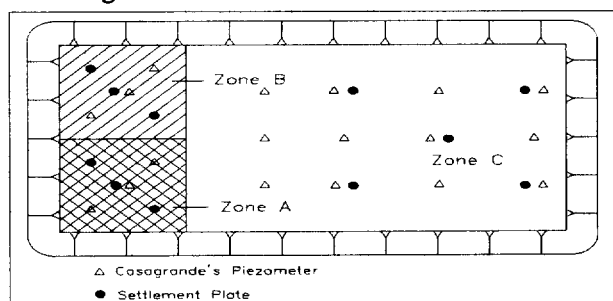


Figure 6 Plant View of the Test Embankment

Table 3. Set of instruments installed in the test embankment

Instrument	Quantity
Casagrande's piezometer	11
Settlement plate	18
Extensometer	3 (60 m length)
Continue Settlement line	4

These instruments allow for the measurement of settlements at the foundation level and to evaluate continuously their space variation.

Table 4. Results of settlement plates

Zone	Settlement (mm)	Instrument
A	80	Settlement plate N° 3
B	115	Settlement plate N° 6
C	158	Settlement plate N° 14

Table 5. Maximum excess of pore water pressure (kPa)

Zone	Depth (m)	Δu (kPa)	Piezometer
A	10	4.9	N°3
	20	21.6	N°1
	30	15.7	N°2
B	10	9.8	N°6
	20	38.3	N°4
	30	30.4	N°5
C	10	1.9	N°11
	20	29.4	N°10
	30	32.4	N°9

Due to space limitations it is not possible to include in this document more detailed information about these provisional test embankment results, but the initial contractor's conclusions are:

- Measured settlements are smaller than those expected and occur at a velocity near to the expected one,
- The greater part of settlements during the construction occurs in the top 20 m of the stratum,
- Apparently there is not important influence of the wick drains on settlements,
- According with the settlement distribution in the test embankment, differential settlements would occur in the runway (in the order of 5 cm). This magnitude of differential settlements have registered in airports with similar foundation conditions than EIDorado Airport (San Francisco Airport, Mexico City Airport)

4.1 Final Embankment

The final embankment foundation was reinforced by a high strength woven geotextile. During construction, no monitoring instruments were installed. At the moment of this writing the contractor is starting a plan of topography measurements. As the contractor has been able to establish through geotechnical studies and embankment tests, settlements will occur on the runway. However thanks to geotextile reinforcement, abrupt differential settlements will not appear. According to the measurements the magnitude of the general settlement because of consolidation is small and will be compensated by repaving maintenance works, which are normal for this type of construction.

5. REQUIRED AND SUPPLIED SPECIFICATIONS FOR THE GEOTEXTILES

5.1 Geotextile for the Runway and Platforms

The contractor specified the following necessary characteristics of the woven geotextile to reinforce the runway and platforms:

Property	Un	Value
Ultimate tensile strength	KN/m	70 x 56
Elongation at break	%	< 13
O ₉₅	µm	< 300

5.2 Geotextile for the Perimeter Roadways

The contractor specified the following necessary characteristics of the separation woven geotextile for perimeter roadways:

Property	Un	Value
Ultimate tensile strength	KN/m	25 x 25
Elongation at break	%	50 to 70
O ₉₅	µm	< 150
Flow Capacity Normal to the plane	L/m ² .s	0.0319
Thickness	Mm	>3.00
Puncture Strength	N	4000

5.3 Geotextiles for Filtration in Drainage System

The pavement drainage system leads infiltrated and ground water, by the open graded asphalt base, to the lateral drainage lines, which are trench drains filled with open graded material including a 100 mm size pipe, wrapped up by nonwoven needle punched geotextile.

Table 6. Characteristics of the geotextiles used.

a) Woven geotextile Geotex 4x4 for runway

Property	UN	MARV	Typical
Polymer Type		PP	
Wide Width	KN/m	70x70	81.4x80.5
Tensile Strength			
Wide Width	%	14x12	19x19
Elongation			
Mullen Burst	kPa	8270	8960
Trapezoidal Tear	N	820x845	1335x1310
AOS	Mm	0.600	0.600-0.425
Permittivity	s ⁻¹	0.60	
Permeability	L/m ² /s		54
Water Flow Rate	l/m/m ²	1830	
UV Resistance	%	80	80

b) Woven geotextile Geotex 200 ST for the perimeter roadways

Property	UN	MARV	Typical
Polymer Type		PP	
Wide Width	KN/m	21x21	22.7x27.1

Tensile Strength			
Wide Width	%	15	11x19
Elongation			
Mullen Burst	kPa	3100	3440
Trapezoidal Tear	N	330	420x420
AOS	Mm	0.425	0.300
Permittivity	Sec ⁻¹	0.07	
Permeability	l/m ² /s		11
Water Flow Rate	L/m/m ²	240	
UV Resistance	%	90	90

c) Nonwoven geotextile NT1600 for filtration in drainage system

Property	UN	Typical
Polymer Type		PP
Grab Tensile Strength	N	420
Elongation at Break	%	80
Mullen Burst	kPa	1205
Trapezoidal Tear	N	160
AOS	Mm	0.150
Permittivity	Sec ⁻¹	2.2
Permeability	Cm/s	4.8 x 10 ⁻²

6. METHOD OF CONSTRUCTION

6.1 Preparation of the Foundation Soil

Geosynthetics installation guidelines for reinforcement of embankments foundation on soft soils recommend: (a) to install the reinforcement over the terrain, without removing the vegetation and (b) to induce - within adequate limits - the development of the resistance in the reinforcement. However, in this case, the organic soil was removed.

6.2 Placement and Joint Systems of the Geotextile

The geotextile was extended in the normal direction along the centerline of the runway, in such a way that the greatest stress was applied in the roll direction.

At first, an instruction was given to sew the geotextile through the interlocking method, recommended by the British Standard Guides 8006 (see Figure 7), in order to guarantee the maximum possible stress transmission. In Colombia neither high strength yarn nor sewing machines to make double chain stitch were available. In consequence, in some spots it was observed that seams could not support the stress due to the extension and compactness of the fill material. To fix that, a new instruction was given to use overlaps whose dimension was adjusted according to the CBR value of the foundation soil in the different zones of the project.

6.3 Extension and Compacting of the Fill Material.

This operation was initiated in the zones where the foundation soil was found to have the greatest bearing

capacity. The material was discharged over the geotextile, on firm areas and was distributed in such a way that, when it was spread out a layer of 0.35 m of thickness, before compacting, was obtained. Bulldozers were used on this job of the type CAT D-7 equipped with caterpillars of standard width. Although this kind of equipment exerts high pressure on the soil, the geotextile was able to support those high construction loads. But the seams (see reasons in 6.2) gave way in some places, something which was made evident by observing local failures.

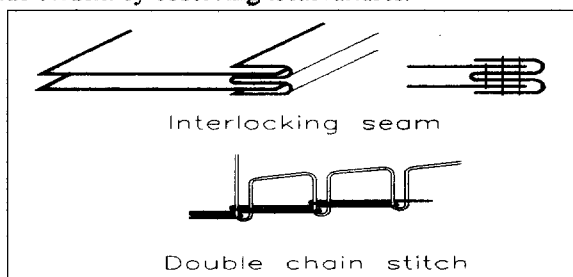


Figure 7. Types of seams.

An initial compacting was applied with the bulldozers and then the final compacting was applied with a vibrator roller until the specified density was achieved.

Some points that showed rutting during construction, due to faults in the subgrade soil, were repaired by adding material, until the geotextile was deformed sufficiently so as to supply the required strength in order to stabilize the filling.

When the adequate bearing capacity was obtained in the first layer, two more layers were added and compacted, until the final projected level was obtained.

On the embankment crest level a hot asphalt spray was applied, on top of which the structure of the pavement was constructed. It was made up of a layer 8 cm of open graded asphalt base, a 30-cm thick standard asphalt base and a carpet layer of 13 cm. The open graded layer was specified for the purpose of improving the drainage conditions of the structure which has a lateral slope of 1.5% and is interconnected with a system of lateral drainage lines, that discharge every 50 m (see Figure 4).

7. CONCLUSIONS

The final design of the embankment foundation reinforced with geotextiles has sped up the construction and it is functioning in accordance with what was established by the contractor. This is without the necessity of overload and drainage and has also resulted in being more economical.

This job demonstrates that geosynthetics offer economic alternatives in construction, that are reliable and of great use for modern engineering projects in both developed countries and in those countries found to be in the process of development. In this case, the geotextiles have made it possible:

- (a) to obtain and make uniform the stability conditions of the embankment, which are required by the project, without the necessity of improving the characteristics of the subgrade soil;
- (b) to carry out the work in a shorter period of time and
- (c) To utilize embankment filling material that is available near the construction site, which translates into considerable savings on transport costs.

The construction job represents an important contribution to the development of the specification, design and construction of works carried out with geosynthetics in Colombia, a country where a tremendous academic effort is required in order to ensure that these products are used according to rational criteria.

The relative extensive use of geosynthetics in Colombia is based generally on the intuition of engineers who have seen proof of beneficial effects of these products in their different applications. Only in some cases, such as the second runway at EIDorado International Airport, do the required specifications of the reinforcement correspond to a technically calculated design.

The lack or absence of adequate design has led to partially or totally faulty projects, which have been carried out with geosynthetics in Colombia and this also has meant a lower pace of growth in this market.

The reduced diffusion of rational analytic methods for design with geosynthetics means that only a handful of engineers have the necessary technical information for designing with these products.

As a result, we continue resolving a lot of geotechnical problems by means of traditional technologies that are more costly, not only in terms of money but also in terms of time and the environment.

We hope that the importance and good results of this project will encourage engineers in Colombia, as well as other countries to construct with geosynthetics. To do this we need to utilize sound geotechnical principles to analyze, design and specify geosynthetics and to construct according with the designer and manufacturer recommendations.

ACKNOWLEDGMENTS

The writer would like to thank Engineers Fernando Bolinaga and Fernando Roman of Dragados and Intecsa, for their help to get the necessary data for this document. The writer also acknowledges the cooperation of the Project Directors, Engineers José Antonio López, Fernando Abadía and José Ignacio Quirós; of the Project Field Director Eng. José Luis Pasión and the Project Technical Director Eng. Pablo Quirós, and of the contractor consortium field engineers, not only because of their cooperation, but especially because of their interest to get the best results in this geosynthetics reinforced job. Finally I would like to thank Engineers Henry Angulo and Rodrigo Arévalo who have made the graphics and Mr. Albert Klein for the translation necessary for this paper.

Testing and Analysis of Soft Foundation Treatment for Donggang Diking Project

Q. Y. Luo

Senior Engineer, Zhejiang Institute of Water Conservancy and Hydraulic Power, Huajiachi, Hangzhou, China

ABSTRACT: A seawall for Donggang diking project is 3635m long and 5.3m to 7.5m high, with a diked area of 2.45km². The foundation consists of silty clay with high water content, high compressibility and low strength. A seawall section having a height of 5.3m to 6.0m was treated with geotextile reinforced foundation mattress; meanwhile, a seawall section having a height of 6.0m to 7.5m was improved using plastic drainage plates. To meet the needs of two treatment schemes the observation instruments had been installed in the seawall, covering observation duration of 830 days and 710 days, respectively. The test results obtained are mainly presented and analysed in this paper. Findings show that the two treatment schemes adopted for this project have achieved excellent effect and the construction of the seawall was smoothly accomplished with faster speed and shorter time. Also, it shows that there is difference in consolidation effect between the two schemes and the popularization and application should be carried out in line with local conditions.

KEYWORDS: Seawall, Soft foundation, Plastic drainage plate, Geotextile, Observation result analysis

1 INTRODUCTION

Donggang diking project is located in Shenjiamen of Zhoushan City, Zhejiang Province, which is the largest fishing harbour in China, and is close to Putu Island of Zhoushan Archipelago which ranks among the most celebrated Buddhist Meccas in China. The diked area during the first construction period covers 2.45km² and has been already completed, in which the development and construction of harbour, industry, commerce and tourism are being conducted.

The seawall for Donggang project involves a total length of 3635m. The beach ground elevation of the seawall line ranges from -1.3m to -3.5m (Huanghai Elevation, the same below). The top elevation of the seawall is 4.0m and the seawall height varies from 5.3m to 7.5m. The design high and low tide levels are 2.84m and -2.8m, respectively. It is a sea area with strong wind, high wave and larger tidal range. The seawall foundation consists of silty soft clay which has high water content and compressibility as well as low strength. The foundation stabilization treatment consists mainly of;

- Geotextile reinforced foundation mattress. The applied area of geotextile included the seawall of less than 6m high. The seawall sections were connected with the land areas at both ends and were 1505m long in total, in which the geotextiles laid were more than 100000m².

- Plastic drainage plate. It was used for the 6m to 7.5m high seawall which was extended into the sea area so as to make the foundation be precompressed, drained and consolidated. The seawall length was 2130m and the plastic drainage plates of 850000m were

driven into the foundation.

In order to verify the stabilization effect of the soft clay foundation, control the construction rate and realize information construction, in accordance with the two treatment schemes a representative seawall with a length of 100m was selected as a test section, respectively. Instruments were embedded to carry out long-term observation. The series of readings which have been obtained started on November 29th, 1992 and ended on March 13th, 1995 and an observation duration lasted eight hundred and thirty days. Now, the test results derived in the course of construction are described as follows.

2 FINDINGS FOR GEOTEXTILE SCHEME

The top elevation of the seawall is 4.0m and the seawall is 6.0m high. The cross-section of the seawall is shown in Figure 1. The seawall cross-section was chosen through stability calculation and analysis for several schemes. The cross-section of the seawall treated by geotextile reinforced foundation mattress is more economical than a conventional scheme (natural foundation), in which a counter weight fill of 15m was shortened. The mattress with a thickness of 1.0m, consisted of two layer polypropylene woven fabrics and a crushed stone layer, is an important component part of the seawall. The geotextile utilized was a 60kN/m product and the characteristic indexes are shown in Table 1. The foundation can be divided into four soil strata and the buried elevation and soil characteristic indexes for each layer are listed in Table 2. The observation instruments were installed in November, 1992 and the location is shown in Figure 1. The instruments which were buried in the seawall include five ground

settlement plates(s), four settlement pipes (Fs) in layers, two clinometers(F), fifteen pore water pressure meters(u), six earth pressure cells (P) and two water level pipes (c). Also, the strength measurement was carried out with vanes(Cu). The seawall was filled in five stages starting on November 29th, 1992 and the crest elevation of the dyke reached 4.0m up to September, 1994. Earth material used for closure was placed in four stages. The top elevation of the seawall reached 2.6m up to November, 1994.

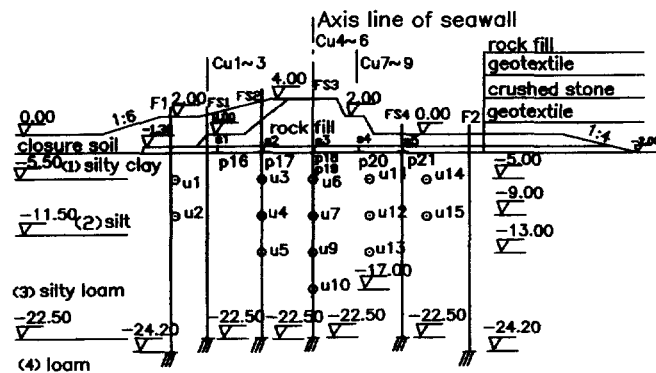


Figure 1. Seawall cross-section and observation instrument layout

Table 1. Main characteristic indexes of geotextile

Mass per unit area	Trapezoidal tearing strength		Ball rupture strength	Strip tensile 10 × 5			
	Longitudinal	Lateral		Tensile strength	Tensile strength rate	Tensile strength	Tensile strength rate
(g/m ²)	(kN)	(kN)	(kN)	Radial (kN)	Radial (%)	Lateral (kN)	Lateral (%)
285	1.26	0.59	2.13	3.34	31	1.53	22

Table 2. Main characteristics of the foundation soil

Soil type	Water content (%)	Void ratio	Coef. of consolidation (cm/s ²)	Quick shear	
				Cohesion (kPa)	Angle of inter. friction (°)
Silty clay	44.3	1.24	2.9×10^{-3}	11.8	8.5
Silt	54.3	1.47	1.29×10^{-3}	8.7	3.5
Silty loam	35.6	0.96	2.69×10^{-3}	13.9	13.5
Loam	26.4	0.71	2.75×10^{-3}	1.92	12.2

2.1 Ground Settlement

The graph of the settlement quantity of $S_1 \sim S_3$ and time is shown in Figure 2. The settlement curve under the action of each stage loading is presented in Figure 3. Up to the end of March, 1995, the accumulated settlement quantities of S_2 and S_3 at the top of the seawall

were 116.7cm and 115.7cm, respectively. The steady settlement quantity was 152cm based on the calculation of their measured settlement curves.

2.2 Stratified Settlement

Taking FS_3 as an example, as can be seen in Figure 4, the settlement quantity of ninety percent occurred in the first and second earth layers having a thickness of 9.5m below the ground surface. The accumulated settlement quantities of FS_2 and FS_3 at the top of the seawall were 114.2cm and 103.2cm, separately, basically identical with that of the corresponding ground settlement plates.

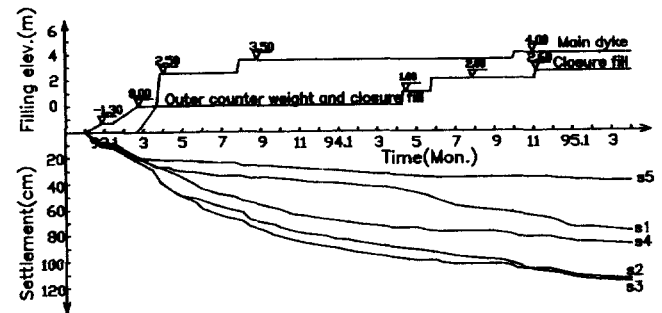


Figure 2. Graph of filling elevation and ground settlement

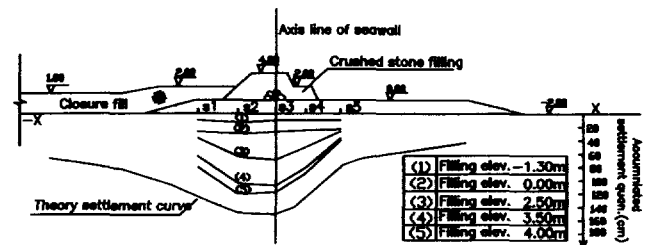


Figure 3. Settlement curve of each stage loading

2.3 Pore Water Pressure

Presenting some measuring points nearby the centre line of the seawall as examples, the graph of the foundation pore water pressure and time in the course of filling the seawall is plotted in Figure 5. It can be seen from Figure 5 that the pore water pressure of U_6 in a shallow layer was more easily dissipated than that of U_9 and U_{10} . Loading in a thin layer was advantageous to the dissipation of pore water pressure. The pore pressure increment of U_6 was dissipated by twenty percent after one month for the third-stage loading and by thirty-nine percent after four months. It was dissipated by sixty-one percent after one month for the fourth-stage loading and fully dissipated after four months.

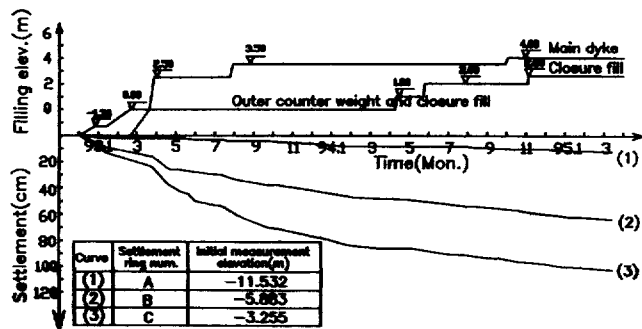


Figure 4. Graph of filling elevation and stratified settlement

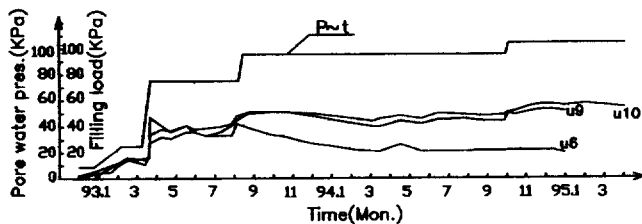


Figure 5. Graph of filling load and pore water pressure

Figure 6 that, if the elevation of -8m was looked upon as a demarcation line, the foundation strength above it would be increased in varying degrees, in which the foundation strength increased greatly near the ground surface; taking the foundation of elevation of -5m as an example, the strength had risen to 1 to 1.8 times; it did not almost increase below the elevation of -8m .

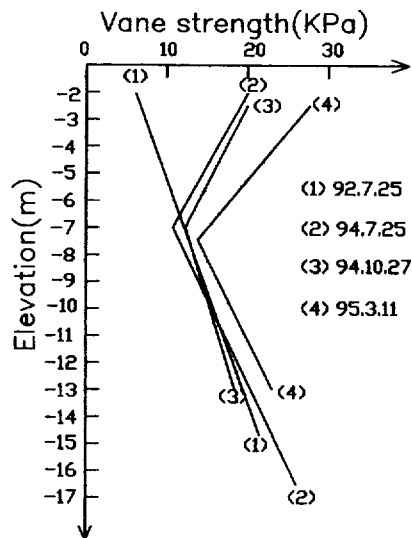


Figure 6. Test results of vane strength

2.4 Horizontal Displacement

The accumulated displacement quantity of F_1 started from December, 1992 and ended in January, 1994 was 110mm. The horizontal displacement quantity was increased and developed to a deeper layer as the height of the seawall was raised and the maximum displacement occurred in the foundation surface layer.

2.5 Earth Pressure

Six earth pressure cells were embedded into the foundation below a geotextile reinforced foundation mattress and five of them are functioning normally. The average value of the ratio of the measured earth pressure was raised along with the increase of load, i. e. it was 0.26 for the second - stage loading, 0.43 for the third - stage loading, 0.66 for the fourth - stage loading and 0.73 for the fifth - stage loading.

2.6 Foundation Strength

The experimental results of vanes in the natural foundation and during three different construction periods are summarised in Figure 6. It can be known from

3 FINDINGS FOR PLASTIC DRAINAGE PLATE SCHEME

The crest elevation of the seawall is 4.0m and the seawall is 7.5m high. The cross - section of the seawall is given in Figure 7. The seawall cross-section was chosen after stability of conventional (natural foundation) and plastic drainage plate schemes had been calculated and analysed according to different water levels and loading. The stability and safety coefficient of the cross-section adopted was only about 0.8 if a conventional (natural foundation) scheme was used. It shows that the effect of plastic drainage plate scheme is excellent. Plastic drainage plates were driven at a range of 36m, with a spacing of 1.4m and a driven depth of 15m. The drainage blanket consisted of crushed stone of less than 10cm in grain diameter was 2.2m in thickness. The plastic drainage plate used is made of polythene cross core bonded with nonwoven fabrics and its performance indexes are listed in Table 3. The beach ground elevation of the seawall was -3.5m , in which the foundation is divided into five soil layers. The buried elevation and property indexes for each soil layer are listed in Table 4 and the location of instruments is given in Figure 7.

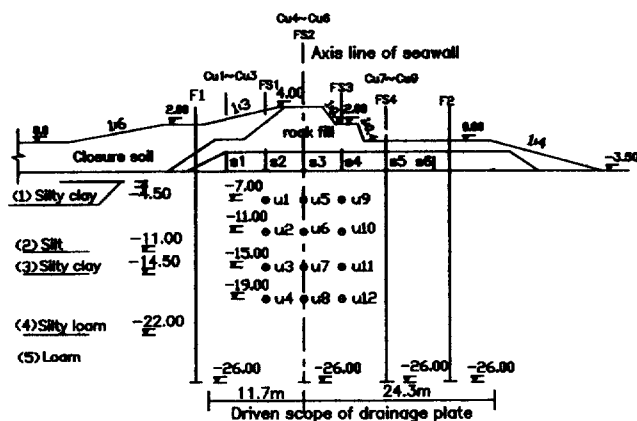


Figure 7. Seawall cross-section and observation instrument layout

Table 3. Main characteristic indexes of plastic drainage plate

Item	Unit	Indexes	Conditions	
Thickness	mm	4		
Wideness	mm	100		
Longitudinal passing water	cm ³ /s	25	Lateral pressure 350kPa	
Filter film permeability coefficient	cm/s	5×10^{-4}	Specimen submerged in water for 24h	
Filter film equivalent aperture	mm	0.075	Equal to O_{80}	
Composite tensile strength	kN/10cm	1.3	At elongation rate of 10%	
Filter film tensile strength	Longitudinal	N/cm	25	At elongation rate of 10%
	Lateral	N/cm	20	At elongation rate of 10%

Table 4. Main characteristics of the foundation soil

Soil type	Water content (%)	Void ratio	Coef. of consolidation (cm ² /s ²)	Quick shear	
				Cohesion (kPa)	Angle of inter. friction (°)
Silty clay	49.3	1.38	2.53×10^{-3}	11.7	7
Silt	59.2	1.63	5.88×10^{-4}	13.0	2
Silty clay	49.6	1.35	8.67×10^{-4}	21.0	2
Silty loam	36.9	1.00	2.88×10^{-3}	15.0	17
Loam	32.0	0.88	1.60×10^{-3}		

The observation items covered six ground settlement plates (s), four stratified settlement pipes (Fs), two clinometers (F) and twelve pore water pressure meters (u); meanwhile, the strength measurement was conducted with vanes (Cu). The installation of obser-

vation instruments was finished from June 14th to June 25th, 1993. All observation work ended till March 27th, 1995 and it took us seven hundred and ten days.

The construction of the seawall, which was divided into six stages, was accomplished between April 9th, 1993 and October 27th, 1994. The work lasted five hundred and sixty days, including an intermittent period. The construction of earth material for closure was performed in four times and lasted five hundred and four days from October 1st, 1993 to February 28th 1995. The filling graph of the seawall is given in Figure 8.

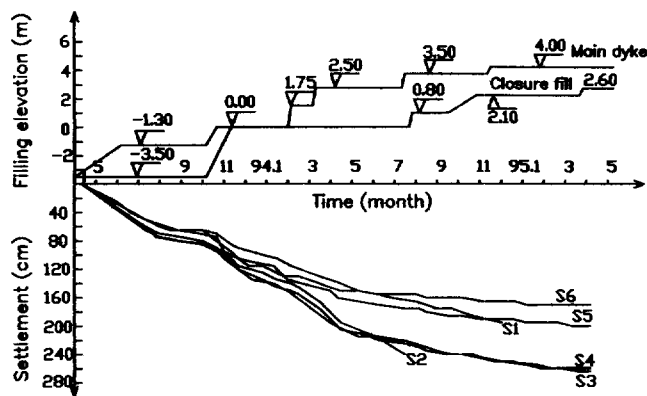


Figure 8. Graph of filling elevation and ground settlement

3.1 Ground Settlement

The graph of the settlement quantity and time is plotted in Figure 8 and the settlement curve of the seawall foundation is shown in Figure 9. As for the first and second stage loading the settlement increment of filling height per metre was larger, about 41cm, respectively; for the third to sixth stage loading the increment was very near, about 28.5cm, respectively. This was because the settlement increment for the first and second stage loading included an instantaneous settlement and an additional settlement induced by disturbed foundation in the course of driving plastic drainage plates. The settlement rate during load stage was all larger, in which the maximum settlement rate amounted to 4.6cm per day. At the end of observation the accumulated settlement quantity of S₃ near the seawall axis line was 260.2cm and the consolidation degree was about ninety percent.

3.2 Stratified Settlement

There are numerous data about stratified settlement. Citing FS₂ near the seawall axis line as an example the settlement graph at different measuring points is shown in Figure 10. The total settlement quantity of each soil

layer amounted to 254.8cm, close to 260.2cm for the accumulated settlement quantity of S_3 . The settlement quantity in silty layer (Elevation-3.5m to -11.0m) made up fifty-nine percent of the total, the settlement quantity in silty clay layer (Elevation -11.0m to -14.5m) twenty percent and the settlement quantity in silty loam (Elevation -14.5m to -22.0m) twenty-one percent.

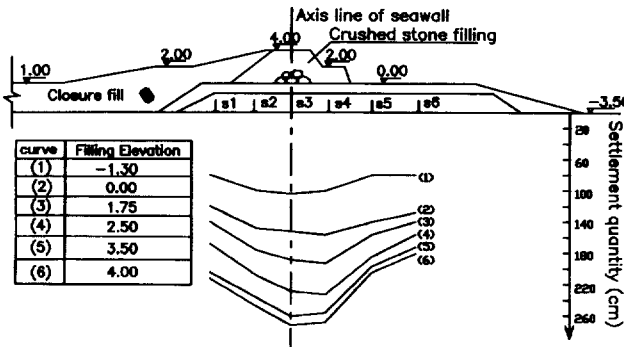


Figure 9. Settlement curve of seawall foundation

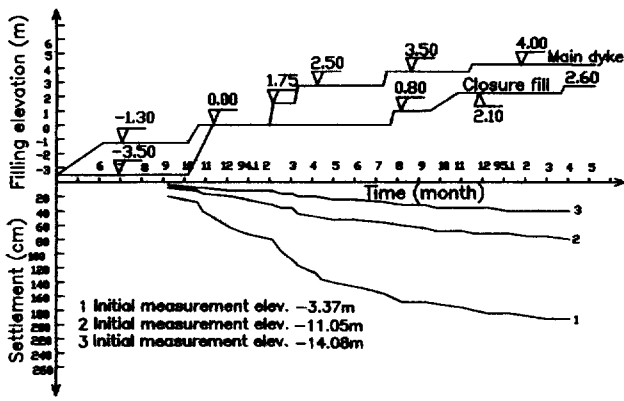


Figure 10. Graph of FS2 stratified settlement

3.3 Horizontal Displacement

Taking F_2 embedded near the sea side as an example, the distribution curve of the horizontal displacement quantity along the direction of depth in different construction period is presented in Figure 11. The horizontal displacement quantity increased as the addition of load. The maximum horizontal displacement quantity was equal to 203.6mm, which occurred near the elevation of -8.0m and affected the silty loam layer at the elevation of -22m.

3.4 Foundation Strength

The vane strength at the elevation of 2.5m increased more obviously than that of the natural foundation

under the action of the fourth-stage loading in May, 1994. At the elevation of -7.25m (half of the seawall height) it was 2.11 times higher than the natural strength. It was 1.78 times at the elevation of -11.0m and it was 1.57 times at the elevation of -14.75m. It was obvious that the foundation strength would further rise with the increase of loading and pre-compression time. The vane tests had not been done afterwards because of the reasons of construction and management.

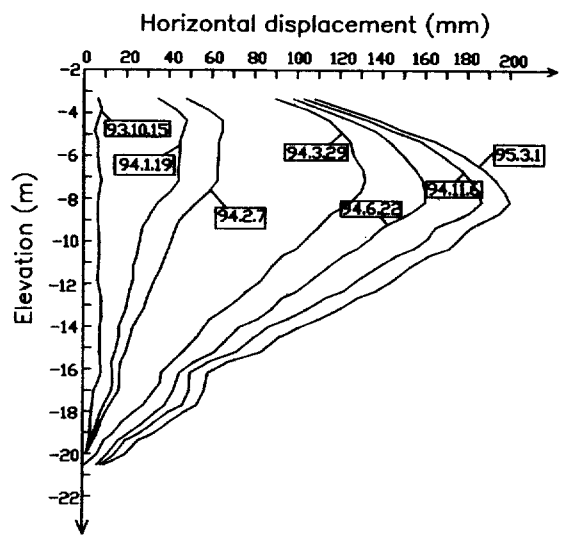


Figure 11. Curve of horizontal displacement along depth

3.5 Pore Water Pressure

According to the statistics of the data obtained from twelve pore pressure cells the pore water pressure rose with filling of the seawall, but it was quickly dissipated. Presenting U_1 , U_2 and U_3 as examples, the coefficients of pore pressure under the action of second-stage loading were greatest. Its average value equalled 0.79 and surpassed the normal standard limit. However, the coefficients of the pore pressure under the action of other different stage loading were smaller, i.e. 0.49 for the third-stage loading, 0.38 for the fourth-stage loading, 0.34 for the fifth-stage loading and 0.25 for the sixth-stage loading. Practice shows that plastic drainage plates have achieved the excellent effects of drainage and stabilization.

4 CONCLUSIONS

Based on the results analysed above, the main conclusions can be concluded as follows:

4.1 The seawall foundation of Donggang diking project is a silty clay with high water content, high

compressibility and low shear strength. For a treatment of this kind of foundation, geotextiles were used as a reinforced foundation mattress and plastic drainage plates as precompression, drainage and stabilization according to the seawall height. The information construction was performed based on the in-situ test results. The seawall was successfully accomplished with faster speed and shorter time and the desired results have been achieved. The methods also have a reference role for a design and construction of similar projects on a soft clay foundation.

4.2 The seawall of 6.0m high which was treated with geotextile reinforced foundation mattress was actually accomplished within twenty-two months. It reveals from the analysis of the test data that the intermittent time of the fourth-stage loading can be reduced from fourteen months to four months. Therefore, if it was not due to untechnical reasons, the seawall would be finished during twelve months. The seawall of 7.5m high, treated with plastic drainage plates, was practically finished during eighteen months. According to the analysis of measured data, the intermittent time for each loading could be shortened except the third-stage loading and it was entirely possible to construct the seawall within twelve months.

4.3 The settlement rate, horizontal displacement rate and pore water pressure coefficient are three main indexes of monitoring the stability of a project and controlling construction rate. As for the seawall treated with two approaches the maximum settlement rate reached 3.2cm to 5.2cm per day, the maximum horizontal displacement rate 4.8mm per day and the pore

water pressure coefficient 0.76 during loading. These three indexes greatly exceed the conventional standard limit and in fact the seawall is always in a stable state.

4.4 The approaches to treating seawall by geotextiles and plastic drainage plates attain the purpose of stabilization foundation. The former exerts a less influence on the stabilization foundation depth, amounting to 6m to 9m, i. e. equivalent to 1 to 1.5 times of the seawall height. The latter's influence scope surpasses the driven depth of plastic drainage plates with a length of 15m; it comes up to the whole silty clay layer, i. e. equivalent to 2.5 times of the seawall height.

ACKNOWLEDGMENTS

The author wishes to thank Senior Engineers Liao Shude and Hu Henan, as well as Engineers Zhang Mingqiang, Chen Xiuliang, Wu Wenhua and Wu Yunbiao for finishing the study work cooperatively.

REFERENCES

- Sun Pengzhou et al (1991) "Geological Report on Donggang Reclamation Development Project in Putu", Zhoushan Water Survey Office, Zhoushan, Zhejiang, China.
- Min Longyou et al (1993) "Preliminary Design on Polder for Donggang Polder Development No. 1 Project in Zhoushan", Zhejiang Design Institute of Water Conservancy & Hydroelectric Power, Hangzhou, China.

Electrokinetic Geosynthetics and their Applications

I. M. Nettleton * +, C.J.F.P. Jones *, B.G. Clarke * & R. Hamir #

* Geotechnical Group, Department of Civil Engineering, Newcastle University, UK

+ Transport Research Laboratory, Riccarton, Edinburgh, Scotland, UK.

Department of Civil Engineering, University Sains Malaysia, Malaysia

ABSTRACT: Increasing demands for construction materials, land and the redevelopment of derelict land are leading to the development of new technologies, and the integration of existing ones. It is with the above challenges in mind that the development of electrically conductive geosynthetics (Electrokinetic Geosynthetics EKGs) has come about. EKGs may provide filtration, drainage and reinforcement, which can be enhanced by electrokinetic processes, such as electro-osmosis and ion migration. In addition to the electrokinetic processes, it is possible to incorporate enhanced transmissivity, sorption, wicking, and hydrophilic characteristics into the new geosynthetics. The availability of new materials and production techniques, together with the need for new engineering solutions, to complex environmental and ground engineering situations, have rendered feasible and desirable the inclusion of these properties into a new range of geosynthetics. This paper describes the concepts behind the development of a new generation of geosynthetics, and the laboratory testing of prototype materials and experimental applications.

A series of laboratory experiments have been undertaken which investigated the feasibility of employing EKGs and electro-osmotic consolidation for the improvement of fine grained low permeability fills. These tests showed accelerated dissipation of pore pressures; reduction of moisture contents; and increases in soil strength and adhesion to reinforcement, over and above that from conventional consolidation. Investigations into environmental applications for EKGs have demonstrated that they can be used for integrated electrode and wellpoint installations for electrokinetic remediation of contaminated ground. Investigations have demonstrated the sorption properties of EKGs, in respect of heavy metals.

KEYWORDS: Geosynthetics, Reinforcement, Electrokinetic, Drainage, Environmental Engineering.

1. INTRODUCTION

The increasing demands for construction materials, land and the redevelopment of derelict land are leading to the development of new technologies, and the integration of existing technologies. The development of *electrically conductive geosynthetics* (EKGs) is an example of this. The concept is to develop a range of geosynthetics which in addition to providing filtration, drainage and reinforcement can be enhanced by electrokinetic techniques for the transport of water and chemical species within fine grained low permeability soils, which are otherwise difficult or impossible to deal with.

The ability of electrokinetic phenomena to move water, charged particles and free ions through fine grained low permeability soil is well established. Electrokinetic phenomena will occur in any soil; however, in medium to coarse grained soils electrokinetic phenomena provide a less effective transport mechanism than hydraulic flows, due to high permeability of the soil.

The first application of electrokinetic phenomena for civil engineering processes was undertaken by Casagrande in 1939 for the dewatering and stabilisation of railway cuttings at Salzgitter, Germany, Casagrande (1952). Since then there have been many other applications of electroosmosis for dewatering and stabilisation of soils, including: (i) The use of electroosmosis for dewatering and strengthening Norwegian quick clays, Bjerrum *et al* (1967); (ii) Electroosmotic stabilisation of West Branch Dam, Fetzer (1967); (iii) Electroosmotic treatment to improve pile friction, Milligan (1994).

2. ELECTROKINETIC TRANSPORT PHENOMENA

There are five principle electrokinetic phenomena within soil: Streaming Potential, Migration Potential, Electroosmosis, Ion Migration and Electrophoresis. The first two of these phenomena are concerned with the generation of electrical potential due to the movement of charges and charged particles respectively. The remaining three are concerned with the transport mechanisms developed upon application of an electrical field across a soil mass.

2.1 Electroosmosis

When an electrical field is applied across a fine grained soil mass cations are attracted to the cathode and anions to the anode, Fig. 1. As the ions migrate they carry their hydration water with them, and exert a frictional force on the water around them. Hence, there is a flow of water to both the anode and the cathode. In order to maintain charge neutrality, however, there are more cations than anions in the pore fluid of a soil containing negatively charged clay particles. Therefore, there is a net flow of water to the cathode, Gray & Mitchell (1967).

The electroosmotic flow of water through a soil can be expressed in the form of Darcy's equation for water flow:

$$q_A = k_e i_e A \quad (1)$$

where q_A is the flow rate, i_e is the potential gradient $\Delta V/\Delta L$, A is the cross-sectional area and k_e is the coefficient of electroosmotic permeability.

The electroosmotic permeability (k_e) for most soils lies in the range 1×10^{-9} to 1×10^{-8} m²/Vs, Lageman *et al* (1989),

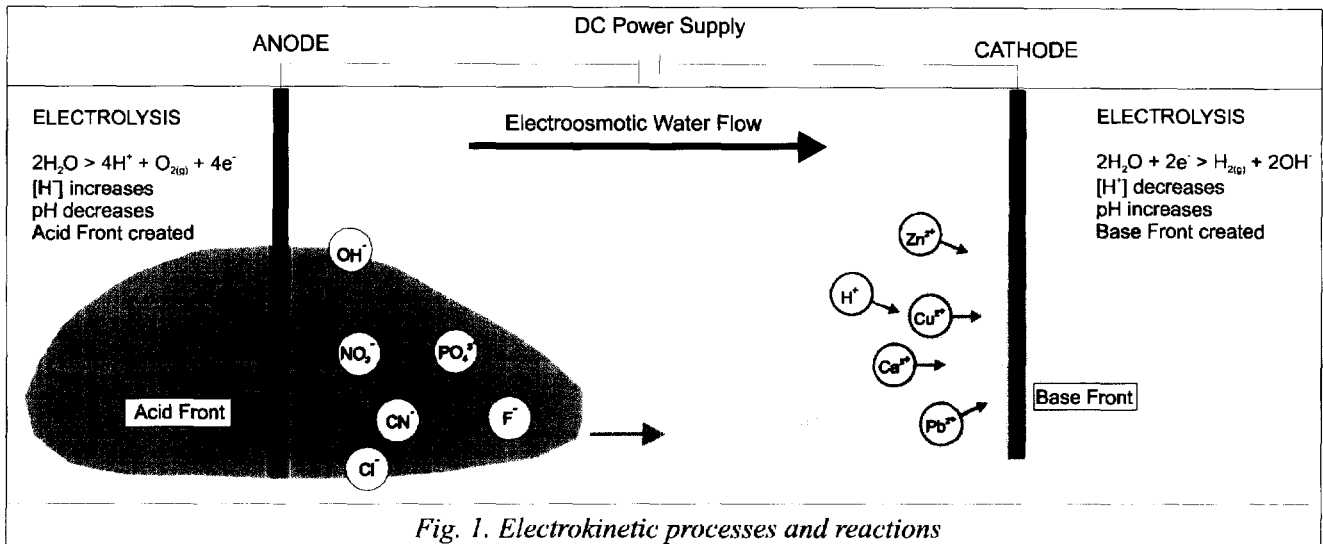


Fig. 1. Electrokinetic processes and reactions

and is independent of pore size, Casagrande (1949).

If both the anode and cathode are open (to water flow) then electroosmosis will “pump” water through a soil. However, if the anode is closed and the cathode open, then electroosmosis will generate negative pore pressures. The magnitude of these is given by:

$$u = \frac{k_e}{k_h} \gamma_w V \quad (2)$$

where k_e is the electroosmotic permeability, k_h is the hydraulic permeability, γ_w is the unit weight of water and V is the applied voltage. If the total stress does not change during electroosmosis then the magnitude of the effective stress is proportional to the negative pore pressure generated at the anode.

2.2 Electromigration or Ion Migration

The application of an electrical field across a soil mass causes migration of the free ions and ion complexes, which are present within the pore fluid, to the appropriate electrode, Lageman *et al* (1989) and Hellowell (1994).

Lageman *et al* (1989) report the average mobility of ions in soils as $5 \times 10^{-8} \text{ m}^2/\text{Vs}$, which is an order of magnitude greater than the electroosmotic permeability. Hence, anions can usually overcome the electroosmotic flow and migrate towards the anode.

2.3 Electrophoresis

When a DC electrical field is applied across a particulate suspension positively charged particles are attracted to the cathode and negatively charged particles are attracted to the anode. Most clay colloids are negatively charged and are therefore, attracted to the anode.

Electrophoretic mobilities reported by Lageman *et al* (1989) and by van Olphen (1977) are in the ranges 1×10^{-10} to $3 \times 10^{-10} \text{ m}^2/\text{Vs}$ and 1×10^{-8} to $3 \times 10^{-8} \text{ m}^2/\text{Vs}$ respectively. Hellowell (1994) attributes the discrepancy to differences in the moisture content of the medium. Electrophoresis has found applications in the densification of sludges and mine tailings, Lo *et al* (1991a). Esrig (1968) reports that the process is inconsequential for most naturally occurring soils.

3. GROUND IMPROVEMENT AND REINFORCEMENT USING EKGS

Electroosmotic treatment of soils generates negative pore pressures and thereby increases the effective stress, leading to consolidation of the soil. The end result is similar to that gained by the application of a surcharge; however, unlike vertically surcharging a soil mass, there are no stability problems, as the pore pressures generated are negative rather than positive. Electroosmosis may also be used to accelerate the dissipation of positive pore pressures resulting from vertical surcharging. Indeed, once the positive pore pressures have been dissipated electroosmosis can be continued for further consolidation, due to the generation of negative pore pressures. The maximum negative pore pressure due to electroosmotic consolidation will be generated at the anode, Esrig (1968). These processes increase the *strength* of the soil and the *bond* characteristics of the soil and the reinforcement.

Electroosmosis often leads to increases in strength of cohesive soils, due to chemical cementing of the soil fabric, Mitchell (1991).

3.1 Laboratory Tests - Consolidation

A number of laboratory tests have been conducted to evaluate the use of conductive geotextiles as electrodes in electroosmotic consolidation. The tests using an electroosmotic cell simulated the reinforcement, electrodes and the drainage configuration expected in reinforced soil applications.

A number of geosynthetic electrodes were considered and compared with a perforated copper disk. The initial type 1 geosynthetic electrode was formed from a non-woven, needle punched geotextile. A copper wire of 300 mm length and 1 mm diameter was inserted at the centre of the geotextile. Copper wire was chosen to inhibit the generation of oxygen at the anode. Any oxygen generated at the anode combined with the copper to form copper oxide, which is a good conductor of electricity.

The samples were prepared from Grade E Kaolinite (SILT) slurry at water contents of 1.5 times the liquid limit to ensure they would be fully saturated. The electroosmotic permeability was $k_e = 3.4 \times 10^{-9} \text{ cm/sec per volt/cm}$ and hydraulic permeability $k_h = 6 \times 10^{-7} \text{ cm/sec}$.

Initially the soil was consolidated with an effective stress of 25 kPa. Electroosmotic tests were conducted with vertical pressures of 50 and 100 kPa to simulate the imposed load of fill material. During the tests, pore pressures, current and voltage variations across the soil sample were recorded. After treatment, tests were carried out to determine the water content and strength of the soil.

Negative Pore Pressure

Figure 2 shows the change in pore pressure at the anode during electroosmotic consolidation using type 1 geosynthetic electrodes with different applied voltages.

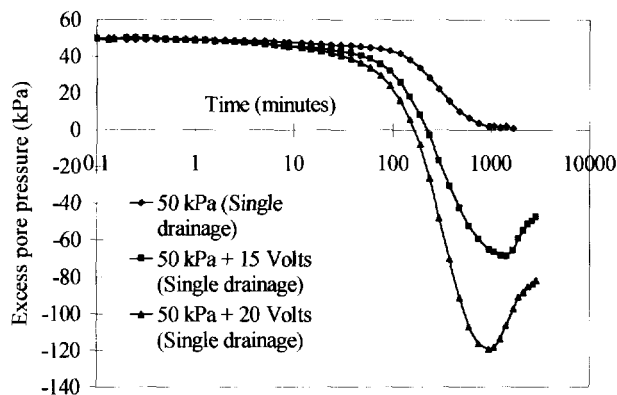


Fig. 2. Excess pore pressure versus time for normal consolidation and for electroosmotic consolidation.

Initially the back pressure was lowered by 50 kPa to simulate an applied vertical pressure. After the current was switched on the pore pressure at the anode decreased until it equalised the back pressure, signifying full dissipation of the positive pore pressure. As the test continued, the pore pressure at the anode decreased to a value lower than the back pressure, signifying the generation of the negative pore pressure. Upon reaching a maximum negative value, the pore pressure increased before stabilising at a lower negative value. Figure 2 shows that the positive pore pressure generated by the vertical loading was reduced to zero in a shorter time by the application of electroosmosis. The results concur with the theoretical solution by Wan *et al* (1976).

Vertical Strain

The vertical strain-time curves are as shown in Figure 3. The electroosmotically induced vertical strain curve was similar to the consolidation due to vertical load. The vertical strain increased from 9.7% for consolidation with a normal load to 13% with the incorporation of electroosmotic consolidation.

Water Content

The moisture content profile is as shown in Figure 4. It indicates that moisture content for soil consolidated by a combination of vertical load and electroosmotic consolidation is lower than soil consolidated only with a vertical load.

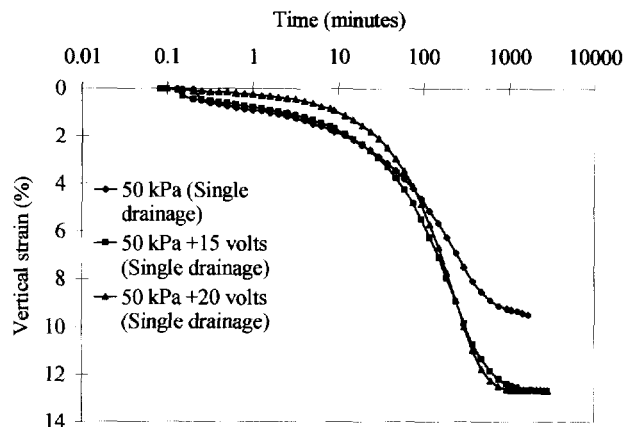


Fig. 3. Vertical strain versus time for normal consolidation and for electroosmotic consolidation.

The shape of the water content distribution indicates that the lowest water content was at the centre of the specimen. However, the water content at the anode was still significantly reduced. The water content profile agrees with the finding of Lo *et al* (1991b).

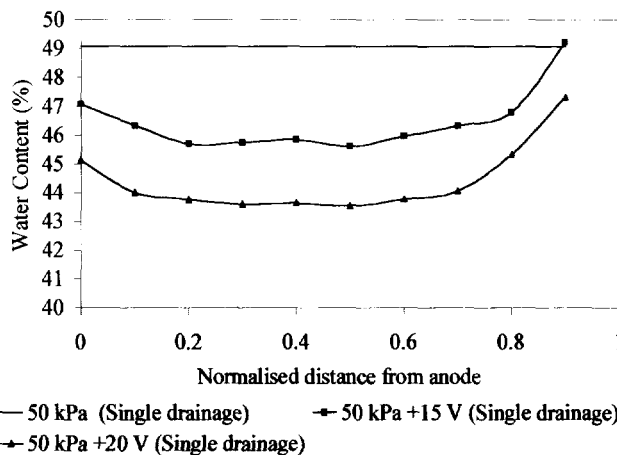


Fig. 4. Water content variation across soil specimens consolidated by vertical loading and by electroosmosis, with a closed anode.

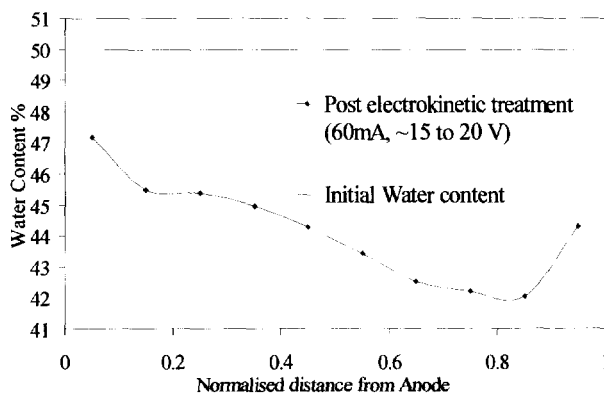


Fig. 5. Moisture content profile across electrokinetically treated soil, open anode and cathode conditions.

As a comparison Figure 5 shows the water content profile across a soil sample subjected to electrokinetic treatment, but with an an "open" anode and cathode. This allows water into and out of the soil. The largest degree of dewatering occurs at the cathode, due to a high resistance zone which develops close to the cathode. This high resistance zone causes a localised increase in the voltage gradient and, hence, an increase in electroosmotic flow in this region.

Shear Strength

The undrained shear strength of the soil was determined at a depth of 30 mm from the surface. The test showed an increase in the shear strength up to 128% for an applied voltage of 20 volts, Table 1.

Table 1. Increase in shear strength when using electrokinetic geosynthetic reinforcement.

Soil	Shear Strength kPa	% Increase
50 kPa vertical pressure	11	-
50 kPa vertical pressure + 15V	19	72
50 kPa vertical pressure + 20V	26	128

3.2 Laboratory Tests - Soil-Reinforcement Bond

The use of electrically conductive geosynthetic reinforcement can be shown to increase soil-reinforcement bond. A series of pullout tests have been undertaken at Newcastle University to illustrate this concept. The objective of the tests was to study the effect of an electroconductive reinforcement on bond performance under undrained conditions. This represented the most severe case in the use of cohesive fill in a reinforced soil structure.

The tests were performed in a specially designed pullout cell and were conducted on soil strengthened by vertical overburden and also by a combination of overburden and electroosmotic consolidation.

Commercially available grade E kaolin was used for the tests. The soil was mixed at a water content of about 52% which was about 3% below the liquid limit.

A drainage layer which also served as the cathode was first placed at the bottom of the cell. The soil was then placed in the cell and compacted manually. The anode was inserted at mid height of the sample. Another layer of conductive geosynthetic was placed at the top of the soil sample forming a second cathode. Hence a two way drainage configuration was used to accelerate the consolidation process.

The soil was consolidated by the application of vertical pressure or by a combination of vertical pressure and electroosmotic consolidation. The vertical pressure was applied by a hydraulic jack capable of providing a constant vertical pressure. A potential difference of 30 volts was

applied by means of a direct current power supply unit with a maximum output current of 1 ampere.

After the completion of the consolidation process, the cell was turned sideways and bolted to the platen of the frame of the triaxial testing machine. A slit cover was then removed, exposing the geosynthetic reinforcement. The pullout resistance and the vertical displacement were automatically recorded by a load cell and LVDT respectively. After the pullout tests, laboratory vane shear tests were carried out on the soil sample close to the anode. A small portion of the soil sample was also taken for the determination of the water content.

Bond Strength

The increase in reinforcement-soil bond due to the use of electrically conductive reinforcement is shown in Table 2. The results show that the increase ranged from 54% to 209% at different overburden pressures.

Table 2. Increase in Shear and Soil Reinforcement Bond strengths using an electrokinetic geosynthetic.

Consolidation Pressure kPa	% Increase in Shear Strength	% Increase in Bond Strength
110	150	209
140	203	113
356	72	54

4. ENVIRONMENTAL APPLICATIONS OF ELECTROKINETIC GEOSYNTHETICS

The electrokinetic processes described in Section 2 can be applied to the remediation and containment of contaminants within the ground. Indeed, electrokinetic remediation is the only technique for the in situ remediation of contaminated fine-grained soils and the groundwater within them (NATO/CCMS 1993). The following are the electrokinetic processes which can be utilised for contaminant remediation and containment:

- Ion migration may be utilised to transport metals and polar contaminants to the relevant electrode, where they may be removed (Lageman *et al* 1989).
- Ion migration may be utilised to transport nutrients to enhance bioremediation (Figure 6).
- Electroosmosis may be utilised to flush contaminants from the soil (Lageman *et al* 1989).
- Electrosorption of contaminants.

In addition because the soil mass acts as a resistor the ground heats up (Lageman *et al* 1989 reports temperature rises of between 20 and 40 °C) and this phenomena may be used to volatilise organic contaminants (Lageman 1995), and to stimulate bioremediation action.

Electrokinetic transport of nutrients has been investigated in a tank containing grade E Kaolinite (Section 3.1). The tank was 400mm long with three wellpoints inserted at 100mm spacings along the length. Nitrate solution (500mg/l) was placed in the electrode reservoirs, an electrical current of 60mA was set across the tank, and porewater samples were taken from the three wells twice a

day. Figure 6 shows the Nitrate breakthrough curves obtained. Well/01 was located 100mm from the anode, well/02 was located at the centre of the tank, and well/03 was located 100mm from the cathode.

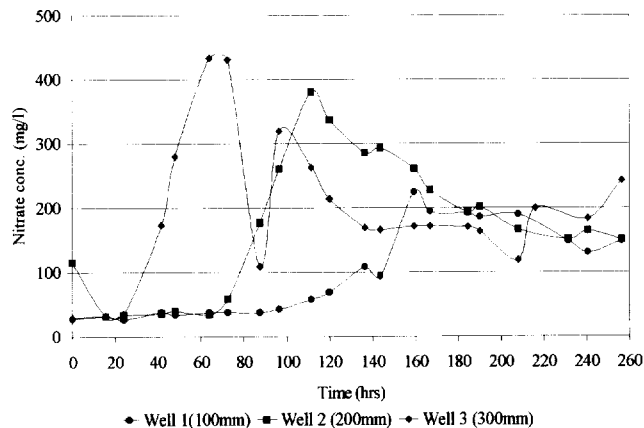


Fig. 6. Graph showing transport of Nitrate by ion migration.

5. ELECTROKINETIC GEOSYNTHETICS

The new EKGs can take the form of single materials, which are electrically conductive, or composite materials, in which at least one element is electrically conductive. They can be of the same basic form as present day filter, drainage, separator and reinforcement materials, but offer sufficient electrical conduction to allow the application of electrokinetic techniques for ground improvement and remediation.

There are a number of materials which can be used to produce electrically conductive geosynthetics. The principle conductive materials which have been considered and evaluated at Newcastle include:

- Carbon Fibre Materials.
- Conductively Filled Polymers.
- Metallic Fibres (Metal fibres, metallised fibres or metal coated fibres).
- Composites formed from conductive/non conductive elements.

The metallic fibres have been discounted due to corrosion durability problems. Both the carbon fibre and conductively filled polymer materials show great promise as base materials for the new EKGs, and are discussed below.

5.1 Conductively Filled Polymers

Organic polymers with all carbon backbones are insulators (eg polyethylene PE, polyvinylchloride PVC, ethylvinylacetate EVA) and can be used for electrical insulation. However, if carbon black, carbon fibres or finely divided metals are used as fillers in such organic polymers, then conductive (10^{-5} to 1 s/cm) composites may be created, Cowie (1991). In these composites it is the filler which conducts and not the polymer.

If carbon black is used as the conductive filler then a loading of between 20 and 30 wt % will be required to

produce a suitable conductivity. The structure and mixing of the carbon black filler plays an important role in determining the properties of the conductive polymer. There are two main types of carbon structure of interest, the Low structure, which is a jumbled array of carbon spheres, and the High structure, which is a chain of spheres, giving a higher conductivity.

An activated carbon black or carbon fibre filler may also be introduced to increase the sorption characteristics of polymeric materials. Sorption is another potential function of EKGs.

5.2 Carbon Fibre Materials

Carbon fibres are representative of graphite materials; they are electrically conductive ($> 10^2$ s/cm) and chemically stable. High modulus carbon fibres are expensive and their use is limited to specialist applications where high stresses, high temperatures and radiation exposure are expected. The lower modulus carbon fibres are cheaper, their production simpler and the raw materials more abundant, Ermolenko *et al* (1990).

Activated carbon fibres (ACFs) have an open microporous structure which provides sorption sites. They provide similar or higher sorption than activated carbon particles and their shape allows more rapid and greater sorption than is found with carbon particles, Ermolenko *et al* (1990). The low modulus materials have many of the features required for the production of electrically conductive geosynthetics.

5.3 EKG functions and design

During electrokinetic treatment utilising EKGs water will flow from the soil and into the EKG at the cathode, and oxygen and hydrogen will be formed and flow into the anode and cathode respectively. The gas and water have to be dissipated to prevent the build up of pore pressures. Hence, the EKG must act as a filter and a drainage material:

- Filtration - to allow the free passage of water from the soil to the drainage system.
- Transmissivity - to transport water and gas out of the system without hindrance.

The EKG must also distribute the electrical current to the pore fluid within the fine grained soil being treated. Any interface resistance to the transfer of current from the electrodes to the soil is a potentially large source of electrical inefficiency for electrokinetic treatment. The higher the interface resistance, the lower will be the effective voltage gradient or current flow for electrokinetic treatment. Factors affecting the pore fluid/electrode interface resistance include:

- Form of the electrodes
- Gas generation during the process
- Current densities - high values lead to electrode polarisation.

Electrode configuration plays an important role in determining the magnitude of interface resistance. An important consideration is the presence of ground water in the porous structure of the geosynthetic. This makes its

whole surface act as an electrode. A major advantage of the use of a geosynthetic electrode is that the surface area can be much larger than traditional electrodes, and the structure is open to the flow of water and gas.

From a study of the electrode requirements for electrokinetic treatment it is clear that a band drain type electrode seems to be the most promising design (Nettleton, 1996). A band drain can be made to act as a local distributor of electrical current by incorporating carbon black fillers into the base polymer for either the geotextile filter or the drainage component of the band drain. Due to the electrical current requirements for electrokinetic treatment a stringer will be required to conduct and distribute the bulk of the current throughout the band drain. The stringer could take the form of a metallic wire coated with a conductive polymer to prevent corrosion due to electrolysis at the electrodes (Nettleton, 1996).

6. CONCLUSIONS

The development of electrically conductive geosynthetic materials offers significant new application areas for geosynthetic products, ranging from accelerated consolidation of soft soils to soil decontamination and pollution control. The use of electrically conductive reinforcement in reinforced soil structures is beneficial as the concept is fully compatible with, and has a positive influence on, the parameters controlling the reinforcement mechanisms.

ACKNOWLEDGEMENTS

The authors would like to express their thanks to the Engineering and Physical Sciences Research Council and the British Council in Japan for their support during this research. In addition the authors would like to thank Mitsui Petrochemical Industrial Products Ltd. and Netlon Ltd. for supplying materials and production facilities.

REFERENCES

- Bjerrum, L., Mowm, J. and Eide, O. (1967). "Application of electro-osmosis to a foundation problem in a Norwegian quick clay", *Geotechnique*, Vol. 17, pp. 214-235.
- Casagrande, I. L. (1949). "Electro-osmosis in soils", *Geotechnique*, Vol.1(3), pp. 159-177.
- Casagrande, L. (1952). "Electrical stabilisation in earthwork and foundation engineering", *Proc. Conf. on Soil Stabilisation*, Massachusetts, USA.
- Casagrande, L. (1952). "Electro-osmotic stabilisation of soils", *Journal of the Boston Society of Civil Engineers*, Vol. 39, pp. 51-83.
- Cowie, J. M. G. (1991). *Polymers: Chemistry & Physics of Modern Materials* (2nd ed.), Blackie, Glasgow, UK. 436 p.
- Ermolenko, I. N., Lyubliner, I. P. and Gulko, N. V. (1990). *Chemically modified carbon fibers and their applications*, Verlagsgesellschaft mbH, Weinheim, Germany. 304 p.
- Esrig, M. I. (1968). "Pore pressures, consolidation and electrokinetics", *Journal of Soil Mechanics and Foundation Division*, ASCE, Vol. 94 (SM4), pp. 899-921.
- Fetzer, C. A. (1967). "Electro-osmotic stabilisation of West Branch Dam", *Journal of Soil Mechanics and Foundations Division*, ASCE, Vol. 93 (SM4), pp. 85-106.
- Gray, D. H. and Mitchell, J. K. (1967). "Fundamental aspects of electro-osmosis in soils", *Journal of the Soil Mechanics and Foundations Division*, ASCE, Vol.93 (SM6), pp. 209-236.
- Hellawell, E. (1994). *Modelling transport processes in soil due to hydraulic density and electrical gradients*, PhD Thesis, Cambridge University, UK.
- Lageman, R. (1995). Personal Communication.
- Lageman, R., Pool, W. and Seffinga, G. A. (1989). "Electro-reclamation: state-of-the-art", *In NATO/CCMS 3rd Int. Conf. on Demonstration of Remedial Action Technologies for Contaminated Land and Groundwater*, Nov. 6-9 1989, Montreal, Canada, pp. 115-136.
- Lo, K. Y., Ho, K. S., & Incullet, I. I. (1991a). "A novel technique of electrical strengthening of soft sensitive clays by dielectrophoresis". *Canadian Geotechnical Journal*, Vol. 29, pp. 599-608.
- Lo, K. Y., Ho, K. S. and Incullet, I. I. (1991b). "Field tests of electroosmotic strengthening of soft sensitive clay", *Canadian Geotechnical Journal*, Vol. 28, pp. 74-83.
- Milligan, V. (1994). "First applications of electro-osmosis to improve friction pile capacity - three decades later", *In Proc. 13th Int. Conf. on Soil Mechanics and Foundation Engineering*, Jan. 5-10 1994, , New Delhi, India. Balkema: Rotterdam, The Netherlands, Vol. 5, pp. 1-5.
- Mitchell, J. K. (1991). "Conduction phenomena: from theory to geotechnical practice", *Geotechnique*, Vol. 41 (3), pp. 299-340.
- NATO/CCMS (1993). "Demonstration of Remedial Action Technologies for Contaminated Land and Groundwater". (Final Report No. EPA/600/R-93/012a) North Atlantic Treaty Organisation, Committee on the Challenges of Modern Society.
- Nettleton, I. M. (1996). *Electro-Bioremediation*. 1st year interim report for EPSRC Contract No. GR/K20590. Geotechnical Group, University of Newcastle upon Tyne, UK.
- van Olphen, H. (1977). *An introduction to clay colloidal chemistry*, (2nd Ed.), Wiley Interscience: New York, USA. 318 p.
- Wan, T. W. and Mitchell, J. K. (1976). "Electro-osmotic consolidations of soils", *Journal of Soil Mechanics and Foundation Division*, ASCE, Vol. 102, (GT5), pp. 503-507.

A Study of the Behavior of Geogrid Reinforced Stone Column

J.S. Sharma

NTU-PWD Geotechnical Research Centre, Nanyang Technological University, Singapore

ABSTRACT: The bearing capacity of a stone column is mainly governed by the bulging failure near its top end. The performance of a stone column can be improved by providing layers of reinforcement in the top region. In this paper, the behavior of geogrid reinforced stone column is explored using the finite element method. Results are presented from a parametric study using a unit cell finite element mesh in which the number, spacing and the stiffness of the geogrid were varied. It was found that increasing the number of geogrid layers results in an increase in the bearing capacity and a reduction in the bulging of the stone column. Decreasing the spacing of geogrid layers also increases the bearing capacity of the stone column. However, decreasing the spacing to less than 0.5 times the diameter of the stone column does not result in appreciable increase in bearing capacity. An inexpensive, low stiffness reinforcement installed at correct spacing is good enough to provide significant increase in the bearing capacity of the stone column.

KEYWORDS: Bearing Capacity, Finite Element Analysis, Geogrids, Soft Soils, Stone Columns

1 INTRODUCTION

It has become a common practice to install stone columns for improving the bearing capacity of soft clay deposits. When a soft clay layer installed with stone columns is loaded, a redistribution of vertical stress takes place. Most of the vertical stress is carried by the stone column because it is significantly stiffer than the soft clay. As a result, the stone column deforms laterally into the surrounding soil. For stone columns with lengths greater than a certain critical length, it is widely accepted that their load carrying capacity is governed by the bulging failure near their top end irrespective of whether they are end bearing or penetrate partially into a medium stiff soil layer (Madhav and Miura, 1994). The reason for this is the shear strength of the surrounding soft soil near the top end of the stone column is fairly low and therefore, the soil is unable to provide sufficient lateral resistance to the bulging. Experiments on stone columns have indicated that maximum bulging occurs at a depth approximately equal to 1 to 1.5 times the diameter of the stone column (Hughes et al., 1975; Madhav, 1982). The occurrence of bulging failure limits the ultimate load carrying capacity of a stone column regardless of the stiffness of the stone column material.

The magnitude of lateral stresses imposed by the stone column on the surrounding soil can be reduced by reinforcing the stone column near its top end using layers of geogrid. As a result, the bulging of stone column is reduced and its load carrying capacity is increased. The effectiveness of this technique has been demonstrated experimentally by Madhav (1982). Madhav et al. (1994) have proposed a limit equilibrium based method for the design of such stone columns. Their method is simple to use but it does not take into account the effect of slip at the stone column-soil interface and the stiffness of the reinforcement. In this paper, the behavior of geogrid reinforced stone columns is explored using the finite element method. A parametric study was conducted using a

“unit cell” finite element mesh in which the number, the spacing and the stiffness of the geogrid were varied. The finite element code was validated against the results of a field trial on a single stone column (Hughes et al., 1975) prior to its deployment in the parametric study.

2 FINITE ELEMENT ANALYSIS

2.1 The Mesh

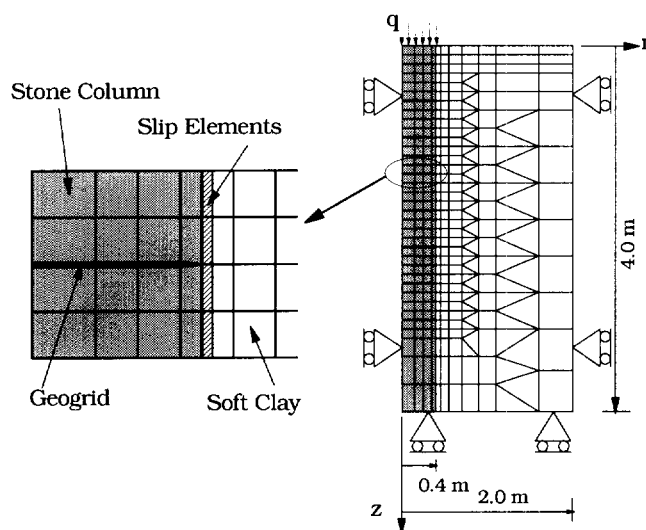


Figure 1. The finite element mesh

Figure 1 shows the details of the finite element mesh used in the present study. It is an axisymmetric unit cell mesh with the central axis of the stone column as the axis of symmetry. The diameter of the stone column is 0.8 m whereas the diameter of the unit cell soil cylinder is 4 m, giving the replacement ratio, i.e. the ratio of the volume of stone column to the volume of the unit cell soil cylinder, equal to 0.04 or 4%. Only top 4 m of the stone column has been

modelled. The justification for this the fact that at depths greater than 2 to 3 diameters, the deformation of the stone column is negligible (Hughes and Withers, 1974).

The stone column has been modelled using 8-noded quadrilateral elements with displacements unknown. The surrounding soil has been modelled using 6-noded triangular and 8-noded quadrilateral elements with displacements and pore pressures unknown. The geogrid has been modelled using very thin (0.01 m thickness) 8-noded quadrilateral elements. The interface between the stone column and the surrounding soil has been modelled using 6-noded slip elements. No slip elements are provided at the geogrid-stone column interface.

2.2 Constitutive Modelling of Materials

The stone column has been modelled as Elastic-Perfectly Plastic material with Mohr-Coulomb failure criterion. The surrounding soft clay is considered as normally consolidated and is modelled as an Elastic-Perfectly Plastic material but with Tresca failure criterion. The undrained shear strength of the soft clay increases linearly with depth. The geogrid has been modelled as Linear Elastic material. The slip elements at stone column-soft clay interface have also been modelled as Elastic-Perfectly Plastic material with Mohr-Coulomb failure criterion. Following the experience of Balaam and Poulos (1982), the stone column-soft clay interface is assumed as purely cohesive, i.e. zero angle of friction but a finite value of cohesion. The cohesion at the stone-column-soft clay interface at any level is taken as 80% of the undrained shear strength of soft clay at that level. Table 1 lists all the parameters chosen for the above four types of materials.

Table 1. Parameters for the stone column, soft clay, geogrid and the stone-column-soft clay interface

Parameter	Stone Column	Soft Clay	Geogrid	Inter-face
c_o (kPa)	1.0	1.2	—	1.0
m_c (kPa/m)	0.0	1.94	—	1.55
ϕ (Degrees)	40.0	0.0	—	0.0
E_o (kPa)	40,000	720	2,500,000	600
m_E (kPa/m)	9200	1150	0.0	900
ν	0.3	0.49	0.3	—
γ_{bulk} (kN/m ³)	18.0	18.0	18.0	—
t (m)	—	—	0.01	0.04

Notes: c_o — cohesion at ground level, m_c — rate of increase of cohesion with depth, ϕ — angle of internal friction, E_o — Young's modulus at ground level, m_E — rate of increase of Young's modulus with depth, ν — Poisson's ratio, γ_{bulk} — bulk unit weight, t — thickness.

2.3 Stages in a Typical Analysis

A typical finite element analysis in the present study has following stages:

1. In-situ stage: This is the start of the analysis. At this stage of the analysis, the whole mesh contains only the soil elements.
2. Installation of stone column and geogrid layers: In this stage, the soil elements that are occupying stone column space are removed from the mesh and the elements representing stone column and geogrid are added to the mesh.
3. Loading of stone column: In this stage, the stone column is loaded at its top end using displacement control. The displacement is applied in very small increments (0.0002 m per increment) to prevent any divergence from the stress-strain curve.

2.4 Validation of the Finite Element Code

Before a finite element mesh is used for a parametric study, it is imperative to validate it against good quality experimental data. The main purposes of the validation are to ensure that the mesh is sufficiently refined and to check that the constitutive models used are satisfactory. For the validation, it was decided to make use of the results of a field trial on a single stone column reported by Hughes et al. (1975). This field trial is supplemented with extensive site investigation data which includes undrained shear strength profile of the soil, in-situ lateral stresses, and the soil modulus obtained from in-situ pressuremeter tests. Almost all the input parameters were taken directly from the site investigation data with the exception of the permeability of the soil which was taken to be 2×10^{-9} m/s in horizontal direction and 1×10^{-9} m/s in the vertical direction. Since the full loading of the stone column was very quick (total time = 0.5 hour), the soil can be assumed to be undrained. Therefore, the finite element simulation can be considered to be insensitive to small differences in permeability of the soil.

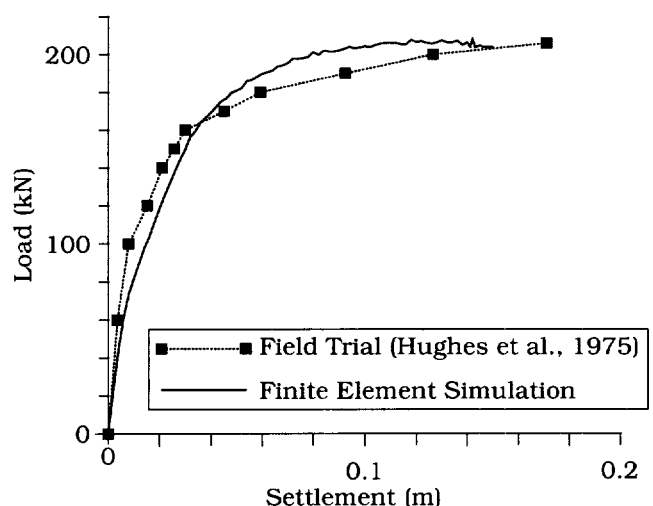


Figure 2. Measured and simulated load-settlement curves (after Hughes et al., 1975)

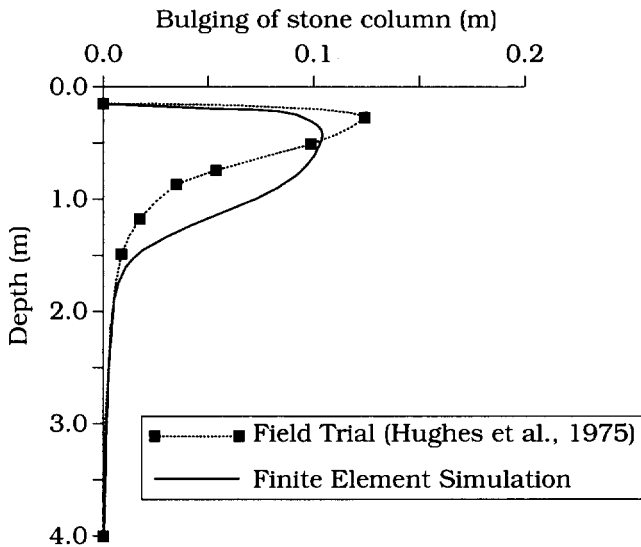


Figure 3. Measured and simulated bulging of stone column (after Hughes et al., 1975).

Detailed account of the finite element simulation can be found in Sharma (1997). Due to lack of space, only two main comparisons are described here. Figure 2 shows the comparison between the measured and the simulated load settlement curves. As seen from Figure 2, there is good agreement between the two curves. The measured and simulated deformation of the stone column at the end of loading are shown in Figure 3. Once again, the agreement between the two curves is satisfactory.

3 PARAMETRIC STUDY

As mentioned previously, the main parameters in the present study are: the number, spacing and the stiffness of the geogrid. Table 2 lists these parameters and their range.

Table 2. Range of parameters for the geogrid

Parameter	Range
Number of geogrid layers	0 to 5, in steps of 1
Spacing of geogrid layers	0.5 to 3 times the diameter of stone column
Elastic Modulus of geogrid (kPa)	100,000 to 2,500,000

3.1 Effect of Number of Reinforcement Layers

In this series of finite element runs, the number of geogrid layers was increased from 0 to 5 in steps of 1. The spacing of these layers was kept constant at 0.5 times the diameter of the stone column (d_{sc}) and the elastic modulus (E_r) of the geogrid was taken equal to 2.5×10^9 N/m². Figure 4 shows the load-settlement curves for the stone column.

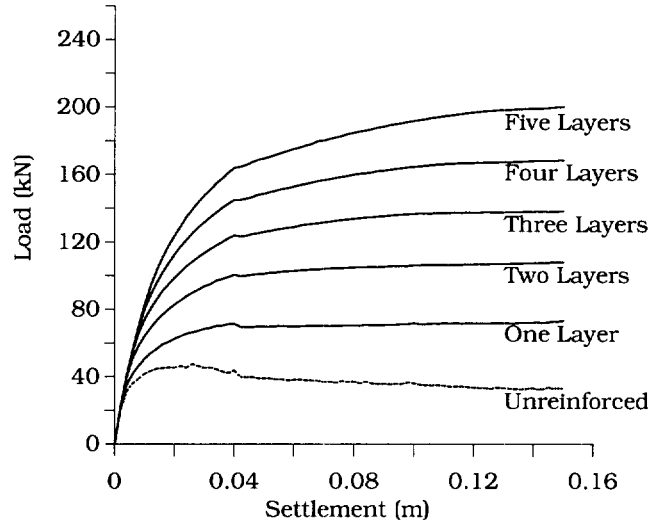


Figure 4. Effect of number of layers on the load-settlement response of stone column

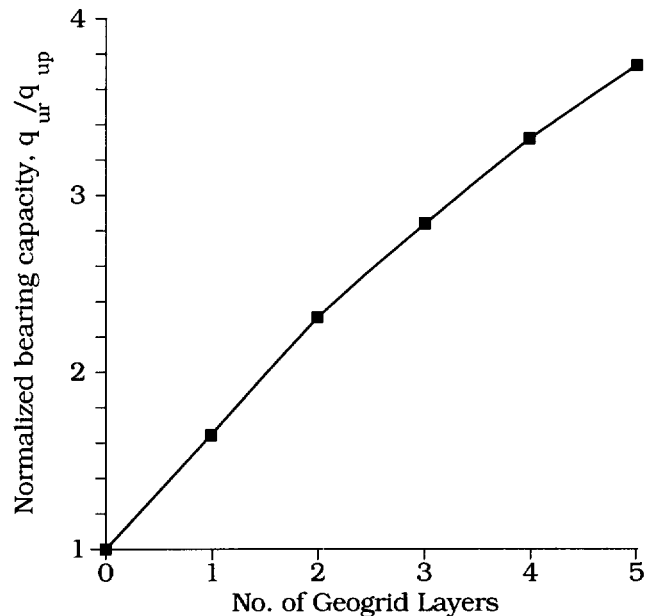


Figure 5. Variation of normalized bearing capacity of stone column with number of geogrid layers

Figure 5 shows the normalized bearing capacity of the stone column ($\theta = q_{ur}/q_{up}$) plotted against number of geogrid layers. In figure 5 and in subsequent figures, q_{ur} is the ultimate bearing capacity of a reinforced stone column and q_{up} is the ultimate bearing capacity of an unreinforced stone column. It is clear from figures 4 and 5 that inclusion of geogrid layers in the stone column results in significant improvement in the load bearing capacity of the stone column. For example, the load bearing capacity of a stone column reinforced with three layers of geogrid is more than

twice that of an unreinforced stone column. The variation between θ and the number of geogrid layers is almost linear. However, it does tend to flatten slightly as the number of layers are increased beyond 3 which implies that it may not be economical to put more than 3 layers of reinforcement.

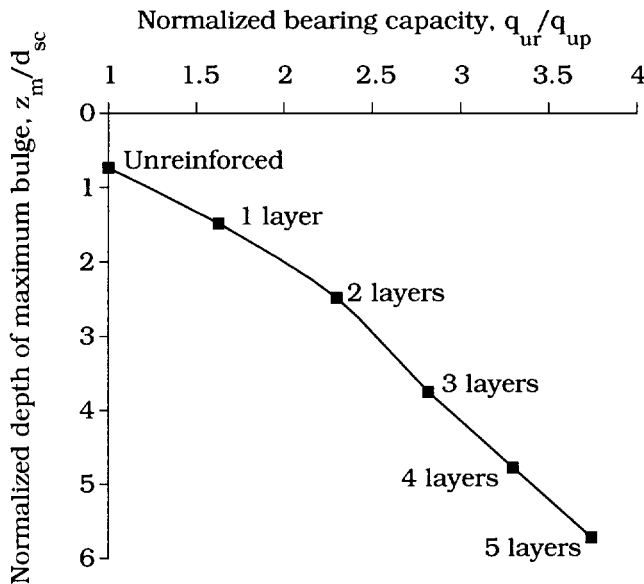


Figure 6. Variation of normalized depth of maximum bulging with normalized bearing capacity of stone column.

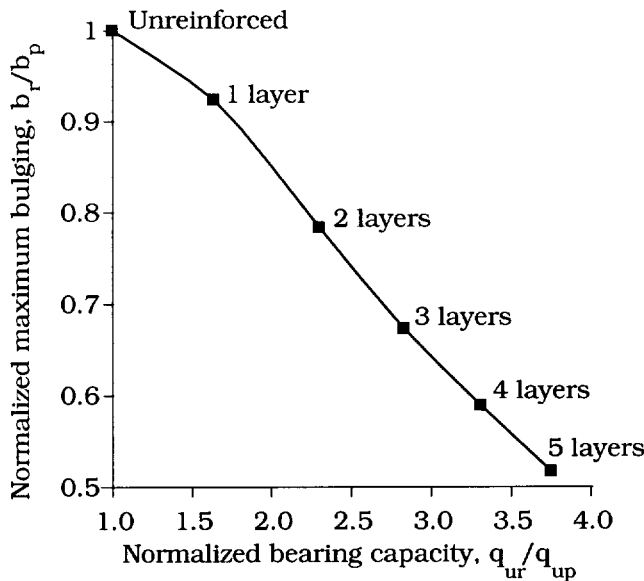


Figure 7. Variation of normalized maximum bulging with normalized bearing capacity of stone column

Figure 6 shows normalized depth of maximum bulging ($\zeta = z_m/d_{sc}$) of stone column plotted against θ . In this figure, z_m is the depth at which maximum bulging takes place. It can be seen from figure 6 that the increase in bearing capacity is

achieved by pushing the point of maximum bulging deeper, i.e. the failure mechanism is now benefiting from higher lateral resistance from the surrounding soil.

Increasing number of geogrid layers not only pushes the point of maximum bulging deeper but also reduces the amount of maximum bulging as seen from Figure 7 which shows normalized maximum bulging ($\beta = b_r/b_p$ where b_r is maximum bulging for reinforced stone column and b_p is the maximum bulging for unreinforced stone column) plotted against θ . For example, the amount of maximum bulging for a stone column reinforced with 3 geogrid layers is less than 70% of that for an unreinforced stone column. The reduction in amount of maximum bulging is achieved by redistribution of the lateral deformation of stone column over a longer section as shown in Figure 8.

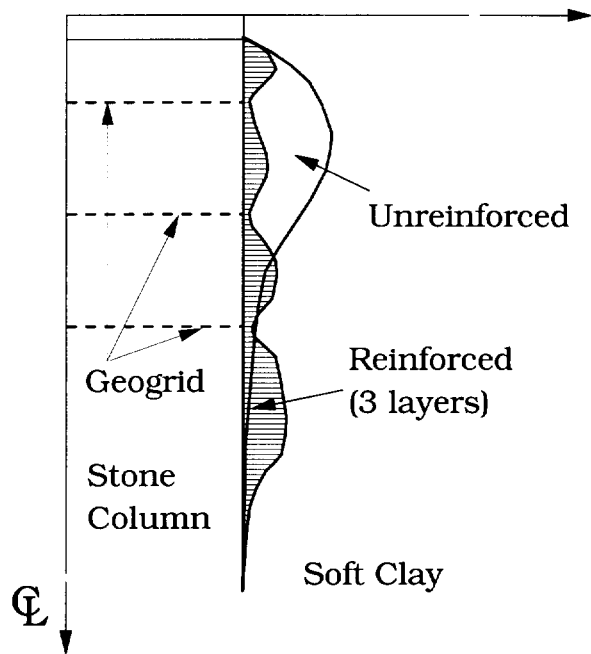


Figure 8. Redistribution of lateral deformation of stone column due to the presence of geogrid layers.

3.2 Effect of Spacing of Reinforcement Layers

For this series of finite element runs, the stone column was reinforced with three geogrid layers. E_r for geogrid was taken equal to $2.5 \times 10^9 \text{ N/m}^2$. Figure 9 shows normalized spacing of the geogrid layers ($\lambda = s_r/d_{sc}$ where s_r is the spacing of geogrid layers) plotted against θ . It can be seen from figure 9 that the maximum benefits of reinforcing the stone column are achieved when the spacing of reinforcement is between 0.5 to 1.5 times the diameter of the stone column. A spacing closer than 0.5 times the diameter would not result in any significant increase in the bearing capacity. Also, the combined action of multiple

layers of reinforcement, i.e. redistribution of lateral deformation of stone column, is not achieved effectively if the spacing of the reinforcement is greater than twice the diameter of the stone column. As a result, the increase in bearing capacity of the stone column is not significant.

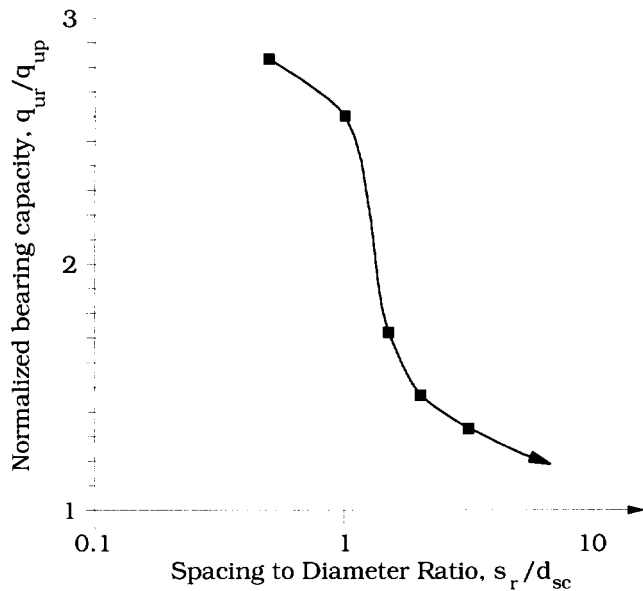


Figure 9. Effect of spacing of geogrid on the bearing capacity of the stone column

3.3 Effect of Stiffness of Reinforcement

In this series of finite element runs, the stone column was reinforced with three layers of geogrid spaced at 0.5 times the diameter of the stone column. Figure 10 shows elastic modulus of the geogrid (E_r) plotted against θ . The bearing capacity of a reinforced stone column increases as the stiffness of the reinforcement is increased. The increase is very dramatic when the stiffness is increased from $E_r = 0$ (unreinforced case) to $E_r = 1 \times 10^8 \text{ N/m}^2$. However, beyond a certain stiffness ($E_r > 10 \times 10^8 \text{ N/m}^2$), the increase is not significant. This implies that one need not use an expensive high stiffness reinforcement in order to improve the bearing capacity of stone column. Even a cheap, low stiffness reinforcement installed at correct spacing would provide significant increase in the bearing capacity of the stone column.

Figure 11 shows maximum tension in the geogrid plotted against E_r . It can be seen from figure 11 that a stiffer reinforcement attracts more tension but does not contribute significantly towards improving the bearing capacity of the stone column. Provision of a low stiffness reinforcement would result in a relatively flexible stone column with low levels of tension in the reinforcement. Such a flexible stone column would deform more uniformly than the one installed with very stiff reinforcement. This would result in the

bulging being distributed over a greater length, thus preventing localised bulging failure and resulting in improved bearing capacity.

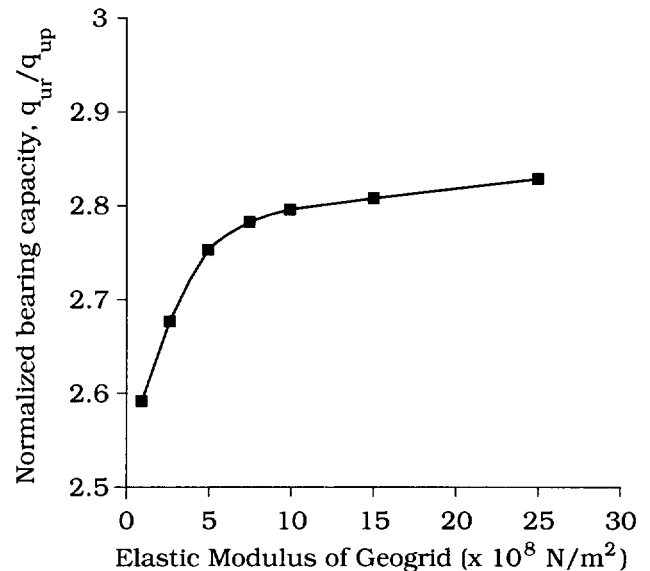


Figure 10. Effect of stiffness of geogrid on the bearing capacity of stone column

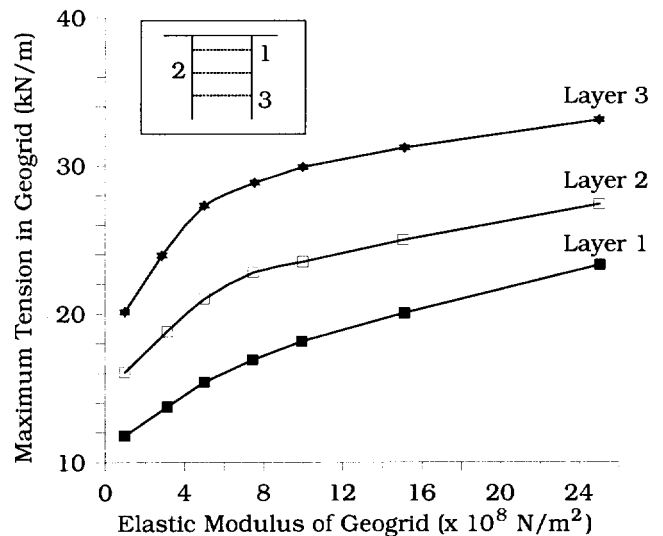


Figure 11. Effect of the stiffness of the geogrid on the magnitude of maximum tension induced in the geogrid

4 CONCLUSIONS

A parametric study of the behavior of geogrid reinforced stone column has been conducted using a finite element unit cell mesh which has been validated against the results of a field trial. The number, the spacing and the stiffness of

geogrid were the main parameters. It was found that increasing number of layers of geogrid increases the bearing capacity of the stone column. It also reduces the bulging of stone column and pushes the point of maximum bulging deeper. The inclusion of geogrid layers results in redistribution of lateral deformation of stone column and therefore, facilitates much more effective transfer of lateral stresses from stone column to the soft clay.

Installing geogrid layers at closer spacing also increases the bearing capacity of the stone column. The optimum spacing of geogrid layers was found to be between 0.5 to 1.5 times the diameter of the stone column. Installation of geogrid layers at spacing closer than 0.5 times the diameter of stone column does not result in appreciable increase in the bearing capacity of the stone column.

The increase in bearing capacity of stone column due to increase in stiffness of geogrid is quite dramatic when the elastic modulus of geogrid is increased from zero (unreinforced) to 1×10^8 N/m². However, increasing the elastic modulus beyond 10×10^8 N/m² does not result in appreciable increase in the bearing capacity. A stiffer reinforcement also tends to attract more tension. Based on these two observations, it can be concluded that it is better to reinforce the stone column using a less stiff reinforcement installed at a spacing between 0.5 and 1.5 times the diameter of the stone column. Such a system would be more flexible and would be able to deform more uniformly than the one installed with stiff reinforcement. This would in turn result in bulging being distributed over a greater length, thus preventing localised bulging failure and improving the bearing capacity of the stone column.

ACKNOWLEDGEMENT

The author has benefited greatly from numerous stimulating discussions with Prof. M.R. Madhav of Indian Institute of Technology, Kanpur and would like to take this opportunity to thank him for all his help and encouragement.

REFERENCES

- Balaam, N.P. and Poulos, H.G. (1982). The Behaviour of Foundations Supported by Clay Stabilised by Stone Columns. *Research report No. R424*, School of Civil and Mining Engineering, University of Sydney.
- Hughes, J.M.O. and Withers, N.J. (1974). Reinforcing of soft cohesive soils with stone columns. *Ground Engineering*, Vol. 7, pp 42-49.
- Hughes, J.M.O., Withers, N.J. and Greenwood, D.A. (1975). A Field Trial of the Reinforcing Effect of a Stone Column in Soil. *Geotechnique*, Vol. 25, No. 1, pp 31-44.
- Madhav, M.R. (1982). Recent Development in the Use and Analysis of Granular Piles. *Symposium on Recent Development in Ground Improvement Techniques*, Bangkok, pp 117-129.

Madhav, M.R., Alamgir, M. and Miura, N. (1994). Improving Granular Column Capacity by Geogrid Reinforcement. *Fifth International Conference on Geotextiles, Geomembranes and Related Products*, Singapore, Vol. 1, pp 351-356.

Madhav, M.R. and Miura, N. (1994). Soil Improvement, Panel Report on Stone Columns, *Thirteenth ICSMFE*, New Delhi, India, Vol. 5, pp 163-164.

Sharma, J.S. (1997). A Parametric Study of the Behaviour of Reinforced Stone Columns. *Technical Report No. NTU/GRC/97-2*, NTU-PWD Geotechnical Research Centre, Nanyang Technological University, Singapore.

Geosynthetic Reinforced Unpaved Roads on Very Soft Soils: Construction and Maintenance Effects

E.M. Palmeira

Associate Professor, Department of Civil Engineering, University of Brasilia, Brasilia, Brazil

ABSTRACT: Geosynthetics can be used in unpaved roads on soft subgrades to increase bearing capacity and reduce fill consumption. When unpaved roads are built on very soft soils and with poor construction techniques excessive deformations of the geosynthetic layer can occur during the construction of the road caused by the traffic of bulldozers and trucks on thin layers of fill. This paper examines the effects of the road construction on the strains in extensible geosynthetic reinforcements. A methodology to estimate geosynthetic strains caused by construction is presented and its results suggest that significant geosynthetic strains can be developed during road construction. The influence of surface maintenance on the bearing capacity of reinforced and unreinforced unpaved roads is also investigated. A methodology to estimate the bearing capacity of this type of road after surface repair is presented. The predictions by this methodology compared well with model tests results available in the literature.

KEYWORDS: geosynthetic, reinforcement, unpaved roads, geotextile strains, surface maintenance.

1 INTRODUCTION

The construction of embankments on soft soils is generally a problem in routine geotechnical engineering works. In the case of unpaved roads the main load on the embankment is usually due to the weight of the trucks rather than the weight of the fill material itself. High vertical stresses can reach the soft foundation causing excessive deformation or local failures that may lead to interruptions of the traffic and to transportation cost increases. The use of geosynthetics for the reinforcement of unpaved roads on soft subgrades has been a common solution for the increase of road bearing capacity, besides minimizing fill consumption, foundation deformation and road surface rutting.

Several methodologies have been presented so far dealing with the design of reinforced unpaved roads or with the estimate of bearing capacity of this type of structure (Ferreira Jr, 1995). A common feature of these methodologies is to assume the geometrical characteristics of the problem as shown in Figure 1. This assumption does not take into account geosynthetic or subgrade deformations caused by the construction of the road. However, in the case of very soft subgrades (undrained strength at the surface below 15 kPa) large deformations of the subgrade can be caused by construction vehicles such as bulldozers and loaded trucks that bring the fill material for the road construction. In such cases the first deformations on the geosynthetic layer will be caused by these vehicles while spreading and compacting the fill or trafficking on thin layers of fill. In many cases the compaction of the fill material is simply provided by the bulldozer weight and the traffic of the trucks used in the construction of the road.

This paper deals with geosynthetic deformations caused during construction of the road and how they can be

estimated. The behaviour of this type of road after surface maintenance is also approached, particularly for the case of narrow unpaved roads.

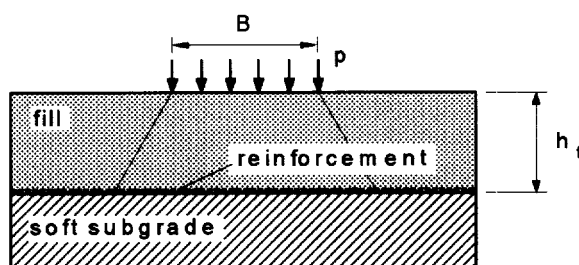


Figure 1. Typical approach for reinforced unpaved roads.

2 GEOSYNTHETIC DEFORMATIONS CAUSED BY ROAD CONSTRUCTION

The construction of unpaved roads on soft soils usually involves the following steps: cleaning of the ground surface, laying of the geosynthetic layer (if present), spreading of the fill material and fill compaction by appropriate equipments. Because of site conditions or project characteristics some of these steps may not be executed in many cases, such as cleaning of the ground surface and fill compaction by usual compaction equipments. Frequently the compaction of the fill is provided by the bulldozer and the traffic of trucks and at this initial stage the road is continuously repaired until a final height of compacted fill is reached for which further loads can be sustained for a certain period of time until maintenance is required. During spreading of fill on the geosynthetic layer the bulldozer operator can cause severe rutting and geosynthetic deformations due the combination

of the bulldozer weight and thin fill layers. A simple analysis of the mechanics of the problem is shown in Figure 2, where the vertical stress caused by the bulldozer weight is assumed as a uniformly distributed stress (strip load). If the fill strength is neglected, equilibrium along the vertical direction leads to an expression for a conservative estimate of the minimum compacted fill layer below the bulldozer track in order to avoid failure of the fill and excessive rutting:

$$h_0 = \frac{b}{\tan\theta} \left(\frac{p}{N'_c c_0} - 1 \right) \quad [1]$$

where: h_0 is the minimum fill height (when the factor of safety equals to unity), p is the vertical stress on the surface, b is half of the track width, θ is the load spreading angle, N'_c is the bearing capacity factor for the foundation and c_0 is the soft soil undrained strength at the surface.

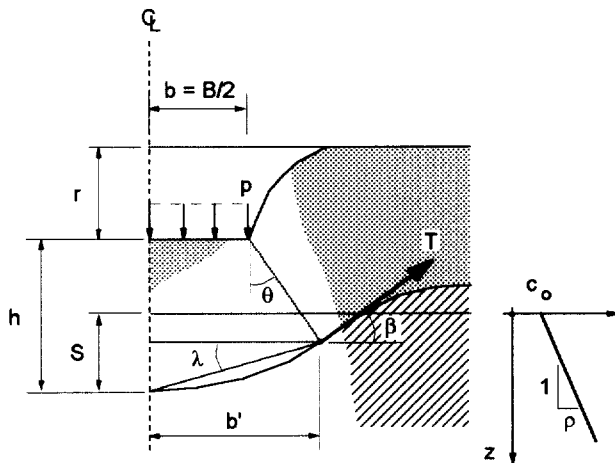


Figure 2. Failure mechanism during spreading of the fill.

A mean value for the subgrade undrained strength can replace the value of c_0 if a less conservative estimate is desired. However, the value of c_0 is chosen at this stage because not all the efforts acting on the system are being considered in expression 1, such as inertia forces and vibrations. For the case of reinforced roads the value of N'_c to be used is equal to $\pi + 2$ and for unreinforced roads the value given by the expression below (Houlsby et al, 1989) is suggested:

$$N'_c = 1 + \frac{\pi}{2} + \cos^{-1}\alpha + \sqrt{1 - \alpha^2} \quad [2]$$

where α is the ratio between the mobilized outward shear stress and the undrained strength at the subgrade surface.

If the bulldozer moves on a fill layer with thickness equal or smaller than the value given by equation 1 a significant vertical displacement at the foundation soil surface will occur. This settlement will reach to a depth where equilibrium is maintained depending on the subgrade undrained strength and on the force mobilized in the reinforcement. This depth can be also estimated considering the vertical equilibrium in Figure 2, which for the reinforced case yields to:

$$S = \frac{pb - T \sin\beta}{\rho N_c (b + h \tan\theta)} - \left(\frac{c_0}{\rho} + 2b \right) \quad [3]$$

where S is the maximum settlement at the subgrade surface, T is the geosynthetic tensile force, β is the inclination of T to the horizontal direction, N_c is the bearing capacity factor for a foundation with inclined base (λ , in Fig. 2) and θ is the load spreading angle in the reinforced case. Due to the assumed trapezoidal shape of the deformed fill below the load (Fig. 2) and assuming no shear stress at the geotextile-subgrade interface the bearing capacity factor in this case (N_c) can be obtained by (Houlsby and Wroth, 1983, and Palmeira and Cunha, 1993):

$$N_c = \pi + 2 - 2\lambda \quad [4]$$

where λ is the angle between the fill wedge base and the horizontal (Fig. 2).

Palmeira and Cunha (1993) performed model tests with unpaved roads reinforced with extensible geotextiles subjected to severe rutting caused by successive stages of footing loading and surface repair. Empirical expressions were obtained to estimate β , λ and the average geosynthetic tensile strain (ϵ) as a function of the maximum vertical displacement at the fill-subgrade interface normalized by the footing width. These expressions were developed for roads with ratios $h_f/B \leq 0.7$ (Fig. 1) and are presented below:

$$\frac{\beta}{\pi} = 0.237 + 0.19 \log_{10} \frac{S}{B} \quad (\beta \text{ in radians}) \quad [5]$$

$$\frac{\lambda}{\pi} = 0.156 + 0.133 \log_{10} \frac{S}{B} \quad (\lambda \text{ in radians}) \quad [6]$$

$$\epsilon = 0.5 \sqrt{1 + 3.5 \tan^2 \lambda} + \frac{0.27}{\tan \lambda} \ln(1.87 \tan \lambda + \sqrt{1 - 3.5 \tan^2 \lambda}) - 1 \quad [7]$$

Figure 3 presents some comparisons between values of geotextile strain (ϵ) versus S/B predicted by equation 7 and observed by different researchers (for $h_f/B \leq 0.7$). The results from model tests were inferred from deformed

shapes of the reinforcement layer or obtained by strain measurements in the reinforcement. A good agreement between predicted and observed values can be noted.

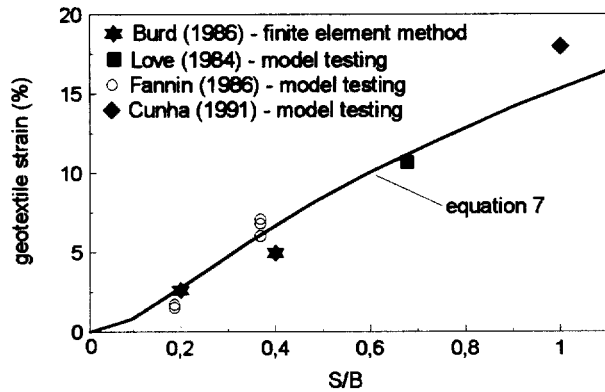


Figure 3. Predicted and observed values of geotextile strains.

Laboratory tests on model unpaved roads have also consistently shown that the load spreading angle in the reinforced fill can be significantly greater than in the unreinforced fill (Love, 1984, Palmeira and Cunha, 1993 and Palmeira and Ferreira, 1994). Palmeira and Ferreira (1994) observed load spreading angles between 21 to 34° for reinforced roads and between 6 to 17° for the unreinforced ones.

The value of S depends on the fill thickness (h in Fig. 2) below the bulldozer track. This thickness depends on the bulldozer operator experience and is likely to be highly variable in different parts of the road depending on the subgrade undrained strength and stiffness at its surface. If h is significantly smaller than h_0 (equation 1) and depending on the subgrade strength the rut depth required for equilibrium can be even greater than h and soft soil may reach the fill surface through fill cracks. This is certainly more critical for the unreinforced case, but depending on the value of h high geotextile strains can be developed because of this excessive deformation of the system. These strains are not taken into account if the available design methods are applied for unpaved roads on very soft soils or when poor construction techniques are employed.

Assuming a linear relationship between tensile force and tensile strain for the geotextile, expressions 1 and 3 can be combined to obtain the following expression relating maximum vertical displacement at the fill-subgrade interface (S) to geotextile strain (ϵ) in dimensionless terms:

$$\frac{S}{B} = \frac{\frac{p}{c_0} - 2 \sin \beta \frac{J}{c_0 B} \epsilon}{N_c \frac{\rho B}{c_0} \left\{ 1 + k \left[\frac{1}{(\pi + 2) c_0} p - 1 \right] \right\}} - \left(\frac{c_0}{\rho B} + 1 \right) \quad [8]$$

where k is the ratio between h and h_0 .

Figures 4 to 6 show charts obtained from the iterative solution of equations 4 to 8 to estimate the geotextile deformation for $k = 0.5$ and for different values of the dimensionless terms. The geotextile strain due to road construction may then be taken into account in conjunction with the strains caused by the traffic of vehicles on the road to estimate the total geotextile strain. The associated settlement S can be estimated by equation 8 and can then be compared with the value of h ($h = k h_0$, with h_0 given by equation 1).

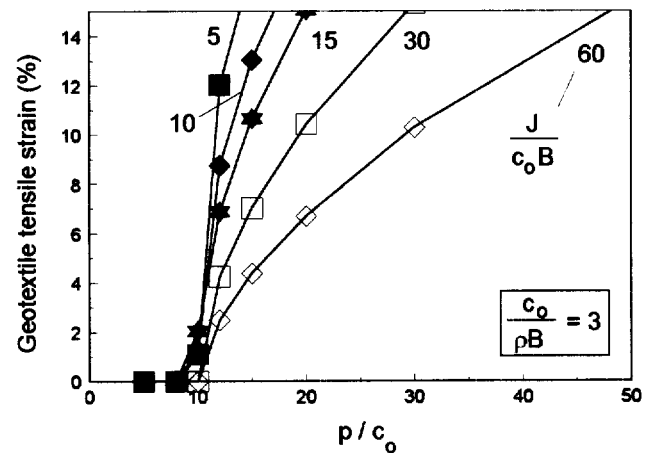


Figure 4. Geotextile strain versus p/c_0 for $c_0/(\rho B) = 3$.

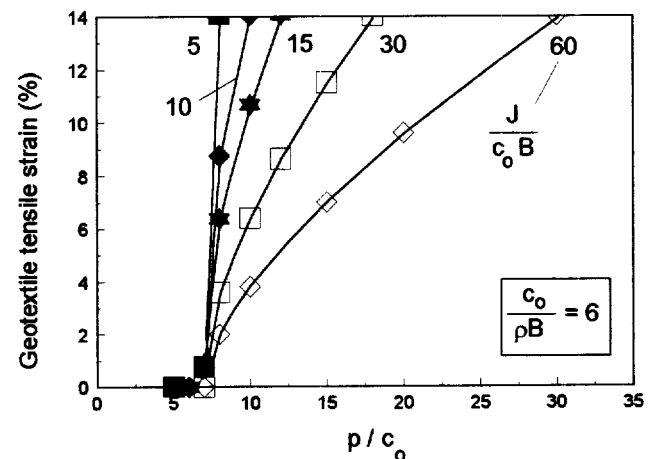


Figure 5. Geotextile strain versus p/c_0 for $c_0/(\rho B) = 6$.

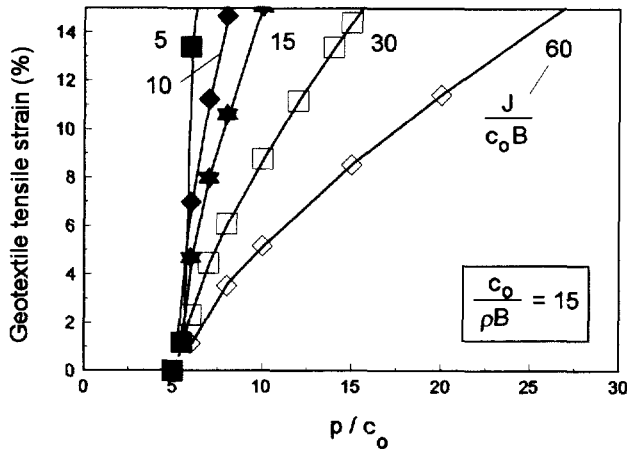


Figure 6. Geotextile strain versus p/c_0 for $c_0/(\rho B) = 15$.

3 BEARING CAPACITY OF UNPAVED ROADS AFTER SURFACE MAINTENANCE

3.1 Theoretical Development

Figure 7 shows the failure mechanism assumed after a repair of the road surface after excessive rutting has occurred under plane strain conditions. This is the case of narrow roads and poor maintenance conditions, where the surface repair is made just by filling the rut and compacting the new material. The region ABCD is inside the compacted material while the block CDEF is composed of the original failed road. It is assumed that failure in the repaired region will develop along vertical planes (plane BC in Fig. 7) due to the punching mechanism of the block underneath. This is consistent with the observation of failure mechanisms in model roads which suffered successive stages of surface repair and loading (Palmeira and Cunha, 1993). For stiff fill materials the block ABCFED is assumed to behave as a rigid mass being pushed into the soft subgrade. A vertical stress distribution throughout the repaired region ABCD similar to the one employed by Terzaghi (1943) for the study of tunnels in soil is adopted (Fig. 8). The yielding base DC controls the failure mechanism of the repaired region and the horizontal stresses along plane BC drops during loading, being assumed that active conditions are reached. This assumption is corroborated by predictions of horizontal stresses in a elastic layer with a yielding base (Poulos and Davis, 1974). Based on these hypotheses the vertical stress at the base of the rut can be derived:

$$\sigma_b = p.e^{-2k_{ap} \tan \phi' \frac{r}{B}} - \frac{2c' - \gamma B}{2k_{ap} \tan \phi'} (1 - e^{-2k_{ap} \tan \phi' \frac{r}{B}}) \quad [9]$$

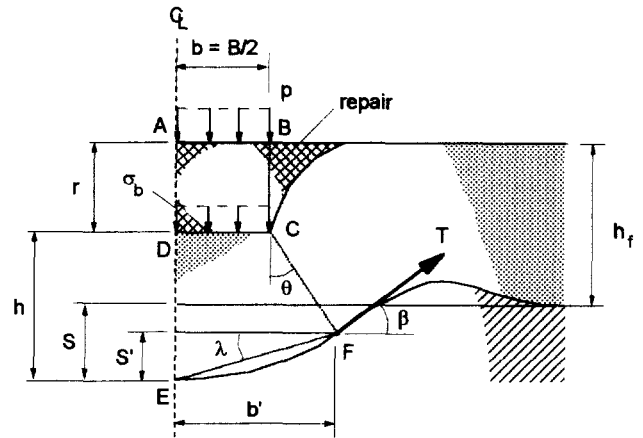


Figure 7. Failure mechanism after surface repair.

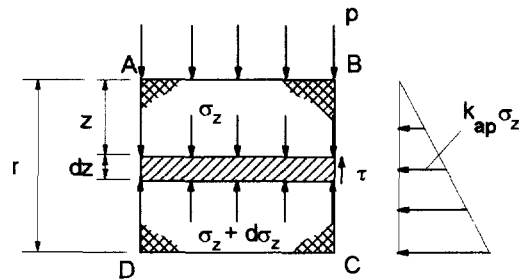


Figure 8. Vertical stress distribution in block ABCD

where γ is the specific weight of the fill, k_{ap} is the active earth pressure coefficient and c' and ϕ' are the shear strength parameters of the soil used for the repair (peak values).

According to Figure 9 the study of the equilibrium of block CDEF and the bearing capacity of the subgrade yields to:

$$\sigma_b = \frac{b'}{b} \sigma + \frac{b'}{b} \tan \lambda \tau - \frac{W}{b} + \frac{T \sin \beta}{b} \quad [10]$$

where σ is the foundation bearing capacity, τ is the shear stress at the reinforcement-subgrade interface (assumed equal to the undrained strength of the subgrade), W is the weight of block DCEF and T is the tensile force in the reinforcement (if present).

The bearing capacity of the foundation soil is given by (Palmeira and Cunha, 1993, Figs. 7 and 9):

$$\sigma = N_c C_u + \gamma h_f + \gamma_s (S - S') \quad [11]$$

where γ_s is the specific weight of the subgrade material and h_f , S and S' are the dimensions given in Figure 7. The value of N_c is given by Equation 4, where λ is given by

between predicted and observed values of p/C_u and the scatter can be partially explained by the scatter of the values of undrained strength besides some limitations of the approach.

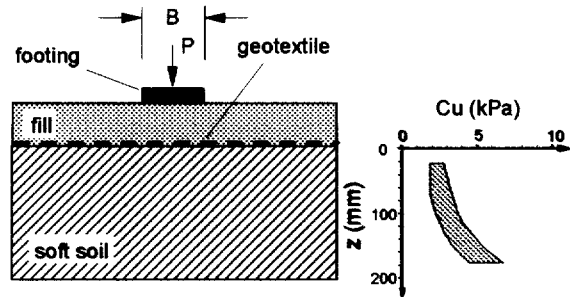


Figure 11. Schematic view of the model tests performed.

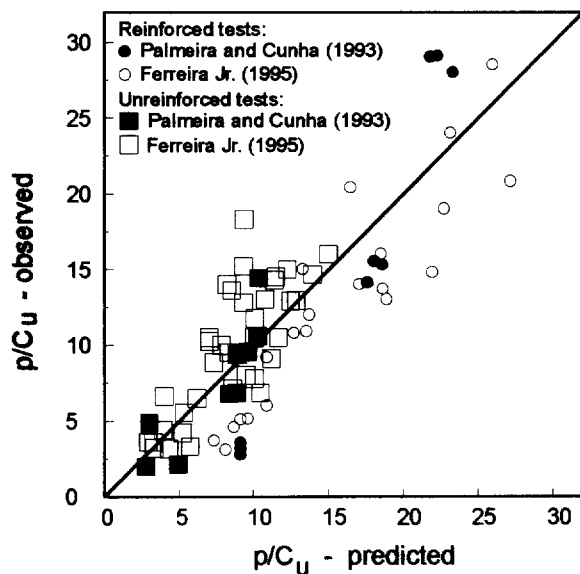


Figure 12. Comparisons between predicted and observed values of p/C_u .

4 CONCLUSIONS

This paper presents some aspects regarding geotextile deformation during unpaved road construction and bearing capacity of this type of road after surface maintenance. It is observed that significant strains can be mobilized in extensible geotextiles during road construction on very soft subgrades. A methodology is presented for the estimate of these strains. In spite of the limited amount of data available, results from model tests and finite element analyses compared well with predicted values of the variation of geotextile strain (ϵ) with the normalized settlement at the soft soil surface (S/B).

The presence of the geosynthetic has a marked effect on the bearing capacity of the unpaved road after maintenances. A proposed methodology has also been presented which improves a similar methodology previously presented in Palmeira and Cunha (1993). Good comparison was observed between predictions by this methodology and model tests results.

ACKNOWLEDGEMENTS

The Authors would like to thank the University of Brasilia, CNPq, CAPES/Brazilian Ministry of Education and Rhodia-Ster for supporting the present work.

REFERENCES

- Burd, H. J. (1986) "A Large Displacement Finite Element Analysis of a Reinforced Unpaved Road", *D.Phil. Thesis*, University of Oxford, UK, 222 p.
- Cunha, M.G. (1991) "Model Studies of Geotextile Reinforced Unpaved Roads", *MSc Thesis*, University of Brasilia, Brazil (in Portuguese), 130 p.
- Fannin, R.J. (1986) "Geogrid Reinforcement of Granular Layers on Soft Clay - A Study at Model and Full Scale", *D.Phil. Thesis*, University of Oxford, UK, 221 p.
- Ferreira Jr., L.G.F. (1995) "Model Studies on the Influence of Geotextile Reinforcement on the Failure and Deformation Mechanisms of Unpaved Roads", *MSc. Thesis*, University of Brasilia, Brazil (in Portuguese), 181 p.
- Houlsby, G.T. and Wroth, C.P. (1983) "Calculation of Stresses on Shallow Penetrometers and Footings", *OUEL Report No.1503/83*, Univ. of Oxford, UK, 18p.
- Houlsby, G.T., Milligan, G.W.E., Jewell, R.A. and Burd, H.J. (1989) "A New Approach to the Design of Unpaved Roads - Part I", *Ground Engineering*, April, pp. 25-29.
- Love, J.P. (1984) "Model Testing of Geogrids in Unpaved Roads", *D.Phil. Thesis*, University of Oxford, 216 p.
- Palmeira, E.M. and Cunha, M.G. (1993) "A Study of the Mechanics of Unpaved Roads with Reference to the Effects of Surface Maintenance", *Geotextiles and Geomembranes*, Vol. 12, No. 2, pp. 109-131.
- Palmeira, E.M. and Ferreira Jr., L.G.F. (1994) "The Behaviour of Unpaved Roads Under Large Rutting Conditions", *Fifth International Conference on Geotextiles, Geomembranes and Related Products*, Singapore, Vol. 1, pp. 135-138.
- Poulos, H.G and Davis, E.H. (1974) "Elastic Solutions for Soil and Rock Mechanics", John Wiley and Sons, New York, USA, 411 p.
- Terzaghi, K. (1943) *Theoretical Soil Mechanics*, John Wiley and Sons, New York, USA.

Numerical Analysis of a Pavement Base Reinforced with Geogrid

Mauricio Abramento

IPT- Instituto de Pesquisas Tecnológicas do Estado de São Paulo, Brasil

ABSTRACT: This paper presents results of a detailed numerical analysis, using the finite differences software FLAC, comparing the behavior of an unreinforced and geogrid reinforced pavement base. The study was developed for designing a flexible pavement (pavers over crushed stone and sand) to be built in an intermodal yard located in Brazil. Preliminary studies showed that the crushed stone layer collapses under the high imposed loads (transtainers with design wheel load of 35tf), suggesting its reinforcement with geogrids. The results of numerical analysis showed that the pavement performance improved substantially with three layers of geogrid (long-term strength of 50kN/m) evenly spaced in the crushed stone, inhibiting plastification of the materials and reducing the magnitude of plastic displacements at surface.

KEYWORDS: Geogrid, Base reinforcement, Pavement, Numerical analysis.

1 INTRODUCTION

One of the many applications of geosynthetics is reinforcement of coarse material for sustaining heavy loads. For example, Walls and Galbreath (1987) present a case of ballast reinforcement with geogrid, while Raymond et al. (1993) show the use of a layer of geogrid for reinforcing a sand for gantry cranes tracks. This paper presents results of a detailed numerical analysis, using the finite differences software FLAC, comparing the behavior of an unreinforced and geogrid reinforced pavement base. The study was developed for designing a flexible pavement to be built in an intermodal yard located in Brazil. Very heavy vehicles (transtainers) for handling containers from large ships will circulate in the area. The vehicles have a very high design wheel load of 35tf, corresponding to an unusual applied pressure on the pavement of about 12kgf/cm².

2 PAVEMENT LAYERS

Figure 1 shows the pavement system and main soil layers involved in the problem, from top to bottom: a) 15cm thick high strength articulated concrete blocks (pavers); b) crushed stone compacted with high energy (pavement base), with thickness to be determined, ranging from 0.6m (geogrid-reinforced) to 1.2m (unreinforced); c) 3.0m thick dense sand; and d) 8.0m thick compressible clay layer. Geotechnical and pluviometric peculiarities resulted in this system, in particular large differential settlements expected due to consolidation of the soft clay layer. The pavement

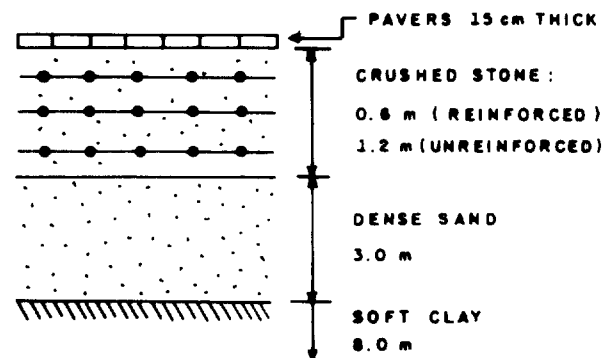


Figure 1. Pavement system (not to scale)

system should act as a reservoir, holding large volumes of water from heavy rainfalls. A numerical analysis was carried out to assess the stability and possible reinforcement of the crushed stone layer, considering heavy wheel loads.

3 SOIL PARAMETERS

In order to analyze the pavement behavior, it is necessary to estimate the strength (friction angle) and deformability parameters for the sand and the crushed stone layers. The friction angle is the most important parameter, since it indicates the possibility of failure of pavement as well as magnitude of plastic displacements due to the wheel load.

The following equation, proposed Barton and Kjaernsli (1981) was used for determining the crushed stone peak friction angle ϕ_p :

$$\phi_p = R \log (S/\sigma'_n) + \phi_b \quad (1)$$

In this equation, R is a particle shape factor (which depends on the crushed stone porosity after compaction), S is a factor depending on the unconfined compressive strength of the original rock (gneiss), σ'_n is the mean confining stress, and ϕ_b the residual friction angle of crushed stone. Depending on the position of the wheel, two conditions for confining stresses were considered. Far from the wheel, stresses due to compaction prevail in the crushed stone (estimated as 0.1MPa) and immediately under the wheel the static load from the transtainer is dominant (1.0MPa). Stiffness of the crushed stone was estimated from the literature. For the sand, the strength and deformability parameters were determined from triaxial compression tests. Table 1 summarizes the parameters used in the analysis:

Table 1. Parameters used in the numerical analysis.

Condition	Crushed Stone		Sand	
	E (MPa)	ϕ_p	E (MPa)	ϕ_p
minimum σ'_n (far from wheel)	300	55°	170	37°
maximum σ'_n (under wheel)	100	46°	140	33°

In all FLAC analyses, the Mohr-Coulomb constitutive model was used for simulating the behavior of dense sand and crushed stone layers, while elastic model was considered for the reinforcement layers. The effect of dilatancy for the dense sand and crushed stone layers was explicitly included in all analyses. The Poisson's ratio was assumed as 0.33 for both materials.

4 UNREINFORCED CRUSHED STONE BASE

The bearing capacity of the unreinforced crushed stone was initially verified through the classical Terzaghi (1943) formulation, considering a cohesionless soil and rectangular load at the surface. The N_y factors were determined as proposed by Kumbhojkar (1993) for the range of friction angles assumed in the analysis. The safety factor with respect to general failure for the crushed stone decreases from as high as 7.7 considering small confining pressures (far from the wheel load in Table 1), to as low as 0.96 for high confining pressures, immediately under the wheel. The results suggested that the crushed stone could

be reinforced in order to avoid its plastification due to the heavy loads prevailing in the pavement.

The thickness of the crushed stone layer determines the magnitude of loads on the dense sand layer underneath. This problem was analyzed supposing the stress distribution proposed by Giroud and Noray (1981). The results indicated that the crushed stone layer should be over 80cm thick in order to yield a factor of safety $FS > 2.0$ with respect to bearing capacity for the sand layer, and over 100cm for $FS > 3.0$. If the sand is required to work within elastic conditions, it is generally recommended a high value of factor of safety with respect to bearing capacity. These results motivated the use of reinforcement layers in the crushed stone.

5 GEOGRID REINFORCED CRUSHED STONE BASE

In order to minimize plastic deformations and rutting, and maximize safety factor against failure for the crushed stone and dense sand layer, reinforcement the crushed stone layer is proposed. The use of three layers of geogrid within the crushed stone layer was preferred in order to achieve better stress distribution (Huang and Tatsuoka, 1990). A single layer of reinforcement could also be used in the crushed stone, but the stress redistribution in the layer would not be as much efficient, and the loads carried by the geogrid would be much higher.

Loads in the reinforcement layers were initially quantified using the analytical model proposed by Binquet and Lee (1975). In this model, the loads along the reinforcements are expressed as a function of the depth, number and spacing of reinforcements, width of applied load and bearing capacity of the soil. The crushed stone layer was taken as 60cm, in order to verify the efficiency of the reinforcement on the bearing capacity of the sand layer. Considering three layers of reinforcements evenly spaced in the crushed stone at 20cm, loads in the reinforcements were estimated as varying from 47kN/m for the top layer to 56kN/m for the bottom layer.

Both the unreinforced and reinforced 60cm crushed stone behavior were further analyzed using the finite differences program FLAC (Fast Lagrangian Analysis of Continua). This program, developed by Itasca Consulting Group (USA), allows flexibility in modeling the behavior of the many materials involved (crushed stone, sand, reinforcement layers). Figure 2 shows the grid used in the numerical simulation. Conditions presented in Table 1 were analyzed, each one with and without reinforcement, resulting a total of four cases. The following properties were considered for the reinforcement layers, corresponding to those of commercially available geogrids: Elastic modulus 500MPa, thickness 2.5mm and ultimate tensile strength 100kN/m. These values do not account for installation damage.

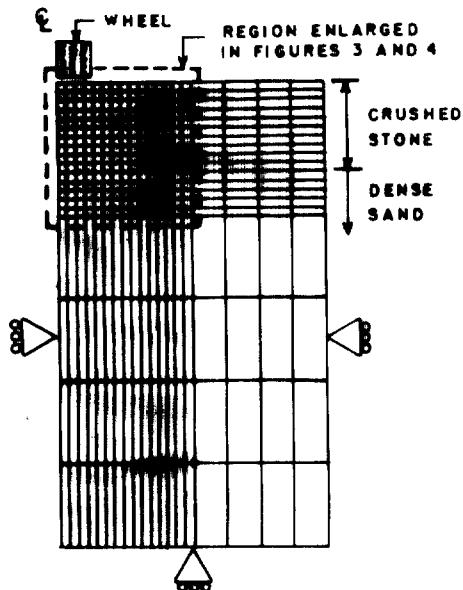


Figure 2. Grid for FLAC analysis.

The following additional hypotheses were considered for the problem: plane strain conditions, Mohr-Coulomb plastification criteria for both the sand and crushed stone and elastic behavior for the reinforcements. Only half of the geometry was considered in the grid due to symmetry of the problem (Figure 2).

Results are presented in Figures 3 and 4 for the critical case of minimum strength parameters presented in Table 1 (immediately under the wheel), without and with reinforcement, respectively. Basically, the failure mechanism for the unreinforced crushed stone observed in the analytical model is confirmed in the numerical analysis, as shown in Figure 3. In this case, there are large upward displacements at the surface and downward displacements immediately under the wheel. There is a general plastification in both crushed stone and dense sand layers. The results show that introducing three reinforcements in the crushed stone layer is very efficient, inhibiting almost completely plastification in both crushed stone and dense sand layers, as shown in Figure 4. Displacements at the surface and within the layer are also drastically reduced. The loads in the reinforcement layers vary from 47kN/m for the bottom layer to 24kN/m for the superficial layers. The maximum value for the axial load in the bottom layer compares relatively well with the one determined with the analytical model of Binquet and Lee (1975), while their model overestimates the loads for the more superficial reinforcement layer. Table 2 summarizes the results obtained in the numerical analysis. In general, the results show that reinforcement is generally more efficient in the critical case of minimum peak friction angle, when loads along geogrids and benefits in the system are maximized.

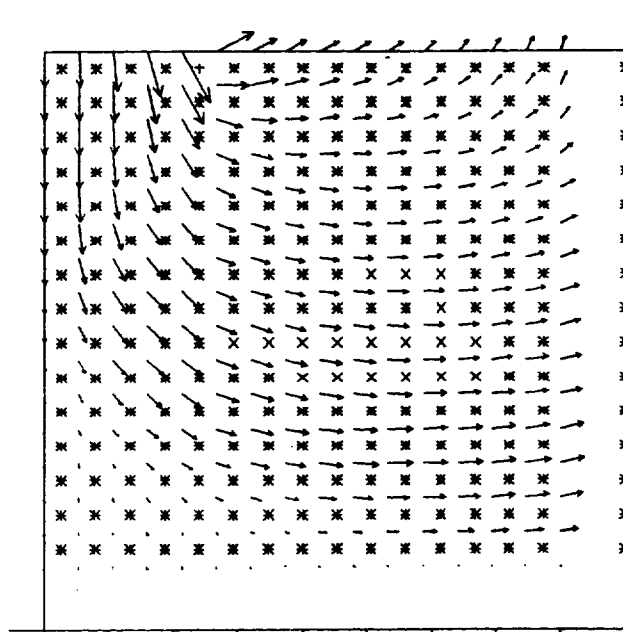


Figure 3. FLAC results, unreinforced crushed stone case. Legend: Max. displacement vector=30cm. Plastification: * At yield; X Elastic.

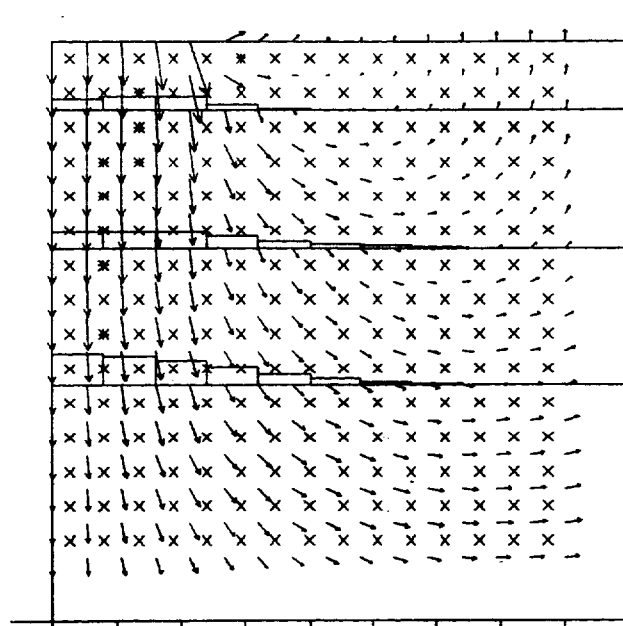


Figure 4. FLAC results, reinforced crushed stone case. Legend: Max. displacement vector=4.5cm. Plastification: * At yield; X Elastic. Reinforcements load distribution also shown.

Table 2: Summary of numerical analyses and results.

Case	Maximum displacements (cm)	Plastification	Geogrid loads (kN/m)
1: ϕ p max unreinf.	1.9	localized	-
2: ϕ p max reinf.	1.8	no	5.5 to 9.5
3: ϕ p min unreinf.	>30	generalized (failure)	-
4: ϕ p min reinf.	4.5	no	24 to 47

6 GEOGRID CHARACTERISTICS AND INSTALLATION

In order to choose the correct reinforcement, it is necessary to multiply the maximum loads determined in the numerical analyses by a general factor of safety. One of the most important aspects to be accounted for is the installation damage of reinforcement, since very high energy will be employed for compacting the crushed stone layer. The amount of damage should be assessed by means of large scale laboratory tests. For example, Watts and Brady (1994) carried out a series of high energy compaction tests using crushed stones over geogrids, suggesting factor of safety against damage varying from 1.3 to 1.7. Koerner (1993) also suggests FS values in this range. Creep, chemical and biological damage should also be taken into account for determining the suitable reinforcement. In order to minimize the effects of installation damage, the reinforcement could be placed within two thin layers of grit, avoiding direct contact of the coarse material with the geogrid layers for improved protection.

7 CONCLUSIONS

This paper presents results of a numerical analysis with FLAC on the behavior of unreinforced and geogrid reinforced pavement base to be constructed in a intermodal yard. The results show that the unreinforced crushed stone base collapses under the high imposed loads, suggesting its reinforcement with geogrids. The number and position of geogrid layers were initially estimated using simplified closed-form solutions originally developed for reinforcement of shallow foundations, which resulted in a reinforcement configuration consisting of three layers of geogrids with long-term strength of 50kN/m evenly spaced within the crushed stone base. Results of numerical finite difference analyses on this reinforcement configuration showed that the pavement performance improved in the

following ways: a) inhibiting the plastification of the crushed stone base and the dense sand layer; b) reducing the magnitude of plastic and elastic displacements at the pavement surface and within the layers; and c) reducing the thickness of the crushed stone base from 1.2m to 0.6m, without causing collapse of the dense sand layer underneath. The introduction of reinforcement could also drastically reduce maintenance frequency, one of the major aspects related to container terminal management (Meletiou and Knapton, 1987).

ACKNOWLEDGEMENTS

The author is grateful to IPT and CNPq for support in the research work.

REFERENCES

- Barton, N. and Kyaernsli, B. (1981) "Shear Strength of Rockfill", *ASCE Journal of Geotechnical Engineering*, Vol. 107, No. GT7, July, p. 873-891.
- Binquet, J. and Lee, K.L. (1975) "Bearing Capacity Analysis of Reinforced Earth Slabs", *J. Geot. Eng. Div. Proc. ASCE*, Vol. 101, GT12, p. 1257-1276.
- Giroud, J.P. and Noiray, L. (1981) "Design of Geotextile Reinforced Unpaved Roads", *J. Geot. Eng. Div. ASCE*, Vol. 107, n. GT9, pl. 1233-1254.
- Huang, C.C. and Tatsuoka, F. (1990) "Bearing Capacity of Reinforced Horizontal Sandy Ground", *Geotextiles and Geomembranes*, v. 9, p. 51-82.
- Koerner, R. (1993) "Designing with Geosynthetics", Prentice Hall.
- Kumbhojkar, A.S. (1993) "Numerical Evaluation of Terzaghi's $N\gamma$ ", *ASCE Journal of Geotechnical Engineering*, Vol. 119, n.3, pp. 598-607.
- Meletiou, M. and Knapton, J. (1987) "Container Terminal Pavement Management", *UNCTAD Monographs on Port Management*, Monograph n.5., 51 p.
- Raymond, G.P. Abdel-Baki, M. Karpurapu, R.G. and Bathurst, R.J. (1993) "Reinforced Granular Soil for Track Support", *ASCE Special Conference on Grouting, Soil Improvement and Geosynthetics*, p.1104-1115.
- Terzaghi, K. (1943) "Theoretical Soil Mechanics", John Wiley and Sons, NY.
- Walls, J.C. and Galbreath, L.L. (1987) "Railroad Ballast Reinforcement Using Geogrids", *Geosynthetics '87*, New Orleans, p. 38-45.
- Watts, G.R.A. and Brady, K.C. "Geosynthetics: Installation Damage and the Measurement of Tensile Strength", *5th International Conference on Geosynthetics*, Singapore, p. 1159-1164.

Improvement of Bearing Capacity of Soft Clay Using Geogrids

Y. Tanabashi

Civil Engineering Dept., Nagasaki University, Bunkyo-machi 1-14, Nagasaki 852, Japan

K. Yasuhara

Dept. of Urban and Civil Engineering, Ibaraki University, Hitachi, Ibaraki 316, Japan

K. Hirao

Dept. of Civil Engineering, Nishinippon Institute of Technology, Kanda 1633, Fukuoka-ken, 80003, Japan

N. Kiyokawa

Mitsui Petrochemical Industrial Products Co., Ltd., Yushima, Tokyo, 101, Japan

H. Itoh

CTI Engineering Co., Ltd., Nihonbashi Honmachi, Tokyo, 103, Japan

ABSTRACT: A number of 1g laboratory model footing tests have been carried out to find out which geosynthetics and methods of placement are optimal for giving sufficient bearing capacity for both the trafficability of construction machines and the construction of earth structures on soft soils. To study the effect of sand mat placement, in particular, a numerical simulation was performed using a procedure in which the Sekiguchi-Ohta constitutive model for soft clay was combined with a truss element for the geogrid and Goodman's joint element for interaction between the sand and geogrid. Based on Biot's theory of three-dimensional consolidation, a finite element model was formulated to analyse the deformation and failure mode of the soft clay in the laboratory model tests both with and without the geogrid and sand mat. Typical results from the calculations give a good prediction of the effectiveness of sand mat placement for decreasing settlement, and, therefore, improving the bearing capacity of soft clay. It is concluded that this must be due to an increase in bending stiffness caused by combining the sand mat with the geogrid.

KEYWORDS: Bearing capacity, Geosynthetics clay liners (GCL), Model tests, Finite element analysis, Friction

1 INTRODUCTION

In previous papers (Hirao et al., 1992; Yasuhara et al., 1994), the authors have emphasized that composite geosynthetics which are non-woven geosynthetics reinforced with woven geosynthetics in-between are best for improving the bearing capacity of soft clay. This composite geosynthetic has a higher tensile strength than the non-woven geosynthetic hitherto used, and in addition has the advantage of giving high friction in soft clay (Hirao et al., 1992). There is no significant improvement in bearing capacity when a geogrid is placed directly over the surface of a soft clay, because the frictional force developed between the geogrid and soft clay is very small (Hirao et al., 1992) and it cannot follow the large deformations of the soft clay.

In order to establish a suitable procedure for the use of geogrids to improve the bearing capacity of soft clay, 1g laboratory model tests were conducted. In particular, a focus was placed on which effect of (i) restraintment, (ii) combination with woven or non-woven geosynthetics and (iii) combination with sand mat contributes most to increasing bearing capacity.

2 EXPERIMENTAL PROGRAMME

2.1 Outline of Model Tests

A soil tank with 2 m width, 0.5 m length and 1.0 m depth, as illustrated in Fig. 1, was used for the model tests. The properties of the clay were: $G_s = 2.62$, $w_L = 107\%$, $I_p = 66$. Details are given in previous papers (Hirao et al., 1992, 1996). Soft clay mixed with water to a moisture content w_i of 130% was poured into the soil tank to form a 40cm or 80cm thickness clay layer. The average vane shear strength of the model clay layer after

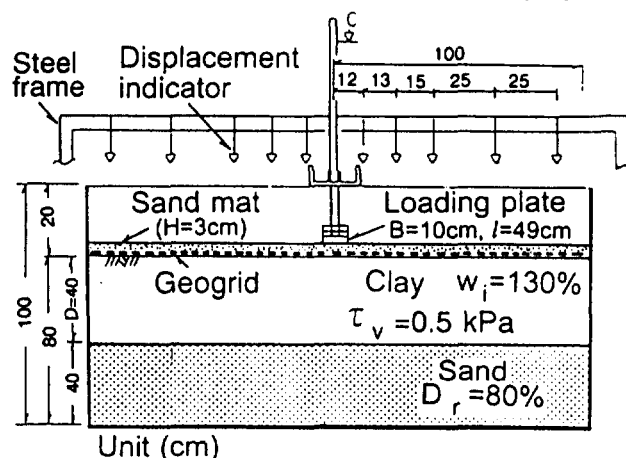


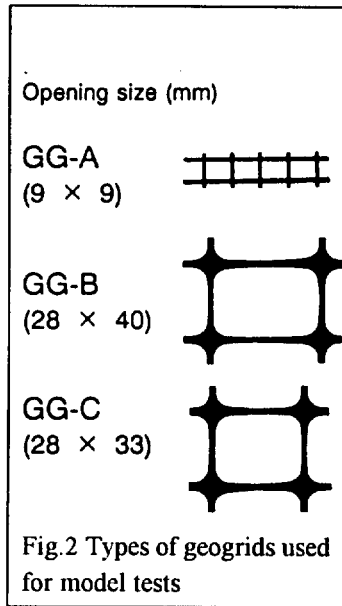
Fig. 1 Testing apparatus for model tests

pouring was 0.5 kPa and was almost constant with depth.

A layer of geogrid was firstly placed directly over whole the surface of the clay layer with a 2m width and 0.5m length. Then a sand mat of 3cm thickness was laid onto the geogrid. To obtain the load versus settlement curves, several kinds of model footing tests were carried out in which step loads were applied to the soft clay reinforced with a geogrid. For comparing the effects of different reinforcements, plate loading tests were also conducted on soft clay without a sand mat and geogrid as well as tests with the combined use of geogrids with non-woven geofabrics.

A vertical load of 1.0 kPa was applied in each step to a plate 10cm wide, 49cm long and 48 Pa in weight until the clay layer failed. The loading duration of each step was 15 min.

A lateral restraint was provided by a tension force developed by a counter weight on the edge of geogrids as is shown in Fig. 1.



2.2 Properties of Geogrids Used

Table 1 summarizes the mechanical properties of the three kinds of geogrids used. The differences between the three geogrids illustrated in Fig. 2 were in the size of the opening, tensile strength, frictional force and bending stiffness of which the later two were determined using methods proposed by Hirao et al. (1992, 1996).

Table 1 Mechanical properties of geotextiles used

Material	Symbol	Thickness or Opening (mm)	Bending Stiffness B_G ($N \cdot cm^2$)	Stiffness I (cm)	Description
Woven Fabric	WF	0.5	9.3	11.3	-----
Composite Fabric	CF-B	4.0	11.3	16.0	=====
Geogrid	GG-A	9 × 9	23.1	33.9	-----
	GG-B	28 × 40	129.4	75.3	-----
	GG-C	28 × 33	185.2	85.3	-----

As will be mentioned later, the size of the opening is an important factor in the improvement of the bearing capacity of soft clay because of its relation to the magnitude of mobilized friction and the interlocking effect.

3 RESULTS FROM EXPERIMENTS

The bearing capacity for reinforced models is defined by the applied load at the yielding point, $p_{y,n}$ for non-reinforced and $p_{y,r}$ for reinforced cases in the settlement, S , versus load, p , curves. The results relating to the improvement of the bearing capacity of soft clays reinforced with geogrids were taken from the model

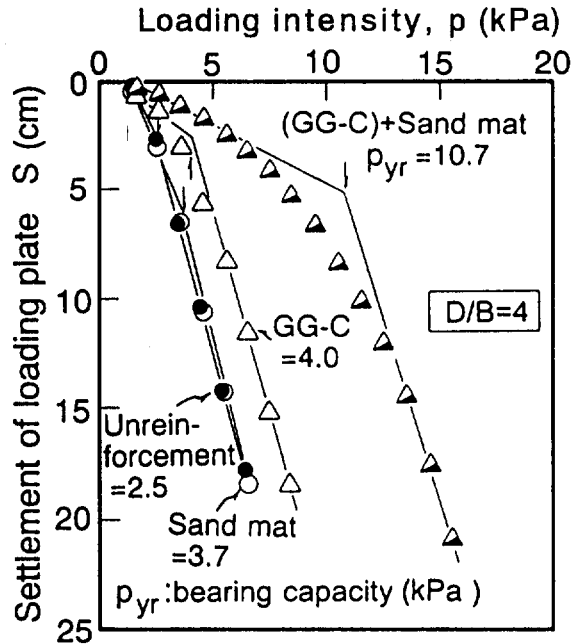


Fig. 3 Representative p vs. S curves obtained by model tests

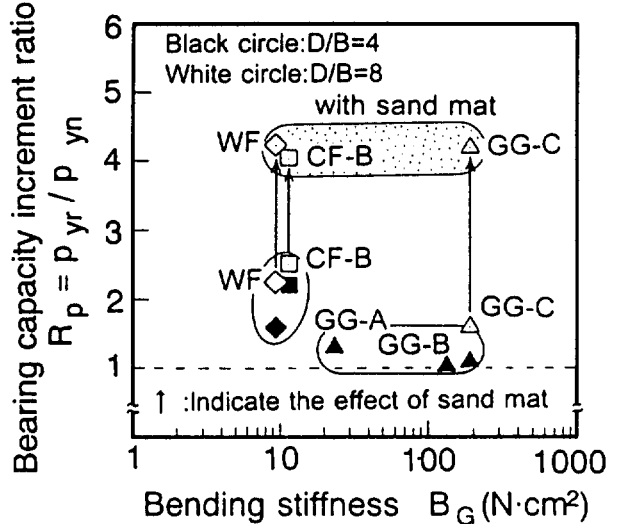


Fig. 4 Effect of bending stiffness on increase in bearing capacity of soft clay

tests described in the previous section. Figs. 3 to 6 illustrate the effects of the above-mentioned factors on the settlement, S , vs. vertical stress, p , curves.

As can be seen in Fig. 3, the bearing capacity with no reinforcement is very small because the model ground consists of extremely soft clay. A small increase in bearing capacity can be observed in Fig. 3 due to the size of the geogrid's mesh.

The ratio of the bearing capacity, p_{yr} , of soft clay improved by reinforcement with geogrids to that, p_{ym} , for no geogrids, is denoted by R_p . Fig. 4 and Fig. 5 show the effects of both the bending stiffness of geogrids and the stiffness of woven and composite geofabrics, respectively. It can be seen from these results in Figs. 4 and 5 that the placement of a geogrid with a large bending stiffness does not necessarily increase the bearing capacity of soft clay, although the bending stiffness of the geogrid is larger than the composite geofabric. This tendency is irrespective of the thickness of the clay (Hirao et al., 1996). On the other hand, it is also seen from these figures that a combination of sand mat with each geosynthetic markedly increases the bearing capacity, independent of the kind of geosynthetic. The reason for these differences will be discussed later.

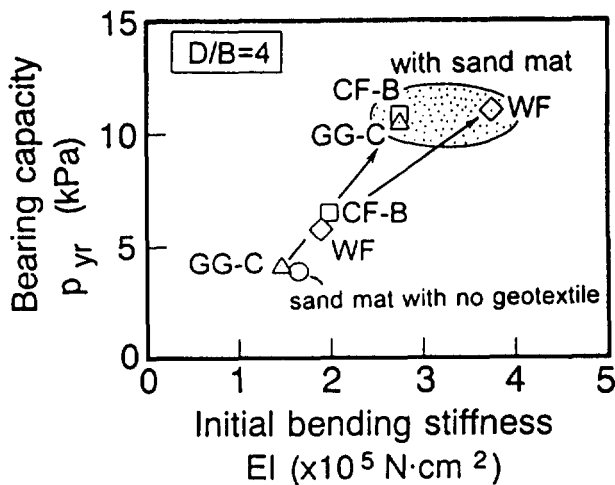


Fig. 5 Relation between initial bending stiffness and bearing capacity with and without sand mat

4 EVALUATION OF SAND MAT EFFECT USING FEM ANALYSIS

4.1 Analysis of Laboratory Model Tests

A FEM analysis of the behaviour of an embankment on soft clay with and without geogrids and sand mats was conducted using a model incorporating the effect of the interaction of the geogrid

and soft clay, as summarized in Table 1. The analytical procedure used the elasto-visco-plasticity model developed by Sekiguchi and Ohta (1977) for clay, by using a beam element for modeling the geogrid and a joint element for the interaction between geogrid and soil, respectively. The model also incorporated Biot's theory of three-dimensional consolidation for a coupled analysis. In a previous paper (Tanabashi et al., 1992), the model was successfully applied to the results from model footing tests on soft clay with and without geogrid and sand mat.

The geometry of the model analyzed is shown in Fig. 6 and corresponds to the laboratory model test where the width of the loading plate B was 10 cm, the depth of the clay layer D was 40 cm and the thickness of the sand layer was 3 cm. The analysis focused on the effect of the sand mat on the improvement of bearing capacity of a soft clay with and without a geogrid. The embankment on clay was modeled with and without sand mat

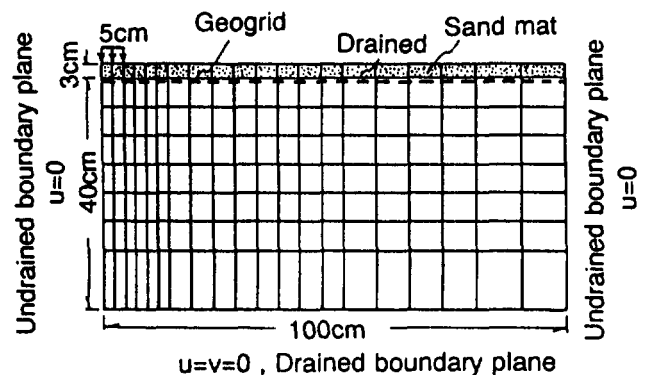


Fig. 6 Finite element mesh and boundary condition used for model tests

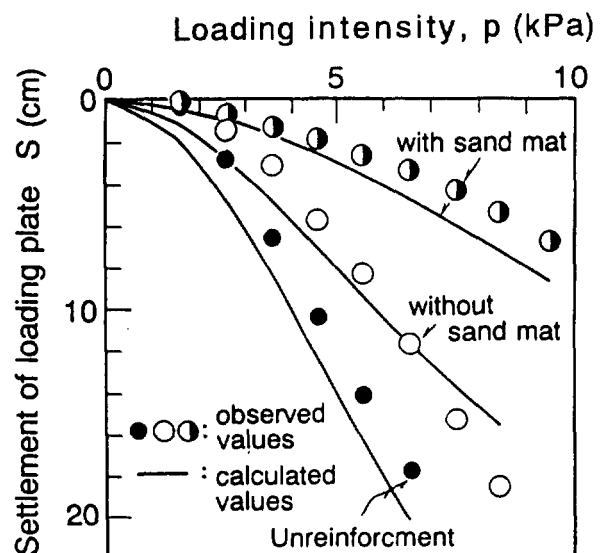


Fig. 7 Comparison of p vs. S curves for model tests with and without sand mat

and geogrid and was divided into 210 nodes and 200 elements for the FEM analysis as is also shown in Fig. 6. The boundary conditions for displacement were complete restraint on the bottom and horizontal restraint on lateral surfaces. In addition, the hydraulic boundary conditions were assumed to be drained at the bottom and surface and undrained on the sides. The parameters necessary for the present analysis were determined indirectly from plasticity indices, as proposed by Iizuka and Ohta (1987). The settlement versus load curves calculated using the FE analysis based on the Sekiguchi and Ohta model (Sekiguchi and Ohta, 1977) were compared in Fig. 7 with those observed in laboratory model tests which includes the results without geogrid and sand mat. Fig. 7 suggests that the method proposed for analyzing the reinforcement effect gives a reasonable prediction of the settlement versus load relations with and without geogrid and sand mat.

The model was also capable of simulating the deformation of the soft clay model both with and without reinforcement. Fig. 8 illustrates a family of results from model tests with and without a sand mat under an applied load, $q = 8.4$ kPa. It can be seen

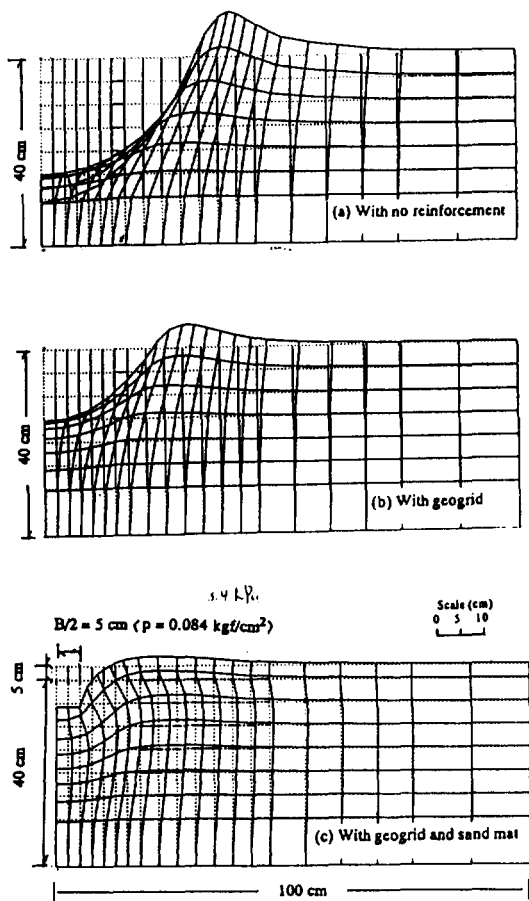


Fig. 8 Typical deformation diagrams obtained from numerical simulations

from Fig. 8 that in the case of soft clay alone or with a geogrid the ground deforms as if it is failing, while for soft clay with a geogrid and sand mat the settlements and lateral displacements are clearly restrained. This is due to the composite effect in which the sand mat restricts the movement of the geogrid and thus produces an increase in bearing capacity.

4.2 Numerical Verification for Field Conditions

Numerical experiments using the proposed model were carried out to demonstrate the effect of a sand mat on the improvement of the bearing capacity of soft clay with a geogrid, under in-situ conditions with a typical profile just like as under model footing test condition as illustrated in Fig. 7. For this calculation, the following conditions were assumed: (i) depth of clay layer, D , 4, 6, 8, 10, 12 m; (ii) depth of clay layer to loaded area ratio, D/B , 1.33, 2.00, 2.67, 3.33, 4.00, and; (iii) the thickness of sand mat was kept constant equal to 30 cm. The boundary and drainage

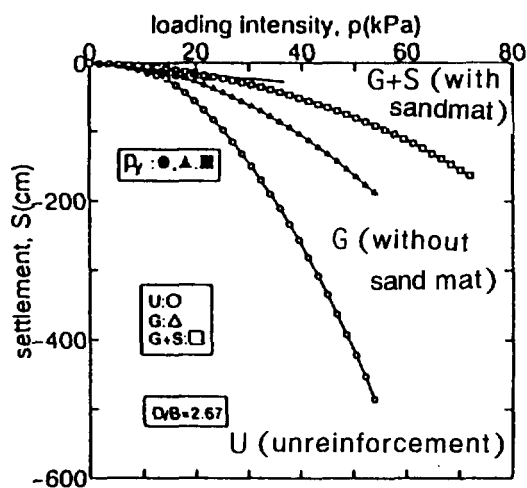


Fig. 9 Typical p vs. S curves obtained from numerical simulations

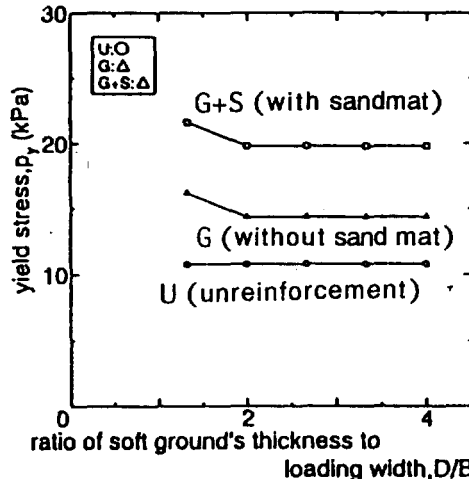


Fig. 10 Calculated relationship between p_y and D/B

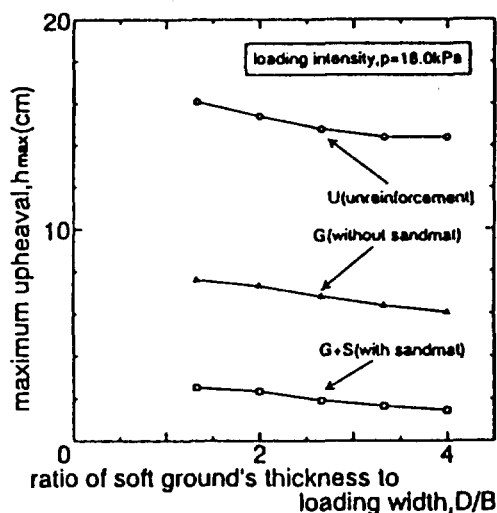


Fig. 11 Calculated relationship between maximum upheaval, h_{max} and D/B

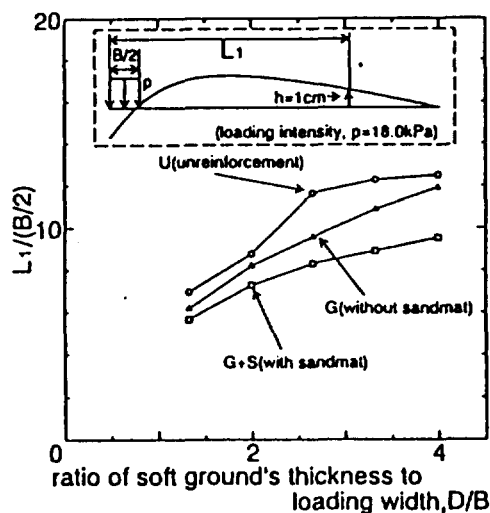


Fig. 12 Relation between normalized critical distance, $L_1/(B/2)$ and D/B

conditions were the same as those adopted in the analysis of the laboratory model tests. Typical settlement versus load relations for $D/B = 2.67$ are shown in Fig. 9. The effect of geogrid and geogrid with sand mat on settlement control in soft clay is illustrated in the p versus S curves in Fig. 9 by the fact that the settlement increases linearly beyond the yield point with increasing applied loads, but increases abruptly in the case of no reinforcement. However, it is interesting to note that this yielding load becomes larger for reinforced compared with unreinforced models but is independent of the D/B as shown in Fig. 10. It is also notable that the bearing capacity improvement

due to a sand mat combined with a geogrid is considerable. The applied yielding load, increases by up to 1.8 times compared with no reinforcement. The advantage of a sand mat with geogrids is also observed in the deformation of soft clay under applied load. The amounts of maximum settlement, maximum heave and lateral distance of heave in soft clay are shown in Fig. 11 and Fig. 12 for cases with and without sand mat and geogrid. It is concluded from these comparisons that both settlement and lateral displacement of soft clay reinforced with geogrid and sand mat are not influenced by D/B .

The results calculated using the proposed model are presented in Fig. 13 in the form of the relation between S/D and d/S which is conventionally used for the stability control of soft clay under embankments (Matsuo and Kawamura, 1977). In this representation, it is assumed that soft clay fails when a S/D versus d/S path reaches the line for $1/F = 1$ where F is a safety factor for stability. When we read off from data in Fig. 13, obtained by calculating for cases with and without a sand mat and $D/B = 2.67$, it is clear that the applied load p_{pr} for $F = 1$ with sand mat and geogrid is larger than that for no reinforcement.

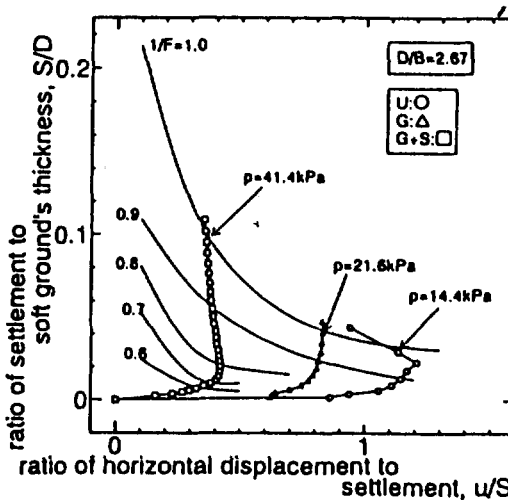


Fig. 13 Calculated relationship between S/D and d/S

5 CONCLUSIONS

- 1) The direct placement of geogrids on the surface of a soft clay does not improve its bearing capacity.
- 2) There is little increase in the bearing capacity of a soft clay if a tensile force is applied by weighting the edge of a geogrid. The reason for no improvement is due to either the frictional

force or the interlocking effect being not exerted between the geogrid and clay.

3) Combined non-woven geosynthetics with geogrid gives an advantage by increasing bearing capacity.

4) The bearing capacity is markedly improved by an underlying sand mat combined with a geogrid. This effect is caused by an increase in bending stiffness of the composite of geogrid and sand mat as well as the higher frictional force developed between sands and geogrids compared with a geogrid only.

5) The effect of a sand mat on bearing capacity improvement and displacement control in soft clay has been successfully analyzed using a modified model which incorporates the effect of the interaction of the geogrid and sand mat.

ACKNOWLEDGEMENT

The authors would like to express their gratitude to Ikegami, M. (the executive director of Mitsui Petrochemical Industrial Products Co., Ltd.) who offered some kinds of geosynthetics and the 1g model footing testing apparatus used in this study.

REFERENCES

- Hirao, K., Yasuhara, K., Takaoka, K., Nishimura, J. and Tanabashi, Y. (1992) : Laboratory model tests on the application of composite fabrics to soft clay ground, Proc. IS-KYUSHU92, Vol. 1, pp. 601 - 606.
- Hirao, K., Yasuhara, K. and Tanabashi, Y. (1996) : Effect of bending stiffness of geotextiles on bearing capacity improvement of soft clay, Proc. IS-KYUSHU96, Vol. 1, pp. 591 - 596.
- Iizuka, A. and Ohta, H. (1987) : A determination procedure of input parameters in elasto-viscoplastic finite element analysis, Soils and Foundations, Vol. 27, No. 3, pp. 71 - 87.
- Matsuo, M. and Kawamura, K. (1977) : Diagram for construction control of embankment on soft ground, Soils and Foundations, Vol. 17, No. 3, pp. 37 - 52.
- Sekiguchi, H. and Ohta, H. (1977) : Induced anisotropy and time dependency in normally consolidated clay, Proc. 9th Intn'l Conf. SMFE, Specialty Session, No. 9, pp. 163 - 175.
- Tanabashi, Y., Hirao, K. and Yasuhara, K. (1992) : Numerical analysis for bearing capacity improvement of soft clay ground reinforced with geotextiles, Proc. IS-KYUSHU92, Vol. 1, pp. 701 - 706.
- Tanabashi, Y., Itoh, H., Hirao, K. and Yasuhara, K. (1996) : In-situ investigation and numerical estimation for bearing capacity improvement of very soft ground reinforced with geotextiles, Proc. IS-KYUSHU96, Vol. 1, pp. 685 - 690.
- Yasuhara, K., Hirao, K. and Tanabashi, Y. (1994) : Geofabrics

application to reinforcement of soft ground, Proc. Intn'l. Symp. Fiber Science and Technology, Vol. 1, pp. 511 - 512.

The Bearing Capacity of a Reinforced Sand Layer Overlying a Soft Clay Subgrade

M.J. Kenny

Lecturer, Department of Civil Engineering, University of Strathclyde, Glasgow, UK

ABSTRACT: Recent interest has developed in the use of geosynthetics for forming a fill layer over soils which have very low bearing capacity. However, the reinforcement mechanism is not clearly understood. A programme of laboratory scale plane-strain bearing capacity tests under monotonic loading has been carried out which considers the reinforcing mechanism of the geosynthetic. Analysis of the test results show that the interpretation of the reinforcing mechanism is highly dependent upon the values assumed for the various model parameters. The results further suggest that in order to function effectively as a reinforcement over very soft clays, the geosynthetic should possess a significant component of in-plane bending stiffness.

KEYWORDS: Bearing capacity, Reinforcement, Shallow foundations, Soft soils, Unpaved roads.

1 INTRODUCTION

Recent interest has developed in the use of geosynthetics for forming a fill layer over soils which have very low bearing capacity, so that a construction platform can be formed. Although the technique has been successful in practice, there has been considerable disagreement concerning the reinforcement mechanism. After carrying out dimensional analysis of model loading tests, Fagher et al. (1996) concluded that the in-plane bending stiffness is the dominant factor when constructing over very soft soils. However, the current design methods for unpaved roads consider only tensile stiffness in the analysis of the mechanisms of reinforcement.

Many of the design methods have been developed from laboratory scale plane-strain bearing capacity tests under monotonic loading. This paper reports the results of a programme of such model tests carried out at the University of Strathclyde. Although the reinforcement used possessed insignificant bending stiffness, analysis of the reinforcing mechanism has allowed consideration of the relative importance of both tensile and bending stiffness in the bearing capacity of a reinforced sand layer over a soft clay subgrade.

2 BACKGROUND

In recent years, two different approaches have been adopted for the design of unpaved roads. The first approach is typified by the design method of Giroud and Noiray (1981). It attributes the improvement in the road performance to the reinforcement acting as a tensioned membrane as rutting develops and an increased subgrade bearing capacity due to subgrade confinement. Burd (1995) further developed membrane theory to produce a model in which the deformed reinforcement shape is obtained from a set of membrane equations. In contrast, the second

approach proposed by Milligan et al. (1989) neglects membrane action but considers that the reinforcement reduces the shear stresses developed at the surface of the subgrade, thus increasing the subgrade bearing capacity. It is thus more appropriate for small deformations. Despite these differences, the two approaches have the following common features :

1. They are derived from a stress distribution model common in the bearing capacity analysis of layered soils (Kenny and Andrawes, 1997). Giroud and Noiray (1981) assume a value of $\tan^{-1}0.6$ for the stress distribution angle α (see Figure 5) for both the unreinforced and reinforced road, while Milligan et al. (1989) state that the stress distribution angle should be derived from observation and experience.
2. The allowable subgrade bearing capacity is greater in the reinforced than in the unreinforced case. Both Giroud and Noiray (1981) and Milligan et al. (1989) have proposed modified subgrade bearing capacity factors.
3. The recommended stress distribution angles are the same in both the unreinforced and reinforced cases, although the presence of the reinforcement has been shown to improve the stress distribution.

3 EXPERIMENTAL SET UP

A strip footing 0.12 m wide was used in all tests. The test tank has inner dimensions of 2.0 m length, 1.4 m height, and 0.3 m width and parallel glass sides, as shown in Figure 1, and contained a soft clay subgrade overlain by Leighton Buzzard sand. The displacement fields were recorded at intervals of 10 mm footing penetration and analysed using the stereo-photogrammetric technique.

The soft clay subgrade was simulated by an artificial clay known as Glyben (Kenny and Andrawes, 1997), which is manufactured by mixing a sodium-bentonite clay

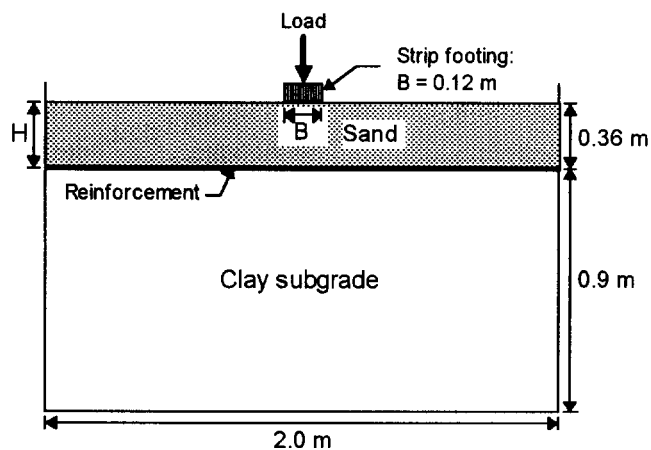


Figure 1. The experimental set up.

(Fulbent 570) and glycerine, the resulting shear strength depending on the mix proportions. A large number of undrained triaxial tests and vane shear tests were carried out over the period of the study, which demonstrated that Glyben behaved generally as a $\phi_u = 0$ material under quick undrained loading, with an average c_u of 10.6 kN/m^2 . Since Glyben samples are formed by compaction, the material unavoidably contains a small proportion of trapped air (approx. air voids content = 8%). However, the material was completely insensitive to handling and gave excellent repeatability during testing.

The fill material used was a uniformly graded coarse Leighton Buzzard sand placed using an air activated spreader in a dense state, with a mean porosity of 34.5% (porosity limits ; 34.0% - 44.5%). The operational angle of friction ϕ' for the sand placed at this density was found to be 48.5° .

The reinforcement of the upper sand layer was provided by a single layer of geogrid type reinforcement placed at the sand-clay interface. Although no attempt was made to correctly scale all aspects of the problem, the reinforcement used can be considered to be a reduced scale model geogrid. It consists of welded polypropylene filaments of 0.5 mm diameter with grid openings of $6.1 \text{ mm} \times 7.1 \text{ mm}$ on average. The load-extension properties of the geogrid were investigated using a range of strain rates of relevance to the current investigation.

In the experimental programme, bearing capacity tests were carried out for clay subgrade alone ($H/B = 0$), and with and without the reinforcement layer for H/B ratios of 0.25, 0.75, 1.0, 1.5 and 2.0.

4 EXPERIMENTAL RESULTS

The stress-settlement relationships for unreinforced and reinforced sand overlying clay shown in Figure 2 are representative of the test programme as a whole. Since

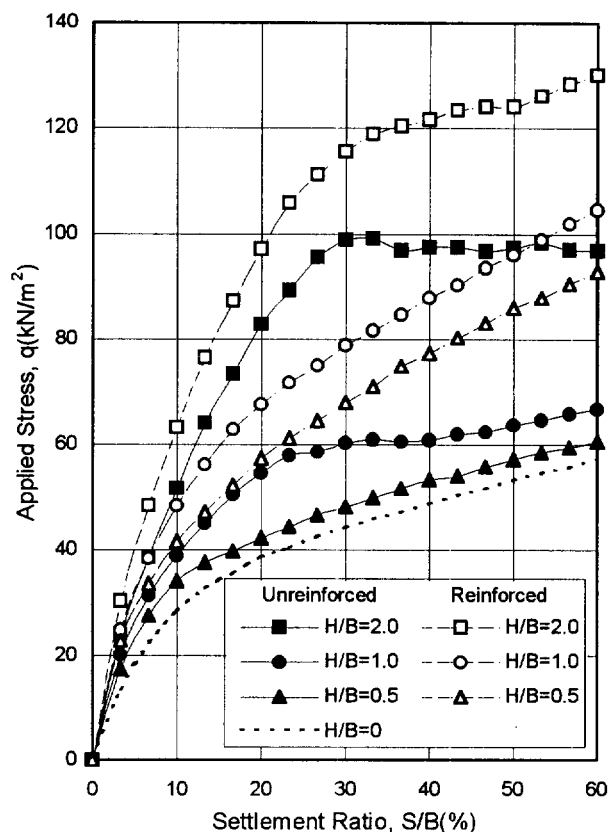


Figure 2. Stress-settlement relationships for unreinforced and reinforced sand over clay.

there is no observable post-peak, strain softening for the clay alone, this stress-settlement behaviour is consistent with a local shear failure of the subgrade due to the compressibility of the material. For unreinforced sand over clay, the ultimate stress can be more readily identified from the peak in the stress-settlement curve, particularly for large H/B ratios. As for clay alone, there is no clearly defined failure point in the reinforced case. In unpaved road design, a maximum rut depth (i.e. footing settlement) is a more appropriate criteria.

The displacement fields recorded during the later stages of footing penetration are given in Figures 3 and 4 for H/B ratios of 0.5 and 2.0 respectively. In general it was observed that for small sand depths the deformation of the sand/clay interface was more uniform when reinforcement was present. This indicates improved stress-distribution in the reinforced case. There was also a tendency for the sand beneath the footing to be displaced outwards when no reinforcement was present, particularly for large sand depths and at low footing settlements. This lateral displacement reduced when reinforcement was used. This is consistent with observations of Milligan et al. (1989), but the effect was less pronounced.

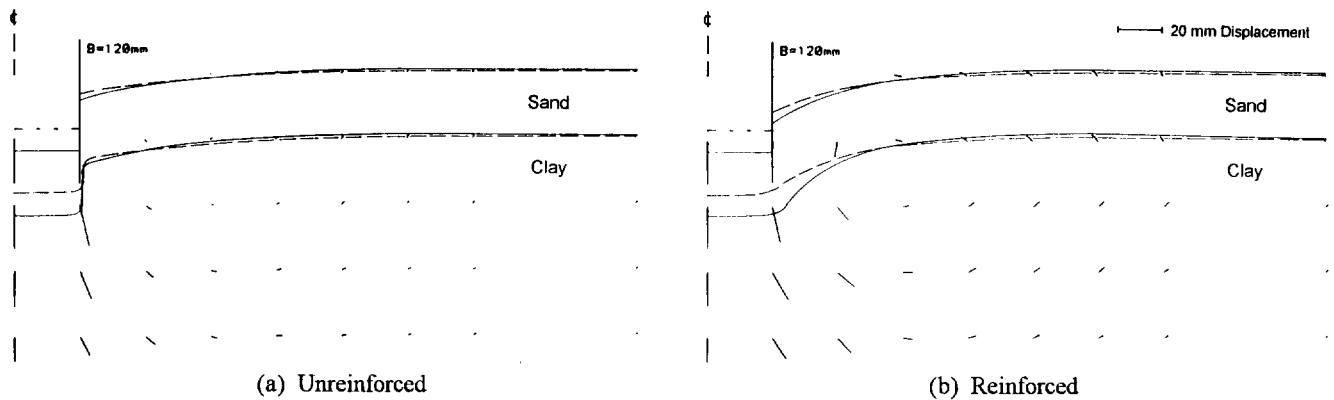


Figure 3. Displacement vectors for $H/B = 0.5$ (Footing settlement, $S/B = 42-58\%$).

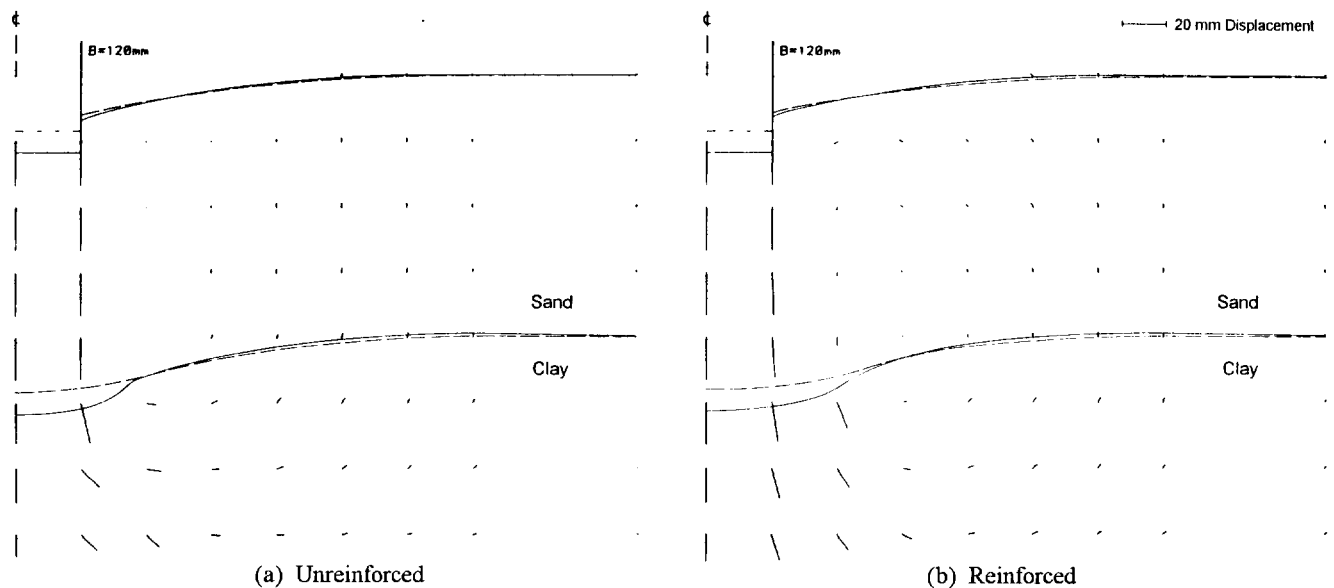


Figure 4. Displacement vectors for $H/B = 2.0$ (Footing settlement, $S/B = 42-58\%$).

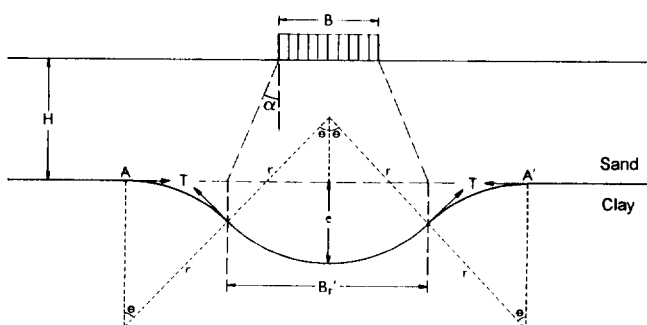


Figure 5. Analysis of membrane forces (after Gourc, 1983).

5 THE REINFORCEMENT MECHANISM

If we consider a typical stress distribution model with membrane action, as shown in Figure 5, the contribution of the reinforcement tension to the bearing capacity can be

calculated. Since very little subgrade heave was observed during footing penetration, the membrane analysis proposed by Gourc (1983) assuming four circular segments was adopted. This method is sufficient for illustrative purposes, although Burd (1995) gives a more rigorous treatment of reinforcement equilibrium.

From Figure 5 it can be seen that the contribution to the bearing capacity from stress distribution through the upper sand layer, q_d , is:

$$q_d = q_c \frac{B'_r}{B} \quad (1)$$

The subgrade reaction q_c was taken from the clay alone curve in Figure 2 at the same footing settlement. The membrane force which opposes the applied stress is equivalent to the vertical projection of the reinforcement tension at the stationary points. The maximum reinforcement tension is limited by the anchorage capacity.

Denoting the contribution to the bearing capacity due to membrane action by q_m , it follows that:

$$q_m = \frac{2T \sin \theta}{B} \quad (2)$$

The angle θ and the reinforcement strain depends on the footing settlement, S . Having determined the strain in the reinforcement and estimating the strain rate from the rate of penetration of the footing, the tension T was obtained from the load-strain properties of the reinforcement. The bearing capacity of the footing, q , can be determined by summing the contributions from stress distribution, q_d , and membrane action, q_m . The bearing capacities were calculated using a commonly assumed stress distribution angle of $\alpha = 30^\circ$ and using the actual values measured during the test programme. These are compared with the experimental values, q_{exp} , in Table 1.

Table 1. Comparison of experimental and predicted bearing capacities for reinforced sand over clay.

Test details			Bearing capacity (kN/m ²)			
H/B	S/B	B' _r /B	q _d	q _m	q	q _{exp}
0.5	0.33	1.58*	78.7	3.7	82.4	71.0
		1.2**	59.9	7.0	66.9	71.0
0.5	0.58	1.58*	78.7	12.2	90.9	92.0
		1.2**	72.7	21.8	94.5	92.0
1.0	0.33	2.16*	107.8	1.8	109.6	81.8
		1.58**	78.6	3.8	82.4	81.8
1.0	0.58	2.16*	130.9	6.0	136.9	103.6
		1.6**	97.0	12.3	109.3	103.6

Note : * denotes values calculated using $\alpha = 30^\circ$; ** denotes values calculated using measured values of B'_r (distance between points of inflection of sand/clay interface).

It can be seen that by using a stress distribution angle α of 30° , the calculated membrane forces are approximately 50% of those calculated using the observed values of α . In addition, the bearing capacity tends to be overpredicted using $\alpha = 30^\circ$. A similar analysis of the unreinforced tests gave a larger overprediction, particularly at small displacements when the sand thickness is large, which can be attributed to the lack of lateral restraint of the sand.

6 CONCLUSIONS

Based on the experimental results and analysis presented above, the following conclusions can be drawn:

1. In the present investigation, the commonly assumed values of the stress distribution angle were larger than those observed experimentally and resulted in overprediction of the bearing capacity. This seems to oppose the observation of Burd (1995) that the stress distribution angle tends to be greater for soft than firm

clays. This discrepancy could be due to the compressibility of the subgrade.

2. It has often been concluded that the improvements in the load carrying capacity of unpaved roads due to membrane action are insignificant and may therefore be neglected. However, these conclusions appear to be based on the method by which they are calculated rather than on observed behaviour. In the present investigation, the use of a more realistic stress distribution angle rather than the commonly assumed values greatly increased the calculated membrane forces, suggesting that membrane action does make a significant contribution, particularly for small subbase thicknesses. Unpaved road field trials carried out by Sigurdsson and Fannin (1997) confirmed the importance of membrane action for small subbase thicknesses.
3. In reinforcing very soft ground, the contribution to the bearing capacity from the subgrade reaction after load spreading through the fill would be insignificant so that a tensile reinforcement would rely upon membrane action to support the traffic loading. Even assuming that adequate anchorage and subbase-geogrid interlock is maintained, deformation is likely to be excessive under traffic loading. Therefore a geosynthetic with significant in-plane bending stiffness would be beneficial to the performance of the structure.

REFERENCES

- Burd, H.J. (1995) "Analysis of membrane action in reinforced unpaved roads", *Canadian Geotechnical Journal*, Vol. 32, pp. 946-956.
- Fakher, A., Jones, C.J.F.P., & Zakaria, N.A.B. (1996) "The influence of dimensional analysis on the interpretation of model loading tests on reinforced ground", *Proc. Int. Symposium on Earth Reinforcement*, Kyushu, Japan, pp. 585-589.
- Giroud, J.P. & Noiray, L. (1981) "Geotextile-reinforced unpaved road design", *Jour. Geotech. Eng. Div.*, ASCE, Vol. 107, No. GT9, pp. 1233-1254.
- Gourc, J.P. (1983) "Quelques aspects du comportement des geotextiles en mecanique des sols", *PhD thesis*, University of Grenoble, France.
- Kenny, M.J., & Andrawes, K.Z. (1997) "The bearing capacity of footings on a sand layer overlying soft clay", *Geotechnique*, Vol. 47, No. 2, pp. 339-345.
- Milligan, G.W.E., Jewell, R.A., Houslyby, G.T. & Burd, H.J. (1989) "A new approach to the design of unpaved roads - part II", *Ground Engineering*, Vol. 22, No. 8, pp. 37-42.
- Sigurdsson, O., & Fannin, R.J. (1997) "Construction and performance of a geosynthetic reinforced unpaved road", *Proc. Ground Improvement Geosystems*, Thomas Telford, London, pp. 322-328.

Supporting Capability of Geogrid Reinforced Soil Foundations

N. Yasufuku

Associate Professor, Department of Civil Engineering, Kyushu University, Fukuoka, Japan

H. Ochiai

Professor, Department of Civil Engineering, Kyushu University, Fukuoka, Japan

K. Kawamata

Engineer, Electric Power Development Co. Ltd.

ABSTRACT: Geogrid reinforced sandy soil foundations are often used to improve the supporting capability of soft soil foundations. The vertical load applied on a geogrid reinforced foundation is transmitted to the supporting soil over a wider area, thus, improving the soil's ability to support the foundation load. In order to examine the effect of the vertical load propagation due to geogrid reinforced sandy soils foundation, a series of model loading tests was carried out with different reinforced soil foundation thicknesses and number of geogrids horizontally placed in sandy soils. In addition, a method estimating the effective thickness for geogrid reinforced foundation design is presented based on experimental and theoretical considerations.

KEYWORDS: reinforcement, geogrid, soil foundation, vertical load propagation, bearing capacity

1 INTRODUCTION

The working platform usually consists of geogrid reinforcement laid within a uniform layer of cohesionless fill on the surface of soft soils. Although a number of methods have been used to construct a fill layer over the soft soil, there seems to be no general agreement with respect to the reinforcement mechanism and load spreading effects.

Reinforced sandy soil foundations with geogrid horizontally placed on soft soil ground are often used to improve the supporting capability of soft soil ground in an economical way. The vertical load applied on the reinforced soil foundations is transmitted to the supporting foundation within a wider area, subsequently, providing the supporting foundation with greater bearing capacity. It is considered that the spreading effects depend on the factors shown in Table 1. It is therefore essential to investigate the properties of vertical load propagation in the reinforced soil foundation with geogrids with reference to the influence factors in

Table 1. Typical factors related to load spreading effects in reinforced sandy soil foundations with geogrid

Term	Influence factors
Reinforced soil ground with geogrid	1. Thickness, 2. Number and position of reinforcement layers, 3. Reinforcement length
Soil property	1. Unit weights of soils, 2. Strength parameters
Geogrid property	1. Tensile strength, 2. Friction property

Table 1. This will develop a rational way of determining the reinforced geogrid soil foundation thickness in practical design. In this paper, the effects of the foundation thickness and the number of reinforcement layers on the spreading effects in reinforced sandy soil foundations with geogrid are investigated using the results of model loading tests and a few theoretical considerations.

2 EXPERIMENTAL PROCEDURE

Figure 1 shows the layout of the experiment. On the floor of a 1.08 m wide, 0.4 m deep, 0.8 m high container, twenty-one aluminium blocks (0.05 m wide, 0.4 m long) were lined up.

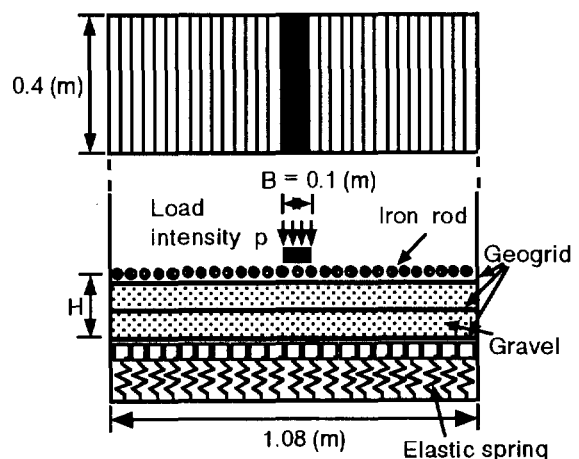


Figure 1 Experimental setup

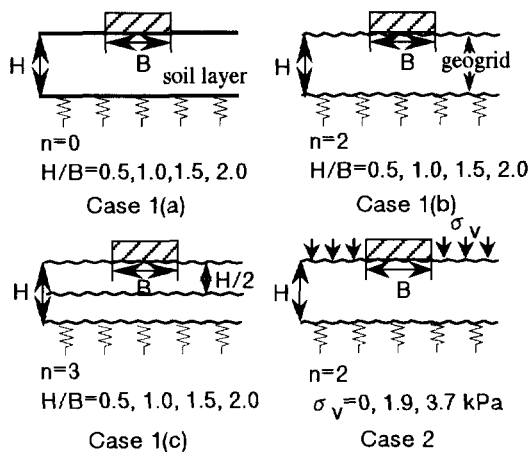


Figure 2 Groups of tests

Two elastic springs were fixed under each aluminium block and the vertical deformation of each spring was measured by a dial gauge attached alongside. The elastic springs with an elastic stiffness of $k=3.14$ (kgf/mm) were used to represent the supporting soil, possessing an elastic modulus of subgrade reaction $k_g=3077$ kPa/m. The model reinforced soil foundation with geogrid were made of fine gravel. The average dry density was 16.4 kN/m³ and the internal friction angle was 41 degrees (Ochiai et.al.,1994). The tests performed are schematically shown in Figure 2. They consists of the following two cases:

Case 1 aims to study the effects of number of reinforcement layers on the vertical load propagation properties. The spreading effect is also investigated in relation to the thickness of reinforcement layer. Case 2 aims to discuss the spreading effect of vertical load through reinforced gravel foundations with geogrid under different overburden pressures. The tensile strength of geogrid used is 14.7 (kN/m). The size of each model is 1.08 m wide, 0.40 m long and 0.05, 0.1, 0.15 or 0.20 m thick. The loading plate of 0.1 m wide and 0.4 m long is placed on the model reinforced gravel foundation, which is then vertically loaded while controlling displacement. The rate of displacement was 1 mm/min.

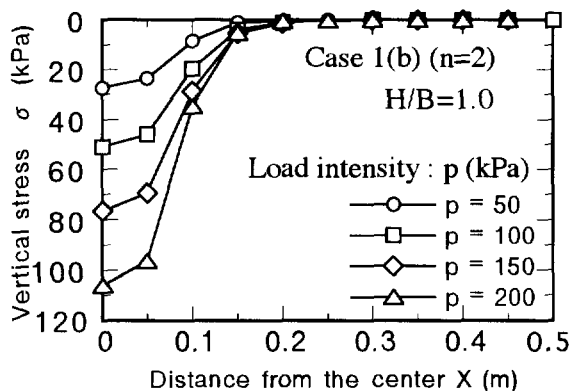


Figure 3. Typical vertical stress distribution

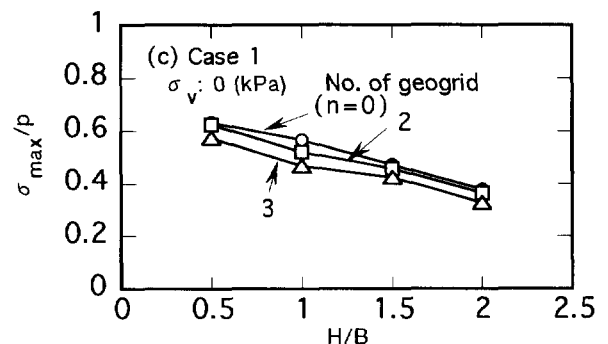
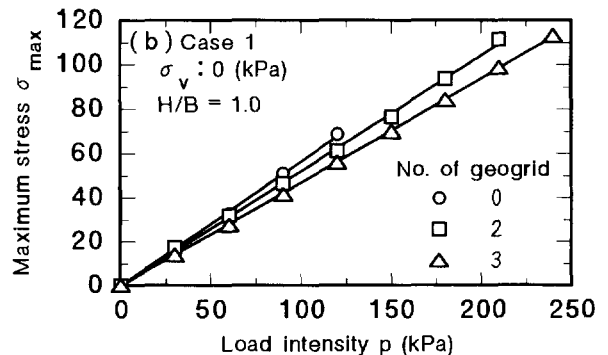
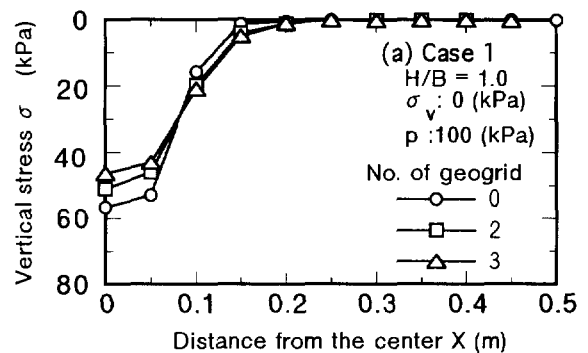


Figure 4 Characteristics of load spreading effect related to number of reinforcement layer

3 EXPERIMENTAL RESULTS

3.1 Vertical Stress Propagation

Figure 3 shows the vertical stress distribution at the supporting foundation under the reinforced gravel layer with two geogrids (Case 1(b) at $H/B=1.0$) generated by several load intensities p . It can be seen from this figure that the vertical stress distribution was convex with a maximum vertical stress σ_{max} at the center. It is also obvious that the magnitude of σ_{max} increases with the increasing load intensity p , and that the magnitude is always smaller than the values of p .

3.2 Maximum Vertical Stress

Figures 4 and 5 show the effects of number of reinforcement

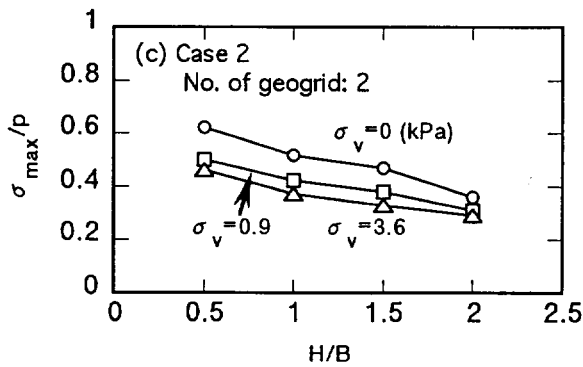
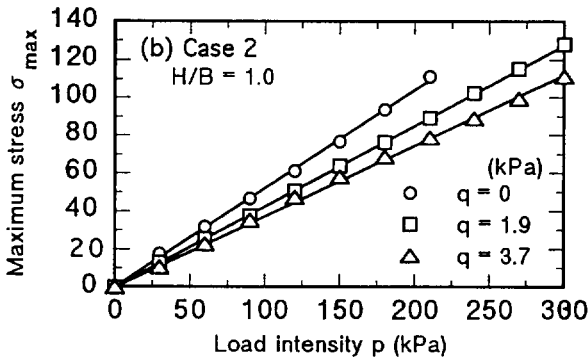
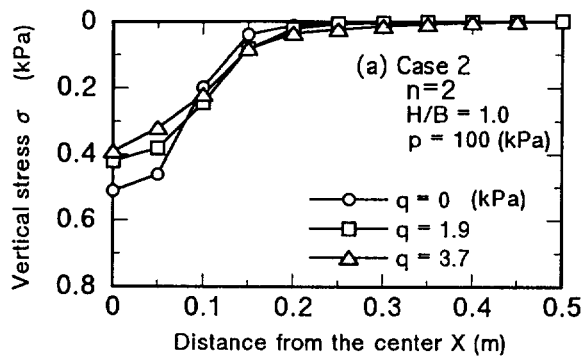


Figure 5 Characteristics of load spreading effect related to overburden pressure

layer and overburden pressure on the magnitude of maximum vertical stress σ_{max} . It is found from these figures that 1) σ_{max} decreases with the increasing number of reinforcement layer and overburden pressure (see Figures 4(a) and 5(a)), and that 2) the σ_{max} develops in proportion to the applied vertical stress over a wide load intensity region, irrespective of the two factors mentioned above (see Figures 4(b) and 5(b)), and also that 3) not only the values of σ_{max}/p decrease with the increasing H/B but also the influence of the two factors on σ_{max}/p gradually decreases with the increasing H/B (see Figures 4(c) and 5(c)). Similar properties have already been shown in the results of geogrid-mattress loading tests (Ochiai, et. al.,(1994); Yasufuku, et. al.,(1996)).

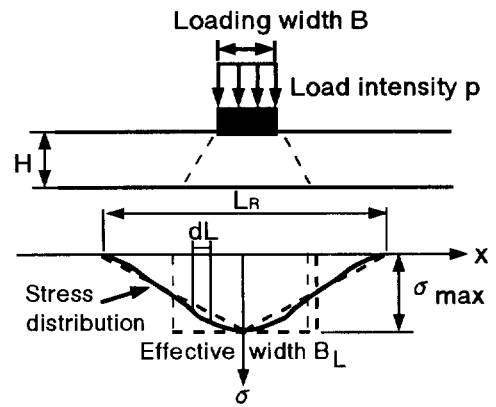


Figure 6 Definition of effective width B_L

4 THEORETICAL CONSIDERATIONS

4.1 Definition of Effective Width

When loading is applied to a reinforced gravel layer with geogrid, the resulting stress distribution becomes convex with a maximum vertical stress σ_{max} at the center of the base as is schematically shown in Figure 6. Here, in order to reasonably estimate the spreading effects of the reinforced gravel foundation, effective width B_L is introduced which is defined as an apparent stress distribution width. When considering that σ_{max} is uniformly transmitted to a given supporting subgrade due to a load intensity p , and then the $\sigma_{max}B_L$ balances with pB , the following equation can be given (see Figure 6):

$$pB = \int \sigma dL = \sigma_{max} B_L \quad (1)$$

Eq.(1) can also be rewritten as;

$$\frac{B_L}{B} = \frac{1}{\frac{\sigma_{max}}{p}} \quad (2)$$

As shown in Figures 4 and 5, σ_{max}/p is constant irrespective of load intensity, and it is therefore obvious from Eq.(2) that B_L/B also becomes constant. In addition, it is important to point out that as the σ_{max}/p becomes smaller and B_L/B becomes larger, the spreading effect of reinforced gravel layer increases.

When a triangular stress distribution with width L_R is assumed as shown in Figure 6 which is approximately true (see Figures 4 and 5), the relationship between L_R and B_L is represented by

$$L_R = 2B_L \quad (3)$$

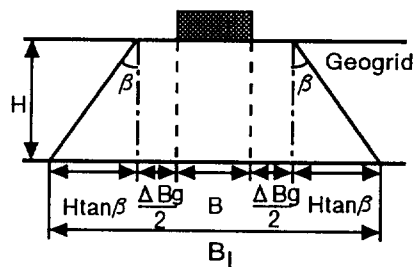


Figure 7 Schematic view of load spreading effect

4.2 Geogrid Spreading Effects ΔB_g

When a loading plate of width B is placed on a reinforced gravel layer with geogrid, the applied vertical load is transmitted to the supporting subgrade through the gravel layer. An idea of load spreading is schematically shown in Figure 7. Based on this idea, the total spreading effect B_L can be divided into two parts: one is geogrid spreading effect ΔB_g , which is due to soil-geogrid interaction and the other is $2H \tan \beta$, which is due to thickness of gravel layer. Thus, the net spreading effect normalized by B is given by

$$\frac{B_L - B}{B} = \frac{\Delta B_g}{B} + 2 \frac{H}{B} \tan \beta \quad (4)$$

where, β is defined as spreading angle through a reinforced gravel layer.

The computed relationship between $(B_L - B)/B$ and $2H/B$ are shown in Figure 8, together with the experimental data, in which Figure 8(a) indicates the effects of number of reinforcement layers on the net spreading effect, and also Figure 8(b) clarifies the dependence of the effect on the overburden pressure. Here the experimental plots were obtained from Eq.(1) with measured values of σ_{max}/p , and the solid lines are based on Eq.(4), in which spreading angle β was estimated to be 27 degrees, that is $\tan \beta = 0.5$, irrespective of number of reinforced layers and overburden pressure. It can be found from these figures that the normalized spreading effect of geogrid $\Delta B_g/B$, which is evaluated as the value of B_L/B at $H/B = 0$, increases with the increase in the number of reinforcement layers and overburden pressure, at least in the case of normalized thickness H/B less than 2. In addition, it can be seen that Eq.(5) can reasonably represent the mechanism of spreading effects in the reinforced gravel layer with geogrid.

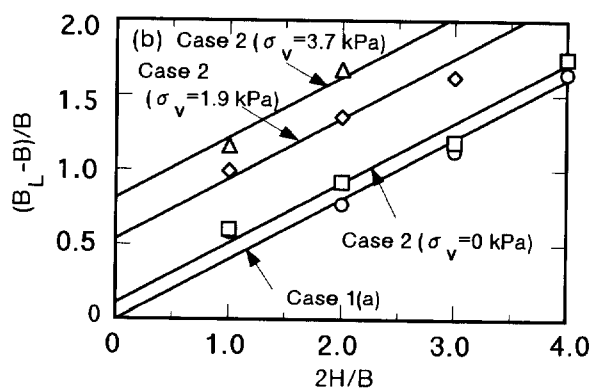
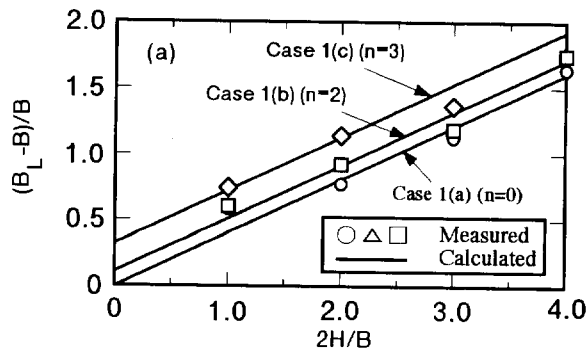


Figure 8 Relationship between $(B_L - B)/B$ and $2H/B$

4.3 Estimation of Geogrid Reinforced Thickness

In a practical design, it is necessary to properly estimate the thickness of reinforcement layer H against an allowable bearing capacity q_a in the supporting soft layer. When q_a is considered to be σ_{max} , and substituting Eq.(4) into Eq.(1), the following equation is obtained;

$$pB = q_a (B + 2H \tan \beta) + q_a \Delta B_g \quad (5)$$

where $q_a \Delta B_g$ represents an internal force taken by the reinforcement spreading effect ΔB_g . As was discussed by Ochiai et. al., (1986), taking the spreading effect as G_e and comparing with Eq.(5), G_e is given by ;

$$\begin{aligned} G_e &= q_a \Delta B_g \\ &= pB - q_a (B + 2H \tan \beta) \end{aligned} \quad (6)$$

Further, considering that $\tan \beta = 0.5$ ($\beta = 27^\circ$), Eq.(6) is easily rewritten as:

$$\frac{H}{B} = \frac{p}{q_a} \left(1 - \frac{G_e}{pB} \right) - 1 \quad (7)$$

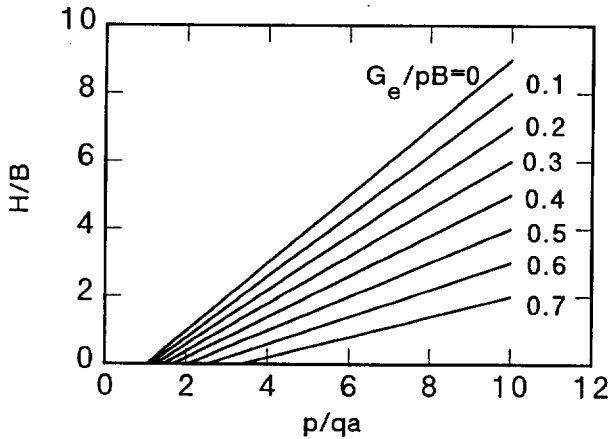


Figure 9 Chart of determining reinforcement thickness H against geogrid spreading effect G_e

Figure 9 shows the H/B - p/q_a relationship calculated from Eq.(7) with various values of G_e/pB . It is important to note that the estimation of G_e is needed in order to obtain the thickness of reinforcement layer using Eq.(7). To estimate G_e in a concrete way, the following assumption can be made; 1) the spreading effects can be produced due to the maximum tensile force F_{Tmax} in geogrids and the direction is perpendicular to line ab (cd) as shown in Figure 10, that is, the angle between the direction of the force and that of the horizontal plane becomes the load spreading angle β ($\tan\beta=0.5$). 2) F_{Tmax} can be mobilized by maximum tensile shear stress τ_{max} in the range of the load spreading width $2H\tan\beta$ and 3) the shear stress τ_{max} is due to the internal friction between soil and geogrid. A similar idea has been reported by Yang et. al.,(1994).

Base on these assumptions, the tensile force F_{Tmax} is represented by

$$F_{Tmax} = \tau_{max}(2H \tan \beta) = \sigma_v \tan \delta (2H \tan \beta) = \sigma_v H \tan \delta \quad (8)$$

where, δ and σ_v are the friction angle in the soil-geogrid interaction and vertical stress acting on the geogrid respectively. Here, for simplicity σ_v is assumed to be equal to the overburden pressure. Therefore, the spreading effect G_e in geogrid is estimated by ;

$$G_e = \sum_{i=1}^n F_{Tmax,i} \sin \beta = \sum_{i=1}^n \sigma_{v,i} H \tan \delta \sin \beta \quad (9)$$

where, n is defined as numbers of reinforcement layer and,

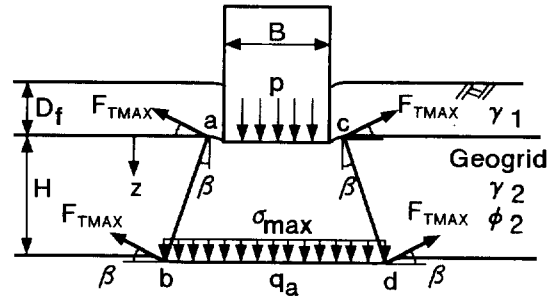


Figure 10 Idea of load spreading effect

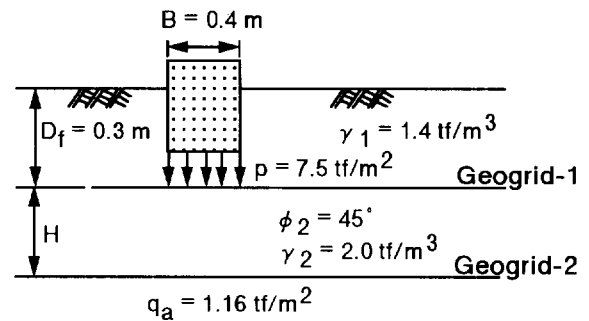


Figure 11 Example of design condition

$\sin\beta$ is almost equal to 0.45 from the definition of β . It is easy to understand that when substituting Eq.(9) into Eq.(7), the proper thickness, H , can be obtained under a certain design condition.

Now, as an application of this model, the following example is considered. The design condition is shown in Figure 11. In this case, the vertical stresses σ_{v1} on geogrid-1 and σ_{v2} on geogrid-2 are evaluated as :

$$\sigma_{v1} = \gamma_1 d_f \quad ; \quad \sigma_{v2} = \gamma_2 (d_f + H) \quad (10)$$

and substituting Eqs.(8), (9) and (10) into Eq.(7), and after some calculation, the thickness H is computed as follows:

$$H = \frac{-A_2 + \sqrt{A_2^2 - 4A_1A_3}}{2A_1} \quad (11)$$

where, $A_1 = \gamma_2 \tan \delta \sin \beta$, $A_2 = 2\gamma_1 d_f \tan \delta \sin \beta + q_a$ and $A_3 = -(p - q_a)B$. It is important to note that in this case, using this equation, the thickness, H , is computed as 1.20 m which is about a half compared with the thickness in the case without geogrid ($G_e=0$) which is about 2.18 m calculated using Eq.(7).

5 CONCLUSIONS

The vertical load spreading effect of reinforced soil foundation with geogrids is investigated both experimentally and theoretically. The main conclusions obtained are as follows :

1. The vertical load propagation on the surface of subgrade has a convex shape with the maximum vertical stress σ_{max} at the center of applied vertical stress p .
2. The maximum vertical stress σ_{max} developed is proportional to the applied vertical stress p . The ratio, σ_{max}/p , is influenced by the thickness of reinforced soil foundations, numbers of geogrids and the overburden pressure.
3. Effective width B_e is proposed to express the load spreading effect in reinforced soil foundation with geogrid which has two parts: one is geogrid spreading effect and the other is the effect due to the thickness of soil layer.
4. An estimating method is proposed to calculate the thickness of reinforced foundations in design practice using the proposed effective width B_e and the considered soil-geogrid interaction mechanism.

ACKNOWLEDGMENTS

The authors would like to thank Prof. J.W. Ju of Suncheon National University, Korea and Mr. M. Nakashima of Kyushu University, Japan for their support during the experiments.

REFERENCES

- Ochiai, H., Matsushita, H. and Hayashi, S. (1986) "Foundations for Buildings on Grounds Contained Sulphuric Ion", *Tsuchi-to-Kiso*, Vol.34, No.6, pp.45-50 (in Japanese).
- Ochiai, H., Tsukamoto, Y., Hayashi, S., Otani, J. and Ju, J.W. (1994) "Supporting Capability of Geogrid-Mattress Foundation", *5th International Conference on Geotextiles, Geomembranes and Related Products*, Singapore, pp.321-326.
- Yang, J, Ochiai, H. and Hayashi, S. (1994) "Evaluation of Bearing Capacity of Geogrid Reinforced Foundation", *Jour. of Geotechnical Engineering, JSCE*, No.505/III-29, pp.123-132, (in Japanese).
- Yasufuku, N, H.Ochiai, K.Omine, S.Ohno, K.Kawamata and Y.Tsukamoto (1996) "Evaluation of the Bearing Capacity Improvement of Geogrid Mattress", *Proc. of Int. Symp. on Earth Reinforcement (IS Kyushu '96)*, Vol.1, pp.703-708.

Theoretical Solutions for Stress and Strain Fields of a Geosynthetic-Reinforced Foundation Vertically Loaded by a Concentrated Force

Jie Han

Design Engineer, Ph.D., Tensar Earth Technologies, Inc., Atlanta, GA 30328, USA

ABSTRACT: Geosynthetics can be used as reinforcements in soils to provide improved bearing capacity and reduced settlement for structural footings or pavement systems. Existence of geosynthetics in a foundation tends to alter the stress and strain fields due to the difference in elastic moduli and strengths between geosynthetics and soils. Geosynthetic-reinforced soil system can be treated as inhomogeneity and inclusion problems as studied in micromechanics of composites. The concept is to represent the inhomogeneities of geosynthetics in soil as the inclusions of eigenstrains in a homogeneous medium. Derivation of the solutions to determine stress and strain fields of the geosynthetic-reinforced foundation vertically loaded by a concentrated load is presented in this paper, in which the Eshelby eigenstrain tensor is introduced.

KEY WORDS: Geosynthetic, reinforcement, foundations, inclusion, stress-strain relations.

1 INTRODUCTION

Early studies conducted by Binquet and Lee (1975a, b) on geosynthetic-reinforced foundations demonstrated the effectiveness of geosynthetics in increasing bearing capacity of soils. The use of this kind of foundation has attracted more attention in the past few years. A number of model tests have been performed by several researchers (Huang and Tatsuoka 1990; Omar et al. 1994; Yetimoglu et al. 1994). Those tests mainly focused on finding out the optimized configuration of the geosynthetic layers in soil such as the location of the top layer, the spacing between adjacent layers, the width of reinforcement, and the number of layers. However, very few theories have been developed so far to study the mechanisms behind the experimental results. Binquet and Lee (1975b) assumed that the normal and shear stresses along the upper surface of the geosynthetic reinforcement follow Boussinesq's solution. Shukla and Chandra (1994) established a model to analyze the settlement response by treating a geosynthetic layer as an elastic membrane and solving the equilibrium equations under vertical and horizontal loads on the membrane. In those papers, the existence of the geosynthetics was not taken into account in the calculation of applied stresses on the geosynthetics due to the external loads on the upper surface. In reality, the existence of geosynthetics in the foundation disturbs the whole stress and strain fields as indicated by Kurian et al. (1997) using a finite element method.

2 THEORIES OF INHOMOGENEITY AND INCLUSION PROBLEMS

A material Ω with different elastic moduli from those of a matrix $D-\Omega$ as shown in Figure 1 is called an inhomogeneity in micromechanics. The existence of the material D will disturb the applied stresses in the domain $D-\Omega$ (Mura 1983).

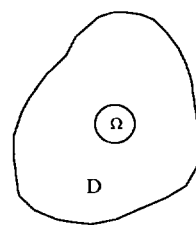


Figure 1 Inhomogeneity and inclusion (Mura 1982)

The disturbed stress field can be simulated by an eigenstress field resulting from a fictitious eigenstrain ϵ_{ij}^* in the domain Ω in a homogeneous material. The so-called eigenstrain was defined by Mura (1982) as a nonelastic strain such as thermal expansion, phase transformation, initial strains, plastic, and misfit strains, etc. Eigenstress is a self-equilibrated internal stress induced by one or several eigenstrains in a body without any other external force and surface constraint. The domain Ω with the eigenstrain ϵ_{ij}^* and the same elastic moduli as those in the matrix $D-\Omega$ is called an inclusion.

Due to applied external forces, the stress-strain relation for the inhomogeneity problem can be expressed as (Mura 1982)

$$\sigma_{ij}^0 + \sigma_{ij} = C_{ijkl}^* (\epsilon_{kl} + \epsilon_{kl}^0) \quad \text{in } \Omega \quad (1)$$

$$\sigma_{ij}^0 + \sigma_{ij} = C_{ijkl} (\epsilon_{kl} + \epsilon_{kl}^0) \quad \text{in } D-\Omega \quad (2)$$

where σ_{ij}^0 and ϵ_{kl}^0 are the stress and the strain induced by external forces without any inhomogeneity, and σ_{ij} and ϵ_{kl} are the stress and the strain due to the presence of the inhomogeneity. As pointed out by Eshelby (1957), the

inhomogeneity problem can be treated as an equivalent inclusion problem by including the eigenstrains as follows:

$$\sigma_{ij}^0 + \sigma_{ij} = C_{ijkl}(\epsilon_{kl} + \epsilon_{kl}^0 - \epsilon_{kl}^*) \quad \text{in } \Omega \quad (3)$$

Equalizing Equation (1) and Equation (3) yields

$$C_{ijkl}^*(\epsilon_{kl} + \epsilon_{kl}^0) = C_{ijkl}(\epsilon_{kl} + \epsilon_{kl}^0 - \epsilon_{kl}^*) \quad \text{in } \Omega \quad (4)$$

3 MODELING OF A GEOSYNTHETIC-REINFORCED FOUNDATION

Figure 2a is a case occurring in geotechnical practice. The geosynthetic layer has two major functions in resisting the applied load P on the surface: soil confinement and membrane effect. This problem can be modeled as an ellipsoidal inhomogeneity or inclusion in a half space as shown in Figure 2b. This model can be further decomposed into two problems as shown in Figure 3. The problem in Figure 3a is a Boussinesqi problem while the problem in Figure 3b is an inclusion problem. The solutions to the stresses σ_{ij}^0 and strains ϵ_{kl}^0 for Boussinesqi's problem can be found in many textbooks. Therefore, the aim of this paper is to investigate the inclusion problem.

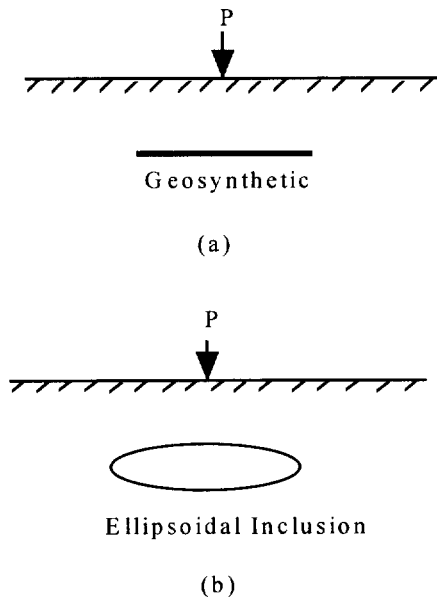


Figure 2 Modeling of a Geosynthetic-Reinforced Foundation

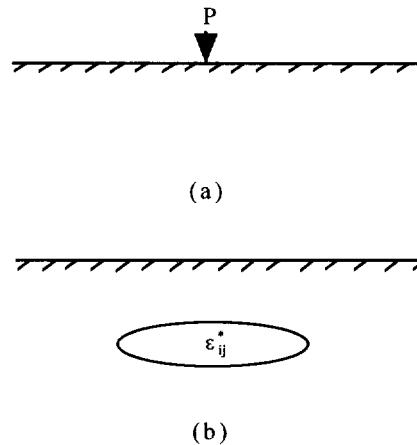


Figure 3 Decomposition of the Problem

4 SOLUTION FOR STRESS AND STRAIN FIELDS

The displacement $u_i(\bar{x})$ induced by the eigenstrain ϵ_{ij}^* in the semi-infinite domain can be expressed by (Seo and Mura 1979)

$$u_i(\bar{x}) = \int_{\Omega} C_{jkmn} \epsilon_{mn}^*(\bar{x}') \frac{\partial}{\partial x'_k} G_{ij}(\bar{x}, \bar{x}') d\bar{x}' \quad (5)$$

where $G_{ij}(\bar{x}, \bar{x}')$ are Green's functions and C_{jkmn} are elastic constants. Green's functions $G_{ij}(\bar{x}, \bar{x}')$ for the semi-infinite isotropic medium have been obtained by Mindlin (1936) and rewritten by Seo and Mura (1979) in their paper as follows:

$$G_{ij}(\bar{x}, \bar{x}') = \frac{1}{16\pi\mu(1-\nu)} \left\{ \frac{3-4\nu}{R_1} \delta_{ij} + \frac{1}{R_2} \delta_{ij} + \frac{(x_i - x'_i)(x_j - x'_j)}{R_1^3} \right. \\ \left. + \frac{(3-4\nu)(x_i - x'_i)(x_j - x'_j)}{R_2^3} + \frac{2x_3x'_3}{R_2^3} \left[\delta_{ij} - \frac{3(x_i - x'_i)(x_j - x'_j)}{R_2^2} \right] \right. \\ \left. + \frac{4(1-\nu)(1-2\nu)}{R_2 + x_3 + x'_3} \left[\delta_{ij} - \frac{(x_i - x'_i)(x_j - x'_j)}{R_2(R_2 + x_3 + x'_3)} \right] \right\}$$

$$G_{3j}(\bar{x}, \bar{x}') = \frac{(x_j - x'_j)}{16\pi\mu(1-\nu)} \left[\frac{(x_3 - x'_3)}{R_1^3} + \frac{(3-4\nu)(x_3 - x'_3)}{R_2^3} \right. \\ \left. - \frac{6x_3x'_3(x_3 + x'_3)}{R_2^5} + \frac{4(1-\nu)(1-2\nu)}{R_2(R_2 + x_3 + x'_3)} \right]$$

$$G_{13}(\bar{x}, \bar{x}') = \frac{(x_i - x'_i)}{16\pi\mu(1-\nu)} \left[\frac{(x_3 - x'_3)}{R_1^3} + \frac{(3-4\nu)(x_3 - x'_3)}{R_2^3} \right. \\ \left. + \frac{6x_3x'_3(x_3 + x'_3)}{R_2^5} - \frac{4(1-\nu)(1-2\nu)}{R_2(R_2 + x_3 + x'_3)} \right]$$

$$G_{33}(x, x') = \frac{1}{16\pi\mu(1-\nu)} \left[\frac{3-4\nu}{R_1} + \frac{8(1-\nu)^2 - (3-4\nu)}{R_2} \right. \\ \left. + \frac{(x_3 - x'_3)^2}{R_1^3} + \frac{(3-4\nu)(x_3 + x'_3)^2 - 2x_3x'_3}{R_2^3} + \frac{6x_3x'_3(x_3 + x'_3)^2}{R_2^5} \right] \\ i, j = 1, 2 \quad (6)$$

where $R_1^2 = (x_1 - x'_1)^2 + (x_2 - x'_2)^2 + (x_3 - x'_3)^2$;
 $R_2^2 = (x_1 - x'_1)^2 + (x_2 - x'_2)^2 + (x_3 + x'_3)^2$;
 μ = shear modulus;
 ν = Poisson's ratio.

The effect of the free surface has been included in the above equations by containing the term R_2 .

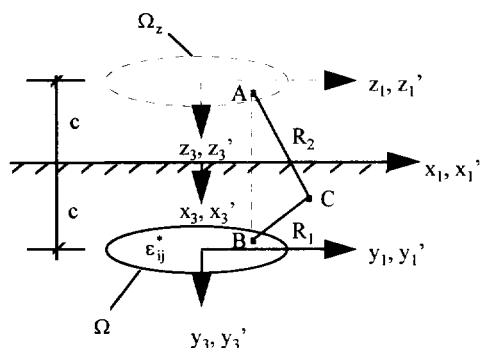


Figure 4 An Ellipsoidal Inclusion in a Half Space (After Seo and Mura 1979)

Assume a circular geosynthetic sheet with a radius R horizontally buried in a half space has a constant thickness t in x'_3 direction, which is much less than the dimensions in x'_1 and x'_2 directions. The vertically applied load P passes through the center of the geosynthetic sheet. The variation of eigenstrains in the thickness direction is negligible. Due to the geometric symmetry and the location of the applied load, the eigenstrains are symmetric to x'_1 and x'_2 axes.

From Equation (5), the relationship between the strain disturbance and the eigenstrain can be expressed by

$$\varepsilon_{kl} = \frac{1}{2} (u_{k,l} + u_{l,k}) = \int_{\Omega} C_{opmn} \varepsilon_{mn}^* (\bar{x}') g_{klop}(\bar{x}, \bar{x}') d\bar{x}' \quad (7)$$

$$\text{where } g_{klop}(\bar{x}, \bar{x}') = \frac{1}{2} \left[\frac{\partial^2 G_{ko}(\bar{x}, \bar{x}')}{\partial x_l \partial x_p} + \frac{\partial^2 G_{lo}(\bar{x}, \bar{x}')}{\partial x_k \partial x_p} \right]$$

Substituting Equation (7) into Equation (4) yields

$$\varepsilon_{kl}^* (\bar{x}) = K \int_{\Omega} C_{opmn} \varepsilon_{mn}^* (\bar{x}') g_{klop}(\bar{x}, \bar{x}') d\bar{x}' + F_{kl}(\bar{x}) \text{ in } \Omega \quad (8)$$

where $K = I - C_{ijkl}^{-1} C_{klij}^*$ and $F_{kl}(\bar{x}) = K \varepsilon_{kl}^0$.

A variety of numerical methods can be adopted to solve Equation (8). A numerical integration technique is introduced herein. Equation (8) can be expressed as (Wang et al 1977):

$$\varepsilon_{kl}^* (\bar{x}_1) = F_{kl}(\bar{x}_1) + KC_{opmn} A_{\Omega} t \sum_{j=1}^n w_j \varepsilon_{mn}^* (\bar{x}_j) g_{klop}(\bar{x}_1, \bar{x}_j) \quad (9)$$

where \bar{x}_1 and \bar{x}_j are integral points, $\bar{x}_1 = (x_1, x_2)$, $\bar{x}_j = (x'_1, x'_2)$, and $x_1^2 + x_2^2 \leq R^2$ and $(x'_1)^2 + (x'_2)^2 \leq R^2$; w_j = weight factor; n = number of integral point; A_{Ω} = integral area, equal to the area of geosynthetic sheet.

Equation (9) can be rewritten in matrix forms as

$$\mathbf{E} = \mathbf{F} + \lambda \mathbf{G} \mathbf{W} \mathbf{E} \quad (10)$$

$$\text{or } \mathbf{H} \mathbf{E} = \mathbf{F} \quad (11)$$

where $\mathbf{H} = \mathbf{I} - \lambda \mathbf{G} \mathbf{W}$; $\mathbf{I} = n \times n$ unit matrix;
 $\lambda = K C A_{\Omega} t$; $\mathbf{G} = (G_{ij})$; $\mathbf{E} = (\varepsilon_{kl}^* (\bar{x}_1), \varepsilon_{kl}^* (\bar{x}_2), \dots, \varepsilon_{kl}^* (\bar{x}_n))^T$;
 $\mathbf{F} = (F(\bar{x}_1), F(\bar{x}_2), \dots, F(\bar{x}_n))^T$; $\mathbf{W} = (w_1, w_2, \dots, w_n)$.

After solving the eigenstrains ε_{kl}^* at integral points from Equation (11), the strain disturbance ε_{kl} can be computed by using the numerical integration technique and substituting ε_{kl}^* into Equation (7). Then, the stress and strain fields can be obtained from Equation (1) and Equation (2).

5 FUTURE STUDIES

This paper only focuses on the development of theoretical solutions for stress and strain fields of a geosynthetic-reinforced foundation vertically loaded by a concentrated force. Parametric studies need to be done in the future to investigate influential factors and develop design charts for this problem, which will be very beneficial to researchers and engineers.

6 SUMMARY

By mean of the concepts and methodologies in micromechanics, the geosynthetic-reinforced foundation is modeled as an inclusion problem. The stress and strain disturbance due to the presence of a geosynthetic sheet in a half space is simulated by applying an eigenstrain in the region of the geosynthetic sheet. Using the solutions obtained by Mindlin (1936) for a force at a point in the interior of a semi-infinite solid and the stress-strain

relationship proposed by Eshelby (1957) for a general inclusion problem, the eigenstrain for the inclusion is computed. The stress and strain fields for a geosynthetic-reinforced foundation vertically loaded by a concentrated force is formulated.

ACKNOWLEDGMENTS

The author would like to thank Mr. Philip Egan, the President of Tensar Earth Technologies, Inc., for his review and comments.

REFERENCES

- Binquet, J. and Lee, K.L. (1975a). "Bearing Capacity Tests on Reinforced Earth Slabs", *Journal of Geotechnical Engineering*, ASCE, Vol. 101, No. 12, pp. 1241-1255.
- Binquet, J. and Lee, K.L. (1975b). "Bearing Capacity Analysis of Reinforced Earth Slabs", *Journal of Geotechnical Engineering*, ASCE, Vol. 101, No. 12, pp. 1257-1276.
- Eshelby, J.D. (1957). "The Determination of the Elastic Field of an Ellipsoidal Inclusion and Related Problems", *Proceedings of the Royal Society, Series A*, Vol. 241, pp. 376-396.
- Huang, C.C. and Tatsuoka, F. (1990). "Bearing Capacity of Reinforced Horizontal Sandy Ground", *Geotextiles and Geomembranes*, Vol. 9, pp. 51-82.
- Kurian, N.P., Beena, K.S., and Kumar, R.K. (1997). "Settlement of Reinforced Sand in Foundations." *Journal of Geotechnical and Geoenvironmental Engineering*, Vol. 123, No.9, pp. 818 - 827.
- Mindlin, R.D. (1936). "Force at a Point in the Interior of a Semi-Infinite Solid", *Physics*, Vol. 7, May, pp. 195-202.
- Mura, T. (1982). *Micromechanics of Defects in Solids*, Martinus Nijhoff Publishers, The Hague, 587p.
- Omar, M.T. (1994). "Bearing Capacity of Foundation on Geogrid-Reinforced Sand", *XIII CIMSTF*, New Delhi, India, pp. 1279-1282.
- Seo, K. and Mura, T. (1979). "The Elastic Field in a Half Space due to Ellipsoidal Inclusions with Uniform Dilatational Eigenstrains", *Journal of Applied Mechanics*, Vol. 46, September, pp. 568-572.
- Shukla, S. and Chandra, S. (1994). "A Generalized Mechanical Model for Geosynthetic-Reinforced Foundation Soil", *Geotextiles and Geomembranes*, Vol. 13, pp. 813-825.
- Wang, L.X., et al. (1977). *Mathematical Handbook* (in Chinese), Higher Education Publisher, Beijing, 1398p.
- Yetimoglu, T., Wu, J.T.H., and Saglamer, A. (1994). "Bearing Capacity of Rectangular Footings on Geogrid-Reinforced Sand", *Journal of Geotechnical Engineering*, Vol. 120, No. 12, pp. 2083-2099.

Bearing Capacity of Strip Footing on Geogrid-Reinforced Slope

C. S. Yoo

Assistant Professor, Department of Civil Engineering, Sung Kyun Kwan University, Seoul, Korea

D. Y. Lee

Researcher, Geotechnical Engineering Division, Korea Institute of Construction Technology, Seoul, Korea

ABSTRACT: This paper presents the results of laboratory model footing tests on the bearing capacity behavior of strip footing on geogrid reinforced slopes. For the model tests, the reinforced slopes were artificially created using the raining technique with sand. A wide range of conditions were analyzed by varying geogrid reinforcing patterns. Furthermore, model tests were simulated using finite element analysis with the aim of investigating the mechanics behavior of the reinforced slope such as failure mechanism and force distribution in geogrid. Based on the results of model tests, both qualitative and quantitative relationships were established between the bearing capacity and the geogrid design parameters such as depth, length, and number of geogrid layers.

KEYWORDS: Geogrid, Bearing capacity, Slope, Model test, Strip footing, Finite element analysis.

1. INTRODUCTION

Geogrids are often used as slope reinforcement for construction of slopes to angles steeper than those constructed with the fill material being used. When a strip footing is constructed adjacent to such a reinforced slope, the bearing capacity behavior of the footing would be significantly different than that of unreinforced slope. To design such a strip footing on a reinforced slope requires a bearing capacity determination method. Most of the previous studies mentioned above, however, have been focused on horizontally leveled ground, and therefore, no rational method of bearing capacity determination for a shallow foundation on reinforced slope is available up to date. Therefore, much still needs to be investigated in order to develop a generally acceptable design method for shallow foundations on reinforced slope.

This study was undertaken with the aim of investigating the mechanistic behavior of geogrid-reinforced slope under strip load as well as the bearing capacity behavior of strip footings on reinforced ground using experimental and numerical studies.

2. LABORATORY MODEL TESTS AND FINITE ELEMENT ANALYSIS

2.1 Laboratory Model Tests

The laboratory model tests were conducted in a test box made of 60 mm-thick wood, having an internal dimension of 1.2m (length) x 0.8m (depth) x 0.3m (width). One side of the test box was cleared using a plexiglass for ease of observing failure mechanism during the test. The

inside walls of the test box were greased to minimize the friction with ground and the edges of the foundations as much as possible. Although no slip sheets were attached onto the inside walls, no appreciable friction was observed during the test. Furthermore, a rough base condition of a 80mm-wide model footing made of steel was achieved by attaching a sand paper at the bottom.

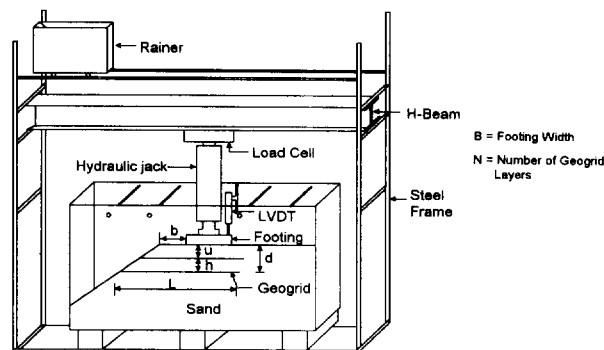


Figure 1. A schematic view of model test box with symbols used in this study.

The artificial ground was constructed with fine sands by the raining technique. The effective size (D_{10}), uniformity coefficient (C_u), and coefficient of gradation (C_c) for sand were 0.36 mm, 1.61, and 1.1, respectively. The tests were conducted on a ground with a slope of 1(H):0.67(V) at a relative density of approximately 70%. The slope of the ground was artificially formed by removing the sand with a vacuum after forming horizontally leveled ground. In order to

evaluate the consistency of the placement density during raining, small cans were placed at different locations in the test box. In the test, the Fortrac geogrids by Huesker Synthetic GmbH Co, which has relatively smaller size of apertures, were used in order to reduce a possible size effect. The mechanical properties of the ground and the geogrid are summarized in Table 1. Note that the Young's modulus of the geogrid was back calculated after performing several computer runs.

During the tests, the model footing was loaded using a hydraulic jack at a rate of 1.0 mm/min. The applied footing load and the settlement were measured using a load cell and two LVDTs, respectively. A schematic view of model test box with the symbols used in this study is seen in Fig.1.

Table 1. Mechanical property of the ground and geogrid.

	Ground	Model Footing	Geogrid
Young's modulus E (kN/m ²)	2500	2.1E08	1700000
Poisson's ratio ν	0.35	0.17	-
Friction angle φ (degree)	42	-	-
Cohesion (kN/m ²)	0	-	-
Unit weight(kN/m ³)	16	-	-
Tensile strength (kN/m)	-	-	55

2.2 Finite Element Analysis

A series of finite element analysis using a commercial code DIANA(1996) were conducted on selected conditions in order to investigate the mechanistic behavior of reinforced slope under strip load. In the finite element modeling, the foundation ground was discretized using isoparametric 8-node elements, while the geogrid using embedded reinforcement element. The embedded reinforcement element is a special type of element provided by DIANA, which can model the grid pattern of reinforcement. The vertical and horizontal boundaries were modeled by placing the y and x direction rollers, respectively, and were placed in accordance with the test configuration.

In the analysis, the footing and geogrid were characterized as a linear elastic material, while the foundation soil being an elasto-plastic material obeying Mohr-Coulomb failure criterion. The mechanical properties tabulated in Table 1 were used as input parameter for analysis. Fig. 2 shows a typical finite element mesh used in the analysis.

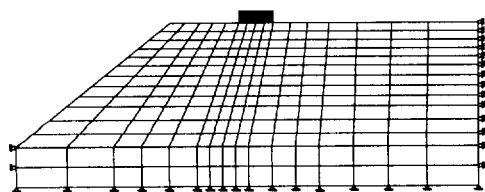


Figure 2. Finite element mesh used in the analysis.

3. MECHANICAL BEHAVIOR OF REINFORCED SLOPE UNDER STRIP LOAD

3.1 Failure Mechanism

The failure mechanism was investigated using the results of model tests and finite element analysis. To observe the failure mechanism during the model tests, horizontal layers of colored sand were placed and photos were taken at various stages of loading to trace the failure surface. The failure patterns for the finite element analysis, on the other hand, were traced using the maximum shear strain ($\epsilon_1 - \epsilon_3$) contours. Figs 3 and 4 show the failure patterns for unreinforced and reinforced slopes, respectively. Note that the results were obtained at the footing settlement level of $S_v/B=0.15$ (S_v =footing settlement; B =footing width), which is beyond its ultimate level for both cases, and that the failure patterns both from the model tests and finite element analysis shown in Figs 3 and 4 are qualitative drawings.

As can be seen in Fig 3 for unreinforced slope, a typical slope failure pattern is observed, which initiates from the footing edge opposite to the slope and progresses toward the slope. The failure pattern for a reinforced slope with three layers of geogrid presented in Fig. 4 demonstrated that due to the reinforcement, the failure surface is not well developed in the reinforced zone, indicating the improved load bearing capacity of the slope. Inspection of the failure pattern reveals that it is desirable to place the geogrids across the potential failure line for unreinforced case so that the geogrid can tie back the potential sliding wedge against outward movement.

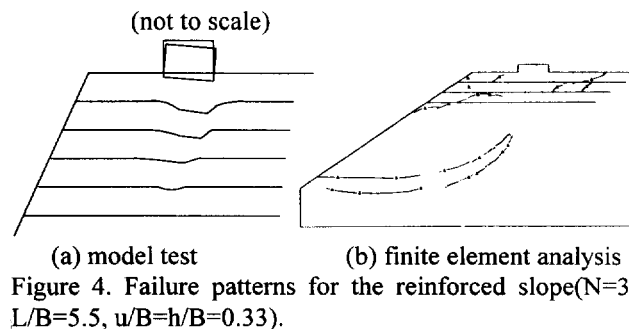
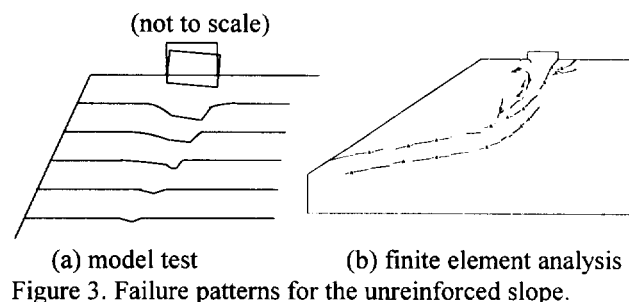


Figure 4. Failure patterns for the reinforced slope ($N=3$, $L/B=5.5$, $u/B=0.33$).

3.2 Traction Force Distribution in Geogrid

Fig. 5 shows typical examples of the traction force distributions in geogrids obtained from the finite element analysis at different footing settlement levels ($S_v/B=0.05$ and 0.1). It is seen that the peak values of tensile force in each layer of geogrid occurs at the points where the slip surface and the geogrid intersect, as one can expect. Furthermore, it is also observed that as the footing load level increases, the traction force in the lower level of geogrid considerably increases while no significant increase is seen in the upper level.

Another finding in this figure is that the traction force distributions are approximately symmetrical from the potential failure surface, and reach nearly zero values at about $2.0B$ from the peak point. This trend indicates that the geogrid needs to be extended beyond the potential failure surface with at least a length of $2.0B$ for anchoring effect. Therefore, it seems reasonable to assume in the relevant design calculation a symmetrical triangular reinforcement force distribution at its apex at the intersection point with a potential failure surface for unreinforced case.

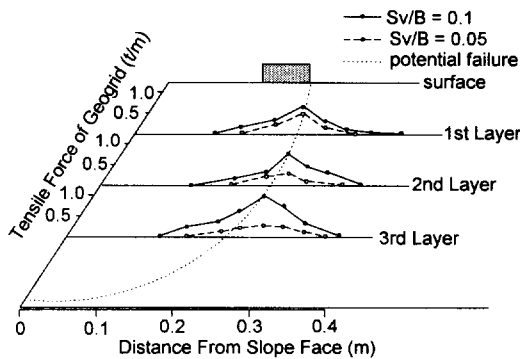


Figure 5. Traction force distributions in geogrids

4. BEARING CAPACITY BEHAVIOR

Based on the results obtained from the model tests, the bearing capacity behavior of strip footing on reinforced slope was analyzed. In the analysis, the normalized bearing capacity ratio ($BCR=q_r/q_{ur}$) was used, where q_r and q_{ur} being bearing capacity values for reinforced and unreinforced slope, respectively.

4.1 Effect of length of geogrid

Das et al.(1994) has reported that there exists a critical length of geogrid beyond which the geogrid has no further reinforcing effect. In order to investigate the variation of bearing capacity with the length of geogrid(L/B), several conditions were tested by varying L/B for $N=3.0$ and $u/B=h/B=0.33$. Fig. 6 shows the relationship between BCR and L/B for $b=1.5B$, indicating that BCR increases

with increasing L/B until L/B reaches its critical value of approximately 5.5 from the slope and becomes almost constant thereafter, indicating $(L/B)_{cr}=5.5$ in this case.

A similar trend can be observed for $b=3.0B$ as seen in Fig. 6, showing the critical length of approximately $7.0B$. The extended length beyond the failure surface corresponds to approximately $3.0B$ for both cases($b=1.5B$ and $3.0B$), implying that the geogrid must be extended approximately $3.0B$ beyond the potential failure surface to have maximum reinforcing effect. This trend supports the traction force distribution pattern.

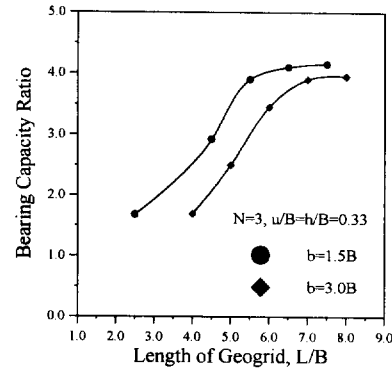


Figure 6. Variation of BCR with L/B

4.2 Effect of depth of reinforced zone

The variation of bearing capacity with the depth of reinforced zone(d/B) was investigated by increasing the number of layers(N) while maintaining $L/B=(L/B)_{cr}$ and $u/B=h/B=0.33$. The relationship between BCR and d/B for $b=1.5B$ and $0B$ is summarized in Fig. 7. As can be seen in this figure, BCR increases almost linearly with d/B until $d/B=2.5$ and becomes nearly constant thereafter, indicating $(d/B)_{cr}=2.5$. Note that Das et al.(1994) reported $(d/B)_{cr}$ of 2.0 for horizontally leveled ground for both sand and clay. This discrepancy may be attributed to the fact that the influencing zone is deeper for a sloped ground than a leveled ground.

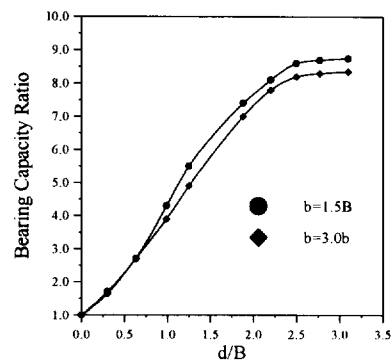


Figure 7. Variation of BCR with d/B

4.3 Effect of u/B and h/B

The effects of u/B and h/B on the bearing capacity were investigated while keeping L/B at a constant value of $(L/B)_{cr} = 5.5$. Fig. 8 shows the variation of BCR with u/B for $N=1, 2$, and 3 cases with $h/B=0.75$. As can be seen in this figure, for $N=1$, the BCR increases with u/B up to approximately a maximum value of $1.0B$ and decreases thereafter, indicating $(u/B)_{cr}=1.0$. Note that Das et al.(1994) reported $(u/B)_{cr}$ of approximately 0.4 for horizontally leveled ground. For $N=2$ and 3 , although a similar trend is observed, $(u/B)_{cr}$ appears to decrease with increasing the number of geogrid layers(N); i.e., $(u/B)_{cr} = 0.8$ for $N=2$ and $(u/B)_{cr} = 0.6$ for $N=3$. This trend may be explained in terms of deep footing effect suggested by Huang et al.(1994). The deep footing effect is a mechanism that a part of reinforced zone behaves as a part of the footing and transfers a major part of the footing load into a deeper zone. Therefore, as the reinforced zone becomes thicker, the reinforced zone acting as a part of the footing should be located closer to the footing in order to maximize its reinforcing effect.

The variation of BCR with h/B can be observed in Fig. 9 for $N=2.0$ and 3.0 . The results obtained for the conditions at a fixed value of $u/B=0.33$. As noticed, the trend is similar to that for the variation of BCR with u/B . However, the critical value of h/B appears to be nearly constant approximately $(h/B)_{cr}=0.8$ regardless of d/B .

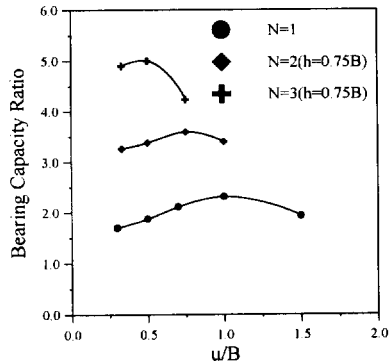


Figure 8. Variation of BCR with u/B

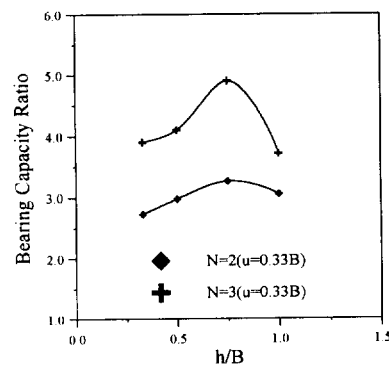


Figure 9. Variation of BCR with h/B

5. CONCLUSIONS

The mechanistic behavior of geogrid-reinforced slope and the bearing capacity behavior of a strip footing on the slope were investigated using both experimental and numerical approaches. A wide range of boundary conditions were tested by varying the reinforcing pattern. The results of model tests and finite element analysis were used to identify the failure mechanism and the traction force distribution in geogrids, and also to establish both qualitative and quantitative relationships between the bearing capacity of a strip footing on reinforced slope and the reinforcing pattern. Based on the results of this study, the following conclusions can be drawn:

1. A symmetrical force distribution with its apex at the intersection point with a potential failure plane can be assumed for traction force distribution in geogrid.
2. The geogrid must be extended at least $3.0B$ beyond a potential failure surface in order to maximize the reinforcing effect.
3. The reinforced zone must be extended to approximately $2.5B$ below footing base for maximum reinforcing effect.
4. The critical value of u/B varies between $0.6 \sim 1.0$ depending on the number of geogrid layers(N), while $(h/B)_{cr}$ being nearly constant value of 0.8 regardless of N

REFERENCES

- Akinmusuru, J. O. and Akinbolade, J. A.(1981) "Stability of Loaded Footings on Reinforced Soil", *Journal of the Geotechnical Engineering*, ASCE, Vol. 107, pp. 819-827.
- Das, B. M., Khing, K. H., Shin, E. C., Puri, V. K., and Yen, S. C.(1994) "Comparison of bearing capacity of strip foundation on geogrid-reinforced sand and clay", *Proc. 8th Inter. Conf. on Computer Methods and Advances in Geomechanics*, Morgantown, WA, USA, pp 1331-1336.
- DIANA(1996), User's Manual, Release 6.1, TNO Building Construction Research
- Fragaszy, R. J. and Lawton, E.(1984) "Bearing Capacity of Reinforced Sand Subgrades", *Journal of the Geotechnical Engineering*, ASCE, Vol. 110, pp.1501-1507.
- Giroud, J. P. and Noiray, L.(1981) "Geotextile-Reinforced Unpaved Road Design", *Journal of The Geotechnical Engineering*, ASCE, pp. 1233-1252.
- Huang, C., Tatsuoka, F., and Sato, Y.(1994) "Failure Mechanisms of Reinforced Sand Slopes Loaded with a Footing", *Soils and Foundations*, Vol. 24, No. 2, pp. 27-40

A Study on the Coir Reinforcement for Strengthening Soft Soil Subgrades

Dr. K. Rajagopal
Associate Professor
Department of Civil Engineering
Indian Institute of Technology Madras
Chennai, India 600 036

Mr. S. Ramakrishna
Assistant Engineer
National Highways Department
Secretariat of Public Works, MS Building
Bangalore, India 560001

ABSTRACT: Coir is a naturally occurring fibre available at relatively low cost in many tropical countries. A number of products can be manufactured from coir fibre for geotechnical applications. The strength and other properties of these products compare favourably with those made of synthetic materials. Through laboratory plate load model tests, this paper examines the suitability of coir geotextiles for construction of unpaved roads over soft soil subgrades. The soft subgrades of 1 m depth (CBR < 0.5) were prepared in a test tank of plan dimensions 1.5 m × 1.5 m. Base course layers of varying thickness values (with and without coir reinforcement) were constructed on top of this subgrade. The results from these tests have clearly illustrated the benefit of using coir reinforcement in such cases.

Key Words: geotextiles, coir reinforcement, subgrades, plate load tests, unpaved roads

1 INTRODUCTION

The coir is a naturally occurring fibre derived from the husk of coconut fruit. It is abundantly available at very low cost in many tropical countries. A number of products can be manufactured from coir fibre for geotechnical applications, such as geogrids, geotextiles, geomats etc. These products were found to last for as long as four to six years within the soil environment depending on the physical and chemical properties of the soil, Ramakrishna (1996). In many instances, the strength of subgrade soil increases in course of time as the soil undergoes consolidation induced by the traffic loads. For such applications the natural reinforcement products are ideally suitable, Rao and Balan (1994). The current paper describes the results from investigations carried out on coir geotextile reinforced soft soil subgrades.

2 MATERIALS USED IN TESTS

2.1 Clay Soil

The clay soil used in this investigation had plastic and liquid limits of 15% and 42% respectively. This soil can be classified as CI according to the Indian Standard Classification System, IS 1498-1978. The cohesive strength and friction angle of the clay soil are 21.2 kPa and 1.3° respectively.

2.2 Gravel Soil (murum)

The gravel soil (murum) contains 48% gravel size particles, 48% sand size particles and 4% silt and clay size particles. The specific gravity of this soil was found to be

2.75. This soil is classified as A-2-4 (0) as per AASHTO classification system and is rated as a good sub-base material. The cohesive strength and friction angle of this soil are 10 kPa and 44.9° respectively.

2.3 Coir Geotextile

The coir geotextiles used in this investigation are commercially available floor mats which are woven from coir fibres. The coir fibres are twisted into a rope form and these ropes are woven in weft and warp directions to form the mat. These mats have approximately the same strength in both the principal directions. The thickness of these mats is dependent on the diameter of the twisted ropes used in forming the mat. The geotextile (coir mat) used in this investigation had a thickness of 7.2 mm at a standard normal pressure of 2 kPa. The mass per unit area of this mat was 1,396 g/m² at a room temperature of 30°C.

The ultimate tensile capacity of this mat was found to be 37 kN/m at a strain of 43% from wide-width tensile tests performed according to ASTM D4595 standards. The secant modulus of this material at 10% strain is 110 kN/m. The seam strength, determined according to the suggested ASTM procedures, was found to be 24 kN/m. The seams were stitched using strong nylon thread with 25 mm overlap on both sides of the seam.

The cohesive strength and friction angle of clay-coir geotextile interface were found to be 22.6 kPa and 8.2° respectively. The same properties for gravel-coir interface are 40 kPa and 32.3° respectively. A comparison of these strength properties with those of individual materials shows that coir geotextile has excellent interface strength properties. This may be because of the rough nature of the coir and its natural affinity towards the water and clay because of surface charges.

3 LABORATORY PLATE LOAD TESTS

3.1 Test Facility

The plate load tests were performed within a test tank of plan dimensions 1.5 m × 1.5 m and 1.2 m deep. The loading was applied through a 100 kN capacity proving ring using a hydraulic jack. The test tank was centrally located below a reaction frame for applying plate loads. The plate was of 300 mm diameter (D) to simulate the Equivalent Single Wheel Load (ESWL).

3.2 Preparation of Test Bed

The soft clay soil bed was prepared by sedimentation technique under vacuum pressure to simulate the soft natural subgrade. The soil was initially mixed manually using crowbars at 160% water content. This slurry was kept under a low vacuum pressure of 19.6 kPa for three days to drain out the water and remove the entrapped air. Then it was subjected to a consolidation pressure of 98 kPa until the rate of deformation has decreased to less than 0.01 mm per minute. The method of test bed preparation was adapted from the work reported by Kuntiwattanukul et al. (1995). The entire consolidation process took approximately 8 to 10 days for each preparation. This procedure had created soft subgrades with a CBR value of approximately 0.4. The thickness of soft clay layer was maintained at around 900 mm for all the tests.

The gravel sub-base course was prepared directly on top of this clay layer. The gravel layer was compacted at optimum moisture content using a 10 kg drop hammer falling through a height of 500 mm.

The gravel layer was compacted to 80% maximum density in all the tests. The compacted sub-base course was allowed to mature for one day by covering it with a polythene sheet. The coir geotextile reinforcement was introduced during the compaction stage itself.

The above procedure of preparing the clay and gravel layers was repeated for all the tests performed in this present investigation so that the test conditions remain uniform for the entire range of tests.

3.3 Test Programme

The following series of plate load tests were carried out in this investigation with the following four configurations.

- Series 1: soft clay subgrade alone
- Series 2: gravel sub-base course over soft clay subgrade.
- Series 3: gravel sub-base course over soft clay subgrade and one layer of coir geotextile at clay-gravel interface.

- Series 4: gravel sub-base course over soft clay subgrade and two layers of coir geotextile, one at clay-gravel interface and the other at mid-depth of gravel layer.

In Series 2-4, six sub-base layer thickness (h) values of 100, 150, 200, 250, 300 and 350 mm were considered. In subsequent sections, the results from these tests are referred to by these series numbers.

3.4 Test Procedure

The general test procedure for plate load tests as described in *Indian standard IS 1888:1982 (Reaffirmed 1988)* was adopted for all the tests. The loading was applied through a 300 mm diameter plate. The applied load was measured using a pre-calibrated 100 kN capacity proving ring. The settlement of plate and the soil surface were measured using a total of six dial gauges. In the case of tests with reinforcement layers, the coir geotextile was placed at the required levels after wetting.

Each load increment was applied as either 10% of the estimated ultimate load or the load required to produce 1 mm settlement, whichever is lesser. Each load increment was kept constant until the rate of settlement reduces to less than 0.025 mm per minute. The load and the corresponding deformations were recorded after the settlements have stabilised under each load increment, which was typically 6 to 12 hours. The loading was continued until a total plate settlement of 150 mm has occurred which took approximately 6 days.

After each test, the gravel layer was carefully removed. After that, the top 400 mm thick clay soil in the tank bed was replaced with puddled clay having 40% water content. This test bed was once again pre-consolidated under 98 kPa surcharge pressure which took 2 to 3 days to stabilise. This re-formed clay bed had the same properties as the originally prepared clay bed as confirmed by results from in situ vane shear tests. On this, fresh gravel layer of required thickness was laid in the same manner as discussed earlier.

4 RESULTS AND DISCUSSIONS

The plate load test carried out on clay bed showed that it is an extremely soft subgrade with an ultimate bearing capacity of 20 kPa. Hence, it can be expected that the provision of gravel sub-base with or without coir reinforcement will significantly improve its load bearing capacity. Typical improvement in the performance obtained with the provision of gravel layer with and without reinforcement layers is illustrated in Figure 1.

Handwritten text at the bottom of the page, possibly a signature or reference number.

In general, the performance has improved with the increase in the thickness of gravel layer. The provision of a geotextile layer at the clay-gravel interface has further increased the load bearing capacity of subgrade. When an additional layer of geotextile was placed at the mid-height of the gravel layer, the ultimate capacity and stiffness has tremendously increased.

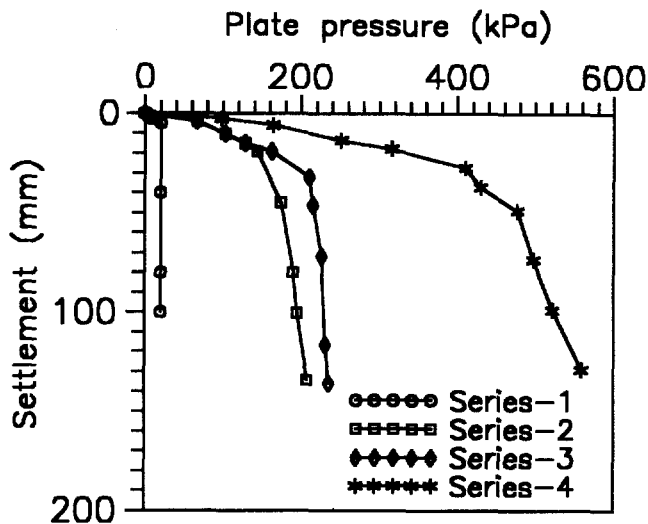


Figure 1. Performance with 150 mm thick gravel layer

The ultimate pressures developed from various tests are compared in Table 1 which clearly show the improvement in the performance with the provision of coir geotextile reinforcement.

From the results shown in Figure 1 and Table 1, it can be seen that the provision of a single layer reinforcement at the clay-gravel interface does not improve the load bearing capacity very much. The effect of single layer of geotextile is significant when gravel layer is thicker than 200 mm. When a thin layer of gravel is provided, there may not have been an adequate bond with the coir geotextile for the load transfer to take place. In the case of two layers of coir geotextile, the reinforcement layer at the mid-depth of gravel prevents its lateral spread and hence higher loads are mobilised in coir reinforcement which contributes to the increase in ultimate pressures. This can also be explained by the good bond between the coir and the gravel as shown from the interface shear strength properties (Section 2.3).

In the case of unreinforced and single layer reinforcement cases, the ultimate pressures have developed within a settlement of 15 to 40 mm whereas the two layer system had developed ultimate pressures at much higher settlements in the range of 100 mm (Figure 1). This result once again confirms the advantage of placing the additional reinforcement layer within the gravel layer.

In addition to the reinforcement action, the geotextile layer at clay-gravel interface functions as a separator and filtration and drainage medium as it has good compressibility characteristics. On the other hand, the layer within the subbase contributes mainly to the strength and stiffness of subgrade. It is evident from this experimental results that stiffness of the coherent mass is also an important parameter as reported by Douglas and Valsangkar (1992).

Table 1 Ultimate pressures (kPa) from plate load tests

Thickness of gravel layer (h)	unreinforced subbase layer	one layer of reinforcement	two layers of reinforcement
100 mm	100	120	400
150	200	220	550
200	240	250	750
250	300	360	900
300	370	440	1000
350	400	500	1150

From the plate load test data, the pressures developed for different thicknesses of gravel layers at various rut depths (settlement levels) were developed. This data is plotted in a non-dimensional form in Figure 2 for a rut depth of 75 mm. Similar charts were developed for other rut depths also. In these figures the thickness of gravel layer (h) is normalised with respect to the diameter of plate (D) and the plate pressure at any settlement is normalised with respect to the ultimate bearing capacity of soft clay layer (20 kPa) denoted as the Bearing Capacity Ratio (BCR). This term BCR indicates the relative improvement in the bearing capacity of subgrade with the provision of gravel layers with or without reinforcement. These charts can be used for designing the thickness of subbase layer over soft subgrades for a given BCR and the diameter of wheel base.

The above data is presented in a different form in Figure 3 for Indian Road Congress (IRC) standard wheel load of 22.25 kN. Similar curves have also been developed for other standard wheel loads. It is evident from this chart that the thickness of subbase can be substantially reduced with the use of coir geotextile reinforcement. At rut depths less than approximately 10 mm, the gravel layer can not mobilise enough shear strength which results in the requirement of very thick subbases, as is evident from the initial steep slope of curves.

5 ILLUSTRATIVE EXAMPLE

Design a subbase course to increase the load bearing capacity to 500 kPa of soft clay subgrade whose ultimate bearing pressure is 25 kPa. Consider the Equivalent

Single Wheel Loads (ESWL) of 28 kN and 48 kN having a tire pressure of 580 kPa. Design the subbase course for allowable rut depths of 25, 50 and 75 mm.

Design: The following step-by-step procedure illustrates the design process using the design charts developed in this investigation.

Step 1: Calculate the Bearing Capacity Ratio (BCR) at the ultimate bearing pressures.

$$BCR = \frac{\text{required ultimate bearing pressure on subbase course}}{\text{ultimate bearing capacity of subgrade}}$$

In the present example, $BCR = \frac{500}{25} = 20$

Step 2: Calculate the contact area of the wheel as the ratio of ESWL and the tire pressure. From these, the equivalent diameters of contact area are calculated for the two wheel loads as 250 mm and 325 mm respectively.

Step 3: Obtain the required h/D ratios for rut formations of 25, 50 and 75 mm from the design charts. The results are given in Table 2.

Table 2 Design of subbase thickness over soft subgrades

Design Case	Design base course thickness (mm)			Savings in thickness (mm)	
	gravel alone (A)	gravel + one layer reinf. (B)	gravel + two layer reinf. (C)	Savings for B over A	Savings for C over A
i) r = 25 mm P = 28 kN P = 48 kN	300 360	268 321	153 183	32 39	147 177
ii) r = 50 mm P = 28 kN P = 48 kN	288 345	255 310	108 129	33 35	180 216
iii) r = 75 mm P = 28 kN P = 48 kN	275 330	250 300	83 100	25 30	192 230

in which r is the rut depth and P is the wheel load. As can be seen, the single layer reinforcement does not result in much savings in subbase thickness. On the other hand, when an additional layer is provided within the subbase, significant savings are achieved.

6 CONCLUSIONS

The use of coir geotextiles for construction of subbase layer over soft subgrades is studied in this paper. Various engineering properties of coir geotextiles have been reported in this paper. These properties are comparable to those of intermediate to high density polypropylene based geotextiles. The plate load tests have clearly indicated the capability of coir geotextiles in improving the stiffness and load bearing capacity of soft subgrades. Hence, the coir geotextiles are suitable for cost-effective field applications.

REFERENCES

- Douglas, R. A. and Valsangakar, A.J. (1992) "Unpaved Geosynthetic-Built Resource Access Roads: Stiffness Rather than Rut Depth as the Key Design Criterion", *Journal of Geotextiles and Geomembranes*, 11, pp. 45-59.
- Kuntiwattanukul, P., Towhata, I, Oshishi, K. and Seko, I. (1995) "Temperature Effects on Undrained Shear Characteristics of Clay", *J. Soils and Foundations*, 35, pp. 147-162.
- Ramakrishna, S. (1996) *Investigation on Applications of Coir Reinforcement in Geotechnical Engineering*, Thesis submitted for award of Master of Science degree, Indian Institute of Technology Madras, Chennai.
- Rao, G.V. and Balan. K. (1994) "Coir Geotextiles-A Perspective", *Proc. of 2nd Int. Workshop on Geotextiles*, CBIP, New Delhi, India, pp. 119-126.

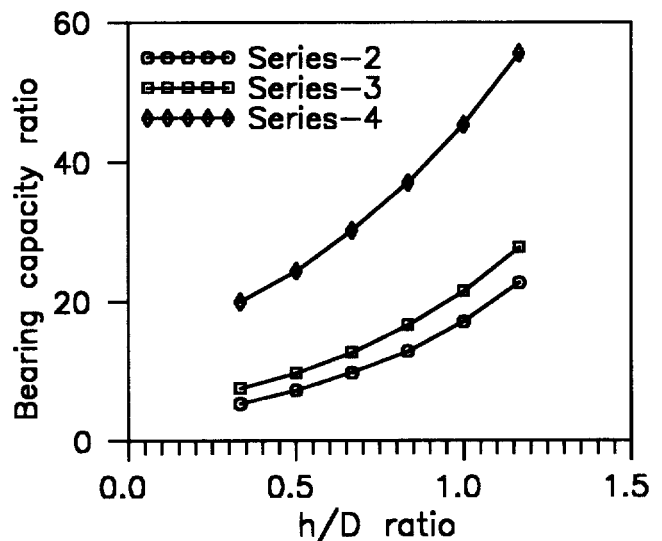


Figure 2 BCR for a rut depth of 75 mm

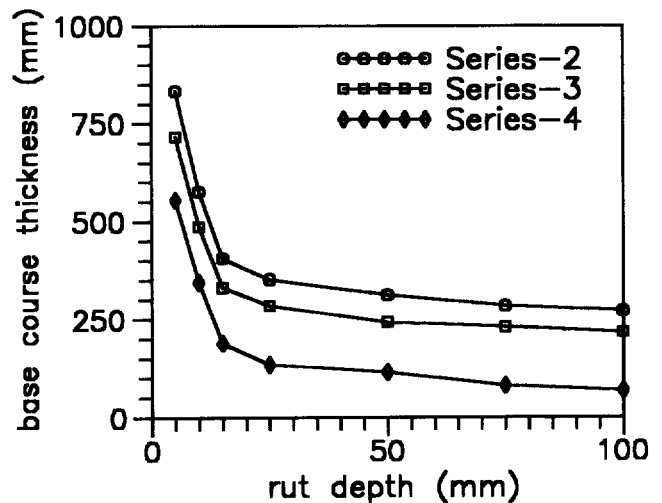


Figure 3. Design chart for wheel load of 22.25 kN

Treatment of container stockyard using Stress distribution ability of geonet

Hong Zhu

General Manager, YiChang Netlon Geosynthetics Ltd, Hubei Province, China

Dao hong Ruan

Engineer, YiChang Netlon Geosynthetics Ltd, Hubei Province, China

ABSTRACT: This paper presents the technical characteristics of geonet, the effect of stress distribution of geonet was initially observed in eastern China in the winter by a lively trial which can be defined as "NET - ICE TRIAL", The interacting mechanism between geonet and soft soil was analyzed based on lots of laboratory tests, three in - situ plate load tests were carried out on the site which is close to Yangtze River with extensive dredged sand areas of soft soil depth up to 8m. The results showed that bearing capacity of soft soil can be increased about one times undisturbed soil bearing capacity after a layer of geonet was paved horizontally, two layers of geonets lead to four times the bearing capacity of soft soil. The total amount of settlement was reduced by 22% , differential settlement was reduced by 35% . compared with the method of dynamic consolidation, the new technique has advantage of quick speed construction and low cost.

KEYWORDS: Container stockyard, Geonet, Stress distribution

1 INTRODUCTION OF APPLICATIONS

The use of geonets in China dates back to the early 1980's when the materials were first manufactured in China. The early projects were mainly in soil reinforcement, drainage and filtration. In the late 1980's the applications increased to projects involving embankment foundation consolidation, bridge approach details, reflection cracking of asphalt pavements, slope protection, leachate collection, leakage detection in landfills and coastal erosion protection. The application areas range from highways and railways to hydraulic engineering.

As the applications of geonets increased the construction departments required more information with regard to calculations and theory and this generated large interest in the academic world. A large number of Universities and Research Institutions became involved in studying the principles of geonets in different applications.

The Ministry of Communications considered the setting up of a project to research the mechanism of geonets and then the National Eight - Five Plan research project entitled "Application Research of Geonets in Bridge Abutment and Soft Soil Treatment of High Grade Road" was appraised by them on October 1995. The research into the mechanisms of geonets was promoted very deeply at this stage and this research became a history of the development of geonets in China.

A typical application of geonets is described as "Reinforce-

ment of Soft Soil Container Stockyard Project"

2 SELECTION OF GEONET MESH

Geonets have a great number of application areas which can be described as follows:

- 1) Soft soil reinforcement
- 2) Slope protection
- 3) Drainage

Laboratory tests have shown that the mesh shape is very important for stress distribution and that a hexagonal shaped aperture is the best as it is both stable and has low elongation. The order of stability of geonets according to tensile tests is: Hexagonal mesh > diamond mesh > square mesh. Although the tensile strengths are different in the longitudinal and transverse directions this is not important as long as the difference is not too large. If the difference is too large then the reinforcement of soft soil can not be achieved.

The selection of the appropriate mesh is also dependent on the grading of the fill material. In the project described later in this paper, the container stockyard, granular materials (dredged sand) were used and therefore a larger mesh size was selected.

The actual tensile strength of the geonet used, weight 660g/m², tested in the laboratory is greater than the specified value of 5.8 KN/m but it is still not high. Is it possible for this material; to reinforce the soft soil? The answer will be found af-

ter the field tests and laboratory trial are completed.

3 THE PHENOMENON OF NET - ICE STRESS DISTRIBUTION

On a container stockyard project where the soft soil foundation was overlain by a geonet reinforced pavement the mesh had been placed on a compacted surface when suddenly the weather became worse. It snowed and the mesh became frozen in ice.

The same load was then imposed on two different ice surfaces, one with the mesh and one without, and the stress distribution of the geonet was observed directly in the two ice surfaces.

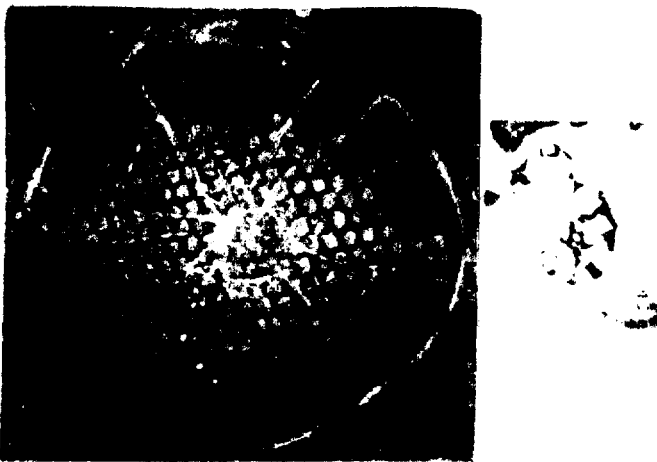


photo 1

photo 2

IN photo 1, with the geonet, the thin ice surface cracked but didn't break with white stress circles radiating from the central load. This showed how the load was distributed over a large area with the same geometry as the loaded area. In photo 2 the ice was broken and no distribution occurred.

This was the first time that the phenomenon of "live" stress distribution had been seen on a working site and this was defined as the NET - ICE TRIAL.

now given

R: radius of stress distribution

r: radius of central load

S_R : area of stress distribution

S_r : area of central load

An equation was obtained by measure on the construction site

$$\text{so } R = 5r$$

$$\frac{S_R}{S_r} = \frac{\pi R^2}{\pi r^2} = \frac{(5r)^2}{r^2} = 25 \quad (1)$$

This equation means that the area of stress is increased by 25 times as compared with the loaded area and shows how the bearing capacity of soft soil can be increased. The NETICE TRIAL shows the distribution mechanism in transmitting the load evenly onto a much larger bearing area.

25 times as compared with the loaded area and shows how the bearing capacity of soft soil can be increased. The NETICE TRIAL shows the distribution mechanism in transmitting the load evenly onto a much larger bearing area.

4 LABORATORY TEST

In order to illustrate quantitatively the geonet mechanism in improving bearing capacity of soft soil lot of tests have been completed in the past five years.

The trial chooses the mid liquid limit silty clay to do three trial cylinder shape samples.

Sample c is pure clay.

Sample d one layer of geonet is used

sample E three layers of geonets are used c (see fig 1)

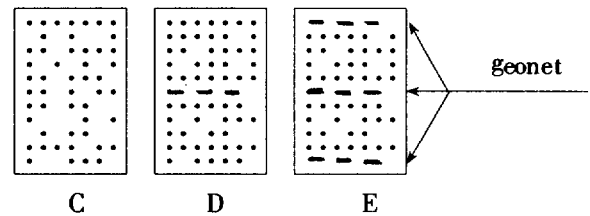


Figure 1.

The trial is unconfined compression strength test, test results are as follows (table 1)

Table 1:

Sample mode	C			D			E		
Sample no.	1	2	3	1	2	3	1	2	3
load(kg)	720	722	722	1520	1522	1523	5239	5240	5241
compression strength(kpa)	408.1	409	409	860.6	861.7	862.3	2966.2	2966.7	2967.3
(mean) strength	408.4			861.1			2966.8		

The bearing capacity is increased significantly by geonet, the value of sample D is 2.1 times the value of sample C and sample E is 7.3 times sample C, results show:

- 1) the bearing capacity of soil is improved with the increase of quantity of geonet.
- 2) the bearing capacity is increased by one time when a layer of geonet is paved.

NET - ICE TRIAL and laboratory test of using geonet to increase the bearing capacity of soil provide enough evidences for construction projects, but all the research data in theory need to be confirmed by actual applications.

5 CONTAINER STOCKYARD TREATMENT

5.1 soil properties

The container stockyard is situated in Jiang Shu province. The harbour area is about two hundred thousand square metres, forty thousand of which will be used as a container stockyard.

The soil profile can be divided into three layers which are described, from top to bottom, as follows:

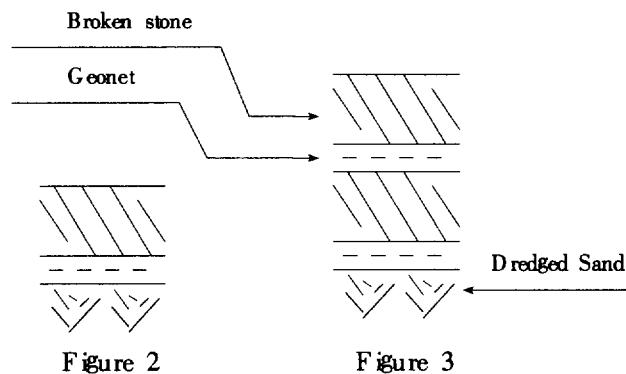
Layer 1: 4 – 5m of pump – dredged yellow fine sand mixed with cohesive soils, saturated and highly compressible. This soil is very susceptible to liquefaction. Particle sizes range from 0.074mm to 0.25mm.

Layer 2: 2 – 3m of mucky clay, brownish yellow and grey in colour, saturated and highly compressible.

Layer 3: Fine sand and intermittent silty clay layers. Moderate to low compressibility with a higher bearing capacity.

The dredged sand was placed two years ago and consolidation of the mucky clay had already occurred due to the overburden load. The groundwater level is not influenced significantly by the water levels of the Yangtze River because of the cofferdam. The only water ingress is due to natural rain water.

The conventional method of treating container stockyard is dynamic consolidation but this method has high cost and slow construction speed, moreover, easily effected by weather. The cross section of new method is shown as follows. (see fig 2):



5.2 construction procedure

- 1). Dredged sand is compacted by bulldozer twice times.
- 2). Geonet is unrolled and laid directly over the dredged sand, with an overlap of 150mm between individual sheets, and pinned with "U" shape steel pins at 1.0m spaces.
- 3). Backfill broken stone with 60% clay and 40% granular material.
- 4). Compact backfill, using vibratory roller operating without vi-

bration twice at the begining and with the vibration for another twice times at one hour interval. The maxium vibrating force is 30 tons.

- 5). Pave the second layer geonet repeat the same procedure.

During the compacting operation in one area in Fig 2 liquefaction occurred. This was assumed to be because the placing and compacting operation had taken place too quickly. It was then suggested that there should be a 1 hour interval between compaction passes and that the fill thickness should be no more than 0.8m – 1m.

5.3 bearing capacity test

Three in situ plate load tests were carried out, two of them were finishd on the structure of Fig 2 and Fig 3 respectively, another one is for ground which had been treated by dynamic consolidation with 10 tonnes hammer at 10 meters high. The size of plate is 1m by 1m. The results see table 2.

Table 2

load(kn)	meansured settlement (mm)		dynamic consolidation
	one layer of geonet	two layers of geonets	
50	7.86	4.42	8.30
100	9.53	5.84	12.23
150	14.38	6.06	16.35
200		6.64	
250	32.58	9.04	
300	39.83		
designed bearing capacity(Mpa)	80	150	150
tested value	125	250	155

Notes: The bearing capacity of undisturbed soil is 60 kpa

Table 2 shows the bearing capacity of two layers of geonets structure is twice times the one layer geonet structure. Interlock between geonet and granular material forms a high density and shear resistant layer which distribute vertical loads also indicate the horizontal elasticity of geonet and granular material is very good, thus the total settlement can be reduced. This concept is confirmed by modulus of resilience test.

Table 3.

Structure mode	one lager of geonet	two layers of geonets
modulus of resilience (Mpa)	711.25	991.89
mean valve	706.21	1061.48

Note: The modulus of resilience of undisturbed soil can't be measured.

5.4 Unit weight test (table 4)

Table 4.

Item	Natural soil	one layer of geonet	two layers of geonets	dynamic consolidations
water content %	17.71	13.13	12.56	
unit weight kn/m ³	16.2	18.3	18.6	18.3

The unit weight of geonet structure changes little. It is increased by 10% to 13%, compared with nature soil the compactness can reach 93.8% to 95.9%.

6 ANALYSIS

It can be seen from Table 2 that the bearing capacity of soft soil has increased significantly. when granular material is compacted over geonet, it partially is penetrates and projects through the apertures creating an interlocking action between granular material and geonet mesh. This interlock enables the mesh to resist horizontal shear from the fill and thereby mobilise the maximum bearing capacity of the soft soil. Mechanical interlock creates a flexurally stiff platform which distributes load evenly and minimizes different settlement, geonet prevents lateral movement of particles at the base of the fill layer, helps the fill to retain its full design strength by preventing contamination by soft soil thus controlling the amount of the more expensive fill.

7 CONCLUSIONS

The following conclusions are drawn:

1. Geonet can increase the bearing capacity of soft soil of dredged sand significantly, reduce the total amount of settlement and control the different settlement.
2. Geonet can distribute vertical load evenly, mechanical interlock between geonet and granular fill plays an important role in reinforcement of soft soil.
3. Tensile strength of geonet is not the main factor in improving soft soil.
4. The further rules of stress distribution of geonet need to be researched.

ACKNOWLEDGEMENTS.

The authors would like to thank Chang Sha University of Communications for its support. The authors also acknowledge Netlon Ltd Uk for its technical help.

REFERENCES

- Ali Fakher and Colin Jones (1996) "Land Reclamation Using Super Softclay Proceedings of the Second International Conference on Soft Soil Engineering, Nanjing, China" pp. 775 - 780
- D. H Ruan and Y. J. Pang (1996) "NETE Geonet Applications In Civil Engineering Foundation Treatment" pp. 37 - 40
- Y. Chen, R. H. Ying and Q. S. Zhang (1993) "Laboratory Research Using Netlon Geonets Consolidate Embankment"

A GEOTEXTILE-WRAPPED AGGREGATE HIGHWAY DRAIN EVALUATION

Gerald P. Raymond

Professor Emeritus, Queen's University, Kingston, Ontario, Canada, K7L 3N6.

Richard J. Bathurst

Professor, Department of Civil Engineering, Royal Military Collage of Canada, Kingston, Ontario, Canada.

Jerry Hajek

Senior Pavement Management Engineer, Ministry of Transportation of Ontario, Downsview, Ontario, Canada.

ABSTRACT: Presented are results from excavations at two edge drain locations adjacent to a freeway pavement (i.e., a limited access divided highway with at least two lanes in each direction). The pavement was built on a high fill of recompacted clayey gravel (GC). Typical Atterberg limits of the fines were $LL \approx 25$; $PL \approx 16$; $PI \approx 9$. Directly on the clayey gravel subgrade was a 152 mm cement treated base followed by 229 mm of structural portland cement concrete pavement. Adjacent to the pavement edge was a 3 metre-wide paved shoulder ending in a continuous curb and gutter fitted with catch basins about every 100 m. In 1982 a geotextile-wrapped aggregate pavement edge drainage system was retrofitted through the paved shoulder. The objective of the investigation was to evaluate the performance of the drainage system. From the observations and tests made on the recovered soil samples conclusions and recommendations are stated.

KEYWORDS: Drainage, Edge drain, Geotextile, Pavement, Performance evaluation.

INTRODUCTION

As part of an evaluation of Ontario's highway pavement drainage practice, excavations were made at two edge drain locations adjacent to a freeway pavement on June 4/1992. The pavement was built in 1970 on a high fill of recompacted clayey gravel (GC, $LL \approx 25$; $PL \approx 16$; $PI \approx 9$) and the drains were added in 1982. Figure 1 is a schematic of the pavement edge and edge drain cross section obtained from the construction drawings. Built directly on the clayey gravel subgrade was a 152 mm thick cement treated base followed by 229 mm thick portland cement concrete slab. Adjacent to the pavement edge was a 3 metre wide paved shoulder ending with a continuous curb and gutter and catch basins about every 100 m. The edge drainage system was retrofitted through the paved shoulder as a geotextile-wrapped coarse open graded aggregate (OGA) containing a 100 mm corrugated perforated polyethylene pipe placed 50 mm above the trench base (and base portion of the geotextile). The pipe centre line was to be located 762 mm from the edge of the concrete pavement. The wrapped stone was to be 325 mm thick and its top level with the cement treated base.

OBJECTIVE

The objective of the investigation was to evaluate the effectiveness of the pavement drainage system some ten years after installation. Also of interest was the condition of the geosynthetics (geotextile and plastic pipe) used in the

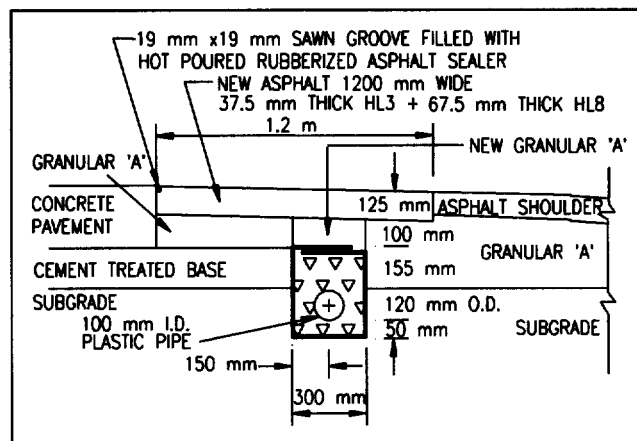


Figure 1. Cross section from construction drawings.

drainage system.

GEOSYNTHETICS

The geotextile was a needlepunched staple fibre product with the following properties: filtration opening size = 100 μm ; mass/unit area = 230 g/m^2 ; grab strength = 550 N at an elongation of 75% at failure. The pipe was a corrugated perforated polyethylene product with a nominal inside diameter of 100 mm, and a nominal outside diameter of 125 mm.

WEATHER AND STORM DRAINAGE CONDITIONS

The weather the day and night before the excavations had been intermittent rainfall. On the day of the excavations the weather was overcast with intermittent sunshine. The temperature at 7:00 am, which was the start of the excavating, was 14°C. The highway surface drainage was discharged via curb and gutters to catch basins. The catch basins were connected to a deep storm sewer.

POSITION OF EXCAVATIONS AND OUTLETS

Both excavations were made on the shoulder side of the shoulder/pavement edge area of six contiguous same direction traffic lanes near catch basins which were located at the curb. The longitudinal grade of the Highway was about 2%. The cross-sectional slope of the pavement was about 2.5% and the shoulder about 6%.

EXCAVATION TP1 (STATION 16+568)

The first excavation (TP1) was made adjacent to a transverse pavement joint at chainage 16+568. The shoulder/pavement surface showed considerable settlement of the shoulder. Figure 2 shows the surface profile measurements taken at both excavations. Figure 3 shows the typical cross section observed at the first excavation TP1. The cross section measurements were taken at both ends of this excavation some 300 mm apart. Little difference was noted between the measurements of the same items. The drainage pipe was not connected to the catch basin at this location. The structural concrete portion of the pavement is about 240 mm thick. The cement treated base was of poor quality either due to deterioration or initial mix. Its thickness was estimated to be 150 mm in accordance with the construction drawing. The geotextile-wrapped aggregate drain was installed adjacent to the edge of the cement treated base. Its centre line was located 780 mm from the edge of the pavement and its width was 420 mm. It extended from the surface elevation of the cement treated base layer into the clayey gravel subgrade for a total thickness of 300 mm. Thus the portion of geotextile forming the base of the drainage system was 540 mm below the pavement surface elevation. Above the upper (top) portion of the geotextile was a thickness of 140 mm of Granular 'A' covered by a thickness of 100 mm of asphalt concrete which formed the shoulder surface.

Figure 4 shows the pipe and the clean condition of the aggregate beside and above the pipe inside the geotextile. Figure 5 shows the fouled cemented condition of the aggregate on the bottom inside of the geotextile wrap. Migration of subgrade fines through the geotextile into the clear stone was visible. Seepage water has washed some of the fines through the clear stone and deposited them on the geotextile. The base portion was wet and once the geotextile was removed a very thin depth of ponded water was evident.

Overall, the top of the drainage pipe was approximately at the same level as the bottom of the cement treated base.

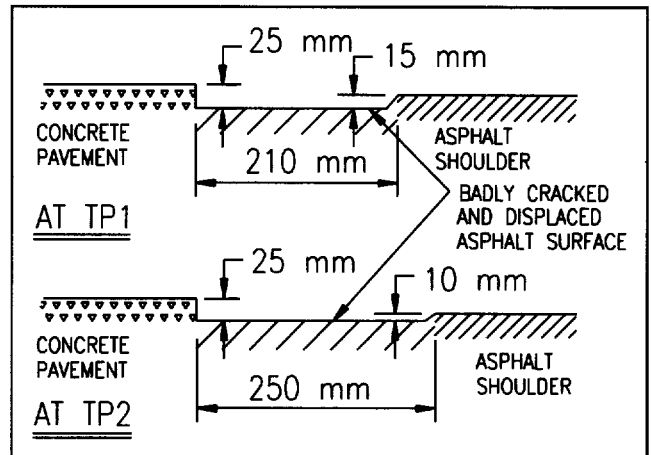


Figure 2. Surface profiles at pavement edge/shoulder.

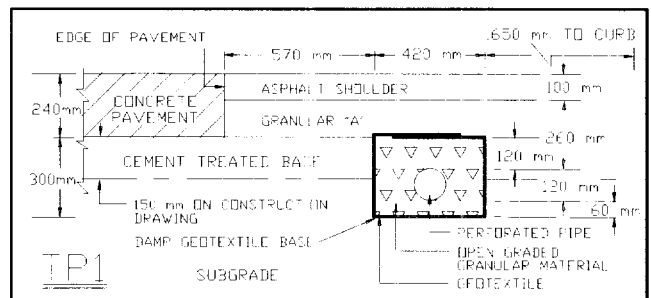


Figure 3. Cross section at Excavation TP1.



Figure 4. Open graded aggregate and pipe within geotextile.

Once the geotextile had been sampled the excavation was extended back to the pavement edge where a transverse joint existed. It was noted that pumping had eroded a portion of the pavement at this joint. Deposited in the eroded portion was black granular type material. This black material was probably fines from the asphalt pavement shoulder. Sampling

the black soil proved difficult and no representative sample was obtained.

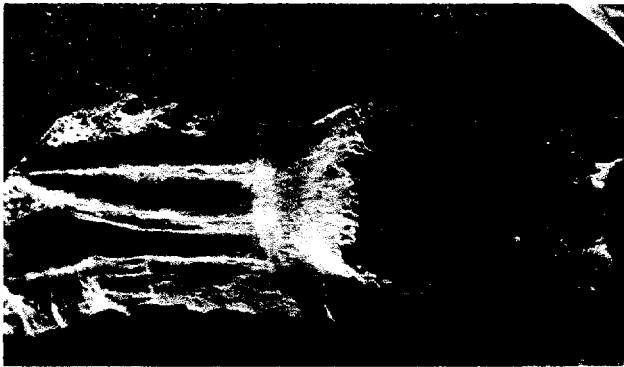


Figure 5. Geotextile condition: side and base.

EXCAVATION TP2 (CHAINAGE 16+532)

The second excavation (TP2) was made near a catch basin and resulted (prior to enlargement) in much the same findings as the first excavation (TP1). Figure 2 shows the settlement between the pavement edge and the geotextile drain. Figure 6 shows the cross section measurements observed.

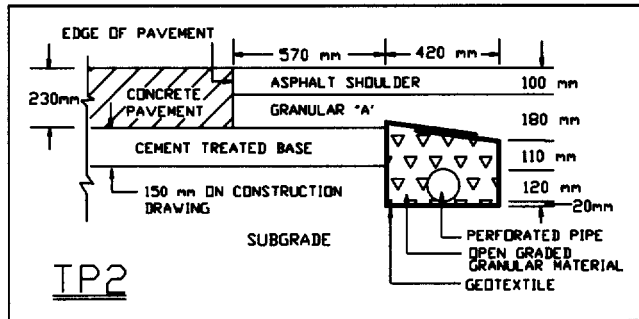


Figure 6. Cross section at Excavation TP2.

The curb catch basin was offset about 1.5 metres from the aggregate drain. The excavation was then enlarged to determine if the edge drain was connected, via an outlet pipe, to the catch basin. Indeed it was, and at the outlet chainage, the drainage pipe was turned down slightly. Figure 7 is a plan of the T-junction connecting a non-perforated outlet pipe, running at a right angle to the pavement, to the catch basin. The T-junction was wrapped in geotextile that was bedded on about 150 mm of Granular 'A'. Figure 8 shows a profile view along the perforated pipe highlighting the turned down condition at the T-junction. The slight turndown at the junction of the two pipes (perforated and non-perforated) picked up any water draining along the 50 mm of aggregate located below the perforated pipe in the geotextile-wrapped aggregate drain. Figure 9 shows a profile view along the

outlet non-perforated pipe connection. The connection pipe was cemented into the catch basin wall. Water collecting in the Granular 'A' below the T-junction and below the outlet pipe was trapped by the surrounding clayey gravel since there was no allowance for drainage at the catch basin connection.

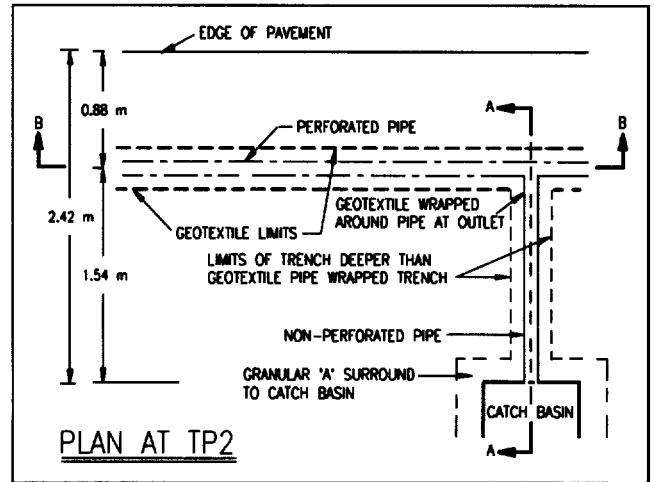


Figure 7. Plan view of outlet connection.

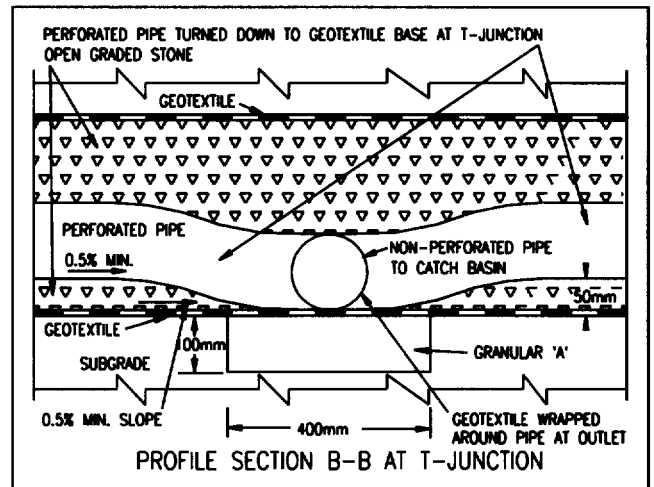


Figure 8. Section B-B: Profile of pipe at T-junction.

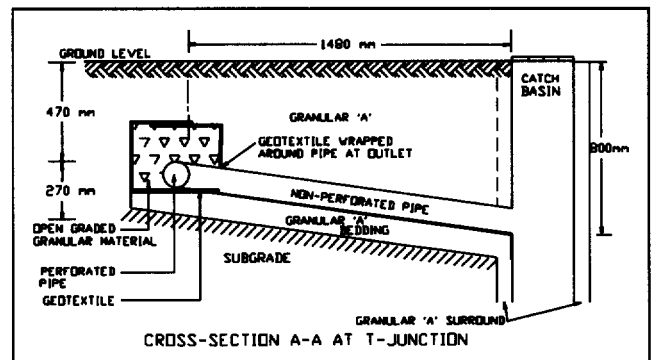


Figure 9. Section A-A: Connection to catch basin.

LABORATORY RESULTS

All soil samples recovered from the excavations were subject to grain size analysis. Figure 10 shows the grain size analysis curves from Excavation TP2. The samples from within the geotextile were open graded aggregate with only small amounts of material passing the 75 μm sieve. The material trapped in the geotextile graded from 1 mm down to 50% passing the 75 μm sieve. The Granular 'A' materials graded in accordance with the MTO specification except at the 75 μm limit which was slightly greater than permissible (i.e. 10% to 12 % compared with MTO limits of 2%-8% for Granular 'A'). This quantity of fine sized material within a broad grading granular material indicated the probability of a relatively low permeability of Granular 'A'. Confirmation was obtained by permeability tests on the recovered Granular 'A' samples. The average coefficient of permeability of the as-recovered samples was 2.8×10^{-5} cm/s and after washing on a 75 μm sieve 2.6×10^{-2} cm/s; an increase of nearly 1000 times.

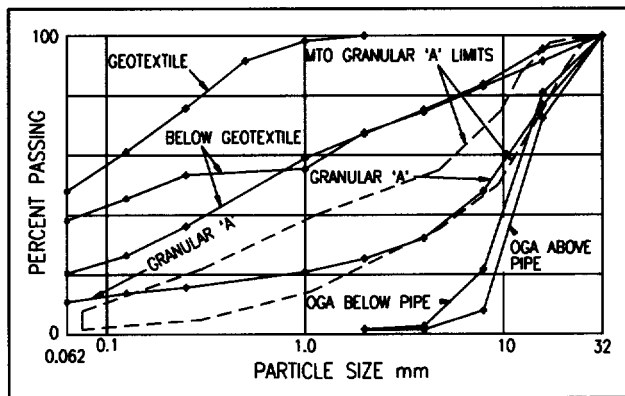


Figure 10. Grading of Excavation TP2 soil samples.

The geotextiles examined in the field and on return to the laboratory showed no sign of obvious damage. There were no holes or severely worn areas that might cause concern that the properties were less than those originally specified in 1982. A good indication of the remaining overall strength was the considerable force needed to remove a small area of the geotextile in the field. This considerable force inflicted no observable damage.

DISCUSSION

The results of the investigation show that placing a geotextile-wrapped trench drain some distance away from, and separated from, the pavement edge by relatively impermeable Granular 'A' prevented or significantly reduced internal drainage of the area below the structural concrete. The results of this poor drainage were clearly seen at the transverse joint uncovered at the first excavation. At this

joint there was evidence of (a) pumping, (b) erosion of the concrete at the joint base, (c) heave/settlement on the shoulder at the pavement edge (Figure 2) and (d) deterioration of the quality of the cement treated base. Retrofit geotextile-wrapped trench drains should be located adjacent to the pavement edge with the geotextiles against the supporting pavement layers. To prevent subgrade pumping, a filter capping granular material continuously graded down to the 75 μm sieve should be used with any cement treated base.

There was no evidence that the geotextile or the pipe had sustained any damage that would cause concern regarding its ability to continue to function as it has over its ten years in-situ. The sides and top of the geotextile were relatively clean. The main fouling was at and above the base, which is the whole purpose of the clear stone bedding below the pipe. Provision should be made to allow drainage of any granular bedding material placed below any outlet pipes connected to catch basins.

CONCLUSIONS AND RECOMMENDATIONS

Excavations were made at two granular edge drain locations on the shoulder of a major Ontario freeway. From the observations and tests made on the recovered soil samples, the following conclusions and recommendations are made.

Retrofit geotextile-wrapped trench drains should be located next to the pavement edge.

Geotextiles, if used, should be placed tight against the supporting layers of the concrete pavement.

The need for a 50 mm bedding of open graded aggregate at the base of trench drains was clearly demonstrated at both excavations. The bedding material trapped sediment that otherwise would have accumulated in the drainage pipe reducing the pipe's ability to function effectively.

Evidence of migration of subgrade fines into the open graded aggregate above the cement treated base was observed. Drainage alone does not stop subgrade pumping.

No evidence was noted of loss of ability to function of either the geotextile or pipe.

Evidence of accumulation of fines in the trench drain demonstrated that a geotextile is required.

The T-junction detail illustrated in Figure 8 is recommended.

ACKNOWLEDGEMENT

Gratefully acknowledged is the considerable cooperation and help provided by Ministry of Transportation of Ontario (MTO) personnel who provided the excavation equipment and manpower. Particular thanks are extended to Ms. P. Marks and Mr. S. Senior of the MTO for their significant contributions to this paper. The views expressed in this paper are those of the authors and not necessarily the MTO.